Macromolecules

Perspective

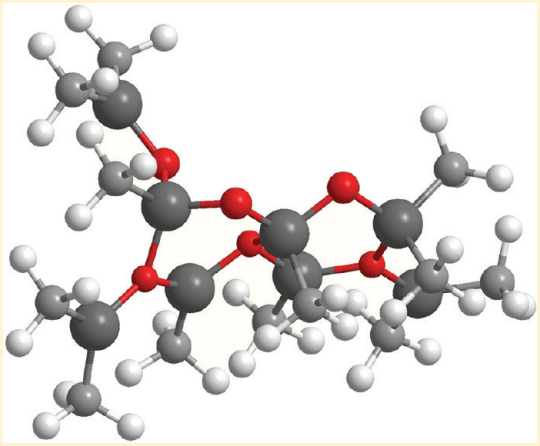
pubs.acs.org/Macromolecules

Discovery of Methylaluminoxane as Cocatalyst for Olefin Polymerization

Walter Kaminsky

Institute for Technical, Macromolecular Chemistry, University of Hamburg, Bundesstr. 45, D-20146 Hamburg, Germany

ABSTRACT: The discovery of methylaluminoxane (MAO) was the start for investigations and innovations of new classes of highly active olefin polymerization catalysts. Different transition metal complexes together with MAO as cocatalyst allow the synthesis of polymers with a highly defined microstructure, tacticity, and stereoregularity as well as new cycloolefin, long chain branched, or blocky copolymers with excellent properties. These new polyolefins could not be obtaind with such a purity before by Ziegler–Natta catalysts. The single site catalyst character of metallocene and other transition metal complexes activated by MAO leads to a better understanding of the mechanism of the olefin polymerization.



INTRODUCTION

There are few inventions that have pushed the polyolefin industry in such a way that they produce in 2010 with about 145 million tons more than 50% of all polymers. The first invention was the high-pressure polymerization by ICI,[1] followed by the catalytic olefin polymerization by Ziegler,[2] Natta,[3] and Phillips.[4] The supporting of Ziegler–Natta catalysts on magnesium dichloride and deactivation of the atactic working polymerization active sites by internal and external donors were the start for a fast growing polypropylene production.[5] The latest invention, carried out at the Chemical Department of the University of Hamburg, is the use of methylaluminoxane (MAO) containing catalysts for the tailored synthesis of polyolefins.[6,7] Catalysts formed by MAO and metallocenes or other transition metal containing complexes have widened up the possibility to design the microstructure of polyolefins in a way which was not possible in years before. These "single site" catalysts show only one kind of active sites and are used today mainly for the rapidly increasing production of linear low density polyethylene (LLDPE) and some special copolymers.[8]

Before the invention of methylaluminoxane as cocatalyst, homogeneous Ziegler–Natta catalysts have been preferentially studied in order to understand the elementary steps of the polymerization, which is simpler in soluble systems than in heterogeneous systems.

Metallocenes, in combination with the conventional aluminum alkyl cocatalysts used in Ziegler systems, are indeed capable of polymerizing ethylene, but at a very low activity. Only with the discovery and application of methylaluminoxane (MAO) was it possible to enhance the activity, surprisingly, by a factor of 10 000[9] or more. Therefore, MAO plays a crucial part in the olefin polymerization by metallocenes and other complexes and has motivated research groups to thousands of publications in the past 20 years.[10]

Impressive is the industrial use of MAO-based catalysts, too. In 2010, over 5 million tons of polyolefins, especially different kinds of polyethylene, are produced in commercial processes using MAO as cocatalyst. Nearly every second new plant for EP or EPDM elastomers based on MAO activated catalysts. For a use in new or excisting plants (drop-in technology) MAO is heterogenized by absorption on silica, aluminia, or other supports.[11] By this procedure, gas phase polymerization is possible, too. Therefore, the amount of industrial used MAO increased rapidly, mainly produced by Albermale, Akzo, Chemtura, and Tosoh.

Kinetic studies and the application of various methods have helped to define the nature of the active centers, to explain the aging effects of Ziegler catalysts, to establish the mechanism of interaction with olefins, and to obtain quantitative evidence of some elementary steps.[12−15] It is necessary to differentiate between the soluble catalyst system itself and the polymerization system. The homogeneous systems are soluble, but they become heterogeneous when polyethylene is formed up to polymerization temperatures of 50 °C. By higher temperatures (Dow solution process) they stay homogeneous.

Before 1980, the most investigated homogeneous catalyst systems are based on bis(cyclopentadienyl)titanium(IV), bis(cyclopentadienyl)zirconium(IV), tetrabenzyltitanium, vanadium chloride, with trialkylaluminum, or alkylaluminum halides.

Received: November 7, 2011
Revised: February 13, 2012
Published: March 8, 2012

ACS Publications © 2012 American Chemical Society

dx.doi.org/10.1021/ma202453u | *Macromolecules* 2012, 45, 3289–3297

Breslow[16] discovered that bis(cyclopentadienyl)titanium(IV) compounds, which are readily soluble in aromatic hydrocarbons, could be used instead of titanium tetrachloride as the transition metal compound together with aluminum alkyls for ethylene polymerization. Subsequent research on this and other systems with various alkyl groups has been conducted by Natta,[17] Patat and Sinn,[18] Shilov,[19] Henrici-Olivé and Olivé,[20] Reichert and Schoetter,[21] and Fink et al.[22] With respect to the kinetics of polymerization and side reactions, this soluble system is probably the one that is best understood. It is found that the polymerization takes place primarily into a titanium carbon bond were the titanium exists as titanium(IV) alkyl cation[23] formed by alkylation and dissociation (eqs 1 and 2).

$$(C_5H_5)_2TiCl_2 + AlR_2Cl \rightarrow (C_5H_5)_2TiRCl + AlRCl_2 \quad (1)$$

$$(C_5H_5)_2TiRCl + AlRCl_2 \rightarrow [(C_5H_5)_2TiR]^+ + [AlRCl_3]^- \quad (2)$$

The polymerization of olefins, promoted by homogeneous Ziegler catalysts based on biscyclopentadienyltitanium(IV) or analogous compounds and aluminum alkyls, is accompanied by a series of other reactions such as alkylation, hydrogen transfer, and reduction that greatly complicate the kinetic interpretation of the polymerization.

In the case of β-hydrogen transfer by ethyl alkylated titanium complexes, Ti−CH_2−CH_2−Ti structure units are formed (eq 3), which are unstable and decompose within some seconds into titanium(III) species and ethylene (eq 4).[12]

$$2Cp_2Ti(Cl)CH_2{-}CH_3 \rightarrow Cp_2Ti(Cl){-}CH_2{-}CH_2{-}Ti(Cl)Cp_2 + CH_3{-}CH_3 \quad (3)$$

$$Cp_2Ti(Cl){-}CH_2{-}CH_2{-}Ti(Cl)Cp_2 \rightarrow 2Cp_2TiCl + CH_2{=}CH_2 \quad (4)$$

The bridged titanium complexes as well as the reduced titanium(III) species are polymerization inactive. Analogous zirconium complexes were used to isolate intermediates and to study alkyl exchange and β-hydrogen transfer since zirconium is less easily reduced compared to titanium.[24]

METHYLALUMINOXANE

The research group of Hansjörg Sinn at the University of Hamburg investigate these side reactions, especially the α-hydrogen transfer reaction of biscyclopentadienyltitanium dimethyl and trimethylaluminum and the formation of new CH_2-bridged titanium aluminum complexes (eq 5).[25] This

$$Cp_2Ti(CH_3)_2 + Al(CH_3)_3 \rightarrow Cp_2Ti(CH_3)\,CH_3\text{-}Al(CH_3)_2 \rightarrow Cp_2Ti(CH_3)\text{-}CH_2\text{-}Al(CH_3)_2 + CH_4 \quad (5)$$

reaction is very slow, and no reduction of titanium(IV) takes place so that NMR measurements are possible of the complexation with ethylene by NMR analysis at low temperature. To start the reaction, a toluene solution of the titanium complex and a solution of trimethylaluminum were mixed together at −78 °C by the Schlenk technique and filled into a NMR tube (Figure 1). This NMR tube was then sealed with a

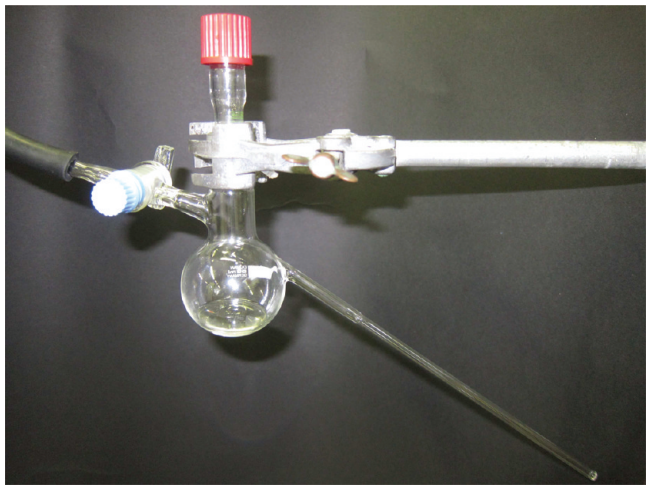


Figure 1. Used glass equipment to fill and seal a NMR tube with a solution of metallocene, trimethylaluminum, and ethylene.

torch by a glass blower, introduced into the NMR equipment at −40 °C, and slowly warmed to room temperature. This procedure was very time-consuming, and the PhD student involved with these measurements in 1975 simplified the preparation method by filling the reaction mixture directly into a simple NMR tube and putting a plastic lid on.[26] Comparing the C NMR spectra obtained with the simple method with those obtained with the sealed NMR tubes, he discovered after 5 h reaction time a small peak by 8.59 ppm in the area of CH_2 bonds in the NMR spectrum which he had never seen before (Figure 2). Fortunately, the student did not ignore these results using the safe procedure again but discussed the effect with me. To recognize such effects and details, a deep knowledge of the investigated subject is necessary. We decided to scale up the experiment and repeat it in a 1 L glass autoclave which was cooled down to −40 °C and subsequently warmed to −14 °C. After pressing on ethylene, the pressure decreased very slowly. The autoclave was opened to take a sample of the solution for NMR control. After the addition of new ethylene to a pressure of 8 bar, the pressure decreased much faster than in the beginning. This procedure was repeated several times, and the reactivity increased each time; for details see ref 27. What was the reason for this increasing polymerization rate of ethylene by a system known before to be polymerization inactive? We discussed the results with our supervisor Hansjörg Sinn and came to the conclusion that traces of chloride, oxygen, or water, introduced by opening the autoclave, could be responsible for the activity.

In the following experiments, using titanium complexes ($Cp_2Ti(CH_3)_2$) containing traces of chloride or oxygen, no polymerization of ethylene was observed. Finally, we added small amounts of water, as a last possibility since water has been discussed to be a strong poison for olefin polymerization catalysts. Surprisingly, a high polymerization rate was observed depending on the amount of water.[28] The polymerization rate reached a maximum when the molar ratio of water to trimethylaluminum was 1:1. Some years before Reichert[29] had found an increase of the activity of about a factor 2 by the addition of small amounts of water to the halogen-rich homogeneous system $Cp_2TiEtCl/EtAlCl_2$, and Breslow[30] obtained similar results by the system Cp_2TiCl_2/Me_2AlCl. Obviously, there are great differences in the halogen-free and halogen-containing catalysts.

dx.doi.org/10.1021/ma202453u | Macromolecules 2012, 45, 3289−3297

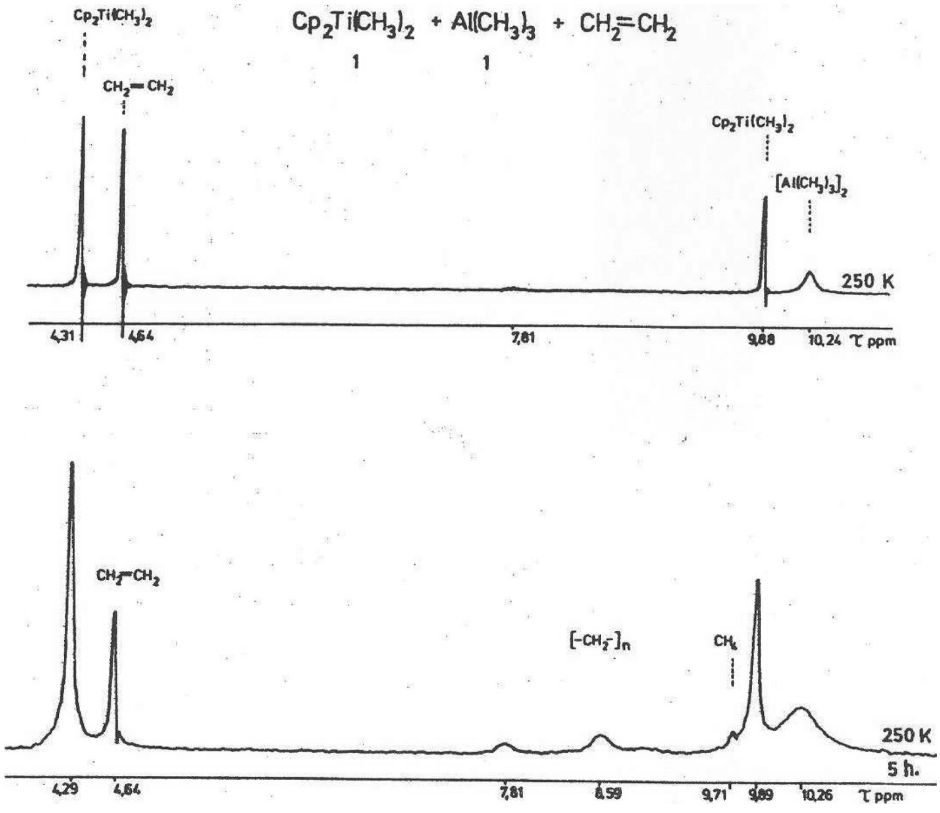


Figure 2. Original NMR spectrum of the first measurements of $Cp_2Ti(CH_3)_2$, $Al(CH_3)_3$, and ethylene in toluene.

It was clear that trimethyaluminum reacts rapidly with water in a toluene solution. The next step was therefore to isolate the product formed in the 1:1 mixture of water and trimethylaluminum. The general reaction is shown by eq 6. At higher water

$$n H_2O + (n+1)Al(CH_3)_3 \rightarrow (H_3C)_2Al-[O-Al]_n-CH_3 + 2nCH_4 \quad (6)$$

levels, explosions could happen; therefore, inorganic salts were used containing bonded water, such as $CuSO_4 \cdot 5H_2O$ or $Al_2(SO_4)_3 \cdot 14H_2O$ in toluene suspension.[31] After 20 h, the reaction mixture was filtrated and the solvent evaporated. The white powder obtained was dried and analyzed. The compound was named methylaluminoxane (MAO).

MAO was investigated by elementary analysis, cryoscopy, NMR measurements, and decomposition with HCl. It was found that MAO is a mixture of different oligomers, including some ring structures (Figure 3). Even today the exact structure is not known because there are equilibria between the oligomers and complexation of the oligomers with each other and with unreacted TMA. MAO is a compound in which aluminum and oxygen atoms are arranged alternately and free valences are saturated by methyl substituents. According to investigations by Sinn[32] and Barron,[33] it consists mainly of units of the basic structure $[Al_4O_3Me_6]$, which contains four aluminum, three oxygen atoms, and six methyl groups. As the aluminum atoms in the unit structures are coordinatively unsaturated, the units join together forming clusters and cages. These have molecular weights from 1200 to 1600 measured by cryoscopy in benzene and are soluble in hydrocarbons especially in aromatic solvents.

The use of this separately produced MAO together with $Cp_2Ti(CH_3)_2$ further increased the activity by a factor of 100

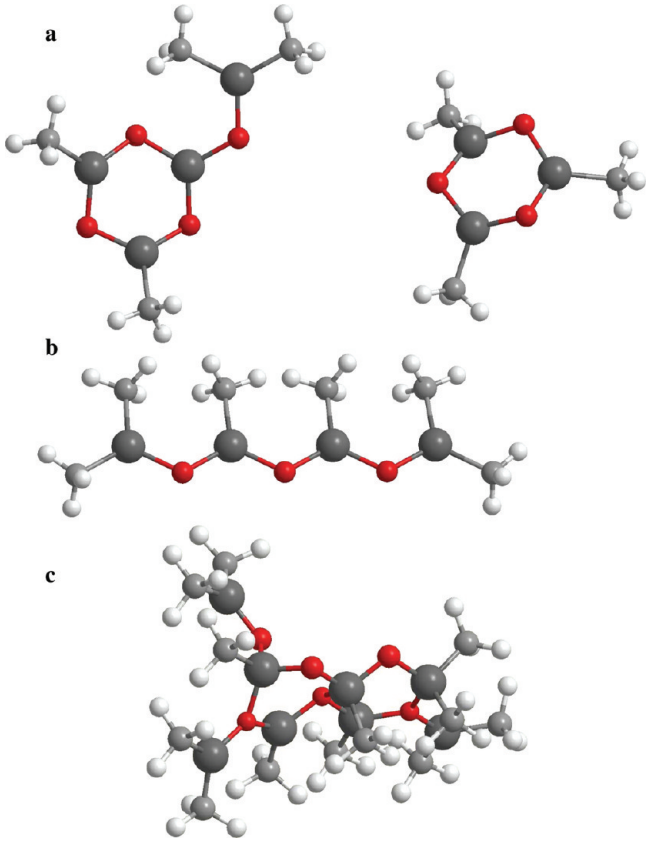


Figure 3. Unit cyclic (a), linear (b), and associate (c) structures of methylaluminoxane (MAO); red balls: oxygen; gray balls: aluminum and methyl groups.

dx.doi.org/10.1021/ma202453u | *Macromolecules* 2012, 45, 3289–3297

Table 1. Polymerization Activities of Metallocene/Aluminoxane Catalysts in 330 mL of Toluene by 8 bar Ethylene Pressure[a]

metallocene	aluminoxane	temp (°C)	activity (g PE/(g Zr h bar))	mol wt (g/mol)
$Cp_2Ti(CH_3)Cl$	MAO	20	50000	350000
Cp_2TiCl_2	MAO	20	90000	n.d.
$Cp_2Zr(CH_3)_2$	MAO	70	700000	190000
Cp_2ZrCl_2	MAO	20	620000	730000
Cp_2ZrCl_2	MAO	70	1000000	190000
Cp_2ZrCl_2	MAO	90	3100000	150000
$Cp_2Hf(CH_3)_2$	MAO	70	60000	300000
Cp_2ZrCl_2	ethylaluminoxane	60	23000	n.d.
$Cp_2Zr(CH_3)_2$	tertaisobutyldialuminoxane	70	175000	400000

[a]Polymerization conditions: 330 mL of toluene, ethylene, pressure: 8 bar, metallocene amount: 10^{-6}–10^{-8} mol, aluminoxane amount: 5×10^{-3} mol Al units.

compared to the system of $Cp_2Ti(CH_3)_2/Al(CH_3)_3/H_2O$.[31] For the first time it was possible to polymerize propylene with a soluble biscyclopentadienyltitanium/MAO catalyst to obtain atactic polypropylene and to generate ethylene–propylene copolymers. Pino and Mülhaupt,[34] who analyzed a sample, found that the polypropylene synthesized with this catalyst was the purest atactic PP they had ever seen.

In 1978, Hansjörg Sinn became Minister of Science and Research of the City State of Hamburg, and 1 year later I received the position of a full professor at the University of Hamburg. At this time my co-workers and I used bis-(cyclopentadienyl)zirconium dimethyl and MAO for ethylene and propylene polymerization and obtained extremely high activities, higher than for the titanium system. Up to this date, biscyclopentadienylzirconium complexes, activated by aluminum alkyls, were described to be totally inactive for olefin polymerization. A patent application was written covering these exciting results.[6] It was discovered, too, that the Cp_2ZrCl_2, which can easier be synthesized and is more stable than $Cp_2Zr(CH_3)_2$, is an active catalyst precursor in combination with MAO.

In 1980 and 1981, I reported for the first time on zirconocene/MAO catalysts on the IUPAC Polymer Congress in Firenze[35] and the Macromolecular Meeting in Midland.[36] In those years we synthesized the analogue ethylaluminoxane and a tetraisobutyldialuminoxane. The results for ethylene polymerization are compared for different metallocenes and aluminoxanes in Table 1.[37]

It can be seen that titanocenes are less active than zirconocene catalysts. They cannot be used at higher temperatures and for longer polymerization times because the titanium(IV) is then reduced into the inactive titanium(III). Hafnocenes are about 10 times less active than titanocenes but produce polyethylene with a higher molecular weight. Under the condition that every zirconocene complex formed a polymerization active site, shown by Peter Tait[30] and Jimmy Chien,[31] the most active zirconocene produces about 15 000 polymer chains per hour at a polymerization temperature of 90 °C. The insertion time of one ethylene unit is only 3×10^{-5} s. The use of ethylaluminoxane instead of MAO decreases the activity by a factor of 40. Tetraisobutylaluminoxane is more active, but still 6 times less than MAO. Compared with classical Ziegler catalyst, zirconocene catalysts are 10–100 times more active and show an activity which is maintained at nearly the same level for several days.

For the first time, we could show that a soluble catalyst and highly active Cp_2ZrCl_2/MAO catalyst is able to produce polyethylene with molecular weights up to 1 million g/mol and with a narrow molecular weight distribution of ~2. Only traces (0.1%) of low molecular weight oligomers are formed compared to Ziegler catalysts (2–5%).[38]

In the following years, we continued polymerizations of ethylene using methylaluminoxane in combination with different transition metal complexes such as $VOCl_3$ and the acethylacetonate (acac) complexes $V(acac)_3$ $VO(acac)_2$, $Cr(acac)_3$, $Co(acac)_2$, $Ni(acac)_2$, and $Fe(acac)_3$.[39]

Surprisingly all these complexes were able to polymerize ethylene. Vanadium-based catalysts were most active, but less than zirconocenes. Copolymers were carried out with ethylene, 1-butene, 1-hexene, 1,7-octadiene, and butadiene.[40]

There was a question which became stronger by every polymerization success with our homogeneous metallocene/MAO catalyst. Is it possible to synthesize pure isotactic polypropylene by a homogeneous catalyst? There was no positive example in the past.

The first idea was to use (cyclopentadienyl)-(pentamethylcyclopentadienyl)zirconium (methyl) chloride ($CpCp^*Zr(CH_3)Cl$), a zirconocene with four different substituents, which could have a chiral structure, which was necessary by a hypothesis of Giulio Natta, that the formation of isotactic polypropylene depends on chiral titanium centers on the surface of $TiCl_3$ crystals. We were disappointed that this complex together with MAO produced only atactic polypropylene. Discussion with colleagues from the inorganic institute indicated that the movement of the four ligands around the metal center is much faster than insertion of an olefin. Such a complex does not have one stable enantiomer and therefore yields atactic polypropylene.

At that time Hans-Herbert Brintzinger (University of Konstanz, Germany) had just published a paper of a chiral ansa ethylidenebis(4,5,6,7-tetrahydroindenyl)titanium dichloride.[41] I contacted him and asked for some milligrams of such an ansa metallocene, if possible with zirconium as metal, since Cp_2ZrCl_2 had been much more active than Cp_2TiCl_2. In spring 1984, my PhD student Klaus Kuelper traveled from Hamburg to Konstanz to pick up the zirconocene. Back in Hamburg, we carried out the first polymerization runs using this complex together with MAO. After some minutes isotactic polypropylene was formed. This could clearly be seen by the formation of a suspension of insoluble polymer in the autoclave while all our previous experiments had given a clear solution of atactic polypropylene.

The ansa zirconocene $[En(THind)_2]ZrCl_2$ exists in three structures (Figure 4). The rotation of the indenyl rings is hindered by the CH_2–CH_2–bridge. Beside the racemic mixture of the R and the S form, a meso form is possible. In the case of

dx.doi.org/10.1021/ma202453u | Macromolecules 2012, 45, 3289–3297

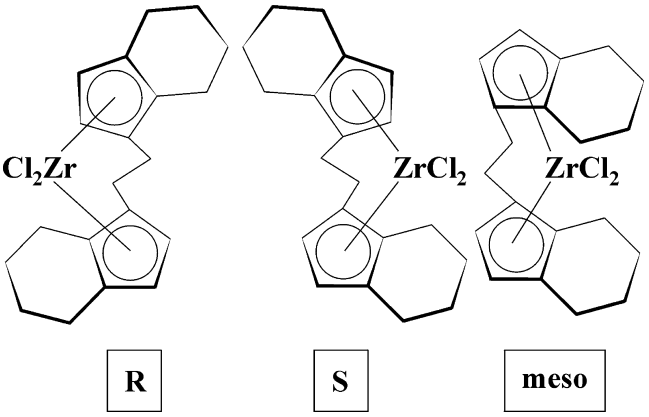


Figure 4. Structures of the R, S, and meso form of $[C_2H_4(THInd)_2]$-$ZrCl_2$.

$[En(THind)_2]ZrCl_2$ only traces of the meso form are obtained, which can be eliminated by recrystallization of the complexes.

The meso form has no asymmetric symmetry and produces therefore atactic polypropylene similar to the unbridged Cp_2ZrCl_2/MAO catalyst. We investigated the influence of temperature and catalyst concentration on molecular weight and isotacticity and wrote together with the research group of Hans Brintzinger a publication.[42] At the same time John Ewen,[43] working for Exxon, had carried out similar experiments with the ansa-$[En(Ind)_2TiCl_2]$/MAO catalyst and had obtained a mixture of isotactic and atactic polypropylene due to the fact that the complex had not been clean and had contained a high amount of meso-complex. These results and the separation of the racemic mixture of the ansa-zirconocene into the optically pure enantiomers confirm the hypothesis that the formation of isotactic polypropylene needs an asymmetric (chiral) active site. Optically active tri- and tetramers of propylene were obtained using the S-enantiomer (Figure 3) together with MAO by high catalyst concentration.[44]

The discovery of the production of isotactic polypropylene by a highly active homogeneous metallocene/MAO catalyst increased the interest of research groups working worldwide in the field of olefin polymerization. In the following years, the number of patents increased from 1 in 1980 up to more than 10 000 until 2010. Similarly high is the amount of publications. An overview can be found in refs 45−55. The new catalyst provided the opportunity to tailor not only the polymer structure but also the tacticity of polyolefin resins in combination with an extremely high activity.

■ NEW POLYMERS

Using zirconocene/MAO catalysts, it is possible to produce polypropylenes with different kinds of microstructures in a purity, which cannot be obtained by Ziegler−Natta catalysts (Figure 5).

Stereo errors in polypropylenes produced by $[En(Ind)_2]$-$HfCl_2$/MAO are randomly distributed along the polymer chain while in polypropylene made with Ziegler−Natta catalysts the errors are concentrated at chain ends and in oligomers. This isoblock-polypropylene is characterized by a higher film transparency because the crystal size is in the nano scale.

Researchers of the Hoechst Co. optimized later the ansa zirconocene complexes by using different bridges and substituents at the indenyl rings.[56] They were able to obtain isotactic polypropylene with an activity of 900 000 kg PP/

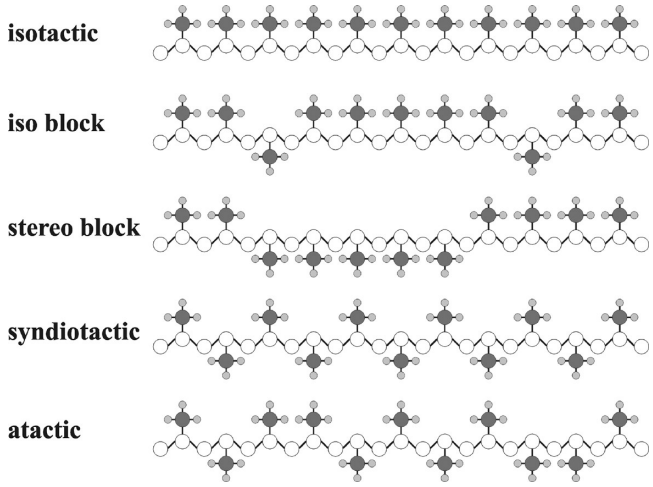


Figure 5. Microstructures of polypropylenes produced by different metallocene/MAO catalysts. (The hydrogen atoms of the backbone are not shown.)

(mol_{Zr} h), a molecular weight of 700 000 g/mol, an isotacticity of 99%, and a melting point of 160 °C.

In 1987, Ewen, Jones, and Razavi[57] obtained pure syndiotactic polypropylene using a C_s-symmetric zirconocene complex with a bridged cyclopentadienyl and a fluorenyl ring. This metallocene offers two different bonding positions for the inserted propylene in an alternating structure. We discovered that unbridged biscyclopentadienyl zirconocenes with bulky substitutions such as neomentyl produces syndioblock polypropylenes with elastic properties.[58] Such a bulky ligand could stabilize an asymmetric (chiral) active site for a short time. During this time, some propylene units could be inserted with the same stereospecificity forming an isotactic block, followed by a change in conformation.

Table 2 summarizes the polymerization of propylene by different metallocene/MAO catalysts.

Polypropylenes with molecular weights up to 700 000 g/mol and by activities of 15 000 kg/(g Zr h cP) could be obtained. Using different ligand substituents, it was now possible to obtain isotactic, isoblock, stereoblock, syndiotactic, and atactic polypropylenes in high purity.

Encouraged by this success, we used metallocene/MAO catalysts for the first time for different copolymerizations, such as ethylene/propylene (EP),[31] ethylene/propylene/diene (EPDM),[59] ethylene/1-butene, ethylene/1-hexene (LLDPE)[59] ethylene/1,3-butadiene or isoprene, and ethylene/cyclopentene or norbornene (COC).[60] The comonomers in these copolymers are distributed randomly in the polymer chain. The low amount of oligomers compared to copolymers produced with Ziegler−Natta catalysts is responsible for a high tensile strength.

Surprisingly, it was also possible to homopolymerize cyclic olefins such as cyclopentene and norbornene to partially crystalline materials and to copolymerize them with ethylene.[43] We observed only double bond opening by the homo- and copolymerization of cyclic olefins in contrast to Ziegler−Natta catalysts, where ring and double bond opening occur simultaneously. Poly(cyclopentene), synthesized by isotactic working metallocene catalysts, are crystalline and have a low solubility and a melting temperature of 395 °C. The unusual formation of 100% of 1,3-enchainments for poly(cyclopentene) was later shown by Collins.[61]

dx.doi.org/10.1021/ma202453u | *Macromolecules* 2012, 45, 3289−3297

Table 2. Propylene Polymerization[a] with Metallocene/Methylaluminoxane Catalysts

metallocene[b]	activity[c]	mol wt (g/mol)	isotacticity mmmm (%)	microstructure[d]	mp (°C)
Cp_2ZrCl_2	140	2000	7	a	
$(NmCp)_2ZrCl_2$	170	3000	23	sb	118
$[En(Ind)_2]ZrCl_2$	1690	32000	91	i	136
$[En(Ind)_2]HfCl_2$	610	446000	85	ib	126
$[En(2,4,7Me_3Ind)_2]ZrCl_2$	750	418000	>99	i	162
$[Me_2Si(Ind)_2]ZrCl_2$	1940	79000	96	i	148
$[Ph_2Si(Ind)_2]ZrCl_2$	2160	90000	96	i	136
$[Me_2Si(2,4,7Me_3Ind)_2]ZrCl_2$	3800	192000	95	i	155
$[Me_2Si(2Me\text{-}4PhInd)_2]ZrCl_2$	15000	650000	99	i	160
$[Me_2Si(2Me\text{-}4,5BenzInd)_2]ZrCl_2$	6100	380000	98	i	157
$[Ph_2C(Fluo)(Cp)]ZrCl_2$	1980	729000	0.4	s	141
$[Me_2C(Fluo)(Cp)]ZrCl_2$	1550	159000	0.6	s	138
$[Me_2C(Fluo)(Cp)]HfCl_2$	130	750000	0.7	s	138
[Me2C(Fluo)(3-*t*-BuCp)]$ZrCl_2$	1045	52000	89	ib	130

[a]Propylene pressure = 2 bar, temperature = 30 °C, [metallocene] = 6.25×10^{-6} M, metallocene/MAO = 250, solvent = toluene. [b]Cp = cyclopentadienyl; Nm = neomenthyl; Ind = indenyl; En = C_2H_4; BenzInd = benzoindenyl; Flu = fluorenyl. [c]In kg/(mol Zr or Hf h) concentration of propylene . [d]a = atactic; i = isotactic; s = syndiotactic; sb = stereoblock; ib = isoblock.

For polynorbornenes it was shown by hydro-oligomerization that norbornene is inserted into the metal−carbon bonds of the growing polymer chain by 1,2-insertion in a cis−exo fashion.[62]

While the tactic homopolymers of cycloolefins cannot be processed because of their high melting points there is much interest in the copolymers of norbornenes or cyclopentene with ethylene or propylene, respectively (Figure 6). These copolymers (COC) are amorphous with an useful glass transition temperature between 80 and 200 °C.[63]

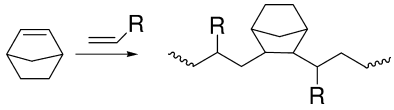


Figure 6. Reaction of ethylene and norbornene.

Cyclopentene, norbornene, or other cyclic olefins are incorporated exclusively by 1,2-insertion into the growing copolymer chain, and no ring-opening occurs. The insertion of the huge norbornene monomer is very fast by metallocene/MAO catalysts.

Table 3 compares activities and incorporation of norbornene by different catalysts. Under special conditions the polymerization rate of a 1:1 molar mixture of ethylene is higher than the homopolymerization of ethylene (comonomer effect).[63]

The $[Ph_2C(Ind)(Cp)]ZrCl_2$/MAO catalyst not only shows high activities for the copolymerization of ethylene with norbornene but also gives an alternating structure, too. Most metallocenes produce polymers with a statistical structure. The melting point of the alternating copolymer depends on the molar ratio of norbornene units in the polymer while the glass transition temperature is nearly independent of this. A maximum melting point of 320 °C was reached.[64,65]

COC materials characteristically have an excellent transparency and low density (1.02 g/mL) and show low adsorption of water and a very high continuous service temperature. From cycloolefin insertion rates of 10 mol % upward, these cycloolefin copolymers (COC) are no longer crystalline but amorphous. They are very resistant toward solvents and chemicals; they exhibit high softening temperatures (glass temperatures of up to 200 °C) and can be processed on a thermoplastic basis.[66] A further peculiarity of these materials is

Table 3. Copolymerization[a] of Norbornene (N) and Ethylene by Different Metallocene/MAO Catalysts

metallocene[b]	*t* [min]	activity (kg/(mol h))	incorp of norbornene (wt %)
Cp_2ZrCl_2	30	1200	21.4
$[En(Ind)_2]ZrCl_2$	10	9120	26.1
$[Me_2Si(Ind)_2ZrCl_2$	15	2320	28.4
$[En(IndH_4)_2]ZrCl_2$	40	480	28.1
$[Me_2C(Flu)(Cp)]$ $ZrCl_2$	10	7200	28.9
$[Ph_2C(Flu)(Cp)]$ $ZrCl_2$	10	6000	27.3
$[Ph_2C(Ind)(Cp)]$ $ZrCl_2$	15	2950	33.3

[a]Ethylene pressure = 2 bar, *c*(N) = 0.05 mol/L, temperature = 30 °C, [metallocene] = 5×10^{-6} mol/L, metallocene/MAO = 200, solvent = toluene. [b]Cp = cyclopentadienyl, Me = methyl, Ind = indenyl, En = C_2H_4, Flu = fluorenyl.

their tendency to absorb little light, which makes them suitable for optoelectronic applications. Norbornene−ethylene copolymers are most interesting for technical uses because of their readily available monomers. COC polymers are already being used for the production of compact discs, lenses, optical fibers, and films.

■ FUTURE TRENDS

Mechanistic studies of metallocene/methylaluminoxane catalysts have strongly increased the knowledge of the olefin polymerization catalysis. This knowledge have made it possible to find new bulky and weakly coordinating cocatalysts such as perfluorophenylborate anions and boranes. The discovery is not completed of new transition metal complexes activated by MAO or other cocatalysts with special polymerization properties. It would be another task to decrease the amount of MAO, needed for the activation.

In recent years, there is an increasing interest to synthesize polyolefin nanocomposites because of their high potential as materials with novel properties.[67] The properties of the nanocomposites are influenced not only by the kind of fillers but also by the microstructure of the polyolefins and the preparation process. As nanofillers are used metal oxides,

dx.doi.org/10.1021/ma202453u | *Macromolecules* 2012, 45, 3289−3297

sulfides, silica, layered silica as well as fibers such as carbon nanotubes, carbon nanofibers, and polymer fibers.[68−71]

Most composites have been prepared by mechanical blending of the particles or fibers above the melting temperature of the desired matrix. Melt compounding of polyolefins with nanoparticles often leads to an insufficient filler dispersion, especially at a high filler content, what leads to aggregation and intercalation, which in turn deteriorates the mechanical properties. Such disadvantages can be solved by in situ polymerization with metallocene/MAO catalysts. Methylaluminoxane is soluble in hydrocarbons, and therefore it can be perfectly adsorbed or anchored on the surface of the nanofillers such as particles, fibers, carbon nanofiber (CNF), and multiwalled carbon nanotubes (MWCNT), changing the surface to a hydrophobic one.[72]

Excess MAO is washed out. In a second step, the metallocene is added forming catalytically active polymerization sites on the nanosurface. The thickness of the polymer films, formed by addition of ethylene or propylene, depends on the polymerization time and the pressure of the monomer. The in situ polymerization leads to composite materials, where the particles or fibers are intensively covered with the polymer. The composite materials show, for example, an improved stiffness with a negligible loss of impact strength, high gas barrier properties, significant flame retardance, better clarity, and gloss as well as high crystallization rates.

Multiwalled carbon nanotubes (MWCNT) are specially attractive class of fillers for polymers because of their intriguing mechanical and thermal properties.[73] High molecular weight isotactic polypropylene filled with MWCNT is an exceptionally strong composite material (Figure 7).

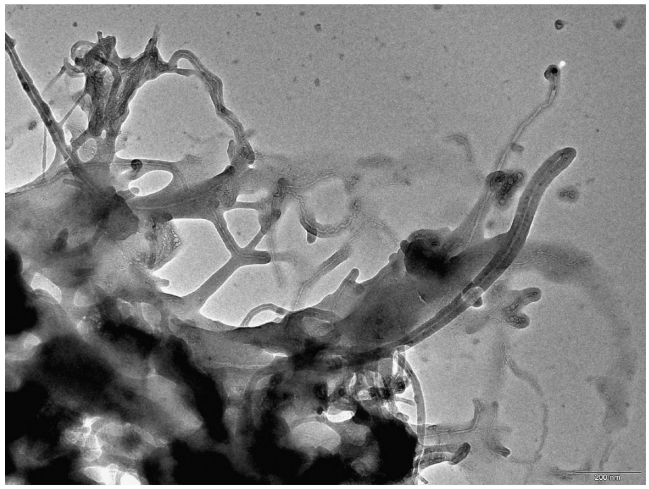


Figure 7. TEM micrograph of an iPP/MWCNT composite material containing 14 wt % of nanotubes.

As expected for in situ polymerization, the polymer grew directly on the fiber surface and covers them with a thin PP layer. Nearly every tube is coated. The diameter of the carbon nanotubes and the polypropylene covering is about 36 nm (20 nm for the MWCNT and 8 nm for the polymer coat). There is a good adhesion on the tubes. The morphology of nanocomposites prepared by in situ polymerization is, in comparison to melt compounded ones, generally characterized by a homogeneous tube distribution in the matrix and a good adhesion of the polymer on the MWCNT surface.[72]

The main advantage of CNT or MWCNT filled PP is the change of mechanical properties. The tensile strength of a composite film increases by 20% if only 1 wt % of MWCNT is incorporated, but also the form stability and the crystallization rate from a melt increase strongly and make this composite material suitable for new applications such as in the automotive plastic industries.

Metallocene and other single site catalysts allow the synthesis of tailored polyolefin structures in a way that was impossible in the years before. The known dependence of the kind of metallocene-based polymers from the catalyst structure allows the modeling of their reaction kinetics.[74] Reactor models could be developed using mass and energy balances, and they describe the polymer composition as well as reactor operating conditions, required for a given polymer design. It would be possible to design polyolefins with tailored molecular weight comonomer content, long chain branching,[75] and comonomer distribution independent and controlled. Late transition metal complexes, which are more stable in water, can be used for emulsion polymerization.[76,77]

A lot can be done to tailor the microstructure of copolymers. Today it is only possible to create statistically ordered or alternating copolymers of polyolefins.[78] It is not possible to design polyolefins with a wanted sequence order of two or more monomers, which will be essential to establish self-organization of the polymer chain. To design three-dimensional crystallizing polyolefins for materials with special properties such as cages for catalysts or membranes, the controlled self-organization will be necessary. Important for this and for blends is the easier synthesis of polyolefins with polar comonomers.[79]

There is first success to form block copolymers by single site catalysts which shows no or only a slow chain transfer reaction like living systems.[80] In a first step only propylene is polymerized forming a hard polypropylene block; then, by addition of ethylene a soft ethylene/propylene copolymer or a polyethylene block follows because ethylene is much faster inserted.

Another method is described to use a chain-shuttling agent to form block copolymers.[81] Two different single site catalysts and monomers are used in one reactor. Cocatalyst is a fluorinated phenylborate. One catalyst is able to homopolymerize from a mixture of ethylene and 1-octene only or mainly ethylene forming a hard polyethylene segment; the other catalyst copolymerizes ethylene and 1-octene to a soft copolymer segment. By the addition of zinc diethyl as a chain transfer agent, the growing polymer chain is shuttling between the two catalysts. A blocky copolymer results with soft and hard segments with elastomeric properties. It could become possible to use MAO activated catalysts for chain-shuttling, too.

The development and commercialization of metallocene/MAO and other single site catalysts have just started and have already expanded the product ranges of polyolefins. New designed catalysts will enlarge the polyolefin industries and the applications of polymers.

AUTHOR INFORMATION

Notes

The authors declare no competing financial interest.

Biography



Walter Kaminsky is Emeritus Professor of Technical and Macromolecular Chemistry at the University of Hamburg. He obtained his Diploma degree and PhD (1971) in Chemistry under the supervision of Dr. Hansjörg Sinn from the University of Hamburg where he was promoted to Full Professor in 1979. His research interest includes aspects of olefin polymerization by metallocene/methylaluminoxane catalysts and feedstock recycling of plastics by a fluidized bed process. He has published more than 400 papers. Among others, Kaminsky has received the Carothers Award (1997), the Walter Ahlström Prize (1998), the Benjamin Franklin Medal in Chemistry (1999), and the Hermann Staudinger Prize (2003), and he was awarded Honorary Fellowship from RSC (1996) and Honorary Professor of the Zhejiang University (1998) and of the East China University (2008).

REFERENCES

(1) Fawcett, E. W.; Gibson, R. U.; Perrin, M. W.; Paton, J. G.; Williams, E. G. Brit. Pat. 471,590 to ICI 1936, C.A. 1938, 32, 1362.
(2) Ziegler, K.; Holzkamp, E.; Breil, H.; Martin, H. *Angew. Chem.* **1955**, *67*, 541.
(3) Natta, G. *J. Am. Chem. Soc.* **1955**, *77*, 1708.
(4) Clark, A.; Hogan, J. P.; Banks, R. L.; Lanning, W. C. *Ind. Eng. Chem.* **1956**, *48*, 1152.
(5) Kashiwa, N.; Tsutsui, T. *Makromol. Chem., Rapid Commun.* **1983**, *4*, 491.
(6) Sinn, H.; Kaminsky, W.; Vollmer, H. J.; Woldt, R. DE Patent 3007725, Feb 29, 1980.
(7) Sinn, H.; Kaminsky, W.; Vollmer, H. J. *Angew. Chem., Int. Ed. Engl.* **1980**, *19*, 390.
(8) Chum, P. S.; Swogger, K. W. *Prog. Polym. Sci.* **2008**, *33*, 797.
(9) Sinn, H.; Kaminsky, W. *Adv. Organomet. Chem.* **1980**, *18*, 99.
(10) Busico, V. *Dalton Trans.* **2009**, *41*, 8794.
(11) Severn, J.; Robert, L. In *Handbook of Transition Metal Polymerization Catalysts*; Hoff, R., Mathers, R. T., Eds.; John Wiley and Sons: New York, 2010; p 157.
(12) Waters, J. A.; Mortimer, G. A. *J. Polym. Sci., Part A1* **1972**, *10*, 905. Chien, J. C. W. *J. Am. Chem. Soc.* **1959**, *81*, 86.
(13) Kaminsky, W.; Vollmer, H.-J.; Heins, E.; Sinn, H. *Makromol. Chem.* **1974**, *175*, 443.
(14) Bochmann, M. *Angew. Chem.* **1992**, *104*, 1206.
(15) Keii, T. *Kinetics of Ziegler-Natta Polymerization*; Kodansha Ltd.: Tokyo, 1972.
(16) Breslow, D. S.; Newburg, N. R. *J. Am. Chem. Soc.* **1959**, *81*, 81.
(17) Natta, G.; Pino, P.; Mazzanti, G.; Longi, P. *Gazz. Chim. Ital.* **1957**, *87*, 549.
(18) Patat, F.; Sinn, H. *Angew. Chem.* **1958**, *70*, 496.
(19) Shilov, A. E. *Dokl. Akad. Nauk SSSR* **1960**, *132*, 599.
(20) Henrici-Olivé, G.; Olivé, S. *J. Organomet. Chem.* **1969**, *16*, 339.
(21) Reichert, K. H.; Schoetter, E. *Z. Phys. Chem.* **1968**, *57*, 74.
(22) Fink, G.; Rottler, R. *Angew. Makromol. Chem.* **1981**, *94*, 2.
(23) Eisch, J. J.; Pombrick, S. I.; Zheng, G. X. *Organometallics* **1993**, *12*, 3856.
(24) Kaminsky, W.; Sinn, H. *Justus Liebigs Ann. Chem.* **1975**, 424.
(25) Sinn, H.; Hinck, H.; Bandermann, F.; Grützmacher, H. F. *Angew. Chem.* **1968**, *80*, 190.
(26) Mottweiler, R. Thesis, University of Hamburg, 1975.
(27) Kaminsky, W. *J. Polym. Sci., Part A: Polym. Chem.* **2004**, *42*, 3911.
(28) Andresen, A.; Cordes, H. G.; Herwig, J.; Kaminsky, W.; Merck, A.; Mottweiler, R.; Pein, J.; Sinn, H.; Vollmer, H. J. *Angew. Chem., Int. Ed. Engl.* **1976**, *15*, 630.
(29) Reichert, K. H.; Meyer, K. R. *Makromol. Chem.* **1973**, *169*, 163.
(30) Long, W. P.; Breslow, D. S. *Justus Liebigs Ann. Chem.* **1975**, 463.
(31) Herwig, J.; Kaminsky, W. *Polym. Bull.* **1983**, *9*, 464.
(32) Sinn, H. *Macromol. Symp.* **1995**, *97*, 27.
(33) Koide, Y.; Bott, S. G.; Barron, A. R. *Organometallics* **1996**, *15*, 2213.
(34) Pino, P.; Muelhaupt, R. *Angew. Chem.* **1980**, *92*, 869.
(35) Kaminsky, W.; Sinn, H.; Woldt, R. *IUPAC International Symposium on Macromolecules*, 7–12 Sept 1980, Firenze, Abstract Vol. *2*, p 59.
(36) Kaminsky, W. *11th Midland Macromolecular Meeting*, 17–21 Aug 1981, Midland, Proceedings, Transition Metal Catalyzed Polymerizations; Quirk, R. P., Ed.; MMI Press: New York, 1983; Part A, p 225.
(37) Kaminsky, W.; Sinn, H. *IUPAC 28th Macromolecular Symposium*, 12 July 1982, Amherst, Proceedings, p 247.
(38) Kaminsky, W.; Miri, M.; Sinn, H.; Woldt, R. *Makromol. Chem., Rapid Commun.* **2000**, *21*, 1333.
(39) Herwig, J. Thesis, University of Hamburg, 1979.
(40) Kaminsky, W. *Nachr. Chem. Tech. Lab.* **1981**, *29*, 373.
(41) Wild, F. R.; Zsolnai, L.; Huttner, G.; Brintzinger, H. H. *J. Organomet. Chem.* **1982**, *232*, 233.
(42) Kaminsky, W.; Kuelper, K.; Brintzinger, H. H.; Wild, F. R. *Angew. Chem., Int. Ed. Engl.* **1985**, *24*, 507.
(43) Ewen, J. A. *J. Am. Chem. Soc.* **1984**, *106*, 6355.
(44) Kaminsky, W.; Ahlers, A.; Moeller-Lindenhof, N. *Angew. Chem.* **1989**, *101*, 1304.
(45) Coates, G. W. *Chem. Rev.* **2000**, *100*, 1223.
(46) Nomura, K.; Liu, K. J. *Dalton Trans.* **2011**, *40*, 7666.
(47) Keii, T. *Heterogeneous Kinetics: Theory of Ziegler-Natta-Kaminsky Polymerization*; Springer Series in Chemical Physics Vol. *77*; Springer: Berlin, 2004.
(48) Rieger, B., Baugh, L. S., Kacker, S., Striegler, S., Eds. *Late Transition Metal Polymerization Catalysis*; Wiley-VCH: Weinheim, 2003.
(49) Heurtefen, B.; Bouilhac, C.; Cloutet, E.; Taton, D.; Deffieux, A.; Cramail, H. *Prog. Polym. Sci.* **2011**, *36*, 89.
(50) Baugh, L. S., Canich, J.A.M., Eds. *Stereoselective Polymerization with Single-Site Catalysts*; CRC: Boca Raton, FL, 2008.
(51) Brintzinger, H. H.; Fischer, D.; Mülhaupt, R.; Rieger, B.; Waymouth, R. M. *Angew. Chem.* **1995**, *107*, 1255; *Angew. Chem., Int. Ed. Engl.* **1995**, *34*, 1143.
(52) Scheirs, J., Kaminsky, W., Eds. *Metallocene-Based Polyolefins: Preparation, Properties, and Technology*; Wiley: Chichester, UK, 2000; Vols. *1* and *2*.

(53) Razavi, A.; Thewalt, U. *Coord. Chem. Rev.* **2006**, *250*, 155.
(54) Kaminsky, W., Ed.; Olefin Polymerization. *Macromol. Symp.* **2005**, *236*, 1−258.
(55) Delferro, M.; Marks, T. J. *Chem. Rev.* **2011**, *111*, 2450.
(56) Spaleck, W.; Aulbach, M.; Bachmann, B.; Kueber, F.; Winter, A. *Macromol. Symp.* **1995**, *89*, 237.
(57) Ewen, J. A.; Jones, R. L.; Razavi, A.; Ferrara, J. P. *J. Am. Chem. Soc.* **1988**, *110*, 6255.
(58) Grubbs, R. H.; Coates, G. W. *Acc. Chem. Res.* **1996**, *29*, 85.
(59) Kaminsky, W.; Miri, M. *J. Polym. Sci.* **1985**, *23*, 2151.
(60) Kaminsky, W.; Spiehl, R. *Makromol. Chem.* **1989**, *190*, 515.
(61) Collins, S.; Kelly, W. M. *Macromolecules* **1992**, *25*, 233.
(62) Kaminsky, W.; Bark., A.; Arndt, M. *Makromol. Chem., Macromol. Symp.* **1991**, *47*, 83.
(63) Cherdron, H.; Brekner, M.-J.; Osan, F. *Angew. Makromol. Chem.* **1994**, *223*, 121.
(64) Kaminsky, W. *J. Polym. Sci., Part A: Polym. Chem.* **2004**, *42*, 3911.
(65) Coates, G. W. *Chem. Rev.* **2000**, *100*, 1223.
(66) M. Arndt, M.; Kaminsky, W.; Schauwienold, A.-M.; Weingarten, U. *Macromol. Chem. Phys.* **1998**, *199*, 1135.
(67) Dong, M.; Wang, L.; Jiang, G.; Sun, T.; Zhao, Y.; Yu, H.; Chen, T. *J. Appl. Polym. Sci.* **2006**, *101*, 1291.
(68) Alexandre, M.; Martin, E.; Dubois, P.; Garcia-Marti, M.; Jerome, R. *Macromol. Rapid Commun.* **2000**, *21*, 931.
(69) Xalter, R.; Halbach, T. S.; Muelhaupt, R. *Macromol. Symp.* **2006**, *236*, 145.
(70) Funck, A.; Kaminsky, W. *Composites, Part A: Technol.* **2007**, *67*, 906.
(71) Kaminsky, W. *Macromol. Chem. Phys.* **2008**, *209*, 459.
(72) Kaminsky, W.; Funck, A.; Klinke, C. *Top. Catal.* **2008**, *48*, 84.
(73) Kaminsky, W. *J. Chem. Soc., Dalton Trans.* **2009**, 8803.
(74) Busico, V.; Cipullo, R.; Corradini, P. *Macromol. Chem., Rapid Commun.* **1993**, *117*, 195.
(75) Stadler, F. J.; Arikan, B.; Kaschta, J.; Kaminsky, W. *Macromol. Chem. Phys.* **2010**, *211*, 1472.
(76) Ittel, S. D.; Johnson, L. K.; Brookhart, M. *Chem. Rev.* **2000**, *100*, 1169.
(77) Mecking, S. *Colloid Polym. Sci.* **2007**, *285*, 605.
(78) Kaminsky, W. *Macromol. Chem. Phys.* **2008**, *209*, 459.
(79) Heinemann, J.; Muelhaupt, R.; Brinkmann, P.; Luinstra, G. A. *Macromol. Chem. Phys.* **1999**, *200*, 384.
(80) Saito, J.; Mitani, M.; Matsui, S.; Kashiwa, N.; Fujita, T. *Macromol. Rapid Commun.* **2000**, *21*, 1333.
(81) Arriola, D. J.; Carnahan, E. M.; Hustad, P. D.; Kuhlman, R. L.; Wenzel, T. T. *Science* **2006**, *312*, 714.

Macromolecules

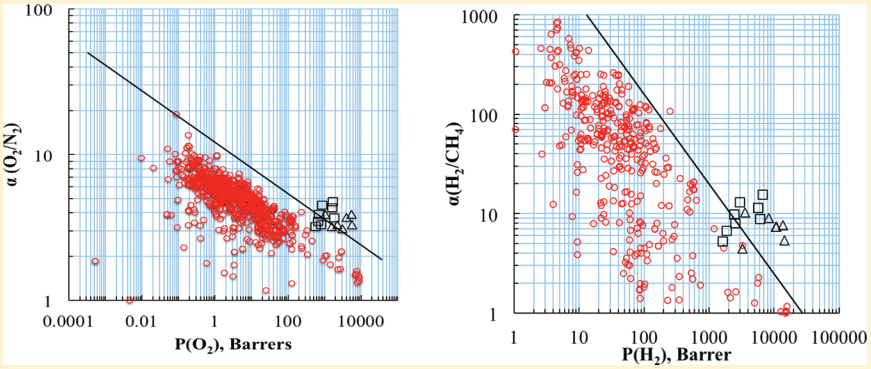
Perspective

pubs.acs.org/Macromolecules

Polymeric Gas Separation Membranes

Yuri Yampolskii*

A.V. Topchiev Institute of Petrochemical Synthesis, Russian Academy of Sciences, 29 Leninsky Prospect, 119991, Moscow, Russia



ABSTRACT: This short Perspective conveys to the general reader of *Macromolecules* basic approaches of materials science of polymeric membranes for gas and vapor separation. The relations between the polymer structure and transport properties of rubbery and glassy membrane materials are considered. On the basis of acquired information, several methods for quantitative prediction of permeability were developed, and their comparative analysis is given in the Perspective. The past decade was marked by the appearance of a number of novel interesting membrane materials, which will be briefly described in the text. In conclusion, novel approaches for achieving highly permeable and permselective materials (e.g., mixed matrix membranes) will be considered as well as several relevant but not solved so far problems of membrane gas separation.

1. INTRODUCTION

The principles of gas separation by means of nonporous polymeric membranes were formulated earlier than those for other membrane separation methods. As early as the 19th century, because of the works by J. K. Mitchell, A. Fick, and T. Graham,[1] it became clear that the mass transfer in polymeric and liquid films is possible in the absence of through pores. While measuring the permeation rates of different gases through polymeric films, for example, films of natural rubber, T.Graham noted that there was no relation between the permeation rates and known gas diffusion coefficients. Therefore, great permeation rate was observed for carbon dioxide distinguished by the largest solubility in membrane materials among all gases tested. These observations led to the "solution−diffusion" mechanism of transport through polymeric membranes. According to this model, the characteristic of the permeation rate, permeability coefficient, P, can be presented as the product

$$P = DS \tag{1}$$

where D is the diffusion coefficient and S is the solubility coefficient. The permeability coefficient characterizes the flux J (mol/m^2 s) through a membrane under the pressure drop (driving force) Δp (Pa) and normalized to the unit thickness of the membrane L (m). The unit of P in the SI system is mol/s m Pa. However, a more widely used and accepted nonsystem unit for P is 1 Barrer = 10^{-10} cm^3(STP) cm/cm^2 s cm Hg. The permeability coefficients of various gases in polymers vary in a wide range from 10^{-4} to 10^4 Barrer.

Another key characteristic of gas-separating membranes is their selectivity. The ideal selectivity (or separation factors) can be defined as

$$\alpha_{AB} = P_A/P_B \tag{2}$$

where P_A and P_B are the permeability coefficients of gases A and B, respectively. Commonly, the more permeable gas is taken as A, so that $\alpha_{AB} > 1$. Keeping in mind eqs 1 and 2, the ideal selectivity can be partitioned into diffusion and solubility selectivity

$$\alpha_{AB} = (D_A/D_B)(S_A/S_B) = \alpha^D{}_{AB}\alpha^S{}_{AB} \tag{3}$$

These simple relationships hold for gases that weakly interact with each other and with polymer matrix during the separation process. This is true for permanent gases at relatively low pressure. For gases having high solubility (e.g., carbon dioxide or hydrocarbons), the ideal separation factors give a rather inaccurate measure of the "actual" selectivity of a membrane in the process of mixture separation. In such cases, the following equation

$$\alpha^*{}_{AB} = (y_A/y_B)/(x_A/x_B) \tag{4}$$

is more suitable. Here y_A and y_B are the mole fractions of the components in the permeate (the stream permeated through

Received: January 30, 2012
Revised: March 6, 2012
Published: March 28, 2012

 © 2012 American Chemical Society dx.doi.org/10.1021/ma300213b | *Macromolecules* 2012, 45, 3298−3311

the membranes) while x_A and x_B are the corresponding mole fractions in the feed.

Although polymeric membranes can be used today for separation of nearly all imaginable gas mixtures, large industrial applications have been realized only for the following processes:[2−6]

- air separation (obtaining of technical grade nitrogen or oxygen enriched air)
- hydrogen separations (separation of the mixtures H_2/N_2, H_2/CH_4, and H_2/CO in refineries and petrochemical industry)
- separation of CO_2/CH_4 mixtures (natural gas "sweetening") and CO_2/N_2 (treatment of flue gas, etc.)
- vapor/gas separations (numerous systems)

Table 1 presents some of the leading industrial companies that are active in membrane gas separation and the principal membrane materials used.

Table 1. Principal Membrane Companies and Membrane Materials Used[2,4]

company	principal membrane materials used
Permea (Air Products)	polysulfone
MEDAL (Air Liquid)	polyimides
Generon	tetrabromopolycarbonate
Separex (UOP)	cellulose acetate
Aquila	poly(phenylene oxide)
Ube	polyimide
MTR	silicon rubber
Helmholtz Centrum (formerly GKSS)	silicon rubber
Grasys[a]	polyimide, polysulfone
Kryogenmash[a]	poly(vinyltrimethylsilane), tetrabromopolycarbonate
Air Liquid	ethyl cellulose
OPW Vaposaver	poly(trimethylsilyl propyne)

[a]Producer of membrane modules and installations only.

Although hundreds of polymers have been investigated so far as potential membrane materials, only several ones, as can be seen from Table 1, found actual application in industrial gas-separating plants. It is a long way from a polymer that showed a good combination of permeability and selectivity to industrial application of membranes based on it. The requirements for production of robust gas separation membranes include sufficiently good mechanical and film-forming properties, absence of microdefects in thin layers of composite membranes, thermal and chemical stability under the conditions of the separation process, and absence of aging in thin films (reduction of permeability in time). Often, high cost of production of potential membrane materials is regarded as the main obstacle for using a polymer as the material of industrially produced gas-separation membranes.

2. "STRUCTURE−PROPERTIES" RELATIONS

The history of membrane gas separation shows that every period had its favorite types of polymeric materials of separating membranes. In the early years of membrane studies, Thomas Graham had at his disposal only natural polymers − gutta percha, natural rubber, and gelatin. On the advent of polymer science in the middle of the 20th century, numerous synthetic polymers became available, and so diverse studies of gas permeation properties were carried out with polyolefins,[7−9] vinylic polymers, like poly(vinyl acetate),[10] polytetrafluoroethylene,[11] siloxane,[12] and other rubbers,[13] cellulose derivatives.[14] These studies indicated that there exist straightforward correlations between chemical structure of polymer repeat unit and the observed gas permeation parameters.

2.1. Rubbers. The most detailed results were obtained for siloxane polymers with different side groups attached to Si atom. It was shown[15] that when the size of the side groups increases, the chains become less flexible, as is shown by the increases in the glass transition temperature and the decreases in permeability (Table 2). In this respect, rubbery polymers differ from glassy polymers, where the introduction of larger side groups often results in an increased permeability, as will be later discussed. The variations of the flexibility of the main chains, while the side chains are intact, is also a strong way to change the permeability, as Table 3 indicates for polydimethylsiloxane, polydimethylsilmethylene, and polyisobutylene. The correlations between T_g values and permeability for structurally less related hydrocarbon rubbers shows that the effects of chemical structure of repeat units are exerted mainly via the flexibility of the main chains of rubbery polymers.

Table 2. Permeability Coefficients, *P*, of Siloxanes with Different Side Groups[15]

			P, Barrer		
R_1	R_2	T_g, K	CO_2	CH_4	C_3H_8
CH_3	CH_3	150	4570	1450	8580
CH_3	C_3H_7	153	1520	531	2950
CH_3	$C_2H_4CF_3$	203	1214	201	584
CH_3	C_6H_5	245	226	36	139

Table 3. Effects of the Variation of the Structure of Main Chains in Rubbery Polymers[12,16−18]

		P, Barrer			
polymer	T_g, K	H_2	O_2	N_2	CH_4
$-Si(CH_3)_2O-$	150	650	600	280	950
$-Si(CH_3)_2CH_2-$	181		99	40	130
$-C(CH_3)_2CH_2-$	208	6.4	1.2	0.3	

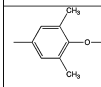
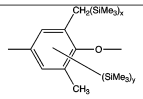
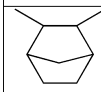
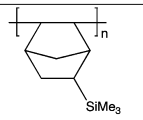
It is interesting that flexible Si−O bonds that enhance the chain mobility and thus increase permeability can exert effects, even if they are located in the side chains. Therefore, polystyrenes substituted in para position with radicals containing several Si−O bonds (e.g., $Si[CH_3][OSi(CH_3)_2]$ or $Si[CH_3]_2[OSi(CH_3)_3]$, etc.) reveal decreased glass-transition temperatures, increased gas permeability, and reduced separation factors as compared with unsubstituted polystyrene.[19] Recently, similar effects were demonstrated for another type of polymers, substituted metathesis polynorbornenes.[20]

2.2. Polyolefins. Extensive studies were performed during the 1960s to 1980s on gas permeation properties of polyolefins (polyethylene of high and low density, polypropylene, poly(4-methylpentene), etc.).[8,21−24] However, the polymers of this important class are semicrystalline, so their transport properties are affected mainly by the degree of crystallinity and morphology of the heterophase structure.[25]

2.3. Glassy Polymers. The gas permeation properties of glassy polymers are much more sensitive to chemical structure of repeat units than those of rubbers. It is sufficient to point out that the permeability coefficients in the glassy state can be as low as $P(CO_2)$ = 0.0003 Barrer for polyacrylonitrile[26] or as

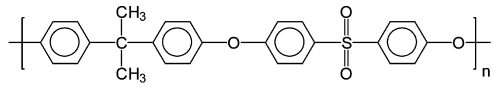
dx.doi.org/10.1021/ma300213b | Macromolecules 2012, 45, 3298−3311

Table 4. Enhancement of Permeability Due to Introduction of $Si(CH_3)_3$ Groups

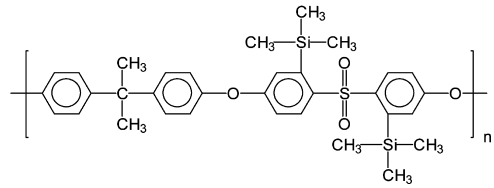
Polymer	Silylated polymer	Polymer		Silylated polymer		Ref.
		$P(CO_2)$, Barrer	$\alpha(CO_2/CH_4)$	$P(CO_2)$, Barrer	$\alpha(CO_2/CH_4)$	
$-CH_2CH_2-$[1]	$-CH_2CH(SiMe_3)-$	12.6	4.4	190	14.6	8, 30
$-CH_2CH(Ph)-$	$-CH_2CH(PhSiMe_3)-$	12.4	15.7	227	6.7	31, 32
		82	12.8	294	9.8	33
		33.6	12.9	4350	5.5	34
PSF[2]	PSF-$SiMe_3$[3]	4.92	20	15.8	15	35

[1]Low density PE (0.91 g/cm^3).

[2]PSF:



[3]PSF-$SiMe_3$



large as $P(CO_2)$ = 27 000 Barrer in poly(trimethylsilyl propyne).[27] The most spectacular demonstration of strong effects of polymer chemical structure on permeation rate was obtained with polymers of different classes containing bulky side groups: $(Si(CH_3)_3$, $Ge(CH_3)_3$, and $CH(CH_3)_2)$. Table 4 summarizes some data on the effect of the introduction of $Si(CH_3)_3$ groups into different main chains. It is seen that independently of the structure of main chains the appearance of this group as the side chain results in a substantial increase in the permeability coefficients, sometimes accompanied by some growth of the separation factors. The most detailed information on such effects was obtained for polyacetylenes.[28] Examination of numerous Si-substituted glassy polymers allows a formulation of the rules for stronger enhancement of permeability:

(1) Symmetry of side groups. The strongest effects are observed for completely symmetrical substituents; for example, the effect of $SiMe_3$ group is stronger than that of $SiMe_2Et$.[28]
(2) A bulky group should be attached directly to the main chain and not via a spacer.
(3) Long linear substituents (e.g., $SiMe_2$-*n*-C_6H_{13}) show significant decreases in permeability.

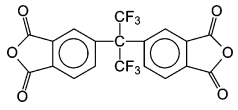
A compelling explanation of such behavior can be given on the basis of free volume theory and application of probe methods.[29]

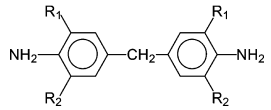
In polymers with aromatic backbones (polyimides, polycarbonates, polysulfones), a marked increase in permeability can be achieved by symmetrical or asymmetrical substitution of phenylene rings.[36] Different radicals were used in such substitution, for example, CH_3 and other linear and branched alkyls, CF_3, Cl, and so on. Examples of the effects of such modification of diamine moyety of 6FDA polyimides are given in Table 5. The increases in permeabiluity correlate with the total size of side groups shown in the last column. These data indicate that substitution results in a more loose chain packing (growth of free volume, which is accompanied by decreases in permselectivity $\alpha(O_2/N_2)$).

Table 5. Properties of 6FDA Polyimides Containing Various Substituted Diamine Fragments[37] [a]

R_1	R_2	$P(O_2)$, Barrer	$\alpha(O_2/N_2)$	substituent volume, Å^3
H	H	2.8	5.65	16.5
H	CF_3	5.2	5.71	79.0
Me	Me	11.0	4.17	90.8
Et	Et	18.4	4.20	158.8
i-Pr	i-Pr	47.1	3.76	226.8

[a]Structure of 6FDA dianhydride and diamine fragments



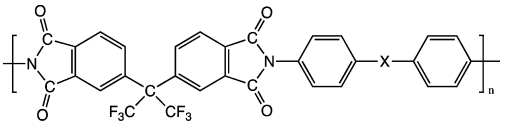


Another element of the design of polymers with aromatic backbones is the structure of connector groups. These effects are also revealed in the transport properties of polycondensation materials.[36] Bulkier connector groups can stiffen the chain backbones, inhibit their dense packing, and thus increase free

dx.doi.org/10.1021/ma300213b | Macromolecules 2012, 45, 3298−3311

volume and permeability. This situation is illustrated for the family of polyimides in Table 6.

Table 6. Effects[38] of the Connector Groups in 6FDA Polyimides of General Formula:



connector group X	$P(CO_2)$, Barrer	$\alpha(CO_2/CH_4)$
−O−	23	60.5
$-CH_2-$	19.3	44.9
$-C(CH_3)_2-$	30	42.9
$-C(CF_3)_2$	63.9	39.9

So far, only the effects of nonpolar groups were considered. Meanwhile, the introduction of the substituents that are capable to dipole−dipole interactions or can form hydrogen bonds can strongly influence the transport parameters due to increasing interchain interactions or interactions with some penetrants. For example, in carboxylated poly(vinyltrimethylsilane) when the content of −COOH groups amounted to 20 mass %, permeability coefficients of hydrocarbon gases decreased two-fold, whereas permeability coefficients of water vapors increased by a factor of 4.5.[30] The introduction of the −COOH group in the *m*-plenylenediamine moyety of 6FDA polyimide results in a decrease in $P(O_2)$ from 3 Barrer (for nonsubstituted polymer) to 1 Barrer with a certain accompanying increase in separation factor α (O_2/N_2): 8 versus 6.7.[39]

3. PREDICTIONS AND MODELING

As soon as a sufficient body of the data had accumulated on gas permeation parameters for polymers with different chemical structure, especially for polymers that belong to the same classes, it became tempting to proceed from qualitative analysis of the data to the development of quantitative models with predictive ability. A detailed discussion of different approaches for predictions was made by Alentiev and Yampolskii.[40] The methods for predictions were conceived for facilitating directed search for advanced membrane materials − not studied so far or even synthesized. Several approaches for predictions were proposed. The most successful ones are based on the group contribution methods that are common in analyzing, for example, thermodynamic and kinetic properties of various compounds. A key question in such methods is the way of "splitting" polymer repeat units into fragments for which corresponding increments (group contributions) are being sought after. The smallest fragments can be atoms in different valence states (e.g., $C(sp^3)$ or $C(sp^2)$).[40] Robeson et al.[41] proposed to split repeat units into larger fragments (e.g., phenylene rings). An important class of membrane materials, polyimides, can be treated as alternating copolymers of diamine and dianhydride fragments. The prediction of the transport parameters of polyimides is more successful if the increments characteristic for such groups are found, especially bearing in mind that the number of chemical structures of polyimides of different chemical structure is very big (more than 300).[42] There were also attempts to use the graph theory approach[43] and artificial neural networks[44] for the prediction of the gas permeation parameters.

If the splitting of repeat units is appropriate and the number of the input parameters is sufficiently great, then it is possible to make relatively accurate predictions within the coefficient of 2 to 3. Such accuracy seems to be really good because the range of variation of the permeability coefficients in polymers amounts to 5 to 8 decimal orders (depending on the gas molecule). Better accuracy is hardly possible because it is mainly determined by "noise" in the input parameters: thus, several authors who studied polyimide Kapton reported the values of $P(O_2)$ in the range 0.2 to 0.8 Barrer, so such big variation should affect the group contributions parameters deduced from these data. It is interesting that the accuracy of the predictions of separation factors is usually better. Apparently, this is a due to similar influences of the aforementioned "noise" on the permeability coefficients of both gases, $P(A)$ and $P(B)$, so it affects the ratio $P(A)/P(B)$ to a smaller extent. This is equally true for predictions using molecular dynamics, and the illustration of this will be given later on in this section.

Meanwhile, it must be admitted that the group contribution and other similar approaches have their limitations. They are based on the input parameters, that is, on the increments obtained for already studied polymers with diverse chemical structure. Therefore, they do not provide means for strong breakthrough, for example, for the methods to overcome the upper bounds on the Robeson diagrams[45,46] or predict transport properties of polymers that include entirely new components of chemical structure, because the corresponding increments are absent.

Such weakness is not characteristic of computer modeling of nanostructure of membrane materials and calculation, on this basis, the *S*, *D*, and *P* values for different gases. These methods of computer simulation made great progress during the past decade.[47−50] The method of molecular dynamics was used by most of the authors.[51−53] Recently, different variants of the Monte Carlo (MC) methods also acquired some popularity.[54,55] It is important that the MC methods allow us to take into account connectivity[56] of membrane materials, an issue especially important for glassy polymers that reveal size sieving permeation.

The accuracy of the prediction differs in different works. Some authors claim that it is easier to predict accurately the solubility coefficients. Often, the predicted *S* values coincide with the experimental ones within the range of 20−30%.[51] The predictions are much less reliable in the case of the diffusion and, hence, permeability coefficients. It is commonly accepted that if the D_{pred} and D_{exp} values differ by a factor 2−5 then the prediction is considered to be as successful. According to the opinion of other research,[50,57,58] the accuracy of the predictions of the S values is less accurate. Such predictions are sensitive to many factors, and the appropriate choice of the force field is maybe the most crucial. It can be assumed that realistic assessment of the accuracy of the *S* values for small penetrants based on contemporary computer simulations corresponds to the factor 2 as compared with the experimental values, which also show some scatter. As for the diffusion coefficients for such penetrants as O_2, N_2, CO_2, the predicted values are within a factor of 1.5 to 2 from the experimental values.

As has been mentioned, the predictions of the separation factors are often more successful than those of the permeability and diffusion coefficients. It is illustrated in Table 7 by a comparison of the experimental and predicted permeability coefficients and separation factors for two substituted

dx.doi.org/10.1021/ma300213b | *Macromolecules* 2012, 45, 3298−3311

Table 7. Experimental and Predicted Gas Permeation Parameters[51] for *p*-Substituted Polystyrenes $-(CH_2-CHPhR)-$

method	$P(O_2)$, Barrer	$P(N_2)$, Barrer	$\alpha(O_2/N_2)$
	$R = SiMe_3$		
calc	323	102	3.2
exp	55.8	16.1	3.5
	$R = SiMe_2(CH_2CH_2CF_3)$		
calc	338	90.9	3.7
exp	38	12	3.2

polystyrenes. The predictions were made by molecular dynamics method.

However, the progress of the programs of simulations (rates of computing) and the sizes of supercomputers used is so fast that it can be imagined that soon computer simulations will successfully compete with experimental procedures for the determination of *D*, *P*, and *S* values as well as sorption isotherms.

4. NOVEL MEMBRANE MATERIALS

The efforts of membrane scientists are traditionally directed to the creation of more permeable and more permselective materials, which, in addition, must be sufficiently robust and resistant to plasticization effects that reduce the selectivity of mixture separation.

Until the 1970s, it was commonly accepted that glassy polymers have low permeability, although sometimes high permselectivity. However, the discovery of, first, poly(vinyltrimethyl silane) (PVTMS)[59,60] and, more importantly, poly(trimethylsilyl propyne) (PTMSP)[61,62] disproved this viewpoint. The design of these polymers (presence of a bulky $Si(CH_3)_3$ substituent attached to the main chain) and the highest permeability coefficients found for PTMSP among all of the polymers known for a long time determined the directions of the search for advanced membrane materials with great permeability (mainly polyacetylenes).

Meanwhile, some highly permeable polymers with entirely different design also showed rather high gas permeability. Thus, amorphous Teflon AF2400 or glassy copolymer containing 87 mol % 2,2-bis(trifluoromethyl)-4,5-difluoro-1,3-dioxole and 13 mol % tetrafluoroethylene has permeability coefficients for O_2 and CO_2 about 1000 and 2500 Barrer, respectively.[63,64] The reason for high permeability of this and related polymers is the rigidity of the main chain (high-energy barriers for rotation of adjacent dioxole rings) and low tendency to interchain interactions that cause a loose packing of the chains.[65] In addition, it was shown that all amorphous perfluorinated polymers exhibit unusual solubility behavior: reduced hydrocarbon gas and vapor solubility.[66] This results in attractive positions at Robeson diagrams[46] of the data points that correspond to perfluorinated polymers for such gas pairs as He/CH_4, N_2/CH_4, and He/H_2 and low tendency for plasticization of membranes in the presence of hydrocarbon vapors, common impurities in gas mixtures.[66] These circumstances justify the growing interest in perfluorinated and partially fluorinated polymers as membrane materials.

The stiffness of main chains was shown to be the governing factor that determines physicochemical and transport properties in another group of novel polymers synthesized by English researchers – polymers of intrinsic microporosity (PIM).[67] These are ladder polymers without any single bond in the backbone. A feature of these materials is that they incorporate sites of contortion or spiro-center that force the polymer chains to form a loosely packed matrix. These polymers are distinguished by great inner porosity (~700 m^2/g), as measured by the BET method, as well as gas and vapor solubility coefficients larger than those reported for any studied polymers, including PTMSP, the great free volume as measured by positron annihilation lifetime spectroscopy and ^{129}Xe/NMR, and relatively large permeability coefficients (Table 8). The data points of archetypal PIM, referred to as PIM-1, are located on some Robeson diagrams above the upper bound of 2008.[67] Interestingly, PIM-1 also shows unprecedented sensitivity to the protocol of film formation: treatment of the films of this polymer by alcohols increases the observed permeability by a factor of three to four. Unusual properties of PIM-1 were also confirmed by the results obtained by other research groups.[68] The works with PIM-1 and other PIMs showed that high permeability combined with good selectivity can be achieved not only by means of bulky $Si(CH_3)_3$ groups attached to rigid main chains. The interest in this polymer is confirmed by further recent publications[69] on cross-linking and UV irradiation of the parent PIM-1 structure that resulted in polymers with attractive membrane properties.

Despite the fact that the transport properties of amorphous polyacetylenes are extensively studied,[28] recently it was shown that even within the class of disubstituted polyacetylenes another design can result in extremely high gas permeability. Hu et al.[70] demonstrated that a group of indan-based polyacetylenes exhibits permeability coefficients larger than those known for PTMSP, which had been considered as the polymer having the highest gas permeability among known polymers. Permeability coefficients of indan-based polyacetylenes are combined, however, with very poor selectivity of separation of light gases (Table 9). It is an indication of the extremely opened pore structure of these polymers.

The introduction of one or more $Si(CH_3)_3$ groups into other stiff backbone chains can also result in the formation of novel highly permeable polymers with unusual properties – Si-substituted additional type norbornene polymers, whose properties will be discussed in more detail in Section 6.3.[20,34,71,72]

5. NEW APPROACHES FOR CONTROL OF THE GAS PERMEATION PARAMETERS

5.1. Mixed Matrix Membranes. The experience accumulated in numerous studies of membrane materials having different structure indicates that there are limitations in achieving, using such an approach, materials with very advanced membrane properties. Since the 1990s, it has become clear that there exists another way to influence the gas permeation properties of membrane materials. This approach, very popular currently, is known as "mixed matrix membranes" (MMM). It implies the introduction of inorganic or organic–inorganic fillers with small particle size (desirably in the range of 10–100 nm) into polymeric matrices. In many cases, such a strategy resulted in enhancing either permeability or permselectivity (or often both) and some data points on Robeson diagrams[46] that are located above the upper bound of 1991 or even 2008 are based namely on MMMs. Preparation of MMMs, investigation of their transport and mechanical properties, and study of their nanostructure have attracted the attention of the membrane community during the past decade; hundreds of articles have been published, including some reviews.[73–75] This direction of

dx.doi.org/10.1021/ma300213b | *Macromolecules* 2012, 45, 3298–3311

Table 8. Permeability Coefficients (Barrer) and Separation Factors of PIM-1 and PIM-Polyimides[67]

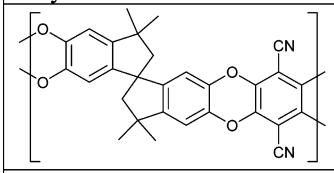
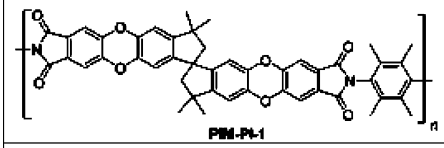
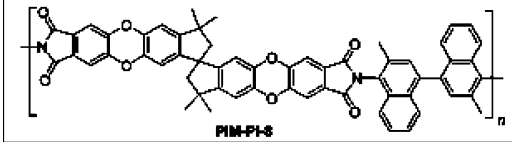
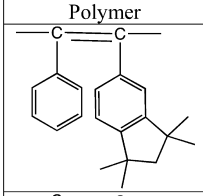
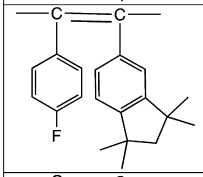
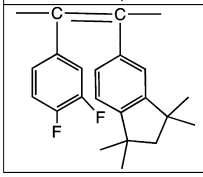
Polymer	$P(O_2)$	$P(N_2)$	$\alpha(O_2/N_2)$
	1610	500	3.2
	730	216	3.4
	1150	416	2.8

Table 9. Permeability Coefficients (Barrer) and Separation Factors of Indan-Based Polyacetylenes[70]

Polymer	$P(O_2)$	$P(N_2)$	$P(CO_2)$	$\alpha(O_2/N_2)$	$\alpha(CO_2/N_2)$
	14400	11600	38700	1.24	3.3
	17900	15600	47000	1.15	3.0
	18700	16600	44200	1.13	2.7

research is seemingly a further development of numerous studies of filled polymers. (See, e.g., refs 76 and 77.) However, new phenomena became clear when the size of the fillers approached nanoscale. In filled polymers, the introduction of nonporous inorganic fillers into polymers resulted, as a rule, in a decrease in permeability with no changes of permselectivity. In MMMs, the opposite behavior is observed: permeability increases upon the introduction of nanofillers, and these changes are caused, in the most cases, by increasing the diffusion coefficients. It is important that these changes are different for different penetrants; hence, selectivity can be changed as compared with pure polymer matrices.

Numerous polymers have been studied as continuous matrices in MMMs: high permeability polyacetylenes,[78] amorphous Teflons AF,[79,80] and also conventional glassy polymers[81,82] and even some rubbers.[83] Nanoadditives of different structures have been introduced into these polymers, for example, fumed silica,[78,79] carbon nanotubes and carbon molecular sieves,[84,85] zeolites,[80,81] TiO_2,[86,87] and so forth.

A common feature of most MMMs studied is an increase in permeability with respect to various gases when the volume fraction of nanoparticles in the membrane increases significantly. (See, e.g., refs 78, 79, 82, and 87.) This is in contrast with the prediction of Maxwell's equation for nonpermeable particles of the dispersed phase, which holds for common filled polymers and which predicts a decrease in permeability and diffusivity for larger loadings of fillers.[76,77]

It is important that strong effects on permeability are observed only for larger concentrations of nanoparticles (>20−30%), whereas at small loading the P values do not depend on the concentration of nanoparticles or sometimes slightly decrease. It can be assumed that marked changes of P are observed above the percolation threshold. This is in line with the qualitative model proposed by Takahashi and Paul,[88] who assumed that at larger loading of the nanoparticles additional microcavities on the boundary nanoparticle−polymer matrix form infinite cluster.

In some cases, the transport properties observed for MMM are entirely different as compared with those of pure polymers. For example, pure amorphous Teflon AF2400 is characterized by size-sieving patterns: the permeability coefficients decrease when the size of penetrants (gaseous hydrocarbons) increases.[64] However, MMMs based on this polymer combined with zeolites and fumed silica become solubility-controlled permeation materials: permeability coefficients for butane are larger than those of methane.[79,80]

dx.doi.org/10.1021/ma300213b | Macromolecules 2012, 45, 3298−3311

Certain combinations of polymer matrices and nanoadditives show common trade-off between P_i and α_{ij} (e.g., systems polysulfon/fumed silica[82] or polyimide Matrimid/MOF[89]); however, in many cases, a more attractive behavior has been reported: joint increases in both P_i and α_{ij}. (See, e.g., systems amorphous Teflon AF2400/fumed silica[79] or polybenzimidazole/metal organic frameworks (MOFs).[90])

Some of the studied nanoparticles (zeolites, or MOF) can be considered as the fillers with inner porosity, whereas other ones do not have empty inner cavities (fumed silica, TiO_2, MgO). Hence, qualitatively different effects can be expected for these two types of nanofillers. Meanwhile, numerous studies showed that different types of nanoparticles (those with inner porosity and its absence) reveal similar trends for permeability and permselctivity for various gases. This seeming contradiction requires elucidation.

An extremely important problem is a substantiated search for optimal combinations of polymer matrices and nanoparticles. There are examples when the introduction of different nanoparticles into the same polymer led to quite different results. Ahn et al.[91] added silica nanoparticles into the polymer of intrinsic microporosity PIM-1 and observed a typical trade-off between $P(O_2)$ and $\alpha(O_2/N_2)$, so the data points on Robeson diagram did not overcome the upper bound of 2008. The introduction of a kind of MOF, zeolitic imidazolate framework ZIF-8, into the same polymer resulted in a more permeable and more permselective systems, so the data points for various content of nanoadditive are above these upper bounds (Figure 1).[92]

Despite obvious advantages that are provided by MMMs and a wide field of further studies, there are many problems that are to be solved.

1. *Preparation of membranes.* There exists no well-defined procedure for preparation of dense films or composite membranes based on MMMs. It is not clear how to prepare membranes with uniform (and maybe nonuniform) distribution of nanoparticles and how to avoid agglomeration of nanoparticles.
2. *Problems of functionalization.* A common wisdom is that without appropriate functionalization it is difficult to achieve a good compatibility of nanoadditives and polymer matrix. However, the formation of additive free volume at the boundary between nanoparticles and the matrix implies that complete compatibility might be detrimental for achieving greater increases in permeability and diffusivity. There are examples that prove that nonfunctionalized additives give good results and opposite examples that demonstrate that under the condition of good miscibility produced membranes show only weak increases in permeability or even decreases. No approaches have been proposed for the calculation of the surface energy of the introduced nanoparticles in advance.
3. *Aging.* It is known that polymers with extra high gas permeability are prone to physical aging, that is, a reduction of permeability in time.[28] Because the introduction of nanoparticles into such polymers as polyacetylenes, amorphous Teflons AF, or PIM-1 results in a further increases in their permeability (already high in pure polymers), the problem of aging becomes very relevant.
4. *Mechanical properties.* The introduction of some nanoparticles (e.g., carbon nanotubes) leads to reinforcing of mechanical properties of polymers, which can make MMMs more robust. However, it is true only for small concentrations of the fillers. At larger concentration (20−40%), an opposite effect is often observed: the membranes become brittle. So this problem desperately requires a solution.
5. *Modeling.* Unfortunately, relatively little has been made regarding modeling MMMs.[93] Good contemporary models require simulation of rather big unit volumes of composite system (cubes with the edge at least 500 nm). Such scale is beyond now the possibility of molecular dynamics, so new approaches are desperately needed.
6. It is really a challenge to transfer the achievements reached with MMMs based on experiments with dense films (thickness of 30 μm or more) and nanoparticles having the size in the range 20−200 nm to industrially used composite membranes (often in the form of hollow fibers) with the thickness of thin selective layers of 100−300 nm. It means that much smaller nanoparticles must be introduced into polymer matrices. Again, any clustering that typically occurs in the process of the preparation of MMMs would be detrimental to the resulting properties of the membranes. These technological problems still wait for their solution.
7. *A selection of combination of polymer matrix and nanoparticles.* A logical requirement to polymers used as matrices in prepared MMMs is that they must have sufficiently good combinations of permeability and permselectivity, even in pure state. Therefore, the introduction of nanoparticles will only further improve these characteristics. However, overcoming the upper bounds on Robeson diagrams is only a part of the story. Practice requires certain values of the permeability coefficients and separation factors. So a search for optimal combinations of polymers and nanoparticles should not be made at random. The demands of further industrial application must be taken into account.

5.2. Desililation. It was demonstrated recently that there are alternatives to the principle of control of free volume in polymers via the introduction of bulky substituents and, hence, obtaining highly permeable polymers. Diphenylacetylene can easily polymerize; however, the obtained poly(diphenylacetylene) is insoluble in any organic solvents, so it is impossible to prepare and test films of this polymer. Meanwhile, its close structural analog, poly[1-phenyl-2-*p*-(trimethylsilyl) phenylacetylene)], is soluble in common organic solvents, like toluene or chloroform. Teraguchi and Masuda proposed[94] carrying out solid-state desililation of the films produced from this polymer and thus obtained the film of poly(diphenylacetylene). Trifluoroacetic acid was used as the desiliation agent. Interestingly, it was found that poly(diphenylacetylene) obtained in this manner has high permeability: its permeability coefficient $P(O_2)$ = 6000 Barrer, much higher than that of the parent Si-containing polymer (1550 Barrer). It can be assumed that this effect is caused by large free volume elements that form in solid film in the sites, where originally presented $Si(CH_3)_3$ groups were removed. This also means that these large free volume elements are retained in the matrix due to highly stiff polymer structure. Although subsequent studies showed that permeability of the

dx.doi.org/10.1021/ma300213b | *Macromolecules* 2012, 45, 3298−3311

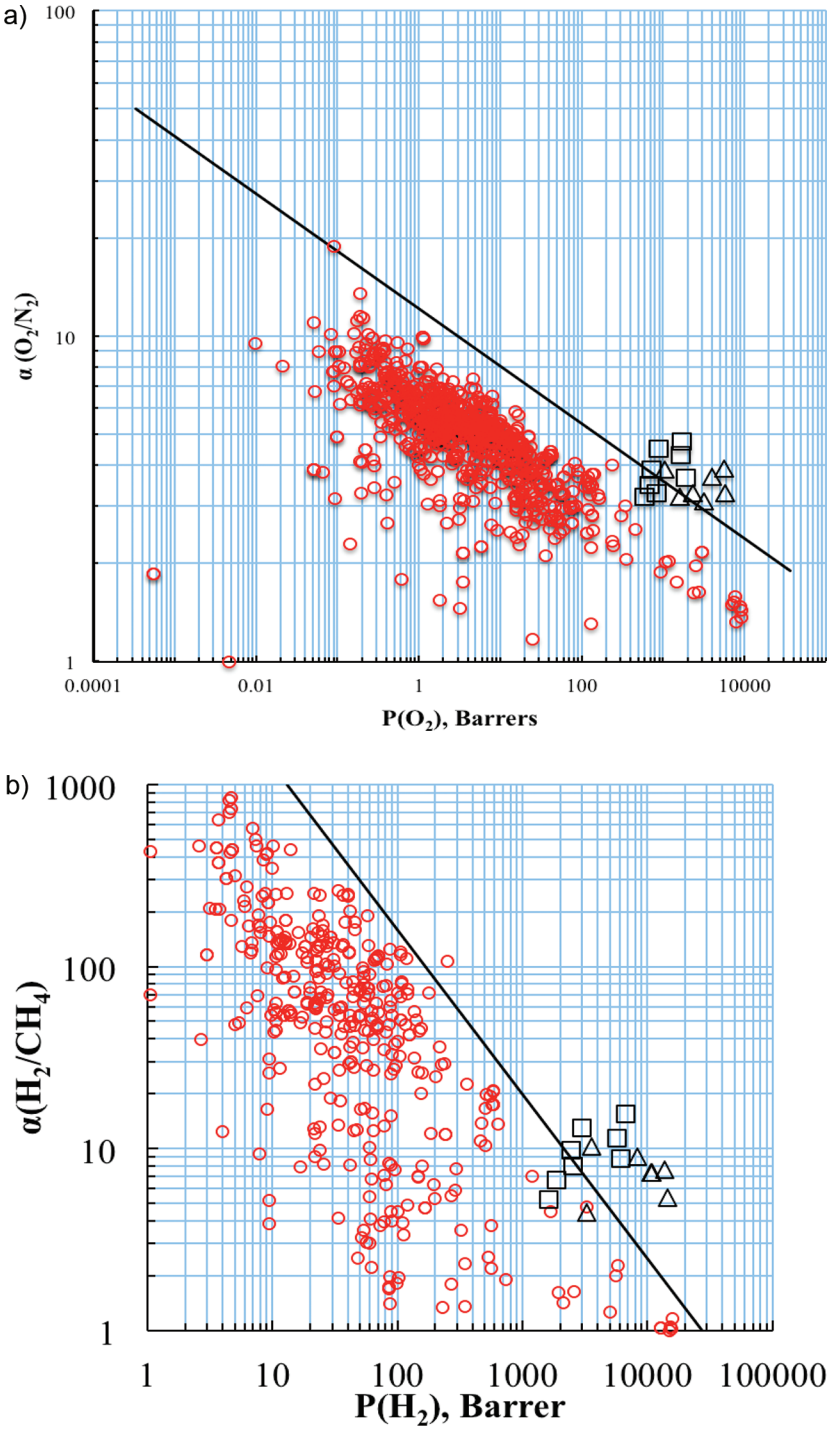


Figure 1. Correlation of permeability and permselectivity for the O_2/N_2 (a) and H_2/CH_4 (b) gas pairs.[92] The solid line is the upper bound of 2008.[46] Triangles indicate PIM-1/ZIF-8 films after ethanol treatment, squares indicate PIM-1/ZIF-8 films as cast.

desililated polyacetylene depends on some not completely clarified factors and can be not so great ($P(O_2)$ = 910−1100 Barrer),[95] for other Si-containing side groups, even greater effects were noted:[95,96] thus, removal of the much larger side group, $Si(CH_3)_2C_8H_{17}$, resulted in an increase $P(O_2)$ from 28 to 3300 Barrer.[95] According to Wang et al.,[97] desililation leads to some reduction of the permeability coefficients, and the reason for this is a decrease in the diffusion coefficients. Computer simulation of nanostructure of free volume in poly[1-phenyl-2-*p*-(trimethylsilyl) phenylacetylene)] and poly(diphenylacetylene)[97] also did not clarify the situation: it was shown that in the latter polymer size distribution of free volume elements is shifted to smaller radii (average cavity size of 5 Å), whereas in the Si-containing polymer the average cavity size is larger (7.5 Å). All this means that further studies of this interesting method for production of highly permeable polymers are quite desirable.

5.3. Thermal Rearrangement of Membrane Polymers. Thermal transformation of polymers can result in entirely new structures, and some of them show very interesting membrane properties. In particular, pyrolysis of polyimides at 500−700 °C leads to carbon membranes with an excellent combination of

dx.doi.org/10.1021/ma300213b | *Macromolecules* 2012, 45, 3298−3311

permeability and selectivity.[98] Therefore, it is possible to speak about another "structure−properties" relationship: structure of the pyrolyzed polyimides and resulting properties of carbon membranes. However, if thermal rearrangement process is carried out at lower temperatures (e.g., at 350−450 °C), it is possible to obtain *polymeric* products with the transport properties significantly changed as compared with those of the parent polyimides. It was suggested[99,100] that mild thermal treatment of polyimides with −OH and −SH side groups in the ortho position results in thermal rearrangement with the formation of insoluble polybenzoxazoles or polybenzothiazoles, respectively, that revealed good combination of $P(CO_2)$ and $\alpha(CO_2/CH_4)$: the corresponding data points are above the upper bound line on Robeson diagram. Insolubility of the obtained membranes makes them less sensitive to the impurities of liquid hydrocarbons in the separated natural gas. Although there are some doubts regarding the proposed mechanism of thermal transformations,[101,102] the quality of the obtained membranes makes quite desirable further investigations of this new method for preparation of gas-separating membranes.

6. UNSOLVED PROBLEMS OF GAS SEPARATION

The existing technologies of gas separation based on polymer membranes have been briefly considered in Section 1. Such processes as production of technical grade nitrogen from air, separation of hydrogen from industrial streams of ammonia synthesis, and refinery and petrochemical industry have been realized on large scale. Thousands of such industrial plants are now working worldwide.[2−6] However, there are several problems of membrane separation that have not found (or found only partly) a technical solution. Some of them will be considered in this section with emphasis on novel membrane materials that can improve the parameters of eventual separation processes.

6.1. Separation of He from Natural Gas. The problem of separation of helium from natural gases is one of the oldest in membrane technologies. The first attempts to use polymeric membranes for this purpose were made as early as the 1960s.[103] Helium molecule has a minimal size, and hence very large diffusion and permeability coefficients are typical for He in polymers.[104] The main problem in the membrane separation of helium is that its concentrations in natural gases are very low: the content of 0.4 to 0.5% of helium is considered to be high. Meanwhile, demands for He are growing in electronic industry, atomic power engineering, and other industries. Therefore, specialists in membrane science keep trying to find materials with sufficiently good combinations of $P(He)$ and $\alpha(He/CH_4)$.[46,105] Because of low content of helium in natural gases, high selectivity is the key issue in the search for such materials.

Because of their unusual thermodynamic properties, perfluorinated polymers are a good choice for such membrane materials. Amorphous Teflons AF and perfluorinated copolymers Hyflons are examples of polymers with relatively high permeability $P(He)$ and sufficiently good permselectivity.[46,106] Recently, promising results were obtained for a novel amorphous perfluorinated polymer−poly(hexafluoropropylene).[107]

The data points of several polyimides on Robeson diagrams for He/CH_4 pair are also located above or in vicinity the upper bound of 1991. The common feature of these polymers is the presence of $C(CF_3)_2$ connection groups in the main chains.[108,109] Very permselective membranes can be obtained by direct fluorination of polyimide Matrimid.[110] Zimmerman and Koros[111] also reported very permselective membranes based on fluorine containing polypyrrolone.

6.2. Separation of CO_2 from Gas Mixtures. These processes are also among the oldest in membrane technology. Membrane removal of carbon dioxide from natural gases ("sweetening" of natural gases) before they can be passed to the pipeline has obtained wide distribution since the early 1980s.[2,6] Capture of CO_2 acquired especially great importance because of the problems of environmental protection (related to global warming). Therefore, a search for membrane materials with high permeability $P(CO_2)$ and separation factors $\alpha(CO_2/N_2)$ became very relevant. For the treatment of synthesis gas, another and even more difficult separation problem appears: treatment of H_2/CO_2 mixtures. The challenge of this task is caused by large and similar permeability coefficients of the both components in most polymers.

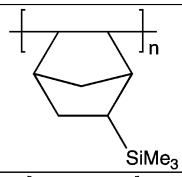
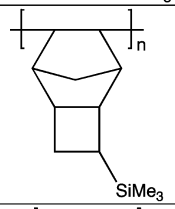
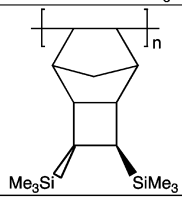
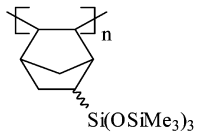
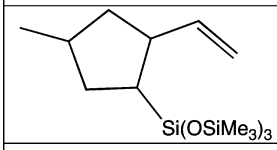
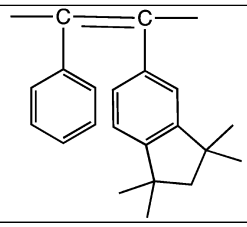
Two types of membrane materials were proven to be the most attractive in this regard. They will be briefly discussed below.

Pebax Copolymers. It was shown that multiblock copolymers having the general formula HO-[C(O)-PA-C(O))-PE-O]$_n$-H, where PA is a hard block of nylon-6 or nylon-12 and PE-O is flexible block of polyethylene oxide, are suitable for the removal of carbon dioxide from gaseous mixtures.[112] Subsequent studies[113−115] showed that high permeability $P(CO_2)$ and separation factors $\alpha(CO_2/N_2)$ and $\alpha(CO_2/CH_4)$ are caused by exceptionally large solubility coefficients of carbon dioxide due to interactions with the PEO component of the material. Cross-linking of poly(ethylene oxide) suppresses the crystallinity normally found in high-molecular-weight, linear poly(ethylene oxide) and makes the membrane even more permeable.[116,117] Some of the cross-linked Pebax membranes showed very impressive transport parameters: CO_2 permeability coefficient of ∼500 Barrer and a mixed gas CO_2/H_2 selectivity of 30 at −20 °C.[116,117] Further investigations of Pebax copolymers and related structures also gave interesting results: $P(CO_2)$ = 110−130 Barrer and $\alpha(CO_2/N_2)$ = 37−49[118] or $P(CO_2)$=98 Barrer and $\alpha(CO_2/N_2)$ = 48.[119]

Composite Membranes Containing Ionic Liquids. Ionic liquids are organic salts having melting points below ambient temperature or at least <100 °C. Examples of ionic liquids are: 1-ethyl-3-methylimidazolium dicyanamide that melts at −21 °C or 1-butyl-3,5 -dimethylpyridinium bromide, which becomes a glass below −24 °C. Among the most common anions of task-specific ionic liquid are bis(trifluoromethylsulfonyl)imide, tetrafluoroborate, and trifluoromethanesulfone. Despite their high cost, ionic liquids offer interesting perspectives for use in membranes for gas separations, especially for capture and removal of CO_2.[120,121] Different types of membranes based on ionic liquids can be fabricated. In supported ionic liquids, selective layer is formed from pure ionic liquid, and a membrane (e.g., inorganic) serves only as a support. The configuration of such membranes is the same as that in well-known impregnated liquid membranes. The advantage of using ionic liquids is a possibility to work at higher temperatures (ionic liquids have high thermal stability and low vapor pressure). Another and maybe more promising type of ionic liquid implies covalent bonding of ionic liquid and polymers. For example, such membrane was prepared by reaction of 6FDA-MDA polyimide with diamino-functionalized ionic liquids.[122] Specific interactions of basic nitrogen of ionic liquids with carbon dioxide make them selective to CO_2 in membrane separations.

dx.doi.org/10.1021/ma300213b | *Macromolecules* 2012, 45, 3298−3311

Table 10. Permeability Coefficients of Hydrocarbons C_1-C_4

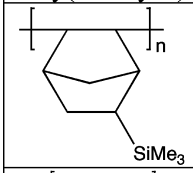
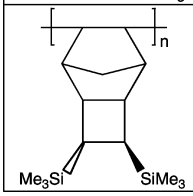
Polymer	*P*, Barrer				Ref
	CH_4	C_2H_6	C_3H_8	C_4H_{10}	
	900	1430	1740	17500	34
	1010	1360	1470	13030	72
	3300	6040	7530	26900	72
	1250	2370	3490	22200	20
	180	270	290	1940	20
PIM-1	430	1500	5500	25100	69
	23100			49600	70

Therefore, separation factors $\alpha(CO_2/N_2)$ as high as 50−55 have been reported for the membranes containing *N*-aminopropyl-3-methylimidazolium bis(trifluoromethylsulfonyl)-imide.[123] A study of supported ionic liquid membranes with the pores of poly(vinylidene fluoride-*co*-hexafluoropropylene) filled with 1-ethyl-3-methyl-imidazolium bis(trifluoromethylsulfonyl)imide showed that common trade-off between permeability and selectivity characteristic for all gas pairs was not observed for CO_2/H_2 pair.[124,125] A good performance of supported liquid membranes using porous ceramic supports was demonstrated by Blath et al.:[126] Permeability coefficients of 600 Barrer and $\alpha(CO_2/N_2) = 20$ can be achieved at 200 °C and pressure drop of 6 bar. However, separation of carbon dioxide from hydrogen or nitrogen can be complicated by the presence of impurities, for example, H_2S.[127] An interesting example[128] indicates that the use of triblock copolymer with the middle block capable of interactions with added ionic liquid results in very permeable and permselective membranes for the separation of carbon dioxide: $P(CO_2)$ is about 1000 Barrer for individual and mixed gas permeation with selectivity $\alpha(CO_2/N_2) = 39$. Hence, this composite membrane exhibits performance somewhat above Robeson's upper bound (2008).

6.3. Separation of Hydrocarbons C_1-C_4 of Natural and Associated Petroleum Gas. The removal of organic vapors from their mixtures with permanent gases, separation of natural and associated petroleum gases, capture of gasoline vapors from air, and so on − all of these technical problems are very important from a practical point of view but found only partial solution. As has been mentioned in Section 2, polymers above their glass-transition temperatures are characterized by higher permeability of heavier hydrocarbons than that of methane. (See, e.g., Table 2.) However, subsequent studies of the polymers with extra-high permeability showed that the same trend is observed for glassy polyacetylenes.[129−132] Such behavior is known as solubility-controlled permeation because in these polymers the variations of the permeability coefficients correlate with the changes of the solubility and not diffusion coefficients, like in other glassy polymers. It was explained by open porosity in highly permeable polyacetylenes.[129] Interestingly, high permeability and high free volume of a membrane

dx.doi.org/10.1021/ma300213b | *Macromolecules* 2012, 45, 3298−3311

Table 11. Transport Parameters for the System CH_4/C_4H_{10}: Individual versus Mixed Gas Permeation

Polymer	Individual gases			Mixed gases			Ref
	$P(C_4)$	$P(C_1)$	$\alpha(C_4/C_1)$	$P(C_4)$	$P(C_1)$	$\alpha(C_4/C_1)$	
PTMSP	78000	15400	5	53500	1800	30	129
Poly(2-nonyne)	1850	64	29	250	55	4.5	130
	17500	900	19	5900	280	21	133
	26900	3300	8.1	11900	920	12.9	133

material are not prerequisites of solubility-controlled permeation: thus, amorphous Teflon AF2400 reveals diffusivity-controlled permeation like conventional glassy polymers.[64]

Recently, it was shown that solubility-controlled permeation of gaseous hydrocarbons C_1-C_4 is characteristic also for addition-type polynorbornenes with Si-containing side groups and for some other polymers. Table 10 indicates that such a trend is not a distinctive feature of polyacetylenes.

There are several common peculiarities in the behavior of the novel polymers and polyacetylenes previously studied. High separation factors $\alpha(C_4H_{10}/CH_4)$ are also observed in mixed gas experiments, where these selectivity are often higher than ideal separation factors, as is seen from Table 11.

In mixed gas permeation in these polymers, the rate of the mass transfer of the less permeable component (CH_4) is not accelerated in the presence of the more permeable component (C_4H_{10}). That is, the plasticization effects that are very important for conventional glassy polymers are not exhibited in the case of polymers described in Tables 10 and 11. A reduction of the P value of the less permeable component is observed in the presence of vapor (C_4H_{10}).[133,134] Such a conclusion was made in the study of the CH_4/C_4H_{10} system[129] and mixtures of SF_6 with He and N_2,[132] in PTMSP, and it is also valid for the norbornene polymers. In contrast with common cases (a trade-off between permeability and permselectivity for different gas pairs), a positive correlation is observed between $P(C_4)$ and $\alpha(C_4/C_1)$ for the polymers described in this Table.

The increases in selectivity in separation of hydrocarbon mixture are caused mainly by the reduction of $P(CH_4)$ and can be explained, as it has been made in ref 129 and 132, by partial blocking of the pores in these membrane materials. These observations make novel Si-containing norbornene polymers potential materials for membranes for the separation of hydrocarbon mixtures if the technical problems of aging and deterioration of membranes under the action of liquid hydrocarbon droplets often present in gas streams are solved.

A development of membrane materials for the separation of hydrocarbons encounters one additional problem. On one hand, the polymers must be soluble, preferably, in hydrocarbon solvents, to cast membranes. On the other hand, the membranes can contact, in the process of exploitation, with droplets of liquid hydrocarbons or aerosols, so reduced solubility in hydrocarbons will be a desirable property. A solution of this contradiction in the case of polyacetylenes was proposed by Khotimsky et al.,[135] who polymerized disubstituted acetylene derivatives in the presence of various catalysts ($TaCl_5$, $NbCl_5$) and cocatalysts and at different temperatures with obtaining polymers having the content of cis configurations of the double bonds in the main chains in the range of 5−80% and different solubility in aliphatic and aromatic hydrocarbons. Meanwhile, these polyacetylenes can be dissolved in such solvents as THF or CCl_4, so there were no problems with film casting.

7. CONCLUDING REMARKS

Therefore, during the past decade, material science of membranes for gas separation made big advances. New ideas appeared. Membrane transport parameters reached the level inaccessible earlier. However, the industry still uses membranes based on polymers developed many years ago. An argument often being advanced in support of such conservatism is that novel membrane materials are too expensive for practical implementation. According to the recommendations issued by DOE (see the references in the review by Ockwig and Nenoff[3]) the cost of membranes had to be less than 100 USD/ft^2 in 2010. Bearing in mind that in contemporary composite membranes the thickness of the selective layers is ∼1 μm (in fact it can be even smaller) and the mass of permselective polymers per 1 m^2 of membrane is ∼1 g, it means that the limiting cost of a membrane polymer must be less than 1000 USD/g. The cost of production of most of the membrane materials discussed in this Perspective is well below this limit. So such an argument seems to be a sort of prejudice.

According to the forecast made in 2002,[2] the total market of membrane gas separation in 2010 would be 350 million USD. However, according to R. W. Baker,[136] the rate of its growth was faster than expected, and it amounted to about 500 million USD in 2010, mainly because of the expansion of the processes of air membrane separation. Therefore, the researchers that work in this field can look forward with optimism.

AUTHOR INFORMATION

Corresponding Author

*E-mail: Yampol@ips.ac.ru.

Notes

The authors declare no competing financial interest.

Biography



Yuri Yampolskii graduated Chemistry Faculty of Lomonosov Moscow State University in 1961 and immediately joined Institute of Petrochemical Synthesis of Russian Academy of Sciences. During the first 15 years of his research, he was involved in the studies of kinetics of hydrocarbon pyrolysis and free radical reactions. Since the mid-1970s he has been engaged in studies in polymer and membrane science, material science of membranes, and membrane gas separation. Yu.Yampolskii is the author and coeditor of 6 monographs and about 300 peer review articles.

REFERENCES

(1) *J. Membr. Sci.* Special Issue, Böddeker, K. W., Ed.; **1995**, *100*, 1−68.
(2) Baker, R. W. *Ind. Eng. Chem. Res.* **2002**, *41*, 1393−1411.
(3) Ockwig, N. W.; Nenoff, T. M. *Chem. Rev.* **2007**, *107*, 4078−4110.
(4) (a) Bernardo, P.; Drioli, E.; Golemme, G. *Ind. Eng. Chem. Res.* **2009**, *48*, 4638−4663. (b) Brunetti, A.; Bernardo, P.; Drioli, E.; Barbieri, G. *Membrane Gas Separation*; Wiley: Chichester, 2010, pp 281−312.
(5) Bernardo, P.; Drioli, E. *Pet. Chem.* **2010**, *50*, 271−282.
(6) Baker, R. W.; Lokhandwala, K. *Ind. Eng. Chem., Res.* **2008**, *47*, 2109−2121.
(7) Barrer, R. M.; Skirrow, G. *J. Polym. Sci.* **1948**, *3*, 549−563.
(8) Michaels, A. S.; Bixler, H. J. *J. Polym. Sci.* **1961**, *50*, 413−439.
(9) Rogers, C. E.; Stannett, V.; Szwarc, M. *J. Polym. Sci.* **1960**, *45*, 61−82.
(10) Meares, P. *J. Am. Chem. Soc.* **1954**, *76*, 3415−3422.
(11) Brandt, W. W.; Anysas, G. A. *J. Appl. Polym. Sci.* **1963**, *7*, 1919−1931.
(12) Robb, W. L. *Ann. N.Y. Acad. Sci.* **1968**, *146*, 119−137.
(13) van Amerongen, G. J. *Rubber Chem. Technol.* **1964**, *37*, 1065−1152.
(14) Hsieh, P. Y. *J. Appl. Polym. Sci.* **1963**, *7*, 1743−1756.
(15) Stern, S. A.; Shah, V. M.; Hardy, B. J. *J. Polym. Sci., Part B: Polym. Phys.* **1987**, *25*, 1263−1298.
(16) Alentiev, A.; Economou, I. G.; Finkelshtein, E.; Petrou, J.; Raptis, V. E.; Sanopoulou, M.; Soloviev, S.; Ushakov, N.; Yampolskii, Yu. *Polymer* **2004**, *45*, 6933−6944.
(17) *Encyclopedia of Polymers*; Soviet Encyclopedia Publishers: Moscow, 1972; Vol. *1*, p 806.
(18) Bartenev, G. M.; Reitlinger, S. A.; Rubinshtein, B. E. *Russ. J. Phys. Chem.* **1956**, *30*, 532−536.
(19) Kawakami, Y.; Sugisaka, T.; Yamashita, Y. *Polym. J.* **1988**, *20*, 685−692.
(20) Bermeshev, M. V.; Syromolotov, A. V.; Gringolts, M. L.; Starannikova, L. E.; Yampolskii, Yu. P.; Finkelshtein, E. Sh. *Macromolecules* **2011**, *44*, 6637−6640.
(21) Harvey, A. *J. Polym. Sci.* **1962**, *57*, 925−935.
(22) Flynn, J. H. *Polymer* **1982**, *23*, 1325−1344.
(23) Vieth, W. R.; Wuerth, W. R. *J. Appl. Polym. Sci.* **1969**, *13*, 685−712.
(24) Puleo, A. C.; Paul, D. R.; Wong, P. K. *Polymer* **1989**, *30*, 1357−1366.
(25) Kanehashi, S.; Kusakabe, A.; Sato, S.; Nagai, K. *J. Membr. Sci.* **2010**, *365*, 40−51.
(26) Allen, S. M.; Fujii, M.; Stannett, V. T.; Hopfenberg, H. B.; Williams, J. L. *J. Membr. Sci.* **1977**, *2*, 153−163.
(27) Merkel, T. C.; Bondar, V. I.; Nagai, K.; Freeman, B. D. *J. Polym. Sci., Part B: Polym. Phys.* **2000**, *38*, 273−296.
(28) Nagai, K.; Masuda, T.; Nakagawa, T.; Freeman, B. D.; Pinnau, I. *Prog. Polym. Sci.* **2001**, *26*, 721−798.
(29) Yampolskii, Yu. *Russ. Chem. Rev.* **2007**, *76*, 59−78.
(30) Plate, N. A.; Yampolskii, Yu. P. In *Polymeric Gas Separation Membranes*; Paul, D. R., Yampolskii, Yu.P., Eds.; CRC Press, Boca Raton, FL, 1994; p 155−207.
(31) Puleo, A. C.; Muruganandam, N.; Paul, D. R. *J. Polym. Sci., Part B: Polym. Phys.* **1989**, *27*, 2385−2406.
(32) Khotimskii, V. S.; Filippova, V. G.; Bryantseva, I. S.; Bondar, V. I.; Shantarovich, V. P.; Yampolskii, Yu. P. *J. Appl. Polym. Sci.* **2000**, *78*, 1612−1620.
(33) Perego, G.; Roggero, A.; Sisto, R.; Valentini, C. *J. Membr. Sci.* **1991**, *55*, 325−331.
(34) Finkelshtein, E.; Makovetsii, K.; Gringolts, M.; Rogan, Yu.; Golenko, T.; Starannikova, L.; Yampolskii, Yu.; Shantarovich, V.; Suzuki, T. *Macromolecules* **2006**, *39*, 7022−7029.
(35) Kim, H.-J.; Hong, S.-I. *J. Appl. Polym. Sci.* **2000**, *76*, 391−400.
(36) Pixton, M. R.; Paul, D. R. In *Polymeric Gas Separation Membranes*; Paul, D. R., Yampolskii, Y. P., Eds.; CRC Press: Boca Raton, FL, 1994; pp 83−154.
(37) Langsam, M.; Burgoyn, W. F. In *The 1990 International Congress on Membranes and Membrane Processes*, Proceedings of ICOM '90, Chicago, IL, 1990; Vol. *1*, pp 809−811.
(38) Coleman, M. R.; Koros, W. J. *J. Membr. Sci.* **1990**, *50*, 285−297.
(39) (a) Hirayama, Y.; Yoshinaga, T.; Nakanishi, S.; Kusuki, Y. In *Polymer Membranes for Gas and Vapor Separation: Chemistry and Materials Science*; Freeman, B. D., Pinnau, I., Eds.; American Chemical Society: Washington, DC; pp 194−214, 1999. (b) Tanaka, K.; Okano, M.; Toshino, H.; Kita, H.; Okamoto, K.-I. *J. Polym. Sci., Part B: Polym. Phys.* **1992**, *30*, 907−914.
(40) Alentiev, A.; Yampolskii, Yu. In *Materials Science of Membranes for Gas and Vapor Separation*, Yampolskii, Yu., Pinnau, I., Freeman, B. D., Eds.; Wiley: Chichester, U.K., 2006; pp 211−229.
(41) Robeson, L. M.; Smith, C. D.; Langsam, M. *J. Membr. Sci.* **1997**, *132*, 33−54.
(42) Alentiev, A.; Loza, K.; Yampolskii, Yu. *J. Membr. Sci.* **2000**, *167*, 91−106.
(43) Bicerano, J. *Prediction of Polymer Properties*; Marcel Decker: New York, 1996.
(44) Wessling, M. Ph.D. Thesis, Twente University, Twente, The Netherlands, 1993.
(45) Robeson, L. M. *J. Membr. Sci.* **1991**, *62*, 165−185.
(46) Robeson, L. M. *J. Membr. Sci.* **2008**, *320*, 390−400.
(47) Hofmann, D.; Fritz, L.; Ulbrich, J.; Schepers, C.; Böning, M. *Macromol. Theory Simul.* **2000**, *9*, 293−327.
(48) Theodorou, D. N. In *Materials Science of Membranes for Gas and Vapor Separation*; Yampolskii, Yu., Pinnau, I., Freeman, B.D., Eds.; Wiley: Chichester, U.K., 2006; pp 49−94.
(49) Fried, J. In *Materials Science of Membranes for Gas and Vapor Separation*; Yampolskii, Yu., Pinnau, I., Freeman, B.D., Eds.; Wiley: Chichester, U.K., 2006; pp 95−136.
(50) Neyertz, S. In *International Congress on Membranes, Book of Abstracts*; ICOM2011, Amsterdam, The Netherlands, 2011; ICOM1856.

(51) Hofmann, D.; Heuchel, M.; Yampolskii, Yu.; Khotimskii, V.; Shantarovich, V. *Macromolecules* **2002**, *35*, 2129−2140.
(52) Neyertz, S.; Brown, D. *Macromolecules* **2009**, *42*, 8521−8533.
(53) Neyertz, S.; Brown, D. *Macromolecules* **2008**, *41*, 2711−2721.
(54) Wang, X. Y.; Lee, K. M.; Lu, Y.; Stone, M. T.; Sanchez, I. C.; Freeman., B. D. *Polymer* **2004**, *45*, 3907−3912.
(55) Neyertz, S.; Brown, D. *J. Chem. Phys.* **2001**, *115*, 708−717.
(56) Willmore, F. T.; Wang, X.; Sanchez, I. C. *J. Polym. Sci., Part B: Polym. Phys.* **2006**, *44*, 1385−1393.
(57) Neyertz, S., private communication.
(58) Neyertz, S.; Brown, D.; Pandiyan, S.; van der Vegt, N. F. A. *Macromolecules* **2010**, *43*, 7813−7827.
(59) Teplyakov, V. V.; Evseenko, A. L.; Novitskii, E. G.; Durgaryan, S. G. *Plast. Massy* **1978**, *#5*, 49−51.
(60) Yampolskii, Yu. P.; Durgaryan, S. G.; Nametkin, N. S. *Vysokomol. Soedin., Ser. B* **1979**, *21*, 616−621.
(61) Masuda, T.; Isobe, E.; Higashimura, T.; Takada, K. *J. Am. Chem. Soc.* **1983**, *105*, 7473−7474.
(62) Ichiraku, Y.; Stern, S. A.; Nakagawa, T. *J. Membr. Sci.* **1987**, *34*, 5−18.
(63) Pinnau, I.; Toy, L. G. *J. Membr. Sci.* **1996**, *109*, 125−133.
(64) Alentiev, A.; Yampolskii, Yu.; Shantarovich, V.; Nemser, S. M.; Plate, N. *J. Membr. Sci.* **1997**, *126*, 123−132.
(65) Tokarev, A. V.; Bondarenko, G. N.; Yampolskii, Yu. P. *Vysokomol. Soed., A* **2007**, *49*, 1510−1523.
(66) Merkel, T. C.; Pinnau, I.; Prabhakar, R.; Freeman, B. D. In *Materials Science of Membranes for Gas and Vapor Separation*; Yampolskii, Yu., Pinnau, I., Freeman, B. D., Eds.; Wiley: Chichester, U.K., 2006; pp 251−270.
(67) (a) McKeown, N. B.; Makhseed, S.; Budd, P. M. *Chem. Commun.* **2002**, 2780−2781. (b) McKeown, N. B.; Budd, P. M.; Msayib, K. J.; Ghanem, B. S.; Kingstone, H. J.; Tettershall, C. E.; Makhseed, S.; Reynolds, K. J.; Fritsch, D. *Chem.—Eur. J.* **2005**, *11*, 2610−2620. (c) Budd, P. M.; Msayib, K. J.; Tettershall, C. E.; Ghanem, B. S.; Reynolds, K. J.; McKeown, N. B.; Fritsch, D. *J. Membr. Sci.* **2005**, *251*, 263−269. (d) Budd, P. M.; McKeown, N. B.; Ghanem, B. S.; Msayib, K. J.; Fritsch, D.; Starannikova, L.; Belov, N.; Sanfirova, O.; Yampolskii., Yu.; Shantarovich, V. *J. Membr. Sci.* **2008**, *325*, 851−860. (e) Ghanem, B.; McKeown, N. B.; Budd, P. M.; Al-Harbi, N. M; Fritsch, D.; Heinrich, K.; Starannikova, L.; Tokarev, A.; Yampolskii, Yu. *Macromolecules* **2009**, *42*, 7881−7888. (f) Emmler, T.; Heinrich, K.; Frotsch, D.; Budd, P. M.; Chaukura, N.; Ehlers, D.; Rätzke, K.; Faupel, F. *Macromolecules* **2010**, *43*, 6075−6084.
(68) (a) Staiger, C. L.; Pas, S. J.; Hill, A. J.; Cornelius, C. J. *Chem. Mater.* **2008**, *20*, 2606−2608. (b) Thomas, S.; Pinnau, I.; Du, N.; Guiver, M. D. *J. Membr. Sci.* **2009**, *333*, 125−131.
(69) (a) Li, F. Y.; Xiao, Y.; Chung, T.-S.; Kawi, S *Macromolecules* **2012**, *45*, 1427−1437. (b) Li, F. Y.; Xiao, Y.; Ong, Y. K.; Chung, T.-S. *Adv. Energy Mater.* **2012**, submitted.
(70) Hu, Y.; Shiotsuki, M.; Sanda, F.; Freeman, B. D.; Masuda, T. *Macromolecules* **2008**, *41*, 8525−8532.
(71) Starannikova, L.; Pilipenko, M.; Belov, N.; Yampolskii, Yu.; Gringolts, M.; Finkelshtein, E. *J. Membr. Sci.* **2008**, *323*, 134−143.
(72) Gringolts, M.; Bermeshev, M.; Yampolskii, Yu.; Starannikova, L.; Finkelshtein, E. *Macromolecules* **2010**, *43*, 7165−7172.
(73) Aroon, M. A.; Ismail, A. F.; Matsuura, T.; Montazer-Rahmati, M. M. *Sep. Purif. Technol.* **2010**, *75*, 229−242.
(74) Chung, T.-S. L.; Jiang, Y.; Li, Y.; Kulprathipanja, S. *Prog. Polym. Sci.* **2007**, *32*, 483−507.
(75) Cong, H.; Radosz, M.; Towler, B. F.; Shen, Y. *Sep. Purif. Technol.* **2007**, *55*, 281−291.
(76) Lipatov, Yu. S. *Physical Chemistry of Filled Polymers*; Naukova Dumka Publishers, Kiev, Ukraine, 1967.
(77) Barrer, R. M. In *Diffusion and Permeation in Heterogeneous Media*; Crank, J., Park, G.S., Eds.; Academic Press: London, 1968; p 165.
(78) Merkel, T. C.; Freeman, B. D.; Spontak, R. J.; He, Z.; Pinnau, I.; Meakin, P.; Hill, A. J. *Science* **2002**, *296*, 519−522.
(79) Merkel, T. C.; He, Z.; Pinnau, I.; Freeman, B. D.; Meakin, P.; Hill, A. J. *Macromolecules* **2003**, *36*, 8406−8414.
(80) Golemme, G.; Jansen, J. C.; Muoio, D.; Bruno, A.; Manes, R.; Buonomenna, M. G.; Choi, J.; Tsapatsis, M. In *Membrane Gas Separation*; Yampolskii, Yu., Freeman, B. D., Eds.; Wiley: Chichester, U.K., 2010; pp 113−124.
(81) Sen, D.; Kalipcilar, H.; Yilmaz, L. *J. Membr. Sci.* **2007**, *303*, 194−203.
(82) Ahn, J.; Chung, W.-J.; Pinnau, I.; Guiver, M. D. *J. Membr. Sci.* **2008**, *314*, 123−133.
(83) Matteucci, S.; Raharjo, R. D.; Kusuma, V. A.; Swinnea, S.; Freeman, B. D. *Macromolecules* **2008**, *41*, 2144−2166.
(84) Kwon, S.-M.; Sik, H.-S.; Kim, D.-Y.; Yun, Y. S.; Jin, H.-J. *J. Appl. Polym. Sci.* **2008**, *110*, 3737−3744.
(85) Vu, D. Q.; Koros, W. J.; Miller, S. J. *J. Membr. Sci.* **2003**, *211*, 311−334.
(86) Hu, Q.; Marand, E.; Dhingra, S.; Fritsch, D.; Wen, J.; Wilkes, G. *J. Membr. Sci.* **1997**, *135*, 65−79.
(87) Yave, W.; Peinemann, K.-V.; Shishatskiy, S.; Khotimskiy, V.; Chirkova, M.; Matson, S.; Litvinova, E.; Lecerf, N. *Macromolecules* **2007**, *40*, 8991−8998.
(88) Takahashi, S.; Paul, D. R. *Polymer* **2006**, *47*, 7519−7534.
(89) Zhang, Y.; Musselman, I. H.; Ferraris, J. P.; K. Balkus, J. *J. Membr. Sci.* **2008**, *319*, 170−181.
(90) Yang, T.; Xiao, Y.; Chung, T.-S. *Energy Environ. Sci.* **2011**, *4*, 4171−4180.
(91) Ahn, J.; Chung, W.-J.; Pinnau, I.; Song, J.; Du, N.; Robertson, G. P.; Guiver, M. D. *J. Membr. Sci.* **2010**, *346*, 280−287.
(92) Bushell, A. F.; Attfield, M. P.; Mason, C. R.; Budd, P. M.; Yampolskii, Yu.; Starannikova, L.; Rebrov, A.; Bazzarelli, F.; Bernardo, P.; Jansen, J. C.; Lanč, M.; Friess, K. *J. Membr. Sci.* **2012**, submitted.
(93) (a) Hill, R. J. *Ind. Eng. Chem. Res.* **2006**, *45*, 6890−6898. (b) Gonzo, E. E.; Parentis, M. L.; Gottifredi, J. C. *J. Membr. Sci.* **2006**, *277*, 46−54. (c) Moore, T. T.; Koros, W. J. *J. Mol. Struct.* **2005**, *739*, 87−98. (d) Pal, R. J. *Colloids Interface Sci.* **2008**, *317*, 191−198.
(94) Teraguci, M.; Masuda, T. *Macromolecules* **2002**, *35*, 1149−1151.
(95) (a) Sakaguchi, T.; Yumoto, K.; Shiotsuki, M.; Sanda, F.; Yoshikawa, M.; Masuda, T. *Macromolecules* **2005**, *38*, 2704−2709. (b) Sakaguchi, T.; Shiotsuki, M.; Masuda, T. *Macromolecules* **2004**, *37*, 4104−4108.
(96) Sakaguchi, T.; Kwak, G.; Masuda, T. *Polymer* **2002**, *43*, 3937−3942.
(97) Wang, X.-Y.; Raharjo, R. D.; Lee, H. J.; Lu, Y.; Freeman, B. D.; Sanchez, I. C. *J. Phys. Chem. B* **2006**, *110*, 12666−12672.
(98) Kita, H. In *Materials Science of Membranes for Gas and Vapor Separation*; Yampolskii, Yu., Pinnau, I., Freeman, B. D., Eds.; Wiley: Chichester, U.K., 2006; pp 337−354.
(99) Park, H. B.; Jung, C. H.; Lee, Y. M.; Hill, A. J.; Pas, S. J.; Mudie, S. T.; Van Wagner, E.; Freeman, B. D.; Cookson, D. J. *Science* **2007**, *318*, 254−258.
(100) Choi, J. I.; Jung, C. H.; Han, S. H.; Park, H. B.; Lee, Y. M. *J. Membr. Sci.* **2010**, *349*, 358−368.
(101) Hodgkin, J. H.; Dao, B. N. *Eur. Polym. J.* **2009**, *45*, 3081−3092.
(102) Hodgkin, J. H.; Liu, M. S.; Dao, B. N.; Mardel, J.; Hill, A. J. *Eur. Polym. J.* **2011**, *47*, 394−400.
(103) Stern, S. A.; Sinclair, T. F.; Gareis, P. J.; Vahldieck, N. P.; Mohr, P. H. *Ind. Eng. Chem.* **1965**, *57*, 49−60.
(104) Pauli, S. In *Polymer Handbook*; Brandrup, J., Emmergut, E. H., Grulke, E. A., Eds.; Wiley Interscience: New York, 1999; Vol. 2; p VI/543.
(105) Merkel, T. C.; Pinnau, I.; Prabhakar, R.; Freeman, B. D. Gas and Vapor Transport Properties of Perfluoropolymers. In *Materials Science of Membranes for Gas and Vapor Separation*; Yampolskii, Yu., Pinnau, I., Freeman, B. D., Eds.; Wiley, Chichester, U.K., 2006; pp 251−270.
(106) Jansen, J. C.; Maccione, M.; Drioli, E. *J. Membr. Sci.* **2007**, *287*, 132−137.
(107) Belov, N. A.; Zharov, A. A.; Shashkin, A. V.; Shaikh, M. Q.; Raetzke, K.; Yampolskii, Yu.P. *J. Membr. Sci.* **2011**, *383*, 70−77.

(108) Costello, L. M.; Koros, W. J. *J. Polym. Sci., Part B: Polym. Phys.* **1995**, *33*, 135−146.
(109) Coleman, M. R.; Koros, W. J. *J. Polym. Sci., Part B: Polym. Phys.* **1994**, *32*, 1915−1926.
(110) D.A Syrtsova, D. A.; Kharitonov, A. P.; Teplyakov, V. V.; Koops, G.-H. *Desalination* **2004**, *163*, 273−279.
(111) Zimmerman, C. M.; Koros, W. J. *J. Polym.Sci.: Part B: Polym. Phys.* **1999**, *37*, 1235−1249.
(112) Blume, I.; Pinnau, I. U.S. Patent 4,963,165, 1990.
(113) Bondar, V. I.; Freeman, B. D.; Pinnau, I. *J. Polym. Sci., Part B: Polym. Phys.* **2000**, *38*, 2051−2062.
(114) Kim, J. H.; Ha, S. Y.; Lee, Y. M. *J. Membr. Sci.* **2001**, *190*, 179−193.
(115) Bondar, V. I.; Freeman, B. D.; Pinnau, I. *J. Polym. Sci., Part B: Polym. Phys.* **1999**, *37*, 2463−2475.
(116) Lin, H.; van Wagner, E.; Freeman, B. D.; Toy, L. G.; Gupta, R. P. *Science* **2006**, *311* (5761), 639−642.
(117) Freeman, B. D. In *International Congress on Membranes, Book of Abstracts*; ICOM2011, Amsterdam, The Netherlands, 2011; ICOM1788.
(118) Car, A.; Yave, W.; Peinemann, K.-V.; Stropnik, C. In *Membrane Gas Separation*; Yampolskii, Yu., Freeman, B. D., Eds.; Wiley: Chichester, U.K., 2010; pp 227−253.
(119) Nguyen, Q. T.; Sublet, J.; Langevin, D.; Chappey, C.; Marais, S.; Valleton, J.-M.; Poncin-Epaillard, F. In *Membrane Gas Separation* Yampolskii, Yu.; Freeman, B. D., Eds.; Wiley: Chichester, U.K., 2010; pp 255−277.
(120) Scovazzo, P. *J. Membr. Sci.* **2009**, *343*, 199−211.
(121) Scovazzo, P.; Kieft, J.; Finan, D. A.; Koval, C.; DuBois, D.; Noble, R. D. *J. Membr. Sci.* **2004**, *238*, 57−63.
(122) Li, P.; Coleman, M. In *International Congress on Membranes, Book of Abstracts*; ICOM2011, Amsterdam, The Netherlands, 2011; ICOM580.
(123) Iaarikov, D. D.; Hacarlioglu, P.; Oyama., S. T. *Chem. Eng. J.* **2011**, *166*, 401−406.
(124) Jansen, J. C.; Friess, K.; Clarizia, G.; Bernardo, P.; Bazzarelli, F.; Schauer, J.; Jarmarova, V.; Kacirkova, M.; Izak, P. In *International Congress on Membranes, Book of Abstracts*; ICOM2011, Amsterdam, The Netherlands, 2011; ICOM1067
(125) Jansen, J. C.; Clarizia, G..; Friess, K.; Schauer, J.; Izák, P. *Macromolecules* **2011**, *44*, 39−45.
(126) Blath, J.; Hirth, T.; Schiestel, T. In *International Congress on Membranes, Book of Abstracts*; ICOM2011, Amsterdam, The Netherlands, 2011; ICOM545.
(127) Myers, C. R.; Luebke, D. R.; Pennline, H. W.; Ilconich, J. B.; Wickramanayake, S. In *Membrane Gas Separation*; Yampolskii, Yu., Freeman, B. D., Eds.; Wiley: Chichester, U.K., 2010; pp 183−199.
(128) Gu, Y.; Lodge, T. P. *Macromolecules* **2011**, *44*, 1732−1736.
(129) Pinnau, I.; Toy, L. G. *J. Membr. Sci.* **1996**, *116*, 199−209.
(130) Pinnau, I.; Morisato, A.; He, Z. *Macromolecules* **2004**, *37*, 2823.
(131) Morisato, A.; Pinnau, I. *J. Membr. Sci.* **1996**, *121*, 243−250.
(132) Srinivasan, R.; Auvil, S. R.; Burban, P. M. *J. Membr. Sci.* **1994**, *86*, 67−86.
(133) Grinevich, Yu.; Starannikova, L.; Yampolskii, Yu.; Gringolts, M.; Finkelshtein, E. *J. Membr. Sci.* **2011**, *378*, 250−256.
(134) Grinevich, Yu.; Starannikova, L.; Yampolskii, Yu.; Gringolts, M.; Finkelshtein, E. *Pet. Chem.* **2011**, *51*, 585−594.
(135) (a) Khotimsky, V. S.; Tchirkova, M. V.; Litvinova, E. G.; Rebrov, A. I.; Bondarenko, G. N. *J. Polym. Sci., Part A: Polym. Chem.* **2003**, *41*, 2133−2155. (b) Sultanov, E. Yu.; Ezhov, A. A.; Shishatskiy, S. M.; Buhr, K.; Khotimskiy, V. S. *Macromolecules* **2012**, *45*, 1222−1229.
(136) Baker, R. W., personal communication.

Macromolecules

Article

pubs.acs.org/Macromolecules

Hybrid Copolymerization of ε-Caprolactone and Methyl Methacrylate

Hongjun Yang,[†] Jinbao Xu,[‡] Stergios Pispas,*[,§] and Guangzhao Zhang*[,†,‡]

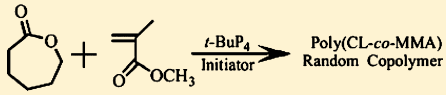
[†]Hefei National Laboratory for Physical Sciences at Microscale, Department of Chemical Physics, University of Science and Technology of China, Hefei 230026, P. R. China

[‡]Faculty of Materials Science and Engineering, South China University of Technology, Guangzhou 510640, P. R. China

[§]Theoretical and Physical Chemistry Institute, National Hellenic Research Foundation, 48 Vassileos Constantinou Avenue, 11635 Athens, Greece

Supporting Information

ABSTRACT: Copolymerization of ε-caprolactone and methyl methacrylate with (1-*tert*-butyl-4,4,4-tris(dimethylamino)-2,2-bis[tris(dimethylamino)-phophoranylidenamino]-2Λ5,Λ5-catenadi(phosphazene) (*t*-BuP$_4$) as the catalyst has been studied. Nuclear magnetic resonance (NMR) and differential scanning calorimetry (DSC) measurements indicate that the cyclic ester and vinyl monomer form a random copolymer. Thermogravimetric analysis (TGA) measurements demonstrate that such a random copolymer exhibits a decomposition temperature higher than those of the corresponding homopolymers. The present study reveals a "hybrid copolymerization" i.e., a combination of vinyl polymerization and ring-opening polymerization, which makes the incorporation of cyclic and vinyl monomers into the same polymer chain possible. Hybrid copolymerization is expected to produce a number of new interesting polymers.



INTRODUCTION

Copolymerization of cyclic monomers with vinyl monomers is very interesting because it can produce new types of copolymers and open up new research directions in the fields of polymer chemistry and of polymer applications. However, it is very difficult because the reactivity and polymerization mechanism of the two types of monomers are extremely different. So far, only the copolymerization of *N*-phenylmaleimide (electrophilic) with some nucleophilic cyclic monomers via zwitterion was reported.[1−4] For common vinyl monomers and cyclic monomers, the copolymerization has not been realized yet.

(1-*tert*-Butyl-4,4,4-tris(dimethylamino)-2,2-bis[tris-(dimethylamino)-phosphoranylidenamino]-2Λ^5,4Λ^5-catenadi-(phosphazene) (*t*-BuP$_4$) can independently catalyze ring-opening polymerization (ROP) of cyclic esters and anionic addition polymerization of vinyl monomers with alcohol or ethyl acetate (EA) as the initiator.[5−15] In the present work, we report that *t*-BuP$_4$ can catalyze the copolymerization of ε-caprolactone (CL) with methyl methacrylate (MMA,) yielding a random copolymer.

EXPERIMENTAL SECTION

Materials. ε-Caprolactone (CL) from Aldrich was dried over calcium hydride (CaH$_2$) and distilled under reduced pressure prior to use. Ethylene glycol (EG) and methanol (MeOH) from Aldrich were dried over sodium with nitrogen protective atmosphere and distilled under vacuum after refluxing for hours. Ethyl acetate (EA) from Sinopharm was washed with aqueous 5% Na_2CO_3, dried with K_2CO_3, and then distilled from CaH_2. Methyl methacrylate (MMA) from Sinopharm was distilled from CaH_2 and stored under a nitrogen atmosphere at −20 °C. Tetrahydrofuran (THF) and toluene (TOL) from Sinopharm were freshly distilled from sodium/benzophenone and stored under an argon atmosphere. *t*-BuP$_4$ and 1-naphthalene-methanol (NMA) from Aldrich were used as received. Other reagents from Sinopharm were used as received.

Characterization. *Nuclear Magnetic Resonance.* ^{1}H NMR, ^{13}C NMR, and 2D NMR spectra (^{1}H−^{1}H COSY and ^{1}H−^{13}C HMBC NMR spectra) were recorded on a Bruker AV400 NMR spectrometer by using deuterated chloroform ($CDCl_3$) as solvent and tetramethylsilane (TMS) as internal standard.

Size Exclusion Chromatography (SEC). The molecular weight and polydispersity index (PDI) were measured at 35 °C on a Waters SEC equipped with a model 510 pump, a differential refractive index detector model 410 (RI), and a Waters 2487 UV detector working at a wavelength of 254 nm. A series of monodisperse polystyrenes were used as standards. THF was used as the eluent at a flow rate of 1.0 mL/min.

Thermal Analysis. Thermogravimetric analysis (TGA) was performed on a TA SDT Q600 instrument under nitrogen atmosphere at a heating rate of 10 °C/min in the range 25−500 °C. Differential scanning calorimetry (DSC) was conducted on a TA Instruments Q2000 under a nitrogen flow of 50 mL/min. Samples were quickly heated to 150 °C and kept for 10 min to remove thermal history and then cooled to −80 °C at a rate of 10 °C/min. Finally, they were reheated to 150 °C at the same rate.

Polymerization of CL in the presence of t-BuP$_4$. A typical polymerization was performed as follows. CL (0.46 g, 4 mmol, 100 equiv), EA (3.90 μL, 0.04 mmol, 1.0 equiv), and toluene (0.5 mL) were placed in a flamed and nitrogen purged round-bottom flask equipped with a magnetic stirrer. *t*-BuP$_4$ (40 μL, 0.04 mmol, 1.0 equiv

Received: February 11, 2012
Revised: March 29, 2012
Published: April 12, 2012

 © 2012 American Chemical Society

Table 1. Characterization Data of the Polymers[a]

sample	f^b (mol/mol)	initiator	$M_n \times 10^{-4}$ (g/mol)	M_w/M_n	$f_p{}^c$ (mol %)	conv.$_{CL}$ (mol %)	conv.$_{MMA}$ (mol %)
S1	0/100	MeOH	2.34	1.96	100		100
S2	25/75	MeOH	2.05	2.32	76.1	100	99.0
S3	50/50	MeOH	2.82	1.72	55.9	100	100
S4	75/25	MeOH	1.61	1.54	29.0	97.2	99.3
S5	100/0	MeOH	1.91	1.45	0	100	
S6	100/0	EA	1.87	1.50	0	100	
S7	50/50	MeOH	1.47	1.84	54.8	99.0	100
S8	50/50	MeOH	1.93	1.71	53.2	100	100
S9	50/50	EG	3.14	4.36	49.6	99.5	98.1
S10	50/50	EA	2.56	2.26	62.3	100	100
S11	25/25	MeOH	0.81	1.44	54.5	100	100
S12	100/100	MeOH	4.13	1.67	50.2	99.6	100
S13	50/50	NMA	4.73	2.01	49.6	100	100
S14[d]	10/10	MeOH	0.18	2.87	54.2	87.4	76.8
F1[e]	50/50	MeOH	2.14	1.39	55.7		
F2[f]	50/50	MeOH	5.06	1.23	56.1		

[a]Molar ratio of monomer to initiator is 100/1 except samples S11 (50/1), sample S12 (200/1) and sample S14 (20/1), reaction temperature is 25 °C except that in S8 (−25 °C), solvent is THF except that in S7 (toluene). [b]Molar ratio of CL to MMA. [c]Molar fraction of MMA units in the copolymer determined by ^{1}H NMR. [d]The reaction time is 2 min. [e]The low molecular weight fraction from sample S3. [f]The high molecular weight fraction from sample S3.

in hexane) was added through a rubber septum with a syringe to start the polymerization at 25 °C. The reaction was terminated with hydrochloric acid/methanol (1/20 v/v) after one hour. The product was dissolved in CH_2Cl_2 and precipitated into a large excess of cold methanol. The polymer was dried under vacuum. Polymerizations of CL or MMA initiated by MeOH were carried out using a similar procedure.

Copolymerization of CL and MMA. A typical copolymerization was performed as follows. CL (0.23 g, 2 mmol, 50 equiv), MMA (0.20 g, 2 mmol, 50 equiv), MeOH (2.24 μL, 0.04 mmol, 1.0 equiv), and toluene (0.5 mL) were placed in a flamed and nitrogen purged round-bottom flask equipped with a magnetic stirrer. The flask was placed in an oil bath at 25 °C. *t*-BuP_4 (40 μL, 0.04 mmol, 1.0 equiv in hexane) was added through a rubber septum with a syringe to start the polymerization. The polymerization was completed in 12 h and was terminated with hydrochloric acid/methanol (1/20 v/v). The product was dissolved in THF and precipitated into a large excess of cold methanol. The polymer was dried under vacuum. Copolymerization of CL and MMA under other reaction conditions was carried out using a similar procedure, and the results are summarized in Table 1.

RESULTS AND DISCUSSION

Copolymerization of CL and MMA was first investigated in THF at room temperature with MeOH as the initiator. The molar ratio of [MMA]/[CL]/[*t*-BuP_4]/[MeOH] was 50/50/1/1. Figure 1 shows the typical ^{1}H NMR spectra of the resulting copolymer. The signals at 1.25−1.47, 1.51−1.71, 2.18−2.40, and 3.96−4.17 ppm are due to the protons in CL units. The signals at 0.72−1.16, 1.72−2.14, and 3.51−3.71 ppm are assigned to MMA units. Note that for PMMA homopolymer, a singlet peak at around 3.5−3.7 ppm can be observed for the methoxy proton (−OCH_3). However, the peak corresponding to the methoxy proton of MMA unit for the copolymer shows splitting, indicating the presence of the comonomeric sequence with different configurations or the formation of CL/MMA copolymer.[16] In addition, the molar fraction (f_p) of MMA in the copolymer determined by ^{1}H NMR was approximately equal to the feed ratio (f) (Table 1). To further verify the copolymerization, we synthesized a low molecular weight sample (S14) with degree of polymerization (DP) of 17, where the polymerization was terminated with hydrochloric acid/methanol (1/20 v/v) within two minutes. The ^{1}H NMR spectrum (Figure S1 in Supporting Information) of the sample is similar to that of the sample (S3) with DP of 100, indicating that copolymerization is rapid and occurs at the initial stage of the allowed polymerization time. This is also supported by the high degree of conversion for both monomers at the short polymerization time.

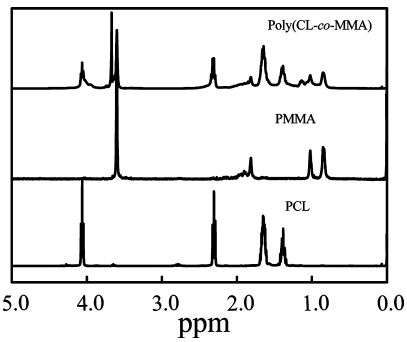


Figure 1. ^{1}H NMR spectra for poly(CL-*co*-MMA) copolymer (sample S3), PCL (sample S5), and PMMA (sample S1).

Figure 2 shows the ^{13}C NMR spectra for poly(CL-*co*-MMA) copolymer. In comparison with the spectra of PCL and PMMA homopolymers (see Figures S2 and S3 in Supporting Information), we can observe three new peaks. The peaks at 33.9.7−33.9 and 51.4−51.5 ppm are assigned to the quaternary (−$CH_2C(CH_3)(COOCH_3)CO$−) and secondary carbons (−$OCH_2C(CH_3)(COOCH_3)$−) in MMA unit in the proximity of the CL unit. The peak at 173.9−174.0 ppm is due to the ester carbonyl (−$C(CH_3)(COOCH_3)CO$−) of CL unit adjacent to a MMA unit. Clearly, CL and MMA copolymerize into a random copolymer (poly(CL-*co*-MMA) with mixed triad sequences.

Figure 3 shows the two-dimensional ^{1}H−^{13}C HMBC NMR spectra of a poly(CL-*co*-MMA) copolymer. Clearly, the protons of −CH_3 in MMA units at 0.78−1.01 ppm are related to that of the −OCH_2 carbon atom, indicating the presence of CL-MMA sequences in the copolymer chain. On the other hand, the

dx.doi.org/10.1021/ma300291q | *Macromolecules* 2012, 45, 3312−3317

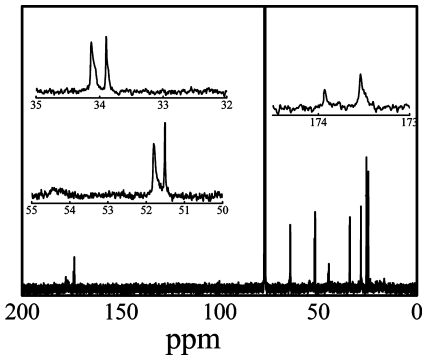


Figure 2. ^{13}C NMR spectra for poly(CL-*co*-MMA) copolymer (sample S3).

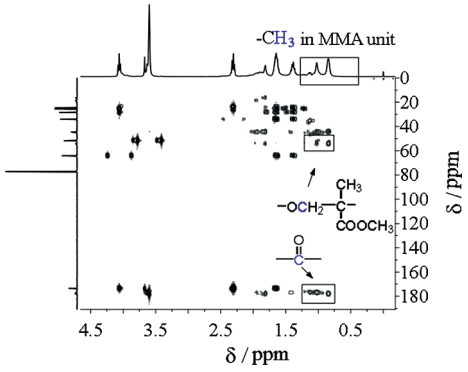


Figure 3. ^{1}H−^{13}C HMBC NMR spectra for the copolymers initiated by MeOH (sample S3).

protons of $-CH_3$ in MMA units have a correlation with the ester carbonyl atom in CL units at 173.9−174.0 ppm, indicating that the copolymer chain has MMA-CL sequences. These observations further demonstrate that the derived poly(CL-*co*-MMA) is a random copolymer.

Figure 4 shows SEC curves for the resultant polymer (RI detection). The SEC-RI curve displays a bimodal distribution,

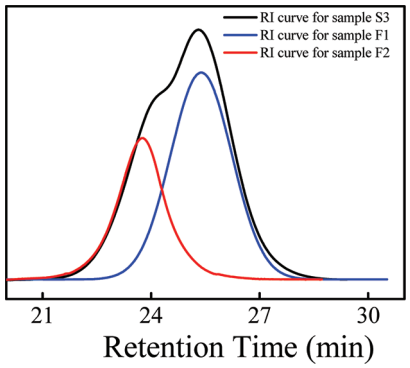


Figure 4. SEC curves for the poly(CL-*co*-MMA) copolymer before and after fractional precipitation (sample S3).

suggesting the presence of two components with quite different molecular weights. The two components (samples F1 and F2) were separated by fractional precipitation. It was found, by NMR, that they have similar compositions (f_p), although they possess different molecular weights (Table 1). Accordingly, the bimodal molecular weight distribution may be due to the nucleophile attack on carbonyl group of MMA, which often happens during anionic polymerization of MMA.[17−19] However, probably because of their low content, signals related to such bonds were not detected in NMR spectra.

Figure 5 shows the DSC curves for the resulting copolymers. All the copolymers exhibit only one glass transition. Sample S4

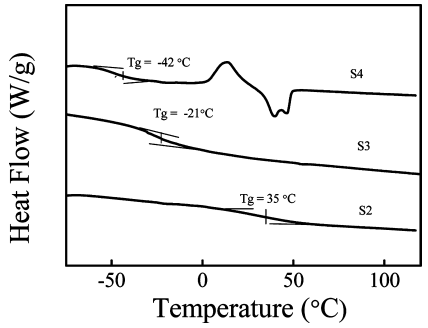


Figure 5. DSC curves for the poly(CL-*co*-MMA) copolymers (S2−S4) at a heating rate of 10 °C/min.

with higher CL content also shows a melting point, presumably due to crystallization of CL segments. The glass transition temperature (T_g) is between those of poly(methyl methacrylate) (PMMA) ($T_g \sim 115$ °C) and poly(ε-caprolactone) (PCL) ($T_g \sim -60$ °C) homopolymers (see Figures S4 and S5 in Supporting Information), and T_g decreases with CL content in the copolymer. Particularly, the T_g values agree with those predicted by the Fox equation.[20] Similar results were obtained at the scanning rate of 5 °C/min. Thus, the NMR and DSC results indicate that CL and MMA segments are randomly distributed along the polymer chain. In addition, when CL content is low enough (e.g., for samples S2 and S3), the melting endotherm specific to PCL is no longer observed, further indicating the random incorporation of MMA and CL units. In the case of sample S4, CL sequences are long enough for the formation of crystallites.

Figure 6 shows the TGA curves of poly(CL-*co*-MMA), together with those for PMMA and PCL homopolymers. PCL

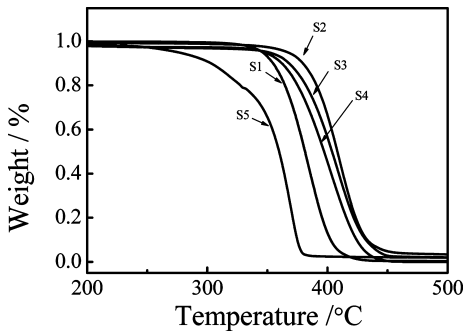


Figure 6. TGA curves for poly(CL-*co*-MMA) (samples S2 to S4), PMMA (sample S1), and PCL (sample S5) homopolymers.

starts to degrade at about 250 °C in a nitrogen atmosphere, and degradation is completed at about 380 °C. For PMMA, the degradation begins at about 330 °C and ends at about 420 °C. All copolymers exhibit improved thermostability in comparison with the two homopolymers, and the thermal decomposition temperature increases with MMA content in the range of f_p from 29.0 mol % to 76.1 mol %. This should be associated with the chemical connection of the CL and MMA units in the

dx.doi.org/10.1021/ma300291q | *Macromolecules* 2012, 45, 3312−3317

copolymer. Anyhow, this fact further indicates that CL and MMA form random copolymers under the applied polymerization conditions.

We also investigated the effect of different initiators (MeOH, EA, and EG) on the copolymerization (Table 1). Each SEC curve for the copolymer in Figure 7 shows multiple peaks,

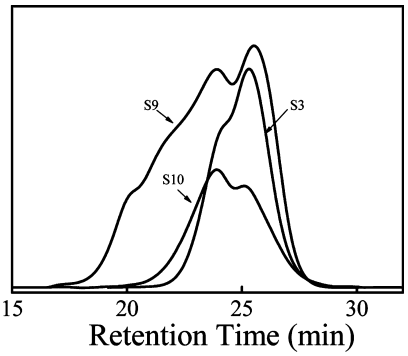


Figure 7. SEC curves for the copolymers initiated by MeOH (sample S3), EA (sample S10), and EG (sample S9), respectively.

indicating several species with different molecular weights. The polymerization with EA or MeOH as the initiator makes a little difference in the molecular weight and molecular weight distribution of the copolymer. However, the initiation by EG (a potential difunctional initiator) results in a higher molecular weight (M_n = 3.14 × 10^4 g/mol) and a broader PDI (M_w/M_n = 4.36). This is probably because the chain grows from the two active centers in EG.[21]

To gain some insight into initiator efficiency, 1-naphthalenemethanol with a UV-active aromatic moiety was also used to initiate the copolymerization. Figure 8 shows SEC curves for

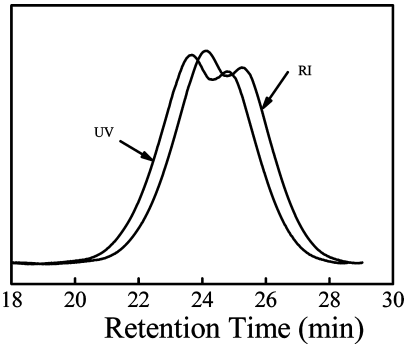


Figure 8. SEC curves for the copolymer initiated by 1-naphthalenemethanol by RI and UV detection, respectively.

the resultant polymer (RI and UV detection). Either the SEC trace monitored with RI detector or that obtained with UV detector has a bimodal distribution, suggesting two components with quite different molecular weights. More importantly, they are similar in shape and are characterized by the same retention time, indicating that the two components should have similar chemical structures,[22] and that the initiator group is incorporated onto the chain end without chain scission taking place.

To ensure that *t*-BuP_4 acts as the organocatalyst, the polymerization without initiator has been examined. The yield was found to be only 7.2%. The limited polymerization observed in this case may be initiated by trace amounts of active hydrogens present in the monomers or *t*-BuP_4 solution.[23] The experimental results demonstrate that *t*-BuP_4 acts as a catalyst in the particular copolymerization. In addition, a number of experiments carried out in parallel show that NaOMe cannot initiate the CL/MMA copolymerization. Thus, a simple deprotonation mechanism under the influence of *t*-BuP_4 should not be operative in this copolymerization system.

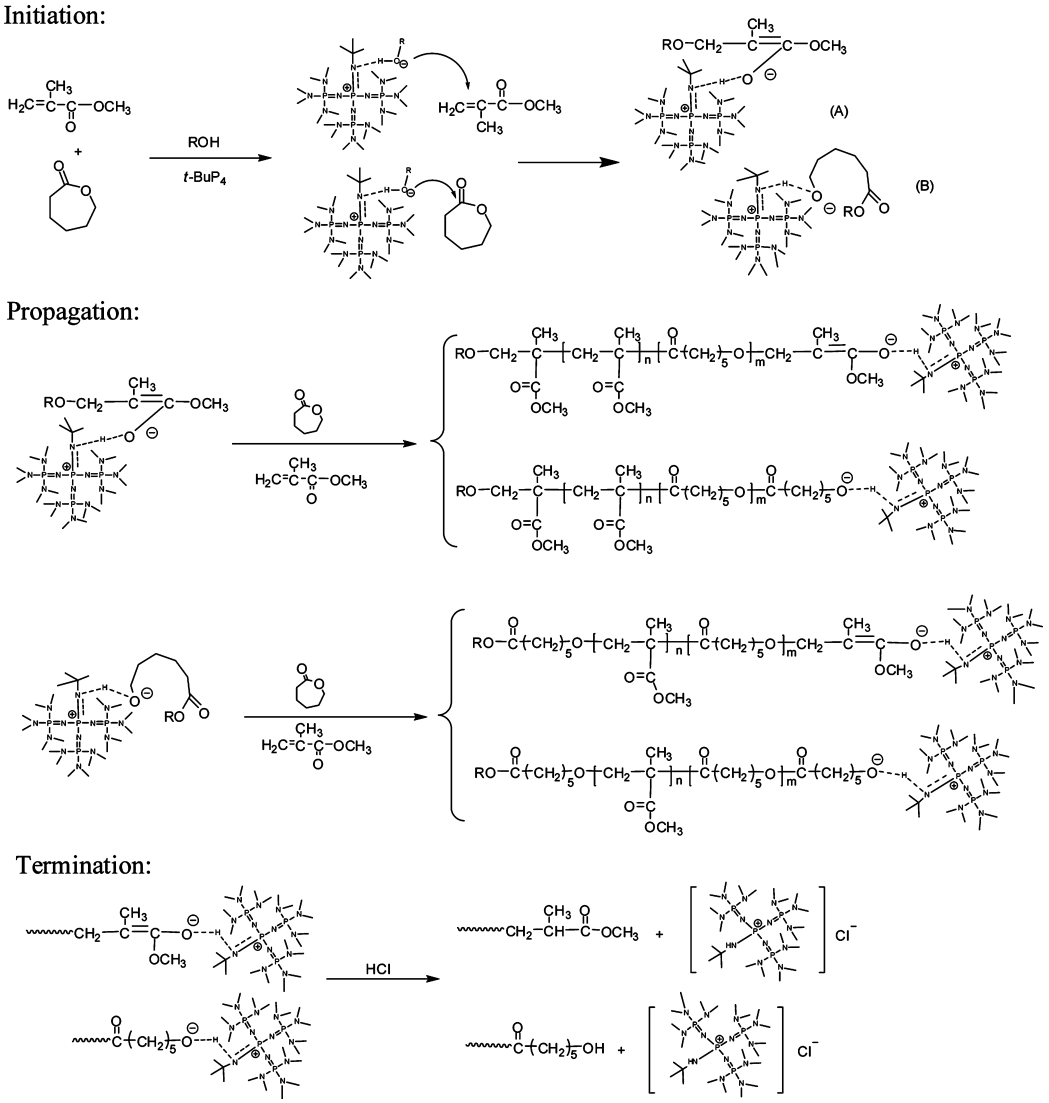
The polymerization was also conducted in toluene, and no significant effects were observed by changing the solvent. Polymerization at a temperature as low as −25 °C shows that temperature has little effect on the polymerization outcome (Table 1). The results summarized in Table 1 also show that the molecular weight distribution (M_w/M_n) of the copolymer increases as the molar ratio of MMA increases in the feed. This is probably because the propagating nucleophile adds to the carbonyl of MMA segments.[17−19]

On the basis of the results at hand, we suggest that the copolymerization of CL and MMA catalyzed by *t*-BuP_4 involves the following steps (Scheme 1). (1) Initiation. This step follows a hydrogen bonding mechanism.[24−27] Phosphazene base (*t*-BuP_4) first activates the alcohol by the intermolecular hydrogen bonding, and the nucleophilic attack on the monomer produces two kinds of active centers (A and B). (2) Propagation. Both of the active centers react with either MMA or CL to form new active centers, and the reactive intermediate is continuously regenerated by addition of monomers leading to a long active chain. (3) Termination. The propagating chain is deactivated by the addition of hydrochloric acid.

The scheme shown above does not represent all details during polymerization but depicts some general aspects of the polymerization process. The mechanism of the copolymerization seems complex, and some parallel reactions/transformations and side reactions may happen. For example, the nucleophilic active centers may add onto the carbonyl of MMA segments,[17−19] leading to a broader molecular weight distribution. Isomerization of hydrogen bonded stabilized "pseudo-enolate" type ions (where the negative charge is located mostly on the O atom) to vinyl type carbanions (where the negative charge is located on the terminal vinylic C atom) may take place so that the monomers are incorporated into the copolymer main chain via addition to the C═C bonds. Multicenter interactions involving the dimethylamino groups of *t*-BuP_4 are also possible. Chain transfer and chain termination in other ways could occur, e.g., reaction of active centers with CL carbonyl or complete abstraction of H from protonated phosphazene by reaction with a MMA type active chain end carbanion, leading to the regeneration of the free base. More studies are needed to fully elucidate all aspects of the reaction mechanism which, however, are beyond the scope of the present manuscript but will be the subject of future work. It should be noted that this copolymerization is quite different from that taking place via zwitterions, where the electrophilic and nucleophilic monomers react to generate a zwitterionic intermediate and the resulting copolymers usually have alternating structures.[28,29] In the present copolymerization, each monomer can form propagating species, which can further combine with either similar or dissimilar monomers, forming a random copolymer. Therefore, we propose the term "hybrid polymerization" for this type of copolymerization between cyclic and vinyl monomers via organocatalysis with *t*-BuP_4 base.

dx.doi.org/10.1021/ma300291q | *Macromolecules* 2012, 45, 3312−3317

Scheme 1. Possible Mechanism for CL/MMA Hybrid Copolymerization



CONCLUSIONS

In conclusion, copolymerization of CL with MMA is possible and can be carried out using *t*-BuP_4 as the organocatalyst. Characterization data demonstrate that the resulting copolymer has a random structure and exhibits a decomposition temperature higher than those of the homopolymers. The hybrid polymerization presented here is applicable to a common cyclic ester and a vinyl monomer. Thus, a number of new polymers with interesting properties can be produced by this polymerization. Studies are in progress that are aiming at a better control of the polymerization reaction in order to produce more well-defined polymers, i.e., by the use of different phosphazene bases. The elucidation of the mechanism of the hybrid copolymerization is another future goal.

ASSOCIATED CONTENT

Supporting Information

DSC curves and NMR spectra of some samples. This material is available free of charge via the Internet at http://pubs.acs.org.

AUTHOR INFORMATION

Corresponding Author

*Phone: +86-20-22236373. Fax: +86-20-22236373. E-mail: msgzzhang@scut.edu.cn.

Notes

The authors declare no competing financial interest.

ACKNOWLEDGMENTS

The financial support of National Program on Key Basic Research Project (2012CB933802), the National Distinguished Young Investigator Fund (20725414), and the Fundamental Research Funds for the Central Universities is acknowledged.

REFERENCES

(1) Simionescu, C. I.; Grigoras, M.; Bicu, E.; Onofrei, G. *Polym. Bull.* **1985**, *14*, 79−83.
(2) Rivas, B. L.; del C. Pizarro, G.; Canessa, G. S. *Polym. Bull.* **1988**, *19*, 123−128.
(3) Hagiwara, T.; Takeda, M.; Hamana, H.; Narita, T. *Macromolecules* **1989**, *22*, 2025−2026.
(4) Ikeda, Y.; Yoshida, Y.; Ishihara, K. *Macromol. Rapid Commun.* **1996**, *17*, 713−721.

(5) Zhang, L.; Nederberg, F.; Pratt, R. C.; Waymouth, R. M.; Hedrick, J. L.; Wade, C. G. *Macromolecules* **2007**, *40*, 4154−4158.
(6) Winter, J. D.; Coulembier, O.; Gerbaux, P.; Dubois, P. *Macromolecules* **2010**, *43*, 10291−10296.
(7) Pietzonka, T.; Seebach, D. *Angew. Chem., Int. Ed.* **1993**, *32*, 716−717.
(8) Makiguchi, K.; Satoh, T.; Kakuchi, T. *Macromolecules* **2011**, *44*, 1999−2005.
(9) Zhang, L.; Pratt, R. C.; Nederberg, F.; Horn, H. W.; Rice, J. E.; Waymouth, R. M.; Wade, C. G.; Hedrick, J. L. *Macromolecules* **2010**, *43*, 1660−1664.
(10) Boileau, S.; Illy, N. *Prog. Polym. Sci.* **2011**, *36*, 1132−1151.
(11) Nederberg, F.; Connor, E. F.; Müller, M.; Glauser, T.; Hedrick, J. L. *Angew. Chem., Int. Ed.* **2001**, *40*, 2712−2715.
(12) Lohmeijer, B. G. G.; Pratt, R. C.; Leibfarth, F.; Logan, J. W.; Long, D. A.; Dove, A. P.; Nederberg, F.; Choi, J.-S.; Wade, C.; Waymouth, R. M.; Hedrick, J. L. *Macromolecules* **2006**, *39*, 8574−8583.
(13) Pratt, R. C.; Lohmeijer, B. G. G.; Long, D. A.; Waymouth, R. M.; Hedrick, J. L. *J. Am. Chem. Soc.* **2006**, *128*, 4556−4557.
(14) Schmalz, H.; Lanzendörfer, M. G.; Abetz, V.; Müller, A. H. E. *Macromol. Chem. Phys.* **2003**, *204*, 1056−1071.
(15) Kakuchi, T.; Chen, Y.; Kitakado, J.; Mori, K.; Fuchise, K.; Satoh, T. *Macromolecules* **2011**, *44*, 4641−4647.
(16) Grabe, N.; Zhang, Y.; Agarwal, S. *Macromol. Chem. Phys.* **2011**, *212*, 1327−1334.
(17) Bhattacharya, A.; Misra, B. N. *Prog. Polym. Sci.* **2004**, *29*, 767−814.
(18) Hong, K. L.; Uhrig, D.; Mays, J. W. *Curr. Opin. Solid State Mater. Sci.* **1999**, *4*, 531.
(19) Allen, P. E. M.; Casey, B. A.; Dankiw, W. *J. Macromol. Sci., , Part A: Pure App.l Chem.* **1970**, *4*, 1091−1103.
(20) Fox, T. G. *Bull. Am. Phys. Soc.* **1956**, *1*, 123−124.
(21) Warzelhan, V.; Höcker, H.; Schulz, G. V. *Makromol. Chem.* **1980**, *181*, 149−163.
(22) Laguna, M. T. R.; Gallego, J.; Mendicuti, F.; Saiz, E.; Tarazona, M. P. *Macromolecules* **2002**, *35*, 7782−7790.
(23) Zhao, J. P.; Zhang, G. Z.; Pispas, S. *J. Polym. Sci., Part A: Polym. Chem.* **2011**, *48*, 2320−2328.
(24) Mori, S.; Suzuki, T. *J. Liq. Chromatogr.* **1981**, *4*, 1685−1696.
(25) Zhang, L.; Nederberg, F.; Messman, J. M.; Pratt, R. C.; Hedrick, J. L.; Wade, C. G. *J. Am. Chem. Soc.* **2007**, *129*, 12610−12611.
(26) Kamber, N. E.; Jeong, W.; Waymouth, R. M.; Pratt, R. C.; Lohmeijer, B. G. G.; Hedrick, J. L. *Chem. Rev.* **2007**, *107*, 5813−5840.
(27) Kiesewetter, M. K.; Shin, E. J.; Hedrick, J. L.; Waymouth, R. M. *Macromolecules* **2010**, *43*, 2093−2107.
(28) Saegusa, T.; Kobayashi, T.; Kimura, Y; Chow, T.; Kobayashi, S. *Macromolecules* **1979**, *12*, 533−535.
(29) Saegusa, T.; Kimura, Y; Ishikawa, N.; Kobayashi, S. *Macromolecules* **1976**, *9*, 724−727.

Macromolecules

Article

pubs.acs.org/Macromolecules

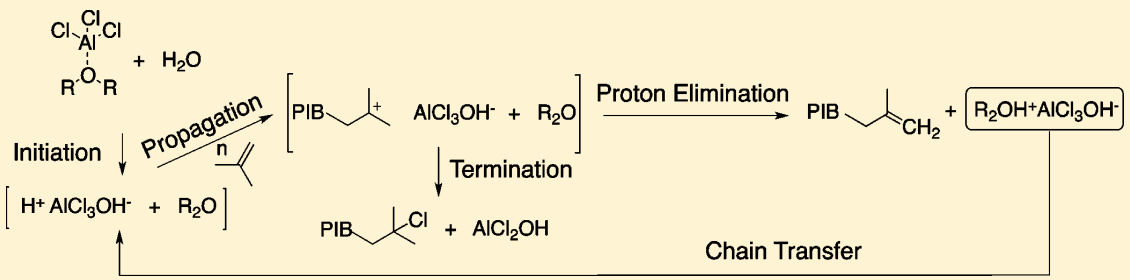
Polymerization of Isobutylene by $AlCl_3$/Ether Complexes in Nonpolar Solvent

Philip Dimitrov,[†] Jack Emert,[‡] and Rudolf Faust*[,†]

[†]Polymer Science Program, Department of Chemistry, University of Massachusetts Lowell, One University Avenue, Lowell, Massachusetts 01854, United States

[‡]Infineum USA, 1900 E. Linden Avenue, Linden, New Jersey 07036, United States

Supporting Information



ABSTRACT: The carbocationic polymerization of isobutylene (IB), co-initiated by $AlCl_3$/ether complexes, has been reexamined and extended to different dialkyl ethers. In the absence of a proton trap, 2,6-di-*tert*-butylpyridine (DTBP), the polymerization of IB by the cumyl alcohol (CumOH)/$AlCl_3$·nBu_2O initiator/co-initiator system in dichloromethane/hexanes (80/20 v/v) at −40 °C gave high conversion to polyisobutylene (PIB) comprising exo-olefins with high selectivity, similar to that reported before by Vasilenko et al.[1,2] However, in the presence of DTBP, polymerization was absent, suggesting that CumOH is not an initiator in conjunction with $AlCl_3$·Bu_2O, and the true initiator is adventitious water. Similarly, in the presence of DTBP in hexanes at 0 °C, polymerizations were absent not only with CumOH but with CumCl, *tert*-butanol, and 2-chloro-2,4,4-trimethylpentane. The polymerization of IB could be initiated only with adventitious water in the absence of DTBP, but monomer conversions and exo-olefin content (60−70%) were much lower than in a polar solvent and the PIBs exhibited M_n = 700−4200 with high polydispersities (PDI ∼ 3−5). The separate addition of ether followed by $AlCl_3$ to the polymerization mixture resulted in conventional PIB with high trisubstituted olefinic content. The previously proposed mechanism is inadequate, as it cannot explain all the observations. Mechanistic studies suggest that the reaction of water with $AlCl_3$·R_2O yields $H^+AlCl_3OH^-$, which initiates the polymerization, and free ether, which abstracts a β-proton from the growing chain end before it diffuses from the immediate vicinity of the polymer cation. Accordingly, the role of the complex is to deliver the ether to close proximity of the propagating end.

INTRODUCTION

The carbocationic polymerization of isobutylene (IB) is a subject of great scientific and industrial interest.[3] Low molecular weight (M_n ∼ 500−5000) olefin end-functional PIB is a precursor to motor oil and fuel additives with worldwide production in excess of 750 000 tons per year. Two major industrial methods are currently employed to produce low molecular weight IB homo- or copolymers with olefinic end groups. The "conventional" process uses a C_4 mixture and $AlCl_3$- or $EtAlCl_2$-based catalyst systems and gives polybutenes with high trisubstituted olefinic content.[4,5] A mechanism has been proposed recently to explain the complex set of isomerization reactions responsible for tri- and tetrasubstituted olefinic content.[6] Because of the low reactivity of the tri- and tetrasubstituted olefinic end groups, polybutenes need to be chlorinated to react with maleic anhydride to give polybutenylsuccinic anhydride, which is reacted with oligoalkylenimines to yield polybutenylsuccinimide ashless dispersants. The other method employs pure IB and BF_3 complexes with either alcohols or ethers and yields highly reactive PIBs (HR PIBs) with 75−85% exo-olefinic end-group content.[7] PIB exo-olefins readily react with maleic anhydride in a thermal "ene" reaction to produce PIB succinic anhydride. Because the final product does not contain any chlorine, HR PIB is more desirable than polybutenes.

In recent decades, several new methods for the synthesis of HR PIB were reported (adequately reviewed in ref 1), but none of them gained industrial acceptance, likely due to the high cost (low temperature, expensive chemicals). Recently, Vasilenko et al.[1] and Liu et al.[8] reported that $AlCl_3$·dibutyl ether and $AlCl_3$·diisopropyl ether complexes in dichloromethane (DCM) or in DCM/hexanes 80/20 (v/v) mixtures at moderate

Received: February 23, 2012
Revised: April 4, 2012
Published: April 13, 2012

 © 2012 American Chemical Society dx.doi.org/10.1021/ma3003856 | *Macromolecules* 2012, 45, 3318−3325

Table 1. Polymerization of [IB] = 1 M at −40 °C in DCM/Hex = 80/20 v/v for 3 min ([CumOH] = 0.018 M)

no.	[Bu_2O·$AlCl_3$] (M)	[DTBP] (M)	conv (%)	initiator effic (%)	M_n (SEC)	PDI (SEC)	M_n (NMR)	[PIB] (M)[b]	exo (%)	endo (%)
1[a]	0.020	0	80	74	3700	2.1	2500	0.0179	100	0
2	0.022	0	78	69	3300	2.1	2500	0.0175	100	0
3	0.022	0	89	80	2300	2.1	3300	0.0151	97	3
[ref 1]	0.022	0	62	75	1560	1.5	n.d.	0.022	91	
4	0.022	0.006	0	0						
5	0.028	0.006	0	0						
6	0.032	0.006	1	3			1000	0.0006	97	3

[a][CumOH] = 0.02 M. [b]M_n(NMR) were used for the calculation of [PIB]; M_n(SEC) was used for the calculation of [PIB] if M_n(NMR) was not available.

temperatures give HR PIB with exo-olefinic end-groups in excess of 90%. Later, Liu et al. also reported the use of $FeCl_3$·diisopropyl ether complexes for the polymerization of IB to yield HR PIB in DCM.[9] Most recently, Vasilenko et al. studied the effect of solvent polarity, temperature, and initiator.[2] With the CumOH/$AlCl_3$·Bu_2O system in hexane, monomer conversions and initiator efficiencies were low,[10] and the PIBs exhibited broad molecular weight distributions. The exo-olefinic end group content was also lower compared to that obtained in polar solvent.

This new technique is intriguing from a mechanistic point of view and may replace the BF_3 process if it can be applied in nonchlorinated hydrocarbon solvents. In the present contribution, the polymerization of IB co-initiated by $AlCl_3$/ether complexes in hexanes was studied with emphasis on the possible initiators, mechanisms of initiation, chain transfer and termination, and mechanisms of deactivation of the $AlCl_3$/ether co-initiator.

EXPERIMENTAL SECTION

Materials. Hexanes and dichloromethane (DCM) were purified as described previously.[6] Isobutylene (IB, Matheson Tri Gas) gas was dried by passing it through in-line gas-purifier columns packed with BaO and then condensed in a receiver flask at −80 °C before use. $AlCl_3$ (Aldrich 99.99%), cumyl alcohol (CumOH, 97%, Aldrich), *tert*-butyl alcohol (tBuOH, 99.6%, anhydrous, Aldrich), dibutyl ether (Bu_2O, Aldrich anhydrous 99.3%), diisopropyl ether (iPr_2O, Aldrich, anhydrous 99%), di-*sec*-butyl ether (sec-Bu_2O, 96%, Aldrich), diisobutyl ether (iBu_2O, 99%, TCI America), and di-*tert*-butylpyridine (DTBP, 97%, Aldrich) were used as received. 2-Chloro-2,4,4-trimethylpentane (TMPCl) was synthesized according to ref 11.

Polymerization of IB. Polymerizations were performed under a dry N_2 atmosphere in a MBraun 150-M glovebox (Innovative Technology Inc., Newburyport, MA). IB was condensed and distributed to the polymerization reactors, screw-top culture tubes (75 mL), at −40 °C. Polymerization were done in DCM/hexanes 80/20 (v/v), or in hexanes, co-initiated with $AlCl_3$/ether complex (typically from 0.005 to 0.02 M) at monomer concentrations of [IB] = 0.2−1 M, at temperatures ranging from −40 to 0 °C and terminated with NH_4OH. The polymer was recovered from the organic layer, solvents were evaporated, and the final PIB was dried until constant weight.

Preparation of $AlCl_3$/Ether Complexes. $AlCl_3$/ether complexes were prepared shortly before the polymerization of IB. In the glovebox, dry DCM was added to $AlCl_3$ powder, which was only partially soluble. Then, an equimolar amount of ether was added slowly while stirring to form a 1 M $AlCl_3$/ether complex solution.

Characterization. *Size Exclusion Chromatography.* Molecular weights and dispersities of the polymers were obtained from size exclusion chromatography (SEC) with universal calibration using a Waters 717 Plus autosampler, a 515 HPLC pump, a 2410 differential refractometer, a 2487 UV−vis detector, a MiniDawn multi angle laser light scattering (MALLS) detector (measurement angles are 44.7°, 90.0°, and 135.4°) from Wyatt Technology Inc., a ViscoStar viscosity detector from Wyatt, and five Ultrastyragel GPC columns connected in the following order: 500, 10^3, 10^4, 10^5, and 100 Å. RI was the concentration detector. Tetrahydrofuran was used as the eluent at a flow rate of 1.0 mL/min at room temperature. The results were processed by the Astra 5.4 software from Wyatt Technology Inc.

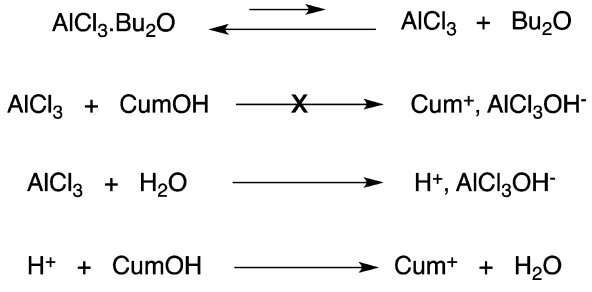
Nuclear Magnetic Resonance. Proton nuclear magnetic resonance (^{1}H NMR) spectra were recorded on a Bruker 500 MHz spectrometer using $CDCl_3$ or CD_2Cl_2 as solvents (Cambridge Isotope Lab., Inc.). ^{27}Al NMR spectra were taken on a Bruker spectrometer operating at 62.9 MHz. Reference was $[Al(H_2O)_6]^{3+}$ in H_2O as external standard.[12]

RESULTS AND DISCUSSION

Polymerization of IB by $AlCl_3$/Ether Complexes in DCM/Hexanes 80:20 (v/v). It was reported previously that the polymerization of IB by CumOH/$AlCl_3$·Bu_2O initiator/co-initiator system in DCM/hexane (80/20 v/v) at −40 °C gives HR PIB with relatively high IB conversion in 3 min of polymerization time.[1] The proposed mechanism suggested ionization of CumOH with free $AlCl_3$ generated by the dissociation of $AlCl_3$·Bu_2O complex, propagation, and proton abstraction by the free ether. Interestingly, in the absence of CumOH, IB conversion and exo-olefin content were similar. We performed polymerizations of IB under the same conditions in the absence and in the presence of the proton trap DTBP in order to evaluate the significance of adventitious water for the overall process. Polymerization results are collected in Table 1. It was possible to reproduce the previously reported results—the obtained PIBs had up to 100% exo-olefin content, and the apparent initiator efficiency was around 80%. The only difference was the observed molecular weight, which in our case was up to 2 times higher. However, in the presence of DTBP, polymerization was not observed, even at increased $AlCl_3$·Bu_2O concentrations (runs 4, 5, and 6, Table 1).

Thus, it can be concluded that CumOH is not an initiator with $AlCl_3$·Bu_2O alone (Scheme 1). We suggest that ionization

Scheme 1



dx.doi.org/10.1021/ma3003856 | Macromolecules 2012, 45, 3318−3325

Table 2. Polymerization of [IB] = 0.91 M Initiated by $AlCl_3$·Bu_2O in Hexanes at −20 °C ([$AlCl_3$·Bu_2O] = 0.022 M)

no.	time (min)	yield (%)	M_n (NMR)	M_n	PDI	tri (%)	exo (%)	endo (%)	tetra (%)
7	20	14	1800	2600	4.4	0	85	8	7
8	40	16	1782	2100	12.0	0	81	9	10
9	60	21	1970	2300	8.7	0	82	8	10
10[a]	60	21	2000	1800	2.3	0	79	9	11

[a][TMPCl] = 0.015 M.

Table 3. Polymerization of IB (1 M) by $AlCl_3$/Ether Systems in Hexanes at 0 °C for 20 min

									PIB end groups distribution		
no.	initiator	[initiator] (M)	conv (%)	[DTBP] (M)	M_n (NMR)	M_n (SEC)	PDI (SEC)	[PIB][f] (M)	exo (%)	tri + endo (%)	tetra (%)
11[a]	adventitious H_2O	~4×10^{-4}	35	0	4100	4 000	4.1	0.0048	60	14	26
12[b]	TMPCl	0.015	0	0.006							
13[c]	CumCl	0.015	0	0.006							
14[d]	CumOH	0.02	0	0.006							
15[e]	tBuOH	0.02	0	0.006							

[a][$AlCl_3$·iPr_2O] = 0.010 M. [b][$AlCl_3$·Bu_2O] = 0.022 M. [c][$AlCl_3$·iPr_2O] = 0.022 M. [d][$AlCl_3$·Bu_2O] = 0.020 M. [e][$AlCl_3$·iPr_2O] = 0.020 M. [f]M_n(NMR) were used for the calculation of [PIB].

Table 4. Polymerization of IB in Hexanes at 0 °C for 20 min Co-initiated by [R_2O·$AlCl_3$] = 0.005 M (R = Bu, iPr, sec-Bu, or iBu)

								PIB end groups distribution		
no.	[IB] (M)	LA·LB	conv (%)	M_n (NMR)	M_n (SEC)	PDI	[PIB][a] (M)	exo (%)	endo + tri (%)	tetra (%)
16	0.2	$AlCl_3$·Bu_2O	1	1000			0.0001	72	13	15
17	0.4		2	1800			0.0002	66	16	18
18	0.6		4	2400	2400	5.8	0.0006	63	15	21
19	0.8		9	2800	2600	6.8	0.0014	63	15	22
20	0.2	$AlCl_3$·iPr_2O	10	700	620	5.2	0.0016	74	14	12
21	0.4		13	1200	1100	4.3	0.0024	70	14	16
22	0.6		18	1700	1800	4.6	0.0036	65	15	20
23	0.8		30	2000	2000	4.9	0.0067	65	14	21
24	0.2	$AlCl_3$·sec-Bu_2O	26	860	1000	4.5	0.0034	60	24	16
25	0.4		35	1500	1800	4.6	0.0052	53	25	22
26	0.6		43	1800	2000	5	0.0080	54	22	24
27	0.8		56	2400	2800	4.5	0.0105	47	24	29
28	0.2	$AlCl_3$·iBu_2O	20	1400	1400	5.8	0.0032	54	25	21
29	0.4		28	2200	2400	5.1	0.0076	54	21	25
30	0.6		33	3100	3600	4.9	0.0036	54	19	26
31	0.8		52	3700	4200	4.4	0.0063	52	18	30

[a]M_n(NMR) were used for the calculation of [PIB].

of CumOH is an indirect process and requires an initial reaction of the $AlCl_3$ with the adventitious H_2O to give $H^+AlCl_3OH^-$, which ionizes CumOH (Scheme 1).

As expected, when tBuOH was used instead of CumOH at the same conditions (Table S2), polymerization was also absent in the presence of 0.006 M DTBP.

Polymerization of IB by $AlCl_3$/Ether Complexes in Hexanes. In hexanes, IB conversions (Table 2) were generally much lower than in DCM/hexanes (80/20 v/v) and also lower than that (65% in 30 min) reported by Vasilenko and co-workers at −20 °C, possibly due to the lower concentration of adventitious water in our case.[2] As expected in the presence of TMPCl conversions and M_ns remained unchanged, indicating that TMPCl does not initiate the polymerization in conjunction with $AlCl_3$·Bu_2O.

Polymerizations were also performed in hexanes at 0 °C typically for 20 min. Similarly to the DCM/hexanes (80/20 v/v) system, CumOH and tBuOH did not initiate the polymerization of IB (Table 3). Also, even the most efficient cationic initiators for IB polymerization such as TMPCl and CumCl could not initiate polymerization in the presence of a proton trap (Table 3). Apparently, the reactivity of $AlCl_3$/ether complex is too low, and active cationic species could be generated only from adventitious moisture.

The results of polymerizations utilizing different dialkyl ethers as a function of IB concentration are summarized in Table 4. The polydispersity indices of the polymers were high (PDI = 4.3−6.8), which may be attributed to the heterogeneous nature of the polymerization. Indeed, upon the addition of $AlCl_3$/ether complex to the polymerization mixture, a fine white precipitate was observed. Other PIB end groups as well as tri- and tetrasubstituted olefins were also observed as a result of carbocationic rearrangements and chain scission at the end of the PIB chain due to delayed proton abstraction from the growing PIB^+ by the ether molecule (Figure 1).[13] The yields and the exo-olefinic content of the PIBs were directly related to

dx.doi.org/10.1021/ma3003856 | Macromolecules 2012, 45, 3318−3325

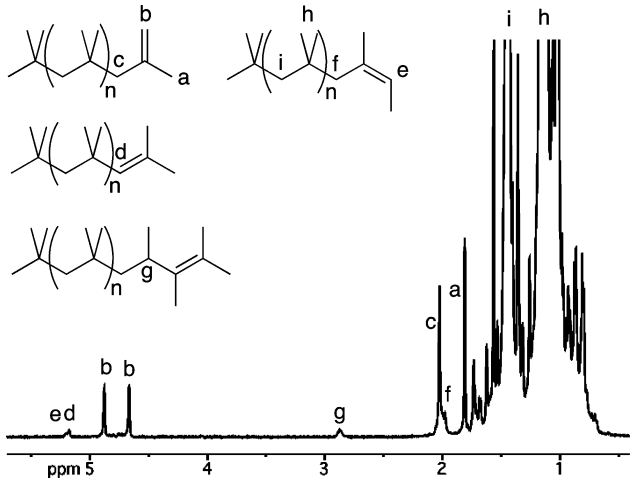


Figure 1. ^{1}H NMR spectrum of PIBs obtained by polymerization of IB in hexanes at 0 °C for 20 min co-initiated by [$AlCl_3$·Bu_2O] = 0.005 M and adventitious H_2O.

the type of ether used. The ethers employed have similar proton affinities (Table S1) so steric factors must have influenced the proton abstraction process. $AlCl_3$·Bu_2O gave PIB with high exo-olefinic end-group content, but yields were below 10%. $AlCl_3$·iPr_2O gave similar end-group distribution and somewhat higher IB conversions. More sterically hindered ethers, such as sec-Bu_2O and iBu_2O, gave higher IB conversions up to 56%, but the exo-olefinic end-group content was lower. With increasing solvent polarity conversions and exo-olefinic content increased (Table S3) up to 100% and 89%, respectively, with $AlCl_3$·iPr_2O in DCM/hexanes (80/20 v/v) at 0 °C.

An attempt to increase monomer conversion was made by saturating hexanes with water ($[H_2O]_{sat}$ = 4 × 10^{-4} M at 0 °C)[14] by washing with deionized water. As seen in Table 4, the IB conversion increased to 90% while the exo-olefin content remained similar. Attempts were also made to increase the exo-olefin content by increasing the concentration of free ether. The exo-olefin content did increase (Table 5), suggesting faster proton abstraction; however, monomer conversion decreased.

Time studies in Table 6 revealed that the polymerization was very rapid, and 60% conversion was obtained within the first minute of polymerization. Additional $AlCl_3$·iPr_2O introduced after 20 min increased the yield only marginally (sample 40, Table 6), indicating that water was already consumed. At the same time, if the co-initiator was aged (Table 7), the yield dropped significantly. Most likely, in that case, the co-initiator was deactivated by hydrolysis of $AlCl_3$ that led to the release of HCl, which is not an initiator in conjunction with $AlCl_3$·ether complexes.

Polymerization of IB in Hexanes Co-initiated by $AlCl_3$ and Separately Added Ether. Polymerizations with separately added iPr_2O and $AlCl_3$ were performed in hexanes at 0 °C in the presence of TMPCl. If free iPr_2O is responsible for proton abstraction, adding iPr_2O separately would be a convenient way to obtain HR PIB of high yields due to the introduction of the efficient initiator TMPCl. Unfortunately, as seen in Table 8, only conventional PIB with mainly trisubstituted olefin ends was obtained even if the concentration of iPr_2O was orders of magnitude higher than the apparent concentration of $AlCl_3$, which is largely insoluble in hexanes.

Mechanistic Studies. *Formation of $AlCl_3$/Ether Complexes.* The formation of $AlCl_3$/ether complexes is an exothermic process, which is possible only in polar solvents, such as DCM. Complexation of $AlCl_3$ with ethers does not proceed in nonpolar solvents such as hexanes. Most $AlCl_3$ also remained undissolved in pure iPr_2O, but $AlCl_3$ formed a 1:1 complex readily with iPr_2O in DCM at 25 °C though $AlCl_3$ has low solubility in DCM (~1.2 × 10^{-3} M at room temperature).[15] There is no conclusive data whether $AlCl_3$ is in monomeric or dimeric form in DCM.

In order to investigate the complexation of $AlCl_3$ with ethers in detail, ^{1}H NMR and FTIR spectroscopies were used. The FTIR spectrum of iPr_2O is presented in Figure 2, where the characteristic peaks for ether C−O bond stretching are situated at 1010, 1108, and 1130 cm^{-1}. Upon complexation of iPr_2O with $AlCl_3$, the peak at 1010 cm^{-1} disappeared completely and two new peaks appeared at 902 and 1097 cm^{-1}. For $AlCl_3$·iPr_2O at a 1:1 ratio, there was no detectable peak at 1010 cm^{-1} (Figure 2), which indicates a very low concentration of free ether and free $AlCl_3$. Provided that saturated solutions of $AlCl_3$ in DCM are around ~1.2 × 10^{-3} M, this concentration should be also the upper limit for the uncomplexed species. An additional half equivalent of iPr_2O ($AlCl_3$:iPr_2O = 1.5) did not lead to the appearance of the peak at 1010 cm^{-1}. However, a broad peak appeared between 902 and 1010 cm^{-1}, suggesting the existence of another complex with a higher ratio of ether to $AlCl_3$ (e.g., $AlCl_3$·$2R_2O$). Free ether was only observed at stoichiometries of 1:2 or higher (Figure 2). This behavior is different than in the case of $FeCl_3$/iPr_2O complexes, where only 1:1 complexes were reportedly formed.[9]

The ^{1}H NMR spectra in DCM-d_2 of $AlCl_3$·iPr_2O, $AlCl_3$·Bu_2O, and $AlCl_3$·iBu_2O are presented in Figure 3, Figure S1, and Figure S2, respectively. All of the characteristic ether peaks move downfield as a result of complexation with $AlCl_3$, especially the protons on the carbons next to oxygen. For $AlCl_3$·Bu_2O and $AlCl_3$·iBu_2O, the peaks, most notably the CH_2−O peak at 4.2 ppm, were also broadened by complexation to $AlCl_3$.

Table 5. Polymerization of [IB] = 1 M by [$AlCl_3$·iPr_2O] = 0.01 M in Hexanes Saturated with H_2O at 0 °C for 20 min

							PIB end group distribution		
no.	added [iPr_2O] (M)	conv (%)	M_n (NMR)	M_n (SEC)	PDI (SEC)	[PIB][a] (M)	exo (%)	tri + endo (%)	tetra (%)
32	0	90	2100	1 900	4.5	0.0240	62	15	23
33	0.005	27	1600	1 000	7.3	0.0095	78	8	14
34	0.010	16	1300	800	8.7	0.0069	80	8	12
35	0.015	7	1100	600	8.9	0.0036	84	7	9
36	0.020	4	984			0.0023	88	4	9

[a] M_n(NMR) were used for the calculation of [PIB].

dx.doi.org/10.1021/ma3003856 | Macromolecules 2012, 45, 3318−3325

Table 6. Polymerization of [IB] = 1 M by [$AlCl_3$·iPr_2O] in Hexanes Saturated with Water at 0 °C

no.	time (min)	conv (%)	M_n (SEC)	PDI (SEC)	M_n (NMR)	[PIB]^b (M)	exo (%)	tri + endo (%)	tetra (%)
37	1	60	4000	2.8	3700	0.0091	63	15	21
38	20	75	3100	3.5	2900	0.0145	62	16	22
39	40	90	2300	4.4	2400	0.0210	63	18	20
40^a	20 + 20	83	2700	5.2	3100	0.0150	61	13	25

^{a}[$AlCl_3$·iPr_2O] = 0.01 M. After 20 min another [$AlCl_3$·iPr_2O] = 0.01 M was added. $^b M_n$(NMR) were used for the calculation of [PIB].

Table 7. Polymerization of [IB] = 1 M by [iPr_2O·$AlCl_3$] = 0.02 M at 0 °C for 20 min

no.	conv (%)	M_n (SEC)	PDI (SEC)	M_n (NMR)	[PIB]^b (M)	exo (%)	tri + endo (%)	tetra (%)
41	86	2500	3.9	1900	0.0253	60	17	23
42^a	25	2000	5.1	1900	0.0074	56	18	26

^{a}iPr_2O·$AlCl_3$ was initially aged in hexanes for 20 min at 0 °C. $^b M_n$(NMR) were used for the calculation of [PIB].

In the case of $AlCl_3$·iPr_2O, two types of complexes were observed (Figure 3-2) as also suggested by the FTIR spectra. One complex exhibits peaks at 5.15 ppm (OC<u>H</u>, m) and at 1.65 ppm ($C\underline{H}_3)_2$CH, d) that are well resolved and appear more downfield with the chemical shift independent of the amount of ether. Another set of resonance peaks at 4.2 ppm (OC<u>H</u>, m) and 1.4 ppm (($C\underline{H}_3)_2$CH, d) are further upfield, consistent with a lower electron-withdrawing environment. The second set of peaks also have broader line widths, indicating ongoing exchange reactions.[16] By lowering the temperature to 0 °C both peaks move downfield to 4.6 and 1.5 ppm.

At iPr_2O-starved conditions ($AlCl_3$:iPr_2O = 2:1, Figure 3-1), the peak (Figure 3-2) at 4.2 ppm was absent. At this ratio, about half of the added $AlCl_3$ remained undissolved, so the real ratio of the formed complex is closer to 1:1 with a small amount of free $AlCl_3$ at a concentration determined by its solubility. This resulted in formation of a stable complex, where the peak at 5.2 ppm is well resolved due to decreased exchange reactions. As more ether is added, a small peak appears at 4.2 ppm (C<u>H</u>O) which grows with increasing amounts of iPr_2O moving upfield due to exchange with free ether (Figure 3-3). This suggests the presence of an additional, less stable complex where the iPr_2O is in an environment of lower acidity (Scheme 2).

Initiation Step. In order to investigate the initiation process, a 1:1 $AlCl_3$·iPr_2O complex was reacted with tBuOH and H_2O, and the products of these reactions were monitored in situ by ^{1}H NMR spectroscopy.

As a result of the addition of tBuOH (0.015 M) to a 0.02 M solution of $AlCl_3$·iPr_2O in DCM-d_2, the C<u>H</u>O peak characteristic of the complex at 5.15 ppm (Figure 4-1) decreased in area, and the C<u>H</u>O peak characteristic of the second complex at 4.2 ppm shifted upfield and increased in intensity (Figure 4-2). At the same time, the added tBuOH formed a complex with $AlCl_3$

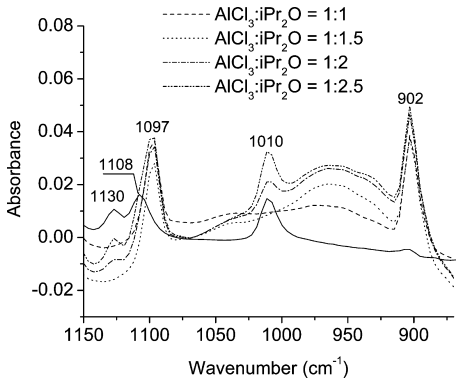


Figure 2. ATR-FTIR spectra overlay of [iPr_2O] = 0.1 M (solid line) and $AlCl_3$·iPr_2O complexes at different $AlCl_3$/iPr_2O ratios at 25 °C where [$AlCl_3$] = 0.1 M.

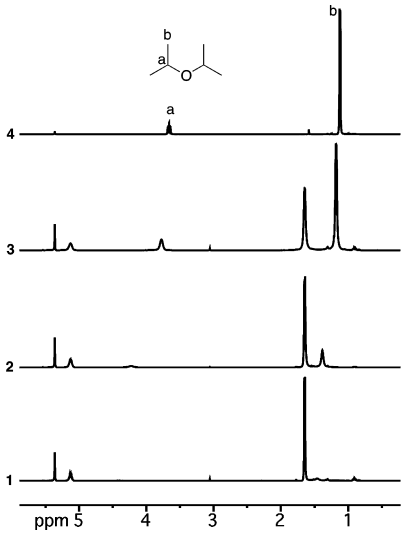


Figure 3. ^{1}H NMR spectra overlay of $AlCl_3$·iPr_2O complexes in DCM-d_2 at 25 °C [$AlCl_3$] = 0.02 M: (1) $AlCl_3$:iPr_2O = 2:1 (soluble portion); (2) $AlCl_3$:iPr_2O = 1:1; (3) $AlCl_3$:iPr_2O = 1:2; (4) spectrum of iPr_2O.

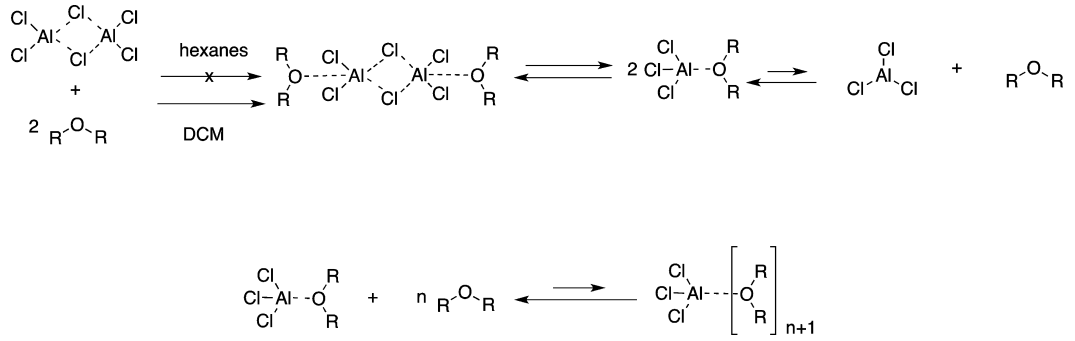
Table 8. Polymerization of [IB] = 1 M by [$AlCl_3$] = 0.035 M and [TMPCl] = 0.02 M in Hexanes at 0 °C for 20 min^a

							PIB end groups distribution		
no.	[iPr_2O] (M)	conv (%)	M_n (SEC)	PDI (SEC)	M_n (NMR)	[PIB]^b (M)	exo (%)	tri + endo (%)	tetra (%)
43	0.005	98	350	3.6	599	0.0917	4	75	21
44	0.010	85	400	3.9	830	0.0574	7	73	20
45	0.015	84	360	3.6	705	0.0668	8	71	20
46	0.020	79	370	3.5	768	0.0577	11	70	19

^{a}The hexane solution of IB, iPr_2O, and TMPCl was added to a glass culture tube containing $AlCl_3$. $^b M_n$(NMR) were used for the calculation of [PIB].

dx.doi.org/10.1021/ma3003856 | *Macromolecules* 2012, 45, 3318−3325

Scheme 2



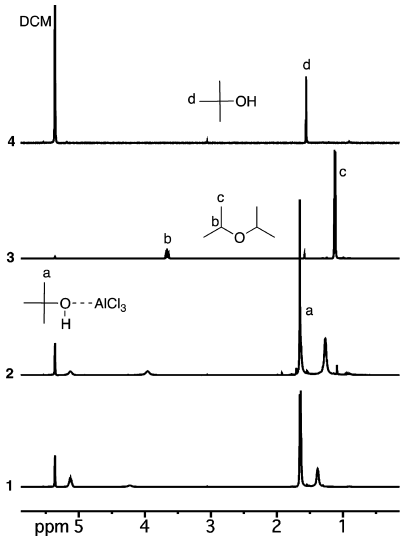


Figure 4. ^{1}H NMR spectra overlay of $AlCl_3{\cdot}iP_2O$ complexes in DCM-d_2 at 25 °C: (1) $AlCl_3{\cdot}iPr_2O$; (2) $AlCl_3{\cdot}iPr_2O$ and $AlCl_3{\cdot}$tBuOH; (3) spectrum of free iPr_2O; (4) spectrum of free tBuOH.

(a, Figure 4-2), as indicated by the shift of the characteristic peak for the *tert*-butyl group downfield from 1.5 to 1.7 ppm. The $AlCl_3{\cdot}$tBuOH complex was formed at the expense of the $AlCl_3{\cdot}iPr_2O$ complex due to the displacement of iPr_2O by tBuOH or the additional tBuOH added to an existing $AlCl_3{\cdot}iPr_2O$ complex forming the more exchangeable tBuOH·$AlCl_3{\cdot}iPr_2O$. In both of these cases the released free iPr_2O would interact with other $AlCl_3{\cdot}iPr_2O$ complexes, leading to complexes with higher stoichiometry of iPr_2O.

When an equimolar amount of water was added to a 1:1 $AlCl_3{\cdot}iPr_2O$ complex, similar results were observed. The characteristic peaks for the complex at 5.15 and 1.65 ppm were still present, but the amount of free ether also increased due to its displacement by water (Figure 5). The released free ether was in equilibrium with the complex species from which the minor CHO peak (from 4.2 to 3.8 ppm) originates. With a decrease of the temperature, the quantity of the major species (with CHO peak at 5.2 ppm) increases (Figure 5). This as an indication that the two complex species are indeed in dynamic equilibrium.

Nature of Counteranion. The original publications by the Vasilenko[1] and Liu[8] and co-workers suggest that the ether molecules remain associated with the MX_nOH^- counteranions. This is difficult to rationalize since both are Lewis bases. In order to clarify this issue $AlCl_3$/ether complex was mixed with TBAOH in DCM-d_2 and the products of the reaction were

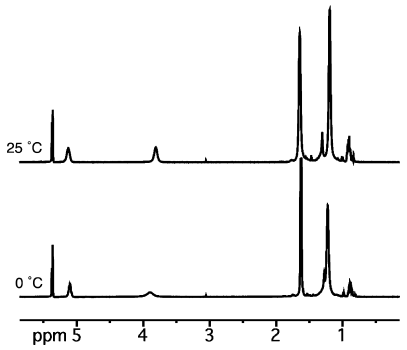


Figure 5. ^{1}H NMR spectrum of the soluble fraction of $[AlCl_3{\cdot}iPr_2O]$ = 0.02 M in DCM-d_2 after treatment with $[H_2O]$ = 0.02 M.

characterized by ^{1}H NMR and ^{27}Al NMR spectroscopies. ^{1}H NMR spectroscopy revealed that iPr_2O was completely released after the formation of $AlCl_3OH^-$, as indicated by the almost

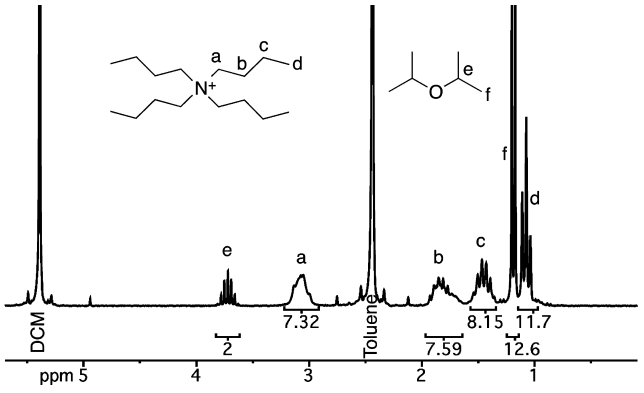


Figure 6. ^{1}H NMR spectrum of products of reaction between $AlCl_3{\cdot}iPr_2O$ and TBAOH in DCM-d_2.

quantitative integral values of TBA^+ and iPr_2O (Figure 6). The ^{27}Al NMR spectrum of the $AlCl_3{\cdot}iPr_2O$ complex shows a broad singlet at around 100 ppm and a much smaller narrow singlet at 103 ppm, corresponding to $AlCl_3OH^-$ formed by adventitious water (Figure 7-1). After the reaction of $AlCl_3{\cdot}iPr_2O$ with TBAOH, only the sharp singlet at 103 ppm remained (Figure 7-2), which confirmed that $AlCl_3$ was no longer complexed with iPr_2O.

Termination Reactions. PIBs obtained by $AlCl_3$/ether systems in hexanes at 0 °C possessed a detectable amount of PIB-Cl end-groups (Figure S3), formed by ion collapse (Scheme 3), which cannot be reionized by the $AlCl_3{\cdot}$ether

dx.doi.org/10.1021/ma3003856 | *Macromolecules* 2012, 45, 3318−3325

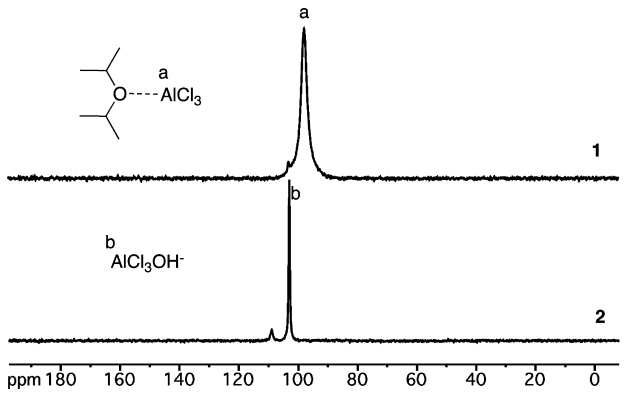


Figure 7. ^{27}Al NMR spectra overlay in DCM/DCM-d_2 = 66/33 (v/v) of (1) [$AlCl_3$·iPr_2O] = 0.1 M and (2) $AlCl_3$·iPr_2O + TBAOH = 0.1 M.

Scheme 3



complex. This reaction also contributed to the overall deactivation of the co-initiator by releasing $AlCl_2OH$ (Scheme 3). Because of the overlapping peaks in the ^{1}H NMR spectra, it was not possible to accurately determine the amount of PIB-Cl.

In order to determine the content of PIB-Cl more accurately, end-capping of the PIB-Cl groups with ditolylethylene (DTE) was performed at the following conditions: [PIB] = 0.01 M, [$TiCl_4$] = 0.036 M, [DTBP] = 0.005 M, [DTE] = 0.01 M, hexanes/MeCl (60/40, v/v), −80 °C for 30 min. Under these conditions PIB-Cl group can be ionized by $TiCl_4$, and the resulting PIB^+ is end-capped with DTE to form $PIB\text{-}DTE^+$. The [$PIB\text{-}DTE^+$] = 2.7 × 10^{-4} M could be determined from the absorbance at 460 nm characteristic for DTE^+ (Figure 8),

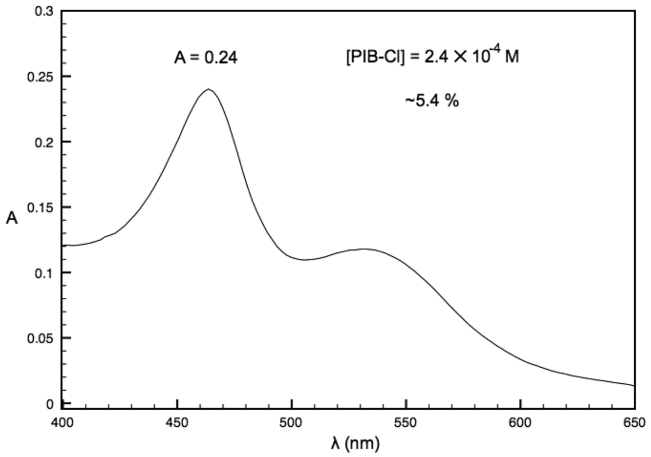


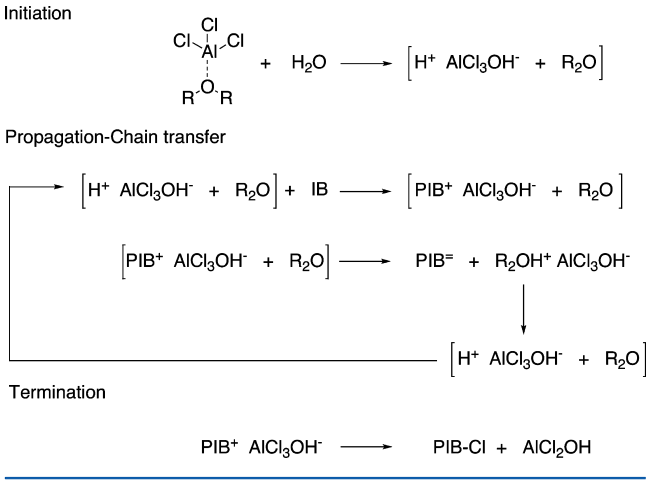
Figure 8. UV−vis spectrum of $PIB\text{-}DTE^+$ obtained at [PIB] = 0.01 M, [$TiCl_4$] = 0.036 M, [DTBP] = 0.005 M, [DTE] = 0.01 M, hexanes/MeCl = 60/40, −80 °C, 10 min.

which corresponds to ∼5.4% of PIB-Cl chains from PIB of M_n = 2000 obtained by polymerization of IB co-initiated by $AlCl_3$·iPr_2O in hexanes for 20 min.

$PIB\text{-}DTE^+$ was also terminated with the hydride donor [Bu_3SiH] = 0.01 M for 30 min followed by rigorous reprecipitation of the polymer five times from hexanes/methanol. According to ^{1}H NMR spectroscopy, which is less sensitive than UV−vis, ∼ 2% from PIB was capped with DTE, which corresponds to 2% PIB-Cl end-groups (Figure S4).

Proposed Mechanism. Since in the presence of DTBP polymerization of IB was absent when CumOH, tBuOH, tBuCl, or TMPCl initiators were used, the true initiator for IB polymerization is adventitious water. It is also unlikely that free uncomplexed $AlCl_3$ is the true co-initiator, as proposed by Vasilenko and co-workers.[1] Free uncomplexed $AlCl_3$ should be able to ionize tBuCl or TMPCl that would lead to a rapid polymerization of IB, which was not observed. The reaction of water with $AlCl_3$·ether complex yields $H^+AlCl_3OH^-$ with the simultaneous release of the ether. Protonation of the monomer and propagation takes place until ether assisted chain transfer to monomer yields PIB exo-olefin and a new protonated monomer. Termination by ion collapse yields PIB-Cl, which cannot be reionized. This mechanism adequately explains all but one observation, i.e., that adding $AlCl_3$ and an ether separately does not produce PIB exo-olefin. In order to explain this finding, we reconsider the data in Table 3. Even if all ether molecules are simultaneously displaced from the complex by water, its maximum concentration would be 0.005 M. Considering that the propagation rate constant of IB is close to diffusion limited and the proton abstraction from PIB^+ by the ether molecule at maximum could also be diffusion limited, the DP_ns controlled by the [M]/[R_2O] ratio should be >40−160 at low conversion. Clearly the observed DP_ns are much lower. To explain these findings, we propose that the ether molecules are brought into the vicinity of propagating ends by the complex and remain there for the duration of the propagation (perhaps solvating the cation), so their local concentration is higher than in the bulk. The proposed mechanism is shown in Scheme 4. This mechanism also

Scheme 4



explains why alkyl halides, which are generally efficient initiators with $AlCl_3$, are completely inactive with the ether complexes.

CONCLUSIONS

A reexamination of the polymerization of IB with the CumOH/$AlCl_3$·Bu_2O initiator/co-initiator system in dichloromethane/hexanes (80/20 v/v) or in hexanes reported by Vasilenko and co-workers before[1,2] revealed that CumOH is not an initiator in conjunction with $AlCl_3$·Bu_2O, and the true initiator is

dx.doi.org/10.1021/ma3003856 | Macromolecules 2012, 45, 3318−3325

adventitious water. Similarly, in hexanes at 0 °C none of the conventional cationic initiators such as CumCl or TMPCl could initiate the polymerization of IB. The polymerization of IB can only be initiated with water in the absence of DTBP, but monomer conversions and exo-olefin content (60−70%) are much lower than in polar solvent and the polymers exhibit broad molecular weight distributions. Among the $AlCl_3$ complexes with Bu_2O, iPr_2O, sec-Bu_2O, and iBu_2O, the highest IB conversions and exo-olefin content could be reached with $AlCl_3$·iPr_2O. Mechanistic studies suggest that the reaction of water with $AlCl_3$·R_2O yields $H^+AlCl_3OH^-$ that initiates the polymerization and free ether, which abstracts a β-proton from the growing chain end before it diffuses from the immediate vicinity of the polymer cation. A separate addition of $AlCl_3$ and ether to the polymerization mixture results in conventional PIB with high trisubstituted olefinic end groups due to slow proton abstraction. Accordingly, the role of the complex is to deliver the ether to the close proximity of the propagating end. Since the $AlCl_3$·R_2O complex yields PIB exo olefins with high selectivity only in polar solvent and only water initiates the polymerization, the industrial relevance of this process is questionable.

■ ASSOCIATED CONTENT

Supporting Information

^1H NMR spectra of $AlCl_3$/ether complexes, PIB-Cl, and PIB end-capped with DTE; tables with additional polymerization data and DFT calculations for the proton affinities of the ethers. This material is available free of charge via the Internet at http://pubs.acs.org.

■ AUTHOR INFORMATION

Corresponding Author

*E-mail: e-mail:Rudolf_Faust@uml.edu.

Notes

The authors declare no competing financial interest.

■ ACKNOWLEDGMENTS

Financial support from Infineum is greatly appreciated.

■ REFERENCES

(1) Vasilenko, I. V.; Frolov, A. N.; Kostjuk, S. V. *Macromolecules* **2010**, *43* (13), 5503−5507.
(2) Vasilenko, I. V.; Shiman, D. I.; Kostjuk, S. V. *J. Polym. Sci.* **2012**, *50* (4), 750−758.
(3) De, P.; Faust, R. Carbocationic Polymerization. In *Macromolecular Engineering. Precise Synthesis, Materials Properties, Applications*; Matyjaszewski, K., Gnanou, Y., Leibler, L., Eds.; Wiley-VCH Verlag GmbH & Co. KGaA: Weinheim, 2007; pp 1−45.
(4) Puskas, I.; Banas, E. M.; Nerheim, A. G. *J. Polym. Sci., Polym. Symp.* **1976**, *56*, 191−202.
(5) Puskas, I.; Meyerson, S. *J. Org. Chem.* **1984**, *49*, 258−262.
(6) Dimitrov, P.; Faust, R. *Macromolecules* **2010**, *43* (4), 1724−1729.
(7) Mach, H.; Rath, P. *Lubr. Sci.* **1999**, *11−2*, 175−185.
(8) Liu, Q.; Wu, Y.-X.; Zhang, Y.; Yan, P.-F.; Xu, R.-W. *Polymer* **2010**, *51*, 5960−5969.
(9) Liu, Q.; Wu, Y.; Yan, P.; Zhang, Y.; Xu, R. *Macromolecules* **2011**, *44*, 1866−1875.
(10) In ref 8, the initiator efficiencies for CumOH were calculated by the formula $I_{eff} = M_{n,theor}/M_{n,exp} \times 100$. This is correct only when initiation from adventitious water and chain transfer are absent. Based on the low F_n values especially for hexane where less than half of the chains contain the Cum moiety, this is not the case. The corrected I_{eff}s ∼ 23%.
(11) Fodor, Zs.; Faust, R. *J. Macromol. Sci., Pure Appl. Chem.* **1996**, *A33*, 305.
(12) Cerný, Z.; Machácek, J.; Fusek, J.; Císenský, B.; Kriz, O.; Tuck, D. G. *J. Chem. Soc., Dalton Trans.* **1998**, 1439−1446.
(13) Dimitrov, P.; Emert, J.; Hua, J.; Keki, S.; Faust, R. *Macromolecules* **2011**, *44*, 1831−1840.
(14) Englin, B. A.; Plate, A. F.; Tugolukov, V. M.; Pryanishnikova, M. A. *Khim. Technol. Topl. Masel* **1965**, *9*, 42−46.
(15) Masure, M.; Sauvet, G.; Sigwalt, P. *J. Polym. Sci.* **1978**, *16*, 3065−3076.
(16) Saunders, M.; Kate, M. R. *J. Am. Chem. Soc.* **1978**, *100*, 7082−7083.

Macromolecules

Article

pubs.acs.org/Macromolecules

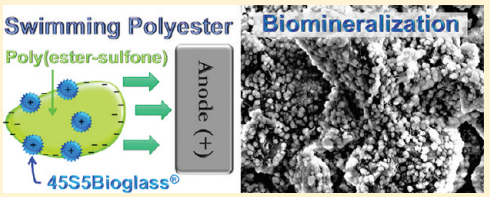
Anode-Selective Electrophoretic Deposition of a Bioactive Glass/Sulfone-Containing Click Polyester Composite

Yu Nagao,[†] Akinori Takasu,[†,*] and Aldo R. Boccaccini[‡]

[†]Department of Frontier Materials, Graduate School of Engineering, Nagoya Institute of Technology, Gokiso-cho, Showa-ku, Nagoya 466-8555, Japan

[‡]Institute of Biomaterials, University of Erlangen-Nurnberg, 91058 Erlangen, Germany

ABSTRACT: A room temperature thiol−ene click polymerization afforded a poly(ester−sulfide) (M_n = 1.4−6.9 × 10^4), which represents the first in a new class of click polyesters. Subsequent oxone oxidation of the poly(ester−sulfide) led to the corresponding poly(ester−sulfone), which had improved thermal stability in comparison with the parent poly(ester−sulfide). A bioactive glass/poly(ester−sulfone) composite could be deposited on a stainless-steel anode by electrophoretic deposition (EPD). Hydroxyapatite was found on the surface of electrophoretically deposited bioactive glass/poly(ester−sulfone) composites that had been immersed in simulated body fluid (SBF) for 2 weeks. This bioactive glass/poly(ester−sulfone) composite might therefore find use as a surface coating for implantable medical devices on which a hydroxyapatite layer can form post implantation to strengthen the interface between the implant and host bone.



INTRODUCTION

The design of high performance polyesters and their composites with inorganic phases for biomedical applications is an expanding field.[1] Although polyesters are usually produced by condensation of a diol and a dicarboxylic acid or a hydroxylcarboxylic acid[2] or by ring-opening polymerization of a lactone,[3] the former method requires severe reaction conditions even when a customized catalyst is used[4] and the latter uses highly strained cyclic monomers, which makes it difficult to synthesize polyesters with specific functionalities and/or properties. We have reported on low-temperature polycondensations of diols and dicarboxylic acids,[5] which allowed us to use thermally labile monomers that contained functional groups.[6]

Conversely, click chemistry, introduced by Sharpless and coworkers,[7] is an efficient tool for the preparation of a wide range of organic compounds. Cu(I)-catalyzed click chemistry involves an efficient 1,3-dipolar cycloaddition between an azide and an alkyne under mild conditions, without formation of byproduct, with high chemoselectivity,[8] and shows promise for preparation of macromolecules and biomacromolecules.[9] We have also reported on the syntheses of polyesters that contain main-chain triazole units by Cu(I)-catalyzed click polymerization of dialkynes and diazides.[10] Because the azides used for this method are prepared *in situ*, the danger of an explosion is minimized.[10b]

Because Cu in high concentration is toxic, its use may be limited;[11] therefore, development of metal-free click reactions is desirable.[12] The thiol−ene click reaction is an efficient method for the production of many types of polymers.[13] Thiol−ene click polymerizations proceed via a thiyl-radical-mediated, mechanism, involving alternating propagation and chain-transfer steps (Figure 1). The reactions are highly efficient, proceed rapidly, even in the presence of oxygen, and do not use metal catalysts. One round of polymerization involves the addition of a thiyl radical to a vinyl, followed by abstraction of a hydrogen from a second thiol to give a thioether, and regenerate the thiyl radical (Figure 1b). Click thiol−ene polymerization can be used in conjunction with many different

Table 1. Photo-Initiated Thiol−ene Click Polymerizations of Bis(butenyl) Methylsuccinate 1,4-Butanedithiol Using Irgacure 184 as the Catalyst

entry	time (min)	$[M]_0/[cat]$	M_n[a]	M_w/M_n[a]	yield (%)	atmosphere
1	15	100	35 000	1.6	94	N_2
2	30	100	49 000	1.5	92	N_2
3	30	100	14 000	1.6	89	air
4	15	50	53 000	1.5	89	N_2
5	30	50	69 000	1.5	90	N_2
6	30	50	29 000	1.7	90	air

[a]M_n and M_w/M_n were determined by SEC with DMF as the solvent. Poly(styrene) served as the standard.

Table 2. Oxidation of Poly(ester−sulfide) to Poly(ester−sulfone)

entry	oxone[a] (equiv)	time (h)	conversion[b] (%)	yield[c] (%)
1	1	6	53	0
2	2	1	90	88
3	2	1.5	91	89
4	2	3	98	87
5	2	6	100	80

[a]Equivalent to one sulfide per poly(ester−sulfide) repeat unit. [b]Determined *in situ* by ^{1}H NMR spectroscopy. [c]After reprecipitation.

Received: February 25, 2012
Revised: April 2, 2012
Published: April 10, 2012

 © 2012 American Chemical Society

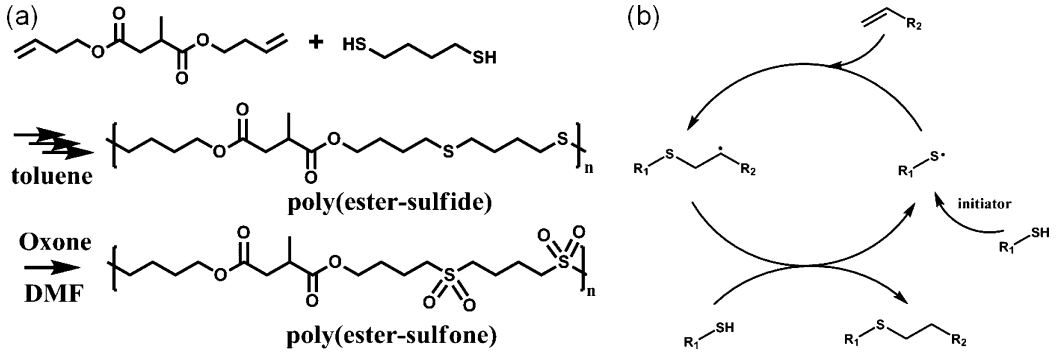
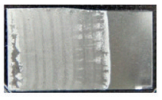
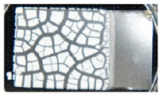


Figure 1. (a) Schematic of a the thiol−ene polymerization reported herein and subsequent oxone oxidation of the poly(ester−sulfide) to produce the poly(ester−sulfone). (b) Reaction cycle for one round of a thiol−ene click reaction.

Table 3. Films Formed on the Stainless Steel Electrodes by EPD

Entry	Matrix	Concentration Polymer/Bioglass® (g/L)	Solvent (v/v)	Suspension	Coating[a] Electrode selectivity	Coating[a] States
1	Poly(ester-sulfone)	6/0	DMF/Ethanol (1/1)	Stable	Anode	 (Clacked)
2	Poly(ester-sulfone)	4/0	DMF/Ethanol (1/1)	Stable	Anode	 (Thin)
3	none	0/20	DMF/Ethanol (1/1)	Unstable	N.D.	
4	none	0/20	DMF/*n*-Butanol (1/1)	Stable	Cathode	 (Thin)
5	Poly(ester-sulfone)	6/20	DMF/Ethanol (1/1)	Stable	Anode	 (Thick)
6	Poly(ester-sulfone)	6/20	DMF/*n*-Butanol (1/1)	Stable	Anode	 (Thin)
7	Poly(ester-sulfone)	12/20	DMF/Ethanol (1/1)	Stable	Anode	 (Cracked)

[a]After deposition, the coatings were dried in air at 50 °C for 6 h and then under reduced pressure for 6 h.

thiol- and vinyl-containing compounds, which should allow for orthogonal and site-selective functionalization of polymers.

Thiol−ene click polymerization might be an attractive route to synthesize polymers that can be used in applications that require materials with specific physical and/or chemical properties.[14] Sulfur-containing polymers have excellent optical properties and biocompatibility.[15] Introduction of sulfurs into a polyester should increase their refractive index, thermal stability, and affinity toward metals in comparison with the analogous nonsulfur-containing polyesters.[15c,f]

dx.doi.org/10.1021/ma300396p | *Macromolecules* 2012, 45, 3326−3334

In the field of biomedical materials, new bioactive materials that can effectively coat a targeted metal substrate at nano- to micrometer scales are needed.[16] Electrophoretic deposition (EPD) is a promising technique for the fabrication of inorganic and organic films.[16a,17] EPD is based in the controlled electric–field-induced deposition of charged particles or molecules in an orderly manner onto an electrode. Nano- to micrometer films can be made, including those formed by organic/inorganic composites.[16a,17h,i]

45S5Bioglass was the first silicate material found to bind directly to bone.[18] This glass contains SiO_2, P_2O_5, CaO, and Na_2O. When in contact with a biological fluid, a thin layer of carbonate hydroxyapatite—a substance similar to carbonated calcium-deficient hydroxyapatite, the main mineral found in bone, dental enamel, and dentin—can form on the surface of Bioglass.[18d] In addition, metal surfaces of orthopedic implants are usually coated with bioactive ceramics and bioactive glasses to prevent the release of harmful metal ions and to form a native-like bond between the implant and the bone surfaces. However, the mechanical strength of Bioglass is poor, which precludes its incorporation into load-bearing prostheses. Therefore, attempts have been made to improve the mechanical strength of Bioglass by developing composites based on Bioglass and biopolymers.[17b,18e] As an alternative, polymer-bioceramic composite coatings for orthopedic applications have been suggested.[17d] These coatings should provide an improved connection to host tissue given that they are softer than pure ceramic or Bioglass coatings and thus a lower mismatch of mechanical properties exists between the implant and host bone tissue. Moreover, the polymer causes the bioactive glass particles to adhere to the metallic substrate at low temperatures, which avoids the need for high temperature sintering of monolithic bioceramic or Bioglass coatings.[16a,17c,d,h,i] Bioglass/polymer films deposited on different substrates have been prepared by low temperature EPD, including polyetheretherketone (PEEK)/Bioglass[17j] and chitosan/Bioglass.[17d] In addition, hydroxyapatite/polycaprolactone (PCL) composite has been prepared by EPD,[19] which suggests that appropriately designed click polyesters might also be used in combination with bioactive inorganic particles to produce an evolutional polyester-based bone-regenerating coating materials by EPD.

In this article, we present a thiol–ene click polymerization for the synthesis of a sulfide-containing polyester that was then converted to a sulfone-containing polyester via oxone oxidation (Figure 1). Given the electrical characteristics of sulfones, i.e., electrochemical stability, oxidation potential, and ionic conductivity, we were able to selectively deposit a Bioglass/poly(ester–sulfone) soft film onto a stainless steel anode by EPD. Finally, we found that a thin layer of hydroxyapatite formed on the surface of the Bioglass/poly(ester–sulfone) film when it was exposed to a simulated body fluid (SBF) confirming the bioactivity of the new soft composite coatings developed here.

EXPERIMENTAL SECTION

Materials and Methods. Chemicals were obtained from commercial sources and used without further purification. ^{1}H NMR spectra were acquired at 27 °C using a Bruker Analytik DPX200 spectrometer (200 MHz). Tetramethylsilane was the internal standard (0 ppm). FT-IR spectra of the polyesters in KBr disks were obtained using a JASCO/IR-430 spectrometer. Number-average molecular weight (M_n) and polydispersity indexes (M_w/M_n) for the polyesters were estimated using a size exclusion chromatography (SEC) system consisting of a Tosoh DP8020 pump system, a Tosoh RI-8020 differential refractometer, and Tosoh TSK-gel α-3000 and α-5000 columns (Tosoh, Tokyo, Japan). The eluent was 0.05% (w/v) LiBr, 100 mM tetramethylethylenediamine in *N*,*N*-dimethylformamide (DMF). The flow rate was 0.5 mL/min, and the temperature was 40 °C. Differential scanning calorimetry (DSC), which used a DSC6220S calorimeter (Seiko Instruments Inc., Chiba, Japan), was performed from −90 to +180 to −90 °C, at 10 °C/min. The instrument was calibrated with indium and tin. Each polyester sample weighted between 5 and 7 mg and was contained in an aluminum pan that was covered with a lid within the calorimeter. The glass-transition temperature (T_g) was taken as the inflection point of the DSC heat-capacity jump. The melting temperature (T_m) was defined as the minimum point in the endothermic trough. Thermogravimetric analyses (TGA) were performed under nitrogen at 10 °C/min between 20 and 600 °C (TG/DTA 220U; Seiko Instruments Inc., Chiba, Japan).

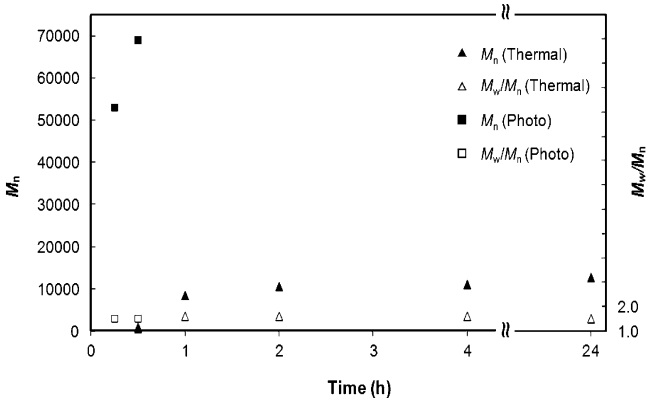


Figure 2. Thermal and photo thiol–ene click polymerizations of bis(butenyl) methylsuccinate and 1,4-butanedithiol. $[M]_0/[cat]$ = 50, M_n and M_w/M_n were determined by SEC with DMF as the solvent. Poly(styrene) served as the standard.

Preparation of Bis(butenyl) Methylsuccinate. Methylsuccinic acid (2.0 g, 15 mmol), $Sc(OTf)_3$ (74 mg, 0.15 mmol), and 3-buten-1-ol (4.3 g, 60 mmol) were added into a 50-mL round-bottom flask. The mixture was stirred at 60 °C for 12 h under reduced pressure (90 mmHg) then diluted with 30 mL of chloroform, washed with 10 mL of saturated $NaHCO_3$(aq), and dried over $MgSO_4$. After filtration and solvent evaporation, bis(butenyl) methylsuccinate was obtained as a white liquid in 91% yield (3.3 g). ^{1}H NMR (200 MHz, $CDCl_3$, δ): 5.89–5.68 (m, C=C*H*CH$_2$, 2H), 5.16–5.05 (m, C*H*$_2$=C, 4H), 4.19–4.10 (m, CH$_2$C*H*$_2$OC=O, 4H), 2.89 (quin, O=CC*H*(CH$_3$)-CH$_2$, 1H, 6.8 Hz), 2.73 (dd, O=CC*H*$_2$CH(CH$_3$), 1H, 8.0 and 16 Hz), 2.45–2.34 (m, O=CC*H*$_2$CH(CH$_3$) and C=CHC*H*$_2$CH$_2$, 5H), 1.21 (d, 3H, C(*CH*$_3$), 7.1 Hz).

Synthesis of the Poly(ester–sulfide) by Thermal Polymerization. To examine reaction variables, a series of 10 mL round-bottom flasks were prepared that contained bis(butenyl) methylsuccinate (1.0 mmol), the thermal initiator azobis(isobutyronitrile) (2.0×10^{-2} mmol), and 1,4-butanedithiol (1.0 mmol) in 1 mL of distilled toluene. The mixtures were stirred at 70 °C under a nitrogen atmosphere for various times and then diluted with $CHCl_3$. The poly(ester–sulfide) preparations were individually precipitated twice from $CHCl_3$ by addition of *n*-hexane, and dried under vacuum. White syrups were obtained. The polymer preparations were physically characterized by NMR and SEC and thermally characterized by DSC (data not shown).

Synthesis of the Poly(ester–sulfide) by Photo-Polymerization. To examine reaction variables, a series of 10 mL round-bottom flasks were prepared that contained bis(butenyl) methylsuccinate (1.0 mmol), 1-hydroxycyclohexyl phenyl ketone (Irgacure 184) (1.0×10^{-2} or 2.0×10^{-2} mmol), and 1,4-butanedithiol (1.0 mmol) in 1 mL of distilled toluene. The mixtures were stirred at room temperature under nitrogen and UV-irradiated using a Toshiba H-400P high-pressure mercury lamp (400 W and 250–400 nm) for various times. Then the mixtures were individually diluted with

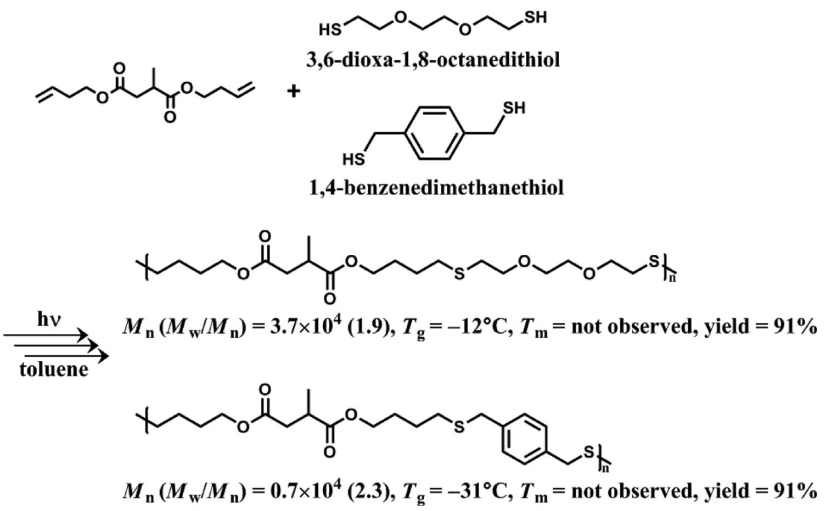


Figure 3. Thiol–ene click polymerization of bis(butenyl) methylsuccinate with 3,6-dioxa-1,8-octanedithiol and 1,4-benzenedimethanethiol. Conditions: 1 mmol scale, 1 mL of toluene as the solvent, room temperature, 30 min, $[M]_0/[cat]$ = 50, UV irradiation.

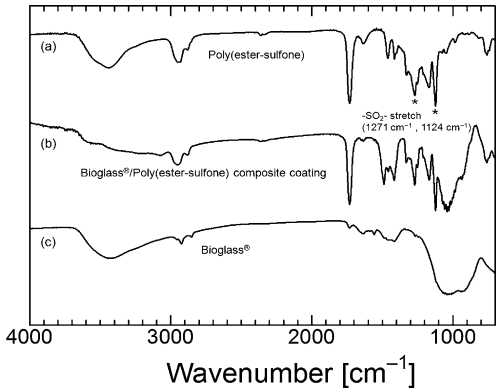


Figure 4. FTIR spectra of (a) poly(ester–sulfone), (b) Bioglass/poly(ester–sulfone) composite film, and (c) pure Bioglass.

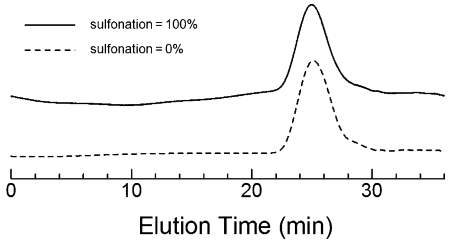


Figure 5. Size exclusion chromatograms of poly(ester–sulfide) and poly(ester–sulfone). The poly(ester–sulfone) was prepared from the poly(ester–sulfide) used for the chromatography.

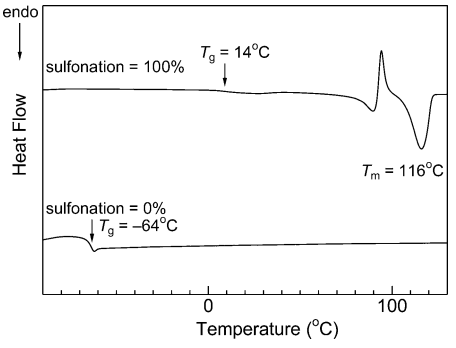


Figure 6. DSC traces for the poly(ester–sulfide) (M_n = 11000) and the poly(ester–sulfone) (M_n = 12000).

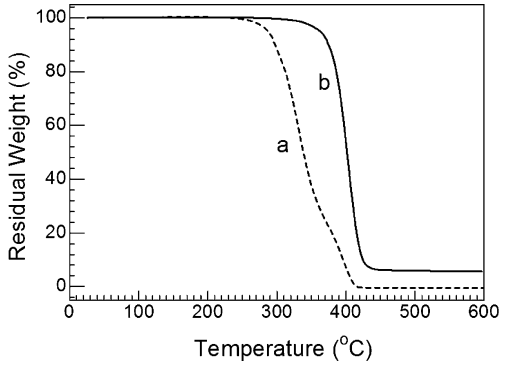


Figure 7. Thermogravimetric curves for (a) the poly(ester–sulfide) (M_n = 11000) and (b) the poly(ester–sulfone) (M_n = 12000).

$CHCl_3$. The poly(ester–sulfide)s were individually precipitated twice from $CHCl_3$ by addition of *n*-hexane and dried under vacuum. White syrups were obtained. Details for the syntheses are summarized in Table 1. The polymer preparations were characterized by ^{1}H NMR and IR spectroscopy, and SEC. The thermal properties were determined by DSC and TGA. ^{1}H NMR (200 MHz, $CDCl_3$, δ): 4.13–4.06 (brm, $CH_2CH_2OC{=}O$, 4H), 2.89 (quin, $O{=}CCH(CH_3)$-CH_2, 1H, 6.8 Hz), 2.73 (dd, $O{=}CCH(H)CH(CH_3)$, 1H, 8.0 and 16 Hz), 2.57–2.50 (brm, CH_2SCH_2, 8H), 2.40 (dd, $O{=}CCH(H)CH$-(CH_3), 1H, 6.0 and 16 Hz), 1.78–1.62 (brm, $CH_2CH_2CH_2CH_2$, 12H), 1.21 (d, 3H, $C(CH_3)$, 7.0 Hz). IR (KBr) cm^{-1}: 2939 (ν_{C-H}), 1732 [$\nu_{C=O}$(ester)], 1275 and 1163 [ν_{C-O}(ester)].

Oxone Oxidation of the Poly(ester–sulfide) to the Poly(ester–sulfone). A variety of conditions were examined, an example (Table 2, entry 5) follows. The poly(ester–sulfide) (402 mg, 1.1 mmol repeat unit) and Oxone (1.36 g, 2.2 mmol) in DMF (8 mL) were added into a 30 mL round-bottom flask. After stirring at 30 °C for 6 h, the mixture was filtered, and the solvent was evaporated under reduced pressure to give a white solid that was then dissolved in 5 mL of DMF and precipitated by addition of 90 mL of H_2O/CH_3OH (9/1, v/v). A total of 427 mg of the poly(ester–sulfone) was obtained as a white solid. The product was characterized by ^{1}H NMR and FTIR spectroscopy, and by SEC. The conversion of sulfide into sulfone was calculated by ^{1}H NMR intensity ratio of signals at 1.21 and 3.13 ppm. Its thermal properties were determined using DSC and TGA. ^{1}H NMR (200 MHz, DMSO-d_6, δ): 4.05 (brs, $CH_2CH_2OC{=}O$, 4H), 3.18–3.07 (brm, $CH_2CH_2SO_2$, 8H), 2.80 (quin, $O{=}CCH(CH_3)CH_2$,

dx.doi.org/10.1021/ma300396p | Macromolecules 2012, 45, 3326–3334

1H, 6.4 Hz), 2.62 (dd, O=CCH(*H*)CH(CH_3), 1H, 7.9 and 17 Hz), 2.55–2.43 (brm, O=CC*H*(H)CH(CH_3) and C=CHCH_2CH_2, 5H), 1.83 (brs, $SO_2CH_2CH_2CH_2CH_2SO_2$, 4H), 1.72 (brs, $SO_2CH_2CH_2CH_2CH_2$, 8H), 1.21 (d, 3H, C(CH_3), 7.1 Hz). IR(KBr) cm^{-1}: 2938 (ν_{C-H}), 1732 [$\nu_{C=O}$(ester)], 1330 and 1123 ($\nu_{S=O2}$), 1269 and 1169 [ν_{C-O}(ester)].

Preparation of Stainless Steel Electrodes Coated with Bioglass/Poly(ester–sulfone) Composites. Bioglass powder of composition 45S5 (45 wt % SiO_2, 24.5 wt % Na_2O, 24.5 wt % CaO, and 6 wt % P_2O_5) of mean particle size <7 μm was used. A suspension of Bioglass powder in 15 mL of ethanol or *n*-butanol was agitated in an ultrasonicator for 15 min and then stirred for 5 min. The poly(ester–sulfone) was stirred in 15 mL of DMF for 15 min at 50 °C to obtain a homogeneous solution. Then the Bioglass and poly(ester–sulfone) solutions were mixed, ultrasonically agitated for 15 min and then stirred for 5 min. To deposit Bioglass/poly(ester–sulfone) composites onto stainless steel electrodes by EPD, the distance between the electrodes was 7.5 mm, and the deposition time was 90 s at a voltage of 30 V. The depositions were carried out on 0.2 × 15 × 25 mm of stainless steel SUS 301 electrodes obtained from The Nilaco Corporation (Tokyo, Japan). Pure poly(ester–sulfone), prior to EPD and recovered from the electrode after EPD, was characterized by ^{1}H NMR and FTIR spectroscopy. Pure Bioglass and poly(ester–sulfone) preparations were also subjected to EPD at similar EPD conditions.

Biomineralization of Bioglass/Poly(ester–sulfone) Composite Films. The surface composition of the Bioglass/poly(ester–sulfone) composite coating deposited on the anode was investigated after immersion of samples in SBF. The composition of SBF, which was buffered with tri[hydroxymethyl]aminomethane and hydrochloric acid to maintain a pH of 7.4, has been described in the literature.[20] After holding the samples in SBF 30 mL for 1 or 2 weeks at 37 °C, the composites were removed and washed with distilled water.

The microstructures of the Bioglass/poly(ester–sulfone) composite and of pure poly(ester–sulfone) films were visualized by scanning electron microscopy (SEM) (dual-stage JSM-6010LA; JEOL Ltd., Tokyo, Japan). Elemental composition was determined by energy-dispersive X-ray spectroscopy (EDX). The elemental distribution was determined using Smart Map, which simultaneously acquired X-ray data from each pixel in an image (JEOL Ltd., Tokyo, Japan). X-ray diffraction (XRD) was used to determine the crystalline composition of the film surfaces and was performed with an automated diffractometer (RINT2000/PC; Rigaku, Tokyo, JAPAN) at a scan rate of 2° min^{-1}, between 0 and 60°.

RESULTS AND DISCUSSION

Synthesis of the Poly(ester–sulfone). We first attempted to prepare the sulfide-containing polyester by thiol–ene thermal radical polymerization that used bis(butenyl) methylsuccinate and 1,4-butanedithiol with azobis(isobutyronitrile) as the thermal initiator at 70 °C. Polymerization proceeded gradually and was complete within several hours (Figure 2). ^{1}H NMR spectrum of the poly(ester–sulfide) (thermal polymerization for 2 h) before reprecipitation showed existence both of terminal double bond (5.10 ppm) and thiol (1.31 ppm), indicating that the thiol moieties was not consumed by undesired oxidative coupling. Because the reaction did not produce a polymer of relatively high M_n, photopolymerization was next attempted.

Thiol–ene photopolymerization was then conducted with Irgacure 184 as the photoinitiator under UV irradiation at room temperature. Polymerizations using this photoinitiator proceeded rapidly even in an air atmosphere (Table 1, entries 3 and 6). Within short time periods (15–30 min), the photopolymerizations gave poly(ester–sulfide)s of greater M_ns than did the thermal polymerization (Figure 2, Table 1) and in excellent yields (89%–94%, Table 1). The SEC data

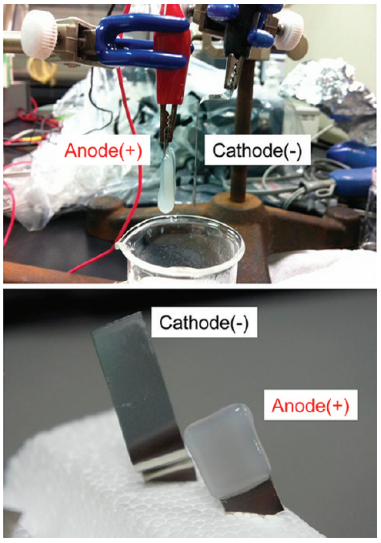


Figure 8. Anode selective electrophoretic deposition of poly(ester–sulfone) from the suspension.

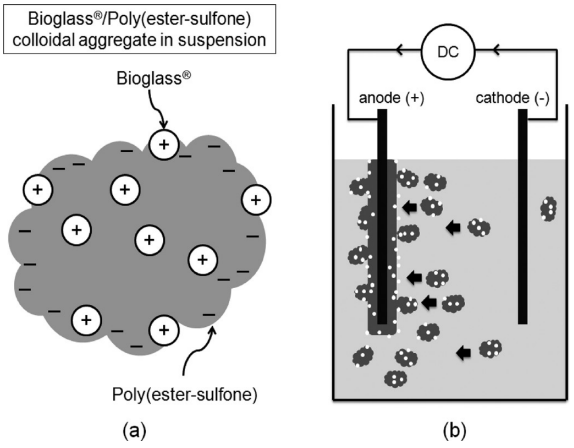


Figure 9. (a) Schematic of a charged Bioglass/poly(ester–sulfone) colloidal suspension in organic solution. (b) Schematic of the electrophoretically controlled deposition of the Bioglass/poly(ester–sulfone) colloid.

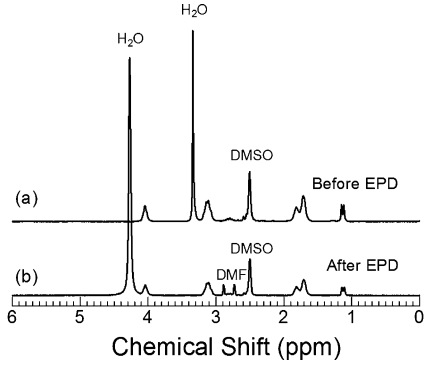


Figure 10. ^{1}H NMR spectra of the poly(ester–sulfone) (a) before EPD and (b) after EPD.

demonstrated that the poly(ester–sulfide)s have a M_w/M_n range (M_w/M_n = 1.5–1.7), which is commonly found for ordinary A–A- and B–B-type step-growth polymerizations.[21] The M_n of the polyester could be controlled by the amount of

dx.doi.org/10.1021/ma300396p | *Macromolecules* 2012, 45, 3326–3334

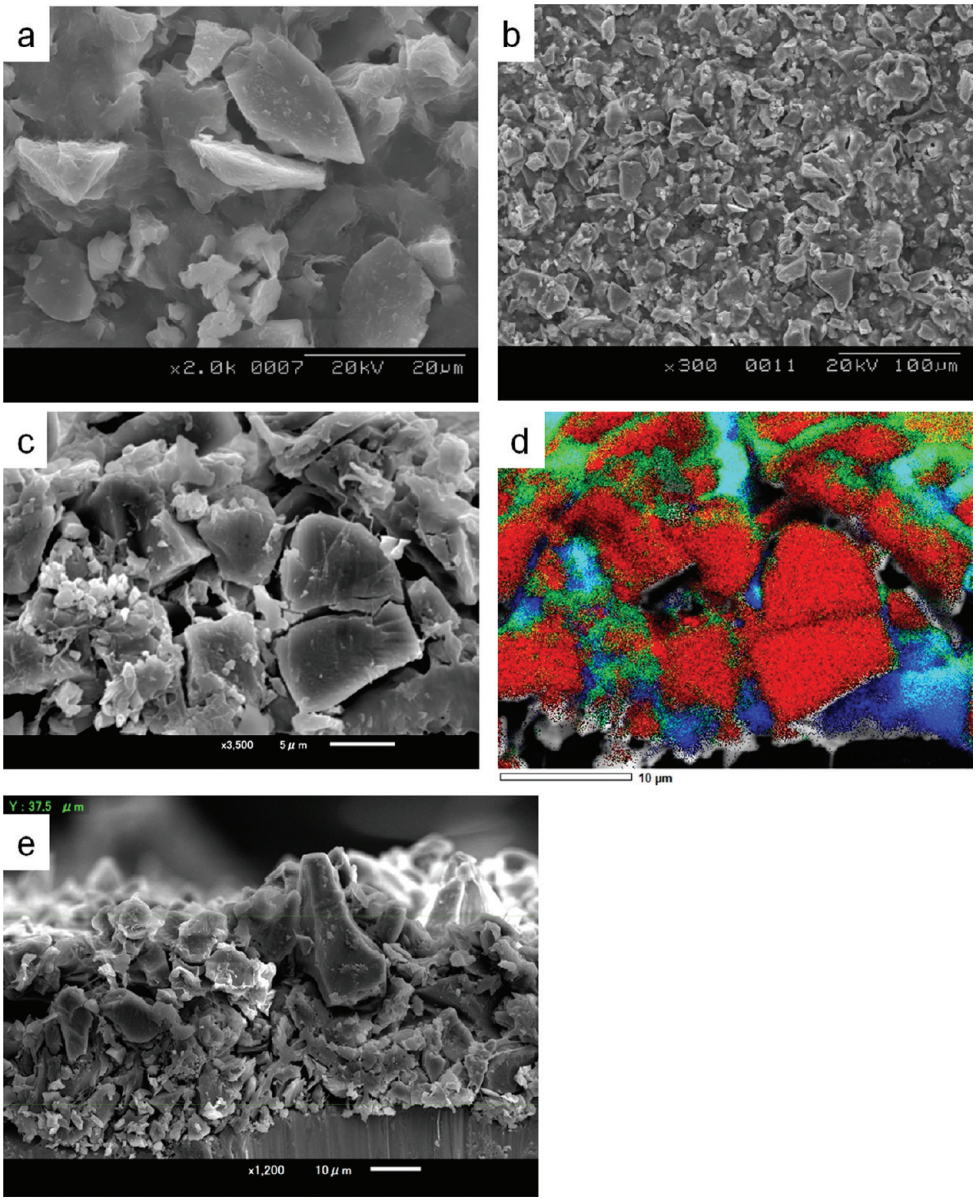


Figure 11. Scanning electron micrographs of Bioglass/Poly(ester−sulfone) films. Surfaces of the composite (a) at high magnification (×1000) and (b) at low magnification (× 300). (c) Cross section of the composite (×3500 magnification). (d) Cross section of an EDX map showing the distribution of silicon (red), carbon (green), and sulfur (blue) (×3500 magnification). (e) Thickness of the composite (×1200 magnification).

photoinitiator used without substantial loss of yield (compare entries 1 and 4, 2 and 5, and 3 and 6 in Table 1). The poly(ester−sulfide) (entry 6, Table 1; M_n = 29000) had a T_g of −64 °C, which is much lower than room temperature, and its T_m was not observed.

Additionally, we conducted photoinitiated thiol−ene polymerization using two other types of dithiol monomers (Figure 3). When the ether-type dithiol monomer was used, we readily obtained a poly(ester−sulfide) with a large M_n. However, the M_n for the 1,4-benzenedimethanethiol-containing polyester was substantially smaller. 1,4-Benzenedimethanethiol has a planar aromatic structure whereas 3,6-dioxa-1,8-octanedithiol represents a linear and flexible chain. Steric hindrance and rigidity of the thiol-monomer seems to inhibit to produce a high molecular weight polyester.[22]

Next, we investigated the oxone oxidation of the poly(ester−sulfide) (M_n = 5600 and M_w/M_n = 1.7) to produce the corresponding poly(ester−sulfone) (Figure 1). Initially, we examined the influence of the oxone concentration and the reaction time (Table 2). Only when 2 equiv of oxone per sulfide were used did quantitative conversion to sulfones occur. IR absorbance bands (1070−1030 cm^{-1}) ascribable to sulfoxide (the reaction intermediate) were not observed (Figure 4a) nor were any ^1H NMR resonances that would be influenced by the presence of a sulfoxide. However, the presence of sulfone was confirmed by their IR absorbencies at 1271 and 1124 cm^{-1}.

The M_n (∼12000) of the poly(ester−sulfone) (sulfonation conversion = 100%) was similar to that of its parent poly(ester−sulfide) (M_n = 11000). Moreover, the M_w/M_ns for the two polyesters were similar, indicating that neither degradation nor side reactions occurred during the oxidation (Figure 5). DSC heating traces for the poly(ester−sulfide) and the poly(ester−sulfone) are shown in Figure 6. The poly(ester−sulfide) had a higher T_g than did the parent polyester, probably because of the restricted molecular rotation neighboring the sulfone units and its high polarity inducing

dx.doi.org/10.1021/ma300396p | *Macromolecules* 2012, 45, 3326−3334

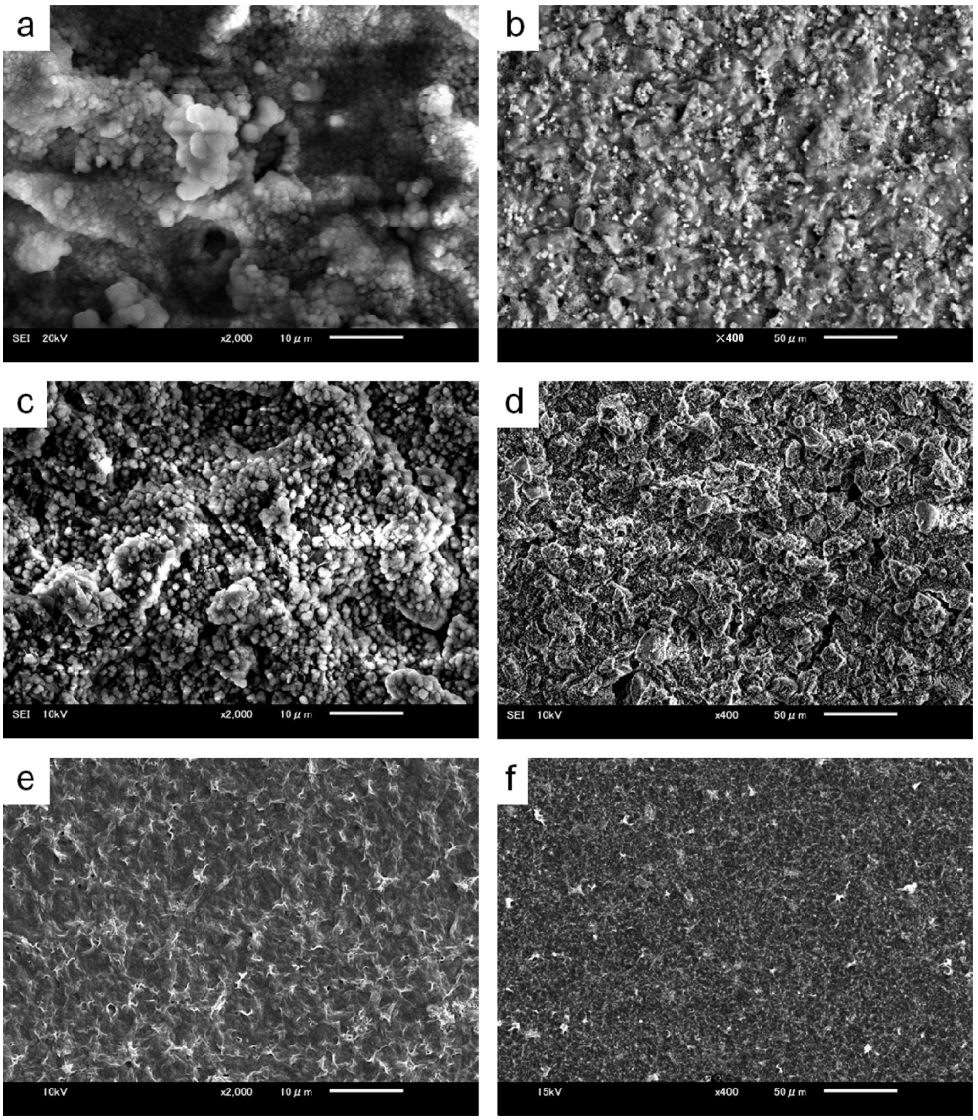


Figure 12. Scanning electron micrographs of Bioglass/Poly(ester−sulfone) films that had been immersed in SBF. (a, b) 1-week immersion (magnification ×2000, × 400, respectively) and (c, d) 2-week immersion (magnification ×2000, ×400, respectively) at 37 °C. (e, f) Control experiment using a pure poly(ester−sulfone) film (magnification ×2000, ×400, respectively).

significant intermolecular interaction. For the poly(ester−sulfone), T_m was 116 °C. The degradation temperatures associated with a 5% weight loss [T_d(5%)] were 363 °C for the poly(ester−sulfone) and 288 °C for the poly(ester−sulfide) (Figure 7). Obviously the presence of the sulfones improved the thermal stability of the polyester.

Electrophoretic Deposition of Bioglass/Poly(ester−sulfone) Coatings. Mixtures of Bioglass and poly(ester−sulfone) (M_n = 12000) formed colloidal suspensions in mixed solvents of DMF and ethanol or *n*-butanol and could be deposited onto a stainless-steel anode by EPD. The results are summarized in Table 3. Notably, isolated Bioglass particles moved toward the cathode in the same system (entry 4) because the surface of these Bioglass particles were covered with Ca^{2+} and Na^{+}.[17d] Conversely, we found an interesting phenomenon that the deposition of pure poly(ester−sulfone) is achieved via electrophoretic motion of polar sulfone to the anode in suspension ("swimming polyester", entries 1 and 2 and Figure 8). It is suggested that the polarized sulfones must dominate the surface charge of the composite (Figure 9a). The ^{1}H NMR spectra (Figure 10) of the poly(ester−sulfone) before and after deposition on the electrode (Table 3, entry 1) indicate that EPD did not alter the structure/composition of the poly(ester−sulfone). Ordinary aliphatic polyesters, e.g., polycaprolactone or polylactic acid, are not charged, and, when they are part of composites, are deposited onto the cathode by EPD,[18] which makes the deposition of the Bioglass/poly(ester−sulfone) onto the anode an unusual phenomenon. Therefore, control of the electrophoretic behavior of a Bioglass/polyester composite can probably be controlled by the choice of the polyester.

There were cracks in the films prepared from a pure poly(ester−sulfone) suspension (6 g/L; Table 3, entry 1) and in Bioglass/poly(ester−sulfone) films prepared from colloidal suspension that contained twice the concentration of the poly(ester−sulfone) (12 g/L; Table 3, entry 7). To deposit a smooth pure poly(ester−sulfone) film on the anode, a smaller concentration (4 g/L) of the poly(ester−sulfone) was used (compare entry 2 in Table 3). In general, *n*-butanol, rather than ethanol, more effectively controlled the stability of the Bioglass suspension (compare entries 3 and 4 in Table 3). [17k] However,

dx.doi.org/10.1021/ma300396p | *Macromolecules* 2012, 45, 3326−3334

as a consequence of the lower electric permittivity of *n*-butanol, the films were thinner when *n*-butanol, rather than ethanol, was the cosolvent (compare entries 5 and 6 in Table 3). Therefore, we selected a film prepared with DMF/ethanol as the solvent (Table 3, entry 5) for the experiments shown in Table 3.

We assessed the surface and cross-section morphology of the Bioglass/poly(ester−sulfone) film by SEM and EDX. The SEM images of the film show that Bioglass particles are well dispersed in a matrix formed by the poly(ester−sulfone) (Figure 11a,b). Parts c and d of Figure 11 show a SEM image and an EDX map for a cross-section of the film, respectively. The colors in the EDX map identify silicon (red), carbon (green), and sulfur (blue) and indicate that the Bioglass particles were homogeneously dispersed, i.e., the poly(ester−sulfone) surrounds and is in close contact with the Bioglass particles. Additionally, the nearer to the surface of the electrode, the greater is the sulfur density. (The bottom of the micrograph in Figure 11d is the region closest to the electrode.) Our results strongly indicate that a Bioglass/poly(ester−sulfone) colloidal diphasic suspension has formed (see Figure 9) and that the sulfone moieties were responsible for anode-selective deposition. The composite thickness was 38 μm on average (Figure 11e).

After a 1-week immersion in SBF, SEM images of the Bioglass/poly(ester−sulfone) film revealed a dense deposit covering the film (Figure 12a,b). Such deposits were absent prior to soaking the film in SBF (Figure 11a,b). At the higher magnification, many spherical particles are seen on the surface of the film (Figure 12a). For the film soaked for 2 weeks in SBF, more densely packed spherical particles were seen (Figure 12c). The morphology of these deposits is very similar to that of hydroxyapatite deposited on titanium or a bioactive glass/ceramic composite by biomimetic methods, i.e. upon exposure to SBF.[17b,j,19,20] As a control experiment, the pure poly(ester−sulfone) film on the stainless steel electrode (Table 3, entry 2) was also immersed in SBF for 1 week at 37 °C. No new deposit, similar in appearance to hydroxyapatite crystals, formed on the surface of the film (Figure 12e,f). The substances deposited on the surface of the Bioglass/poly(ester−sulfone) film were identified by XRD as dicalcium phosphate dihydrate (DCPD) and hydroxyapatite, which is a hydrolysis product of DCPD[23] (Figure 13). Phase analysis by XRD also indicated that the amount of hydroxyapatite had increased, and the amount of DCPD had decreased after the 2-week immersion in SBF. The extent to which DCPD was hydrolyzed to hydroxyapatite was therefore dependent on immersion time.

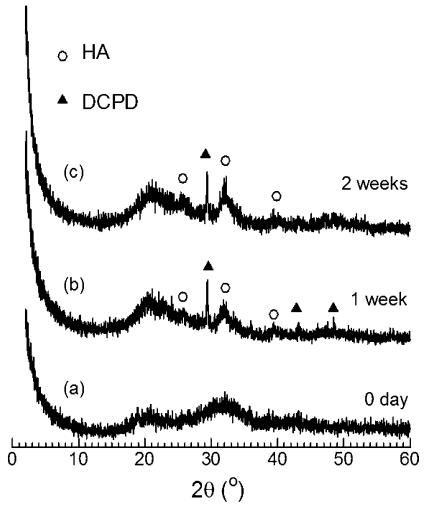


Figure 13. XRD patterns for (a) the Bioglass/poly(ester−sulfone) film before immersion in SBF and after immersion in SBF for (b) 1 and (c) 2 weeks. DCPD, dicalcium phosphate dihydrate. HA, hydroxyapatite.

CONCLUSION

The demand for implantable medical devices is steadily increasing, especially the demand for spinal and orthobiologic implants, and improved technologies and biomaterials are therefore required. In this study, we prepared a Bioglass/click poly(ester−sulfone) colloid, which could be deposited onto a stainless steel surface by EPD to form a soft composite coating. The Bioglass/click poly(ester−sulfone) film developed a surface layer of hydroxyapatite when immersed in SBF confirming the bioactive behavior of the new composite coating. The easy deposition and the ability to produce surface hydroxyapatite layers are properties required for bone-related implants, e.g. bioactive coatings on metallic substrates. The synthesis of the poly(ester−sulfone) was facile, and the poly(ester−sulfone) was stable in the EPD cell, e.g., under electric fields. The results reported herein therefore provide a foundation upon which new bioactive composite materials may be developed as soft coatings for bone-related implants.

AUTHOR INFORMATION

Corresponding Author

*Telephone: +81-52-735-7159. Fax: +81-52-735-5342. E-mail: takasu.akinori@nitech.ac.jp.

Notes

The authors declare no competing financial interest.

ACKNOWLEDGMENTS

This work was funded by the Ministry of Education, Science, and Culture of Japan (Grant-in-Aid for Development Scientific Research, no. 24550132). The authors are grateful to Dr. Kenji Nagata of the Nagoya Institute of Technology for valuable advice and fruitful discussions. This work was supported by the JSPS International program for Young Researcher Overseas Visits.

REFERENCES

(1) (a) Vert, M. *Biomacromolecules* **2005**, *6*, 538−546. (b) Takwa, M.; Xiao, Y.; Simpson, N.; Malmström, E.; Hult, K.; Koning, C. E.; Heise, A.; Martinelle, M. *Biomacromolecules* **2008**, *9*, 704−710. (c) Misra, S. K.; Valappil, S. P.; Roy, I.; Boccaccini, A. R. *Biomacromolecules* **2006**, *7*, 2249−2258. (d) Seyednejad, H.; Vermonden, T.; Fedorovich, N. E.; Eijik, R.; Steenbergen, M. J.; Dhert, W. J. A.; Nostrum, C. F.; Hennink, W. E. *Biomacromolecules* **2009**, *10*, 3048−3054. (e) Naolou, T.; Busse, K.; Kressler, J. *Biomacromolecules* **2010**, *11*, 3660−3667. (f) Zhang, P.; Wu, H.; Wu, H.; Lu, Z.; Deng, C.; Hong, Z.; Jing, X.; Chen, X. *Biomacromolecules* **2011**, *12*, 2667−2680. (g) Moglia, R. S.; Holm, J. L.; Sears, N. A.; Wilson, C. J.; Harrison, D. M.; Cosgriff-Hernandez, E. *Biomacromolecules* **2011**, *12*, 3621−3628.

(2) (a) Carothers, W. H.; Dorough, G. L. *J. Am. Chem. Soc.* **1930**, *52*, 711−721. (b) Takiyama, E.; Niikura, I.; Hatano, Y. Japan Patent 189,823, 1995. (c) Miura, M.; Watanabe, H.; Fujiwara, M. Japan Patent 53, 695, 1995. (d) Buzin, P.; Lahcini, M.; Schwarz, G.; Kricheldord, H. R. *Macromolecules* **2008**, *41*, 8491−8495. (e) Garaleh, M.; Lahcini, M.; Kricheldorf, H. R.; Weidner, S. M. *J. Polym. Sci.; Part A: Polym. Chem.* **2009**, *47*, 170−177.

(3) (a) Kricheldorf, H. R.; Kreiser-Saunders, I. *Macromol. Chem. Phys.* **1990**, *191*, 1057−1066. (b) Lofgren, A.; Albertsson, A. C.; Dubois, P.; Jerome, R. *J. Macromol. Sci.; Rev. Macromol. Chem. Phys.* **1995**, *35*,

379−418. (c) Kim, S.; Han, Y. K.; Kim, Y. H.; Hong, S. I. *Macromol. Chem. Phys.* **1992**, *193*, 1623−1631.
(4) (a) Ajioka, M.; Enomoto, K.; Suzuki, K.; Yamaguchi, A. *Bull. Chem. Soc. Jpn.* **1995**, *68*, 2125−2131. (b) Ni: Mochizuki, M.; Mukai, K.; Yamada, K.; Ichise, N.; Murase, S.; Iwaya, Y. *Macromolecules* **1997**, *30*, 7403−7407. (c) $HfCl_4(THF_2)$: Ishihara, K.; Ohara, S.; Yamamoto, H. *Science* **2000**, *290*, 1140−1142. (d) Sn distannoxane: Ishii, M.; Okazaki, M.; Shibasaki, Y.; Ueda, M. *Biomacromolecules* **2001**, *2*, 1267−1270.
(5) (a) Takasu, A.; Oishi, Y.; Iio, Y.; Inai, Y.; Hirabayashi, T. *Macromolecules* **2003**, *36*, 1772−1774. (b) Takasu, A.; Iio, Y.; Oishi, Y.; Narukawa, Y.; Hirabayashi, T. *Macromolecules* **2005**, *38*, 1048−1050. (c) Takasu, A.; Iio, Y.; Mimura, T.; Hirabayashi, T. *Polym. J.* **2005**, *37*, 946−953. (d) In water: Takasu, A.; Takemoto, A.; Hirabayashi, T. *Biomacromolecules* **2006**, *7*, 6−9. (e) PLA: Takasu, A.; Narukawa, Y.; Hirabayashi, T. *J. Polym. Sci.; Part A: Polym. Chem* **2006**, *44*, 5247−5253. (f) Combination with ROP: Takasu, A.; Tsuruta, H.; Narukawa, Y.; Shibata, Y.; Oshimura, M.; Hirabayashi, T. *Macromolecules* **2008**, *41*, 4688−4693. (g) Customized catalyst: Takasu, A.; Makino, T.; Yamada, S. *Macromolecules* **2010**, *43*, 144−149. (h) Microwave-assisted: Yamada, S.; Takasu, A. *Polym. J.* **2011**, *43*, 1003−1007.
(6) (a) Hydroxyl: Takasu, A.; Shibata, Y.; Narukawa, Y.; Hirabayashi, T. *Macromolecules* **2007**, *40*, 151−153. (b) Hydroxyl: Shibata, Y.; Takasu, A. *J. Polym. Sci.; Part A: Polym. Chem.* **2009**, *47*, 5747−5759. (c) Mercapto: Yamamoto, K.; Takasu, A. *Macromolecules* **2010**, *43*, 8519−8523. (d) Disulfide: Sato, Y.; Takasu, A. *Polym. J.* **2010**, *42*, 956−959.
(7) Kolb, H. C.; Finn, M. G.; Sharpless, K. B. *Angew. Chem., Int. Ed.* **2001**, *40*, 2004−2021.
(8) (a) Rostovtsev, V. V.; Green, L. G.; Fokin, V. V.; Sharpless, K. B. *Angew. Chem., Int. Ed.* **2002**, *41*, 2596−2599. (b) Chan, T. R.; Hilgraf, R.; Sharpless, K. B.; Fokin, V. V. *Org. Lett.* **2004**, *17*, 2853.
(9) (a) Adhesive polymer: Diaz, D. D.; Punna, S.; Holzer, P.; Mcpherson, A. K.; Sharpless, K. B.; Fokin, V. V.; Finn, M. G. *J. Polym. Sci.; Part A: Polym. Chem.* **2004**, *42*, 4392. (b) Polyketone: Tang, B. Z.; Qin, A.; Jim, C. K. W.; Lu, W.; Lam, J. W. Y.; Häussler, M.; Dong, Y.; Sung, H. H. Y.; Williams, I. D.; Wong, G. K. L. *Macromolecules* **2007**, *40*, 2308−2317. (c) Helical polymer: Kobayashi, S.; Itomi, K.; Morino, K.; Iida, H.; Yashima, E. *Chem. Commun.* **2008**, 3019−3021. (d) Poly(ethylene glycol): Liu, X. M.; Thakur, A.; Wang, D. *Biomacromolecules* **2007**, *8*, 2653−2658. (e) Biomass-based polymer: Michinobu, T.; Inazawa, Y.; Hiraki, K.; Katayama, Y.; Masai, E.; Nakamura, M.; Ohara, S.; Shigehara, K. *Chem. Lett.* **2008**, 154−155. Michinobu, T.; Hirai, K.; Inazawa, Y.; Katayama, Y.; Masai, E.; Nakayama, M.; Ohara, S.; Shigehara, K. *Polym. J.* **2011**, *43*, 648−653. (f) Review: Binder, W. H.; Sachsenhofer, R. *Macromol. Rapid Commun.* **2007**, *28*, 15−54. (g) Review: Binder, W. H.; Sachsenhofer, R. *Macromol. Rapid Commun.* **2008**, *29*, 952−981. (h) Review: Johnson, J. A.; Finn, M. G.; Koberstein, J. T.; Turro, N. J. *Macromol. Rapid Commun.* **2008**, *29*, 1052−1072. (i) New "click" chemistry: Koyama, Y.; Yonekawa, M.; Takata, T. *Chem. Lett.* **2008**, *37*, 918−919. (j) Lee, Y. G.; Koyama, Y.; Yonekawa, M.; Takata, T. *Macromolecules* **2009**, *42*, 7709−7717. (k) α-Azide-ω-alkyne monomers: Binauld, S.; Damiron, D.; Hamaide, T.; Pascault, J. P.; Fleury, E.; Drockenmuller, E. *Chem. Commun.* **2008**, 4138−4140. Binauld, D.; Fleury, E.; Drockenmuller, E.; Huang, F. *J. Polym. Sci.; Part A: Polym. Chem.* **2010**, *48*, 2470−2476. (l) Functional polymer: Schwartz, E.; Breitenkamp, K.; Fokin, V. V. *Macromolecules* **2011**, *44*, 4735−4741. (m) Polytriazoleimide: Zhou, X.; Wan, L.; Hu, Y.; E, Y.; Huang, F.; Du, L. *Polym. J.* **2010**, *42*, 216−222.
(10) (a) Nagao, Y.; Takasu, A. *Macromol. Rapid Commun.* **2009**, *30*, 199−203. (b) Nagao, Y.; Takasu, A. *J. Polym. Sci.; Part A: Polym. Chem.* **2011**, *48*, 4207−4218.
(11) (a) Sletten, E. M.; Bertozzi, C. R. *Org. Lett.* **2008**, *10*, 3097−3099. (b) Codelli, J. A.; Baskin, J. M.; Agrad, N. J.; Bertozzi, C. R. *J. Am. Chem. Soc.* **2008**, *130*, 11486−11493. (c) Jewett, J. C.; Sletten, E. M.; Bertozzi, C. R. *J. Am. Chem. Soc.* **2010**, *132*, 3688−3690.
(12) Koyama, Y.; Yonekawa, M.; Takata, T. *Chem. Lett.* **2008**, *37*, 918−919.
(13) (a) Jacobine, A. F. *In Radiation Curing in Polymer Science and Technology III*; Fouassier, J. D., Rabek, J. F., Eds.; Elsevier: London, 1993, *7*, 219−268. (b) Hoyle, C. E.; Lee, T. Y.; Roper, T. *J. Polym. Sci., Part A: Polym. Chem.* **2004**, *42*, 5301−5338.
(14) (a) Wilderbeek, H. T. A.; Goossens, J. G. P.; Bastiaansen, C. W. M.; Broer, D. J. *Macromolecules* **2002**, *35*, 8962−8968. (b) Wilderbeek, H. T. A.; Meer, M. G. M.; Bastiaansen, C. W. M.; Broer, D. J. *J. Phys. Chem. B* **2002**, *106*, 12874−12883. (c) Killops, K. L.; Campos, L. M.; Hawker, C. J. *J. Am. Chem. Soc.* **2008**, *130*, 5062−5064. (d) Kwinsnek, L.; Nazarenko, S.; Hoyle, C. E. *Macromolecules* **2009**, *42*, 7031−7041. (e) Kloxin, C. J.; Scott, T. F.; Bowman, C. N. *Macromolecules* **2009**, *42*, 2551−2556. (f) Shin, J.; Matsushima, H.; Chan, J. W.; Hoyle, C. E. *Macromolcules* **2009**, *42*, 3294−3301. (g) Lluch, C.; Ronda, J. C.; Galia, M.; Lligadas, G.; Cádiz, V. *Biomacromolecules* **2010**, *11*, 1646−1653.
(15) (a) Santerre, J. P.; Brash, J. L. *Macromolecules* **1991**, *24*, 5497−5503. (b) Marianucci, E.; Berti, F.; Pilati, F.; Manaresi, P. *Polymer* **1994**, *35*, 1564−1566. (c) Lu, C.; Cui, Z.; Wang, Y.; Li, Z.; Guan, C.; Yang, B.; Shen, J. *J. Mater. Chem.* **2003**, *13*, 2189−2195. (d) Rydholm, A. E.; Bowman, C. N.; Anseth, K. S. *Biomaterials* **2005**, *26*, 4495−4506. (e) Rydholm, A. E.; Reddy, S. K.; Anseth, K. S.; Bowman, C. N. *Biomacromolecules* **2006**, *7*, 2827−2836. (f) Huang, Y.; Paul, D. R. *Macromolecules* **2006**, *39*, 1554−1559.
(16) (a) Boccaccini, A. R.; Keim, S.; Ma, R.; Zhitmirsky, L. I. *J. R. Soc. Interface* **2010**, *7*, 581−613. (b) Gastillo, J.; Dimaki, M.; Svendsen, W. E. *Integr. Biol.* **2009**, *1*, 30−42. (c) Lee, S. W.; Belcher, A. M. *Nano Lett.* **2004**, *4*, 387−390. (d) Guo, L. J. *Adv. Mater.* **2007**, *19*, 495−513.
(17) (a) Sarker, P.; Nicholson, P. S. *J. Am. Ceram. Soc.* **1996**, *79*, 1987−2002. (b) Roether, J. A.; Boccaccini, A. R.; Hench, L. L.; Maquet, V.; Gautier, S.; Jérôme, R. *Biomaterials* **2002**, *23*, 3871−3878. (c) Corni, I.; Neumann, N.; Novak, S.; König, K.; Veronesi, P.; Chen, Q.; Ryan, M. P.; Boccaccini, A. R. *Surf. Coat. Technol.* **2009**, *203*, 1349−1359. (d) Pishbin, F.; Simchi, A.; Ryan, M. P.; Boccaccini, A. R. *Surf. Coat. Technol.* **2011**, *205*, 5260−5268. (e) Rodriguez, H. H.; Vargas, G.; Cortés, D. A. *Ceram. Int.* **2008**, *34*, 1303−1130. (f) Van der Biest, O. O.; Vandeperre, L. J. *Annu. Rev. Mater. Sci.* **1999**, *29*, 327−352. (g) Boccaccini, A. R.; Zhitomirsky, I. *Curr. Opin. Solid State Mater. Sci.* **2002**, *6*, 251−260. (h) Ma, R.; Zhitomirsky, I. *J. Alloys Compd.* **2011**, *509*, S510−S513. (i) Wang, Y.; Deen, I.; Zhitomirsky, I. *J. Colloid Interface Sci.* **2011**, *362*, 367−374. (j) Boccaccini, A. R.; Peters, C.; Roether, J. A.; Eifler, D.; Misra, S. K.; Minay, E. J. *J. Mater. Sci.* **2006**, *41*, 8152−8159. (k) Xiao, X. F.; Liu, R. F. *Mater. Lett.* **2006**, *60*, 2627−2632.
(18) (a) Hench, L. L.; Splinter, R. J.; Allen, W. C.; Greenlee, T. K. *J. Biomed. Mater. Res.* **1971**, *2*, 117−141. (b) Hench, L. L. *J. Am. Ceram. Soc.* **1998**, *81*, 1705−1728. (c) Hench, L. L. *J. Eur. Ceram. Soc.* **2009**, *29*, 1257−1265. (d) Oonishi, H.; Hench, L. L.; Wilson, J.; Sugihara, F.; Tsuji, E.; Matsuura, M.; Kin, S.; Yamamoto, T.; Mizokawa, S. *J. Biomed. Mater. Res.* **2000**, *51*, 37−46. (e) Misra, S. K.; Nazhat, S. N.; Valappil, S. P.; Torbati, M. M.; Wood, R. J. K.; Roy, I.; Boccaccini, A. R. *Biomacromolecules* **2007**, *8*, 2112−2119.
(19) Xiao., X.; Liu, R.; Tang, X. *J. Mater. Sci.: Mater. Med.* **2009**, *20*, 691−697.
(20) Kokubo, T.; Kushitani, H.; Sakka, S. *J. Biomed. Mater. Res.* **1990**, *24*, 721−734.
(21) (a) Carothers, C. H. *Trans. Faraday Soc.* **1936**, *32*, 39. (b) Flory, P. J. *Chem. Rev.* **1946**, *39*, 137.
(22) Wutticharoenwong, K.; Soucek, M. D. *Macromol. Mater. Eng.* **2008**, *293*, 45−46.
(23) Fulmer, M. T.; Brown, P. W. *J. Mater. Sci.: Mater. Med.* **1998**, *9*, 197−202.

Macromolecules

Article

pubs.acs.org/Macromolecules

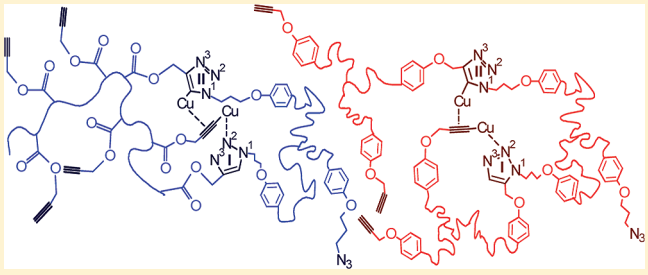
Autocatalysis in the Room Temperature Copper(I)-Catalyzed Alkyne–Azide "Click" Cycloaddition of Multivalent Poly(acrylate)s and Poly(isobutylene)s

Diana Döhler,[†] Philipp Michael,[†] and Wolfgang H. Binder*

Chair of Macromolecular Chemistry, Institute of Chemistry, Division of Technical and Macromolecular Chemistry, Faculty of Natural Science II (Chemistry, Physics and Mathematics), Martin-Luther-University Halle-Wittenberg, Halle D-06120, Germany

Supporting Information

ABSTRACT: The concept of self-healing polymers requires fast and efficient cross-linking processes, ideally based on catalytic reactions. We investigate autocatalytic effects in cross-linking processes based on the copper(I)-catalyzed alkyne–azide "click" cycloaddition reaction (CuAAC), taking advantage of the 1,3-triazole rings formed during the CuAAC-based cross-linking, which act as ligands for subsequent "click"-reactions in turn accelerating the reaction rate of subsequent CuAAC-reactions. Catalysis during the cross-linking reactions of multivalent polymeric alkynes and azides (nine atactic random poly(propargyl acrylate-*co*-*n*-butyl acrylate)s, M_n = 7000–23400 g/mol) prepared via nitroxide mediated polymerization (NMP) and displaying alkyne-contents ranging from 2.7 mol % to 14.3 mol % per chain were studied via melt-rheology and differential scanning calorimetry (DSC), revealing significant increases of the reaction rate with increasing alkyne-concentrations. A kinetic analysis showed autocatalytic effects (up to a factor of 4.3) now enabling a deeper understanding of the catalysis as well as on the achievement of a "click"-cross-linking concept acting at room temperature. Effects exerted by the molecular weight were investigated by reacting five three-arm-star azido-telechelic poly(isobutylene)s (PIB's) (M_n = 5500–30000 g/mol) and one three-arm-star alkyne-telechelic PIB (M_n = 6300 g/mol) in the cross-linking-reaction, thus linking molecular mobility to changes in CuAAC-reactivity revealing faster network formation with lower molecular weights. The now designable significant autocatalytic effects together with the optimized reaction rate via the lowest molecular weight compounds enabled the design of a new, highly efficient and fast cross-linking system acting at room temperature.



INTRODUCTION

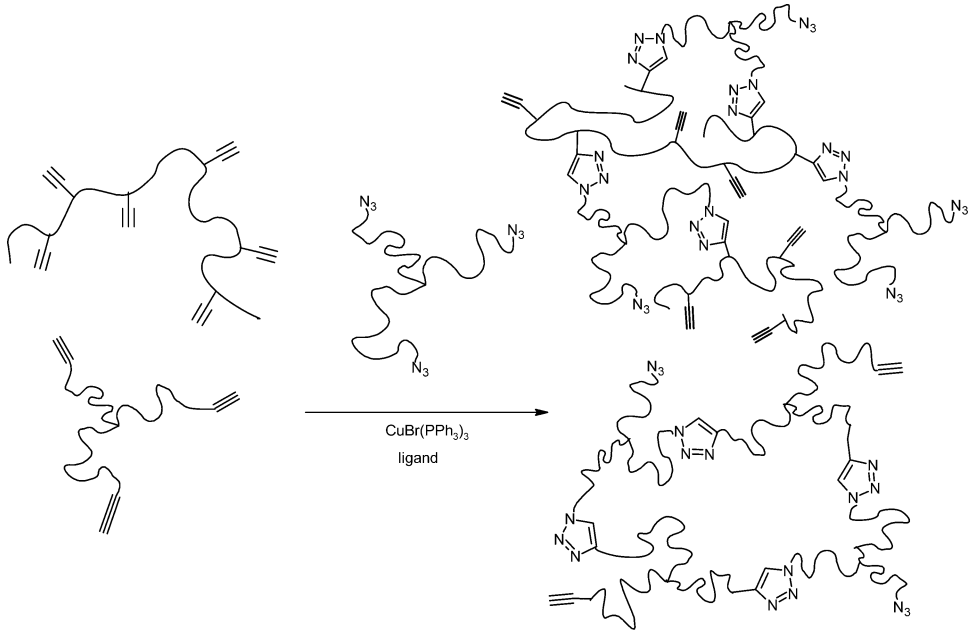
Network formation based on cross-linking and postcross-linking reactions is of great interest for materials scientists as these reactions can be used to build up new complex architectures or to improve existing materials in their physicochemical and thermomechanical properties, most of all self-healing polymeric materials. Therefore, a permanent strive for reactions enabling cross-linking under mild reaction conditions as well as the quest for new reactants has been generating efficient reactions such as Diels–Alder (DA) reactions, or "click"-type-reactions like the CuAAC,[1−7] which proceed at moderate temperature[1,2] with high efficiency and substrate insensitivity. The "click"-type reactions in particular are valuable tools for the design of self-healing polymers,[8−11] which to a large extend rely on efficient and insensitive cross-linking chemistry. In contrast to the previously used epoxide-[12−14] or metathesis-[8,10,15−21] based cross-linking reactions, many approaches using DA-type reactions have been investigated, featuring furane/maleimide linkers[22] or other maleimides,[23−28] thus generating polymers with switchable mechanical properties.[29−32] However, in most of these cases the underlying DA reactions proceeded at temperatures significantly above room temperature, often at 80–100 °C, leading to cross-linked materials such as hydrogels, shape-memory materials, in nanoscale probe lithography, adhesives or coatings.[33−40]

To overcome the described disadvantage of required high temperatures we intensely investigated the use of the CuAAC as cross-linking reaction, specifically for the purpose of self-healing polymers.[41,42] The CuAAC in particular opens suitable pathways for cross-linking approaches that have been used for the preparation of hydro- or microgels based on poly(vinyl alcohol)s,[43] poly(ethylenimine)s,[44] poly(ethylene glycol)-s,[43,45,46] hyaluronic acids,[47−49] or for the stabilization of organogels.[50] For this purpose copper(II) sulfate pentahydrate/sodium ascorbate or ascorbic acid in aqueous conditions as well as CuBr, CuI, or CuCl in organic solutions were used as catalytic systems[43−50] and the corresponding "click" reactions proceeded at moderate, but still elevated temperatures.[43−50] In other concepts, the CuAAC has been applied to synthesize cellulose nanoplatelet gels[51] and polyester nanoparticles[52] as well as particle-like structures[53] and polymeric nanoparticles[54]

Received: February 27, 2012
Revised: April 2, 2012
Published: April 13, 2012

 © 2012 American Chemical Society

Scheme 1. CuAAC of Multivalent Poly(acrylate)s and PIB's Functionalized with Alkyne and Azide Groups, Respectively, Applying Bromotris(triphenylphosphine)copper(I) and a Ligand as Catalytic System at 20 °C



via intramolecular cross-linking reactions, often by use of cross-linking reactions based on low-molecular-weight[55] or polymeric precursors.[41,42]

Our concept of using the CuAAC as cross-linking-principle relies on the use of liquid monovalent or three-arm-star azido-telechelic polymers, namely PIB's with different liquid multivalent alkynes for their use in self-healing materials.[41,42] When studying different copper-catalysts the resulting kinetic behavior of the cross-linking reaction in solution and in the solid state revealed that bromotris(triphenylphosphine)copper(I) was the best catalyst for a cross-linking reaction, also observing an acceleration of the reaction rate in solution when using NMR-spectroscopy.[41,42] Therefore, we hypothesized that the autocatalytic effects observed in solution should operate in the melt-state of polymers as well, in particular for the herein described cross-linking of multivalent poly(acrylate)s and PIB's via "click" chemistry.

Ligands containing triazole rings and accelerating the reaction rate of the CuAAC are known in literature,[56] with TBTA (tris[(1-benzyl-1*H*-1,2,3-triazol-4-yl)methyl]amine)[56] being one prominent example completely encasing the catalytically active copper(I) center and protecting it against degradation. Such tetradentate ligands seem to be so effective because of their tertiary amine accelerating the catalytic process while increasing the electron density on the copper(I) center.

Within this publication we report on the catalysis during the cross-linking reaction of multivalent polymeric alkynes and azides via a CuAAC-process (see Scheme 1), aiming at a deeper understanding of the catalytic effects as well as on the achievement of a "click"-cross-linking concept acting at room temperature. Beside this we focus on the autocatalysis during the cross-linking reaction due to the *in situ* formation of triazole rings, investigating their influence with respect to density when present in various amounts within a random copolymer of propargyl acrylate (PA) and *n*-butyl acrylate (*n*BA). Furthermore, we evaluate autocatalytic effects with respect to the molecular weight of five three-arm-star azido-telechelic PIB's and one three-arm-star alkyne-telechelic PIB on the cross-linking-reaction, trying to link molecular mobility to changes in CuAAC-reactivity.

EXPERIMENTAL SECTION

Materials. The destabilization of commercial available *n*BA was done by passing through a short column of neutral alumina into a flask with calcium hydride and stored overnight into freezer. Before using *n*BA was distilled freshly. PA and TMSPA were prepared according to Thelakkat et al.[57] 1,3,5-Tris(2-methoxy-2-propyl)benzene was synthesized according to previous descriptions.[58,59] Trimethyl(3-phenoxy-1-propynyl)silane was synthesized according to Morgan et al.[60] Tris[(1-benzyl-1*H*-1,2,3-triazol-4-yl)methyl]amine (TBTA) was prepared according to Lee et al.[61] All other chemicals were purchased from Sigma-Aldrich and used without further purification.

Instrumentation. *NMR spectra* were recorded on a Varian Gemini 2000 (400 MHz) or on a Varian Unity Inova 500 (500 MHz) at 27 °C. Deuterated chloroform ($CDCl_3$) was used as solvent. All chemical shifts were given in ppm. MestRec-C software (version 4.9.9.6) was used for interpretation of the NMR-spectra.

ATR-IR spectra were performed on a Bruker Tensor VERTEX 70 equipped with a Golden Gate Heated Diamond ATR Top-plate. Opus 6.5 was used for analyzing data.

Gel permeation chromatography (GPC) measurements were performed on a Viscotek GPCmax VE 2002 using a $H_{HR}H$ Guard-17369 and a GMH_{HR}-N-18055 column in THF at 40 °C and via detection of the refractive index with a VE 3580 RI detector of Viscotek. For external calibration PIB-standards (320 g/mol to 578000 g/mol) or PS-standards (1050 g/mol to 115000 g/mol) from Viscotek were used. The concentration of all samples was 3 mg/mL and the flow rate was 1 mL/min.

Rheological measurements were performed on an oscillatory plate rheometer MCR 501/SN 80753612 from Anton Paar (Physica). For all measurements a PP08 measuring system (parallel plated, diameter 8 mm) was used. Measurements were performed at 20 °C and the sample temperature was regulated by thermoelectric heating and cooling. For evaluation of data the RheoPlus/32 software (V 3.40) and OriginPro7 was used. For sample preparation a 1: 1 mixture of an azido-functionalized polymer and an alkyne-functionalized polymer was placed in a flask (100.0−150.0 mg) and was dissolved in THF (approximately 3.0 mL). The solvent was removed and the sample was dried in high vacuo. The frequency sweep of the pure polymer mixture

which was used as basic measurement was performed with a strain γ of 10.0% and with an angular frequency ω ranging from 100 to 1 rad/s. TBTA (0.2 equiv per functional group) was added to the polymer mixture in case of poly(acrylate)s. $CuBr(PPh_3)_3$ (0.1 equiv per functional group) was dissolved in $CHCl_3$ (40.0 μL) and was added as a stock solution to all investigated polymer mixtures. Subsequently, the reaction mixture was mixed with a spatula and was immediately put on the rheometer plate. Measurements were performed with a strain γ of 0.1% or 0.5% and with an angular frequency ω ranging from 100 to 1 rad/s. A frequency sweep was performed every 20 minutes. All samples were measured at 20 °C. For samples **1a**−**i** + **3** a measurable torque could be achieved after approximately 100 min whereas in case of samples **4a**,**b** + **2** a reliable torque was observed only after reaction times of approximately 200 min. The gelation time[62] was determined as crossover of the storage (G') and loss modulus (G''). Measurements were stopped after a total time (46−160 h) when the values of the storage and the loss modulus stayed constant (second decimal place) for at least 60 min. The plateau moduli corresponded to the storage moduli measured at 100 Hz and total time and were in the range of soft technical rubbers or soft natural gums.[62] The rate constants k were analyzed over time up to the gel point. The factor of autocatalysis was determined by comparing the rate constant k_0 and the rate constant $k_{crossover}$ corresponding to the gelation time.

Differential scanning calorimetry (DSC) measurements were performed on a differential scanning calorimeter 204F1/ASC Phoenix from Netzsch. Crucibles and lids made of aluminum were used. Measurements were performed in a temperature range from 20 to 200 °C using heating rates of 2, 5, and 10 K/min. As purge gas a dry nitrogen flow of 20 mL/min was used for all experiments. For evaluation of data the Proteus Thermal Analysis Software (version: 5.2.1) and OriginPro7 was used. For sample preparation a 1: 1 mixture of an azido-functionalized polymer and an alkyne-functionalized polymer was placed in a flask (100.0−150.0 mg) and was dissolved in THF (approximately 3.0 mL). The solvent was removed and the sample was dried in high vacuo. $CuBr(PPh_3)_3$ (0.1 equiv per functional group) and in case of poly(acrylate)s TBTA (0.2 equiv per functional group) was added to the polymer mixture which was mixed with a spatula and immediately put in a crucible and closed with a pinhole-pricked lid.

Synthesis. *General Procedure for the NMP of Random Copolymers Consisting of PA and nBA (Poly(propargyl acrylate-co-ran-n-butyl acrylate)) (**1a**−**i**).* The polymerization was performed according to a general procedure with modifications as described by Thelakkat et al.[57] Previously destabilized *n*BA (687 μL, 4.77 mmol), TMSPA (91 μL, 0.47 mmol) and alkoxyamine 2,2,5-trimethyl-3-phenylethoxy-4-phenyl-3-azahexane (7.5 mg, 23.1 μmol) were added to a Schlenk tube. The free nitroxide TIPNO (0.1 mol equiv based on alkoxyamine, 2.31 μmol, 21 μL) was added by means of a stock-solution with a concentration of 25 mg/mL in *o*-dichlorobenzene. Further *o*-dichlorobenzene (557 μL) was added to achieve a monomer concentration of 9 mol/L. The Schlenk tube was sealed, degassed with argon for at least 30 min, subjected to four freeze−thaw cycles and immersed into a previously on 125 °C heated oil bath. Subsequently, the polymerization was quenched after 42 h by cooling to 0 °C, the solvent and the residual monomers were removed by precipitating two times into cold MeOH. After drying in high vacuum a colorless, highly viscous polymer was obtained.

The deprotection of the alkyne groups was accomplished by dissolving the polymer (767 mg, 0.52 mmol based on TMSPA units) into 40 mL dry THF and the reaction mixture was degassed with argon for 30 min. After being cooled to −20 °C, a likewise degassed solution of 1.0 M tetrabutylammonium fluoride (TBAF) solution in THF (1.57 mL, 1.57 mmol) and acetic acid (90 μL, 1.57 mmol) in 10 mL dry THF was added. The reaction mixture was stirred for 30 min at −20 °C and further 24 h at room temperature. The final product (**1e**) was obtained as viscous, slightly yellow polymer after three times of precipitation into cold MeOH and drying in high vacuum. The obtained polymer was stored under an inert gas in the dark. ^{1}H NMR (400 MHz, $CDCl_3$): δ (ppm) 4.66 (2H, OCH_2 of PA), 4.04 (2H, OCH_2 of *n*BA), 2.52 (1H, C≡C*H* of PA), 2.29−1.39 (7H, $CHCH_2$ of polymer backbone and CH_2CH_2 of *n*BA), 0.95 (3H, CH_3 of *n*BA). T_g = − 45.6 °C

Polymerization of Isobutylene (IB) and End Group Modification. All PIB syntheses were done according to Binder et al.[63] and Morgan et al.[60,64] and were further modified to obtain three-arm-star PIB's. Polymerizations were done under an atmosphere of argon. Total reaction volumes (80−120 mL, DCM and *n*-hexane v/v = 40/60) were placed in a 250 mL round-bottom flask equipped with mechanical stirrer, septum and stopcock. The solution was started to cool down and during the cooling D*t*BP (5.0 mM), DMA (5.0 mM) and 1,3,5-tris(2-methoxy-2-propyl)benzene (2.0−16.0 mM, dissolved in 1.0−3.0 mL *n*-hexane) was added. At − 80 °C isobutylene (0.75−1.0 M) was added and the polymerization was started by addition of $TiCl_4$ (10.0−15.0 mM). After 15 min the corresponding alkoxybenzene quenchers were added. To yield trimethylsilyl protected three-arm-star alkyne-telechelic PIB, trimethyl(3-phenoxy-1-propynyl)silane (4.0 equiv per chain end) was used as quencher and quenching proceeded during 18 hours at −70 °C, however, only when using an extra portion of $TiCl_4$ (3 equiv of initial portion) to accelerate the quenching reaction. In order to obtain three-arm-star bromine-telechelic PIB 3-(bromopropoxy)benzene (2.5 equiv per chain end) was used as quencher and quenching proceeded for 150 min at −60 °C. After quenching an excess of MeOH was added and the solvent was removed. The crude polymer was dissolved in *n*-hexane and precipitated in a 10 to 15 time excess of MeOH for three times. Obtained trimethylsilyl protected three-arm-star alkyne-telechelic PIB was converted into compound **2** and obtained three-arm-star bromine-telechelic PIB's were transformed in compounds **3** and **4a**−**d**.

*Synthesis of Three-Arm-Star Alkyne-Telechelic PIB (**2**).* Under an atmosphere of nitrogen trimethylsilyl protected three-arm-star alkyne-telechelic PIB (1 equiv, 1.1 mmol, 4.6 g) was dissolved in THF (24 mL) and TBAF (1.0 M solution in THF, 13.6 equiv, 15.0 mmol, 15 mL). The reaction mixture was stirred at room temperature overnight. The polymer solution was extracted with water (50 mL) and the desired polymer precipitated. It was subsequently dissolved in DCM (35 mL) and extracted with water (two times 50 mL). The organic layer was separated and dried over Na_2SO_4 and the solvent was removed. The crude polymer was dissolved in *n*-hexane, precipitated into a 10 to 15 time excess of MeOH and dried in high vacuo. ^{1}H NMR ($CDCl_3$, 400 MHz): δ 7.13 (s, 3H, Ar−*H* of initiator), 6.89 (d, 6H, Ar−*H* of quenching agent), 4.66 (d, 6H, O−CH_2), 2.50 (t, 3H, C−*CH*), 1.41 (s, CH_2 of repetitive unit), 1.11 (s, CH_3 of repetitive unit), 0.79 (s, 18H, CH_3 of initiator part). ^{13}C NMR ($CDCl_3$, 100 MHz): δ 155.4, 148.4, 143.7, 127.2, 117.6, 114.2, 79.0, 77.9, 77.4, 76.6, 75.4, 61.9, 59.7, 59.2, 58.7, 57.5, 56.0, 51.0, 48.3, 39.1, 38.5, 38.4, 38.3, 38.2, 38.2, 38.1, 38.1, 38.0, 32.6, 32.3, 31.7, 31.4, 31.3, 31.2, 30.8, 29.2, 27.1.

*Synthesis of Three-Arm-Star Azido-Telechelic PIB's (**3**, **4a**−**d**).* Under an atmosphere of nitrogen three-arm-star bromine-telechelic PIB (1.0 equiv, 775.0 mg, 126.0 μmol) was dissolved in a 1:1 mixture of *n*-heptane (30 mL) and DMF (30 mL). Sodium azide (30.0 equiv, 246.0 mg, 3.8 mmol) was added to the reaction mixture subsequently heating to 90 °C for 8 h. After the reaction mixture was cooled down, the *n*-heptane layer was separated and extracted with water (three times, 50 mL). The organic layer was dried over Na_2SO_4 and the solvent was removed, obtaining the crude polymer which was dissolved in *n*-hexane and was then precipitated into a 10 to 15 time excess of MeOH for three times and dried in high vacuo. ^{1}H NMR ($CDCl_3$, 500 MHz): δ 6.81 (d, 6H, Ar−*H* of quenching agent), 4.03 (t, 6H, O−CH_2), 3.49 (t, 6H, CH_2−N_3), 2.04 (q, 6H, CH_2−CH_2−CH_2), 1.80 (m, 6H, CH_2 next to repetitive unit), 1.41 (s, CH_2 of repetitive unit), 1.11 (s, CH_3 of repetitive unit), 0.80 (s, 18H, CH_3 of initiator part). ^{13}C NMR ($CDCl_3$, 125 MHz): δ 156.2, 148.4, 142.8, 127.1, 127.0, 126.9, 113.6, 113.6, 64.4, 59.6, 59.5, 59.4, 58.4, 48.3, 38.2, 38.1, 38.0, 37.9, 37.8, 32.1, 31.3, 31.2, 31.1, 30.9, 30.6, 28.9. IR (cm^{-1}): 2950, 2893, 2098, 1470, 1389, 1366, 1231, 950, 924, 827, 668, 630

Scheme 2. Synthesis of Poly(propargyl acrylate-co-ran-*n*-butyl acrylate)s (1a-i) via NMP and of Three-Arm-Star Alkyne- (2) and Three-Arm-Star Azido-Telechelic (3, 4a-d) PIB's via LCCP

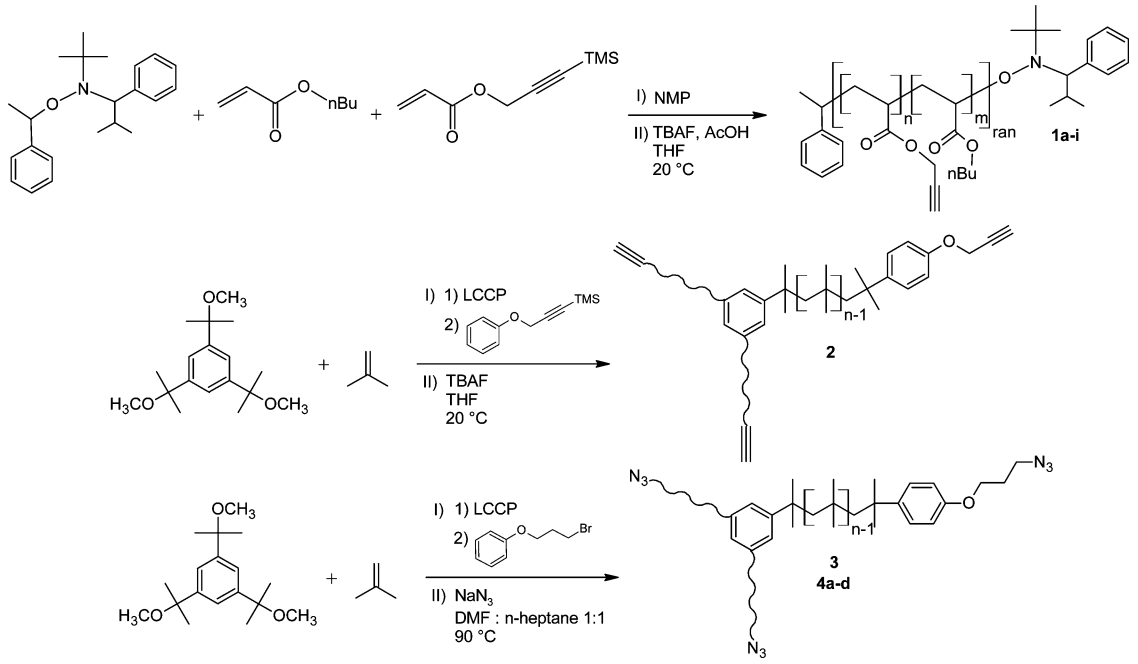


Table 1. Characterization of the Poly(propargyl acrylate-*co-ran-n*-butyl acrylate)s (1a-i) Prepared via NMP and of the Three-Arm-Star Alkyne- (2) and Three-Arm-Star Azido-Telechelic (3, 4a-d) PIB's Prepared via LCCP

ent.	polymer	polymer composition PA-*n*BA[a]	$M_{n,theor}$ [g/mol]	$M_{n,GPC}$[b] [g/mol]	$M_{n,NMR}$[c] [g/mol]	number of functional groups/chain[d]	PDI[e]	yield[f] [%]
1	**1a**	1:6	30 000	7000	–	7.6	1.8	30
2	**1b**	1:6	30 000	18 000	–	20.1	1.8	53
3	**1c**	1:12	50 000	9600	–	5.6	1.4	45
4	**1d**	1:12	30 000	12 500	–	7.4	1.6	48
5	**1e**	1:12	30 000	19 100	–	11.4	1.8	70
6	**1f**	1:24	30 000	15 200	–	4.7	1.5	85
7	**1g**	1:24	50 000	22 200	–	6.9	2.3	69
8	**1h**	1:36	75 000	14 200	–	2.9	3.5	57
9	**1i**	1:36	30 000	23 400	–	4.9	1.6	91
10	**2**		6000	6300	5700	3	1.3	90
11	**3**		5000	6200	6300	3	1.2	87
12	**4a**		6000	6500	5500	3	1.4	86
13	**4b**		12 000	10 400	11 600	3	1.5	85
14	**4c**		18 000	16 700	23 600	3	1.3	87
15	**4d**		30 000	20 200	30 000	3	1.4	88

[a]Determined via ^{1}H NMR: integration of O−CH_2−resonance of PA at 4.62 ppm and O−CH_2−resonance of *n*BA at 4.02 ppm. [b]PS standards were used for polymers **1a−i**; PIB standards were used for polymers **2**, **3**, **4a−d** [c]Determination for polymers **1a−i** not possible due to overlapping resonances; for polymers **2**, **3**, **4a−d** determined via ^{1}H NMR: integration of resonances of initiator at 0.78 ppm to 0.82 ppm and of polymer at 1.08−1.10 ppm or at 1.37−1.40 ppm. [d]For **1a-i** calculated from $M_{n,GPC}$ subtracted by the molecular weight of head and end group, divided by the average molecular weight of the monomers and divided by the ratio of PA to *n*BA detected via NMR. [e]Determined via GPC. [f]Yield of isolated product.

RESULTS AND DISCUSSION

The investigation of catalysis during cross-linking via the CuAAC is based on liquid telechelic and orthogonal functionalized polymers, all of them displaying the reactive groups (azide/alkyne) as well as a glass transition temperature (T_g) below room temperature in order to ensure molecular mobility. The polymers are based on poly(acrylate)s as well as PIB's using living polymerization techniques, namely NMP and LCCP for their preparation. In order to understand the influence of functional-group density and molecular weight in relation to catalysis, nine atactic random poly(propargyl acrylate-*co*-*n*-butyl acrylate)s were prepared via NMP, gradually changing the composition of the alkyne bearing copolymers with respect to the alkyne content from 2.7 to 14.3 mol % PA per chain.

The newly generated 1,3-triazole functionalities during the CuAAC are expected to provide more labile N-donor atoms which in turn can bind to the catalytic copper(I) center strongly while allowing to open coordination sites temporarily for the formation of the copper(I)−acetylide/ligand complex. A related effect is known experimentally by acceleration of a

dx.doi.org/10.1021/ma300405v | *Macromolecules* 2012, 45, 3335−3345

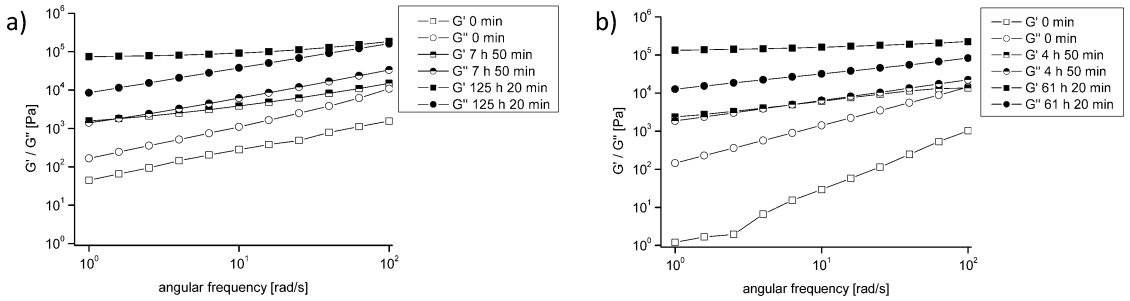


Figure 1. *In situ* rheology for cross-linking (a) **1e** (1:12, 19100 g/mol) and **3** applying bromotris(triphenylphosphine)copper(I) and TBTA as catalytic system at 20 °C, (b) **2** and **4a** (5500 g/mol) applying bromotris(triphenylphosphine)copper(I) as catalyst at 20 °C.

"click"-process,[65] enabling preferential formation of a bistriazole product via catalysis of the monotriazole product based on spatial proximity of the just formed triazole ring to the reactive center. On the basis of these two aspects a preorientation of functional groups (azide/alkyne) and therefore an autocatalytic effect within the "click" reaction seems to be possible due to the *in situ* formation of triazole rings acting as **internal** ligands and therefore as N-donors as well.

Preparation of Multivalent Functionalized Poly(acrylate)s and PIB's. The synthesis of poly(propargyl acrylate-*co*-ran-*n*-butyl acrylate) via NMP and of three-arm-star alkyne- and three-arm-star azido-telechelic PIB's via LCCP is illustrated in Scheme 2.

Synthesis of Random Copolymers Consisting of PA and *n*BA via NMP. NMP of random poly(propargyl acrylate-*co-ran-n*-butyl acrylate)s (**1a-i**) was performed according to a modified procedure described in literature[57] adapted to the synthesis of copolymers using an alkoxyamine-initiator in *o*-dichlorobenzene. Important for the achievement of low polydispersities was the dilution with *o*-dichlorobenzene in order to prevent restricted diffusion and to minimize the impact of the increasing viscosity. Deprotection of trimethylsilyl protected poly(propargyl acrylate-*co-n*-butyl acrylate) was done according to literature[57] using a mixture of TBAF and acetic acid, in order to suppress the decomposition of the propargyl ester under alkaline conditions. The pure product (**1e**) showed a T_g of −45.6 °C proving the applicability of random copolymers consisting of PA and *n*BA for self-healing materials. In Table 1 the theoretical molecular weights calculated for 100% conversion as well as the molecular weights determined via GPC and NMR are listed, together with the average number of functional groups/chain, the PDIs and the yields of the synthesized multivalent poly(acrylate)s and PIB's.

The molecular weights of the prepared polymers were in a range between 7000−23400 g/mol. Although increasing PDIs with increasing conversion are a well-known issue for NMP reactions,[66] acceptable low PDIs also at higher conversions could be achieved up to a theoretical molecular weight of 30000 g/mol by using the described procedure. In case of polymers **1g** and **1h** higher PDIs were observed because of higher theoretical molecular weights and therefore longer reaction times. In general, the copolymerization was limited by the amount of TMSPA (1: 6 molar ratio of TMSPA to *n*BA) in the copolymer because of increasing reaction times. The average number of functional groups/chain (2.9−20.1) was calculated from the molecular weight determined via GPC and the ratio of PA to *n*BA investigated via NMR spectroscopy providing a large range for studying the influence of the alkyne density (and thus of the subsequently formed triazole rings) on the kinetic behavior of the cross-linking reaction.

Synthesis of Three-Arm-Star Functionalized PIB's via LCCP and End Group Functionalization. For the synthesis of three-arm-star functionalized PIB's[60,63,64] LCCP was used, applying 1,3,5-tris(2-methoxy-2-propyl)benzene as initiator in all cases. In order to obtain polymer **2**, trimethyl(3-phenoxy-1-propynyl)silane was added as quenching agent leading to trimethylsilyl protected three-arm-star alkyne-telechelic PIB. Although already described in literature[60] this approach was applied to the synthesis of three-arm-star PIB's for the first time, requiring a quenching reaction at −70 °C for 18 h. In order to shift the equilibrium of the quenching reaction to the side of the final product, an additional portion of $TiCl_4$ had to be added during the quenching reaction. For deprotection of the trimethylsilyl group an excess of TBAF was used as deprotecting agent.[60] In a similar mode, 3-(bromopropoxy)-benzene was applied as quencher in order to synthesize three-arm-star bromide-telechelic PIB's as developed by Storey et al.[64] for bivalent telechelic PIB. During the quenching reaction the temperature was adjusted to −60 °C as the quencher was hardly soluble at the needed high concentrations for the three-arm-star quenching reaction. Subsequently, the polymers **3** and **4a−d** were obtained by treating bromide functionalized PIB's with an excess of sodium azide in a 1:1 mixture of DMF and *n*-heptane and heating up to 90 °C.[64] In contrast to literature[64] the reaction time had to be increased from 2 to 8 h to achieve quantitative end group functionalization. Results of the synthesis of **2**, **3**, and **4a−d** are shown in Table 1 proving living polymerization conditions with a good match between desired and observed molecular weights.

Cross-Linking Experiments via *in Situ* Rheology. *In situ* rheology was performed to investigate the network formation as illustrated in Scheme 1 depending on the alkyne content, the molecular weight and the absolute concentration of functional groups. Of peculiar interest was the determination of the gelation time[62] to draw conclusions about the rate of the catalytic process even at room temperature.

Copolymers **1a−i** (bearing 20.1−2.9 alkyne moieties/chain) were mixed with the three-arm-star azido-telechelic PIB polymer **3**; alternatively the PIB-alkyne polymer **2** was reacted with the polymers **4a−d** using bromotris(triphenylphosphine)-copper(I) (stock solution) as catalyst. Figure 1a and 1b show the graphs obtained via *in situ* rheology, as illustrated as example for cross-linking **1e** with **3** and **2** with **4a**.

With progressing network formation due to the "click" reaction, the crossover of the storage and the loss modulus could be observed after 7 h and 50 min in case of cross-linking **1e** and **3** or after 4 h and 50 min in case of cross-linking **2** and

dx.doi.org/10.1021/ma300405v | *Macromolecules* 2012, 45, 3335−3345

Table 2. Results Obtained by *in Situ* Rheology and Kinetic Data for Cross-Linking 1a−i with 3 Applying Bromotris(triphenylphosphine)copper(I) and TBTA as Catalytic System at 20 °C and by Cross-Linking 2 and 4a−d Applying Bromotris(triphenylphosphine)copper(I) as Catalyst at 20 °C

ent.	polymer mixture	c [M][a]	η_0[b] [Pa·s]	gel. time[c] [min]	c_{Cu} [M] (10^{-2})	k_0 [$M^{-3}\cdot min^{-1}$]	$k_{crossover}$ [$M^{-3}\cdot min^{-1}$]	r_0 [$M\cdot min^{-1}$] (10^{-3})
1	**1a** + **3**	0.302	89.0	142	3.0	29.9	47.8	2.4
2	**1b** + **3**	0.302	336.0	601	3.4	10.8	37.3	1.1
3	**1c** + **3**	0.245	60.0	213	2.4	42.2	76.0	1.5
4	**1d** + **3**	0.245	73.8	400	2.4	26.6	73.7	0.92
5	**1e** + **3**	0.245	123.0	468	2.4	22.7	49.9	0.81
6	**1f** + **3**	0.179	59.1	328	1.8	98.5	229.6	1.1
7	**1g** + **3**	0.179	147.0	724	1.8	19.5	29.4	0.21
8	**1h** + **3**	0.139	56.0	585	1.4	89.1	158.0	0.32
9	**1i** + **3**	0.139	74.3	1940	1.5	33.0	91.1	0.14
10	**2** + **4a**	0.238	44.0	290	2.4	706.9	2676.8	23
11	**2** + **4b**	0.155	33.4	375	1.6	522.8	1889.2	3.2
12	**2** + **4c**	0.093	32.9	467	0.95	377.4	820.4	0.29
13	**2** + **4d**	0.076	30.8	855	0.81	323.0	686.5	0.13

[a]Absolute concentration of functional groups (azide/alkyne) in the reaction mixture. [b]Absolute initial viscosity at 100 Hz. [c]Crossover, $G' = G''$.

4a corresponding to the gelation times (gelation point).[62] After 125 h and 20 min (**1e** and **3**) or after 61 h and 20 min (for **2** and **4a**) the moduli changed only slightly due to the stagnant network formation. The results of all rheology investigations are shown in Table 2, together with the viscosity of the polymer mixture at the beginning of the experiment (η_0), the gelation time and the kinetic data of the cross-linking reactions.

According to Fokin et al.[65] the rate law for kinetic controlled "click" reactions can be assumed as first order for the azide, as first to second order for the alkyne and at least as second order (x) for the copper resulting in an overall reaction rate $r_{\text{"click"}}$ of $r_{\text{"click"}} = k[\text{alkyne}]^{2,3}[\text{Cu(I)}]^x$ (assuming [azide] = [alkyne]). Thus, for higher concentrations of functional groups (azide/alkyne) higher reaction rates as well as a faster crossover and therefore a faster network formation should be expected.

To prove this assumption the cross-linking of polymers with decreasing concentration of functional groups but with comparable molecular weight was studied (Table 2, entries 2, 5, 6 and 8, composition PA-*n*BA: 1:6, 1:12, 1:24, 1:36) comparing the kinetic behavior of **1b** (entry 2, 20.1 alkynes/chain), **1e** (entry 5, 11.4 alkynes/chain), **1f** (entry 6, 4.7 alkynes/chain) and **1h** (entry 8, 2.9 alkynes/chain) cross-linked with the three-arm-star polymer **3**. The gelation time of **1b** with **3** corresponding to the highest concentration took the longest time (entry 2, 601 min), whereas the gelation time of **1f** with **3** was significantly shorter (entry 6, 328 min). An explanation for this behavior can be given by the strongly increased starting viscosity η_0 of the polymer mixtures with rising PA content (entry 6, **1f** + **3**: 59.1 Pa·s; entry 2, **1b** + **3**: 336.0 Pa·s), indicating that the gelation time in these cases is primarily dominated by the initial viscosity of the polymer mixture. A similar behavior could be observed by comparing the cross-linking of polymer mixtures **1c** (entry 3, 5.6 alkynes/chain), **1d** (entry 4, 7.4 alkynes/chain) and **1e** (entry 5, 11.4 alkynes/chain) with **3**, which displayed an equal concentration of functional groups (0.245 M, composition PA-nBA: 1: 12) but increasing viscosities due to their increasing molecular weights (entry 3, **1c** + **3**: 60.0 Pa·s; entry 4, **1d** + **3**: 73.8 Pa·s; entry 5, **1e** + **3**: 123.0 Pa·s).

In contrast for the cross-linking of the three-arm-star alkyne-telechelic PIB **2** with the three-arm-star azido-telechelic PIB's **4a−d** (Table 2, entries 10−13) the gelation time increased from 290 to 855 min with increasing molecular weights from 5500 g/mol to 30000 g/mol and with decreasing concentration of the reactive functional groups from 0.238 to 0.076 M. As this observation is in accordance to Fokin et al.[65] we assume a kinetically controlled "click" reaction when cross-linking **2** with **4a−d**. The increased gelation time for cross-linking **2** and **4d** (entry 13, 855 min) could be explained by the high molecular weight and the molecular weight distribution of **4d** (30000 g/mol), reaching the range of the entanglement molecular weight which is 17000 g/mol for linear PIB[67] assuming partial entanglement of **4d**.

In order to exclude viscosity effects in case of poly(acrylate)s the gelation times of cross-linking the polymers **1a**, **1c**, **1f**, and **1h** with polymer **3** (Table 2, entries 1, 3, 6 and 8) were compared. This series of poly(acrylate)s **1a** (entry 1, 7.6 alkynes/chain), **1c** (entry 3, 5.6 alkynes/chain), **1f** (entry 6, 4.7 alkynes/chain), and **1h** (entry 8, 2.9 alkynes/chain) showed decreasing concentrations of functional groups (composition PA-*n*BA: 1:6, 1:12, 1:24, 1:36) but comparable starting viscosities η_0 (56.0−89.0 Pa·s). Clearly the gelation times increased with decreasing concentrations of the reactive functional groups (entry 1, **1a** + **3**, 142 min; entry 8, **1h** + **3**, 585 min) and the expected behavior based on the mentioned kinetic law could thus be proven.

Autocatalysis during the Cross-Linking Reactions. When analyzing the development of the rate constants k as well as the dk values (derivative of the rate constant k with respect to time) as a function of time an autocatalytic effect of the herein described "click" reactions of multivalent poly(acrylate)s and PIB's was observed. On the basis of the assumption of a pseudofirst reaction order near the gel point[62] corresponding to Ampudia[68] and Barton[69] the rate constants k could be determined according to eq 1 (for mathematical derivation see Supporting Information).

$$k = \frac{e^{(k'\cdot t)} - 1}{t\cdot[A]_0} \quad (1)$$

By using eq 1, the rate constant k_0 correlating to the first measurable value for the real part of the viscosity and the corresponding reaction rate r_0 as well as the rate constant $k_{crossover}$ at the gel-point were calculated. The values of k_0, $k_{crossover}$, and r_0 are listed in Table 2 for all performed cross-linking reactions.

dx.doi.org/10.1021/ma300405v | *Macromolecules* 2012, 45, 3335−3345

For the cross-linking reactions of the series **1c−e** with **3** characterized by increasing molecular weights of **1c−e** (Table 1, entries 3−5) the curves of the rate constants *k* were analyzed over time. The corresponding results for the cross-linking reaction of **1c−e** with **3** are shown in Figure 2.

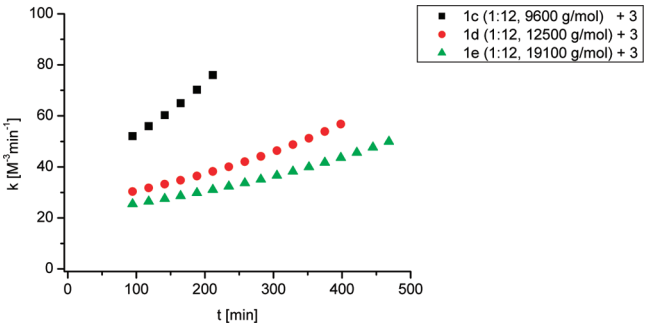


Figure 2. Correlation of the rate constants *k* vs time *t* for cross-linking **1c-e** with **3** applying bromotris(triphenylphosphine)copper(I) and TBTA as catalytic system at 20 °C.

As all rate constants *k* as well as the *dk* values (see Supporting Information, Figure S2) increased exponentially with increasing time a strong autocatalytic effect (of a factor up to 2.5) during the cross-linking reaction of **1c-e** with **3** can be assumed. Furthermore, the absolute values of the rate constants *k* decreased from **1c** and **3** to **1d** and **3** to for **1e** and **3**, thus following the trends of the observed gelation times corresponding to the starting viscosities of the polymer mixtures.

The autocatalytic behavior of poly(acrylate)s **1a−i** cross-linked with **3** was analyzed according to Figure 3 by incorporating the concentration of copper(I) catalyst.

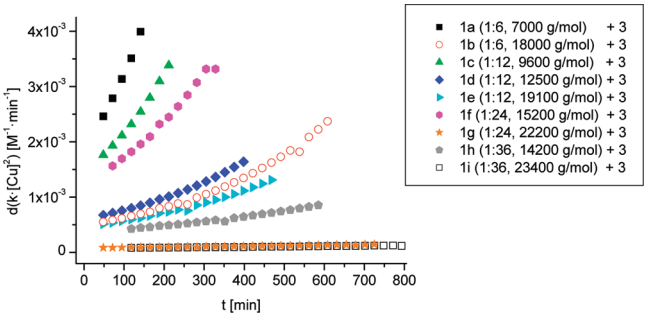


Figure 3. Correlation of the derivative of the reaction rate *k* with respect to time *t* vs time *t* for cross-linking **1a−i** with **3** applying bromotris(triphenylphosphine)copper(I) and TBTA as catalytic system at 20 °C incorporating the concentration of copper(I) catalyst.

Autocatalysis could be observed for cross-linking polymers **1a**, **1c**, **1f** and **1h** with polymer **3**. As these polymer mixtures showed increasing gelation times with decreasing concentrations of functional groups (Table 2, entry 1, **1a** + **3**: 142 min; entry 8, **1h** + **3**: 585 min) the d*k* values proved this trend increasing stronger for **1a** and **3** than for **1c** and **3** than for **1f** with **3** than for **1h** with **3**.

When cross-linking the polymer mixtures with the same composition of PA to *n*BA but with a higher molecular weight a less pronounced autocatalytic effect could be observed due to the different starting viscosities of the polymer mixtures. (Table 2, entry 6, **1f** + **3**: 59.1 Pa·s; entry 7, **1 g** + **3**: 147.0 Pa·s). Thus, for the polymer mixtures **1d** and **1e** with **3** displaying a lower concentration of functional groups (composition PA−*n*BA: 1:12) the increase of the d*k* values was comparable or even stronger than for cross-linking **1b** with **3** (composition PA−*n*BA: 1:6) due to the higher starting viscosity of this polymer mixture (Table 2, entry 2, **1b** + **3**: 336.0 Pa·s; entry 4, **1d** + **3**: 73.8 Pa·s; entry 5, **1e** + **3**: 123.0 Pa·s).

The same analysis of the rate constants *k* over time was done for cross-linking **2** with **4a-d** as illustrated in Figure 4, determining the rate constant *k* independently from the used copper(I) concentrations.

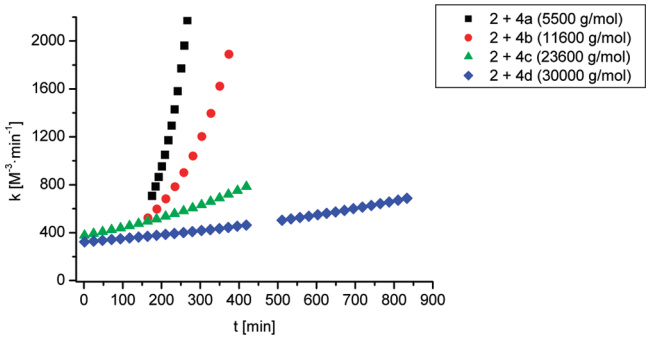


Figure 4. Correlation of the rate constants *k* vs time *t* for cross-linking **2** with **4a−d** applying bromotris(triphenylphosphine)copper(I) as catalyst at 20 °C.

For these polymer mixtures, the values of the rate constants *k* and the d*k* values (see Supporting Information, Figure S3) reflected the already discussed trends shown by *in situ* rheology experiments (see Table 2). The strongest increase of the rate constants *k* as well as the highest absolute values of the *k* values could be observed for cross-linking **2** with **4a** showing the shortest gelation time due to the highest concentration of functional groups (entry 10: 290 min, 0.238 M) and therefore the most prominent autocatalytic behavior of a factor of 3.8. Consequently the rate constants *k* increased stronger for the cross-linking reaction of **2** with **4b** (entry 11: 375 min, 0.155 M) in comparison to the reaction of **2** with **4c** (entry 12: 467 min, 0.093 M) and of **2** with **4d** (entry 13: 855 min, 0.076 M). The same trends were observed for the d*k* values. The absolute values of the rate constants *k* as well as the d*k* values for the "click" reactions of **2** with **4a−d** were one magnitude higher compared to cross-linking **1a−i** with **3**.

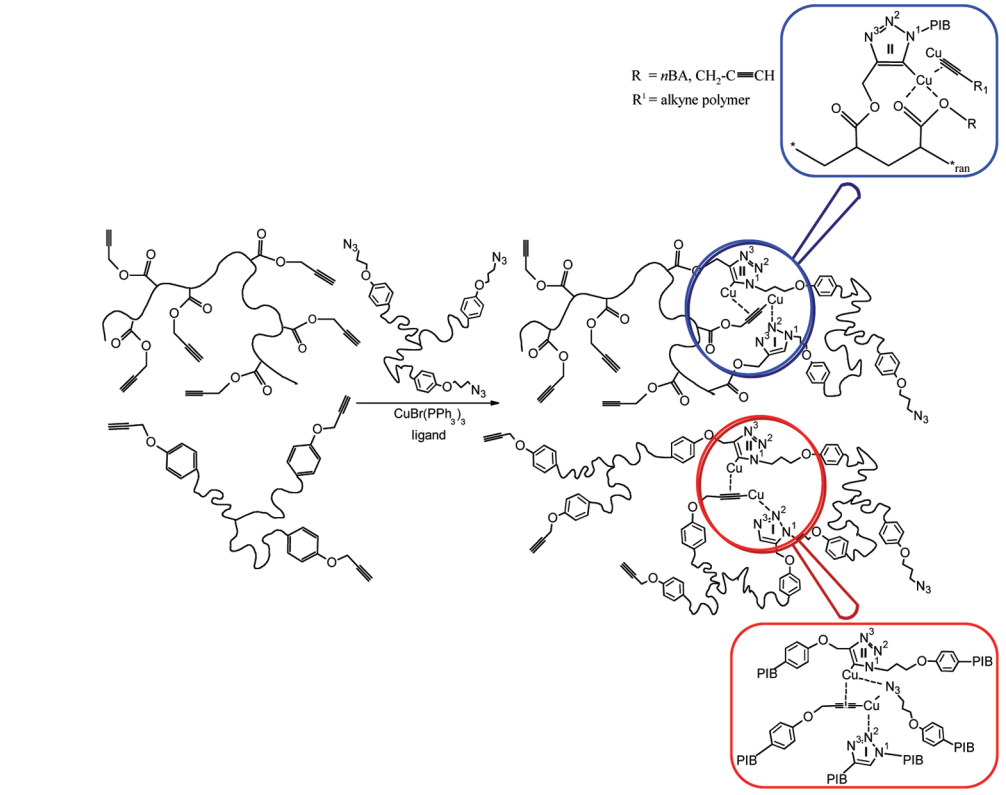
On the basis of our results we proposed a mechanism to explain the observed autocatalytic behavior for cross-linking multivalent poly(acrylate)s and PIB's as shown in Scheme 3.

According to Scheme 3 triazole rings with different functions could be identified. One triazole functionality (**I**) is assumed to act as **internal ligand** using either the N^2-atom or the N^3-atom of the triazole ring as donor atom while forming the copper(I)−acetylide/ligand complex.[70] Additionally, it can be assumed that a second triazole functionality (**II**) can preorientate the functional groups (azide/alkyne) near the copper(I) center resulting in spatial proximity of all reaction components (shown in the blue and red framed image details). Thus, the formation of the next triazole ring is promoted while retarding the cleavage of the Cu−C bond of the Cu triazolyl-intermediate in the proteolysis step as described by Fokin et al.[65]

The calculated values of the rate constants k_0 and therefore also of the reaction rates r_0 were comparable to rate constants

dx.doi.org/10.1021/ma300405v | *Macromolecules* 2012, 45, 3335−3345

Scheme 3. Proposed Mechanism of Autocatalysis for Cross-Linking Multivalent Poly(acrylate)s and PIB's Functionalized with Alkyne or Azide Groups, Respectively, Applying Bromotris(triphenylphosphine)copper(I) and a Ligand as Catalytic System at 20 °C



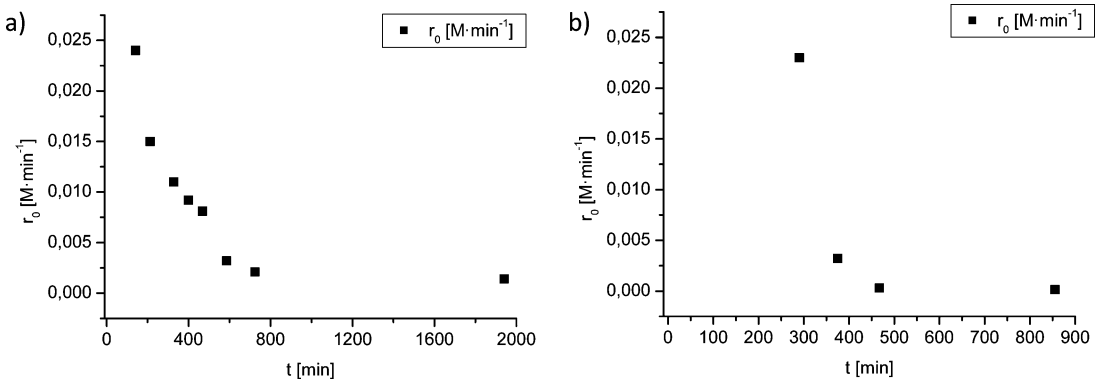


Figure 5. Correlation of gelation time and reaction rate r_0 for cross-linking (a) **1a−i** with **3** applying bromotris(triphenylphosphine)copper(I) and TBTA as catalytic system at 20 °C and (b) **2** and **4a−d** applying bromotris(triphenylphosphine)copper(I) as catalyst at 20 °C.

of DA reactions being in the range of 1.25×10^{-5} M^{-1} s^{-1} to 4.83×10^{-5} M^{-1} s^{-1} by assuming second-order kinetics.[33,71,72] Correlations of the gelation times and the reaction rates r_0 are illustrated in Figure 5a for cross-linking **1a−i** with **3** and in Figure 5b for cross-linking **2** with **4a-d**.

The reaction rate r_0 decreased with increasing gelation time resulting in an exponential decay for cross-linking **1a-i** with **3** as well as for cross-linking **2** with **4a−d** as illustrated in Figure 5, parts a and b. According to the shown correlations the order of magnitudes of the reaction rate r_0 could be derived directly in case of performing further cross-linking experiments between the discussed multivalent polymers.

Calculation of Network Strand Densities. Plateau moduli[62,73] and network strand densities[73,74] as a function of the absolute concentration of functional groups were explored to prove the suitability of the represented "click" reaction for self-healing purpose. The network strand density is an average value for the cross-linking points per volume segment providing information about the completeness of the "click" reaction. The relationship between the observed plateau modulus G_N, the network strand density υ_x, the density of the polymer mixture ρ and the average molecular weight between two network points M_c and the molecular weight M_n is given according to eq 2[73,74]

$$G_N = \upsilon_x RT = \frac{\rho RT}{M_c}\left(1 - \frac{2M_c}{M_n}\right) \quad (2)$$

where R is the universal gas constant, R = 8.3145 J·mol^{-1}·K^{-1} and T the temperature, T = 298.15 K. According to eq 2 the maximum network strand densities $\upsilon_{x,\,max}$ could be calculated

dx.doi.org/10.1021/ma300405v | Macromolecules 2012, 45, 3335−3345

assuming complete cross-linking. Furthermore, the experimental network strand densities $\upsilon_{x,\,exp}$ were determined using the plateau moduli and the ratios between the two network strand densities were calculated to obtain an impression about the formed network points during the performed "click" reaction (see Table 3).

Table 3. Obtained Results based on eq 2 for Cross-Linking 1a−i with 3 Applying Bromotris(triphenylphosphine)copper(I) and TBTA as Catalytic System at 20 °C and for Cross-Linking 2 and 4a−d Applying Bromotris(triphenylphosphine)copper(I) as Catalyst at 20 °C

ent.	polymer mixture	c [M][a]	$G_N{}^b$ [Pa] 10^5	$\upsilon_{x,\,max}$ [mol/m^3]	$\upsilon_{x,\,exp}$ [mol/m^3]	$\upsilon_{x,\,exp}/\upsilon_{x,max}$ [%]
1	**1a** + **3**	0.302	1.69	807	69	8.6
2	**1b** + **3**	0.302	2.55	972	105	10.8
3	**1c** + **3**	0.245	*c*	385	*c*	*c*
4	**1d** + **3**	0.245	2.11	431	87	20.2
5	**1e** + **3**	0.245	2.68	485	110	22.7
6	**1f** + **3**	0.179	2.42	179	99	55.3
7	**1g** + **3**	0.179	1.40	220	57	25.9
8	**1h** + **3**	0.139	0.89	71	37	52.1
9	**1i** + **3**	0.139	0.38	125	16	12.8
10	**2** + **4a**	0.238	2.25	244	91	37.3
11	**2** + **4b**	0.155	0.13	158	6	3.8
12	**2** + **4c**	0.093	0.19	93	8	8.6
13	**2** + **4d**	0.076	0.078	77	3	3.9

[a]Absolute concentration of functional groups (azide/alkyne) in the reaction mixture. [b]Constant value at 100 Hz. [c]Measurement finished after 1900 min.

In the case of cross-linking polymer mixtures **1a−i** with **3**, the best values for the experimental network strand density were in the range of 100 mol/m^3. CuAAC of polymer **3** with poly(acrylate)s with the same concentration of functional groups but with higher molecular weights resulted in higher network strand densities. Thus, the "click" reaction between **1a** + **3** (entry 1, **1a**, 7000 g/mol, composition PA-*n*BA: 1:6) resulted in a network strand density of 69 mol/m^3 compared to 105 mol/m^3 for cross-linking **1b** + **3** (entry 2, **1b**: 18000 g/mol, composition PA-*n*BA: 1:6). The ratio between the experimental and the maximal network strand density varied between 8.6 and 55.3%, increasing with decreasing concentration of functional groups presumably due to steric hindrance. For cross-linking polymer **3** and poly(acrylate)s with a composition of PA to *n*BA of 1:6 or 1:12 higher ratios were observed for higher molecular weights (entry 1, **1a**, 7000 g/mol, 8.6%; entry 2, **1b**, 18000 g/mol, 10.8%). In contrast, a higher ratio between experimental and maximal network strand density could be achieved for the "click" reaction between polymer **3** and poly(acrylate)s with lower molecular weights and with a composition of PA to *n*BA of 1:24 or 1:36 (entry 6, **1f**, 15200 g/mol, 55.3%; entry 7, **1g**, 22200 g/mol, 25.9%).

For cross-linking polymer **2** with polymers **4a−d** the values of the maximal network strand density decreased with decreasing concentrations (entries 10−13, from 244 to 77 mol/m^3), as less network points could be formed. The experimental determined network strand density showed this tendency as well (entries 10−13, 91−3 mol/m^3). Therefore, the relation of the maximal and experimental network strand density varied between 37 and 4% implying that the experimentally determined network strand density decreased relatively and absolutely, the values, however, remaining within the limits observed for hydrogels.[75]

Calculation of Activation Energies. DSC experiments were performed for selected cross-linking reactions in order to determine their activation energies according to Kessler et al.[76] DSC measurements were run in a temperature range from 20 to 200 °C using heating rates of 2, 5, and 10 K/min. With increasing heating rate β a shift of the peak temperature T_p to higher temperatures could be observed. The activation energy E_a as well as the pre-exponential factor A could be calculated by applying Kissinger's equation[76] which is shown in eq 3

$$\ln\left(\frac{\beta}{T_p{}^2}\right) = \ln\left(\frac{AR}{E_a}\right) - \frac{E_a}{RT_p} \tag{3}$$

where R is the universal gas constant, R = 8.3145 J·mol^{-1}·K^{-1}, β the given heating rate, and T_p the measured peak temperature. The so obtained results are illustrated in Table 4 for cross-linking **1a**, **1f**, and **1h** with **3** and for cross-linking **2** with **4a** and **4d**.

Table 4. Results Obtained via DSC Experiments for Cross-Linking 1a, 1f, and 1h with 3 Applying Bromotris(triphenylphosphine)copper(I) and TBTA as Catalytic System and for Cross-Linking 2 and 4a and 4d Applying Bromotris(triphenylphosphine)copper(I) as Catalyst

entry	polymer mixture	E_a [kJ/mol]	ln A
1	**1a** + **3**	60.3	17.1
2	**1f** + **3**	38.5	10.5
3	**1h** + **3**	23.1	4.4
4	**2** + **4a**	41.7	13.2
5	**2** + **4d**	44.5	16.1

All determined activation energies were in the range of CuAAC reported by Kessler et al.[76] and Binauld et al.[77] as well as being located in between the activation energy of 32 and 96 kJ/mol described by Liu et al.[33] and Chen et al.[24] for DA-reactions of furan and maleimide compounds. This indicates clearly that the rate-determining step of the CuAAC remains unchanged by the observed autocatalysis.

The cross-linking reaction of the polymer mixtures **1a**, **1f** and **1h** with **3** followed the rate law of Fokin et al.[65] due to comparable starting viscosities (56.0−89.0 Pa·s). Therefore, with decreasing concentration of functional groups increased gelation times could be observed (see Table 2, entries 1, 6, and 8). Nevertheless, the activation energy displayed the highest value for the cross-linking reaction of **1a** with **3**, followed by the cross-linking of **1f** and **1h** with **3**. This aspect might be explained by an increased steric hindrance due to a higher concentration of functional groups within sample **1a** (0.302 M).

CONCLUSIONS

We have investigated autocatalytic effects in cross-linking processes based on the CuAAC, aiming at the design of generating polymeric networks for future self-healing materials without the need of an external stimulus like increased temperature. Specifically, we planned to take advantage of the 1,3-triazole rings formed during the CuAAC-based cross-linking, thus enabling to act as internal ligands in turn accelerating the reaction rate of subsequent "click"-reactions.

dx.doi.org/10.1021/ma300405v | *Macromolecules* 2012, 45, 3335−3345

To this effect, we have synthesized multivalent polymeric alkynes and azides (nine atactic random poly(propargyl acrylate-*co*-*n*-butyl acrylate)s, M_n = 7000−23400 g/mol) via NMP displaying alkyne-contents ranging from 2.7 mol % to 14.3 mol % per chain. Furthermore, five three-arm-star azido-telechelic PIB's (M_n = 5500−30000 g/mol) and one three-arm-star alkyne-telechelic PIB (M_n = 6300 g/mol) were prepared via LCCP with perfect end group-functionalization, thus studying the influence of functional group density, viscosity and molecular weight on the cross-linking process. Cross-linking reactions were studied via *in situ* melt-rheology and DSC, revealing increasing reaction rates with increasing concentration of functional groups (**1c** + **3**, composition PA-*n*BA, 1:12, r_0 = 1.5 × 10^{-3} M·min^{-1}; **1a** + **3**, composition PA-*n*BA, 1:6, r_0 = 2.4 × 10^{-3} M·min^{-1}). A kinetic analysis showed significant autocatalytic effects ranging from a factor of 1.6 to 4.3 for cross-linking the polymers **1a-i** with **3** and from a factor of 2.1 to 3.8 for cross-linking the polymers **2** with **4a**−**d** now enabling control of the catalytic effects. Therefore, it is assumed that clustering effects of the generated triazole rings prompted the catalysis of the CuAAC thus explaining the observed autocatalysis. Furthermore, a "click"-cross-linking concept acting at room temperature with very short gelation times (**1a** + **3**, 142 min; **2** + **4a**, 290 min), with experimental network strand densities about 100 mol/m^3 (**1b** + **3**, 105 mol/m^3; **2** + **4a**, 91 mol/m^3) and ratios between experimental and maximal network strand densities up to 55.3% (**1f** + **3**) could be achieved. Effects exerted by the molecular weight reacting five three-arm-star azido-telechelic PIB's and one three-arm-star alkyne-telechelic PIB on the cross-linking-reaction, linked molecular mobility to changes in CuAAC-reactivity featuring increased reaction rates with decreasing molecular weights (**2** + **4b** (11600 g/mol), r_0 = 3.2 × 10^{-3} M·min^{-1}; **2** + **4a** (5500 g/mol), r_0 = 23 × 10^{-3} M·min^{-1}). The now designable significant autocatalytic effects enabled the design of new, highly efficient and fast cross-linking systems acting at room temperature.

■ ASSOCIATED CONTENT

Ⓢ Supporting Information

Derivation of eq 1 and correlation of the derivative of the reaction rate k with respect to time t vs time t for cross-linking **1c**−**e** with **3** and **2** with **4a**−**d**. This material is available free of charge via the Internet at http://pubs.acs.org.

■ AUTHOR INFORMATION

Corresponding Author

*E-mail: wolfgang.binder@chemie.uni-halle.de. Fax: (+49) 345 55 27392.

Author Contributions

[†]D.D. and P.M. contributed equally to this work.

Notes

The authors declare no competing financial interest.

■ ACKNOWLEDGMENTS

We gratefully acknowledge Grant DFG BI 1337/8-1 (within the SPP 1568 "Design and Generic Principles of Self-Healing Materials").

■ ABBREVIATIONS

(CuAAC) Copper(I)-catalyzed alkyne−azide "click" cycloaddition; (DA) Diels−Alder; (DSC) differential scanning calorimetry; (LCCP) living carbocationic polymerization; (MeOH) methanol; (*n*BA) *n*-butyl acrylate; (NMP) nitroxide mediated polymerization; (PA) propargyl acrylate; (PIB) poly(isobutylene); (TBTA) tris[(1-benzyl-1*H*-1,2,3-triazol-4-yl)methyl]amine; (T_g) glass transition temperature; (TIPNO) 2,2,5-trimethyl-4-phenyl-3-azahexane-3-nitroxide; (TMSPA) 3-(trimethylsilyl)prop-2-ynyl acrylate

■ REFERENCES

(1) Kolb, H. C.; Finn, M. G.; Sharpless, K. B. *Angew. Chem., Int. Ed.* **2001**, *40* (11), 2004−2021.
(2) Tillet, G.; Boutevin, B.; Ameduri, B. *Prog. Polym. Sci.* **2011**, *36*, 191−217.
(3) Binder, W. H.; Sachsenhofer, R. *Macromol. Rapid Commun.* **2007**, *28* (1), 15−54.
(4) Iha, R. K.; Wooley, K. L.; Nystrom, A. M.; Burke, D. J.; Kade, M. J.; Hawker, C. J. *Chem. Rev.* **2009**, *109* (11), 5620−5686.
(5) Binder, W. H.; Sachsenhofer, R. *Macromol. Rapid Commun.* **2008**, *29* (12−13), 952−981.
(6) Vestberg, R.; Malkoch, M.; Kade, M.; Wu, P.; Fokin, V. V.; Sharpless, K. B.; Drockenmuller, E.; Hawker, C. J. *J. Polym. Sci., Part A: Polym. Chem.* **2007**, *45* (14), 2835−2846.
(7) Malkoch, M.; Schleicher, K.; Drockenmuller, E.; Hawker, C. J.; Russell, T. P.; Wu, P.; Fokin, V. V. *Macromolecules* **2005**, *38* (9), 3663−3678.
(8) Blaiszik, B. J.; Kramer, S. L. B.; Olugebefola, S. C.; Moore, J. S.; Sottos, N. R.; White, S. R. *Annu. Rev. Mater. Res.* **2010**, *40* (1), 179−211.
(9) Weder, C. *Nature* **2009**, *459*, 45−46.
(10) Blaiszik, B. J.; Caruso, M. M.; McIlroy, D. A.; Moore, J. S.; White, S. R.; Sottos, N. R. *Polymer* **2009**, *50* (4), 990−997.
(11) Wu, D. Y.; Meure, S.; Solomon, D. *Prog. Polym. Sci.* **2008**, *33* (5), 479−522.
(12) Guadagno, L.; Longo, P.; Raimondo, M.; Naddeo, C.; Mariconda, A.; Sorrentino, A.; Vittoria, V.; Iannuzzo, G.; Russo, S. *J. Polym. Sci., Part B: Polym. Phys.* **2010**, *48* (23), 2413−2423.
(13) Montarnal, D.; Tournilhac, F.; Hildago, M.; Leibler, L. *J. Polym. Sci., Part A: Polym. Chem.* **2010**, *48*, 2413−2423.
(14) McIlroy, D. A.; Blaiszik, B. J.; Caruso, M. M.; White, S. R.; Moore, J. S.; Sottos, N. R. *Macromolecules* **2010**, *43* (4), 1855−1859.
(15) Jackson, A. C.; Bartelt, J. A.; Marczewski, K.; Sottos, N. R.; Braun, P. V. *Macromol. Rapid Commun.* **2011**, *32* (1), 82−87.
(16) Jones, A. S.; Rule, J. D.; Moore, J. S.; White, S. R.; Sottos, N. R. *Chem. Mater.* **2006**, *18* (5), 1312−1317.
(17) Brown, E. N.; White, S. R.; Sottos, N. R. *J. Mater. Sci.* **2004**, *39*, 1703−1710.
(18) Blaiszik, B. J.; Baginska, M.; White, S. R.; Sottos, N. R. *Adv. Funct. Mater.* **2010**, *20*, 3547−3554.
(19) Kessler, M. R.; Sottos, N. R.; White, S. R. *Compos. Part A: Appl. S.* **2003**, *34* (8), 743−753.
(20) Brown, E. N.; Kessler, M. R.; Sottos, N. R.; White, S. R. *J. Microencapsulation* **2003**, *20* (6), 719−730.
(21) White, S. R.; Sottos, N. R.; Geubelle, P. H.; Moore, J. S.; Kessler, M. R.; Sriram, S. R.; Brown, E. N.; Viswanathan, S. *Nature* **2001**, *409* (6822), 794−797.
(22) Hizal, G.; Tunca, U.; Sanyal, A. *J. Polym. Sci., Part A: Polym. Chem.* **2011**, *49* (19), 4103−4120.
(23) Chen, X.; Wudl, F.; Mal, A. K.; Shen, H.; Nutt, S. R. *Macromolecules* **2003**, *36* (6), 1802−1807.
(24) Chen, X.; Dam, M. A.; Ono, K.; Mal, A. K.; Shen, H.; Nutt, S. R.; Sheran, K.; Wudl, F. *Science* **2002**, *295*, 1698−1702.
(25) Park, J. S.; Takahashi, K.; Guo, Z.; Wang, Y.; Bolanos, E.; Hamann-Schaffner, C.; Murphy, E.; Wudl, F.; Hahn, T. *J. Compos. Mater.* **2008**, *42* (26), 2869−2881.
(26) Murphy, E. B.; Bolanos, E.; Schaffner-Hamann, C.; Wudl, F.; Nutt, S. R.; Auad, M. L. *Macromolecules* **2008**, *41* (14), 5203−5209.
(27) Liu, Y. L.; Chen, Y. W. *Macromol. Chem. Phys.* **2007**, *208*, 224−232.

(28) Kavitha, A. A.; Singha, N. K. *Macromolecules* **2010**, *43* (7), 3193−3205.
(29) Ishida, K.; Yoshie, N. *Macromolecules* **2008**, *41* (13), 4753−4757.
(30) Ishida, K.; Nishiyama, Y.; Michimura, Y.; Oya, N.; Yoshie, N. *Macromolecules* **2010**, *43* (2), 1011−1015.
(31) Ishida, K.; Weibel, V.; Yoshie, N. *Polymer* **2011**, *52* (13), 2877−2882.
(32) Ishida, K.; Yoshie, N. *Macromol. Biosci.* **2008**, *8* (10), 916−922.
(33) Liu, Y.-L.; Hsieh, C.-Y.; Chen, Y.-W. *Polymer* **2006**, *47* (8), 2581−2586.
(34) Kavitha, A. A.; Singha, N. K. *J. Polym. Sci., Part A: Polym. Chem.* **2007**, *45*, 4441−4449.
(35) Kavitha, A. A.; Singha, N. K. *Macromol. Chem. Phys.* **2007**, *208* (23), 2569−2577.
(36) Adzima, B. J.; Aguirre, H. A.; Kloxin, C. J.; Scott, T. F.; Bowman, C. N. *Macromolecules* **2008**, *41* (23), 9112−9117.
(37) Nimmo, C. M.; Owen, S. C.; Shoichet, M. S. *Biomacromolecules* **2011**, *12* (3), 824−830.
(38) Wei, H.-L.; Yang, Z.; Chen, Y.; Chu, H.-J.; Zhu, J.; Li, Z.-C. *Eur. Polym. J.* **2010**, *46* (5), 1032−1039.
(39) Defize, T.; Riva, R.; Raquez, J.-M.; Dubois, P.; Jérôme, C.; Alexandre, M. *Macromol. Rapid Commun.* **2011**, *32* (16), 1264−1269.
(40) Raquez, J.-M.; Vanderstappen, S.; Meyer, F.; Verge, P.; Alexandre, M.; Thomassin, J.-M.; Jérôme, C.; Dubois, P. *Chem.—Eur. J.* **2011**, *17* (36), 10135−10143.
(41) Schunack, M.; Gragert, M.; Döhler, D.; Michael, P.; Binder, W. H. *Macromol. Chem. Phys.* **2012**, *213*, 205−214.
(42) Gragert, M.; Schunack, M.; Binder, W. H. *Macromol. Rapid Commun.* **2011**, *32* (5), 419−425.
(43) Ossipov, D. A.; Hilborn, J. *Macromolecules* **2006**, *39* (5), 1709−1718.
(44) Liu, J.; Jiang, X.; Xu, L.; Wang, X.; Hennink, W. E.; Zhuo, R. *Bioconjugate Chem.* **2010**, *21* (10), 1827−1835.
(45) Malkoch, M.; Vestberg, R.; Gupta, N.; Mespouille, L.; Dubois, P.; Mason, A. F.; Hedrick, J. L.; Liao, Q.; Frank, C. W.; Kingsbury, K.; Hawker, C. J. *Chem. Commun.* **2006**, *26*, 2774−2776.
(46) Liu, S. Q.; Ee, P. L. R.; Ke, C. Y.; Hedrick, J. L.; Yang, Y. Y. *Biomaterials* **2009**, *30* (8), 1453−1461.
(47) Crescenzi, V.; Cornelio, L.; Di Meo, C.; Nardecchia, S.; Lamanna, R. *Biomacromolecules* **2007**, *8* (6), 1844−1850.
(48) Testa, G.; Di Meo, C.; Nardecchia, S.; Capitani, D.; Mannina, L.; Lamanna, R.; Barbetta, A.; Dentini, M. *Int. J. Pharm.* **2009**, *378*, 86−92.
(49) Huerta-Angeles, G.; Šmejkalová, D.; Chládková, D.; Ehlová, T.; Buffa, R.; Velebný, V. *Carbohyd. Polym.* **2011**, *84* (4), 1293−1300.
(50) Díaz, D. D.; Punna, S.; Holzer, P.; McPherson, A. K.; Sharpless, K. B.; Fokin, V. V.; Finn, M. G. *J. Polym. Sci., Part A: Polym. Chem.* **2004**, *42* (17), 4392−4403.
(51) Filpponen, I.; Argyropoulos, D. S. *Biomacromolecules* **2010**, *11* (4), 1060−1066.
(52) van der Ende, A. E.; Harrell, J.; Sathiyakumar, V.; Meschievitz, M.; Katz, J.; Adcock, K.; Harth, E. *Macromolecules* **2010**, *43* (13), 5665−5671.
(53) Cengiz, H.; Aydogan, B.; Ates, S.; Acikalin, E.; Yagci, Y. *Des. Monomers. Polym.* **2011**, *14*, 69−78.
(54) de Luzuriaga, A. R.; Ormategui, N.; Grande, H. J.; Odriozola, I.; Pomposo, J. A.; Loinaz, I. *Macromol. Rapid Commun.* **2008**, *29* (12−13), 1156−1160.
(55) Li, C.; Finn, M. G. *J. Polym. Sci., Part A: Polym. Chem.* **2006**, *44* (19), 5513−5518.
(56) Chan, T. R.; Hilgraf, R.; Sharpless, K. B.; Fokin, V. V. *Org. Lett.* **2004**, *6* (17), 2853−2855.
(57) Lang, A. S.; Neubig, A.; Sommer, M.; Thelakkat, M. *Macromolecules* **2010**, *43* (17), 7001−7010.
(58) Rother, M. Diploma Thesis, Martin-Luther-Universität Halle-Wittenberg, 2009.
(59) Mishra, M. K.; Wang, B.; Kennedy, J. P. *Polym. Bull.* **1987**, *17* (4), 307−314.
(60) Morgan, D. L.; Martinez-Castro, N.; Storey, R. F. *Macromolecules* **2010**, *43* (21), 8724−8740.
(61) Lee, B.-Y.; Park, S. R.; Jeon, H. B.; Kim, K. S. *Tetrahedron Lett.* **2006**, *47* (29), 5105−5109.
(62) Metzger, T. G., *The Rheology Handbook: For users of rotational and oscillatory rheometers*, 2nd revised ed.; Vincentz Network: Hannover, Germany, 2006.
(63) Binder, W. H.; Kunz, M. J.; Kluger, C.; Hayn, G.; Saf, R. *Macromolecules* **2004**, *37* (5), 1749−1759.
(64) Morgan, D. L.; Storey, R. F. *Macromolecules* **2009**, *42* (18), 6844−6847.
(65) Rodionov, V. O.; Fokin, V. V.; Finn, M. G. *Angew. Chem.* **2005**, *117* (15), 2250−2255.
(66) Hawker, C. J.; Bosman, A. W.; Harth, E. *Chem. Rev. (Washington, DC)* **2001**, *101* (12), 3661−3688.
(67) Fox, T. G.; Flory, P. J.*Further studies on the melt viscosity of polyisobutylene*; Research Laboratory of the Goodyear Tire and Rubber Company: Akron, OH, 1950; pp 221−234
(68) Ampudia, J.; Larrauri, E.; Gil, E. M.; Rodríguez, M.; León, L. M. *J. Appl. Polym. Sci.* **1999**, *71* (8), 1239−1245.
(69) Barton, J. M.; Greenfield, D. C. L.; Hodd, K. A. *Polymer* **1992**, *33* (6), 1177−1186.
(70) Schweinfurth, D.; Deibel, N.; Weisser, F.; Sarkar, B. *Nachr. Chem.* **2011**, *59* (10), 937−941.
(71) Kavitha, A. A.; Singha, N. K. *ACS Appl. Mater. Interfaces* **2009**, *1* (7), 1427−1436.
(72) Goiti, E.; Heatley, F.; Huglin, M. B.; Rego, J. M. *Eur. Polym. J.* **2004**, *40* (7), 1451−1460.
(73) Feldman, K. E.; Kade, M. J.; Meijer, E. W.; Hawker, C. J.; Kramer, E. J. *Macromolecules* **2009**, *42* (22), 9072−9081.
(74) Müller, M.; Seidel, U.; Stadler, R. *Polymer* **1995**, *36* (16), 3143−3150.
(75) Goiti, E.; Huglin, M. B.; Rego, J. M. *Eur. Polym. J.* **2004**, *40* (2), 219−226.
(76) Sheng, X.; Mauldin, T. C.; Kessler, M. R. *J. Polym. Sci., Part A: Polym. Chem.* **2010**, *48* (18), 4093−4102.
(77) Binauld, S.; Boisson, F.; Hamaide, T.; Pascault, J.-P.; Drockenmuller, E.; Fleury, E. *J. Polym. Sci., Part A: Polym. Chem.* **2008**, *46* (16), 5506−5517.

Macromolecules

Article

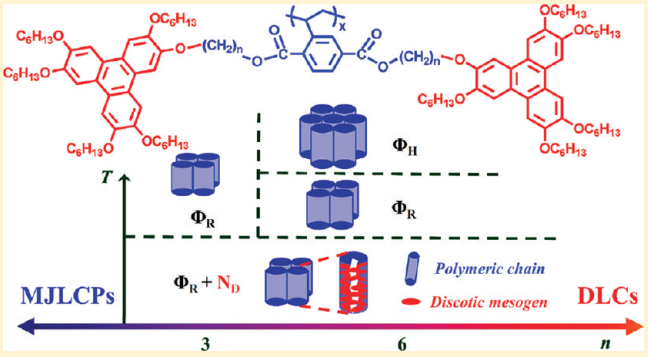
pubs.acs.org/Macromolecules

Competition and Promotion between Two Different Liquid-Crystalline Building Blocks: Mesogen-Jacketed Liquid-Crystalline Polymers and Triphenylene Discotic Liquid Crystals

Yu-Feng Zhu, Xiao-Lin Guan,† Zhihao Shen,* Xing-He Fan,* and Qi-Feng Zhou

Beijing National Laboratory for Molecular Sciences, Department of Polymer Science and Engineering, and Key Laboratory of Polymer Chemistry and Physics of Ministry of Education, College of Chemistry and Molecular Engineering, Peking University, Beijing 100871, China

ABSTRACT: Mesogen-jacketed liquid-crystalline polymers (MJLCPs) containing two triphenylene (Tp) units in the side chains, denoted as PP*n*V (n = 3 or 6, which is the number of the methylene units between the terephthalate core and Tp moieties in the side chains), were synthesized through conventional free radical polymerization, and the phase behaviors of these new combined main-chain/side-chain liquid-crystalline (LC) polymers were investigated. The chemical structures of the monomers were confirmed by elemental analysis, high-resolution mass spectrometry, and $^{1}H/^{13}C$ NMR. The molecular characterizations of the polymers were performed with ^{1}H NMR, gel permeation chromatography, and thermogravimetric analysis. LC behaviors of the polymers were investigated by differential scanning calorimetry (DSC), polarized light microscopy, and wide-angle X-ray diffraction (WAXD). Both polymers exhibit excellent thermal stabilities. DSC and WAXD results indicate that covalently incorporating Tp discotic liquid crystals has a tremendous effect on the LC behaviors of MJLCPs. As expected, the glass-transition temperature decreases as the spacer length increases. Both polymers form rectangular columnar (Φ_R) phases at relatively high temperatures. At low temperatures, however, Tp moieties in the side chains form a discotic nematic (N_D) phase in conjunction with the Φ_R phase developed by the rod-like supramolecular mesogen − the MJLCP chain as a whole, owing to the self-organization of the Tp moieties. For PP6V in particular, a higher symmetry hexagonal columnar (Φ_H) phase forms when temperature exceeds 225 °C. Individual ordered structures developed by these two LC building blocks are not only competitive but also promotive to each other.



INTRODUCTION

Liquid crystalline (LC) ordering offers possibilities for organic semiconducting materials to circumvent their main drawbacks owing to low charge carrier mobility.[1−4] It has been intensively investigated that the packing of discotic liquid crystals (DLCs) into hierarchical ordered structures on both microscopic and macroscopic length scales influences the charge carrier mobility of organic semiconducting materials.[2,5−7] The packing is dominated by the formation of columnar (Φ) LC phases based on the strong self-organizing tendency of DLCs. Because of the $\pi-\pi$ stacking of the planar aromatic cores and the van der Waals interactions of the peripheral chains, DLCs can self-organize into well-ordered, self-healable supramolecular columns, which then tend to arrange in 2D lattices. Within the columns of discotic mesogens, adjacent molecules experience a large π-orbital overlap, which results in the 1D charge-transport property with a high value of charge carrier mobility.[4,5,8−11] Plenty of triphenylene (Tp)-containing side-chain LC polymers (LCPs) with flexible spacers as linkers have been investigated.[12−20] For example, several polysiloxanes[12−14] and poly(meth)acrylates[14−17] containing Tp moieties in the side chains can form stable Φ phases. However, from the viewpoint of polymer conformation, utilizing polymers with more rigid backbones, like mesogen-jacketed LCPs (MJLCPs) or polypeptides that tend to adopt a more extended conformation, may be an alternative way to weaken the interactions between the polymer backbone and the discotic mesogens in the side chains. A series of Tp-containing polyacetylenes with different peripheral chain lengths show a typical hexagonal Φ (Φ_H) phase and a hexagonal lattice with mixed structures.[21] A Tp-containing side-chain LCP with polythiophene as the polymer backbone exhibits a peculiar lamello-columnar mesophase where a 2D oblique columnar lattice and the lamellar piling coexist in the same structure.[22]

Recently, calamitic mesogens have been introduced into the side chains of poly[di(alkyl)vinylterephthalate] (PDAVT, with the alkyl ranging from propyl/isopropyl to hexyl), a representative MJLCP with nonmesogenic side chains showing a 2D long-range-ordered Φ_H phase.[23,24] By introducing

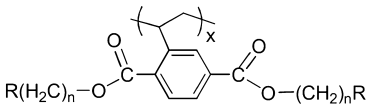
Received: March 15, 2012
Published: April 2, 2012

ACS Publications © 2012 American Chemical Society

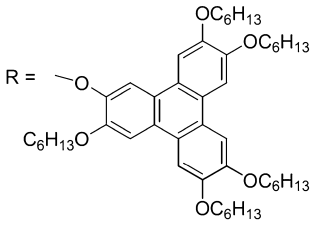
biphenyl groups to both ends of the PDAVT side chain, the resultant main-chain/side-chain LCPs (MCSCLCPs) with sufficient high molecular weights (MWs) exhibit hierarchical supramolecular structures with ordering on both nanometer and subnanometer length scales at low temperatures. Whereas the latter one is attributed to the packing of the biphenyl groups in the side chains, the former one is associated with a scaffold of the supramolecular structure with a 2D rectangular positional order constructed by the packing of thick MJLCP main chains. Altering the calamitic mesogen from biphenyl to azobenzene results in a similar hierarchical supramolecular structure.[25] Calamitic mesogens have also been introduced to other polymer backbones with a rod-like nature, such as polypeptides and ethyl cellulose (EC), to construct functional hierarchical ordered structures.[26−28] Hence, combining rod-like LC main chains and calamitic mesogen-containing side chains can provide LCPs with hierarchical ordered structures. However, discotic mesogens have completely different self-assembling tendencies compared with the calamitic mesogens. To the best of our knowledge, attempts to construct MCSCLCPs with discotic mesogens have so far been unsuccessful.[29] Therefore, whether discotic mesogens act the same way as the calamitic mesogens in the supramolecular self-organization of MCSCLCPs is intriguing.

Herein, we designed a series of combined LCPs utilizing an MJLCP as the main-chain LC building block and a Tp DLC as the side-chain LC building block. At the molecular structure level, two Tp moieties are connected to the repeating unit of the poly(vinyl terephthalate) main chain through several methylene units to derive the target polymer, PP*n*V (Chart 1), where

Chart 1. Chemical Structure of PP*n*V



PPnV, n = 3, 6.



n represents the number of methylene units. The structure of PP*n*V is designed on the basis of four considerations: (i) PDAVT and Tp DLC are selected as the main-chain and side-chain LC building blocks, respectively, because of their ready accessibility and potential capability of forming ordered Φ phases. (ii) Hexyloxy chains, unbranched alkyl chains with a medium chain length, are selected as the peripheral chains of Tp moieties to facilitate the formation of discotic Φ phases.[30,31] (iii) Methylene units are selected as the flexible spacer owing to the easily variable length and good thermal stability. (iv) The number of methylene units, *n*, is determined on the basis of the critical alkyl chain length for PDAVT to form a highly ordered Φ phase. Mainly based on the wide-angle X-ray diffraction (WAXD) experiments, we investigated the phase structure evolution of PP3V and PP6V. The interplay between the individual phase formation of the two fundamentally distinct LC building blocks, namely MJLCPs and Tp DLCs, is also discussed. The spacer length affects the interplay between the two LC building blocks tremendously. To the best of our knowledge, this is the first report of combined LC polymers containing discotic mesogens exhibiting fascinating ordered structures, and it can guide the design of ordered functional LCPs bearing discotic mesogens.

EXPERIMENTAL SECTION

Materials. 2,2′-Azobis(isobutyronitrile) (AIBN, Beijing Chemical, 95%) was purified by recrystallization from ethanol. Chlorobenzene was washed with sulfuric acid and then distilled under reduced pressure. Tetrahydrofuran (THF, Beijing Chemical) was refluxed over sodium and distilled before use. Dichloromethane (CH_2Cl_2, Beijing Chemical) was dried over magnesium sulfate anhydrous. All other reagents and solvents were used as received from commercial sources.

Measurements. Elemental analysis, gel permeation chromatographic (GPC) measurements, thermogravimetric analysis (TGA), differential scanning calorimetry (DSC), polarized light microscopy (PLM), and 1D and 2D WAXD experiments were performed according to the procedures previously described.[32] ^{1}H NMR (400 MHz) and ^{13}C NMR (100 MHz) spectra were obtained with a Bruker ARX400 spectrometer using tetramethylsilane as the internal standard at ambient temperature and deuterated chloroform as the solvent. The chemical shifts were reported on the ppm scale. Mass spectra were recorded on a Bruker Apex IV Fourier transform ion cyclotron resonance mass spectrometer by electrospray ionization (ESI).

Synthesis of Monomers. The chemical structures and synthetic procedures of the monomers and polymers are illustrated in Scheme 1. The experimental details are described as follows. 2-Hydroxyl-3,6,7,10,11-pentakis(hexyloxy)triphenylene (PHT) and 2-vinylterephthalic acid (VTA), were facilely synthesized according to the reported procedures.[21,33]

Synthesis of 2-(3-Hydroxypropyl)-3,6,7,10,11-pentakis(hexyloxy)-triphenylene, PHT3. PHT (7.4 g, 10.0 mmol), potassium carbonate (1.4 g, 10.0 mmol), and acetonitrile (300 mL) were charged in a 500 mL three-necked flask. Then a solution of 3-bromopropan-1-ol (2.1 g, 15.0 mmol) in acetonitrile (10 mL) was added dropwise, and the mixture was refluxed for 10 h. After cooled to ambient temperature, the precipitate was dissolved in CH_2Cl_2 (50 mL). After it was filtered, the filtrate was concentrated by a rotary evaporator to give the crude product. The purified product was obtained by passing through a silica gel column with ethyl acetate and petroleum ether (v:v, 1:5) as eluent and subsequent recrystallization from petroleum ether as a white powder. Yield: 98%. ^{1}H NMR (δ): 7.80−7.84 (m, 6H), 4.44 (t, 2H), 4.23 (m, 10H), 3.98 (t, 2H), 2.50 (s, 1H), 2.19 (quint, 2H), 1.91−1.98 (m, 10H), 1.34−1.62 (m, 30H), 0.93 (t, 15H). HRMS(ESI): calcd. $(M + H^+)/z$, 803.5826; found $(M + H)^+/z$, 803.5844. Anal. Calcd. for $C_{51}H_{78}O_7$: C, 76.27; H, 9.79. Found: C, 76.12; H, 9.84.

Synthesis of 2-(6-Hydroxyhexyl)-3,6,7,10,11-pentakis(hexyloxy)-triphenylene, PHT6. PHT6 was prepared in the same manner as described for PHT3, except that 6-bromohexan-1-ol was used instead of 3-bromopropan-1-ol. Yield: 96%. ^{1}H NMR (δ): 7.84 (s, 6H), 4.22−4.25 (t, 12H), 3.68−3.71 (t, 2H), 1.91−1.98 (m, 12H), 1.39−1.60 (m, 36H), 0.94 (t, 15H). HRMS(ESI): calcd. $(M + H^+)/z$, 803.5826; found $(M + H)^+/z$, 845.5844. Anal. Calcd. for $C_{54}H_{84}O_7$: C, 76.73; H, 10.02. Found: C, 76.69; H, 10.14.

Synthesis of 2,5-Bis[(3,6,7,10,11-pentakis(hexyloxy)triphenylen)-2-oxypropyloxycarbonyl]styrene, P3V. VTA (1.9 g, 10.0 mmol), PHT3 (16.0 g, 20.0 mmol), *N*,*N*′-dicyclohexylcarbodiimide (DCC, 6.2 g, 30.0 mmol), 4-(dimethylamino)pyridine (DMAP, 0.2 g, 2.0 mmol), and dried CH_2Cl_2 (100 mL) were mixed in a 250 mL round-bottomed flask and stirred at ambient temperature for 24 h. The floating solid was filtrated, and the solvent was evaporated under reduced pressure. The crude product was purified by silica gel column chromatography with CH_2Cl_2 as eluent and subsequent recrystallization from petroleum ether as a white powder. Yield: 50%. ^{1}H NMR (δ): 7.82−8.23 (m, 15H), 7.36−7.43 (q, 1H), 5.67−5.71 (d, 1H),

dx.doi.org/10.1021/ma300538h | *Macromolecules* 2012, 45, 3346−3355

Scheme 1. Synthetic Route of the Polymers (PP*n*V)

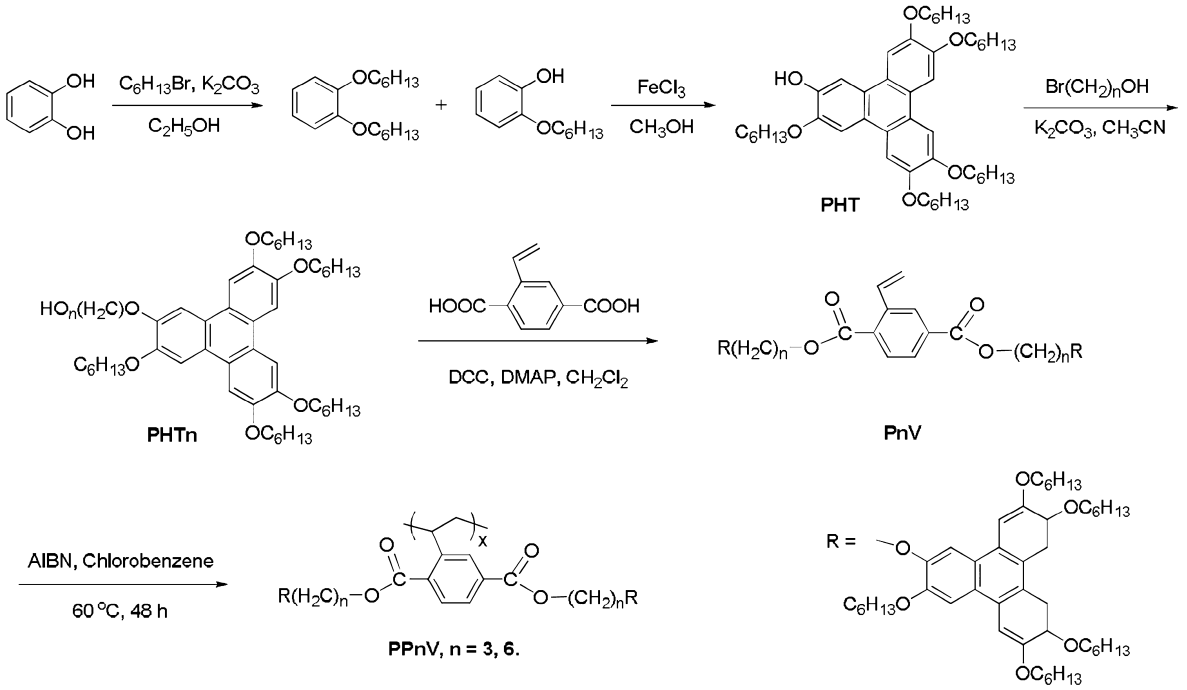


Table 1. Molecular Characterizations and Thermal Properties of PP*n*V

polymer	yield (%)	M_n (× 10^4 g/mol)[a]	M_w/M_n[a]	T_d (°C)[b]	T_g (°C)[c]	$T_{transition}$ (°C) and corresponding enthalpy change (J/g)[c]	
PP3V	78	15.2	1.97	387	60		
PP6V	56	7.1	1.65	380	21	114 (0.3)	225 (0.2)

[a]Determined by GPC in THF using polystyrene standards. [b]5% weight loss temperature evaluated by TGA under a nitrogen atmosphere at a heating rate of 10 °C/min. [c]Evaluated by DSC during the second heating cycle at a rate of 40 °C/min.

5.31−5.34 (d, 1H), 4.64−4.69 (q, 4H), 4.39 (m, 4H), 4.19−4.25 (m, 20H), 2.38−2.43 (m, 4H), 1.90−1.97 (m, 20H), 1.38−1.59 (m, 60H), 0.89−0.95 (t, 30H). ^{13}C NMR (δ): 166.7, 165.6, 149.1, 149.0, 148.4, 139.5, 134.7, 133.2, 130.3, 128.3, 124.1, 123.8, 123.6, 123.5, 123.4, 107.5, 107.4, 107.3, 107.1, 69.7, 69.5, 66.5, 62.5, 31.7, 31.6, 29.4, 29.3, 29.1, 25.8, 22.7, 22.6, 14.0. HRMS(ESI): calcd. $(M + H^+)/z$, 1763.1863; found $(M + H)^+/z$, 1763.1847. Anal. Calcd. for $C_{112}H_{160}O_{16}$: C, 76.33; H, 9.15. Found: C, 76.30; H, 9.16.

Synthesis of 2,5-Bis[(3,6,7,10,11-pentakis(hexyloxy)triphenylen)-2-oxyhexyloxycarbonyl]styrene, P6V. P6V was prepared in the same manner as described for P3V, except that PHT6 was used instead of PHT3. Yield: 58%. ^{1}H NMR (δ): 8.23 (s, 1H), 7.83−7.95 (m, 14H), 7.39−7.46 (q, 1H), 5.72−5.77 (d, 1H), 5.39−5.42 (d, 1H), 4.35−4.39 (m, 4H), 4.22−4.25 (m, 24H), 1.84−1.98 (m, 28H), 1.57−1.60 (m, 28H), 1.40−1.45 (m, 40H), 0.91−0.96 (t, 30H). ^{13}C NMR (δ): 166.7, 165.7, 148.9, 148.8, 139.4, 134.9, 133.2, 132.5, 130.2, 128.2, 127.9, 123.6, 123.5, 117.4, 107.3, 107.1, 69.6, 69.5, 69.4, 65.3, 31.6, 29.4, 28.6, 25.8, 22.6, 14.0. HRMS(ESI): calcd. $(M + H^+)/z$, 1847.2757; found $(M + H)^+/z$, 1847.2763. Anal. Calcd. for $C_{118}H_{172}O_{16}$: C, 76.75; H, 9.39. Found: C, 76.81; H, 9.36.

Polymerization. As shown in Scheme 1, the two polymers were obtained by conventional free-radical polymerization in solution. The detailed procedure was carried out as follows. P3V (1.000 g), chlorobenzene (3.250 g), and AIBN (0.91 mg) were mixed in a glass tube with a magnetic stir bar. The reaction mixture was purged with nitrogen and subjected to three freeze−pump−thaw cycles and sealed under vacuum. Polymerization was performed at 60 °C for 48 h. Subsequently, the polymerization was stopped by dipping the tube in ice/water. After the tube was broken, the solution was diluted with THF (5 mL) and then added dropwise to vigorously stirred acetone (300 mL). To eliminate the unreacted monomer completely, we repeated the precipitation process three times. By filtration and drying in vacuum at 35 °C for 24 h, the target polymer poly{2,5-bis[(3,6,7,10,11-pentakis-(hexyloxy)triphenylen)-2-oxypropyloxycarbonyl]styrene}, PP3V, was obtained as a white solid. Yield: 78%. Poly{2,5-bis[(3,6,7,10,11-pentakis-(hexyloxy)triphenylen)-2-oxyhexyloxycarbonyl]styrene}, PP6V, was obtained similarly compared with PP3V.

RESULTS AND DISCUSSION

Synthesis and Characterization of Monomers and Polymers. As shown in Scheme 1, monomers can be prepared in two efficient steps. PHT*n* was first synthesized by Williamson etherification with PHT and bromhydrin in a nearly 100% yield. Then PHT*n* reacted with VTA via Steglich esterification to obtain the monomers. The chemical structures of the monomers were confirmed by elemental analysis, high-resolution mass spectrometry, and ^{1}H/^{13}C NMR.

Polymers were synthesized in satisfactory yields through conventional free radical polymerization in chlorobenzene with AIBN as the initiator. The molecular characterizations of the polymers are summarized in Table 1. GPC analysis of the polymers shows that number-average MWs (M_n) of the PP3V and PP6V are 1.5×10^5 to 7.1×10^4 g/mol, with polydispersities of 1.97 and 1.65, respectively, confirming their polymeric nature. Figure 1 gives ^{1}H NMR spectra of P6V and PP6V in $CDCl_3$. The characteristic resonances of vinyl H appearing at δ 5.41−5.78 and 7.39−7.46 completely disappear after polymerization, and the resonance peaks of PP6V are rather broad and consistent with the expected polymer structure, indicating the successful polymerization as well.

dx.doi.org/10.1021/ma300538h | *Macromolecules* 2012, 45, 3346−3355

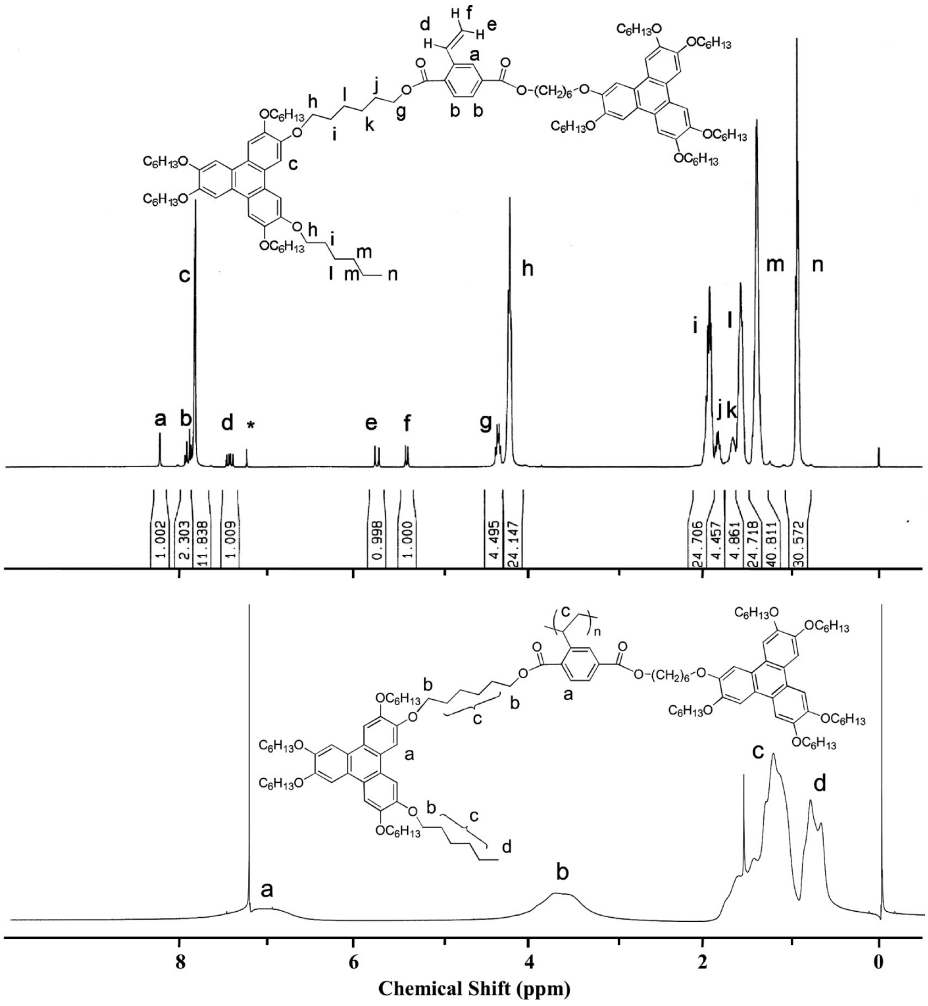


Figure 1. ^{1}H NMR spectra of P6V (top) and PP6V (bottom) in $CDCl_3$.

Thermal and Liquid-Crystalline Properties of the Polymers. The thermal and liquid-crystalline properties of the polymers were investigated by TGA, DSC, and PLM. As shown in Table 1, both polymers exhibit excellent thermal stabilities with the temperatures at 5% weight loss above 370 °C in nitrogen.

The phase-transition behaviors of the polymers were investigated by DSC. With the consideration of the effect of thermal history, the samples were heated from ambient temperature to 250 °C at a rate of 20 °C/min first. DSC experiments were carried out at a heating rate of 40 °C/min under a nitrogen atmosphere following a cooling process at a rate of 2 °C/min. The glass-transition temperatures (T_g's) and the data corresponding to phase transitions of PP*n*V are summarized in Table 1. As expected, T_g decreases as the spacer length increases owing to the lower steric hindrance and the stronger internal plasticization effect of the longer alkyl spacers. The DSC thermograms of both polymers during the second heating process are shown in Figure 2. The DSC profile of PP3V from −50 to 250 °C shows only a glass-transition step but no endothermic peak correlating to a phase transition. For PP6V, two endothermic peaks are observed at 114 and 225 °C besides the glass-transition step. Considering the small value of the enthalpic changes of transitions, these two endothermic peaks might be attributed to two transitions involving LC phases. According to the literature,[5] the endothermic peak at

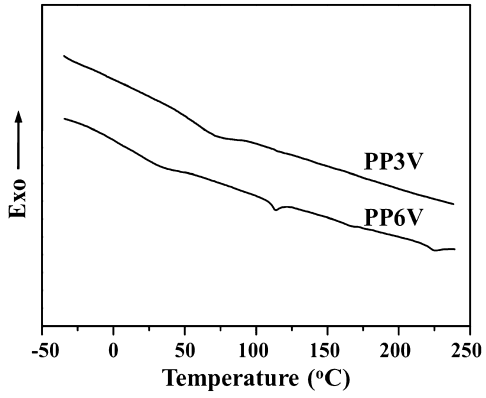


Figure 2. DSC traces of PP*n*V at a heating rate of 40 °C/min under a nitrogen atmosphere following cooling at 2 °C/min.

114 °C may be correlated to the isotropization of Tp DLCs. Interestingly, this phase-transition temperature is higher than that of 2,3,6,7,10,11-hexahexyloxytriphenylene (ca. 100 °C)[34] and Tp containing poly(meth)acrylates (ca. 40−80 °C),[14,16,17] which suggests that ordered structures formed by Tp DLCs are stabilized by incorporating Tp moieties into the side chains of rod-like MJLCPs. In other words, the rod-like MJLCPs stabilize the ordered structures of Tp DLCs, whereas the

dx.doi.org/10.1021/ma300538h | *Macromolecules* 2012, 45, 3346−3355

flexible poly(meth)acrylates disrupt the regular packing of Tp DLCs.

Birefringence of the polymers was observed by PLM with powder samples. A typical PLM texture of PP6V is shown in Figure 3. Both polymers exhibit strong birefringence that always remains, and the isotropic state was not observed in the whole temperature range before degradation, indicating that LC phases of the polymers are rather stable. However, no characteristic textures were observed.

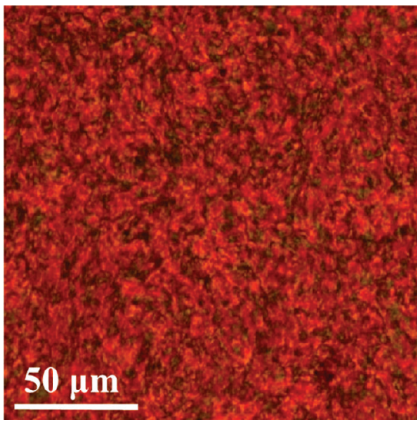


Figure 3. Representative texture of PP6V at 80 °C from PLM observation. The powder sample was cooled from 250 °C.

Phase Structure Identification of the Polymers. Because the PLM textures were ambiguous for the phase structure identification of PP*n*V, variable-temperature 1D and 2D WAXD experiments were performed. Film samples for 1D WAXD experiments were cast from the homogeneous solutions in hexane onto a copper substrate. Solvent was then allowed to evaporate at ambient temperature, and the samples were dried overnight at 35 °C in a vacuum oven before characterization. The samples were under a nitrogen atmosphere during 1D WAXD experiments to avoid thermal degradation. In 2D WAXD experiments, oriented film samples of PP3V and PP6V were sheared from the bulk polymer with a relatively large mechanical force at 170 and 150 °C, respectively, during cooling from higher temperatures. All samples were thermally annealed overnight at an appropriate temperature above T_g of the corresponding polymers before 2D WAXD experiments. 2D WAXD patterns were recorded with the X-ray incident beam perpendicular to the shear direction.

1D WAXD profiles of PP3V during the first heating and subsequent cooling processes are shown in Figure 4a,b, respectively. The patterns of the low-angle region during cooling are shown in Figure 4c for clarity. During the first heating process, the as-cast sample renders two peaks in the low-angle region, indicating the existence of some ordered structure. The broad halo in the wide-angle region is characteristic of the amorphous packing of the alkyl chain. After heating to higher temperatures, more peaks develop in the low-angle region, and the broad halo in the wide-angle region slightly shifts to lower angles due to thermal expansion. At 270 °C, seven sharp peaks are observed in the low-angle region (Figure 4c), and they remain during the cooling process. The corresponding *d*-spacing values of the seven peaks are 3.74, 3.20, 2.30, 1.88, 1.60, 1.50, and 1.23 nm, which can be assigned as (100), (010), (110), (200), (020), (120), and (300) diffractions of a rectangular structure with a = 3.74 nm, b = 3.20 nm, and $\gamma = 90°$, as identified in Figure 4c. The absence of (hkl) diffractions with $l \neq 0$ indicates that this rectangular structure possesses only a 2D positional order, exhibiting features of a columnar phase, similar to many other MJLCPs.[23,25,35] The simulated length of the Tp moiety with all-trans conformation of C6 alkyl arms is ca. 2.3 nm. Because of the possible rotation of the flexible spacer and ester linkage, the whole side-chain length cannot be precisely estimated. However, depending on the relative position of Tp moieties in the side chain, the dimension of the whole side chain should be in the range of 2.3−4.6 nm. This range includes the sizes of the aforementioned 2D rectangular structure (a = 3.74 nm and b = 3.20 nm). Therefore, we speculate that PP3V forms a 2D rectangular columnar (Φ_R) phase developed by the rod-like supramolecular mesogen − the MJLCP chain as a whole at 270 °C.

After cooling to ambient temperature, all diffraction peaks developed at high temperatures remain with slightly lower intensities, whereas no diffraction peak is observed at $2\theta \approx 25°$ which represents the π−π stacking, indicating that Tp moieties do not self-organize into a well-ordered supramolecular

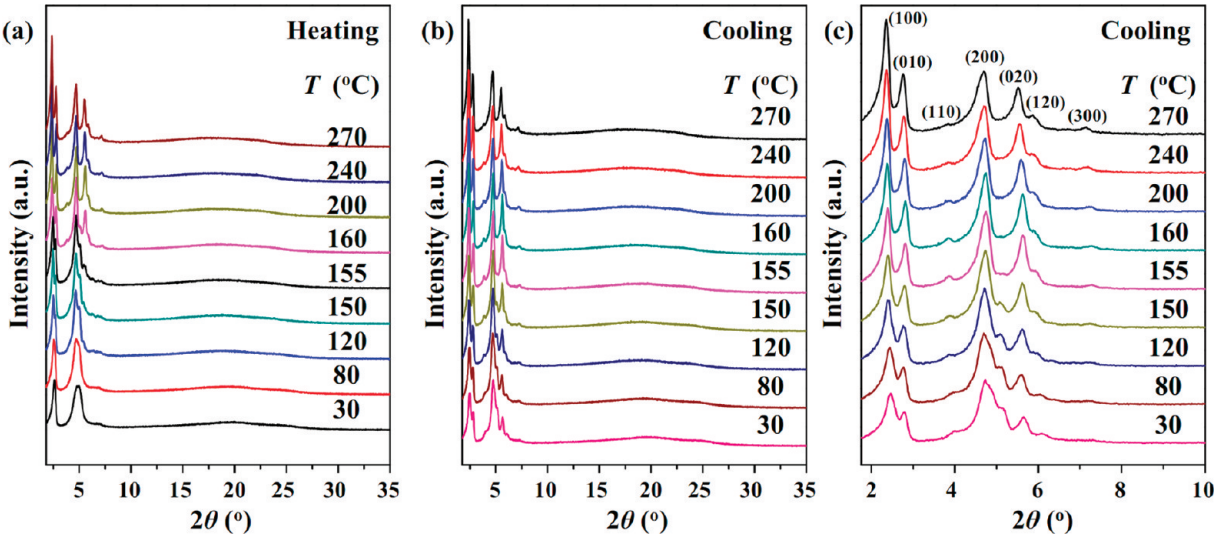


Figure 4. 1D WAXD patterns of PP3V during the first heating (a) and subsequent cooling (b) and the pattern in the low-angle region during cooling (c).

column. Notably, a new diffraction peak appears at $2\theta = 5.16°$ which corresponds to a *d*-spacing of 1.71 nm. This *d*-spacing cannot be fitted into the 2D rectangular structure developed at high temperatures. Actually, several Tp-containing molecules[36,37] and LCPs[18,38,39] have a diffraction peak at 2θ of ca. 5° (ca. 1.7 to 1.8 nm) in their powder WAXD patterns. Hence, this peak may be characteristic of ordered structures of Tp derivatives. Considering the intensity and shape of this peak, we reason that the new diffraction peak can be attributed to an ordered structure formed by Tp DLCs in conjunction with the 2D rectangular scaffold constructed by MJLCPs, although there can be other possibilities. The ordered structure corresponding to the 2θ value of 5.16° (1.71 nm) formed by Tp moieties can be attributed to the lateral spacing of a discotic nematic (N_D) mesophase of Tp moieties. Therefore, the high-temperature phase of PP3V is a 2D Φ_R phase developed by the rod-like MJLCP chain as a whole, whereas the low-temperature phase is the same Φ_R phase in conjunction with an N_D phase owing to the self-organization of the Tp moieties.

It is difficult to calculate the density of PP3V using the above-mentioned supramolecular structure at ambient temperature. However, we can roughly estimate the density of PP3V using the 2D Φ_R structure based on the MJLCP scaffold. Taking the values of *a* and *b* measured at ambient temperature and assuming a value of 0.25 nm for *c* (the projection length of one repeating unit on the *c* axis with C−C bond length and angle of 0.154 nm and 109.5°, respectively),[40] we estimate the density of PP3V to be ca. 1.04 g/cm^3, which is slightly larger than the measured value of 0.94 g/cm^3 at ambient temperature. The slightly larger estimated density is reasonable with the consideration of the poor packing of the Tp moieties in the side chain and the structural imperfection of the whole polymer in the LC state than in the crystalline state.

The 1D WAXD profiles in the second heating process follow the opposite transition pathways to those in the first cooling process, indicating the enantiotropic phase behavior of PP3V. Figure 5 shows plots of the *d*-spacing of the (100) diffraction (d_{100}) against temperature. A discontinuous increase of d_{100} is observed at ~150 °C during heating, even though the transition cannot be detected in DSC. This indicates a first-order phase transition upon heating.[40−42] Upon cooling, the first-order transition with a less dramatic *d*-spacing change compared with that in the heating process is observed at ~130 °C, indicating the formation of a new phase. However, the degree of order of this low-temperature phase does not change much compared with the high-temperature one, which is consistent with the DSC results and our preceding speculation on the phase behavior of PP3V.

Owing to the dimensionality limit of 1D WAXD, 2D WAXD experiments were conducted with mechanically sheared samples. Figure 6a shows the 2D WAXD pattern of PP3V at 170 °C, and similar patterns were recorded at low temperatures due to the limited resolution of our equipment. Nonetheless, several pairs of sharp arcs in the low-angle region appear on the equator, indicating the existence of ordered structures on the nanometer scale with lattice planes oriented primarily parallel to the meridian direction. In general, the polymer chain will be oriented parallel to the direction of the shear force. Hence, the absence of the diffractions on other directions except those on the equator in the low-angle region ensured that all of the low-angle diffractions can be attributed to (*hk*0) diffractions. This observation is consistent with the assignment of the diffraction peaks in 1D WAXD patterns. In addition, the weak scattering

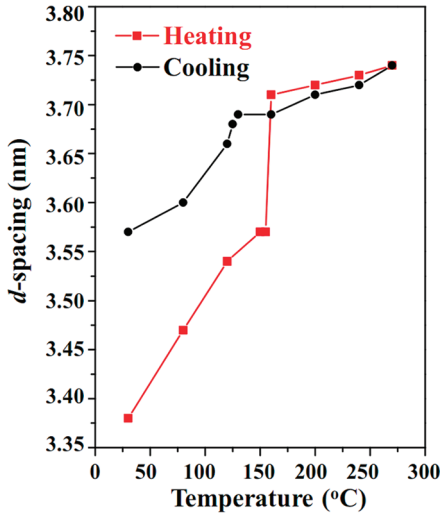


Figure 5. *d*-Spacing values of the first diffraction peak in the 1D WAXD patterns of PP3V during the first heating (solid squares) and subsequent cooling (solid circles) processes as a function of temperature.

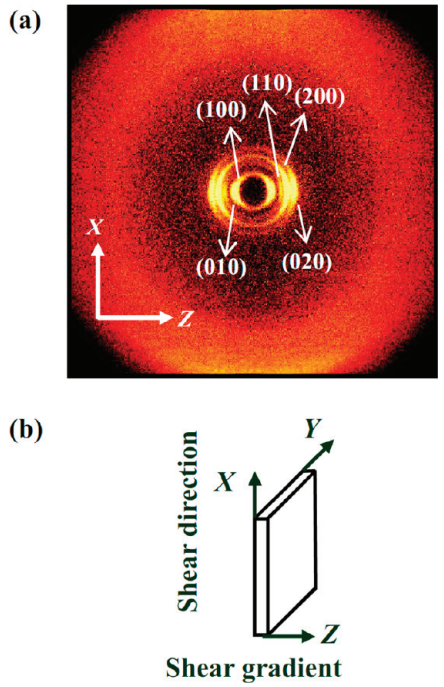


Figure 6. 2D WAXD pattern of PP3V at 170 °C with the X-ray beam perpendicular to the shear direction (a) and the shearing geometry (b), where *X* and *Z* are the shear direction and shear gradient, respectively.

halo at $2\theta \approx 25°$ (*d*-spacing of ~0.36 nm) corresponding to the vertical distance between neighboring aromatic rings is more or less concentrated on the meridian with rather broad azimuthal distributions, indicative of subnanometer structures with a short-range order existing with lattice planes mainly parallel to the equatorial direction. Therefore, all Tp moieties are aligned with the aromatic plane perpendicular to the polymer main chain to form a low ordered N_D phase. 2D WAXD patterns serve as the additional evidence to support our preceding speculation on the phase structures of PP3V.

dx.doi.org/10.1021/ma300538h | *Macromolecules* 2012, 45, 3346−3355

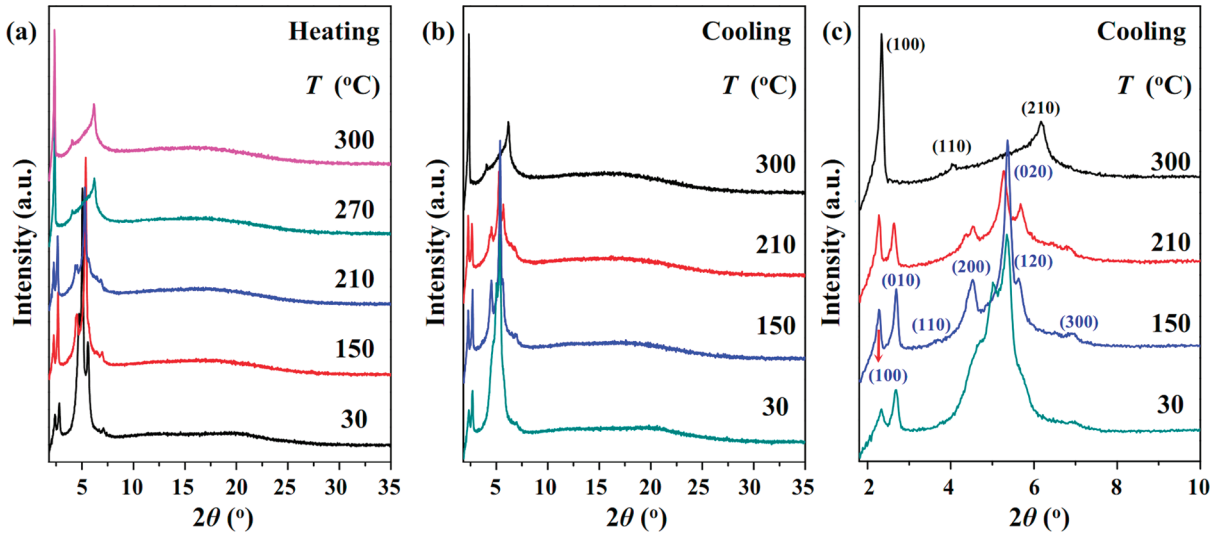


Figure 7. 1D WAXD patterns of PP6V during the first heating (a) and subsequent cooling (b) and the pattern in the low-angle region during cooling (c).

One-dimensional WAXD profiles of PP6V during the first heating and subsequent cooling processes are shown in Figure 7a,b, respectively. The low-angle patterns during cooling are shown in Figure 7c for clarity. The 1D WAXD profiles of PP6V are similar to those of PP3V to some extent. As shown in Figure 7a, several peaks are observed in the low-angle region at 30 °C, indicative of an ordered structure in the as-cast film. Seven peaks also develop at elevated temperatures. The corresponding *d*-spacing values of the seven peaks at 150 °C are 3.89, 3.28, 2.40, 1.96, 1.64, 1.57, and 1.28 nm, which can be assigned as (100), (010), (110), (200), (020), (120), and (300) diffractions of a 2D Φ_R phase with a = 3.89 nm, b = 3.28 nm, and $\gamma = 90°$, as identified in Figure 7c. The larger a and b values in the 2D rectangular unit cell of PP6V compared with PP3V are owing to the increased spacer length from three methylene units to six. Notably, when the temperature goes to 300 °C, three peaks with a scattering vector ratio of $1:3^{1/2}:7^{1/2}$ appear, demonstrating a long-range ordered hexagonal lattice with $a = b =$ 4.35 nm and $\gamma = 120°$. The three peaks are indexed as the (100), (110), and (210) diffractions, as identified in Figure 7c. Upon cooling, the seven peaks representing the 2D Φ_R phase develop again, indicating the enantiotropic phase behavior of PP6V. As the temperature further decreases to ambient temperature, intensities of all diffraction peaks slightly decrease, with the diffractions from the 2D Φ_R scaffold of MJLCPs developed at 150 °C remaining. Similar to 1D WAXD profiles of PP3V during cooling, a new diffraction peak appears at a 2θ value of 5.01° corresponding to a *d*-spacing of 1.76 nm. Interestingly, its intensity is higher than that for PP3V. The difference of intensity may be related to the competition between the two LC building blocks, which will be discussed in the next section. No diffraction peak is observed at $2\theta \approx 25°$, which represents the $\pi-\pi$ stacking at ambient temperature, indicating that Tp moieties do not self-organize into a well-ordered supramolecular LC column. This new diffraction peak appearing at a 2θ value of 5.16° (1.71 nm) is also assigned to the lateral distance of an N_D mesophase formed by Tp moieties due to the absence of higher-ordered diffractions and the characteristic $\pi-\pi$ stacking in the discotic LC column (~0.35 nm).

Figure 8a,b shows the 2D WAXD patterns of PP6V at 150 and 30 °C, respectively. Variable-temperature 2D WAXD experiments at 300 °C were not conducted because the sample began to decompose in air at such a high temperature. As shown in Figure 8a, the 2D WAXD pattern of PP6V at 150 °C is similar to that of PP3V at high temperatures, indicative of the existence of a 2D Φ_R structures on the nanometer scale with the supramolecular rod oriented primarily parallel to the meridian direction. The 2D WAXD film pattern of PP6V at 30 °C (Figure 8b) shows that the diffraction arcs on the equator in the low-angle region are similar to those at 150 °C. In addition, the intensity of the scattering halo at $2\theta \approx 25°$ (0.36 nm) in the high-angle region becomes much stronger upon cooling, although the scattering halo at $2\theta \approx 25°$ (0.36 nm) in 1D WAXD patterns of PP6V is not observed even after an overnight thermal treatment. This intensity increase indicates that a more ordered N_D phase is formed. This phenomenon suggests that the discotic mesogens in the side chains of PP6V can be further oriented and packed into a higher ordered structure. Therefore, PP6V possesses three LC phases with two enantiotropic phase transitions according to the DSC and WAXD studies. The high-temperature phase of PP6V is a 2D Φ_H phase developed by the rod-like supramolecular mesogen — the MJLCP chain as a whole — while the medium-temperature one is a 2D Φ_R phase developed by the rod-like MJLCP supramolecular mesogen. Furthermore, the low-temperature phase is the same 2D Φ_R phase as the medium-temperature one in conjunction with an N_D phase owing to the self-organization of the Tp moieties.

Interplay between the Two LC Building Blocks. Figure 9 depicts a schematic drawing of the molecular packing of PP*n*V at different temperatures. From the whole phase evolution diagram, we found that with two fundamentally distinct LC building blocks in one polymer, PP*n*V exhibits a complex phase behavior involving the competition of these two building blocks. Specifically, comparing the diffraction peaks at $2\theta \approx 5°$ (1.7 to 1.8 nm) in the 1D WAXD patterns during cooling at ambient temperature (Figure 10), we found that the diffraction peak of PP6V exhibits higher intensity, indicating that the ordered structure formed by Tp moieties in PP6V is more ordered. This intensity difference suggests that longer flexible spacers between MJLCP main chain and Tp moieties in the side chains offer a stronger decoupling effect, which allows

dx.doi.org/10.1021/ma300538h | *Macromolecules* 2012, 45, 3346−3355

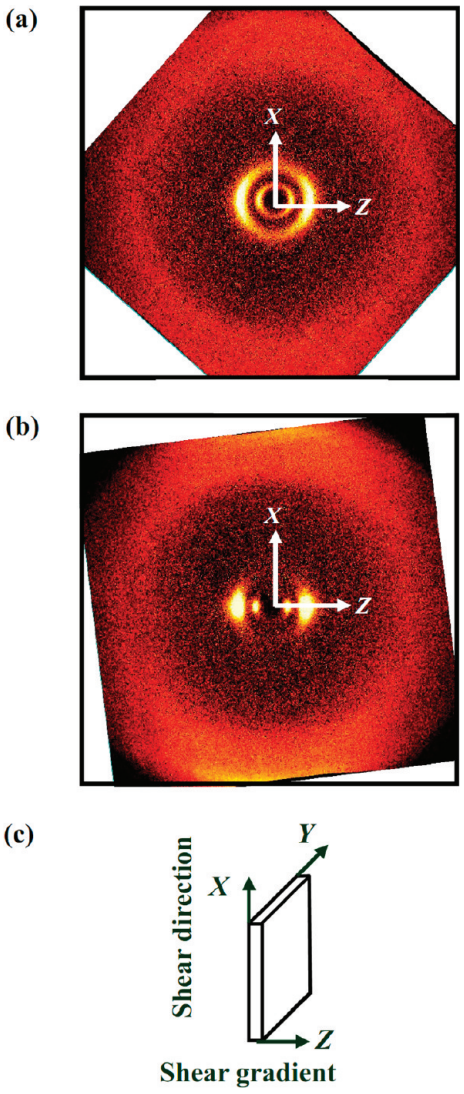


Figure 8. 2D WAXD patterns of PP6V at 150 °C (a) and 30 °C (b), respectively, with the X-ray beam perpendicular to the shear direction and the shearing geometry (c), where *X* and *Z* are the shear direction and shear gradient, respectively.

for the two LC building blocks to act more independently. Therefore, we can speculate that when the flexible spacer is shorter between the main-chain MJLCP and the side-chain

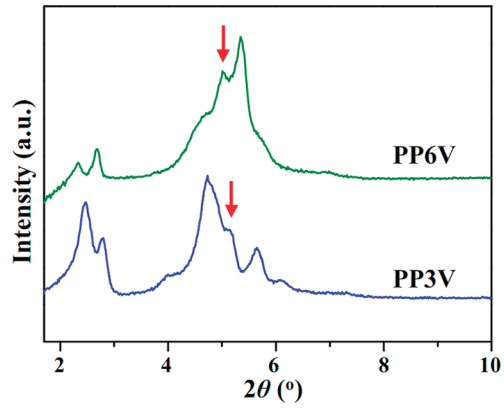


Figure 10. 1D WAXD patterns of PP3Vand PP6V at ambient temperature during cooling, with the arrows pointing out the diffraction peaks associated with the discotic mesogens.

DLC, the whole polymer behaves more like the individual MJLCPs, and Tp moieties become more-or-less part of the side chains of the MJLCP because of the strong coupling effect of the DLC moieties and the MJLCP main chain. With the length of the flexible spacer increasing, however, the interaction between the two LC building blocks, the MJLCP and the Tp DLC, is gradually weakened, and then both LC building blocks act more independently and tend to display their individual self-organizing properties. Moreover, when the flexible spacer is sufficiently long, the coupling between the two LC building blocks will diminish, and the resultant polymer may have fascinating self-assembling behaviors. To this end, further work is currently in progress.

Ordered structures developed by the two LC building blocks separately stabilize each other. Of particular interest is the fact that PP6V can retain the Φ_R phase during cooling with merely a slight intensity decrease, whereas its homologous polymer, PDAVT with hexyl tails, is relatively disordered after cooling to ambient temperature.[24] Retaining of the ordered structures may be associated with the stabilizing effect of the discotic moieties, and this stabilizing effect may be originated from the increased "jacketing" effect due to the attachment of the Tp units. Moreover, DSC results suggest that ordered structures formed by Tp DLCs are also stabilized by incorporating Tp moieties into the side chain of rod-like MJLCPs. Therefore, individual ordered structures developed by these two LC building blocks are not only competitive but also promotive to each other.

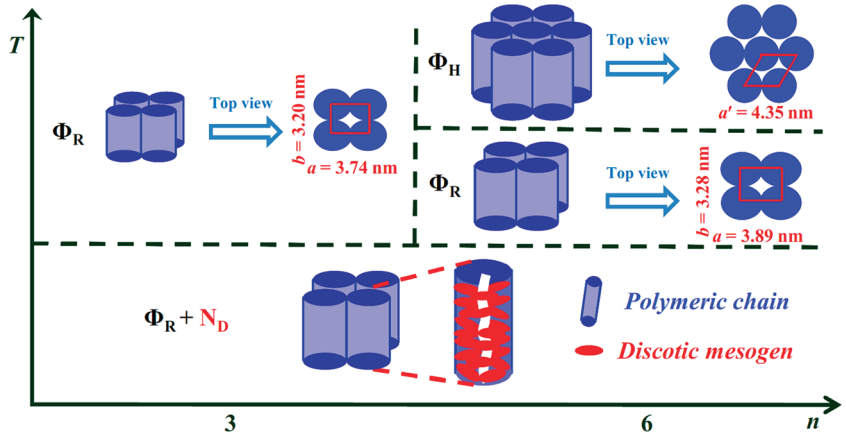


Figure 9. Schematic drawing of the whole phase evolution diagram for PP*n*V at different temperatures.

dx.doi.org/10.1021/ma300538h | *Macromolecules* 2012, 45, 3346−3355

CONCLUSIONS

Using conventional free-radical polymerization, we synthesized a series of MJLCPs bearing Tp DLCs as pendant groups, PP*n*V, with sufficiently high MW (M_n > 10^4 g/mol) to construct MCSCLCPs with DLCs as the side-chain LC building block. With the increasing length of the flexible spacer, which links the two fundamentally distinct LC building blocks, the phase behaviors of PP*n*V vary tremendously. PP3V exhibits two mesophases. The high-temperature one is a 2D Φ_R phase developed by the rod-like MJLCP supramolecular mesogen as a whole, and the low-temperature one is the same 2D Φ_R scaffold in conjunction with an N_D phase owing to the poor packing of the Tp moieties. However, PP6V displays three different mesophases. At high temperatures, PP6V exhibits a 2D Φ_H phase developed by the supramolecular MJLCP mesogen, whereas the medium-temperature phase is a 2D Φ_R phase formed by the same mesogen. The low-temperature phase is the same 2D Φ_R phase as the medium-temperature one in conjunction with an N_D phase, which is similar to the low-temperature phase of PP3V. Both polymers act like MJLCPs with Φ phases (Φ_R or Φ_H) when Tp DLCs isotropilize at relatively high temperatures. When temperature decreases to ambient temperature, however, Tp moieties in the side chain tend to self-organize into an N_D phase. In conjunction with the Φ_R scaffold developed by the rod-like supramolecular mesogen of the MJLCP chain, an N_D phase coexists in the low-temperature phases for both polymers. With the flexible spacer length increasing, the two LC building blocks act more independently, and ordered structures developed by these two LC building blocks are not only competitive but also promotive to each other.

As expected, introducing DLCs into the side chains of MJLCPs can enrich the phase behaviors of LC polymers, which is of great importance for both fundamental research and real applications. On the basis of our work, LC building blocks with various topologies and functions can be covalently linked together and investigated to exploit new functional materials with fine-tuning ordered structures.

AUTHOR INFORMATION

Corresponding Author

*E-mail: fanxh@pku.edu.cn (X.-H.F.); zshen@pku.edu.cn (Z.S.).

Notes

The authors declare no competing financial interest.

[†]Joint first authors

ACKNOWLEDGMENTS

This work was supported by the National Natural Science Foundation of China (grants 20974002, 20990232, and 21134001).

REFERENCES

(1) O'Neill, M.; Kelly, S. M. *Adv. Mater.* **2011**, *23*, 566−584.
(2) Pisula, W.; Zorn, M.; Chang, J. Y.; Mullen, K.; Zentel, R. *Macromol. Rapid Commun.* **2009**, *30*, 1179−1202.
(3) Funahashi, M. *Polym. J.* **2009**, *41*, 459−469.
(4) Kaafarani, B. R. *Chem. Mater.* **2011**, *23*, 378−396.
(5) Kumar, S. *Chemistry of Discotic Liquid Crystals: From Monomers to Polymers*; CRC Press: Boca Raton, FL, 2011.
(6) Sergeyev, S.; Pisula, W.; Geerts, Y. H. *Chem. Soc. Rev.* **2007**, *36*, 1902−1929.
(7) Debije, M. G.; Piris, J.; de Haas, M. P.; Warman, J. M.; Tomović, Ž.; Simpson, C. D.; Watson, M. D.; Müllen, K. *J. Am. Chem. Soc.* **2004**, *126*, 4641−4645.
(8) Schmidt-Mende, L.; Fechtenkötter, A.; Müllen, K.; Moons, E.; Friend, R. H.; MacKenzie, J. D. *Science* **2001**, *293*, 1119−1122.
(9) Feng, X.; Marcon, V.; Pisula, W.; Hansen, M. R.; Kirkpatrick, J.; Grozema, F.; Andrienko, D.; Kremer, K.; Mullen, K. *Nat. Mater.* **2009**, *8*, 421−426.
(10) Chandrasekhar, S.; Sadashiva, B.; Suresh, K. *Pramana* **1977**, *9*, 471−480.
(11) Adam, D.; Schuhmacher, P.; Simmerer, J.; Haussling, L.; Siemensmeyer, K.; Etzbachi, K. H.; Ringsdorf, H.; Haarer, D. *Nature* **1994**, *371*, 141−143.
(12) Hüser, B.; Spiess, H. W. *Macromol. Rapid Commun.* **1988**, *9*, 337−343.
(13) Hueser, B.; Pakula, T.; Spiess, H. W. *Macromolecules* **1989**, *22*, 1960−1963.
(14) Werth, M.; Spiess, H. W. *Macromol. Rapid Commun.* **1993**, *14*, 329−338.
(15) Ringsdorf, H.; Wüstefeld, R.; Zerta, E.; Ebert, M.; Wendorff, J. H. *Angew. Chem., Int. Ed.* **1989**, *28*, 914−918.
(16) Boden, N.; Bushby, R. J.; Lu, Z. B. *Liq. Cryst.* **1998**, *25*, 47−58.
(17) Stewart, D.; S. Mchattie, G.; T. Imrie, C. *J. Mater. Chem.* **1998**, *8*, 47−51.
(18) Weck, M.; Mohr, B.; Maughon, B. R.; Grubbs, R. H. *Macromolecules* **1997**, *30*, 6430−6437.
(19) Catry, C.; Van der Auweraer, M.; De Schryver, F. C.; Bengs, H.; Häussling, L.; Karthaus, O.; Ringsdorf, H. *Macromol. Chem. Phys.* **1993**, *194*, 2985−2999.
(20) Imrie, C. T.; Inkster, R. T.; Lu, Z.; Ingram, M. D. *Mol. Cryst. Liq. Cryst.* **2004**, *408*, 33−43.
(21) Xing, C. M.; Lam, J. W. Y.; Zhao, K. Q.; Tang, B. Z. *J. Polym. Sci., Part A: Polym. Chem.* **2008**, *46*, 2960−2974.
(22) Tahar-Djebbar, I.; Nekelson, F.; Heinrich, B.; Donnio, B.; Guillon, D.; Kreher, D.; Mathevet, F.; Attias, A.-J. *Chem. Mater.* **2011**, *23*, 4653−4656.
(23) Xie, H.-L.; Jie, C.-K.; Yu, Z.-Q.; Liu, X.-B.; Zhang, H.-L.; Shen, Z.; Chen, E.-Q.; Zhou, Q.-F. *J. Am. Chem. Soc.* **2010**, *132*, 8071−8080.
(24) Yin, X. Y.; Ye, C.; Ma, X.; Chen, E. Q.; Qi, X. Y.; Duan, X. F.; Wan, X. H.; Cheng, S. Z. D.; Zhou, Q. F. *J. Am. Chem. Soc.* **2003**, *125*, 6854−6855.
(25) Xie, H.-L.; Wang, S.-J.; Zhong, G.-Q.; Liu, Y.-X.; Zhang, H.-L.; Chen, E.-Q. *Macromolecules* **2011**, *44*, 7600−7609.
(26) Schaefer, K. E.; Keller, P.; Deming, T. J. *Macromolecules* **2005**, *39*, 19−22.
(27) Hu, T. H.; Xie, H.-L.; Xiao, J. B.; Zhang, H. L.; Chen, E. Q. *Cellulose* **2010**, *17*, 547−558.
(28) Hu, T.; Yi, J.; Xiao, J.; Zhang, H. *Polym. J.* **2010**, *42*, 752−758.
(29) Karthaus, O.; Ringsdorf, H.; Ebert, M.; Wendorff, J. H. *Macromol. Chem. Phys.* **1992**, *193*, 507−513.
(30) Deibel, C.; Janssen, D.; Heremans, P.; De Cupere, V.; Geerts, Y.; Benkhedir, M. L.; Adriaenssens, G. J. *Org. Electron.* **2006**, *7*, 495−499.
(31) Green, M. M.; Ringsdorf, H.; Wagner, J.; Wüstefeld, R. *Angew. Chem., Int. Ed.* **1990**, *29*, 1478−1481.
(32) Xu, Y. D.; Yang, Q.; Shen, Z. H.; Chen, X. F.; Fan, X. H.; Zhou, Q. F. *Macromolecules* **2009**, *42*, 2542−2550.
(33) Tu, H. L.; Zhang, D.; Wan, X. H.; Chen, X. F.; Liu, Y. X.; Zhang, H. L.; Zhou, Q. F. *Macromol. Rapid Commun.* **1999**, *20*, 549−551.
(34) Boden, N.; Borner, R. C.; Bushby, R. J.; Cammidge, A. N.; Jesudason, M. V. *Liq. Cryst.* **1993**, *15*, 851−858.
(35) Chen, X.-F.; Shen, Z.; Wan, X.-H.; Fan, X.-H.; Chen, E.-Q.; Ma, Y.; Zhou, Q.-F. *Chem. Soc. Rev.* **2010**, *39*, 3072−3101.
(36) Paraschiv, I.; Giesbers, M.; van Lagen, B.; Grozema, F. C.; Abellon, R. D.; Siebbeles, L. D. A.; Marcelis, A. T. M.; Zuilhof, H.; Sudhölter, E. J. R. *Chem. Mater.* **2006**, *18*, 968−974.
(37) Paraschiv, I.; de Lange, K.; Giesbers, M.; van Lagen, B.; Grozema, F. C.; Abellon, R. D.; Siebbeles, L. D. A.; Sudholter, E. J. R.; Zuilhof, H.; Marcelis, A. T. M. *J. Mater. Chem.* **2008**, *18*, 5475−5481.

(38) Wan, W.; Monobe, H.; Tanaka, Y.; Shimizu, Y. *Liq. Cryst.* **2003**, *30*, 571−578.
(39) Talroze, R. V.; Otmakhova, O. A.; Koval, M. A.; Kuptsov, S. A.; Platé, N. A.; Finkelmann, H. *Macromol. Chem. Phys.* **2000**, *201*, 877−881.
(40) Tu, H. L.; Wan, X. H.; Liu, Y. X.; Chen, X. F.; Zhang, D.; Zhou, Q. F.; Shen, Z. H.; Ge, J. J.; Jin, S.; Cheng, S. Z. D. *Macromolecules* **2000**, *33*, 6315−6320.
(41) Yu, Z. N.; Tu, H. L.; Wan, X. H.; Chen, X. F.; Zhou, Q. F. *J. Polym. Sci., Part A: Polym. Chem.* **2003**, *41*, 1454−1464.
(42) Zhang, L.; Wu, H.; Shen, Z.; Fan, X.; Zhou, Q. *J. Polym. Sci., Part A: Polym. Chem.* **2011**, *49*, 3207−3217.

Macromolecules

Article

pubs.acs.org/Macromolecules

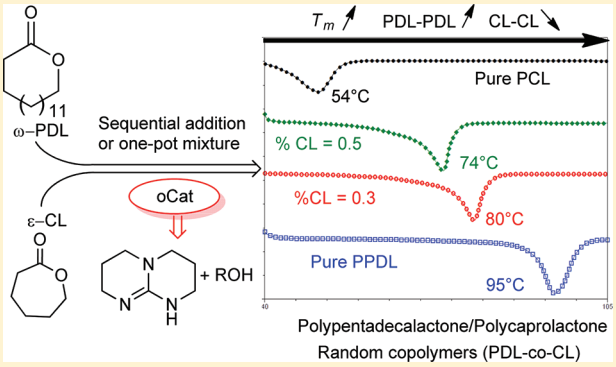
ω-Pentandecalactone Polymerization and ω-Pentadecalactone/ε-Caprolactone Copolymerization Reactions Using Organic Catalysts

Miloud Bouyahyi,[†] Mark P. F. Pepels,[†] Andreas Heise,[‡] and Rob Duchateau*[,†]

[†]Laboratory of Polymer Chemistry, Department of Chemical Engineering and Chemistry, Eindhoven University of Technology, Den Dolech 2, P.O. Box 513, 5600 MB Eindhoven, The Netherlands

[‡]School of Chemical Sciences, Dublin City University, Dublin 9, Ireland

ABSTRACT: The catalytic behavior of several inexpensive and simple N-heterocyclic organic catalysts in ring-opening polymerization (ROP) of ω-pentadecalactone (PDL) and ε-caprolactone (CL) has been studied. The polymerization reactions, carried out in bulk monomer and in toluene solution at 100 °C, identified 1,5,7-triazabicyclo[4.4.0]dec-5-ene (TBD) in combination with benzyl alcohol (BnOH) as initiator as the only active catalyst for the ring-opening polymerization of PDL and for the copolymerization of PDL and CL. The guanidine *N*-methyl-TBD (MTBD), 1,2,3-triisopropylguanidine, the amidine 1,8-diazabicycloundec-7-ene (DBU), and other N-heterocyclic organic catalysts such as dialkylaminopyridine (DMAP), imidazole, indoles, and N-heterocyclic carbenes (NHC's) tested in this study proved to be inactive in the ROP of PDL even for the long reaction times. The polymerization mechanism, kinetic studies, temperature, and monomer concentration effects were investigated both in solution and in bulk monomer. The pseudoliving character of the TBD/BnOH system has been proven by kinetic studies in both toluene solution and bulk monomer. By varying the experimental conditions and the monomer feed composition, highly crystalline poly(PDL-*co*-CL) random copolymers of various compositions have been prepared using the binary system TBD/ROH as catalyst/initiators. Thermal analysis and ^{13}C NMR spectroscopy show a linear relation of the variation of the random copolymers melting temperatures as a function of comonomer content.



INTRODUCTION

During the past years, aliphatic polyesters have received an increasing attention due to their physical properties, biocompatibility, and biodegradability, which makes them very suitable for biomedical and pharmaceutical applications.[1] These polymers can be prepared by classical polycondensation of α,ω-hydroxyl acids or diols and diacids,[2] but for better control over the polymer's microstructure ring-opening polymerization (ROP) of the corresponding cyclic ester monomers is the preferred approach. Several routes that have been reported in the literature leading to these thermoplastic polyesters include anionic, cationic, coordination−insertion, and nucleophilic polymerization using enzymes or organic catalysts.[3]

Compared to the vast number of publications describing the ROP of small and medium ring-sized cyclic esters (lactides, glycolide, caprolactone, etc.),[4] the ROP of macrolactones like ω-pentadecalactone (PDL) or 16-hexadecalactone is underexposed, and only few reports have been published to date.[5] Mainly enzymatic ring-opening polymerization of macrolactones has been reported.[6] Enzymes, such as Candida Antarctica Lipase B, are very active in the enzymatic ring-opening polymerization (*e*ROP) of large ring lactones and produce high molecular weight products including copolymers consisting of macrolactones and smaller ring-sized lactones (Figure 1, route A).[7] Since enzymes are costly and *e*ROP is a transesterification reaction with little control over the polymer microstructure, researchers have been looking for alternative catalysts for the catalytic ring-opening polymerization (*c*ROP) of macrolactones.

Metal-based catalysts (mCat) clearly dominate the *c*ROP of ring-strained cyclic esters,[8] and several attempts have been undertaken to also develop suitable catalysts for the *c*ROP of macrolactones. Some homoleptic metal complexes like diethylzinc,[9] yttrium isopropoxide,[5a,10] and some alkali metal alkoxides[11] have been reported as ring-opening polymerization catalysts of macrolactones following the coordination−insertion and anionic mechanism. Generally, long polymerization times were necessary to reach high conversions, and only relatively low molecular weight polymers have been obtained. Recently, some aluminum−salen complexes have been studied in our group and were found to be remarkably efficient catalysts for the *c*ROP of macrolactones and medium-sized lactones, producing high molecular weight polymacrolactones (M_w up to 300 kDa) (Figure 1, route B).[12]

Received: January 25, 2012
Revised: March 29, 2012
Published: April 9, 2012

 © 2012 American Chemical Society dx.doi.org/10.1021/ma3001675 | *Macromolecules* 2012, 45, 3356−3366

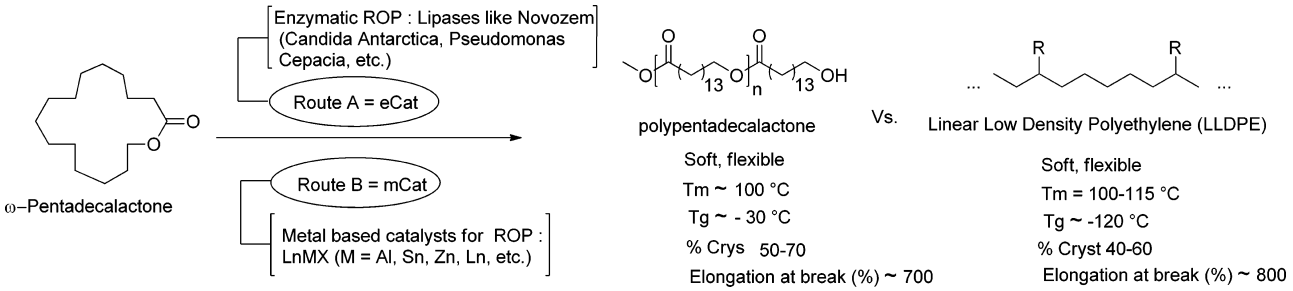
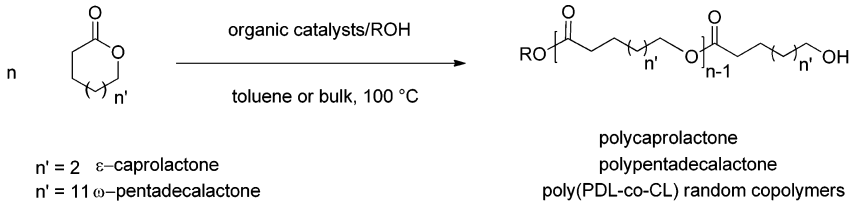
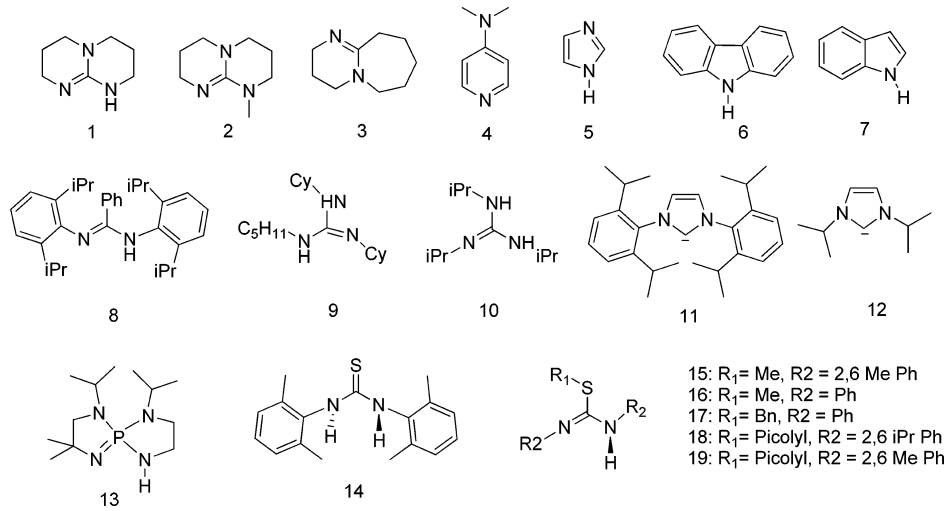


Figure 1. Schematic representation summarizing different routes toward polypentadecalactone synthesis: (route A) see refs 6 and 7; (route B) see refs 8−10 and 12.

Chart 1. Ring-Opening Polymerization of CL and PDL Using Organic Catalysts



Organic molecules tested in this work:



Despite recent advances in the use of inexpensive, metal-free catalysts for the ROP of a large variety of ring-strained cyclic esters (caprolactone, δ-valerolactone, lactide, etc.) and cyclic carbonates,[13,14] there is no example to date of the use of organic catalysts in the *c*ROP of macrolactones. In the context of our interest in ROP of macrolactones, we have investigated the *c*ROP of PDL catalyzed by a variety of N-heterocyclic organic molecule such as guanidines, amidines, and N-heterocyclic carbenes (NHCs).

RESULTS AND DISCUSSION

Ring-Opening Polymerization of ε-Caprolactone Using N-Heterocyclic Organic Catalysts. Generally, the relief of the ring strain of lactone monomers dictates the driving force for the ring-opening polymerization. The large ring size of macrolactones is associated with low ring strain, and consequently polymerization reactions are driven mainly by entropy.[2,15] In order to test the effectiveness of the binary catalyst/initiator systems consisting of the N-heterocyclic catalyst plus benzyl alcohol (BnOH) in lactone ring-opening polymerization, first several polymerization reactions of caprolactone (CL) were conducted as benchmark. Among all the above-mentioned systems (Chart 1), only the bicyclic guanidine 1,5,7-triazabicyclo[4.4.0]dec-5-ene (TBD, **1**), 1,2,3-triisopropylguanidine (**10**), and diisopropyl-substituted carbene (**12**) proved to be catalytically active in CL polymerization.

The organocatalyst/initiator system TBD/BnOH readily polymerizes CL at room temperature and 100 °C either in toluene solution at different concentration or in bulk monomer. Representative results are reported in Table 1. The lack of catalytic activity of *N*-methyl-TBD (MTBD) is not surprising since previous reports have demonstrated that CL polymerization occurs only in the presence of thiourea as cocatalyst. In this bicatalytic system the thiourea activates the CL monomer while the MTBD activates the initiator group or polymer chain end (ROH).[13b,16] The efficiency of the *c*ROP of CL is clearly sensitive to the steric nature of the organic catalysts. While the guanidine bearing the *i*-Pr groups (**10**) was found to be active

dx.doi.org/10.1021/ma3001675 | *Macromolecules* 2012, 45, 3356−3366

Table 1. Ring-Opening Polymerization of CL Mediated by Binary Catalyst/Initiator Systems[a]

entry	Cat.	ROH	$[CL]_0/[oCat.]_0/[ROH]_0$	T (°C)	time[b] (min)	conv[c] (%)	TOF[d] (h^{-1})
1	**1**	BnOH	100:1:1	100	5	100	1200
2	**1**	BnOH	100:1:0	100	300	0	
3	**1**	BnOH	150:1:1	20	60	100	150
4[e]	**1**	BnOH	150:1:1	20	60	100	150
5	**1**	Triol[f]	120:1:1	100	5	100	1440
6	**1**	Triol[f]	300:1:1	100	10	85	1530
7	**10**	BnOH	100:1:1	100	1080	81	5
8	**12**	BnOH	100:1:1	100	10	88	550

[a]Reactions performed in bulk monomer unless noted otherwise. [b]Reaction times were not necessarily optimized. [c]Conversion of CL as determined by ^{1}H NMR. [d]Turnover frequency determined from the conversion and reaction time. [e]Reaction performed at RT in toluene solution $[CL]_0$ = 4.9 M. [f]Reactions performed using 1,1,1-tris-(hydroxymethyl)ethane as initiator.

in CL polymerization, the bulkier guanidine **9** was not. Similarly, of the two NHCs **11** and **12** tested in ROP of CL, only the carbene bearing the least bulky substituent (*i*-Pr, **12**) proved to be efficient in the *c*ROP of CL (TOF ~ 550 h^{-1}).[17]

Ring-Opening Polymerization of ω-Pentadecalactone Catalyzed by TBD/BnOH. In view of the low solubility of PPDL and the high melting temperature of PPDL, the ROP of PDL is commonly carried out at elevated temperatures to prevent monomer diffusion limitations and precipitation of the product.[12] Thus, initially the PDL polymerization reactions were carried out in toluene and in bulk monomer at 100 °C. Representative results are reported in Table 2. Not surprising based on the results obtained for CL polymerization, only the combination of TBD/BnOH proved to be an efficient organocatalyst system to promote the cROP of PDL. The dual activation of monomer and growing polymer chain by TBD as reported for CL is also the most likely mechanism for PDL polymerization.[13a,b] The fact that MTBD is inactive indicates the absence of a general base mechanism. Addition of thiourea as cocatalyst to MTBD did not result in an active catalyst for PDL polymerization while it proved to be for CL polymerization.[16] With TOFs up to 17 h^{-1}, the bulk polymerization ($[PDL]_0$ = 3.7 M) afforded higher activities than the corresponding solution polymerizations (Table 2). Reducing the PDL concentration during solution polymerizations also resulted in a lower catalytic activity consistent with first-order behavior (Table 2, entries 9−12). The catalytic activity of TBD/BnOH in *c*ROP of PDL is considerably lower than of CL, and longer reaction times are required to reach full conversion. No polymerization was observed for a reaction conducted in bulk at 100 °C in the absence of BnOH, indicating that an initiator is essential in this system (Table 2, entry 4). Increasing the initiator:catalyst ratio (BnOH:TBD = 1, 5, 10, 20) results in a significant increase in polymerization rate. For bulk polymerizations the TOF increases most strongly (TOF = 17 → 70 h^{-1}), but in solution the polymerization rate also increases noticeably (TOF = 7 → 30 h^{-1}) (Table 2, entries 5, 17−19, and 2, 16, respectively). The increase of the polymerization rates and the high conversions reached with excess BnOH is most likely due to the lower viscosity as a result

Table 2. Ring-Opening Polymerization of ω-Pentadecalactone Mediated by TBD/BnOH[a]

entry	com	$[PDL]_0/[Cat.]_0/[BnOH]_0$	[PDL] (mol L^{-1})	time[b] (h)	conv[c] (%)	$M_{n,calc}$[d] (kg mol^{-1})	$M_{n,exp}$[e] (kg mol^{-1})	M_w/M_n[e]	TOF (h^{-1})[f]
1	**1**	100:1:1	3.7[g]	5	47	11.4	8.6	1.5	9.4
2	**1**	100:1:1	2.5	5	37	9.0	8.3	1.4	7.4
3	**1**	100:1:1	3.7[g]	3	35	8.5			11.6
4	**1**	100:1:0	2.5	5	0				
5[h]	**1**	100:1:1	3.7[g]	1.5	26	6.4			17.3
6	**1**	200:1:1	3.7[g]	3	22	10.7			14.7
7	**1**	200:1:1	2.5	3	13	6.3			8.6
8	**1**	350:1:1	3.7[g]	3	14	11.7			16.3
9	**1**	200:1:1	1.0	5	≤5	2.0	2.5	1.4	≤5
10	**1**	200:1:1	1.7	5	8	3.9	3.9	1.3	≤5
11	**1**	200:1:1	2.2	5	12	5.7	6.3	1.4	≤5
12	**1**	200:1:1	2.5	14	55	26.5	26.5	1.6	8
13	**1**	200:1:1	2.5	96	99	47.6	18.5	1.7	≤5
14	**1**	200:1:1	3.7[g]	96	99	47.6	23.8	1.5	≤5
15	**1**	400:1:1	2.5	96	63	60.6	27.1	1.4	≤5
16	**1**	100:1:5	2.5	1	30	1.5			30.0
17	**1**	100:1:5	3.7[g]	1	42	2.0			42.0
18	**1**	100:1:10	3.7[g]	1	68	1.6	4.7	1.4	68.0
19	**1**	100:1:20	3.7[g]	1	70	0.9	3.5	1.5	70.0
20[i]	**1**	100:1:1	3.7[g]	1.7	43	3.5	6.3	1.9	25.9
21[i]	**1**	100:1:1	2.5	1.7	33	2.7	11.6	1.5	19.9
22[i]	**1**	200:1:1	3.7[g]	1.7	18	8.7	3.6	2.1	21.7
23	**12**	100:1:1	3.7[g]	18	30	7.3	10.3	1.4	≤5

[a]Reactions were conducted at 100 °C in bulk or toluene solution. [b]Reaction times were not necessarily optimized. [c]Conversion of PDL as determined by ^{1}H NMR from the α-methylene of PDL and PPDL resonances. [d]Number molecular weight calculated from $[PDL]_0/[BnOH]_0 \times$ conv × 240.0. [e]Experimental number-average molecular weight and molecular weight distribution determined by HT-SEC in TCB at 160 °C and referenced to polyethylene standards. [f]Turnover frequency determined from the conversion and reaction time. [g]Reaction performed in bulk PDL, without solvent. [h]Conversion determined immediately after stopping the agitation. [i]Reactions performed using 1,1,1-tris(hydroxymethyl)ethane as initiator.

dx.doi.org/10.1021/ma3001675 | Macromolecules 2012, 45, 3356−3366

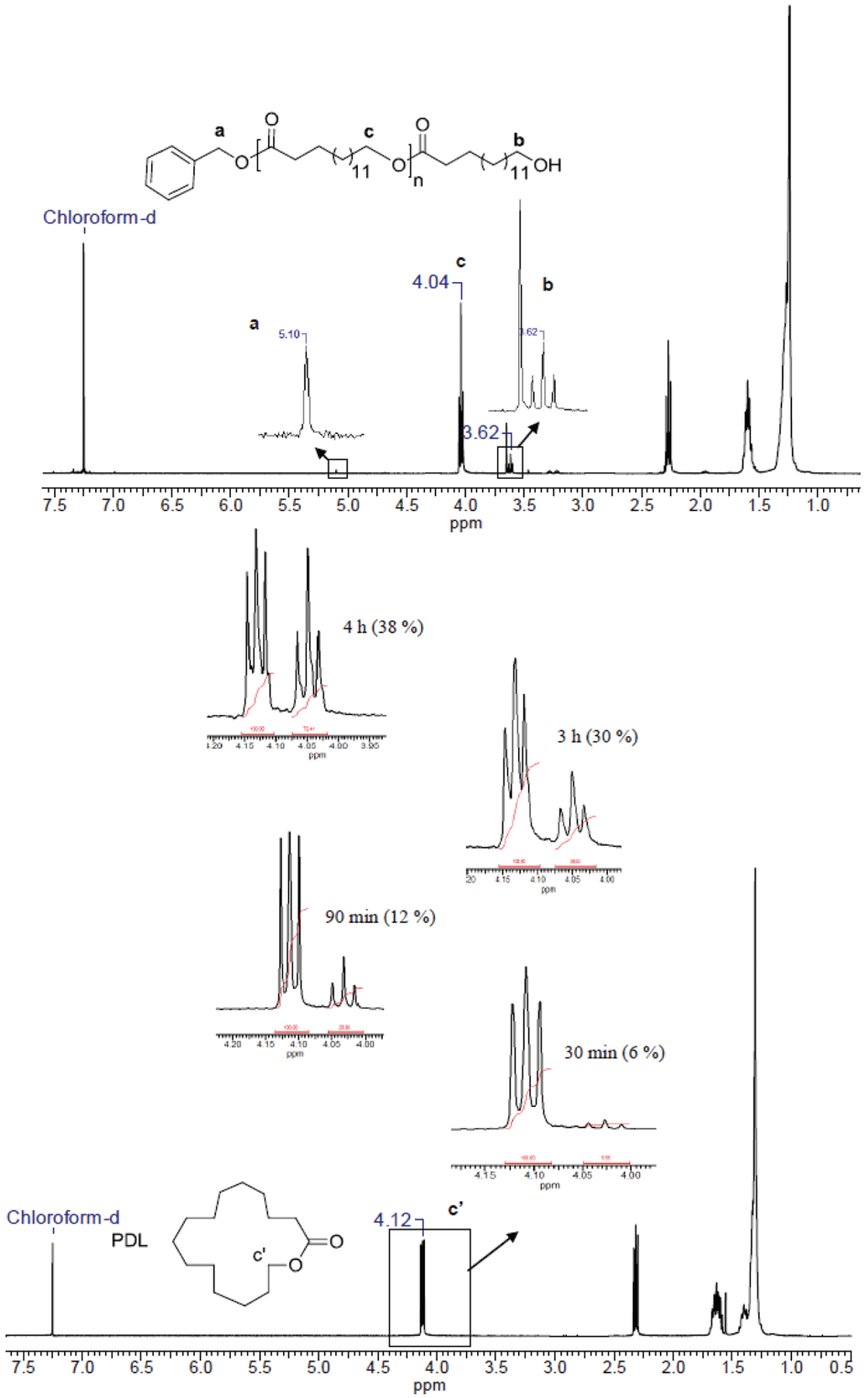


Figure 2. ^{1}H NMR spectra of PDL (bottom) and PPDL (top) illustrating the polymer end groups and ^{1}H NMR monitoring of the PDL polymerization (middle spectra) using TBD/BnOH/PDL (1:1:100).

of the lower molecular weight of the polymers. Clearly, this effect is stronger in bulk than in solution. The low polydispersities of the polymers and the fact that the molecular weight of the polymers is inversely related to the amount of BnOH indicates that the latter functions as an effective chain transfer agent. This trend was confirmed using a trifunctional initiator bearing three alcohol groups (1,1,1-tris-(hydroxymethyl)ethane) which afforded comparable PDL conversions as obtained using an excess of BnOH (Table 2, entries 20−22). It is important to emphasize that using triols (Table 2) or polyols allows the preparation of PPDL starlike polymers.

The kinetics of the PDL polymerization can easily be followed using ^{1}H NMR spectroscopy. The conversion rate can

dx.doi.org/10.1021/ma3001675 | *Macromolecules* 2012, 45, 3356−3366

be calculated by determining the ratio of the integrals of the proton signals of the $-C(=O)OCH_2-$ repeat units in the polymer chains to the corresponding PDL monomer (*c* and *c*′, Figure 2). The ^1H NMR spectra show the signals *a* and *b*, assignable to *α*-methylene protons of the $-CH_2OH$ end group at 3.62 ppm and the methylene protons of benzyl alkoxide initiator residue at 5.10 ppm (Figure 2). The catalytic activity of TBD/BnOH is considerably lower than the aluminum salen/BnOH catalyst system, which reached full conversion within an hour at 100 °C.[12]

The polymerization reactions can roughly be divided in two stages. During the first stage, the polymerizations follow first-order kinetics (Figure 3). During the second stage the

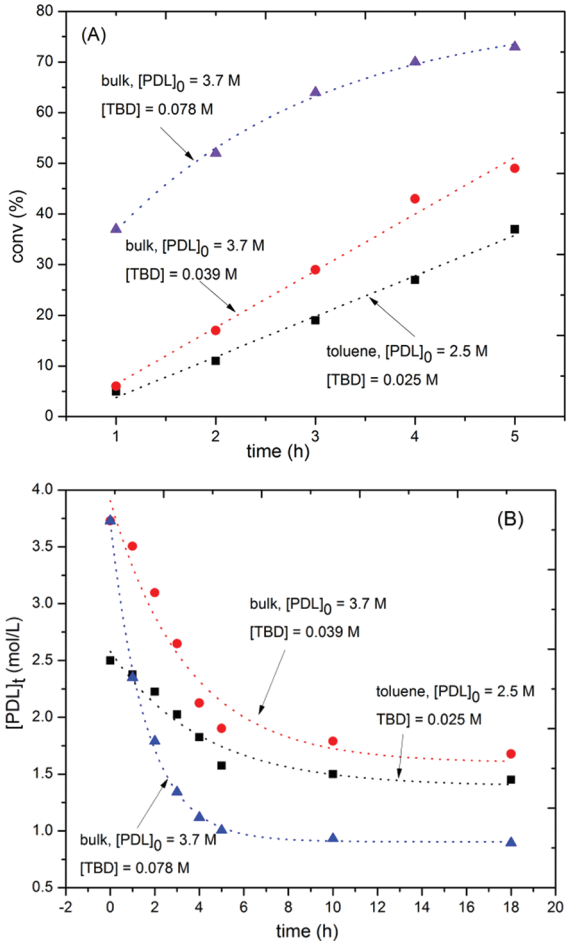


Figure 3. (A) Conversion versus time plots for PDL polymerizations in toluene at 100 °C with $[PDL]_0/[BnOH]_0 \sim 100$ ($[PDL]_0$ = 2.5 M, [TBD] = 0.025 M) and in bulk monomer ($[PDL]_0 \sim 3.7$ M, [TBD] = 0.039 and 0.078 M). (B) Kinetic plot of [PDL] versus time fitted using first-order decay equation ($[PDL]_t = [PDL]_0 \exp(-kt)$): ■ ($[PDL]_0$ = 2.5 M, [TBD] = 0.025 M); ● ($[PDL]_0 \sim 3.7$ M, [TBD] = 0.039) ▲.

monomer diffusion limitation clearly slows down the reaction, and for the 200:1:1 PDL:TBD:BnOH ratio full conversion is only reached after ~96 h (Table 2, entries 13 and 14). During the first stage the polymerization is relatively fast, and the M_n increases almost linearly with monomer conversion and also with increasing $[PDL]_0/[TBD]_0$ molar ratio (Table 2). Doubling the catalyst concentration (▲ 73% versus ● 47%, Figure 3A) significantly improves the polymerization rate. The M_n values of the PPDL produced using TBD/BnOH system are in most cases close to the theoretical ones, especially for the polymerization carried out in toluene solution (Figures 3 and 4). This linear correlation between M_n and conversion is

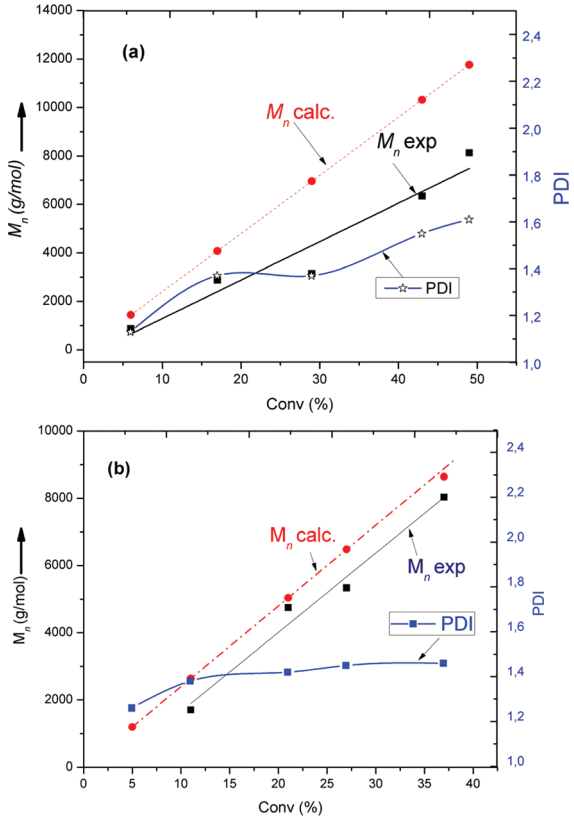


Figure 4. Dependence of M_n and polydispersity index (M_w/M_n) of PPDL on monomer conversion. (a) Bulk polymerization ($[PDL]_0$ = 3.7 M). (b) Solution polymerization in toluene ($[PDL]_0$ = 2.5 M).

typically characteristic for a living-catalytic behavior. However, the polydispersity indices (PDI) of the obtained PPDL gradually increase to about 1.5 at 50% conversion and to 1.7 at full conversion. At full conversion the number-average molecular weight (M_n) is lower than the theoretical value (23.8 and 47.6 kg mol^{-1}, respectively, Table 2, entry 14), suggesting that at increasing monomer conversion competitive intramolecular and intermolecular transesterification is becoming more pronounced.

The effect of temperature on the PDL polymerizations was also studied (Table 3). Maintaining the PDL/TBD molar ratio at 100 and 200 equiv, the PDL polymerizations were conducted at 60, 100, 130, and 160 °C for 3 and 5 h. The polymerization rate increases with increasing temperature but does not follow a linear relationship (Figure 5). For the 100:1:1 ratio, between 60 and 100 °C a clear increase in the conversion can be observed, whereas between 100 and 130 °C hardly any acceleration of the polymerization rate is noticeable. Increasing the temperature further to 160 °C leads to a significant further increase in activity. Most probably, this is a viscosity effect. Above 40% conversion, even at 130 °C the medium becomes rather viscous. However, increasing the temperature to 160 °C leads to a reduction of the viscosity and thus an increase in conversion. For the 200:1:1 ratio a similar trend can be observed. For example, after 5 h at 60 °C only 17% of the PDL was converted while during the same time at 100 °C a

dx.doi.org/10.1021/ma3001675 | Macromolecules 2012, 45, 3356−3366

Table 3. Ring-Opening Polymerization of ω-Pentadecalactone Carried Out at Different Temperatures

entry	$[PDL]_0/[TBD]_0/[BnOH]_0$	time (h)	T (°C)	conv (%)	$M_{n,calc}$ (kg mol^{-1})	$M_{n,exp}$ (kg mol^{-1})	M_w/M_n	TOF (h^{-1})
1	100:1:1		60	7	1.7	–[a]	–[a]	2.3
2	100:1:1	3	100	35	8.5	–[a]	–[a]	11.6
3	100:1:1	5	100	47	11.3	8.6	1.51	9.4
4	100:1:1	5	130	48	11.6	8.2	2.05	9.6
5	100:1:1	5	160	83	20.2	11.0	2.10	16.6
6	200:1:1	5	60	17	8.2	–[a]	–[a]	6.8
7	200:1:1	5	100	40	19.3	12.2	1.85	16.0
8	200:1:1	5	130	42	20.3	9.6	2.12	16.8
9	200:1:1	5	160	42	20.3	11.6	2.05	16.8

[a]MW's were too low to be determined accurately.

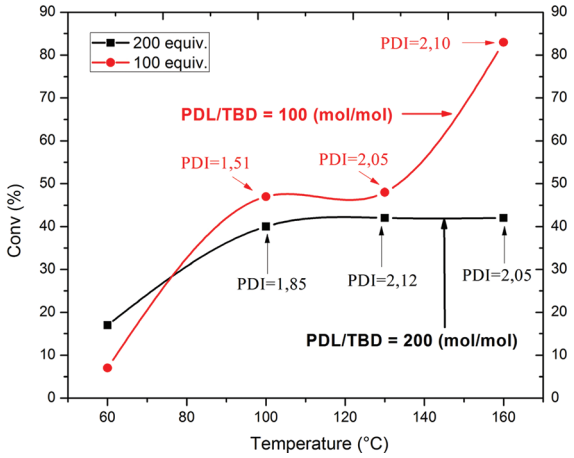


Figure 5. Effect of reaction temperatures on the PDL polymerization rates.

conversion of 40% was reached. Increasing the temperature further did not lead to a significantly higher conversion, indicating that for the 200:1:1 ratio the viscosity becomes a severe problem even at temperatures as high as 160 °C. Both for 100 and 200 equiv ratio, the polymerizations at high temperatures (>100 °C) are less controlled as reflected by the broadening of the molecular weight distributions of the PPDL polymers compared to those produced at 100 °C (Table 3). The lack of control is believed to be caused by the transesterification side reactions, which is less dependent on viscosity and therefore becomes more notable at higher temperatures. The presence of transesterification reactions has been clearly evidenced by MALDI-ToF-MS analysis. For example, the MALDI-ToF-MS of the sample produced at 100 °C using a low PDL/TBD ratio (50 equiv) and recovered after several reprecipitations in methanol shows two sets of peaks, with a difference of 240 g/mol corresponding to the PDL monomer unit. Interestingly, the least intense distribution corresponds to the expected linear PPDL terminated with a benzyloxy (BnO) group, while the most intense distribution corresponds to linear PPDL containing a methoxy (OMe) end group. The formation of these methoxy-terminated PPDL is due to chain scission as a result of transesterification reactions during the precipitation of the polymer in methanol.[18] The work-up procedure does not involve any heating, which indicates that the TBD-induced transesterification is very fast.

To confirm this finding, a crude PPDL sample was analyzed by MALDI-ToF-MS without any work-up. The major distribution (Figure 6, bottom) corresponds to linear PPDL end-capped by benzyloxy groups, while the minor distribution corresponds to cyclic PPDL formed by "backbiting" side reactions. Further confirmation of transesterification reaction was obtained by the addition of an excess of hexadecanol (HDOH) to the crude PPDL. As shown in Figure 6 (middle), the presence of two sets of peaks corresponding to the linear PPDL terminated by hexadecanoloxy and benzyloxy end groups clearly indicates the occurrence of transesterifications. Since transesterification during work-up with added alcohols or traces of water in the precipitation solvent (THF) results in random chain scission this process is expected to result in a lowering of the molecular weight, which was indeed demonstrated using HT-SEC. As expected, the drop in molecular weight and molecular weight distribution was observed in the following order: MeOH > HDOH > THF ~ crude PPDL (Figure 7). The broadening of the molecular weight distribution after work up in MeOH and HDOH provided further evidence that intermolecular transesterification reactions occurs in the presence of protic solvents and residual TBD. Based on these latest results, and in order to limit the shortening of the PPDL molecular weight as a results of backbiting side reactions during the polymerization (formation of cyclic product) and the work-up step (intra- and intermolecular chains scission), the use of nonprotic solvents for the precipitation step (toluene, THF, etc.) could certainly contribute to improvement of the molecular weight of the PPDLs.

PDL and CL Copolymerization. Since TBD also effectively ring-opens CL, we attempted the copolymerization of PDL and CL. Mixtures of both monomers with initial CL:PDL feed composition ranging from 0:100 to 100:0 allows the preparation of random copolymers poly(PDL-*co*-CL) with T_m values that linearly decrease with composition from that of PPDL (~95 °C) to that of PCL (~50 °C) (Figure 8). The random copolymers poly(PDL-*co*-CL) remain highly crystalline over the whole composition range as a result of cocrystallization and isomorphism phenomena.[7,19] The melting enthalpy follows the same trend with ΔH_f ranging from 138.1 J g^{-1} for pure PPDL, 110.7 for copolymer with a 30:70 CL:PDL molar ratio, 97.1 J g^{-1} for copolymer containing 50 mol % of CL, to 50.3 J g^{-1} for pure polycaprolactone (Figure 8b). Although sequential addition of different comonomers has been reported as an efficient route for the preparation of block copolyesters,[20] all attempts to prepare PDL–CL block copolymers using the system TBD/BnOH or triol were unsuccessful and only random copolymers were obtained, again emphasizing the existence of rapid competitive intra- and intermolecular transesterification.

Details concerning the PDL–CL copolymers composition were obtained using ^{13}C NMR characterization. The expansion

dx.doi.org/10.1021/ma3001675 | Macromolecules 2012, 45, 3356–3366

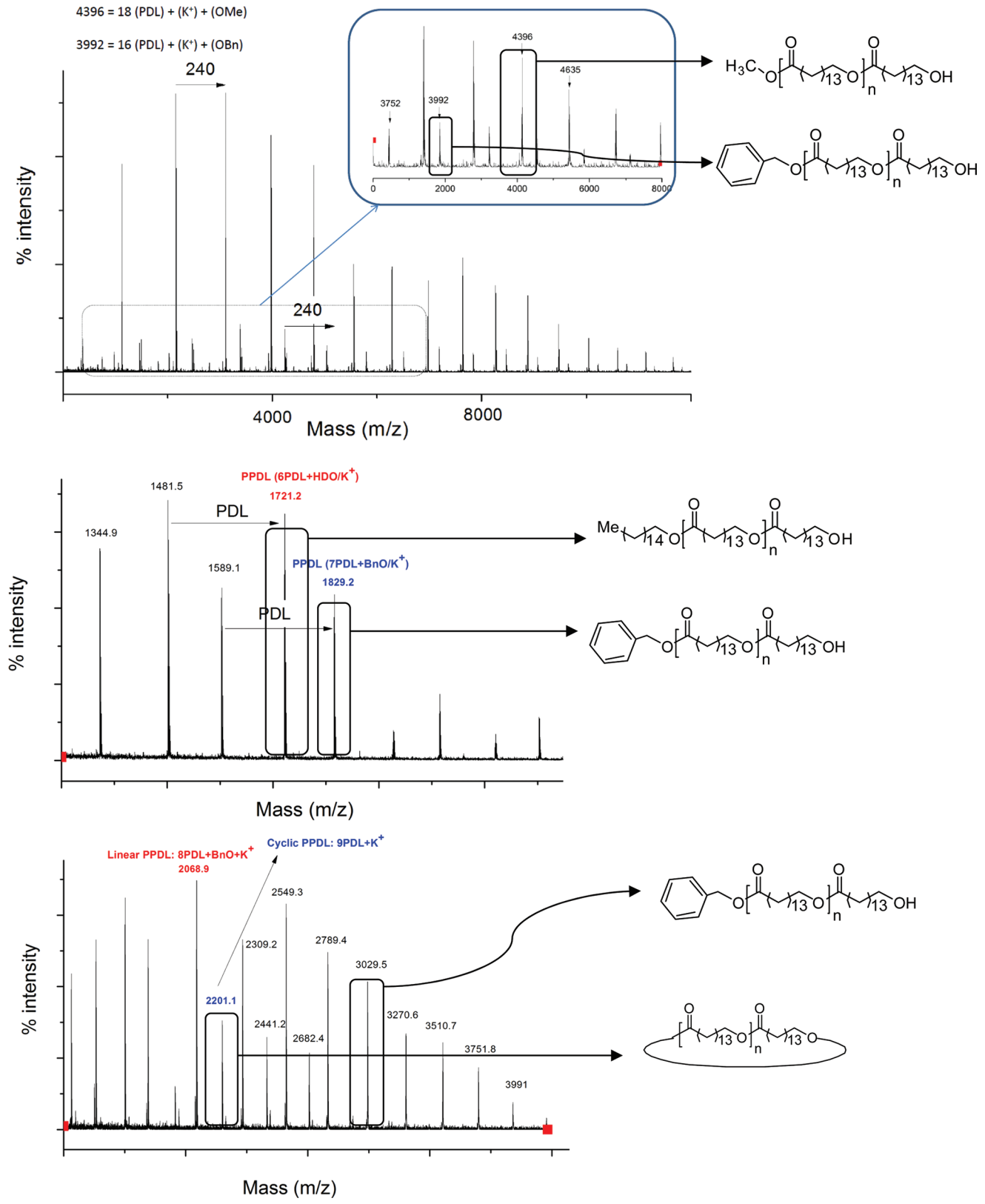


Figure 6. MALDI-ToF-MS of BnOH-initiated PPDL after work-up in methanol (top), after addition of excess 1-hexadecanol (middle), and of a crude PPDL sample (bottom).

of the α-methylene region shows four resonances corresponding to diad sensitivity. A schematic representative of copolymer diads and the corresponding linkages between units is shown in Figure 9a–d. The resonance at 64.11 ppm corresponds to the linkage between two CL monomer units, whereas the linkage between two PDL units is indicated by the signal at 65.35 ppm. The CL–PDL and PDL–CL linkages give resonances at 64.46 and 63.97 ppm, respectively. Lowering the CL content clearly

dx.doi.org/10.1021/ma3001675 | *Macromolecules* 2012, 45, 3356–3366

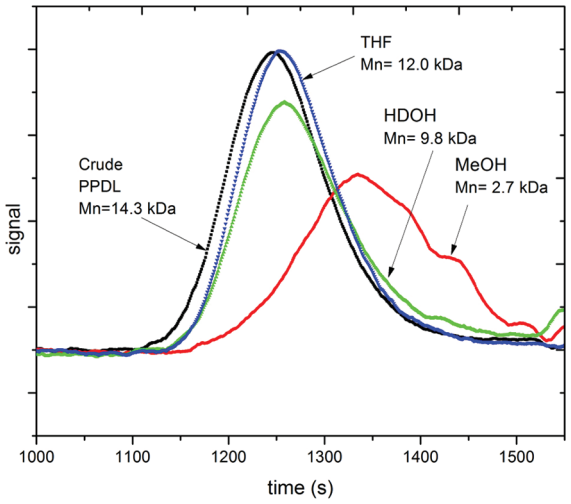


Figure 7. Comparison between SEC traces of the PPDL samples isolated after work-up in MeOH, HDOH, THF, and crude PPDL.

shows a drop in intensity of the CL−CL resonance, indicating that the polymers are indeed completely random.

Finally, the MALDI-ToF-MS has been used to analyze the PDL−CL random copolymers and estimate the reactivity ratios of the PDL and CL in the experiments reported in Table 4 (entries 2 and 3). First of all, the spectra obtained are in good agreement with those simulated using the model developed recently in our group.[21] For example, the experimental MALDI-ToF-MS in Figure 10 shows one set of picks separated by a unit of ∼126 g/mol, which indeed confirm the randomness of those copolymers [MW(PDL) − MW(CL) ∼ 126 g/mol]. On the other hand, using in-house developed MALDI-ToF-MS simulation software,[21a] the average monomer fractions in copolymers (F_1 and F_2) have been calculated and reported in Table 4 of both feed compositions (1:1 and 0.5:1 ratios of CL_0:PDL_0) which are 0.53 (CL) and 0.47 (PDL), whereas the average fractions for 0.5:1 (CL_0:PDL_0) are 0.48 (CL) and 0.52 (PDL). On the other hand, the reactivity ratios have also been calculated using the analytical method developed by our group based on the terminal model and taking into account the conversion rates of both ratios reported in Table 4.[21b] For this end, since the simulated spectrum match with the experimental one at more than 95%, this simulated spectrum has been used to calculate the reactivity ratios of both monomers. The results obtained are summarized in Table 4, and the calculated PDL−CL reactivity ratios are completely different compared to the relative intrinsic reactivity of each monomer in homopolymerization reactions. Those calculated numbers r_{CL} = 1.51 and r_{PDL} = 0.79 for 1:1 ($[CL]_0/[PDL]_0$, mol/mol) feed ratio and r_{CL} = 0.94 and r_{PDL} = 1.47 for 0.5:1 ($[CL]_0/[PDL]_0$, mol/mol) are in good agreement with the experimental observations since the formation of random structures are expected with those

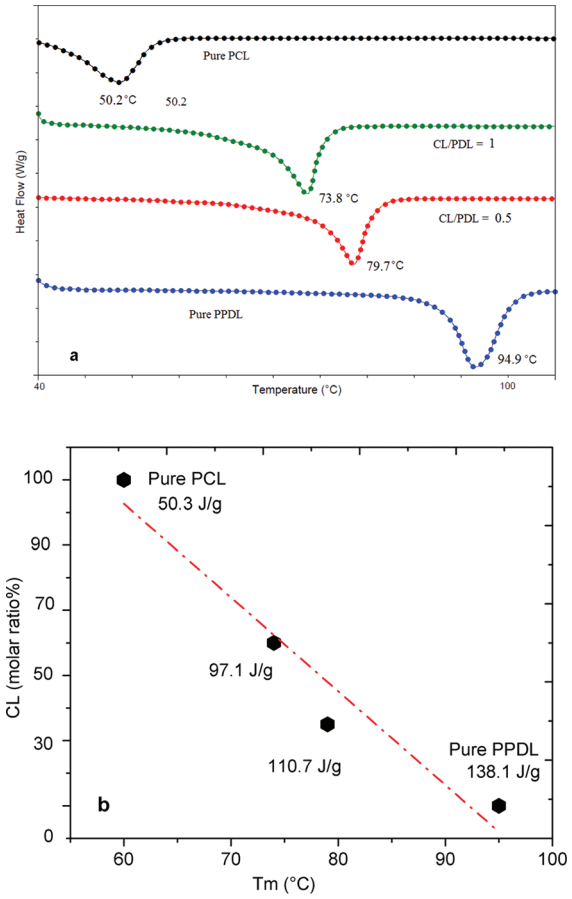


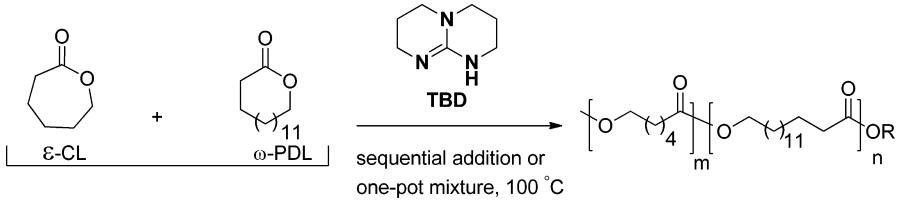
Figure 8. (a) DSC heating curves (10 °C/min) of PDL−CL random copolymers. (b) Composition dependence of the melting temperature and ΔH_f of PDL−CL random copolymers.

reactivity ratios values ($r_1 r_2 \sim 1 \pm 0.2$). However, as the conversions were relatively high for both reactions (entries 2 and 3, Table 4) and reaction times were long, it should be taking into consideration that competitive transesterification reactions (vide supra) under these conditions obviously result in a random copolymer. Shorter reaction times and lower conversions might well lead to block or gradient copolymer using the TBD/BnOH catalyst system.

CONCLUSIONS

Here we have reported the first effective route for PDL polymerization using an N-heterocyclic organic catalyst. Of all catalysts screened, TBD, in combination with an initiator alcohol (BnOH, triol), proved to be the only active system for the ROP of the macrolactone PDL as well as for the copolymerization of PDL and CL. Kinetic studies revealed first-order behavior of the TBD/BnOH system in the first stage of the reaction or at high catalyst concentration. At higher

Scheme 1. PDL/CL Copolymerization Reactions Using TBD/BnOH



dx.doi.org/10.1021/ma3001675 | Macromolecules 2012, 45, 3356−3366

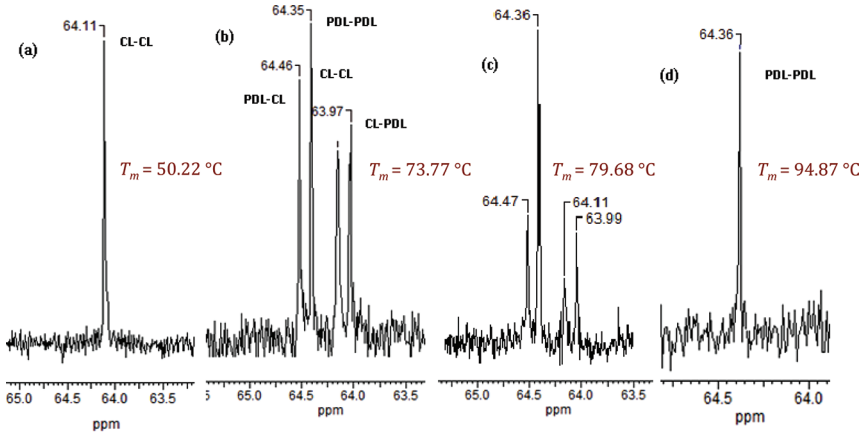


Figure 9. ^{13}C NMR spectrum (400 MHz, $CDCl_3$, 25 °C) of PCL and PPDL homopolymers (a, d) and random poly(PDL-*co*-CL) copolymers prepared using TBD/BnOH (b, c).

Table 4. Dependence of Copolymers Chemical Composition Distribution on Monomers Feed and Reactivity Ratios of PDL and CL Monomers[a]

					diads sequence distribution (%)[b]										
entry	CL/PDL (mol %)	$[CL]_0/[PDL]_0/[oCat.]_0/[ROH]_0$	time (h)	conv(%)	CL–CL	CL–PDL	PDL–CL	PDL–PDL	r_{CL}[c]	r_{PDL}[c]	F_1[c]	F_2[c]	M_n (10^3)	PDI	T_m (°C)
1	PCL	100:0:1:1	24	99	100	0	0	0			1	0	8.6	1.55	50.2
2	100	100:100:1:1	18	75	29	18	29	24	1.51	0.79	0.54	0.46	11.5	1.53	73.8
3	50	50:100:1:1	18	81	15	16	27	42	0.94	1.47	0.48	0.52	9.5	1.44	79.7
4	0	0:100:1:1	72	99	0	0	100	0			0	1	11.3	1.75	94.9

[a]Reactions performed in bulk monomer at 100 °C. [b]Diad sequence distribution content was determined by ^{13}C NMR. [c]Fraction of the comonomer in the copolymers and reactivity ratios determined by MALDI-ToF-MS.

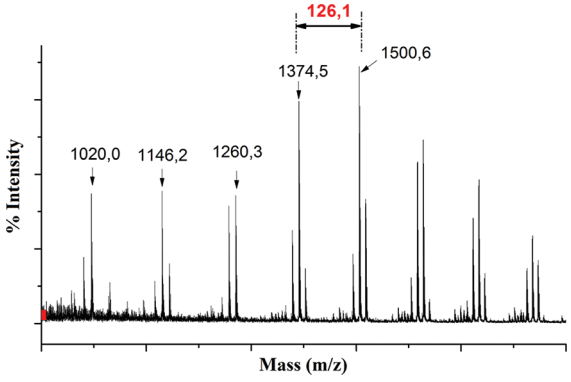


Figure 10. MALDI-ToF-MS of random poly(PDL-*co*-CL) copolymer prepared using TBD/BnOH.

conversions, transesterification starts to play an increasingly important role leading to broader polydispersities and a decrease in molecular weight (intramolecular transesterification). Transesterification also became more prominent at higher polymerization temperatures but more importantly also at low temperatures in the presence of conventional protic extraction solvents (MeOH). Hence, to obtain high molecular weight products, the catalyst should be deactivated before work-up of the polymer.

Using the binary system TBD/BnOH as catalyst/initiator and a mixtures of PDL and CL, poly(PDL-*co*-CL) random copolymers with tunable comonomer composition and melting temperatures can be obtained. The random copolymers poly(PDL-*co*-CL) remain highly crystalline over the whole composition range as a result of cocrystallization and isomorphism phenomena and show a linear relationship between the random copolymers melting temperatures (T_m) and comonomer content. Although rapid competitive transesterification prevents the formation of block copolymers, the preparation of PPDL homo- or copolymers with specific functional end groups and variable architectures (branched, star-shaped, etc.) is potentially possible by a meticulous selection of the initiator group.

EXPERIMENTAL SECTION

General Considerations. Organic compounds **1**–**7** are commercially available and were purchased from Sigma-Aldrich and Acros Organics and were used without further purification. The amidine compounds **8**, **9**, and **10** were synthesized according to literature procedures.[22] PDL and CL were purchased from Sigma-Aldrich and were freshly distilled from CaH_2 under nitrogen and degassed thoroughly by freeze–thaw–vacuum cycles prior to use. Toluene (Sigma-Aldrich) was passed through purification columns before use. Benzyl alcohol was purchased from Sigma-Aldrich and was distilled from CaH_2 and stored under nitrogen.

Analytical Techniques. ^1H and ^{13}C NMR spectra of PPDLs and PCLs were recorded in 5 mm tubes on a Varian Mercury 400 and 200 MHz spectrometers at ambient probe temperature in $CDCl_3$. Chemical shifts are reported in ppm versus tetramethylsilane ($SiMe_4$) and were determined by reference to the residual solvent. Size exclusion chromatography (SEC) of PPDLs was performed at 160 °C and performed on a Polymer Laboratories PLXT-20 Rapid GPC Polymer Analysis System (refractive index detector and viscosity detector) with 3 PLgel Olexis (300 × 7.5 mm, Polymer Laboratories) columns in series. 1,2,4-Trichlorobenzene was used as eluent at a flow rate of 1 mL min^{-1}. The molecular weights were calculated with respect to polyethylene standards (Polymer Laboratories). A Polymer Laboratories PL XT-220 robotic sample handling system was used as autosampler. Differential scanning calorimetry (DSC) analyses of

dx.doi.org/10.1021/ma3001675 | *Macromolecules* 2012, 45, 3356–3366

PPDL homopolymers and poly(PDL-*co*-CL) copolymers were carried out on a DSC Q100 from TA Instruments at a heating rate of 5 °C min^{-1}. First and second runs were recorded after cooling down to ca. −20 °C. The melting temperatures reported correspond to second runs.

MALDI-ToF-MS Analysis. MALDI-ToF-MS analysis was performed on a Voyager DE-STR from Applied Biosystems equipped with a 337 nm nitrogen laser. An accelerating voltage of 25 kV was applied. Mass spectra of 1000 shots were accumulated. The polymer samples were dissolved in $CHCl_3$ at a concentration of 1 mg mL^{-1}. The cationization agent used was potassium trifluoroacetate (Fluka, >99%) dissolved in THF at a concentration of 5 mg mL^{-1}. The matrix used was *trans*-2-[3-(4-*tert*-butylphenyl)-2-methyl-2-propenylidene]-malononitrile (DCTB) (Fluka) and was dissolved in THF at a concentration of 40 mg mL^{-1}. Solutions of matrix, salt, and polymer were mixed in a volume ratio of 4:1:4, respectively. The mixed solution was hand-spotted on a stainless steel MALDI target and left to dry. The spectra were recorded in the reflectron mode. All MALDI-ToF-MS spectra were recorded from the crude products.

Typical Polymerization Procedure (Table 2, Entry 2). In the glovebox, PDL (1.73 g, 7.2 mmol), TBD (10.0 mg, 0.072 mmol), and an equimolar amount of BnOH (7.8 mg, 0.072 mmol) were placed in a small glass crimp cap vial. Dry toluene (1.0 mL) was added, and the vial was capped. The reaction mixture was removed from the glovebox and stirred for 3 h at 100 °C. For all reactions, an aliquot of crude polymer was withdrawn at the end of the polymerization time and dissolved in $CDCl_3$ in order to determine the conversion by NMR spectroscopy. The reaction was then stopped by cooling the mixture, removal of toluene under vacuum, and addition of excess methanol (∼2 mL) to precipitate the polymer. The produced PPDL polymer was isolated and dried in vacuo at RT over 18 h.

Kinetics (Figure 4). Data for the PDL polymerization kinetics (conversions, M_n, and PDI) were obtained by collecting and analyzing of ∼0.2 mL of crude polymer from the reaction mixture at appropriate time intervals. The conversions were determined by the ^1H NMR analysis of these samples, and the M_n and PDI data were determined by HT SEC analysis of the isolated polymers after removal of the $CDCl_3$ in vacuo.

Copolymerization Reactions (Table 4, Entry 2). In the glovebox, PDL (1.73 g, 7.2 mmol), CL (0.82 g, 7.2 mmol), TBD (10.0 mg, 0.072 mmol), and an equimolar amount of BnOH (7.8 mg, 0.072 mmol) were placed simultaneously in a small glass crimp cap vial. The vial was capped, removed from the glovebox, and heated at 100 °C for 18 h. For all reactions, an aliquot of crude polymer was removed for the determination of copolymerization conversion. The copolymer was then precipitated in THF, dried under vacuum for 18 h, and characterized by size-exclusion chromatography (SEC), differential scanning calorimetry (DSC), and ^1H, ^{13}C nuclear magnetic resonance spectroscopy (NMR).

AUTHOR INFORMATION

Corresponding Author

*Ph +31 40 247 4918; Fax +31 40 246 3966; e-mail r.duchateau@tue.nl.

Notes

The authors declare no competing financial interest.

ACKNOWLEDGMENTS

This research is financially supported by a MarieCurie Intra-European Fellowship (IEF) within the seventh European Community Framework Programme (FP7).

REFERENCES

(1) (a) Vert, M.; Li, S.; Spenlehauer, G.; Guerin, P. *J. Mater. Sci.: Mater. Med.* **1992**, *3*, 432. (b) Chiellini, E., Sunamoto, J., Migliaresi, C., Ottenbrite, R. M., Cohn, D., Eds.; *Biomedical Polymers and Polymer Therapeutics*; University of Pisa: Pisa, Italy, 2002. (c) Vert, M. *Angew. Makromol. Chem.* **1989**, *166*, 155.

(2) For example, see: (a) Carothers, W. H.; Dorough, G. L. *J. Am. Chem. Soc.* **1930**, *52*, 711. (b) Ishihara, K.; Ohara, S.; Yamamoto, H. *Science* **2000**, *290*, 1140. (c) Takasu, A.; Makino, T.; Yamada, S. *Macromolecules* **2010**, *43*, 144. (d) Liu, C.; Liu, F.; Cai, J.; Xie, W.; Long, E. T.; Turner, S. R.; Lyons, A.; Gross, R. A. *Biomacromolecules* **2011**, *12*, 3291.

(3) Dubois, P.; Coulembier, O.; Raquez, J.-M. *Handbook of Ring-Opening Polymerization*; Wiley-VCH: Weinheim, 2009.

(4) For general reviews, see: (a) Dechy-Cabaret, O.; Martin-Vaca, B.; Bourissou, D. *Chem. Rev.* **2004**, *104*, 6147. (b) Dove, A. P. *Chem. Commun.* **2008**, 6446. (c) Labet, M.; Thielemans, W. *Chem. Soc. Rev.* **2009**, *38*, 3484. (d) Albertsson, A.-C.; Varma, K. I. *Biomacromolecules* **2003**, *4*, 1466.

(5) For nonenzymatic routes, see: (a) Nakayama, Y.; Watanabe, N.; Kusaba, K.; Sasaki, K.; Cai, Z.; Shiono, T.; Tsutsumi, C. *J. Appl. Polym. Sci.* **2011**, *121*, 2098. (b) Wang, Y.; Kuniko, M. *Macromol. Symp.* **2005**, *224*, 193.

(6) For example, see: (a) van der Mee, L.; Helmich, F.; de Bruijn, R.; Vekemans, J. A. J. M.; Palmans, A. R. A.; Meijer, E. W. *Macromolecules* **2006**, *39*, 5021. (b) Namekawa, S.; Suda, S.; Uyama, H.; Kobayashi, S. *Int. J. Biol. Macromol.* **1999**, *25*, 145. (c) Bisht, K. S.; Henderson, L. A.; Gross, R. A. *Macromolecules* **1997**, *30*, 2705. (d) Focarete, M. L.; Scandola, M.; Kumar, A.; Gross, R. A. *J. Polym. Sci., Part B: Polym. Phys.* **2001**, *39*, 1721. (e) de Geus, M.; van der Meulen, I.; Goderis, B.; van Hecke, K.; Dorschu, M.; van der Werff, H.; Koning, C. E.; Heise, A. *Polym. Chem.* **2010**, *1*, 525. (f) van der Meulen, I.; Geus, M. D.; Antheunis, H.; Deumens, R.; Joosten, E. A. J.; Koning, C. E.; Heise, A. *Biomacromolecules* **2008**, *9*, 3404.

(7) (a) Ceccorulli, G.; Scandola, M.; Kumar, A.; Kalra, B.; Gross, R. A. *Biomacromolecules* **2005**, *6*, 902. (b) Kumar, A.; Kalra, B.; Dekhterman, A.; Gross, R. A. *Macromolecules* **2000**, *33*, 6303.

(8) For reviews describing organometallic catalysis of lactides and lactones, see: (a) Wu, J.; Yu, T.-L.; Chen, C.-T.; Lin, C.-C. *Coord. Chem. Rev.* **2006**, *250*, 602. (b) O'Keefe, B. J.; Hillmyer, M. A.; Tolman, W. B. *J. Chem. Soc., Dalton Trans.* **2001**, 2215. (c) Wheaton, C. A.; Hayes, P. G.; Ireland, B. J. *Dalton Trans.* **2009**, 4832. (d) Ajellal, N.; Carpentier, J.-F.; Guillaume, C.; Guillaume, M. S.; Helou, M.; Poirier, V.; Sarazin, Y.; Trifonov, A. *Dalton Trans.* **2010**, *39*, 8363.

(9) Lebedev, B.; Yevstropov, A. *Makromol. Chem.* **1984**, *185*, 1235.

(10) Zhong, Z.; Dijkstra, P. J.; Feijen, J. *Macromol. Chem. Phys.* **2000**, *201*, 1329.

(11) Jedliriski, Z.; Juzwa, M.; Adarnus, G.; Kowalczuk, M. *Macromol. Chem. Phys.* **1996**, *197*, 2923.

(12) Van der Meulen, I.; Gubbels, E.; Huijser, S.; Sablong, R.; Koning, C. E.; Heise, A.; Duchateau, R. *Macromolecules* **2011**, *44*, 4301.

(13) For organic catalytic ROP of lactide and lactones, see: (a) Chuma, A.; Horn, H. W.; Swope, W. C.; Pratt, R. C.; Zhang, L.; Lohmeijer, B. G. G.; Wade, C. G.; Waymouth, R. M.; Hedrick, J. L.; Rice, J. E. *J. Am. Chem. Soc.* **2008**, *130*, 6749. (b) Pratt, R. C.; Lohmeijer, B. G. G.; Long, D. A.; Waymouth, R. M.; Hedrick, J. L. *J. Am. Chem. Soc.* **2006**, *128*, 4556. (c) Dove, A. P. R; Pratt, C.; Lohmeijer, B. G. G.; Culkin, D. A.; Hagberg, E. C.; Nyce, G. W.; Waymouth, R. M.; Hedrick, J. L. *Polymer* **2006**, *47*, 4018. (d) Kamber, N. E.; Jeong, W.; Waymouth, R. M.; Pratt, R. C.; Lohmeijer, B. G.; Hedrick, J. L. *Chem. Rev.* **2007**, *107*, 5813. (e) Kiesewetter, M. K.; Shin, E. J.; Hedrick, J. L.; Waymouth, R. M. *Macromolecules* **2010**, *43*, 2093.

(14) (a) Helou, M.; Miserque, O.; Brusson, J.-M.; Carpentier, J.-F.; Guillaume, S. M. *Chem.—Eur. J.* **2010**, *16*, 13805. (b) Pratt, R. C.; Nederberg, F.; Waymouth, R. M.; Hedrick, J. L. *Chem. Commun.* **2008**, 114.

(15) (a) Strandman, S.; Gautrot, J. E.; Zhu, X. X. *Polym. Chem.* **2011**, *2*, 791. (b) Duda, A.; Kowalski, A.; Penczek, S.; Uyama, H.; Kobayashi, S. *Macromolecules* **2002**, *11*, 4266.

(16) Lohmeijer, B. G. G.; Pratt, R. C.; Leibfarth, F.; Logan, J. W.; Long, D. A.; Dove, A. P.; Nederberg, F.; Choi, J.; Wade, C.; Waymouth, R. M.; Hedrick, J. L. *Macromolecules* **2006**, *39*, 8574.

(17) This behavior is in agreement with the conclusions reported by previous reports, demonstrating that the efficiency of the ROP of ε-CL is sensitive to the steric nature of the carbene catalyst. For example, see: Nyce, G. W.; Glauser, T.; Connor, E. F.; Mock, A.; Waymouth, R. M.; Hedrick, J. L. *J. Am. Chem. Soc.* **2003**, *125*, 3046.
(18) Schuchardt, U.; Vargas, R. M.; Gelbard, G. *J. Mol. Catal. A: Chem.* **1995**, *99*, 65.
(19) (a) Allegra, G.; Bassi, I. W. *Adv. Polym. Sci.* **1969**, *6*, 549. (b) Kamiya, N.; Sakurai, M.; Inoue, Y.; Chujo, R. *Macromolecules* **1991**, *24*, 3888.
(20) For example, see: (a) Coulembier, O.; Mespouille, L.; Hedrick, J. L.; Waymouth, R. M.; Dubois, P. *Macromolecules* **2006**, *39*, 4001. (b) Kim, B. J.; White, J. L. *J. Appl. Polym. Sci.* **2003**, *88*, 1429.
(21) For more details concerning the MALDI-ToF-MS methods used, see: (a) Huijser S. Synthesis and characterization of biodegradable polyesters. PhD Thesis, Eindhoven, 2009. (b) Daswani, P.; Rheinhold, F.; Ottink, M.; Staal, B.; Van Herk, A. *Eur. Polym. J.* **2012**, *48*, 296.
(22) (a) Kurzer, F.; Douraghi-Zadeh, K. *Chem. Rev.* **1967**, *67*, 107−152. (b) Quast, H.; Ross, K.-H.; Philipp, G.; Hagedorn, M.; Hahn, H.; Banert, K. *Eur. J. Org. Chem.* **2009**, 3940−3952.

Macromolecules

Article

pubs.acs.org/Macromolecules

Decreasing the Alkyl Branch Frequency in Precision Polyethylene: Effect of Alkyl Branch Size on Nanoscale Morphology

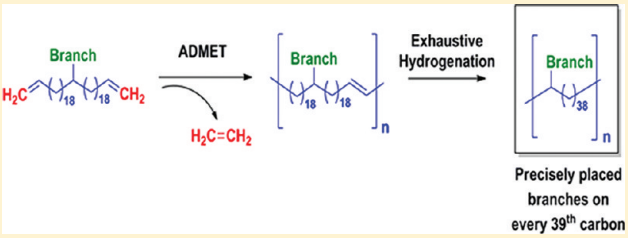
Bora Inci,[†,§] Ingo Lieberwirth,[‡] Werner Steffen,[‡] Markus Mezger,[‡] Robert Graf,[‡] Katharina Landfester,[‡] and Kenneth B. Wagener*[,†]

[†]Center for Macromolecular Science and Engineering, The George and Josephine Butler Polymer Research Laboratory, Department of Chemistry, University of Florida, Gainesville, Florida 32611-7200, United States

[‡]Max Planck Institute for Polymer Research, Ackermannweg 10, 55128 Mainz, Germany

Supporting Information

ABSTRACT: Synthesis and morphological characterization are reported for a series of 13 precision branched polyethylene structures, the branch being placed on every 39th carbon and varying in size from methyl to pentadecyl group. A recently established synthetic scheme for preparation of the symmetrical α,ω-diene monomer was employed to increase the number of methylene carbons between the branch points from 20 to 38, yielding polymers with 5.26 mol % α-olefin incorporation. The morphology of these polymers was investigated using differential scanning calorimetry (DSC), wide-angle X-ray diffraction (WAXD), and transmission electron microscopy (TEM). Methyl branching significantly reduces the melting point and single crystal lamellae thickness of unbranched polyethylene. On the other hand, all further branches from ethyl to pentadecyl produce polymers that have similar melting points and single crystal lamellae thicknesses. A clear change in the morphology of both solution and melt-grown crystals of these polymers was observed from a situation where the methyl branch is incorporated in the polymer's unit cell to one where branches of greater mass are mostly expelled from the unit cell.



INTRODUCTION

The structure of polyethylene has been extensively investigated[1,2] and is considered as the model for polymer crystallization studies.[3−6] Linear polyethylene (high density polyethylene) crystallized from solution or the melt forms folded chain crystals having the orthorhombic unit cell.[7] The branched versions of polyethylene (low density and linear low density polyethylene) have attracted more attention due to their wide-ranging thermal and mechanical properties governed by branching.[8,9] The effect of branching on crystal structure of polyethylene has been examined in chain polymerized ethylene/α-olefin copolymers with comonomers propylene,[10,11] 1-butene,[10,12,13] and 1-octene.[14] It is known that the ethylene/propylene copolymers show evidence for methyl branch inclusion into the crystal unit cell, whereas ethylene/1-butene and ethylene/1-octene polymers display the exclusion of ethyl and hexyl branches due to their larger branch sizes.[9,15] The validity of this generalization is limited, and partial ethyl branch inclusion is suggested for some of the ethylene/1-butene copolymer systems.[16,17] For the case of ethylene/1-octene copolymers, X-ray investigations show the existence of a complex multiphase morphology which hinders the deeper examination of hexyl branch placement within the polymer structure.[14]

The ambiguity in morphology determination of ethylene copolymers is governed by the heterogeneously distributed nature of branches using either Ziegler−Natta,[18−20] metallocene,[21−23] and late transition metal[24] catalytic systems. By its nature, chain-propagation chemistry incorporates structural defects via inevitable chain transfer and chain walking processes which produce alkyl branches of varying lengths randomly spaced along the polyethylene backbone.[25]

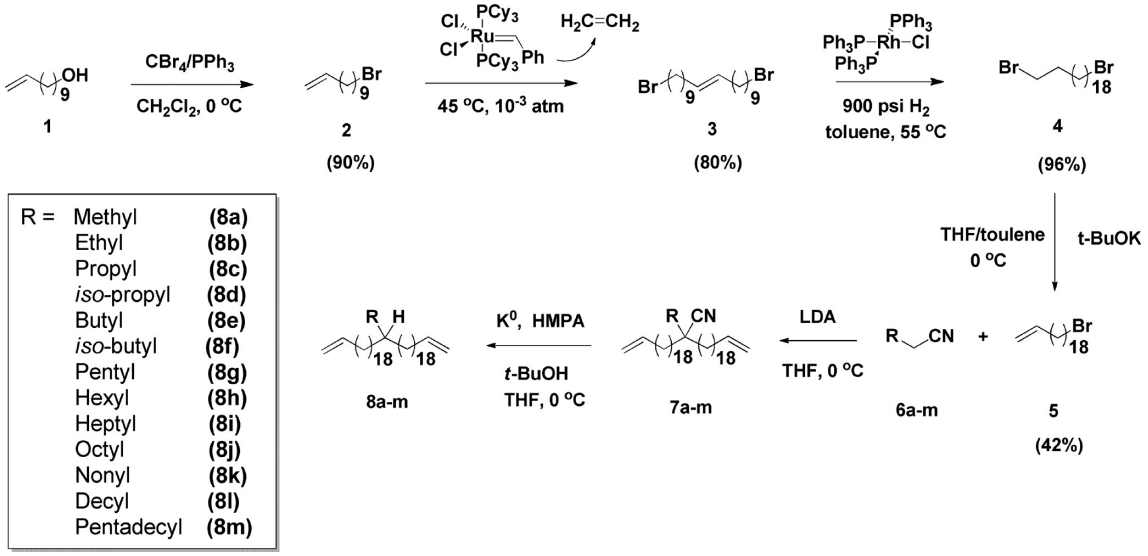
Recently, we have employed step polycondensation chemistry (the ADMET reaction) to generate precisely branched ethylene copolymers.[26−31] Symmetrical α,ω-diene monomers (having built-in branches) are condensed into unsaturated polymers, which upon saturation generate precision branched polyethylenes.[32,33] This approach circumvents the random nature of branching in polyethylene with the elimination of chain transfer and chain walking processes. The design of the symmetrical α,ω-diene monomer obviates the ethylene/comonomer reactivity ratio problems and ensures the precise placement of branches along the polymer backbone. We are now able to prepare polymers where both the identity of the branch and its position are known without equivocation. Systematic alterations in branch identity and position on the polymer backbone can be made during monomer synthesis to yield predictable changes in physical properties.[31]

Linear polyethylene prepared via ADMET by polycondensation of 1,9-decadiene melts at 134 °C. Introduction of branches

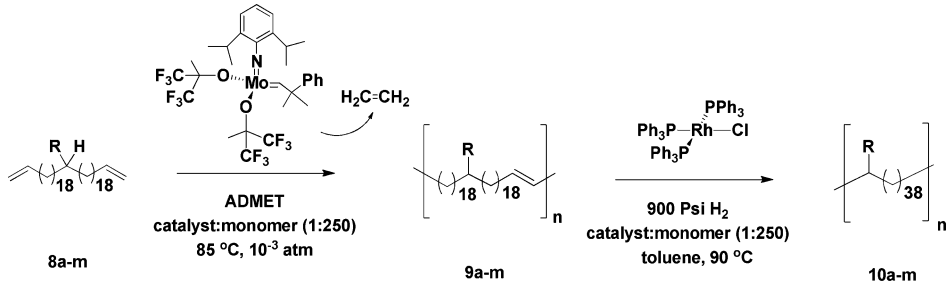
Received: February 6, 2012
Revised: April 4, 2012
Published: April 15, 2012

 © 2012 American Chemical Society

Scheme 1. Synthesis of 21-Alkylhentetraconta-1,40-dienes (8a−m)



Scheme 2. Synthesis of Precisely Sequenced Polymers



Unsaturated polymer	Branch (R)	Saturated polymer
9a	Methyl	10a
9b	Ethyl	10b
9c	Propyl	10c
9d	*iso*-propyl	10d
9e	Butyl	10e
9f	*iso*-butyl	10f
9g	Pentyl	10g
9h	Hexyl	10h
9i	Heptyl	10i
9j	Octyl	10j
9k	Nonyl	10k
9l	Decyl	10l
9m	Pentadecyl	10m

onto the polyethylene backbone disrupts the crystallinity and results in a decrease in melting point.[26,34] For example, insertion of butyl branches on every 21st carbon (i.e., 20 methylene carbons between consecutive branch points) generates a semicrystalline polymer that melts at 12 °C.[29] More frequent butyl branch placement on the polymer backbone can also be achieved with this technique to prepare polymers with lower melting points and, in some cases, amorphous materials (with as few as four methylene groups between branches).[35] A recently developed synthetic scheme for preparation of the symmetrical α,ω-diene monomer has been employed to decrease the total concentration of butyl branches by increasing the number of methylene carbons between the branch points from 20 to 38. This synthetic methodology yields a semicrystalline polymer that melts at 75 °C.[36] The thermal and morphological behavior of this polymer was compared to that of an ethylene/1-hexene copolymer having the same net concentration of butyl branches along the polymer backbone but prepared via chain polymerization with a metallocene catalyst.[37] Both polymers show the existence of (110) and (200) orthorhombic unit cell reflection planes, with the ADMET polymer having a sharper melting transition and narrower lamella thickness distribution.

Herein, we report the synthesis and the characterization of precisely sequenced polyethylenes containing 13 different branches, each being placed on every 39th carbon on the polymer backbone. This paper extends the scope of the precision polyethylene study to provide a better understanding for the effect of the branch identity on polymer properties.

dx.doi.org/10.1021/ma3002577 | *Macromolecules* 2012, 45, 3367−3376

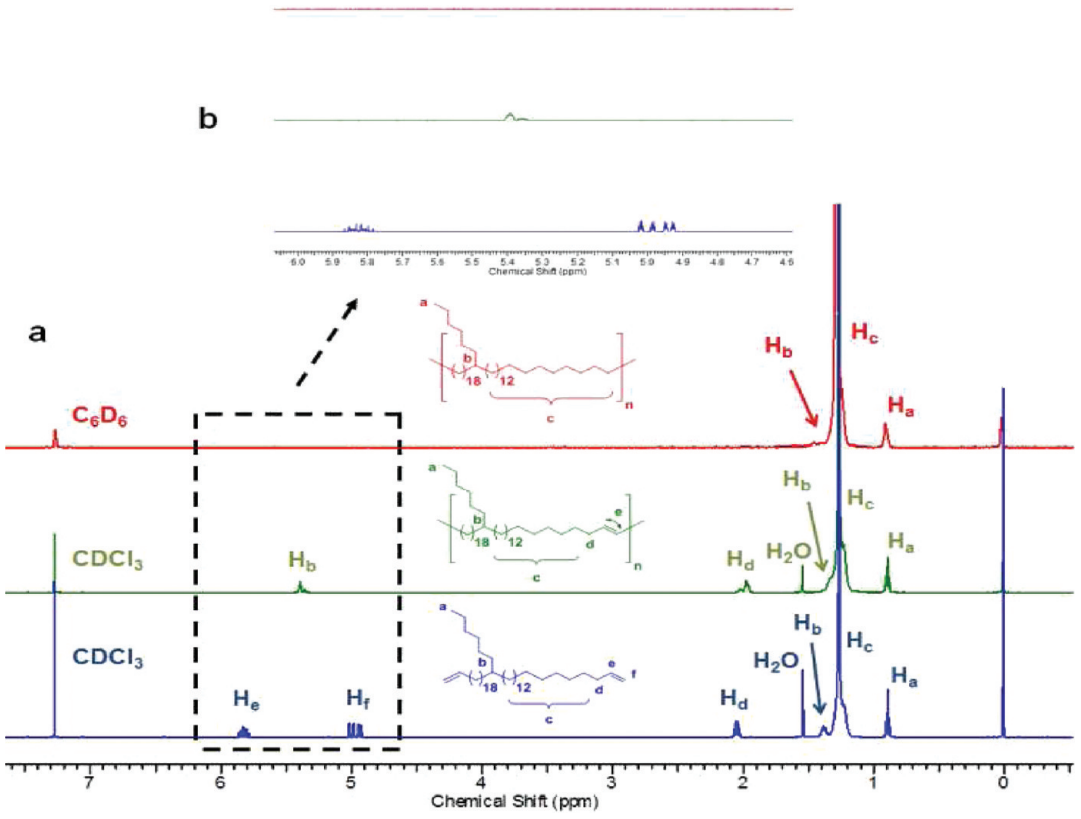


Figure 1. (A) ^{1}H 500 MHz NMR spectra of monomer **8h-(hexyl)**, unsaturated **9h-(hexyl)**, and saturated **10h-(hexyl)** polymers. (B) Olefinic region shown in higher magnification.

RESULTS AND DISCUSSION

A. Synthesis and Primary Structure Characterization of Precisely Branched Polymers. Successful preparation of symmetrical α,ω-diene monomers is the key in this research, where a multistep synthetic route was required for each monomer (**8a−m**). Scheme 1 illustrates the elaborate synthetic effort, which consisted of a six-step procedure including alkenyl bromide (**5**) preparation,[38] dialkylation of nitriles (**6a−m**),[39] and decyanation of alkylcyano α,ω-dienes (**7a−m**).[40]

The spacing between the two consecutive branch points along the polyethylene backbone (see structures of polymers **10a−m** in Scheme 2) was set in the dialkylation step of nitriles, where the alkenyl bromide run length (in this case 18 methylene units) played a crucial role. Systematic increase of run length from 9 to 18 required challenging purification steps. For example, in the dehydrohalogenation of alkyl dibromide (**4**) with *t*-BuOK, the crude mixture contained the desired alkenyl bromide (20-bromoicos-1-ene **5**), the dielimination product, and unreacted starting material, all with close retardation factors by thin layer chromatography. Consecutive column chromatography passes and the relatively low room temperature solubility of compound **5** in hexane (used as an eluent for the separation) made the purification of the desired compound, 20-bromoicos-1-ene (**5**), tedious.

Alkenylation of nitriles **6a−m** in the presence of lithium diisopropylamide (LDA) and 20-bromoicos-1-ene produced the alkylcyano α,ω-dienes 7**a−m** in high yields. Decyanation of nitriles 7**a−m** was achieved with potassium metal via radical chemistry. The resulting tertiary radical after decyanation was further quenched by abstraction of hydrogen from *t*-BuOH to give α,ω-diene monomers **8a−m** in moderate to high yields.

Monomers **8a−m** were condensed to form the corresponding unsaturated ADMET polymers (Scheme 2). Because of the relatively high melt viscosity of the resulting polymers (**9a−m**), the polymerization temperature was set to 85 °C. At that elevated temperature, Ru-based catalysts are prone to have low turnover numbers and to generate Ru−H species,[41−43] which would cause isomerization problems and disrupt the symmetrical nature of the monomer.[44,45]

Therefore, monomers **8a−m** were condensed to form unsaturated ADMET polymers using Schrock's [Mo] catalyst for clean metathesis chemistry. Because of the oxophilic nature of [Mo] catalysts, all the manipulations prior to polymerization and catalyst addition (catalyst to monomer ratio 1:500) were performed in a glovebox. Polymerization was initiated by melting the monomer at 50 °C, and the temperature was set to 85 °C to be able to stir the viscous polymer melt. After 24 h of reaction, the polymer was cooled to RT, another portion of [Mo] catalyst (catalyst to monomer ratio 1:500) was added in the glovebox, and the temperature was set back to 85 °C.

ADMET polymerization proceeded smoothly to give the desired unsaturated linear polymers **9a−m** with no detectable side reactions. Disappearance of terminal olefin signals in ^{1}H NMR spectra (Figure 1) proved the complete conversion, which is necessary for any step-growth polymerization. Unsaturated polymers (**9a−m**) were hydrogenated using Wilkinson's catalyst (catalyst to monomer ratio 1:250) to yield the precision polyethylenes (polymers **10a−m**) having branches from methyl to pentadecyl on every 39th carbon.

The polymerization and hydrogenation steps were followed by ^{1}H nuclear magnetic resonance (NMR) spectroscopy. As an example, Figure 1 illustrates the ^{1}H NMR spectra of hexyl branched polymer, **10h-(hexyl)**, and its precursors. ADMET

dx.doi.org/10.1021/ma3002577 | *Macromolecules* 2012, 45, 3367−3376

polymerization of monomer **8h-(hexyl)** yielded the unsaturated polymer, **9h-(hexyl)**. Formation of the ADMET polymer resulted in loss of the terminal olefin signals (5.0 and 5.8 ppm) and the appearance of the internal olefin at 5.4 ppm (Figure 1). Exhaustive hydrogenation of the internal olefins with Wilkinson's catalyst generated **10h-(hexyl)**, corresponding to polyethylene with hexyl branches on every 39th carbon, with complete loss of the olefinic signals in ^{1}H NMR.

Polymerization and hydrogenation of monomer **8h-(hexyl)** was also monitored with ^{13}C NMR spectroscopy (Figure 2).

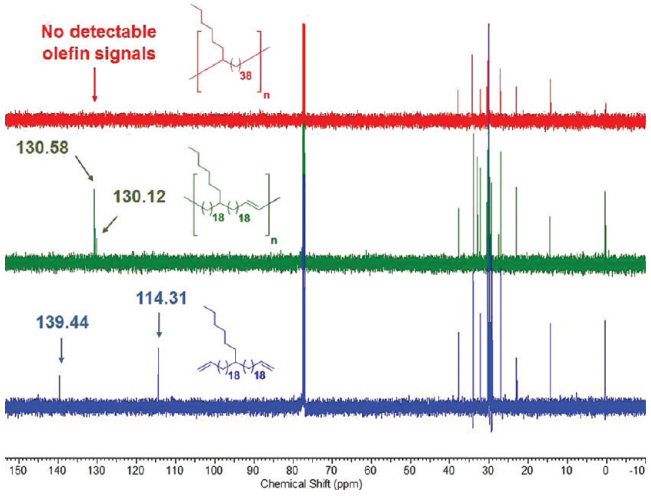


Figure 2. ^{13}C 126 MHz NMR spectra of monomer **8h-(hexyl)**, unsaturated **9h-(hexyl)**, and saturated **10h-(hexyl)** polymers.

Comparison of the ^{13}C NMR spectra for the monomer **8h-(hexyl)** and unsaturated polymer **9h-(hexyl)** indicates the disappearance of the signals belonging to the terminal olefin at 114.31 and 139.44 ppm and formation of the new internal olefin (*cis* olefin at 130.12 ppm, minor product, and *trans* olefin at 130.58 ppm, major product) generated by the metathesis chemistry. Hydrogenation of the internal olefin with Wilkinson's catalyst yielded the saturated polymer **10h-(hexyl)** with no detectable trace of olefins.

Infrared (IR) spectroscopy was also used to monitor this transformation (Figure 3). Disappearance of the out-of-plane C−H bend absorption at 969 cm^{-1} indicates the complete absence of C=C in the polymer backbone and proves the full conversion for the hydrogenation step.

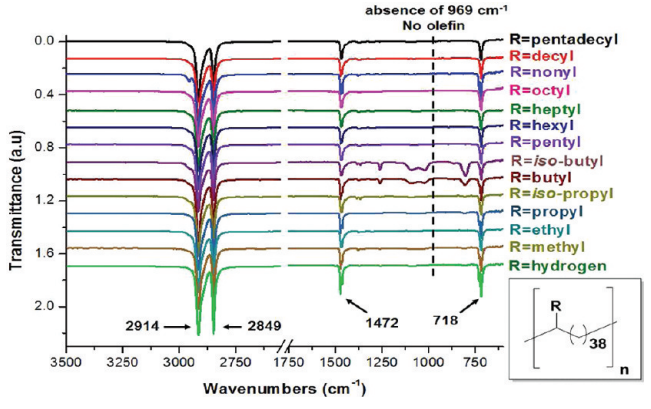


Figure 3. Infrared spectra of the precisely branched polymers **10a-(methyl)**, **10b-(ethyl)**, **10c-(propyl)**, **10d-(iso-propyl)**, **10e-(butyl)**, **10f-(iso-butyl)**, **10g-(pentyl)**, **10h-(hexyl)**, **10i-(heptyl)**, **10j-(octyl)**, **10k-(nonyl)**, **10l-(decyl)**, **10m-(pentadecyl)**, and **ADMET PE**.

After hydrogenation, solutions of saturated polymers were concentrated and precipitated into methanol. It is important to note that the solubility characteristics of polymers **10a−m** (soluble in toluene, dichlorobenzene, trichlorobenzene, etc., at high temperatures) are similar to those of polyethylenes prepared by chain polymerization. Molecular weight data were obtained using high temperature gel permeation chromatography (GPC) in 1,2,4-trichlorobenzene at 135 °C relative to polystyrene standards. Table 1 illustrates the weight-average molecular weights for the precisely branched unsaturated and saturated polymers.

Table 1. Molecular Weights and Thermal Data for Precisely Branched Polymers

			$\bar{M}_w$ (kg/mol)[a] (PDI[b])	
branch identity on every 39th carbon	T_m (°C) (peak)	ΔH_m (J/g)	unsaturated	saturated
no branch	134	211	70.2 (2.7)	70.2 (2.7)
methyl	92	137	33.7 (2.2)	92.7 (2.0)
ethyl	76	93	56.7 (2.2)	53.1 (2.4)
propyl	78	71	217 (3.1)	225 (3.0)
isopropyl	77	74	107 (2.0)	144 (3.5)
butyl	75	66	60.2 (2.3)	66.5 (2.5)
isobutyl	73	51	22.6 (2.5)	54.8 (2.4)
pentyl	74	88	29.3 (2.2)	30.2 (2.0)
hexyl	73	85	30.5 (2.3)	30.5 (1.9)
heptyl	74	85	76.6 (3.0)	74.2 (2.9)
octyl	74	73	200 (3.6)	181 (3.3)
nonyl	73	84	35.9 (2.4)	34.3 (2.2)
decyl	71	76	28.0 (2.4)	27.7 (1.8)
pentadecyl	70	83	58.0 (2.4)	55.9 (2.4)

[a]Molecular weight data were collected by GPC in 1,2,4-trichlorobenzene at 135 °C relative to polystyrene standards. [b]PDI, polydispersity index $\bar{M}_w/\bar{M}_n$.

Control over the primary structure of the final precision polymer is governed by the precision established on the molecular level. The purity of the monomers and the absence of any side reactions during the polymerization ensure the successful polycondensation chemistry and the level of control. Upon close inspection of the ^{13}C NMR data for the polymers, it can be concluded that the branches are precisely placed along the polyethylene backbone with none of the undesired branches due to chain transfer typically observed during chain-growth chemistry. As an example, Figure 4 shows a portion (10−55 ppm) of the ^{13}C NMR spectra for precise polymers having branches from methyl to propyl. All spectra are dominated by a singlet at 29.99 ppm corresponding to methylenes on the main polyethylene chain. Note that the presence of alkyl branches precisely placed along the main chain affects the chemical shifts of carbons located within three CH_2 units from an individual branch.[26]

In the spectrum for **10a-(methyl)**, which is polyethylene containing methyl branches on every 39th backbone carbon (Figure 4A), the resonances belonging to the methyl branch, 19.84 ppm, as well as main chain carbons, 37.45, 27.98, 30.34, and 29.99 ppm and the carbon at the branch point (33.12 ppm) indicate that only methyl branches are present, in good agreement with previously reported[26] experimental data and predicted values.[46]

dx.doi.org/10.1021/ma3002577 | *Macromolecules* 2012, 45, 3367−3376

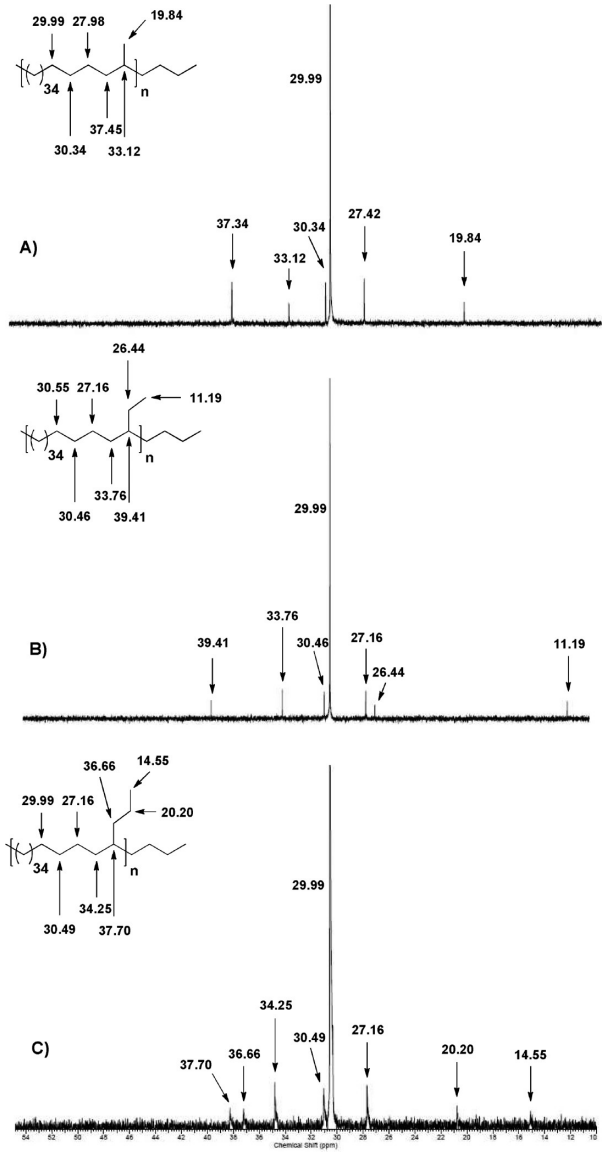


Figure 4. Comparison of ^{13}C NMR spectra for precision polymers (A) **10a-(methyl)**, (B) **10b-(ethyl)**, and (C) **10c-(propyl)**.

Introduction of ethyl branches changes the chemical shifts of both backbone and side chain carbons (Figure 4B). The terminal methyl carbon is now more shielded by the presence of a methylene unit, which results in a predictable shift upfield (11.19 ppm). On the other hand, the methine carbon is deshielded with more electron delocalization and shifts downfield (39.41 ppm) compared to the methyl branched polymer. All the chemical shifts shown in Figure 4B for the polymer **10b-(ethyl)** are in good agreement with previously reported ethylene/1-butene and hydrogenated polybutadiene systems.[47−50]

In the spectrum for **10d-(propyl)** (Figure 4C), the resonances belonging to the propyl branch, 14.55, 20.20, and 36.66 ppm, as well as main chain carbons, 34.25, 27.16, 30.49, and 29.99 ppm and the methine carbon (37.70 ppm) indicate that only propyl branches are present, in good agreement with previously reported data on chain-growth polymers obtained by copolymerization of ethylene with 1-pentene.[51−53]

B. Melting Behavior of Precisely Branched Polymers. Figures 5 and 6 present the differential scanning calorimetry (DSC) thermograms of linear **ADMET PE** and precise polymers having branches from methyl to pentadecyl increasing in both length and bulkiness.

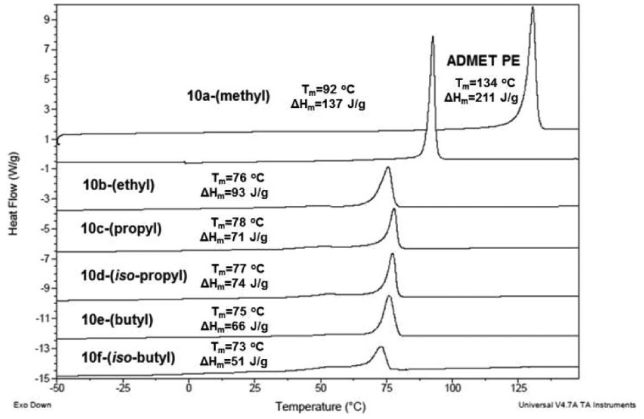


Figure 5. Differential scanning calorimetry thermograms for second heating cycles of **ADMET PE**, **10a-(methyl)**, **10b-(ethyl)**, **10c-(propyl)**, **10d-(iso-propyl)**, **10e-(butyl)**, and **10f-(iso-butyl)** with 10 °C/min heating rate.

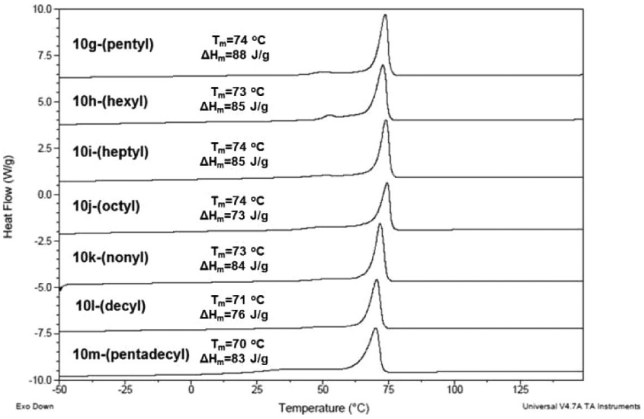


Figure 6. Differential scanning calorimetry thermograms for second heating cycles of precision polymers **10g-(pentyl)**, **10h-(hexyl)**, **10i-(heptyl)**, **10j-(octyl)**, **10k-(nonyl)** and **10l-(decyl)**, and **10m-(pentadecyl)** with 10 °C/min heating rate.

It is immediately obvious that methyl branching significantly reduces the melting point of ADMET polyethylene. On the other hand, all further branches, from ethyl to pentadecyl, produce polymers that have very similar (in some cases identical) melting points. As discussed further below, this behavior may be attributed to a change in morphology from a situation where the methyl branch is incorporated into the polymer crystal to one where larger branches are expelled from the crystal. It is important to note that the ethyl branch is incorporated into the polymer crystal when the branches are placed on every 21st carbon.[31] Increasing the distance between two consecutive branches from 20 carbons (10.0 mol % α-olefin incorporation) to 38 carbons (5.26 mol % α-olefin incorporation) expels the ethyl branches from the crystal lattice into the amorphous phase. Similar observations were also reported for chain polymerized ethylene/1-butene copolymers, where the ethyl branch is mostly found in the amorphous region.[9,54]

As shown in Figure 5, unbranched **ADMET PE** displays thermal behavior virtually the same as that of high density polyethylene (T_m = 134 °C, ΔH_m = 211 J/g). Incorporation of

dx.doi.org/10.1021/ma3002577 | *Macromolecules* 2012, 45, 3367−3376

methyl branches precisely placed on every 39th carbon, polymer **10a-(methyl)**, disrupts the crystal structure and decreases the melting temperature to 92 °C and the enthalpy of fusion to 137 J/g. A similar trend is observed when the branch is an ethyl group, **10b-(ethyl)**; the melting point decreases below that of **10a-(methyl)** (T_m = 76 °C with a heat of fusion ΔH_m = 93 J/g). Depression of both the melting temperature and the heat of fusion suggests a reduction of crystal thickness for polymer **10b-(ethyl)**. Transmission electron microscopy (TEM) measurements of solution-grown single crystals for polymer **10b-(ethyl)** also support this observation (see section C). Extension of the branch size from ethyl to propyl, **10c-(propyl)**, does not lead to further decreases in melting temperature and enthalpy of fusion (T_m = 78 °C and ΔH_m = 71 J/g). Similar melting behavior is observed for precision polyethylene possessing longer branches (Figure 7).

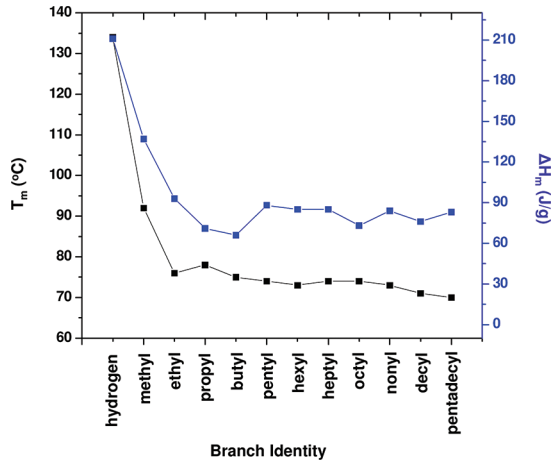


Figure 7. Effect of branch identity on melting point and heat of fusion.

Incorporation of defects in polyethylene crystal along with the melting behavior of chain-polymerized ethylene copolymers has been extensively studied.[9,15,54] Alamo et al. reported that only small groups, such as CH_3, Cl, O, and OH, are incorporated into the crystal lattice, whereas the bigger defects are expelled from the crystal.[9] Hosoda et al. prepared various ethylene/α-olefin copolymers with a vanadium catalyst system.[54] They determined that the probability of branch inclusion into the crystal is strongly dependent on branch identity and is in the order of methyl > ethyl > butyl = hexyl = decyl > isobutyl. Interestingly, ethylene/1-octene and ethylene/1-dodecene copolymers reported by the same group with 5.14 and 4.54 mol % α-olefin incorporation ratios exhibit melting points (70−75 °C) very similar to those of precision polymers **10h-(hexyl)** and **10l-(decyl)** with 5.26 mol % α-olefin incorporation. More recently, Hosoda et al. compared the melting behavior of precision polymer **10e-(butyl)** with the ethylene/1-hexene copolymer having the same net concentration of butyl branches along the polymer backbone but prepared via chain polymerization with a metallocene catalyst.[37] The melting profile of polymer **10e-(butyl)** displays a melting curve at 75 °C with width less than 20 °C. Even though the two polymers have the same net concentration of butyl branches, ethylene/1-hexene copolymer melts over a broader range from 50 to 105 °C with a melting point of 99 °C. The distinctly different melting behavior of these polymers was attributed to the broader lamella thickness distribution of chain-polymerized ethylene/1-hexene copolymer due to random positioning of butyl branches along the polymer backbone.[37]

C. Morphology and Crystal Structure Determination of Precisely Branched Polymers. Wide-angle X-ray and selected area electron diffraction measurements further support the observation of a change in unit cell as a function of branch size. WAXD diffractograms of precision polymers having branches from methyl to pentadecyl are shown in Figures 8 and 9.

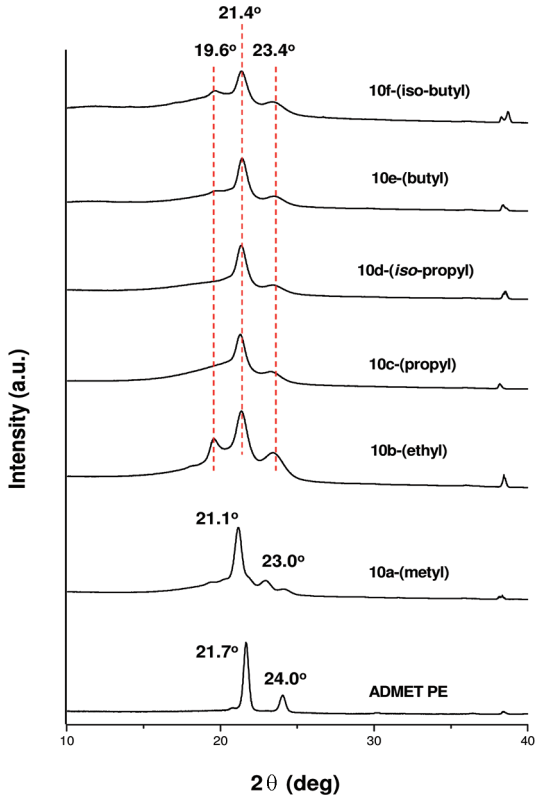


Figure 8. Wide-angle X-ray diffraction (WAXD) patterns for precision polymers **10a-(methyl)**, **10b-(ethyl)**, **10c-(propyl)**, **10d-(iso-propyl)**, **10e-(butyl)**, **10f-(iso-butyl)**, and **ADMET PE** obtained at RT. Prior to data acquisition, all samples were heated to 20 °C above the melting temperature of each polymer to remove the thermal history and then cooled to room temperature at a rate of 50 °C/min.

WAXD data were collected using the Cu Kα radiation (λ = 0.154 17 nm) induced by a generator operating at 40 kV and 150 mA. Diffraction patterns were recorded for 2(theta) values ranging from 10° to 40°. The peak at 38.5° observed in all WAXD diffractograms is the (111) reflection of the Al cubic closed packed structure. Aluminum foil was used to sandwich the polymer sample between copper holders.

For the sake of comparison, **ADMET PE** is displayed at the bottom of Figure 8. It exhibits the typical orthorhombic crystal structure (lattice parameters a = 7.40 Å, b = 4.93 Å, and c = 2.54 Å) with two characteristic crystalline peaks, exactly the same as for high density polyethylene made by chain propagation chemistry.[55] The more intense peak at scattering angle 21.7° and the less intense one at 24.0° correspond to reflection planes (110) and (200), respectively.

Introduction of precisely placed methyl branches on every 39th carbon (see polymer **10a-(methyl)** in Figure 8) disturbs

dx.doi.org/10.1021/ma3002577 | Macromolecules 2012, 45, 3367−3376

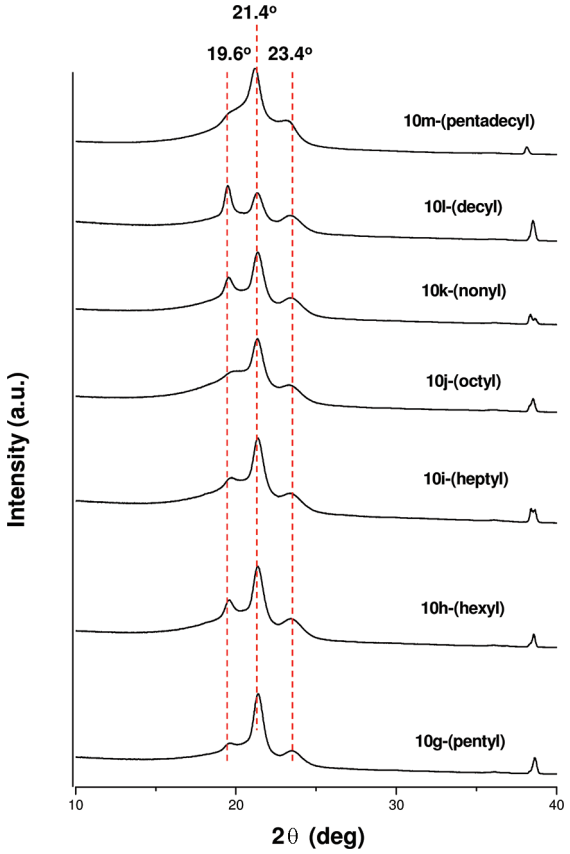


Figure 9. Wide-angle X-ray diffraction patterns for precision polymers **10g-(pentyl)**, **10h-(hexyl)**, **10i-(heptyl)**, **10j-(octyl)**, **10k-(nonyl)**, **10l-(decyl)**, and **10m-(pentadecyl)** obtained at RT. Prior to data acquisition, all samples were heated to 20 °C above the melting temperature of each polymer and then cooled to room temperature at a rate of 50 °C/min.

the unit cell of **ADMET PE** and shifts the two strong scattering peaks to 21.1° and 23.0°, corresponding to (110) (d = 4.19 Å) and (200) (d = 3.87 Å) reflection planes with lattice parameters a = 7.74 Å and b = 5.00 Å. An expansion of the unit cell by 4.6% and 1.4% along the a- and b-axes proves the distortion in the orthorhombic unit cell governed by the incorporation of the methyl branches in the unit cell. A similar expansion in unit cell parameters was also reported for ethylene/propylene copolymers prepared via chain polymerization, thus confirming the methyl branch inclusion into the unit cell.[11] In the case of the ethyl branched polymer **10b-(ethyl)**, WAXD and electron diffraction data suggest the existence of the orthorhombic crystal structure with lattice parameters of a = 7.58 Å and b = 4.98 Å. WAXD diffractograms of precision polymers having branches larger than ethyl (from propyl to pentadecyl) show nearly identical scattering patterns, indicating the formation of the orthorhombic crystal structure.

To better understand these observations, the scattering angles of two strong diffraction peaks are plotted as a function of branch identity in Figure 10. The decrease of scattering angles for methyl branched polymer **10a-(methyl)** indicates the larger d-spacing between the diffraction planes, suggesting the inclusion of the methyl branches into the unit cell. A clear structural change for polymers ranging from **10b-(ethyl)** to **10l-(decyl)** is evidenced by the increase of scattering angles, confirming the exclusion of branches from the unit cell. It is important to note that precision polymer **10m-(pentadecyl)**

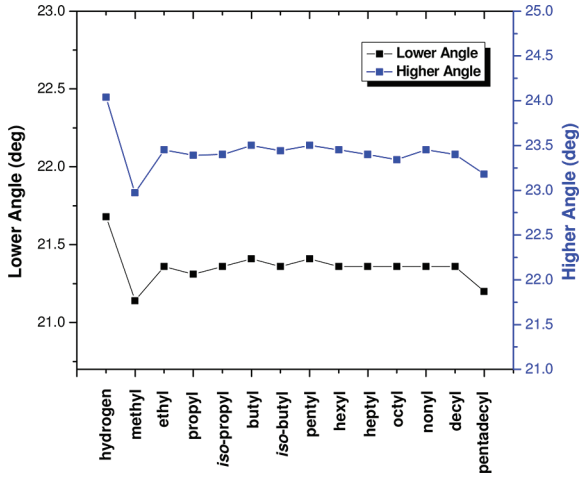


Figure 10. Scattering angles of two strong reflections for alkyl branched precision polymers. The blue line corresponds to reflection at higher angle, while the black line corresponds to reflection at lower angle.

exhibits a distinct morphological behavior, in which the relatively long pentadecyl branch presumably cocrystallizes with the main polymer chain, thereby increasing the d-spacing between the diffraction planes. Cocrystallization of branches longer than 10 carbon atoms in length with the main chain was previously reported for chain polymerized polyolefins.[56]

An interesting aspect of the WAXD patterns for the precision polymers ranging from **10b-(ethyl)** to **10m-(pentadecyl)** is that the 19.6° peak, which is sharper than that of the amorphous halo, suggests the possible coexistence of a dominant orthorhombic crystal and another metastable crystal structure as a minor component. Selected area electron diffraction (SAED) measurements on solution-grown polymer **10b-(ethyl)** crystals confirm the formation of a monoclinic crystal with lattice parameters of a = 8.04 Å, c = 4.80 Å, and β = 109.4°. The metastable monoclinic polyethylene structure was previously reported by Seto[57] with unit cell parameters a = 8.08 Å, b = 2.54 Å, c = 4.79 Å, and β = 107.9°. Please note that the notation of crystallographic directions for the monoclinic crystal structure differs from the orthorhombic case. Here the crystalline b-direction is the direction parallel to the polymer chain.

Formation of monoclinic crystalline phase is known for chain-polymerized ethylene/α-olefin copolymers (having branches larger than methyl) with high comonomer content.[58] Hu et al. reported ethylene/1-butene and ethylene/1-octene copolymers with α-olefin concentrations ranging from 7.50 to 19.7% prepared with single site metallocene catalyst.[58] Monoclinic crystals were found to coexist with the dominant orthorhombic crystalline phase for polymers having comonomer content higher than 9.00 mol %. The authors proposed that the formation of monoclinic crystals is strongly dependent on the nature of the crystalline−amorphous interface.[58] Polymers with high comonomer content display low crystallinity by populating the crystalline−amorphous interfacial area and favor the formation of monoclinic crystals. It is interesting that the precision polymers discussed here also exhibit monoclinic crystals even with 5.26 mol % comonomer incorporation. Because the defects larger than methyl are expelled from the crystal, they presumably "agglomerate" at the fold surface of the crystal. This might lead to a packing problem

dx.doi.org/10.1021/ma3002577 | Macromolecules 2012, 45, 3367−3376

Table 2. Observed WAXD and SAED Lattice Plane Distances for 10a-(methyl) and Their Corresponding Allocation to Orthorhombic and Monoclinic Crystal Planes[a]

$WAXD_{obs}$ d [Å]	$SAED_{obs}$ d [Å]	$intensity_{obs}$ WAXD/SAED	index (hkl)	$d_{(hkl)calc}$ [Å]
4.58	4.61	w/s	(001)mono	4.58
4.19	4.19	vs/vs	(110)ortho	4.20
3.87	3.88	s/s	(200)ortho/(200)mono	3.88/3.87
3.58	3.62	w/s	(−201)mono	3.60
2.50	2.52	w/s	(020)ortho/(201)mono	2.50/2.57

[a]Abbreviations: obs, observed; calc, calculated; mono, monoclinic; ortho, orthorhombic; w, weak; s, strong; vs, very strong.

with too high a density of bulky defects and finally cause the crystal lattice to shear to a metastable, in this case, monoclinic lattice. There should be a limit in metastable crystal phase formation for precisely branch polyethylene structures. That limit was recently reached by positioning branches on every 75th carbon (2.70 mol % comonomer incorporation) where the butyl branches are fully expelled from the crystalline phase, yielding pure orthorhombic crystals with none of the metastable crystal structure formation.[59]

SAED measurements were performed for solution-grown crystals of precision polymer **10a-(methyl)**. Along with the orthorhombic crystalline phase, monoclinic crystals were also found with lattice parameters a = 8.22 Å, c = 4.85 Å, and β = 109.3°. Table 2 illustrates WAXD and SAED analysis of polymer **10a-(methyl)**. A strong reflection corresponding to a d-spacing of 4.19 Å indicates that the orthorhombic crystal structure is the dominant form. However, some of the single crystals show a nonorthorhombic electron diffraction pattern which can be indexed as a monoclinic unit cell. Methyl branches in chain-polymerized ethylene/1-propene copolymers drive the change of orthorhombic crystal toward a hexagonal/rotator crystalline phase instead of monoclinic phase.[10] Observation of this unusual behavior in precision polymer **10a-(methyl)** is subject to further investigation.

Figure 11 shows the TEM images of solution-grown single crystals for precision polymers and **ADMET PE**. Lozenge-shaped rhombohedral single crystals were observed for all polymers, consistent with previous reports on solution-grown HDPE single crystals.[3,4] It is noteworthy that, although the crystallization conditions were similar for all the branched polymers, the morphology of solution-grown crystals changed based on the branch size.

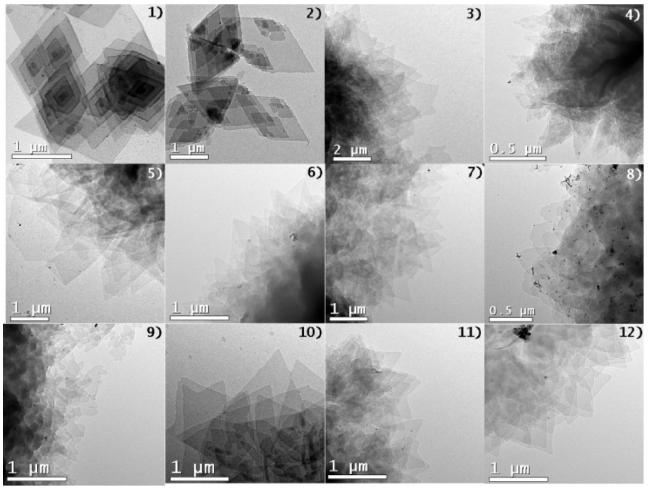


Figure 11. Transmission electron microscopy (TEM) micrographs of (1) **ADMET PE**, (2) **10a-(methyl)**, (3) **10b-(ethyl)**, (4) **10c-(propyl)**, (5) **10e-(butyl)**, (6) **10g-(pentyl)**, (7) **10h-(hexyl)**, (8) **10i-(heptyl)**, (9) **10j-(octyl)**, (10) **10k-(nonyl)**, (11) **10l-(decyl)**, and (12) **10m-(pentadecyl)**. **ADMET PE** crystals were grown from 0.03 wt % C_2Cl_4 solution, and all the other polymer single crystals were grown from 0.03% o-xylene solution.

Besides the **ADMET PE** single crystals, which clearly show secondary nucleation via screw dislocations, only the single crystals of polymer **10a-(methyl)** exhibit secondary nucleation. This may be an indication of a well-defined crystalline fold surface and hence the incorporation of methyl branches into the polymer crystal.

The lamella thicknesses of the solution-grown single crystals were determined using energy-filtered TEM measurements.[60,61] Taking two consecutive images from the same TEM sample, one with the slit positioned at the zero-loss peak and one without the slit, yielded two images, the elastically filtered image I_0 and the inelastic image I_t. After aligning both images for possible sample drift, the relative thickness, t, at each point of the images was given by $t/\lambda = \ln(I_0/I_t)$, in which λ is the mean free path of the respective material for the respective electron energy (200 kV). Calculation of the mean free path scales the image to an absolute thickness mapping.[61] Table 3 illustrates such single crystal lamella thicknesses of **ADMET PE** and precision polymers.

Table 3. Lamellae Thicknesses of ADMET PE and Precision Polymers Determined by TEM

polymer	thickness (nm)	polymer	thickness (nm)
ADMET PE	9.75	**10i-(heptyl)**	4.39
10a-(methyl)	7.09	**10j-(octyl)**	4.06
10b-(ethyl)	4.79	**10k-(nonyl)**	4.67
10e-(butyl)	4.25	**10l-(decyl)**	4.16
10g-(pentyl)	5.03	**10m-(pentadecyl)**	5.33
10h-(hexyl)	4.17		

Methyl branching reduces the lamella thickness of unbranched polyethylene; on the other hand, all further branches produce polymers that have very similar lamella thicknesses. Single crystal thickness data provide good evidence for the positioning of branches. Assuming the all-trans conformation of methylene units in the crystalline phase (lattice constant c = 2.54 Å), the distance between the two consecutive branch points (38 methylene units) can be estimated to be 4.8 nm. The length matches quite well with the observed crystal thickness of polymer **10b-(ethyl)** and precision polymers having branches longer than ethyl, suggesting the exclusion of such branches from the crystal phase. However, the single crystal thickness of polymer **10m-(pentadecyl)** is slightly increased to a value of ∼5.3 nm, which

dx.doi.org/10.1021/ma3002577 | Macromolecules 2012, 45, 3367−3376

may be attributed to cocrystallization of the pentadecyl branch onto the crystal surface.

Solution-grown single crystal lamella thickness measurements provide additional evidence of a clear change in the morphology of these polymers from a situation where the methyl branch is incorporated into the solution-grown single crystal to one where branches of greater mass are mostly expelled from the crystal.

CONCLUSIONS

Metathesis polycondensation chemistry has been employed to control the crystalline morphology of a series of 13 precision branched polyethylene structures, the branch being placed on every 39th carbon and varying in size from methyl to pentadecyl. The primary structures of both monomers and polymers have been confirmed via ^{1}H NMR, ^{13}C NMR, and IR spectroscopy to prove the purity of the monomers and the absence of any undesired side reactions during polycondensation and hydrogenation steps. Methyl branches, being incorporated into the polymer crystal, decrease the melting point and the heat of fusion of **ADMET PE**. On the other hand, increasing the size of the branch to ethyl and larger yields a set of polymers with a completely different morphology, with the branches mostly expelled from the polymer crystal. WAXD patterns of melt-grown crystals and lamella thicknesses of the solution-grown single crystals also support this argument.

ASSOCIATED CONTENT

Supporting Information

Experimental procedures and spectral data for all monomers and polymers. This material is available free of charge via the Internet at http://pubs.acs.org.

AUTHOR INFORMATION

Corresponding Author

*E-mail: wagener@chem.ufl.edu.

Present Address

[§]Department of Chemistry and the Beckman Institute for Advanced Science and Technology, University of Illinois at Urbana−Champaign, Urbana, IL 61801.

Notes

The authors declare no competing financial interest.

ACKNOWLEDGMENTS

The authors thank the National Science Foundation (DMR-0703261) and the International Max Planck Research School for Polymer Materials (IMPRS) for financial support. The Army Research Office contributed to the catalyst work necessary to make proper selections. We also thank Michael Bach at Max Planck Institute for Polymer Research for his help with X-ray measurements and Sandra Seywald at Max Planck Institute for Polymer Research for her help with GPC measurements.

REFERENCES

(1) Till, P. *J. Polym. Sci.* **1957**, *24* (106), 301−306.
(2) Strobl, G. *Progress in Understanding of Polymer Crystallization*; Springer: Heidelberg, 2007.
(3) Organ, S.; Keller, A. *J. Mater. Sci.* **1985**, *20* (5), 1571−1585.
(4) Organ, S.; Keller, A. *J. Mater. Sci.* **1985**, *20* (5), 1586−1601.
(5) Organ, S.; Keller, A. *J. Mater. Sci.* **1985**, *20* (5), 1602−1615.
(6) Ungar, G.; Stejny, J.; Keller, A.; Bidd, I.; Whiting, M. *Science* **1985**, *229* (4711), 386−389.
(7) Bunn, C. *Trans. Faraday Soc.* **1939**, *35* (1), 0482−0490.
(8) Alamo, R.; Mandelkern, L. *Macromolecules* **1989**, *22* (3), 1273−1277.
(9) Alamo, R.; Mandelkern, L. *Thermochim. Acta* **1994**, *238*, 155−201.
(10) Hu, W.; Srinivas, S.; Sirota, E. *Macromolecules* **2002**, *35* (13), 5013−5024.
(11) deBallesteros, O.; Auriemma, F.; Guerra, G.; Corradini, P. *Macromolecules* **1996**, *29* (22), 7141−7148.
(12) Crist, B.; Howard, P. *Macromolecules* **1999**, *32* (9), 3057−3067.
(13) Crist, B.; Williams, D. *J. Macromol. Sci., Phys.* **2000**, *B39* (1), 1−13.
(14) Androsch, R.; Blackwell, J.; Chvalun, S.; Wunderlich, B. *Macromolecules* **1999**, *32* (11), 3735−3740.
(15) Richardson, M.; Flory, P.; Jackson, J. *Polymer* **1963**, *4* (2), 221−236.
(16) Perez, E.; Vanderhart, D.; Crist, B.; Howard, P. *Macromolecules* **1987**, *20* (1), 78−87.
(17) Howard, P.; Crist, B. *J. Polym. Sci., Part B: Polym. Phys.* **1989**, *27* (11), 2269−2282.
(18) Ziegler, K.; Holzkamp, E.; Breil, H.; Martin, H. *Angew. Chem., Int. Ed.* **1955**, *67* (16), 426−426.
(19) Ziegler, K.; Holzkamp, E.; Breil, H.; Martin, H. *Angew. Chem., Int. Ed.* **1955**, *67* (19−2), 541−547.
(20) Tait, P. *CHEMTECH* **1975**, *5* (11), 688−692.
(21) Sinn, H.; Kaminsky, W.; Vollmer, H.; Woldt, R. *Angew. Chem., Int. Ed. Engl.* **1980**, *19* (5), 390−392.
(22) Kaminsky, W.; Miri, M.; Sinn, H.; Woldt, R. *Makromol. Chem., Rapid Commun.* **1983**, *4* (6), 417−421.
(23) Kaminsky, W.; Hoff, M.; Derlin, S. *Macromol. Chem. Phys.* **2007**, *208* (13), 1341−1348.
(24) Gates, D.; Svejda, S.; Onate, E.; Killian, C.; Johnson, L.; White, P.; Brookhart, M. *Macromolecules* **2000**, *33* (7), 2320−2334.
(25) Mattice, W. *Macromolecules* **1983**, *16* (3), 487−490.
(26) Sworen, J.; Smith, J.; Wagener, K.; Baugh, L.; Rucker, S. *J. Am. Chem. Soc.* **2003**, *125* (8), 2228−2240.
(27) Sworen, J.; Smith, J.; Berg, J.; Wagener, K. *J. Am. Chem. Soc.* **2004**, *126* (36), 11238−11246.
(28) Sworen, J.; Wagener, K. *Macromolecules* **2007**, *40* (13), 4414−4423.
(29) Rojast, G.; Wagener, K. *Macromolecules* **2009**, *42* (6), 1934−1947.
(30) Rojas, G.; Berda, E.; Wagener, K. *Polymer* **2008**, *49* (13−14), 2985−2995.
(31) Rojas, G.; Inci, B.; Wei, Y. Y.; Wagener, K. B. *J. Am. Chem. Soc.* **2009**, *131* (47), 17376−17386.
(32) Wagener, K.; Valenti, D.; Hahn, S. *Macromolecules* **1997**, *30* (21), 6688−6690.
(33) Smith, J.; Brzezinska, K.; Valenti, D.; Wagener, K. *Macromolecules* **2000**, *33* (10), 3781−3794.
(34) Lieser, G.; Wegner, G.; Smith, J.; Wagener, K. *Colloid Polym. Sci.* **2004**, *282* (8), 773−781.
(35) Baughman, T.; Sworen, J.; Wagener, K. *Macromolecules* **2006**, *39* (15), 5028−5036.
(36) Zuluaga, F.; Inci, B.; Nozue, Y.; Hosoda, S.; Wagener, K. *Macromolecules* **2009**, *42* (14), 4953−4955.
(37) Hosoda, S.; Nozue, Y.; Kawashima, Y.; Suita, K.; Seno, S.; Nagamatsu, T.; Wagener, K.; Inci, B.; Zuluaga, F.; Rojas, G.; Leonard, J. *Macromolecules* **2011**, *44* (2), 313−319.
(38) Baughman, T.; Sworen, J.; Wagener, K. *Tetrahedron* **2004**, *60* (48), 10943−10948.
(39) Rojas, G.; Baughman, T.; Wagener, K. *Synth. Commun.* **2007**, *37* (22−24), 3923−3931.
(40) Rojas, G.; Wagener, K. *J. Org. Chem.* **2008**, *73* (13), 4962−4970.
(41) Ulman, M.; Grubbs, R. *J. Org. Chem.* **1999**, *64* (19), 7202−7207.
(42) Hong, S.; Day, M.; Grubbs, R. *J. Am. Chem. Soc.* **2004**, *126* (24), 7414−7415.

(43) Hong, S.; Wenzel, A.; Salguero, T.; Day, M.; Grubbs, R. *J. Am. Chem. Soc.* **2007**, *129* (25), 7961−7968.
(44) Courchay, F.; Sworen, J.; Ghiviriga, I.; Abboud, K.; Wagener, K. *Organometallics* **2006**, *25* (26), 6074−6086.
(45) Fokou, P.; Meier, M. *J. Am. Chem. Soc.* **2009**, *131* (5), 1664−1665.
(46) Grant, D.; Paul, E. *J. Am. Chem. Soc.* **1964**, *86* (15), 2984−2990.
(47) Liu, W.; Ray, D.; Rinaldi, P. *Macromolecules* **1999**, *32* (11), 3817−3819.
(48) Axelson, D.; Levy, G.; Mandelkern, L. *Macromolecules* **1979**, *12* (1), 41−52.
(49) Kuroda, N.; Nishikitani, Y.; Matsuura, K.; Ikegami, N. *Macromolecules* **1992**, *25* (11), 2820−2827.
(50) Rossi, A.; Zhang, J.; Odian, G. *Macromolecules* **1996**, *29* (7), 2331−2338.
(51) Luruli, N.; Heinz, L.; Grumel, V.; Brull, R.; Pasch, H.; Raubenheimer, H. *Polymer* **2006**, *47* (1), 56−66.
(52) Randall, J. C. *J. Polym. Sci., Part B: Polym. Phys.* **1973**, *11* (2), 275−287.
(53) Striegel, A. M.; Krejsa, M. R. *J. Polym. Sci., Part B: Polym. Phys.* **2000**, *38* (23), 3120−3135.
(54) Hosoda, S.; Nomura, H.; Gotoh, Y.; Kihara, H. *Polymer* **1990**, *31* (10), 1999−2005.
(55) Butler, M.; Donald, A.; Bras, W.; Mant, G.; Derbyshire, G.; Ryan, A. *Macromolecules* **1995**, *28* (19), 6383−6393.
(56) Russell, K.; McFaddin, D.; Hunter, B.; Heyding, R. *J. Polym. Sci., Part B: Polym. Phys.* **1996**, *34* (14), 2447−2458.
(57) Seto, T.; Hara, T.; Tanaka, K. *Jpn. J. Appl. Phys.* **1968**, *7* (1), 31−42.
(58) Hu, W.; Sirota, E. *Macromolecules* **2003**, *36* (14), 5144−5149.
(59) Inci, B.; Wagener, K. *J. Am. Chem. Soc.* **2011**, *133* (31), 11872−11875.
(60) Iakoubovskii, K.; Mitsuishi, K.; Nakayama, Y.; Furuya, K. *Microsc. Res. Tech.* **2008**, *71* (8), 626−631.
(61) Egerton, R. F. *Electron Energy Loss Spectroscopy in the Electron Microscope*; Plenum Press: New York, 1996.

Macromolecules

Article

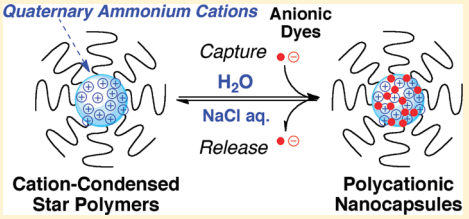
pubs.acs.org/Macromolecules

Cation-Condensed Microgel-Core Star Polymers as Polycationic Nanocapsules for Molecular Capture and Release in Water

Kaoru Fukae, Takaya Terashima,* and Mitsuo Sawamoto*

Supporting Information

ABSTRACT: Cation-condensed microgel-core star polymers with poly(ethylene glycol) (PEG)-based arms were designed as unimolecular polycationic nanocapsules (hosts) to encapsulate and stimuli-responsively release hydrophilic and anionic dyes (guests) in water. Typically, a cation-condensed star polymer (core cations: ~670/star) was directly synthesized in high yield (>90%) by the linking reaction of a PEG macroinitiator (**1**) with a quaternary ammonium cation-carrying linking agent (**2**) in ruthenium-catalyzed living radical polymerization. Analyzed by UV−vis spectroscopy, the star polymer efficiently encapsulated various hydrophilic dyes carrying sulfonate anions (methyl orange: MO; orange G: OG; methyl blue: MB) in water (UV−vis: ~400 OG per a single star). The efficient dye encapsulation is due to the high concentration of quaternary ammonium cations in the core. The number of core-bound dyes increased with increasing the number of core-bound cations. The ligation structure of dyes within the core was proposed: the immobilization of one OG molecule involves two in-core ammonium cations. Additionally, stimuli-responsive release of dyes from cation-condensed star polymers was successfully achieved via ion exchange with NaCl aqueous solution.



INTRODUCTION

Globular macromolecules often carry interior compartments that may serve as nanocapsules. Macromolecular or polymeric capsules comprising well-defined and spatially isolated cavities are now key materials for delivery (drug, gene, and imaging agents), catalyst scaffolds, microreactors, and biomedical applications, among others.[1] Depending on their constructive aspects, these nanocapsules may be divided into two categories, physical and chemical: The physical capsules involve aggregates of amphiphilic molecules and block copolymers, such as micelles,[2,3] vesicles (polymersomes),[4,5] and nanogels.[6] The chemical capsules implies cross-linked and/or branched molecules, such as nanogels,[6a−c,7] cross-linked micelles,[8] microgel-core star polymers,[9−18] hyperbranched polymers,[19] and dendrimers.[20,21] Though polymeric scaffolds and capsules, either physical or chemical, can be designed to meet specific objectives and applications, sophisticated functions often require complex architectures and thus impose cumbersome and multistep preparation.

Microgel-core star polymers,[9−18] a unique class in nanogels, carry nanoscale cross-linked central cores (10−30 nm in diameter) that are covered by multiple linear polymeric arms with which, despite the gel core, the entire molecules are totally soluble in common solvents. Different from other complex capsules and dendrimers, their synthesis is straightforward, efficient, and versatile, simply based on a living polymerization followed by an in-situ polymer "linking", in which linear living polymers (for arms) are linked with a small amount of divinyl compounds (for cores).[9] Living radical polymerization[22] is especially suitable for microgel-core star polymers[10] because it proceeds via the neutral propagating species to facilely afford direct functionalization, either on arms or cores or both, with the use of functional monomers and/or linking agents without protection and deprotection. These star polymers are thus expected to be soluble, unimolecular compartments (nanocapsules) with the core network structures.

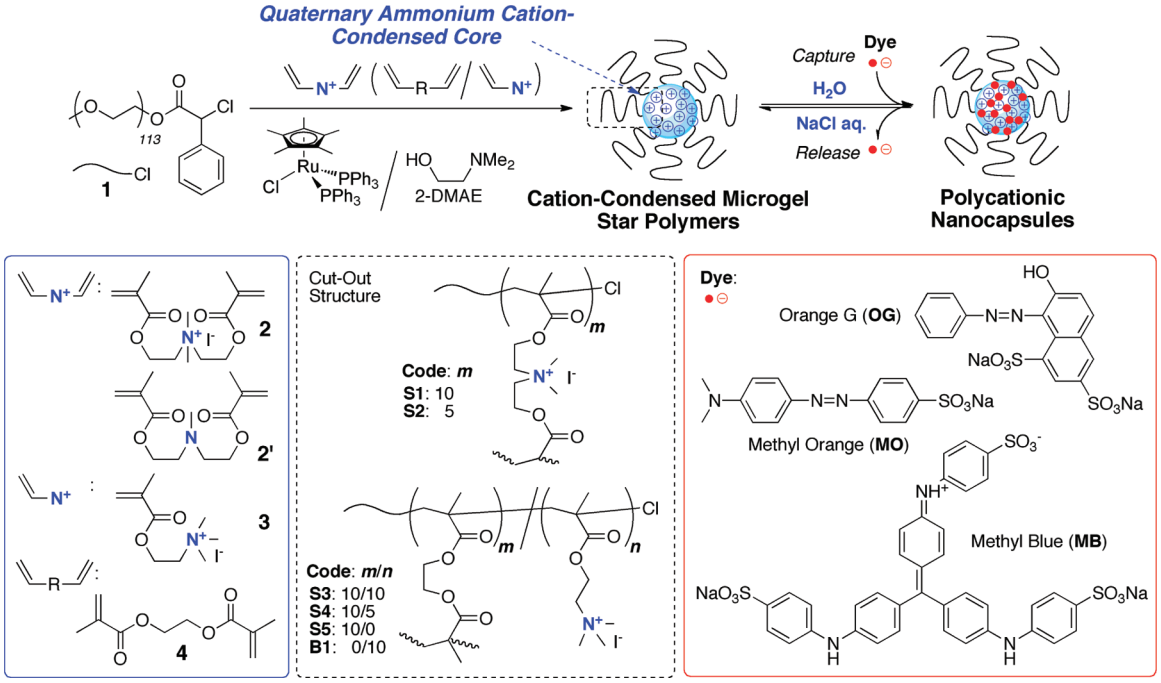
Focused on the characteristic environment of the microgel core, core-functionalized star polymers[12−18] have been designed by living radical polymerization to create inherent functions. We have already obtained various core-functionalized star polymers[12−14] by the arm-linking reaction with functional linking agents and/or monomers (cores) in ruthenium-catalyzed living radical polymerization.[22a,b,23] The "core" functional groups including amide or hydroxyl groups,[12] perfluoroalkanes,[14] phosphine ligands, and metals[13] are introduced and condensed into their cores to perform unique molecular recognition[12,14] and catalysis.[13] For examples, amide-functionalized microgel star polymers worked as molecular-recognition hosts that selectively interact with acids (guests) via hydrogen bonding.[12b] Other examples include, among others, fluorinated or "fluorous" microgel star polymers, which not only solubilized perfluoroalkanes in organic media but also selectively and efficiently entrapped the compounds into the core via fluorous interaction.[14] These unique recognitions are specifically derived from the microgel core that owns a fixed, rigid network structure with highly condensed functional groups. These results suggest that the condensation of functional groups into star polymer cores is a key to efficiently entrap guest molecules via specific interaction, leading to star polymers as unique, stable unimolecular nanocapsules.

In this work, we now directed our efforts to "ionic" microgel cores and thus designed water-soluble star polymers with

Received: February 8, 2012
Revised: March 16, 2012
Published: April 2, 2012

 © 2012 American Chemical Society dx.doi.org/10.1021/ma300266k | *Macromolecules* 2012, 45, 3377−3386

Scheme 1. Synthesis of Cation-Condensed Microgel Star Polymers via Ru-Catalyzed Living Radical Polymerization and Encapsulation and Release of Hydrophilic Dyes in Water



cation-condensed microgel cores. The expected functions therefore include unimolecular polycationic nanocapsules (hosts) to capture and stimuli-responsively release hydrophilic and anionic dyes (guests) in water (Scheme 1). Typically, these star polymers were directly and homogeneously synthesized in high yield (>90%) by ruthenium-catalyzed living radical polymerization, and in the core-forming linking step, a small amount of a quaternary ammonium cation-bearing linking agent (**2**) was polymerized with a chlorine-capped poly(ethylene glycol) methyl ether macroinitiator (PEG-Cl: **1**) in the presence of ruthenium pentamethylcyclopentadienyl bistriphenylphosphine chloride [RuCp*Cl(PPh_3)$_2$][23a] (catalyst) and 2-(dimethylamino)ethanol [2-DMAE][23d,f,24] (cocatalyst) in ethanol and *N*,*N*-dimethylformamide (DMF). The high activity and versatility of ruthenium-mediated system for functional monomers[23b,d−f] allowed the direct and selective incorporation of quaternary ammonium cations[25] into the core without any postquaternization of amines often required in the synthesis of similar polymers.[26]

Because of their high charge density, polycations[27−33] and related polyelectrolytes are known to bind counterions in solution more effectively than monomeric electrolytes with free counterions.[27,29−32] Thus, focusing on the unique cation-enriched cores in our star polymers, we investigated the encapsulation of hydrophilic anionic dyes [methyl orange (MO), orange G (OG), and methyl blue (MB)] into the core (Scheme 1). The molecular recognition was examined in water under homogeneous conditions, although similar molecular encapsulation by polycationic scaffolds generally occurs in organic/aqueous biphasic media.[19,21b,c] With the high local concentration of quaternary ammonium cations, the star polymers effectively captured these anionic dyes via the anion exchange between the in-core iodide (the original counteranion) and the sulfate moiety in the dye. The controlled release of core-bound dyes was also examined via the anion exchange using sodium chloride water. UV−vis analysis of the interacting cores further indicated unique environments of the cores with dyes, in addition to the contents of core-bound dyes. Discussion was especially directed to the unique performance of the star polymers as unimolecular polycationic nanocapsules in water, in sharp contrast to that of quaternary ammonium block copolymers.

EXPERIMENTAL SECTION

Materials for a Macroinitiator, a Linking Agent, and a Monomer. Poly(ethylene glycol) methyl ether (Aldrich, M_n = 5000, averaged ethylene oxide units: 113), *N*-methyldiethanolamine (TCI, purity >99%), and methyl iodide (TCI, purity >99.5%) were used as received. 2-(Dimethylamino)ethyl methacrylate (TCI, purity >98.5%) was purified by passing through inhibitor remover (Aldrich). *α*-Chlorophenylacetyl chloride (Aldrich, purity >90%), methacryloyl chloride (TCI, purity >80%), and triethylamine (Wako, purity >99%) were purified by distillation before use. Dichloromethane (Wako, dehydrated), acetonitrile (Wako, dehydrated), diethyl ether (Wako, purity >99.5%), and 25% ammonia solution (Wako) were used as received. Toluene was purified by passing it through a purification column (Glass Contour Solvent Systems by SG Water).

Materials for Polymers. A chlorine-capped poly(ethylene glycol) methyl ether macroinitiator [PEG-Cl (**1**)] was prepared according to the literature.[34] A cationic linking agent (**2**) and monomer (**3**) were synthesized as shown below. Ethylene glycol dimethacrylate (**4**: Aldrich, purity >98%) was purified by distillation from calcium hydride before use. RuCp*Cl(PPh_3)$_2$[23a] (Cp*: pentamethylcyclopentadienyl, Aldrich, purity >97%) was handled in a glove box under a moisture- and oxygen-free argon atmosphere (H_2O < 1 ppm, O_2 < 1 ppm). 2-(Dimethylamino)ethanol (2-DMAE: TCI, purity >99%) and 4-(dimethylamino)-1-butanol (4-DMAB: TCI, purity >98%)[23d,24] were degassed by reduced pressure before use. Tetralin (1,2,3,4-tetrahydronaphthalene: Kisida Chemical, purity >98%)] as an internal standard for **4** in gas chromatography or **2** and **3** in ^{1}H NMR was dried over calcium chloride overnight and distilled twice from calcium hydride. Ethanol (Wako, dehydrated), dimethylformamide (Wako, dehydrated), and water (Wako, deionized) for polymerization solvents were purged by argon before use. Regenerated cellulose dialysis

dx.doi.org/10.1021/ma300266k | *Macromolecules* 2012, 45, 3377−3386

membranes (Spectra/Por 6; MWCO 15 000 or 1000) were used as received.

Materials for Molecular Recognition. Orange G (OG: Wako), methyl orange (MO: Wako), and methyl blue (MB: Kanto Chemical) were used as received. Sodium chloride (Wako, purity >99.5%) and a regenerated cellulose dialysis membrane (Spectra/Por 6; MWCO 1000) were used as received.

Characterization. The MWD, M_n, and M_w/M_n ratios of polymers were measured by SEC in DMF containing 10 mM LiBr at 40 °C (flow rate: 1 mL/min) on three linear-type polystyrene gel columns (Shodex KF-805 L; exclusion limit = 4×10^6; particle size = 10 μm; pore size = 5000 Å; 0.8 cm i.d. × 30 cm) that were connected to a Jasco PU-2080 precision pump, a Jasco RI-2031 refractive index detector, and a Jasco UV-2075 UV/vis detector set at 270 nm. The columns were calibrated against 10 standard samples of poly(ethylene glycol) and poly(ethylene oxide) (Polymer Laboratories; M_n = 1460−737 000; M_w/M_n = 1.03−1.07). ^{1}H NMR spectra were recorded in $CDCl_3$, DMSO-d_6, CD_3OD, and D_2O at 25 °C on a JEOL JNM-LA500 spectrometer, operating at 500.16 MHz. Matrix-assisted laser desorption/ionization time-of-flight mass spectrometry (MALDI-TOF-MS) analysis was performed on a Shimadzu AXIMA-CFR instrument equipped with 1.2 m linear flight tubes and a 337 nm nitrogen laser with dithranol (1,8,9-anthracenetriol) as an ionizing matrix and sodium trifluoroacetate as a cationizing agent. Electorospray ionization mass spectrometry (ESI-MS) was performed on Waters Quattro micro API. The absolute weight-average molecular weight (M_w) and radius of gyration (R_g) for star polymers were determined by multiangle laser light scattering (MALLS) equipped with SEC in DMF containing 10 mM LiBr at 40 °C on a Dawn E instrument (Wyatt Technology; Ga−As laser, λ = 690 nm). The refractive index increment (dn/dc) was measured in DMF at 40 °C on an Optilab DSP refractometer (Wyatt Technology; λ = 690 nm, c < 2.5 mg/mL). Dynamic light scattering (DLS) was measured on Otsuka Photal ELSZ-0 equipped with a semiconductor laser (wavelength: 658 nm) at 25 °C. The measuring angle was 165°, and the data were analyzed by the CONTIN fitting method. Ultraviolet−visible (UV/vis) spectra were obtained from Shimadzu MultiSpec 1500 in H_2O at room temperature (optical path length = 1.0 cm). The amounts of polymer-bound orange G were determined by using the absorbance at 478 nm in water and the calibration plots for orange G (4.4−66 μM) at the same wavelength in water. Differential scanning calorimetry (DSC) was performed for polymer samples (ca. 3 mg: filled in aluminum pans) under dry nitrogen flow on a DSCQ200 calorimeter (TA Instruments) equipped with a RCS90 electric freezing machine. The heating and cooling rates were performed at 10 and −10 °C/min, respectively, between −80 and 150 °C.

Synthesis of PEG-Cl (1). In 300 mL round-bottomed flask filled with argon, α-chlorophenylacetyl chloride (8.14 mmol, 1.29 mL) was added dropwise to a solution of poly(ethylene glycol) methyl ether (5.43 mmol, 27.14 g) and triethylamine (8.14 mmol, 1.13 mL) in dry CH_2Cl_2 (200 mL) at 0 °C. The reaction mixture was stirred at 0 °C for 2 h and then at 25 °C for an additional 22 h. After the reaction, the solution was filtrated and precipitated into diethyl ether twice. The resultant product was dried overnight under reduced pressure. Quantitative esterification of the terminal hydroxyl group in a poly(ethylene glycol) methyl ether was confirmed by MALDI-TOF MS. SEC (DMF, PEG/PEO standard): M_n = 4800; M_w/M_n = 1.06. ^{1}H NMR [500 MHz, $CDCl_3$, rt, δ = 0 (TMS)]: δ 7.5−7.3 (aromatic, 5H), 5.4 (COCHPhCl, 1H), 4.3−4.2 (−$CH_2C\underline{H}_2$OCO, 2H), 3.8−3.4 (−CH_2CH_2O−), 3.3 ($C\underline{H}_3O$−, 3H).

Synthesis of a Linking Agent (2) and a Monomer (3). Quaternary ammonium cation-bearing linking agent (**2**) and monomer (**3**) (Scheme 1) were synthesized by the quaternization of their corresponding amine-bearing linking agent (**2′**) and monomer (DMAEMA) with methyl iodide, respectively.

2: In 500 mL round-bottomed flask filled with argon, methacryloyl chloride (176 mmol, 17 mL) was added dropwise to a solution of *N*-methyldiethanolamine (80 mmol, 9.17 mL) and triethylamine (176 mmol, 24.5 mL) in dry CH_2Cl_2 (250 mL) at 0 °C. The reaction mixture was stirred at 0 °C for 2 h and then at 25 °C for an additional 22 h and poured into distilled water (200 mL). The organic layer was then separated and concentrated under reduced pressure. The condensed organic solution was diluted with 200 mL of diethyl ether and washed with 200 mL of 25% ammonia−water, followed by 200 mL of distilled water twice. The organic layer was dried on sodium sulfate overnight and evaporated to dryness under reduced pressure. The product (*N*-methylaminodiethanol dimethacrylate: **2′**; yield: 67%) was applied to the next reaction without further purification. In 100 mL round-bottomed flask filled with argon, a 2069 mM toluene solution of **2′** (23.8 mmol, 11.5 mL) was stirred with methyl iodide (23.8 mmol, 2.52 mL) in dry acetonitrile (20 mL) at 25 °C for 12 h under shading. The solution was precipitated into diethyl ether (100 mL) twice, and the resulting white solid product (**2**) was dried overnight. Yield: 63%. ^{1}H NMR [500 MHz, DMSO-d_6, rt, δ = 2.49 ppm (DMSO)]: δ 6.07, 5.75 (olefin, 4H), 4.55 (4H, −OC$\underline{H}_2CH_2$N−), 3.85 (4H, −OCH$H_2C\underline{H}_2$N−), 3.22 (6H, N-(CH_2−)$_2$($C\underline{H}_3$)$_2$I), 1.88 (6H, −C(CO)CH_3). ^{13}C NMR [125 MHz, DMSO-d_6, rt, δ = 39.7 ppm (DMSO)]: δ 166.0, 135.5, 126.9, 62.6, 58.2, 51.4, 18.1. ESI-MS: m/z: 270.1 $[M - I^-]^+$.

3: In 100 mL round-bottomed flask filled with argon, 2-(dimethylamino)ethyl methacrylate (50 mmol, 8.43 mL) and methyl iodide (50 mmol, 2.52 mL) were stirred in dry toluene (30 mL) at 25 °C for 12 h under shading. The solution was precipitated into diethyl ether (100 mL) twice, and the resulting white solid product (**3**) was dried overnight. Yield: 88%. ^{1}H NMR [500 MHz, CD_3OD, rt, δ = 3.3 ppm ($C\underline{H}_3OH$)]: δ 6.16, 5.71 (olefin, 2H), 4.62 (m, 2H, −OC$\underline{H}_2CH_2$N−), 3.78 (m, 2H, −$OCH_2C\underline{H}_2$N−), 3.24 (s, 9H, −N($C\underline{H}_3$)$_3$I), 1.96 (t, 3H, −C(CO)CH_3). ^{13}C NMR [125 MHz, CD_3OD, rt, δ = 49.0 ppm (CH_3OH)]: δ 167.6, 137.0, 127.4, 66.2, 59.3, 54.6, 18.4. ESI-MS: m/z: 172.2 $[M - I^-]^+$.

Synthesis of Polymers. The synthesis of polymers (**S1**−**S5**, **B1**) was carried out by the syringe technique under argon in baked glass tubes equipped with a three-way stopcock via ruthenium-catalyzed living radical polymerization.

S1: **1** (0.103 mmol, 0.53 g) was placed in a 30 mL glass tube. Into the tube, ethanol (1.28 mL), tetralin (0.10 mL), a 500 mM ethanol solution of 2-DMAE (0.205 mmol, 0.41 mL), a 733 mM DMF solution of **2** (1.03 mmol, 1.40 mL), and a 5.3 mM ethanol solution of $RuCp^*Cl(PPh_3)_2$ (0.0103 mmol, 1.94 mL) were added sequentially in this order at 25 °C under argon. The total volume of the reaction mixture was thus 5.6 mL. The tube with the mixture was placed in an oil bath at 40 °C. In predetermined intervals, the reaction was terminated by cooling the mixture to −78 °C. The conversion of **2** was determined by ^{1}H NMR with tetralin as an internal standard. After 25 h (conversion = 90%), the quenched reaction mixture was evaporated to dryness under reduced pressure. The resulting crude was dialyzed in methanol with a regenerated cellulose membrane (Spectra/Por 6; MWCO 15 000) for 1 day and in dichloromethane for an additional 1 day. The inner purified solution was evaporated to dryness under reduced pressure to give a white solid product (**S1**). Star yield (SEC): 91%. dn/dc (DMF) = 0.076. SEC-MALLS (DMF, 0.01 M LiBr): $M_{w,star}$ = 617 000 g/mol; arm number = 68; R_g = 11 nm. ^{1}H NMR [500 MHz, CD_3OD, δ = 3.3 ($C\underline{H}_3OH$)]: δ 7.5−7.2 (aromatic), 3.8−3.5 (−OCH_2CH_2O−), 3.36−3.34 (−OCH_3), 1.8−0.7 (−$CH_2C\underline{H}_3$− in core, broad). **S2** was similarly synthesized with the different mole ratio of **2** (r_2 = 5.0): dn/dc (DMF) = 0.068.

S3: **1** (0.0996 mmol, 0.51 g) and **3** (0.996 mmol, 0.27 g) were placed in a 30 mL glass tube. Into the tube, ethanol (1.29 mL), H_2O (1.25 mL), tetralin (0.10 mL), a 500 mM ethanol solution of 2-DMAE (0.199 mmol, 0.40 mL), a 1842 mM ethanol solution of **4** (0.996 mmol, 0.53 mL), and a 7.04 mM ethanol solution of $RuCp^*Cl(PPh_3)_2$ (0.009 96 mmol, 1.46 mL) were added sequentially in this order at 25 °C under argon. The total volume of the reaction mixture was thus 5.8 mL. The tube with the mixture was placed in an oil bath at 40 °C. In predetermined intervals, the reaction was terminated by cooling the mixture to −78 °C. The conversion of **3** and **4** was determined by ^{1}H NMR and gas chromatography, respectively, with tetralin as an internal standard. After 8 h (conversion **3**/**4** = 91/97%), the quenched reaction mixture was evaporated to dryness under reduced pressure. The resulting crude was dialyzed in methanol with a regenerated cellulose

dx.doi.org/10.1021/ma300266k | *Macromolecules* 2012, 45, 3377−3386

membrane (Spectra/Por 6; MWCO 15 000) for 1 day and in dichloromethane for an additional 1 day. The inner purified solution was evaporated to dryness to give a white solid product (**S3**). Star yield (SEC): 89%. dn/dc (DMF) = 0.077. SEC-MALLS (DMF, 0.01 M LiBr): $M_{w,star}$ = 950 000 g/mol; arm number = 97; R_g = 21 nm. ^{1}H NMR [500 MHz, CD_3OD, δ = 3.3 ($C\underline{H}_3OH$)]: δ 7.5–7.2 (aromatic), 3.8–3.5 ($-OCH_2CH_2O-$), 3.5–3.2 ($-N(CH_3)_3I$), 3.36–3.34 ($-OCH_3$), 2.2–2.0 ($-C\underline{H}_2CCH_3-$ in core, broad), 1.8–0.7 ($-CH_2CC\underline{H}_3-$ in core, broad). **S4** and **S5** were similarly synthesized with the different mole ratio of **3** (r_3 = 5.0, 0): dn/dc (DMF) = 0.064 (**S4**), 0.055 (**S5**).

B1: **1** (0.0848 mmol, 0.44 g) and **3** (0.848 mmol, 0.23 g) were placed in a 30 mL glass tube. Into the tube, ethanol (1.15 mL), H_2O (1.06 mL), tetralin (0.10 mL), a 500 mM ethanol solution of 2-DMAE (0.170 mmol, 0.34 mL), and a 5.33 mM ethanol solution of $RuCp^*Cl(PPh_3)_2$ (0.008 48 mmol, 1.59 mL) were added sequentially in this order at 25 °C under argon. The total volume of the reaction mixture was thus 4.9 mL. The tube with the mixture was placed in an oil bath at 40 °C. In predetermined intervals, the reaction was terminated by cooling the mixture to −78 °C. The conversion of **3** was determined by gas chromatography with tetralin as an internal standard. After 10 h (conversion = 89%), the quenched reaction mixture was evaporated to dryness under reduced pressure. The resulting crude was dialyzed in methanol with a regenerated cellulose membrane (Spectra/Por 6; MWCO 1000) for 1 day and in dichloromethane for an additional 1 day. The purified inner solution was evaporated to dryness to give a white solid product (**B1**). SEC (DMF, 0.01 M LiBr, PEG standard): M_n = 3800 g/mol; M_w/M_n = 1.19. ^{1}H NMR [500 MHz, CD_3OD, δ = 3.3 ($C\underline{H}_3OH$)]: δ 7.4–7.2 (5H, aromatic), 4.4–4.6 ($-OC\underline{H}_2CH_2N-$), 4.2–3.8 ($-OCH_2C\underline{H}_2N-$), 3.7–3.6 ($-OCH_2CH_2O-$), 3.6–3.3 ($-N^+(CH_3)_3$), 3.3–3.4 ($-OCH_3$), 2.3–1.9 ($-C\underline{H}_2CCH_3-$), 1.4–1.1 ($-CH_2CC\underline{H}_3-$); M_n (NMR) = 7900 g/mol.

Encapsulation of Dyes into Polymers in Water. A typical procedure to capture orange G (OG) into **S1** in water was given: In a 10 mL vial, **S1** (8.7 mg) and OG (4.35 mg) were stirred in water (8.7 mL) for 2 h. The mixture was dialyzed in water with a regenerated cellulose membrane (Spectra/Por 6; MWCO 1000), in which the water was changed every 3 h for 1 day and every 12 h for 1 week. The inner solution was then evaporated to dryness under reduced pressure. The resulting product was dissolved in water and analyzed by UV–vis spectroscopy. UV–vis (calibration plots of OG at 478 nm): 672 μmol OG/g-polymer; the number of OG in a polymer ($N_{OG/polymer}$) = 414.

Release of Orange G from Polymers with NaCl(aq). Release of OG from polymers (**S1** and **B1**) was investigated via anion exchange with the dialysis of aqueous solutions of OG-bearing polymers with 0.1 M NaCl aqueous solutions. A typical procedure for OG-carrying **S1** was given: Three aliquots (1.0 mL each) of 1 mg/mL aqueous solutions of OG-containing **S1** (3 mL) were distributed into dialysis membranes (Spectra/Por 6; MWCO 1000), and the membranes were placed in 0.1 M NaCl aqueous solutions (100 mL). In predetermined intervals (2, 10, and 24 h), one of the membranes was placed in pure water (1000 mL) and dialyzed for 24 h, where the water was changed three times. The inner solution was evaporated to dryness. The resulting product was dissolved in water and analyzed by UV–vis to determine the content of OG (moles) per gram of polymer.

RESULTS AND DISCUSSION

Synthesis and Characterization of Ion-Condensed Microgel Star Polymers. Water-soluble and cation-condensed microgel-core star polymers (**S1**–**S4**) were directly synthesized by ruthenium-catalyzed living radical polymerization of a quaternary linking agent (**2**) or copolymerization of a quaternary monomer (**3**) and ethylene glycol dimethacrylate (**4**), in conjunction with a PEG-based chloride initiator [PEG-Cl (**1**): M_n = 4800; M_w/M_n = 1.06 (DMF, PEG/PEO standard)] (Scheme 1, Figures 1 and S1, Table 1). A ruthenium pentamethylcyclopentadienyl (Cp*) complex [$RuCp^*Cl(PPh_3)_2$][23a] was employed as a catalyst because the ruthenium shows the high controllability and functionality tolerance to be applicable to alcohol and/or water-mediated polymerization of polar functional monomers.[23d]

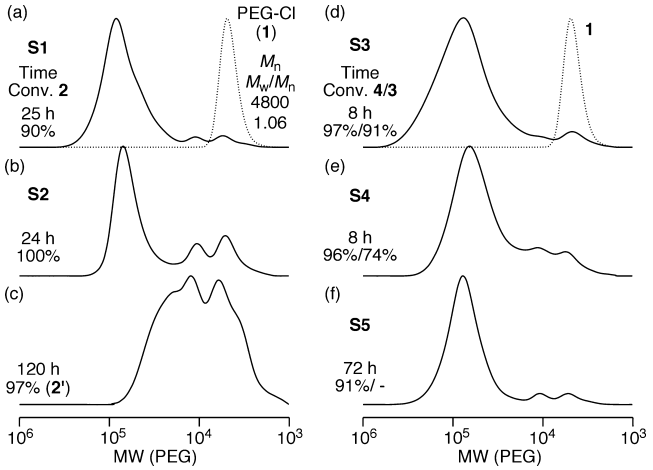


Figure 1. SEC curves of cation-condensed microgel star polymers (a: **S1**; b: **S2**; d: **S3**; e: **S4**), an amine-bearing polymer (c), and a nonionic microgel star polymer (f: **S5**), obtained from ruthenium-catalyzed living radical polymerization of **2**, (**3** and **4**), **2′**, and **4** with PEG-Cl (**1**). (a–c) [**1**]/[**2** (**S1**, **S2**) or **2′** (c)]/[$RuCp^*Cl(PPh_3)_2$]/[2-DMAE] = 20/200 (**S1**, c) or 100 (**S2**)/2.0/40 mM in EtOH/DMF (3/1, v/v) at 40 °C. (d–f) [**1**]/[**4**]/[**3′**]/[$RuCp^*Cl(PPh_3)_2$]/[2-DMAE (**S3**, **S4**) or 4-DMAB (**S5**)] = 20/200/200 (**S3**), 100 (**S4**), 0 (**S5**)/2.0/40 mM in EtOH/H_2O (3/1, v/v: **S3**, **S4**) or EtOH (**S5**) at 40 °C.

Typically for **S1**, **2** was polymerized with **1**, $RuCp^*Cl(PPh_3)_2$, and 2-(dimethylamino)ethanol (2-DMAE)[23d] in EtOH/DMF (3/1, v/v) at 40 °C. The feed ratio of **2** to **1** ($r_2 = [\mathbf{2}]_0/[\mathbf{1}]_0 = \boldsymbol{m}$) was set as 10. **2** was smoothly consumed up to 90% conversion in 25 h (Figure S1a). Analyzed by size exclusion chromatography (SEC), a cation-condensed microgel star polymer (**S1**) with narrow molecular weight distribution (MWD: M_w/M_n <1.2) was obtained in high yield (90%) (Figures 1a and S1b). The intermediates and/or products were further analyzed by ^{1}H NMR spectroscopy (Figure S2). Their olefin signals gradually broadened and decreased as the polymerization proceeded, meaning that PEG block arms carrying pendant olefins were initially formed and subsequently intermolecularly cross-linked to form cation-condensed microgel cores. Similarly, a star polymer (**S2**) with a small content of **2** (r_2 = 5) was also obtained (Figure 1b, Table 1).

Cation-condensed star polymers (**S3**, **S4**) with core-bound quaternary ammonium pendants and a cation-pendant block copolymer (**B1**) were efficiently and homogeneously synthesized by $RuCp^*Cl(PPh_3)_2$/2-DMAE-mediated copolymerization of **3** and/or **4** with **1** in EtOH/H_2O (3/1, v/v) in high yield (80–90%) {$r_4 = [\mathbf{4}]_0/[\mathbf{1}]_0 = \boldsymbol{m}$, $r_3 = [\mathbf{3}]_0/[\mathbf{1}]_0 = \boldsymbol{n}$, r_4/r_3 = 10/10 (**S3**), 10/5 (**S4**), 0/10 (**B1**)} (Figure 1d–f, Table 1). A noncationic PEG star with narrow MWD (**S5**: r_4/r_3 = 10/0; $M_w/M_n \sim$ 1.1) was also obtained with **4** and **1** in EtOH in high yield. On the contrary, a tertiary amine bearing-linking agent (**2′**), the precursor of **2**, never efficiently gave star polymers, independent of catalytic systems (Figures 1c and S3). Thus, the most stable conformation of **2′** was compared with that of **2**, calculated by a MO-G program (a semiempirical molecular orbital program) with AM1 (Hamiltonian) on SCIGRESS, FUJITSU. The distance between two divinyl groups of **2′** (~5.1 Å) was closer than that of **2** (~6.8 Å) (Figure S4). Owing to

dx.doi.org/10.1021/ma300266k | Macromolecules 2012, 45, 3377–3386

Table 1. Characterization of Star Polymers by SEC-MALLS[a]

code	L[a]	r_L[a]	r_3[a]	time (h)	conv[b] (L/3, %)	yield[c] (%)	M_w[d] (SEC)	M_w/M_n[d]	$M_{w,star}$[e] (MALLS)	M_n[f] (NMR)	N_{arm}[g]	R_g[e] (nm)	N_{N+}[h]
S1	**2**	10		25	90/–	91	99 000	1.14	617 000		68	16	666
S2	**2**	5		24	100/–	70	70 000	1.10	298 000		42	14	206
S3	**4**	10	10	8	97/91	89	107 000	1.63	950 000		97	22	880
S4	**4**	10	5	8	96/74	80	76 000	1.24	500 000		61	18	228
S5	**4**	10		72	91/–	91	92 000	1.11	513 000		74	10	
B1			10	10	–/89		4600	1.16		7900			9.3

[a] $[L]_0/[3]_0/[1]_0/[RuCp^*Cl_2(PPh_3)_2]_0/$[2-DMAE (**S1**–**S4**, **B1**) or 4-DMAB (**S5**)]$_0$ = 200, 100/10, 5, 0/20/2/40 mM in EtOH/DMF (3/1, v/v: **S1**, **S2**), EtOH/H_2O (3/1, v/v: **S3**, **S4**, **B1**), and EtOH (**S5**) at 40 °C: L (linking agent) = **2** or **4**; $r_L = [L]_0/[1]_0 = m$, $r_3 = [3]_0/[1]_0 = n$. [b] Determined by ^{1}H NMR (**2**, **3**) and G.C. (**4**) with tetralin as an internal standard. [c] Yield of star polymers calculated from the area ratio in SEC curves. [d] M_w (SEC) and M_w/M_n of polymers determined by SEC in DMF (10 mM LiBr) with PEG/PEO standards. [e] $M_{w,star}$ (MALLS) and R_g of star polymers determined by SEC-MALLS in DMF (10 mM LiBr). [f] Number-average molecular weight [M_n (NMR)] determined by ^{1}H NMR. [g] The number of arms per a single star polymer: N_{arm} = (weight fraction of arms) × $M_{w,star}$ (MALLS)/$M_{w,arm}$ (SEC) [**1**: $M_{w,arm}$ (SEC) = 5100]. [h] The number of quarternary ammonium cations in a single polymer: $N_{N+} = N_{arm} \times (r_2$ or $r_3) \times$ (conv/100).

the relatively adjacent location of the respective olefins, **2′** would often tend to induce intramolecular cyclopropagation in addition to the intermolecular cross-linking of PEG block arms, resulting in low yield of star polymers. Rather interestingly, the quarternization of the spacer of **2′** triggered the efficient formation of star polymers.

Star polymers (**S1**–**S5**) were characterized by multiangle laser light scattering coupled with SEC (SEC-MALLS) in DMF (Table 1). They had 298 000–950 000 of absolute weight-average molecular weight (M_w), 42–97 of the number of PEG arms (N_{arm}), and 10–22 nm of radius of gyration (R_g). Their M_ws determined by SEC were smaller than their M_ws by SEC-MALLS because star polymers form globular structures that are more compact than linear counterparts. The number of quaternary ammonium cations in a single star core (N_{N+}) was calculated from N_{arm}, the feed ratio of a cationic linking agent or monomer (r_2, r_3), and their conversions [$N_{N+} = N_{arm} \times (r_2$ or $r_3) \times$ (conv/100)]. **S1**–**S4** had about 200–880 of ammonium cations in single cores, indicating that the cations were highly condensed and localized in nano-cross-linked cores.

S1, **S3**, and **B1** were analyzed by ^{1}H NMR in CD_3OD at room temperature (Figure 2). The core-bound cation spacers and polymethacrylate backbones in **S1** were hardly detected, while the linear polycationic segment in **B1** was clearly observed.[11] Even quaternary ammonium pendants (*h*) in a **S3** core showed much less extent than those in **B1**. These results demonstrate that the ammonium cations in star polymers were rigidly fixed within the cores to show low mobility.

Solid properties of **S1**, **S5**, and **B1** were evaluated by differential scanning calorimetry (DSC) (Table S1, Figure S5). Owing to their PEG segments,[35] all of the products showed clear melting temperatures [T_m = 59.6 (**1**), 56.2 (**B1**), 49.4 (**S5**), 40.3 (**S1**)] and crystalline temperatures [T_c = 36.2 (**1**), 38.8 (**B1**), 3.2 (**S5**), and 1.0 (**S1**)] as well as PEG-Cl (**1**). Both of T_m and T_c for star polymers (**S1**, **S5**) were smaller than those for linear counterparts (**B1** and **1**), suggesting that the crystallinity of PEG chains in star polymers was smaller than that in linear ones. This is probably because PEG arms in star polymers are tethered to the cores to interfere the effective intermolecular crystallization.

Encapsulation and Release of Dyes in Water. Since cation-condensed cores of star polymers (**S1**–**S4**) are compartmentalized by multiple PEG arms, the cores are expected to behave as unimolecular polycationic nanocapsules for anionic compounds in water. Thus, we examined the

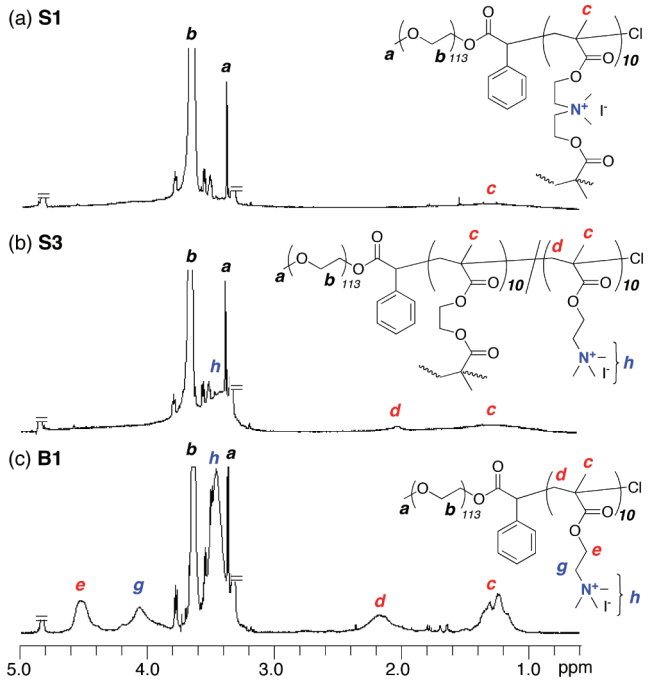


Figure 2. ^{1}H NMR spectra (500 MHz) of star polymers (a: **S1**; b: **S3**) and a block copolymer (c: **B1**) in CD_3OD at 25 °C.

encapsulation of water-soluble anionic dyes (guests) into cation-condensed microgel-core star polymers (**S1**–**S4**: hosts) in water, compared with a nonionic core star polymer (**S5**) and a cationic block counterpart (**B1**) (Figure 3). Methyl orange (MO), orange G (OG), and methyl blue (MB) were employed as guest molecules that carried mono-, di-, and trisubstituted sulfonate anions, respectively. The methodology was the following: (1) mixing a polymer and a dye in water to encapsulation dyes; (2) dialysis of the mixture in water to remove nonbound dyes; (3) UV–vis analysis of the aqueous polymer solution to evaluate polymer-bound dyes.

Dye Capture in Water. A cation-condensed star polymer (**S1**: N_{N+} = ~670) was first mixed with various dyes (MO, OG, MB) in water for 2 h at room temperature ($[dye]_0/[S1]_0$ = 0.5/1 mg/mL), respectively. After purified by dialysis in water, all of the polymer solutions exhibited orange or blue colors (see inset pictures in Figure 3) and UV–vis spectra originating from core-bound dyes (Figure 3a,c,d). Thus, **S1** efficiently encapsulated water-soluble MO, OG, and MB even in water, independent of their structures and the number of sulfonate anions.

dx.doi.org/10.1021/ma300266k | *Macromolecules* 2012, 45, 3377–3386

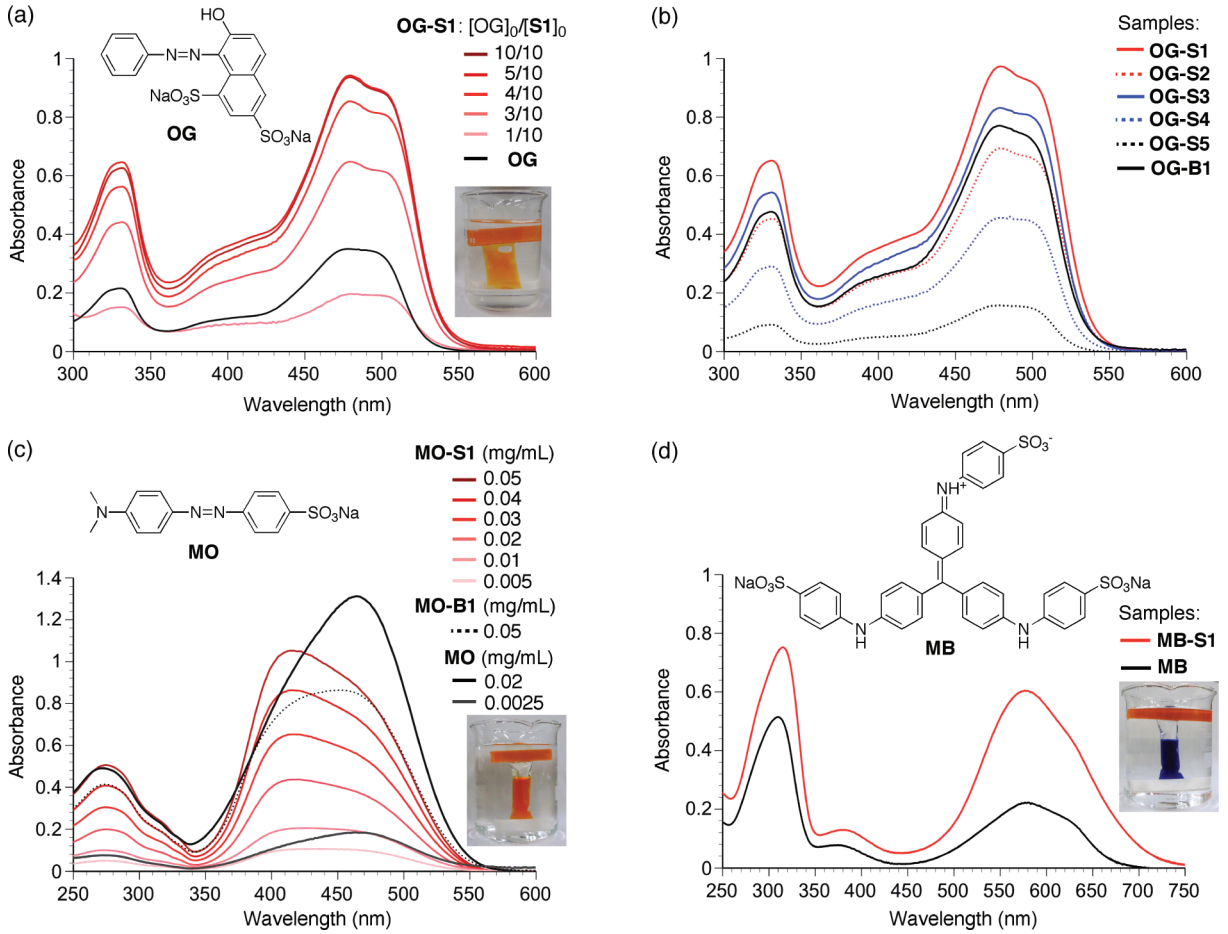


Figure 3. UV−vis measurements of dye-bearing polymers (dye-**S1**−**S5**, **B1**: prepared by mixing polymers and dyes in H_2O at rt for 2 h) in H_2O at rt. (a) OG-bearing **S1** obtained from various feed ratio of OG to **S1** ($[OG]_0/[S1]_0$ = 1/10, 3/10, 4/10, 5/10, 10/10 mg/mL): [OG-**S1**] = 0.1 mg/mL; [OG] = 0.01 mg/mL. (b) OG-bearing polymers (**S1**−**S5**, **B1**: $[OG]_0/[polymer]_0$ = 0.5/1 mg/mL): [OG-polymer] = 0.1 mg/mL. (c) MO-bearing polymers ($[MO]_0/[S1$ or $B1]_0$ = 0.5/1 mg/mL): [MO-**S1**] = 0.05−0.005 mg/mL; [MO-**B1**] = 0.05 mg/mL; [MO] = 0.02 and 0.0025 mg/mL (6.1×10^{-5} and 7.6×10^{-6} M, respectively). (d) MB-bearing **S1** ($[MB]_0/[S1]_0$ = 0.5/1 mg/mL): [MB-**S1**] = 0.05 mg/mL; [MB] = 0.01 mg/mL. Inset pictures: OG-**S1** (a), MO-**S1** (c), MB-**S1** (d) in water.

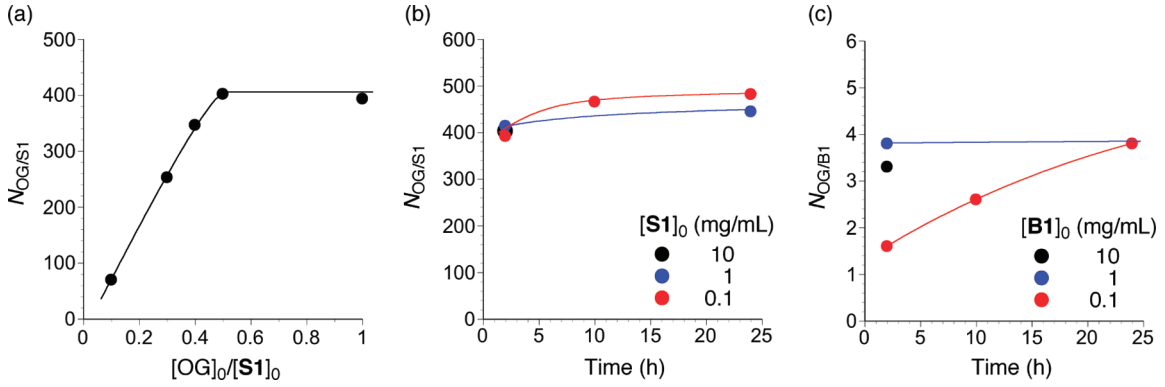


Figure 4. Quantitative analysis of polymer-bound OGs. (a) The number of **S1**-bound OGs ($N_{OG/S1}$) as a function of the mixing ratio of OG to **S1** ($[OG]_0/[S1]_0$): $[OG]_0/[S1]_0$ = 1/10−10/10 mg/mL in H_2O at rt for 2 h. (b) $N_{OG/S1}$ and (c) $N_{OG/B1}$ as a function of the mixing time of OG and polymers (b: **S1**; c: **B1**): $[OG]_0/[polymer]_0$ = 5/10 (black), 0.5/1 (blue), 0.05/0.1 (red) mg/mL in H_2O at rt.

Among them, MO-bearing **S1** showed unique UV−vis spectra in water (Figure 3c: red lines). The absorption maximum wavelength of MO was blue-shifted to 415 nm in the presence of **S1**, compared with that of MO alone at 460 nm ([MO] = 10^{-5}−10^{-6} M) (Figure S6). More importantly, the blue shift was completely independent of the total concentration of MO-bearing **S1**, where the absorption maximum was maintained at 415 nm even in quite low total concentration of MO: $[core\text{-}bound\ MO]_{total}$ = ~10^{-5} to ~10^{-6} M ([MO-**S1**] = 0.05−0.005 mg/mL). Though a block copolymer with a short polycationic segment (**B1**), a linear cut-out mimic of **S1**, also bound MO, such a blue shift was not so clearly observed ([MO-**B1**] = 0.05 mg/mL: Figure 3c, dashed line). In general, MO shows a blue shift of the absorption maximum in high

dx.doi.org/10.1021/ma300266k | *Macromolecules* 2012, 45, 3377−3386

concentration (>10^{-3} M) owing to the aggregation, which is often induced in the presence of cationic polyelectrolytes.[36−39] Thus, these results indicate that core-bound MOs are highly condensed in polycationic microgel compartments even in quite low total concentration of MO in water. This further suggests that the quaternary ammonium cations are locally concentrated in microgel cores.

Quantitative Analysis. In contrast to MO, OG within **S1** showed UV−vis spectra with shape and absorption maximum (478 nm) identical to OG alone (Figure 3a). Thus, we determined the number of polymer-bound OGs by UV−vis spectroscopy, coupled with the calibration plot for OG at 478 nm. OG was mixed with **S1** in various feed ratios of OG to **S1** ($[OG]_0/[S1]_0$ = 1/10−10/10 mg/mL) in water for 2 h. As shown in Figure 3a, the UV−vis intensity for **S1**-bound OG increased with increasing the feed ratio of OG to **S1** ($[OG]_0/[S1]_0$) from 1/10 to 5/10 and was finally saturated over 5/10 of the ratio. The number of OG per a single **S1** molecule ($N_{OG/S1}$) also increased with increasing $[OG]_0/[S1]_0$ and finally reached 400 as the maximum value (Figure 4a and Table 2).

We further compared **S1** with **B1** on time-dependent encapsulation of OG (Figure 4b,c and Table S2). In the respective polymers, the total polymer concentration ($[polymer]_0$) was changed from 0.1 to 10 mg/mL under the constant feed ratio of OG to polymers ($[OG]_0/[polymer]_0$ = 0.5/1). The mixtures of a polymer and OG were sampled at the predetermined periods (2, 10, and 24 h) to determine $N_{OG/S1}$ and $N_{OG/B1}$ by UV−vis. $N_{OG/S1}$ was almost independent of both the total polymer concentration and the mixing time. In contrast, $N_{OG/B1}$ gradually increased with increasing the mixing time at the low polymer concentration ($[polymer]_0$ = 0.1 mg/mL). The final maximum value of $N_{OG/B1}$ was however independent of total polymer concentration and was estimated as 3.8. These results demonstrated that **S1** quickly entrapped OG within the core even at the low total concentration of the host, in sharp contrast to **B1**. This would be due to the locally high concentration of ammonium cations in the core.

Other cation-condensed star polymers (**S2**−**S4**) were also quite effective for the encapsulation of OG in water ($[OG]_0/[polymer]_0$ = 0.5/1 mg/mL; Figure 3b). The number of OG in **S1**−**S4** ($N_{OG/polymer}$) was estimated as 514−131 (Table 2), where $N_{OG/polymer}$ is dependent on the number of quaternary ammonium cations in a single star (N_{N+}). A noncationic core PEG star polymer (**S5**) was, in turn, much less effective for OG than cationic counterparts (**S1**−**S4**). These results revealed that quaternary ammonium cations play a critical role to efficiently entrap anionic dyes into host polymers in water.

Ligation Structure. The immobilization of OG onto polycationic hosts (**S1**−**S4**, **B1**) is triggered by the anion exchange between sodium sulfonate in OG ($-SO_3^-Na^+$) and quaternary ammonium iodide in their hosts ($polyNR_4^+I^-$): i.e., the poly(ammonium cation)s ligate an anionic OG to form quaternary ammonium sulfonate ($R-SO_3^-polyNR_4^+$).[40] To propose the ligation structure, the number ratio ($N_{N+/OG}$) of N_{N+} to polycation-bound OG (N_{OGonN+}) was estimated by the following equation: $N_{N+/OG} = N_{N+}/N_{OGonN+} = N_{N+}/(N_{OG/polymer} - N_{OG/PEG})$; $N_{OG/PEG} = N_{arm} \times [N_{OG/polymer}$ (**S5**)$/N_{arm}$ (**S5**)] (Table 2 and Figure 5). It should be noted that N_{OGonN+} was calculated by the subtraction of the number of PEG segment-bound OG ($N_{OG/PEG}$) from the number of polymer-bound OG ($N_{OG/polymer}$) because a noncationic **S5** also slightly carried OG in water (Figure 3b). $N_{OG/PEG}$ was further estimated, assuming that a single PEG chain on polycationic hosts still bears OG in the same extent as that on **S5**.

Table 2. Encapsulation of OG into Polymers in Water[a]

entry	polymer	$[OG]_0/[polymer]_0$ (mg/mL)	$OG_{polymer}$[b] (μmol/g)	$N_{OG/polymer}$[c]	$N_{N+/OG}$[d]
1	**S1**	5/10	652	402	1.9
2	**S1**	0.5/1	672	414	1.8
3	**S1**	0.05/0.1	637	392	1.9
4	**S2**	0.5/1	433	129	2.0
5	**S3**	0.5/1	542	514	1.9
6	**S4**	0.5/1	263	131	2.3
7	**S5**	0.5/1	80	41	
8	**B1**	0.5/1	477	3.8	2.9

[a]Polymers (**S1**−**S5**, **B1**) and orange G (OG) were stirred in H_2O at rt for 2 h, followed by the dialysis of the mixtures in H_2O. [b]The amount of OG per gram of polymer, determined by UV−vis measurements of OG-bearing polymers in H_2O with the calibration plot of OG at 478 nm. [c]The number of OG in a single polymer: $N_{OG/polymer} = OG_{polymer} \times [M_{w,star}$ (MALLS): **S1**−**S5**, or M_n (NMR): **B1**] $\times 10^{-6}$. [d]The number ratio of polymer-bound ammonium cations (N_{N+}) to polycation-bound OGs (N_{OGonN+}): $N_{N+/OG} = N_{N+}/N_{OGonN+} = N_{N+}/(N_{OG/polymer} - N_{OG/PEG})$; $N_{OG/PEG} = N_{arm} \times [N_{OG/S5}/N_{arm}$ (**S5**)].

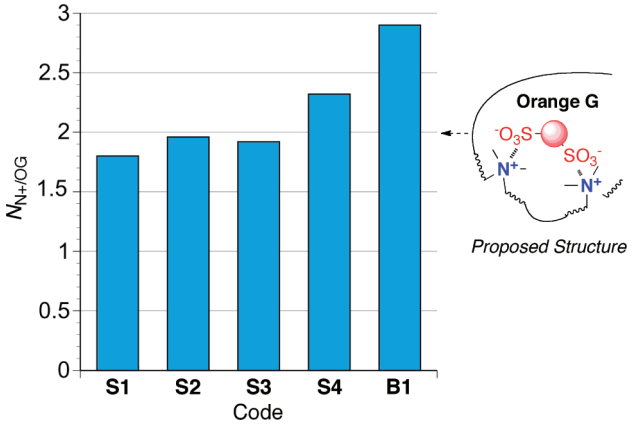


Figure 5. Effects of host polymers (**S1**−**S4**, **B1**) on the number ratio of polymer-bound ammonium cations to polycation-bound OGs ($N_{N+/OG}$).

$N_{N+/OG}$s for cation-condensed star polymers (**S1**−**S3**) were estimated as about 2 (Table 2). As proposed in Figure 5, the star polymers involve about two ammonium cations to immobilize one OG molecule. Since OG originally carried two sulfonates, all of the core-bound ammonium cations in **S1**−**S3** would serve as ionic ligands to catch OGs in their core. The $N_{N+/OG}$s were independent of both the total concentration of **S1** ($[polymer]_0$) (entries 1−3) and N_{N+}s originating from **2** (entries 2 and 4: N_{N+} = 666 (**S1**), 206 (**S2**); Table 1 and Figure 5). On the other hand, $N_{N+/OG}$ for **S4** (∼2.3) was larger than that for **S2** (∼2.0) (entries 4 and 6, Figure 5) in spite of their almost identical N_{N+}s (∼200, Table 1). These results suggest that $N_{N+/OG}$ is dependent on the local concentration of quaternary ammonium cations (N^+). **S1** has the same N^+ local concentration as **S2** because both of the cores consist of a cation-bearing dimethacrylate (**2**) alone: $[N^+]/[methacrylate]$ = 1/2. In contrast, the N^+ local concentration in **S4** is diluted by ethylene glycol dimethacrylate (**4**) against that in **S2**: i.e., the

dx.doi.org/10.1021/ma300266k | *Macromolecules* 2012, 45, 3377−3386

S4 core is prepared by the copolymerization of a cation-bearing monomer (**3**) and **4** in 5/10 of $[\mathbf{3}]_0/[\mathbf{4}]_0$; $[N^+]/[\text{methacrylate}] = 1/5$. Thus, a certain remote location of ammonium cations in **S4** probably reduces the efficiency to immobilize OG. Additionally, **B1** was much less efficient for the immobilization of OG ($N_{N+/OG} = \sim 3$) than cation-condensed star polymers (**S1**–**S4**) (Table 2, entry 8; Figure 5). Therefore, $N_{N+/OG}$ was also dependent on the three-dimensional structures of host polymers, in addition to the local concentration of quaternary ammonium cations.

Efficient capture of OG with cation-condensed star polymers can be further explained by the following reasons. Generally, the counterion binding in polyelectrolytes are enhanced as the local ion concentration increased.[27,29−32] Thus, OG is confined as a counteranion more strongly within cation-condensed segments (cores) of **S1**–**S3** than those in **S4** and **B1**. Additionally, OG is a divalent anion to involve the bidentate chelate ligation on polycationic hosts, in sharp contrast to an original monovalent iodide anion in the hosts. Such a chelate binding structure also contributes to the steady encapsulation of dyes.[30]

The mobility of OG on polycations (**S1**, **B1**) was evaluated by proton nuclear magnetic resonance (^{1}H NMR) analysis (Figure 6). **S1**-bound OG was hardly detected in D_2O, in contrast to sharp signals of OG alone around 6.5–9.0 ppm (Figure 6a,b). OG in the presence of **B1** in turn became

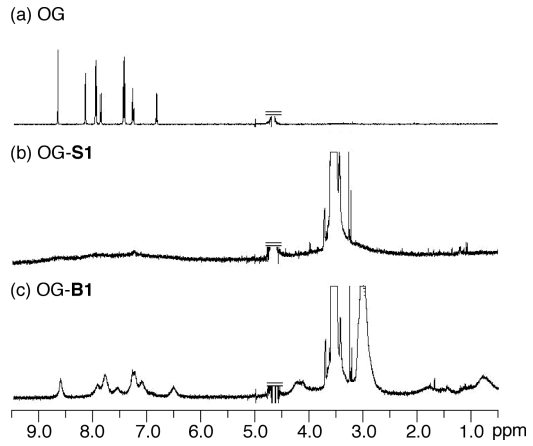


Figure 6. ^{1}H NMR spectra (500 MHz) of (a) OG, (b) OG-bearing **S1**, and (c) OG-bearing **B1** in D_2O at room temperature.

broader than OG alone (Figure 6a,c). This means that **S1** tightly ligates OG within a cross-linked polycationic core to dramatically reduce the mobility of OG, though **B1** dynamically immobilizes OG. The steady binding of OG in **S1** was further confirmed by proton diffusion-ordered NMR spectroscopy (^{1}H DOSY, Figure S6).[14] OG-bearing **S1** exhibited a single series of diffusion coefficient ($D_{NMR} = 8.3 \times 10^{-11}$) derived from the PEG chains in D_2O without that from free OG (OG alone in D_2O: $D_{NMR} = 4.5 \times 10^{-10}$). Thus, all of OGs were tightly enclosed within the **S1** core.

Conformation. Dynamic light scattering (DLS) measurements of star polymers (**S1**–**S5**) and a block counterpart (**B1**) were conducted in water (Table 3, Figures 7 and S8). Cation-condensed star polymers (**S1**–**S4**) with OG showed monomodal distributions with 12–24 nm of hydrodynamic radius (R_h), while all of the hosts demonstrated bimodal distributions including large aggregates (R_h: ~100 to ~200 nm) in the

Table 3. Hydrodynamic Radius of OG-Bearing Polymers in Water[a]

entry	polymer	concn (mg/mL)	R_h (nm)[b]
1	**S1**	0.1	15, 210
2	OG-**S1**	1	14
3	OG-**S2**	1	12
4	OG-**S3**	1	24
5	OG-**S4**	1	24
6	OG-**S5**	1	28
7	OG-**B1**	10	15
8	OG-**B1**	1	n.d.

[a][Polymer] = 0.1, 1, 10 mg/mL in H_2O at 25 °C. [b]Intensity-average hydrodynamic radius (R_h). n.d.: not detected.

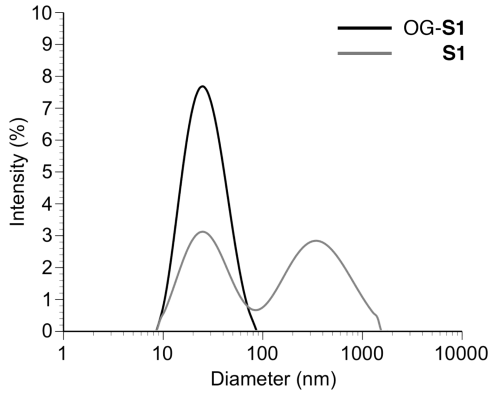


Figure 7. DLS intensity distributions of OG-bearing **S1** (black) and **S1** (gray) in H_2O at 25 °C: [OG-**S1**] = 1 mg/mL; [**S1**] = 0.1 mg/mL.

absence of OG (Figures 7 and S8). These results demonstrate that dye incorporation effectively dissociates some aggregations of polycationic hosts (**S1**–**S4**) in water to provide unimolecular polycationic nanocapsules. On the contrary, the conformation of **B1** was dynamically changed dependent on the total polymer concentration. OG-bearing **B1** mainly formed a micelle structure with 15 nm of R_h via the intermolecular aggregation at the high total concentration (10 mg/mL), whereas **B1** would almost form a unimer conformation below 1 mg/mL owing to the no detection in DLS measurements (Table 3). Thus, the stable, cross-linked, and compartmentalized structure of the cores in **S1**–**S4** is a key factor to achieve such an efficient dye entrapment.

Controlled Release. The release of OG from **S1** or **B1** was investigated via anion exchange by the dialysis of the aqueous solutions of OG-bound **S1** or **B1** with 0.1 M NaCl aqueous solutions. Figure 8 shows mole percent of polymer-bound OG ($[\text{polymer-OG}]_t$) per an initial polymer-bound OG ($[\text{polymer-OG}]_0$) as a function of dialysis time (Table S3). OG was gradually released from **S1**, which was slower than that from **B1**. The controlled release from **S1** most likely arises from the tight ligation of OG within the cation-condensed core. These results revealed that cation-condensed star polymers work as stimuli-responsive nanocarriers to release core-bound anionic compounds via ion exchange.

■ CONCLUSION

We successfully create cation-condensed microgel-core star polymers as unimolecular nanocapsules (hosts) for the encapsulation and stimuli-responsive release of anionic dyes (guests) in water. The water-soluble star polymers with cation-

dx.doi.org/10.1021/ma300266k | Macromolecules 2012, 45, 3377−3386

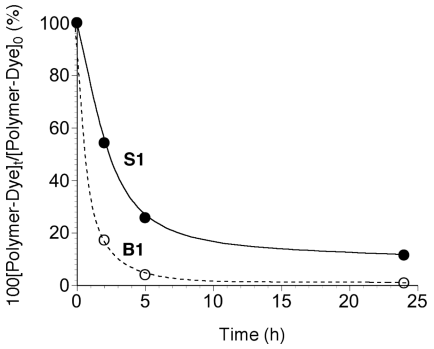


Figure 8. Release of OG from polymers (**S1** or **B1**) via the dialysis of aqueous solutions of OG-bound polymers ([polymer] = 1 mg/mL, 1 mL) with 0.1 M NaCl aqueous solutions (100 mL).

rich cores were directly obtained in high yield from the ruthenium-catalyzed living radical polymerization of a quaternary ammonium-bearing linking agent or monomer with a PEG-based macroinitiator. Owing to the locally high concentration of quaternary ammonium cations in the core, the star polymers afforded efficient and versatile encapsulation of various dyes carrying sodium sulfonate (methyl orange: MO; orange G: OG; methyl blue: MB) in water. The condensation of dyes within the core was confirmed by the unique blue shift of the absorption maximum for MO. OG-bearing star polymers embedded 130−510 of OG per a single star, whose numbers are dependent on the number of core-bound cations. Almost all of quaternary ammonium groups in star polymers served as ionic ligands to encapsulate OG, where the immobilization of one OG molecule involved two in-core ammonium cations. Furthermore, OG within a star polymer was gradually released from the core via simple anion exchange with sodium chloride water. Cation-condensed star polymers would be useful as versatile delivery vessels, contributing to a wide variety of biomedical applications.

■ ASSOCIATED CONTENT

Supporting Information

Polymer characterization (SEC, ^{1}H NMR and DOSY, DSC, DLS); dye capture and release (UV−vis, quantitative analysis). This material is available free of charge via the Internet at http://pubs.acs.org.

■ AUTHOR INFORMATION

Corresponding Author

*Tel +81-75-383-2600; Fax +81-75-383-2601; e-mail terashima@living.polym.kyoto-u.ac.jp (T.T.), sawamoto@star.polym.kyoto-u.ac.jp (M.S.).

Notes

The authors declare no competing financial interest.

■ ACKNOWLEDGMENTS

This research was supported by the Ministry of Education, Science, Sports and Culture through a Grant-in Aid for Creative Scientific Research (18GS0209) and Young Scientist (B) (No. 20750091), for which T.T. is grateful. We thank Prof. Hideki Matsuoka for helpful comments and suggestion about DLS analysis, Mr. Yuta Koda for technical supports on DOSY, and Mr. Yusuke Hibi for helpful support on conformational search with a calculation program.

■ REFERENCES

(1) Van Dongan, S. F. M.; De Hoog, H.-P. M.; Peters, R. J. R. W.; Nallani, M.; Nolte, R. J. M.; Van Hest, J. C. M. *Chem. Rev.* **2009**, *109*, 6212−6274.

(2) (a) Allen, C.; Maysinger, D.; Eisenberg, A. *Colloids Surf., B* **1999**, *16*, 3−27. (b) Kataoka, K.; Harada, A.; Nagasaki, Y. *Adv. Drug Delivery Rev.* **2001**, *47*, 113−131. (c) Nishiyama, N.; Kataoka, K. *Adv. Polym. Sci.* **2006**, *197*, 67−101.

(3) (a) Bronich, T. K.; Keifer, P. A.; Shlyakhtenko, L. S.; Kabanov, A. V. *J. Am. Chem. Soc.* **2005**, *127*, 8236−8237. (b) Yusa, S.; Yokoyama, Y.; Morishima, Y. *Macromolecules* **2009**, *42*, 376−383. (c) Yusa, S.; Sugihara, M.; Endo, T.; Morishima, Y. *Langmuir* **2009**, *25*, 5258−5265.

(4) (a) Lasic, D. D.; Needham, D. *Chem. Rev.* **1995**, *95*, 2601−2628. (b) Discher, D. E.; Eisenberg, A. *Science* **2002**, *297*, 967−973.

(5) (a) Dong, W.-F.; Kishimura, A.; Anraku, Y.; Chuanoi, S.; Kataoka, K. *J. Am. Chem. Soc.* **2009**, *131*, 3804−3805. (b) Oana, H.; Kishimura, A.; Yonehara, K.; Yamasaki, Y.; Washizu, M.; Kataoka, K. *Angew. Chem., Int. Ed.* **2009**, *48*, 4613−4616. (c) Delaittre, G.; Dire, C.; Rieger, J.; Putaux, J.-L.; Charleux, B. *Chem. Commun.* **2009**, 2887−2889.

(6) (a) Kabanov, A. V.; Vinogradov, S. V. *Angew. Chem., Int. Ed.* **2009**, *48*, 5418−5429. (b) Oh, K. J.; Drumright, R.; Siegwart, D. J.; Matyjaszewski, K. *Prog. Polym. Sci.* **2008**, *33*, 448−477. (c) Nayak, S.; Lyon, L. A. *Angew. Chem., Int. Ed.* **2005**, *44*, 7686−7708. (d) Akiyoshi, K.; Deguchi, S.; Moriguchi, N.; Yamaguchi, S.; Sunamoto, J. *Macromolecules* **1993**, *26*, 3062−3068.

(7) (a) Oh, J. K.; Tang, C.; Gao, H.; Tsarevsky, N. V.; Matyjaszewski, K. *J. Am. Chem. Soc.* **2006**, *128*, 5578−5584. (b) Fuji, S.; Dupin, D.; Araki, T.; Armes, S. P.; Ade, H. *Langmuir* **2009**, *25*, 2588−2592. (c) Cheng, C.; Zhu, X.; Pich, A.; Möller, M. *Langmuir* **2010**, *26*, 4709−4716.

(8) (a) Yuan, J.-J.; Mykhaylyk, O. O.; Ryan, A. J.; Armes, S. P. *J. Am. Chem. Soc.* **2007**, *129*, 1717−1723. (b) Jackson, A. W.; Fulton, D. A. *Chem. Commun.* **2011**, *47*, 6807−6809.

(9) Bauer, B. J.; Fetters, L. J. J. *Rubber Chem. Technol.* **1978**, *51*, 406−436.

(10) (a) Gao, H.; Matyjaszewski, K. *Prog. Polym. Sci.* **2009**, *34*, 317−350. (b) Blencowe, A.; Tan, J. F.; Goh, T. K.; Qiao, G. G. *Polymer* **2009**, *50*, 5−32.

(11) (a) Baek, K.-Y.; Kamigaito, M.; Sawamoto, M. *Macromolecules* **2001**, *34*, 215−221. (b) Terashima, T.; Motokawa, R.; Koizumi, S.; Sawamoto, M.; Kamigaito, M.; Ando, T.; Hashimoto, T. *Macromolecules* **2010**, *43*, 8218−8232.

(12) (a) Baek, K.-Y.; Kamigaito, M.; Sawamoto, M. *Macromolecules* **2001**, *34*, 7629−7635. (b) Baek, K.-Y.; Kamigaito, M.; Sawamoto, M. *Macromolecules* **2002**, *35*, 1493−1498.

(13) (a) Terashima, T.; Kamigaito, M.; Baek, K.-Y.; Ando, T.; Sawamoto, M. *J. Am. Chem. Soc.* **2003**, *125*, 5288−5289. (b) Terashima, T.; Ouchi, M.; Ando, T.; Kamigaito, M.; Sawamoto, M. *J. Polym. Sci., Part A: Polym. Chem.* **2006**, *44*, 4966−4980. (c) Terashima, T.; Ouchi, M.; Ando, T.; Sawamoto, M.; Kamigaito, M. *Macromolecules* **2007**, *40*, 3581−3588. (d) Terashima, T.; Ouchi, M.; Ando, T.; Sawamoto, M. *J. Polym. Sci., Part A: Polym. Chem.* **2010**, *48*, 373−379. (e) Terashima, T.; Ouchi, M.; Ando, T.; Sawamoto, M. *J. Polym. Sci., Part A: Polym. Chem.* **2011**, *49*, 1061−1069. (f) Terashima, T.; Ouchi, M.; Ando, T.; Sawamoto, M. *Polym. J.* **2011**, *43*, 770−777. (g) Terashima, T.; Nomura, A.; Ito, M.; Ouchi, M.; Sawamoto, M. *Angew. Chem., Int. Ed.* **2011**, *50*, 7892−7895.

(14) Koda, Y.; Terashima, T.; Nomura, A.; Ouchi, M.; Sawamoto, M. *Macromolecules* **2011**, *44*, 4574−4578.

(15) Bosman, A. W.; Vestberg, R.; Heumann, A.; Fréchet, J. M. J.; Hawker, C. J. *J. Am. Chem. Soc.* **2003**, *125*, 715−728.

(16) (a) Helms, B.; Guillaudeu, S. J.; Xie, Y.; McMurdo, M.; Hawker, C. J.; Fréchet, J. M. J. *Angew. Chem., Int. Ed.* **2005**, *44*, 6384−6387. (b) Chi, Y.; Scroggins, S. T.; Fréchet, J. M. J. *J. Am. Chem. Soc.* **2008**, *130*, 6322−6323.

(17) Rodionov, V.; Gao, H.; Scroggings, S.; Unruh, D. A.; Avestro, A.-J.; Fréchet, J. M. J. *J. Am. Chem. Soc.* **2010**, *132*, 2570−2572.

(18) Syrett, J. A.; Haddleton, D. M.; Whittaker, M. R.; Davis, T. P.; Boyer, C. *Chem. Commun.* **2011**, *47*, 1449−1451.
(19) Burakowska, E.; Quinn, J. R.; Zimmerman, S. C.; Haag, R. *J. Am. Chem. Soc.* **2009**, *131*, 10574−10580.
(20) (a) Bosman, A. W.; Janssen, H. M.; Meijer, E. W. *Chem. Rev.* **1999**, *99*, 1665−1688. (b) Gupta, U.; Agashe, H. B.; Asthana, A.; Jain, N. K. *Biomacromolecules* **2006**, *7*, 649−658.
(21) (a) Radowski, M. R.; Shukla, A.; Von Berlepsch, H.; Böttcher, C.; Pickaert, G.; Rehage, H.; Haag, R. *Angew. Chem., Int. Ed.* **2007**, *46*, 1265−1269. (b) Wan, D.; Pu, H.; Cai, X. *Macromolecules* **2008**, *41*, 7787−7789. (c) Wan, D.; Eang, G.; Pu, W.; Jin, M. *Macromolecules* **2009**, *42*, 6448−6456.
(22) (a) Ouchi, M.; Terashima, T.; Sawamoto, M. *Acc. Chem. Res.* **2008**, *41*, 1120−1132. (b) Ouchi, M.; Terashima, T.; Sawamoto, M. *Chem. Rev.* **2009**, *109*, 4963−5050. (c) Matyjaszewski, K.; Tsarevsky, N. V. *Nat. Chem.* **2009**, *1*, 276−288. (d) Rosen, B. M.; Percec, V. *Chem. Rev.* **2009**, *109*, 5069−5119. (e) Hawker, C. J.; Bosman, A. W.; Harth, E. *Chem. Rev.* **2001**, *101*, 3661−3688. (f) Moad, G.; Rizzardo, E.; Thang, S. H. *Polymer* **2008**, *49*, 1079−1131. (g) Yamago, S. *Chem. Rev.* **2009**, *109*, 5051−5068.
(23) (a) Watanabe, Y.; Ando, T.; Kamigaito, M.; Sawamoto, M. *Macromolecules* **2001**, *34*, 4370−4374. (b) Yoshitani, Y.; Watanabe, Y.; Ando, T.; Kamigaito, M.; Sawamoto, M. In *Controlled/Living Radical Polymerization From Synthesis to Materials*; Matyjaszewski, K., Ed.; ACS Symposium Series 944; American Chemical Society: Washington, DC, 2006; Chapter 2, pp 14−25. (c) Ouchi, M.; Ito, M.; Kamemoto, S.; Sawamoto, M. *Chem.—Asian J.* **2008**, *3*, 1358−1364. (d) Yoda, H.; Nakatani, K.; Terashima, T.; Ouchi, M.; Sawamoto, M. *Macromolecules* **2010**, *43*, 5595−5601. (e) Fukuzaki, Y.; Tomita, Y.; Terashima, T.; Ouchi, M.; Sawamoto, M. *Macromolecules* **2010**, *43*, 5989−5995. (f) Ouchi, M.; Yoda, H.; Terashima, T.; Sawamoto, M. *Polym. J.* **2012**, *44*, 51−58.
(24) Ando, T.; Sawauchi, C.; Ouchi, M.; Kamigaito, M.; Sawamoto, M. *J. Polym. Sci., Part A: Polym. Chem.* **2003**, *41*, 3597−3605.
(25) (a) Ma, Y.; Tang, Y.; Billingham, N. C.; Armes, S. P.; Lewis, A. L.; Lloyd, A. W.; Salvage, J. P. *Macromolecules* **2003**, *36*, 3475−3484. (b) Li, Y.; Armes, S. P.; Jin, X.; Zhu, S. *Macromolecules* **2003**, *36*, 8268−8275.
(26) (a) Plamper, F. A.; Schmalz, A.; Penott-Chang, E.; Drechsler, M.; Jusufi, A.; Ballauff, M.; Müller, A. H. E. *Macromolecules* **2007**, *40*, 5689−5697. (b) Dong, H.; Huang, J.; Koepsel, R. R.; Ye, P.; Russell, A. J.; Matyjaszewski, K. *Biomacromolecules* **2011**, *12*, 1305−1311.
(27) Dobrynin, A. V.; Rubinstein, M. *Prog. Polym. Sci.* **2005**, *30*, 1049−1118.
(28) Williams, S. R.; Long, T. E. *Prog. Polym. Sci.* **2009**, *34*, 762−782.
(29) Manning, G. S. *J. Chem. Phys.* **1969**, *51*, 924−933.
(30) Boussouira, B.; Ricard, A.; Audebert, R. *J. Polym. Sci., Part B: Polym. Phys.* **1988**, *26*, 649−661.
(31) Ríos, H. E.; Gamboa, C.; Ternero, G. *J. Polym. Sci., Part B: Polym. Phys.* **1991**, *29*, 805−809.
(32) (a) Kawaguchi, D.; Kawauchi, S.; Satoh, M.; Komiyama, J. *Polymer* **1998**, *39*, 1387−1392. (b) Yasumoto, N.; Kasahara, N.; Sakaki, A.; Satoh, M. *Colloid Polym. Sci.* **2006**, *284*, 900−908.
(33) (a) Lee, J.-J.; Ford, W. T.; Moore, J. A.; Li, Y. *Macromolecules* **1994**, *27*, 4632−4634. (b) Pan, Y.; Ford, W. T. *Macromolecules* **2000**, *33*, 3731−3738.
(34) Keul, H.; Neumann, A.; Reining, B.; Höcker, H. *Macromol. Symp.* **2000**, *161*, 63−72.
(35) Pfefferkorn, D.; Kyerematen, S. O.; Busse, K.; Kammer, H.-W.; Thurn-Albrecht, T.; Kressler, J. *Macromolecules* **2011**, *44*, 2953−2963.
(36) Quadrifoglio, F.; Crescenzi, V. *J. Colloid Interface Sci.* **1971**, *35*, 447−459.
(37) Vishalakshi, B. *J. Polym. Sci., Part A: Polym. Chem.* **1995**, *33*, 365−371.
(38) Fujieda, T.; Ohta, K.; Wakabayashi, N.; Higuchi, S. *J. Colloid Interface Sci.* **1997**, *185*, 332−334.
(39) Kuiper, J. M.; Buwalda, R. T.; Hulst, R.; Engberts, J. B. F. N. *Langmuir* **2001**, *17*, 5216−5224.
(40) (a) Van De Coevering, R.; Gebbink, R. J. M. K.; Van Koten, G. *Prog. Polym. Sci.* **2005**, *30*, 474−490. (b) Van De Coevering, R.; Alfers, A. P.; Meeldijk, J. D.; Martínez-Viviente, E.; Pregosin, P. S.; Gebbink, R. J. M. K.; Van Koten, G. *J. Am. Chem. Soc.* **2006**, *128*, 12700−12713.

Macromolecules

Article

pubs.acs.org/Macromolecules

Reactive Polymers Bearing Styrene Pendants through Selective Anionic Polymerization of 4-Vinylbenzyl Methacrylate

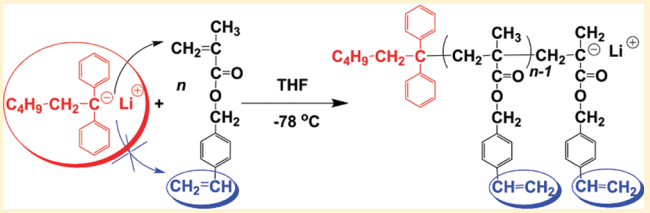
Y. Murali Mohan,[†,⊥] V. Raghunadh,[†,§] S. Sivaram,[†] and D. Baskaran*[,†,‡]

[†]Division of Polymer Science and Engineering, National Chemical Laboratory, Pune 411 008, India

[‡]Department of Chemistry, University of Tennessee, Knoxville, Tennessee 37996, United States

Supporting Information

ABSTRACT: Selective anionic polymerization of 4-vinylbenzyl methacrylate at methacrylate site has been achieved using resonance stabilized anionic initiators such as 1,1-diphenylhexyllithium (DPHLi) and tritylpotassium (TritylK) in tetrahydrofuran (THF) at −78 °C. Polymerization proceeded selectively through methacrylate functionality of the monomer in a controlled manner and produced polymers and copolymers with narrow molecular weight distribution at low temperatures (≤−40 °C). ^{1}H NMR of the polymer showed the presence of styrene pendants in every monomeric repeating unit. The polymerization results confirm that the resonance stabilized carbanions with an optimum pK_a (30 ≤ pK_a ≤ 32) of their conjugate acids such as DPHLi and TritylK do not react with styrene functionality at −78 °C. The selective initiation without cross-linking is attributed to the differences in the electronegativity between polar methacrylate and styrene functionalities and an attenuation of initiator reactivity at low temperature. Poly(4-vinylbenzyl methacrylate) and its copolymers with the vinyl pendant in close proximity with ester linkage are very reactive and unstable, readily undergoing cross-linking in solution or in solid state with or without a radical initiator.



INTRODUCTION

Polymers having polymerizable functional groups at their repeat units are of significant interest as they can be used as thermally reactive polymers in many applications such as cross-linked adsorbents, controlled postgrafting, immobilization of bioactives, and thermal cross-linking agent in the production of high-refractive-index transparent organic glass.[1−3] However, synthesis of polymers with reactive vinyl group at every repeating unit remains a challenge for chemists, and only in a few cases have such polymers been synthesized.[4−6]

Reactive vinyl group containing polymers can be made via either postattachment of a monomer moiety at the repeat units or selective initiation of divinyl monomers. Selective polymerization of one vinyl group in divinyl monomers is a straightforward method. Nevertheless, the reactivity of vinyl groups present in the difunctional monomer must be drastically different otherwise cross-linking will dominate the course of the polymerization.[1,7−10] The difunctional monomers such as divinylbenzene (1,3- and 1,4-isomers),[11−13] diisopropenylbenzene (1,3- and 1,4-isomers),[4,14−16] allyl methacrylate,[17] 4-(α-alkylvinyl)styrene,[18] 4-(1-alkynyl)styrenes,[19] and 4-vinylbenzyl methacrylate[9] have been used for selective initiation in the past. Although the reactivity of the vinyl groups in these difunctional monomers differs considerably, reactive radical initiators do not allow initiation of one of the vinyl groups selectively.[20−22] Linear polymers of ethylene glycol dimethacrylate, and ethylene glycol 4-vinylbenzoate methacrylate have been prepared with a pendant vinyl group through protection of methacrylate functionality with cyclodextrin via inclusion complex.[23] One of the double bonds of 2,5-norbornadiene has been copolymerized with ethylene successfully using metallocene catalyst as an initiator.[24]

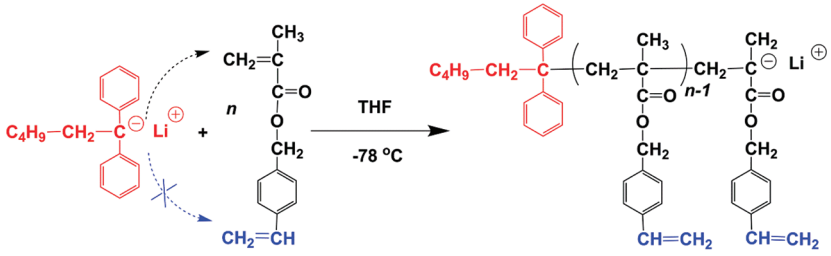
Synthesis of linear polymer from difunctional monomers is possible in some cases with anionic initiators.[4,14] Polymerization of 1,3-diisopropenylbenzene using *n*-butyllithium as anionic initiator in tetrahydrofuran (THF) at a low temperature produced polymer with pendant vinyl groups.[14] Recently, Hirao and co-workers have successfully polymerized 1,4-divinylbenzene selectively through one of its vinyl groups using oligo(α-methylstyryl)lithium initiator complexed with 11-fold excess of potassium *tert*-butoxide.[13] In these cases, the reactivity modulations were achieved through stabilization of anions and ion-pair complexation.

Zhang and Ruckenstein reported selective anionic polymerization of 4-(vinylphenyl)-1-butene at its styrene functionality.[6] The reactivity of the two vinyl groups is substantially different, the olefinic unsaturation being nonreactive. It was possible to selectively initiate styrene polymerization using an anionic initiator. Group transfer polymerization (GTP) using silylketene acetal is effective for polar vinyl monomers such as alkyl (math)acrylates and is ineffective for the polymerization of nonpolar monomer such as styrene.[25] Pugh and Percec polymerized 4-vinylbenzyl methacrylate (VBMA) through its methacrylate double bond using GTP and obtained polymers

Received: December 20, 2011
Revised: March 19, 2012
Published: April 11, 2012

 © 2012 American Chemical Society dx.doi.org/10.1021/ma202750b | *Macromolecules* 2012, 45, 3387−3393

Scheme 1. Anionic Polymerization of 4-Vinylbenzyl Methacrylate Using DPHLi as Initiator in THF at −78 °C



with bimodal molecular weight distribution (M_w/M_n = 8.3) and incomplete monomer conversion.[9] Nonetheless, they prepared successfully controlled molecular weight copolymers of VBMA with methyl methacrylate (MMA). It is also known, based on the relative pK_a values of conjugate acids of propagating enolate (~30) and styryl anions (~44),[26] that the propagating methacrylate anion is not nucleophilic enough to initiate the polymerization of styrene.[27−29] Therefore, a selective initiation is critical in the anionic polymerization of VBMA to produce polymer with styrene pendants.

Herein, we report selective anionic polymerization of VBMA at its polar vinyl functionality using 1,1-diphenylhexyllithium (DPHLi) and tritylpotassium (TritylK) as initiators in THF at −78 °C (Scheme 1).[30] Although DPHLi is routinely used as the initiator for the anionic polymerization of acrylates and methyl methacrylates, it is also known to initiate styrene polymerization in THF at 0 °C.[31] At lower temperature, the reactivity of stabilized anions such as diphenylhexyl or trityl carbanions can be moderated to selectively polymerize VBMA at its methacrylate site.

EXPERIMENTAL SECTION

Materials. Tetrahydrofuran (THF, SD Fine Chemicals, India) was fractionated, refluxed over K metal, and stored over fresh Na−K alloy in a vacuum line. N_2 gas (Industrial Oxygen, Pune) was purified by passing through a heated column containing Cu (200 °C) (2 × 1 m) and a column containing A4 molecular sieves (2 × 1 m) and was finally bubbled through a toluene solution of oligostyrryllithium anion. 1,1-Diphenylethylene (DPE, Aldrich) was distilling over a small amount of *n*BuLi under high vacuum. *p*-Chloromethylstyrene (Aldrich) was distilled over CaH_2 under vacuum, and methacrylic acid (Aldrich) was used as received. $LiClO_4$ (Aldrich) was dried under dynamic high vacuum overnight at 100 °C and then dissolved in a known amount of dry THF. Triphenylmethane (Aldrich) was dried under high vacuum for 2 days at room temperature. Triphenylmethylpotassium was prepared by reacting potassium mirrors and triphenylmethane in THF at room temperature under vacuum. The excess metal was filtered off, and the initiator solution was stored under pure nitrogen. DPHLi initiator was prepared by reacting *n*BuLi with an equimolar amount of DPE in THF at −40 °C and stored under a pure nitrogen atmosphere in a refrigerator.

4-Vinylbenzyl methacrylate (VBMA) was synthesized following Pugh and Percec[9] reported procedure using *p*-chloromethylstyrene and potassium methacrylate in THF and dimethyl sulfoxide as a mixed solvent in the presence of tetrabutylammonium hydrogen sulfate. VBMA was obtained in 70% yield. The obtained VBMA was stirred over a small amount of CaH_2 for 4−6 h under vacuum at 0 °C. Subsequently, it was distilled under dynamic vacuum at 60 °C just prior to the polymerization. It was noticed ~10% of monomer underwent thermal polymerization during distillation. Attempts to purify this monomer using trialkylaluminum treatment failed due to excessive thermal polymerization during distillation.

Methyl methacrylate (MMA, Aldrich) was first distilled under vacuum from CaH_2 after stirring for 12 h at room temperature and then stored under a nitrogen atmosphere at −10 °C. The required amount of the distilled MMA was taken into a flask to which triisobutylaluminum or 10 wt % $AlEt_3$ solution in hexane was added drop by drop until a persistent yellowish-green color was observed. MMA was redistilled under reduced pressure, just prior to polymerization experiments.

Polymerization. The polymerizations were carried out in a flamed glass reactor under a pure nitrogen atmosphere. Solvent, initiator, $LiClO_4$ solution in THF, and monomer were transferred by capillary technique or syringe. The required amount of a solution of $LiClO_4$ in THF was added into a single-neck round-bottom flask containing 100 mL of THF. DPHLi solution was added drop by drop until a persistent red color was observed. Subsequently, the required amount of the initiator was added and the reactor was brought to a desired temperature (−78, or −40, or −20 °C). The purified neat VBMA was added to the initiator solution using a stainless steel cannula under N_2 pressure. The reaction was terminated after 15 min with degassed methanol. In case of block copolymerization, a small amount of sample was withdrawn for analysis, and MMA was added into the reactor and terminated after 30 min with degassed methanol. Poly(4-vinylbenzyl methacrylate) (PVBMA) and poly(4-vinylbenzyl methacrylate-*b*-methyl methacrylate) were recovered by stripping off the solvent, dissolving the residue in a small amount of benzene (10 mL), and freeze-drying at 0 °C. The polymer was not dried in the vacuum as it was noticed in a few early experiments that the polymer underwent thermal cross-linking at 80 °C during drying.

Measurements. Characterization of polymers was carried out using size exclusion chromatography (SEC) consisting of a ThermoSeparation's Spectra System P100 pump, an AS 300 autosampler, a UV-100 detector, and a RI-150 refractive index detector with either 10^2−10^5 linear Å 60 cm and 100 Å 60 cm 5 μm PSS-SDV gel columns or with series of 10^6, 10^4, 10^3, 500, and 100 Å 30 cm 5 μm PSS-SDV gel columns. The data were processed using Polymer Standards Service software (PSS WinGPC). THF was used as the mobile phase at a flow rate of 1 mL min^{-1} at 30 °C. Standard monodisperse poly(styrene)s (PL, UK) were used for calibration. ^{1}H NMR spectra were recorded in $CDCl_3$ on a Bruker 300 MHz spectrometer. A TA Instruments Q10 differential scanning calorimeter (DSC) was used at a heating rate of 10 °C/min. The glass transition temperature (T_g) was measured in first heating scan from 0 to 250 °C. The second heating cycle did not show any endothermic peak due to cross-linking reaction during first heating to 250 °C. The midpoint of endothermic transition was considered as T_g. DSC was calibrated using indium as standard for temperature and enthalpy. A TA Instruments TGA Q5000IR was used to determine thermal degradation of PVBMA in air at a heating rate of 10 °C/min.

RESULTS AND DISCUSSION

Attenuation of DPHLi Reactivity at −78 °C. To find a most suitable reaction condition for selective initiation of VBMA, the reactivity of DPHLi with styrene was first examined in THF at −78 °C. Accordingly, purified styrene (3 mL) was added under nitrogen into THF (100 mL) containing DPHLi (3.7×10^{-4} mol) at −78 °C. It was found that the red color of the initiator remained unchanged after addition of styrene. As the colors of DPHLi and styryl anions are similar, it is difficult to ascertain the initiation process visually. Nevertheless, the

dx.doi.org/10.1021/ma202750b | Macromolecules 2012, 45, 3387−3393

reaction after termination did not produce any polymer when precipitated in excess methanol. The analysis of the crude reaction mixture by SEC confirmed the absence of polystyrene and established the inability of DPHLi to initiate styrene polymerization in THF at −78 °C.

Selective Anionic Polymerization of VBMA. Based on this observation, selective anionic initiation of VBMA was attempted using DPHLi and TritylK as initiators in THF at −78 °C (Table 1). Polymerizations were performed in the presence of excess $LiClO_4$ to control the equilibrium dynamics of propagating enolate anions.[32] Upon addition of VBMA into the DPHLi solution in THF (Scheme 1), the red color of the initiator disappeared, immediately indicating a fast initiation at the methacrylate functionality. The viscosity of the homogeneous polymerization solution slightly increased during the polymerization. After termination, poly(4-vinylbenzyl methacrylate) (PVBMA) was recovered by precipitation in excess methanol; the gravimetric yield indicated that the conversion was nearly 100%.

Table 1. Anionic Polymerization of 4-Vinylbenzyl Methacrylate (*M*) Using DPHLi and TritylK as Initiators (I) in the Presence of $LiClO_4$ ($[LiClO_4]_0/[I]_0$ = 10) in THF at −78 °C[a]

run	$[I] \times 10^3$ (mol/L)	[M] (mol/L)	*T* (°C)	$M_{n,th}$[b] (g/mol)	$M_{n,SEC}$[c] (g/mol)	M_w/M_n	*f*[d]
1	1.24	0.115	−78	18 700	19 300	1.19	0.97
2	5.72	0.216	−78	7 640	8 300	1.18	0.92
3[e]	5.07	0.091	−78	3 600	5 100	1.15	0.70
4[f]	1.75	0.189	−78	21 800	25 100	1.20	0.87
5[f]	2.54	0.189	−78	15 000	16 600	1.17	0.90
6	1.83	0.096	−40	10 570	20 800	1.21	0.51
7	1.83	0.096	−20	10 570	89 000	1.82	0.12

[a]Polymer was freeze-dried from benzene for 10 h. [b]$M_{n,th}$ = grams of monomer/mole of initiator. [c]Apparent molecular weight obtained using SEC calibrated with standard PMMA. [d]Initiator efficiency, $f = M_{n,th}/M_{n,SEC}$. [e]In the absence of $LiClO_4$ additive. [f]TritylK was used as initiator.

The ^{1}H NMR of the synthesized PVBMA showed an absence of signals at 5.6 and 6.18 ppm (*b*) corresponding to methacrylate vinyl protons and an appearance of new signals for the backbone aliphatic protons at ∼1 ppm (*a*) and 1.5 ppm (*b*). The signals corresponding to the styrene moiety at 5.2, 5.7 ppm (doublets, *f*) and 6.6 ppm (multiplet, *e*) are intact in the PVBMAs indicating the styrene pendants were not involved in the polymerization. Furthermore, the proton intensity of the methyl group matched with the vinyl protons of the styrene pendants (Figure 1). Several batch polymerizations were performed. The results are given in Table 1. The obtained PVBMA was completely soluble in solvents such as THF, chloroform, toluene, and benzene, indicating an absence of cross-linking.

The number-average molecular weights (M_n) of PVBMAs were determined using size exclusion chromatography (SEC) with respect to poly(methyl methacrylate) standards, and hence they are apparent ones. However, they agreed well with the molecular weight calculated ($M_{n,th}$) on the basis of the concentration of monomer to the initiator in the feed, indicating the PVBMA has a similar hydrodynamic volume compared to PMMA. As shown in the Table 1, the (PVBMA)s exhibited narrow molecular weight distribution (MWD) (M_w/M_n < 1.2) without high molecular weight fraction, indicating the absence of cross-linking during the polymerization at −78 °C

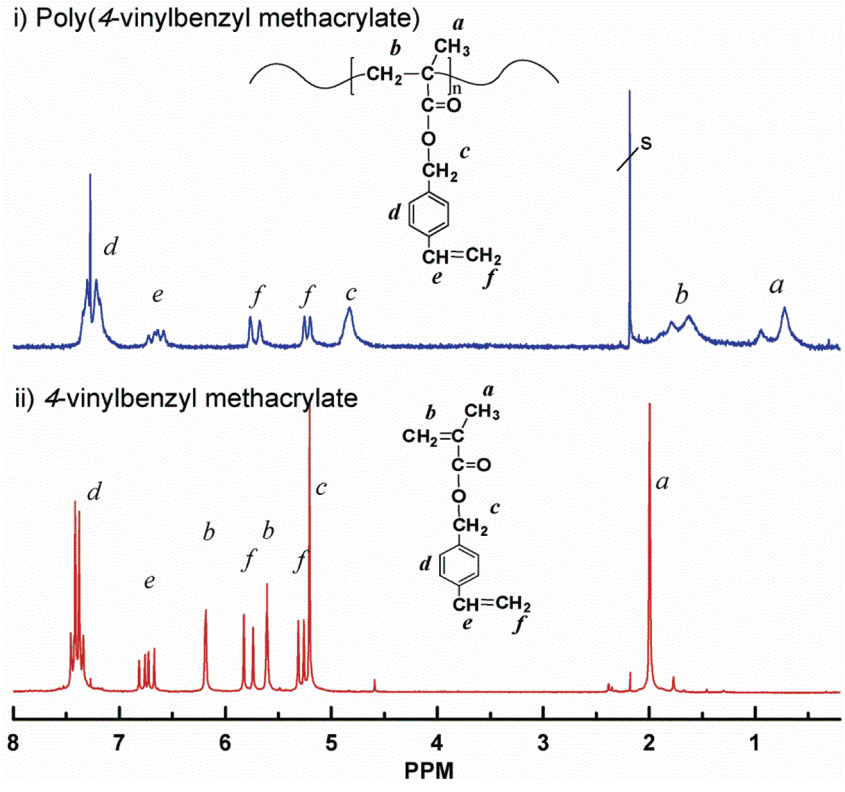


Figure 1. ^{1}H NMR of monomer before and after anionic polymerization using DPHLi as initiator in the presence of $LiClO_4$ as additive in THF at −78 °C: (i) PVBMA and (ii) VBMA ("s" indicates residual solvent).

dx.doi.org/10.1021/ma202750b | Macromolecules 2012, 45, 3387−3393

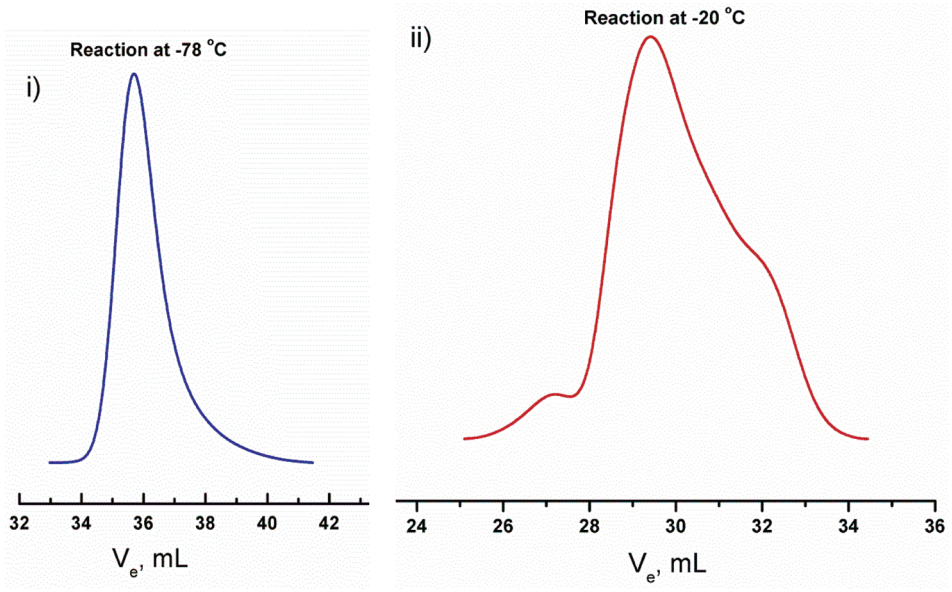


Figure 2. SEC traces of poly(4-vinylbenzyl methacrylate) (PVBMA) using DPHLi as initiator in the presence of $LiClO_4$ as additive in THF. (i) Reaction performed at −78 °C; $M_{n,SEC}$ = 19 260 g/mol, M_w/M_n = 1.19. (ii) Reaction performed at −20 °C in THF; $M_{n,SEC}$ = 89 000 g/mol, M_w/M_n = 1.82.

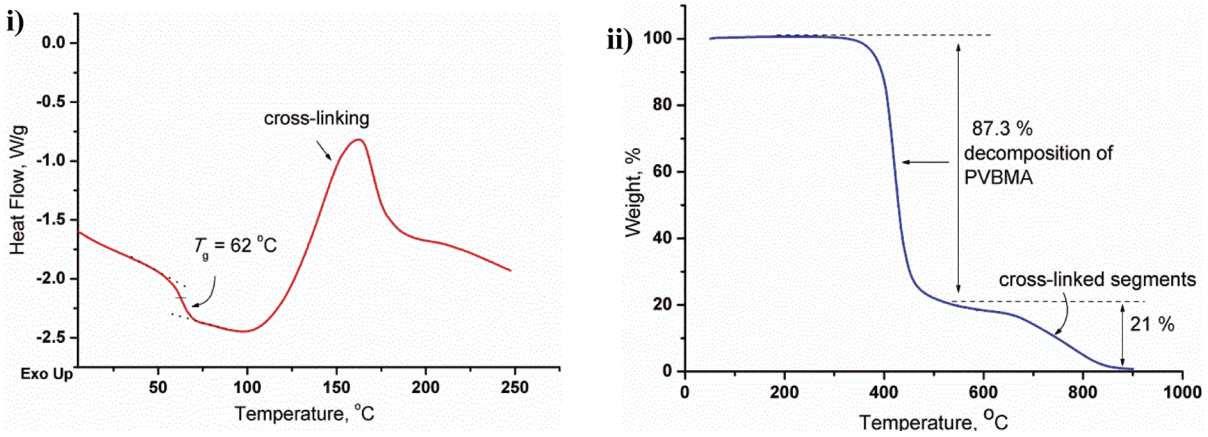


Figure 3. Thermal characterization of PVBMA. (i) DSC at first heating cycle showing T_g at 62 °C and a broad exotherm for cross-linking. (ii) TGA of PVBMA performed in the presence of air showing cross-linking during decomposition at the heating rate of 10 °C/min.

(Figure 2i). However, the precipitated polymer which exhibited narrow MWD (M_w/M_n = 1.19) when dried at 80 °C under vacuum showed a high molecular weight hump in SEC with M_w/M_n > 1.80 (Supporting Information, Tables S1 and S2). This is consistent with the results obtained by Pugh and Percec.[9] Thus, the vinyl pendant in close proximity with ester linkage is highly reactive even in the solid state. Therefore, in subsequent reactions, the polymer was recovered by freeze-drying in benzene at −10 °C and stored in the refrigerator. Polymerization performed in the absence of additive also produced PVBMA with narrow MWD (Table 1, run 3). It appears that the presence of $LiClO_4$ does not have a significant effect in modulating the aggregation dynamics of the enolate anion derived from VBMA. The reason for such a behavior is not clearly understood, a steric factor associated with styrene pendants may be attributed to an ineffective salt complexation.

Similarly, the polymerization initiated using TritylK produced PVBMAs with narrow MWD through selective initiation at methacrylate functionality at −78 °C (Table 1, runs 4 and 5). On the other hand, the polymerization of VBMA carried out using commercial anionic initiators such as *sec*-butyllithum or *n*-butyllithium in THF at −78 °C produced insoluble gel with low yields, indicating the occurrence of cross-linking due to the participation of both the vinyl groups in the monomer. The results confirm that the resonance-stabilized carbanions with an optimum pK_a (30 ≤ pK_a ≤ 32) of their conjugate acids such as DPHLi and TritylK[33] do not react with styrene functionality at −78 °C. It should be mentioned that DPHLi anion has been used as an initiator for styrene to create a wide variety of architectures at room temperature in nonpolar solvents.[31] The temperature-dependent selective initiation can be attributed to the higher electronegativity of the methacrylate group as compared to vinyl group of styrene. The formation of linear PVBMA with styrene pendants at −78 °C in THF indicates the rate of initiation at the vinyl functionality with these initiators is strongly dependent on the temperature. No evidence of cross-linking was observed even when the reaction was performed at −40 °C as evident from the obtained narrow MWD of PVBMA (Table 1, run 6).

dx.doi.org/10.1021/ma202750b | *Macromolecules* 2012, 45, 3387−3393

Table 2. Anionic Diblock Copolymerization of MMA with VBMA Using DPHLi in the Presence of $LiClO_4$ Additive ($[LiClO_4]_0/[DPHLi]_0 = 10$) in THF at −78 °C[a]

		first block					PMMA-*b*-PVBMA				
run	$[DPHLi] \times 10^3$ (mol/L)	[MMA] (mol/L)	$M_{n,calcd}$[b] (g/mol)	$M_{n,SEC}$[c] (g/mol)	M_w/M_n	f[d]	[VBMA] (mol/L)	$M_{n,calcd}$[b] (g/mol)	$M_{n,SEC}$[c] (g/mol)	M_w/M_n	f[d]
1	1.87	0.343	18 300	23 300	1.09	0.80	0.013	19 700	24 300	1.09	0.81
2	1.87	0.487	26 000	28 500	1.09	0.91	0.052	27 600	30 300	1.10	0.91
3[e]	2.84	0.295	10 400	11 500	1.07	0.90	0.105	17 900	19 700	1.11	0.91

[a]Polymer was precipitated from methanol and dried in air at room temperature for 4 h. [b]$M_{n,cal}$ = grams of monomer/mole of initiator. [c]Obtained using SEC calibrated with PMMA standards. [d]Initiator efficiency, $f = M_{n,calcd}/M_{n,SEC}$. [e]VBMA was first polymerized followed by MMA to obtain PVBMA-*b*-PMMA.

However, polymerization carried out at −20 °C gave PVBMA, which exhibited uncontrolled molecular weight with low and high molecular weight humps in SEC, indicating the occurrence of cross-linking through the styrene pendants (Figure 2ii). It should be noted that the homopolymerization of VBMA via GTP using silylketen acetal as the initiator did not proceed to 100% conversion. The synthesized PVBMA exhibited a broad and bimodal distribution.[9] Although the primary fraction showed a narrow molecular weight distribution, the overall polydispersity index was high (M_w/M_n = 8.3). The high molecular weight hump was attributed to an uncontrolled cross-propagation at room temperature due to thermal polymerization of the styrene groups. Nevertheless, in the present study, clearly such cross-propagation does occur even at −20 °C in the anionic polymerization. Although the reaction mixture did not show any indication of the development of a typical red color of styryl anion, the SEC result suggests that the cross propagation of enolate ion pairs occurs with styrene at −20 °C. A multimodal distribution was obtained (Figure 2ii), confirming the local exotherm resulting from the enolate propagating centers complicated the process via thermal initiation of styrene pendants.

The differential scanning calorimetry (DSC) analysis of the PVBMA showed two transitions in the first scan. The midpoint endothermic transition at 62 °C is a glass transition temperature which is in accordance with the reported value[9] and a substantial exothermic broad peak in the region between ~110 and 180 °C is arising from the thermal cross-linking via styrene pendants (Figure 3). Thermogravimetric analysis (TGA) showed two distinct decomposition peaks: a sharp one at T_{max} ~ 445 °C and a broad one at T_{max} ~ 700 °C. The latter is attributed to the decomposition of the segments that had undergone thermal cross-linking while heating the sample at the rate of 10 °C/min.

Synthesis of Block Copolymer with MMA. The living nature of the polymerization of VBMA could be used for the preparation of diblock copolymer through sequential block copolymerization with MMA. The block copolymerization of VBMA with MMA was carried out in the presence of $LiClO_4$ in THF at −78 °C. Well-defined block copolymers with short segments of PVBMA were obtained regardless of the monomer addition sequence (Table 2). The SEC traces of the diblock copolymers showed controlled molecular weight with narrow MWD supporting a noninterfering nature of the styrene pendants during the diblock formation (Figure 4).

High Reactivity of Pendant Styrene Units. Interestingly, the THF solution of PVBMA ($M_{n,SEC}$ = 8300 g/mol, M_w/M_n = 1.18, Table 1, run 2) kept at 35 °C had a slow cross-linking even without an initiator and produced higher molecular weight polymer. The SEC of the aged polymer showed appearance of high molecular weight fractions in the eluogram with broader MWD (Figure 5). The soluble nature of the cross-linked polymer indicates that the extent of cross-linking is very low. The SEC eluogram of PVBMA obtained from an aged sample solution at 60 °C for 2 h shows a multimodal distribution with

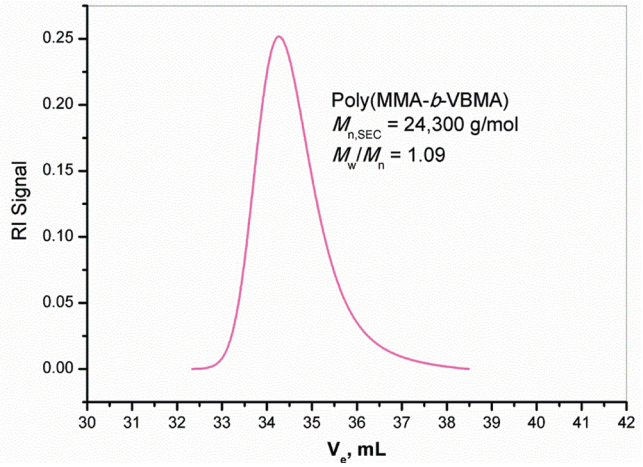


Figure 4. SEC trace of Poly(MMA-*b*-VBMA) via sequential monomer addition in THF at −78 °C; $M_{n,SEC}$ = 24 300 g/mol, M_w/M_n = 1.09 (PMMA block, $M_{n,SEC}$ = 23 300 g/mol, M_w/M_n = 1.09).

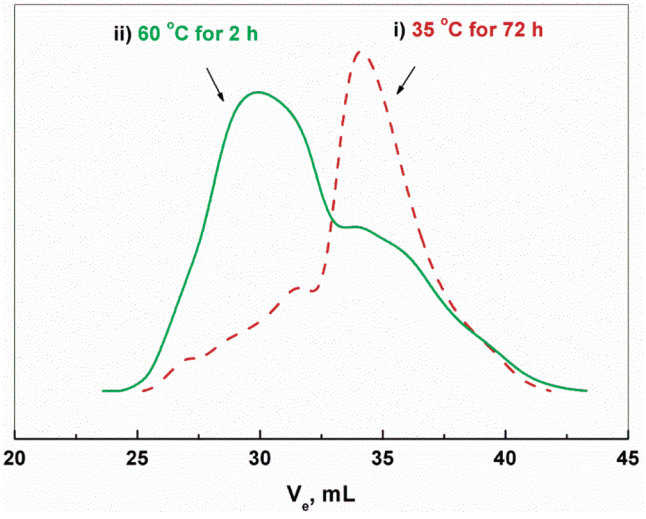


Figure 5. SEC traces of PVBMA (Table 1, run 2) kept at 35 °C for 72 h in THF, $M_{w,SEC}$ = 168 800 g/mol, M_w/M_n = 8.20 and at 60 °C for 2 h, $M_{w,SEC}$ = 411 100 g/mol, M_w/M_n = 15.22 in the absence of radical initiator showing substantial radical cross-linking of pendant styrene units.

dx.doi.org/10.1021/ma202750b | Macromolecules 2012, 45, 3387−3393

an increased higher molecular weight fraction ($M_{w,SEC}$ = 411 100 g/mol, M_w/M_n = 15.22). Thus, PVBMA can be readily cross-linked thermally in the solution with or without a radical initiator and could be photo-cross-linked. However, the polymers can be stored in refrigerator without undergoing cross-linking. The results indicate that the reactivity of the pendant styrene in PVBMA is higher in solution than in the solid state. Thus, the pendant styrene units can serve as a replacement for other cross-linkable segments like polybutadiene, poly(allyl methacrylate), or poly(cinnamoyl methacrylate).

As the styrene pendants are very reactive in the polymer both in solid and in solution, a short PVBMA segment containing PMMA-*b*-PVBMA diblock copolymer was cross-linked using benzyl peroxide as radical initiator in toluene at 80 °C to obtain a cross-linked polystyrene core with starlike PMMA arms emanating from it (Supporting Information, Figure S1). Although the reaction was not complete, the SEC showed a peak at substantially high elution volume, indicating the formation of starlike PMMA with cross-linked PS polymer. The high reactivity of styrene pendants can find usage in many applications such as synthesis of polymer nanoparticles, core cross-linked micelles, and also freezing microphase-separated morphologies of block copolymers containing PVBMA segments via cross-linking at low temperature using solvent swollen (wet) condition.

CONCLUSIONS

Polymers bearing reactive styrene pendants as repeat units have been synthesized through selective anionic initiation of 4-vinylbenzyl methacrylate (VBMA) using resonance stabilized carbanions, 1,1-diphenylhexyllithium (DPHLi) and trityl potassium (TritylK), in THF at −78 °C. We have shown that the nucleophilicity of the stabilized carbanions can be attenuated at −78 °C, for selective anionic initiation of VBMA at its more polar methacrylate site in the presence of styrene functionality. The successful selective polymerization of VBMA through methacrylate group is attributed to a higher activation energy associated with the initiation of styrene using stabilized DPHLi or TritylK initiators. Highly reactive poly(4-vinylbenzyl methacrylate)s and poly(4-vinylbenzyl methacrylate-*b*-methyl methacrylate)s have been synthesized and characterized. The PVBMAs are thermally reactive in solid as well as in solution and will find applications in reactive cross-linking and network formation.

ASSOCIATED CONTENT

Supporting Information

SEC data on cross-linking in solid and in solution (Tables S1 and S2); SEC of star polymer synthesis from PMMA-*b*-PVBMA copolymer. This material is available free of charge via the Internet at http://pubs.acs.org.

AUTHOR INFORMATION

Corresponding Author

*E-mail e-mail:baskaran@utk.edu; phone 865-974-5583.

Present Addresses

[§]GE Global Research, Bangalore, India.

[⊥]Cancer Biology Research Center, Sanford Research/USD, Sioux Falls, SD 57104.

Notes

The authors declare no competing financial interest.

ACKNOWLEDGMENTS

This work was supported by National Chemical Laboratory (Divisional Basic Research Fund), India, and the US Army Research Office (57790-CH). We thank Mr. S. K. Menon, Mrs. Deepa A. Dhoble, and Mr. S. K. Choudhary (Glass Blowing Section) for assistance during this project. D.B. dedicates this work to the Lab-105, Main Building, National Chemical Laboratory, Pune, India, where he worked for several years and has fond memories.

REFERENCES

(1) Li, Z.; Day, M.; Ding, J.; Faid, K. *Macromolecules* **2005**, *38*, 2620−2625.

(2) Percec, V.; Auman, B. C. *Macromol. Chem. Phys.* **1984**, *185*, 2319−2336.

(3) Percec, V.; Auman, B. C. *Macromol. Chem. Phys.* **1984**, *185*, 1867−1880.

(4) Yu, Y. S.; Dubois, P.; Jerome, R.; Teyssie, P. *Macromolecules* **1996**, *29*, 1753−1761.

(5) Ishizone, T.; Uehara, G.; Hirao, A.; Nakahama, S.; Tsuda, K. *Macromolecules* **1998**, *31*, 3764−3774.

(6) Ruckenstein, E.; Zhang, H. *Macromolecules* **1999**, *32*, 6082−6087.

(7) Guan, Z. *J. Am. Chem. Soc.* **2002**, *124*, 5616−5617.

(8) Hirao, A.; Loykulnant, S.; Ishizone, T. *Prog. Polym. Sci.* **2002**, *27*, 1399−1471.

(9) Pugh, C.; Percec, V. *Polym. Bull. (Berlin)* **1985**, *14*, 109−116.

(10) Jiang, J.; Thayumanavan, S. *Macromolecules* **2005**, *38*, 5886−5891.

(11) Nagasaki, Y.; Ito, H.; Tsuruta, T. *Makromol. Chem.* **1986**, *187*, 23.

(12) Baskaran, D. *Polymer* **2003**, *44* (8), 2209−2216.

(13) Hirao, A.; Tanaka, S.; Goseki, R.; Ishizone, T. *Macromolecules* **2011**, *44*, 5479−5482.

(14) Lutz, P.; Beinert, G.; Rempp, P. *Makromol. Chem.* **1982**, *183*, 2787−2797.

(15) Yu, Y. S.; Dubois, P.; Teyssié, P.; Jérôme, R. *Macromolecules* **1997**, *30*, 7356.

(16) Baskaran, D. *Macromol. Chem. Phys.* **2001**, *202*, 1569−1575.

(17) Bywater, S.; Black, P. E.; Wiles, D. M. *Can. J. Chem.* **1966**, *44*, 695.

(18) Sugiyama, K.; Watanabe, H.; Hirao, A.; Hayashi, M. *Macromolecules* **2008**, *41*, 4235−4244.

(19) Ishuizone, T.; Uehara, G.; Hirao, A.; Nakahama, S.; Tsuda, K. *Macromolecules* **1998**, *31*, 3764−3774.

(20) Gao, H. F.; Matyjaszewski, K. *Prog. Polym. Sci.* **2009**, *34*, 317−350.

(21) Paris, R.; de la Fuente, J. L. *J. Polym. Sci., Part A: Polym. Chem.* **2005**, *43*, 2395−2406.

(22) Tobita, H.; Kimura, K.; Fujita, K.; Nomura, M. *Polymer* **1993**, *34*, 2569−2574.

(23) Satav, S. S.; Karmalkar, R. N.; Kulkarni, M. G.; Mulpuri, N.; Sastry, G. N. *J. Am. Chem. Soc.* **2006**, *128*, 7752−7753.

(24) Radhakrishnan, K.; Sivaram, S. *Macromol. Chem. Phys.* **1999**, *200*, 858−862.

(25) Webster, O. W.; Hertler, W. R.; Sogah, D. Y.; Farnham, W. B.; RajanBabu, T. V. *J. Am. Chem. Soc.* **1983**, *105*, 5706−5708.

(26) The pK_a for methyl-α-isobutyrate (a monomeric model conjugate acid for methacrylate propagating anion) is an extrapolated estimate in DMSO calculated by Bordwell et al.[28,29] The pK_a for ethylbenzene (a monomeric model conjugate acid for styrene propagating anion) is not available in the literature. However, the estimated value for toluene is ∼43 in DMSO, and hence we expect that ethylbenzene will have higher pK_a (∼44) than toluene due to methyl group's inductive destabilization of the corresponding anion.

(27) Baskaran, D.; Mueller, A. H. E. Anionic Vinyl Polymerization. In *Controlled and Living Polymerization*; Mueller, A. H. E., Matyjaszewski,

K., Eds.; Wiley-VCH Verlag GmbH & KGaA: Weinheim, 2009; pp 1−56.
(28) Bordwell, F. G. *Acc. Chem. Res.* **1988**, *21*, 456.
(29) Bordwell, F. G.; Fried, H. E. *J. Org. Chem.* **1981**, *46* (22), 4327.
(30) Baskaran, D. Process for the synthesis of reactive polymers and copolymers from vinylbenzyl methacrylate. Indian Patent IN216747, 2008.
(31) Hsieh, H. L.; Quirk, R. P. *Anionic Polymerization: Principles and Practical Applications*; Marcel Dekker, Inc.: New York, 1996.
(32) Baskaran, D.; Sivaram, S. *Macromolecules* **1997**, *30*, 1550−1555.
(33) Although diphenylpotassium (Ph_2CHK) is known to initiate styrene polymerization at −78 °C in THF, the rate of initiation is slow and results in a broad MWD polystyrene. However, it initiates, more reactive, 2-(4-vinylphenyl)pyridine and produces polymer with narrow molecular weight distribution at −78 °C (Kang, N.-G.; Changez, M.; Lee, J.-S. *Macromolecules* **2007**, *40*, 8553−8559).

Macromolecules

Article

pubs.acs.org/Macromolecules

2,2′-Biimidazole-Based Conjugated Polymers as a Novel Fluorescent Sensing Platform for Pyrophosphate Anion

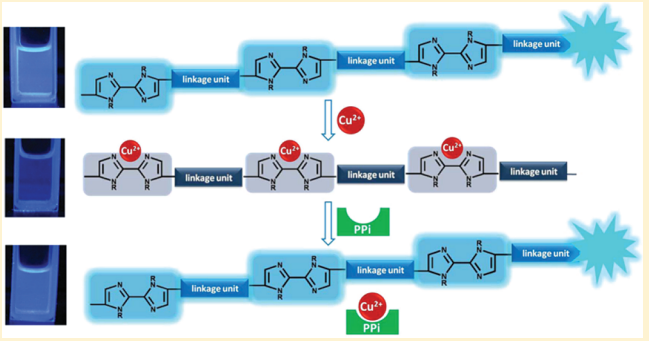
Yinyin Bao,[†] Hu Wang,[†] Qianbiao Li,[†] Bin Liu,[†] Qing Li,[†] Wei Bai,[‡] Bangkun Jin,[†] and Ruke Bai*[,†]

[†]CAS Key Laboratory of Soft Matter Chemistry, Department of Polymer Science and Engineering, University of Science and Technology of China, Hefei 230026, P. R. China

[‡]Department of Chemistry, Louisiana State University, Baton Rouge, Louisiana 70803, United States

Supporting Information

ABSTRACT: Three novel conjugated polymers based on 2,2′-biimidazole have been successfully designed and synthesized through the Suzuki coupling reactions, and their fluorescence sensing ability to metal ions and anions was investigated. The emission of the two polymers with hydrophilic side chains can be efficiently quenched by Cu^{2+} through a photoinduced electron transfer process. Moreover, the polymer−Cu^{2+} complexes exhibit excellent "turn on" sensing properties for detection of pyrophosphate (PPi) anion. These complex sensors possess high selectivity avoiding the interference from other anions, very fast response (less than 3 min) to PPi, and the detection limit of about 0.17 ppm. In addition, the linear detection range of PPi can be tuned conveniently by changing the amount of Cu^{2+} ions. Thus, the conjugated polymers can be used as a novel fluorescent sensing platform, and this work provides a new strategy for the development of PPi sensors.



INTRODUCTION

In recent years, conjugated polymer-based fluorescent sensors have been developed as a highly effective tool for detection of a broad range of environmental and biological analyses.[1] With "molecular wire" effect of the conjugated polymers, the detection sensitivity of the polymer sensors can be greatly enhanced because of the fast energy migration along the conjugated backbone.[2] Thus, conjugated polymers have more advantages over small molecules for sensing applications. Among these polymers, several N-heterocyclic aromatic units have been introduced into the backbone as molecular recognition sites for metal ions, such as bipyridyl,[3] terpyridyl,[4] and phenanthroline.[5] After coordination with different metal ions, the polymers exhibit different fluorescence changes, such as quenching or emission red/blue shift, which can be attributed to electron density variations on the main chains, aggregation of polymer chains, or conjugation enhancement along the polymer backbone.[3−5] However, the selectivity of polymer sensors based on N-heterocycle, especially for the bipyridyl analogue, remains unsatisfactory compared with that of the small molecule sensors.[6] In order to improve the properties of the polymer sensors, the design and synthesis of the conjugated polymer sensors with new aromatic N-heterocycle as a receptor are still a quite important and intriguing theme.

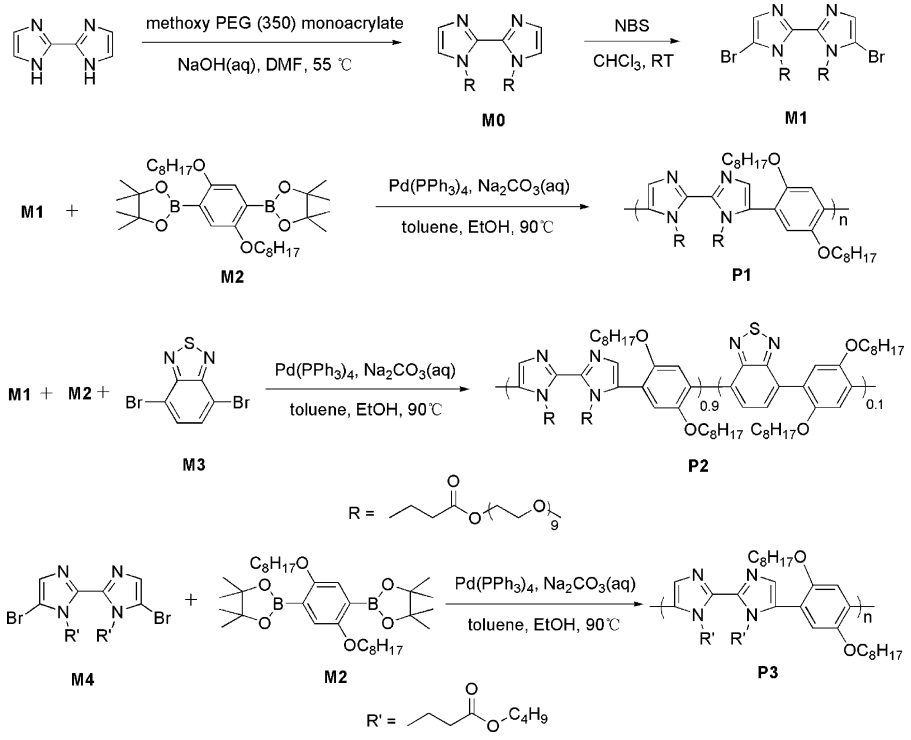
As an important aromatic N-heterocycle, imidazole plays a significant role in biosystems and attractive chemical properties.[7] Most recently, the conjugated polymers with imidazole or imidazolium as the side groups have been synthesized and utilized as excellent fluorescent sensors for detection of metal ions, anions, nitric oxide, and amino acids.[8] 2,2′-Biimidazole, the dimeric analogue of imidazole, is one of the most important derivatives of imidazole and plays a particular role in crystal engineering because of the excellent coordination ability and diverse coordination modes.[9] In addition, 2,2′-biimidazole can be easily functionalized through various ways under mild conditions.[10] However, only very few papers have been devoted to the study of the conjugated polymers containing biimidazole moiety. Yamamoto et al. prepared three 2,2′-biimidazole homopolymers by the dehalogenative polycondensation using a zerovalent nickel catalyst.[11a] Then MacLean et al. reported conjugated polymers of 2,2′-biimidazole obtained through electrochemical polymerization.[11b] The authors did not investigate the fluorescence properties of the polymers; they focused on the structure and chemical properties. From the literature,[12] we know that 2,2′-biimidazole has large M−N (metal−nitrogen) bond length of 4.2 Å, while 2,2′-bipyridine's M−N bond length is only 2.51 Å, which may endow 2,2′-biimidazole containing conjugated polymers with some distinguishing sensing properties.

We have recently incorporated 2,2′-biimidazole into the conjugated polymer and used this kind of polymer as a new

Received: February 21, 2012
Revised: March 30, 2012
Published: April 9, 2012

 © 2012 American Chemical Society dx.doi.org/10.1021/ma300361t | *Macromolecules* 2012, 45, 3394−3401

Scheme 1. Synthesis of Monomers and Polymers



platform for design of different fluorescent sensors.[13] The polymer exhibits distinctive fluorescence response to Ag^+, which is quite different from the features of the conjugated polymers with the oligopyridyl moieties in their backbones and as well as with the imidazole moieties in their side chains. In addition, the polymer−Ag^+ complexes can be used to highly selective detection of cysteine with nanomolar detection limit. In order to further explore new sensors based on the sensing properties of the N-heterocyclic conjugated polymers, we have also designed and prepared three new conjugated polymers based on 2,2′-biimidazole (**P1**, **P2**, and **P3**, Scheme 1) and found that the polymers exhibit high quantum yields in solutions. Moreover, the fluorescence of **P1** and **P2** can be efficiently quenched by Cu^{2+} in DMF−H_2O mixed solvents. Therefore, a new sensing platform utilizing the polymer−Cu^{2+} complexes for detection of pyrophosphate (PPi) anion has been achieved. The complex sensors exhibit high selectivity and fast response to PPi with the detection limit of about 0.17 ppm, and the linear detection range of PPi can be tuned conveniently by changing the amount of Cu^{2+} ions. Herein we report the synthesis, characterization, and sensing properties of the polymers.

EXPERIMENTAL SECTION

Materials. Metal salts such as NaCl, KCl, $MgCl_2$, $CaCl_2$, $FeCl_3$, $ZnCl_2$, $CdCl_2$, $NiCl_2$, $CuCl_2$, $Mn(OAc)_2$, $Pb(OAc)_2$, and $AgNO_3$ were purchased from Shanghai Chemical Co. and used without further purification. Et_3N and 1,4-dioxane were freshly distilled over appropriate drying agents. The reactions that required oxygen-free conditions were carried out under an argon atmosphere using standard Schlenk techniques. All the other reagents were purchased and used without further purification.

Measurements. Fluorescence spectra measurements were performed on a Shimadzu RF-5301PC spectrofluorophotometer. Absorption spectra were determined on a Pgeneral UV−vis TU-1901 spetrophotometer. ^1H and ^{13}C NMR spectra were taken on a Bruker AVANCEII spectrometer with TMS as an internal standard and $CDCl_3$ as solvent. Molecular weights and molecular weight distributions were determined by GPC equipped with a Waters 1515 pump, a Waters 2414 RI detector, and Waters UV/RI detectors (set at 30 °C) using a series of three linear Styragel columns HR3, HR4, and HR6 at an oven temperature of 45 °C. Mass spectra were performed on a ProteomeX-LTQ spectrometer. FT-IR spectra were recorded on a Bruker EQUINOX55 spectrometer. All spectra were measured at room temperature (temperature controlled at 25 ± 3 °C).

Synthesis of M0. Solid 2,2′-biimidazole[14] (0.67 g, 5.0 mmol) was dispersed in DMF (20 mL), and 0.5 N NaOH(aq) (1.0 mL) was added. The suspension was stirred and heated to 50 °C. A solution composed of methoxy poly(ethylene glycol) monoacrylate (5.0 g, 10.3 mmol) solubilized in DMF (10 mL) was added dropwise. After 4 h, the solution was neutralized with aqueous hydrochloric acid and the heating discontinued. The solvent was removed by rotary evaporation, and the product was chromatographed on silica gel (CH_2Cl_2:methanol = 20:1, v/v) to give **M0** (5.5 g) as a pinkish liquid; yield: 98.7%. ^1H NMR (400 MHz, $CDCl_3$): δ = 7.07 (s, 2H), 7.03 (s, 2H), 4.74 (t, 4H), 4.21 (t, 4H), 3.62 (m, 68H), 3.36 (s, 6H), 2.93 (t, 4H). ^{13}C NMR (100 MHz, $CDCl_3$): δ = 171.3, 137.7, 127.8, 122.3, 71.9, 70.5, 68.9, 63.8, 59.0, 43.3, 35.5. MS: m/z = 1098.61.

Synthesis of M1. *N*-Bromosuccinimide (0.38 g, 2.13 mmol) was added to a chloroform solution (15 mL) of **M0** (1.17 g, 1.06 mmol) under vigorous stirring under air. After 2 h, the reaction mixture was neutralized with NaOH(aq), and the product was extracted with chloroform. After being washed with water, the combined organic layers were dried (Na_2SO_4) and chromatographed on silica gel (CH_2Cl_2:methanol = 20:1, v/v) to give **M1** (2.6 g) as light yellow liquid; yield: 65.4%. ^1H NMR (400 MHz, $CDCl_3$): δ = 7.12 (s, 2H), 4.70 (t, 4H), 4.07 (t, 4H), 4.21 (t, 4H), 3.63 (m, 68H), 3.37 (s, 6H), 2.91 (t, 4H). ^{13}C NMR (100 MHz, $CDCl_3$): δ = 170.6, 138.4, 128.9, 105.8, 71.9, 70.5, 68.9, 63.9, 59.0, 42.1, 34.3. MS: m/z = 1256.43.

Synthesis of M2. 1,4-Diiodo-2,5-dioctyloxybenzene[15] (1.67 g, 3.0 mmol), pinacolborane (1.32 mL, 9.0 mmol), Et_3N (2.5 mL), and $PdCl_2$(dppf) (0.05 g, 0.06 mmol) were dissolved in anhydrous 1,4-dioxane (12 mL) under an Ar atmosphere, and the solution was stirred overnight at 90 °C. After cooling to room temperature, the mixture was poured into water (50 mL) and extracted with Et_2O (3 × 20 mL).

dx.doi.org/10.1021/ma300361t | Macromolecules 2012, 45, 3394−3401

The combined organic layers were dried (Na_2SO_4) and chromatographed on silica gel (petroleum ether:ethyl acetate = 20:1, v/v) to give **M2** (1.2 g) as a brown solid; yield: 72%. ^{1}H NMR (400 MHz, $CDCl_3$): δ = 7.08 (s, 2H), 3.93 (t, 2H), 1.74 (m, 2H), 1.47 (m, 2H), 1.34 (s, 12H), 1.30−1.24 (m, 8H), 0.88 (t, 6H). ^{13}C NMR (100 MHz, $CDCl_3$): δ = 157.7, 119.9, 83.4, 69.7, 31.9, 29.6, 29.5, 29.3, 26.1, 24.8, 22.7, 14.1. MS: m/z = 586.46.

Synthesis of P1. **M2** (0.23 g, 0.4 mmol), **M1** (0.5 g, 0.4 mmol), $Pd(PPh_3)_4$ (0.05 g, 0.04 mmol), and Na_2CO_3 (0.85 g, 8.0 mmol) were added to a flask under an Ar atmosphere. A solvent mixture of toluene (8 mL), water (4 mL), and ethanol (2 mL) was degassed and added to the reaction mixture. The resulting mixture was refluxed with vigorous stirring for 48 h. After cooling to room temperature, the mixture was poured into water (30 mL) and extracted with $CHCl_3$ (3 × 30 mL). The collected organic layers were dried (Na_2SO_4) and purified by precipitated from ether to give **P1** (0.11 g) as a brown solid; yield: 19.6%. M_w = 8900, M_w/M_n = 1.27 (GPC, polystyrene calibration). ^{1}H NMR (400 MHz, $CDCl_3$): δ = 7.12 (br, ArH), 6.94 (br, ArH), 4.74 (br, $-CH_2-O-$), 4.13−3.89 (br, $-CH_2-N-$ and $-CH_2-O-$), 3.63−3.54 (br, $-O-CH_2CH_2-O-$), 3.36 ($-O-CH_3$), 2.76 (br, $-CH_2-COO-$), 1.69 (br, $-CH_2-$), 1.24 (br, $-CH_2-$), 0.86 (br, $-CH_3$). UV−vis (DMF, 8.0 × 10^{-6} mol/L): λ_{max} = 335 nm. IR (thin film), υ (cm^{-1}): 2928, 2860 (CH_2 stretching), 1737 (C═O stretching), 1102 (C−O stretching).

Synthesis of P2. **P2** was prepared by reaction of **M2** (0.17 g, 0.3 mmol), **M1** (0.34 g, 0.27 mmol), and 4,7-dibromo-2,1,3-benzothiadiazole (0.009 g, 0.03 mmol) using the same procedure as **P1**. The yield was 23% of **P2** (0.09 g) as a brown solid. M_w = 5200, M_w/M_n = 1.28 (GPC, polystyrene calibration). ^{1}H NMR (400 MHz, $CDCl_3$): δ= 7.47−6.93 (br, ArH), 4.75 (br, $-CH_2-O-$), 4.15−3.93 (br, $-CH_2-N-$ and $-CH_2-O-$), 3.63−3.54 (br, $-O-CH_2CH_2-O-$), 3.37 ($-O-CH_3$), 2.75 (br, $-CH_2-COO-$), 1.81−1.45 (br, $-CH_2-$), 1.23 (br, $-CH_2-$), 0.86 (br, $-CH_3$). UV−vis (DMF, 8.0 × 10^{-6} mol/L): λ_{max} = 326 nm. IR (thin film), υ (cm^{-1}): 2926, 2855 (CH_2 stretching), 1735 (C═O stretching), 1100 (C−O stretching).

Synthesis of P3. **P3** was prepared by reaction of **M2** (0.17 g, 0.3 mmol) and **M4**[13] (0.16 g, 0.3 mmol) using the same procedure as **P1**, except that the polymer was purified by precipitated from methanol to give a slightly gray solid (0.09 g); yield: 45%. M_w = 12 000, M_w/M_n = 1.40 (GPC, polystyrene calibration). ^{1}H NMR (400 MHz, $CDCl_3$): δ = 7.14 (ArH), 6.95 (ArH), 4.78 (br, $-CH_2-N-$), 4.11−3.93 (br, $-CH_2-O-$), 2.76 (br, $-CH_2-COO-$), 1.71−1.53 (br, $-CH_2-$), 1.34−1.25 (br, $-CH_2-$), 0.91−0.85 (br, $-OCHH_3$). UV−vis (DMF, 8.0 × 10^{-6} mol/L): λ_{max} = 336 nm. IR (thin film), υ (cm^{-1}): 2965, 2904 (CH_2 stretching), 1735 (C═O stretching), 1100 (C−O stretching).

Fluorometric Analysis. The stock solutions of **P1**, **P2**, and **P3** were prepared by dissolving the polymers in DMF (1.0 × 10^{-3} M) and were diluted as required before use. The cation stock solutions were prepared by dissolving the metal salts in deionized water with a concentration of 0.01 M. The stock solutions of F^-, Cl^-, Br^-, I^-, NO_3^-, HSO_4^-, AcO^-, HCO_3^-, CO_3^{2-}, $H_2PO_4^-$, HPO_4^{2-}, PO_4^{3-}, and $P_2O_7^{2-}$ were prepared in deionized water with a concentration of 0.01 M. A solution of polymer (2.0 mL) was placed in a quartz cell (10.0 mm width), and the fluorescence spectrum was recorded. The sum volume of each ion solution introduced to the test solution was no more than 50 μL, and the changes of the fluorescence intensity were recorded at room temperature (λ_{ex} = 338 nm). The quantum yields of the polymers were determined according to the equation

$$\Phi_u = \Phi_s \frac{F_u A_s n_u^2}{F_s A_u n_s^2}$$

where Φ is quantum yield, F is integrated area under the corrected emission spectra, A is absorbance at the excitation wavelength, n is the refractive index of the solution, and the subscripts u and s refer to the unknown and the standard, respectively. Quinine bisulfate in 0.05 M H_2SO_4 solution was used as the standard, which has a quantum yield of 0.55.

RESULTS AND DISCUSSION

Design and Synthesis. The polymers **P1**, **P2**, and **P3** were synthesized by Suzuki condensation, and the synthetic routes are illustrated in Scheme 1. 2,2′-Biimidazole was prepared according to the published procedure[14] and then was reacted with methoxy poly(ethylene glycol) monoacrylate through Michael addition reaction to form **M0**. Subsequently, **M0** was brominated with *N*-bromosuccinimide (NBS) at room temperature, resulting 5,5′-dibromo-*N*,*N*′-di(methoxy poly(ethylene glycol) monoacrylate propionato)-2,2′-biimidazole (**M1**) as a hydrophilic monomer. A hydrophobic monomer 5,5′-dibromo-*N*,*N*′-di(*n*-butylpropionato)-2,2′-biimidazole (**M4**) was synthesized by a similar method.[13] Monomer **M2** (1,4-bis(4,4,5,5,-tetramethyl-1,3,2-dioxaborolan-2-yl)-2,5-dioctyloxyphenylene) was synthesized from 1,4-diiodo-2,5-dioctyloxybenzene[15] through borylation reaction catalyzed by $PdCl_2(dppf)$,[16] and monomer **M3** (4,7-dibromo-2,1,3-benzothiadiazole) was prepared according to the literature procedures.[17] **P1** was conveniently formed via Suzuki coupling reaction between **M1** and **M2** catalyzed by the $Pd(PPh_4)_3$, and **P3** was obtained in a similar approach with **M4** and **M2**. **P2** was synthesized utilizing 1.0 equiv of **M2**, 0.9 equiv of **M1**, and 0.1 equiv of **M3**. **P1** and **P2** were purified by precipitation from ether and collected as brown solids, while **P3** was obtained by precipitation from methanol as a slightly gray solid. It is worthy to point out that 2,2′-biimidazole-based monomers were efficiently synthesized under mild conditions, which makes the 2,2′-biimidazole containing polymers more accessible compared with the other N-hetercycle-based main chain conjugated polymers. Utilizing the 2,2′-biimidazole-based monomers, different kinds of conjugated polymers can be prepared conveniently, resulting a new series of fluorescence sensing molecules.

Characterization of Polymers. The purified polymers were characterized by ^{1}H NMR, FT-IR, UV−vis, and GPC analysis (see Experimental Section and Supporting Information for detailed analysis data). In the ^{1}H NMR spectra of the polymers **P1**, **P2**, and **P3** (Figure 1 and Figures S34 and S35),

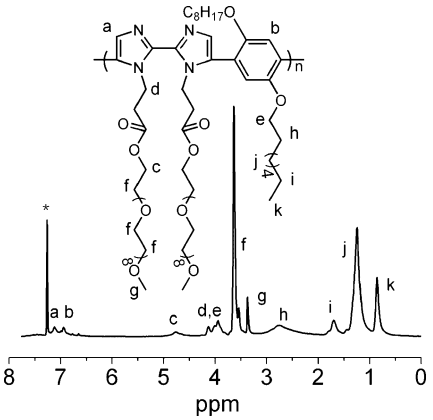


Figure 1. ^{1}H NMR spectra of **P1** in chloroform-*d*. The solvent peak was marked with asterisks.

the chemical shifts are consistent with the proposed structure of the polymers as demonstrated in Scheme 1. Take **P1** for example; as shown in Figure 1, the two peaks at about 7.12 and 6.94 ppm in the downfield can be ascribed to the aromatic protons of biimidazole unit and benzene unit, respectively, indicating **M1** and **M2** have been successfully copolymerized

dx.doi.org/10.1021/ma300361t | Macromolecules 2012, 45, 3394−3401

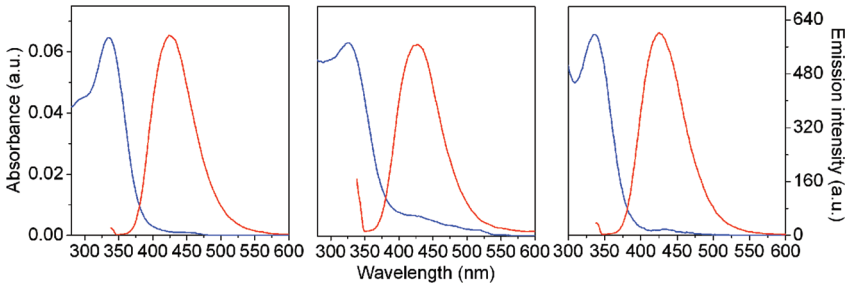


Figure 2. UV−vis absorption (blue line) and fluorescence spectra (red line) of **P1** (left), **P2** (middle), and **P3** (right) in DMF. [**P1**] = [**P2**] = [**P3**] = 8.0×10^{-6} M. λ_{ex} = 338 nm.

through Suzuki condensation. And the existence of the ether side chains and octyl side chains can be confirmed by the peaks at 3.36 and 0.86, which can also be supported by the bands at 2965 and 2904 cm^{-1} of C−H vibration stretching, 1737 cm^{-1} of C═O stretching, and 1102 cm^{-1} of C−O stretching in the FT-IR spectrum of **P1** (Figure S36).

The three polymers readily dissolve in common organic solvents, such as toluene, CH_2Cl_2, THF, and DMF, because of the flexible alkyl or ether side chains. The molecular weights (M_n) and polydispersity index (PDI) of the polymers were determined by gel permeation chromatography (GPC) with polystyrene as the reference standard (Table S1). The molecular weights of the polymers are relatively low, which may be because the polymerization reactivity of the 2,2′-biimidazole-based monomers is not very high. Even so, the molecular weights are high enough for the polymers to have good sensing properties, and a similar phenomenon can be seen in the previous reports[3−5] on polycondensation of N-heterocycle-based monomers. The UV−vis absorption spectra of polymers are shown in Figure 2, **P1**, **P2**, and **P3** have similar maximum absorption wavelengths around 330 nm in DMF because of the similar conjugated backbone. But **P2** has stronger absorption from 400 to 550 nm, which can be attributed to the alkoxybenzene−benzothiadiazole units. All the evidence indicates that the designed polymers have been successfully prepared.

Fluorescence Properties and Ion Recognition. The emission spectra of **P1** and **P2** were measured in various organic solvents at room temperature (Figures S1 and S2). It can be seen that the two polymers exhibit highest emission intensity in DMF, so it was chosen as the main solvent to investigate the fluorescence properties of the polymers. The results show that all the three polymers exhibit a strong blue fluorescence with a maximum around 425 nm in DMF because of the conjugated polymer backbone. However, in the presence of alkoxybenzene−benzothiadiazole units, **P2** shows a little broader emission peak. Simultaneously, a Förster resonance energy transfer (FRET) process may exist in **P2** because the weak absorption peak of the alkoxybenzene−benzothiadiazole unit can be found to overlap with the emission peak of the alkoxybenzene−biimidazole unit. The orange emission peak around 550 nm can be observed more obviously in the solution of THF, dioxane, and toluene than in DMF (Figure S2), and a similar phenomenon has also been observed in our previous report.[13] The fluorescence quantum yields of **P1**, **P2**, and **P3** in DMF were determined to be 0.22, 0.10, and 0.41, respectively. In order to examine the properties of these polymers in aqueous solution, the fluorescence spectra of the three polymers in DMF−H_2O mixed solvents were studied. As shown in Figures S3−S6, the emission intensity of the polymers decreases along with increasing the water content; this can be attributed to the chain aggregation-induced fluorescence quenching. Note that **P3** shows much faster quenching rate than the other two polymers (Figure S7). This phenomenon indicates that both **P1** and **P2** with hydrophilic side chains can be better dispersed in DMF−H_2O mixed solvents. Thus, **P1** and **P2** are more suitable for fluorescence sensing application in aqueous solution compared with **P3**. Moreover, as shown in Figure S5, the fluorescence intensity ratios $F_{550\ nm}/F_{423\ nm}$ of **P2** increases along with raising the water content, and after the water content reaches 90% the emission peak at 423 nm disappeared, resulting a single peak at 550 nm (Figure S4). This result can be largely ascribed to the fact that the FRET effect existing in **P2** system is distinctly enhanced because of water-induced chain aggregation.[13]

Since the polymers **P1** and **P2** show high fluorescence quantum yield (Table S1) and good dispersion in DMF−H_2O (4:1, v/v), we chose the mixed solvent as the detection media, and HEPES was used as the buffer agent. The ion responsive properties of **P1** were studied by fluorescence spectroscopy in DMF−HEPES (pH = 7.4, v/v = 4:1) at a concentration of 8.0×10^{-6} M. The experimental result displays that the fluorescence of **P1** can be efficiently quenched by Cu^{2+} ions. As shown in Figure 3, upon the addition of Cu^{2+}, the emission

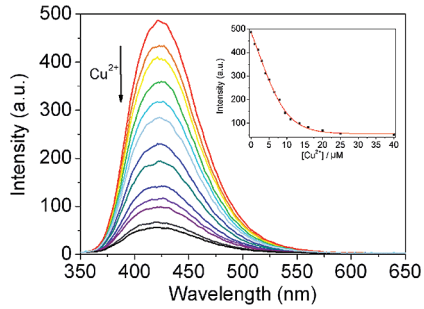


Figure 3. Fluorescence spectra of **P1** upon the titration of Cu^{2+} in DMF−HEPES (pH = 7.4, v/v = 4:1). Inset: fluorescence intensity of **P1** as a function of Cu^{2+} concentration. λ_{ex} = 338 nm. [**P1**] = 8.0×10^{-6} M.

peaks at 423 nm gradually decrease along with increasing the Cu^{2+} concentration. The intensity exhibits a good linear response to a Cu^{2+} concentration change from 0 to 1.0 equiv, and after adding 2.5 equiv of Cu^{2+}, 90% of the fluorescence has been quenched. The quenching efficiency can be described by the Stern−Volmer equation, $I_0/I = K_{sv}[A] + 1$, which related to the fluorescence intensity, I, at different concentrations of analyte quencher, [A], where I_0 is the intensity at [A] = 0 and K_{sv} is the Stern−Volmer constant. According to the

dx.doi.org/10.1021/ma300361t | *Macromolecules* 2012, 45, 3394−3401

fluorescence titration of **P1** in DMF aqueous solution with Cu^{2+}, K_{sv} of the system was determined to be 3.3×10^5 M^{-1} (Figure S8). When the quantum yield of **P1** changed from 0.13 to 0.02 upon interaction with Cu^{2+}, the obvious fluorescence changes could be observed by the naked eye under a UV lamp. For comparison's sake, the Cu^{2+} response properties of **P3** were also studied (Figures S13–S15). However, the Stern–Volmer quenching constant K_{sv} of **P3**–Cu^{2+} was calculated to be only 2.8×10^3 M^{-1} (Figure S15), which is much lower than that of **P1**–Cu^{2+}. And after addition of 20.0 equiv of Cu^{2+}, only 30% of the fluorescence can be quenched. This result indicates that **P1** has much stronger coordination ability with Cu^{2+} than **P3** in DMF–H_2O mixed solvent, which implies that the hydrophilic side chains can promote the interaction between the polymer and Cu^{2+} ions in aqueous solution. Thus, the reasonable design of side chains is important to construct conjugated polymer-based fluorescent sensors.

In general, there are two possibilities that metal ions cause an obvious fluorescence quenching phenomenon of conjugated polymer: one is electron transfer interactions between the polymer backbone and metal ions, and the other is interpolymer aggregation induced by coordination. To further clarify the mechanism, we investigated the fluorescence response properties of **P2** to Cu^{2+} in aqueous DMF solution. If the fluorescence quenching is induced by chain aggregation, after adding enough Cu^{2+} ions the FRET enhancement similar to the phenomenon caused by water (Figure S4) should be observed, leading to a large change of intensity ratios $F_{550\ nm}/F_{423\ nm}$. However, upon interaction with Cu^{2+}, the intensity ratios $F_{550\ nm}/F_{423\ nm}$ exhibits only a slight increment, and no obvious emission peak at 550 nm was actually observed in the **P2** system (Figures S9 and S10), which means aggregation of polymer chains is not the principal contributor to the quenching phenomenon in the system. Thus, we may reasonably conclude that the emission quenching of the polymers is mainly due to electron transfer interactions between the polymer backbone and Cu^{2+} ions, which was also reported in the previous paper.[8c] In addition, this work provides an efficient method to investigate the sensing mechanism of conjugated polymers to metal ions, which was not reported in the literature of other N-heterocycle-based polymer sensors.[3−5,8] At the same time, the Stern–Volmer constant K_{sv} of **P2**–Cu^{2+} was calculated to be 2.6×10^5 M^{-1} (Figure S12), which is of the same order of magnitude as, but a little lower than, that of the **P1**–Cu^{2+} system. This result shows that the fluorescence of **P2** can also be efficiently quenched by Cu^{2+}, and the lower Stern–Volmer constant compared to that of **P1**–Cu^{2+} system may be attributed to the lower molecular weight, resulting in a slightly weaker "molecular wire" effect. Thus, the electron transfer interactions between the polymers and Cu^{2+} can be tuned by changing the molecular weight of the polymer. Therefore, the reasonable design of the backbone is critical to develop efficient conjugated polymer-based fluorescent sensors. In addition, the coordination reaction of **P1** and **P2** with Cu^{2+} has been confirmed by the UV–vis titration experiment (Figures S16 and S17).

As shown in Figures S18–S21, compared with other metal ions, Cu^{2+} ion shows the strongest quenching ability to the polymers. It is well-known that pyrophosphate (PPi) anion has strong interaction with Cu^{2+};[18] thus, we attempted to use these polymer–Cu^{2+} complexes as new sensors for detection of PPi. PPi is a biologically important target because it is the product of ATP hydrolysis under cellular conditions.[19] There are many papers published on the study of PPi fluorescent sensors based on the metal ion complexes[20] and hydrogen-bond or ionic bond interaction.[21] However, only very few PPi sensors based on conjugated polymers have been reported.[22] Herein we prepared the Cu^{2+} complexes of the conjugated polymers containing 2,2′-biimidazole moieties *in situ* by mixing **P1** and **P2** with Cu^{2+} salt in aqueous DMF, respectively, and studied their sensing properties for PPi. The results indicate that the emission spectra of the complexes exhibit remarkable changes upon interaction with PPi. As shown in Figure 4, the emission

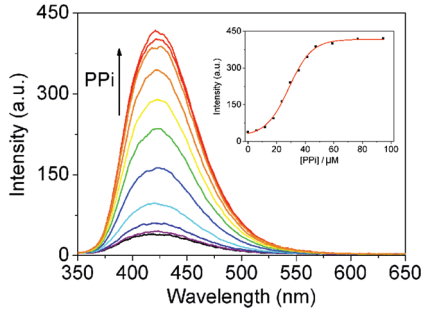


Figure 4. Fluorescence spectra of **P1**–Cu^{2+} complex upon the titration of PPi in DMF–HEPES (pH = 7.4, v/v = 4:1). Inset: fluorescence intensity of **P1**–Cu^{2+} complex as a function of PPi concentration. λ_{ex} = 338 nm. [**P1**] = 8.0×10^{-6} M. [Cu^{2+}] = 2.0×10^{-5} M.

peak of **P1**–Cu^{2+} ([**P1**] = 8.0×10^{-6} M, [Cu^{2+}] = 2.0×10^{-5} M) gradually increases upon addition of different amount of PPi anions, and the intensity at 423 nm exhibits a good linear change with a PPi concentration increasing from 1.0×10^{-5} to 4.8×10^{-5} M. Moreover, when utilizing 1.0×10^{-5} M Cu^{2+} and 8.0×10^{-6} M **P1** as the sensing ensemble, the emission intensity changes linearly with the concentration of PPi from 5.0×10^{-6} to 1.6×10^{-5} M (Figure 5). Thus, the linear change

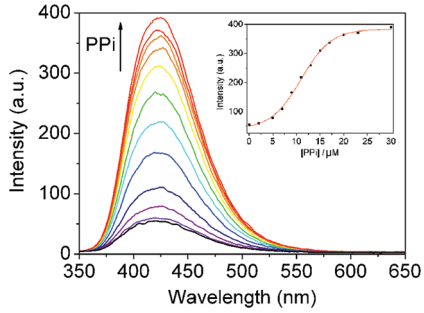
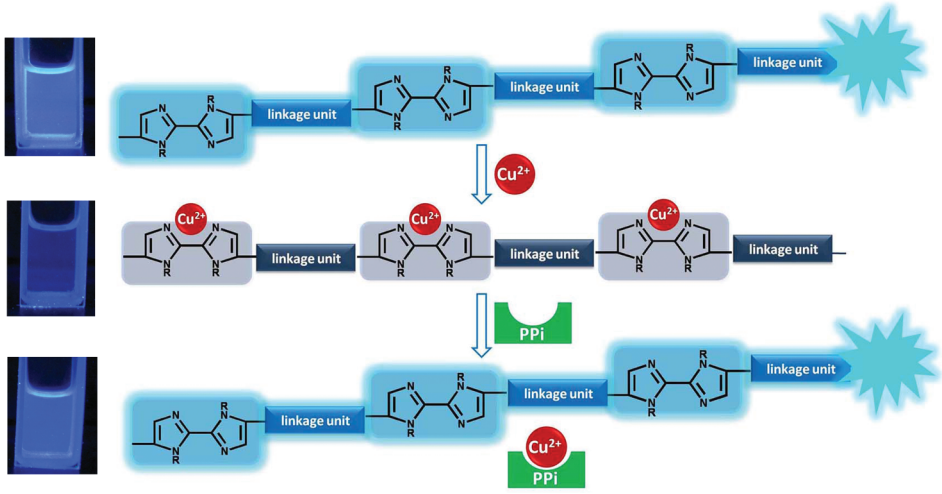


Figure 5. Fluorescence spectra of **P1**–Cu^{2+} complex upon the titration of PPi in DMF–HEPES (pH = 7.4, v/v = 4:1). Inset: fluorescence intensity of **P1**–Cu^{2+} complex as a function of PPi concentration. λ_{ex} = 338 nm. [**P1**] = 8.0×10^{-6} M. [Cu^{2+}] = 1.0×10^{-5} M.

range of PPi can be tuned by varying the amount of Cu^{2+} ions. After adding 5.0 equiv of PPi, a 9-fold emission enhancement can be obtained, and the fluorescence changes under a UV lamp can be distinctly observed by the naked eye (Chart 1). From the fluorescence titration experiment, the detection limit of PPi was estimated to be less than 1.0×10^{-6} M, about 0.17 ppm. Similar to **P1**, **P2** also shows good turn-on sensing properties for PPi in the presence of Cu^{2+} ions (Figures S22–S25). As shown in Figures S23 and S25, the linear range 1.0×10^{-5}–3.6×10^{-5} M can be changed into 5.0×10^{-6}–2.4×10^{-5} M by varying the concentration of Cu^{2+} from 2.0×10^{-5} to 1.0

dx.doi.org/10.1021/ma300361t | *Macromolecules* 2012, 45, 3394–3401

Chart 1. Schematic Representation of PPi Sensors Based on the Fluorescence "On−Off−On" of 2,2′-Biimidazole Containing Conjugated Polymers



× 10^{-5} M. The sensing process is consistent with the displacement approach reported in the previous report[18,20] utilizing metal ion complexes, the fluorescence of the polymers can be recovered once the Cu^{2+} ions are removed by PPi, and the possible sensing mechanism is illustrated in Chart 1. These sensors are based on the interaction of PPi with Cu^{2+} ions coordinated to the biimidazole group on polymer backbone, while the other polymer PPi sensors[22] rely on the interaction of PPi with Cu^{2+} on the polymer side chains or directly with the polymers.

The response time is very important for a sensor; therefore, the effect of the interaction time on the fluorescence emission of the system has been examined, and the results are shown in Figure 6. It can be seen that the emission intensity of **P1**−Cu^{2+}

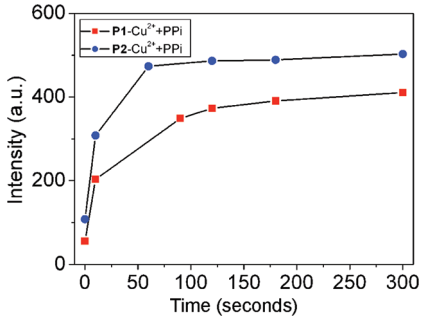


Figure 6. Effect of reaction time on the fluorescence intensity of **P1**−Cu^{2+} and **P2**−Cu^{2+} by PPi ions in DMF−HEPES (pH = 7.4, v/v = 4:1). λ_{ex} = 338 nm. [**P1**] = [**P2**] = 8.0 × 10^{-6} M. [Cu^{2+}] = 2.0 × 10^{-5} M. [PPi] = 4.0 × 10^{-5} M.

reaches to its saturation value in just 3 min due to the strong interaction of Cu^{2+} ions with the PPi anions. On the other hand, the response time of **P2**−Cu^{2+} to PPi is only 1 min, much shorter than that of **P1**−Cu^{2+}. The reason is that **P2** has weaker binding ability to Cu^{2+} than **P1** due to the lower molecular weight, which can be deduced from the Stern−Volmer constants. Since **P2**−Cu^{2+} complex possesses a faster response, it can be used as an excellent sensor for rapid detection of PPi. We can conclude that the fluorescence sensing properties of conjugated polymer based fluorescent sensors can be efficiently optimized through the reasonable structure modification.

To determine the selectivity of the PPi-sensing systems, the fluorescence responses of **P1**−Cu^{2+} and **P2**−Cu^{2+} complexes were further examined with 13 different anions including monovalent anions (F^-, Cl^-, Br^-, I^-, NO_3^-, HSO_4^-, AcO^-, HCO_3^-, $H_2PO_4^-$), divalent anions (CO_3^{2-}, HPO_4^{2-}), and trivalent ion PO_4^{3-}. As shown in Figure 7 and Figures S26 and

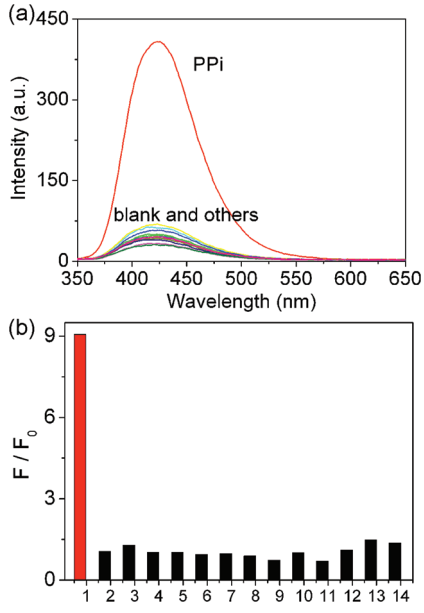


Figure 7. (a) Fluorescence spectra of **P1**−Cu^{2+} complex and (b) intensity ratios F/F_0 of **P1**−Cu^{2+} complex in the presence of 4.0 × 10^{-5} M PPi and 8.0 × 10^{-5} M various anions in DMF−HEPES (pH = 7.4, v/v = 4:1). λ_{ex} = 338 nm. [**P1**] = 8.0 × 10^{-6} M. [Cu^{2+}] = 2.0 × 10^{-5} M. 1, PPi; 2, F^-; 3, Cl^-;4, Br^-; 5, I^-; 6, NO_3^-; 7, HSO_4^-; 8, ClO_4^-; 9, AcO^-; 10, HCO_3^-; 11, CO_3^{2-}, 12, $H_2PO_4^-$; 13, HPO_4^{2-}; 14, PO_4^{3-}.

S27, the experiment results indicate that all of the other anions exhibit weak binding affinities to Cu^{2+} ion and lead to negligible changes in the fluorescence properties of the complexes. Therefore, PPi can be easily differentiated from the other anions, especially from PO_4^{3-}, by the emission intensity. This

dx.doi.org/10.1021/ma300361t | Macromolecules 2012, 45, 3394−3401

result indicates that the novel polymer complexes exhibit a high selectivity for detecting PPi.

CONCLUSIONS

In summary, we have successfully designed and synthesized three novel conjugated polymers based on 2,2′-biimidazole through the Suzuki coupling reaction and also investigated their ability to sense metal ions and anions. The fluorescence of the two polymers with hydrophilic side chains can be efficiently quenched by Cu^{2+} ions through a photoinduced electron transfer process. Based on the unique interaction of Cu^{2+} with the polymers, the two conjugated polymer−Cu^{2+} complexes have been demonstrated to be potential "turn on" fluorescent sensors for detection of pyrophosphate anion. The sensors possess high sensitivity to PPi with the detection limit of about 0.17 ppm and excellent selectivity avoiding the interference from other anions. And the linear detection range of PPi can be tuned conveniently by changing the amount of Cu^{2+} ions. Since the sensors display very fast response (less than 3 min), it provides a rapid and efficient approach for the detection of PPi. The experiment results show that the fluorescence sensing properties of the polymers can be efficiently optimized through the reasonable structure modification. In addition, the facile synthesis of the 2,2′-biimidazole-based conjugated polymers under mild conditions makes the sensors more accessible compared with the other N-heterocycle-based conjugated polymers. To the best of our knowledge, this is the first example utilizing the 2,2′-biimidazole-based conjugated polymers to detect PPi, and this work provides not only a new strategy for the development of PPi sensors but also a novel platform to further design different fluorescent sensors for other analytes.

ASSOCIATED CONTENT

Supporting Information

^{1}H NMR of monomers; ^{13}C NMR of monomers; ^{1}H NMR of **P2** and **P3**; optical data of polymers **P1** and **P2** in various organic solvents; optical data of polymers **P1**−**P3** in aquous DMF solution with different water contents; optical data of polymers **P1** and **P2** in the presence of various metal ions in DMF−HEPES (pH = 7.4, v/v = 4:1); UV−vis absorption and fluorescence titration experiment data of **P1**−**P3** to Cu^{2+} and PPi; selectivity of **P2**−Cu^{2+} to PPi; FT-IR spectra of **P1**−**P3**. This material is available free of charge via the Internet at http://pubs.acs.org.

AUTHOR INFORMATION

Corresponding Author

*Tel 86-551-3600722; Fax 86-551-3631760; e-mail bairk@ustc.edu.cn.

Notes

The authors declare no competing financial interest.

ACKNOWLEDGMENTS

The financial support from National Natural Science Foundation of China (No. 20974104 and No. 21074120) and Ministry of Science and Technology of China (No. 2007CB936401) is gratefully acknowledged.

REFERENCES

(1) (a) Toal, S. J.; Trogler, W. C. *J. Mater. Chem.* **2006**, *16*, 2871−2883. (b) Feng, F.; He, F.; An, L.; Wang, S.; Li, Y.; Zhu, D. *Adv. Mater.* **2008**, *20*, 2959−2964. (c) Fan, L.-J.; Zhang, Y.; Murphya, C. B.; Angell, S. E.; Parkera, M. F.L.; Flynna, B. R.; Jones, W. E., Jr. *Coord. Chem. Rev.* **2009**, *253*, 410−422. (d) Liu, Y.; Ogawa, K.; Schanze, K. S. *J. Photochem. Photobiol., C* **2009**, *10*, 173−190. (e) Feng, X.; Liu, L.; Wang, S.; Zhu, D. *Chem. Soc. Rev.* **2010**, *39*, 2411−2419. (f) Li, K.; Liu, B. *Polym. Chem.* **2010**, *1*, 252−259. (g) Duarte, A.; Pu, K.-Y.; Liu, B.; Bazan, G. C. *Chem. Mater.* **2011**, *23*, 501−515. (h) Rostami, A.; Taylor, M. S. *Macromol. Rapid Commun.* **2012**, *33*, 21−34.

(2) (a) Swager, T. M. *Acc. Chem. Res.* **1998**, *31*, 201−207. (b) McQuade, D. T.; Pullen, A. E.; Swager, T. M. *Chem. Rev.* **2000**, *100*, 2537−2574. (c) Thomas, S. W., III; Joly, G. D.; Swager, T. M. *Chem. Rev.* **2007**, *107*, 1339−1386.

(3) (a) Wang, B.; Wasielewski, M. R. *J. Am. Chem. Soc.* **1997**, *119*, 12−21. (b) Chen, L. X.; Ja1ger, W. J. H.; Gosztola, D. J.; Niemczyk, M. P.; Wasielewski, M. R. *J. Phys. Chem. B* **2000**, *104*, 1950−1960. (c) Liu, B.; Yu, W.-L.; Pei, J.; Liu, S.-Y.; Lai, Y.-H.; Huang, W. *Macromolecules* **2001**, *34*, 7932−7940. (d) Smith, R. C.; Tennyson, A. G.; Lim, M. H.; Lippard, S. J. *Org. Lett.* **2005**, *7*, 3573−3575. (f) Liu, Y.; Zhang, S.; Miao, Q.; Zheng, L.; Zong, L.; Cheng, Y. *Macromolecules* **2007**, *40*, 4839−4847. (g) He, S.; Iacono, S. T.; Budy, S. M.; Dennis, A. E.; Smith, D. W.; Smith, R. C. *J. Mater. Chem.* **2008**, *18*, 1970−1976. (h) Kaes, C.; Katz, A.; Hosseini, M. W. *Chem. Rev.* **2000**, *100*, 3553−3590.

(4) (a) Kimura, M.; Horai, T.; Hanabusa, K.; Shirai, H. *Adv. Mater.* **1998**, *10*, 459−462. (b) Zhang, Y.; Murphy, C. B.; Jones, W. E. *Macromolecules* **2002**, *35*, 630−636.

(5) (a) Yasuda, T.; Yamaguchi, I.; Yamamoto, T. *Adv. Mater.* **2003**, *15*, 293−296. (b) Yasuda, T.; Yamamoto, T. *Macromolecules* **2003**, *36*, 7513−7519. (c) Zhang, M.; Lu, P.; Ma, Y.; Shen, J. *J. Phys. Chem. B* **2003**, *107*, 6535−6538. (d) Liu, X.; Zhou, X.; Shu, X.; Zhu, J. *Macromolecules* **2009**, *42*, 7634−7637.

(6) (a) Ajayaghosh, A.; Carol, P.; Sreejith, S. *J. Am. Chem. Soc.* **2005**, *127*, 14962−14963. (b) Dennis, A. E.; Smith, R. C. *Chem. Commun.* **2007**, 4641−4643. (c) Sreejith, S.; Divya, K. P.; Ajayaghosh, A. *Chem. Commun.* **2008**, 2903−2905. (d) Cockrell, G. M.; Zhang, G.; VanDerveer, D. G.; Thummel, R. P.; Hancock, R. D. *J. Am. Chem. Soc.* **2008**, *130*, 1420−1430.

(7) Fox, S. W. *Chem. Rev.* **1943**, *32*, 47−71.

(8) (a) Ho, H. A.; Leclerc, M. *J. Am. Chem. Soc.* **2003**, *125*, 4412−4413. (b) Zhou, X.-H.; Yan, J.-C.; Pei, J. *Macromolecules* **2004**, *37*, 7078−7080. (c) Xing, C.; Yu, M.; Wang, S.; Shi, Z.; Li, Y.; Zhu, D. *Macromol. Rapid Commun.* **2007**, *28*, 241−245. (d) Zeng, Q.; Cai, P.; Li, Z.; Qina, J.; Tang, B. Z. *Chem. Commun.* **2008**, 1094−1096. (e) Li, Z.; Lou, X.; Yu, H.; Li, Z.; Qin, J. *Macromolecules* **2008**, *41*, 7433−7439. (f) Zeng, Q.; Jim, C. K. W.; Lam, J. W. Y.; Dong, Y.; Li, Z.; Qin, J.; Tang, B. Z. *Macromol. Rapid Commun.* **2009**, *30*, 170−175. (g) Salinas-Castillo, A.; Camprubí-Robles, M.; Mallavia, R. *Chem. Commun.* **2010**, *46*, 1263−1265.

(9) Tadokoro, M.; Nakasuji, K. *Coord. Chem. Rev.* **2000**, *198*, 205−218.

(10) (a) Barnett, M.; Secondo, P.; Collier, H. *J. Heterocycl. Chem.* **1996**, *33*, 1363. (b) Sánchez-García, D.; Borrós, S.; Nonell, S.; Borrell, J. I.; Colominas, C.; Teixidó, J. *J. Heterocycl. Chem.* **2002**, *39*, 733. (c) Matthews, D. P.; McCarthy, J. R.; Whitten, J. P.; Kastner, P. R.; Barney, C. L.; Marshall, F. N.; Ertel, M. A.; Burkhard, T.; Shea, P. J.; Kariyat, T. *J. Med. Chem.* **1990**, *33*, 317−327.

(11) (a) Yamamoto, T.; Uemura, T.; Tanimoto, A.; Sasaki, S. *Macromolecules* **2003**, *36*, 1047−1053. (b) Walker, D. T.; Douglas, C. D.; MacLean, B. J. *Can. J. Chem.* **2009**, *87*, 729−737.

(12) Buist, D.; Williams, N. J.; Reibenspies, J. H.; Hancock, R. D. *Inorg. Chem.* **2010**, *49*, 5033−5039.

(13) Bao, Y.; Li, Q.; Liu, B.; Du, F.; Tian, J.; Wang, H.; Wang, Y.; Bai, R. *Chem. Commun.* **2012**, *48*, 118−120.

(14) Fieselmann, B. F.; Hendrickson, D. N.; Stucky, G. D. *Inorg. Chem.* **1978**, *17*, 2078−2084.

(15) Weder, C.; Wrighton, M. S. *Macromolecules* **1996**, *29*, 5157−5165.

(16) (a) Murata, M.; Watanabe, S.; Masuda, Y. *J. Org. Chem.* **1997**, *62*, 6458−6459. (b) Bao, Y.; Liu, B.; Wang, H.; Du, F.; Bai, R. *Anal. Methods* **2011**, *3*, 1274−1276.
(17) Neto, B. A. D.; Lopes, A. S.; Ebeling, G.; Gonçalves, R. S.; Costa, V. E. U.; Quina, F. H.; Dupont, J. *Tetrahedron* **2005**, *61*, 10975−10982.
(18) (a) Kim, S. K.; Lee, D. H.; Hong, J.-I.; Yoon, J. *Acc. Chem. Res.* **2009**, *42*, 23−31. (b) Fabbrizzi, L.; Marcotte, N.; Stomeo, F.; Taglietti, A. *Angew. Chem., Int. Ed.* **2002**, *41*, 3811−3814. (c) Huang, X.; Guo, Z.; Zhu, W.; Xie, Y.; Tian, H. *Chem. Commun.* **2008**, 5143−5145. (d) Guo, Z.; Zhu, W.; Tian, H. *Macromolecules* **2010**, *43*, 739−744. (e) Kim, M. J.; Swamy, K. M. K.; Lee, K. M.; Jagdale, A. R.; Kim, Y.; Kim, S.-J.; Yooc, K. H.; Yoon, J. *Chem. Commun.* **2009**, 7215−7217. (f) Zhang, J. F.; Park, M.; Ren, W. X.; Kim, Y.; Kim, S. J.; Jung, J. H.; Kim, J. S. *Chem. Commun.* **2011**, *47*, 3568−3570.
(19) Mathews, C. P.; van Hold, K. E. *Biochemistry*; The Benjamin/Cummings Publishing Co., Inc.: Redwood City, CA, 1990.
(20) (a) Mizukami, S.; Nagano, T.; Urano, Y.; Odani, A.; Kikuchi, K. *J. Am. Chem. Soc.* **2002**, *124*, 3920−3925. (b) Lee, D. H.; Kim, S. Y.; Hong, J.-I. *Angew. Chem., Int. Ed.* **2004**, *43*, 4777−4780. (c) Aoki, S.; Kagata, D.; Shiro, M.; Takeda, K.; Kimura, E. *J. Am. Chem. Soc.* **2004**, *126*, 13377−13390. (d) Jang, Y. J.; Jun, E. J.; Lee, Y. J.; Kim, Y. S.; Kim, J. S.; Yoon, J. *J. Org. Chem.* **2005**, *70*, 9603−9606. (e) Lee, H. N.; Xu, Z.; Kim, S. K.; Swamy, K. M. K.; Kim, Y.; Kim, S.-J.; Yoon, J. *J. Am. Chem. Soc.* **2007**, *129*, 3828−3829. (f) Ojida, A.; Takashima, I.; Kohira, T.; Nonaka, H.; Hamachi, I. *J. Am. Chem. Soc.* **2008**, *130*, 12095−12101. (g) Shao, N.; Wang, H.; Gao, X.; Yang, R.; Chan, W. *Anal. Chem.* **2010**, *82*, 4628−4636. (h) Chen, W.-H.; Xing, Y.; Pang, Y. *Org. Lett.* **2011**, *13*, 1362−1365.
(21) (a) Vance, D. H.; Czarnik, A. W. *J. Am. Chem. Soc.* **1994**, *116*, 9397−9398. (b) Nishizawa, S.; Kato, Y.; Teramae, N. *J. Am. Chem. Soc.* **1999**, *121*, 9463−9464. (c) Gunnlaugsson, T.; Davis, A. P.; O'Brien, J. E.; Glynn, M. *Org. Lett.* **2002**, *4*, 2449−2452. (d) Aldakov, D.; Anzenbacher, P., Jr. *Chem. Commun.* **2003**, 1394−1395. (e) Gunnlaugsson, T.; Davis, A. P.; O'Brien, J. E.; Glynn, M. *Org. Biomol. Chem.* **2005**, *3*, 48−56. (f) Zyryanov, G. V.; Palacios, M. A.; Anzenbacher, P., Jr. *Angew. Chem., Int. Ed.* **2007**, *46*, 7849−7852. (g) Kim, I.-B.; Han, M. H.; Phillips, R. L.; Samanta, B.; Rotello, V. M.; Zhang, Z. J.; Bunz, U. H. F. *Chem.—Eur. J.* **2009**, *15*, 449−456.
(22) (a) Zhao, X.; Liu, Y.; Schanze, K. S. *Chem. Commun.* **2007**, 2914−2916. (b) Liu, Y.; Schanze, K. S. *Anal. Chem.* **2008**, *80*, 8605−8612. (c) Zhao, X.; Schanze, K. S. *Chem. Commun.* **2010**, *46*, 6075−6077. (d) Wu, C.-Y.; Chen, M.-S.; Lin, C.-A.; Lin, S.-C.; Sun, S.-S. *Chem.—Eur. J.* **2006**, *12*, 2263−2269. (e) Kim, K. M.; Oh, D. J.; Ahn, K. H. *Chem.—Asian J.* **2011**, *6*, 122−127.

Macromolecules

Article

pubs.acs.org/Macromolecules

Synthesis and Characterization of High Refractive Index and High Abbe's Number Poly(thioether sulfone)s based on Tricyclo[5.2.1.0^{2,6}] decane Moiety

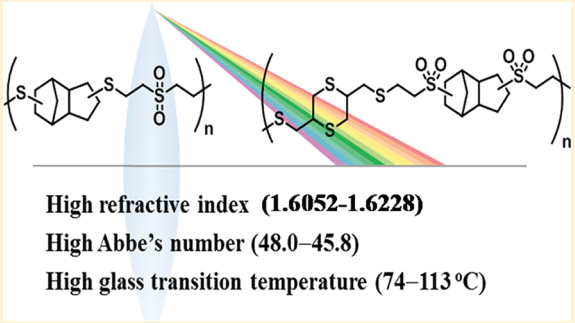
Yasuo Suzuki,[†] Tomoya Higashihara,[†,‡] Shinji Ando,[†] and Mitsuru Ueda*[,†]

[†]Department of Organic and Polymeric Materials, Graduate School of Science and Engineering, Tokyo Institute of Technology, 2-12-1-H-120, O-okayama, Meguro-Ku, Tokyo 152-8552, Japan

[‡]Japan Science and Technology Agency (JST), 4-1-8, Honcho, Kawaguchi, Saitama 332-0012, Japan

Supporting Information

ABSTRACT: Novel thermoplastic poly(thioether sulfone)s, poly(TCDSH/DVS) and poly(BSMD/VSTCD), with high refractive indices and high Abbe's numbers have been developed using disulfanyltricyclo[5.2.1.0^{2,6}]decane (TCDSH) and bis(vinylsulfone)-tricyclo[5.2.1.0^{2,6}]decane (VSTCD) based on tricyclo[5.2.1.0^{2,6}]-decane moiety. TCDSH and VSTCD were easily prepared from dicyclopentadiene via two or three steps and polymerized with divinyl sulfone (DVS) or 2,5-bis(sulfanylmethyl)-1,4-dithiane (BSMD) to give high molecular weight polymers (M_n = 19 300 and 28 400). The flexible, transparent, and amorphous films of poly(TCDSH/DVS) and poly(BSMD/VSTCD) were successfully prepared. They showed a good thermal stability with the 5% weight loss temperatures of around 300 °C in nitrogen, the glass transition temperatures of 74 and 113 °C, high refractive indices of 1.6052 and 1.6228, and high Abbe numbers of 48.0 and 45.8, respectively. Poly(TCDSH/DVS) and poly(BMMD/VSTCD) with highly balanced thermal and optical properties are promising candidates for optical application, especially for lens materials.



INTRODUCTION

Development of highly functional materials has been increasingly indispensable for the progress of advanced optical devices. Polymeric materials with a high refractive index (high-n) and a high Abbe's number (high-ν) attract significant interest because of their application as optical materials such as lenses, prisms, and waveguides, with the advantage of lightweight, impact resistance, processability, and dying ability compared to inorganic glasses.[1,2] Polymeric materials include thermosets and thermoplastics. The former such as resins from episulfides,[3] polythiols,[4] and polyisocyanates[5] have been developed for consumer use such as eyeglasses that are manufactured by cast molding. On the other hand, the latter such as poly(methyl methacrylate), polycarbonate, and cyclo-olefin polymers[6] are used in camera, pick-up, and projector lenses where injection molding is applied.

A general approach for increasing the refractive indices of polymers is the introduction of substituents with a high molar refraction and low molar volume according to the Lorentz–Lorenz equation.[7] Among the various substituents, the sulfur element is commonly selected because of its high polarizability, stability, and facility to introduce to polymers. Meanwhile, the Abbe's number (ν), which is a measure for the refractive index dispersion, is also a key parameter for optical materials used in the visible region. The Abbe's number is given by the following equation

$$\nu_D = (n_D - 1)/(n_F - n_C) \quad (1)$$

where n_D, n_F, and n_C are the refractive indices of the material at the wavelengths of the sodium D (589.3 nm), hydrogen F (486.1 nm), and hydrogen C (656.3 nm) lines, respectively.[8] A high Abbe's number corresponds to a lower dispersion in the refractive index. It has been reported that high-n materials generally exhibit small Abbe's numbers (Figure 1).[9] Development of polymeric materials with both high-n and high-ν is, therefore, a challenging topic.

Various kinds of high-n and high-ν polymers containing the sulfur elements were reported.[11−13] Recently, in our group, a high-n and high-ν poly(thioether sulfone) (PES) from 2,5-disulfanyl-1,4-dithiane and divinyl sulfone (DVS) was developed by the simultaneous introduction of sulfide and sulfone groups.[14] Generally, polymers with a high sulfur content show a high refractive index and a relatively low Abbe's number (<40) because a sulfide has a high atomic refraction ([R] = 7.80) and high atomic dispersion ([ΔR] = 0.22).[8,15,16] On the other hand, a sulfone has a low [ΔR] of 0.07 for [R] of 9.76, and thus the PES containing both groups exhibited high-n and high-ν.[14] However, a brown coloration of the PES started at around 150

Received: February 23, 2012
Revised: April 4, 2012
Published: April 13, 2012

 © 2012 American Chemical Society

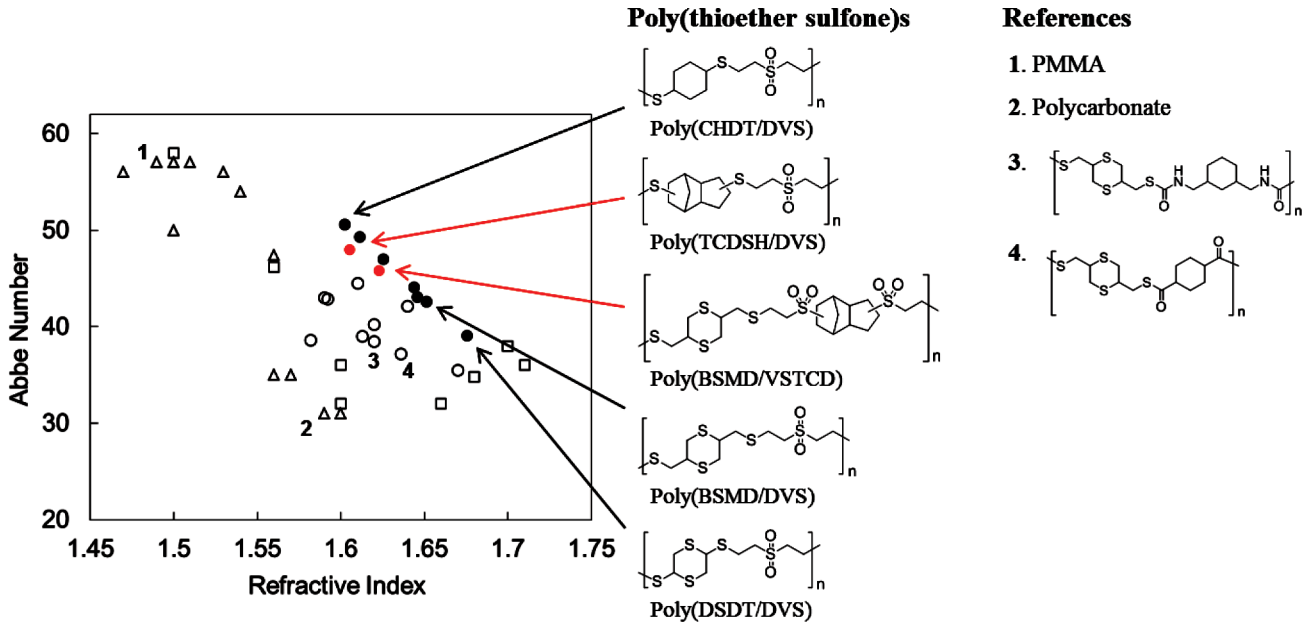


Figure 1. Abbe's numbers and refractive indices of optical materials: (□) thermosets; (Δ) thermoplastics; (○) sulfur-containing thermoplastics; (●) poly(thioether sulfone)s.[10]

°C, probably due to the thioacetal group in the main chain, which means the injection molding process cannot be applied.

To prevent this coloration of the PES, other PESs without a thioacetal group were prepared from DVS and 2,5-bis-(sulfanylmethyl)-1,4-dithiane (BSMD) or cyclohexane-1,4-dithiol.[17,18] They indeed exhibited high thermal stability, no coloration even at 200 °C in air, as well as high refractive indices (1.60−1.65) and high Abbe's numbers (50.6−42.6). The n_D and ν_D values of these and other PESs are plotted in the highest $n_D-\nu_D$ area among the organic materials while polythioesters[19] and polythiourethanes show a relatively lower n_D and ν_D (Figure 1). It reveals that PESs are the highest class of thermoplastics for high-n and high-ν materials.

However, their T_g values were low around 50 °C, which must be increased to over 100 °C for practical lens application. The low T_g values can be attributed to the flexible sulfide group and alkyl chain in the main chain. One of the most promising methods to increase the T_g of polymers is introduction of a rigid structure such as polycyclic hydrocarbons.[6,20,21] In this work, tricyclo[5.2.1.0^{2,6}]decane (TCD) consisting of three condensed cyclopentanes was selected as a monomer unit since TCD has a rigid structure and the derivatives are easily accessible from dicyclopentadiene, which is low cost and usually used as a precursor of cyclopentadiene (Figure 2A). For example, tricyclo[5.2.1.0^{2,6}]decane dimethanols are well-known compounds as a monomer for high-T_g polymers.[22,23] In practice, disulfanyl tricyclo[5.2.1.0^{2,6}]decane (TCDSH) and bis(vinylsulfone)tricyclo[5.2.1.0^{2,6}]decane (VSTCD) were newly synthesized and polymerized with DVS or BSMD to give thermoplastic PESs, poly(TCDSH/DVS) and poly-(BSMD/VSTCD), respectively. The simultaneous introduction of sulfide and sulfone groups endowed the polymer with high-n and high-ν, and the rigid structure of TCD successfully increased their T_gs. The combined thermal and optical properties of poly(BSMD/VSTCD) satisfied the requirements for thermoplastic lens applications for the first time.

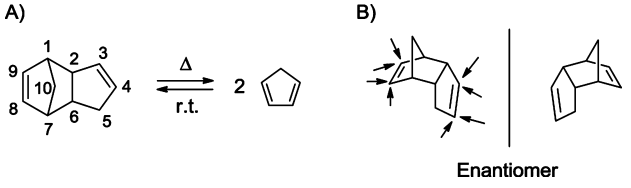


Figure 2. (A) Diels−Alder reaction of cyclopentadiene. (B) *endo*-Dicyclopentadiene and the attack positions of the thiol or thiocarboxylic acid in the thiol−ene reactions.

EXPERIMENTAL SECTION

Materials. Dicyclopentadiene (TCI, Japan), thioacetic acid (Aldrich), trimethylsilyl chloride (TMSCl, TCI, Japan), 2-mercaptoethanol (TCI, Japan), thionyl chloride (TCI, Japan), 2,2′-azobis-(isobutyronitrile) (AIBN, Wako, Japan), and the other chemicals were used as received. BSMD was prepared according to a reported procedure.[8]

Synthesis. *Bis(acetylsulfanyl)tricyclo[5.2.1.0^{2,6}]decane (**1**, Isomer Mixture).* To a flask charged with dicyclopentadiene (2.64 g, 20 mmol), thioacetic acid (4.27 mL, 60 mmol) was added slowly in an ice-bath. After addition of AIBN (0.164 g, 1 mmol), the solution was stirred at 65 °C for 36 h under nitrogen. After the reaction, unreacted thioacetic acid was removed in vacuo at 65 °C. The crude product was purified by column chromatography (silica gel, dichloromethane (DCM)/hexane 2:1) to give colorless liquid **1** (3.56 g, 63% yield). FT-IR (NaCl, cm^{-1}): 2954 (−CH_2−), 2870 (−CH−), 1689 (C═O). ^{1}H NMR (300 MHz, $CDCl_3$, 25 °C, ppm): δ = 3.87−3.62 (2H, −C*H*−SAc), 2.33−2.26 (6H, CH_3−C═O), 2.64−1.15 (m, 14H).

Disulfanyltricyclo[5.2.1.0^{2,6}]decane (TCDSH, Isomer Mixture). A solution of **1** (1.42 g, 5 mmol) and TMSCl (0.1 mL, 0.73 mmol) in methanol (10 mL) was stirred at 60 °C for 12 h. After evaporation of the solvent, the crude product was purified by column chromatography (silica gel, $CHCl_3$/hexane 1:2) to give colorless liquid TCDSH (0.893 g, 89% yield). FT-IR (NaCl, cm^{-1}): 2954 (−CH_2−), 2870 (−CH−), 2546 (−SH). ^{1}H NMR (300 MHz, $CDCl_3$, 25 °C, ppm): δ = 3.25−3.00 (2H, −C*H*−SH), 1.75−1.71 (d, 1H, −SH), 1.64−1.60 (d, 1H, −SH), 2.68−1.22 (m, 14H).

*Bis(2-hydroxyethylsulfanyl)tricyclo[5.2.1.0^{2,6}]decane (**2**, Isomer Mixture).* To a flask charged with dicyclopentadiene (2.64 g, 20

dx.doi.org/10.1021/ma300379w | *Macromolecules* 2012, 45, 3402−3408

mmol), 2-mercaptoethanol (3.44 g, 44 mmol) was added slowly in an ice-bath. After addition of AIBN (0.164 g, 1 mmol), the solution was stirred at 65 °C for 24 h under nitrogen. Additional AIBN (0.164 g, 1 mmol) was added to the solution and kept stirring at 65 °C for 48 h. Then the solution was cooled to room temperature, and 5% aqueous NaOH was added to remove the unreacted 2-mercaptoethanol. The mixture was extracted with DCM several times, the combined organic layer was dried over $MgSO_4$, and the solvent was evaporated. The residue was purified by column chromatography (silica gel, acetone/DCM 1:5) to give a highly viscous colorless liquid **3** (3.64 g, 60% yield). FT-IR (NaCl, cm^{-1}): 3379 (−OH), 2947 (−CH_2−), 2870 (−CH−), 1458 (−CH_2−). ^{1}H NMR (300 MHz, $CDCl_3$, 25 °C, ppm): δ = 3.82−3.67 (t, 4H, CH_2−OH), 3.22−2.87 (m, 2H, CH−S), 2.83−2.68 (m, 4H, S−CH_2), 2.83−1.10 (m, 14H). Anal. Calcd for $C_{14}H_{24}O_2S_2{\cdot}0.25H_2O$: C, 57.39; H, 8.43. Found: C, 57.26; H, 8.28.

*Bis(2-chloroethylsulfanyl)tricyclo[5.2.1.0^{2,6}]decane (**3**, Isomer Mixture).* To a flask charged with **3** (1.15 g, 4 mmol) in $CHCl_3$ (4 mL), thionyl chloride (1.0 mL, 13.8 mmol) in $CHCl_3$ (1 mL) was added slowly in an ice-bath. After complete addition of thionyl chloride, the solution was stirred at room temperature for 3 h. Then, the reaction mixture was quenched with aqueous $NaHCO_3$, it was extracted with DCM. The crude product was purified by column chromatography (silica gel, DCM/hexane 1:2) to give viscous colorless liquid **4** (1.04 g, 80% yield). FT-IR (NaCl, cm^{-1}): 2954 (−CH_2−), 2869 (−CH−), 1442 (−CH_2−). ^{1}H NMR (300 MHz, $CDCl_3$, 25 °C, ppm): δ = 3.73−3.59 (t, 4H, CH_2−Cl), 3.27−2.77 (m, 6H, CH−S−CH_2), 2.71−1.10 (m, 12H). Anal. Calcd for $C_{14}H_{22}Cl_2O_2$: C, 51.68; H, 6.82. Found: C, 51.73; H, 6.72.

Bis(vinylsulfonyl)tricyclo[5.2.1.0^{2,6}]decane (VSTCD, Isomer Mixture). To a solution of **4** (1.00 g, 3.07 mmol) in acetic acid (5 mL) and acetone (5 mL), $KMnO_4$ (2.14 g, 13.5 mmol) was added slowly in an ice-bath. After complete addition, the mixture was stirred at room temperature for 2 h. Then, DCM (50 mL), H_2O, and K_2CO_3 were added, and residual $KMnO_4$ was reduced with Na_2SO_3. The brown mixture was filtered through Celite and the brown solid was washed well with hot DCM. To the two phase filtrate, triethylamine (1 mL) was added and stirred vigorously for 30 min. After complete elimination was confirmed by TLC, the organic layer was collected and washed with dilute HCl solution. The crude product was purified by column chromatography (silica gel, acetone/DCM 1:20) to give sticky white paste **VSTCD** (1.04 g, 80% yield). FT-IR (KBr, cm^{-1}): 3109 (−CH=CH_2), 3055 (−CH=CH_2), 2962 (−CH_2−), 2884 (−CH−), 1612 (−C=C−), 1458 (−CH_2−), 1304 (−SO_2−), 1126 (−SO_2−). ^{1}H NMR (300 MHz, $CDCl_3$, 25 °C, ppm): δ = 6.67−6.55 (m, 2H, CH=CH_2), 6.50−6.39 (m, 2H, CH=CH_2), 6.25−6.16 (m, 2H, CH=CH_2), 3.58−1.42 (m, 14H). Anal. Calcd for $C_{14}H_{20}O_4S_2$: C, 53.14; H, 6.37. Found: C, 53.03; H, 6.17.

Polymerization. *Poly(TCDSH/DVS).* To a solution of TCDSH (3 mmol, 0.600 g) and DVS (96%, 3 mmol, 0.369 g) in dimethyl sulfoxide (DMSO, 1.5 mL) was added a catalytic amount of triethylamine. The solution was stirred for 24 h at 65 °C. The resulting viscous liquid was poured into methanol. The precipitate was collected to give white powder poly(TCDSH/DVS) (0.821 g, yield: 85%). FT-IR (KBr, cm^{-1}): 2947 (alkyl C−H), 2870 (alkyl C−H), 1319 (−SO_2−), 1119 (−SO_2−). ^{1}H NMR (300 MHz, DMSO-d_6, 40 °C, ppm): δ = 3.51−3.34 (4H), 2.98−2.78 (4H), 3.34−1.04 (14H). Anal. Calcd for $C_{20}H_{32}O_4S_6$: C, 52.79; H, 6.69. Found: C, 52.37; H, 6.62.

Poly(BSMD/VSTCD). To a solution of BSMD (0.5 mmol, 0.106 g) and VSTCD (0.5 mmol, 0.158 g) in DMSO (1 mL) was added a catalytic amount of triethylamine. The solution was stirred for 24 h at room temperature. The resulting highly viscous liquid was poured into methanol. The precipitate was collected to give white powder poly(BSMD/VSTCD) (0.206 g, yield: 78%). FT-IR (KBr, cm^{-1}): 2954 (alkyl C−H), 1304 (−SO_2−), 1119 (−SO_2−). ^{1}H NMR (300 MHz, DMSO-d_6, 40 °C, ppm): δ = 3.84−3.27 (6H), 3.14−2.82 (14H), 2.80−1.36 (12H). Anal. Calcd for $C_{20}H_{32}O_4S_6$: C, 45.42; H, 6.10. Found: C, 45.09; H, 5.83.

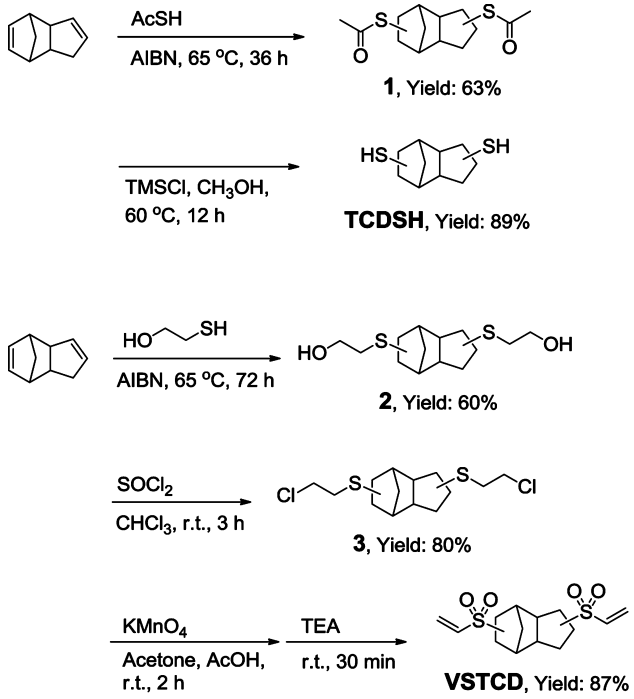
Measurements. FT-IR spectra were obtained on a Horiba FT-720 spectrometer. Solution state ^{1}H NMR spectra were recorded with a Bruker DPX300S spectrometer using $CDCl_3$ or DMSO-d_6 as a solvent and trimethylsilane as the reference (0 ppm). Number- and weight-average molecular weights (M_n and M_w) were evaluated by gel permeation chromatography (GPC) on a JASCO PU-2080 Plus with two polystyrene gel columns (TSK GELS GMH_{HR}-M). DMF containing 0.01 M LiBr was used as a solvent at a flow rate of 1.0 mL·min^{-1} calibrated by standard polystyrene samples. UV−vis transmittance spectra were recorded on a JASCO V-560 UV/vis spectrometer in the range 250−800 nm. Thermal analysis was performed on a Seiko EXSTAR 6000 TG/DTA 6300 thermal analyzer at a heating rate of 10 °C/min for thermogravimetry (TG) and a Seiko EXSTAR 6000 DSC 6200 at a heating rate of 20 °C/min for differential scanning calorimetry (DSC) under nitrogen. The refractive indices of polymer films were measured at the wavelengths of 486, 589, 656 nm by changing monochromatic filters with an Abbe refractometer (Atago, DR-M4). A halogen lamp with high brightness was used as a white light source.

DFT Calculation. The wavelength-dependent refractive indices of models for poly(BSMD/VSTCD), poly(TCDSH/DVS), and poly(BSMD/DVS) were calculated based on the Lorentz−Lorenz theory. The 6-311G(d) basis set was used for geometry optimizations under no constraints, and the 6-311++G(d,p) was used for the calculations of frequency-dependent linear polarizabilities. The three-parameter Becke-style hybrid functional (B3LYP) was adopted as the functional and all the calculations were performed using the software package of Gaussian-09 (Rev.B01). A packing coefficient (K_p) of 0.67 was used for evaluating the intrinsic molecular volumes of the models. The details of the calculation method were reported elsewhere.[24]

RESULTS AND DISCUSSION

PESs were prepared by Michael polyaddition of dithiols and bis(vinylsulfone)s. We newly designed each monomer containing TCD moiety, TCDSH for a dithiol and VSTCD for a bis(vinylsulfone). TCDSH was synthesized by a procedure of the thiol−ene addition reaction of thioacetic acid to dicyclopentadiene, followed by an ester exchange reaction with methanol in the presence of a catalytic amount of HCl produced from TMSCl (Scheme 1).[25] The ^{1}H NMR spectra of

Scheme 1. Synthesis of TCDSH and VSTCD



dx.doi.org/10.1021/ma300379w | Macromolecules 2012, 45, 3402−3408

1 and TCDSH show characteristic signals at 3.75 ppm for the acetylsulfanylmethyne group of **1**, 2.29 ppm for the acetyl group of **1**, 3.11 ppm for the sulfanylmethyne group of TCDSH, 1.73 and 1.62 ppm for the thiol group of TCDSH (Figure 3). The FT-IR spectra of **1** and TCDSH showed absorption of the C═O of **1** at 1689 cm^{-1} and the S−H of TCDSH at 2546 cm^{-1}.

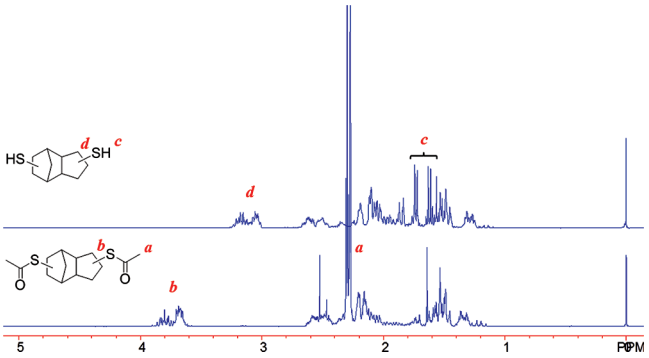


Figure 3. ^{1}H NMR spectra of **1** and TCDSH in $CDCl_3$.

On the other hand, VSTCD was synthesized in three steps of thiol−ene reaction, chlorination, and oxidation/elimination. Diol **2** was prepared by a similar reaction to that of **1** in the solvent-free condition using AIBN at 65 °C. In spite of several trials of oxidation of the sulfide to sulfone using H_2O_2 or *m*-chloroperbenzoic acid, the reactions were too slow to give a product in good yield. To use a stronger oxidant, $KMnO_4$, hydroxyl groups were converted first to chlorides to prevent oxidation of the alcohols. After oxidation of the chloride compound, HCl was eliminated from it to afford VSTCD. Figure 4 shows the ^{1}H NMR spectra of **2**, **3**, and VSTCD in

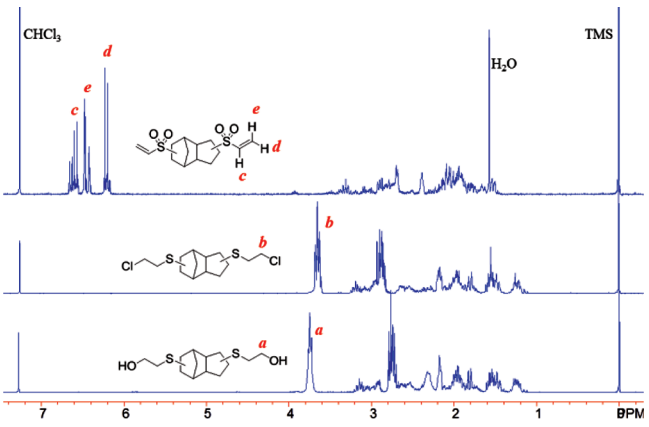


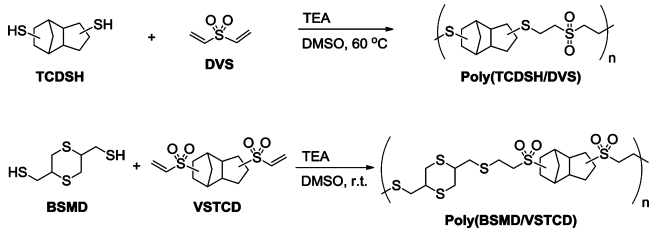
Figure 4. ^{1}H NMR spectra of **2**, **3**, and VSTCD in $CDCl_3$.

$CDCl_3$. Characteristic signals were observed at 3.75 ppm for the hydroxymethylene group of **2**, 3.66 ppm for the chloromethylene group of **3**, and 6.62, 6.45, and 6.21 ppm for the vinylsulfone group of VSTCD. Also, the FT-IR spectrum of VSTCD showed the absorptions of the vinyl C−H at 3109 and 3055 cm^{-1}, and the sulfone group at 1304 and 1126 cm^{-1}. In addition, all the compounds were characterized by elemental analysis.

All the derivatives of TCD include a lot of structural isomers. Diels−Alder dimerization of cyclopentadiene gives preferentially an *endo* isomer while both the *endo* and *exo* isomers can exist. Commercially available dicyclopentadiene used in this work has >95% *endo* structure, and it was used in this work. Also, the cyclopentadiene contains enantiomers. In the thiol−ene reactions, the thiol or thioacetic acid can react at one of the four positions for each double bond of cyclopentadiene (Figure 2B). The mixture of various isomers makes the assignments of signals in the ^{1}H spectra very complicated especially at 1.2−3.4 ppm, while the integral ratio of the characteristic protons, a−d in Figure 3 and a−e in Figure 4, and the other protons of the alicyclic group agrees well with the theoretical ones. Although the existence of enormous kinds of isomers makes the precise characterization of the compounds difficult, the mixture of many isomers must be helpful to increase solubility and decrease birefringence of the polymers derived from this monomer.

TCDSH and VSTCD were polymerized with DVS and BSMD to give poly(TCDSH/DVS) and poly(BSMD/VSTCD), respectively. The polymerizations proceeded by the Michael addition reaction under a similar condition of previous works, in the presence of a catalytic amount of triethylamine in DMSO at 60 °C or room temperature (Scheme 2). The

Scheme 2. Synthesis of Poly(TCDSH/DVS) and Poly(BSMD/VSTCD)



resulting polymers were soluble in *N*,*N*-dimethylformamide (DMF), *N*-methylpyrrolidone (NMP), and DMSO and were insoluble in $CHCl_3$, tetrahydrofuran (THF), and cyclohexanone. In spite of their rigid structures, the solubility is higher than those of previous PESs probably because of the structural isomers. The molecular weights of the polymers were determined by GPC eluted with DMF. The number-average molecular weight (M_n) and the polydispersity (M_w/M_n) were 19 300 and 1.96 for poly(TCDSH/DVS), and 28 400 and 2.38 for poly(BSMD/VSTCD), respectively. The ^{1}H NMR spectra of the polymers were taken in DMSO-d_6. The signals of the protons of vinyl groups in VSTCD and DVS disappeared, and new signals assignable to methylene and methyne protons next to the sulfone group were clearly observed (see Figure S1 in Supporting Information). Also, the polymers were characterized by elemental analysis.

Thermal stability can be evaluated by decomposition temperature and glass transition temperature (T_g). In general, optical materials manufactured by the injection molding process require a T_g of above 100 °C or preferably even 120 °C. Also, the stability of the materials at a temperature in the process is very important. The decomposition temperature was evaluated as a 5% weight loss temperature ($T_{5\%}$) by TGA, and the T_g was determined by DSC measurement. The TGA curves of poly(TCDSH/DVS) and poly(BSMD/VSTCD) are shown in Figure 5, and they exhibited good thermal stability without any weight loss up to around 270 °C. The $T_{5\%}$ values of poly(TCDSH/DVS) and poly(BSMD/VSTCD) were 296 and 303 °C (Table 1), respectively, and they are comparable with

dx.doi.org/10.1021/ma300379w | *Macromolecules* 2012, 45, 3402−3408

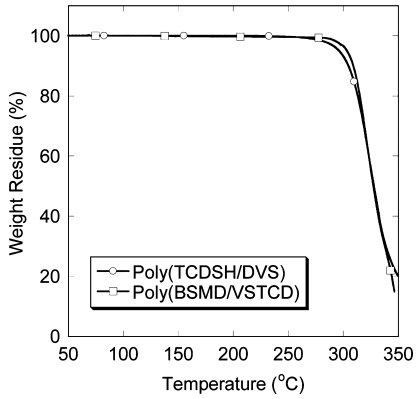


Figure 5. TGA curves of poly(TCDSH/DVS) and poly(BSMD/VSTCD) under nitrogen.

Table 1. Thermal and Optical Properties of PESs

	M_n[a]	M_w/M_n[a]	$T_{5\%}$[b]	T_g[c]
poly(TCDSH/DVS)	19 300	1.96	296	74
poly(BSMD/VSTCD)	28 400	2.38	303	113
poly(CHDT/DVS)[18]	11 600	1.62	300	46
poly(BSMD/DVS)[17]	–	–	303	50

[a]Determined by GPC (DMF, PSt standard). [b]5% weight loss temperature. [c]Glass transition temperature.

the previous PESs, indicating that PESs decompose in the same manner, probably starting with retro Michael addition reaction followed by some decomposition. No coloration was observed in both polymers at a heating of 200 °C under the air. On the other hand, clear glass transitions of poly(TCDSH/DVS) and poly(BSMD/VSTCD) were observed at 74 and 113 °C, respectively, in the DSC measurement, and no crystalline property was detected reflecting the many isomeric structures in the TCDSH and VSTCD (Figure 6). The T_g values of

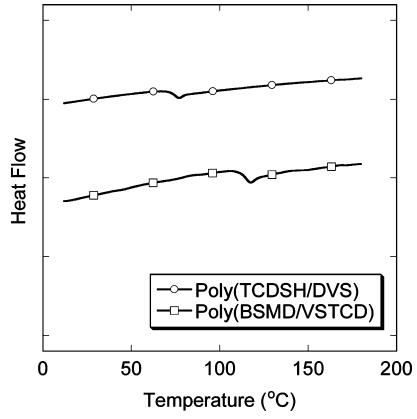


Figure 6. DSC curve of poly(TCDSH/DVS) and poly(BSMD/VSTCD) at heating rate of 20 °C/min.

poly(TCDSH/DVS) and poly(BSMD/VSTCD) were much improved compared with those of the previous PESs because the TCD unit is rigid due to the cyclic and condensed structure. Poly(TCDSH/DVS) possessing TCD showed a higher T_g value by 28 °C than that of poly(CHDT/DVS) with cyclohexane instead of TCD (see Figure 1). Furthermore, the T_g value of poly(BSMD/VSTCD), containing additional TCD and a sulfone group to poly(BSMD/DVS), reached to 113 °C. Thus, poly(BSMD/VSTCD) satisfied the required thermal properties for lens applications as high-n and high-ν PESs for the first time.

Optical properties such as transparency, refractive indices, and Abbe's numbers were evaluated with a UV−vis spectrometer and an Abbe refractometer. Figure 7 shows the

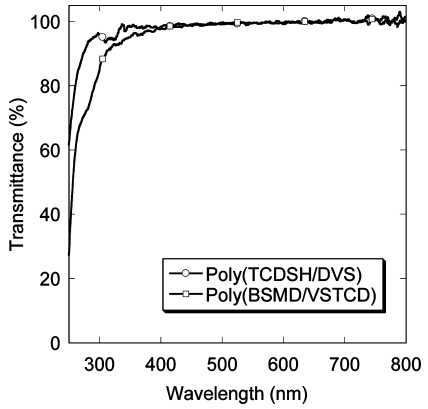


Figure 7. UV−vis absorption spectra of films of poly(TCDSH/DVS) (3.7 μm thickness) and poly(BSMD/VSTCD) (10 μm thickness).

UV−vis absorption spectra of poly(TCDSH/DVS) and poly(BSMD/VSTCD) films with a thicknesses of 3.7 and 10 μm, respectively. They exhibit high transparency in the visible region (>400 nm) like the previously reported transparent PESs.[17,18] The transmittance of the films at 400 nm is over 98% (without Fresnel reflection), which is suitable for optical applications. Figure 8 shows a photograph of poly(BSMD/



Figure 8. Picture of a film of poly(BSMD/VSTCD).

VSTCD) film. The aliphatic structures and inherent amorphous nature derived from the isomeric structures endow the polymers with colorlessness and good transparency in the visible region.

The refractive indices at 486, 589, and 656 nm, and the Abbe's number of the poly(TCDSH/DVS) and poly(BSMD/VSTCD) films with two referential PESs are summarized in Table 2. The wavelength dispersion of the refractive indices (n_λ) is plotted in Figure 9a with a fitted curve using the simplified Cauchy's formula.

$$n_\lambda = n_\infty + D/\lambda^2$$

The estimated refractive index at the infinite wavelength (n_∞) and the dispersion coefficient (D) are listed in Table 2. Both the poly(TCDSH/DVS) and poly(BSMD/VSTCD) exhibited high refractive indices at 589 nm (n_D) of 1.6052 and 1.6228 with high Abbe's numbers (ν_D) of 48.0 and 45.8, respectively. It has been reported that the simultaneous introduction of a sulfur (−S−) element with high atom

dx.doi.org/10.1021/ma300379w | Macromolecules 2012, 45, 3402−3408

Table 2. Refractive Indices (n) and Abbe's Numbers (ν) of PESs

				experimental						calculated[h]	
polymer	sulfur content (wt %)	d[a] (μm)	$T_{400\ nm}$[b] (%)	n_F[c]	n_D[d]	n_C[e]	ν_D[f]	n_∞[g]	D[g]	n_D	ν_D
poly(TCDSH/DVS)	30.2	3.7	98	1.6142	1.6052	1.6016	48.0	1.5862	6609	1.605	37.8
poly(BSMD/VSTCD)	36.4	10	98	1.6322	1.6228	1.6186	45.8	1.6022	7090	1.634	35.0
poly(CHDT/DVS)[18]	36.1	13	99	1.6107	1.6022	1.5988	50.6	1.5843	6242	1.602	36.3
poly(BSMD/DVS)[17]	48.5	26	97	1.6627	1.6512	1.6474	42.6	1.6236	7948	1.652	32.3

[a]Film thickness. [b]Transmittance at 400 nm without Fresnel reflection. [c]Measured at 486 nm. [d]Measured at 589 nm. [e]Measured at 656 nm. [f]Abbe number. [g]Estimated from curve fitting using the simplified Cauchy's formula. The unit of D is nm^2. [h]Calculated from the wavelength dependent molecular polarizabilities from DFT calculations with a constant packing coefficient (K_p = 0.67).

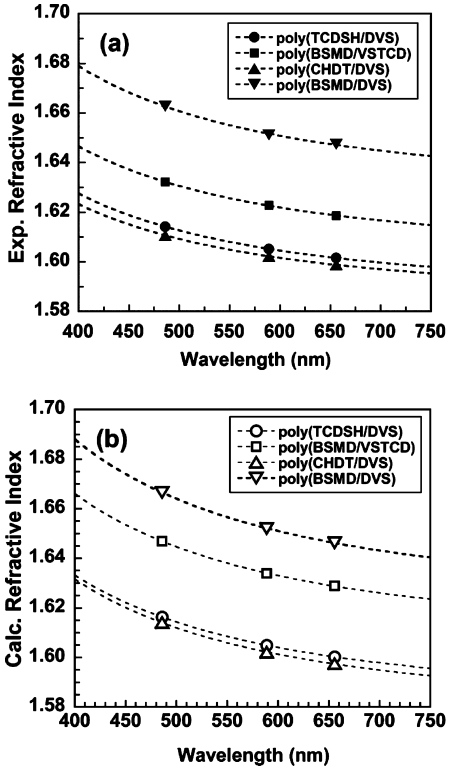


Figure 9. Wavelength dispersion of (a) experimental and (b) calculated refractive indices of four PESs. The dispersions are fitted by the simplified Cauchy's formula.

refraction and a sulfone (−SO_2−) group with low molecular dispersion is effective to develop high-n and high-ν polymers.[14] The n_D of poly(BSMD/VSTCD) (1.6228) is higher than that of poly(CHDT/DVS) (1.6022) despite the similar sulfur contents of 36.4% and 36.1%, respectively.[17,18] This could be due to the rigid and condensed structure of TCD which reduces the molecular volume and thus increases the refractive index of the polymer. On the other hand, the refractive index of poly(BSMD/VSTCD) (1.6228) including a TCD structure in the main chain is lower than that of poly(BSMD/DVS) (1.6512). This is essentially due to the much lower sulfur content (36.4%) of the former than the latter (48.5%), but a significant improvement in T_g (+63 °C) caused by the incorporation of a rigid TCD structure is quite beneficial for optical polymers. As shown in Figure 1, the n_D and ν_D values of the PESs including poly(TCDSH/DVS) and poly(BSMD/VSTCD) are sequentially located in the highest n_D−ν_D area with a linear relation. This could be a novel limiting line between n_D and ν_D for polymers composed of aliphatic, sulfide, and sulfone groups. The wavelength dispersions of calculated refractive indices are plotted in Figure 9b with fitted curves. The DFT calculations well reproduce the experimental refractive indices of PESs, although the calculated n_Ds of poly(BSMD/VSTCD) are slightly overestimated. This suggests that the combination of sulfur-containing cyclic BSMD structure and two sulfone linkages induces additional free volume. The calculated Abbe's numbers (ν_D) are smaller than those of the experimental values, which is caused by the slightly overestimated refractive indices at 486 nm. The higher optical transparency of the PESs in the near UV region (320−400 nm) (Figure 7) effectively suppresses the increase in refractive indices at shorter wavelengths. The notably high n_D and ν_D values with enhanced thermal stability (T_g) of these PESs make them promising optical materials for lens application.

CONCLUSION

Novel thermoplastics, poly(TCDSH/DVS) and poly(BSMD/VSTCD), with high refractive indices and high Abbe's numbers have been developed. The new monomers, TCDSH and VSTCD based on tricyclo[5.2.1.$0^{2,6}$]decane moiety were easily prepared from dicyclopentadiene via two or three steps starting from the thiol−ene reaction. Michael polyaddition of these monomers produced high molecular weight polymers of M_n = 19 300 for poly(TCDSH/DVS) and M_n = 28 400 for poly(BSMD/VSTCD). Because of the rigid structure of the TCD moiety, the T_gs of poly(TCDSH/DVS) and poly(BSMD/VSTCD) are effectively enhanced as 74 and 113 °C, respectively. These are much higher than those of other reported PESs (around 50 °C). Furthermore, no coloration was observed on heating up to 200 °C in air. They also exhibited the high refractive indices of 1.6052 and 1.6228, and the high Abbe's numbers of 48.0 and 45.8, respectively, as thermoplastics containing sulfur, sulfone, and a dense structure of TCD moiety. In particular, the highly balanced thermal and optical properties of poly(BSMD/VSTCD) have never been achieved by other polymers, which demonstrates that this polymer is one of the best candidates for optical applications, such as lens materials.

ASSOCIATED CONTENT

Supporting Information

^{1}H NMR spectrum of poly(BSMD/VSTCD) in DMSO-d_6. This material is available free of charge via the Internet at http://pubs.acs.org.

AUTHOR INFORMATION

Corresponding Author

*Fax: +81-3-5734-2127. E-mail: ueda.m.ad@polymer.titech.ac.jp.

Notes

The authors declare no competing financial interest.

■ ACKNOWLEDGMENTS

This work is supported by JSR Corporation.

■ REFERENCES

(1) Gao, C.; Yang, B.; Shen, J. *J. Appl. Polym. Sci.* **2000**, *75*, 1474−1479.
(2) Matsuda, T.; Funae, Y.; Yoshida, M.; Yamamoto, T.; Takaya, T. *J. Appl. Polym. Sci.* **2000**, *76*, 45−49.
(3) Morishiri, H.; Kobayashi, S. *Jpn. Kokai.* Tokkyo Koho JP 2005325274A, 2005.
(4) Morishiri, H.; Kobayashi, S. *Jpn. Kokai.* Tokkyo Koho JP 2006131724A, 2006.
(5) Okada, R.; Ohkubo, T.; Kosaka, M. Eur. Pat. Appl. EP 530757A1, 1993.
(6) Kohara, T. *Macromol. Symp.* **1996**, *101*, 571−9.
(7) Dislich, H. *Angew. Chem.* **1979**, *91*, 52−61.
(8) Okubo, T.; Kohmoto, S.; Yamamoto, M. *J. Appl. Polym. Sci.* **1998**, *68*, 1791−1799.
(9) Yang, C.-J.; Jenekhe, S. A. *Chem. Mater.* **1995**, *7*, 1276−85.
(10) Although poly(DSDT/DVS) was reported as n_D = 1.686 and ν_D = 48.6,[14] the repeating measurements of DSDT/DVS prepared again here gave the values of n_D = 1.676 and ν_D = 39.1 as more reliable data. These values are plotted in Figure 1, and it agrees well with the tendency of n_D and ν_D values for PESs.
(11) Matsuda, T.; Funae, Y.; Yoshida, M.; Yamamoto, T.; Takaya, T. *J. Appl. Polym. Sci.* **2000**, *76*, 45−49.
(12) You, N.-H.; Higashihara, T.; Yasuo, S.; Ando, S.; Ueda, M. *Polym. Chem.* **2010**, *1*, 480.
(13) Okutsu, R.; Ando, S.; Ueda, M. *Chem. Mater.* **2008**, *20*, 4017−4023.
(14) Okutsu, R.; Suzuki, Y.; Ando, S.; Ueda, M. *Macromolecules* **2008**, *41*, 6165−6168.
(15) Okubo, T.; Kohmoto, S.; Yamamoto, M. *J. Macromol. Sci., Part A* **1998**, *35*, 1819−1834.
(16) Okubo, T.; Kohmoto, S.; Yamamoto, M.; Nakahira, T. *J. Mater. Sci.* **1999**, *34*, 337−347.
(17) Suzuki, Y.; Higashihara, T.; Ando, S.; Ueda, M. *Polym. J.* **2009**, *41*, 860−865.
(18) Suzuki, Y.; Higashihara, T.; Ando, S.; Ueda, M. *Eur. Polym. J.* **2010**, *46*, 34−41.
(19) Higuchi, C.; Otsuji, A.; Sugimoto, K.; Nakamura, M.; Takagi, M.; Nukii, Y.; Okazaki, K. Eur. Pat. Appl. EP 1279692, 2002.
(20) Tsuda, T.; Mathias, L. J. *Macromolecules* **1993**, *26*, 4734−4735.
(21) Matsumoto, A.; Watanabe, H.; Otsu, T. *Bull. Chem. Soc. Jpn.* **1992**, *65*, 846−852.
(22) Yu, A. G.; Liu, H. P.; Blinco, J. P.; Jack, K. S.; Leeson, M.; Younkin, T. R.; Whittaker, A. K.; Blakey, I. *Macromol. Rapid Commun.* **2010**, *31*, 1449−1455.
(23) Oshima, K.; Shida, Y. Eur. Pat. Appl. EP 1674496, 1989.
(24) Ando, S. *J. Photopolym. Sci. Technol.* **2006**, *19*, 351−360.
(25) Awano, H. *Jpn. Kokai.* Tokkyo Koho JP 2008063276A, 2008.

Macromolecules

Article

pubs.acs.org/Macromolecules

Water-Soluble Poly(vinylferrocene)-*b*-Poly(ethylene oxide) Diblock and Miktoarm Star Polymers

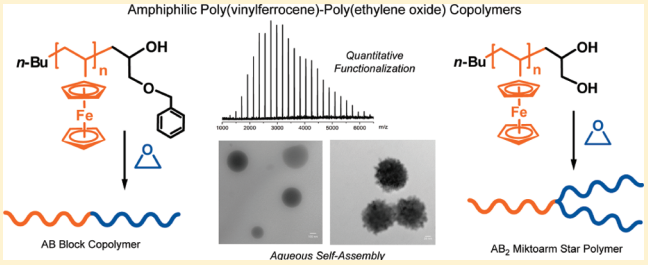
Christoph Tonhauser,[†] Markus Mazurowski,[‡] Matthias Rehahn,[‡] Markus Gallei,[‡,*] and Holger Frey[†,*]

[†]Institute of Organic Chemistry, Organic and Macromolecular Chemistry, Johannes Gutenberg-University (JGU), Duesbergweg 10-14, D-55099 Mainz, Germany

[‡]Ernst-Berl Institute for Chemical Engineering and Macromolecular Science, Darmstadt University of Technology, Petersenstraße 22, D-64287 Darmstadt, Germany

Supporting Information

ABSTRACT: We describe the synthesis of water-soluble diblock and miktoarm star polymers consisting of poly(vinylferrocene) (PVFc) and poly(ethylene oxide) (PEO) blocks. First, end-functionalized poly(vinylferrocene) was generated by end-capping the living carbanionic PVFc chains with benzyl glycidyl ether (BGE) or ethoxy ethyl glycidyl ether (EEGE). Acidic hydrolysis of the EEGE-terminated PVFc partially oxidized the PVFc backbone. However, the dihydroxyl end-functional PVFc was obtained in quantitative yields by hydrogenolysis of the BGE-terminated PVFc. A series of block copolymers and AB_2 miktoarm star copolymers was obtained in a second polymerization step, utilizing the respective end-functionalized PVFc as a macroinitiator for the ring-opening polymerization (ROP) of ethylene oxide. All polymers were analyzed in detail, using NMR spectroscopy and size-exclusion chromatography (SEC). Online SEC-viscosimetry as well as MALLS was carried out, confirming the formation of miktoarm structures. Quantitative functionalization and subsequent removal of the acetal and benzyl protective groups, respectively were confirmed by MALDI–ToF mass spectrometry. Molecular weights of the end-functionalized PVFcs range between 1000 and 3600 g mol^{-1}, and block copolymers with 10 000 to 50 000 g mol^{-1} overall molar masses were synthesized. In addition, the water-soluble block copolymers were investigated by differential scanning calorimetry (DSC) and thermogravimetric analysis (TGA). For characterization of the morphology in aqueous solution, transmission electron microscopy (TEM) was performed, showing micelles and multicompartment micellar structures.



INTRODUCTION

Ferrocene-containing polymers offer a promising combination of different characteristic features such as redox, catalytic, mechanical, semiconductive, photophysical, optoelectronic, and magnetic properties.[1−7] Furthermore, these polymers demonstrate high potential for applications in fields like amperometric glucose/*L*-glutamate sensors, as demonstrated by Hale et al., who attached a ferrocene unit to a flexible polysiloxane backbone. The resulting polymer can be utilized as an efficient electron-transfer relay system (glucose oxidase/electrode) to improve the sensor response time.[8] Biosensors containing the ferrocene/ferrocenium redox couple and a carbon electrode are highly explored.[9−14] Moreover, ferrocene-containing materials show promise for various biomedical application,[15] e.g., as antimalarial-[16] or anticancer-active drugs.[17−20]

The first synthesis of polymers containing ferrocene units dates back to the 1950s and was based on radical and step growth polymerization techniques. However, at this time no single material with well-defined structure and high molecular weight could be obtained, due to side reactions, low solubility, and insufficient chemical stability of the formed products.[21−26] This limitation was overcome by the seminal discovery of the controlled living ring-opening polymerization (ROP) of *ansa*-metallocenophanes by Manners and co-workers,[27,28] which leads to high-molecular-weight poly(ferrocenylsilanes) (PFS). Manifold PFS-based (both, linear and hyperbranched) block copolymers, star polymers, and graft copolymers were developed utilizing this synthetic pathway.[29−34] These polymers exhibit various intriguing self-assembled nanostructures in bulk and solution (e.g., micelles, rods, and nanotubes).[34−39]

Other established ferrocene-based monomers are ferrocenylmethyl methacrylates (FMMA)[40−42] and vinylferrocene (VFc),[43−45] which possess a high stability toward thermal treatment and atmospheric exposure. The latter monomer (VFc) can be utilized to attach ferrocene units to a preformed polymer backbone.[46] First reports dealing with anionic polymerization of vinylferrocene were published by Nuyken et al. in the 1990s.[43] The authors not only synthesized PVFc homopolymes, but also described PVFc block copolymers (comonomers: methyl methacrylate, styrene, and propylene sulfide) with narrow molecular-weight distributions. Similar procedures were used by Durkee[47] and Higashihara[44] to

Received: January 2, 2012
Revised: March 25, 2012
Published: April 6, 2012

 © 2012 American Chemical Society dx.doi.org/10.1021/ma3000048 | *Macromolecules* 2012, 45, 3409−3418

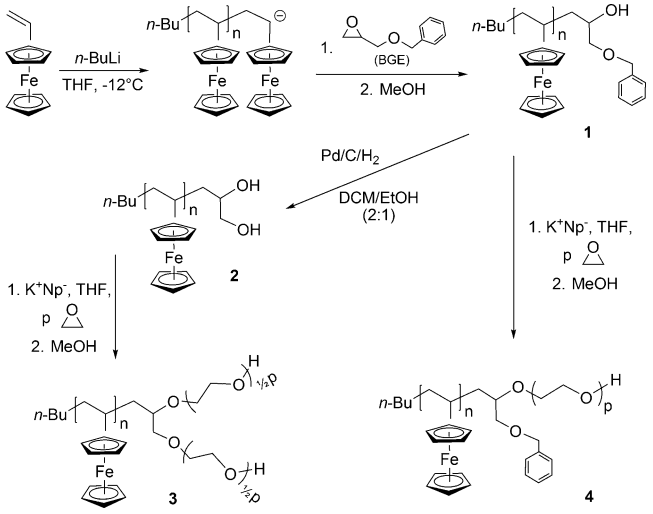
synthesize PVFc-based block copolymers with poly(isoprene) and poly(isobutylene), respectively. "Living" radical homo- and block copolymerization of VFc with styrene—mediated by TEMPO—was developed by our group.[48] Most of those block copolymers exhibit low-molecular-weight PVFc blocks only. In the case of controlled radical chain growth, side reactions prevent the formation of longer PVFc blocks, while for living anionic approaches this is due to tremendously decreasing reactivity of the living chains with increasing chain length.[44] Recently, however, we could demonstrate that reactivation of the "sleeping" state formed by the anionic chain termini can be achieved by adding a mixture of 1,1-dimethylsilacyclobutane (DMSB) and 1,1-diphenylethylene (DPE) (activating agent and end-capping reagent, respectively), yielding well-defined block copolymers.[45,49] This method is known as the so-called "carbanion pump" technique.[50,51] The synthetic strategy provides access to a large variety of well-defined block copolymers in a broad range of molecular weights.

Despite all recent progress in this field, well-defined amphiphilic or water-soluble ferrocene-based block copolymers have hardly been reported in literature.[52,53] Manners and co-workers developed two synthetic routes to PFS-*b*-poly(ethylene oxide) (PFS−PEO) block copolymers. In a first approach, SiH-functionalized PEO was utilized as a macroinitiator for the transition metal-catalyzed ROP of dimethylsila[1]-ferrocenophanes[54] and second two homopolymers (PEO, PFS) were combined with a bis(terpyridine)ruthenium(II) complex.[55] The former strategy reveals spherical structures, whereas the latter leads to intriguing rod-like micelles in aqueous media, due to deviating crystallization behavior of the two organometallic block copolymers.

The established route for amphiphilic block copolymers with a PEO-block (combination of oxy- and carbanionic polymerization) relies on the termination of living carbanionic polymers with ethylene oxide.[56,57] By utilizing epoxide derivatives as capping reagents, a wide variety of end-functionalized polymers can be obtained, either with a single hydroxyl group or multiple orthogonal functionalities.[58−60] Subsequently, the terminal functionalities can be used to initiate the synthesis of well-defined polymer architectures (e.g., in-chain functionalized block copolymers,[61,62] star polymers,[63,64] or hyperbranched polymers[65]). To the best of our knowledge, epoxide termination has not been used for PVFc to obtain end-functional polymers to date. Therefore, the initial goal of this work was to develop a strategy for the combination of PVFc and PEO by sequential monomer addition (oxy- and carbanionic polymerization). A facile approach to amphiphilic metal-containing block copolymers without suffering from the redox-lability of VFc was the foremost objective of this work.

In this contribution, we describe a powerful and versatile synthetic strategy to novel amphiphilic organometallic macromolecular architectures containing PVFc blocks (Scheme 1). PEO was employed as the polar component in this initial study.[66] In the first step of the reaction sequence "living" poly(vinylferrocene) anions were end-capped with benzyl glycidyl ether (BGE) to obtain one hydroxyl group and one benzyl-protected hydroxyl group at the chain termini (PVFc-BGE, **1**). The terminal hydroxyl group was then utilized to initiate anionic ring-opening polymerization (AROP) of ethylene oxide, affording a series of poly(vinylferrocene)-*block*-poly(ethylene oxide) copolymers (PVFc-BGE-PEO, **4**). After release of the second hydroxyl group of PVFc-BGE, **1**, by hydrogenolysis, on the other hand, the resulting dihydroxyl

Scheme 1. Synthetic Strategy to Amphiphilic Ferrocene-Containing Block Copolymers (PVFc-BGE-PEO, 4) and AB_2 Miktoarm Star Polymers (PVFc-$(PEO)_2$, 3)[a]



[a] K^+Np^-: potassium naphthalide. BGE: benzyl glycidyl ether.

end-functionalized PVFc (PVFc-$(OH)_2$, **2**) was used as a macroinitiator for polymerization of EO. This approach resulted in a series of novel AB_2 miktoarm star polymers containing two hydrophilic PEO blocks (PVFc-$(PEO)_2$, **3**). The materials have been characterized in detail and studied regarding their thermal stability and aqueous self-assembly.

EXPERIMENTAL SECTION

Reagents. All solvents and reagents were purchased from Acros Organics or Sigma-Aldrich and used as received, unless otherwise stated. Chloroform-d_1 was purchased from Deutero GmbH. Tetrahydrofuran (THF) was distilled from sodium/benzophenone under reduced pressure (cryo-transfer) prior to the addition of 1,1-diphenylethylene and *n*-BuLi as well as a second cryo-transfer. Benzyl glycidyl ether (BGE) and ethoxy ethyl glycidyl ether (EEGE) were dried over calcium hydride (CaH_2) or trioctylaluminium 2−3 times and cryo-transferred prior to use. Vinylferrocene (VFc) was synthesized according to a recently published procedure.[49]

Instrumentation. All syntheses were carried out under an atmosphere of nitrogen or argon, using the Schlenk technique or a glovebox equipped with a Coldwell apparatus. ^1H NMR spectra were recorded at 300 or 400 MHz on a Bruker AC300 or Bruker AMX 400, respectively and are referenced internally to residual proton signals of the deuterated solvent. Size exclusion chromatography (SEC) measurements were carried out in $CHCl_3$ on an instrument consisting of a Waters 717 plus autosampler, a TSP Spectra Series P 100 pump, a set of three MZ SDV columns (10^4/500/50 Å), RI- and UV-detectors (absorption wavelength: 254 nm). All SEC diagrams show the RI detector signal unless otherwise stated, and the molecular weight refer to linear poly(styrene) (PS) standards provided by Polymer Standards Service (PSS). In addition, SEC was performed with THF as the mobile phase (flow rate 1 mL min^{-1}) on a Mixed Gel column set from PL (PL Mixed Gel B, PL Mixed Gel C, PL Mixed Gel D) or an SDV column set from PSS (SDV 1000, SDV 100000, SDV 1000000) at 30 °C. Here, calibration was carried out using poly(styrene) (PS; from Polymer Standard Service (PSS), Mainz) and PVFc (self-made) calibration standards.[49] For the SEC−MALLS experiments, a system composed of a Waters 515 pump (Waters, Milford, CT), a TSP AS100 auto sampler, a Waters column oven, a Waters 486 UV detector operating at 254 nm, a Waters 410 RI-detector, and a DAWN DSP light scattering detector (Wyatt Technology, Santa Barbara, CA) was used. For data acquisition and evaluation of the light-scattering experiments, Astra version 4.73 (Wyatt Technology, Santa Barbara,

CA) was used. The light-scattering instrument was calibrated using pure toluene, assuming a Rayleigh ratio of 9.78×10^{-6} cm^{-1} at 690 nm. An injection volume of 118 μL, a sample concentration of 1−2 g L^{-1}, a column temperature of 35 °C, and a THF flow rate of 1 mL min^{-1} was used, and SEC analysis was performed on a high resolution column set from PSS (SDV 5 μm 10^6 Å, SDV 5 μm 10^5 Å, SDV 5 μm 1000 Å). The online viscosity was analyzed in THF at room temperature on linear M column (UV, RI, visco, and light scattering detectors) by PSS-company in Mainz.

Matrix-assisted laser desorption and ionization time-of-flight (MALDI−ToF) measurements were performed on a Shimadzu Axima CFR MALDI−TOF mass spectrometer equipped with a nitrogen laser delivering 3 ns laser pulses at 337 nm. Dithranol (1,8,9-trihydroxyanthracene) was used as a matrix. Samples were prepared by dissolving the polymer in THF at a concentration of 10 g L^{-1}. A 10 μL aliquot of this solution was added to 10 μL of a 10 g L^{-1} solution of the matrix. A 1 μL aliquot of the mixture was applied to a multistage target to evaporate THF and create a thin matrix/analyte film. The samples were measured in linear or reflection mode of the spectrometer. DSC curves were recorded on a Perkin-Elmer DSC 8500. TGA measurements were conducted on a Perkin-Elmer Pyris 6 TGA. A Philips EM420 transmission electron microscope (TEM) using a LaB_6 cathode at an acceleration voltage of 120 kV was used to obtain TEM images. TEM grids (carbon film on copper, 300 mesh) were obtained from Electron Microscopy Sciences Hatfield, PA, USA. Additional TEM experiments were carried out using a Zeiss EM 10 electron microscope operating at 80 kV. In all cases no staining was necessary. As autoclave a high-pressure laboratory autoclave Model II form Carl Roth GmbH + Co. KG was used.

Poly(vinylferrocene)benzyl Glycidyl Ether (PVFc-BGE, 1). *Exemplary Synthesis Procedure for $PVFc_4$-BGE.* In an ampule equipped with a stirring bar, 520 mg (2.45 mmol) neat VFc was dissolved in 12 mL of dry THF and the solution was cooled to −12 °C. A 325 μL (0.52 mmol) sample of a 1.6 M solution of *n*-BuLi in hexane was added quickly. The solution was stirred for 3 h to ensure complete conversion. A sample was taken for SEC measurement. After that time 3.9 mL of freshly distilled BGE (2.59 mmol, 5 equiv concerning the living chain ends) were added via a syringe. The solution was allowed to warm up to room temperature and stirred for 2 h. A small amount of degassed methanol was added and the reaction mixture was poured into a 10-fold excess of methanol. The end-functionalized PVFc precipitated quantitatively and was collected by filtration, washed with methanol, and dried *in vacuo* (yield: quantitative).

^{1}H NMR (300 MHz, $CDCl_3$, δ in ppm): 7.51−7.08 (m, BGE aromatic), 4.61−3.25 (br, PVFc aromatic −C*H*-), 2.71−0.73 (br, PVFc backbone −CH_2−C*H*−). ^{13}C NMR (75 MHz, $CDCl_3$, δ in ppm): 128.4 (BGE aromatic) 127.8 (BGE aromatic) 95.8 (PVFc C_{quat}) 70.3−64.5 (PVFc aromatic), 43.0 (PVFc backbone CH_2−CH), 32.1 (PVFc backbone CH_2−CH) 22.7 (PVFc initiator CH_2) 14.2 (PVFc initiator CH_3).

Poly(vinylferrocene)-$(OH)_2$ ($PVFc-(OH)_2$, 2). The reaction flask (laboratory autoclave) was filled with 500 mg (0.19 mmol) of **1**, 40 mL of DCM, 20 mL of EtOH, and 100 mg of palladium catalyst on activated carbon (Pd/C, 10%). The flask was flushed with hydrogen (50−80 bar) and stirred for 72 h. Subsequently the catalyst was removed by filtration over Celite, and the solvent was removed *in vacuo*. $PVFc-(OH)_2$ was obtained by precipitation in methanol and drying *in vacuo*. Strong interaction of the polymer with Pd/C resulted in yields of 50−70% only. ^{1}H NMR (300 MHz, $CDCl_3$, δ in ppm): 4.61−3.25 (br, PVFc aromatic −C*H*−), 2.71−0.73 (br, PVFc backbone CH_2−C*H*). ^{13}C NMR (75 MHz, $CDCl_3$, δ in ppm): 96.0 (PVFc C_{quat}) 70.8−64.5 (PVFc aromatic), 43.7 (PVFc backbone CH_2−CH), 32.4 (PVFc backbone CH_2−CH) 22.8 (PVFc initiator CH_2) 14.3 (PVFc initiator CH_3).

Poly(vinylferrocene)-*b*-poly(ethylene oxide) (PVFc-BGE-PEO, 4). *Exemplary Synthesis Procedure for $PVFc_4$-BGE-PEO_{92}.* The terminally functionalized polymer **1** (280 mg, 0.15 mmol) was dissolved in 20 mL of THF and the hydroxyl group was deprotonated by titration with potassium naphthalide (K^+Np^-, 0.5 M, 0.35 mL) until a slightly greenish color remained. Ethylene oxide (EO, 0.88 g, 20 mmol) was cryo-transferred into a graduated ampule and subsequently into the reaction flask at approximately −80 °C. The greenish color disappeared rapidly. The reaction mixture was heated up to 60 °C and stirred for 24−48 h. The polymerization was terminated with degassed methanol. PVFc-BGE-PEO was obtained as a bright yellow powder using precipitation in cold diethyl ether and drying *in vacuo* at room temperature (yield: 91%). ^{1}H NMR (400 MHz, $CDCl_3$, δ in ppm): 4.68−3.74 (br, PVFc aromatic −C*H*−), 3.96−2.77 (br, PEO backbone CH_2−CH_2) 2.71−0.73 (br, PVFc backbone CH_2−C*H*). ^{13}C NMR (100 MHz, $CDCl_3$, δ in ppm): 95.7 (PVFc C_{quat}) 72.4 (BGE: −CH_2−), 71.7−68.6 (PEO backbone CH_2−CH_2), 68.6−65.6 (PVFc aromatic −C*H*−), 61.0 (CH_2−OH), 32.9−28.5 (PVFc backbone CH_2−C*H*).

Poly(vinylferrocene)-*b*-(poly(ethylene oxide))$_2$ ($PVFc-(PEO)_2$, 3). *Exemplary Synthesis Procedure for $PVFc_{11}$-$(PEO_{61})_2$.* A 200 mg (0.08 mmol) of **2** were utilized as macroinitiator for the anionic polymerization of EO analogous to the preparation of **4**. A THF solution of **2** was titrated by K^+Np^- and EO (0.88 g, 20 mmol) was added. The reaction mixture was stirred for 24 h at 60 °C and was terminated with degassed methanol. Precipitation in cold diethyl ether and drying *in vacuo* yields $PVFc-(PEO)_2$ as bright yellow powder (yield: 90%). ^{1}H NMR (400 MHz, $CDCl_3$, δ in ppm): 4.68−3.92 (br, PVFc aromatic −C*H*−), 3.90−2.97 (br, PEO backbone CH_2−CH_2) 2.84−0.63 (br, PVFc backbone CH_2−C*H*). ^{13}C NMR (100 MHz, $CDCl_3$, δ in ppm): 95.7 (PVFc C_{quat}) 72.5 (core, −CH_2−), 71.5−68.4 (PEO backbone CH_2−CH_2), 68.9−65.8 (PVFc aromatic −C*H*−), 61.2 (CH_2−OH), 33.1−28.7 (PVFc backbone CH_2−C*H*).

RESULTS AND DISCUSSION

A. Synthesis of Linear and Star-Shaped PVFc-*block*-PEO Copolymers. A series of block copolymers and AB_2 miktoarm star polymers containing one PVFc block and either one or two PEO blocks have been prepared by living anionic polymerization. Vinylferrocene was synthesized as described in literature,[49] and the polymerization was initiated by *n*-BuLi. To the best of our knowledge, neither water-soluble PVFc block copolymers have been synthesized, nor has epoxide termination been used in the context of the carbanionic synthesis of PVFc to date. As it is known from the epoxide-termination of poly(styrene),[58,67] the strong coordination of the lithium counterion with alkoxides prevents undesired further propagation and direct oxyanionic polymerization.[59,68] The living anionic polymerization of VFc was terminated by the addition of two different epoxide derivatives, i.e., benzyl glycidyl ether (BGE) and ethoxy ethyl glycidyl ether (EEGE), thereby generating a first hydroxyl group at the chain termini. In both cases, a second hydroxyl group can be released, utilizing different deprotection protocols (hydrogenolysis and acidic hydrolysis, respectively). Initially EEGE was utilized as the end-capping reagent to obtain mono- and dihydroxyl end-functional PVFcs, because we assumed facile and rapid release of the second hydroxyl group by acidic hydrolysis, and because of its high stability toward the aggressive reaction conditions of carbanionic polymerization (Scheme S1).

A series of PVFc-EEGEs was synthesized and characterized by SEC (Figure 1) and MALDI−ToF MS. Table 1 summarizes the molecular weights determined by SEC, using PS and PVFc standards. The difference between these values increases with increasing molecular weights. PVFc chains show considerably smaller hydrodynamic volumes compared to PS samples with

dx.doi.org/10.1021/ma3000048 | *Macromolecules* 2012, 45, 3409−3418

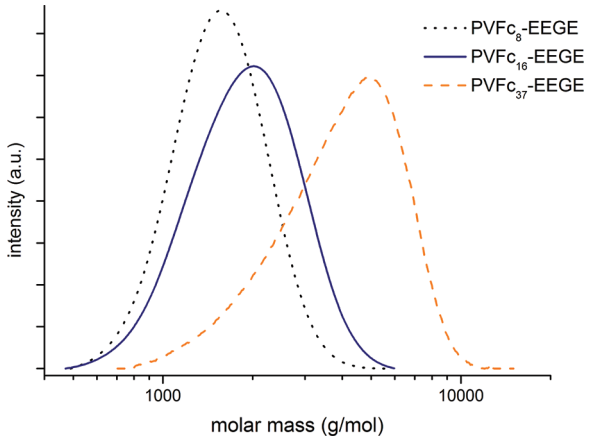


Figure 1. MWDs determined via SEC of PVFc-EEGE samples no. I–III (THF, RI-Signal, PS standard).

Table 1. Characterization Data of PVFc-EEGE

no.	polymer	M_n[a]	M_n[b]	M_w/M_n[b]
I	$PVFc_8$-EEGE[c]	1500	1800	1.17
II	$PVFc_{16}$-EEGE[c]	1700	3500	1.20
III	$PVFc_{37}$-EEGE[c]	3400	8000	1.26

[a]Molecular weight determined by SEC in g mol^{-1}(PS standards, THF). [b]Molecular weight in g mol^{-1} and molecular-weight distribution characterized by SEC in THF (PVFc standards[49]). [c]Degree of polymerization calculated by SEC (PVFc standards).

similar molar mass, due to the very compact chain conformation of the ferrocene-containing polymer.[49] According to the MALDI–ToF results the end-capping process was not quantitative. The highest degree of functionalization for the PVFc-EEGE was approximately 80% (Figure S1, Supporting Information). In addition, acidic hydrolysis of this polymer even under mild reaction conditions afforded yields of less than 50% dihydroxyl end-functionalized polymer (cf. MALDI–ToF MS: Figure S2, Supporting Information). Partial oxidation of the iron centers, which are located laterally to the polymer backbone, occurred. As a simple indication of the undesired oxidation process a color change of the reaction mixture from amber yellow to green was observed.

As an alternative synthetic pathway, BGE instead of EEGE was utilized as protected epoxide derivative for the termination step. The reaction was terminated with a 5-fold excess of BGE to introduce simultaneously (i) an active hydroxyl group and (ii) a benzyl-protected hydroxyl group at the chain terminus. In contrast to the former strategy the second hydroxyl group can be released by hydrogenolysis, and hence without the unwanted oxidizing processes. The BGE end-functionalized polymers were precipitated in methanol and characterized using SEC, ^{1}H NMR spectroscopy and MALDI–ToF MS. The corresponding characterization data are summarized in Table 2. ^{1}H NMR spectra were recorded in $CDCl_3$ (Figure S3 Supporting Information, bottom). A characteristic challenge of the NMR spectra of PVFc polymers in general is the appearance of very broad and unstructured resonances (see Supporting Information).[49] Nevertheless, the successful end-capping reaction with benzyl glycidyl ether could be verified, since the signal of the benzylic proton (7.49–7.25 ppm) is separated from the polymer signals. Unfortunately, the unstructured resonances in the PVFc spectra prevent accurate integration of the initiator

Table 2. Characterization Data of the PVFc-BGE Samples

no.	polymer[c]	M_n[a]	M_n[b]	M_w/M_n[b]
1	$PVFc_4$-BGE	860	980	1.07
2	$PVFc_5$-BGE	1180	1110	1.07
3	$PVFc_{11}$-BGE	1150	2630	1.09
4	$PVFc_{13}$-BGE	1510	3050	1.11
5	$PVFc_{16}$-BGE	1990	3650	1.10

[a]Molecular weight determined by SEC in g·mol^{-1} (THF, PS standards). [b]Molecular weight in g·mol^{-1} and molecular-weight distribution characterized by SEC in THF (PVFc standards[49]). [c]Degree of polymerization calculated by SEC (PVFc standards).

signals, and therefore precise end-group analysis based on NMR spectroscopy is complicated.

MALDI–ToF MS has been utilized instead to carry out a precise end-group analysis. The respective measurements of PVFc-BGE demonstrate quantitative terminal functionalization of PVFc with BGE. Figure 2 shows the MALDI–ToF mass

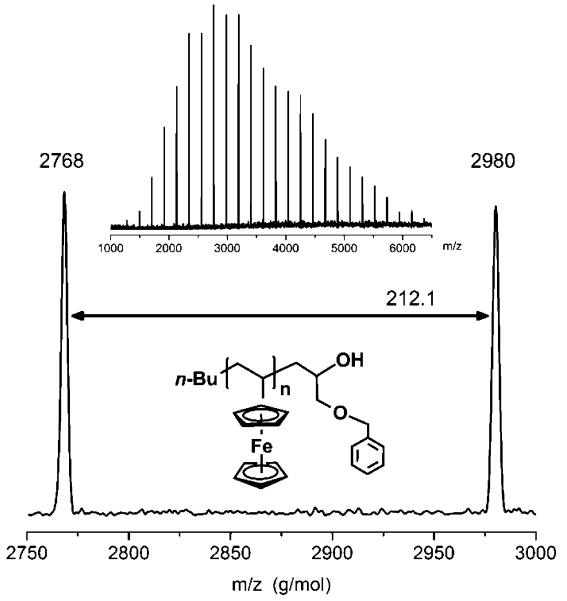


Figure 2. MALDI–ToF spectrum of $PVFc_{16}$-BGE (no. 5, Table 2) synthesized by anionic polymerization and a termination process with BGE as end-capping reagent; matrix, dithranol.

spectrum of $PVFc_{16}$-BGE as an example (no. 5, Table 2). The spectrum reveals only one distribution mode, which can unequivocally be assigned to BGE-functionalized poly(vinylferrocene) (**1**). This confirms the high functionalization efficiency of epoxide derivatives for the end-capping of PVFc. In the spectrum shown, representative signals are enlarged. The mass peak at m/z 2768.0 corresponds to the 12-mer of PVFc-BGE ($C_4H_9(C_{12}H_{12}Fe)_{12}C_{10}H_{13}O_2$; calculated value, 2767.2 g mol^{-1}). Showing a constant mass difference (molecular mass of the monomer repeating unit: 212.1 g mol^{-1}) between each signal, the complete spectrum is in good agreement with the calculated values. Furthermore, it should be emphasized that no signals corresponding to the mass peak of proton-terminated, and thus unfunctionalized PVFc ($C_4H_9(C_{12}H_{12}Fe)_{13}H$; calculated value, 2815.1 g mol^{-1}) can be observed in the MALDI–ToF spectrum, which again supports quantitative BGE functionalization. The MALDI–ToF investigation of all PVFc-BGE samples (see Table 2) confirmed the high

dx.doi.org/10.1021/ma3000048 | Macromolecules 2012, 45, 3409–3418

functionalization efficiency of the BGE end-capping method (see Supporting Information, Figure S4).

All synthesized PVFc samples showed a narrow and monomodal molecular-weight distribution (M_w/M_n = 1.09–1.11) and average molecular weights in the range of 770–1760 g mol^{-1} (vs PS standards[69]) and 980–3650 g mol^{-1} (vs PVFc standards) according to SEC results (cf. Figure 3 and Table 2).

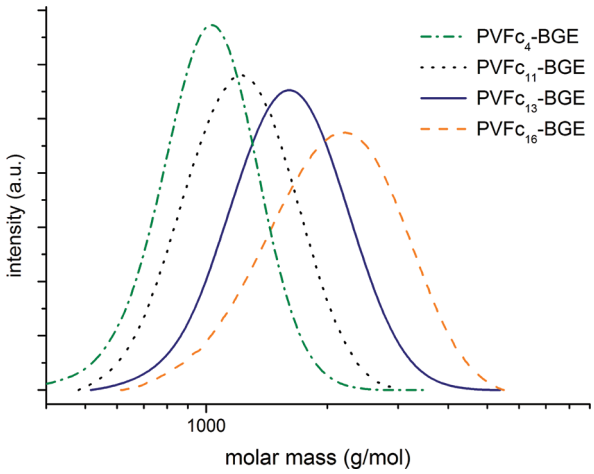


Figure 3. MWDs determined via SEC of selected PVFc-BGE samples no. 1 and no. 3–5 of Table 2 (THF, RI signal, PS standard).

Because of the aforementioned misleading values of the molar masses when evaluated using PS standards, it is necessary to consider molecular weights determined by SEC using PVFc standards (~500–50 000 g mol^{-1}). In summary, monohydroxyl end-functional PVFc samples were obtained in quantitative yields.

As mentioned above, the benzyl protecting group can now be released by catalytic hydrogenolysis to obtain dihydroxyl end-functionalized poly(vinyferrocene)s (PVFc-(OH)$_2$, **2**). By adjusting several parameters including solvent, time, and temperature the reaction conditions were optimized. Using the polar solvent mixture of dichloromethane and ethanol (2:1), Pd/C as a catalyst, and a hydrogen pressure of 50–80 bar, the best hydrogenolysis results were obtained.[70] The progress of the deprotection reaction was monitored by ^{1}H and ^{13}C NMR spectroscopy. Figure S3, Supporting Information shows ^{1}H NMR spectra of PVFc before (PVFc-BGE, no. 4) and after (PVFc-(OH)$_2$) the release of the benzyl groups. The disappearance of the aromatic proton signals in the δ = 7.49–7.25 ppm region confirms successful deprotection. ^{13}C NMR analysis verifies the results additionally, as the disappearance of the aromatic signals in the region between 127.4 and 128.9 ppm is evident (Figure S5, Supporting Information).

MALDI–ToF MS was employed to verify successful and quantitative removal of the benzyl group. Figure 4 shows an overlay of the MALDI–ToF spectra recorded before (PVFc$_{16}$-BGE, no. 5) and after (PVFc$_{16}$-(OH)$_2$) hydrogenolysis. A shift of the signals to lower masses is observed, indicating successful removal of the protecting group. The upper right part of Figure 4 depicts a magnification of the spectrum in the region between 1900 and 2500 g mol^{-1}, which highlights the expected shift (90.1 g mol^{-1} for the leaving group C_7H_7). Furthermore, it has to be emphasized that only the desired distribution mode can be observed in the MALDI–ToF spectrum of PVFc$_{16}$-(OH)$_2$, but no signals corresponding to the PVFc$_{16}$-BGE, even if the

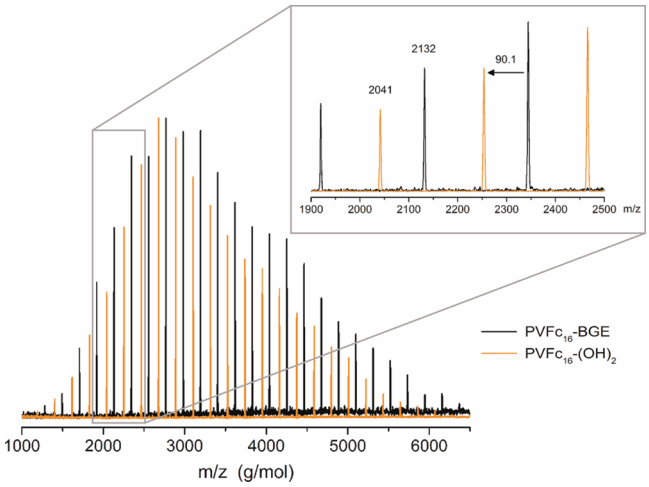


Figure 4. Overlay of MALDI–ToF mass spectra PVFc$_{16}$-BGE (Table 2 sample no. 5, black) and the respective PVFc$_{16}$-(OH)$_2$ (Table S1, Supporting Information sample no. S4, orange). The magnification highlights the successful release of the benzyl protecting group.

same experimental conditions were used as for the analysis of PVFc$_{16}$-BGE (cf. Figure S6, Supporting Information). SEC characterization of PVFc-(OH)$_2$ samples (Table S1 and Figure S7, Supporting Information) underlined narrow molecular-weight distributions (M_w/M_n = 1.09–1.15, THF, PS standards). The molecular weights as determined for these polymers using SEC are in good agreement with their protected counterparts.

The successful synthesis of two different end-functionalized poly(vinylferrocene)s with either one or two terminal hydroxyl groups paves the way to different PVFc-based block copolymer architectures.[57] To illustrate the potential of the approach, some representative amphiphilic PVFc block copolymers and AB$_2$ miktoarm star polymers have been prepared. The detailed results will be discussed in the following sections.

Linear (PVFc-BGE)-b-PEO Diblock Copolymer ***4***. BGE-end-capped PVFc was used as an initiator and EO as a monomer. The polymerization of EO is usually initiated by cesium or potassium alkoxides.[71–74] In our present case, the initiating species for EO polymerization is a potassium alkoxide, which was obtained by potassium naphthalide titration: The slightly greenish colored reaction mixture was cooled to −70 °C, and the corresponding amount of EO was added. After stirring the reaction mixture for 24 h at 60 °C, the copolymer (**4**) was precipitated into cold diethyl ether. The material was obtained in high yields (91%). After drying a bright yellow powder was obtained. When dissolving the powder in water, successful incorporation of the PVFc block is already visually indicated by the absence of precipitated PVFc homopolymer. Block copolymers in the range of 10 000 to 50 000 g mol^{-1} with a constant PVFc block of 1 000 g mol^{-1} were synthesized to investigate the influence of varying PEO block length on the copolymer properties. ^{1}H NMR spectroscopy was employed to study the block copolymer structure and composition. However, similar to the spectra of PVFc homopolymers, broad and unstructured signals are observed throughout, due to limited chain mobility. Nevertheless, the main signals of the two different polymer blocks can clearly be distinguished. The expected signals reflecting the PVFc backbone appear at 2.7–0.7 ppm. The signals of the PEO backbone and the ferrocene units overlap in the region between 4.5 and 3.0 ppm. In addition, ^{13}C NMR analyses were carried out. The signals of

dx.doi.org/10.1021/ma3000048 | Macromolecules 2012, 45, 3409–3418

both blocks (PVFc: backbone 34−29 ppm; ferrocene units 68−65 ppm; PEO 73−69 ppm) are clearly visible in analogy to the ^{1}H NMR spectrum. The presence of all expected signals in ^{1}H and ^{13}C NMR analysis confirms the successful synthesis of the desired diblock copolymers (Table 3 and Figure S8, Supporting Information).

Table 3. Characterization Data of Block Copolymers PVFc-BGE-PEO and AB_2 Miktoarm Star Polymers PVFc-$(PEO)_2$

no.	polymer[a]	M_n[b]	M_n[c]	M_w/M_n[c]
6	$PVFc_4$-BGE-PEO_{92}	10 000	10 000	1.11
7	$PVFc_4$-BGE-PEO_{206}	20 000	20 000	1.12
8	$PVFc_4$-BGE-PEO_{795}	43 000	37 000	1.07
9	$PVFc_4$-BGE-PEO_{1045}	44 000	48 000	1.06
10	$PVFc_{11}$-$(PEO_{61})_2$	11 000	8000	1.19
11	$PVFc_{11}$-$(PEO_{73})_2$	11 000	9000	1.25
12	$PVFc_{13}$-$(PEO_{273})_2$	25 000	27 000	1.10
13	$PVFc_{13}$-$(PEO_{420})_2$	50 000	40 000	1.10

[a]PVFc: degree of polymerization corresponds to the protected precursor (nos. 1−10). PEO: degree of polymerization determined by SEC. [b]Theoretical value of the number-average of the molecular weight in g mol^{-1} [c]Molecular weight in g mol^{-1} and molecular-weight distribution characterized by SEC in $CHCl_3$ (PS standard).

NMR characterization provides important information about the copolymers, but final proof of successful block formation is not possible by this technique. Thus, SEC was applied to study all polymer samples subsequent to the work up procedure. Figure 5 presents the MWDs of a diblock copolymer (no. 8) and the corresponding precursor PVFc-BGE (no. 1), demonstrating efficient block formation. A characteristic shift of the molecular weights from approximately 2000 to 40 000 g mol^{-1} can be observed. Since the PEO block does not induce a signal in the UV detector, the pronounced UV absorption of the block copolymers evidence successful incorporation of the PVFc chains. The corresponding characterization data for all copolymers are listed in Table 3 (no. 6−9) and the respective SEC traces are depicted in Figure S9, Supporting Information. In comparison, theoretical values of the molecular weight agree well with SEC results, showing good control of the polymerization process.

It has to be emphasized that all synthesized polymers show excellent water solubility. By dissolving the bright yellow product in water, the formation of a clear, slightly amber colored solution is observed. In addition, UV−vis spectra have been measured in $CHCl_3$ and H_2O, showing the characteristic strong absorption[75] of PVFc between 400 and 450 nm (Figure S10, Supporting Information). Comparable solubility properties are not observed for any other amphiphilic ferrocene-containing polymer published so far.[55]

The use of BGE as the capping reagent provides facile access to terminal orthogonal hydroxyl functionalities. The first hydroxyl group can directly be applied for further reactions (as shown herein) and the second hydroxyl group can be released by hydrogenolysis. The presented synthetic strategy generates block copolymers with a single protected functionality at the block junction, which is suitable for additional reactions subsequent to the release of the benzyl group. It may be worth mentioning that also ABC block copolymers with poly(vinylferrocene) segment should be available in this manner. Detailed studies employing the functionality at the interface yielding novel macromolecular architectures are subject of future research.

PVFc-$(PEO)_2$ AB_2 Miktoarm Star Polymer ***3***. After the successful release of the benzyl group, PVFc-$(OH)_2$ was subsequently used as a difunctional macroinitiator-functionalized PVFc, offering access to water-soluble AB_2 miktoarm star polymers. The procedure was carried out similar to the linear block copolymer synthesis, and both hydroxyl groups were deprotonated using potassium naphthalide prior to the addition of EO. Because of the rapid cation-exchange equilibrium (compared to the propagation), both hydroxyl groups can be expected to react with the monomer units in the same manner and with the same propagation rate.[76] In comparison to PVFc-PEO block copolymers, similar reaction conditions with 24−48 h reaction time, 60 °C and an identical work up procedure was applied to obtain PVFc-$(PEO)_2$ (**3**) miktoarm star polymers as a bright yellow powder. As expected, the materials are water-soluble as well.

Molecular weights in the range of 8000 to 40 000 g mol^{-1} with low PDIs (M_w/M_n < 1.25) were synthesized. The corresponding characterization data of all PVFc-$(PEO)_2$ samples are also summarized in Table 3 (no. 10−13, cf. Figure S11, Supporting Information). All signals of ^{1}H NMR and ^{13}C

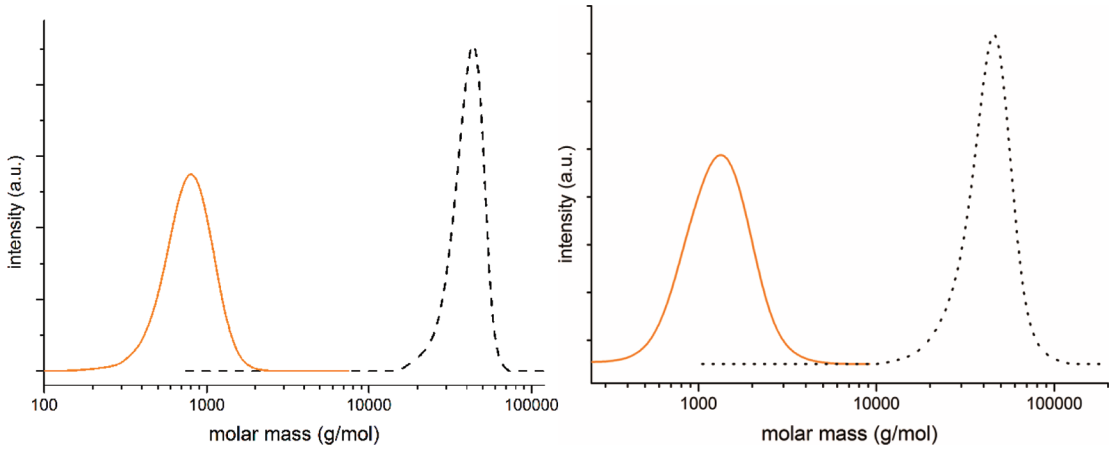


Figure 5. Linear block copolymer formation evidenced by UV-signals in SEC. MWDs of $PVFc_4$-BGE and $PVFc_4$-BGE-PEO_{795} (no. 1 and no. 13, *left*) as well as $PVFc_{13}$-$(OH)_2$ and $PVFc_{13}$-$(PEO_{420})_2$ (corresponds to no. 4 and no. 18, *right*). ($CHCl_3$, PS standard).

dx.doi.org/10.1021/ma3000048 | *Macromolecules* 2012, 45, 3409−3418

NMR spectra can be assigned to the respective hydrogens and carbons of PVFc-$(PEO)_2$ and are analogous to the respective linear block copolymers. Because of high molecular weights and therefore low signal intensity of the junction carbons, no significant difference between linear block and miktoarm star polymers was observable in NMR spectroscopy (cf. Figure S12, Supporting Information). To confirm block formation, in Figure 5 the SEC results obtained from the miktoarm star polymer no. 13 and the dihydroxyl PVFc-precursor are combined. In analogy to the linear block copolymer a molecular weight shift from 3000 to 40 000 g mol^{-1} can be observed and the presence of an intense UV absorption in SEC analysis indicates successful incorporation of the PVFc block into the 3-arm star polymer. Again, the comparison of experimentally observed and theoretically expected values for molar masses demonstrates good control over molecular weights. In contrast to the linear block copolymers the SEC results underestimate the molecular weights slightly. This is due to the macromolecular architecture of the star-shaped polymer, which shows a reduced hydrodynamic volume compared to linear block copolymer with similar contour length.[77,78]

It is obvious that it is a key issue, whether the formation of the miktoarm structures has been achieved. Additional information on the polymers was obtained by investigating two selected samples with conventional SEC, SEC−MALLS and SEC online viscometry. The corresponding results are listed in Table 4. Characterization by light-scattering demonstrated similar molecular weights for both samples (block and star polymer), whereas in the case of the conventional SEC (linear PS standards) the molecular weight of the star polymer was strongly underestimated. This is obviously a consequence of the decreased hydrodynamic volume of the star-shaped polymer. In addition, the data of the viscosity detector present a distinct difference between linear and star shaped polymers concerning the intrinsic viscosity (see Table 4 and Figure S13, Supporting Information). These results support the successful synthesis of ferrocene-containing AB_2 miktoarm star polymers, i.e., growth of both PEO arms, and mirror the different hydrodynamic volume of linear and miktoarm star polymer prepared.

Table 4. Characterization Data of a Selected Block Copolymer PVFc-BGE-PEO and an AB_2 Miktoarm Star Polymer PVFc-$(PEO)_2$ (Conventional SEC vs SEC−MALLS)

no.	polymer	M_n [a]	M_w [a]	M_w/M_n [a]	M_w [b]	$[\eta]$ [c]
6	$PVFc_4$-BGE-PEO_{92}	9600	12 200	1.27	9700	17.3
10	$PVFc_{11}$-$(PEO_{61})_2$	6800	8100	1.19	9900	8.7

[a]Number-average and weight-average of molecular weight in g mol^{-1} and molecular-weight distribution characterized by SEC in THF. [b]Weight-average of molecular weight in g mol^{-1} characterized by SEC−MALLS in THF,[79] [c]Intrinsic viscosity determined by SEC online viscosity measurements in THF.

B. Properties of Linear and Star-Shaped PVFc-*block*-PEO Copolymers. The main objective of this work was the development of a versatile synthetic strategy to generate water-soluble block copolymers containing PVFc blocks. Nevertheless, first results of preliminary studies of their behavior in solution, thermal properties and morphological characteristics will be given in the following.

DSC measurements of both types of block copolymers (linear and AB_2 star polymers) have been performed to evaluate the effect of the different chain architectures. The long PEG chain of both polymer structures provides clearly visible glass transition temperatures (T_g: ∼−50 °C) and melting points (T_m: ∼ 60 °C), whereas the T_g of the PVFc chains, which is expected in the region of approximately 200 °C,[49] could not be observed. This is most probably due to the low weight fraction of the PVFc blocks (2−25%). However, an increased stability of the synthesized polymeric structures was observed by TGA analysis. The degradation threshold compared to PEO homopolymers (380−400 °C[80,81]) was slightly higher for the organometallic structures (420 °C).

As mentioned above, all presented PVFc-PEO structures show water solubility (see Figure S10, Supporting Information). This is of interest, since amphiphilic ferrocene-containing block copolymers based on poly(ferrocenylsilane) can form redox-active micelles, allowing e.g., for the storage and release of encapsulated drugs in aqueous media.[82−85] The morphologies of block and miktoarm star copolymers in solution were studied by transmission electron microscopy (TEM) using the drop-casting method. The polymers were initially dissolved in THF. Subsequent slow addition of water by a syringe pump was employed to lock the core structures ("frozen micelles") as described by Eisenberg et al.[86] To obtain the micelles in pure water, the organic cosolvent was gradually eliminated by dialysis. One drop of the aqueous solution ($c \approx 0.5$ g L^{-1}) was deposited on a carbon-coated copper TEM grid. The water was allowed to evaporate under vacuum, before the polymer structures on the grid were investigated by TEM.

Representative images of PVFc-BGE-PEO and PVFc-$(PEO)_2$ (M_n of approximately 40 000 g mol^{-1}) are shown in Figure 6A−C. As expected for the given block ratios with rather small content of the insoluble PVFc block and high content of PEO, micellar structures were observed. The diameters of the spherical aggregates varied between 100 and 400 nm. Neither the shape nor the diameters show a difference, comparing the TEM images of block copolymers and AB_2 miktoarm star polymers. However, the TEM images of star polymers with lower molecular weight (sample no. 11, ∼10 000 g mol^{-1}) exhibit a spherical structure consisting of several agglomerated spherically shaped micelles (Figure 6D−F). In Figure 6F an intriguing microphase separation within the block copolymer micelles can be distinguished. Obviously, the dark regions represent the cores of the micelles consisting of PVFc, whereas the brighter regions in proximity represent the PEO blocks. In addition, rather uniform diameter of the micelles of approximately 100 nm can be observed. In our current understanding, the appearance of different agglomerated micelles depends on the molecular weight of the block copolymers and the fraction of PVFc. Furthermore, the degree of crystallization of the high molecular weight PEO in the initially swollen and subsequently dried shell of the micelle might play a role for the formation of the structures observed. Morphologies and potential application (e.g., redox-active micelles) of block copolymers with increasing PVFc ratio are currently investigated in a systematic manner and will be presented in forthcoming work.

■ CONCLUSION

A synthetic pathway to water-soluble block copolymers and AB_2 miktoarm star polymers containing a poly(vinyl ferrocene) (PVFc) block and either one or two poly(ethylene oxide)

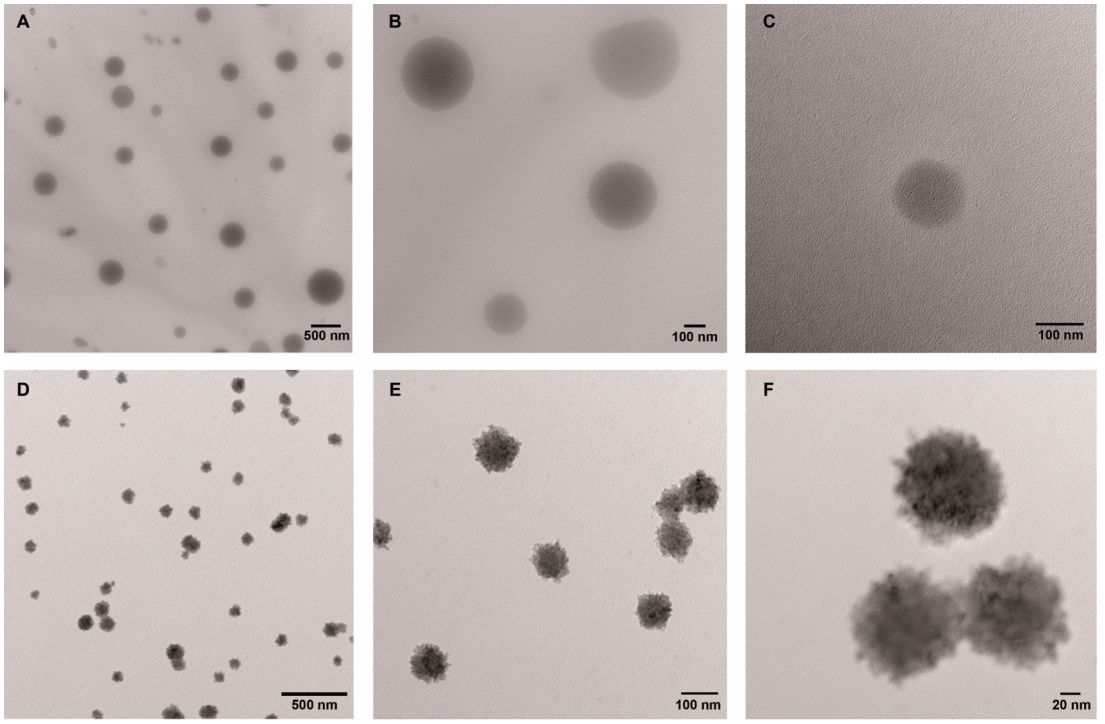


Figure 6. TEM images of PVFc-BGE-PEO block copolymers and PVFc-$(PEO)_2$ star polymers prepared from aqueous solution using the drop-casting method. (A and B: $PVFc_{13}$-$(PEO_{420})_2$, no. 13, C: $PVFc_4$-BGE-PEO_{795}, no. 8, D-F: $PVFc_{11}$-$(PEO_{73})_2$, no. 11).

(PEO) blocks has been developed. For the first time, the combination of carb- and oxyanionic polymerization has been implemented for poly(vinylferrocene), utilizing a protected epoxide derivative as end-capping reagent. Two different glycidyl ethers (BGE and EEGE) were employed for the functional end-capping of the PVFc block. In order to switch from the PVFc block to PEO, a procedure had to be developed that permits to overcome the redox-sensitivity of the metal-containing PVFc block. The benzyl glycidyl ether (BGE) was found to be the best suited capping reagent, since cleavage of the benzyl protecting group by hydrogenolysis does not lead to degradation of the PVFc polymer chain in contrast to the acidic treatment, which is necessary to remove the acetal protecting group of EEGE. Quantitative end-capping (and deprotection) led to mono and dihydroxyl end-functionalized PVFc, as evidenced by MALDI–ToF MS.

In the following step, the respective polymers have been used as macroinitiators for the ring-opening polymerization of ethylene oxide to obtain a series of water-soluble PVFc-BGE-PEO block copolymers and PVFc-$(PEO)_2$ AB_2 miktoarm star polymers with molecular weights in the range of 8000 to 50 000 g mol^{-1}, as confirmed by a combination of SEC, SEC–MALLS and online viscosimetry. These metal-containing amphiphilic block copolymers exhibit good solubility in water, and the synthetic pathway provides an efficient approach to water-soluble and redox-active complex polymer architectures. First studies dealing with the morphologies in aqueous solution showed agglomerated micelle structures.

The general synthetic pathway demonstrated herein provides a facile route to a large variety of macromolecular architectures containing PVFc blocks combined with polyether chains. In view of the versatile application potential for water-soluble ferrocene-containing compounds, the presented structures are promising materials for bio-organometallic applications,[15,17] which are currently investigated.

■ ASSOCIATED CONTENT

Ⓢ Supporting Information

Synthetic strategy, MALDI–ToF, NMR, UV–vis, viscosity, and SEC results (Scheme S1, Figure S1–S12). This material is available free of charge via the Internet at http://pubs.acs.org.

■ AUTHOR INFORMATION

Corresponding Author

*E-mail: (M.G.) mgallei@dki.tu-darmstadt.de; (H.F.) hfrey@uni-mainz.de.

Notes

The authors declare no competing financial interest.

■ ACKNOWLEDGMENTS

C.T. thanks MPGC (Max Planck Graduate Center with Johannes Gutenberg-University) and the Excellence Initiative (DFG/GSC 266) for a scholarship and financial support. The authors would like to thank the Landesoffensive zur Entwicklung Wissenschaftlich-ökonomischer Exzellenz (LOEWE Soft Control) for financial support of this work. We acknowledge Daniela Held und Michael Krämer (PSS company Mainz) for detailed SEC analysis and on-line viscosity measurements. Support in performing the SEC analyses by Marion Trautmann (PVFc) is acknowledged.

■ REFERENCES

(1) Whittell, G. R.; Manners, I. *Adv. Mater.* **2007**, *19* (21), 3439–3468.

(2) Abd-El-Aziz, A. S.; Manners, I. *Frontiers in Transition Metal-Containing Polymers*; Wiley-Interscience: Hoboken, NJ, 2007.

(3) Manners, I. *Synthetic Metal-Containing Polymers*; VCH: Weinheim, Germany, 2004.

(4) Wöhrle, D.; Pomogailo, A. D. *Metal Complexes and Metals in Macromolecules: Synthesis, Structure and Properties*; Wiley-VCH: Weinheim, Germany, 2003.

(5) Carraher, C. E.; Abd-El-Aziz, A. S.; Pittman, C.; Sheats, J.; Zeldin, M. *A Half Century of Metal and Metalloid Containing Polymers*; Wiley: New York, 2003.
(6) Rehahn, M. Organic-Inorganic Hybrid Polymers. In *Synthesis of Polymers*; Schlüter, A.-D., Ed.; Wiley-VCH: Weinheim, Germany, 1999; p 319.
(7) Smith, T. M.; Nelson, G. L. *Polym. Adv. Technol.* **2006**, *17* (9−10), 746−753.
(8) Hale, P. D.; Inagaki, T.; Karan, H. I.; Okamoto, Y.; Skotheim, T. A. *J. Am. Chem. Soc.* **1989**, *111* (9), 3482−3484.
(9) Tatsuma, T.; Saito, K.; Oyama, N. *Anal. Chem.* **1994**, *66* (7), 1002−1006.
(10) Saito, T.; Watanabe, M. *React. Funct. Polym.* **1998**, *37* (1−3), 263−269.
(11) Saito, T.; Watanabe, M. *Polym. J.* **1999**, *31* (11−2), 1149−1154.
(12) Patel, H.; Li, X.; Karan, H. I. *Biosens. Bioelectron.* **2003**, *18* (8), 1073−1076.
(13) Gülce, A.; Gülce, H. *J. Biochem. Bioph. Methods* **2005**, *62* (1), 81−92.
(14) Cass, A. E. G.; Davis, G.; Francis, G. D.; Hill, H. A. O.; Aston, W. J.; Higgins, I. J.; Plotkin, E. V.; Scott, L. D. L.; Turner, A. P. F. *Anal. Chem.* **1984**, *56* (4), 667−671.
(15) van Staveren, D. R.; Metzler-Nolte, N. *Chem. Rev.* **2004**, *104* (12), 5931−5986.
(16) Biot, C.; Pradines, B.; Dive, D. Ferroquine: A Concealed Weapon. In *Apicomplexan Parasites*; Wiley-VCH Verlag GmbH & Co. KGaA: Weinheim, Germany, 2011; pp 397−411.
(17) Top, S.; Vessières, A.; Leclercq, G.; Quivy, J.; Tang, J.; Vaissermann, J.; Huché, M.; Jaouen, G. *Chem.—Eur. J.* **2003**, *9* (21), 5223−5236.
(18) Top, S.; Dauer, B.; Vaissermann, J.; Jaouen, G. *J. Organomet. Chem.* **1997**, *541* (1−2), 355−361.
(19) Köpf-Maier, P.; Köpf, H.; Neuse, E. W. *Angew. Chem., Int. Ed.* **1984**, *23* (6), 456−457.
(20) Ornelas, C. *New J. Chem.* **2011**, *35* (10), 1973−1985.
(21) Arimoto, F. S.; Haven, A. C. *J. Am. Chem. Soc.* **1955**, *77* (23), 6295−6297.
(22) Neuse, E. W.; Rosenberg, H. *J. Macromol. Sci., Rev. Macromol. Chem.* **1970**, *4* (1), 1−145.
(23) Neuse, E. W. *J. Macromol. Sci., Chem.* **1981**, *16* (1), 3−72.
(24) Withers, H. P.; Seyferth, D.; Fellmann, J. D.; Garrou, P. E.; Martin, S. *Organometallics* **1982**, *1* (10), 1283−1288.
(25) Walter, S. *Russ. Chem. Rev.* **1991**, *60* (7), 784.
(26) Brandt, P. F.; Rauchfuss, T. B. *J. Am. Chem. Soc.* **1992**, *114* (5), 1926−1927.
(27) Foucher, D. A.; Tang, B. Z.; Manners, I. *J. Am. Chem. Soc.* **1992**, *114* (15), 6246−6248.
(28) Manners, I. *Can. J. Chem.* **1998**, *76* (4), 371−381.
(29) Hirano, T.; Yoo, H.-S.; Ozama, Y.; Abou El-Magd, A.; Sugiyama, K.; Hirao, A. *J. Inorg. Organomet. Polym.* **2010**, *20* (3), 445−456.
(30) Hudson, R. D. A. *J. Organomet. Chem.* **2001**, *637*−*639*, 47−69.
(31) Gilroy, J. B.; Patra, S. K.; Mitchels, J. M.; Winnik, M. A.; Manners, I. *Angew. Chem., Int. Ed.* **2011**, *50* (26), 5851−5855.
(32) Wurm, F.; Frey, H. *Prog. Polym. Sci.* **2011**, *36* (1), 1−52.
(33) Wurm, F.; Villanueva, F. J. L.; Frey, H. *J. Polym. Sci., Part A: Polym. Chem.* **2009**, *47* (10), 2518−2529.
(34) Bellas, V.; Rehahn, M. *Angew. Chem., Int. Ed.* **2007**, *46* (27), 5082−5104.
(35) Wurm, F.; Hilf, S.; Frey, H. *Chem.—Eur. J.* **2009**, *15* (36), 9068−9077.
(36) Massey, J. A.; Winnik, M. A.; Manners, I.; Chan, V. Z. H.; Ostermann, J. M.; Enchelmaier, R.; Spatz, J. P.; Müller, M. *J. Am. Chem. Soc.* **2001**, *123* (13), 3147−3148.
(37) Mohd Yusoff, S. F.; Gilroy, J. B.; Cambridge, G.; Winnik, M. A.; Manners, I. *J. Am. Chem. Soc.* **2011**, *133* (29), 11220−11230.
(38) Eloi, J.-C.; Rider, D. A.; Cambridge, G.; Whittell, G. R.; Winnik, M. A.; Manners, I. *J. Am. Chem. Soc.* **2011**, *133* (23), 8903−8913.
(39) Qian, J.; Guerin, G.; Lu, Y.; Cambridge, G.; Manners, I.; Winnik, M. A. *Angew. Chem., Int. Ed.* **2011**, *50* (7), 1622−1625.
(40) Pittman, C. U.; Lai, J. C.; Vanderpool, D. P. *Macromolecules* **1970**, *3* (1), 105−107.
(41) Gallei, M.; Schmidt, B. V. K. J.; Klein, R.; Rehahn, M. *Macromol. Rapid Commun.* **2009**, *30* (17), 1463−1469.
(42) Herfurth, C.; Voll, D.; Buller, J.; Weiss, J.; Barner-Kowollik, C.; Laschewsky, A. *J. Polym. Sci., Part A: Polym. Chem.* **2012**, *50* (1), 108−118.
(43) Nuyken, O.; Burkhardt, V.; Hübsch, C. *Macromol. Chem. Phys.* **1997**, *198* (11), 3353−3363.
(44) Higashihara, T.; Faust, R. *Macromolecules* **2007**, *40* (21), 7453−7463.
(45) Gallei, M.; Tockner, S.; Klein, R.; Rehahn, M. *Macromol. Rapid Commun.* **2010**, *31* (9−10), 889−896.
(46) Chauhan, B. P. S.; Rathore, J. S. *J. Am. Chem. Soc.* **2005**, *127* (16), 5790−5791.
(47) Durkee, D. A.; Eitouni, H. B.; Gomez, E. D.; Ellsworth, M. W.; Bell, A. T.; Balsara, N. P. *Adv. Mater.* **2005**, *17* (16), 2003−2006.
(48) Baumert, M.; Fröhlich, J.; Stieger, M.; Frey, H.; Mülhaupt, R.; Plenio, H. *Macromol. Rapid Commun.* **1999**, *20* (4), 203−209.
(49) Gallei, M.; Klein, R.; Rehahn, M. *Macromolecules* **2010**, *43* (4), 1844−1854.
(50) Kloninger, C.; Rehahn, M. *Macromolecules* **2004**, *37* (5), 1720−1727.
(51) Zundel, T.; Baran, J.; Mazurek, M.; Wang, J.-S.; Jerome, R.; Teyssie, P. *Macromolecules* **1998**, *31* (9), 2724−2730.
(52) Wang, X.-S.; Winnik, M. A.; Manners, I. *Macromol. Rapid Commun.* **2002**, *23* (3), 210−213.
(53) Schacher, F. H.; Elbert, J.; Patra, S. K.; Mohd Yusoff, S. F.; Winnik, M. A.; Manners, I. *Chem.—Eur. J.* **2012**, *18* (2), 517−525.
(54) Resendes, R.; Massey, J.; Dorn, H.; Winnik, M. A.; Manners, I. *Macromolecules* **2000**, *33* (1), 8−10.
(55) Gohy, J.-F.; Lohmeijer, B. G. G.; Alexeev, A.; Wang, X.-S.; Manners, I.; Winnik, M. A.; Schubert, U. S. *Chem.—Eur. J.* **2004**, *10* (17), 4315−4323.
(56) Hillmyer, M. A.; Bates, F. S. *Macromolecules* **1996**, *29* (22), 6994−7002.
(57) Natalello, A.; Tonhauser, C.; Berger-Nicoletti, E.; Frey, H. *Macromolecules* **2011**, *44*, 9887−9890.
(58) Tonhauser, C.; Frey, H. *Macromol. Rapid Commun.* **2010**, *31* (22), 1938−1947.
(59) Tonhauser, C.; Wilms, D.; Wurm, F.; Berger-Nicoletti, E.; Maskos, M.; Löwe, H.; Frey, H. *Macromolecules* **2010**, *43* (13), 5582−5588.
(60) Quirk, R. P.; Gomochak, D. L. *Rubber Chem. Technol.* **2003**, *76* (4), 812−831.
(61) Tonhauser, C.; Obermeier, B.; Mangold, C.; Löwe, H.; Frey, H. *Chem. Commun.* **2011**, *47* (31), 8964−8966.
(62) Zhang, W.-B.; Sun, B.; Li, H.; Ren, X.; Janoski, J.; Sahoo, S.; Dabney, D. E.; Wesdemiotis, C.; Quirk, R. P.; Cheng, S. Z. D. *Macromolecules* **2009**, *42* (19), 7258−7262.
(63) Li, Z.; Kesselman, E.; Talmon, Y.; Hillmyer, M. A.; Lodge, T. P. *Science* **2004**, *306* (5693), 98−101.
(64) Higashihara, T.; Kitamura, M.; Haraguchi, N.; Sugiyama, K.; Hirao, A.; Ahn, J. H.; Lee, J. S. *Macromolecules* **2003**, *36* (18), 6730−6738.
(65) Bender, J. T.; Knauss, D. M. *Macromolecules* **2009**, *42* (7), 2411−2418.
(66) Dingels, C.; Schömer, M.; Frey, H. *Chem. unserer Zeit* **2011**, *45* (5), 338−349.
(67) Quirk, R. P.; Ma, J. J. *J. Polym. Sci., Part A: Polym. Chem.* **1988**, *26* (8), 2031−2037.
(68) Furukawa, J.; Saegusa, T.; Tsuruta, T.; Kakogawa, G. *Macromol. Chem. Phys.* **1960**, *36* (1), 25−39.
(69) SEC data of PVFc polymer with PS standards are listed to enable the reproducibility of this works for other groups even if no PVFc standards are available.
(70) Deschenaux, R.; Even, M.; Guillon, D. *Chem. Commun.* **1998**, *5*, 537−538.

(71) Mangold, C.; Wurm, F.; Obermeier, B.; Frey, H. *Macromol. Rapid Commun.* **2010**, *31* (3), 258−264.
(72) Mangold, C.; Dingels, C.; Obermeier, B.; Frey, H.; Wurm, F. *Macromolecules* **2011**, *44* (16), 6326−6334.
(73) Hofmann, A. M.; Wurm, F.; Hühn, E.; Nawroth, T.; Langguth, P.; Frey, H. *Biomacromolecules* **2010**, *11* (3), 568−574.
(74) Wilms, D.; Schömer, M.; Wurm, F.; Hermanns, M. I.; Kirkpatrick, C. J.; Frey, H. *Macromol. Rapid Commun.* **2010**, *31* (20), 1811−1815.
(75) Pittman, C. U.; Lai, J. C.; Vanderpool, D. P.; Good, M.; Prado, R. *Macromolecules* **1970**, *3* (6), 746−754.
(76) Sunder, A.; Hanselmann, R.; Frey, H.; Mülhaupt, R. *Macromolecules* **1999**, *32* (13), 4240−4246.
(77) Hadjichristidis, N.; Pitsikalis, M.; Pispas, S.; Iatrou, H. *Chem. Rev.* **2001**, *101* (12), 3747−3792.
(78) Hadjichristidis, N. *J. Polym. Sci., Part A: Polym. Chem.* **1999**, *37* (7), 857−871.
(79) Due to the difference in polymer architecture the dn/dc values were determined for both samples with 0,0802 for $PVFc_4$-BGE-PEO_{92} and 0,0778 for $PVFc_{11}$-$(PEO_{61})_2$
(80) Costa, L.; Gad, A. M.; Camino, G.; Cameron, G. G.; Qureshi, M. Y. *Macromolecules* **1992**, *25* (20), 5512−5518.
(81) Hoevetborn, T.; Hoelscher, M.; Keul, H.; Höcker, H. *Rev. Roum. Chim.* **2006**, *51*, 781−793.
(82) Xiao, Z.-P.; Cai, Z.-H.; Liang, H.; Lu, J. *J. Mater. Chem.* **2010**, *20* (38), 8375−8381.
(83) Power-Billard, K. N.; Spontak, R. J.; Manners, I. *Angew. Chem., Int. Ed.* **2004**, *43* (10), 1260−1264.
(84) Takeoka, Y.; Aoki, T.; Sanui, K.; Ogata, N.; Yokoyama, M.; Okano, T.; Sakurai, Y.; Watanabe, M. *J. Controlled Release* **1995**, *33* (1), 79−87.
(85) Ma, Y.; Dong, W.-F.; Hempenius, M. A.; Möhwald, H.; Julius Vancso, G. *Nat. Mater.* **2006**, *5* (9), 724−729.
(86) Zhang, L.; Eisenberg, A. *Science* **1995**, *268* (5218), 1728−1731.

Macromolecules

Article

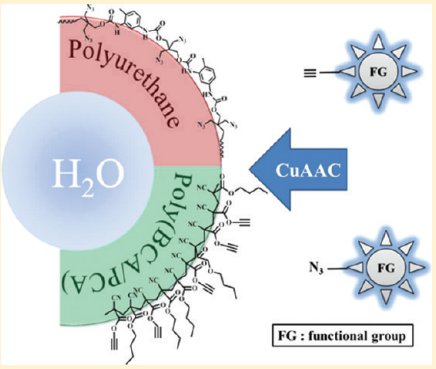
pubs.acs.org/Macromolecules

Surface Click Reactions on Polymeric Nanocapsules for Versatile Functionalization

Grit Baier, Joerg Max Siebert, Katharina Landfester, and Anna Musyanovych*

Max Planck Institute for Polymer Research, Ackermannweg 10, 55128 Mainz, Germany

ABSTRACT: One-step synthesis of poly(butyl cyanoacrylate-*co*-propargyl cyanoacrylate) (P(BCA/PCA)) and polyurethane (PUR) azide nanocapsules for direct covalent and variable functionalization is reported. The capsules in the size range between 230 and 350 nm were synthesized in an inverse (water-in-oil) miniemulsion system through either interfacial anionic polymerization (in the case of P(BCA/PCA)) or interfacial polyaddition reaction with 2,4-toluene diisocyanate (PUR azide). Surface functionalization of nanocapsules was achieved by different copper-catalyzed azide−alkyne cycloaddition (CuAAC) reactions, which were carried out under mild and ambient conditions. Click reactions of rhodamine azide and anthracene azide to P(BCA-*co*-PCA) nanocapsules were performed for quantitative determination of the surface alkyne bonds. PUR-azide nanocapsules were functionalized with propiolic acid and fluorescent alkyne dye. The reaction kinetics between propiolic acid and the azide monomer was studied by ^{1}H NMR spectroscopy. Furthermore, the functionalization of nanocapsules with propiolic acid was extended to copper-free azide−alkyne cycloaddition, thus making the system suitable for copper-sensitive materials.



INTRODUCTION

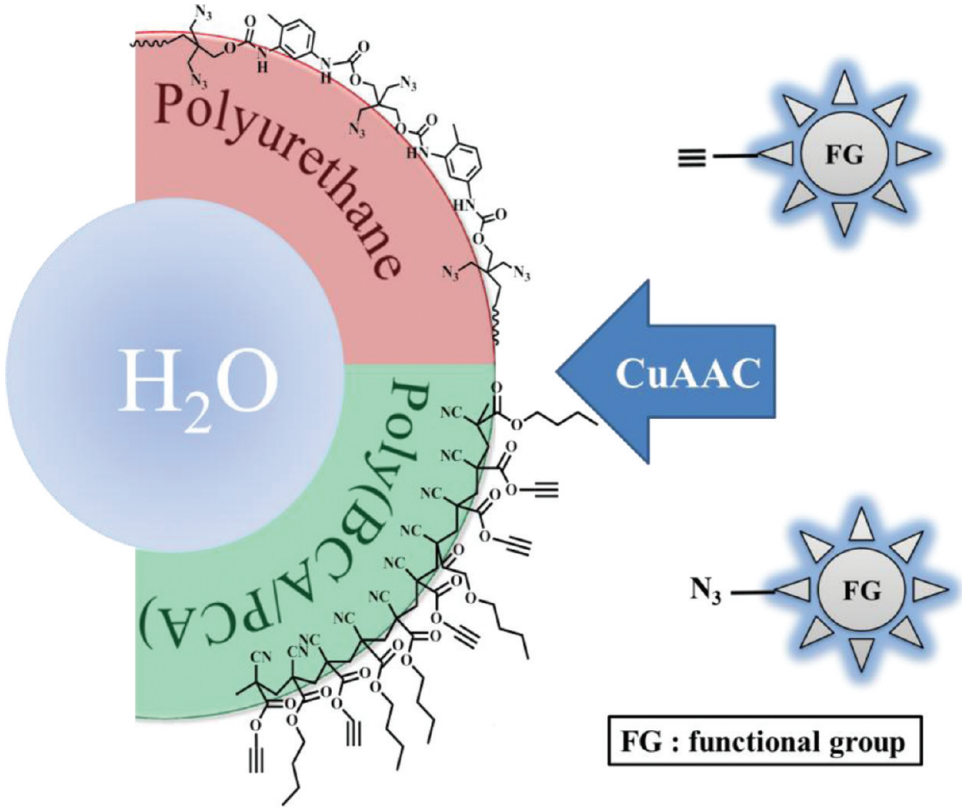
In the past decades there is a growing interest in the development of nanocarriers with well-defined structures and tailorable properties for drug delivery systems. The particle size, shape, and surface functionality are the most important factors that influence the distribution of the particles within the body, their interaction, and uptake by living cells.[1−4] Colloidal carriers such as liposomes, micelles, dendritic polymers, and nanoparticles or nanocapsules are the most promising candidates with regards to the site-specific targeting and controlled drug release.[5−8] The main advantages to use nanocapsules for drug delivery are the efficient protection of a drug against degradation caused by the influence of the environment, and preventing desorption of a drug, as it could be the case with physically adsorbed drug molecules onto the particle surface.

In recent years, the fabrication of polymer nanocapsules made from different materials and using various approaches was described by many research groups ranging from the layer-by-layer approach of preformed polymer(s) to the interfacial reactions of monomers at stable nanodroplets.[9−13] For the drug delivery application it is of immense interest that the capsules are biocompatible and possess functional groups on the surface that enable covalent attachment of biomolecules for the site-specific targeting. The covalent attachment can be achieved by numerous coupling reactions, such as amine/epoxide, amine/glutaraldehyde, thiol/maleimide, carbodiimide, and so on.[14−16] Click chemistry, which is based on the copper-catalyzed azide−alkyne cycloaddition, reported simultaneously in 2001/2002 by Sharpless et al.[17,18] and Meldal et al.,[19] is a very efficient strategy for the functionalization as it proceeds at the mild reaction conditions and results in high yields.[20,21] To date, numerous click-chemistry-based strategies have been reported for the modification of surfaces. Over the past few years, several click reactions have been particularly elaborated for the modification of curved surfaces, i.e., micro- and nanoparticles. Ranjan and Brittain[22] combined living radical polymerization with click chemistry to modify the surface of silica nanoparticles with polymers. The possibilities of postfunctionalization of poly(6-azidohexyl methacrylate)-grafted silica nanoparticles with various functional alkynes via click reactions were also demonstrated by Li and Benicewicz.[23] Using Cu-catalyzed click reaction, the modification of polymeric particles with azide- or alkyne-functionalized dyes and macromolecules, i.e., poly(ethylene oxide), was successfully achieved in aqueous and nonaqueous environments.[24−26] Ouadahi et al.[27] reported the synthesis of azide-functionalized polystyrene nanoparticles, which were used as clickable polymeric scaffolds for the grafting of dansyl and fluorescein derivatives through copper(I)-catalyzed azide−alkyne cycloaddition. For localized cell delivery, self-assembled polymeric nanoparticles containing azide groups were modified with targeting alkyne-functionalized ligands by the aqueous Huisgen's 1,3 dipolar cycloaddition reaction, catalyzed by copper sulfate and sodium ascorbate.[28] Magnetic poly(*N*-propargylacrylamide) microspheres were used as the anchor to enable a "click" reaction with an azido-end-functionalized model peptide.[29] The versatility of copper-

Received: February 15, 2012
Revised: March 30, 2012
Published: April 11, 2012

 © 2012 American Chemical Society dx.doi.org/10.1021/ma300312n | *Macromolecules* 2012, 45, 3419−3427

Scheme 1. Schematical Presentation of the Alkyne-Functionalized PBCA/P(BCA-*co*-PCA) and Azide-Functionalized Polyurethane Nanocapsules



catalyzed alkyne–azide coupling (CuAAC) in functionalizing drug-loaded polymer nanoparticles was demonstrated via the modification of surface of acetylene-functionalized nanoprticles with folate, biotin, and gold nanoparticles[30] Using click chemistry, the surface functionalization of poly(*N*-vinylpyrrolidone) capsules with antibodies that are specific to colorectal cancer cells was recently published by Caruso et al.[31]

Poly(alkyl cyanoacrylates) (PACAs) have gained an increased clinical interest mainly due to their biodegradability, low toxicity, and enhancement of the drug intracellular penetrations. In the mid-1960s, cyanoacrylates were widely employed as bioadhesives in surgery and later in the 1980s as the polymeric carriers for delivery of biomolecules.[32−37] However, the attachment of specific target molecules onto the surface of PACAs nanocarriers still remains a big challenge. The most commonly used systems for preparing of the drug-loaded (PACA) particles/capsules is the anionic polymerization initiated by a nucleophilic group. Depending on the used surfactant (or cosurfactant), a certain amount of functional groups might remain on the surface of nanocarriers after polymerization. Recently, Nicolas et al.[38] described the preparation of functionalized PACA-based nanoparticles made from a preformed poly(hexadecyl cyanoacrylate)-*co*-azidopoly(ethylene glycol) cyanoacrylate copolymer. The obtained nanoparticles display azide functionalities at the extremity of the PEG chains, which were further reacted with the model alkynes by click chemistry.

In this work we describe the one-step synthesis of poly(butyl cyanoacrylate-*co*-propargyl cyanoacrylate) (P(BCA/PCA)) and polyurethane (PUR) azide nanocapsules for direct covalent and variable functionalization. Both types of capsules were synthesized in inverse (water-in-oil) miniemulsion through either interfacial anionic polymerization (P(BCA/PCA)) or interfacial polyaddition reaction (PUR azide). The presence of propargyl and azide groups on the surface of P(BCA/PCA) and PUR nanocapsules, respectively, enables to achieve high yields of functionalization using the click chemistry. Different fluorescent markers were attached onto the surface of P(BCA/PCA) and PUR nanocapsules through Cu(I)-catalyzed azide–alkyne cycloaddition (CuAAC) reactions performed under mild and ambient conditions (Scheme 1). Furthermore, in order to avoid any cytotoxic and side effects related to the copper,[39] the concept was extended to the copper-free azide alkyne cycloaddition. In this way, PUR capsules functionalized with any functional group can be obtained; as an example we show here the functionalization with carboxylic groups by using propiolic acid. We believe that the approach disclosed in this paper can be applied to prepare a wide range of hybrid polycyanoacrylate- and polyurethane-based capsules with advanced properties.

EXPERIMENTAL SECTION

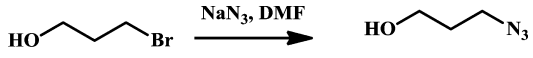
Materials. All chemicals were used as received without further purification. Demineralized water was used throughout the experiments. The monomers *n*-butyl cyanoacrylate and propargyl cyanoacrylate (^{1}H NMR ($CDCl_3$, 400 MHz, δ in ppm): 2.59 (t, J = 2.5 Hz, alkyne), 4.88 (t, J = 2.5 Hz, 2H, =CH_2), 6.72 (s, 1H, vinyl), 7.13 (s, 1H, vinyl) were kindly donated by Henkel AG & KGaA, Duesseldorf, Germany. The oil Miglyol 812N (caprylic/capric triglycerides) was a donation from Sasol, Germany. 2,4-Toluene diisocyanate (TDI, 99%) and cyclohexane (>99.9%) were purchased from Sigma-Aldrich. The oil-soluble block copolymer surfactant poly[(ethylene-*co*-butylene)-*b*-(ethylene oxide)], P(E/B-*b*-EO), consisting of a poly(ethylene-*co*-butylene) block (M_w = 3700 g mol^{-1}) and a poly(ethylene oxide) block (M_w = 3600 g mol^{-1}) was synthesized

dx.doi.org/10.1021/ma300312n | *Macromolecules* 2012, 45, 3419−3427

starting from ω-hydroxypoly(ethylene-*co*-butylene), which was dissolved in toluene, by adding ethylene oxide under the typical conditions of an anionic polymerization.[40] P(E/B-*b*-EO) was vacuum-dried prior to use. The anionic surfactant sodium dodecyl sulfate (SDS, 99%) was purchased from Fluka. The nonionic block copolymer Lutensol AT50 (BASF), which is a poly(ethylene oxide) hexadecyl ether with an EO block length of about 50 units, was used as surfactant. The surfactants Span80 and Tween80 were supplied by Aldrich. Ethanol (Aldrich), dimethylformamide (Aldrich), ethyl acetate (VWR), methylene chloride (<50 ppm water content) (Acros Organics), methanol (Fisher Scientific), dichloromethane (VWR), and chloroform (VWR) were of HPLC grade. Alexa Fluor488 alkyne dye was purchased from Invitrogen molecular probes, and Rhodamine B (90%) was purchased from Aldrich. Sodium azide (98%) was purchased from SERVA. 9-Chloromethylanthracene (97%) was purchased from Riedel de Haen. Dicyclohexylcarbodiimide (DCC), sodium hydrogen carbonate, (dimethylamino)pyridine, ascorbic acid, magnesium sulfate, and sodium chloride were purchased from Aldrich. 1-Bromo-3-propanol (97%), propiolic acid (95%), and 2,2-bis(bromomethyl)-1,3-propanediol were purchased from Acros Organics. PBS buffer was purchased from Invitrogen. The used copper complex $Cu(II)Br_2$/PMDETA was synthesized using a literature procedure.[41]

Synthesis of 1-Azido-3-propanol. 25 g of 1-bromo-3-propanol (180 mmol, 1.0 equiv) was dissolved in 100 mL of dimethylformamide, and 23.4 g of sodium azide (353 mmol, 2.0 equiv) was added. The mixture was heated to 50 °C for 24 h using an oil bath. The formed precipitate was filtered out, and DMF was removed at 60 °C using a rotoevaporator. The resulting liquid was dissolved in 250 mL of ethyl acetate and washed with 200 mL of water and brine each. The organic phase was dried using magnesium sulfate and filtered, and ethyl acetate was distilled out, using a rotoevaporator. 10.1 g (56%, 100 mmol) of a colorless liquid were obtained. ^{1}H NMR ($CDCl_3$, 300 MHz, δ in ppm): 3.70 (m, 2H), 3.41 (t, 2H, ^3J = 3.41 Hz), 1.79 (m, 2H). ^{13}C NMR ($CDCl_3$, 75 MHz, δ in ppm): 60.0, 48.6, 31.6.

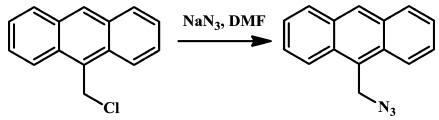
Scheme 2. Synthesis of 1-Azido-3-propanol



Synthesis of 1-Azido-3-propylrhodamine Ester (Rho-N_3). The synthesis was performed using a modified literature procedure[42] (Scheme 3). 5.3 g of Rhodamine B (11 mmol, 1.0 equiv) was dissolved in 100 mL of dry dichloromethane under an argon atmosphere in a flame-dried Schlenk vessel. 1.2 g of 1-azido-3-propanol (12 mmol, 1.1 equiv) and 12 mg of (dimethylamino)pyridine (0.1 mmol, 0.01 equiv) were added, and the solution was cooled to 0 °C in an ice bath. 4.12 g of dicyclohexylcarbodiimide was added, and the solution was stirred and warmed to room temperature over 12 h. The formed white precipitate was filtered out, and 100 mL of dichloromethane (DCM) was added. The organic solution was washed with 2 × 200 mL of saturated $NaHCO_3$ solution and 200 mL of water. The organic phase was dried over magnesium sulfate and filtered, and the solvent was evaporated using a rotoevaporator. The resulting dark violet solid was submitted to column chromatography, using a DCM/methanol (MeOH) mixture (9:1). 4.6 g of a dark violet solid was obtained after removal of the solvent (79%, 8.7 mmol). R_f (DCM/MeOH, 9:1): 0.36. ^{1}H NMR ($CDCl_3$, 300 MHz, δ in ppm): 8.25 (1H, dd, ^4J = 1.37 Hz, ^3J = 7.8 Hz), 7.82−7.69 (m, 4H), 7.28 (dd, 1H, ^4J = 1.3 Hz, ^3J = 7.5 Hz), 7.04 (d, 2H, ^3J = 9.0 Hz), 6.88 (dd, 2H, ^4J = 2.4 Hz, ^3J = 9.2 Hz), 6.78 (d, 2H, ^3J = 2.4 Hz), 4.08 (m, 2H), 3.61 (q, 8H, ^3J = 7.1 Hz), 3.17 (t, 2H, ^3J = 6.7 Hz), 1.71 (m, 2H), 1.29 (t, 12H, ^3J = 7.1 Hz). ^{13}C NMR ($CDCl_3$, 75 MHz, δ in ppm): 165.1, 158.8, 157.9, 155.8, 133.7, 133.4, 131.5, 131.4, 130.7, 130.5, 129.9, 114.5, 113.7, 96.6, 76.8, 63.9, 62.7, 48.9, 48.2, 46.3, 29.4, 28.1, 12.8. ESI-MS: 526 (100, M^+), 527 (25, $[M + H]^+$).

Synthesis of 9-Methylenazidoanthracene (Anth-N_3). The synthesis was performed following a slightly modified procedure

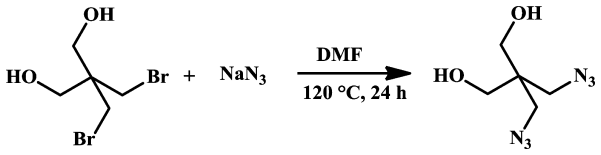
Scheme 4. Synthesis of Anthracene-N_3 (Anth-N_3)



described by Xie et al.[43] (Scheme 4). Briefly, 2.26 g of 9-chloromethylanthracene (10 mmol) was dissolved in 50 mL of dimethylformamide (DMF), and 1.95 g of sodium azide (30 mmol) was added. The solution was heated for 24 h to 50 °C using an oil bath. After the reaction was finished, DMF was evaporated using a rotoevaporator, and the resulting solid was dissolved in 100 mL of chloroform and washed twice with 150 mL of water. The organic phase was dried over magnesium sulfate and filtered, and the solvent was evaporated. The resulting solid was recrystallized from ethanol, and the solution was cooled to 0 °C using an ice bath, where it crystallized to yellow needlelike structures. After drying the substance in vacuum, 1.5 g of yellow solid was obtained (64%). ^{1}H NMR ($CDCl_3$, 300 MHz, δ in ppm): 8.49 (s, 1H), 8.28 (dd, 2H, ^3J = 9.0 Hz), 8.03 (d, 2H, ^3J = 9.0 Hz), 7.58 (m, 2H), 7.50 (m, 2H), 5.31 (s, 2H). ^{13}C NMR ($CDCl_3$, 75 MHz, δ in ppm): 131.6, 130.9, 129.5, 129.2, 127.1, 125.9, 125.4, 123.7, 46.6. IR (ν in cm^{-1}): 3446 (b), 2096 (s), 2055 (s), 1228 (s), 858 (s), 738 (s). FD-MS: 233.3 M^+(100), 234.4 $(M + H)^+$ (22).

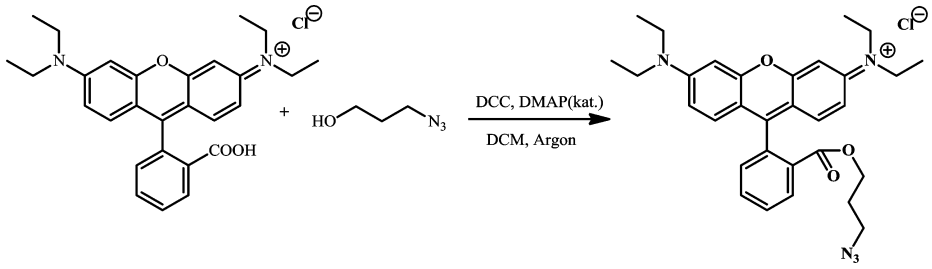
Synthesis of 2,2-Bis(azidomethyl)-1,3-propanediol (BAP). BAP was synthesized using a modified literature procedure[44] (Scheme

Scheme 5. Synthesis of 2,2-Bis(azidomethyl)-1,3-propanediol (BAP)



5). 15 g of 2,2-bis(bromomethyl)-1,3-propanediol (57.3 mmol) was dissolved in 200 mL of dimethylformamide, and 15 g of sodium azide

Scheme 3. Synthesis of 1-Azido-3-propylrhodamine Ester (Rho-N_3)



dx.doi.org/10.1021/ma300312n | *Macromolecules* 2012, 45, 3419−3427

was dispersed in the solution. The mixture was heated for 24 h at 120 °C and formed sodium bromide after cooling. The excess sodium azide was filtered out. DMF was evaporated using a rotoevaporator, and the resulting liquid was dissolved in 200 mL of ethyl acetate. The organic phase was washed twice with 200 mL of water and dried over magnesium sulfate. After filtration the solvent was evaporated by a rotoevaporator. After drying in an oil pump vacuum for 2 days, the obtained colorless oil solidified into white crystals upon standing. 10.1 g of a white solid were obtained (95%). ^{1}H NMR ($CDCl_3$, 300 MHz, δ in ppm): 4.74 (t, 2H, ^3J = 4.9 Hz), 3.28 (m, 8H). ^{13}C NMR ($CDCl_3$, 75 MHz, δ in ppm): 59.8, 51.1, 45.5.

Synthesis of PBCA/P(BCA-*co*-PCA) Nanocapsules. The PBCA/P(BCA-*co*-PCA) nanocapsules were prepared through anionic polymerization at the inverse (water-in-oil) miniemulsion droplets interface using the previously published procedure with slight changes.[37] The used amounts of both monomers, namely *n*-butyl cyanoacrylate (BCA) and propargyl cyanoacrylate (PCA), are shown in Table 1. The miniemulsions were stabilized with a mixture of surfactants (Span80 and Tween80). The continuous phase (7.6 g) consisted of 0.152 g of Span80, 0.228 g of Tween80, and Miglyol 812N as oil. Different amounts of PBS buffer (see Table 1) were used as an aqueous phase. The aqueous phase was slowly added to the oil phase under stirring and ice cooling. Thereafter, stirring was continued for half an hour at 4 °C. Afterward, the samples were homogenized using a Branson 450 W sonifier with an inverse cup tip (60 s, 5 s sonication, 10 s pause, 50% amplitude) at 4 °C. Shortly after the homogenization, an earlier prepared mixture of BCA/chloroform or BCA/PCA/chloroform was added dropwise to the miniemulsion under gentle stirring, and the formation of polymer around the aqueous droplets took place over 4 h at 25 °C. The monomer(s) to chloroform volume ratio corresponds to 100 μL/300 μL, and it was kept constant for all experiments. After polymerization the obtained nanocapsules were separated from the oil phase by centrifugation (Sigma, 3k-30, RCF 17968, 20 min), washed in ethanol, and used for click reaction experiments.

Table 1. Characterization Data for the Poly(BCA-*co*-PCA) Capsules

sample	BCA/PCA, mmol	PBS buffer, g	diam, nm/ (std dev, %)	mol wt (M_w), g/mol
GB-cc-1	0.94/–	1	305/(28)	37 218
GB-cc-2	0.70/0.24	1	280/(24)	34 789
GB-cc-3	0.47/0.47	1	235/(33)	19 547
GB-cc-4	0.24/0.70	1	230/(32)	23 049
GB-cc-5	0.94/–	2	310/(27)	98 146
GB-cc-6	0.70/0.24	2	350/(30)	54 916
GB-cc-7	0.47/0.47	2	340/(27)	37 690
GB-cc-8	0.24/0.70	2	340/(28)	30 408

Synthesis of Azide-Functionalized Polyurethane Nanocapsules. The azide-functionalized polyurethane nanocapsules were prepared through polyaddition reaction at the inverse (water-in-oil) miniemulsion droplets interface using the previously published procedure.[13,45] The formulation process is shown in Scheme 6. Initially, 100 mg of 2,2-bis(azidomethyl)-1,3-propanediol was mixed with 30 mg of sodium chloride and 1.3 g of demineralized water. Then, 100 mg of P(E/B-*b*-EO) was dissolved in 7.5 g of cyclohexane at 50 °C using an ultrasonication for 180 s with a 90% amplitude in a pulse regime (20 s sonication, 10 s pause) bath. Both solutions were mixed together, stirred over 1 h at 25 °C, and ultrasonicated using a Branson W450-Digital sonifier (1/2 in. tip) under ice cooling in order to prevent evaporation of the solvent. A solution consisting of 5 g of cyclohexane, 30 mg of P(E/B-*b*-EO), and 100 of mg TDI was added dropwise over 5 min to the earlier prepared mixture. The reaction was carried out overnight at 25 °C. After synthesis the nanocapsules were washed twice with cyclohexane. The azide-functionalized polyurethane nanocapsules were centrifuged, the supernatant was removed, and 2.0 g of the nanocapsules was redispersed either in 10.0 g of SDS solution (0.3 wt %) or in 10.0 g of Lutensol AT50 solution (0.3 wt %). Then, the samples were redispersed for 20 min in a sonication bath (power 50%, 25 kHz) and 24 h dialyzed (MWCO 12 000 g mol^{-1}) against demineralized water in order to remove residues of the surfactant. Afterward, the obtained azide-functionalized polyurethane nanocapsules were subjected to the click reaction experiments.

Click Reaction of Rho-N_3 and Anth-N_3 to P(BCA-*co*-PCA) Nanocapsules. The click reaction between either the azide end group-functionalized rhodamine (Rho-N_3) or anthracene (Anth-N_3) and P(BCA-*co*-PCA) nanocapsules was performed in the following way: For the Rho-N_3 click reaction, either PBCA or P(BCA-*co*-PCA) nanocapsules (500 μL, solid content 1 wt %) were redispersed in a Rho-N_3 (12.4 mg, 0.0235 mmol), ethanol, Tween80 solution (0.6 wt %). The obtained dispersion and the Cu(II)Br_2/PMDETA (0.94 mg, 0.0024 mmol) were mixed together and put into an argon-flushed Schlenk tube. The dispersion was degassed by argon bubbling for 15 min. The click reaction was initiated by injection of 1 equiv (100 μL) of ascorbic acid (0.03 M in water) into the nanocapsules dispersion under an argon atmosphere. The mixture was stirred for 24 h at 23 °C. After the clicking procedure the nanocapsules were cleaned four times by repetitive centrifugation/redispersion in ethanol in order to remove the residuals of the clicking reagents and the nonreacted Rho-N3. The efficiency of click reaction was determined by fluorescence spectroscopy, measuring the fluorescence intensity of the PBCA and P(BCA-*co*-PCA) freeze-dried and dissolved in THF nanocapsules.

For the click reaction with Anth-N_3, 5.5 mg (0.0235 mmol) of Anth-N_3 was used, and the reaction with PBCA and P(BCA-*co*-PCA) nanocapsules was performed in the same manner as described above.

Clicking of Alkyne Dye to Azide-Functionalized Polyurethane Nanocapsules. For the alkyne dye click reaction, 2 mL (solid content 1 wt %) of the azide-functionalized polyurethane nanocapsules redispersed in Lutensol AT50, the alkyne dye (0.5 mg, 6.46 × 10^{-4} mmol), and Cu(II)Br_2/PMDETA (0.94 mg, 0.0024 mmol) were put into an argon-flushed Schlenk tube and degassed by argon bubbling through the dispersion for 15 min. The click reaction was initiated by injection of 1 equiv (100 μL) of ascorbic acid (0.03 M in water) into the nanocapsules dispersion under an argon atmosphere. The mixture was stirred for 48 h at 25 °C. After the click reaction the nanocapsules were cleaned four times by repetitive centrifugation in order to remove the residuals of the reagents. The supernatant was analyzed for the presence of nonbonded residual dye.

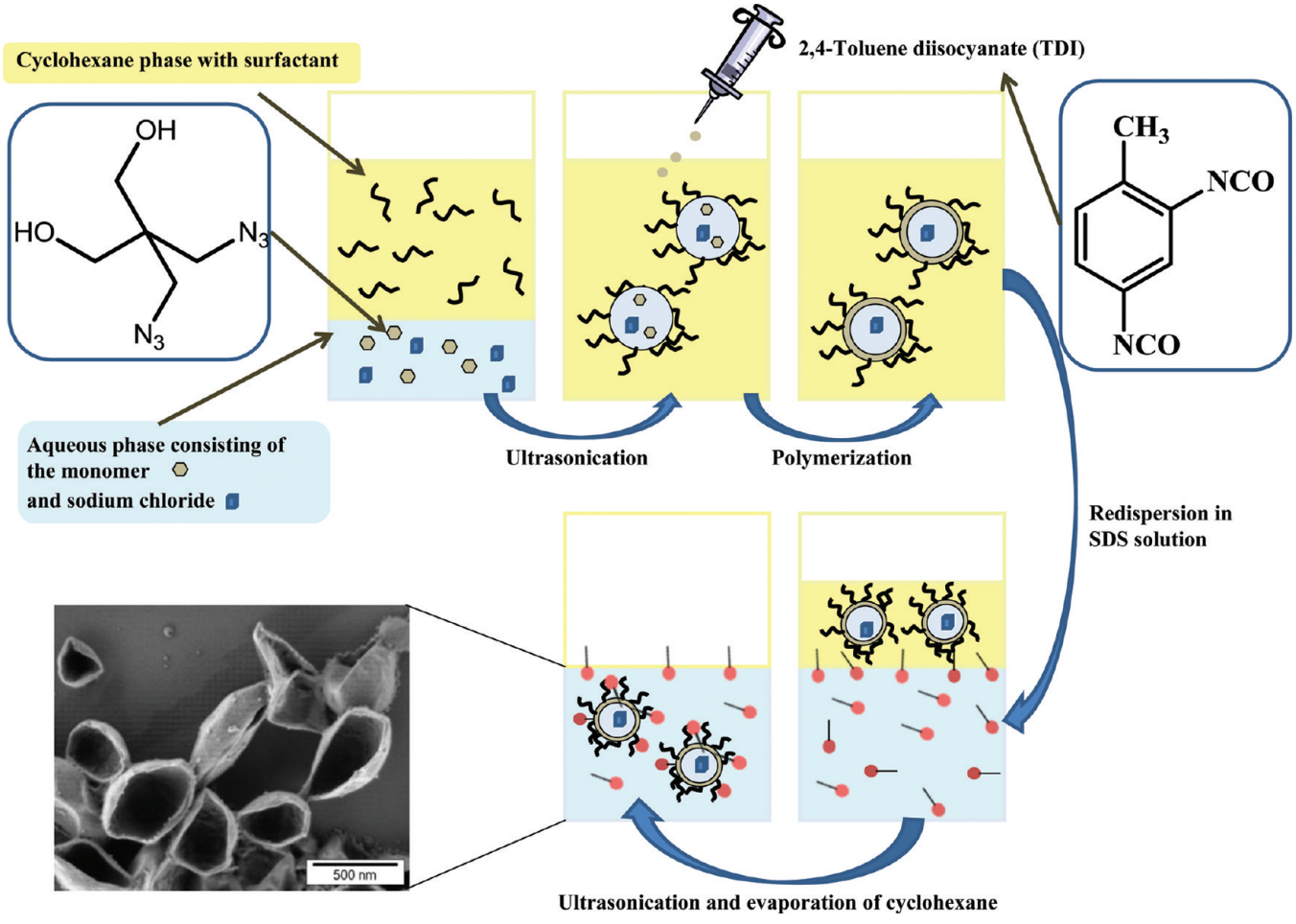
Cu-Free Reaction between Propiolic Acid and Azide-Functionalized Polyurethane Nanocapsules. For the propiolic acid click reaction, 111.5 mg (100 μL, 0.166 mmol) of propiolic acid was added to 5.0 mL (solid content 1 wt %) of azide-functionalized polyurethane nanocapsules redispersed in SDS solution. The mixture was stirred for 48 h at 25 °C. After the click reaction the nanocapsules were dialyzed (MWCO 12 000 g mol^{-1}) against demineralized water for 2 days in order to remove any residuals of the nonreacted propiolic acid.

Investigation of Cu-Free Reaction Kinetics between Propiolic Acid and Azide Monomer in Solution. 100 mg of 2,2-bis(azidomethyl)-1,3-propanediol (0.054 mmol, 1.0 equiv) was dissolved in 0.7 mL of d_6-DMSO and filled into a NMR tube. The reaction was started by adding 72.5 mg of propiolic acid (65 μL, 0.108 mmol, 2.0 equiv). After defined periods of time the NMR spectra were recorded.

Characterization. The average size and the size distribution of the nanocapsules were measured by means of dynamic light scattering (DLS) at 20 °C using a PSS Nicomp Particle Sizer 380 (Nicomp Particle Sizing Systems) equipped with a detector for a scattering angle of 90°. The zeta potential of the nanocapsules was measured in 10^{-3} M potassium chloride solution with a Zeta Nanosizer (Malvern Instruments, U.K.) at 20 °C. Scanning electron microscopy (SEM) images were recorded by using a field emission microscope (LEO (Zeiss) 1530 Gemini, Oberkochen, Germany) working at an acceleration voltage of 170 V. The samples were prepared by diluting the capsule dispersion in cyclohexane or demineralized water (in case of the redispersed samples) to about of 0.01% solid content. Then, one

dx.doi.org/10.1021/ma300312n | Macromolecules 2012, 45, 3419–3427

Scheme 6. Synthesis of Azide-Functionalized Polyurethane Nanocapsules and Their Subsequent Redispersion in the Aqueous Phase



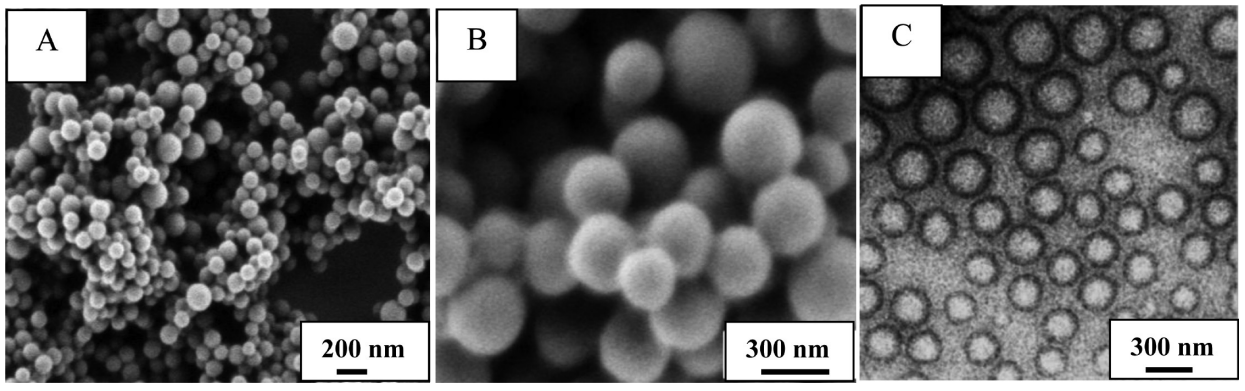


Figure 1. (A, B) SEM images of redispersed PBCA (sample GB-cc-5) and P(BCA-*co*-PCA) (sampleGB-cc-8) nanocapsules, respectively. (C) TEM image of P(BCA-*co*-PCA) (sampleGB-cc-7) nanocapsules. Dark circles correspond to the polymeric shell.

droplet of the sample was placed onto a silica wafer and dried under ambient conditions overnight. The solid content of the capsule dispersion was measured gravimetrically. The analysis of the polymer was performed by FTIR measurements. The sample powder was obtained by freeze-drying the capsule dispersion for 48 h at −60 °C under reduced pressure. Then 3 mg of the dry sample was pressed with KBr to form a pellet, and a spectrum between 4000 and 400 cm^{-1} was recorded by using the IFS 113v Bruker spectrometer. Size exclusion chromatography (SEC) experiments were performed at 20 °C using a Waters WISP 717 autosampler, a Waters 515 HPLC pump, and a PSS-SDV 300 × 8 mm column with a particle size of 10 mm and a pore size of 500, 10^5, and 10^6 Å. A RI detector from SOMA and a UV detector from ERC were used for detection. THF was used as a solvent. For nuclear magnetic resonance (NMR) analysis ^{1}H NMR spectra were recorded on a Bruker Avance 300 spectrometer operating with a 300 MHz frequency. The polymers were dissolved in an appropriate solvent. The spectra were calibrated against the solvent peak. The amount of carboxylic groups was calculated from the results of the titration experiments performed on a particle charge detector (Mütek GmbH, Germany) in combination with a Titrino automatic titrator (Metrohm AG, Switzerland). The carboxylic groups were titrated against the positively charged polycation poly-

dx.doi.org/10.1021/ma300312n | *Macromolecules* 2012, 45, 3419−3427

(diallyldimethylammonium chloride) (poly-DADMAC). The titration was performed using 10 mL of the dispersion with a solid content of 1 g/L. The amount of groups per nm^2 was calculated from the consumed volume of the polyelectrolyte solution. The fluorescence intensities were measured using a plate reader (Infinite M1000, Tecan, Switzerland). Mass spectroscopy and ESI mass spectra were obtained from a Q-ToF Ultima 3 spectrometer with LockSpray interface from Micromass (Waters). The sample was dissolved in methanol with a concentration of about 1 mg/mL.

RESULTS AND DISCUSSION

Synthesis of PBCA/P(BCA-*co*-PCA) Nanocapsules. PBCA nanocapsules containing PBS buffer as aqueous core were synthesized via anionic polymerization of BCA or a mixture of BCA and PCA at the water/oil miniemulsion droplets' interface. The oil phase consists of Miglyol 812N (density 0.95 g cm^{-3}, viscosity 30 mPa·s) and a mixture of surfactants Span80 and Tween80. Different amounts of monomers BCA, BCA/PCA (in total 0.94 mmol), and dispersed phase, i.e., PBS buffer solution, were used in order to study their influence on the physicochemical parameters of the obtained capsules (Table 1). No precipitation, coagulation, or flocculation of the nanocapsules was observed throughout the experiments. After the synthesis and redispersion of the nanocapsules in an aqueous medium they were analyzed in terms of average size, size distribution, morphology, and molecular weight of the formed polymer. The obtained results are summarized in Table 1. SEM studies (Figure 1A,B) reveal that the obtained capsules are in a size range between 70 and 150 nm. Moreover, the capsules shell is quite stable and did not lead to the collapse of the capsules upon drying. Transmission electron images clearly identify the capsule (core−shell) morphology (Figure 1C).

The size of the capsules measured by DLS is slightly higher than that measured by microscopy (Table 1). The hydrodynamic size of the capsules was in the range between 235 and 350 nm with a size distribution between 24% and 33%, which is in the range of an inverse miniemulsion system. When using 1.0 g of PBS buffer, a decrease in the initial BCA/PCA monomer ratio results in the reduction of the capsule size. The size of nanocapsules remained approximately the same when using 2.0 g of PBS buffer as dispersed phase. The molecular weight of the obtained (co)polymer decreases with the decrease in the initial BCA/PCA monomer ratio. The capsules with the highest molecular weight were obtained from pure BCA and using 2.0 g of PBS as dispersed phase.

The chemical composition of PBCA and P(BCA-*co*-PCA) nanocapsules was studied by FT-IR spectroscopy. The obtained spectra are shown in Figure 2.

The region between 3000 and 1100 cm^{-1} is known as the functional group region. In all spectra following bands were found: 2900 cm^{-1} (CH_2 group), at 2250 cm^{-1} (−CN group), 1730 cm^{-1} (C═O), and 1100 cm^{-1} (−C−O group). In the FT-IR spectra of P(BCA-*co*-PCA) nanocapsules, an additional band at 2130 cm^{-1}, which is characteristic for the alkyne bond from the PCA comonomer, could be seen.

Click Reaction of Rho-N_3 and Anth-N_3 to P(BCA-*co*-PCA) Nanocapsules. Although the FT-IR studies confirm that the P(BCA-*co*-PCA) capsules contain the alkyne bond, it is still important to know how many of these groups are able to participate in the click reaction. Therefore, click reactions of Rho-N_3 and Anth-N_3 to P(BCA-*co*-PCA) nanocapsules were performed for quantitative determination of the surface alkyne bonds as well as to show the simplicity of the described click procedure.

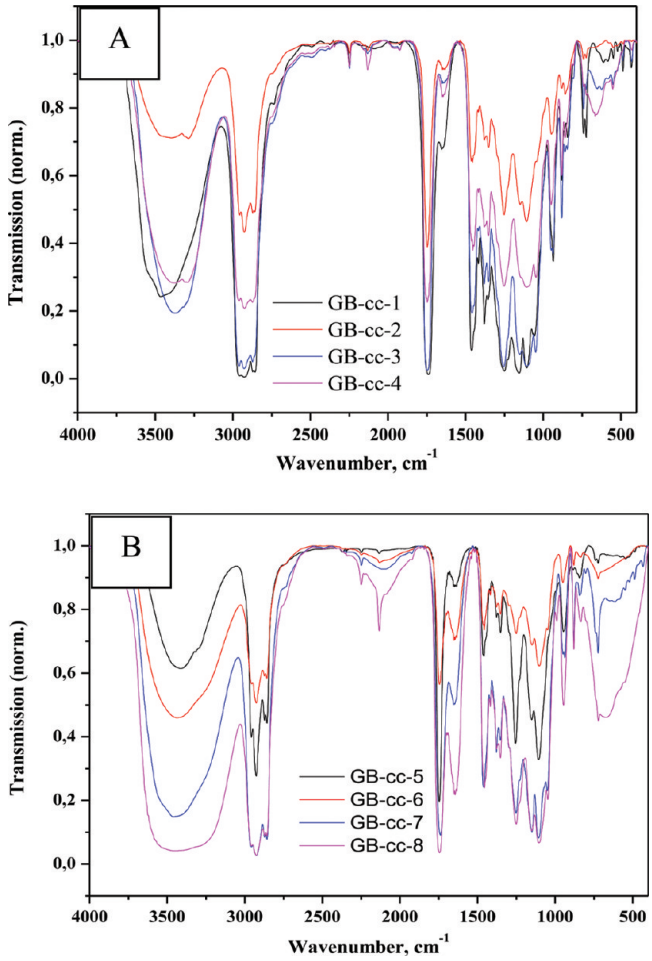


Figure 2. FTIR spectra of PBCA and P(BCA-*co*-PCA) nanocapsules synthesized using 1.0 g (A) or 2.0 g (B) of PBS buffer as dispersed phase.

The Anth-N_3 click reaction was performed to study the formation of the covalent bond between the azide group of the anthracene and the alkyne groups of the nanocapsules' surface. Because of the enhancement of the fluorescent intensity the formation of a covalent attachment of the dye was proved by a fluorogenic reaction. The fluorescence of anthracene azide is quenched due to a photoinduced electron transfer (PET) process which is not the case in the formation the triazole, resulting in a 48-fold increase of quantum yield.[43] From the fluorescent enhancement Ω (eq 1), the amount of reacted azide groups (eq 2) can be calculated. The obtained values are summarized in Table 2.

$$\Omega = \frac{I}{I_0} \tag{1}$$

$$n_{\text{react-Azido}} = \left(\frac{\Omega}{48}\right) n_{(\text{Anth-N}_3)} \tag{2}$$

The introduction of PCA as a comonomer results in the increase of fluorescence enhancement value. The amount of covalently attached Anth-N_3 onto the capsule surface is slightly higher when 2 g of the disperse phase was used, and it increases proportionally to the introduced PCA amount (Figure 3 and Table 2).

dx.doi.org/10.1021/ma300312n | *Macromolecules* 2012, 45, 3419−3427

Table 2. Results of Fluorescent Measurements Obtained After Click Reaction with Anth-N_3 and Rho-N_3

sample	Ω	$n_{reac\text{-}Azido}$, mmol	amt of alkyne groups per capsule/per nm^2 [a]	
			Anth-N_3	Rho-N_3
GB-cc-1	1.0			
GB-cc-2	2.4	0.001 17	3.44×10^5/1.4	4.18×10^5/1.7
GB-cc-3	3.4	0.001 66	4.84×10^5/2.8	6.05×10^5/3.5
GB-cc-4	4.4	0.002 15	6.14×10^5/3.7	7.14×10^5/4.3
GB-cc-5	1.1			
GB-cc-6	4.7	0.002 30	5.78×10^5/1.5	7.70×10^5/2.0
GB-cc-7	5.9	0.002 88	8.33×10^5/2.3	11.94×10^5/3.3
GB-cc-8	7.9	0.003 86	11.58×10^5/3.2	14.84×10^5/4.1

[a]The values are calculated from the fluorescence measurements data, obtained after click reaction with Rho-N_3 or Anth-N_3.

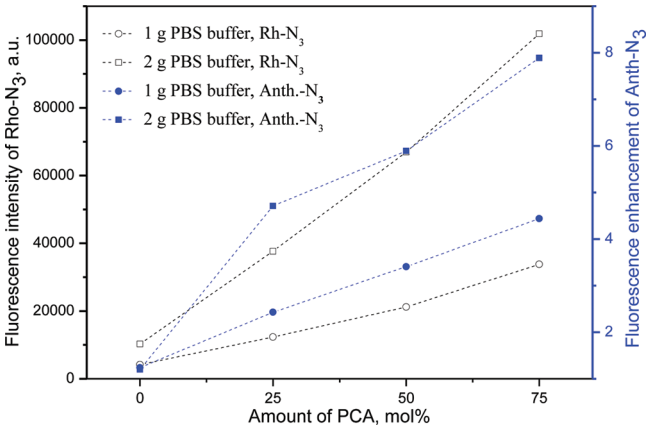


Figure 3. Fluorescence intensity of Rho-N_3 (open symbols) and fluorescence enhancement of Anth-N_3 (solid symbols) after click reaction.

In further experiments, the fluorescent dye rhodamine azide was covalently attached to the surface of P(BCA/PCA) capsules to study the influence of the used amounts of BCA/PCA on the resulting numbers of alkyne groups on the nanocapsules' surface. After the click reaction, as described in the Experimental Section, the PBCA and P(BCA-*co*-PCA) nanocapsules were subjected to the fluorescence measurements. The results are shown in Figure 3 (samples synthesized using 1.0 and 2.0 g of PBS buffer).

A steeper slope was obtained when 2.0 g of PBS buffer was used as a disperse phase. Assuming that the density of alkyne groups remains constant for a given amount of PCA, the number of surface groups depends on the diameter of the nanocapsules. Using 1.0 g of PBS buffer, the diameter decreases by increasing amount of PCA, while remaining constant when 2.0 g of PBS buffer was used. The graphs obtained from the experiments of the click reaction between Rho-N_3 and the alkyne-functionalized P(BCA-*co*-PCA) nanocapsules show the same shape like the graphs obtained from the experiments of the click reaction between Anth-N_3 and the alkyne-functionalized P(BCA-*co*-PCA) nanocapsules. From the fluorescent data, the number of alkyne groups per capsule and nm^2 was calculated (Table 2). The values obtained from the reaction with Rho-N_3 are slightly higher as compared to those with Anth-N_3. This could be explained by the presence of some Rho-N_3 molecules that are strongly adsorbed to the capsule's surface (not covalently bonded) and were not removed by the centrifugation.

Synthesis of the Azide-Functionalized Polyurethane Nanocapsules. An interfacial polyaddition reaction using the inverse miniemulsion technique was employed to synthesize the azide-functionalized polyurethane nanocapsules. The reaction between OH groups from 2,2-bis(azidomethyl)-1,3-propanediol and NCO groups from TDI occurs at the water-in-oil droplets' interface and results in the formation of a cross-linked polymeric shell. The formulation process is illustrated in Scheme 6. After redispersion of the capsules in the aqueous phase, some amounts of azide groups are present on the surface and could be used for further surface modification through click chemistry.

The azide-functionalized polyurethane nanocapsules were characterized in terms of size, size distribution (Table 3), and morphology. SEM studies reveal "core−shell" morphology for the obtained capsules. The collapses of the nanocapsules' shell is due to the drying effects and electron beam. The collapse of the capsules was not observed in the case of PBCA and P(BCA-*co*-PCA) capsules (see Figure 1), which might be due to the formation of a thicker and more stable poly(cyanoacrylate) shell.

Table 3. Characterization Data for the Azide-Functionalized Polyurethane Nanocapsules before and after Click Reaction (BAP to TDI Molar Ratio Was 0.9 to 1.0)

sample	diam, nm/STD, %	zeta potential, mV	amt of alkyne dye per capsule/per nm^2	amt of carboxylic groups per capsule/per nm^2
GB-MS-100	285/29	−26		
GB-MS-100-PA	300/34	−40		2.22×10^5/0.78
GB-MS-100-Alexa	310/29	−15	2.15×10^5/0.71	2.02×10^5/0.67

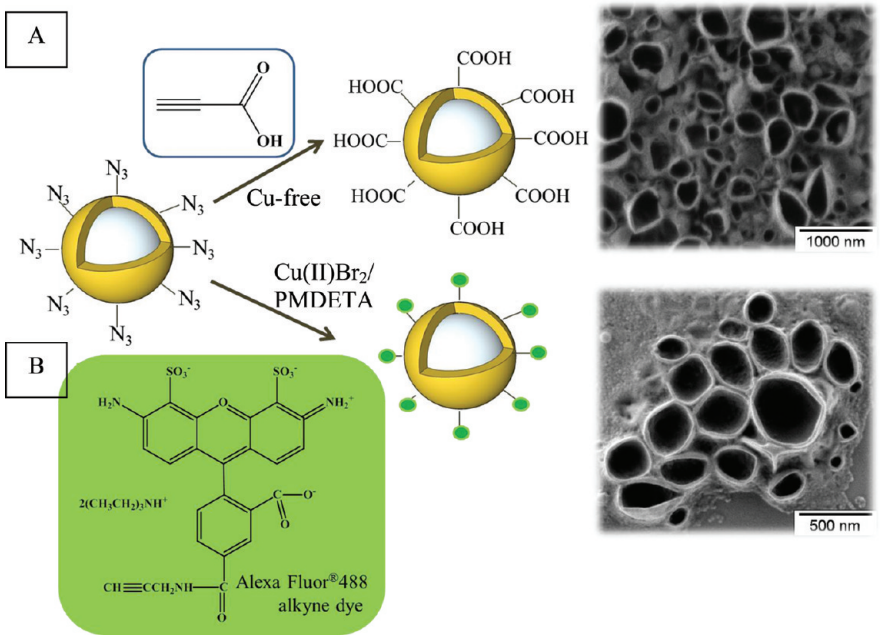
Click Reaction of Propiolic Acid (Cu-Free Reaction) and of an Alkyne Dye to Azide-Functionalized Polyurethane Nanocapsules. Two different click reactions between the azide-functionalized polyurethane nanocapsules and either propiolic acid or alkyne fluorescent dye were performed to show the versatility in the functionalization (Scheme 7).

In the first reaction, azide-functionalized polyurethane nanocapsules were functionalized with propiolic acid (sample GB-MS-100-PA) by Cu-free click chemistry. The reaction was performed under normal ambient conditions, without additional heating and without using a catalyst, thus making the system interesting for various applications, where the presence of Cu residues affects the properties of the material. The reaction conditions can be applied for many other alkyne-functionalized molecules, resulting in the formation of nanocapsules with variable functionalities.

In the second click reaction, fluorescent alkyne dye was reacted with azide-functionalized polyurethane nanocapsules (sample GB-MS-100-Alexa) in order to demonstrate the possibility of fluorescent labeling of nanocapsules that could be used for trafficking. Before addition of CuAAC, the fluorescent signal (λ_{ex} = 488 nm, λ_{em} = 520 nm) was measured and set as a reference signal. After click reaction the nanocapsules were centrifuged and the fluorescent signal of the supernatant was measured and compared to the reference.

dx.doi.org/10.1021/ma300312n | *Macromolecules* 2012, 45, 3419−3427

Scheme 7. Surface Click Reaction between Azide-Functionalized Polyurethane Nanocapsules and (A) Propiolic Acid (Cu-Free Reaction) or (B) Alkyne Fluorescent Dye



The obtained results reveal that about 94% of the alkyne dye was attached to the nanocapsules surface. The calculated amount of alkyne dye molecules per capsule and per nm^2 are given in Table 3.

The average diameter of capsules before click reaction was about 285 nm. A slight increase of size and size distribution was observed after the click reaction, confirming the presence of "clicked" molecules on the surface. Both clicking procedures did not influence the capsule's morphology as it could be seen from the SEM images of nanocapsules made after the reactions (Scheme 7). The zeta potential values after click reaction are different from the nonfunctionalized capsules. The decrease (sample GB-MS-100-PA) or increase (sample GB-MS-100-Alexa) of value mainly depends on the charge of molecules that were used for the click reaction. The amount of carboxylic groups that are present on the nanocapsules surface was calculated from the particle charge detector (PCD) measurements. The determined amount of carboxylic groups was slightly higher when the surface of capsules was functionalized with the propiolic acid.

Investigation of the Cu-Free Reaction Kinetics between Propiolic Acid and Azide Monomer. The reaction kinetics between the propiolic acid and the azide monomer (2,2-bis(azidomethyl)-1,3-propanediol) was studied by NMR spectroscopy in DMSO. The results are presented in Figure 4.

It can be seen that the characteristic peak from the used monomers (3.28 ppm) decreases, and the new peaks corresponding to triazole ring evolve. Furthermore, two new signals between 8.45 and 8.55 ppm were observed. These are originated from the proton of the C−C double bound of the triazole ring. The reaction proceeded smoothly under ambient conditions within 48 h. A 1,4-isomer as well as an 1,5-isomer was found.

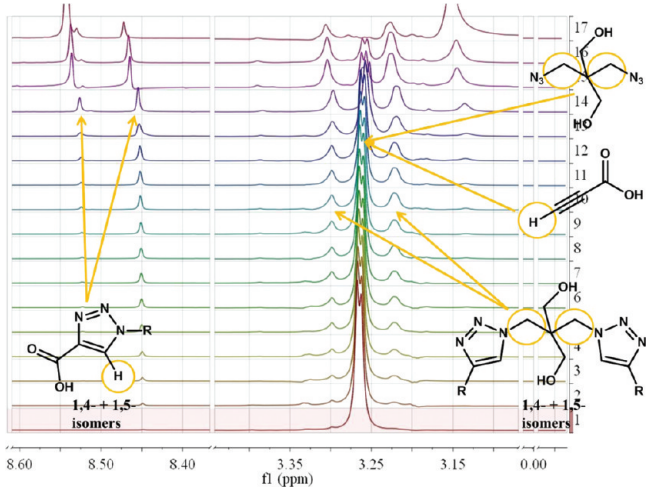


Figure 4. ^{1}H NMR spectra in d_6-DMSO of the Cu-free click reaction between 2,2-bis(azidomethyl)-1,3-propanediol and propiolic acid after certain time periods.

CONCLUSION

In this work, we have demonstrate for the first time the ability to prepare polycyanoacrylate- and polyurethane-based nanocapsules with several types of surface functionalization, while utilizing different Cu(I)-catalyzed azide alkyne cycloaddition (CuAAC) reactions as well as in the absence of copper. In the case of polycyanoacrylate-based capsules, the density of functionalization can be adjusted by using different amounts of propargyl cyanoacrylate comonomer. The results of click reaction between nanocapsules and anthracene azide reveal that the amount of surface available propargyl groups increases by a factor of 0.65 as compared to the introduced amount of propargyl cyanoacrylate. Click reaction performed on the surface of polyurethane azide nanocapsules with copper catalysis (alkyne dye) or under copper-free conditions (propiolic acid) results in similar functionalization density

dx.doi.org/10.1021/ma300312n | Macromolecules 2012, 45, 3419−3427

(0.70 vs 0.78 groups per nm^2), thus making the described copper-free reaction promising for the biological applications. The proposed concept for surface functionalization of polycyanoacrylate- and polyurethane-based nanocapsules through click reactions could be extended to many others alkyne or azide molecules, thus leading to the formation of novel materials for diverse applications.

AUTHOR INFORMATION

Corresponding Author

*E-mail musyanovych@mpip-mainz.mpg.de, Tel +49(0)6131 379-248, Fax +49(0)6131 379-100.

Notes

The authors declare no competing financial interest.

ACKNOWLEDGMENTS

We thank Elke Muth, Gunnar Glasser, and Christoph Sieber for their help in FTIR, TEM, and SEM measurements. We also thank Dr. Andreas Taden (Henkel KGaA, Düsseldorf, Germany) for his assistance in providing the propargyl cyanoacrylate monomer.

REFERENCES

(1) Gratton, S. E. A.; Ropp, P. A.; Pohlhaus, P. D.; Luft, J. C.; Madden, V. J.; Napier, M. E.; DeSimone, J. M. *Proc. Natl. Acad. Sci. U. S. A.* **2008**, *105*, 11613−11618.

(2) Cortez, C.; Tomaskovic-Crook, E.; Johnston, A. P. R.; Scott, A. M.; Nice, E. C.; Heath, J. K.; Caruso, F. *ACS Nano* **2007**, *1*, 93−102.

(3) Zauner, W.; Farrow, N. A.; Haines, A. M. R. *J. Controlled Release* **2001**, *71*, 39−51.

(4) Musyanovych, A.; Dausend, J.; Dass, M.; Walther, P.; Mailänder, V.; Landfester, K. *Acta Biomater.* **2011**, *7*, 4160−4168.

(5) Zhang, L.; Gu, F. X.; Chan, J. M.; Wang, A. Z.; Langer, R. S.; Farokhzad, O. C. *Clin. Pharmacol. Ther.* **2008**, *83*, 761−769.

(6) Zhang, S.; Uludağ, H. *Pharm. Res.* **2009**, *26*, 1561−1580.

(7) Jain, R. K.; Stylianopoulos, T. *Nat. Rev. Clin. Oncol.* **2010**, *7*, 653−664.

(8) Petros, R. A.; DeSimone, J. M. *Nat. Rev. Drug Discovery* **2010**, *9*, 615−627.

(9) Caruso, F.; Caruso, R. A.; Möhwald, H. *Science* **1998**, *282*, 1111−1114.

(10) Dowding, P. J.; Atkin, R.; Vincent, B.; Bouillot, P. *Langmuir* **2004**, *20*, 11374−11379.

(11) Huang, C.-J.; Chang, F.-C. *Macromolecules* **2009**, *42*, 5155−5166.

(12) Tiarks, F.; Landfester, K.; Antonietti, M. *Langmuir* **2001**, *17*, 908−917.

(13) Crespy, D.; Stark, M.; Hoffmann-Richter, C.; Ziener, U.; Landfester, K. *Macromolecules* **2007**, *40*, 3122−3135.

(14) Das, M.; Mardyani, S.; Chan, W. C. W.; Kumacheva, E. *Adv. Mater.* **2006**, *18*, 80−83.

(15) Ramos, J.; Martin-Molina, A.; Sanz-Izquierdo, M. P.; Rus, A.; Borque, L.; Hidalgo-Alvarez, R.; Galisteo-Gonzalez, F.; Forcada, J. *J. Polym. Sci., Part A: Polym. Chem.* **2003**, *41*, 2404−2411.

(16) Yang, X.; Grailer, J. J.; Rowland, I. J.; Javadi, A.; Hurley, S. A.; Steeber, D. A.; Gong, S. *Biomaterials* **2010**, *31*, 9065−9073.

(17) Kolb, H. C.; Finn, M. G.; Sharpless, K. B. *Angew. Chem., Int. Ed.* **2001**, *40*, 2004−2021.

(18) Rostovtsev, V. V.; Green, L. G.; Fokin, V. V.; Sharpless, K. B. *Angew. Chem., Int. Ed.* **2002**, *41*, 2596−2599.

(19) Tornøe, C. W.; Christensen, C.; Meldal, M. *J. Org. Chem.* **2002**, *67*, 3057−3064.

(20) Binder, W. H.; Sachsenhofer, R. *Macromol. Rapid Commun.* **2008**, *29*, 952−981.

(21) Nandivada, H.; Jiang, X.; Lahann, J. *Adv. Mater.* **2007**, *19*, 2197−2208.

(22) Ranjan, R.; Brittain, W. J. *Macromolecules* **2007**, *40*, 6217−6223.

(23) Li, Y.; Benicewicz, B. C. *Macromolecules* **2008**, *41*, 7986−7992.

(24) Evans, C. E.; Lovell, P. A. *Chem. Commun.* **2009**, *17*, 2305−2307.

(25) Breed, D. R.; Thibault, R.; Xie, F.; Wang, Q.; Hawker, C. J.; Pine, D. J. *Langmuir* **2009**, *25*, 4370−4376.

(26) Haschick, R.; Klapper, M.; Wagener, K. B.; Müllen, K. *Macromol. Chem. Phys.* **2010**, *211*, 2547−2554.

(27) Ouadahi, K.; Allard, E.; Oberleitner, B.; Larpent, C. *J. Polym. Sci., Part A: Polym. Chem.* **2012**, *50*, 314−328.

(28) Lu, J.; Shi, M.; Shoichet, M. S. *Bioconjugate Chem.* **2009**, *20*, 87−94.

(29) Macková, H.; Proks, V.; Horák, D.; Kučka, J.; Trchová, M. *J. Polym. Sci., Part A: Polym. Chem.* **2011**, *49*, 4820−4829.

(30) Krovi, S. A.; Smith, D.; Nguyen, S. T. *Chem. Commun.* **2010**, *46*, 5277−5279.

(31) Kamphuis, M. M. J.; Johnston, A. P. R.; Such, G. K.; Dam, H. H.; Evans, R. A.; Scott, A. M.; Nice, E. C.; Heath, J. K.; Caruso, F. *J. Am. Chem. Soc.* **2010**, *132*, 15881−15883.

(32) Couvreur, P.; Roblot-Treupel, L.; Poupon, M. F.; Brasseur, F.; Puisieux, F. *Adv. Drug Delivery Rev.* **1990**, *5*, 209−230.

(33) Chouinard, F.; Kan, F. W. K.; Leroux, J.-C.; Foucher, C.; Lenaerts, V. *Int. J. Pharm.* **1991**, *72*, 211−217.

(34) Miyazaki, S.; Takahashi, A.; Kubo, W.; Bachynsky, J.; Löbenberg, R. *J. Pharm. Pharm. Sci.* **2003**, *6*, 238−645.

(35) Sanchez de Juan, B.; von Briesen, H.; Gelperina, S. E.; Kreuter, J. *J. Drug Targeting* **2006**, *14*, 614−622.

(36) Hillaireau, H.; Le Doan, T.; Chacun, H.; Janin, J.; Couvreur, P. *Int. J. Pharm.* **2007**, *331*, 148−152.

(37) Musyanovych, A.; Landfester, K. *Prog. Colloid Polym. Sci.* **2008**, *134*, 120−127.

(38) Nicolas., J.; Bensaid, F.; Desmaële, D.; Grogna, M.; Detrembleur, C.; Andrieux, K.; Couvreur, P. *Macromolecules* **2008**, *41*, 8418−8428.

(39) Wang, T.; Guo, Z. *Curr. Med. Chem.* **2006**, *13*, 525−537.

(40) Schlaad, H.; Kukula, H.; Rudloff, J.; Below, I. *Macromolecules* **2001**, *34*, 4302−4304.

(41) Lonsdale, D. E.; Bell, C. A.; Monteiro, M. J. *Macromolecules* **2010**, *43*, 3331−3339.

(42) Goldmann, A. S.; Schoedel, C.; Walther, A.; Yuan, J.; Loos, K.; Mueller, A. H. E. *Macromol. Rapid Commun.* **2010**, *31*, 1608−1615.

(43) Xie, F.; Sivakumar, K.; Zeng, Q.; Bruckman, M. A.; Hodges, B.; Wang, Q. *Tetrahedron* **2008**, *64*, 2906−2914.

(44) Besset, C.; Bernard, J.; Fleury, E.; Pascault, J.-P.; Cassagnau, P.; Drockenmuller, E.; Williams, R. J. J. *Macromolecules* **2010**, *43*, 5672−5678.

(45) Baier, G.; Musyanovych, A.; Dass, M.; Theisinger, S.; Landfester, K. *Biomacromolecules* **2010**, *11*, 960−968.

Macromolecules

Article

pubs.acs.org/Macromolecules

Comparison between Free Volume Characteristics of Composite Membranes Fabricated through Static and Dynamic Interfacial Polymerization Processes

Quanfu An,[†,‡] Wei-Song Hung,*[,‡] Shen-Chuan Lo,[§] Yueh-Hsien Li,[‡] Manuel De Guzman,[‡] Chien-Chieh Hu,[‡] Kueir-Rarn Lee,*[,‡] Yan-Ching Jean,[‡,⊥] and Juin-Yih Lai[‡]

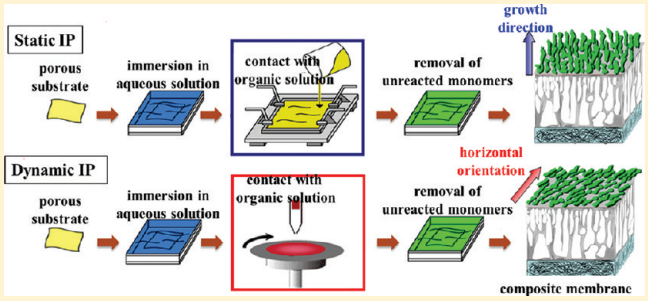
[†]MOE Key Laboratory of Macromolecular Synthesis and Functionalization, Department of Polymer Science & Engineering, Zhejiang University, Hangzhou 310027, China

[‡]R&D Center for Membrane Technology, Department of Chemical Engineering, Chung Yuan University, Chung-Li 32023, Taiwan

[§]Materials and Chemical Research Laboratories, Industrial Technology Research Institute, Hsin-Chu 31040, Taiwan

[⊥]Department of Chemistry, University of Missouri—Kansas City, Kansas City, Missouri 64110, United States

ABSTRACT: For fabricating a polyamide (PA) selective film by interfacial polymerization (IP), we selected a linear structure of succinyl chloride, an acyl chloride monomer, and of 1,3-diaminopropane, an amine monomer. It was not by conventional IP; instead, the technique of spin-coating was successfully integrated into the process of IP. We called such integrated systems as dynamic IP. Spin-coating provided a strong centrifugal force which induced arrangement and orientation of molecular chains in the horizontal direction. Hence, a dense and thin selective film of PA formed. In characterizing the different layers of the PA composite membrane in terms of free volume elements, we exploited the advantages of probing it with positron annihilation spectroscopy (PAS). PAS data revealed a shorter o-Ps lifetime (τ_3 = 1.71 ns) and a lower free volume intensity (I_3 = 7.9%) for the case of the PA film fabricated through the dynamic IP process, in contrast to a longer τ_3 of 1.86 ns and a higher I_3 of 9.1% for the film produced from applying the static IP process. Transmission electron miscroscopy (TEM) results complemented the free volume data obtained. TEM described cavities with sizes outside the sensitivity of the PAS instrument. TEM micrographs showed that the cavities present in the PA film formed by applying the IP process without the integration of spin-coating ranged in size between 40 and 60 nm, whereas those in the film obtained from the IP process integrated with spin-coating ranged 15−30 nm. Separation performance data indicated a simultaneous enhancement of flux and selectivity for the composite membrane fabricated through the combined techniques of IP and spin-coating. This outcome is different from the common behavior known as the trade-off phenomenon.



INTRODUCTION

Pervaporation separation processes are economical alternatives to conventional ones for separating liquid mixtures that cannot be separated or concentrated by distillation. These processes are especially attractive in separation applications involving azeotropic and close boiling point mixtures.[1−3] Alcohol dehydration is one of the important developing areas in membrane pervaporation separation. Therefore, an integral part of the investment should be in the membrane technology because membrane separation processes involve low-energy consumption and minimum operating cost.[4−6] As such, it is worth pursuing to develop industries that would also delve into basic and applied researches on membrane fabrication and characterization.

Thin film composite membranes consist of a film of polymer uniformly distributed over the surface of another polymer that functions as substrate. This film has a dense structure, which is responsible for giving a high selectivity. The substrate not only provides mechanical strength but also induces high flux due to its porous structure. Many studies have made use of interfacial polymerization as a technique for preparing a thin selective film of polyamide (PA).[7,8] In 1965, Morgan prepared a PA selective film by IP, and he proposed that the film forms and gradually grows in a disordered or random fashion from the aqueous to the organic phase. The resulting interfacial film has appropriate mechanical strength and compact structure.[9] In 2008, Lee validated Morgan's theory based from the viewpoint of the free volume obtained with the use of the positron annihilation lifetime technique. One of his experimental results demonstrated that at the point of contact between aqueous and organic phases a dense thin film forms at the interface.[10] The presence of this first layer of film hinders further penetration of

Received: January 18, 2012
Revised: April 5, 2012
Published: April 10, 2012

 © 2012 American Chemical Society

the aqueous solution into the organic solution. Hence, the PA film grows in an erratic or irregular way. As such, the surface structure of the resulting film is loose.

Techniques that produce uniform thin films include coating methods by means of spinning, dipping, or spraying. Because it results in very thin films of good uniformity, spin-coating is widely used. For example, microelectronics industries often adopt the spin-coating technique, which also finds applications in polymeric composite films, integrated circuits, polymer light-emitting diodes, and liquid crystal display panels.[11,12] During the process of spin-coating, a solution is dispensed onto the middle part of the substrate. It then spreads away from the axis of rotation toward the substrate outer edge due to the centrifugal force. At the end of the process, a film of uniform thickness forms. The thickness of the film is inversely proportional to the square roof of the rotation speed, and it also depends on time and the solution viscosity.[13,14]

For fabricating PA composite membranes, we introduced the concept of integrating spin-coating into IP. We proposed a more effective way of reacting acyl chloride monomer with amine monomer: spin-coating an organic solution of the former monomer onto a substrate soaked with an aqueous solution of the latter monomer. The accompanying powerful centrifugal force oriented the molecular chains in the growing interfacial PA film in the horizontal direction, leading to the formation of an ultrathin and compact PA film. We then analyzed the microstructure of the fabricated PA composite membrane by the positron annihilation lifetime technique complemented with TEM.

EXPERIMENTAL SECTION

Materials. Polyacrylonitrile (PAN) polymer was supplied by Tong-Hua Synthesis Fiber Co., Ltd., in Taiwan. *N*-Methyl-2-pyrrolidone (NMP) of reagent grade was used as solvent for PAN. Succinyl chloride (SCC) and 1,3-diaminopropane (DAPE) were purchased from TCI Co. DAPE was the aqueous phase monomer and SCC the organic phase monomer. These two monomers were reacted with each other during the interfacial polymerization process to form an active film of PA. In preparing aqueous amine solution and organic solution of acyl chloride, distilled water was the solvent in the former solution and reagent grade toluene the solvent in the latter.

Fabrication of Porous Modified PAN Support Membrane. We cast a 15 wt % PAN–NMP solution on a nonwoven polyester fabric with the use of a 200 μm gap casting knife. On immersion in a bath of water, the cast solution precipitated to form a film of PAN. We then obtained a porous PAN membrane, which was washed overnight in a water bath and dried at atmospheric conditions. The next step was modifying this dry PAN membrane through hydrolysis with a 2 M NaOH(aq) solution at 50 °C to improve the surface hydrophilicity and to ease the spread of aqueous amine solution over the modified membrane. During hydrolysis, the −CN groups on the surface of PAN could be converted into −COOH groups. In addition to −COOH groups as the product of hydrolysis, $-CONH_2$ or −CONH groups as byproducts may also form.[15] The final step was washing the resulting porous modified PAN (mPAN) membrane in a bath of water for several hours and then drying at atmospheric conditions. We used this mPAN as a substrate or flat support membrane.

Static and Dynamic Processes of Fabricating Polyamide Thin Film Composite Membranes. We fabricated a PA thin film composite membrane through a static (upper half of Figure 1) or a dynamic (lower half of Figure 1) IP process. For both processes, we dissolved a DAPE monomer in deionized water to prepare a 0.1 wt % aqueous solution and mixed an SCC acyl chloride monomer with toluene to form a 0.2 wt % organic solution. Next was immersion of the substrate in the aqueous amine solution for 30 s. Then, we fixed the wet substrate on a tailor-made holding device. Static and dynamic

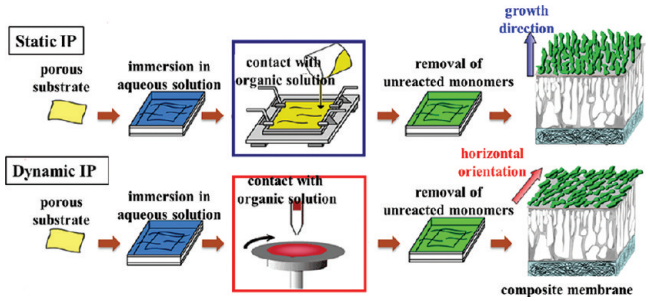


Figure 1. Illustration of procedures for fabrication of polyamide composite membranes through static and dynamic interfacial polymerization processes.

IP processes differed in the step of the interfacial polymerization reaction between DAPE and SCC, i.e., in the way the organic phase got in contact with the aqueous phase. In the former process, the organic acyl chloride solution was poured onto the surface of the substrate soaked with the aqueous solution, and the two monomer solutions were allowed to stand and contact each other for 10 s. In the latter process, the organic solution was spin-coated over the surface of the substrate at different spin-coating rates. Spin-coating provided a powerful centrifugal shearing force which affected the arrangement and the orientation of molecular chains in the polymer film that formed at the interface between the organic and the aqueous phase. As a result, the molecular chains simultaneously oriented in the horizontal direction and stacked up closer to one another.

After the step of the interfacial polymerization reaction, we dried the composite membrane by exposing it to air at room temperature for 30 min. Immersion in methanol followed to remove unreacted monomers and residual solvents. The final step was drying the composite membrane and storing it for later measurement of its characteristics.

Pervaporation and Sorption Measurements. Our previous work[16] gives a detailed description of the pervaporation and sorption measurements conducted in this study. For determining the performance of synthesized PA composite membranes, we applied them to dehydrate a 90 wt % aqueous ethanol solution at 30 °C by pervaporation. The feed solution was in direct contact with the composite membrane. Permeation flux (J) and permeability (Q) were calculated according to the following equations:[16,17]

$$J = \frac{w}{St} \tag{1}$$

$$Q_i = \frac{J_i L}{P_i - PY_i} \tag{2}$$

$$P_i = X_i \gamma_i P \tag{3}$$

where w is the weight of permeate collected in traps immersed in liquid nitrogen during the operation time t, S is the membrane effective area, Q_i is the permeability for component i, L is the membrane thickness, P is the downstream pressure, Y_i is the mole fraction of component i in the permeate, P_i is the fugacity of component i in the feed, X_i is the mole fraction of component i in the feed, P is the vapor pressure of component i, and γ_i is the activity coefficient. The compositions of feed solution and permeate were determined using gas chromatography (GC Chromatograph 8700 T, China).

For the sorption measurement, we used a device whose description was detailed in another study.[16] Only the TFC membrane PA film was in contact with the feed solution at 30 °C. After attaining equilibrium sorption, the PA film was blotted with a filter paper to remove the excess solution. Afterward, the composite membrane was immediately placed in the left tube of a twin-tube setup. This left tube was put into liquid nitrogen to freeze the swollen membrane. Then, the system was evacuated with a vacuum pump. The next step was replacing the container of liquid nitrogen in which the left tube was immersed with a container of hot water to heat and evaporate completely the liquid

dx.doi.org/10.1021/ma3001324 | Macromolecules 2012, 45, 3428–3435

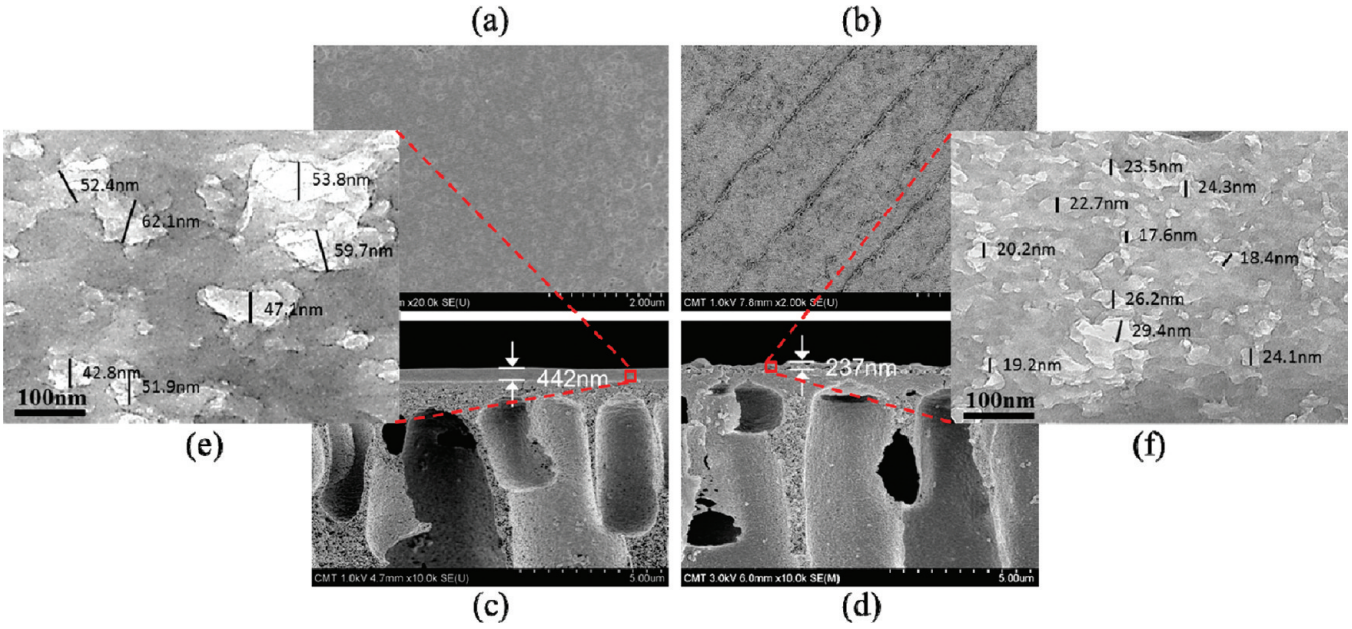


Figure 2. Micrographs of polyamide composite membranes fabricated through static (a, c, e) and dynamic (b, d, f) interfacial polymerization processes. For dynamic IP, spin-coating rate = 6000 rpm. (a–d) SEM surface and cross-sectional images; (e, f) TEM cross-sectional images.

sorbed in the membrane. The ensuing vapor was trapped in the right tube, which was cooled with liquid nitrogen and subsequently condensed with tap water. GC was used to measure the composition of the liquid permeate collected.

Positron Annihilation Spectroscopy. We made use of a novel variable monoenergy slow positron beam (VMSPB), housed in the R&D Center for Membrane Technology in Chung Yuan University in Taiwan,[18] to probe the composite membrane. This new radioisotope beam used 50 mCi of ^{22}Na as the positron source. Sputtering a few atomic layers of platinum (1 nm) on the PA composite membrane completely removed the charging effect induced by VMSPB applications on insulators.[19] We operated the beam in the range of 0–30 keV positron incident energy, equivalent to a mean depth of 0–10 μm.

When a positron enters a polymeric surface, it loses its energy through the process of inelastic collisions within the time scale of 10^{-12} s, and its energy distribution can be expressed by a Makhovian implantation profile. The mean depth Z of polymeric materials where the positron annihilation occurs is calculated from E_+ using the equation[20−22]

$$Z(E_+) = (40/\rho)E_+^{1.6} \quad (4)$$

where Z is expressed in nm, ρ is the density in g/cm,^{3} and E_+ is the positron incident energy in keV. The corresponding distribution of the mean depth Z is broadened with an increase in the positron energy E_+, and the depth resolution is better near the surface than in the bulk. A typical depth resolution is estimated to be about 10% of the depth of interest.

Connected to the beam was Doppler broadening energy and positron annihilation lifetime spectroscopes. These two positron annihilation spectroscopes used secondary electrons, which were emitted from the surface of a sample. An HP Ge detector identified and recorded the spectra from Doppler broadening energy spectroscopy (DBES) at a counting rate of ∼1800 cps. The energy resolution of the solid-state detector was 1.5 keV at 0.511 MeV (corresponding to a positron 2γ annihilation peak). For a DBES spectrum, the total number of counts was 1.0 million. Positron annihilation lifetime spectroscopy (PALS) data were obtained by taking the coincident events between the start signal detected by a multichannel plate from the secondary electrons and the stop signal given by a BaF_2 detector from the annihilation photons at a counting rate of approximately 200–250 cps. Each PALS spectrum contained 2.0 million counts.

In analyzing the PALS data from the slow beam using PATFIT, we found that the three-lifetime analysis consistently gave better χ^2 values (χ^2 < 1.5) and stability with reasonable errors than the four-lifetime analysis. Analyzed results of positron lifetimes (τ_1, τ_2, τ_3) and intensities (I_1, I_2, I_3) from PAL spectra are attributed to the positron and positronium annihilation in polymeric materials. The lifetimes are described as follows: τ_1 = 0.125 ns (fixed in our final PATFIT analysis) is the shortest and is from p-Ps annihilation, τ_2 ∼ 0.45 ns is from the free positron annihilation, and τ_3, which is on the order of 1–5 ns in polymeric materials, is due to o-Ps annihilation, the so-called pickoff annihilation with electrons in molecules. Since positronium is known to preferentially localize in defect sites,[23] particularly in the free volume before annihilation takes place, parameters from o-Ps annihilation have been successfully used to obtain electron properties and depth profiles of free volumes in thin film polymers.[24−27]

Morphological Characterization. Surface and cross-sectional morphologies of the PA film on DAPE-SCC/mPAN composite membranes were obtained by using scanning electron microscopy (SEM, Hitachi model S4800, Japan), transmission electron microscopy (TEM, JEOL JEM-2100F, Japan), atomic force microscopy (AFM, Digital Instruments MultiMode, DI-NS3a, USA), and water contact angle measurement (FACE, model PD-VP, Japan). The preparation of the specimen for the cross-sectional TEM image was based on the technique of ultramicrotomy or DB-FIB (dual-beam focused ion beam). Applied was a JEOL JEM-21000F TEM operated at 200 kV and equipped with a Schottky field emission gun with a point-to-point resolution of 1.9 Å. High-resolution TEM micrographs were used to examine the microstructure of the sample.

■ RESULTS AND DISCUSSION

Figure 2 presents SEM and TEM micrographs of surface and cross-sectional structures of PA composite membranes fabricated through static (Figure 2a,c,e) and dynamic (Figure 2b,d,f) IP processes. Figure 2a shows that the surface of the composite membrane is smooth. This result conforms to the surface morphology of PA composite membrane generally fabricated by conventional interfacial polymerization,[10,24,28] which we called static IP, where aqueous and organic monomer solutions contact each other and stand for some time until a polymer film forms at the interface between the aqueous and the organic phase. Figure 2b indicates that the surface of the

dx.doi.org/10.1021/ma3001324 | Macromolecules 2012, 45, 3428–3435

composite membrane is rough and displays several parallel lines of raised or protruding parts. These lines represent part of the wavy fluid flow pattern on the membrane surface, which forms due to the effect of the rotation. Because of the strong shearing force associated with the dynamics of the spin-coating process, the casting solution being coated on the mPAN substrate has unstable flow patterns. As such, a turbulent flow may be produced. Factors that affect the fluid flow pattern include centrifugal force, fluid surface tension, solid−liquid interface between the substrate and the casting solution, and liquid−vapor interface between the casting solution and the surrounding air. A variety of flow patterns on the fluid surface have been identified: helical, spiral, wavelike, and other related shapes of flow currents.[29−31]

The cross-sectional SEM image in Figure 2c illustrates that the thickness of the PA film is about 442 nm. The structure of the supporting layer of PAN substrate consists of fingerlike macrovoids. These giant holes form because of the rapid exchange between the solvent and the nonsolvent during the substrate preparation using the wet-phase inversion method. Under the same polymerization conditions, the composite membrane cross section in Figure 2d shows that the thickness of the PA film is about 237 nm. This thickness is only about half of that indicated in Figure 2c. During the dynamic IP process, a high shearing force provided by a strong centrifugal force affects the PA film that forms at the time of contact between the solutions of acyl chloride and amine monomers in such a way that the PA molecular chains grow along the substrate surface and orient themselves in the horizontal direction. This setup of horizontal arrangement and orientation is a plausible explanation why the thickness of the polyamide film from the dynamic IP process is less than that from the static IP process.

The PA film shown by the cross-sectional SEM images in Figure 2c,d appears to be dense. However, a TEM image of a part of this PA film (Figure 2e,f) demonstrates that cavities exist in the film. These cavities may be linked to the diffusion of the aqueous phase through the organic phase during the IP reaction.[9,10] When the amine monomer present in the aqueous solution reacts with the acyl chloride monomer in the organic solution to form a continuous PA film, the remaining aqueous solution does occupy a space and leaves cavities in the PA film when the solvent water evaporates. With TEM, electrons are passed through the composite membrane. Few electrons fall on the polymer part, which appears as dark regions in Figure 2e,f. More electrons are easily scattered in cavities, which appear as light or bright regions in Figure 2e,f. Across the depth of the membrane, therefore, the dark or thick areas referring to the PA polymer are contrasted with the light or low mass areas representing the cavities.

A comparison of the TEM micrographs indicates that the microstructure of the PA film produced from static IP consists of bigger cavities of about 40−60 nm (Figure 2e) compared to that of the film from dynamic IP with smaller cavities of about 15−30 nm (Figure 2f). Because of the powerful centrifugal force provided by spin-coating, some amount of the aqueous solution that has diffused in the PA film gets drawn out, so that less amount of the solvent water remains, which evaporates on drying and leaves behind a small cavity. Hence, cavities shown in Figure 2f are smaller than those in Figure 2e.

AFM can measure contours of the surface structure of PA composite membranes and can give information about the surface roughness. Figure 3 contrasts the rougher surface of the

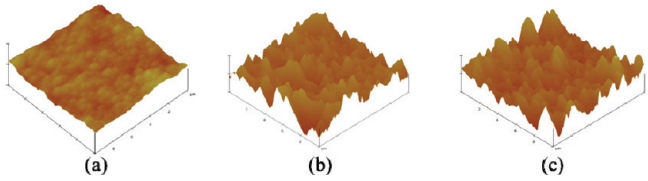


Figure 3. AFM images of polyamide composite membranes: (a) static IP; (b) dynamic IP, spin-coating rate = 3000 rpm; (c) dynamic IP, spin-coating rate = 6000 rpm.

PA composite membrane fabricated through the IP process integrated with the spin-coating technique relative to the smoother surface of that produced by means of the IP process without the integration of spin-coating. Table 1 summarizes

Table 1. Surface Roughness of Polyamide Composite Membranes[a]

membrane from	R_{ms} (nm)	R_a (nm)	R_{max} (nm)
static IP	12.5	18.7	197.9
dynamic IP, 3000 rpm	76.2	55.3	475.3
dynamic IP, 6000 rpm	81.2	62.7	563.4

[a] R_{ms}, R_a, and R_{max} are mean square, average, and maximum roughness, respectively.

surface roughness parameters, such as average roughness (R_a) and mean-square roughness (R_{ms}), to compare the surface roughness of different PA films. With the static IP process, R_a and R_{ms} values for the PA film are 18.7 and 12.5 nm, respectively. When the process applied is dynamic IP at a spin-coating rate of 3000 rpm, R_a and R_{ms} data are higher at 55.3 and 76.3 nm, respectively. This rougher surface of the PA film may be attributed to the combined effects of centrifugal force and its resolved upward force. The following two conditions contribute to the generation of the upward force: (1) Bumps on the rough surface of mPAN substrate induce upward force as the casting solution spreads outward on the influence of the horizontal centrifugal shearing force. (2) The volatile nature of the NMP present in the organic phase causes upward movement or force associated with the occurrence of mass transfer by solvent evaporation from the surface of the casting solution to the surrounding air.[32] For the dynamic IP at a spin-coating rate of 6000 rpm, it is interesting to note that the R_{max} of 563 nm (Table 1) is greater than the PA film thickness of 237 nm indicated by the SEM image in Figure 2d. The reason is that the AFM we used, which operates by tapping mode, measures the composite membrane surface that is characterized with parallel lines of raised or protruding parts.

During the process of IP integrated with the spin-coating technique, we varied the spin-coating rate. Different rates had an effect on the water contact angle. Figure 4 plots the relationship between them. The composite membrane produced from the IP process without the integration of spin-coating gives a water contact angle of about 81°. With spin-coating integrated into IP at 1000 rpm, the resulting composite membrane has a lower water contact angle of 69°. As the spin-coating rate increases, the water contact angle decreases. It drops to 59° at 8000 rpm. In the literature, it has been proposed that in the case of water contact angle above 90° the rougher the surface becomes, the greater the surface contact area and the lower the surface energy, and the water contact angle gets higher than 90°. To balance the decreased energy

dx.doi.org/10.1021/ma3001324 | Macromolecules 2012, 45, 3428−3435

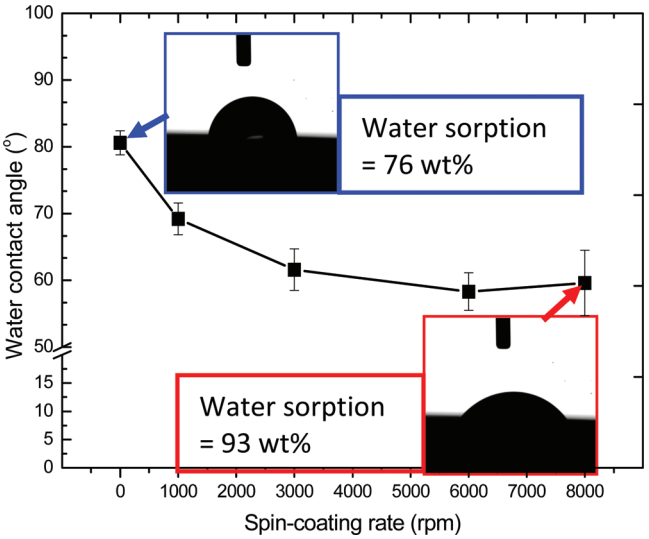


Figure 4. Effect of different spin-coating rates on water contact angle and sorption data for DAPE-SCC/mPAN composite membranes (feed: 90 wt % aqueous ethanol solution).

between the surface and the water droplet, the water contact angle has to increase. For the case of water contact angle below 90°, increased roughness results in greater surface area for the water droplet and in higher nominal or apparent surface energy, and the value of the water contact angle is lower than 90°. The water contact angle has to decrease to balance the increased surface energy.[33] Therefore, the data in Figure 4 indicate that the rougher the PA film surface, the more hydrophilic it is. The greater surface contact area for the water droplet leads to a decrease in the water contact angle. The sorption data also indicated in Figure 4 demonstrate further the rougher and more hydrophilic properties of the PA film surface at faster spin-coating rates. Results of sorption with a 90 wt % aqueous ethanol solution show that the water content of 76 wt % in the membrane produced with the use of static IP is lower than that of 93 wt % in the membrane obtained from applying the dynamic IP process. The powerful shearing force associated with spin-coating results in the preferential arrangement of the molecular chains in the growing PA film in the horizontal direction, forming a compact or dense structure. Hence, more water molecules of shorter dynamic radius would diffuse into the membrane as opposed to ethanol molecules of longer dynamic radius that would have difficulty passing through the membrane.

SEM, AFM, and water contact angle results correspond with each other. Both SEM and AFM data discussed above indicate that the surface of the PA composite membrane fabricated from the dynamic IP process is rough. This rough surface leads to a decline in the water contact angle.

In pervaporation separation processes, the general tendency is that high selectivities of polymeric membranes are counter-balanced by low permeation fluxes due to the high membrane resistance. Conversely, membranes with large pores deliver high fluxes but have low selectivities. However, we found a rather interesting result shown in Figure 5a, which contrasts the pervaporation performance of PA composite membranes fabricated through interfacial polymerization with and without the integration of the spin-coating technique. A spin-coating rate of 0 rpm represents static IP, and that greater than 0 rpm describes dynamic IP. From a spin-coating rate of 0−1000 rpm

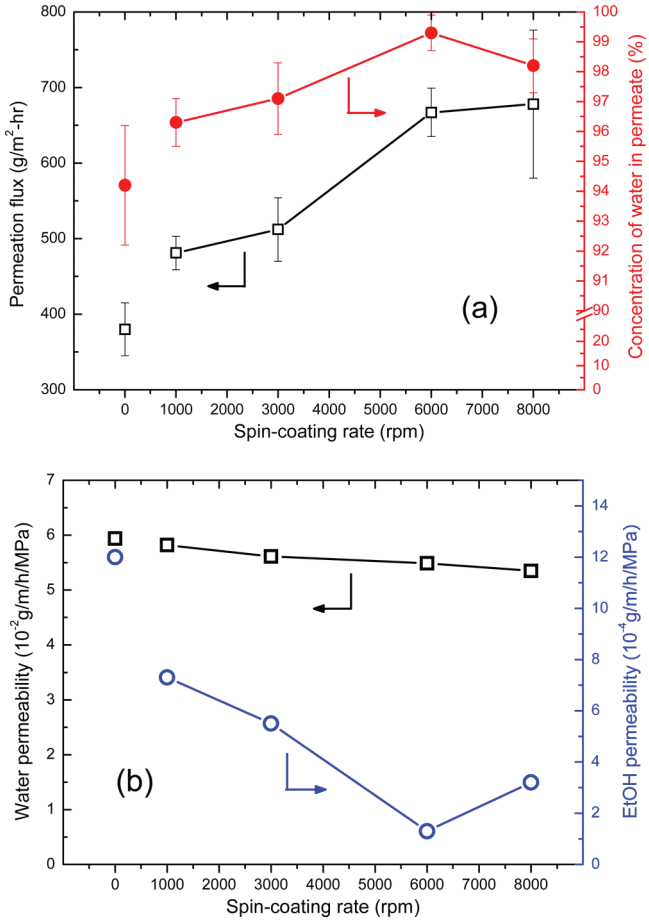


Figure 5. Effect of different spin-coating rates on pervaporation performance (a) and permeability (b) of polyamide composite membranes (feed: 90 wt % aqueous ethanol solution).

and then to a higher rate of 6000 rpm, the permeation flux increases from 382 to 481 g/(m^2 h) and then to a much higher flux of 678 g/(m^2 h), corresponding to the improvement in the concentration of water in permeate from 94.2 to 96.3 wt % and then to 99.3 wt %. For the dynamic IP process, there is a simultaneous increase in the permeation flux and the concentration of water in permeate. This result is different from the common behavior for membrane separations known as the trade-off phenomenon between permeability and selectivity.[34] However, when the spin-coating rate reaches 8000 rpm, the selectivity slightly decreases and the error bar, even for the corresponding permeation flux, turns out to be bigger. These results are likely attributed to the very high spin-coating rate. The casting solution dispensed onto the spinning substrate would have very high kinetic energy, resulting in the solution being thrown out of place. Hence, the solution would not completely cover the surface of the substrate. Less amount of the organic solution, therefore, would react with the aqueous solution by interfacial polymerization. The result would be defects in some regions of the substrate surface. Thus, both the membrane selectivity and stability would drop.

Figure 5b shows the decreasing trend of both the permeability of water and of ethanol as a function of the spin-coating rate. But the decrease in the water permeability is not as drastic as the ethanol permeability in the spin-coating rate range of 0−6000 rpm. As the ethanol permeability is much lower than the water permeability, the ratio of the latter

dx.doi.org/10.1021/ma3001324 | Macromolecules 2012, 45, 3428−3435

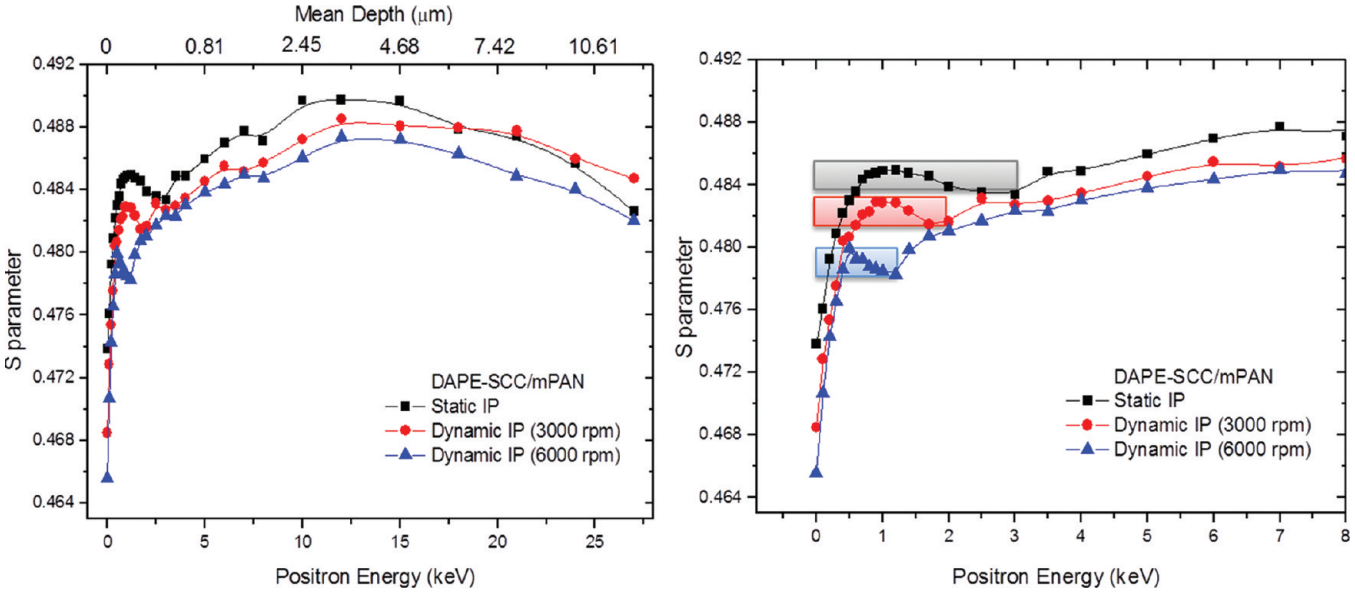


Figure 6. *S* parameter as a function of positron incident energy in keV (or mean depth in μm) for DAPE-SCC/mPAN composite membranes fabricated through static and dynamic IP processes. The right plot is the magnified part of the left plot from 0 to 8 keV.

permeability to the former increases with the spin-coating rate. This ratio is directly proportional to the selectivity, which is why the concentration of water in permeate increases, as depicted in Figure 5a. Moreover, the changes in the permeability of water and of ethanol with the spin-coating rate indicate that the PA film structures are all different. The film gets denser as it gets thinner, in connection with the preferential horizontal orientation of the film molecular chains due to the influence of the spin-coating centrifugal force. A denser film offers stronger resistance to diffusion, which in turn leads to lower permeability. On the other hand, a thinner film offers lower resistance to permeation, that is why the flux in Figure 5a is shown to increase.

We conducted experiments on DBES. This DBES technique provides qualitative information about free volume and structure of multilayered membranes.[10,18,24] Parameters that describe DBES include the *S* parameter. Defined as the central part at 511 keV of the annihilation radiation, *S* measures free volumes between 0.1 and 1 nm based on 2γ annihilation.[35] In general, larger *S* values represent bigger size and greater amount of free volume, which lead to the increase in the polymer chain mobility and then to the formation of a looser structure correlated to a smaller polymer density.

Figure 6 compares different PA composite membranes fabricated by means of static and dynamic IP processes based on the results of *S* parameter vs positron incident energy (mean depth). The right plot in Figure 6 illustrates by using rectangular bars that the PA film formed from applying the static IP process is thicker than either of the films from dynamic IP processes at different spin-coating rates. These rectangular bars are results of the analysis using a VEPFIT program[36] that deconvolutes positron energies into an implantation profile. During the analysis of the composite membrane multilayer structure, we tried to apply different models with the use of the VEPFIT program. The two-layer model could not give reasonably good χ^2 values (>3.5), whereas the four-layer model gave slightly better χ^2 values than the three-layer model, but the fitted results were unstable and the resultant errors were larger than the fitted layer thicknesses and diffusion lengths. Thus, we found appropriate fitting results descriptive of a three-layer model, based on consistently good χ^2 values (<1.8) and reasonable errors. We therefore report the results of the three-layer analysis in this paper. The three layers indicated are as follows: (I) polyamide film, (II) transition layer from dense skin to porous support layer of mPAN, and (III) porous support layer of mPAN. By varying the density input for each of the three layers, best fitting of the results from the VEPFIT program analysis was obtained, as judged from $\chi^2 < 1.8$. The resulting density values are as follows: $\rho_I = 1.2$, $\rho_{II} = 1.0$, and $\rho_{III} = 0.8$ g/cm^3, where the subscripts I, II, and III denote the three layers. These densities agree with the previously reported data.[18,24] With a spin-coating rate of 0, 3000, and 6000 rpm, the thickness of the respective PA films is 417, 352, and 209 nm. For the dynamic IP process, the higher the spin-coating rate, the thinner the layer. Therefore, the decreasing thickness is a function of the increasing spin-coating rate. As to how dense the different PA films are, we can deduce it based on their corresponding *S* parameters. The *S* value is directly proportional to the size or the amount of free volume. Lower *S* values indicate smaller size or amount of free volume, which means that the structure is denser. From the right plot in Figure 6, the relationship between the PA films obtained, depending on the applied spin-coating rate (0, 3000, and 6000 rpm), and their corresponding *S* parameters can be described as follows: as spin-coating rate increases, *S* value decreases. Hence, the higher the spin-coating rate, the denser the PA film. For the case of integrating spin-coating into the process of IP at faster spin-coating rates, the reason why the PA film formed is denser can be attributed to the corresponding stronger centrifugal force. Because of the accompanying powerful shearing force, the molecular chains in the growing PA film arrange themselves in the horizontal direction to form a compact or dense structure. In regard to the thinner PA film obtained from the dynamic IP process at higher spin-coating rates, the volatilization of the NMP solvent in the organic phase becomes faster. This lost amount of solvent inhibits the monomer diffusion, which in turn limits the thickness of the PA film.

dx.doi.org/10.1021/ma3001324 | *Macromolecules* 2012, 45, 3428−3435

We can deduce from Figure 6 that the microstructure of the different layers of composite membranes depends on the S values, which vary as a function of the positron energy as follows: (1) S values rise in low-energy positron implantation range (<0.7 keV). (2) Next, S values exhibit a shoulder at positron incident energy range of 1−3 keV. (3) Then, S values increase to a point, after which they reach a plateau. (4) Finally, S values slightly decline after the plateau region.

Possible reasons for the changes in the S values are the following. (1) Back-diffusion and scattering of positron and positronium from the membrane surface cause the sharp rise in the value of S at the onset (<0.7 keV). Some positrons are reflected back to the vacuum chamber, and the positronium that diffuses near the membrane surface is sent back to vacuum where it undergoes 3γ annihilation. Hence, the S value very close to the membrane surface is low, as S is based on the detection of 2γ annihilation. (2) In the 1−3 keV range of positron incident energy, the PA film structure dictates that S values decrease following their sudden increase near the membrane surface, resulting in a shoulder in the S curve. The first layers of the PA film instantly form at the point of contact between the organic and aqueous solutions. These layers are dense, as indicated by low S values within the 1−3 keV range, and offer resistance to the further diffusion of the aqueous phase through the organic phase. Such a behavior leads to a loose structure of the remaining layers of the PA film, as indicated by high S values in the 0.5−1.5 keV range. (3) The region >3 keV represents the transition layer from the PA film layer to the mPAN layer, in which S values increase. This further region denotes the porous mPAN substrate layer. (4) The decrease in S values at positron incident energy from 10 to 27 keV is ascribed to macrovoids in the mPAN substrate (see Figure 2), wherein the low momentum causes the o-Ps to give 3γ annihilation, resulting in the reduction of the pick off o-Ps 2γ annihilation rate. Hence, S values decrease.[19]

We used PALS to analyze the variation in the o-Ps lifetime (τ_3) and intensity (I_3) in each layer of PA composite membranes. Figure 7 indicates that the τ_3 in the dense PA film formed from applying the static IP process is 1.86 ns and that in the film from the dynamic IP process is 1.71 ns; the corresponding I_3 is 9.1% and 7.9%, respectively. When solutions of acyl chloride and amine monomers contact each other, a film of PA immediately forms, and concurrent with the application of strong centrifugal shearing force, the molecular chains in the growing PA film arrange and stack themselves close to each other, leading to the formation of short τ_3. Near the PA film surface region (~1 keV), the I_3 of the composite membrane is higher with the application of the dynamic IP process than with the static IP process. The rapid volatilization of the NMP solvent creates a driving force that influences the growth of PA molecular chains toward the formation of not only a rough surface but also a loose structure.[10] Data on positron implantation energy or depth reveal that the PA film thickness is 412 nm for the case of static IP, and it is 209 nm for the dynamic IP process. These results have a trend similar to those from SEM.

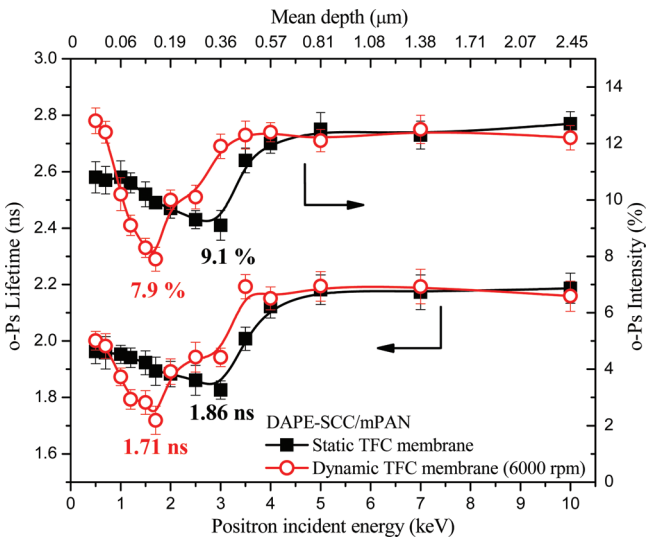


Figure 7. o-Ps lifetime or intensity vs positron incident energy for DAPE-SCC/mPAN composite membranes fabricated through static and dynamic IP processes.

CONCLUSION

We successfully integrated the technique of spin-coating into the process of IP. With this technology called as dynamic IP, we fabricated PA composite membranes; characterized them using SEM, AFM, contact angle measurement, TEM, and PALS; and applied them to the pervaporation separation of a solution consisting of 90 wt % ethanol in water. Results obtained are indicated as follows.

1. SEM and AFM showed that the surface of the PA composite membrane fabricated through dynamic IP was rougher than that obtained from the static IP process. The contact angle measurement indicated the hydrophilicity of the interfacial PA film, with the rougher surface having a lower water contact angle than the smoother surface.
2. TEM demonstrated that smaller nanopores of 15−30 nm existed in the PA film formed from applying the dynamic IP process and that bigger nanopores of 40−60 nm were present in the film formed using the static IP process.
3. PALS data revealed a shorter o-Ps lifetime (τ_3 = 1.71 ns) and a lower free volume intensity (I_3 = 7.9%) for the case of the PA film fabricated through the dynamic IP process compared to a longer τ_3 of 1.86 ns and a higher I_3 of 9.1% for the film obtained from the static IP process. Results of the PA film thickness based on the PALS data conformed to those from SEM.
4. Pervaporation results showed better performance of PA composite membranes fabricated through interfacial polymerization with the integration of the spin-coating technique compared to that without spin-coating. The effect of increasing spin-coating rates on the pervaporation performance was to improve both the permeation flux and the concentration of water in permeate. This result is different from the commonly known trade-off phenomena for membrane separation processes. Moreover, faster spin-coating rates led to the formation of denser PA films, which had lower permeability.

AUTHOR INFORMATION

Corresponding Author

*Tel +886-3-2654190, Fax +886-3-2654198, e-mail krlee@cycu.edu.tw (K.R.L.); Tel +886-3-2654190, Fax +886-3-2654198, e-mail wshung@cycu.edu.tw (W.S.H.).

Notes

The authors declare no competing financial interest.

■ ACKNOWLEDGMENTS

The authors sincerely thank the Ministry of Education Affairs and the National Science and Technology Program-Energy from NSC of Taiwan (NSC 100-3113-E-033-001 and NSC 100-2218-E-033-009) for financially supporting this work.

■ REFERENCES

(1) Aptel, P.; Challard, N.; Neel, J. *J. Membr. Sci.* **1976**, *1*, 271−289.
(2) Dutta, B. K.; Sikdar, S. K. *AIChE J.* **1991**, *37*, 581−588.
(3) Garcia-Villaluenga, J. P.; Tabe-Mohammadi, A. *J. Membr. Sci.* **2000**, *169*, 159−174.
(4) Baker, R. W.; Cussler, E. L.; Eykamp, W.; Koros, W. J.; Riley, R. L.; Strathmann, H. In *Membrane Separation Systems: Recent Developments and Future Directions*; Noyes Data Corporation: Park Ridge, NJ, 1991.
(5) Ulbricht, M. *Polymer* **2006**, *47*, 2217−2262.
(6) Huang, Y.; Baker, R. W.; Vane, L. M. *Ind. Eng. Chem. Res.* **2010**, *49*, 3760−3768.
(7) Hwang, S. T.; Kammermeyer, K. In *Membrane in Separation*; John Wiley and Sons: New York, 1975.
(8) Baker, R. W. In *Membrane Technology and Applications*; McGraw-Hill: New York, 2000.
(9) Morgan, P. W. In *Condensation Polymers: By Interfacial and Solution Methods*; Interscience Publishers: New York, 1965.
(10) Huang, S. H.; Hung, W. S.; Liaw, D. J.; Li, C. L.; Kao, S. T.; Wang, D. M.; De Guzman, M.; Hu, C. C.; Jean, Y. C.; Lee, K. R.; Lai, J. Y. *Macromolecules* **2008**, *41*, 6438−6443.
(11) Jiang, P.; McFarland, M. J. *J. Am. Chem. Soc.* **2004**, *126*, 13778−13786.
(12) Caseri, W. *Macromol. Rapid Commun.* **2000**, *21*, 705−722.
(13) Lawrence, C. J. *Phys. Fluids* **1988**, *31*, 2786.
(14) Lee, S. S.; Hong, J. D. *Macromolecules* **2001**, *34*, 5358−5360.
(15) Oh, N. W.; Jegal, J.; Lee, K. H. *J. Appl. Polym. Sci.* **2001**, *80*, 2729−2736.
(16) Chao, W. C.; Huang, S. H.; An, Q. F.; Liaw, D. J.; Huang, Y. C.; Lee, K. R.; Lai, J. Y. *Polymer* **2011**, *52*, 2414−2421.
(17) Wijmans, J. G. *J. Membr. Sci.* **2003**, *220*, 1−3.
(18) Chen, H. M.; Hung, W. S.; Lo, C. H.; Huang, S. H.; Cheng, M. L.; Liu, G.; Lee, K. R.; Lai, J. Y.; Sun, Y. M.; Hu, C. C.; Suzuki, R.; Ohdaira, T.; Oshima, N.; Jean, Y. C. *Macromolecules* **2007**, *40*, 7542−7557.
(19) Hung, W. S.; De Guzman, M.; An, Q. F.; Lee, K. R.; Jean, Y. C.; Lai, J. Y. *Langmuir* **2011**, *27*, 3020−3023.
(20) Jean, Y. C.; Mallon, P. E.; Schrader, D. M. In *Principles and Applications of Positron and Positronium Chemistry*; World Scientific: Singapore, 2003.
(21) Schultz, P. J.; Lynn, K. G. *Rev. Mod. Phys.* **1988**, *60*, 701−779.
(22) Coleman, P. G. In *Positron Beams and Their Application*; World Scientific: Singapore, 2000.
(23) Jean, Y. C. *Macromolecules* **1996**, *27*, 5756−5760.
(24) Hung, W. S.; De Guzman, M.; Huang, S. H.; Lee, K. R.; Lai, J. Y.; Jean, Y. C. *Macromolecules* **2010**, *43*, 6127−6134.
(25) DeMaggio, G. B.; Frieze, W. E.; Gidley, D. W.; Zhu, M.; Hristov, H.; Yee, A. F. *Phys. Rev. Lett.* **1997**, *78*, 1624−1627.
(26) Cao, H.; Zhang, R.; Zhang, J.-P.; Huang, C.-M.; Jean, Y. C.; Suzuki, R.; Ohdaira, T.; Nielsen, B. *J. Phys.: Condens. Matter* **1998**, *10*, 10429−10442.
(27) Algers, J.; Suzuki, R.; Ohdaira, T.; Maurer, F. H. J. *Polymer* **2004**, *45*, 4533−4539.
(28) Freger, V. *Environ. Sci. Technol.* **2004**, *38*, 3168−3175.
(29) Uchiyama, H.; Namba, W.; Kozuka, H. *Langmuir* **2010**, *26*, 11479−11484.
(30) Mellbring, O.; Oiseth, S. K.; Krozer, A.; Lausmaa, J.; Hjertberg, T. *Macromolecules* **2001**, *34*, 7496−7503.
(31) Mao, G.; Dong, W.; Kurth, D. G.; Möhwald, H. *Nano Lett.* **2004**, *4*, 249−252.
(32) Strawhecker, K. E.; Kumar, S. K.; Douglas, J. F.; Karim, A. *Macromolecules* **2001**, *34*, 4669−4672.
(33) Shang, H. M.; Wang, Y.; Limmer, S. J.; Chou, T. P.; Takahashi, K.; Cao, G. Z. *Thin Solid Films* **2005**, *472*, 37−43.
(34) Feng, X.; Huang, R. Y. M. *Ind. Eng. Chem. Res.* **1997**, *36*, 1048−1066.
(35) Nakanishi, N.; Wang, S. J.; Jean, Y. C. In *Positron Annihilation Studies of Fluids*; Sharma, S. C., Ed.; World Scientific: Singapore, 1988.
(36) Van Veen, A.; Schut, H. H.; de Vries, J.; Hakvoort, H. A.; IJpma, M. R. *AIP Conf. Proc.* **1990**, *218*, 171−193.

Macromolecules

Article

pubs.acs.org/Macromolecules

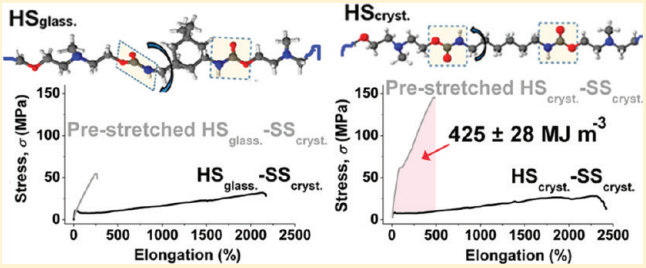
Molecular Engineering of Elastic and Strong Supertough Polyurethanes

Borja Fernández-d'Arlas, Jose A. Ramos, Ainara Saralegi, Marian Corcuera, Iñaki Mondragon, and Arantxa Eceiza*

Grupo "Materiales + Tecnologías" (GMT), Department of Chemical and Environmental Engineering, Polytechnic School, University of the Basque Country (UPV/EHU), Pza. Europa 1, 20018 Donostia-San Sebastián, Spain

Supporting Information

ABSTRACT: Spider silk is an icon of supertough energy absorbing polymeric material which its macromolecular multiblock composition has been attributed to be responsible for such remarkable properties. As in spider silk, polyurethanes can be synthesized with two distinct block which can differ in nature, combining properties like deformability and relatively high strengths. Here we synthesized and studied four different block polyurethanes with two different soft segments (SS) and two different hard segments (HS), with the aim of discovering the best molecular architecture to develop best mechanical performance after macromolecular alignment. The difference between soft segments is the crystalline nature, one in the rubbery state ($T_{g,SS} < T_{room}$) and the other in the semicrystalline state at room temperature ($T_{room} < T_{m,SS}$). In parallel one hard segment was amorphous in the glassy state ($T_{room} < T_{g,HS}$) and the other semicrystalline ($T_{g,HS} < T_{room} < T_{m,HS}$). Results indicate that polyurethane with crystalline soft segments produce stronger materials after drawing than polyurethanes with rubbery soft segments, but the most exciting finding is the influence that hard segment has on the mechanical performance of predrawn materials, having polyurethanes prepared with semicrystalline hard segments more capability to undergo macromolecular alignment than materials with glassy segments, developing stiffer, stronger, and tougher materials.



INTRODUCTION

Extraordinary mechanical properties of spider silk[1−5] have inspired material scientists to undertake research on a new field of science pursuing supertough materials based on molecular engineering and understanding of fracture and toughening mechanisms underlying on spider silk molecular structure[6,7] and materials.[8] Simultaneously, achievement of highly elastic materials, reversibly highly deformable, but with high yield and tensile stresses[9,10] has resulted in an equally challenging goal. In the last years researches have concluded that spider silk's combination of extensibility and strength under tension arises from the copolymeric nature of the silk polypeptidic protein sequences consisting on crystalline, alanine-rich segments in antiparallel β-sheet configuration linked to glycine-rich amorphous domains.[1,7] In addition, the orientated chain anisotropy caused by fiber drawing has been shown to be an equally important factor to that of the chemical composition.[11]

Development of supertough, energy absorbing, materials has been traditionally pursued by either improving the deformability of stiff and strong materials, for example by adding block copolymers,[12] or by strengthening soft and very deformable materials with the inclusion of fibers[9] or nanoparticles.[13] Nevertheless, natural silks, which comprise the toughest materials known to date,[5] are composed of single polymeric molecules not blended with any other nonpolypeptidic structures. Great efforts have been put into understanding structure-properties relationships of spider and worm silks.[14] Even attempts to synthesize *in vivo* silks by genetic engineering of goats mammalian cells[15] have drawn the attention of materials scientists, but not managed to equal natural silk fibers mechanical performance, despite the complexity of the procedure. On the basis of the idea that astonishing mechanical performance of silk relays on its block copolymeric nature of its polypeptidic protein chains and that these are oriented at spinning developing great stiffness and strength,[1,11] we envisioned the idea of creating spider silk like supertough materials supported on our experience on engineering of block polyurethanes.[9,16,17] Here we explore thermoplastic polyurethane copolymers with different block architecture as possible candidates to become industrially scalable synthetic mimics of spider silk like materials. Based on the design possibilities block polyurethanes (PU) offer and on experimental results, we discuss the chain architecture requirements to achieve a strong and highly deformable supertough material.

Polyurethane elastomers share with silks its copolymeric nature consisting on hard segments (HS) linked to soft segments (SS) in an alternative fashion. Thermodynamic incompatibility between HS and SS as well as steric and

Received: February 25, 2012
Revised: April 4, 2012
Published: April 13, 2012

ACS Publications © 2012 American Chemical Society

physicochemical properties of each of the segments[17] lead to certain microphase separated structures, consisting on HS nanocylinders of about 5−25 nm dispersed within a SS matrix.[16] This terminology of HS and SS comes from the idea that in typical polyurethane elastomers the HS are semicrystalline in nature, in the vast majority of the cases with glass-transition and melting temperatures well above ambient temperature ($T_{room} < T_{g,\ HS} < T_{m,\ HS}$) while typically SS are usually in the rubbery state at room temperature with both the glass transition and melting temperatures well below room temperature ($T_{g,\ SS} < T_{m,\ SS} < T_{room}$).[13,17] On the basis of these considerations, in this work we wanted to modestly summarize in four PU cases, the possible situations in which each of the HS and SS display either amorphous (glassy-rubbery) or semicrystalline states at room temperature, and study its performance after orienting their molecules along the stretching axis, as in a fashion of spider silk spinning.

EXPERIMENTAL SECTION

Polyurethanes Synthesis. PU synthesis was realized via two shot polymerization method, in a four necked round-bottom reactor provided with a mechanical stirrer. The molecular weights of the polyols were 2020 and 1980 g mol^{-1} for the $SS_{rubb.}$ and $SS_{cryst.}$, respectively, as measured by backward hydroxyl titration. The polyols were made react with the diisocyanates under N_2 atmosphere. For 1,6-hexamethylene diisocyanate (HDI, Bayer) based PU the reaction time and temperature at this stage were 5 h and 100 °C according to previous kinetic studies.[18] The reaction with 5-isocyanato-1-(isocyanatomethyl)-1,3,3-trimethyl-cyclohexane (also known as Isophorone diisocyanate, IPDI, Bayer) was undergone for 24 h at 100 °C due to the lower reactivity of IPDI. The chain extender MDEA (Aldrich), was added at the end of this first stage and the mixture was stirred vigorously for 10 min and then poured to polytetrafluorethylene (PTFE) coated molds and pressed at 50 bar and 100 °C for 10 h. Hard segments based on IPDI were designated as $HS_{glass.}$ and hard segments based on HDI as $HS_{cryst.}$.The stoichiometric ratio diisocyanate:-poyol:MDEA was in all cases 3:1:2. Molecular weight distributions were calculated by size exclusion chromatography. All polyurethanes presented comparable molecular weights (see Table 1).

Table 1. Molecular Weight Distributions of Polyurethanes[a]

polyurethane	M_w	M_w/M_n	$M_{w,max}$
$HS_{glass.}$-$SS_{rubb.}$	47 520	2.1	323 496
$HS_{glass.}$-$SS_{cryst.}$	44 120	2.2	338 573
$HS_{cryst.}$-$SS_{rubb.}$	54 570	1.5	258 506
$HS_{cryst.}$-$SS_{cryst.}$	50 090	1.4	344 254

[a] M_w, weight average molecular weight; M_w/M_n, polydispersity index; $M_{w,max.}$, maximum M_w for longest chains in the samples.

Size Exclusion Chromatography (SEC). The molecular weights and molecular weight distributions were analyzed by size exclusion chromatography with a PerkinElmer chromatograph equipped with a binary pump and a refractive-index detector. The mobile phase was tetrahydrofuran (THF), and the separation was carried out with three columns packed with particle gels with different nominal pore sizes. Elution rate was of 1 mL min^{-1} at 30 °C. The samples were dissolved to 1 wt % in THF. The molecular weights and molecular weight distributions were based on a calibration curve with monodisperse polystyrene standards.

Differential Scanning Calorimetry (DSC). Differential scanning calorimetry (DSC) analysis between −60 and 250 °C was performed on a Mettler Toledo calorimeter at heating rates of 20 °C min^{-1} under constant N_2 flow. Stretched samples were pre-drawn for 10 min just before being analysed.

Polarized Optical Microscope (POM) and Atomic Force Microscope (AFM) Morphology Monitoring. Samples for POM studies were prepared by casting PU (50 mg mL^{-1}, THF) solutions into PTFE molds and controlled evaporation to produce films which ranged from 100 μm (low magnification images) to 10−50 μm for high magnification images showing spherullitic structures. For deforming the samples and holding them into microscopes set-ups a small stretching device consisting on two clamps and a screw guide with submillimetric precision to control strain, was designed and built (Suguz, Donostia-San Sebastián, Spain). AFM images were taken in the tapping mode in air at room temperature at different strains leaving to relax the samples at each strain for at least 10 min. The used aquipment was a Nanoscope IV, Dimension 3100 from Digital Instruments.

Dynamic Fourier Transformed Infrared Spectroscopy (FTIR). Samples for FTIR studies were prepared by casting PU (50 mg mL^{-1},THF) solutions into PTFE molds and controlled evaporation to produce films with thicknesses between 10 and 50 μm. Spectra at different strains were recorded on the transmission mode on a Nicolet-Nexus-FTIR spectrometer and obtained by averaging 20 scans between 4000 and 400 cm^{-1} with a resolution of 2 cm^{-1} after leaving relax the samples at least 10 min at measuring strains.

Materials Prestretching and Mechanical Testing. Samples for tensile testing were die cut from hot pressed films, prepared by heating up to 180 °C for 5 min with 1 ton of pressure, and slow cooling to 30 °C. Mechanical properties of films casted from tetrahydrofuran and hot-pressed films resulted to be similar. Cross-head deformation speed was of 100 mm min^{-1} for all samples. The prestretching experiments consisting on deforming the samples up to ∼1500% for 10 min. During that time stress were recorded at 0.5, 1, 2, 3, 5, 7, and 10 min for the stress-relaxation studies. The prestretched samples thicknesses and widths were measured again after the prestretching and then clamped in such a way that only the predrawn material suffered the tensile stress.

Molecular Models. Molecular models were drawn using ACD/ChemSketch (Freeware version) from ACD/Labs.

RESULTS AND DISCUSSION

The four PU were synthesized in our lab by the common two-shot polymerization method[17] and temperatures and times were chosen according to previous tests so to achieve high molecular weight PU macromolecules, as can be observed by size exclusion chromatography data gathered in Table 1. As seen in Table 1 the M_w was slightly lower for polyurethanes based on isophorone diisocyanate, IPDI, (those with $HS_{glass.}$) than those based on 1,6-hexamethylene diisocyanate, HDI, (those with $HS_{cryst.}$). This fact is related to the lower reactivity of IPDI respect to HDI. The polydispertity was also higher for IPDI-based polyurethanes and this is also related to the lower reactivity of IPDI respect to HDI. In any case M_w of polyurethanes were close enough to associate the differences observed in this work merely to polyurethanes segments architecture variations.

The chemical structure of the polyurethanes is sketched in Figure 1a. The changing parameters between different PU were the diisocyanate and the polyol employed. The diisocyanates were either HDI or IPDI. The SS employed were either a castor oil derived polyester diol consisting on sebacic acid copolymerized with 1,4-butanediol ($SS_{cryst.}$) or a poly(ester-*co*-carbonate) diol consisting on 1,6-hexamethylene carbonate copolymerized with caprolactone ($SS_{rubb.}$). The subscripts cryst. and rubb. describe the morphology state of each SS at room temperature, crystalline ($T_{room} < T_{m,\ SS}$) and rubbery ($T_{g,\ SS} < T_{m,\ SS} < T_{room}$), respectively. The chain extender was in all cases *N*-methyl-diethanolamine (MDEA). Hard segments formed by MDEA and HDI were semicrystalline ($HS_{cryst.}$) with $T_{g,HS} > T_{room}$ and a $T_{m,\ HS} < T_{room}$, while hard segments formed by MDEA and IPDI were amorphous at the glassy state ($HS_{glass.}$)

dx.doi.org/10.1021/ma300397e | Macromolecules 2012, 45, 3436−3443

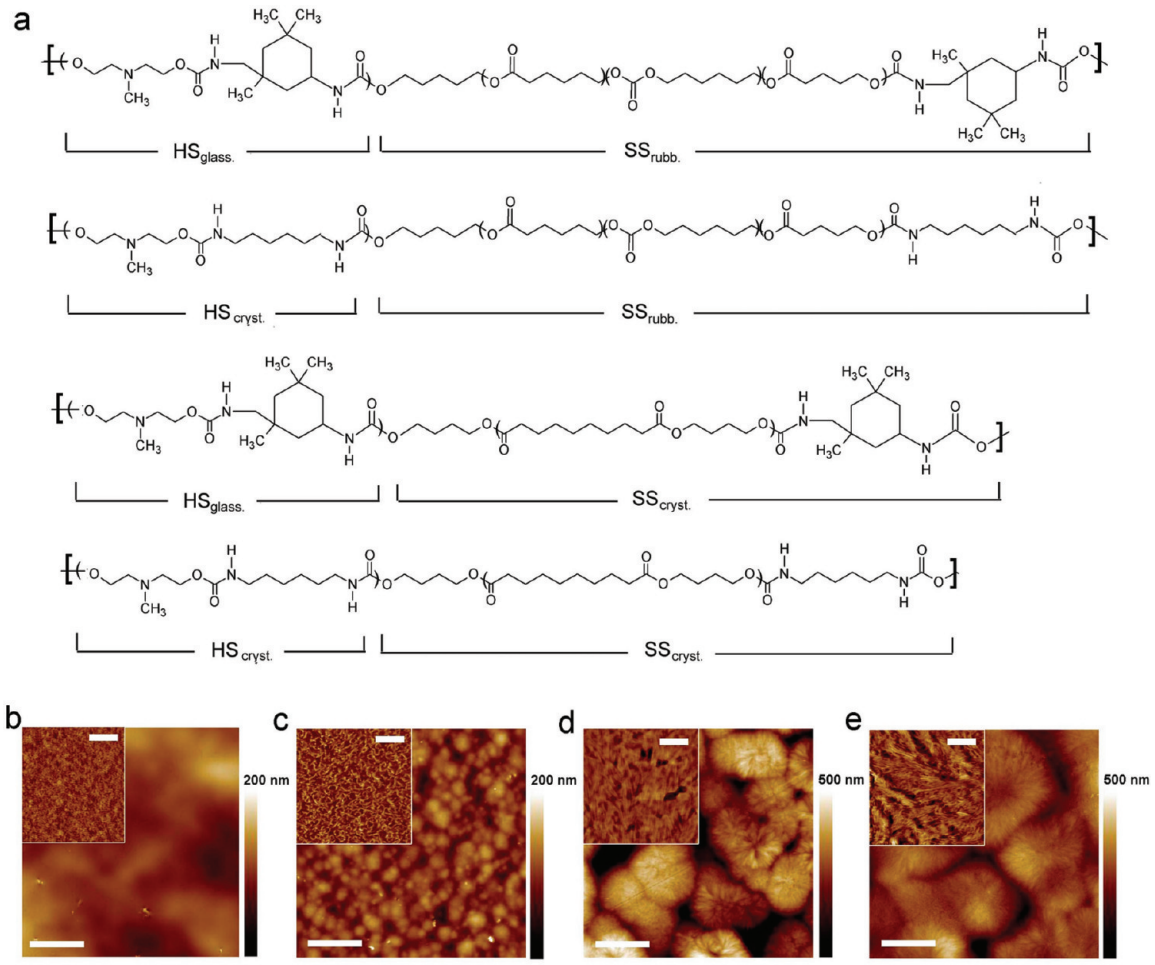


Figure 1. (a) Sketches of polyurethane chain architecture and materials morphology as observed by AFM of (b) $HS_{glass.}$-$SS_{rubb.}$, (c) $HS_{cryst.}$-$SS_{rubb.}$, (d) $HS_{glass.}$-$SS_{cryst.}$, and (e) $HS_{cryst.}$-$SS_{cryst.}$. The height images sizes are 40 μm × 40 μm scan area with a scale bar of 10 μm. The inset images are 1 μm × 1 μm phase images with scale bars of 250 nm.

with $T_{g,\ HS} > T_{room}$. The morphology of each of the polyurethane casted from solution (see Experimental Section) as analyzed by atomic force microscopy (AFM) is included nearby each structure in Figure 1b–e. In the large scale height images it can be observed the increasing tendency to form bigger spherullites as the overall proportion of crystalline fraction is increased from Figure 1b to Figure 1e. In the small range phase images, it is seen that the microphase morphology varies from nanometric scale hard globules (related to HS_{glass} domains) dispersed in the amorphous $SS_{rubb.}$ matrix, in Figure 1b, to worm-like nanocrystals consisting on partially crystallized $HS_{cryst.}$ nanodomains dispersed in $SS_{rubb.}$ matrix, in Figure 1c. Comparing images in Figure 1d and Figure 1e it is seen that both materials develop large lamellas due to the soft segment crystallizing tendency, although in Figure 1e larger, brighter and more defined lamellas are observed due to the higher tendency of the $HS_{cryst.}$ to crystallize than $HS_{glass.}$ (see Figure 2).

Macromolecular alignment was attained by prestretching the samples at 1500% strain for 10 min. At this time stress relaxation with time leveled off down to a quasi-equilibrium stress value, or very slow decrease with time (see Supplementary Figure §1), indicating that at this time most of the polymer chains reached minimum energy conformations and organization for the given strain. Although molecular processes occurring when drawing are complex in PU elastomers it is generalized that arrangements and reorientation of hard domains and alignment and crystallization of soft domains take part.[19,20] Morphology was also studied by thermal analysis (DSC) of nonstretched and stretched samples. Figure 2 show thermograms of non stretched and stretched specimens. Stretching $HS_{glass.}$-SS_{rubb} leads to no noticeable morphological changes detected by DSC. This can be attributed to the amorphous nature of both blocks which cannot promote supramolecular organization upon stretching while, stretching $HS_{cryst.}$-$SS_{rubb.}$ leads to supramolecular organization of $HS_{cryst.}$ segments into an ordered phase with melting transition around 225 °C. Also a mechanically driven phase mixing between $HS_{cryst.}$ and $SS_{rubb.}$ produced an increase of $SS_{rubb.}$ phase glass transition temperature about 3 °C.

Stretching $HS_{glass.}$-$SS_{cryst.}$ leads to $SS_{cryst.}$ strain induced crystallization, as can be observed by the increased area of the $SS_{cryst.}$ phase melting transition around 50 °C. No noticeable changes in transition associated with $HS_{glass.}$ were observed. The increase of the lower melting peak phase enthalpy in the melting transition associated with soft segments, when stretching, suggests a favored formation of the less ordered structure appreciated as a low temperature shoulder peak in both nonstretched and stretched materials. Stretching of $HS_{cryst.}$-$SS_{cryst.}$ produces both a $SS_{cryst.}$ and $HS_{cryst.}$

dx.doi.org/10.1021/ma300397e | Macromolecules 2012, 45, 3436–3443

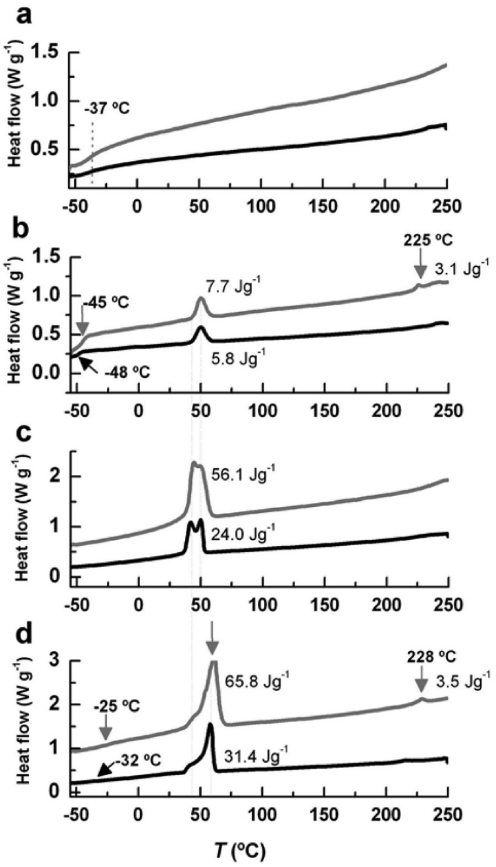


Figure 2. Differential scanning calorimetry (DSC) of nonstretched (black) and prestretched samples to 1500% for 10 min (gray) of (a) $HS_{glass.}$-$SS_{rubb.}$, (b) $HS_{cryst.}$-$SS_{rubb.}$, (c) $HS_{glass.}$-$SS_{cryst.}$ and (d) $HS_{cryst.}$-$SS_{cryst.}$.

ordered phases increase in melting enthalpies, consequence of a better alignment of both segments along the strain direction.

Under the cross-polarized microscope it is observed a change from spherulitic structure to a pure fibrous structure as samples are stretched, more clearly seen in samples with crystallizable segments (Figure 3a and Supplementary Figure §2). Both morphologies contain high level of ordered substructures responsible of birefringence, but with obvious differences in higher levels of macromolecular organization. In the case of completely amorphous polyurethane ($HS_{glass.}$-$SS_{rubb.}$) no brightness contrast is observed after yield, what can be related to the disruption of the enthalpically driven low energy globular structures of $HS_{glass.}$ attained by the slow cooling at processing, and incapability of both segments to undergone self-organization into high level ordered structures with capability to produce optical interferences.

Evolution of morphology with strain at lower scales was also monitored by AFM with samples supported at different strains with a home-designed extensometer (see Experimental Section). Figure 3b,c present AFM phase images of $HS_{cryst.}$-$SS_{cryst.}$ and $HS_{glass.}$-$SS_{cryst.}$ nanostructure at 600% of deformation. While in the case of $HS_{cryst.}$-$SS_{cryst.}$ a clear nanofibrous morphology with fibers separated by ~50 nm (see inset of Figure 3b) the $HS_{glass.}$-$SS_{cryst.}$ strained up to 600% did not present a fibrous morphology at the nanoscale (Figure 3c). This corresponds to a lack in ordering upon drawing due to the $HS_{glass.}$ restricted mobility arising from the intrinsic cyclic nature of IPDI ring and for its bulky methyl groups which hinder crystallization mechanisms.[21] Both the microstructure and nanostructure seemed to present a fractal like fibrous structure, which in addition evolves in an opposite direction producing wider and more separated micropits at the micro level and thinner and more packed fibrils at the nano level (see Supplementary Figure §3). Changes at the micro level are related to spherullite disruption and orientation of the lamellae along the strain direction,[22] and to the collapse of adjacent

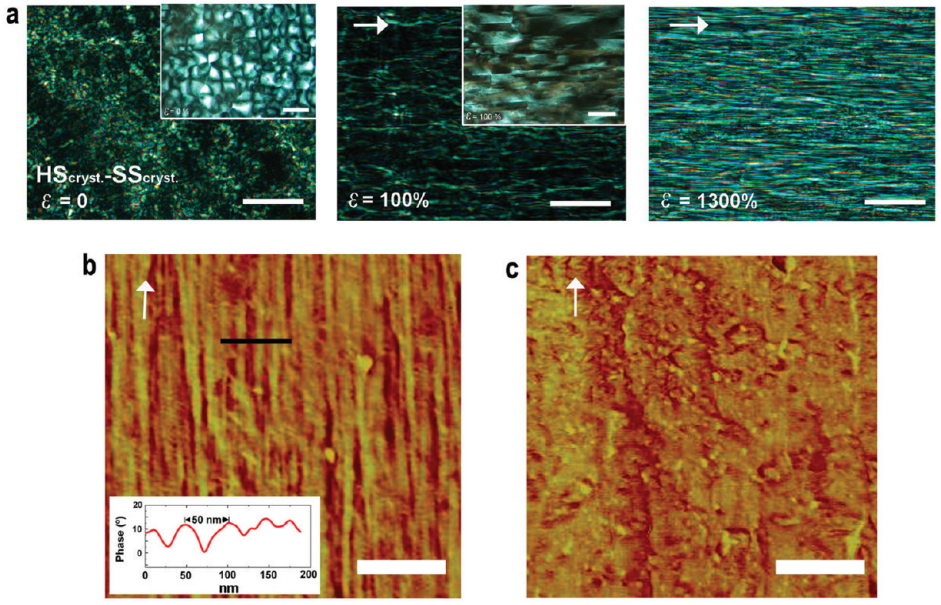


Figure 3. Morphology variation with strain. (a) Cross-polarized optical microscopy images of $HS_{cryst.}$-$SS_{cryst.}$ morphology variation with the indicated strain. The scale bars correspond to 40 μm and to 20 μm for the inset images. (b) AFM 1 μm × 1 μm phase image of the $HS_{cryst.}$-$SS_{cryst.}$ material at 600% strain, indicating the phase profile for a specific set of fibrils indicated with a black line. (c) AFM 1 μm × 1 μm phase image of $HS_{glass.}$-SS_{cryst} material at 600% for comparison with "b". The scale bars of the AFM images are of 250 nm. White arrows indicate strain direction.

dx.doi.org/10.1021/ma300397e | *Macromolecules* 2012, 45, 3436–3443

spherullites due to normal forces arising perpendicular to strain direction. Lack of fibrous nano level order was observed in $HS_{glass.}$-$SS_{cryst.}$ with small range phase AFM images at different elongations.

Molecular conformation evolution with strain was monitored by dynamic Fourier-transform infrared spectroscopy (FTIR) (see Experimental Section). Figure 4a,b show urethane N−H

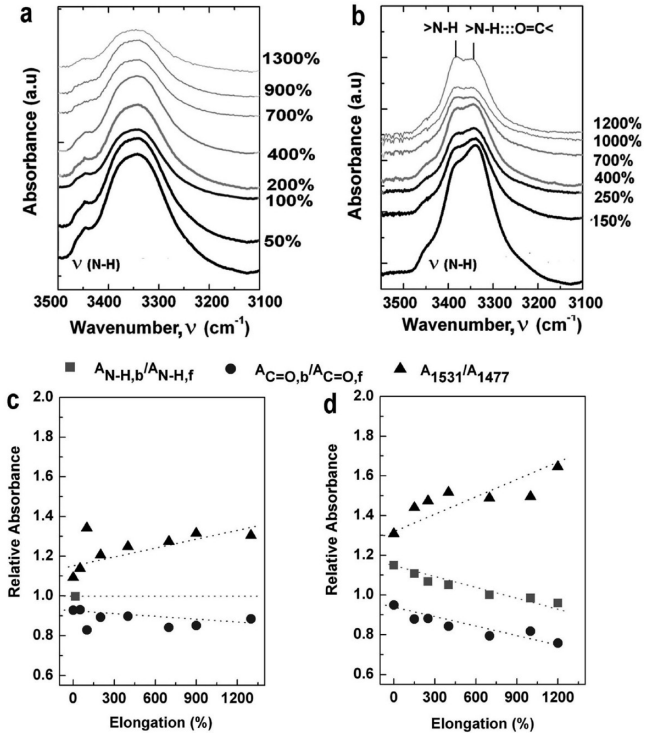


Figure 4. Dynamic FTIR analysis of hydrogen bonding changes with strain. FTIR absorption region of N−H stretching bands for (a) $HS_{glass.}$-$SS_{cryst.}$ and (b) $HS_{cryst.}$-$SS_{cryst.}$ at different strains. Relative absorbancies between the indicated functional groups at different strains for (c) $HS_{glass.}$-$SS_{cryst.}$ and (d) $HS_{cryst.}$-$SS_{cryst.}$.

stretching region of $HS_{glass.}$-$SS_{cryst.}$ and $HS_{cryst.}$-$SS_{cryst.}$, respectively. It is seen that while the $HS_{glass.}$-$SS_{cryst.}$ present a single wide peak which do not vary in shape with strain, $HS_{crys.}$-$SS_{cryst.}$ presents a two peak absorption band typical from partially hydrogen bonded amides and urethanes.[17] In addition, in the later, the relation between hydrogen bonded N−H peak at 3320 cm^{-1} and non-hydrogen bonded N−H peak varies with strain, with a tendency to increase the non-hydrogen bonded N−H absorbance over the hydrogen bonded. In the carbonyl (C═O) region, both the $HS_{glass.}$-$SS_{cryst.}$ and $HS_{cryst.}$-$SS_{cryst.}$ PUs developed higher absorbancies of non-hydrogen bonded carbonyl stretching peak at 1730 cm^{-1} with increasing strain. Parts c and d of Figure 4 present the ratio of absorbancies between different peaks at different strains. For both PUs the ratio between hydrogen bonded carbonyls and non-hydrogen bonded carbonyls, $A_{C=O,b}/A_{C=O,f}$ trends to decrease what, considering molar absorptivities of different species vary in the same ratio with strain, means an overall disruption of hydrogen bonded carbonyls. The ratio between hydrogen bonded and non hydrogen bonded N−H, $A_{N-H,b}/A_{N-H,f}$ only trends to decrease with strain for the $HS_{cryst.}$-$SS_{cryst.}$ PU what indicates N−H group is not as much involved in macromolecular conformation changes with strain in $HS_{glass.}$-$SS_{cryst.}$ as in $HS_{cryst.}$-$SS_{cryst.}$. The tendency to hydrogen bonding disruption upon stretching has also been reported by other researchers, and has been attributed to either lamellae disruption[19] and secondary structures intramolecular hydrogen bonding breakage.[23] The ratio between bending bands of N−H at 1531 cm^{-1} and C−H at 1475 cm^{-1} is higher for $HS_{cryst.}$-$SS_{cryst.}$ than $HS_{glass.}$-$SS_{cryst.}$ due to hard segment composition differences, but increase of the ratio also appears higher, corresponding again to a more profound conformational change of this structure. Band peaks position, which are associated with functional groups bonds energetic levels[24] can be shifted toward different position depending on chemical environment[25] or mechanical stress.[24] In Figure 5a−c, we see that specific peaks of N−H stretching

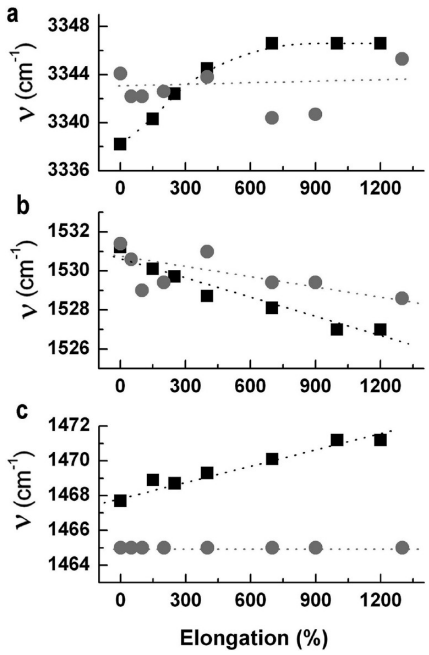


Figure 5. Wavenumber (ν) frequency shifts of peaks from stretching and bending absorption bands of (a) N−H stretching, (b) N−H bending and (c) C−H bending functional groups for both $HS_{glass.}$-$SS_{cryst.}$ (gray circles) and $HS_{cryst.}$-$SS_{cryst.}$ (black squares).

and bending and C−H bending are shifted with strain more pronouncedly for $HS_{cryst.}$-$SS_{cryst.}$. Corresponding these absorption bands to groups embedded within the PU hard segments it is concluded that hard segments of $HS_{cryst.}$ segments participate more on PU overall deformation than $HS_{glass.}$. Figure 6 sketches the above conclusions for spherullitic lamella disruption by the action of the stress on both $HS_{cryst.}$-$SS_{cryst.}$ and $HS_{glass.}$-$SS_{cryst.}$ giving ordered and less ordered fibrils, respectively. It also presents the molecular most stable conformation of both $HS_{glass.}$ and $HS_{cryst.}$. It is observed that urethane groups (OCONH) of $HS_{cryst.}$ repetitive units lay on very similar planes to respect to the chain axis, while in the case of $HS_{glass.}$ OCONH groups lay on very different planes, which obviously restrict inter chain molecular associations.

Tensile mechanical properties of non-prestretched PU were strongly dependent on molecular composition (Figure 7). Materials mechanical properties are resumed in Table 2. The materials with rubbery SS presented low elastic modulus, E, and yield stresses, σ_y, and among them the strength was higher for the $HS_{cryst.}$-$SS_{rubb.}$ because of the partial crystallinity of the HS, which holds the structure via thermally reversible pseudocross-

dx.doi.org/10.1021/ma300397e | Macromolecules 2012, 45, 3436−3443

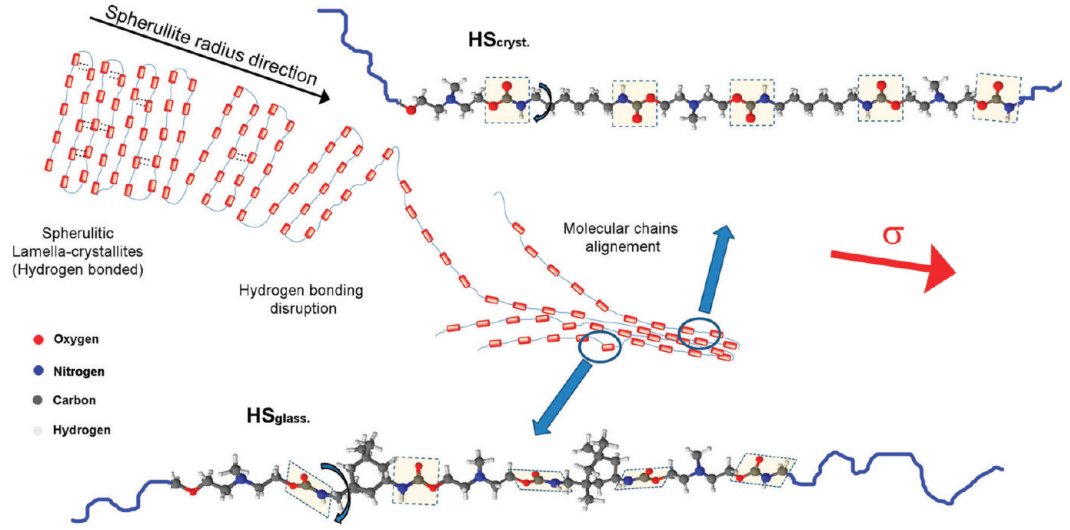


Figure 6. Model for molecular rearrangement of $HS_{glass.}$-$SS_{cryst.}$ and $HS_{cryst.}$-$SS_{cryst.}$ chains upon stretching. Also shown the most stable molecular conformations of $HS_{glass.}$ and $HS_{cryst.}$ segments and the relative positioning of consecutive urethane groups.

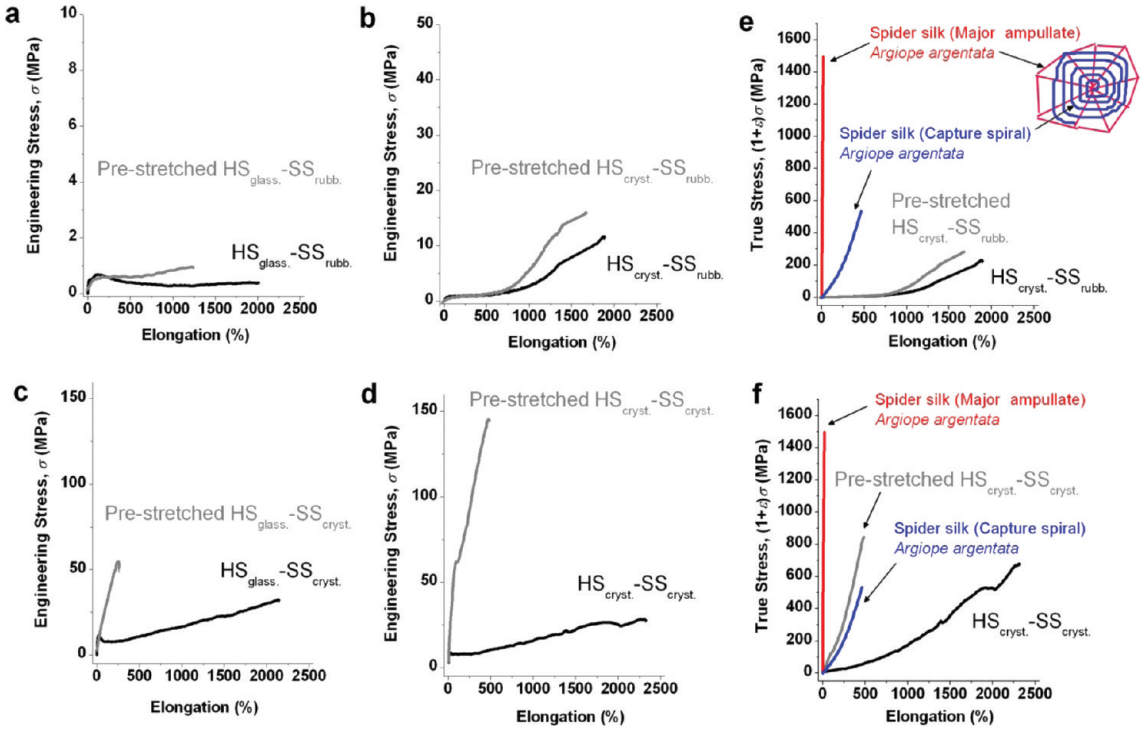


Figure 7. Stress−strain curves of non stretched (black) and prestretched (gray) representative samples of (a) $HS_{glass.}$-SS_{rubb}, (b) $HS_{cryst.}$-SS_{rubb}, (c) $HS_{glass.}$-$SS_{cryst.}$ and (d) $HS_{cryst.}$-$SS_{cryst.}$. In (e) and (f) representative true stress curves of $HS_{cryst.}$-$SS_{rubb.}$ and $HS_{cryst.}$-$SS_{cryst.}$ are plotted along with true stress curves for *Argiope argentata* spider silks.[3] True stress was defined considering a constant samples volume between clamps, as engineering stress (σ) multiplied by $(1 + \varepsilon)$, where ε is the nominal strain (mm mm^{-1}).[26]

Table 2. Resume of the Mechanical Properties of Original and Pre-Drawn Polyurethanes

Polyurethane	E (MPa)	σ_y (MPa)	ε_y (%)	σ_{max} (MPa)	ε_{max} (%)	T (MJ m^{-3})
$HS_{glass.}$-$SS_{rubb.}$	1.3 ± 0.5	0.6 ± 0.1	143 ± 35	0.6 ± 0.1	2500 ± 500	6 ± 2
$HS_{glass.}$-$SS_{rubb.}$-drawn	1.7 ± 0.6	0.7 ± 0.1	90 ± 6	1.5 ± 0.4	1040 ± 170	9 ± 1
$HS_{cryst.}$-$SS_{rubb.}$	2.1 ± 0.3	0.9 ± 0.2	120 ± 45	10.5 ± 3.8	2000 ± 380	75 ± 44
$HS_{cryst.}$-$SS_{rubb.}$-drawn	2.5 ± 0.3	1.2 ± 0.1	78 ± 25	20.4 ± 3.4	1530 ± 460	260 ± 81
$HS_{glass.}$-$SS_{cryst.}$	106.0 ± 27.0	10.6 ± 0.5	21 ± 2	28.4 ± 3.7	2100 ± 190	337 ± 34
$HS_{glass.}$-$SS_{cryst.}$-drawn	44.7 ± 6.9	44.2 ± 10.5	208 ± 41	45.1 ± 10.8	221 ± 41	68 ± 10
$HS_{cryst.}$-$SS_{cryst.}$	61.4 ± 12.0	8.6 ± 0.6	25 ± 6	26.9 ± 2.1	2070 ± 290	350 ± 57
$HS_{cryst.}$-$SS_{cryst.}$-drawn	98.3 ± 14.4	58.8 ± 2.7	95 ± 7	147 ± 14	480 ± 40	425 ± 28

dx.doi.org/10.1021/ma300397e | *Macromolecules* 2012, 45, 3436−3443

linking sites, being the most typical case of PU elastomer.[17] The materials with crystalline SS presented higher modulus and yield stresses, being $HS_{glass.}$-$SS_{cryst.}$ stiffer than $HS_{cryst.}$-$SS_{cryst.}$ but both with similar deformability, ε_{max} and strength, σ_{max}, between them. When prestretching the materials with SS_{rubb}, $HS_{glass.}$-$SS_{rubb.}$ lead to an increase of strength from 0.6 ± 0.1 MPa to 1.5 ± 0.5 MPa while $HS_{cryst.}$-$SS_{rubb.}$ leads to an increase in strength from 10 ± 4 MPa to 20 ± 3 MPa. Variations in mechanical properties of $HS_{glass.}$-$SS_{rubb.}$ were not as significant as variations of $HS_{cryst.}$-$SS_{rubb.}$, especially if we consider the toughness, which varied from 6 ± 2 to 9 ± 1 MJ m^{-3} for the $HS_{glass.}$-$SS_{rubb.}$ and from 75 ± 44 to 260 ± 81 MJ m^{-3} for the $HS_{cryst.}$-$SS_{rubb.}$. This fact was attributed as the aforementioned $HS_{cryst.}$ partial mobility and capability to develop strain induced crystallization. In parallel, prestretching the materials with $SS_{cryst.}$ lead to a stiffening just in the case of $HS_{cryst.}$-$SS_{cryst.}$. In the case of $HS_{glass.}$-$SS_{cryst.}$, despite having a crystalline phase and displaying strain induced anisotropy the elastic modulus decreased respect the nonstretched sample. This is attributed to the disruption of enthalpically driven low energy $HS_{glass.}$ structures upon prestretching, which afterward do not contribute to macromolecular fibrillar organization as $HS_{cryst.}$ does (see Figure 3). In this material the strength was also increased, and this is related to the induced anisotropy and increased overall crystallinity (see Figure 2). In the case of $HS_{cryst.}$-$SS_{cryst.}$ both modulus and strength increased notably (from 59 ± 6 MPa to 98 ± 14 MPa and from 27 ± 2 MPa to 147 ± 14 MPa, respectively). Despite the relatively high modulus and strength for being a thermoplastic, this PU extensibility was as large as 480%. This material presented engineering strengths similar to tendon collagen,[4] but was much more deformable (see Supplementary Table §1). Because of this large deformability a true stress plot was considered convenient in order to account for the cross-section shrinkage occurring during deformation (Figure 7e,f). The combined strength and deformability properties accounted for its remarkable toughness of 425 ± 28 MJ m^{-3} what corresponds to about 2−3 times that of *Araneus diadematus* major ampullate (MA) silk,[3,4,7] about 5−6 times that of *Argiope argentata* capture spiral silk[3] (see Supplementary Table §1), and to authors knowledge the toughest synthetic material reported.

CONCLUSIONS

Four polyurethanes with different segmental nature were synthesized and analyzed mechanically. Mechanical performance of the materials after predrawing was related to their molecular structure. Crystallizable segments resulted to provide higher tensile properties than those based on amorphous segments in spite of these having cyclic nature and bulky groups. In the case of hard segments this has been observed to be due to the capability of semicrystalline hard segments to orient along the stress direction providing macromolecular organization in detriment of hydrogen bonding. Mobility of semicrystalline hard segments allowed transition from spherulitic-lammelar structure to oriented ordered fibrilar organization. Materials combining semicrystalline soft segments with semicrystalline hard segments exhibit relatively high stiffness, great deformability typical from elastomers and high strengths typical of engineered thermoplastics. These combined properties allow proposing this type of engineered PU as materials with potential applicability in different areas like tissue engineering or high loads bearing applications. The molecular design considerations developed in this work pave the way to the future synthesis of new materials with mechanical properties facing traditional confrontations between deformation and strength.

ASSOCIATED CONTENT

Supporting Information

Plots of stress relaxation of polyurethanes, cross-polarized optical microscopy (POM) images of polyurethanes, and morphology variation with strain and a resume of mechanical properties of some high performance fibers and materials. This material is available free of charge via the Internet at http://pubs.acs.org/.

AUTHOR INFORMATION

Corresponding Author

*Telephone: (0034)-943-017185. E-mail: arantxa.eceiza@ehu.es.

Notes

The authors declare no competing financial interest.

ACKNOWLEDGMENTS

B.F.-d'A. acknowledges University of the Basque Country and the (UPV/EHU) postdoc grant "Ayuda a la Especialización de Doctores" for financial support and all authors acknowledge the General Research Services of the University of the Basque Country (SGIker), and especially the *Macroconducta-Mesoestructura-Nanotecnología* unit, for their technical support. Authors also acknowledge funding from the Basque Government through SAIOTEK 10-S-PE10UN22 and SAIOTEK 11-S-PE11UN132 programs and in the frame of *Grupos Consolidados* (IT-365-07).

DEDICATION

This article is dedicated to Proffesor Dr. Iñaki B. Mondragon, who passed away just after his contribution to this work and who founded the research group "Materiales + Tecnologías" (GMT) in 1988. His devotion to science and humanity filled us with lifelong inspiration.

REFERENCES

(1) Simmons, A. H.; Michaes, C. A.; Jelinski, L. W. *Science* **1996**, *271*, 84−87.
(2) Liu, Y.; Shao, Z.; Vollrath, F. *Nat. Mater.* **2005**, *4*, 901−905.
(3) Blackledge, T. A.; Hayashi, C. Y. *J. Exp. Biol.* **2006**, *209*, 2452−2461.
(4) Omenetto, F. G.; Kaplan, D. L. *Science* **2010**, *329*, 528−531.
(5) Agnarsson, I.; Kuntner, M.; Blackledge, T. A. *PLoS ONE* **2010**, *5*, 1−8.
(6) Liu, Y.; Spooner, A.; Porter, D.; Vollrath, F. *Biomacromolecules* **2008**, *9*, 116−121.
(7) Elices, M.; Guinea, G. V.; Plaza, G. R.; Karatzas, C.; Riekel, C.; Agulló-Rueda, F.; Daza, R.; Pérez-Rigueiro, J. *Macromolecules* **2011**, *44*, 1166−1176.
(8) Ritchie, R. O. *Nat. Mater.* **2011**, *10*, 817−822.
(9) Fernández-d'Arlas, B.; Khan, U.; Rueda, L.; Coleman, J. N.; Mondragon, I.; Corcuera, M. A.; Eceiza, A. *Compos. Sci. Technol.* **2011**, *71*, 1030−1038.
(10) Lynd, N. A.; Oyerokun, F. T.; O'Donoghue, D. L.; Handlin, D. L.; Fredrickson, G. H. *Macromolecules* **2010**, *43*, 3479−3486.
(11) Guinea, G. V.; Elices, M.; Pérez-Rigueiro, J.; Plaza, G. R. *J. Exp. Biol.* **2004**, *208*, 25−30.
(12) Ocando, C.; Tercjak, A.; Martín, M. D.; Ramos, J. A.; Campo, M.; Mondragon, I. *Macromolecules* **2009**, *42*, 6215−6224.

(13) Liff, S. M.; Kumar, N.; McKinley, G. H. *Nat. Mater.* **2007**, *6*, 76−83.
(14) Holland, C.; Terry, A. E.; Porter, D.; Vollrath, F. *Nat. Mater.* **2006**, *5*, 870−874.
(15) Lazaris, A.; Arcidiacono, S.; Huang, Y.; Zhou, J. F.; Duguay, F.; Chretien, N.; Welsh, E. A.; Soares, J. W.; Karatzas, C. N. *Science* **2002**, *18*, 472−476.
(16) Fernández-d'Arlas, B.; Rueda, L.; Fernández, R.; Khan, U.; Coleman, J. N.; Mondragon, I.; Eceiza, A. *Soft Mater.* **2011**, *9*, 79−93.
(17) Fernández-d'Arlas, B.; Rueda, L.; de la Caba, K.; Mondragon, I.; Eceiza, A. *Polym. Eng. Sci.* **2008**, *48*, 519−529.
(18) Fernández-d'Arlas, B.; Rueda, L.; Stefani, P. M.; de la Caba, K.; Mondragon, I.; Eceiza, A. *Thermochim. Act.* **2007**, *459*, 94−103.
(19) Waletzko, R. S.; Korley, L. T.; Pate, B. D.; Thomas, E. L.; Hammond, P. T. *Macromolecules* **2009**, *42*, 2041−2053.
(20) Christenson, E. M.; Anderson, J. M.; Hiltner, A.; Baer, E. *Polymer* **2005**, *46*, 11744−11754.
(21) Kijio, K.; Kakamura, S.; Furukawa, M. *Polymer* **2004**, *45*, 8147−8152.
(22) Peterlin, A. In *Man made fibers, science and technology*; Marks, H. F., Atlas, S. M., Cernia, E., Eds.; John Wiley and Sons: New York, 1967; Vol. *1*, pp 283−340.
(23) Melning, V.; Apostu, M. O.; Tura, V.; Ciobanu, C. *J. Membr. Sci.* **2005**, *267*, 58−67.
(24) Papadopoulos, P.; Sölter, J.; Kremer, F. *Eur. Phys. J. E* **2007**, *24*, 193−199.
(25) Fafarman, A. T.; Sigala, P. A.; Herschlag, D.; Boxer, S. G. *J. Am. Chem. Soc.* **2010**, *37*, 12811−12813.
(26) Ward, I. M.; Hadley, D. W. In *An introduction to the mechanical properties of solid polymers*, 1st ed.; John Wiley and Sons: Chichester, England, 1993; pp 213−218.

Macromolecules

Article

pubs.acs.org/Macromolecules

Grafting of Polyester onto Graphene for Electrically and Thermally Conductive Composites

Zhenghai Tang,[†] Hailan Kang,[‡] Zuoli Shen,[†] Baochun Guo,*[,†] Liqun Zhang,*[,‡,§] and Demin Jia[†]

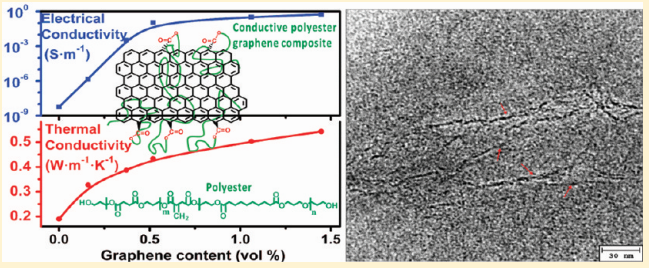
[†]Department of Polymer Materials and Engineering, South China University of Technology, Guangzhou 510640, P. R. China

[‡]Key Laboratory of Beijing City for Preparation and Processing of Novel Polymer Materials, Beijing University of Chemical Technology, Beijing 100029, P. R. China

[§]State Key Laboratory of Organic/Inorganic Composites, Beijing University of Chemical Technology, Beijing 100029, P. R. China

Supporting Information

ABSTRACT: Many reported polymer/graphene composites, even some with excellent graphene dispersion, do not possess impressive conductivity, which may be due to the failure in forming interconnected conductive paths. In this work, a kind of bio-based polyester (BE) is synthesized by polycondensation between plant-derived diols and diacids. It is then grafted onto graphene oxide (GO) via the easterification between hydroxyls of BE and carboxyls of GO. Subsequently, the grafted GO is subjected to reduce by vitamin C. Because of the presence of terminal hydroxyl group in both ends of the BE chains and multiple carboxyl groups on GO, the grafts form specific spatial interconnection structure in BE matrix. The resulting BE/graphene composites possess impressive low threshold percolation of electrical conductivity, in combination of high thermal conductivity.



INTRODUCTION

Graphene, a single-atom-thick sheet of hexagonally arrayed sp^2-bonded carbon atoms, has been under the spotlight owning to its intriguing and unparalleled physical properties.[1] Because of its novel properties, such as exceptional thermal conductivity,[2] high Young's modulus,[3] and high electrical conductivity,[4] graphene has been highlighted in fabricating various micro-electrical devices, batteries, supercapacitors, and composites.[5−7] However, the practical applications of graphene are greatly hampered by its preparation and dispersity in solvents. On one hand, many strategies, including mechanical exfoliation,[1] liquid-phase exfoliation,[8] chemical vapor deposition,[9] and reduction of GO,[10] have been developed to produce graphene. Among these methods, reduction of GO is a promising method to obtain bulk graphene, and it has been regarded as an efficient way to fabricate graphene-based composites for the versatile surface chemistry of GO.[11] On the other hand, graphene has low solubility in both aqueous and organic solutions, which poses a persistent difficulty to manipulate graphene in solutions in which many chemical processes occur. Thereby, functionalization of graphene is widely adopted to improve its dispersibility/processability.[12−14]

Integration of graphene and its derivations into polymer has been highlighted, from the point views of both the spectacular improvement in mechanical, electrical properties, and the low cost of graphite.[15,16] However, the large surface area of graphene and strong van der Waals force among them result in severe aggregation in the composites matrix. To obtain satisfied performance of the final graphene/polymer composites, the issues of the strong interfacial adhesion between graphene−matrix and well dispersion of graphene should be addressed.

GO sheets bear various oxygen-containing groups, mainly epoxides and hydroxyls on their basal planes and carboxyls on the edges, which can facilitate the dispersion of GO in water. Through the noncovalent strategy, chemical reduction of GO can be still stably suspended in water in the presence of dispersants or stabilizers. Recently, GO and reduced graphene have been successfully incorporated into water-soluble polymers such as poly(vinyl alcohol), chitosan, cellulose via simple solution mixing by using water as the media. Unfortunately, similar to carbon nanotubes, the noncovalent methods on graphene are not efficient to afford stable graphene dispersion in organic solvents.[17] Thus, the route of fabrication of graphene/organic-soluble polymer composites based on noncovalent strategy does not work. Alternatively, chemical functionalization of graphene is highly pursued, and it includes "grafting from" or "grafting to" strategies. Through the "grafting-from" approach, vinyl polymer molecules such as polystyrene and poly(methyl acrylate) were successfully bound to the basal plane of graphene, by which the excellent compatibility between graphene and polymer hosts is achieved.[18,19] Nevertheless, in most of the cases, the functional characteristics of the resulting composites such as electrical and

Received: March 5, 2012
Revised: April 8, 2012
Published: April 13, 2012

ACS Publications © 2012 American Chemical Society

thermal conductivity imparted by graphene have not been reported.[19−21] This may be due to that dense polymer chains cover the basal plane of graphene and impede the electron and phonon transfer in the composites. In addition, the "grafting from" method creates the new bonding between graphene and the attached polymer, causing additional defects on the graphitic lattice and weakening the intrinsic properties of graphene, which maybe another origin for the modestly improved in the conductive performance.[22] In contrast, based on the "grafting to" approach, polymer chains can be covalently bonded onto graphene by esterification or amidation; these reactions are conducted between preformed functionalized polymer chains and functional groups on GO edge, which has the advantage of preserving the graphitic lattic. To the best of our knowledge, the studies concerning the "grafting-to" approach and subsequent fabrication of composites are relatively few, which may be due to the difficulty in matching the unique surface chemistry of GO with the specific functionality on polymer chains. More importantly, there are many active sites on preformed polymer and GO sheet, and the selectivity of chemical reaction between these active sites is hardly controlled; thus, the final structure of grafts is ill-defined. For example, the multifunctionalized groups of the preformed polymer chains inevitably act as covalent cross-linker between graphene sheets to form the interconnection of graphene. Although the concept that the well-defined structure and perfect dispersion of graphene in host matrix is essential for the electrical and thermal performances of the matrix is prevalent, we propose that the formation of graphene network in polymer host is the root origin for significantly increased conductivities.

In terms of the above reason, the hydroxyl-terminated bio-based polyester (BE) was synthesized through polycondensation using the industrially available bio-based succinic acid, sebacic acid, itaconic acid, and 1,3-propylenediol as the starting materials. 1,3-Propenediol, succinic acid, and itaconic acid are produced industrially by fermentation of carbohydrates such as glucose. Sebacic acid is derived from castor oil which is a fully sustainable industrial building block. The obtained BE was then coupled onto GO sheets via the "grafting to" method, and the grafted GO was subjected to reduction to recovery its conjugated structure. The final BE/graphene composites exhibit high electrical and thermal conductivities. The uniform dispersion of graphene, strong interfacial covalent bonding between graphene and BE, and the connection of graphene sheets are responsible for the concurrently improved electrical and thermal conductivities.

EXPERIMENTAL SECTION

Materials. Succinic acid (purity of 98.0%), sebacic acid (purity of 99.0%), and itaconic acid (purity of 99.9%) were supplied by Hunan Rivers Bioengineering, Tianjing Damao Chemicals, and Qingdao Kehai Biochemistry, respectively. 1,3-Propylenediol with purity of 99.5% was provided by Sinopec Yangzi Petrochemical. Tetra-*n*-butyl titanate (purity of 98%) and *p*-hydroxyanisole were obtained from SinoPharm Group. Graphite powder (<20 μm) was purchased from Shanghai Colloidal Co. Ltd. 1-Ethyl-3-(3-(dimethylamino)propyl)-carbodiimide (EDC) and 4-(dimethylamino)pyridine (DMAP) were purchased from Sigma-Aldrich Trading Co. Ltd. The reagents for the oxidation of graphite including concentrated sulfuric acid (H_2SO_4), hydrogen peroxide (H_2O_2), potassium permanganate ($KMnO_4$), and sodium nitrate ($NaNO_3$) were analytically pure and used as received.

Synthesis of BE. The reaction mixture with total diols/diacids molar ratio of 1.1 and succinic acid/sebacic acid/itaconic acid molar ratio of 0.72/0.18/0.1 was charged into a 150 mL three-necked flask, and *p*-hydroxyanisole (0.5 wt % relative to the reactants) was added as free radical inhibitor. The precondensation was conducted under nitrogen atmosphere at 190 °C for 1.5 h. Then the catalyst tetra-*n*-butyl titanate (0.5 wt % relative to total of reactants) was added. After gradually heating to 220 °C under vacuum, the polycondensation lasted for 2−3 h until the Weisenberg effect was observed. The purified BE was obtained by dissolving the product in chloroform and precipitating in cold methanol. The number-average molecular weight and molecular weight distribution of BE determined by GPC were 41 106 and 1.83, respectively. BE was characterized by ^{1}H NMR and DSC (Figures S1 and S2).

Exfoliation of GO in DMF. Graphite oxide was prepared by oxidizing natural graphite based on a modified Hummers method.[23] Since graphite oxide is hardly exfoliated in DMF, GO/DMF solution was prepared by a novel solvent-exchange method. Typically, 100 mg of GO was first exfoliated in 20 mL of deionized water under sonication for 1 h. Then a certain amount of DMF was added into the above GO aqueous dispersion. After that, water was removed under reduced pressure to obtain GO/DMF dispersion, in which the GO are well exfoliated and exist as single layer.

Fabrication of BE/Graphene Composites. A desired amount of BE was added into as-prepared GO/DMF dispersion and stirred at room temperature for 24 h. Then EDC (quintuple weight to GO) and DMAP (the same weight to GO) were subsequently added to catalyze the esterification reaction. The reaction was allowed to proceed for 3 days at room temperature. After that, vitamin C (decuple weight to GO) was added as the reducer, and the reduction of GO was accomplished at 80 °C for 24 h. After reduction, the above mixture dispersion was coagulated with methanol under vigorous stirring. The black solid products (BE/graphene composites) were filtered, washed with abundant methanol, and vacuum-dried at 50 °C overnight. The volume contents of graphene in the composites are 0.16%, 0.37%, 0.52%, 1.06%, and 1.45%. To investigate the reaction process, the intermediate products (BE/GO composites) were prepared following the above protocol without reduction.

Preparation of BEGO and BEG. To envisage the successful grafting of BE onto GO or graphene sheets, the resulting BE/GO and BE/graphene composites (0.52 vol % graphene) were subjected to several cycles of filtration and washing with chloroform to remove the free and physically absorbed BE chains and then dried at 50 °C. The resultants were labeled as BEGO and BEG, respectively. As a control experiment, cBEGO and cBEG were prepared following the similar process as that for BEGO and BEG in the absence of the carboxyl activating agents EDC and DMAP.

Characterization. Fourier transform infrared (FTIR) measurements were performed on a Bruker Vector 33 spectrometer. Atomic force microscopy (AFM) was conducted on Veeco Multimode V operated in a tapping mode. The Raman spectra were taken by LabRAM Aramis of HO RIBA Jobin Yvon, equipped with a He−Ne ion laser (532.0 nm) as excitation source. Thermal gravimetric analysis (TGA) was carried out on a TA Q5000 thermogravimetric analyzer at a heating rate of 10 °C/min under a nitrogen atmosphere. DSC was performed on TA Q20. The samples were heated to 160 °C and maintained for 3 min, then cooled to −60 °C, and heated again to 160 °C. The heating or cooling rates were 10 °C/min in all cases. X-ray spectroscopy (XPS) analysis was carried out on a Kratos Axis Ultra DLD with Al Kα radiation (1486.6 eV). X-ray diffraction (XRD) patterns were collected using a Rigaku D/max IIIA X-ray diffractometer with Cu Kα radiation (λ = 0.154 nm). Scanning electron microscopy (SEM) was performed on Nova Nano SEM 430. High-resolution transmission electron microscopy (HRTEM) was conducted on a JEOL2100 instrument. The electrical conductivity was measured on Kisthley 2365A. Thermal conductivity was calculated from the thermal diffusivity which was measured by using a NETZSCH-LFA 447 instrument.

RESULTS AND DISCUSSION

Preparation of Individually Dispersed GO in DMF. GO cannot be fully exfoliated in DMF because the strong

hydrophilicity and hydrogen bonds of GO layers prevent the entrance of organic solvent molecules into interlayer spaces of GO.[24,25] A previous study showed that GO could be dispersed in a mixed solvent of DMF/H_2O, which was successfully predicted by Hansen solubility parameters.[26] In present work, GO is readily exfoliated and stably dispersed in DMF by a simple solvent-exchange method as described in the Experimental Section. As shown in Figure 1a, GO/DMF dispersion

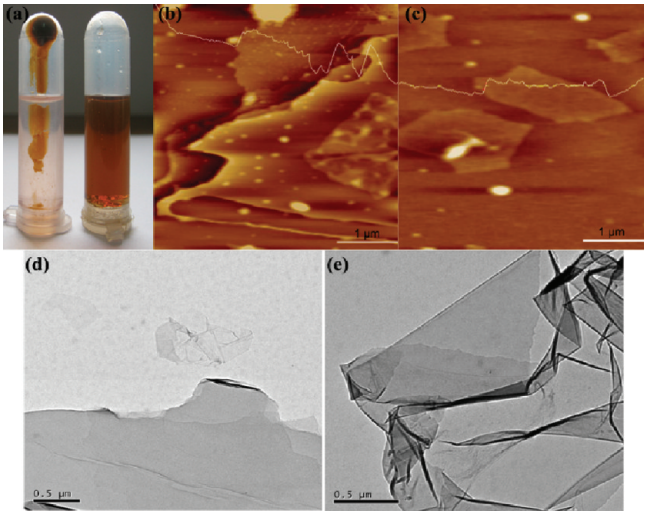


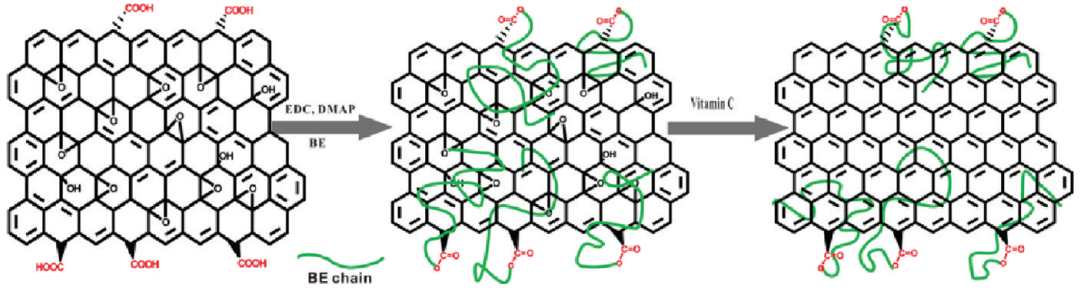
Figure 1. Photos of GO in DMF obtained by direct sonication (left) and solvent exchange (right) after centrifugation (a). AFM images of GO/DMF dispersion obtained by direct sonication (b) and solvent exchange (c). TEM images of GO sheets prepared by direct sonication (d) and solvent exchange (e).

prepared by direct sonication is totally precipitated after centrifugation at 8000 rpm for 10 min. In contrast, for the GO/DMF dispersion obtained by solvent exchange method, there is no sediment at the bottom of centrifuge tube after the same centrifugation process. The exfoliation status of GO in DMF are investigated by AFM measurement. In Figure 1b, it is obvious that GO sheets are multilayers and its height profile exhibits multisteps, indicating that GO are not fully exfoliated into single layers in DMF by direct sonication. Nevertheless, Figure 1c shows that the mean thickness of GO is about 0.92 nm, in agreement with the thickness of an individual GO layer.[27] The same conclusion can also be drawn from the TEM images. The GO sheets obtained by direct sonication in DMF display multilayers (Figure 1d), while the GO sheets obtained by solvent exchange show a wrinkled silk shape, which is the typical characteristic of single GO sheet (Figure 1e). The production of individual GO sheet is very important because the attractive properties of GO are based on its existence of single layer. Herein, the solvent-exchange method is emerging as an efficient and simple way to obtain individually exfoliated GO sheet in DMF. Furthermore, with this method in hand, we also obtain individually dispersed GO sheets in other organic solvents or some liquid oligomers. As shown in Figure S3, although GO can be stably dispersed in DMSO and glycol by direct sonication, the concentration of GO is only about 0.5 mg/mL, which is impractical in many applications. The solvent exchange method can greatly enhance its concentration as high as 3 mg/mL or higher. Even more striking is that GO cannot be wetted in DMF, butanediol, *N*-methylimidazole, PEG100, and D230 (a product of Jeffamine from Huntsman) by direct sonication (even for 12 h). However, the solvent exchange method enables production of homogeneous GO dispersions in these solvents and oligomers. It should be noted that the color of GO dispersion in *N*-methylimidazole and D230 is much darker than that in other solvents, which may be due to the fact that the basic solvents can partly reduce GO.[28,29]

Recently, Zhang et al. reported that liquid exfoliated graphene in *N*-methyl-2-pyrrolidone (NMP) could be transferred into ethanol by repeated diluting and washing NMP/graphene dispersion with ethanol. In contrast, direct sonication of graphite in ethanol results in complete precipitation.[30] It well indicates that the solvent properties that are optimum for initial exfoliation are not necessarily the same as that required to maintain the dispersion. Besides, according to the molecular dynamic simulations on graphene/polar solvent systems, when solvent molecules−graphene interaction is not sufficiently strong to overcome the enormous van der Waals attractive interactions that operate between graphene sheets, the solvent molecules by themselves are not able to exfoliate graphene. Once graphene is dispersed in the solvents, the solvent molecules confined in the graphene intersheet space generate a high energy barrier that hinders the restack of graphene sheets through the steric repulsion between solvent and graphene.[31] Thus, solvent exchange may offer an efficient route to obtain individually dispersed graphene in a wide spectrum of organic solvents and subsequently fabricate graphene-based materials through the solution process.

Covalent Grafting of BE onto GO and Graphene. As schematically illustrated in Scheme 1, synthesis of BEGO, GO graft of BE via ester linkages, is carried out by the esterification reaction between the hydroxyl-terminated BE and GO in DMF with the assistance of EDC and DMAP. BEGO is then subjected to reduction by vitamin C to yield BEG. Vitamin C is utilized as the reducer due to its nontoxic and highly reducing ability toward GO in DMF.[32] The evidence for the covalent bonding between graphene and BE is first provided by FTIR spectra. As shown in Figure 2, the absorption peaks of GO at

Scheme 1. Schematic of Synthesis of BEGO and BEG



dx.doi.org/10.1021/ma300450t | *Macromolecules* 2012, 45, 3444−3451

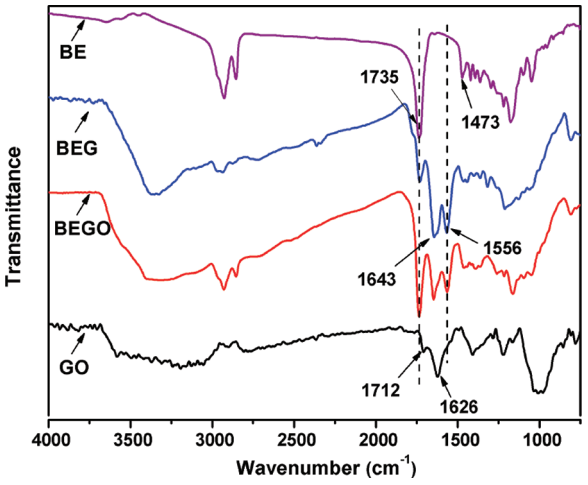


Figure 2. FTIR spectra of GO, BEGO, BEG, and BE.

1712 and 1626 cm^{-1} are assigned to the carbonyl groups (C═O) stretching vibration of −COOH units situated at GO edges and the C═C stretching mode of sp^2 network in GO basal plane, respectively. For BE, the absorption peaks at about 3550, 1735, and 1473 cm^{-1} are corresponded to the O−H stretching vibration, −C═O stretching vibration, and CH_2 bending vibration in BE chain, respectively. After the chemical grafting, in the spectrum of BEGO and BEG, it is distinctly observed that the bands at 1712 cm^{-1} (−COOH of GO) and 3550 cm^{-1} (−OH of BE) disappear, demonstrating that the esterification reaction has occurred between carboxyl and hydroxyl groups. The absorption peak locations of the groups that are not involved into the grafting were significantly changed after grafting. Specifically, in the spectra of BEGO and BEG, the C═C stretching for GO and CH_2 bending vibrations for BE are upshifted from 1626 to 1643 cm^{-1} and from 1473 to 1556 cm^{-1}, respectively. The origins of these shifts are the significant interactions including hydrogen bond and nonspecific CH−π interaction between GO/graphene and the grafted BE.[33] The FTIR profiles of BEG and BEGO are similar, which may be due to the fact that the minute differences between them are indistinguishable under FTIR measurement.

TGA measurement is performed to study the thermal stability and the amount of BE chains grafting onto graphene, as shown in Figure 3. In the TGA curve of GO, there is about 50% weight loss below 250 °C, which is ascribed to removal of

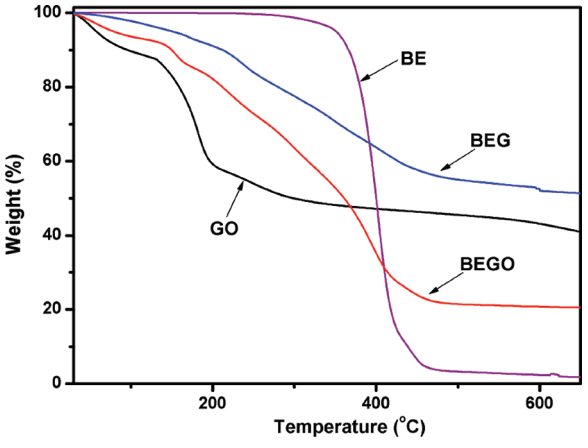


Figure 3. TGA curves of GO, BEGO, BEG, and BE.

the absorbed water and pyrolysis of the oxygen-containing functional groups. The TGA curve for BEGO exhibits two major weight loss stages at 150−250 and 250−500 °C. The former stage is due to the decomposition of the unstable oxygenic groups of the GO component, and the latter stage above 250 °C is mainly attributed to the degradation of the grafted BE. Compared with BEGO, BEG is more thermally stable and the weight loss below 250 °C originating from the decomposition of unstable oxygen-containing groups is quite low, indicating the successful deoxygenation of GO upon reduction. Taking into account of the residue at 600 °C, the quantity of grafted BE in BEGO and BEG is calculated to be ca. 50 wt %, which corresponds to 3.7 BE chains per 10^4 carbon atoms of GO. It is worthy to note that the grafting efficiency in present work is comparable to that of GO covalently modified via click chemistry, suggesting that the grafting by esterification is efficient.[34] Additionally, the reducing ability of vitamin C toward GO is investigated by monitoring the C/O mass ratio of GO and BEG. As displayed in Figure S4, the C/O mass ratio of BEG is 3.45, and the theoretical C/O mass ratio of BE is calculated to about 1.5. Considering that the mass fraction of BE in BEG is about 50% (the TGA results), the C/O mass ratio of graphene can be deduced to be about 5.5. It is much higher than that of GO (2.0) and can be comparable to the value obtained by using the traditional reducers such as sodium borohydride and hydrazine.[35,36]

Raman spectroscopy is a convenient and powerful tool to probe the structure of graphene-based materials. In Figure 4,

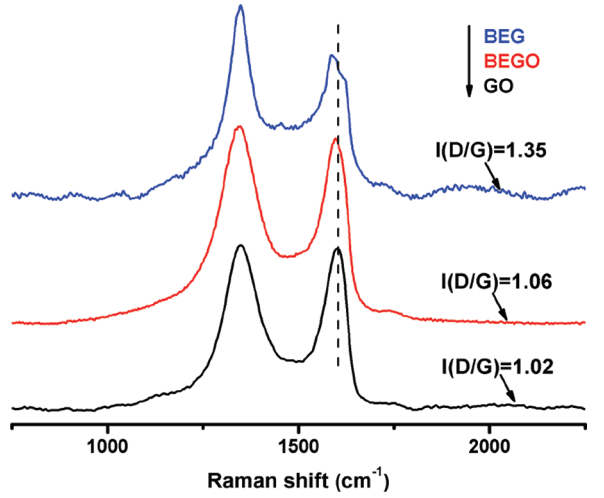


Figure 4. Raman spectra of GO, BEGO, and BEG.

the Raman spectrum of GO displays a D band at 1349 cm^{-1} due to the breathing mode of κ-point phonons of A_{1g} symmetry and a G band at 1603 cm^{-1} corresponding to the first-order scattering of the E_{2g} phonons. The peak positions of D band and G band of BEGO are identical to those of GO. Nevertheless, the G-band of BEG red-shifts to 1586 cm^{-1}, which is close to the value of raw graphite, indicating the successful reduction of GO.[24] The intensity ratio of D and G bands (I(D/G)), correlating to the disordered and ordered crystal structures of carbon, is inverse to the average size of sp^2 domains.[37] The I(D/G) of BEGO (1.06) is similar to that of GO (1.02). This is because that the grafting reaction is taken place by using carboxyl groups situated at the edges of GO as the active sites, and thus the skeletal structure is greatly

dx.doi.org/10.1021/ma300450t | Macromolecules 2012, 45, 3444−3451

preserved after the grafting.[38] In striking contrast, according to others reports, when the covalent functionalization was conducted on functional groups in interbasal platelet of graphene, a substantial enhancement of $I(D/G)$ was observed due to the introduction of additional defects on graphitic lattice; subsequently, the intrinsic properties of graphene may be greatly weakened.[22,25,39] The $I(D/G)$ of BEG is increased from 1.06 to 1.35, which is due to the decrease in the average size of the in-plane sp^2 domain (increase of the edge defects) upon reduction.[27]

As is well-known, neither GO nor reduced GO can be dispersed in chloroform, acetone, or tetrahydrofuran (Figure S5). Shown Figure 5 is the photo of BEGO and BEG

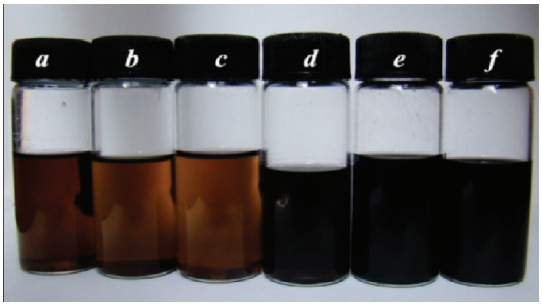


Figure 5. Photos of BEGO (a, b, c) and BEG (d, e, f) in chloroform, acetone, and tetrahyrdofuran.

dispersions in these aforementioned solvents. It can be seen that both BEGO and BEG are well dispersed and do not undergo sedimentation for 2 months. The surface properties of GO and reduced GO are altered by the grafted BE chains, thereby imparting them solubility. The wide spectrum dispersibility of the BEGO and BEG in these low boiling point solvents opens up an opportunity for processing graphene-based composites. The yellow BEGO dispersions are converted to black in BEG dispersions, which is due to the recovery of conjugated structure of GO upon reduction. In addition, to exclude the possible contribution of the physically adsorbed BE chains to the dispersibility of GO or reduced GO, the control samples cBEGO and cBEG were prepared and then dispersed into these solvents. As shown in Figure S6, both cBEGO and cBEG are completely precipitated in the solvents which can suspend BEGO and BEG, which clarify that the dispersibility is as a result of the chemical grafting BE instead of the physically adsorbed BE.

Figure 6a shows the AFM image of BEGO and its height profile. The sample was prepared by depositing a drop of chloroform/GO dispersion onto mica and then drying. It reveals that the thickness of the BEGO sheet varies from 1.6 to 4.9 nm; such large spanning of thickness is attributed to the inhomogeneous distribution of BE on GO platelets. It is obvious that the thickness at the peripheral area is larger than that at the central area. Considering the fact that the carboxyl groups are located at the edge of GO sheets at which the esterification takes place, BE chains are preferentially gathered at the peripheral area of GO sheets. Besides, the thickness of BEGO sheet is much higher than that of the individually exfoliated GO sheets (~0.9 nm) (Figure 1c), which can be rationalized in terms of the grafted BE that covers onto the surface of GO, and a similar phenomenon was also reported in other work.[40,41] The AFM image of BEG is presented in Figure S7, its mean thickness is about 4.3 ± 0.3 nm, and the lateral size

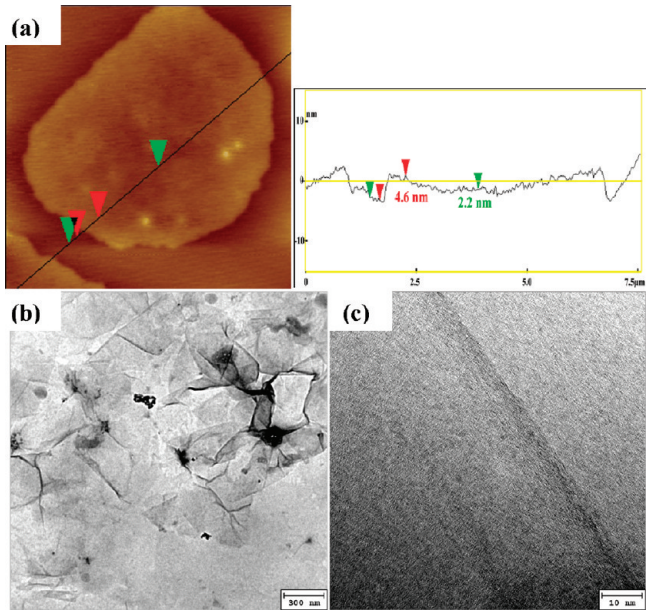


Figure 6. AFM image and its height profile of BEGO (a). TEM images of BEG sheets (b) and (c).

is about 1 μm. Compared with BEGO, BEG sheets do not display remarkable thickness variations. The reduced GO become more hydrophobic and have a decreased lateral size upon reduction; thus, the grafted BE chains are prone to uniformly disperse on its basal plane. The morphology and microstructure of BEG are further characterized by TEM. For TEM measurement, a droplet of diluted BEG/chloroform dispersion was deposited onto a copper grid. From Figure 6b, the graphene sheets are partially interconnected and wrinkled. The dark spots on the graphene surface, mainly on the edge of graphene sheets, are the condensed particles of the grafted BE. After careful observation on the edge of BEG, it reveals that the thickness of single layer BEG is about 3 nm (Figure 6c). Besides, in Figure S8, the coarse surface and desultory stacking of the wrinkled BEG observed from SEM images provide another evident for the grafting of BE onto graphene.

Characterizations and Properties of BE/Graphene Composites. The BE/graphene composite flakes (Figure S9) can be dispersed in chloroform and then dried to form BE/graphene films. The structures of BEGO, BEG, and BE/graphene film are studied by XRD. As depicted in Figure 7, in the XRD pattern of neat BE, the typical diffraction peaks at 2θ = 19.1°, 20.4°, 21.7°, and 22.3° are assigned to (102), (016), (112), and (105) diffractions of the orthorhombic crystal form in the polyester of SA and PDO.[42] In the XRD patterns of BEGO and BEG, diffraction peaks of GO (2θ about 11°) or graphene (2θ about 26.6°) cannot be detected,[43] revealing the disordering and loose stacking of GO or graphene in BEGO and BEG samples. It is well consistent with the observations from SEM images (Figure S8). Besides, compared with the neat BE, the grafted BE component in BEGO and BEG show different XRD diffraction peaks, indicative of the changed crystalline form of BEGO or BEG. DSC results (Figure S10) also indicated the confined crystallization which may be originated from the grafting. The BE/graphene film with 1.06 vol % graphene has the similar XRD profile as the neat BE, and the diffraction peak associated with graphene disappears, indicating the well-dispersed of graphene in BE matrix. Other

dx.doi.org/10.1021/ma300450t | Macromolecules 2012, 45, 3444−3451

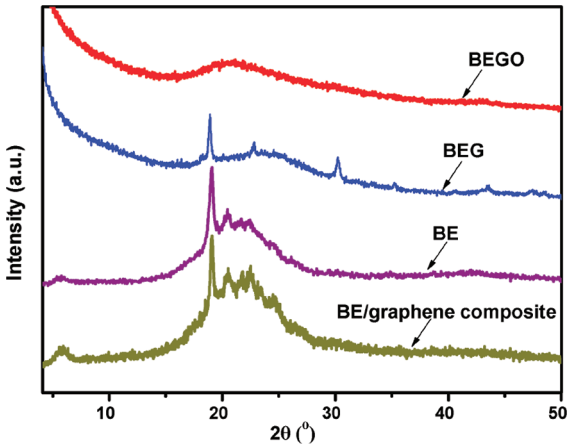


Figure 7. XRD patterns of BEGO, BEG, neat BE, and BE/graphene composite containing 1.06 vol % graphene.

BE/graphene films, regardless of the graphene loadings, also exhibit the similar XRD patterns as the neat BE (not shown).

For providing direct evidence on the excellent compatibility of graphene in composites, SEM measurement on the cryo-fractured surfaces of composite films was conducted. From Figure 8a, it can be seen that graphene is uniformly dispersed in

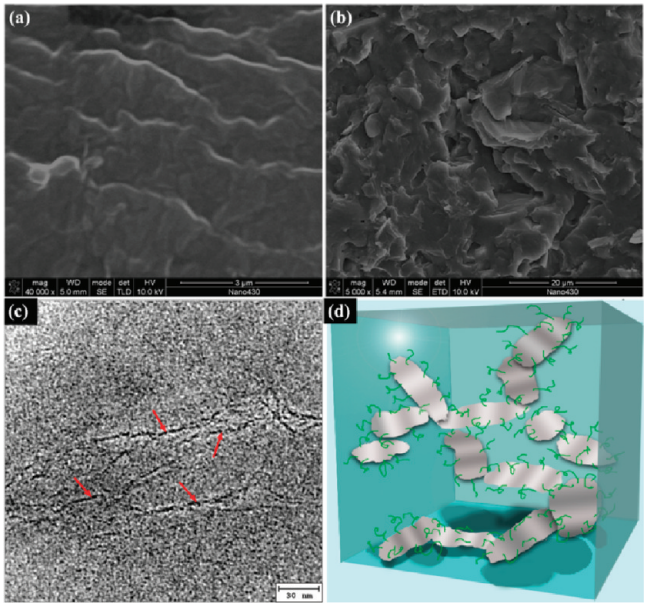


Figure 8. Cross-section SEM images of the composites with 0.16 vol % graphene (a) and 1.06 vol % graphene (b). HRTEM images of the composites containing 0.16 vol % graphene (c). 3D schematic of the interconnected graphene in the composites (d).

BE matrix containing 0.16 vol % graphene. At a higher loading (1.06 vol %), the rough surface comprising of BE wrapped graphene is observed, and the graphene are connected to form consecutive conductivity pathway through the matrix (Figure 8b). HRTEM was employed to further evaluate the dispersion quality of graphene within BE matrix. From the TEM image of composites containing 0.16 vol % graphene, the thin graphene with thickness of about 2 nm is interconnected and forms a conductive path. Much denser conductivity network is resulted in the composite with higher graphene loading at 1.06 vol % (Figure S11). The formation of conductivity pathway at such low graphene content (0.16 vol %) is because: (a) The individually dispersed GO in DMF obtained by solvent-exchange method is prerequisite to produce satisfied dispersion status of graphene in BE matrix. (b) The effective surface functionalization of graphene with BE chains facilitates enhancing the compatibility between graphene and BE matrix. (c) Since each BE chain bears two terminated hydroxyl groups, it is inevitable that one BE chain connects two graphene sheets together, causing the interconnection of graphene layers via BE chain. As illustrated in Figure 8d, the visual effect shows that the graphene sheets are well exfoliated in the matrix and spatially interconnected by BE chains, which favor the formation of conductive paths at lower graphene loading.

Figure 9 shows the direct current electrical conductivity of the composites (σ_c) as a function of graphene volume (Φ). It is

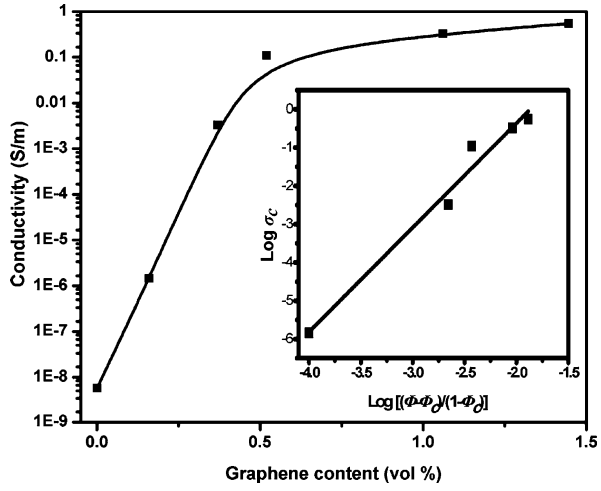


Figure 9. Conductivity as a function of graphene content for BE/graphene composites. The inset is the logarithmic plot for conductivity versus $(\Phi - \Phi_c)/(1 - \Phi_c)$; the straight line in the inset is a linearly fit to the data using the equation described in the text.

evident that even with the incorporation of 0.16 vol % graphene, the electrical conductivity of the composite increases drastically, referring to the neat BE. The conductivity further increases to 0.33 S/m with 1.06 vol % graphene loading. The certain loading fraction, at which the filler forms an infinite network of connected paths leading to a sudden rise of the electrical conductivity of the composites, is known as percolation threshold (Φ_c). The σ_c and Φ above percolation threshold can be expressed as follows.[44,45] $\sigma_c = \sigma_f [(\Phi - \Phi_c)/(1 - \Phi_c)]^t$, where σ_f is the electrical conductivity of the filler and t is the critical exponent. As illustrated in Figure 9, the straight line in the inset shows a good fit to the data with a correlation factor of 0.97. According to the fitted parameters, the t, σ_f, and φ_c are calculated to be 2.73 ± 0.24, $10^{5.09\pm0.65}$ S m^{-1}, and 0.15 vol %, respectively. The value of t is depended on the system dimensionality and is indicative of electron transfer behavior. The t obtained in the present work (2.73) is close to that of phenyl isocyanate-treated graphene-filled polystyrene composite (2.74), indicating a similar geometry of the conducting nanoparticle and electron transport behavior.[45,46] It suggests that the consecutive conductive pathway is originated from contacts of individual graphene sheets in a 3D system segregated in the polymer matrix.[47] The percolation in present work is as low as 0.15 vol %, which is lower than most of the reported values, e.g., 0.52 vol % epoxy/graphene composites[48]

dx.doi.org/10.1021/ma300450t | Macromolecules 2012, 45, 3444−3451

and 3 vol % for graphene/poly(benzoyl-1,4-phenylene)-*co*-(1,3-phenylene).[49] The lower percolation threshold is attributed to the homogeneous dispersion of graphene and the interconnected graphene by BE chains. The fitted filler conductivity ($\sigma_f = 10^{5.09\pm0.65}$ S m^{-1}) in the present work is close to that of phenyl isocyanate-functionalized graphene ($\sigma_f = 10^{4.92\pm0.52}$ S m^{-1})[45] but lower than that of thermally reduced GO ($\sigma_f = 10^{8.55\pm0.69}$ S m^{-1}).[50] Although σ_f is not a real conductivity, it is positively related to the intrinsic conductivity of the pristine filler. Compared with the thermally reduced GO, the lower σ_f may be due to the covalent functionalization and incomplete reduction of GO, which lower the electron transfer in graphene sheets.

The thermal conductivity of graphene/polymer composites received less attention because the modest improvement in thermal conductivity is observed with the incorporation of graphene.[51] However, the composites with good thermal conductivity have numerous applications in thermal interface materials, connectors, and other high-performance thermal management systems. As presented in Figure 10, the thermal

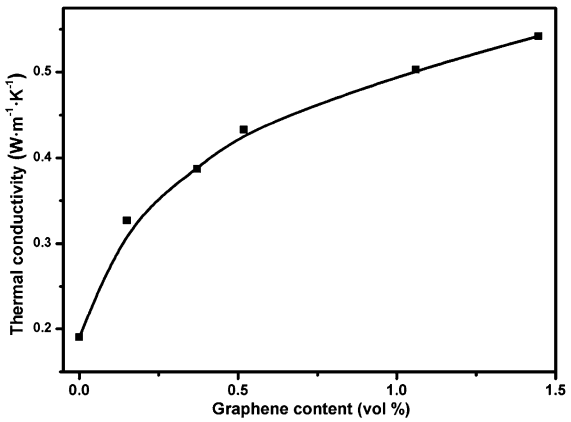


Figure 10. Thermal conductivity of BE/graphene as a function of graphene content.

conductivity of composites increases consistently with increasing graphene content. The thermal conductivity of the composites containing 1.45 vol % graphene increases by 185% (from 0.19 to 0.542 W m^{-1} K^{-1}). On basis of previous investigations on polymer-based composites, dozens volume percent of conventionally thermally conductive fillers were needed to achieve such an increment. For example, 20 vol % nanozinc oxide led to ~110% increase in the thermal conductivity of ethylene propylene rubber,[52] and 10 vol % aluminum oxide generated ~73% increase in the thermal conductivity of silicone rubber.[53] Further, compared with graphene filled polymer, the improvement in present work is still more pronounced. For example, with the incorporation of 0.25 wt % thermal expansion graphene, 6% increase in thermal conductivity of silicone foams was observed.[54] The thermal conductivity of the epoxy composite was increased by 55% at 2 wt % siliane-treated exfoliated graphene.[55] In the composites, since the thermal energy is transferred mainly in the form of phonons, poor coupling in vibration modes at the filler–polymer interface will impart significant thermal resistance.[56] Chemical bonding between filler and matrix can efficiently reduce the acoustic phonon scattering at the interface. In present work, the BE is chemically grafted onto graphene, and thus the improvement in the thermal conductivity is impressive.

Besides the improvement of the electrical conductivity and thermal conductivity, the thermal stability of composites is significantly improved with addition of graphene, which can be explained by the "tortuous path effect" (Figure S12).

As a fascinating carbonaceous material, graphene exhibits versatile characteristics for improving the performance of various polymers, including strength, modulus, conductivities, etc. However, compared with its reinforcing capability, the functional properties associated with its unique sp^2 electron structure are more attractive because many other inorganics may also fulfill the goal of reinforcing polymers. In this regard, we have focused on converting the unusual conductive characteristics into the bio-based polyester effectively.

CONCLUSIONS

The individually dispersed GO sheets in DMF are obtained by the solvent-exchange method. BE is successfully grafted onto GO via esterification, which is then subjected to reduction by vitamin C. The functionalization enhances the compatibility between graphene and BE matrix. The graphene sheets are interconnected by the BE chain, which favors the formation of conductive paths at very low graphene loading. The concurrently increased electrical and thermal conductivity are a consequence of well-dispersion of graphene in BE matrix and the interconnected structure of graphene. The present work provides unique insights in developing bio-based functional polymers with sustainable plant resources and graphene.

ASSOCIATED CONTENT

Supporting Information

DSC data of BE and BEGO, ^{1}H NMR of BE, XPS spectra of BEG and GO, Photo of GO in various solvents or oligomers, Photo of GO, cBEGO, and cBEG in chloroform, acetone, and tetrahydrofuran, AFM image of BEG, SEM images of BEG, TEM image of BE/graphene composites, GO sheets in GO/DMF dispersions obtained by different methods, TGA curves of composites. This material is available free of charge via the Internet at http://pubs.acs.org.

AUTHOR INFORMATION

Corresponding Author

*E-mail: psbcguo@scut.edu.cn (B.G); zhanglq@mail.buct.edu.cn (L.Z).

Notes

The authors declare no competing financial interest.

ACKNOWLEDGMENTS

This work was supported by National Natural Science Foundation of China (50933001), Program for New Century Excellent Talents in University (NCET-10-0393), and Fundamental Research Project for the Central Universities (2012ZG0002).

REFERENCES

(1) Novoselov, K. S.; Geim, A. K.; Morozov, S. V.; Jiang, D.; Zhang, Y.; Dubonos, S. V.; Grigorieva, I. V.; Firsov, A. A. *Science* **2004**, *306*, 666–669.

(2) Balandin, A. A.; Ghosh, S.; Bao, W.; Calizo, I.; Teweldebrhan, D.; Miao, F.; Lau, C. N. *Nano Lett.* **2008**, *8*, 902–907.

(3) Lee, C.; Wei, X.; Kysar, J. W.; Hone, J. *Science* **2008**, *321*, 385–388.

(4) Zhang, Y.; Tan, Y. W.; Stormer, H. L.; Kim, P. *Nature* **2005**, *438*, 201–204.

(5) Zhu, Y. W.; Stoller, M. D.; Cai, W. W.; Velamakanni, A.; Piner, R. D.; Chen, D.; Ruoff, R. S. *ACS Nano* **2010**, *4*, 1227−1233.
(6) Patil, A. J.; Vickery, J. L.; Scott, T. B.; Mann, S. *Adv. Mater.* **2009**, *21*, 3159−3164.
(7) Sudibya, H. G.; He, Q. Y.; Zhang, H.; Chen, P. *ACS Nano* **2011**, *5*, 1990−1994.
(8) Hernandez, Y.; Nicolosi, V.; Lotya, M.; Blighe, F. M.; Sun, Z. Y.; De, S.; McGovern, I. T.; Holland, B.; Byrne, M.; Gun'ko, Y. K.; Boland, J. J.; Niraj, P.; Duesberg, G.; Krishnamurthy, S.; Goodhue, R.; Hutchison, J.; Scardaci, V.; Ferrari, A. C.; Coleman, J. N. *Nat. Nanotechnol.* **2008**, *3*, 563−568.
(9) Dato, A.; Radmilovic, V.; Lee, Z.; Phillips, J.; Frenklach, M. *Nano Lett.* **2008**, *8*, 2012−2016.
(10) Li, D.; Muller, M. B.; Gilje, S.; Kaner, R. B.; Wallace, G. G. *Nat. Nanotechnol.* **2008**, *3*, 101−105.
(11) Dreyer, D. R.; Park, S.; Bielawski, C. W.; Ruoff, R. S. *Chem. Soc. Rev.* **2010**, *39*, 228−240.
(12) Xu, Z.; Gao, C. *Macromolecules* **2010**, *43*, 6716−6723.
(13) Yang, H. F.; Li, F. H.; Shan, C. S.; Han, D. X.; Zhang, Q. X.; Niu, L.; Ivaska, A. *J. Mater. Chem.* **2009**, *19*, 4632−4638.
(14) Qi, X.; Pu, K.; Li, H.; Zhou, X.; Wu, S.; Fan, Q.; Liu, B.; Boey, F.; Huang, W.; Zhang, H. *Angew. Chem., Int. Ed* **2010**, *49*, 9426−9429.
(15) Bai, H.; Li, C.; Shi, G. Q. *Adv. Mater.* **2011**, *23*, 1089−1115.
(16) Kuilla, T.; Bhadra, S.; Yao, D.; Kim, N.; Bose, S.; Lee, J. *Prog. Polym. Sci.* **2010**, *35*, 1035−1055.
(17) Kim, K. K.; Yoon, S. M.; Choi, J. Y.; Lee, J.; Kim, B. K.; Kim, J. M.; Lee, J. H.; Paik, U.; Park, M.; Yang, C. W. *Adv. Funct. Mater.* **2007**, *17*, 1775−1783.
(18) He, H. K.; Gao, C. *Chem. Mater.* **2010**, *22*, 5054−5064.
(19) Fang, M.; Wang, K. G.; Lu, H. B.; Yang, Y. L.; Nutt, S. *J. Mater. Chem.* **2009**, *19*, 7098−7105.
(20) Yang, Y.; Wang, J.; Zhang, J.; Liu, J.; Yang, X.; Zhao, H. *Langmuir* **2009**, *25*, 11808−11814.
(21) Lomeda, J. R.; Doyle, C. D.; Kosynkin, D. V.; Hwang, W. F.; Tour, J. M. *J. Am. Chem. Soc.* **2008**, *130*, 16201−16206.
(22) Hsiao, M.; Liao, S.; Yen, M.; Liu, P.; Pu, N.; Wang, C.; Ma, C. *ACS Appl. Mater. Interfaces* **2010**, *2*, 3092−3099.
(23) Hummers, W., Jr; Offeman, R. *J. Am. Chem. Soc.* **1958**, *80*, 1339−1339.
(24) Stankovich, S.; Piner, R. D.; Nguyen, S. T.; Ruoff, R. S. *Carbon* **2006**, *44*, 3342−3347.
(25) Zhang, B.; Zhang, Y.; Peng, C.; Yu, M.; Li, L.; Deng, B.; Hu, P.; Fan, C.; Li, J.; Huang, Q. *Nanoscale* **2012**, *4*, 1742−1748.
(26) Park, S.; An, J. H.; Jung, I. W.; Piner, R. D.; An, S. J.; Li, X. S.; Velamakanni, A.; Ruoff, R. S. *Nano Lett.* **2009**, *9*, 1593−1597.
(27) Stankovich, S.; Dikin, D. A.; Piner, R. D.; Kohlhaas, K. A.; Kleinhammes, A.; Jia, Y.; Wu, Y.; Nguyen, S. T.; Ruoff, R. S. *Carbon* **2007**, *45*, 1558−1565.
(28) Fan, X. B.; Peng, W. C.; Li, Y.; Li, X. Y.; Wang, S. L.; Zhang, G. L.; Zhang, F. B. *Adv. Mater.* **2008**, *20*, 4490−4493.
(29) Park, S.; An, J. H.; Piner, R. D.; Jung, I.; Yang, D. X.; Velamakanni, A.; Nguyen, S. T.; Ruoff, R. S. *Chem. Mater.* **2008**, *20*, 6592−6594.
(30) Zhang, X.; Coleman, A. C.; Katsonis, N.; Browne, W. R.; van Wees, B. J.; Feringa, B. L. *Chem. Commun.* **2010**, *46*, 7539−7541.
(31) Shih, C. J.; Lin, S.; Strano, M. S.; Blankschtein, D. *J. Am. Chem. Soc.* **2010**, *132*, 14638−14648.
(32) Fernandez-Merino, M. J.; Guardia, L.; Paredes, J. I.; Villar-Rodil, S.; Solis-Fernandez, P.; Martinez-Alonso, A.; Tascon, J. M. D. *J. Phys. Chem. C* **2010**, *114*, 6426−6432.
(33) Zheng, X. L.; Xu, Q.; He, L. H.; Yu, N.; Wang, S. S.; Chen, Z. M.; Fu, J. W. *J. Phys. Chem. B* **2011**, *115*, 5815−5826.
(34) Cao, Y.; Lai, Z.; Feng, J.; Wu, P. *J. Mater. Chem.* **2011**, *21*, 9271−9278.
(35) Shin, H.; Kim, K.; Benayad, A.; Yoon, S.; Park, H.; Jung, I.; Jin, M.; Jeong, H.; Kim, J.; Choi, J. *Adv. Funct. Mater.* **2009**, *19*, 1987−1992.
(36) Stankovich, S.; Piner, R.; Chen, X.; Wu, N.; Nguyen, S.; Ruoff, R. *J. Mater. Chem.* **2006**, *16*, 155−158.
(37) Kudin, K. N.; Ozbas, B.; Schniepp, H. C.; Prud'Homme, R. K.; Aksay, I. A.; Car, R. *Nano Lett.* **2008**, *8*, 36−41.
(38) Zhang, S.; Xiong, P.; Yang, X.; Wang, X. *Nanoscale* **2011**, *3*, 2169−2174.
(39) Wang, H. X.; Zhou, K. G.; Xie, Y. L.; Zeng, J.; Chai, N. N.; Li, J.; Zhang, H. L. *Chem. Commun.* **2011**, *47*, 5747−5749.
(40) Liu, J.; Fu, S.; Yuan, B.; Li, Y.; Deng, Z. *J. Am. Chem. Soc.* **2010**, *132*, 7279−7281.
(41) Xu, C.; Wang, J.; Wan, L.; Lin, J.; Wang, X. *J. Mater. Chem.* **2011**, *21*, 10463−10471.
(42) Guo, B. C.; Chen, Y. W.; Lei, Y. D.; Zhang, L. Q.; Zhou, W. Y.; Rabie, A. B. M.; Zhao, J. Q. *Biomacromolecules* **2011**, *12*, 1312−1321.
(43) Zhang, J. L.; Yang, H. J.; Shen, G. X.; Cheng, P.; Zhang, J. Y.; Guo, S. W. *Chem. Commun.* **2010**, *46*, 1112−1114.
(44) Dutta, P.; Biswas, S.; Ghosh, M.; De, S. K.; Chatterjee, S. *Synth. Met.* **2001**, *122*, 455−461.
(45) Stankovich, S.; Dikin, D. A.; Dommett, G. H. B.; Kohlhaas, K. M.; Zimney, E. J.; Stach, E. A.; Piner, R. D.; Nguyen, S. T.; Ruoff, R. S. *Nature* **2006**, *442*, 282−286.
(46) Stauffer, D. *Introduction to Percolation Theory*; Taylor & Francis: London, 1985.
(47) Gelves, G. A.; Al-Saleh, M. H.; Sundararaj, U. *J. Mater. Chem.* **2010**, *21*, 829−836.
(48) Liang, J. J.; Wang, Y.; Huang, Y.; Ma, Y. F.; Liu, Z. F.; Cai, F. M.; Zhang, C. D.; Gao, H. J.; Chen, Y. S. *Carbon* **2009**, *47*, 922−925.
(49) Biswas, S.; Fukushima, H.; Drzal, L. T. *Composites, Part A* **2011**, *42*, 371.
(50) Yoonessi, M.; Gaier, J. R. *ACS Nano* **2010**, *4*, 7211−7220.
(51) Verdejo, R.; Bernal, M. M.; Romasanta, L. J.; Lopez-Manchado, M. A. *J. Mater. Chem.* **2011**, *21*, 3301−3310.
(52) Wang, Z.; Lu, Y.; Liu, J.; Dang, Z.; Zhang, L.; Wang, W. *J. Appl. Polym. Sci.* **2011**, *119*, 1144−1155.
(53) Sim, L. C.; Ramanan, S.; Ismail, H.; Seetharamu, K.; Goh, T. *Thermochim. Acta* **2005**, *430*, 155−165.
(54) Verdejo, R.; Barroso-Bujans, F.; Rodriguez-Perez, M. A.; de Saja, J. A.; Lopez-Manchado, M. A. *J. Mater. Chem.* **2008**, *18*, 2221−2226.
(55) Ganguli, S.; Roy, A. K.; Anderson, D. P. *Carbon* **2008**, *46*, 806−817.
(56) Zhong, H.; Lukes, J. R. *Phys. Rev. B* **2006**, *74*, 125403.

Macromolecules

Article

pubs.acs.org/Macromolecules

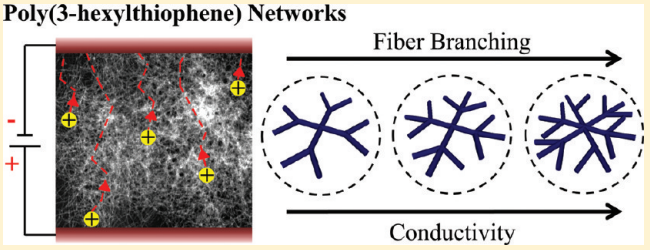
Electrical, Mechanical, and Structural Characterization of Self-Assembly in Poly(3-hexylthiophene) Organogel Networks

Gregory M. Newbloom,[†] Katie M. Weigandt,[†] and Danilo C. Pozzo*

Department of Chemical Engineering, University of Washington, Box 351750, Seattle, Washington 98195-1750, United States

Supporting Information

ABSTRACT: An electrically percolated network structure of conjugated polymers is critical to the development of organic electronics. Herein, we investigate the potential to rationally design an interconnected network of conjugated polymers using the gelation of poly(3-hexylthiophene) (P3HT) as a model system. The three-dimensional network structure is evaluated through small-angle neutron scattering (SANS) and ultrasmall-angle neutron scattering (USANS). The analytical models used for data fitting provide relevant structural parameters over multiple length scales. Structural parameters include the fiber cross section (height and width), the specific surface area, and the network density (i.e., fractal dimension). Simultaneous rheological and conductivity measurements also provide insight into the development of the mechanical and electrical properties of organogels and allow us to propose a detailed gelation mechanism for P3HT. The fiber shape is found to be relatively independent of the solvent type, but P3HT organogels show distinct differences in conductivity, which can be directly linked to differences in the branching network structures. These results suggest that the gelation of fiber-forming conjugated polymers offers an excellent platform for designing electrically percolated networks that can be used for structural optimization in organic electronic devices.



1. INTRODUCTION

Conjugated polymers are a keystone material for developing the next generation of economical electronic devices. The potential for low-temperature and solution-based processing of semiconducting polymers makes it possible to manufacture inexpensive, large area devices directly on a variety of substrates.[1,2] These unique features are embraced in the design of organic light-emitting diodes (OLEDs) that are now being incorporated into high-definition electronic displays and organic field-effect transistors (OFETs).[3] Organic photovoltaic (OPVs) devices, also based on conjugated polymers, offer a lower-cost alternative to traditional solar cell technologies. OPVs are also economically well-positioned to capture a significant fraction of the available solar energy (120 000 TW/year globally).[4,5] However, the overall efficiency and stability of these devices must still be improved before they can make a significant impact.[2,6]

Engineering a network structure that is interconnected and spans the gap between electrodes is one of the grand challenges of designing efficient electronic devices from conjugated polymers.[2,3,7,8] In the case of OPVs, the structure must satisfy important constraints such as being interconnected for effective charge transport, having adequate thickness for photon absorption and having domains that are smaller than the exciton diffusion distance.[6,9−11] Unfortunately, the morphology of conjugated polymers is sometimes loosely characterized in the literature because of difficulties involved with probing the bulk structure of opaque thin films and because of their multiscale nature. Therefore, instead of designing the structure to achieve good performance, it is more common to optimize device properties through changes to the processing parameters. This approach leads to a lack of accurate structure−property relationships that describe the correlation between network structure and device performance.[12]

Achieving a specific network morphology for use in organic electronics also becomes increasingly difficult when structural development is strongly coupled to processing conditions. OPVs, for example, are typically produced by coating a solution of dissolved p-type and n-type materials onto a conductive substrate.[13] This leads to a film that may or may not phase separate into the desired structure depending on parameters related to coating conditions and post-processing annealing (e.g., temperature, solvent vapor pressure, coating speed, etc.).[1,14−16] Given the operating constraints of OPVs, the ideal structure of the photoactive layer should be a bicontinuous network that vertically bridges the anode and cathode, with nanoscale phase segregation of p-type and n-type materials.[1,6−8,10,15,17,18] It is difficult to corroborate that the ideal structure has been achieved because there are few analytical techniques that can directly and quantitatively probe the multiscale structural features of these materials. The top surface of thin films is commonly studied with microscopy techniques, such as atomic force microscopy (AFM), even though it is unlikely that this surface structure will match the bulk morphology underneath.[16,19−21]

Received: November 23, 2011
Revised: February 28, 2012
Published: April 6, 2012

 © 2012 American Chemical Society dx.doi.org/10.1021/ma202564k | *Macromolecules* 2012, 45, 3452−3462

An alternative to adjusting the morphology of the network via post-processing is to directly build the desired network structure prior to coating. The self-assembly of conjugated polymers prior to deposition could ensure the formation of a three-dimensional, stable, and interconnected network that should be beneficial for organic electronic devices. Gelation of conjugated polymers in organic solvents is a very common phenomenon. Poly(3-alkylthiophenes) (P3ATs), poly(9,9-dioctylfluorene-2,7-diyl) (PFO), and poly[2-methoxy-5-(2-ethylhexyloxy)-1,4-henylenevinylene)] (MEH-PPV) have all been shown to form organogels in organic solvents.[22−34] The propensity for π-stacking among conjugated polymers frequently leads to growth of long, semicrystalline fiber structures that can extend for several micrometers.[2,22,24] In particular, the fibrillar structure of P3HT has been shown to be beneficial for charge transport.[12,22] Malik and coworkers further demonstrated that the interconnectivity of P3HT fibers in the gel phase results in increased charge mobility when compared to traditional spin-cast films with the same composition.[29] The ability to engineer the network phase of fiber-forming conjugated polymers could provide a route toward achieving optimized active layer morphologies.

In the past, conjugated polymer gelation has been largely regarded as a hurdle to overcome for the benefit of storing and processing electronic inks.[22,28,35] The elastic nature of interconnected networks makes them difficult to process using traditional coating techniques. To overcome this problem, our lab recently demonstrated the possibility of processing P3HT organogels directly from aqueous dispersions through the preparation of microgel particles. The feasibility of this approach was demonstrated by fabricating prototype solar cells.[36] Other researchers have also demonstrated the feasibility of using conjugated polymer organogels in OPVs through freeze-drying methods and through organogel sonication to form homogeneous solutions.[25,33] These advances in gel processing now make it possible to utilize conjugated polymer gel networks in real applications. Additionally, fundamental research in the field of small-molecule organogels suggests that network structures can be effectively tuned by controlling the solubility of the gelator molecules.[37,38]

Here we present a systematic, multiscale structural analysis of P3HT organogels formed at different concentrations and in various aromatic solvents for the purpose of informing the development of percolated networks for organic electronics. Utilizing multiscale analysis techniques is critical for the development of robust structure−property relationships because structural differences can occur simultaneously on multiple length scales.[12] Small-angle scattering of X-rays and neutrons are promising techniques to nondestructively probe morphology in these materials.[12,14,20,23,36,39−41] Here, we use small-angle neutron scattering (SANS) and ultra small-angle neutron scattering (USANS) to evaluate the structure of P3HT gels over length scales of 1−10 000 nm. Scanning transmission electron microscopy (sTEM) is also utilized to complement the scattering analysis and to directly observe the network structures. Simultaneous rheology and conductivity measurements as well as UV−vis spectroscopy are utilized to further understand the complex self-assembly mechanism and to develop structure−property relationships. Conductivity measurements confirm that structural variations can significantly impact charge transport characteristics in organogels. These results demonstrate that it is possible to engineer a network structure for specific organic electronic applications using gelation as a general platform.

2. EXPERIMENTAL METHODS

2.1. Materials. Two lots of Sepiolid P200 poly(3-hexylthiophene) (P3HT) were used as received from Rieke Metals (Lincoln, NE). The molecular weight (M_w) and polydispersity index (PDI) of each batch were characterized using gel permeation chromatography (GPC) relative to polystyrene standards. Batch 1 (Lot # 31-10-2008) had M_w = 24 060 g/mol and PDI = 2.0. Batch 2 (Lot # 22.10.2009) had M_w = 16 770 g/mol and PDI = 1.6. The regioregularity of both batches was reported by the manufacturer to be greater than 98%. The results presented in this paper are primarily from batch 2 samples, unless otherwise indicated. Some results from batch 1 are also included to illustrate effects originating from batch-to-batch variations. Hydrogenated solvents *p*-xylene, toluene, and benzene were purchased from Sigma-Aldrich (St. Louis, MO) and used as received. Deuterated solvents were used to increase the scattering contrast and to decrease the incoherent scattering background in SANS and USANS experiments. d_{10}-*p*-Xylene (D > 98%), d_8-toluene (D > 99.5%), and d_6-benzene (D > 99.5%) were purchased from Cambridge Isotopes (Andover, MA) and were used as received.

2.2. Sample Preparation. Samples were prepared by adding 5−50 mg/mL P3HT to *p*-xylene, benzene, or toluene and then heating to 80 °C until the polymer was fully dissolved. The polymer is considered fully dissolved when the solution is bright orange, and there are no visible signs of solid polymer (black). The polymer solution was then removed from heat and allowed to gel at a lower temperature for 24 h unless otherwise noted.

2.3. UV−vis Spectroscopy. The fraction of solids in the gels was determined via UV−vis spectroscopy after allowing gels to self-assemble for a specific length of time. At this point, the gels were fractured through vigorous shaking in the presence of a small controlled amount of extra solvent (~2 mL). The fractured P3HT gels were then centrifuged at 21100*g* for 1 min, and the polymer concentration in the supernatant was measured via UV−vis spectroscopy. UV−vis absorbance spectra were obtained using a Thermo Evolution 300 UV−vis spectrophotometer at wavelengths between 350 and 750 nm. The concentration of the dissolved polymer fraction was determined from the maximum absorption at 450 nm using Beer's law with experimentally determined extinction coefficients of 50.3, 50.2, and 51.6 mL/mg cm for dissolved P3HT in *p*-xylene, toluene, and benzene, respectively. The fraction of polymer in the solid phase was calculated from a simple mass balance.

2.4. Rheology and Conductivity. Rheological measurements were made using an Anton Paar Physica MCR301 stress-controlled rheometer. A parallel plate geometry with a 50 mm diameter and 0.4 mm gap was preheated to 50 °C prior to loading the hot polymer solution in the liquid state. Once loaded, the solution was rapidly cooled to induce gelation. After the solution had solidified (~1 min) a fluorinated nonconductive oleophobic liquid, Fomblin Y 25/6, was added to the outer edge of the sample geometry to fully suppress the evaporation of the organic solvent. We have experimentally confirmed that the addition of Fomblin does not impact the rheology of P3HT organogels. The gel was then reheated to 80 °C for 2 min to completely redissolve the gel before the experiments were performed. Small-amplitude oscillatory strain measurements (γ = 0.25% and f = 1 Hz) were used to track changes in mechanical properties during gelation.

Simultaneous conductivity measurements were also made for some experiments. This was accomplished through the use of a special rheometer cell designed for simultaneous dielectric measurements. This cell is electrically isolated from the frame and the electronics of the rheometer. Electrical contact is created between a gold wire and the upper tool geometry (stainless steel) and also from the bottom tool (stainless steel). The conductivity and other electrical properties are then measured across the sample gap with the parallel plates of the rheometer also acting as electrodes. The use of stainless steel plates ensures that corrosion does not impact the electrical measurements. The ac conductivity measurements were made using an Agilent e4980a Precision LCR meter at a frequency of 2 kHz and a small perturbation voltage (200 mV) in the linear impedance region. Although the

dx.doi.org/10.1021/ma202564k | Macromolecules 2012, 45, 3452−3462

contact between the upper tool and the gold wire causes a constant frictional resistance to rotation, its effect is only noticeable when the samples are in the fluid dissolved state. Experiments were reproduced both with and without the gold wire to fully characterize its effect on the measured mechanical properties.

2.5. Scanning Transmission Electron Microscopy. Small quantities of the organogels were transferred to copper TEM grids with Formvar support films by briefly placing the grids in contact with the surface of the gel samples without applying pressure. In this way, only a thin-film of organogel is transferred to the TEM grid. Because of the very thin nature of the samples, the aromatic solvents evaporate under ambient conditions. TEM images were obtained with a FEI Tecnai G2 F20 transmission electron microscope operating at 120 kV in scanning TEM (sTEM) mode.

2.6. Small-Angle Scattering. Ultra small-angle neutron scattering (USANS) and small-angle neutron scattering (SANS) experiments were performed at the NIST Center for Neutron Research in Gaithersburg, MD. SANS measurements were performed on the NG3 and NG7 instruments using standard configurations to cover a broad q-range ($0.001 < q < 0.5$ Å^{-1}).[42] Dissolved polymer solutions were loaded into demountable cells with quartz windows (1 mm path length) and allowed to gel for a minimum of 24 h prior to measurement. The 2D scattering profiles of the sample were placed on an absolute scale by measuring the empty beam flux and correcting for background and empty cell scattering.[43] The 2D scattering profiles were averaged about the azimuthal angle, and the scattering intensity (I) was plotted against the scattering vector (q). USANS measurements were performed at NIST on the BT5 perfect crystal diffractometer extending the q-range to 4×10^{-5} Å^{-1}.[44] The data were reduced and desmeared using the NIST Igor-based algorithms.[43] Model fitting was performed using the NIST Igor-based analysis algorithms as well as the DANSE SansView software.[43,45]

3. RESULTS

3.1. Gelation of P3HT. Poly(3-hexylthiophene) (P3HT) can be solubilized in many aromatic solvents when the temperature is increased. When the solvent quality is lowered, often through temperature reduction, the polymer spontaneously self-assembles into semicrystalline nanofibers.[12,22,46] When the polymer is in dilute concentrations, fibers grow individually or in discrete fiber bundles (colloidal networks). On the other hand, if the concentration is larger than ~5 mg/mL, fiber formation at low temperatures leads to gelation. Rheology was utilized to track the mechanical evolution of a 30 mg/mL P3HT solution in p-xylene during the sol−gel transition (both gelation and redissolution).

Figure 1 shows the temperature-dependent elastic (G') and viscous modulus (G'') of a P3HT organogel formed in p-xylene. As the temperature of the polymer solution is reduced from 80 to 20 °C (at a rate of 2 °C/min), the sample remains a viscous liquid (no elastic component) until about 26 °C when a clear sol−gel transition occurs. At this temperature the elastic response due to the formation of the percolating network overwhelms the viscous response, which is indicated by the crossover ($G' = G''$) of the elastic and viscous moduli. Although gelation occurs rapidly, when the gel is held at 20 °C, the gel continues to stiffen as a function of time for several hours. This steady increase in the elastic modulus indicates that there is ongoing gelation and slow development of the fiber network. The inset frequency sweep in Figure 1 confirms that P3HT is a gel across a wide range of frequencies. Upon reheating (at a rate of 2 °C/min), P3HT shows significant thermal hysteresis prior to full dissolution at about 61 °C. The thermal hysteresis is likely due to the existence of a different dissolution mechanism with slower kinetics for fiber breakup.

Simultaneous rheology and conductivity measurements allow for direct correlation of the evolution of the mechanical and

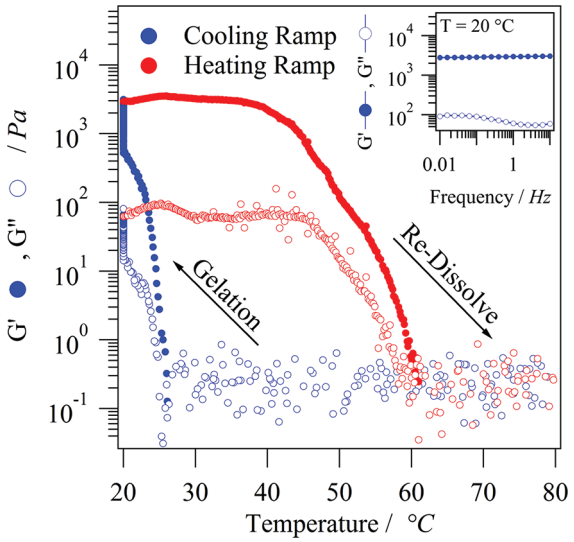


Figure 1. Temperature-dependent oscillatory rheology of a 30 mg/mL P3HT organogel formed and redissolved in p-xylene. The temperature sweep rate is 2 °C/min. When the temperature reached 20 °C, gelation was allowed to proceed to completion for 2 h prior to the heating ramp. Inset: frequency sweep of the fully developed P3HT organogel.

electrical properties during the gelation process. Figure 2a tracks the gelation and dissolution of a sample with 30 mg/mL of P3HT dissolved in p-xylene with simultaneous mechanical and electrical property measurements. For clarity, the mechanical data in Figure 2a are shown in terms of the complex modulus (G^*), which is related to the elastic and viscous moduli (G' and G'') by the equation

$$G^* = \sqrt{(G')^2 + (G'')^2} \quad (1)$$

The complex modulus is effectively equivalent to the elastic modulus for P3HT in the gel phase because $G' \gg G''$. However, it is also important to note that the complex modulus prior to gelation (i.e., in the soluble phase) is significantly affected by the friction between the upper geometry shaft and the gold contact that is necessary for the electrical connection, depicted in Figure 2b. The data shown in Figure 2a suggest that the increase in conductivity develops prior to the increase in G^*. However, this could also be due to the background friction that makes the measurement less sensitive to the initial changes in the elastic modulus. Nevertheless, it is clear that gelation occurs around 26 °C and that it corresponds to an increase of more than 2 orders of magnitude in the conductivity in addition to the observed increase in elasticity (G^*). When self-assembly is allowed to proceed at 20 °C for an additional 2 h, both the elastic modulus and the conductivity continue to increase, indicating a slow evolution of the organogel structure. A figure highlighting this increase can be found in the Supporting Information (Figure S4).

Figure 2a also shows that upon reheating there is significant thermal hysteresis in the mechanical and electronic properties of the gel prior to complete dissolution. This is particularly evident for the conductivity, which shows a significant increase in magnitude upon reheating. This response is due to the Arrhenius behavior of conductivity that is described by eq 2:

$$\sigma = Ae^{[-E_A/k_bT]} \quad (2)$$

Here, σ is the conductivity, A is a proportionality constant, E_A is the activation energy, k_b is Boltzmann's constant, and T is the

dx.doi.org/10.1021/ma202564k | Macromolecules 2012, 45, 3452−3462

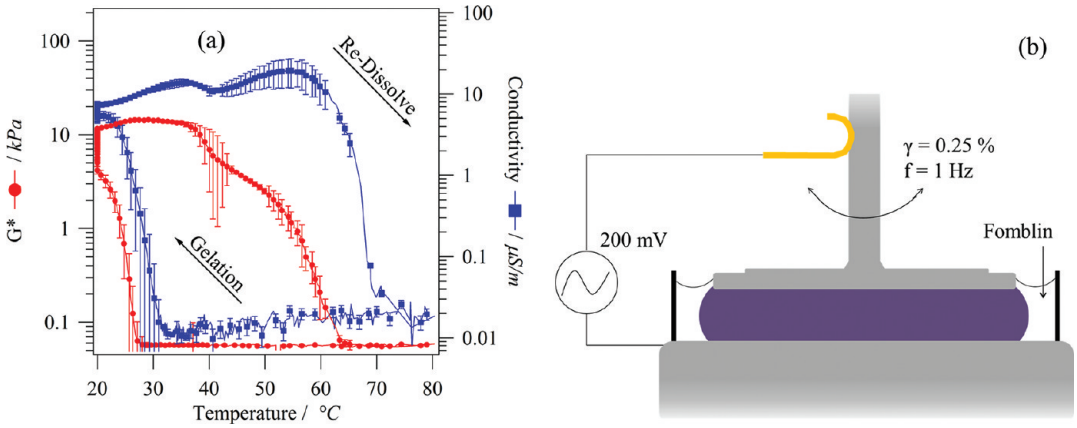


Figure 2. (a) Temperature-dependent, simultaneous oscillatory rheology and ac conductivity of a 30 mg/mL P3HT organogel formed and redissolved in *p*-xylene. The temperature sweep rate is 2 °C/min. When the temperature reached 20 °C, gelation was allowed to proceed to completion for 2 h prior to the heating ramp. (b) Schematic of the experimental configuration for simultaneous rheology and ac conductivity measurements.

temperature. When the initial increase in conductivity is fit to the Arrhenius equation, we find that $E_A = 300 \pm 79$ meV. This value is very similar to what others have reported for solid P3HT films.[47]

3.2. Properties of P3HT Organogels. Time-dependent simultaneous rheology and conductivity measurements were also performed to probe the development of mechanical and electrical percolation in networks. Rheology is only sensitive to fiber interactions that contribute to the transduction of mechanical stress between the two plates of the rheometer. Meanwhile, conductivity measurements are only sensitive to fiber paths that electronically bridge the electrodes (Figure 3a).

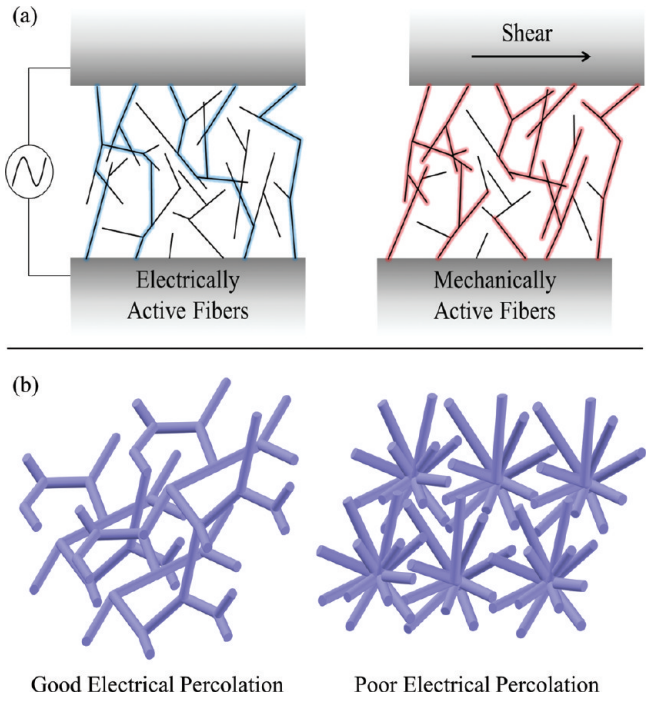


Figure 3. (a) Sketch to illustrate the sensitivity of rheology and conductivity measurements for characterizing the complex network structures. Fibers can contribute differently to the bulk conductivity (σ) and to the elastic modulus (G') of the network. (b) Example of two network structures that could result in similar mechanical properties but different electrical properties.

Thus, a single network can be characterized by two fractal dimensions resulting from these two different macroscopic properties, and we will refer to them as D_f^E for electronic percolation and D_f^M for mechanical percolation. Figure 3b depicts an example of two different network structures that might have very similar mechanical properties but would have drastically different electrical properties.

Liu and co-workers have demonstrated the use of rheology to determine the fractal dimension (D_f) of branching fibrillar organogels by using the Avrami theory to characterize the kinetics of gelation.[48−50] This powerful analysis relies on some basic assumptions including a constant fiber growth rate and branching frequency. Under isothermal conditions, the total extent of gelation is characterized by X_G

$$X_G(t) = 1 - \exp(-k(t - t_{gel})^{D_f}) \quad (3)$$

where k is a constant proportional to the rate of fiber growth, t is the elapsed time, and t_{gel} is the initial gelation time. The extent of gelation (X_G) is related to measurable properties such as the complex modulus (G^*) and the conductivity (σ) using

$$X_G(t) = \frac{G^*(t) - G^*_{bkg}}{G^*_{max} - G^*_{bkg}} \text{ or } X_G(t) = \frac{\sigma(t) - \sigma_{bkg}}{\sigma_{max} - \sigma_{bkg}} \quad (4)$$

where $G^*(t)$ is the time-dependent complex modulus, G^*_{bkg} is the complex modulus prior to gelation, G^*_{max} is the maximum complex modulus associated with kinetic equilibrium, $\sigma(t)$ is the time-dependent conductivity, σ_{bkg} is the conductivity of the solution prior to gelation, and σ_{max} is the maximum conductivity of the gel. To ensure that gelation was monitored at a constant temperature and from identical initial states, the fully dissolved polymer was rapidly cooled from 80 to 20 °C at a rate of 22.5 °C/min. The gelation process was then monitored as a function of time when the test solution reached 20 °C. The time required to reach the test temperature (<3 min) was much smaller than the characteristic gelation time.

Figure 4 shows the isothermal gelation kinetics of P3HT in different organic solvents. Upon close examination, it is evident that the solvent plays an important role in the development of the mechanical and electrical properties. The lower images in

dx.doi.org/10.1021/ma202564k | *Macromolecules* 2012, 45, 3452−3462

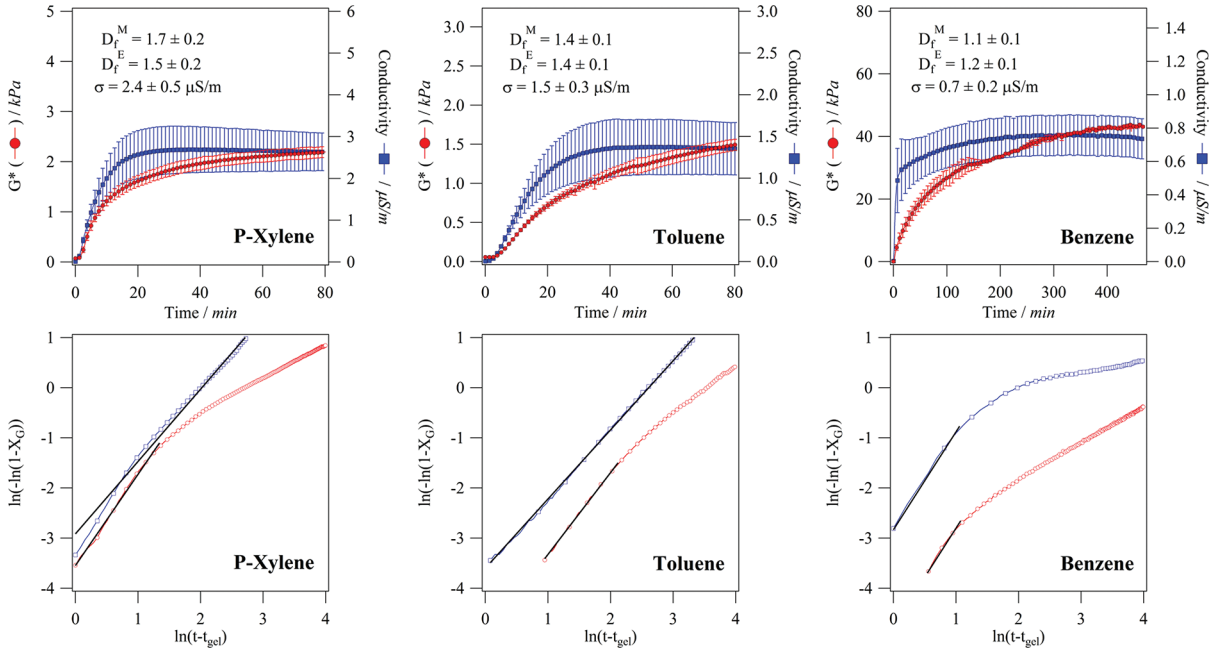


Figure 4. Top row: simultaneous rheology and conductivity collected during the isothermal gelation of 30 mg/mL P3HT in different aromatic solvents at a temperature of T = 20 °C. Bottom row: data represented in the linearized form (eq 5).

Figure 4 show the same data, but plotted in a linearized form of eq 3:

$$\ln[-\ln(1 - X_G(t))] = \ln(k) + D_f \ln(t - t_{gel}) \quad (5)$$

In this plot, the slope represents the fractal dimension and the intercept is related to the rate of gelation (k). In this format it becomes clear that, for all samples, there are two distinct slopes associated with the rheological measurement in the initial growth period and near its end. The slope change occurs near the time when the conductivity is fully developed for *p*-xylene and toluene organogels. In benzene organogels, there is a slope change associated with both the conductivity and the rheological measurement. This change occurs when the conductivity of the benzene sample is ∼50% developed, and unlike the *p*-xylene and toluene samples, the conductivity of benzene gels continues to increase until gelation is complete. As seen in Figure 4, the electrical properties of *p*-xylene and toluene gels fully develop on a shorter time scale than the mechanical properties. In this work, the mechanical (D_f^M) and electrical (D_f^E) fractal dimensions are extracted from the initial growth region, which corresponds to the largest increase in conductivity for all samples.

Table 1 summarizes the fitting results of the kinetic model as well as the equilibrium mechanical and electrical properties from the experiments shown in Figure 4. Benzene gels take significantly longer to reach equilibrium, resulting in a lower fractal dimension and suggesting that fewer fibers are growing simultaneously. According to the fractal dimensions, *p*-xylene and toluene organogels have denser and more branched network structures than benzene gels. Importantly, all three gels show significantly different maximum elastic moduli and conductivity values, indicating that there is potential to tune these properties for specific applications by simply controlling the solvent quality and the kinetics of gelation.

Table 1. Summary of Fitting Results to the Kinetic Gelation Model from Isothermal, Simultaneous Rheology and Conductivity Experiments for 30 mg/mL P3HT Organogels (Batch 2)

	p-xylene	toluene	benzene
k_E (min^{-1})	3.6×10^{-2}	2.4×10^{-2}	1.1×10^{-1}
D_f^E	1.5 ± 0.2	1.4 ± 0.1	1.2 ± 0.1
k_M (min^{-1})	3.9×10^{-2}	1.0×10^{-2}	2.5×10^{-2}
D_f^M	1.7 ± 0.2	1.4 ± 0.1	1.1 ± 0.1
G^*_{max} (kPa)	2.3 ± 0.1	1.7 ± 0.1	46.9 ± 5.3
σ_{max} (μS/m)	2.4 ± 0.5	1.5 ± 0.3	0.7 ± 0.2

Conjugated polymers rarely reach a fully self-assembled state due to their finite solubility in aromatic solvents. Therefore, the total amount of polymer in solid form (i.e., solids fraction) is also an important parameter to consider in evaluating the properties of organogels. The total extent of solidification in the gels can be quantified by tracking the concentration of dissolved polymer over time with the equation

$$\phi = 1 - \frac{C(t)}{C_i} = 1 - \frac{A(t)/(\varepsilon l)}{C_i} d_f \quad (6)$$

where ϕ is the solids fraction, $C(t)$ is the dissolved polymer concentration at time t, C_i is the initial concentration of polymer, $A(t)$ is the absorbance due to dissolved polymer at time t, ε is the extinction coefficient of P3HT in the solvent, l is the path length of the cell, and d_f is the dilution factor. The development of the solids fraction over time can be seen in Figure 5. *p*-Xylene samples take significantly less time to reach the final equilibrium state than organogels formed in toluene and benzene. In contrast, benzene gels form with a slow and continuous evolution but are still able to reach larger equilibrium solid fractions than toluene gels, which contain the largest amounts of dissolved polymer at long times. After more than 16 h of gelation, the equilibrium solids fractions of the organogels are 83%, 81%, and 56% for benzene, *p*-xylene, and toluene, respectively.

3.3. Structural Characterization of P3HT Organogels.

The self-assembly of an interconnected network of semiconducting

dx.doi.org/10.1021/ma202564k | *Macromolecules* 2012, 45, 3452−3462

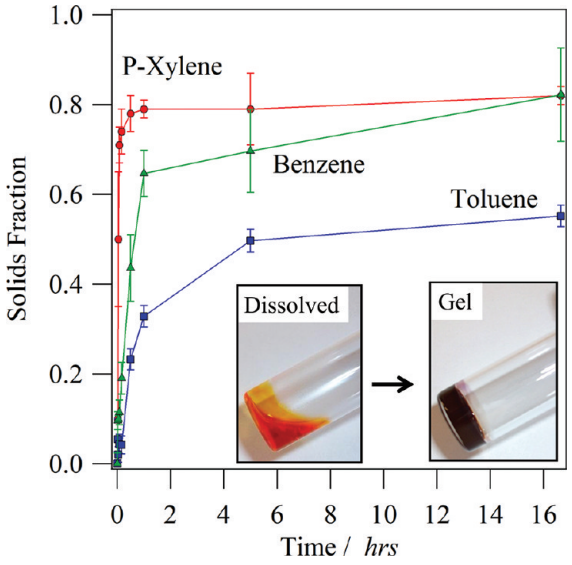


Figure 5. Time evolution of the solids content of 30 mg/mL P3HT organogels self-assembled in aromatic solvents at 20 °C.

fibers makes organogels of P3HT particularly promising for engineering low-cost electronic devices such as solar cells. However, the multiscale structure of these networks must be fully characterized in order to optimize it for relevant applications. Here we use a combination of sTEM and small-angle neutron scattering techniques to characterize the bulk structure of P3HT organogels over a wide range of length scales.

3.3.1. Scanning Transmission Electron Microscopy. Dried P3HT networks were evaluated using sTEM and typical images are shown in Figure 6 highlighting important features. Most notable are dense nucleation centers, fibrillar "ropes" (i.e., lateral fiber bunches), and branching of individual fibers. Dense nucleation centers were primarily observed in samples prepared from batch 1 of the P3HT. Dense radial growth can originate from impurities or from aggregates that act as nucleation sites for new fibers.[51] We believe that this feature could arise in P3HT samples due to impurities, such as residual polymerization catalyst, or due to high molecular weight fractions that may not fully dissolve and may act as nucleation sites. Batch 1, which shows more nucleation, had a significantly larger molecular weight and polydispersity index when compared to batch 2. Dense nucleation centers are expected to be a potential source of trap sites for charge carriers in the organogels due to their disordered nature and because they act as junctions to several fibers. Therefore, to improve transmission of charge, it is desirable to minimize the formation of dense nucleation centers.

The fiber "ropes" observed in this study are also consistent with reported AFM studies of P3HT gels.[23] Fibrillar roping, which is observed in both P3HT batches, results in the lateral aggregation of fibers often with less than 10 nm of space between fibers. Finally, fibrillar branching (or fiber splitting) is also observed in all sTEM images. Bifurcations are expected to be beneficial for electronic properties as they allow for continuous charge transport along fibers through branch points and reduce the total number of potential charge trap sites.[12] Unfortunately, the extent of branching could not be easily quantified in sTEM due to the three-dimensional structure of the gel and the high fiber density.

3.3.2. Small-Angle Neutron Scattering of P3HT Organogels. While sTEM is an effective tool for visualizing the gel structure, it only yields a two-dimensional projection of a three-dimensional structure, it requires a thin sample to resolve the morphology, and it is performed on dry films after solvent evaporation. In contrast, small-angle neutron scattering (SANS) is a proven nondestructive method for quantifying the average bulk structural properties of solvated P3HT gels over all relevant length scales.[12] Figure 7 shows the 1D SANS and USANS profiles for a 30 mg/mL P3HT organogel self-assembled in *p*-xylene. The scattering provides structural information over multiple length scales (~1 to 10 000 nm) to characterize all features of the gel. The morphology of P3HT organogels is modeled using a similar approach to one established in a recent publication.[12]

At high-q, the internal structure and semicrystalline nature of P3HT fibers dominates the scattering intensity. The peak at high-q is characteristic of the lamellar spacing within the P3HT crystal lattice.[14] This region was fit to a Gaussian peak (seen in Figure S5) corresponding to a spacing of 15.8 Å, which is within 1 Å of the expected value reported in the literature.[52] A more detailed analysis of the diffraction peak, with respect to concentration, is not possible due to the incoherent background and the resolution limit of the SANS instrument at high-q.

The cross-sectional shape of the individual fibers, e.g., height (a) and width (b), was fit in the region of $0.01 < q < 0.4$ Å^{-1} using a parallelepiped form factor, $P_{PP}(q)$, while also using a

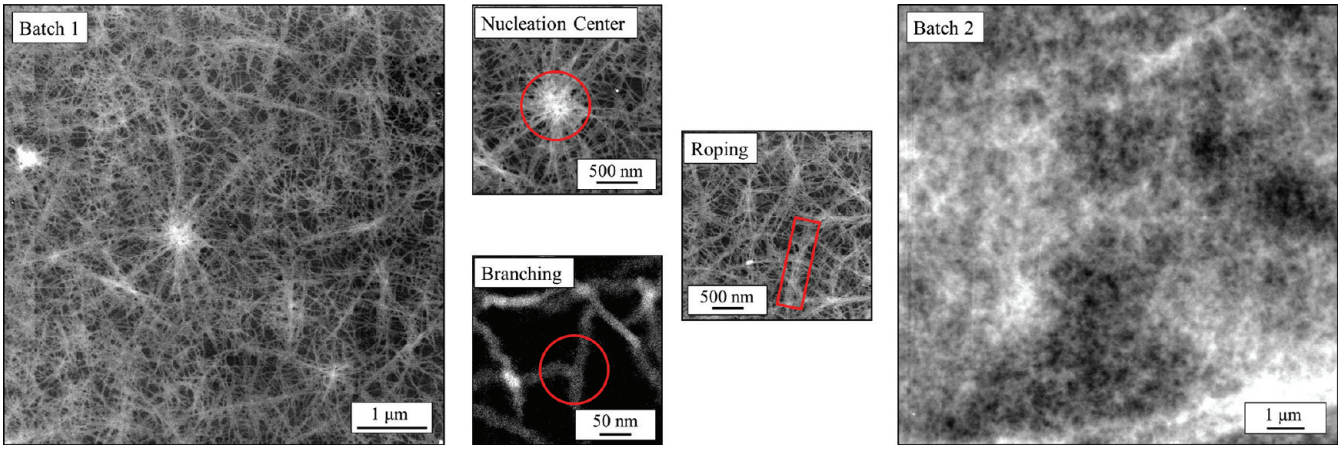


Figure 6. P3HT organogel network features can include dense nucleation centers, fibrillar roping, and fibrillar branching. The sTEM images are made from 27 mg/mL P3HT (batch 1) and 30 mg/mL P3HT (batch 2) in toluene.

dx.doi.org/10.1021/ma202564k | *Macromolecules* 2012, 45, 3452–3462

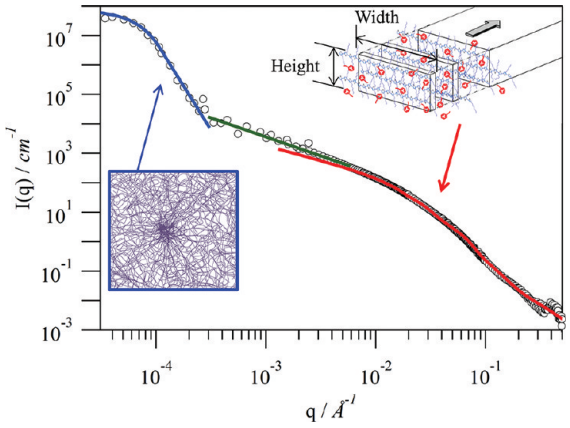


Figure 7. SANS and USANS profile for 30 mg/mL P3HT (batch 1) in *p*-xylene (○). Fits to different models are shown as colored lines; the combined parallelepiped model (red), fractal network power law (green), and Guinier extrapolation (blue). The deviation of the parallelepiped form factor of at q = 0.009 Å^{-1} is due to the increased power-law slope caused by the fractal network structure.

mass balance to account for the dissolved polymer that does not gel.[12,53] The total scattering is defined by

$$I(q) = \phi_v\phi_{PP}(\Delta\rho_{PP})^2 P_{PP}(q) + \phi_v(1-\phi_{PP}) \times (\Delta\rho_{PExV})^2 P_{PExV}(q) \quad (7)$$

where ϕ_v is the total volume fraction of P3HT, $\Delta\rho$ is the scattering length density contrast, and ϕ_{PP} is the fraction of P3HT in parallelepiped form (i.e., fibrillar P3HT). The scattering from the dissolved polymer is modeled using the form factor for a polymer with excluded-volume interactions ($P_{PExV}(q)$).[54] Setting the scattering data in an absolute scale allows for rigorous model fitting with only a few adjustable parameters (ϕ_{PP}, a, and b). A detailed description of the parallelepiped and polymer excluded volume form factors is included in the Supporting Information.

The scattering length density (SLD) is a critically important physical parameter for fitting of neutron scattering data. The SLD contrast between different phases (i.e., fibrillar P3HT vs solvent) is directly related to the scattering intensity. The SLD can be easily calculated if the density and molecular formula of each material are precisely known. Unfortunately, there are too many discrepancies between the reported densities of fibrillar P3HT in the literature with values ranging between 1.1 and 1.3 g/cm^3.[14,20,55,56] Therefore, we performed a careful contrast variation experiment to determine the SLD of P3HT gels in all of our solvent systems. In this experiment, the isotopic composition of the solvent was changed in order to vary the SLD contrast between the two phases. From a linear fit of the square root of the intensity, at low-q, as a function of the hydrogen content in the solvent, the SLD of fibrillar P3HT was determined to be $(1.07 \pm 0.1) \times 10^{-6}$ Å^{-2} with little variability between solvents. Given the known atomic composition of P3HT, the corresponding mass density for a P3HT fiber to yield this SLD would have to be 1.75 g/cm^3. This value is much larger than any published report. Therefore, it is likely that another factor must be causing the SLD of the fibers to be much larger than expected. With an Anton Paar DMA 35 density meter, we measured the mass density of extracted fibers and obtained a value of 1.1 g/cm^3 that is nearly identical to other published values.[14] This suggests that there is likely a considerable amount of deuterated solvent incorporated within the volume of the P3HT fibers (Figure 7, inset). If one assumes the density of solid P3HT to be 1.1 g/cm^3, then the fibers in the organogel would contain ~11 wt % of entrained solvent. This correctly accounts for the higher SLD value of P3HT fibers in the gel when compared reports from neutron reflectivity for solid thin films of P3HT.[20,21,57] This contrast variation experiment verifies that P3HT fibers within solvated gels contain semicrystalline domains as well as entrained solvent.

It is clear from Figure 7 that, at $2 \times 10^{-4} < q < 2 \times 10^{-3}$ Å^{-1}, the combined parallelepiped model deviates significantly from the scattering profiles. The deviation occurs at a q-value that is related to the onset of fractal behavior (d_{onset}), which is the characteristic length where isolated fibers no longer approximate the scattering profiles because of the network structure.[12] In this region, the scattering intensity is fit to a simple power law, $I(q) \sim q^{-D_f^S}$, where D_f^S is related to the fractal dimension of the network. The fractal dimension obtained from scattering experiments (D_f^S) may be different from either the fractal dimensions obtained from electrical (D_f^E) or mechanical measurements (D_f^M). SANS data are sensitive to all fibers located within the scattering volume; therefore, the fractal dimension is related to the total fiber density and arrangement in the network. This contrasts with the growth kinetics experiments, where only some fibers may contribute to the mechanical or electrical properties (Figure 3). Furthermore, the fractal dimension obtained from the power-law fit in scattering will also be sensitive to density fluctuations within the network. Inhomogeneous networks show a higher fractal dimensions in scattering experiments due to bulk concentration gradients that cause an increase in the scattering intensity.[58]

In the low-q region, $7 \times 10^{-5} < q < 2 \times 10^{-4}$ Å^{-1}, there is another increase in the scattering intensity that clearly deviates from fractal behavior. Scattering in this region is attributed to the dense nucleation centers in the gels that are also visible in the electron microscopy images. The characteristic size of these dense nucleation centers can be obtained by performing a simple Guinier extrapolation, which results in a radius of gyration of ~10 μm. This low-q characteristic is most clearly observed in samples prepared from P3HT in batch 1. It is still possible that dense nucleation centers also occur in batch 2, but those domains would need to be larger than the minimum q-range probed by USANS. In contrast, the sTEM images did not show dense nucleation centers in samples prepared from batch 2 so it is likely that they are not present. Scattering data comparing the two polymer batches can be found in Figure S3.

SANS probes the multiscale structure of P3HT organogels without disturbing the gels. Figure 8a,b shows the results of fitting P3HT scattering data to the combined model (eq 7).[45] Interestingly, the fiber width is relatively constant at about 24 nm regardless of the solvent type or the polymer concentration. The fiber height is also found to be independent of the polymer concentration. However, there is a systematic solvent dependence of the fiber height as P3HT fibers formed in benzene are typically 15% thicker than all other samples.

Because exciton dissociation occurs at the interface between donor and acceptor materials, the total interfacial area of the fibers in the gel is an important metric that can significantly affect the overall efficiency of OPV devices. To this end, the specific surface area of the P3HT fibers in each organogel was determined from a standard Porod analysis. In all samples, an intensity proportional to q^{-4} develops between $0.07 < q < 0.1$ Å^{-1} due to the sharp interface between the P3HT fibers and

dx.doi.org/10.1021/ma202564k | *Macromolecules* 2012, 45, 3452−3462

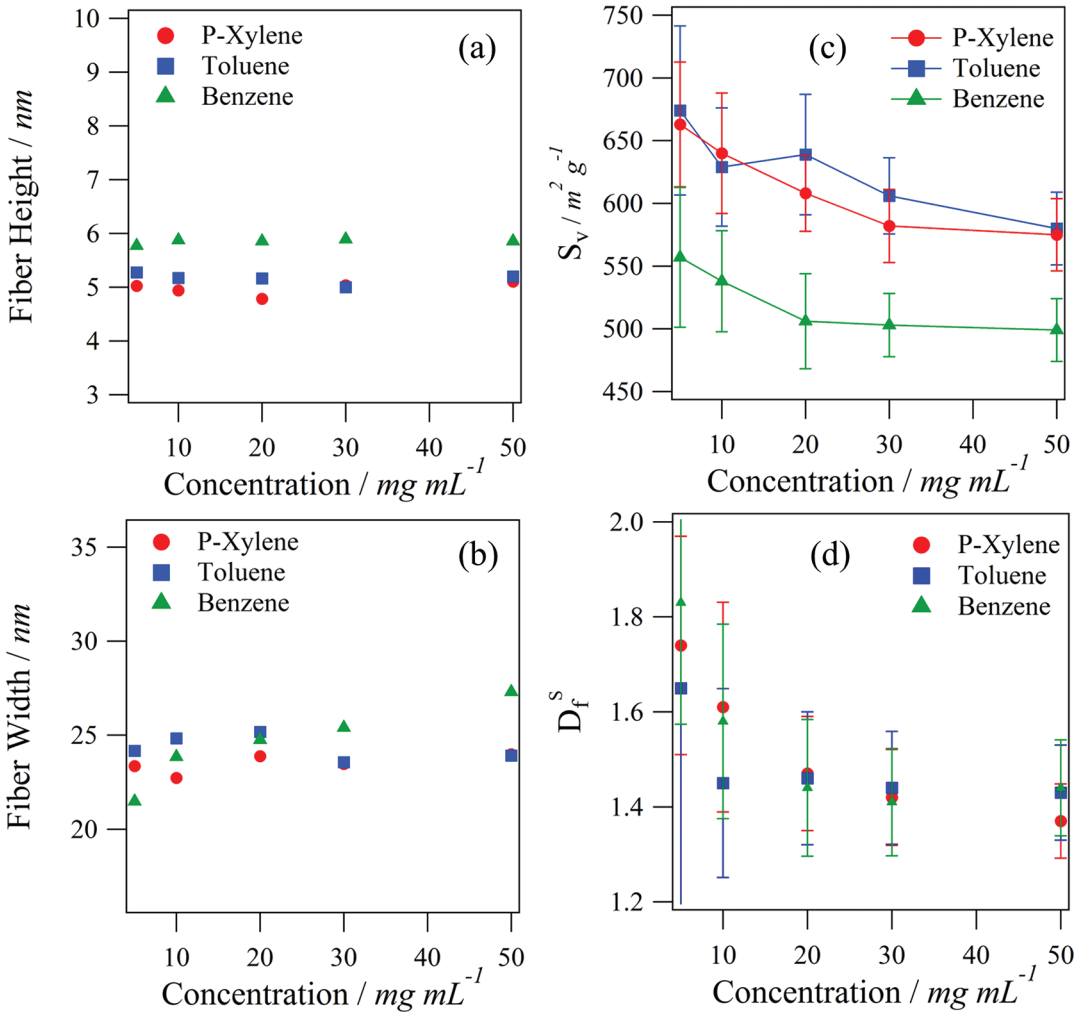


Figure 8. P3HT fibrillar (a) height and (b) width as obtained from parallelepiped model, the (c) specific surface area (S_v) of P3HT fibers obtained from a Porod analysis, and the (d) network fractal dimension (D_f^S) obtained from power law fitting. The error bars reflect the fitting uncertainty. In (a) and (b) the error bars are smaller than the marker size.

the solvent (Figure S2).[36] All of the details and basic equations used in the surface area analysis are also discussed in the Supporting Information. This surface area analysis requires knowledge of the effective SLD in the two phases of the material. For this, we have experimentally determined the SLD of the fibers with entrained solvent ($(1.07 \pm 0.1) \times 10^{-6}$ Å^{-2}) as discussed before and also calculated the SLD of *p*-xylene, toluene, and benzene (5.76×10^{-6}, 5.65×10^{-6}, and 5.40×10^{-6}, respectively). It was determined that the low concentration of dissolved polymer in the solvent did not significantly change the SLD of the continuous phase.

The specific surface area of the P3HT nanofibers is reported in Figure 8c. All of the organogels evaluated have a very high specific surface area that decreases with concentration and that also varies with the solvent type. The slight reduction in the specific surface area with increasing polymer concentration is likely caused by an increase in fiber−fiber contacts leading to lower interfacial area between P3HT and solvent. The reduced specific surface area of P3HT fibers in benzene, relative to the other solvents, can also be fully explained by accounting for the increase in the cross-sectional dimensions of the fibers due to the larger height (Figure 8a).

D_f^S is also plotted as a function of concentration and solvent in Figure 8d. The P3HT gels characterized in this study are described by fractal dimensions between 1.4 and 1.9. The fractal dimension, like the specific surface area, decreases as a function of concentration. At first look, this could be interpreted as a decrease in the network density with increasing concentration. However, it is also important to note that heterogeneous networks with significant density fluctuations show higher apparent fractal dimensions than homogeneous networks.[58] At low concentrations, inhomogeneities will occur due to solvent-rich regions that develop between fiber-rich regions of the organogel. These solvent spaces are more abundant at polymer concentrations that are very close to the onset of percolation. When the concentration increases, the organogels effectively fill all free space and become increasingly more homogeneous.

4. DISCUSSION

We have demonstrated that P3HT dissolved at high concentrations will self-assemble into branching fibrillar organogels, with variable network structure, when the solvent quality is gradually reduced. When evaluating the structure of P3HT organogels for photovoltaic applications, it is important to point out that the cross-sectional dimension of the fibers is always smaller than the maximum exciton diffusion length (~20 nm).[2,11] Therefore, if the solvent phase is later replaced by an n-type semiconductor (e.g., C_{60} or PCBM), most excitons

dx.doi.org/10.1021/ma202564k | *Macromolecules* 2012, 45, 3452−3462

generated within the gel fibers would effectively dissociate into electrons and holes and also be effectively conducted to the corresponding electrodes. The SANS results demonstrate that, regardless of the solvent and concentration, all P3HT organogels in this study have fiber dimensions that lie within this important limit. Furthermore, SANS reveals that the fiber structure is nearly identical across solvents and concentrations, with the exception of organogels prepared in benzene that have a slightly larger fiber height. The larger fiber cross-section of gels prepared in benzene (~15% increase in fiber thickness) contributes to a lower interfacial area and a larger elastic modulus (46.9 kPa) when compared to gels formed in *p*-xylene (2.3 kPa) and toluene (1.7 kPa). On the other hand, P3HT gels prepared in benzene also show lower electrical conductivity values when compared to gels formed in other solvents. This suggests that the macroscopic properties in these materials relate differently to specific structural features in the gels. Scanning TEM also demonstrates that gels are bifurcating networks where fibers split and branch to form interconnected networks. The branching observed in P3HT gels allows for effective charge transport through fiber junctions and along the $\pi-\pi$ stacking direction of the fiber axis, leading to effective and long-range charge propagation (i.e., high conductivity through millimeter thick samples). Charge transport between fibers that are only touching is not expected to be very effective because the exposed alkyl chains of the P3HT act as insulating layers that hinder inter-fiber charge transport.[12,59]

We have also demonstrated that network structures in P3HT organogels can be evaluated using a variety of complementary techniques (rheology, conductivity, and neutron scattering) to characterize different components of the same network (D_f^M, D_f^E, and D_f^S). The mechanical fractal dimension D_f^M is sensitive to fibers that interact and contribute to the transduction of mechanical stress, D_f^E is sensitive to fibers that electrically percolate the electrodes, and D_f^S characterizes the total network density and its inhomogeneities. D_f^S was found to be relatively constant across solvents, but D_f^M and D_f^E differed significantly for the three solvents. In each of the solvents, D_f^M and D_f^E are found to be vey similar during the initial growth region, suggesting that both components develop similarly at short time scales. However, unlike the electrical conductivity, the modulus continues to slowly evolve with time during gelation for samples prepared in *p*-xylene and toluene. The linearized data in Figure 4 (bottom plots) show that the slope corresponding to the mechanical fractal dimension in all samples changes at an intermediate time during the gelation process. In contrast, a single slope characterizes the linearized conductivity data for P3HT gels in toluene and *p*-xylene over the full time range. Benzene gels show changes in slope for the elastic modulus and the electrical conductivity. These combined rheology and conductivity measurements also demonstrate that increasing elasticity does not always result in increasing electrical conductivity. This is because continued fiber growth may not always improve electrical percolation. For example, at long times newly formed fibers can contribute to the increased transduction of mechanical stress but may not bridge the electrodes in order to contribute to increasing the bulk conductivity. Additional studies are currently being pursued to further understand how other self-assembly conditions (e.g., different temperatures) could also impact the mechanical and electrical properties of organogels.

The structure and property measurements presented in this work provide great insight and allow us to propose a detailed gelation mechanism for P3HT in aromatic solvents (Figure 9). The data in Figure 1 shows that P3HT solutions do not have a measurable elastic component until a percolating gel forms abruptly upon cooling. In addition, SANS and sTEM both demonstrate that P3HT polymers self-assemble into interconnected fibers in the gels. The isothermal kinetic experiments (Figure 4) further show that fibers branch to different degrees during the gelation process depending on the solvent quality. These branching sites can also be directly observed in the sTEM images shown in Figure 6. The detailed gelation mechanism that emerges from these new experiments builds upon those presented in pervious works. Koppe and co-workers proposed that P3HT gelation occurred as a result of polymer aggregation followed by physical cross-linking of aggregates.[28] Xu and co-workers suggested that fibers grew in one dimension and subsequently aggregated to produce a percolated network structure.[60] Our results suggest a mechanism in which discrete branched fiber networks form at short times while the sample remains liquid and continue to grow until percolation and gelation is achieved. This is supported by our previous studies on network structures formed in liquid P3HT solutions at lower concentrations.[12] Subsequently, significant fiber and network growth continues to occur long after the first signs of gelation are observed. Yet, fibers formed at long times may contribute differently to the development of various macroscopic properties (i.e., electronic or mechanical) depending on whether or not they result in a net increase in the network interconnectivity. Finally, these results also suggest that the solvent quality can be used to alter branching in growing fibers and to modify the final properties of the organogels.

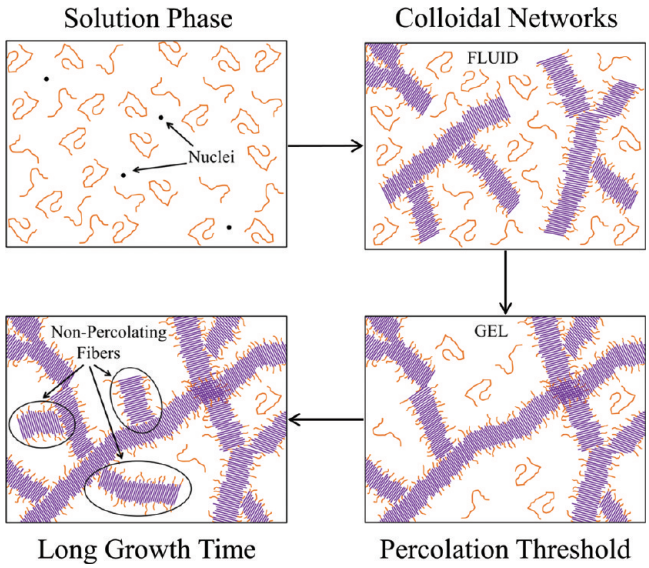


Figure 9. Schematic of the proposed gelation mechanism for P3HT in aromatic solvents. Upon cooling, dissolved polymer grows into fibers from nucleation sites. Lattice dislocations lead to branching and the formation of a colloidal dispersion of isolated fiber networks. Eventually, dispersed networks grow and reach the percolation threshold to form a gel. The network structure continues to develop with time as new fibers grow and may contribute differently to the developing gel properties (i.e., conductivity and elasticity).

Simultaneous rheology and conductivity measurements reveal that different mesoscale structures can be achieved by adjusting self-assembly conditions. Solvent quality has been

dx.doi.org/10.1021/ma202564k | *Macromolecules* 2012, 45, 3452–3462

found to be a primary factor controlling the network formation in a variety of small molecule systems.[50] The equilibrium solids fraction (Figure 5) in different solvents is an indication of supersaturation and therefore solvent quality.[37] Based on these results, toluene is the best solvent for P3HT. However, our data also suggests that relative solubility is not the only factor contributing to the final structure (i.e., D_f^M and D_f^E) and properties (i.e., elasticity and conductivity) of P3HT networks. For example, the incorporation of solvent molecules within growing fibers may also play a substantial role in controlling growth and the resulting structure. More work is therefore needed to fully determine all fundamental dependencies between the driving forces for gelation and the resulting network structures.[37,38]

From our results, it is evident that the network structure of P3HT gels can be manipulated to produce distinctly different mechanical and electrical properties. In fact, there is a direct correlation between increased branching (D_f^M and D_f^E) and the final conductivity of the gels. Branching fibers should increase conductivity more effectively than fibers that only "touch" each other because the insulating alkane layers will hinder inter-fiber charge transport. Since fibers have a nearly identical nanoscale structure, the changes in mechanical and electrical properties can be primarily attributed to differences in the mesoscale structure. That being said, the gels formed in benzene have the highest modulus and lowest conductivity. One possible explanation for this is that the increased fiber thickness in benzene results in significantly stiffer fibers compared to *p*-xylene or toluene. This can easily explain the increased elastic modulus of these gels. On the other hand, both the electrical and mechanical fractal dimensions indicate that fiber growth in benzene is less branched than in any other solvent, and this could lead to the reduced bulk conductivity.

Malik and co-workers also found that gelation of P3HT resulted in an order of magnitude increase in conductivity when compared to thin films.[29,30] Here, we confirm that the conductivity of the gel phase (measured up to 7 μS/m at 20 °C) is significantly larger when compared to thin solid films reported in literature (0.678 μS/m).[47] Furthermore, organogels are able to effectively transport charges over very large distances due to their percolating network structure. In our experiments, samples as thick as 2 mm were found to maintain excellent conductive properties.

Temperature adjustment could be another way to tune the final network structure. Small molecule organogels have been produced with different network structures through control of supersaturation by varying the temperature or the thermal history.[38] When comparing identical samples in Figure 2 (slow cooling ramp of 2 °C/min) and Figure 4a (isothermal gelation at 20 °C), it is found that self-assembly associated with slow cooling results in a network structure with a 3-fold increase in conductivity (measured at 20 °C). Unfortunately, the full Avrami analysis cannot be performed using non-isothermal data such as that presented in Figure 2. Still, the results demonstrate that by adjusting self-assembly conditions it is possible to tune the macroscopic properties of P3HT organogels.

Gelation is a nearly universal phenomenon for fiber-forming conjugated polymers, but to this point it has been poorly characterized and largely avoided. The potential to design network structures for organogels of conjugated polymers opens up numerous possibilities within the field of organic electronics, especially when considering OPVs. We have demonstrated that P3HT organogels have a high specific surface area, high conductivity, fibers that are the correct size for exciton diffusion and that there is ample void space for backfilling with small molecule n-type semiconductors.[25] The challenge for conjugated polymer organogels remains in the possibility of coating them using traditional manufacturing processes. Our lab has recently demonstrated that stable gel dispersions can be processed and used in functioning OPV devices while still maintaining the network structure and properties.[36] Still, significantly more work is necessary, including optimizing the incorporation of the n-type fullerene phase, in order to continue improving the performance of organogel devices.

5. CONCLUSIONS

In summary, dissolved P3HT at high concentration self-assembles into branching fibrillar organogels with high conductivities and high interfacial areas. Simultaneous rheology and conductivity measurements have been used to systematically probe the gelation mechanism, and it was found to be characteristic of classic nucleation and growth for branching fiber systems. Fitting of 1D SANS and USANS profiles has shown that the nanoscale fiber structure of P3HT is relatively constant regardless of solvent or concentration. However, we have also demonstrated that the mesoscale network structure and the resulting mechanical and electrical properties are tunable by adjusting self-assembly conditions. Furthermore, these results demonstrate that higher conductivities can be achieved by increasing branching in the network structure. This work contributes to developing the fundamental understanding that will be necessary to engineer organogels with optimized properties for target applications.

■ ASSOCIATED CONTENT

Supporting Information

Form factor analysis of SANS data; Porod analysis and specific surface area; Figures S1−S5. This material is available free of charge via the Internet at http://pubs.acs.org.

■ AUTHOR INFORMATION

Corresponding Author

*E-mail: dpozzo@u.washington.edu.

Author Contributions

†These authors contributed equally.

Notes

The authors declare no competing financial interest.

■ ACKNOWLEDGMENTS

This work is primarily supported by the Department of Energy Office of Basic Energy Sciences under Award DE-SC0005153. G.M.N. received an IGERT fellowship from NSF DGE Award 0654252, IGERT program on Bioresource Based Energy for Sustainable Societies. We acknowledge the support of the National Institute of Standards and Technology in providing the neutron research facilities used in this work. This work benefitted from DANSE software developed under NSF Award DMR-0520547. We thank Jae Cho (NIST) for providing the combined model for use within the DANSE software package. Part of this work was conducted at the University of Washington NanoTech User Facility, a member of the NSF National Nanotechnology Infrastructure Network (NNIN).

■ REFERENCES

(1) Hoppe, H.; Sariciftci, N. S. *J. Mater. Res.* **2004**, *19*, 1924−1945.

(2) Yang, X.; Loos, J.; Veenstra, S. C.; Verhees, W. J. H.; Wienk, M. M.; Kroon, J. M.; Michels, M. A. J.; Janssen, R. A. J. *Nano Lett.* **2005**, *5*, 579−583.
(3) Halls, J. J. M.; Walsh, C. A.; Greenham, N. C.; Marseglia, E. A.; Friend, R. H.; Moratti, S. C.; Holmes, A. B. *Nature* **1995**, *376*, 498−500.
(4) Department of Energy, Basic Research Needs for Solar Energy Utilization; http://science.energy.gov/~/media/bes/pdf/reports/files/seu_rpt.pdf, 2005.
(5) Wohrle, D.; Meissner, D. *Adv. Mater.* **1991**, *3*, 129−138.
(6) Coakley, K. M.; McGehee, M. D. *Chem. Mater.* **2004**, *16*, 4533−4542.
(7) Yu, G.; Gao, J.; Hummelen, J.; Wudl, F.; Heeger, A. J. *Science* **1995**, *270*, 1789−1791.
(8) Yu, G.; Heeger, A. J. *J. Appl. Phys.* **1995**, *78*, 4510−4515.
(9) van Bavel, S.; Sourty, E.; de With, G.; Frolic, K.; Loos, J. *Macromolecules* **2009**, *42*, 7396−7403.
(10) Rice, A. H.; Giridharagopal, R.; Zheng, S. X.; Ohuchi, F. S.; Ginger, D. S.; Luscombe, C. K. *ACS Nano* **2011**, *5*, 3132−3140.
(11) Shaw, P. E.; Ruseckas, A.; Samuel, I. D. W. *Adv. Mater.* **2008**, *20*, 3516−3520.
(12) Newbloom, G. M.; Kim, F. S.; Jenekhe, S. A.; Pozzo, D. C. *Macromolecules* **2011**, *44*, 3801−3809.
(13) Moule, A. J.; Meerholz, K. *Adv. Funct. Mater.* **2009**, *19*, 3028−3036.
(14) Yin, W.; Dadmun, M. *ACS Nano* **2011**, *5*, 4756−4768.
(15) Zhang, Y.; Yip, H.-L.; Acton, O.; Hau, S. K.; Huang, F.; Jen, A. K.-Y. *Chem. Mater.* **2009**, *21*, 2598−2600.
(16) Treat, N. D.; Brady, M. A.; Smith, G.; Toney, M. F.; Kramer, E. J. Hawker, C. J.; Chabinyc, M. L. *Adv. Energy Mater.* **2011**, *1*, 82−89.
(17) Cravino, A.; Sariciftci, N. S. *J. Mater. Chem.* **2002**, *12*, 1931−1943.
(18) Pingree, L. S. C.; MacLeod, B. A.; Ginger, D. S. *J. Phys. Chem. C* **2008**, *112*, 7922−7927.
(19) Coffey, D. C.; Reid, O. G.; Rodovsky, D. B.; Bartholomew, G. P.; Ginger, D. S. *Nano Lett.* **2007**, *7*, 738−744.
(20) Kiel, J. W.; Kirby, B. J.; Majkrzak, C. F.; Maranville, B. B.; Mackay, M. E. *Soft Matter* **2010**, *6*, 641−646.
(21) Kiel, J. W.; Eberle, A. P. R; Mackay, M. E. *Phys. Rev. Lett.* **2010**, *105*, 168701−168705.
(22) Berson, S.; De Bettignies, R.; Bailly, S.; Guillerez, S. *Adv. Funct. Mater.* **2007**, *17*, 1377−1384.
(23) Chen, C.-Y.; Chan, S.-H.; Li, J.-Y.; Wu, K.-H.; Chen, H.-L.; Chen, J. H.; Huang, W.-Y.; Chen, S.-A. *Macromolecules* **2010**, *43*, 7305−7311.
(24) Chen, J.-H.; Chang, C.-S.; Chang, Y.-X.; Chen, C.-Y.; Chen, H.-L.; Chen, S.-A. *Macromolecules* **2009**, *42*, 1306−1314.
(25) Huang, P.-T.; Chang, Y.-S.; Chou, C.-W. *J. Appl. Polym. Sci.* **2011**, *122*, 233−240.
(26) Huang, W. Y.; Huang, P. T.; Han, Y. K.; Lee, C. C.; Hsieh, T. L.; Chang, M. Y. *Macromolecules* **2008**, *41*, 7485−7489.
(27) Kitts, C. C.; Vanden Bout, D. A. V. *Polymer* **2007**, *48*, 2322−2330.
(28) Koppe, M.; Brabec, C. J.; Heiml, S.; Schausberger, A.; Duffy, W.; Heeney, M.; McCulloch, I. *Macromolecules* **2009**, *42*, 4661−4666.
(29) Malik, S.; Jana, T.; Nandi, A. K. *Macromolecules* **2001**, *34*, 275−282.
(30) Malik, S.; Nandi, A. K. *J. Phys. Chem. B* **2004**, *108*, 597−604.
(31) Malik, S.; Nandi, A. K. *J. Appl. Polym. Sci.* **2007**, *103*, 2528−2537.
(32) Wang, P.-S.; Lu, H.-H.; Liu, C.-Y.; Chen, S.-A. *Macromolecules* **2008**, *41*, 6500−6504.
(33) Kim, B.-G.; Jeong, E. J.; Park, H. J.; Bilby, D.; Guo, L. J.; Kim, J. *ACS Appl. Mater. Interfaces* **2011**, *3*, 674−680.
(34) Lin, Z.-Q.; Shi, N.-E.; Li, Y.-B.; Qiu, D.; Zhang, L.; Lin, J.-Y.; Zhao, J.-F.; Wang, C.; Xie, L.-H.; Huang, W. *J. Phys. Chem. C* **2011**, *115*, 4418−4424.
(35) Alcazar, D.; Wang, F.; Swager, T. M.; Thomas, E. L. *Macromolecules* **2008**, *41*, 9863−9868.
(36) Richards, J. J.; Weigandt, K. M.; Pozzo, D. C. *J. Colloid Interface Sci.* **2011**, *364*, 341−350.
(37) Li, J.-L.; Liu, X.-Y.; Wang, R.-Y.; Xiong, J.-Y. *J. Phys. Chem. B* **2005**, *109*, 24231−24235.
(38) Li, J.-L.; Yuan, B.; Liu, X.-Y.; Xu, H.-Y. *Cryst. Growth Des.* **2010**, *10*, 2699−2706.
(39) Chen, D.; Nakahara, A.; Wei, D.; Nordlund, D.; Russell, T. P. *Nano Lett.* **2011**, *11*, 561−567.
(40) Knaapila, M.; Bright, D. W.; Nehls, B. S.; Garamus, V. M.; Almasy, L.; Schweins, R.; Scherf, U.; Monkman, A. P. *Macromolecules* **2011**, *44*, 6453−6460.
(41) Parnell, A. J.; Cadby, A. J.; Mykhaylyk, O. O.; Dunbar, A. D. F.; Hopkinson, P. E.; Donald, A. M.; Jones, R. A. L. *Macromolecules* **2011**, *44*, 6503−6508.
(42) Glinka, C. J.; Barker, J. G.; Hammouda, B.; Krueger, S.; Moyer, J. J.; Orts, W. J. *J. Appl. Crystallogr.* **1998**, *31*, 430−445.
(43) Kline, S. *J. Appl. Crystallogr.* **2006**, *39*, 895−900.
(44) Barker, J. G.; Glinka, C. J.; Moyer, J. J.; Kim, M. H.; Drews, A. R.; Agamalian, M. *J. Appl. Crystallogr.* **2005**, *38*, 1004−1011.
(45) Butler, P.; Alina, G.; Hernandez, R. C.; Doucet, M.; Jackson, A.; Kienzle, P.; Kline, S.; Zhou, J. Danse SANSView, http://danse.chem.utk.edu/sansview.html, 2011.
(46) Samitsu, S.; Shimomura, T.; Ito, K. *Thin Solid Films* **2008**, *516*, 2478−2486.
(47) Obrzut, J.; Page, K. A. *Phys. Rev. B* **2009**, *80*, 195211−195218.
(48) Avrami, M. *J. Chem. Phys.* **1939**, *7*, 1103−1112.
(49) Avrami, M. *J. Chem. Phys.* **1941**, *8*, 177−184.
(50) Liu, X. Y.; Sawant, P. D. *Adv. Mater.* **2002**, *14* (6), 421−426.
(51) el Maaty, M. I.; Hosier, I. L.; Bassett, D. C. *Macromolecules* **1998**, *31*, 153−157.
(52) Sirringhaus, H.; Brown, P. J.; Friend, R. H.; Nielsen, M. M.; Bechgaard, K.; Langeveld-Voss, B. M. W.; Spiering, A. J. H.; Janssen, R. A. J.; Meijer, E. W.; Herwig, P.; de Leeuw, D. M. *Nature* **1999**, *401*, 685−688.
(53) Mittelbach, P.; Porod, G. *Acta Phys. Austriaca* **1961**, *14*, 185−211.
(54) Hammouda, B. *Adv. Polym. Sci.* **1993**, *106*, 87−133.
(55) Erwin, M. M.; McBride, J.; Kadavanich, A. V.; Rosenthal, S. J. *Thin Solid Films* **2002**, *409*, 198−205.
(56) Prosa, T. J.; Winokur, M. J.; Moulton, J.; Smith, P.; Heeger, A. J. *Macromolecules* **1992**, *25*, 4364−4372.
(57) Lee, K. H.; Schwenn, P. E.; Smith, A. R. G.; Cavaye, H.; Shaw, P. E.; James, M.; Krueger, K. B.; Gentle, I. R.; Meredith, P.; Burn, P. L. *Adv. Mater.* **2011**, *23*, 766−770.
(58) Hecht, A.-M.; Duplessix, R.; Geissler, E. *Macromolecules* **1985**, *18*, 2167−2173.
(59) Samitsu, S.; Shimomura, T.; Heike, S.; Hashizume, T.; Ito, K. *Macromolecules* **2010**, *43*, 7891−7894.
(60) Xu, W.; Tang, H.; Lv, H.; Li, J.; Zhao, X.; Li, H.; Wang, N.; Yang, X. *Soft Matter* **2012**, *8*, 726−733.

Macromolecules

Article

pubs.acs.org/Macromolecules

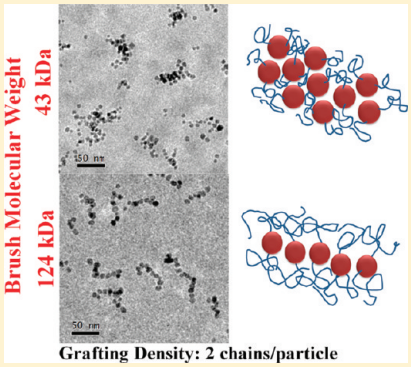
Assembly of Polymer-Grafted Magnetic Nanoparticles in Polymer Melts

Yang Jiao and Pinar Akcora*

Department of Chemical Engineering & Materials Science, Stevens Institute of Technology, Hoboken, New Jersey 07030, United States

Supporting Information

ABSTRACT: Hydrophobic iron oxide nanoparticles grafted with hydrophobic polymer chains of varying molecular weights and graft densities are synthesized to underpin the role of brush entanglement and dipolar forces on creating nanostructures. Grafting density on magnetic nanoparticles is controlled in grafting-to method by changing the concentration of functionalized polymer in solution. The grafting density and brush length have varied systemically to observe the changes in nanostructures. Bridging between grafted chains and dipolar forces become effective only at low grafting density and result in long chains of particles. We demonstrate experimentally that structural transition of magnetic nanoparticles is controlled with the balance between grafted chain entanglements and dipolar forces.



INTRODUCTION

Controlling the state of nanoparticle dispersion in polymer matrices through functionalizing the particles with polymers and ligands is essential to enhance functional properties of polymer nanocomposites.[1−5] Polymer-decorated magnetic nanoparticles can play an essential role in forming equilibrium structures that will lead to significant advances in their macroscopic mechanical and electroactive properties when they are mixed with polymers. Moreover, magnetic polymer nanocomposites find potential applications in microelectronics, biotechnology, sensing, and catalysis.[6−8]

In the context of stabilizing nanoparticles through polymer decoration, the length of the free and grafted chains, the grafting density and the size of the particle core are critical parameters that govern the dispersion state and morphology diagrams of functional particles. It is known that nanoparticles functionalized uniformly with long dense polymer grafts present good dispersion in melt.[3,9,10] On the contrary, polymer-grafted nanoparticles with low grafting density have been found to disperse well when tethered polymers are shorter than the polymer matrix due to repulsive interactions between tethered nanoparticles.[11,12] Furthermore, a recent simulation work presented the structural transitions of solvent-free oligomer grafted nanoparticles with variations of grafting density.[13] Recent experimental work showed that anisotropic organization of spherical nanoparticles could only be achieved by entropic−enthalpic balance between particle and polymer parts.[14] Thus, particles of amphiphilic character can organize into various morphologies where polymer graft length, density and entanglement between brushes and matrix determine the boundaries between different structures. However, it has been difficult to show the effect of entanglement between grafts on the organization of polymer-grafted nanoparticles. While the effect of entanglement between grafted and free chains on mechanical properties has been reported in previous experiments,[15−17] the direct influence of brush−brush entanglement on the formation and presumably on the transitions between different nanostructures has not been shown experimentally. Particle size, length of polymer grafts and low grafting density can play an important role to investigate the brush−brush and brush-matrix interactions.

Assembly of magnetic nanoparticles in polymer solution and films has been a challenge as they tend to aggregate without surface functionalization.[7] It is known that ferromagnetic nanoparticles can assemble into chains due to their directional dipolar interactions in solution[18−21] or between oil−water interphases.[22−24] For superparamagnetic nanoparticles, chains can be formed by applying magnetic fields,[25,26] however chains cannot keep their structures upon removal of fields. In the case of magnetic particles adsorbed with polymer, irreversible chain-like structures are obtained after magnetic fields are removed due to the strong entanglement (bridging) between polymer chains.[27] To improve the dispersion of magnetic nanoparticles in polymers, grafting-from approach was utilized in previous works which yielded high grafting density.[28−30] Iron oxide nanoparticles tethered with high grafting density of polymer resulted in well-dispersion of particles and with short brushes aggregation of particles was observed in homopolymers and block copolymers,[31] typical results expected for polymer decorated particles.

Received: January 8, 2012
Revised: March 30, 2012
Published: April 10, 2012

ACS Publications © 2012 American Chemical Society

dx.doi.org/10.1021/ma3000576 | Macromolecules 2012, 45, 3463−3470

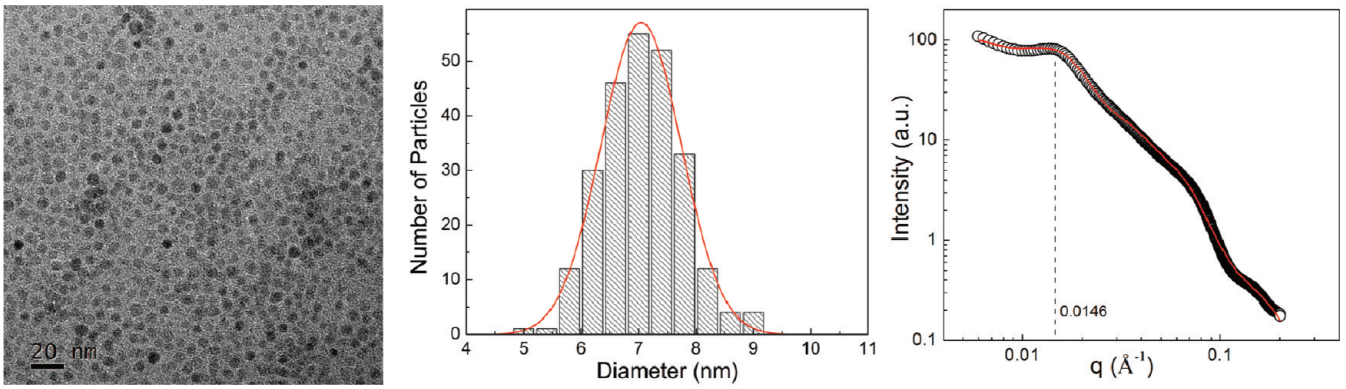


Figure 1. TEM image of bare iron oxide nanoparticles and particle size histogram of corresponding TEM. Small-angle X-ray scattering pattern of bare particles in 156 kDa PS matrix.

In this work, we tethered poly(styrene) of various molecular weights at low and intermediate grafting densities on iron oxide nanoparticles using grafting-to approach through a ligand exchange reaction. Different grafting densities with grafting-to method were obtained by varying the concentration of free chains in dilute solution which is an easy method to obtain different grafting densities with low polydispersity polymers. It is important to note that magnetic nanoparticles and grafted polymers are both hydrophobic in this work. Consequently, with the right choice of magnetic particle size and polymer lengths, steric repulsion and magnetic interactions become effective in the case of low grafting density. Herein, we report the structures of PS grafted iron oxide nanoparticles dispersed in polymer matrices and discuss the effect of brush−brush entanglement and dipolar interactions on assembly of nanoparticles.

EXPERIMENTAL SECTION

Materials. 2,2′-Azobis(isobutyronitrile) (AIBN; 98%) was recrystallized from methanol. Styrene (99%) was distilled under reduced pressure over CaH_2 before use. Benzyl ether (98%), iron(III) acetylacetonate (97%), oleic acid (90%), oleylamine (70%), 1,2-hexadecanediol (90%), and other chemicals were used as received. All chemicals were purchased from Sigma-Aldrich.

Synthesis of Functionalized PS. The oleic acid and oleylamine-stabilized Fe_3O_4 nanoparticle was synthesized by thermal decomposition method.[32] A RAFT agent, 2-[(dodecylsulfanyl)-carbonothioyl]sulfanyl propanoic acid (DCSPA), was synthesized following the reported procedure.[33] Reversible addition−fragmentation chain transfer polymerization of poly(styrene) with carboxyl group containing RAFT agent was followed according to the reported procedure.[34] Chain transfer agent (CTA) (27.5 mg, 78.4 μmol), AIBN (2.5 mg, 15.7 μmol), and styrene (10 mL, 86.4 mmol) were added to a 20 mL Schlenk flask, and degassed through three cycles of freeze−pump−thaw. The flask was then placed in an oil bath preset to 85 °C for 24 h. Polystyrene with different molecular weight was synthesized by changing the ratio of styrene to CTA. The polymerization was stopped by quenching the flask in ice−water. The reaction mixture was dissolved in toluene and the polymer was purified by precipitating in methanol. Product was dried in a vacuum oven for overnight.

Immobilization of PS onto Fe_3O_4 Nanoparticles. Carboxyl group ended PS was associated with oleic acid and oleylamine-stabilized Fe_3O_4 nanoparticles through a ligand-exchange mechanism (as shown in Figure 1). The freshly prepared NPs (50 mg) dispersed in toluene (50 mL) were stirred with the addition of PS at 60 °C for 48 h. Removal of the free PS chains after ligand exchange is critical for determining grafting densities. PS-tethered nanoparticles resemble star polymers where their solubility decreases with the increase in number of arms. Therefore, the solubility of free chains and tethered ones will be different and this difference will increase as the solvent quality decreases, leading to star polymers (tethered polymers) collapsing first. To accomplish this, ethanol was added to the solution of tethered and free PS chains in toluene drop by drop until the homogeneous solution turns to cloudy. The clear upper liquid, containing the free polymer, was removed from the particles by centrifuging the solution at 11000 rpm for 12 min. The dark brown precipitate was collected and redissolved in toluene. After multiple washes, the upper solution was decanted in methanol to confirm that there was no free polymer left in solution. The brown sediment was dispersed and stored in toluene for future use. Sample characteristics used in this work are listed in Table 1.

Table 1. Characteristics of Synthesized PS Grafted Fe_3O_4

		σ	
$\bar{M}_w$ (kg/mol)	PDI	(chains/nm^2)	(chains/particle)
15.6	1.06	0.052	7.6
43.2	1.05	0.017	3.4
		0.044	6.4
		0.066	20.7
68.25	1.15	0.023	4.6
		0.04	12.4
124.1	1.28	0.013	1.9
		0.052[a]	13.8[a]

[a]Sample is synthesized using grafting-from approach.

Surface-Initiated RAFT Polymerization of PS from Fe_3O_4 Nanoparticles Surface. DCSPA was linked to the oleic acid- and oleyl amine stabilized Fe_3O_4 nanoparticles via the ligand exchange reaction. First, the freshly prepared Fe_3O_4 nanoparticles (200 mg) were dispersed in 1,2-dichlorobenzene (20 mL), followed by addition of DCSPA (1 g). The mixture was stirred at 80 °C for 24 h. Then, the reaction mixture was added into a large excess of ethanol, and the precipitate was separated via centrifuge (7000 rpm, 10 min). The precipitated particles were purified by three times of redispersing in toluene and reprecipitating in ethanol to remove all traces of free DCSPA. The DCSPA-anchored Fe_3O_4 nanoparticles were dried under vacuum at room temperature for overnight prior to polymerization.

A stock solution in 1,2-dichlorobenzene (5 mL) comprising DCSPA-anchored Fe_3O_4 nanoparticles (107 mg), styrene (8.2 g, 78.7 mmol), free DCSPA (7.54 mg, 21.5 × 10^{-3} mmol), and AIBN (1.13 mg, 6.89 × 10^{-3} mmol) in a Schlenk flask was degassed through three freeze−pump−thaw cycles. The flask was then placed in an oil bath preset to 85 °C for 48 h. The polymerization was stopped by quenching the flask in ice water. The purification of PS-tethered nanoparticles was identical to the procedure described above. Further, polymer was cleaved from nanoparticles by adding a HCl solution (2 mL at 37 wt %) into PS grafted iron oxide nanoparticles (5 mL at 10

dx.doi.org/10.1021/ma3000576 | Macromolecules 2012, 45, 3463−3470

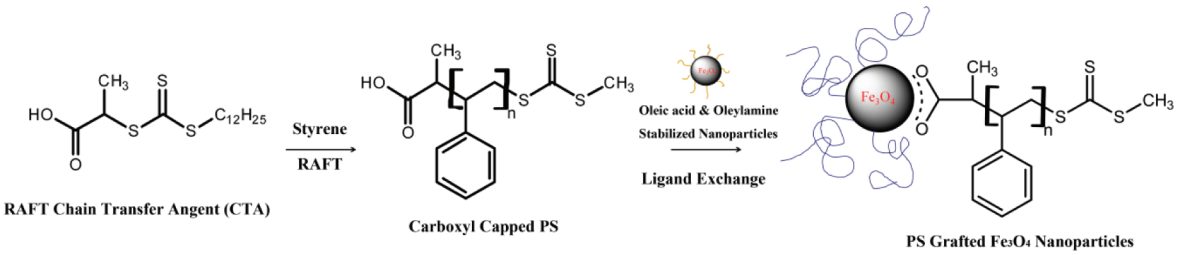


Figure 2. Synthesis schema of CTA-anchored PS and PS-grafted Fe_3O_4 NPs by grafting-to method.

mg/mL). After the organic phase was clear, an excess of methanol was added to the solution to precipitate PS chains. The recovered polymer was collected by centrifugation and dried under vacuum for subsequent GPC analysis.

Polymer-grafted particles in toluene were mixed with the matrix polystyrene homopolymers and then sonicated for 20 s to prepare the composite solutions. The polymer-grafted particle concentration was 5 mass % in all of the samples. The composites, in solution, were cast onto Teflon dishes, dried to remove the solvent in air, and then annealed for 48 h and additional 7 more days in a vacuum oven at 150 °C. Sample thicknesses were approximately 300 μm; therefore, particle dispersions presented for composites are for the bulk samples.

Characterization. Molecular weights were determined by gel permeation chromatography-light scattering (GPC/LS) using a system equipped with a VARIAN PLgel 5.0 μm Mixed−C gel column (7.5 mm ID), a light detector (miniDawn, Wyatt Technology) and a refractive index detector (Optilab rEX, Wyatt). Pure CTA and carboxyl group ended PS were confirmed by H^1 NMR, performed on a Bruker AV 500 spectrometer. Dynamic light scattering (DLS) measurements were carried out with a Zetasizer NanoS, Malvern Instruments. Solutions having particle concentration of 0.3−0.5 mg/mL in toluene were bath sonicated for about 2 min. Measurement duration was set to be 15 s, and data were averaged over 15 runs.

Nanocomposite films were microtomed into 50−80 nm slices with a diamond knife at room temperature and examined in transmission electron microscopy (FEI CM20 FE S/TEM) operated at 200 keV. Many cross-sectional TEM images were captured over different areas and the images presented are representative of observed nanostructures.

TGA measurements were performed on a Q50 TGA (TA Instruments) for grafting density calculations. Measurements were performed under a constant flow of nitrogen of 20 mL/min at a heating rate of 20 °C/min, starting from room temperature up to 580 °C, and then held constant at maximum temperature for 30 min. All samples were dried in a vacuum oven at 60−80 °C prior to each TGA measurement to remove remaining moisture. All reported TGA curves were normalized with respect to the weight at 100 °C to make sure that only the solid fraction was measured.

SAXS measurements were performed at Beamline X27C at the National Synchrotron Light Source (NSLS), Brookhaven National Laboratory.

RESULTS AND DISCUSSION

Bare Iron Oxide Nanoparticles. TEM image of bare particles prepared from a solution drop on a copper grid and the corresponding histogram are presented in Figure 1. The average particle core diameter is measured to be 7.8 ± 1.8 nm. The particle size was also determined by small-angle X-ray scattering (SAXS) from bare particles dispersed in 156 kDa PS. SAXS pattern in Figure 1 was fit to the unified equation[35] where the primary particle size was obtained as 6.8 nm at intermediate-q (see Supporting Information for SAXS analysis). Power law exponent for the larger structure at low q region was found to be 3.78, indicating particles are dispersed like surface fractals. The hydrophobic surfactants on nanoparticles prevent the aggregation of particles into large spherical clusters when they are dispersed in hydrophobic PS polymer matrix and behave as surface fractals. The peak at the low q region indicates interference within particle aggregates which was observed as separated clusters in TEM image (see Supporting Information, Figure S1).

Synthesis and Stability of Poly(styrene) Tethered Iron Oxide Nanoparticles in Solution. The key to critical understanding of various interactions between components of polymer brush nanocomposites is the preparation of low-PDI tethered polymers onto iron oxide nanoparticles with controlled brush chain length and the variation of grafting densities ranging from low to intermediate values. We employ grafting-to method (Figure 2) which is accomplished by a ligand exchange reaction of carboxylic acid functionalized poly(styrene) (PS) of molecular weights ranging between 15 kDa-124 kDa. Different grafting densities (0.01−0.06 chains/nm^2) were achieved by controlling the molar concentration of free PS chains in solution. This method has been used in previous works on silicon surfaces to achieve high grafting density.[36,37]

Iron oxide nanoparticles with oleic acid and oleylamine surfactants are unable to sustain a secondary reaction to bring new functionalities.[38] Ligand exchange reaction has been widely used as the first step to modify nanoparticle surfaces. This surface modification involves adding an excess amount of new ligand containing carboxyls,[39,40] silanes and amines.[38] The structure of carboxylic acid (or chain transfer agent, CTA) functionalized PS was confirmed by the appearance of the peak for methyl in hydrocarbon chain of CTA in ^{1}H NMR spectrum of PS at 0.90−0.86 ppm (not shown here). The attachment of PS to the NP surface was probed by FTIR analysis (Figure 3).

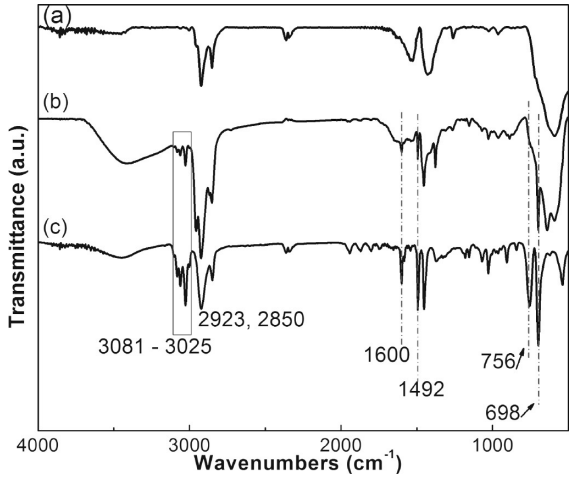


Figure 3. FTIR spectra of (a) oleic acid and oleylamine-stabilized Fe_3O_4 nanoparticles, (b) PS tethered Fe_3O_4 nanoparticles, and (c) PS.

dx.doi.org/10.1021/ma3000576 | Macromolecules 2012, 45, 3463−3470

The appearance of aromatic absorption bands at 3081−3025, 1600, 1492, 756, and 698 cm^{-1} (Figure 3b) demonstrates the presence of PS on particle surface. The successful dispersion of the PS-grafted iron oxide nanoparticles in toluene but their poor dispersion in hexane is also indicative of successful surface modification. It is worth to note that compared with the spectrum for PS (Figure 3c), the peak ratio of aromatic stretches of C−H (3025−3081 cm^{-1}) to CH_2 (2923, 2850 cm^{-1}) decreased after ligand exchange reaction indicating oleic acid and oleylamine remain after tethering polymers. We note that particles are presumably uniformly covered with the oleic acid and oleylamine prior to and after attaching polymers.

Surface modifications by grafting-to method involves coupling of functional groups on the surface and on the end of PS chains, which can be achieved by controlling the number of functional groups on surfaces or the number of chains.[41] Because it is difficult to determine the amount of functional groups on surfaces, changing the number of polymer chains with functional ends is an easy approach in order to achieve controlled grafting densities. Here, we reported that the concentration of free chains can control the extent of ligand-exchange reaction of Fe_3O_4 nanoparticles and hence grafting density of different molecular weights of chains. Figure 4 shows

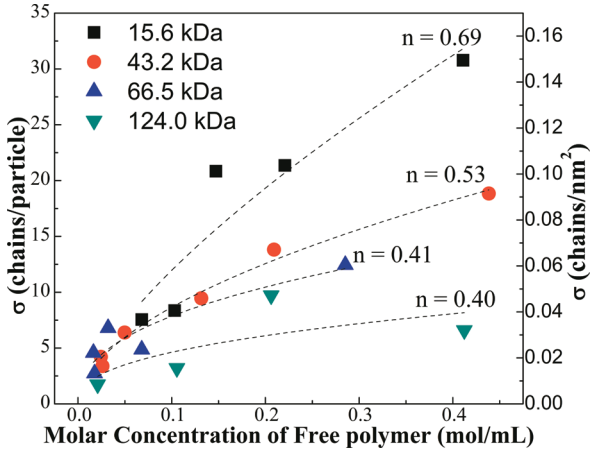


Figure 4. Effect of free polymer concentration in solution on polymer grafting density.

that grafting density increases with the concentration of free PS chains, varying from dilute to semidilute solution.

The existence of a plateau at low grafting density (~5 chains/particle) of 124 kg/mol PS suggests a limited accessibility of chains to the particle surface due to steric hindrance of long chains. It is seen that the grafting density decreases when the chain length increases (Figure 4). The dependence of grafting density on the polymer concentration has been suggested by deGennes[42] and has been confirmed experimentally by Auroy et al.[43] for grafting 145 kg/mol PDMS onto 400 nm porous silica particles that the amount of grafted polymer per unit area is equal to $C_{7/8N}^{1/2}$ where C is concentration and N is degree of polymerization. In their case all chains were irreversibly grafted. The lines in Figure 4 are the power-law fits and the concentration exponents (n) are indicated on each line. Our data deviates from this relationship for 15 kDa PS where the exponent of concentration is 0.69, and it decreases to 0.53 for 43.2 kDa, to 0.41 for 66.5 kDa, and to 0.40 for 124 kDa. We explain this behavior by suggesting that chains are attached reversibly to the surface; therefore, the grafted chains are not at equilibrium at semidilute concentration leading to fast adsorption−desorption of chains, and thus dependence of grafting density on polymer concentration varies from what has been proposed by Auroy et al.[43] We have achieved the grafting density of 0.1 chains/nm^2 (30 chains/particle) for 15 kDa PS sample at high polymer concentration as high osmotic pressure was required to overcome the steric hindrance to form a dense grafted layer. For longer chains, this steric force cannot be compensated by increasing polymer concentration, thus resulted in grafting densities of ~5−10 chains/particle. Additionally, we observed that polymer immobilized nanoparticles are stable in concentrated solution (10 mg/mL), but precipitated easily in dilute concentration (0.6 mg/mL), but adding a small amount (~0.2 mg/mL) of carboxylic group functionalized PS enables the stability of brushes in solution, suggesting the existence of the equilibrium between adsorption−desorption of ligands. With the presence of excess amount of ligands, adsorption of chains are favorable and desorption process becomes negligible. Therefore, the ligand exchange process and the grafting density of chains on nanoparticles can be controlled with the concentration of free chains. On another note, when CTA was attached to nanoparticle and grafting-from polymerization was proceeded, high grafting density with 124 kDa PS could not be achieved which might be due to the desorption of CTA molecules. Adding silane layer on iron oxide nanoparticles is another option to obtain more stable ligands,[38] however silanized iron oxide nanoparticles will have solubility problems because of the short length of silane ligands and thus may cause nonuniformity of grafting density.

Next, we have characterized the average size of polymer-tethered nanoparticles in DLS to confirm their stability in solution. Figure 5 shows the normalized hydrodynamic size,

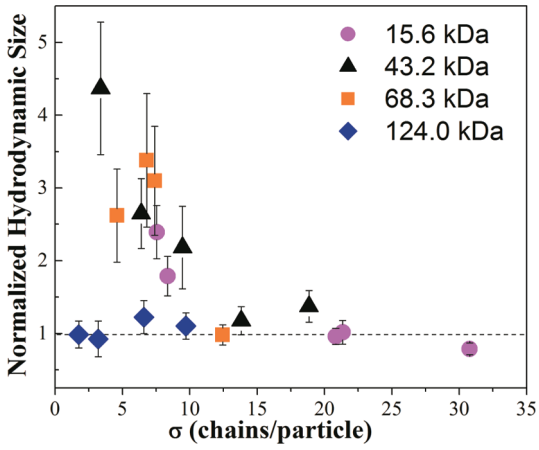


Figure 5. Variation of normalized hydrodynamic size of PS-tethered iron oxide nanoparticles with grafting density.

which is the ratio of measured number-averaged size of clusters ($2R_h$) to calculated brush size with its core, (particle core plus $4R_g$) for the tethered polymers at various grafting densities. It is seen that all of the brushes except 124 kDa PS agglomerated when the number of grafted chains were lower than 10 chains per particle. Well-dispersion was achieved at all of the grafting densities in 124 kDa brush.

Structural Characterization: Dispersion of Polymer Tethered Iron Oxide Nanoparticles in Polymer Melts. We investigate the effect of brush length and grafting density on the

dx.doi.org/10.1021/ma3000576 | Macromolecules 2012, 45, 3463−3470

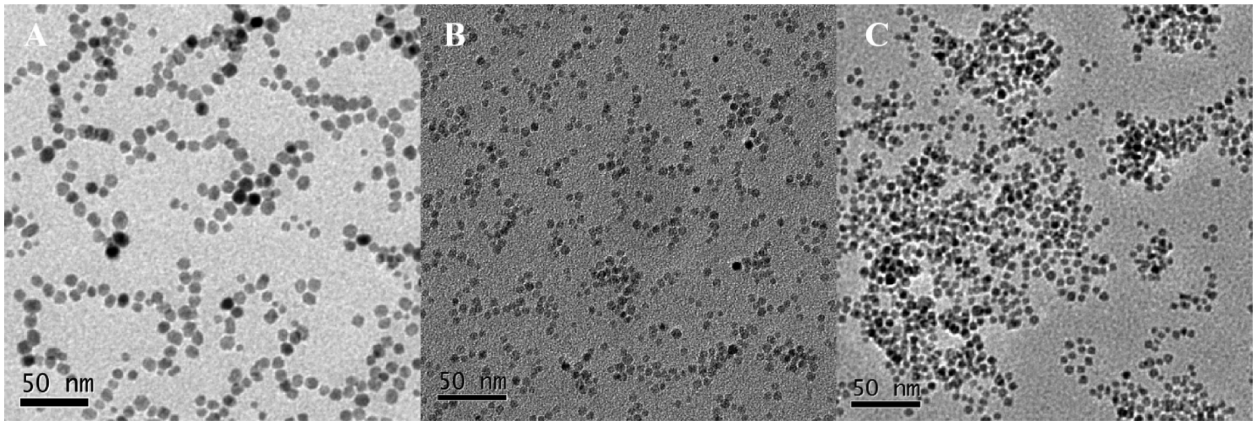


Figure 6. Dispersion of PS-tethered iron oxide nanoparticles (pure magnetic brushes) as cast from solution in toluene: (A) 124 kDa (0.013 chains/nm^2); (B) 124 kDa (0.052 chains/nm^2); (C) 15 kDa (0.052 chains/nm^2).

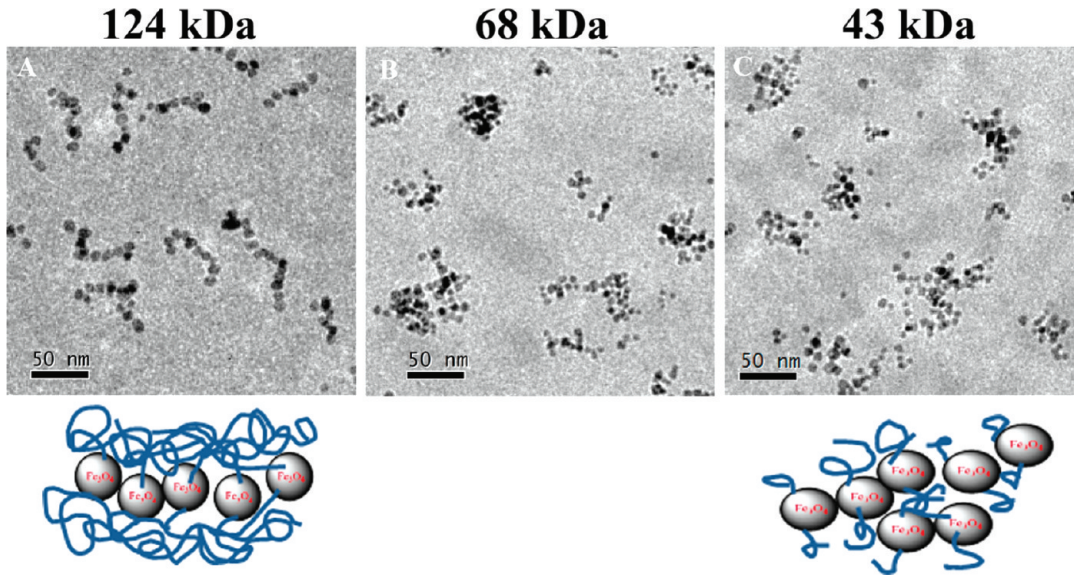


Figure 7. Effect of brush chain length on dispersion of PS grafted magnetic nanoparticles at sparse grafting density in 15 kDa PS matrix: (A) 124 kDa (0.013 chains/nm^2); (B) 68.25 kDa (0.023 chains/nm^2); (C) 43.2 kDa (0.017 chains/nm^2).

dispersion of polymer tethered magnetic oxide nanoparticles primarily to underpin the role of brush−brush entanglements on particle aggregation. It is important to note that PS-grafted iron oxide nanoparticles do not have the amphiphilic character as of PS-grafted silica system[14] and their controlled aggregation will be different as magnetic particles provide different interplays between dipolar, repulsion and van der Waals interactions.

The spherical iron oxide nanoparticles with average diameter of 7.8 ± 1.8 nm are superparamagnetic at room temperature which means that particles cannot organize into 1-D chains purely by dipole magnetic interactions. It has been shown that magnetic coupling occurs in chain-like structures, causing an increase in coercivity.[44,45] For example, superparamagnetic nanoparticles that are covalently linked through their pole points are shown to form chains with induced magnetization moments.[46] In this work, instead of using a molecular linker, we have decorated particles with polymers at low grafting density where the conformation of brush chains enable the brushes and lead to string formation. In addition to this entanglement factor, magnetic coupling among particles in a chain keeps their elongated string structures.

To understand the strength of interactions, we have calculated the van der Waals and dipole−dipole interactions between two superparamagnetic particles of 8 nm in diameter that are in contact with the separation distance of 2 nm.[31] The van der Waals interaction energy is calculated to be around 1 kT and dipole−dipole interaction is calculated as 0.8 kT (see Supporting Infomation for equations). Thus, dipole interaction plays less significant role in the aggregation of particles. In our work, grafted polymers play the physical bridging role between particles through the entanglement of chains, thus dipolar interactions become effective as particles are connected to form chains. We surmise that dipolar interactions, even though structures are not mainly induced by them, help the formation of the equilibrium structures of polymer grafted iron oxide nanoparticles. We have also examined the composite structures after annealing 9 days at 150 °C and have observed similar structures that are seen for 2 days annealed samples as shown in Figures 7−9, indicating that the structures are in equilibrium.

We have synthesized polymers of varying molecular weights (15−124 kDa) and tethered them mainly at two different grafting densities: ∼0.01 and ∼0.05 chains/nm^2 (shown in Table 1). We start our discussion with the structures of pure

dx.doi.org/10.1021/ma3000576 | *Macromolecules* 2012, 45, 3463−3470

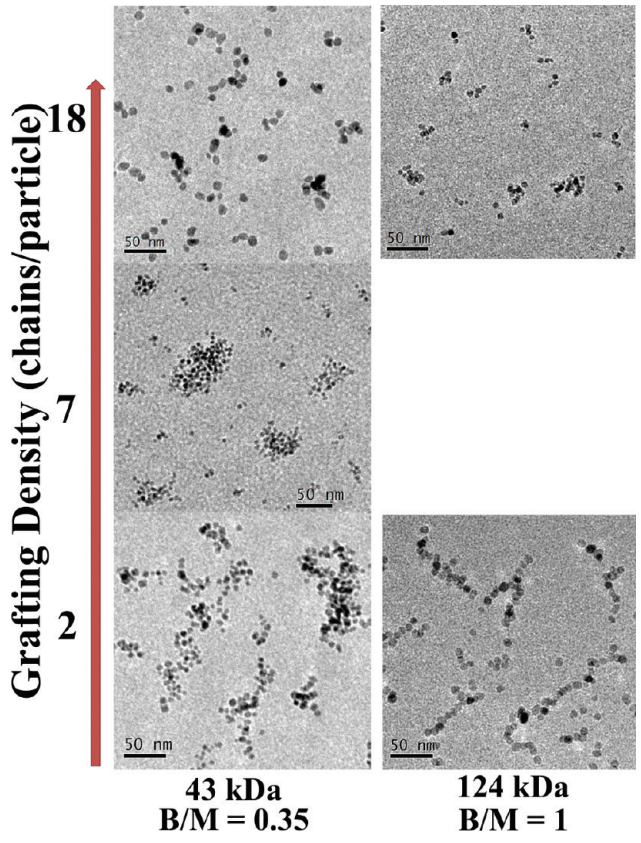


Figure 8. TEM images show transition of nanostructures from large elongated branched chains to spheres and to short chains with the increase of grafting density from bottom to top. The first column is for 43 kDa PS-grafted nanoparticles, the grafting density is 0.017 (bottom), 0.044 (middle) and 0.066 chains/nm^2 (top). The second column is for 124 kDa brush with 0.052 chains/nm^2 (top) and 0.013 chains/nm^2 (bottom). Ratio of brush and matrix molecular weights is 0.35 for 43 kDa and 1 for 124 kDa.

polymer tethered iron oxide nanoparticles with 124 kDa PS with 2 chains and 14 chains per particle (~0.013 and ~0.052 chains/nm^2) which are good representations of particles dispersed in solution as they are prepared by evaporating a drop of solution on a grid. As discussed in previous section, magnetic nanoparticles feel dipolar interactions when the steric repulsion is weaker in the case of 2 tethered chains and form long branched chains (Figure 6a). On the other hand, particles tethered with 15 kDa PS form spherical aggregates as the result of van der Waals interactions dominating the dipolar forces (Figure 6c).

Figure 7 presents the effect of increasing brush length on the aggregation of particles that are grafted at low density. When particles come into contact with attractive interactions, entanglement between the grafted chains of 124 kDa molecular weight at a low grafting density (0.013 chains/nm^2) plays the bridging role and elongated chains are protected with the brush entanglement (Figure 7a). Therefore, the formation of string is not controlled purely with dipolar interactions but also with the entanglement of long brushes (124 kDa) which allows the particles aggregate from the two ends of a string. A shorter brush (43.2 kDa), having the shorter range of repulsion of grafted chains, at the same grafting density has a thinner effective entangled brush layer and dipolar forces become insufficient to keep the chain-like structures, hence they form branched chains and clusters (Figure 7c). We conclude that long strings are stabilized when the effective entanglement is large which is achieved only at low grafting density and also due to the magnetic coupling of uniaxial particles in 1-D chains. We discussed the structures in Figure 7 by simply considering that they are pure brushes in a good solvent as the matrix molecular weight (15 kDa) was below the entanglement molecular weight of PS. Note that TEM images of pure PS-tethered particles (Figure 6a) show similar structure when they are mixed with 15 kDa PS. We discuss the effect of matrix molecular weight in the following section.

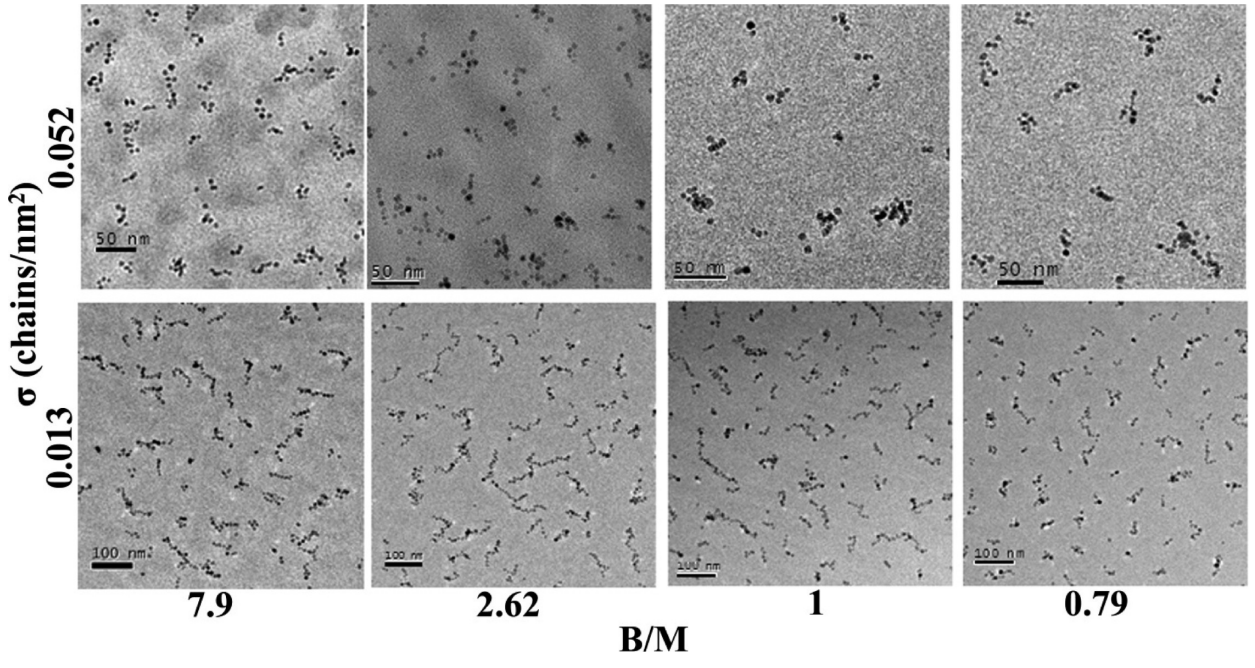


Figure 9. Dispersion of PS (124 kDa)-grafted magnetic nanoparticles in matrices of increasing molecular weight for the two grafting cases: 0.052 and 0.013 chains/nm^2.

dx.doi.org/10.1021/ma3000576 | *Macromolecules* 2012, 45, 3463−3470

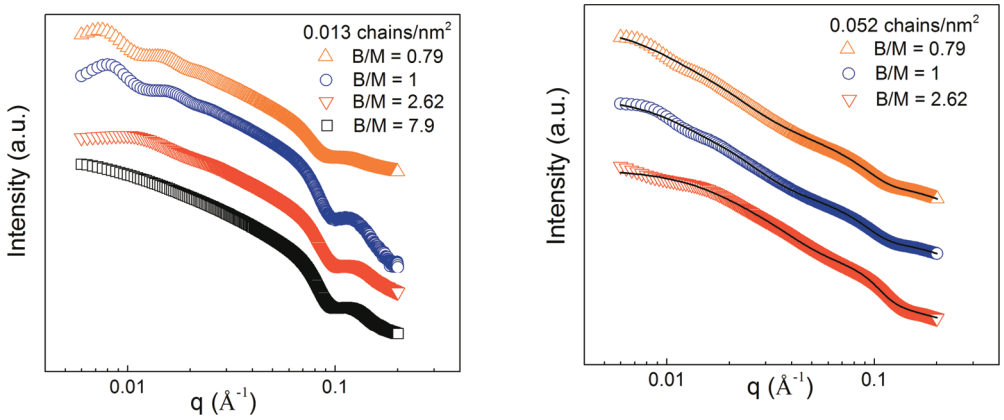


Figure 10. SAXS data of PS (124 kDa)-grafted magnetic nanoparticles in different PS matrix molecular weights: 15, 40, 124, and 156 kDa of (A) 0.013 chains/nm^2 and (B) 0.052 chains/nm^2. Data shifted vertically for clarity.

Next, we look into the effect of grafting density for the two brushes of 124 kDa and 43 kDa molecular weights. Sterically stabilized long strings observed at 0.013 chains/nm^2 for 124 kDa brush break into small aggregates of tetramers and pentamers with the increase of grafting density to 0.05 chains/nm^2 (Figure 8, second column). It is expected that with denser brushes, brush−brush entanglement will not be effective for particles to conserve long strings and steric repulsion separates particles into short chains and isolated particles. We observed that the increase in grafting density has the most influence in 43 kDa brush where the branched chains seen at the low grafting density (0.017 chains/nm^2) collapse into spherical aggregates at 0.044 chains/nm^2 and then are dispersed well as short chains at 0.06 chains/nm^2 (Figure 8, first column). While at low grafting density of 43 kDa brush the dipolar forces are dominant resulting in anisotropic branched structures, at intermediate density dipolar forces are balanced with stronger steric repulsion, hence they collapse. We interpret this behavior as isotropic repulsion of the short brushes counteracting the directional forces and form demagnetized structures through isotropic aggregation. Previous magnetic studies on spherical aggregates of superparamagnetic nanoparticles have reported demagnetizing effect due to random dipole−dipole interactions.[26,47] At increased grafting density of 0.06 chains/nm^2, they are well-dispersed short chains mainly due to stronger repulsion and steric depletion of free chains around particles (see Supporting Information for SAXS data and analysis of 43 kDa brush, Figure S2). The transition in nanostructures is attributed to the entanglement between brushes, which is controlled mainly with grafting density and is determined by the balance between dipolar and steric repulsion forces. Our results validate the recent predictions of Panagiotopoulos et al.[13] where the collapse of string-like structures into isotropic colloidal clusters is obtained at high grafting density in their simulations.

We demonstrate that increasing the brush length at sparse grafting density creates chains (Figure 7), which seems to be analogous to what has been shown for the PS−silica grafted system.[14] In that previous relevant work, amphiphilic nanoparticles with 0.01 chains/nm^2 graft density present a transition from connected structures into strings with the corresponding brush lengths we used in this work. In addition, the amphiphilic nanoparticles show transition from spheres to anisotropic objects or dispersed particles as grafting density increases for given brush length. Here, the particular difference of having hydrophobic magnetic nanoparticles is shown in the structural transition of branched structures into spherical aggregates and then into isolated particles with the increase of graft density. Moreover, in the context of amphiphilic nanoparticles, changing the particle size can play an important role in phase separation of polymer tethered particles at different grafting density. However, the size effect is irrelevant in the physical picture we present here as our particles and chains are both hydrophobic.

To resolve the effect of matrix chains, we varied the ratio of grafted molecular weight and matrix molecular weight (B/M) from 0.79 to 7.9. TEM images have shown clearly that the matrix chains play the solvent role more effectively for 124 kDa brushes at the lower grafting density (Figure 9). Interestingly, we observed that even at $B/M < 1$, matrix chains which are entangled with the brushes at the low grafting density (0.013 chains/nm^2) can create short chains instead of long strings expected to form at the dewetting interface. SAXS patterns of the low grafting density composites in varying matrix molecular weights confirm the strong interference from the ordering of strings giving a main peak at $q = 0.008$ Å^{-1} (Figure 10a). The average spacing between these observed nanostructures is calculated from $d = 2\pi/q$ as 78 nm. It is apparent that with the connectivity of strings (as clearly seen in TEMs of $B/M = 7.9$ and 2.62), the low-q feature disappears, indicating that the structures are large, which cannot be measured in SAXS. TEM images of particles at high grafting density (0.05 chains/nm^2) show that the structures do not change with the increase of matrix molecular weight (top row of Figure 9). Their scattering patterns (Figure 10b) provide that structures are like surface fractals with power-law exponent values between 3 and 4. TEM and SAXS results suggest that matrix-brush entanglements do not influence the structures at high grafting density.

In summary, we demonstrate the structural transitions of polymer grafted iron oxide nanoparticles which depend on the brush lengths and subtle changes of grafting density. Dispersion of nanoparticles was controlled at the particle size level where the formation of tetramers, short chains and long chains were obtained by tethering polymer chains onto magnetic nanoparticles. This system offers controllable aggregation of structures in equilibrium which further brings additional magnetic properties to the polymer nanocomposite systems.

dx.doi.org/10.1021/ma3000576 | *Macromolecules* 2012, 45, 3463−3470

CONCLUSION

Polymer grafted iron oxide nanoparticles of varying grafting densities have been synthesized for the first time using grafting-to method. Previous reported strategy on controlling the grafting density of various molecular weights of brushes have been applied to magnetic oxide nanoparticles and their dispersion in solution and melts has been presented. We showed that brush−brush entanglement plays an effective role only at low grafting density in the string formation. Dipolar forces and entanglement between brushes result in long strings of particles. Structural transitions observed with increase in grafting density and brush length substantiate the interplay between steric repulsion which is enhanced with entanglement, and dipolar forces. Organization of functional magnetic nanoparticles can be tuned differently under applied fields than the previously reported magnetic colloids due to the strong repulsion of tethered polymers. Field-induced extended structures of polymer grafted magnetic nanoparticles are currently under investigation.

ASSOCIATED CONTENT

Supporting Information

TEM of bare iron oxide nanoparticles in 156 kDa PS matrix, interaction energy between two superparamagnetic nanoparticles, SAXS data analysis by unified fits, Power law exponents, cluster size and primary size of particles obtained from the Unified fits. This material is available free of charge via the Internet at http://pubs.acs.org/

AUTHOR INFORMATION

Corresponding Author

*Telephone: (201) 216-5060. E-mail: Pinar.akcora@stevens.edu.

Notes

The authors declare no competing financial interest.

ACKNOWLEDGMENTS

This work is supported by NSF-CAREER award Grant No. 1048865 from DMR. We acknowledge the Multiscale Imaging Lab (LMSI) of Stevens for TEM. Portions of this work were performed at Beamline X27C at the National Synchrotron Light Source (NSLS), Brookhaven National Laboratory. NSLS is supported by the U.S. Department of Energy, Office of Science, Office of Basic Energy Sciences, under Contract No. DE-AC02-98CH10886.

REFERENCES

(1) Pyun, J.; Matyjaszewski, K. *Chem. Mater.* **2001**, *13*, 3436.
(2) Pyun, J.; Zhou, X. Z.; Drockenmuller, E.; Hawker, C. J. *J. Mater. Chem.* **2003**, *13*, 2653.
(3) Lan, Q.; Francis, L. F.; Bates, F. S. *J. Polym. Sci., Part B: Polym. Phys.* **2007**, *45*, 2284.
(4) Zou, H.; Wu, S.; Shen, J. *Chem. Rev.* **2008**, *108*, 3893.
(5) Zhao, Y.; Thorkelsson, K.; Mastroianni, A. J.; Schilling, T.; Luther, J. M.; Rancatore, B. J.; Matsunaga, K.; Jinnai, H.; Wu, Y.; Poulsen, D.; Fréchet, J. M. J.; Paul Alivisatos, A.; Xu, T. *Nat. Mater.* **2009**, *8*, 979.
(6) Sun, S. *Adv. Mater.* **2006**, *18*, 393.
(7) Pyun, J. *Polym. Rev.* **2007**, *47*, 231.
(8) Laurent, S.; Forge, D.; Port, M.; Roch, A.; Robic, C.; Vander Elst, L.; Muller, R. N. *Chem. Rev.* **2008**, *108*, 2064.
(9) Corbierre, M. K.; Cameron, N. S.; Sutton, M.; Laaziri, K.; Lennox, R. B. *Langmuir* **2005**, *21*, 6063.
(10) Wang, X.; Foltz, V. J.; Rackaitis, M.; Böhm, G. G. A. *Polymer* **2008**, *49*, 5683.
(11) Smith, G. D.; Bedrov, D. *Langmuir* **2009**, *25*, 11239.
(12) Cheng, L.; Cao, D. *J. Chem. Phys.* **2011**, 135.
(13) Chremos, A.; Panagiotopoulos, A. Z. *Phys. Rev. Lett.* **2011**, 107.
(14) Akcora, P.; Liu, H.; Kumar, S. K.; Moll, J.; Li, Y.; Benicewicz, B. C.; Schadler, L. S.; Acehan, D.; Panagiotopoulos, A. Z.; Pryamitsyn, V.; Ganesan, V.; Ilavsky, J.; Thiyagarajan, P.; Colby, R. H.; Douglas, J. F. *Nat. Mater.* **2009**, *8*, 354.
(15) Choi, J.; Dong, H.; Matyjaszewski, K.; Bockstaller, M. R. *J. Am. Chem. Soc.* **2010**, *132*, 12537.
(16) Chevigny, C.; Dalmas, F.; Di Cola, E.; Gigmes, D.; Bertin, D.; Boué, F.; Jestin, J. *Macromolecules* **2011**, *44*, 122.
(17) Moll, J. F.; Akcora, P.; Rungta, A.; Gong, S.; Colby, R. H.; Benicewicz, B. C.; Kumar, S. K. *Macromolecules* **2011**, *44*, 7473.
(18) Teixeira, P. I. C.; Tavares, J. M.; Telo Da Gama, M. M. *J. Phys.: Condens. Matter* **2000**, 12.
(19) Cabuil, V. *Curr. Opin. Colloid Interface Sci.* **2000**, *5*, 44.
(20) Lalatonne, Y.; Richardi, J.; Pileni, M. P. *Nat. Mater.* **2004**, *3*, 121.
(21) Klokkenburg, M.; Vonk, C.; Claesson, E. M.; Meeldijk, J. D.; Erné, B. H.; Philipse, A. P. *J. Am. Chem. Soc.* **2004**, *126*, 16706.
(22) Benkoski, J. J.; Bowles, S. E.; Jones, R. L.; Douglas, J. F.; Pyun, J.; Karim, A. *J. Polym. Sci., Part B: Polym. Phys.* **2008**, *46*, 2267.
(23) Khomutov, G. B. *Adv. Colloid Interface Sci.* **2004**, *111*, 79.
(24) Benkoski, J. J.; Bowles, S. E.; Korth, B. D.; Jones, R. L.; Douglas, J. F.; Karim, A.; Pyun, J. *J. Am. Chem. Soc.* **2007**, *129*, 6291.
(25) Butter, K.; Bomans, P. H. H.; Frederik, P. M.; Vroege, G. J.; Philipse, A. P. *Nat. Mater.* **2003**, *2*, 88.
(26) Gross, A. F.; Diehl, M. R.; Beverly, K. C.; Richman, E. K.; Tolbert, S. H. *J. Phys. Chem. B* **2003**, *107*, 5475.
(27) Goubault, C.; Leal-Calderon, F.; Viovy, J. L.; Bibette, J. *Langmuir* **2005**, *21*, 3725.
(28) Garcia, I.; Tercjak, A.; Zafeiropoulos, N. E.; Stamm, M.; Mondragon, I. *J. Polym. Sci., Part A: Polym. Chem.* **2007**, *45*, 4744.
(29) Garcia, I.; Zafeiropoulos, N. E.; Janke, A.; Tercjak, A.; Eceiza, A.; Stamm, M.; Mondracon, I. *J. Polym. Sci., Part A: Polym. Chem.* **2007**, *45*, 925.
(30) Robbes, A. S.; Cousin, F.; Meneau, F.; Chevigny, C.; Gigmes, D.; Fresnais, J.; Schweins, R.; Jestin, J. *Soft Matter* **2012**, *8*, 3407.
(31) Xu, C.; Ohno, K.; Ladmiral, V.; Composto, R. J. *Polymer* **2008**, *49*, 3568.
(32) Sun, S.; Zeng, H.; Robinson, D. B.; Raoux, S.; Rice, P. M.; Wang, S. X.; Li, G. *J. Am. Chem. Soc.* **2004**, *126*, 273.
(33) Yang, Y.; Yang, Z.; Zhao, Q.; Cheng, X.; Tjong, S. C.; Li, R. K. Y.; Wang, X.; Xie, X. *J. Polym. Sci., Part A: Polym. Chem.* **2009**, *47*, 467.
(34) Jung, M. L.; Ok, H. K.; Sang, E. S.; Lee, B. H.; Choe, S. *Macromol. Res.* **2005**, *13*, 236.
(35) Beaucage, G. *J. Appl. Crystallogr.* **1995**, *28*, 717.
(36) Taylor, W.; Jones, R. A. L. *Langmuir* **2010**, *26*, 13954.
(37) Huang, H.; Penn, L. S. *Macromolecules* **2005**, *38*, 4837.
(38) De Palma, R.; Peeters, S.; Van Bael, M. J.; Van Den Rul, H.; Bonroy, K.; Laureyn, W.; Mullens, J.; Borghs, G.; Maes, G. *Chem. Mater.* **2007**, *19*, 1821.
(39) Xiao, Z. P.; Yang, K. M.; Liang, H.; Lu, J. *J. Polym. Sci., Part A: Polym. Chem.* **2010**, *48*, 542.
(40) Bourlinos, A. B.; Bakandritsos, A.; Georgakilas, V.; Petridis, D. *Chem. Mater.* **2002**, *14*, 3226.
(41) Flesch, C.; Delaite, C.; Dumas, P.; Bourgeat-Lami, E.; Duguet, E. *J. Polym. Sci., Part A: Polym. Chem.* **2004**, *42*, 6011.
(42) De Gennes, P. G. *Macromolecules* **1980**, *13*, 1069.
(43) Auroy, P.; Auvray, L.; Leger, L. *Macromolecules* **1991**, *24*, 5158.
(44) Zhang, L.; Manthiram, A. *Phys. Rev. B: Condens. Matter Mater. Phys.* **1996**, *54*, 3462.
(45) Bottoni, G.; Candolfo, D.; Cecchetti, A.; Masoli, F. *J. Magn. Magn. Mater.* **1992**, *116*, 285.
(46) Nakata, K.; Hu, Y.; Uzun, O.; Bakr, O.; Stellacci, F. *Adv. Mater.* **2008**, *20*, 4294.
(47) Franco, V.; Batlle, X.; Labarta, A.; O'Grady, K. *J. Phys. D: Appl. Phys.* **2000**, *33*, 609.

Macromolecules

Article

pubs.acs.org/Macromolecules

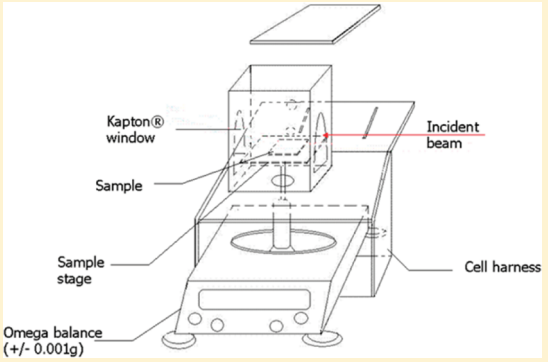
In Situ Measurement of Block Copolymer Ordering Kinetics during the Drying of Solution-Cast Films Using Small-Angle X-ray Scattering

Michael J. Heinzer,*[,†] Sangil Han,[†] John A. Pople,[‡] Donald G. Baird,[†] and Stephen M. Martin[†]

[†]Department of Chemical Engineering, Virginia Polytechnic Institute and State University, Blacksburg, Virginia 24061-0211, United States

[‡]Stanford Synchotron Radiation Lightsource, SLAC National Accelerator Laboratory, Menlo Park, California 94025, United States

ABSTRACT: The ordering of a poly(styrene-*b*-butadiene) block copolymer solution into hexagonally packed cylinders during the extraction of a neutral solvent from a solution-cast film was studied in real time using *in situ* small-angle X-ray scattering (SAXS). By tracking changes in the scattering intensity as solvent is continually removed from the film, information on the ordering rate was obtained as the film progresses from the dilute to the concentrated regime. The ordering rate was found to be controlled by thermodynamics below a critical concentration and by limited chain mobility at higher concentrations. The effect of drying temperature on the ordering kinetics was investigated by extracting solvent at three different temperatures: 30, 40, and 60 °C. The net effect of drying temperature on the ordering rate was found to depend on a competition between the thermodynamics of the drying film and the mobility of the copolymer chains. An intermediate temperature, 40 °C, provided a balance between these competing phenomena, resulting in improved overall ordering in the films. The effect of drying rate was considered by drying films in the presence of a sweep gas. The introduction of a sweep gas to remove solvent resulted in appreciable concentration gradients that hindered ordering in the films.



1. INTRODUCTION

Block copolymers are versatile candidates for numerous applications. In electronics, block copolymers are used to fabricate data storage media, patterned semiconductors, and photonic band-gap materials.[1,2] Block copolymer films can also be used in separation processes. Filter media and nanoporous membranes developed using block copolymers are employed as desalination membranes and biomolecule purification membranes.[1−4] They have also been explored for fuel cell membranes.[5]

Central to making block copolymers such attractive materials is the ability to promote the development of specified microstructures on a nanometer length scale which in turn govern material properties.[6] For instance, block copolymers forming a bicontinuous structure have proven useful in creating efficient solar panels.[7] Lee et al.[5] demonstrated that changes in the dimensions of the lamella microstructure in block copolymer fuel cell membranes are a suitable means for improving proton flux. In other applications, including porous membranes,[8−11] photonics,[12] and sensors,[13] hexagonally packed cylinders have been utilized. As such, it is desirable to be able to control the final microstructure in order to optimize material properties for various applications.

The presence of a solvent allows access to a wider range of microstructures for a given block copolymer composition than can be attained in the melt state. Further, the breadth of structures that can be obtained by the addition of solvent is strongly dependent on the nature of the solvent.[14−21] Lodge et al.[20] extensively studied the phase behavior of poly(styrene-*b*-isoprene) in solution, showing that by changing the solvent selectivity, a block copolymer developing only cylinders in a neutral solvent could form lamella, gyroid, and spheres in selective solvents. Not only was the selective solvent effective in creating new microstructures, but both normal and inverted versions of these structures could be obtained. The equilibrium microstructures obtained by Lodge and co-workers[20] were shown to be a function of the solvent selectivity, solution temperature, and solution composition.

Because of the complexity of the phase behavior of block copolymers in solution, the structure development during the processing of solution-cast films is dependent on the manner in which the solvent is removed. For instance, Wang et al.[22] showed that because of the thermotropic nature of block copolymer phase behavior in solution, changing the temperature at which a block copolymer film was dried changed the microstructure in the final film. Further, Huang et al.[23] and Gong and co-workers[24] demonstrated that the ordered structures developing at a given point during solvent removal is dependent on the concentration of polymer in the film. As the film becomes more concentrated, a block copolymer may

Received: December 5, 2011
Revised: March 20, 2012
Published: April 13, 2012

 © 2012 American Chemical Society dx.doi.org/10.1021/ma2026429 | *Macromolecules* 2012, 45, 3471−3479

go through many metastable states and order−order transitions. As a consequence of this, it has been shown that the film morphology is also a function of the drying rate.[25−28] It is evident from such studies that an understanding of the ordering kinetics during solvent removal is imperative.

Tremendous efforts have been made to understand the mechanism of ordered structure growth in block copolymer films during solution-casting. Consideration has been given to the influence of drying temperature,[5] drying rate,[25,27] solvent selectivity,[5,23,29,30] and solvent annealing[27,29−35] on structure development. However, these studies typically only look at the final morphology following prescribed processing conditions. While many authors attempt to deduce an ordering mechanism, rarely is kinetic data collected during the solvent extraction process itself.

In some instances, groups have monitored structure evolution at certain points during solvent removal. At several concentrations during film drying Gong and co-workers[24] freeze-dried samples and analyzed the morphology using microscopy. The authors were able to show the progression of the morphology from polystyrene spheres in a poly(methyl methacrylate) matrix to polystyrene cylinders to lamellae and finally to PMMA cylinders. Similarly, Huang et al.[23] froze in structures during the removal of a neutral solvent, toluene, from styrenic block copolymer films, observing transitions between inverted and normal spheres and cylinders while moving from dilute to concentrated films. While these studies were capable of demonstrating the lyotropic nature of the drying film, the work did not quantify the kinetics of such transitions.

Recently, Paik et al.[33] demonstrated the ability to track order−disorder and order−order transitions through *in situ* grazing incidence small-angle X-ray scattering measurements. This work, however, was primarily concerned with structure changes during solvent annealing as the films swell or deswell. Though the work did comment on structure development during the addition and removal of solvent, the kinetics of the structure formation and the drying process itself was not the focal point of the work.

Numerous other authors have studied the ordering kinetics of block copolymers in solution.[36−47] These works have tracked growth from a disordered state[37−40,42,43] and transitions between two ordered states.[36,41,44−47] Rheology, SAXS, or a combination of these methods is used to determine the degree of ordering in the solution as a function of time. The ordering kinetics are then quantitatively analyzed using a suitable model, particularly the Avrami model for crystallization, to obtain information regarding the ordering rate and growth mechanism. Others[37,38] have used polarized optical microscopy to directly monitor the growth of ordered domains by measuring the growth front velocity of the grains.

Further work is needed to fully understand the ordering process during solvent removal. The transitions being explored in the above works are thermally induced. That is, the growth of a new state is initiated by heating or cooling through a thermal transition. As such, the studies do not fully account for the ordering kinetics during solvent removal over a full range of concentrations that will be encountered during film drying, concerning themselves primarily with temperature effects. In multiple cases, only a single concentration is considered for a given block copolymer solution.[37,40,41] When multiple concentrations have been considered, only a few concentrations in semidilute solutions are given attention.[39,42] In solvent extraction, one is concerned with changes induced because of the lyotropic nature of the solution. It is important to understand how the ordering process changes as one proceeds through order−disorder transition concentrations and subsequent order−order transitions into the concentrated region of the film.

In the work presented here, *in situ* small-angle X-ray scattering (SAXS) measurements were used to track, in real time, the evolution of ordered structures in a block copolymer film during solvent removal. SAXS is a powerful tool for studying the phase separation process of a block copolymer. Quantitative information regarding the ordered domain can be obtained by analyzing the primary scattering peak. The microstructure spacing, d, can be determined in a manner analogous to the determination of the Bragg spacing as a function of the wave vector of the primary peak, q^*:

$$d = \frac{2\pi}{q^*} \tag{1}$$

The extent of ordering in the sample, ϕ, is related to the integrated intensity of the primary peak through the scattering power, P:

$$P = \frac{1}{2\pi}\int I(q) q \, \mathrm{d}q \tag{2}$$

where $I(q)$ is the relative intensity at a wave vector, q. The scattering power can then be related to the volume fraction of the ordered phase in the material, ϕ, by eq 3:

$$P = \Delta n^2 \phi(1 - \phi) \tag{3}$$

In eq 3, Δn is the difference in the electron densities of the two phases. This relation holds for a binary system. Thus, by monitoring changes in the scattering power as a function of time and polymer concentration during solvent removal, the ordering kinetics can be tracked in real time.

In the current study, changes in the scattering power as solvent was continually removed from a block copolymer film were used to track the development of ordered structures. Because styrenic block copolymers are commonly used in ordering kinetics studies,[36−39,41,42] poly(styrene-*b*-butadiene) was selected as a model system for this work. The kinetics of the ordering process were quantified at concentrations ranging from the dilute to the concentrated regimes during the drying process. Changes in the ordering kinetics with concentration during solvent removal at room temperature are first discussed. The effect of drying temperature on the ordering kinetics during solvent removal is then described. Finally, the effect of changing the drying rate by drying films in the presence and absence of a sweep gas is discussed.

2. EXPERIMENTAL SECTION

2.1. Materials. A block copolymer, poly(styrene-*b*-butadiene) (SB), was purchased from Sigma-Aldrich and used as received. Based on size-exclusion chromatography (SEC), the weight-average molecular weight of the diblock copolymer was determined by SEC to be 119.3 kg/mol and the polydispersity index is 1.01. The polymer is reported to be 33% polystyrene. A neutral solvent, toluene (>99.5% pure), was purchased from Sigma-Aldrich and used as received.

2.2. Solution Preparation. Solutions were prepared by dissolving an appropriate amount of copolymer in toluene to yield a 20 wt % polymer solution. Solutions were made in a sealed vial and sonicated at room temperature overnight (>12 h) or until a clear solution was obtained prior to use. Solutions were used within 24 h of preparation.

2.3. Scattering Cell. The apparatus for SAXS measurements during solvent removal was designed and fabricated in our lab and is

dx.doi.org/10.1021/ma2026429 | *Macromolecules* 2012, 45, 3471−3479

shown in Figure 1. The apparatus consists of an aluminum cell attached to an aluminum harness. Two Kapton windows are present

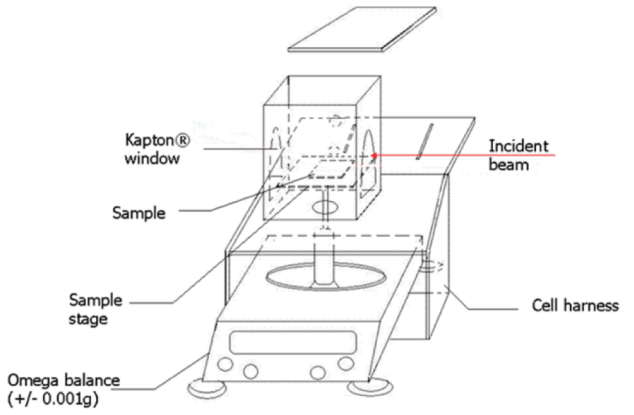


Figure 1. Scattering cell used to simultaneously monitor removal of solvent from block copolymer films and track ordered structure development using SAXS. Sample chamber can be wrapped in heating tape (not shown) to control the solvent removal temperature.

on the side of the cell. On the back of the cell are two ports that serve as inlet and outlets for a nitrogen sweep gas. Nitrogen gas enters through the bottom port and exits through the top port.

The cell is covered by an aluminum lid to create a closed environment within the cell, with the exception of the inlet and outlet gas. A thermocouple (Type K, purchased from Omega) is inserted through a hole in the center of the lid to monitor the temperature inside the cell.

Insulated fiberglass Omegalux heating tape (FGS051-020) purchased from Omega was used to heat the environment surrounding the sample. The tape was wrapped around the unit, extending from the lid down the cell to just above the Kapton windows. The heating tape allowed temperature control from ambient to ~200 °C, which was sufficient for achieving the temperatures desired in these experiments. The heating tape is powered by a variable transformer. During experiments, the temperature fluctuated no more than ±1 °C.

The cell is capable of simultaneously monitoring solvent loss from a polymer solution and continuously obtaining scattering profiles during the solvent removal process. An aluminum stage is attached to a telescopic post that can be adjusted manually. The post runs through the bottom of the cell and attaches to a balance that sits in the harness. The harness attaches to a motorized stage so that the cell, stage, and balance can be moved in the beamline as a single unit. The balance is connected to computer to register the weight of the sample on the stage during experiments.

2.4. *In Situ* SAXS Experiments. A 0.15 g sample of polymer solution was transferred dropwise by pipet from the solution vial onto a 25 mm × 25 mm silica wafer on the stage in the sample cell. The final polymer films had a thickness of 50 μm. While thinner films could be studied with this setup, the sample thickness used in these experiments was necessitated by a balance between the desired volatility of the casting solvent and the drying rate of the sample. The drying time, a function of film thickness and solvent volatility, must be rapid enough that the sample does not equilibrate during the solvent removal but sufficiently long to allow the acquisition of enough data points to characterize the phase transformation kinetics. The speed at which the data can be obtained is primarily a function of the intensity of the incoming X-ray beam.

The initial polymer solutions are a viscous liquid, whose meniscuses are pinned at the edge of the sample substrate. As such, there is no wall at the edges of the sample, and the films must be kept in a horizontal orientation during the experiment. Beamline 1-4 at SSRL is not equipped to allow the incoming X-ray beam to be deflected, so all experiments were performed with the X-ray beam impinging on the film in a direction parallel to the film surface.

The samples were dried in the cell while the weight was recorded every 5 s. As solvent was removed, they were exposed to an incident X-ray beam for 30 s every 60 s. The beam entered through the Kapton window at an angle parallel to the film surface at 0°. The incoming beam had a vertical thickness of 0.6 mm and was thicker than the film for the duration of the experiment. Thus, the beam always impinged on the whole of the sample thickness. For consistency, the sample was positioned such that the same amount of beam was occluded to begin each experiment. The sample position relative to the beam path was not adjusted during the experiment. In total, five different drying conditions were examined. The samples were dried at three different temperatures (30, 40, and 60 °C) without a nitrogen sweep gas, and at 30 and 40 °C, samples were also dried in the presence of a nitrogen sweep gas.

3. RESULTS AND DISCUSSION

3.1. Phase Behavior. SAXS profiles for the SB block copolymer/toluene film recorded during solvent removal at 30 °C are depicted in Figure 2 for polymer weight fractions

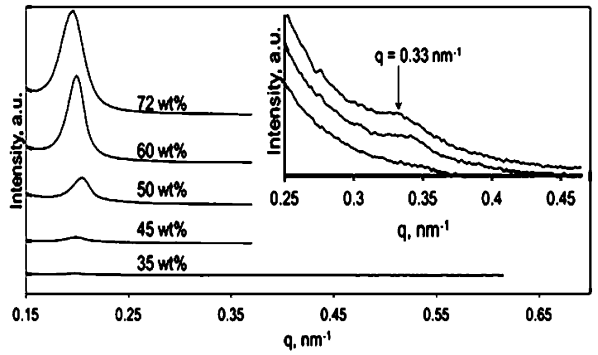


Figure 2. SAXS profiles of an SB/tolune solution during solvent removal at 30 °C. Peaks positioned at n = 1 and $3^{1/2}$ are consistent with hexagonally packed cylinders.

between 0.22 and 0.8. The profiles have been offset along the y-axis for clarity. The primary peak at a wave vector of 0.2 nm^{-1} first appears at 30 wt % polymer. Beginning around a polymer weight fraction of 0.5, secondary peaks appear. The intensity of these secondary peaks is relatively low. Insets in Figure 2 show these secondary peaks more clearly. The secondary peak is located at a q/q_{max} value of $\sqrt{3}$. Based on the relative positions of the peaks in the scattering profiles and the position of the primary peak, the microstructure is hexagonally packed cylinders with a structure spacing of ~30 nm. The relative positions of the peaks are constant over all solvent concentrations, indicating that the structure does not depend on solvent content.

Scattering profiles at a concentration of 60 wt % SB for films dried at 40 and 60 °C are shown in Figure 3. Insets are again included to more clearly show the secondary peaks. Again, these peaks have been offset along the y-axis for clarity. Secondary peaks also appear at a wave vector (0.33 nm^{-1}) that is $\sqrt{3}$ times the primary peak position, indicating hexagonally packed cylinders at 40 and 60 °C.

3.2. Ordering Kinetics during Solvent Removal under Ambient Conditions. The degree of ordering in the block copolymer film is related to the integrated intensity of the primary peak (n = 1) in the SAXS profile. Prior to integration, all profiles are normalized to account for changes in concentration and film thickness. Figure 4 contains a plot of the integrated intensity as a function of concentration for solvent removal from an SB/toluene film at 30 °C. Below the

dx.doi.org/10.1021/ma2026429 | Macromolecules 2012, 45, 3471−3479

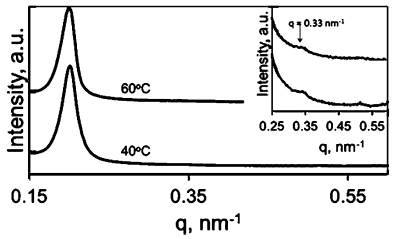


Figure 3. SAXS profiles of an SB/tolune film (60 wt % polymer) during solvent removal at 40 and 60 °C. Peaks positioned at $n = 1$ and $3^{1/2}$ are consistent with hexagonally packed cylinders.

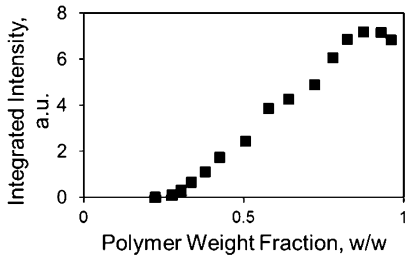


Figure 4. Integrated intensity of the primary SAXS peak ($n = 1$) as a function of the polymer weight fraction in a SB/tolune film during solvent removal at 30 °C.

order−disorder transition (ODT), there is no discernible ordering and the integrated intensity is equal to zero. The onset of ordering is signaled by an increase in the integrated intensity beginning at ∼30 wt % polymer, which is therefore identified as the order−disorder concentration. The integrated intensity increases in a sigmoidal manner above the ODT concentration. The fluctuations observed in the semidilute region are due to interference caused by reflections off the film surface.

The integrated intensity increases as the solvent is removed before leveling off at ∼80 wt % polymer, indicating that the ordered phase has stopped growing. Growth is still observed at relatively high polymer concentrations (>60 wt % polymer) where chain mobility is expected to be limited, but it must be recognized that the concentrations in Figure 4 are average concentrations for a relatively thick film (>50 μm). It is probable that concentration gradients exist in the film, resulting in regions in the film where the local concentration is below the average concentration.[48] The continued growth likely occurs in these more dilute regions of the film where chain movement is still possible.

The sigmoidal shape of the integrated intensity indicates that the ordering rate varies with polymer concentration. The ordering rate during the solvent removal can be quantified by plotting the integrated intensity as a function of time, shown in Figure 5. The data is fit with a third-order polynomial to smooth out the noise due to reflections from the film surface. The derivative at a given time is defined as the instantaneous ordering rate at the corresponding polymer concentration.

The instantaneous ordering rates as a function of polymer concentration are shown in Figure 6. Initially, the instantaneous ordering rate increases as the polymer concentration increases above the ODT concentration (∼30 wt % polymer). A broad maximum is reached between approximately 42 and 50 wt % polymer, followed by a decrease as the sample becomes more concentrated.

The trend depicted in Figure 6 is the result of competition between thermodynamic and kinetic factors. Figure 7 is a

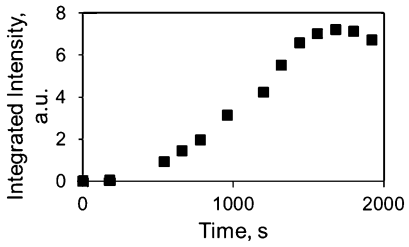


Figure 5. Integrated intensity of the primary SAXS peak ($n = 1$) as a funtion of time collected from a SB film cast in tolune while solvent is simultaneously removed at 30 °C.

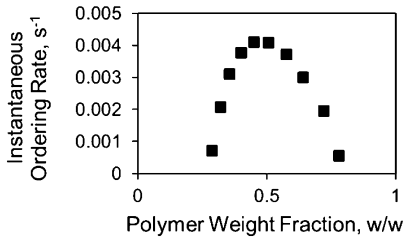


Figure 6. Instantaneous rate of ordering of the SB copolymer into hexagonally packed cylinders in a neutral solvent, tolune, during continual solvent removal at 30 °C.

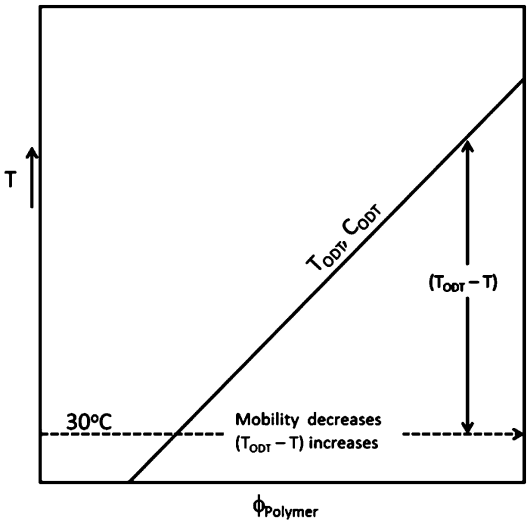


Figure 7. Schematic phase diagram (polymer concentration, $\phi_{Polymer}$, vs temperature, T) illustrating the solvent removal path (dashed line) of the SB/tolune film at 30 °C. T_{ODT} and C_{ODT} represent the order−disorder transition temperature and concentration, respectively.

schematic phase diagram for a block copolymer in solution showing the order−disorder transition (ODT − solid line) and a constant temperature drying path (dashed line) for solvent removal from the copolymer film. Near the order−disorder transition the disordered state is metastable, and the energy barrier for nucleation is large. Moving away from order−disorder transitions makes the disordered state unstable. It has been reported that the half-time for ordering decreases proportionally to the inverse of the square of the quench depth ($\delta = T_{ODT} - T$) for shallow temperature quenches below the ODT temperature.[49] Thus, the ordering is slow near the ODT and increases farther away from it. Similar behavior is responsible for the increase in ordering rate as polymer concentration increases beyond the ODT concentration. Figure

dx.doi.org/10.1021/ma2026429 | Macromolecules 2012, 45, 3471−3479

7 shows that as the solvent is removed from the film, the film moves farther from the order−disorder transition concentration and δ increases. The combination of these effects causes the net thermodynamic driving force for phase separation to increase as the film initially becomes more concentrated. This results in an increased ordering rate.

Increasing the polymer concentration also results in a reduction in chain mobility, so that as the driving force for ordering increases, chain mobility is continually decreasing. At high polymer concentrations the chain mobility decreases to the point that the kinetic factors begin to dominate the thermodynamic factors in dictating the ordering rate. Thus, a continual decrease in the ordering rate is observed as the polymer concentration increases into the concentrated regime. The ordering rate approaches zero at high polymer concentrations when the chains become kinetically trapped.

3.3. Effect of Drying Temperature on Ordering.

3.3.1. Drying Curves. Toluene was removed from poly(styrene-*b*-butadiene) (SB) block copolymer films at three different temperatures (30, 40, and 60 °C). Figure 8 contains drying

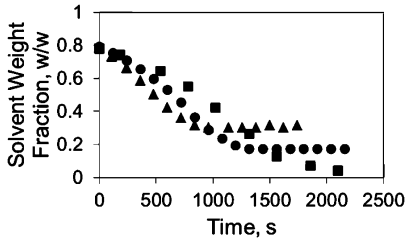


Figure 8. Drying curves for SB copolymer films cast from a 20 wt % tolune solution at 30 (■), 40 (●), and 60 °C (▲).

curves (polymer weight fraction vs time). The drying rate is primarily controlled by evaporation of solvent at the film/air interface at short times, referred to as the constant drying regime, and the rate of solvent removal increases with increasing temperature. At longer times, the solvent removal is diffusion-controlled, resulting in a decreased drying rate. The onset of diffusion-controlled solvent removal occurs at shorter times and higher residual solvent content as temperature is increased.

It is hypothesized that the drying behavior is due to the formation of a skin—a region of high polymer concentration—at the film surface due to a high solvent evaporation rate at the air/film interface relative to the rate of solvent diffusion through the film. A consequence of this phenomenon is the development of sharp concentration gradients near the film surface. Upon the formation of the skin layer, the solvent diffusion near the interface becomes extremely slow. It is further speculated that as the drying temperature increases, the skin forms more rapidly due to higher solvent removal rates at the film−air interface with increasing temperature, leading to a larger disparity between the evaporation rate at the interface and the rate of diffusion of solvent through the film.

Though the vertical concentration gradients in the films could not be directly measured, the amount of residual solvent in the films at long times also suggests that skinning is occurring. The increased residual solvent is evidence of trapping skinning.[50,51] If a skin were not present, the residual solvent at long times would decrease with increasing temperature due to an increased diffusion coefficient.[50] The data support the previous arguments that increasing the drying temperature increases skin formation as the degree of solvent trapping below the skin layer increases with increasing temperature.

3.3.2. Ordering Kinetics. The integrated intensities of the primary SAXS peaks recorded during solvent removal from an SB/toluene film at 30, 40, and 60 °C are plotted as a function of polymer concentration in Figure 9. The integrated intensities

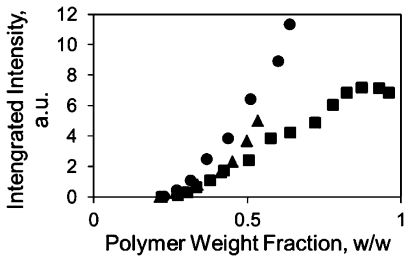


Figure 9. Primary scattering peak integrated intensity as a function of concentration during extraction of tolune from SB copolymer at 30 (■), 40 (●), and 60 °C (▲).

are normalized to account for temperature, solvent content, and film thickness differences.

Beyond the concentrations shown in Figure 9, reflections off the surface interfere with the scattering signal, producing unreliable data at 40 and 60 °C. Only concentrations for which interference is not present are analyzed. It is believed that the larger surface reflections at 40 and 60 °C are due to the skinning phenomenon discussed in section 3.3.1. Similar arguments used to explain the changes in the drying behavior with increasing temperature are valid in discussing the maximum concentration for which useable data were obtained at each temperature. At 30 °C, data were collected at concentrations in excess of 95 wt % polymer, suggesting that reflections off the film surface due to skinning were negligible. It is expected that at a low temperature such as 30 °C the evaporation of solvent at the film−air interface is not drastically faster than the rate of diffusion of solvent through the film, mitigating the formation of sharp the concentration gradients near the film surface. Thus, the formation of a skin was likely prevented at 30 °C, allowing meaningful scattering data to be obtained over all measured concentrations.

At 40 and 60 °C sharp concentration gradients in the film are formed as the diffusion of solvent through the film was exceeded by the rate of solvent evaporation at the surface, leading to skinning at the film surface. The solidlike skin causes larger surface reflections, interfering with the normalization and integration of the scattering data.

Increasing the temperature from 30 to 40 °C resulted in higher integrated intensities for a given concentration despite shorter ordering times due to the higher drying rate. The final integrated intensity at 40 °C, obtained at 66 wt % polymer, is around 12 au while the final integrated intensity obtained at 30 °C at 90 wt % polymer is only 7 au. This indicates that the ordering is more rapid at 40 °C than at 30 °C.

Further increasing the temperature to 60 °C also results in more rapid ordering than observed at 30 °C. At 53 wt % polymer, the integrated intensity from the film dried at 60 °C is 5 au, as opposed to a value of 3 au for the film dried at 30 °C. The film dried at 60 °C has a lower integrated intensity for a given polymer concentration than the film dried at 40 °C; however, the drying rate at 60 °C is faster than the drying rate at 40 °C.

dx.doi.org/10.1021/ma2026429 | *Macromolecules* 2012, 45, 3471−3479

The instantaneous ordering rates for SB−toluene films dried at 30, 40, and 60 °C are shown in Figure 10. At the two

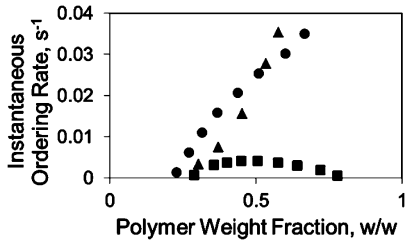


Figure 10. Instantaneous rate of ordering of the SB copolymer into hexagonally packed cylinders in a neutral solvent, tolune, during continual solvent removal at 30 (■), 40 (●), and 60 °C (▲).

elevated temperatures, 40 and 60 °C, the ordering rates are significantly higher than the rates measured at 30 °C for all concentrations. At 40 and 60 °C, the ordering rates continue to increase at concentrations for which the film dried at 30 °C begins to show a decrease in the ordering rate. The data taken at 40 °C show a slowing of the rate of increase of the ordering rate with concentration, which may indicate it is approaching a maximum. This maximum does not occur in the range of measurable data but would be at a higher concentration than the maximum obtained at 30 °C. At 60 °C, the ordering rates do not appear to be approaching a maximum.

The ordering rates at 40 and 60 °C show a crossover at around 55 wt % polymer. At low concentrations, the ordering rates at 40 °C are nearly double the ordering rates at 60 °C. After the crossover, the ordering rate at 60 °C is ∼10% higher than the ordering rate at 40 °C at 53 wt % polymer, the final point for which ordering data were obtained at 60 °C.

The trends in ordering rate with temperature and concentration in Figure 10 can be explained by considering two effects: the changes in the thermodynamic driving force with temperature and the changes in chain mobility with temperature and concentration. The kinetics at a given temperature and concentration are the result of a combination of these effects. To help explain these concepts, Figure 11 depicts a schematic block copolymer/solvent phase diagram, showing the ODT and drying paths for films dried at three different temperatures. As temperature decreases (moving vertically in the phase diagram), the interaction parameter between the styrene and butadiene blocks increases, increasing the driving force for phase separation. As discussed in section 3.2, the ordering time is expected to decrease proportionally to the inverse of the square of the quench depth, δ. Films dried at 60 °C will always be closest to the disordering temperature and will have the lowest driving force for ordering at all concentrations. Disregarding the effect of chain mobility, the ordering rate should increase as temperature decreases. However, decreasing the temperature also decreases chain mobility, so if structure growth is diffusion-driven, decreasing the chain mobility should decrease the ordering rate. The changes in thermodynamics and chain mobility with temperature cannot be decoupled. If the increase in the interaction parameter with lowered temperature is substantial enough to offset the loss of thermal mobility, the net result is an increase in the ordering rate. Alternatively, if the diminished chain mobility cannot be overcome by improved thermodynamics, the ordering rate is slowed.

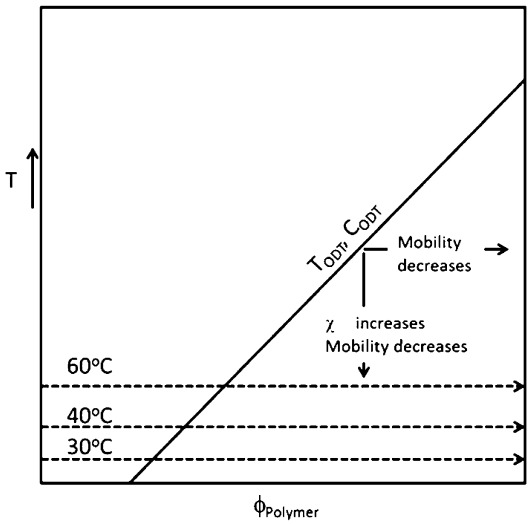


Figure 11. Schematic phase diagram (polymer concentration, $\phi_{Polymer}$, vs temperature, T) illustrating the solvent removal path (dashed lines) of the SB/tolune film at three different temperatures as indicated in the figure. T_{ODT} and C_{ODT} represent the order−disorder transition temperature and concentration, respectively.

The ordering rate at 30 °C is lower than at 40 or 60 °C. At 30 °C, the driving force for chain segregation is the greatest but is offset by the decreased chain mobility, as shown in Figure 11. This results in lower ordering rates at 30 °C than at the higher temperatures.

The ordering rate of the film dried at 40 °C is higher than that of the film dried at 60 °C for low polymer concentrations. As shown in Figure 11, the film dried at 40 °C will have a higher thermodynamic driving force for phase separation but lower chain mobility. In this case, the difference in the chain mobility at these two temperatures appears to be small relative to the difference in the thermodynamic driving forces.

The crossover in the ordering rates at 40 and 60 °C suggests that chain mobility decreases more rapidly with concentration at 40 °C than at 60 °C. As shown in Figure 11, as the film becomes more concentrated, the relative difference in δ decreases. That is, differences in the thermodynamic driving force become less substantial, moving deeper into the phase diagram. Eventually, the difference in thermodynamic driving force is negligible relative to the difference in the chain mobility. The ordering rate crossover observed in Figure 10 is attributed the increased influence of chain mobility at lower temperatures as polymer concentration increases. At higher concentrations, higher temperatures result in higher ordering rates because of improved chain mobility; however, the improved mobility comes at the cost of shorter ordering times, which results in a lower degree of ordering at a given concentration, as seen in Figure 9.

In addition to having different ordering rates, the instantaneous ordering rate curves display different shapes. This results from changes in the thermodynamic driving force as the concentration changes. Increasing the polymer concentration in the film by removing solvent results in an increase in the thermodynamic driving force for phase separation and a reduction in chain mobility. At 30 °C, this was manifested as a maximum in the ordering rate as a function of concentration. The higher ordering rates and lack of an observable maximum at 40 and 60 °C suggest that the

dx.doi.org/10.1021/ma2026429 | Macromolecules 2012, 45, 3471−3479

increased temperature results in a significant increase in chain mobility.

3.4. Effect of Sweep Gas on Ordering Kinetics. The data presented in section 3.3 are sufficient to investigate how ordering kinetics change with drying temperature. However, changing the temperature inherently changes the drying rate, so the effect of drying temperature and drying rate cannot be independently analyzed based solely on temperature changes. To better understand how drying rate influences ordering, the drying rate of films dried at 30 and 40 °C was altered by drying in the presence and absence of a sweep gas.

3.4.1. Drying Curves. The solvent removal rates at 30 and 40 °C were altered by introducing a sweep gas. Films prepared with a sweep gas still exhibited the same cylindrical structure as those formed in the absence of sweep gas. Figures 12a and 12b show the drying curves for films dried with and without a sweep gas at 30 and 40 °C, respectively. At both temperatures, the sweep gas results in a slower drying rate. The presence of a sweep gas should improve mass transfer at the film/air interface, but a slowing of the drying rate was observed instead, and higher residual solvent concentrations were measured at the final plateau in the drying curve. Earlier experimental studies on the drying of polymer films have reported similar observations of the effect of sweep gas flow rate on residual solvent and attributed this to trapping skinning.[50,51] Further, reflection off the surface is again observed. As such, the drying behavior in Figure 12 suggests a skin layer is forming and is responsible for the higher residual solvent content in the presence of a sweep gas. It is hypothesized that the mass transfer at the film/air interface is initially improved by the sweep gas resulting in rapid development of the skin layer. Once the skin layer has developed, it acts as a diffusion barrier and slows the solvent removal rate over a majority of the solvent removal process. Nonetheless, drying with a sweep gas allowed for two different drying rates to be studied at a single drying temperature.

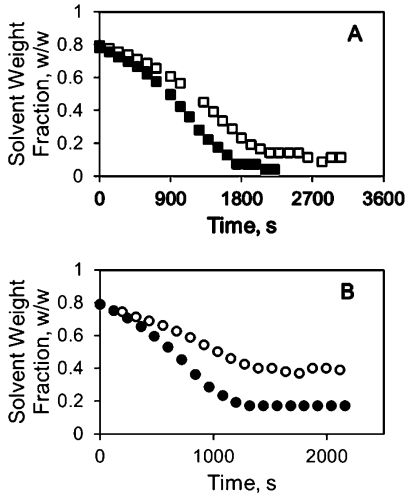


Figure 12. Dying curves for SB copolymer films cast from a 20 wt % tolune solution at 30 °C (A) and 40 °C (B). The curves in each figure represent films dried without a sweep gas (filled points) and with a sweep gas (open points).

3.4.2. Ordering Kinetics. Plots of the integrated intensity as a function of concentration for films dried with and without a sweep gas at 30 and 40 °C are shown in Figures 13a and 13b, respectively. At 30 °C, the range of concentrations over which ordering was observed is different for the two different solvent removal rates. The onset of ordering occurs at a lower concentration with sweep gas than without. It is hypothesized that introducing a sweep gas results in significant concentration gradients. As such, at lower average concentrations, the concentration near the film's free surface is expected to be higher than the order−disorder transition concentration. This results in ordered phase growth at concentrations below the expected ODT. The reflection from the surface of the films dried with a sweep gas prevented data analysis at high polymer concentrations.

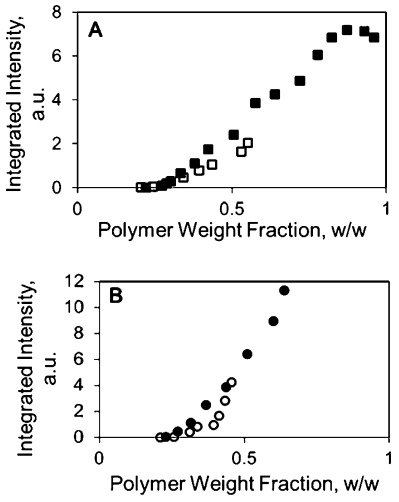


Figure 13. Primary scattering peak integrated intensity as a function of concentration during extraction of tolune from SB copolymer at 30 °C (A) and 40 °C (B). At both temperatures, films were dried without a sweep gas (closed points) and with a sweep gas (open points).

At 30 °C and concentrations below 35 wt % polymer, the rate of change of the integrated intensity with concentration for a film dried in the presence of a sweep gas is comparable to the trend observed for a film dried without a sweep gas. Beyond ∼35 wt % polymer, the integrated intensities of the two films deviate from one another, with the film dried without a sweep gas ordering more rapidly with respect to concentration. This is observed despite the film having a faster solvent removal rate and a shorter time to order.

At 40 °C, no difference in the onset of ordering is discernible. It appears that under both solvent removal conditions the rise in the integrated intensity begins at nearly the same concentration. However, the film dried in the presence of a sweep gas shows a significant degree of scatter in the data at low polymer concentrations. Prior to 35 wt % polymer, the intensities of the films dried under both conditions are comparable as concentration changes. The intensities with respect to concentration diverge at ∼35 wt % polymer. At ∼50 wt % polymer, which is the maximum concentration that reliable data was obtained using a sweep gas, the intensities are comparable once more. Thus, the apparent differences in changes in intensity with concentration may be due to scatter in the data collected from the film dried with a sweep gas.

Figures 14a and 14b show the instantaneous ordering rates for the films dried at 30 and 40 °C, respectively. At both temperatures, films dried without a sweep gas have higher ordering rates than films dried with a sweep gas. This is attributed to the fact that the films dried with a sweep gas have more significant concentration gradients. This results in the

dx.doi.org/10.1021/ma2026429 | Macromolecules 2012, 45, 3471−3479

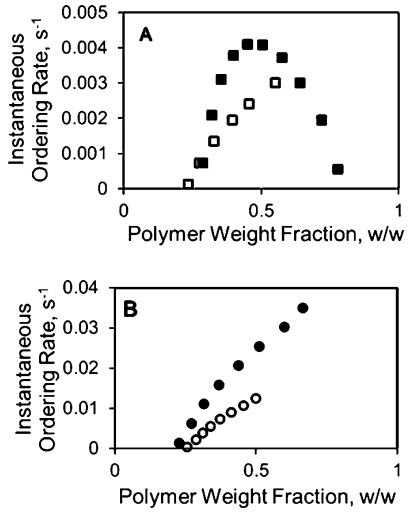


Figure 14. Instantaneous rate of ordering of the SB copolymer into hexagonally packed cylinders in a neutral solvent, toluene, during continual solvent removal at 30 °C (A) and 40 °C (B). At both temperatures, films were dried without a sweep gas (open points) and with a sweep gas (closed points).

formation of a skin with a high polymer concentration at the surface with concentration decreasing rapidly away from the surface. Conditions are unfavorable for ordering due to limited chain mobility in the concentrated skin and a low driving force for ordering in the dilute region of the film. The concentrations in the films dried without a sweep gas are more uniform, resulting in faster ordering throughout the film. Despite these differences, the decreased ordering rates observed in the films dried with a sweep gas are offset by increased ordering times, resulting in a similar degree of ordering for a given concentration, as shown in Figure 13.

Changing the drying rate at 30 °C affects the shape of the ordering rate versus concentration curve. The ordering rate of the film dried with a sweep gas increases with concentration for all measured concentrations. Therefore, it can be inferred that the maximum ordering rate occurs at a higher concentration when removing solvent with a sweep gas than without a sweep gas. This can be attributed to steep concentration gradients in the film dried with a sweep gas resulting in regions with low polymer concentration (i.e., below the average film concentration) where the ordering rate is still high. Further study is necessary to confirm the presence of gradients in the film and their effect on the maximum ordering rate. However, it is clear that the presence of a sweep gas, and resultant change in drying rate, significantly affect the ordering in the film.

4. CONCLUSIONS

In situ SAXS has been used to quantify the kinetics of the development of ordered structures in a block copolymer film during solvent removal in real time. The technique allows the simultaneous determination of the type of ordered structure (e.g., cylinders) and the extent of ordering as a function of the film concentration. Ordering was studied as a function of temperature and in the presence and absence of a sweep gas. The ordering kinetics at a given concentration and temperature are the result of a competition between changes in the thermodynamic driving force for phase separation and chain mobility. In general, the ordering rate increases as the concentration initially progresses beyond the order−disorder transition due to an increased thermodynamic driving force. At high concentrations, chain mobility decreases and the ordering rate decreases until the film becomes kinetically trapped.

Drying the film at elevated temperatures (40 and 60 °C) serves to decrease the effect of lowered chain mobility at high concentrations and improves ordered phase formation during the solvent removal process. The ordering kinetics also become more complex due to the competition between thermodynamics and chain mobility. The intermediate drying temperature, 40 °C, resulted in the highest initial ordering kinetics and the highest final degree of ordering due to the balance between thermodynamic and kinetic effects. The high temperature, 60 °C, exhibited lower initial ordering rates due to the formation of a high polymer concentration "skin" that acted as a diffusion barrier, and the final degree of ordering was limited by the short drying time.

The addition of a sweep gas resulted in a decreased drying rate due to the formation of a high polymer concentration "skin" that limited solvent diffusion. The skin formation decreases the instantaneous ordering rates. At a low temperature, 30 °C, the difference in ordering rates resulted in slight differences in the extent of ordering in the film at a given concentration. At an elevated temperature, 40 °C, there is no net effect on the extent of ordering in the film because the reduction in ordering rate is balanced by longer ordering times due to the slower drying rate.

The sample cell design can be improved, and these efforts are currently underway. In the current setup, the beam path length is quite long due to both thickness of the sample and the length of the sample along the direction of the beam path. Because the scattered intensity is inversely proportional to the thickness of the sample through which it must travel, the scattering intensity is not maximized and information about the bulk sample away from the surface may be lost with the current scheme. An improved design would be one in which the beam enters the sample normal to the film surface allowing for pure transmission SAXS through the entire sample. This would require the ability to bend the incoming X-ray beam, possible using a monochromator crystal. The capacity to bend the beam would also allow the use of reflectivity techniques to study vertical concentration gradients in the films.

AUTHOR INFORMATION

Notes

The authors declare no competing financial interest.

ACKNOWLEDGMENTS

Funding for this work was provided by the Institute for Critical Technology and Applied Science at Virginia Tech. The authors acknowledge Eastman Chemical Company for providing funding through the Eastman Fellowship in Polymer Science. Portions of this research were carried out at the Stanford Synchrotron Radiation Laboratory, a national user facility operated by Stanford University on behalf of the U.S. Department of Energy, Office of Basic Energy Sciences. The SSRL Structural Molecular Biology Program is supported by the Department of Energy, Office of Biological and Environmental Research, and by the National Institutes of Health, National Center for Research Resources, Biomedical Technology Program, and the National Institute of General Medical Sciences.

REFERENCES

(1) Hamley, I. W. Introduction to Block Copolymers. In *Developments in Block Copolymer Science and Technology*; Hamley, I. W., Ed.; John Wiley & Sons, Ltd.: New York, 2004; p 1.
(2) Zhang, J.; Yu, X.; Yang, P.; Peng, J.; Luo, C.; Huang, W.; Han, Y. *Macromol. Rapid Commun.* **2010**, *31*, 591.
(3) Fasolka, M. J.; Mayes, A. M. *Annu. Rev. Mater. Res.* **2001**, *31*, 323.
(4) Wang, F.; Hickner, M.; Kim, Y. S.; Zawodzinski, T. A.; McGrath, J. E. *J. Membr. Sci.* **2002**, *197*, 231.
(5) Lee, M.; Park, J. K.; Lee, H. S.; Lane, O.; Moore, R. B.; McGrath, J. E.; Baird, D. G. *Polymer* **2009**, *50*, 6129.
(6) Lodge, T. P. *Macromol. Chem. Phys.* **2003**, *204*, 265.
(7) Meuler, A. J.; Hillmyer, M. A.; Bates, F. S. *Macromolecules* **2009**, *42*, 7221.
(8) Jackson, E. A.; Hillmyer, M. A. *ACS Nano* **2010**, *4*, 3548.
(9) Kang, M.; Moon, B. *Macromolecules* **2009**, *42*, 455.
(10) Pai, R. A.; Humayun, R.; Schulberg, M. T.; Sengupta, A.; Sun, J. N.; Watkins, J. J. *Science* **2004**, *303*, 507.
(11) Uehara, H.; Kakiage, M.; Sekiya, M.; Sakuma, D.; Yamonobe, T.; Takano, N.; Barraud, A.; Meurville, E.; Ryser, P. *ACS Nano* **2009**, *3*, 924.
(12) Bockstaller, M.; Kolb, R.; Thomas, E. L. *Adv. Mater.* **2001**, *13*, 1783.
(13) Wirnsberger, G.; Scott, B. J.; Stucky, G. D. *Chem. Commun.* **2001**, *01*, 119.
(14) Alexandridis, P.; Olsson, U.; Lindman, B. *Langmuir* **1998**, *14*, 2627.
(15) Alexandridis, P.; Olsson, U.; Lindman, B. *Langmuir* **1997**, *13*, 23.
(16) Alexandridis, P.; Zhou, D.; Khan, A. *Langmuir* **1996**, *12*, 2690.
(17) Forster, S.; Berton, B.; Hentze, H. P.; Kramer, E.; Antonietti, M.; Lindner, P. *Macromolecules* **2001**, *34*, 4610.
(18) Hanley, K. J.; Lodge, T. P.; Huang, C. I. *Macromolecules* **2000**, *33*, 5918.
(19) Lai, C. J.; Russel, W. B.; Register, R. A. *Macromolecules* **2002**, *35*, 841.
(20) Lodge, T. P.; Pudil, B.; Hanley, K. J. *Macromolecules* **2002**, *35*, 4707.
(21) Svensson, B.; Alexandridis, P.; Olsson, U. *J. Phys. Chem. B* **1998**, *102*, 7541.
(22) Wang, Y.; Shen, J. S.; Long, C. F. *Polymer* **2001**, *42*, 8443.
(23) Huang, H.; Hu, Z.; Chen, Y.; Zhang, F.; Gong, Y.; He, T.; Wu, C. *Macromolecules* **2004**, *37*, 6523.
(24) Gong, Y. M.; Huang, H. Y.; Hu, Z. J.; Chen, Y. Z.; Chen, D. J.; Wang, Z. B.; He, T. B. *Macromolecules* **2006**, *39*, 3369.
(25) Gong, Y. M.; Hu, Z. J.; Chen, Y. Z.; Huang, H. Y.; He, T. B. *Langmuir* **2005**, *21*, 11870.
(26) Huang, H.; Zhang, F.; Hu, Z.; Du, B.; He, T.; Lee, F. K.; Wang, Y.; Tsui, O. K. C. *Macromolecules* **2002**, *36*, 4084.
(27) Kim, G.; Libera, M. *Macromolecules* **1998**, *31*, 2569.
(28) Zhang, Q. L.; Tsui, O. K. C.; Du, B. Y.; Zhang, F. J.; Tang, T.; He, T. B. *Macromolecules* **2000**, *33*, 9561.
(29) Leolukman, M.; La, Y. H.; Li, X.; Gopalan, P. *Polym. J.* **2008**, *40*, 825.
(30) Li, Y.; Huang, H.; He, T.; Gong, Y. *J. Phys. Chem. B* **2010**, *114*, 1264.
(31) Guo, R.; Huang, H.; Chen, Y.; Gong, Y.; Du, B.; He, T. *Macromolecules* **2008**, *41*, 890.
(32) Luo, C.; Huang, W.; Han, Y. *Macromol. Rapid Commun.* **2009**, *30*, 1917.
(33) Paik, M. Y.; Bosworth, J. K.; Smilges, D. M.; Schwartz, E. L.; Andre, X.; Ober, C. K. *Macromolecules* **2010**, *43*, 4253.
(34) Peng, J.; Kim, D. H.; Knoll, W.; Xuan, Y.; Li, B. Y.; Han, Y. C. *J. Chem. Phys.* **2006**, *125*, 064702.
(35) Peng, J.; Xuan, Y.; Wang, H. F.; Yang, Y. M.; Li, B. Y.; Han, Y. C. *J. Chem. Phys.* **2004**, *120*, 11163.
(36) Bang, J.; Lodge, T. P. *J. Phys. Chem. B* **2003**, *107*, 12071.
(37) Chastek, T. Q.; Lodge, T. P. *Macromolecules* **2004**, *37*, 4891.
(38) Chastek, T. Q.; Lodge, T. P. *Macromolecules* **2003**, *36*, 7672.
(39) Liu, Z.; Shaw, M.; Hsiao, B. S. *Macromolecules* **2004**, *37*, 9880.
(40) Nie, H. F.; Bansil, R.; Ludwig, K.; Steinhart, M.; Konak, C.; Bang, J. *Macromolecules* **2003**, *36*, 8097.
(41) Park, M. J.; Bang, J.; Harada, T.; Char, K.; Lodge, T. P. *Macromolecules* **2004**, *37*, 9064.
(42) Soenen, H.; Berghmans, H.; Winter, H. H.; Overbergh, N. *Polymer* **1997**, *38*, 5653.
(43) Liu, Z.; Shaw, M.; Hsiao, B. S. *J. Rheol.* **2004**, *48*, 1389.
(44) Liu, Y. S.; Nie, H. F.; Bansil, R.; Steinhart, M.; Bang, J.; Lodge, T. P. *Phys. Rev. E* **2006**, *73*, 061803.
(45) Wang, C. Y.; Lodge, T. P. *Macromol. Rapid Commun.* **2002**, *23*, 49.
(46) Li, M.; Liu, Y.; Nie, H.; Bansil, R.; Steinhart, M. *Macromolecules* **2007**, *40*, 9491.
(47) Liu, Y. S.; Li, M. H.; Bansil, R.; Steinhart, M. *Macromolecules* **2007**, *40*, 9482.
(48) Vinjamur, M.; Cairncross, R. A. *AIChE J.* **2002**, *48*, 2444.
(49) Fredrickson, G. H.; Binder, K. *J. Chem. Phys.* **1989**, *91*, 7265.
(50) Vinjamur, M.; Cairncross, R. A. *Drying Technol.* **2001**, *19*, 1591.
(51) Vinjamur, M.; Cairncross, R. A. *J. Appl. Polym. Sci.* **2001**, *83*, 2269.

Macromolecules

Article

pubs.acs.org/Macromolecules

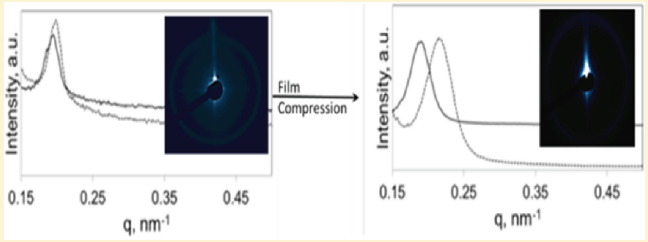
In Situ Tracking of Microstructure Spacing and Ordered Domain Compression during the Drying of Solution-Cast Block Copolymer Films Using Small-Angle X-ray Scattering

Michael J. Heinzer,*[,†] Sangil Han,[†] John A. Pople,[‡] Donald G. Baird,[†] and Stephen M. Martin[†]

[†]Department of Chemical Engineering, Virginia Polytechnic Institute and State University, Blacksburg, Virginia 24061-0211, United States

[‡]Stanford Synchotron Radiation Lightsource, SLAC National Accelerator Laboratory, Menlo Park, California 94025, United States

ABSTRACT: Changes in the spacing of hexagonally packed cylinders in a poly(styrene-*b*-butadiene) copolymer film during the continual extraction of toluene under different solvent removal conditions were studied by *in situ* small-angle X-ray scattering (SAXS) measurements. As the solvent is removed from the film, the structure spacing increases due to increasing segregation power and then decreases as the polymer chains become kinetically trapped while microdomains continue to deswell. The structure spacing in the vertical film direction decreases more drastically due to compression of the domains as the film thickness decreases. The degree of compression increased with increased polymer concentration because of an increase in the chain relaxation time. Increasing the drying temperature resulted in more severe domain compression, which is ascribed to faster solvent removal. Removing solvent in the presence of a sweep gas further increased the domain compression as a result of the formation of a skin at the film surface. When the solvent removal rate was decreased and skinning was avoided by saturating the sample chamber with the casting solvent, domain compression was impeded.



1. INTRODUCTION

Due primarily to their ability to segregate into ordered microstructures, block copolymers are valuable materials in a number of applications. The gyroid[1] and lamella[2] microstructures have been used to fabricate conductive materials. Hexagonally packed cylinders are favored in other applications, such as porous membranes,[3−8] photonics,[9] and sensors.[10] Block copolymers have also received a great deal of attention as candidates for templates for patterned surfaces[11,12] for which other microstructures may be desirable, depending on the surface features necessitated by the end application.

While the specific microstructure is of considerable importance, equally as important in controlling material properties are the orientation and dimensions of these microstructures. For instance, cylinders oriented through the plane of the film are targeted for porous membranes and filters.[6] Similar orientation is necessary in order for cylinders to effectively serve as templates for aligned nanowires.[13,14] By changing the cylinder dimensions, including diameter and length, in membranes for drug delivery, the rate transport of species through a membrane and membrane selective via size-exclusion can be controlled.[5,8,15] Similarly, changes in domain dimensions have been found to improve conductivity of fuel cell membranes prepared from block copolymers.[2] It is, therefore, advantageous to understand how microstructure dimensions and orientation evolve during the preparation of block copolymer films.

While several methods, such as shear alignment,[16−18] electric fields,[19] and graphoepitaxy,[11,12,20] have been demonstrated to successfully control microstructure dimensions and orientation in block copolymer films, the work presented here focuses on the effect of solvent evaporation rate and temperature. Both temperature and drying rate have been shown to dictate the orientation of resultant thin film microstructures. For instance, Kim and Libera[21] were able to switch the orientation of polystyrene cylinders in a poly(styrene-*b*-butadiene-*b*-styrene) film from perpendicular to in-plane by decreasing the drying rate. Liang et al.[22] showed that changing the drying temperature was also effective for manipulating lamella orientation in solution-cast block copolymer films. The current work explores the evolution of hexagonally packed cylinders in a block copolymer film as solvent is continually extracted.

In a separate paper,[23] a set of *in situ* small-angle X-ray scattering experiments that allowed ordering of a poly(styrene-*b*-butadiene) block copolymer in the presence of solvent to be monitored in real time as solvent was extracted from a solvent-cast film were reported. The ability to quantitatively monitor structure development via changes in the scattering profile with concentration and time was demonstrated. The kinetics of the ordering process were reported in terms of the instantaneous

Received: December 5, 2011
Revised: March 18, 2012
Published: April 4, 2012

ACS Publications © 2012 American Chemical Society

ordering rates at several concentrations along the drying path starting at 20 wt % polymer.

In addition to providing information about the extent of ordering in the film, the *in situ* SAXS experiments were also capable of exposing details regarding the ordered domain dimensions and microstructure orientation as the film contracts during solvent removal. Specifically, as solvent is removed, changes in the structure spacing in the vertical film direction were observed. This paper presents experimental results from real-time tracking of the dimensions and orientation of ordered structures during the removal of solvent from a solution-cast block copolymer film consisting of a model poly(styrene-*b*-butadiene) copolymer. Details regarding the analysis of the scattering profiles to extract information about the horizontal and vertical structure spacing will be described. Based on this analysis, the effect of solvent removal temperature on the compression and resulting spacing of ordered microstructures during extraction of solvent from a block copolymer film is presented. Finally, the effect of drying rate on domain compression is discussed. The information presented is part of a larger effort to quantitatively analyze phase separation in block copolymer films during solvent removal.

2. EXPERIMENTAL SECTION

A poly(styrene-*b*-butadiene) block copolymer in a neutral solvent, toluene, was used as a model system to complete this work. All materials were purchased from Sigma-Aldrich. Details regarding the block copolymer composition are available in a separate paper.[23] Toluene is a good solvent for both blocks at all temperatures used in this work (30−60 °C). Calculated interaction parameters between the solvent and the blocks show negligible changes over this temperature range. As such, changes in the neutrality of solvent as the solvent removal temperature changes should not strongly influence the structure development. Experimental procedures are also described in a separate paper[23] and will not be reproduced here.

3. RESULTS AND DISCUSSION

3.1. Peak Splitting. This section describes the analysis of the scattering patterns to obtain information regarding spacing of ordered structures in the vertical and horizontal film directions. Data collected at two concentrations during the removal of solvent at 40 °C will be used for illustrative purposes to facilitate the discussion. Details regarding the cause of the behavior will be discussed in later sections of the paper.

The scattering patterns produced by an SB copolymer film at 45 and 72 wt % polymer during the extraction of toluene at 40 °C are shown in Figures 1a and 1b, respectively. The radial position from the center of the pattern corresponds to different wave vectors, q. The wave vector of the innermost ring, q^*, can be used to determine the separation of microstructures, D, in a manner akin to the Bragg spacing of crystal planes, as shown in eq 1:

$$D = \frac{2\pi}{q^*} \tag{1}$$

The angular position, θ, along the ring relates to orientation in the film. The angle is taken to increase clockwise from zero at the abscissa of the left quadrants. The radial position of the ring at $\theta = 0°$ provides information regarding the horizontal spacing, while the position of the ring at $\theta = 90°$ gives the vertical spacing. Thus, the pattern at 45 wt %, which is a nearly perfect circle, indicates that the ordered domains in the film at this concentration are randomly oriented and the spacing in both the horizontal and vertical film directions are identical. At the elevated concentration (72 wt %) the scattering pattern now forms an ellipse with the major axis along the vertical direction. Based on this pattern, the wave vector of the primary peak in the vertical film direction is higher than the wave vector of the primary peak in the horizontal direction. As such, the spacing in the vertical direction is smaller than the horizontal spacing.

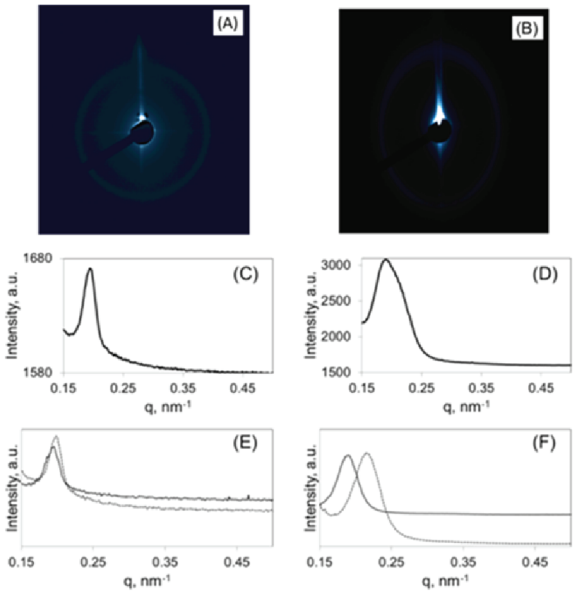


Figure 1. Scattering data from SB copolymer film cast from a 20 wt % solution in toluene dried at 40 °C. Scattering rings collected at 45 and 72 wt % polymer are shown in (A) and (B), respectively. (C) and (D) show the integrated scattering profiles based on (A) and (B), respectively. The peaks in (C) and (D) are decomposed into the vertical and horizontal film primary peaks in (E) and (F), respectively.

The scattering profiles resulting from integrating around the scattering patterns in Figures 1a and 1b are shown in Figures 1c and 1d, respectively. The primary peak obtained from the nearly perfect circle at 45 wt % polymer is sharper than the primary peak based on the ellipse at 72 wt % polymer. The sharp peak is due to the consistency of spacing at all angular positions in Figure 1a. The broad peak in Figure 1d represents the distribution of structure spacing due to the ellipse in Figure 1b. As such, the peak in Figure 1d can be considered to be comprised of multiple primary peaks corresponding to the horizontal and vertical film directions.

In order to determine the horizontal and vertical structure spacings, the peaks in Figures 1c and 1d are decomposed into their constitutive primary peaks by integrating the scattering pattern over incremental angular positions. The results are shown in Figures 1e and 1f. The solid line is the primary peak based on integrating from $\theta = 5°$ to $15°$. This represents the structure spacing in the horizontal film direction. The primary peak shown by the dashed line is determined by integrating from $\theta = 75°$ to $85°$. This peak indicates the structure spacing of microstructures in the vertical film direction. By decomposing the scattering patterns obtained at several concentrations during the removal of solvent from the SB/toluene film, the compression of the ordered domain can be quantitatively analyzed by comparing the vertical and horizontal structure spacings.

dx.doi.org/10.1021/ma2026435 | *Macromolecules* 2012, 45, 3480−3486

3.2. Effect of Solvent Removal Temperature on Structure Spacing. Details regarding the solvent removal rate and phase behavior of the SB copolymer in toluene during solvent extraction can be found elsewhere.[23] At all three solvent removal temperatures (30, 40, and 60 °C), the SB copolymer begins to form hexagonally packed cylinders in toluene between 25 and 30 wt % polymer. Further, the solvent removal rate increased as temperature increased, while the final attainable concentration decreased, which is believed to be due to skin formation at the film surface.[23]

The horizontal (filled symbols) and vertical (open symbols) structure spacing obtained during the extraction of toluene from the SB film at three different temperatures are shown in Figures 2a−2c. Before proceeding with the discussion, it will be useful to define terminology to be used in the subsequent discussion. *Deswelling* refers to shrinkage of the individual ordered domains due to the diffusion of solvent from these ordered domains as the film dries. *Compression*, on the other hand, arises from changes in the film thickness as solvent is extracted from the film. As the film thickness decreases, both individual microstructures and ordered domains are physically pressed closer to one another in the vertical direction as the film surface advances down. Based on these definitions, deswelling will occur in both the horizontal and vertical film direction. Alternatively, assuming the film is pinned in the horizontal direction, compression will affect only the vertical structure spacing. The effects of these two phenomenon will be considered individually. Because the bottom surface of the film is believed to be pinned, which makes the horizontal film structure spacing insensitive to compression, changes in the horizontal structure spacing during solvent extraction will be used to study the effect of deswelling on the structure spacing.

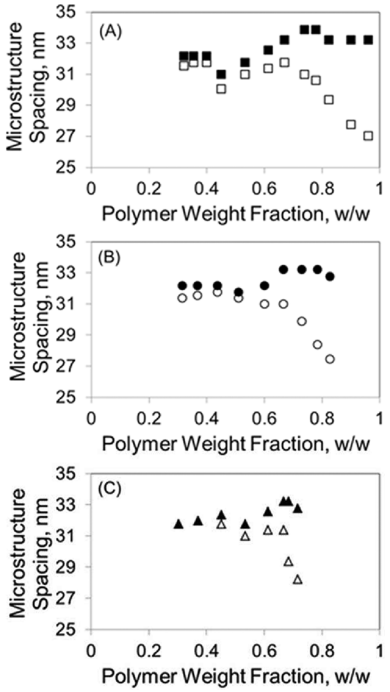


Figure 2. Microstructure spacing in horizontal (closed symbols) and vertical (open symbols) film directions of an SB film cast from a 20 wt % (initial concentration) toluene solution as a function of polymer concentration during solvent removal at 30 (A), 40 (B), and 60 °C (C).

Differences in the vertical and horizontal structure spacing will then be used to study compression during solvent removal.

The structure spacing at all three temperatures is initially the same (~32 nm). It has been shown that in a neutral solvent increasing the temperature can decrease the structure spacing.[24] This result is not confirmed here, but the severity of the temperature dependence of the structure spacing is variable among different molecular weights and polymer compositions. Thus, for the particular copolymer used in this work, the temperature range studied may not be large enough to yield significant differences in the structure spacing. Further, the samples were not given time to equilibrate as solvent is constantly being removed, which may also contribute to the lack of temperature-dependent structure spacing.

The structure spacing changes with polymer concentration, increasing up to a critical concentration, C_{Crit}, and then decreasing. C_{Crit} is typically between 70 and 80 wt % polymer. The increase in the structure spacing is about 2 nm. The trends are observed in both the vertical and horizontal direction and are, therefore, believed to be due to changes in solvent content in the ordered domains. Shibayama et al.[25] observed a similar trend while tracking the structure spacing of poly(styrene-*b*-isoprene) in toluene. The authors note that the increase in structure spacing is observed even as deswelling occurs, as is observed in this work. The authors attribute the increasing structure spacing to increased segregation power between the blocks as the polymer concentration increases. Above C_{Crit}, it was proposed that the reduction in structure spacing is due to deswelling of the domains and slow chain relaxation. The arguments put forth by Shibayama et al.[25] are pertinent to the data presented here and justify the trends in Figures 2a−2c.

The vertical and horizontal structure spacings are initially in agreement at all three temperatures. Thus, the microstructures are oriented randomly with the same structure spacing in all directions. At a certain concentration, ϕ^*, the vertical and horizontal structure spacings deviate from one another. ϕ^* is around 60 wt % at all temperatures, though it is difficult to distinguish the exact value from the data in Figure 2.

Following ϕ^*, the horizontal structure spacing increases more rapidly than the vertical structure spacing prior to C_{Crit}, while after C_{Crit} is reached, the vertical structure spacing decreases more drastically than the horizontal structure spacing. It is speculated that both effects are the consequence of compression the domains in the vertical direction as the film thickness decreases. Below C_{Crit}, the continual compression of the domains in the vertical direction diminishes the effect of the increase in segregation power as concentration increases. Above C_{Crit}, the compression of the domains in the vertical direction exacerbates the effect of deswelling as solvent exits the domains.

The severity of the compression during solvent extraction is quantified by the percent difference between the horizontal and vertical structure spacings, σ. Figure 3 shows σ as a function of concentration at the three temperatures presented above. Around 50 wt % polymer, σ begins to increase at all three temperatures, indicating disparities between the horizontal and vertical structure spacings. Between 65 and 70 wt % polymer, discrepancies in the rate of increase of σ with concentration at the three temperatures are observed. The rate of increase of σ with concentration increases with temperature, and at a given concentration above 65 wt % polymer, σ is most severe at the highest solvent removal temperature.

The following discussion presents a proposed explanation for the trends observed in Figure 3. For the purposes of this

dx.doi.org/10.1021/ma2026435 | *Macromolecules* 2012, 45, 3480−3486

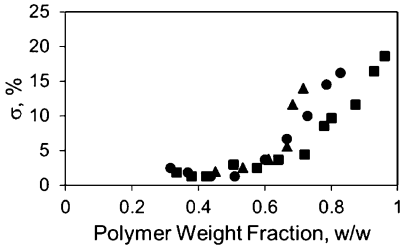


Figure 3. Percent difference (σ) in the horizontal and vertical microstructure spacings of an SB film cast from a 20 wt % toluene solution as a function of polymer concentration during solvent removal at 30 (■), 40 (●), and 60 °C (▲).

discussion, it is assumed that the solvent partitions equally between the ordered and disordered phases in the film, which is reasonable given that the solvent, toluene, is neutral for the SB copolymer. It is recognized that under the conditions that the solvent preferentially swells one of the blocks, these arguments may be invalid. As such, the subsequent section is not proposed as a generalization that can be extended to selective solvents.

The value of σ is believed to be strongly dependent on the relaxation time of the polymer relative to the rate of compression of the film at a given concentration. As the film is compressed, the polymer chains attempt to repack such that the equilibrium spacing is attained once more. The rate at which the repacking process occurs depends on chain mobility and relaxation times. The presence of solvent facilitates this relaxation process. Enough residual solvent remains in the film at low concentrations, in this case below 50 wt % polymer, to make the relaxation process quicker than rate of compression of the domains, as dictated by the rate of decrease of the film thickness. Above 50 wt % polymer, the lack of solvent leads to a loss of chain mobility, slowing the relaxation process. Therefore, when the domains are compressed and the equilibrium spacing is lost, the films do not have enough time to reorder as the film thickness decreases.

The differences in the rate at which σ increases with increasing concentration data among the different temperatures are due to differences in solvent removal rates, which results in different film compression rates. Because the solvent removal rate increases with temperature, the time between compressions and, therefore, the time to relax back to the equilibrium spacing decrease as temperature increases. Though the relaxation time should increase with temperature, this effect appears to be insignificant relative to the differences in the film compression rates. As a result, the film dried at 60 °C displays the most severe compression of the ordered domains in the vertical direction for a given concentration, followed by the film prepared at 40 °C.

3.3. Effect of Drying Rate on Structure Spacing. Solvent was removed at 30 and 40 °C at two different rates per temperature by removing solvent in the presence and absence of a sweep gas. Based on the drying curves provided in an earlier paper,[23] the presence of a sweep gas slows the solvent removal rate at both temperatures. The slower solvent removal is believed to be due to the rapid formation of a skin at the surface of the film resulting from the presence of a sweep gas.[23,26,27] Thus, the presence of a sweep gas affords the opportunity to study domain compression as a function of solvent removal rate.

The horizontal and vertical structure spacings as a function of concentration in films dried in the presence of sweep gas at 30 and 40 °C are shown in Figures 4a and 4b, respectively. Comparing the data in Figure 4 to the corresponding data

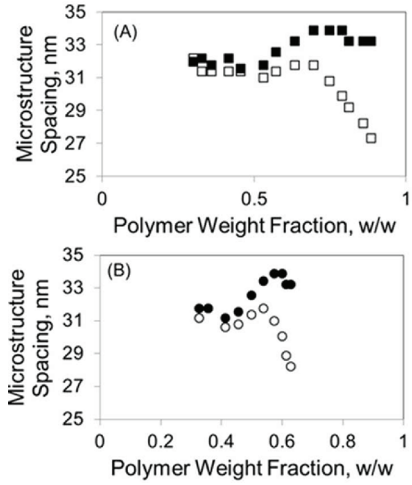


Figure 4. Microstructure spacings in horizontal (closed symbols) and vertical (open symbols) film directions of an SB film cast from a 20 wt % toluene solution as a function of polymer concentration during solvent removal with a sweep gas at 30 (A) and 40 °C (B).

without a sweep gas in Figure 2, it does not appear that changing the drying rate changes the structure spacing at low concentrations. Further, a similar trend in the structure spacing with concentration is seen when a sweep gas is present. However, the presence of a sweep gas shifts C_{Crit} to a lower concentration. C_{Crit} in Figure 4 is now closer to 60 wt % polymer than 70 wt % polymer. It is postulated that the lower C_{Crit} value observed when removing solvent with a sweep gas is due to the development of the skin layer near the film surface. Assuming that a steep concentration gradient exists due to skin formation, the solvent content near the film surface is much lower than in the bulk film. Kinetic trapping of the polymer chains near the surface occurs at a lower average polymer concentration, lowering C_{Crit}.

The domain compression is again analyzed by considering σ as a function of polymer concentration. In Figures 5a and 5b the σ values during the removal of solvent with and without a sweep gas at 30 and 40 °C, respectively, are compared. At both temperatures, the presence of a sweep gas intensifies the domain compression. The effect at 40 °C is substantially more pronounced than at 30 °C. For instance, the maximum difference in the σ values between the samples dried at 30 °C is 5.5% at a polymer concentration of 88 wt %. At 40 °C, the maximum difference in σ values is ~10% at 63 wt % polymer.

The concentration dependence of σ observed using a sweep gas is contradictory to the expected behavior based on the arguments proposed in section 3.2. In section 3.2, rapid solvent removal was the likely cause of the increased domain compression at elevated temperatures. However, it is seen that the presence of a sweep gas yields more severe domain compression despite a slower solvent removal rate. The results observed in Figure 4 are believed to be a consequence of the formation of the skin layer and steep concentration gradients, which are interfering with the effect of the change in the solvent removal rate. As previously discussed, the formation of a skin layer kinetically traps the SB copolymer chains in the region near the film surface. Thus, while the rate of change of the average concentration is slower when a sweep gas is used, the

dx.doi.org/10.1021/ma2026435 | Macromolecules 2012, 45, 3480−3486

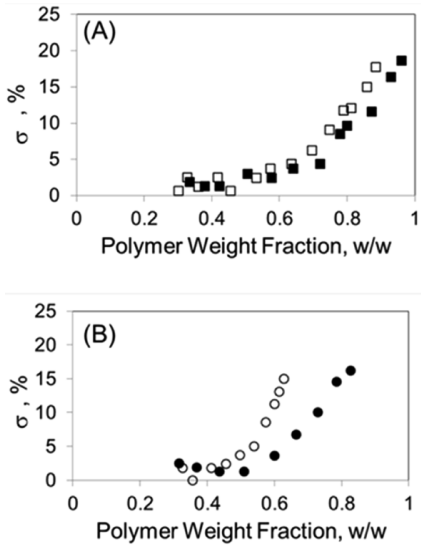


Figure 5. Percent difference (σ) in the horizontal and vertical microstructure spacings of an SB film cast from a toluene solution with an initial concentration of 20 wt % as a function of polymer concentration during solvent removal without a sweep has (closed symbols) and with a sweep gas (open symbols) at 30 (A) and 40 °C (B).

solvent extraction near the surface is rapid and domain compression near the surface is high.

It was desired to examine the effect of drying rate on domain compression without the development of a skin layer interfering with the results. In order to achieve this, an additional solvent removal condition was implemented at 30 °C. A reservoir of the solvent, toluene, was placed in the chamber beneath the sample, effectively saturating the chamber in which the film is dried. The drying curves during the removal of solvent at room temperature under three different conditions are shown in Figure 6. The open and filled squares correspond

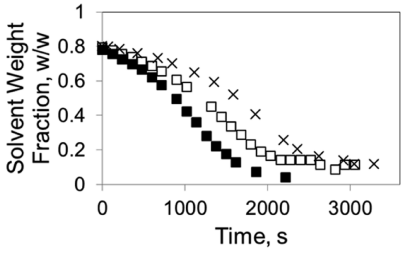


Figure 6. Drying curves during the removal of solvent from an SB film cast from a 20 wt % solution at 30 °C without a sweep gas (■), with a sweep gas (□), and in the presence of excess solvent (×).

to the removal of solvent with and without a sweep gas previously discussed. The curve denoted with the cross-marks represents solvent removal when the chamber was saturated. Saturating the sample chamber decreases the drying rate. It is speculated that under the slow solvent evaporation the formation of a skin at the film surface is avoided, thereby making the only substantial difference between the film dried without a sweep gas and the film dried in the presence of solvent the solvent removal rate. It was noted that when excess solvent was present, reflection off the film surface in the scattering pattern, which was taken to be indicative of skinning, was not present.

The concentration dependence of the horizontal and vertical structure spacings of a film dried in the presence of solvent is shown in Figure 7. The horizontal structure spacing again

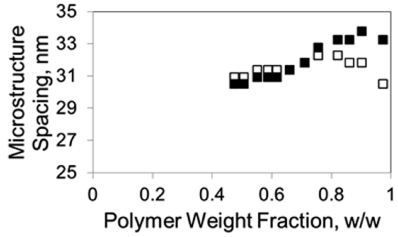


Figure 7. Microstructure spacings in horizontal (■) and vertical (□) film directions of an SB film cast from a 20 wt % toluene solution as a function of polymer concentration during solvent removal in the presence of excess solvent at 30 °C.

shows the expected trend with concentration. However, C_{Crit} is now at a substantially higher concentration than in all previous experiments. The continual presence of solvent at the film surface may be limiting the formation of concentration gradients and imparting appreciable mobility to the polymer in the film, thus allowing resistance to kinetic trapping. This mitigates the effect of deswelling until a higher concentration is reached. It is also seen in Figure 7 that ϕ^* is at a higher concentration (>70 wt %) than observed in any other sample. As such, the microstructures can resist a net decrease in structure spacing due to compression at higher concentrations than achievable under the previously discussed solvent removal conditions.

The σ versus concentration curves for the three films dried at 30 °C are shown in Figure 8. As discussed in the preceding

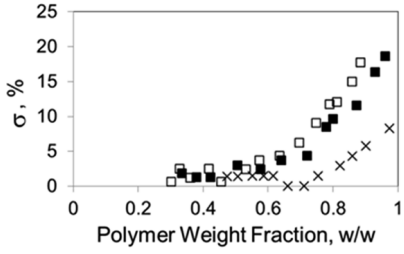


Figure 8. Percent difference (σ) in the horizontal and verical microstructure spacings of an SB film cast from a 20 wt % toluene solution as a function of polymer concentration during solvent removal at 30 °C without a sweep gas (■), with a sweep gas (□), and in the presence of excess solvent (×).

paragraph, the presence of solvent is delaying ϕ^*. Therefore, while the σ of the two films dried in the absence of solvent begin to increase at approximately the same polymer concentration (60 wt %), the film dried in the presence of solvent does not show appreciable σ values until 70 wt %. Above 70 wt % polymer, σ of the film dried in the presence of solvent is lower than the σ values of the films dried without a solvent reservoir.

In order to ensure that the lower σ value at a given concentration obtained by removing solvent in a saturated chamber is not simply an artifact of the delayed onset of residual compression, the rates of change of σ with respect to concentration under the three solvent removal conditions are compared in Figure 9. At all concentrations, the rate of compression with concentration is lowest when a solvent is

dx.doi.org/10.1021/ma2026435 | Macromolecules 2012, 45, 3480−3486

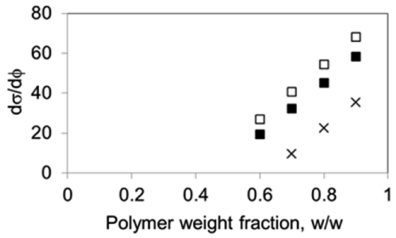


Figure 9. Rate of change of σ with respect to polymer concentration, ϕ, during the removal of solvent from an SB film cast from a 20 wt % solution in toluene at 30 °C without a sweep gas (■), with sweep gas (□), and in the presence of excess solvent (×).

present. The difference between the film dried in the presence of solvent and the film dried with a sweep gas in an unsaturated chamber ranges from 350% at 70 wt % polymer to 160% at 90 wt % polymer. This illustrates that the discrepancy in σ observed in Figure 8 is not just a result of the delayed onset of peak splitting, and the slower drying rate reduces the effect of film shrinkage on structure spacing. These results also support the arguments made in section 3.2 that the net domain compression is a function of the relaxation time of the polymer chains relative to the rate of domain compression, which is controlled by the solvent removal rate. Thus, when the solvent removal is slowed by saturating the chamber with solvent, the ratio of relaxation time to domain compression rate decreases and chains are given longer times to relax. It is also noted, however, that the presence of solvent at the film/air interface may be assisting the relaxation process during the extraction of solvent.

4. CONCLUSIONS

In situ small-angle X-ray scattering measurements as solvent was removed under various conditions from a poly(styrene-*b*-butadiene) copolymer film revealed information regarding changes in the microstructure spacing as a function of solvent concentration in real time. The structure spacing was found to follow a similar trend with respect to concentration as has previously been reported for block copolymers in a neutral solvent.[25] Increasing the polymer concentration in the film initially led to increased segregation of the blocks and larger structure spacing. Above a critical concentration, the polymers were kinetically trapped and the structure spacing decreased as the domains deswelled due to the loss of solvent.

In addition to deswelling effects, it was observed that the vertical spacing of the microstructure decreased due to compression of the ordered domains as the film thickness decreased during solvent extraction. At low concentrations, the polymer chains were able to relax back to their equilibrium spacing between subsequent compressions of the domains, and the structure spacing in the vertical direction was essentially unaffected. At a certain concentration, the rate of domain compression was too rapid for the chains to relax as the film thickness decreased. As such, the structure spacing in the vertical direction continually decreased with concentration.

The compression of the domains was found to increase as the solvent removal temperature increases. It was determined that over the temperature range utilized in this work the severity of domain compression was primarily governed by the rate of solvent removal, which dictates the rate of domain compression. Thus, while increasing the temperature will reduce the relaxation time, this was not sufficient to overcome the increased rate of compression upon faster solvent removal. In spite of this finding, decreasing the solvent removal rate at a given temperature by introducing a sweep gas resulted in an increase in the domain compression. This was ultimately attributed to the formation of the skin at the film surface, which masked the effect of solvent removal rate. This limitation was overcome by drying a film in the presence of excess solvent to slow the solvent removal rate without forming a skin. The reduced solvent removal rate delayed the onset of peak splitting and reduced the rate of domain compression with concentration.

■ AUTHOR INFORMATION

Notes

The authors declare no competing financial interest.

■ ACKNOWLEDGMENTS

Funding for this work was provided by the Institute for Critical Technology and Applied Science at Virginia Tech. The authors acknowledge Eastman Chemical Company for providing funding through the Eastman Fellowship in Polymer Science. Portions of this research were carried out at the Stanford Synchrotron Radiation Laboratory, a national user facility operated by Stanford University on behalf of the U.S. Department of Energy, Office of Basic Energy Sciences. The SSRL Structural Molecular Biology Program is supported by the Department of Energy, Office of Biological and Environmental Research, and by the National Institutes of Health, National Center for Research Resources, Biomedical Technology Program, and the National Institute of General Medical Sciences.

■ REFERENCES

(1) Meuler, A. J.; Hillmyer, M. A.; Bates, F. S. *Macromolecules* **2009**, *42*, 7221.
(2) Lee, M.; Park, J. K.; Lee, H. S.; Lane, O.; Moore, R. B.; McGrath, J. E.; Baird, D. G. *Polymer* **2009**, *50*, 6129.
(3) Pai, R. A.; Humayun, R.; Schulberg, M. T.; Sengupta, A.; Sun, J. N.; Watkins, J. J. *Science* **2004**, *303*, 507.
(4) Kang, M.; Moon, B. *Macromolecules* **2009**, *42*, 455.
(5) Nuxoll, E. E.; Hillmyer, M. A.; Wang, R. F.; Leighton, C.; Siegel, R. A. *ACS Appl. Mater. Interfaces* **2009**, *1*, 888.
(6) Jackson, E. A.; Hillmyer, M. A. *ACS Nano* **2010**, *4*, 3548.
(7) Phillip, W. A.; O'Neill, B.; Rodwogin, M.; Hillmyer, M. A.; Cussler, E. L. *ACS Appl. Mater. Interfaces* **2010**, *2*, 847.
(8) Uehara, H.; Kakiage, M.; Sekiya, M.; Sakuma, D.; Yamonobe, T.; Takano, N.; Barraud, A.; Meurville, E.; Ryser, P. *ACS Nano* **2009**, *3*, 924.
(9) Bockstaller, M.; Kolb, R.; Thomas, E. L. *Adv. Mater.* **2001**, *13*, 1783.
(10) Wirnsberger, G.; Scott, B. J.; Stucky, G. D. *Chem. Commun.* **2001**, *01*, 119.
(11) Segalman, R. A. *Science* **2008**, *321*, 919.
(12) Bita, I.; Yang, J. K. W.; Jung, Y. S.; Ross, C. A.; Thomas, E. L.; Berggren, K. K. *Science* **2008**, *321*, 939.
(13) Zhang, Z. T.; Dai, S.; Blom, D. A.; Shen, J. *Chem. Mater.* **2002**, *14*, 965.
(14) Jung, Y. S.; Jung, W.; Tuller, H. L.; Ross, C. A. *Nano Lett.* **2008**, *8*, 3776.
(15) Yang, S. Y.; Yang, J. A.; Kim, E. S.; Jeon, G.; Oh, E. J.; Choi, K. Y.; Hahn, S. K.; Kim, J. K. *ACS Nano* **2010**, *4*, 3817.
(16) Jain, A.; Hall, L. M.; Garcia, C. B. W.; Gruner, S. M.; Wiesner, U. *Macromolecues* **2005**, *38*, 10095.
(17) Marcencic, A. P.; Adamson, D. H.; Chaikin, P. M.; Register, R. A. *Phys. Rev. E* **2010**, *81*, 011503.

(18) Wu, L.; Lodge, T. P.; Bates, F. S. *J. Rheol.* **2005**, *49*, 1231.
(19) Olszowka, V.; Hund, M.; Kuntermann, V.; Scherdel, S.; Tsarkova, L.; Boker, A. *ACS Nano* **2009**, *3*, 11091.
(20) Xiao, S.; Yang, X. M.; Lee, K. Y.; ver der Veerdonk, R. J. M.; Kuo, D.; Russell, T. P. *Nanotechnology* **2011**, *22*, 305302.
(21) Kim, G.; Libera, M. *Macromolecules* **1998**, *31*, 2569.
(22) Liang, G. D.; Xu, J. T.; Fan, Z. Q. *J. Phys. Chem. B* **2007**, *111*, 11921.
(23) Heinzer, M. J.; Han, S.; Pople, J. A.; Baird, D. G.; Martin, S. M. *Macromolecules* **2011**, manuscript in submission.
(24) Shibayama, M.; Hashimoto, T.; Kawai, H. *Macromolecules* **1983**, *16*, 16.
(25) Shibayama, M.; Hashimoto, T.; Hasegawa, H.; Kawai, H. *Macromolecules* **1983**, *16*, 1427.
(26) Vinjamur, M.; Cairncross, R. A. *Drying Technol.* **2001**, *19*, 1591.
(27) Vinjamur, M.; Cairncross, R. A. *J. Appl. Polym. Sci.* **2001**, *83*, 2269.

Macromolecules

Article

pubs.acs.org/Macromolecules

Tracing a Moving Thin-Film Reaction Front with Nanometer Resolution

Anne Köhnen,[†,⊥] Martin Brücher,[‡,⊥] Anna Reckmann,[†] Heike Klesper,[†] Alex von Bohlen,[‡] Ralph Wagner,[§] Alexej Herdt,[§] Dirk Lützenkirchen-Hecht,[∥] Roland Hergenröder,*[,‡] and Klaus Meerholz*[,†]

[†]Institute of Physical Chemistry, University of Cologne, Luxemburgerstr. 116, 50939 Köln, Germany

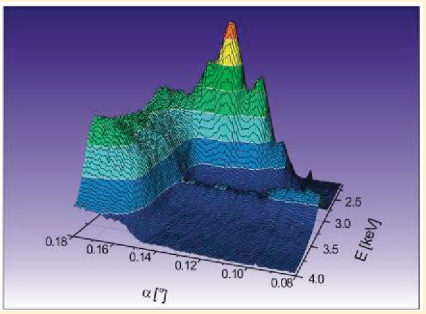
[‡]Leibniz-Institut für Analytische Wissenschaften - ISAS e.V., Bunsen-Kirchhoff-Str. 11, 44139 Dortmund, Germany

[§]DELTA, TU Dortmund, Maria-Goeppert-Mayer-Str. 2, 44227 Dortmund, Germany

[∥]Fachbereich C- Abteilung Physik, Bergische Universität Wuppertal, Gaußstraße 20, 42097 Wuppertal, Germany

Supporting Information

ABSTRACT: X-ray standing waves at grazing incidence are used to trace the position of the reactive chain ends of a surface-initiated (via protons in the underlying PEDOT:PSS layer) polymerization in a bulk polymer film, a procedure recently used to realize insoluble functional films for mutlilayer organic light-emitting diodes. The reactive chain ends as well as their respective counterions are found within a few nanometers thin layer, which moves away from the surface as the reaction proceeds. This reactive front remains narrow for polymerized films that are significantly thicker than the front width. This result can be rationalized by assuming that all oxetane units in contact with the PEDOT:PSS are initiated before the reaction proceeds at elevated temperature.



1. INTRODUCTION

Large-area printed electronics is a scientifically very interesting topic and an economically growing worldwide market, comprising devices such as organic light-emitting diodes (OLEDs),[1−3] organic solar cells (OSCs),[4,5] and organic field-effect transistors (OFETs).[6] One of the main challenges is to achieve large-area homogeneous coatings with nanometer-scale accuracy and low-cost thin-film deposition techniques such as printing.

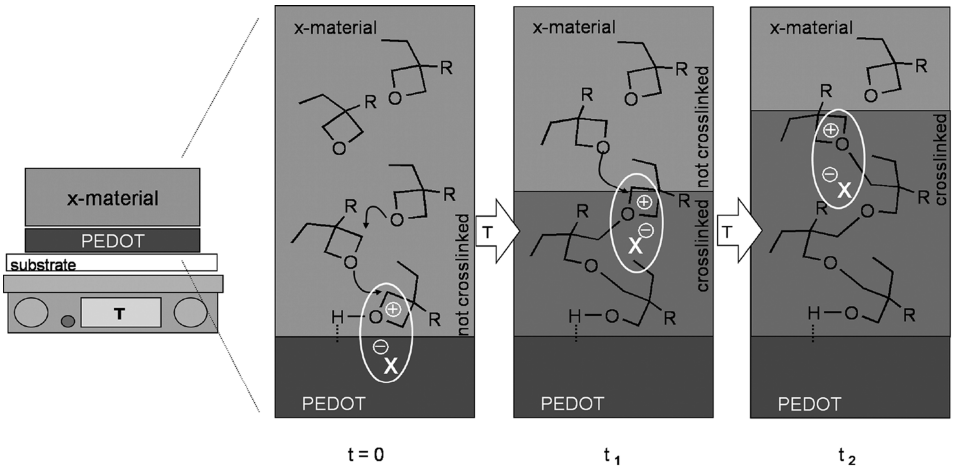
Recently, we demonstrated the so-called PEDOT:PSS (poly(3,4-ethylenedioxythiophene:polystyrenesulfonate))-initiated cross-linking method (PIX),[7] which has the potential to allow fabrication of nanometer-smooth thin films with even the crudest deposition techniques. PIX is a surface-initiated cross-linking method based on the cationic ring-opening polymerization (CROP) of oxetane-functionalized materials. The solid-state CROP reaction is commonly initiated by electrophiles (e.g., protons generated upon illumination of the material in the presence of a photoacid[8]), which is homogeneously dispersed at a small percentage into the cross-linkable precursor layer.

In the case of PIX, the electrophiles are protons provided by the underlying acidic PEDOT:PSS layer, which is commonly used as a hole-injection layer in OLEDs[9] or a hole-collecting contact in OSCs.[4] After initiation, cross-linking is promoted by thermal annealing. Elevated annealing temperatures and prolonged annealing times correspond to more cross-linked material (thicker cross-linked layers). A simple sketch of the PIX process and the chemical structure of the cross-linkable material are shown in Figure 1. PIX resembles the "grafting from" approach that is common in polymer brush sciences;[10−12] however, there are some important differences between the two methods: (1) In our case, since we commonly use materials with two or more oxetane units per molecule, PIX leads to the formation of three-dimensional polymer networks as opposed to one-dimensional polymer strands as in the case of polymer brushes, and (2) in the latter case, the reaction is carried out in solutions, whereas PIX is performed in solid thin films.

In our previous work, we assumed that for reasons of electroneutrality anions (X^- in Figure 1) move along with the reactive chain ends (= cations).[7] Because of its large size and thus negligible diffusional mobility, the polymeric counterion PSS^- was excluded as a candidate. However, it is known that small molecules are present in commercial PEDOT:PSS, where PSS is known to decompose into HSO_4^- and SO_4^{2-}, which are likely the species that migrate with the active chain ends of the cationic polymerization through the layer. Further verification of the proposed impact of these small decomposition products was gained from preclusion experiments, where dialysis-purified PEDOT:PSS samples (i.e., samples where mobile low-molecular-weight ions were removed) were unable to initiate the PIX reaction. However, until now, we were unable to directly prove the presence of the HSO_4^- and SO_4^{2-} counterions or even their distribution in the cross-linked film.

Received: January 27, 2012
Revised: April 4, 2012
Published: April 12, 2012

ACS Publications © 2012 American Chemical Society



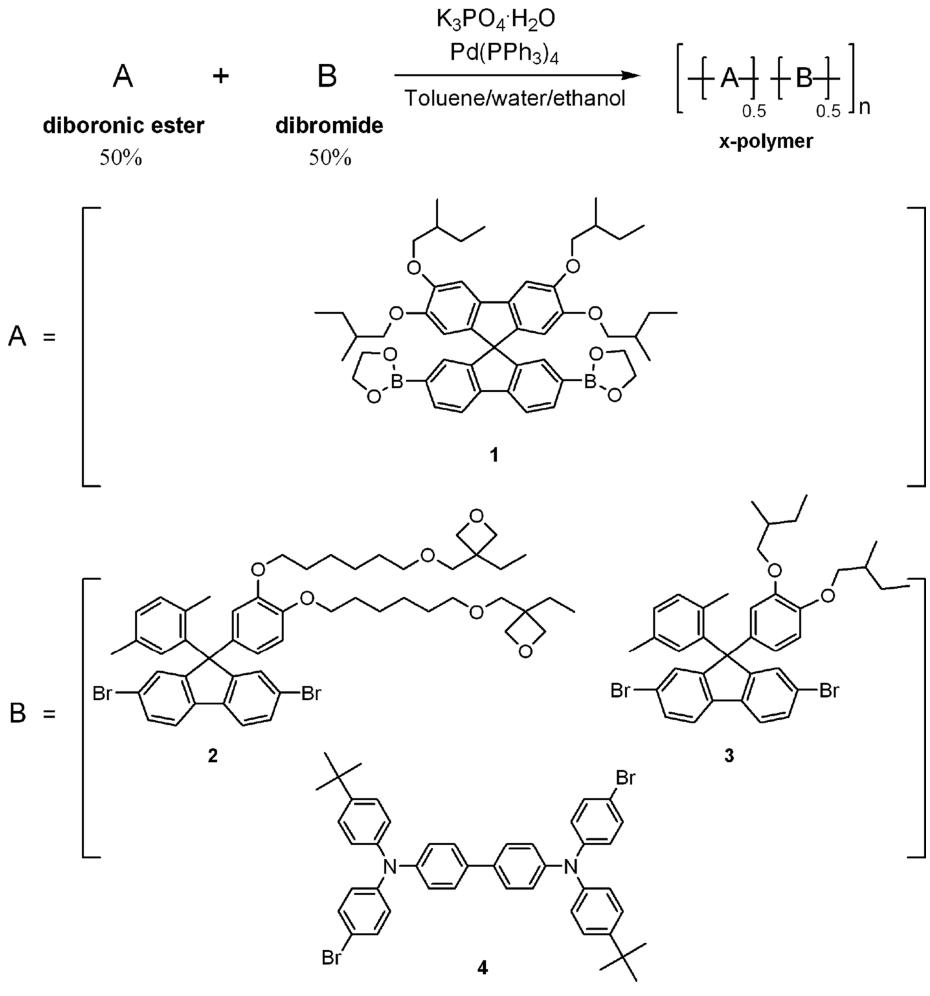


Figure 1. (top) Illustration of the PIX process: The proton that starts the CROP of the oxetane units originates from the surface of the acidic PEDOT:PSS layer. The reaction is promoted by thermal annealing and proceeds in a directional way away from the PEDOT:PSS interface. The counterion X^- (here: HSO_4^- or SO_4^{2-}) is shown in white writing. The cross-linked part of the film is marked in dark gray. (bottom) General scheme for synthesis of the cross-linkable material and chemical structure of the monomers **1**–**4**. The monomer feed ratio is 50 mol % for monomer **1**, 25 mol % for monomer **2**, 15 mol % for monomer **3**, and 10 mol % for monomer **4**.

This information would yield valuable insight into the location of the reactive chain ends to which the anions would be associated and ultimately into the mechanism of the solid-state CROP polymerization in general.

In the past, we found that the PIX process yields a surface topography of the coating that perfectly replicates the underling topography ("conformal" coating). We also indirectly demonstrated the presence of reactive chain ends at the surface of a washed film by initiating a second layer of another oxetane-containing material (layer-by-layer cross-linking; LBLX).[7] However, both facts do not allow drawing conclusions about the exact distribution of the reactive chain ends within the

dx.doi.org/10.1021/ma300204g | *Macromolecules* 2012, 45, 3487–3495

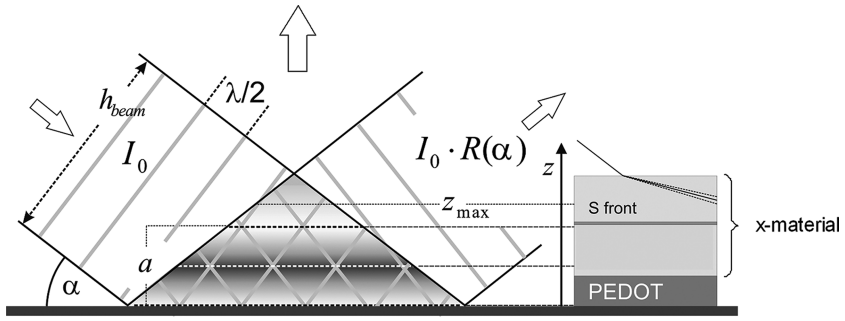


Figure 2. Principle of the XSW measurement of the sulfur distribution in the polymer layer: In the overlap of incoming (I_0) and reflected ($I_0 \cdot R$) radiation, interference of the two beams generates the X-ray standing waves field of period a. The X-ray fluorescence of the elements within the sample (here: sulfur as marker atom in a PEDOT:PSS/x-material stack) is excited by the maxima (antinodes) of the XSW field. The distribution profile of sulfur in both polymer layers is scanned by angular-resolved fluorescence measurements. The vertical measuring range of the method is limited to a value z_{max} due to the finite coherence length of incoming radiation.

Table 1. Parameters of Sample Preparation

sample	temp [°C]	cross-linking time [s]	front position [nm][d]	layer thickness [nm][e]	layer thickness [nm][f]	delta [nm][g]
A	**200**	**15**	**83 ± 3**	**102 ± 2**	**90 ± 3**	**7**
B1/B2	**200**	**60**	**102 ± 3**	**122/110 ± 2**	**109/106 ± 3**	**7/4**
C	**200**	**600**	**146 ± 5**	**142 ± 5**	**151 ± 5**	**5**
D	110	20	69 ± 3			
E	110	40	103 ± 3			
F	110	90	132 ± 3			
G	130	120	148 ± 5			
H	130	300	155 ± 5			
I[a]	130	90	19 ± 2			
R[b]	**200**	**15**	**85 ± 4**	**124 ± 2**	**124 ± 3**	**n.a.**
N1/N2[c]				**137/145 ± 2**	**144/144 ± 4**	**n.a.**

[a]For this sample a PEDOT layer with less initiator is used. [b]Reference sample, without removal of nonpolymerized material (not rinsed). [c]Reference sample, not cross-linked. [d]Height above Si surface. [e]PEDOT plus polymer, X-ray reflectivity measurement. [f]PEDOT plus polymer, evaluation of X-ray scattering. [g]Difference between front position and layer thickness by scattering. Boldface: series 1; lightface: series 2; see Table 2. The samples B and N were scanned twice; the respective measurement is indicated by a number (e.g., B1).

cross-linked film below/behind the reaction front. Because of the limited diffusional mobility of both the covalently attached reactive chain ends and the still non-cross-linked oxetane units above (in front) of the reaction front, it might be expected that some of the reactive chain ends may become "stuck" whenever oxetane units in the vicinity have been consumed previously and are no longer available for reaction. Such chain ends could still be chemically "alive" due to the formal absence of chemical termination steps; nevertheless, these dead ends have to be phenomenologically treated as "terminated" chains. In such case, the spatial distribution of the counterions in the cross-linked film could be expected to be relatively broad. This is in stark contrast to "grafting from" reactions, which are commonly done in solution, where monomers from an infinite reservoir (given concentration) diffuse toward the reactive ends.

In order to obtain information related to the presence of sulfur-containing anions associated with the reactive cationic chain ends in the cross-linking reaction, we took advantage of the X-ray fluorescence signal of the sulfur atoms that are distinct to the counterions. The method of choice was the analysis of the fluorescence excited by X-ray standing waves at grazing incidence (GI-XSW), a versatile tool to characterize multilayer thin films and elemental distributions on a nanometer scale.[13−17] The GI-XSW method relies on total external reflection of coherent X-ray radiation (see Methods Section for detailed method information), where interference of the incoming and reflected beam generates a stationary electromagnetic field that varies periodically normal to the surface (see Figure 2). In contrast to the X-ray standing waves at normal incidence (NI-XSW) technique,[18−21] GI-XSW does not require a periodic crystal structure. The fluorescence of the elements in the near-surface volume is excited by the antinodes of the standing waves, where atoms and ions overlapping with the interference field act as fluorescence markers. The measured fluorescence is the product of the local intensity $I(z)$ and the local marker concentration $C_i(z)$.

By gradually changing the angle of incidence α, the fringes of the periodic XSW field gradually move through the sample, vertically scanning the marker distribution. Thus, the sample characterization is restricted to the direction perpendicular to the surface (z-direction), which is especially suitable for layered samples.[15,16,22−24]

2. RESULTS AND DISCUSSION

PIX Samples. Samples A−I, R, and N were prepared and analyzed by XSW with different experimental parameters (see Table 1 and Experimental Section). The fluorescence and reflected/scattered beam intensity are measured, where the former provides information about the position and concentration of the marker atom and the latter two give information about the entire sample thickness.

Silicon wafers with a native oxide layer were coated via spin-coating with PEDOT:PSS (10−15 nm) followed by ca. 110−140 nm of a polyspirofluorene copolymer (x-material; for the

dx.doi.org/10.1021/ma300204g | Macromolecules 2012, 45, 3487−3495

chemical structure see Figure 1) containing 25 mol % of an oxetane functionalized unit. The films were then heat-treated at varying temperatures (100−200 °C) and heating times (15−600 s) to control the degree of the CROP reaction and, thus, the cross-linked film thickness (see Table 1). After cross-linking, the non-cross-linked material was removed with excess solvent (THF; except in the case of sample R and the noncross-linked sample, N).

An overview of the different samples A−I, R, and N and their different XSW and PIX parameters are given in Tables 1 and 2,

Table 2. Experimental Parameters of the XSW Measurements

samples	series 1	series 2
energy [keV]	**10**	15
detector	**XR-100CR (Si-PIN)**	XR-100SDD (Si-drift)
energy resolution [eV]	**150**	125
channels/spectrum	**2048**	2048
angular step width $\Delta\alpha$ [deg]	**0.001**	0.0005

respectively. For reference purposes, two samples were scanned twice (B1/B2 and N1/N2). The fluorescence, scattering, and reflectivity data of sample B will be discussed exemplary in the following, but the complete set of fluorescence and reflectivity data is given in the Supporting Information (Figures SI_1−SI_3).

Fluorescence Data. For data evaluation, the fluorescence signal of an assumed (plausible) marker distribution $C(z)$ is simulated. The integration of the product of the XSW field intensity and the assumed marker distribution (eq 2 in Methods Section) gives the expected fluorescence signal, which is then compared to the experimental data. Good correlation between the simulated and measured fluorescence spectra implies that the assumed marker distribution is indeed close to reality. Please note that only the range $0.12 < \alpha < 0.17$ contains information about the S distribution. The rise of Si fluorescence of the substrate at $\alpha = 0.17°$ (plotted as crosses in all XSW scans; normalized to the maximum of S count rate) marks the critical angle α_c^{Si} of the polymer/Si interface, above which meaningful interpretation of the data is no longer possible.

Figure 3c shows the X-ray fluorescence scan for the sample that was not thermally annealed (sample N) and was, therefore, not cross-linked at all. The sulfur fluorescence emerges at $\alpha = 0.12°$, the critical angle of the polymer layers, and features a rise of intensity up to a maximum near $\alpha = 0.17°$. The rising of fluorescence intensity occurs due to the overlap of the lowermost antinode of the XSW field with the PEDOT:PSS layer (S in thiophene as well as in sulfonic acid). Since the used polymer does not contain sulfur, the best fit of this measurement only assumes the presence of sulfur in the PEDOT:PSS layer near the silicon surface with slightly descending signal strength (10−15 nm; Figure 3b). There is good agreement between experiment and model calculation (Figure 3c).

Figure 3a shows a typical fluorescence scan for a sample that was annealed at 200 °C for 60 s (sample B1). In this example, the unstructured fluorescence signal observed with sample N is now superimposed by an oscillation generated by the successional passing of XSW maxima through a sulfur-containing layer (S due to counterions accompanying the CROP reaction front). From the oscillation period of the sulfur signal, the z-position (center of the z-distribution) of the sulfur layer is determined to be 102 nm above the Si surface. The corresponding best-fitting sulfur distribution model is shown in Figure 3b. For the additional sulfur-containing layer, a rectangular sulfur distribution with a width of 1 nm was assumed in the model. Assumption of a Gaussian distribution did not lead to a better fit quality. For the remainder of the paper we used the rectangular distribution.

Figure 3d summarizes the sulfur profiles assumed in the respective simulations of all samples. In all cases, the assumed PEDOT layer thickness of ca. 10 nm agrees with the experimental value (profilometer) within its limits of error. Since the amount of sulfur in the PEDOT:PSS was constant, the data were normalized to the PEDOT:PSS signal. For all samples A−I, the additional narrow rectangular sulfur distribution was assumed in the model. As expected, the z-position of this distribution increases with curing time (for example: A through C in series 1). It should also be noted that all data fit onto the same line, independently of the experimental series, pointing out the good reproducibility of the experiments.

In order to prove that the sulfur layer did not result from the rinsing procedure and was present even before, we compare sample A with the nonwashed sample R, which were both cured under identical conditions (T = 200 °C, t = 15 s; see Figure 4). Indeed, both samples feature the identical angular positions of the fluorescence despite the different thickness of the respective samples (Figure 4) and, thus, contain an identical reaction front position as expected. As in both samples the angular positions of fluorescence maxima the occurrence of resonance effects[25−28] causing the oszillaton can be excluded.

Position and Thickness of the Front. We estimated the accuracy in the absolute z-position to ±3 nm, since the assumption of a different lateral position in the distribution model considerably reduces fit quality (Figure 5, left). Also, an estimation of the lateral extension of the front can be concluded from XSW simulation. We estimate the thickness of the front d_f < 9 nm, as the assumption of a broader S distribution representing the front considerably reduces fit quality. Using 1−9 nm, no distinct difference is observed (Figure 5, right).

***z*-Measurement Range.** Considering the normalized concentration profiles shown in Figure 3d, it is observed that the sulfur concentration contained in the layer associated with the front of reactive chain ends decreases linearly with increasing distance from the substrate, i.e., as the migration of the reaction front proceeds further from the PEDOT:PSS interface.

One seemingly possible explanation for this result would be that the number of reactive chain ends in the front (and counterions associated with them) decreases during the proceeding polymerization because they found no reaction partner. In this case, linear regression of our data would predict that polymerization beyond 180 nm would be impossible; however, experimentally we were able to cross-link >250 nm thick films without indication that this constitutes a limit.[7] Furthermore, the difference in sulfur signal intensity between the samples H and I would indicate that 83.3% of reactive chain ends (and associated sulfur-containing ions) would have been "lost" during polymerization. At such high relative concentration of "lost ions" one would have to assume additional sulfur in between the PEDOT layer and the front within the model, which dramatically reduces the fit quality. Therefore, a loss of reactive chain ends can be excluded as an explanation.

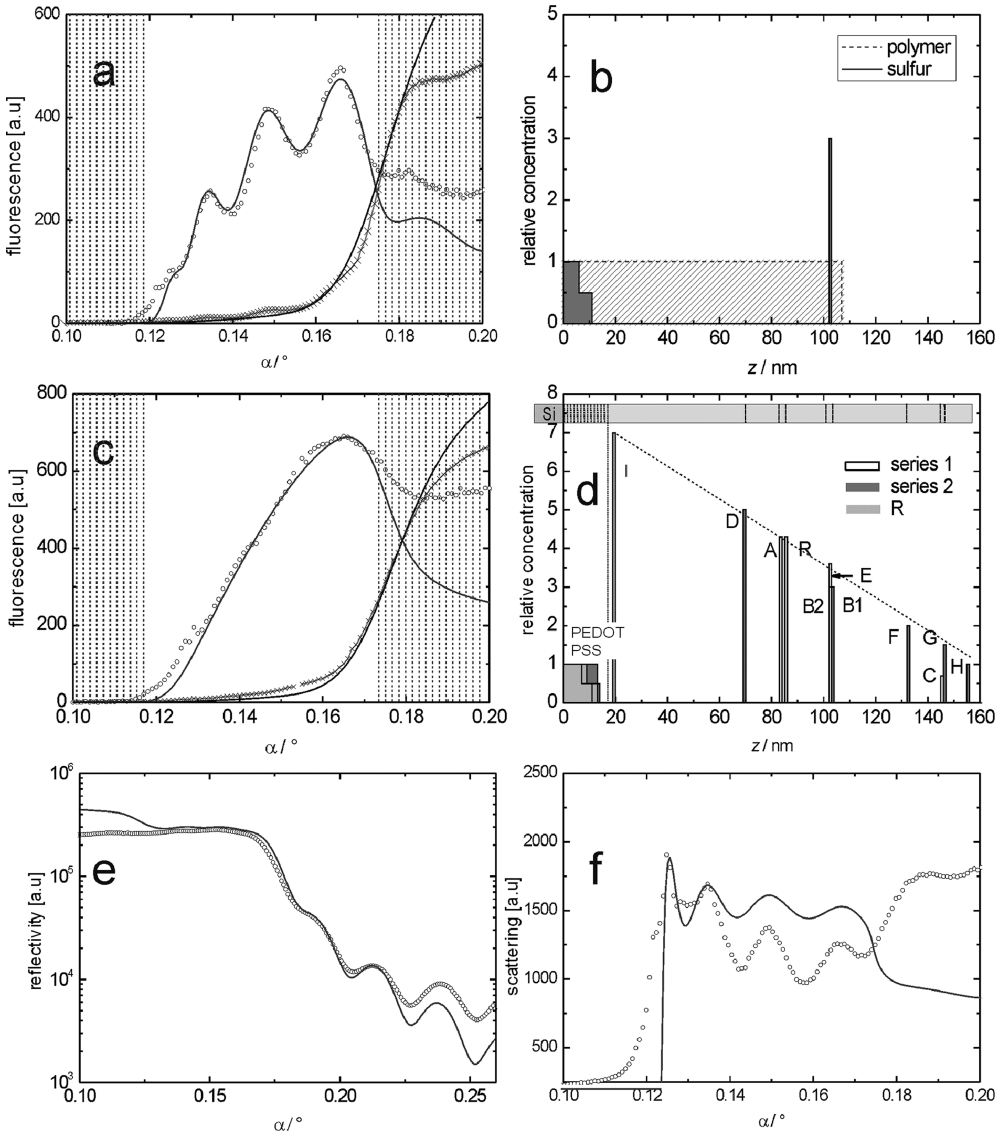


Figure 3. Evaluation of fluorescence and reflectivity data of the XSW scans: (a) Measured fluorescence intensities of S (circles) and Si (crosses) and simulated fluorescence intensities of S (maximum at $\alpha = 0.16°$) and Si (rising at $\alpha = 0.16°$) of sample B1. (b) Corresponding best-fit distribution model. Here, the overall thickness of both polymers (PEDOT + x-material) is deduced from scattering data. (c) Results from the not cross-linked sample N. (d) Summary of all distribution models applied with schematical sample composition including the position of the front. (e, f) Reflectivity and scattering signal of measurement B1, respectively.

Instead, a fading of the node−antinode contrast of the XSW field has to be considered as already observed investigating samples with metal nanoparticles.[29] It results from an inhomogeneous intensity distribution of the XSW field in vertical direction (coherence limit).[30,31] As a consequence, the amplitude of the fluorescence oscillations, indicating the sulfur ion front, decreases linearly as a function of z. For positions on the vertical axis exceeding a certain value z_{max}, indicating the upper limit of the interference range (coherence limit), no front can be detected anymore as the interference field has completely faded. From our experiments we estimate the upper integration limit z_{max} = ca. 180 nm.

From these considerations we can conclude that the relative concentration of reactive chain ends (associated anions, respectively) remains essentially constant as the reactive front moves away from the initiating surface. This view is supported by the finding, that the width of the reactive front remains narrow (<9 nm).

Position of the Sulfur-Containing Anions Relative to the Reactive Chain Ends. The thickness of the polymer layers can be determined from the X-ray reflectivity (XRR) recorded as a function of the incident angle.[32,33] Interference between X-rays reflected at the polymer−Si interface and at the surface of the polymer results in the so-called Kiessig fringes,[32] a characteristic intensity oscillation, from which the distance of the two interfaces can be calculated. An example of a reflectivity curve (sample B1) providing a thickness value of (d) 122 ± 2 nm is shown in Figure 3e.

Additionally, the layer thickness may also be obtained from the scattering signal, which also features oscillations as shown for sample B1 in Figure 3f. Every XSW antinode entering the polymer leads to a rise of the scattering level, corresponding to a maximum in the scattering signal. In the distribution diagrams (Figure 3b and SI_1, center), the thickness of the polymer layers (as detected by scattering) is indicated by the shaded area.

dx.doi.org/10.1021/ma300204g | *Macromolecules* 2012, 45, 3487−3495

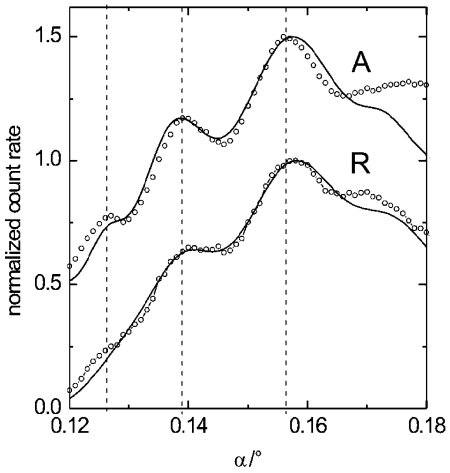


Figure 4. Comparison of the fluorescence signals of sample A (not cross-linked polymer removed) and reference sample R (not removed). The angular positions of the fluorescence maxima are identical, as indicated by the dashed lines. The spectra are stacked for clarity.

Comparing the results obtained by the two methods (see Table 1), one finds differences of some nanometers, which can be explained by the different size of the irradiated areas delivering information about the polymer thickness. The reflectivity measurement averages over the beam area, which amounts to ca. 300 mm^2, whereas the fluorescence detector collects scattering photons from a small spot of ca. 30 mm^2. As the surface of the polymer is not perfectly flat, different orientations of the sample relative to the beam may result in varying values of d, which is the case for the two measurements of sample B. For the scattering measurements, the same spot as for XSW evaluation was used; therefore, a better agreement was found. In comparing the reaction front position to the thickness value obtained from our scattering measurements, we find that the z-position of the sulfur front is ca. 6 nm smaller than the film thickness. Thus, it can be concluded that after rinsing the counterions are located close below the film surface.

This conclusion can be supported by applying XPS (X-ray photoelectron spectroscopy) on the surface of the samples after removing the non-cross-linked material; however, sulfur could not be detected. Thus, the counterions have to be located below the surface, since XPS is an extremely surface sensitive technique.

Evidence for the presence of the sulfur-containing anionic species just below the film surface is further supported by our earlier Kelvin probe measurements that revealed a reproducible change in the surface potential by +0.3 eV between non-cross-linked and fully cross-linked films. This change in the surface potential corresponds to an interface dipole in the direction of the substrate interface, with the negatively charge counterions located below the surface and the positively charged reactive chain ends at the surface.[34]

Cross-Linking Mechanism. Overall, these results support the view that the distribution of cationic reactive chain ends (probed indirectly by the X-ray fluorescence of the associated counterions) is very narrow and localized at an essentially identical distance relative to the PEDOT:PSS/x-material interface over the entire area.

Our results can be rationalized by assuming that all oxetane units in contact with the PEDOT:PSS are initiated before the reaction proceeds (once the layer is heated). This outcome is only possible if more initiator (here: protons) are available at the surface of the PEDOT:PSS layer than oxetane units in direct contact (i.e., all oxetane units at the surface can be initiated). Assuming that one oxetane unit requires a space of 1 nm^2, the areal density would be roughly 10^{14} cm^{-2}. As the volume density of protons in PEDOT:PSS is large (pH = 2−3), it can be safely assumed that this condition is fulfilled. Even though initiation may not happen strictly at the same time for all oxetanes, the z-distribution of initiated chains is still very narrow because, after initiation, the reaction cannot proceed due to the very low diffusional mobility of the reactive oxetane units without thermal activation.

Upon annealing the diffusional mobility of the reactive units is strongly increased and the polymerization/cross-linking reaction may proceed. Since all oxetanes in direct contact with the PEDOT:PSS have been initiated, the reaction can only progress in the direction away from the interface because all oxetane units to the right and the left (and later also below) have already reacted (Figure 6, bottom). Thus, the polymerization proceeds uniformly perpendicular to the surface, leading

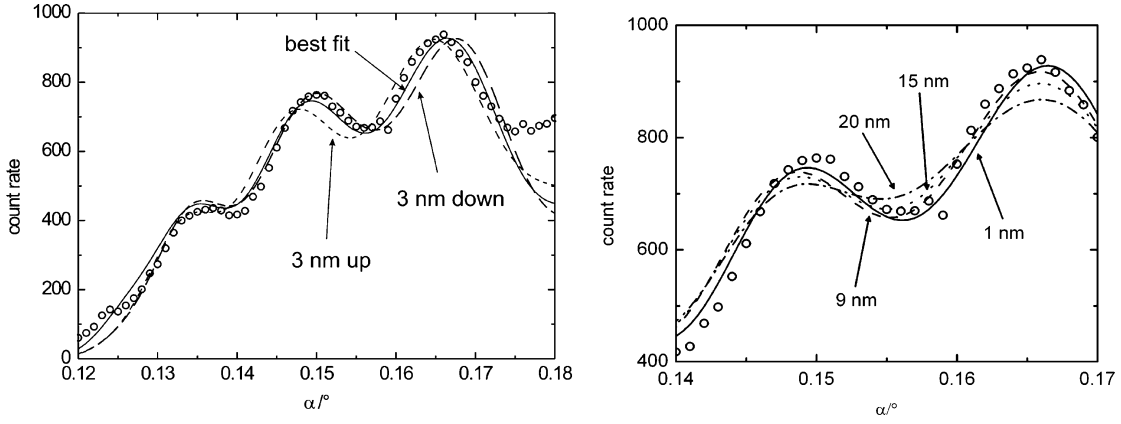


Figure 5. (left) Estimation of the positional accuracy of the XSW method by application of modified distribution models to the simulation of the fluorescence data of sample B2. The short dashed and long dashed curve results from distribution models containing a front shifted 3 nm downward and upward relative to the best-fit profile (z = 102 nm, d_f = 1 nm), respectively. This calculation is valid for front models up to 7 nm thickness. (right) Estimation of the lateral extension of the front by application of modified distribution models (rectangular fit with d_f = 1, 9, 15, and 20 nm) to the simulation of the fluorescence data of sample B2 (z = 102 nm).

dx.doi.org/10.1021/ma300204g | Macromolecules 2012, 45, 3487−3495

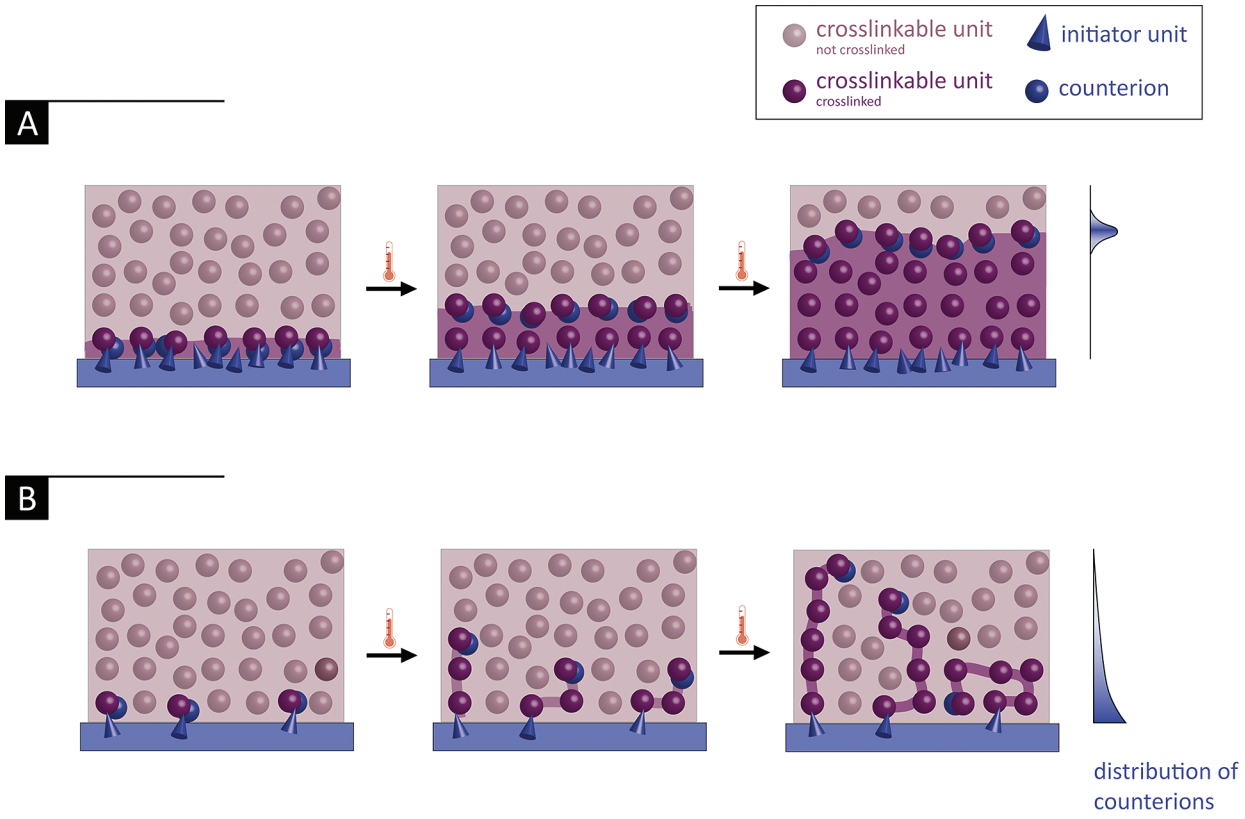


Figure 6. Proposed reaction scheme to rationalize the experimental findings of a narrow distribution of the reactive front (as measured indirectly by the accompanying sulfur-containing counterions): (A) For areal surface densities of the initiator above the critical value, the polymerization is forced to proceed in a directional fashion, since all neighboring reactive units left and right are already consumed. It is assumed that all chains are initiated simultaneously (see main text for details). From left to right the progress of the reaction is shown. (B) For areal surface densities of the initiator below the areal concentration of oxetane units (= critical concentration) the polymerization proceeds statistically, leading to a broader distribution of counterions throughout the cross-linked volume.

to a very narrow distribution of the reactive chain ends and the counterions. The system is self-limiting since no more chains than the areal density of oxetane units can be initiated. By contrast, if less initiators were present at the surface than oxetane units in direct vicinity, the polymerization would proceed statistically, leading to a broader distribution of sulfur within the layer (Figure 6, top).

3. CONCLUSIONS

Until now, the XSW method has proven to be very useful for the investigation of different types of near-surface elemental distributions with relatively large atomic numbers ($Z \geq 29$) and appreciable quantum yields (>40%).[14−16,35] In our experiments, however, the element of interest was a relatively light one (sulfur: $Z = 16$, $E_{K\alpha} = 2.31$ keV) with a fluorescence yield of only ca. 5%. Nonetheless, the distribution of sulfur was reproducibly measured with high accuracy, and the results confirmed the proposed reaction mechanism, where we were able to trace the position of the reactive chain ends of a surface-initiated solid-state polymerization (CROP of oxetane-functionalized materials) in a bulk polymer film using GI-XSW fluorescence spectroscopy.

Unexpectedly, all reactive chain ends were found within a very thin layer that moves away from the initiating interface over time, without a significant loss due to spatial trapping or even chemical termination reactions (constant areal density). This finding can be rationalized by assuming that all oxetane units are initiated simultaneously before the reaction proceeds upon thermal curing. The reactive front, with its associated sulfur-containing anions, remains narrow (<9 nm) even for distances beyond 180 nm (which was the coherence limit in our case). This result explains our earlier experimental finding that the topography of the underlying PEDOT surface is perfectly replicated (conformal process).[7] These findings correlate nicely to experimental findings reported for other surface-initiated polymerizations, explaining the observed 1:1 amplification of templates into cross-linked layer morphologies.[12,36−38]

We believe that GI-XSW fluorescence spectroscopy might be very useful to reveal further insight into other surface-initiated living ionic polymerization,[39−41] surface-initiated atom transfer radical polymerizations (SI-ATRP), and surface-initiated reversible addition−fragmentation chain transfer (SI-RAFT) reactions and their specific problems.[42,43]

4. EXPERIMENTAL SECTION

Dialysis. Commercial PEDOT:PSS suspension (Clevios P VP. Al 4083) was dialyzed against a stirred solution of deionized water (3 × 100 mL) for 2 days in a dialysis tube ZelluTrans (Roth, MWCO 4000−6000). The resultant PEDOT suspension was used as received for layer formation and subsequent cross-linking examinations (see below). Since the suspension was diluted during dialysis, it was concentrated under reduced pressure to allow for the formation of thicker spin-coated layers. No PIX of the cross-linkable polymer was observed.

Sample Preparation, PIX Procedure. Silicon wafers were commercially obtained from Virginia Semiconductor Inc. and carefully

dx.doi.org/10.1021/ma300204g | *Macromolecules* 2012, 45, 3487−3495

cleaned in chloroform, acetone, mucasol, and water. After an ozone treatment for 20 min a homogeneous layer of PEDOT:PSS (Clevios P VP. Al 4083) was spin-coated under clean-room conditions, resulting in a thickness of ca. 10−15 nm and baked at 110 °C for 1 min to remove residual water. The substrates were then transferred to a nitrogen glovebox. Thin films of x-material were prepared by spin-coating from toluene solution on top of the PEDOT-layer and then heat-treated at 200 °C (series 1) and 110−130 °C (series 2) for a given time to promote the CROP of the oxetane moieties. After cross-linking samples were washed with THF to remove the non-cross-linked part of the material.

X-ray Standing Waves. GI-XSW experiments were performed at beamline 8 of the DELTA synchrotron radiation facility (TU Dortmund). The radiation energy was 10 keV, corresponding to a wavelength of 0.124 and 0.083 nm, respectively. In the case of 10 keV, the interval between the critical angles of polymer and Si is larger, so the interesting angular range can be measured with more data points. An adjustment of the energy to 15 keV extends the number of detectable elements; this way potential impurities can be identified.

Radiation was generated by a 5.3 T superconducting asymmetric wiggler and monochromatized by a Si(111) double crystal monochromator. The storage ring was operated with an electron energy of 1.5 GeV and a beam current between 70 and 130 mA. The cross section of the beam irradiating the sample was confined to 5 mm × 100 μm. For the collection of fluorescence photons, two Amptek solid-state detectors with an energy resolution of at least 150 eV were applied, which is sufficient to separate the Kα lines of the interesting elements. Simultaneous to fluorescence collection the intensity of the reflected beam was measured by an argon-filled ionization chamber. The experimental parameters of the measurements are summarized in Tables 1 and 2.

The XSW analysis of the first series (samples A−C: Si wafers of 30 mm in diameter) was done at an X-ray energy of 10 keV. Here, the fluorescence signals of sulfur (analyte) and Si (substrate) and the intensity of in elastic scattered radiation (Compton scattering), recorded by the fluorescence detector, was used for evaluation. Furthermore, series 1 included two reference samples (R: reference sample, without removal of not polymerized part; and N: reference sample with noncross-linked material). The samples B and N were scanned twice; the respective measurement is indicated by a number (e.g., B1).

The second sample series (samples D−H) was produced using smaller wafers with a size of ca. 20% of the substrates of series 1. Therefore, the settings of the fluorescence detector had to be adjusted to the lower amount of sulfur in the layers. As a consequence, the peaks of Si fluorescence and Compton scattering could not fully be recorded.

The z-resolution was shown in this study to be in the nanometer range. The spatial resolution in the xy plane amounts to several centimeters in the direction of the grazing X-ray beam, whereas it is in the millimeter range perpendicular to the beam. The temporal resolution of the experiment depends on the intensity of the used X-ray source (photon flux). At the DELTA facility, the minimum time for a well-resolved measurement (good SNR) is about 10 min for an angle scan of about 0.06°.

5. METHODS SECTION

X-ray Standing Waves. The XSW method uses a beam of monochromatic and parallel X-rays, which hit a flat and plane surface under grazing incidence. For angles below a critical angle α_c, which is determined by the wavelength λ of the radiation and the electron density of the reflector material, the beam is totally reflected. In the overlap of incoming and reflected radiation, interference of the two beams generates a stationary electromagnetic field of alternating minima (nodes) and maxima (antinodes), the so-called X-ray standing waves field. The intensity of the XSW field depends on the incident angle α and the position z relative to the reflecting surface and is given by[17,27,33,44]

$$I_{XSW}(\alpha, z) = I_0[1 + R(\alpha) + 2\sqrt{R(\alpha)}\cos((2\pi z/a) - \phi(\alpha))] \quad (1)$$

Here $R(\alpha)$ is the angle-dependent intensity of the reflected beam, a gives the period of the XSW field, and $\phi(\alpha) = \arccos[2(\alpha/\alpha_c)^2 - 1]$ describes the phase shift between the two beams. The increase of the incident angle α induces a movement of the standing waves toward the surface and a decrease of the field period; this relation is also illustrated in Figure SI_4.

In the near-surface region, the maxima of the XSW field excite to fluorescence any atoms or ions as they move through the distribution of these so-called fluorescence markers. Thus, by the variation of α during the collection of fluorescence photons, the concentration profile of the elements within the field is scanned vertically. Using an energy-dispersive detector, these measurements can be performed in an element-sensitive way. In Figure SI_5, a set of fluorescence spectra recorded during the angle scan is shown for measurement A. The vertical resolution of such scans is determined by the period of the XSW field, given by $a = \lambda/(2 \sin \alpha)$, so that the vertical resolution of the XSW field is highest at the critical angle α_c. For the applied X-ray energy settings of 10 and 15 keV, typical values of a range between 80 and 20 nm, so the XSW method is ideally suited for the investigation of the present sample type.

As for each α the fluorescence photons are collected from the entire irradiated sample volume, the measured signal is the product of the intensity of the XSW field and the concentration profile $C(z)$ of the respective analyte, integrated over the vertical axis:

$$I(\alpha) = \int_0^{z_{max}} I_{XSW}(\alpha, z)C(z)\, dz' \quad (2)$$

For the evaluation of an XSW scan, first $I(\alpha)$ is calculated for a probable element distribution model $C_0(z)$. Then, this initial model is varied until best possible agreement between the measured and simulated fluorescence signal is achieved. Good correlation between the simulated and measured fluorescence spectra implies that the assumed marker distribution is indeed close to reality.

Besides the possibility of element-sensitive measurements with a vertical resolution in the nanometer range, the experiments benefit from other advantages of the XSW method. The total reflection of X-rays greatly reduces the noise in the fluorescence spectra, as a contribution to the signal from the substrate is avoided, so that the detection limit is very low even for light elements like sulfur. Furthermore, matrix effects influencing the intensity of the signal are largely avoided.

An effect which must be taken into account is the influence of the imperfect flatness of the interfaces. The Si wafer as well as the polymer surface is not perfectly flat but features a slight undulation. Although the inhomogeneity of the layer thickness is in the range of only few nanometers, it induces a divergence of the grazing incidence beam inside the polymer. This also lowers the contrast of the XSW field. In the simulation procedure, this divergence was taken into account by the convolution of $I(\alpha,z)$ with a normal distribution. The standard deviation of the convolution function is included as a fit parameter in the calculation of the fluorescence simulation.

As a conclusion from the discussion of the factors influencing the amplitude of the oscillating signal, it can be noted that XSW are ideally suited for the determination of the z-position of the polymerization front, whereas the quantification over the given vertical range of ca. 100 nm is complicated by the influence of the not ideal interfaces of the sample and the limited extension of the XSW field.

In all measurements, certain deviations between measured and calculated curves are observed.

The fit quality of the fluorescence curves, which is good in the angular range of total reflection, considerably decreases for $\alpha > 0.17°$ mainly due to two reasons:

(1) When the beam enters the substrate, the conditions of total reflection, advantageous in terms of avoiding of matrix effects, are not given anymore.

(2) Furthermore, the settings of the fluorescence detector and the multichannel analyzer (amplification, integration time, etc.) are adapted to the low count rates expected for the collection of sulfur fluorescence photons. As the total count rate drastically rises at α_c^{Si}, the optimal working conditions of the fluorescence detector are not given anymore. This leads to the effect that often two Si Kα photons, reaching the detector within one counting interval, are counted as one of double energy. This again raises the level of spectral noise in the energy range up to ca. 3.5 keV. Also for Si fluorescence, measured and calculated signals diverge for after α_c^{Si}, because the excited photons are absorbed in the substrate material, as the beam penetrates deeper into the wafer.

However, as the effects described only occur for $\alpha > \alpha_c^{Si}$, the data in the interesting angle range containing the information about the sulfur distribution and their interpretation are not impaired.

■ ASSOCIATED CONTENT

Supporting Information

Figures SI_1−SI_5. This material is available free of charge via the Internet at http://pubs.acs.org.

■ AUTHOR INFORMATION

Corresponding Author

*E-mail: klaus.meerholz@uni-koeln.de (K.M.), hergenroeder@isas.de (R.H.).

Author Contributions

⊥These authors contributed equally to this publication.

Notes

The authors declare no competing financial interest.

■ ACKNOWLEDGMENTS

This work was funded by the German Ministry of Education and Research (BMBF) through the HOBBIT and OLED-3D projects. We thank Dr. R. Clayton Shallcross for the careful proofreading and revision of this manuscript.

■ REFERENCES

(1) Zacharias, P.; Gather, M. C.; Rojahn, M.; Nuyken, O.; Meerholz, K. *Angew. Chem., Int. Ed.* **2007**, *46*, 4388.

(2) Jungermann, S.; Riegel, N.; Müller, D.; Meerholz, K.; Nuyken, O. *Macromolecules* **2006**, *39*, 8911.

(3) Müller, D. C.; Braig, T.; Nothofer, H. G.; Arnoldi, M.; Gross, M.; Scherf, U.; Nuyken, O.; Meerholz, K. *ChemPhysChem* **2000**, *1*, 207.

(4) Moule, A. J.; Meerholz, K. *Adv. Mater.* **2008**, *20*, 240.

(5) Günes, S.; Neugebauer, H.; Sariciftci, N. S. *Chem. Rev.* **2007**, *107*, 1324.

(6) Klauk, H. *Chem. Soc. Rev.* **2010**, *39*, 2643.

(7) Köhnen, A.; Riegel, N.; Kremer, J. H.-W. M.; Lademann, H.; Müller, C. D.; Meerholz, K. *Adv. Mater.* **2009**, *21*, 879.

(8) Gather, M. C.; Köhnen, A.; Falcou, A.; Becker, H.; Meerholz, K. *Adv. Funct. Mater.* **2007**, *17*, 191.

(9) Jonas, F.; Krafft, W.; Muys, B. *Macromol. Symp.* **1995**, *100*, 169.

(10) Uhlmann, P.; Ionov, L.; Houbenov, N.; Nitschke, M.; Grundke, K.; Motornov, M.; Minko, S.; Stamm, M. *Prog. Org. Coat.* **2006**, *55*, 168.

(11) Zhao, B.; Brittain, W. J. *Prog. Polym. Sci.* **2000**, *25*, 677.

(12) Steenackers, M.; Jordan, R.; Kuller, A.; Grunze, M. *Adv. Mater.* **2009**, *21*, 2921.

(13) Wang, J.; Caffrey, M.; Bedzyk, M. J.; Penner, T. L. *Langmuir* **2001**, *17*, 3671.

(14) Bedzyk, M. J.; Bommarito, G. M.; Schildkraut, J. S. *Phys. Rev. Lett.* **1989**, *62*, 1376.

(15) Krämer, M.; von Bohlen, A.; Sternemann, C.; Paulus, M.; Hergenröder, R. *J. Anal. At. Spectrom.* **2006**, *21*, 1136.

(16) Krämer, M.; von Bohlen, A.; Sternemann, C.; Paulus, M.; Hergenröder, R. *Appl. Surf. Sci.* **2007**, *253*, 3533.

(17) Trainor, T. P.; Templeton, A. S.; Eng, P. J. *J. Electron Spectrosc. Relat. Phenom.* **2006**, *150*, 66.

(18) Battermann, B. W. *Phys. Rev. Lett.* **1969**, *22*, 703.

(19) Zhang, Z.; Fenter, P.; Cheng, L.; Sturchio, N. C.; Bedzyk, M. J.; Machesky, M. L.; Wesolowski, D. J. *Surf. Sci.* **2004**, *554*, L95.

(20) Zhang, Z.; Fenter, P.; Kelly, S. D.; Catalano, J. G.; Bandura, A. V.; Kubicki, J. D.; Sofo, J. O.; Wesolowski, D. J.; Machesky, M. L.; Sturchio, N. C.; Bedzyk, M. J. *Geochim. Cosmochim. Acta* **2006**, *70*, 4039.

(21) Zegenhagen, J. *Surf. Sci. Rep.* **1993**, *18*, 199.

(22) Zhang, R. T.; Itri, R.; Caffrey, M. *Biophys. J.* **1998**, *74*, 1924.

(23) Templeton, A. S.; Trainor, T. P.; Spormann, A. M.; Brown, G. E. *Geochim. Cosmochim. Acta* **2003**, *67*, 3547.

(24) Kohli, V.; Bedzyk, M. J.; Fenter, P. *Phys. Rev. B* **2010**, *81*, xxxx.

(25) de Boer, D. K. G. *Phys. Rev. B* **1991**, *44*, 498LP.

(26) Wang, J.; Bedzyk, M. J.; Caffrey, M. *Science* **1992**, *258*, 775.

(27) Klockenkämper, R. In *Chemical Analysis*; Wiley: New York, 1997; p 140.

(28) Brücher, M.; Jacob, P.; von Bohlen, A.; Franzke, J.; Sternemann, C.; Paulus, M.; Hergenroder, R. *Langmuir* **2010**, *26*, 959.

(29) A. von Bohlen, M. Brücher, Holland, B.; Wagner, R.; R. Hergenröder, in preparation,

(30) von Bohlen, A.; Kramer, M.; Sternemann, C.; Paulus, M. *J. Anal. At. Spectrom.* **2009**, *24*, 792.

(31) von Bohlen, A.; Brucher, M.; Holland, B.; Wagner, R.; Hergenroder, R. *Spectrochim. Acta, Part B* **2010**, *65*, 409.

(32) Kiessig, H. *Ann. Phys.* **1931**, *10*, 769.

(33) Tolan, M. In *X-Ray Scattering from Soft-Matter Thin Films*; Springer: Berlin, 1999; p 148.

(34) Cahen, D.; Kahn, A. *Adv. Mater.* **2003**, *15*, 271.

(35) Guico, R. S.; Narayanan, S.; Jin, W.; Shull, K. R. *Macromolecules* **2004**, *37*, 8357.

(36) Zhou, X. C.; Liu, X. Q.; Xie, Z.; Zheng, Z. J. *Nanoscale* **2011**, *3*, 4929.

(37) Zhou, X. C.; Wang, X. L.; Shen, Y. D.; Xie, Z.; Zheng, Z. J. *Angew. Chem., Int. Ed.* **2011**, *50*, 6506.

(38) Chen, T.; Amin, I.; Jordan, R. *Chem. Soc. Rev.* **2012**, *41*, 3280.

(39) Zhao, B.; Brittain, W. J. *Macromolecules* **2000**, *33*, 342.

(40) Advincula, R.; Zhou, Q. G.; Park, M.; Wang, S. G.; Mays, J.; Sakellariou, G.; Pispas, S.; Hadjichristidis, N. *Langmuir* **2002**, *18*, 8672.

(41) Jordan, R.; Ulman, A.; Kang, J. F.; Rafailovich, M. H.; Sokolov, J. *J. Am. Chem. Soc.* **1999**, *121*, 1016.

(42) Tsujii, Y.; Ejaz, M.; Sato, K.; Goto, A.; Fukuda, T. *Macromolecules* **2001**, *34*, 8872.

(43) Barbey, R.; Lavanant, L.; Paripovic, D.; Schuwer, N.; Sugnaux, C.; Tugulu, S.; Klok, H. A. *Chem. Rev.* **2009**, *109*, 5437.

(44) Parratt, L. G. *Phys. Rev.* **1954**, *95*, 359 LP.

Macromolecules

Article

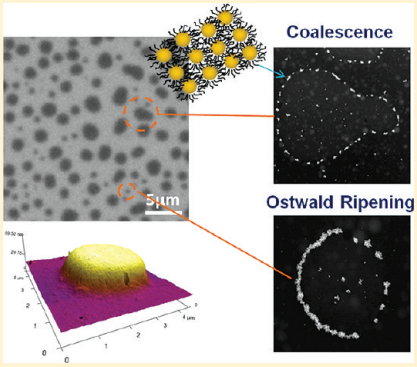
pubs.acs.org/Macromolecules

Time Evolution of the Topography of Structured Hybrid Polymer/Nanoparticle Systems

Jenny Kim[†] and Peter F. Green*[,†,‡]

[†]Department of Materials Science and Engineering and [‡]Department of Chemical Engineering, University of Michigan, Ann Arbor, Michigan 48109, United States

ABSTRACT: An important class of functional hard/soft hybrid nanocomposites is formed when nanoparticles (NPs) are induced to self-assemble within the structures of ordered A-*b*-B diblock copolymers (BCPs). Based on their size, NPs will preferentially reside within edge dislocations, defects, which enable the formation of surface structures, islands or holes, in BCP thin films. The islands (and holes), ubiquitous in BCP thin films, coarsen in a manner reminiscent of 2-dimensional phase ordering systems of binary alloys, where the growth is self-similar, governed by classical capillarity driven Ostwald ripening and coalescence mechanisms. In the pure BCP thin films, coarsening initially occurs via coalescence and at later times via Ostwald ripening. In BCP/nanoparticle systems, the dynamics are considerably slower, and throughout similar time scales, the mechanism of coarsening occurs predominantly via coalescence. Contributions to the structural evolution due to Ostwald ripening are comparatively small over these time scales. Our assessments are based on an analysis of the power law growth exponents and of probability density distribution functions of data obtained from samples using microscopy.



INTRODUCTION

Control of the structure and properties of materials at the nanoscale is a key challenge associated with the development of nanostructured materials for many technological applications. Hybrid soft material/nanoparticle (NP) systems are viable for a wide range of applications, from biosensors and batteries to optoelectronic devices.[1−11] Macromolecules such as conjugated polymers, block copolymers, liquid crystals, and proteins exhibit an ability to self-assemble over various length sales.[12−18] Lithographic processes may be exploited to create templates on which the chemistry and topography may be tailored; such engineered substrates enable additional control over the structure and long-range order of these soft materials that possess an intrinsic ability to self-assemble.[6,15,19−23] Of interest in this study are A-*b*-B diblock copolymers, which self-assemble into different geometrical structures (spherical, hexagonal, lamellar), possessing long-range order. When mixed with nanoparticles, the A/B domains act as scaffolds, directing the self-assembly of nanoparticles, provided the nanoparticles are sufficiently smaller than the A- or B-rich domain dimensions. Defects such as dislocations and grain boundaries are ubiquitous within the structure of these materials.[24,25] These structural disruptions occur randomly during the assembly process often during solvent evaporation; consequently, internal stresses develop and disorientations of ordered domains occur.[26] Controlling the defect formation and distribution in these systems during processing is a major challenge.

With regard to thin A-*b*-B diblock copolymer systems, it is well-known that when the A and B bocks are comparable in size, the material forms a lamellar structure; the lower surface energy component resides at the free, air/vacuum, interface. Specific chemical interactions determine whether the A or B component resides at a substrate.[28,29] The topography of a thin film A-*b*-B copolymer is composed of islands or holes, provided the film thickness, h, does not meet certain selection criteria.[28−30] For the case of symmetric wetting, where the same component resides at both external interfaces, the topographical features, islands or holes, develop when $h \neq 2nL$, where n is an integer. In the asymmetric wetting case the topographies develop when $h \neq (2n + 1)L$. Line defects, specifically edge dislocations, surround and facilitate the existence of islands.[31] For A-*b*-B diblock/nanoparticle systems, the nanoparticles reside at the boundaries of islands, i.e., within the edge dislocation cores that enable formation of islands.[31] We recently showed that when the size of the nanoparticles approaches that of the domain dimensions it becomes energetically more favorable for the nanoparticles to reside within the defect structures.[27] A scanning transmission electron microscopy (STEM) image of the organization of the nanoparticles around an island is shown in Figure 1a. An atomic force microscopy (AFM) image of a typical island is shown in Figure 1c, and a schematic of the nanoparticles in the vicinity of an island is shown in Figure 1b.

This article reports a study of the 2-dimensional structural and temporal evolution of the topography of a symmetrically wetting A-*b*-B diblock thin film of thickness of $h < 2L$. The islands in this film are shown to increase in size, with a growth

Received: February 3, 2012
Revised: March 18, 2012
Published: April 4, 2012

ACS Publications © 2012 American Chemical Society

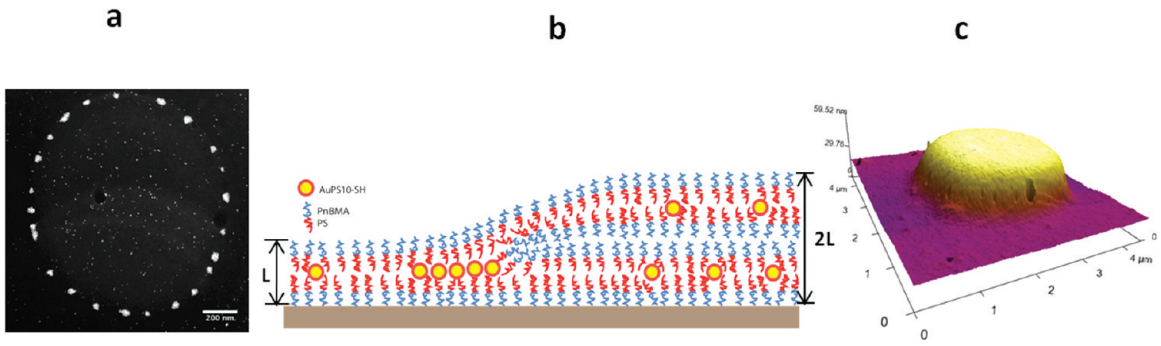


Figure 1. Local structure, island, of a PS-*b*-PnBMA diblock copolymer film containing 3 wt % $AuPS_{10}$. (a) Plan-view of island, imaged using HAADF-STEM, revealing NP clusters at its perimeter (b) schematic of the edge of an islands showing the location of NPs; (c) AFM topographical image of island.

rate that exhibits a power law dependence; this behavior is self-similar. The classical coarsening mechanism, coalescence, is shown to dominate the growth of the islands of the pure BCP during the early stage; Ostwald ripening, where the larger islands grow at the expense of the smaller ones, became the dominant mechanism at later times.[32] In the hybrid system, however, islands grew at a considerably smaller rate, primarily via coalescence, throughout the same duration. The coarsening of the islands is reminiscent of that of 2-dimensional phase ordering systems, including binary alloys, magnetic systems, and others.[33,34]

EXPERIMENTAL SECTION

We begin by discussing the materials. The PS-*b*-PnBMA diblock copolymers of number-average molecular weight, M_n = 93 000 g/mol (M_w/M_n = 1.08), were purchased from Polymer Source, Inc. The molecular weights of PS and PnBMA blocks were M_n = 45 000 and 48 000 g/mol respectively, and the volume fraction of polystyrene was f_{ps} = 0.56 (this system forms a lamellar structure). The nanoparticles were synthesized using the two-phase arrested precipitation method reported by Brust et al.[35] Thiol-terminated polystyrene molecules (PS-SH) of number-average molecular weight M_n = 1000 g/mol (M_w/M_n = 1.4), purchased from Polymer Source, Inc., were then grafted onto the surface of nanoparticles. The resulting brush-coated NPs were characterized by scanning transmission electron microscopy (STEM) to determine the average NP core diameter D_{core} = 5.1 ± 1.2 nm and the overall diameter of the nanoparticle and the brush layer thickness D_{NP} = 8.9 ± 1.1 nm. The grafting density of σ = 2.1 chains/nm^2 was determined based on thermal gravimetric analysis experiments.

Thin films of a poly(styrene-*b*-*n*-butyl methacrylate) (PS-*b*-PnBMA) diblock copolymer mixed with PS-ligand-coated gold nanoparticles (Au NPs) were prepared on silicon substrates; a native oxide layer, 1.5 nm thick, resided on each substrate. While the preparation methods have previously been described,[27] we mention briefly that solutions containing 5 wt % Au nanoparticles, prepared using toluene as the solvent, were spin-cast onto SiO_x substrates to create films of average thickness 53 nm. These films corresponded to thicknesses of h = 1.4L. For the pure BCP, the interlamellar spacing L = 35 nm, whereas L = 37 nm for the BCP/NP mixtures.

The time evolution of the topographies of the films was examined using atomic force microscopy (AFM), optical microscopy (OM), and scanning transmission electron microscopy (STEM). The AFM measurements were performed using the MFP-3D Asylum Research, Inc., atomic force microscope. Silicon cantilevers (Olympus, Inc.), each with a spring constant of 42 N/m and resonant frequency of 300 kHz, were used. The OM studies were performed using an Eclipse LV 150, Nikon, optical microscope. The topographical features, island sizes and shapes, of the images were analyzed by using Image J, Igor Pro (Asylum Research, Inc.), and WSXM software.

The films were annealed under supercritical CO_2 ($scCO_2$) conditions at a temperature of T = 60 °C and a pressure of P = 2000 psi for durations that ranged from t = 150 to 12 000 min. $ScCO_2$ is a poor solvent that plasticizes the samples, thereby enabling the structure to get to equilibrium. A judicious choice of temperature and pressure enables control of the time scale and thermodynamics of the process. This particular choice of T and P for our experiments created a benign environment for processing of this system. We note that we annealed the pure diblock at 150 °C for long periods of time under vacuum and carefully examined the coarsening of the topography. We obtained identical results as we did in $scCO_2$; i.e., the mechanisms that characterize the structural evolution were identical to those that occurred in the high-temperature vacuum environment under which the samples were processed. The low-temperature $scCO_2$ environment was chosen to avoid detachment of the ligands from the nanoparticles, which occurs at high temperatures.

The two sets of samples, pure PS-*b*-PnBMA and 5 wt % $AuPS_{10}$/PS-*b*-PnBMA, were processed simultaneously. The $AuPS_{10}$/PS-*b*-PnBMA samples that were analyzed using STEM were fabricated by spin-casting solutions onto glass substrates, from which they were floated onto a bath of distilled water. They were then picked up onto silicon nitride windows (TEM grid (SPI Supplies)). Images were taken using high annular angle dark field (HAADF) detector (Z-contrast) applying an accelerating voltage of 200 kV.

RESULTS AND DISCUSSION

In-situ images of the topographies, specifically islands, of a pure BCP film and of a BCP/NP film were taken at various times, throughout the interval from 150 minutes 12 000 minutes, using optical microscopy (Figure 2). It is clear from the images of both systems that as the number of islands, $N(t)$, decreases, the average area per island, $\langle S(t)\rangle$, increases, and the average distance between the islands increases, with increasing time t. The rate of evolution of the structure of the pure BCP sample is more rapid than that of the BCP/NP system. The islands in the images, encircled by the broken lines (Figure 1a,c,e), of the pure BCP film, gradually disappear with time; they are no longer visible after 12 000 min. In the BCP/NP system, however, small islands, enclosed within the broken line circles, still exist after 12 000 min.

The process responsible for the gradual disappearance of these islands is believed to be Ostwald ripening, a capillarity driven process, wherein islands of average radius R less than a critical radius, R_c, increase in size and those of $R < R_c$ decrease in size and eventually disappear. This phenomenon is well-known in phase separated two-phase mixtures;[33,34,36,37] we will revisit this question in further detail later.

The solid circles in the images show evidence of structural evolution occurring via coalescence. The three islands initially

dx.doi.org/10.1021/ma300245s | *Macromolecules* 2012, 45, 3496−3502

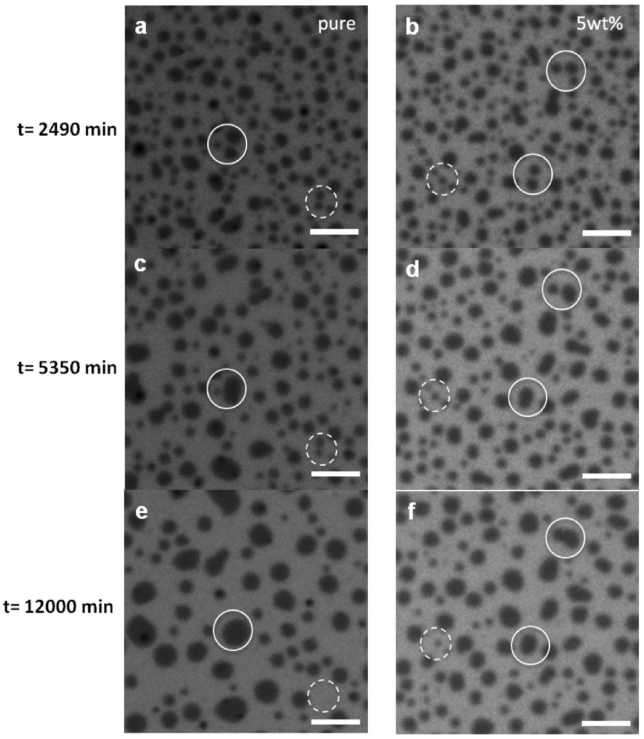


Figure 2. Time evolution of islands on pure thin film PS-*b*-PnBMA (a, c, e), and on PS-*b*-PnBMA containing 5 wt % Au nanoparticles (b, d, f) at times t = 2490 min (a, b), 5335 min (c, d), and 12 000 min (e, f). Total surface area of island for both samples remained at 22−23% throughout the annealing period. The islands enclosed by the solid circles undergo coarsening via a coalescence mechanism. The process associated with the reduction in size of the islands enclosed within the circles denoted by the broken lines present Ostwald ripening. Scale bar corresponds to 5 μm.

enclosed within the solid line circle in Figure 2a (t = 150 min) completely coalesced and reshaped, approaching a circular shape, by time t = 12 000 min (Figure 2e). This coalescence process is much slower in the BCP/NP system than in the pure copolymer. Additionally, we note that the average area occupied by the islands remain constant throughout the entire period of observation. This latter point is important because the coarsening theories we use to describe our observations are based on the conversation of mass.

Classical coarsening theories suggest that the structure may be characterized by a single length scale. Such a length-scale should exhibit a power law dependence on time.[33,34,36,38−40] The average area and number of islands, $\langle S(t)\rangle$ (Figure 3a) and $N(t)$ (Figure 3b), exhibited a power law dependence on time. The behavior of the pure BCP sample is well described by $\langle S_{pure}(t)\rangle \sim t^{0.70\pm0.03}$ and $N_{pure}(t) > \sim t^{-0.64}$. In the case of the BCP/NP system, $\langle S_{BCP/NP}(t)\rangle \sim t^{0.48\pm0.02}$ and $N_{pure}(t) > \sim t^{-0.47}$. It is known that the values of the exponent, β, provide information not only about the relative rates of growth but also about differences between the physics that govern the mechanisms of growth.

The most well-known studies of coarsening have been performed on binary alloy systems that have undergone phase separation. The classical theories, Ostwald ripening as well as static and dynamic coalescence, have successfully been used to describe the late-stage, coarsening, evolution of the structure of these materials.[33,34,36,38−41] Parenthetically, an initially homogeneous A/B mixture, when quenched below a critical temperature, would phase separate into A-rich and B-rich phases; over time the domains increase in size. The late-stage coarsening behavior of a system in 3-dimensions, or in 2-dimensions, may be described within the framework of the classical coarsening mechanisms: Ostwald Ripening or coalescence. In Ostwald ripening the growth of domains larger than a critical radius, R_c, occurs when entities (atoms or molecules) detach and diffuse from the smaller domains to the larger domains. This process is driven by differences between the local chemical potentials, determined by the local radii of curvature, of the larger and smaller domains. Atoms, or molecules, move from the smaller domains to the larger domains, both of which remain stationary. Theories[34,36] based on the earlier work of Lifshitz and Slyozov (LS)[38] showed that late-stage coarsening of a binary phase-separated solution, in the limit of dilute volume fraction of minority phase, where the volume fraction of domains remain constant and where the domain locations are static, $\langle R\rangle \sim t^{\beta}$. When the rate-limiting step for growth is determined by the detachment of an entity

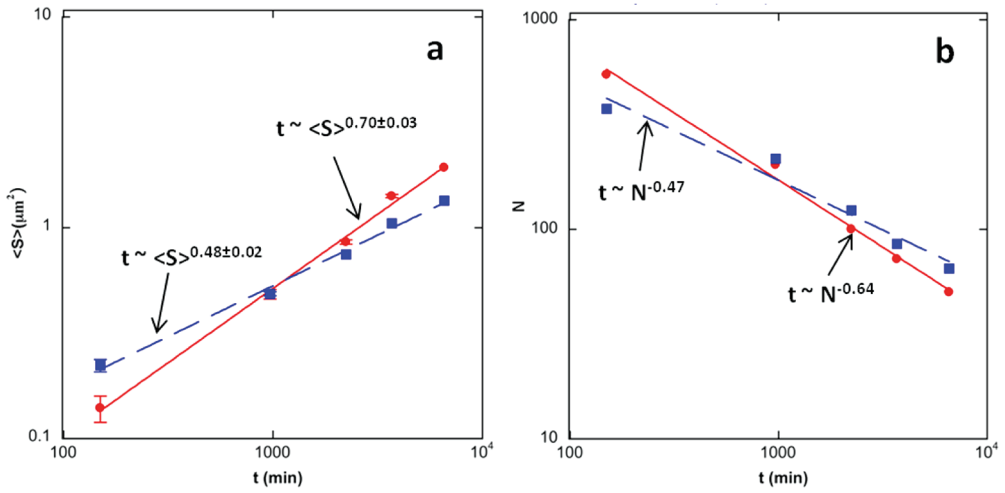


Figure 3. Log−log plots of the time dependencies of average surface area per island, $\langle S(t)\rangle$, and number of islands, $N(t)$, for pure BCP (circle) and 5 wt % NP/BCP (square) samples are plotted in (a) and (b), respectively. The data (pure: solid; 5 wt %: dashed) fitted to power law functions. Error bar is from the area analysis of islands from 4 to 5 AFM images (20 × 20 and 30 × 30 μm^2) of similar areas.

dx.doi.org/10.1021/ma300245s | *Macromolecules* 2012, 45, 3496−3502

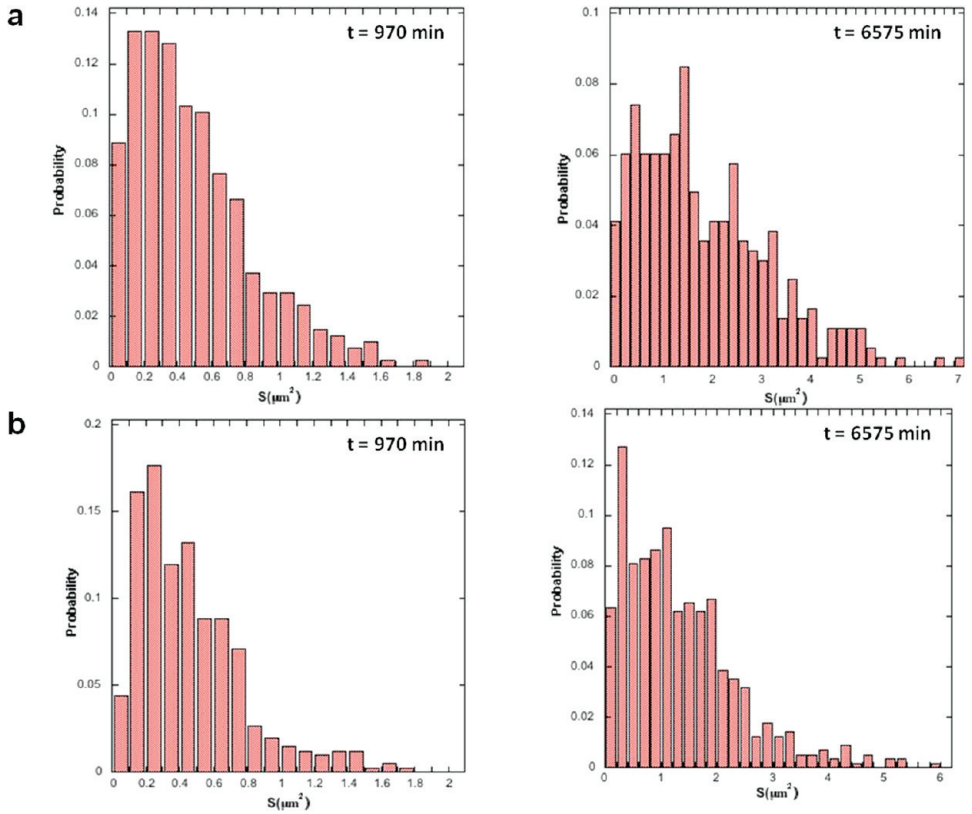


Figure 4. Probability distributions of the island sizes (areas) for pure (a) and 5 wt % (b) samples for annealing times t = 970 and 6575 min.

(atom or molecule) from one domain to another, the growth exponent is $\beta = 1/2$. Alternatively, when domain growth is determined by a diffusion-limited process, the exponent was $\beta = 1/3$. These exponents are valid in 2- and 3-dimensions for the OR mechanism. Further, if the mechanism of growth occurs via dynamic coalescence, then a value of $\beta = 1/3$ is possible if the dynamics of the islands are uncorrelated. The exponent of $\beta = 1/3$, determined from the data in Figure 2 describing dynamics in the pure BCP film, appears to be consistent with that expected for both mechanisms.

The exponent associated with island coarsening in the BCP/NP system is however smaller than that of the pure BCP film; the former is $\beta = 0.24$. It is not immediately clear how to reconcile this apparent discrepancy between the exponents and the relation to the actual coarsening mechanisms. To this end, we note that in general the power law analysis may provide only limited insight into the actual mechanism of coarsening. If, for example, two mechanisms are operational simultaneously, or a different mechanism becomes dominant during different stages of coarsening, then assessments based on the magnitude of the exponent are uncertain.[37,39,40] Therefore, a thorough analysis involving the use of the distribution functions, combined with a careful analysis of the images, would reveal additional insight into details regarding the structural evolution of the system.

The island size distribution function $F(r,t)$ is described in a scale invariant form $F(R'=R/R_c)$ by theories based on Ostwald ripening and coalescence.[34,38,41,42] As mentioned above, when the rate-limiting step for island growth is determined by the detachment of an entity from an island, the exponent $\beta = 1/2$. The associated time invariant distribution function is represented by

$$F(R') = \frac{R'}{2}\left(\frac{2}{2-R'}\right)^4 \exp\left(-\frac{2R'}{2-R}\right) \quad (1)$$

where $F(R') = 0$, when $R' > 2$. However, for the diffusion-limited process, the growth exponent is $\beta = 1/3$, and the distribution function is shown to yield

$$F(R') = \frac{CR'^2 \exp\left(\frac{-1}{3/2-R'}\right)}{\left(\frac{3}{2}-R'\right)^{28/9}(3+R')^{17/9}} \quad (2)$$

where C is a normalization constant and $F(R') = 0$ for $R' > 3/2$.

While dynamic coalescence involves diffusion and subsequent merging of islands, static coalescence occurs due to the fluctuation of the shapes of the islands (their centers of mass remain stationary). In the case of dynamic coalescence, Smoluchowski[41] suggested that $R \sim t^{\beta}$, where $\beta = 1/d(\alpha+1)$ and d is dimension ($d = 2$ for islands on flat surface). The associated distribution function of dynamic coalescence is predicted to be

$$F(R') = \frac{dW(WR')^{d(\alpha+1-(1/d))}}{\Gamma(\alpha+1)} \exp(-WR')^d \quad (3)$$

where $W = \Gamma(\alpha + 1 + 1/d)/\Gamma(\alpha+1)$ and Γ is the gamma function. Thus, the parameter α is related to details of the coarsening behavior during dynamic coalescence: for periphery diffusion $\alpha = 3/2$ and so $\beta = 1/5$; for terrace diffusion (correlated) $\alpha = 1$ and $\beta = 1/4$; for uncorrelated diffusion $\alpha = 1/2$ and $\beta = 1/3$. While the Smoluchowski equation strictly applies to dynamic (Brownian) coalescence, numerical simulations have nevertheless indicated that predictions from static coalescence (islands interact by shape fluctuation)

dx.doi.org/10.1021/ma300245s | Macromolecules 2012, 45, 3496−3502

theories do not provide additional length scales that would describe the behavior of the system.[27]

The experimental distributions, plotted in Figure 4, were determined from measurements of the number of islands within a specific area, normalized by the total number of islands. The data describing the island size distributions in the BCP film are plotted in Figure 4a; those for the BCP/NP film are plotted in Figure 4b. The distributions are plotted for two different times, 970 min and 6600 min. We computed probability densities from the data in Figure 4 for the pure BCP and the BCP/NP samples and compared them with the theoretical probability density distribution functions for coarsening. Shown in Figure 5a are the theoretical probability density distribution functions ($F(R/\langle R\rangle)$ vs $R/\langle R\rangle$) that account for Ostwald ripening (detachment-limited, eq 1, and diffusion-limited, eq 2) and for coalescence (eq 3).[34,37,39,40,43]

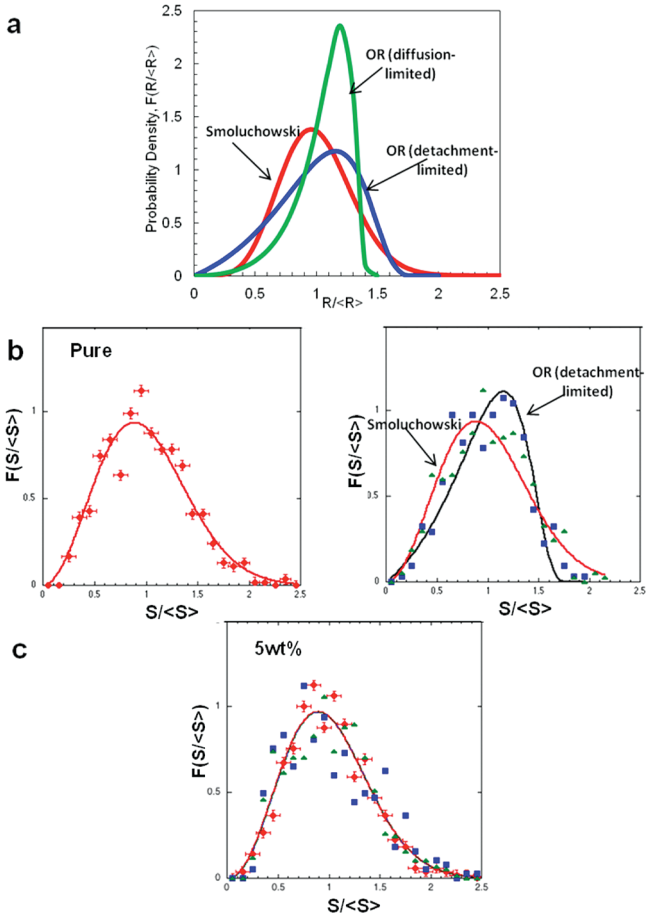


Figure 5. (a) Theoretical probability density distribution functions, $F(R/\langle R\rangle)$ vs $R/\langle R\rangle$, describing Ostwald ripening (detachment-limited and diffusion-limited) and coalescence respectively are plotted. Normalized size distribution of islands ($S/\langle S\rangle$) for pure (part b) and for 5 wt % NP/BCP (part c) samples are shown at different times: t = 150 min (red circles), 3710 min (blue squares), and 6575 min (green triangles). In part b (t = 150 min) the data are best described by the Smoluchowski distribution. At longer times the data are fit by both the Smoluchowski and the detachment-limited OR distributions, in order to illustrate the change in distribution at long times. Note that the peak is shifted slightly to the right, as the positive tail disappeared, when the time increased from 150 to 3710 min. In part c (BCP/NP), the data are well described by the Smoluchowski equation throughout the same time interval.

In the pure BCP film, the coarsening mechanism occurred primarily by coalescence during the initial stages, as shown in Figure 5b, where the Smoluchowski equation is shown to describe the data quite well ($R^2 \sim 0.91$). The growth exponent, β, deduced from the single fitting parameter $\alpha = 1/2$ in Smoluchowski equation turns out to be 1/3, which corresponds well to the experimentally determined exponent ($\beta \sim 0.35$). Notably, for longer time $t > 3710$ min, the data becomes more skewed toward higher values of $S/\langle S\rangle$. The Smoluchowski equation no longer describes the data as well as it did during the earlier stages ($R^2 \sim 0.85$). In fact, these data are now described comparably using the detachment (interface)-limited Ostwald ripening equation ($R^2 \sim 0.86$). This suggests that the Ostwald ripening mechanism becomes more important at later time scales. The images in Figure 2 also confirm the importance of the Ostwald ripening mechanism. The importance of the Ostwald ripening mechanism should not be unexpected: as the distances between the islands increase, it would become increasingly more difficult for a coalescence mechanism to remain operational. A process involving the detachment of chains form the edge of an island, diffusion and attachment to another island, would eventually become energetically more favorable. The transition from coalescence (early growth stage) to Ostwald ripening (later stage) has been observed in other systems such as Cu on Cu(100).[33,34]

The foregoing analysis indicates that the late-stage coarsening of the pure BCP film initially occurs primarily via a coalescence mechanism, but at longer times, as the islands become more separated, the Ostwald ripening mechanism becomes important. The images in Figure 2 are consistent with this assessment. We now return to the BCP/NP system, whose behavior was characterized by a much smaller power law exponent. As shown in Figure 5c, the probability distributions are well described by the Smoluchowski equation for all times, with $R^2 > 0.9$; the fitting parameters were $\alpha = 1/2$ and $\beta = 1/3$. The coarsening rates are clearly much slower than that of the pure BCP film. It follows that because the coalescence process is comparatively fast in the pure BCP system, $\langle S_{BCP}(t)\rangle = t^{0.2}\langle S_{BCP/NP}(t)\rangle$, the average distance between the islands increases more rapidly. Consequently, at later times the coarsening mechanism in the pure BCP proceeds via Ostwald ripening, since long-range mass transport between the islands becomes more favorable. In the BCP/NP system, the islands remain in proximity throughout the same time scales, so coarsening continues to evolve via coalescence.

We found it instructive to examine STEM images of regions of the BCP/NP samples at two very different times (Figure 6) to gain further insight into the details of the coarsening mechanisms, first described in Figure 2. Information in Figures 2 and 6 together provide useful insight into the coalescence processes. The islands labeled 1 and 2, in both Figures 6a and 6b, are typical of islands that have coalesced. The arrows denote the direction of motion of the boundaries. In part b, the coalescence process is more advanced, and the average local curvature is reduced, thereby decreasing the surface area. Examples of this process are shown in Figure 2. The island labeled 3 has decreased in size due to the transfer of chains from its boundaries; this is expected of samples that have undergone Ostwald ripening. The groups of nanoparticles labeled 4 are remnants of islands that have disappeared. The process in the BCP/NP system is very slow due to the larger activation barrier associated with removal of chains from the islands whose cores contain nanoparticles.

dx.doi.org/10.1021/ma300245s | Macromolecules 2012, 45, 3496−3502

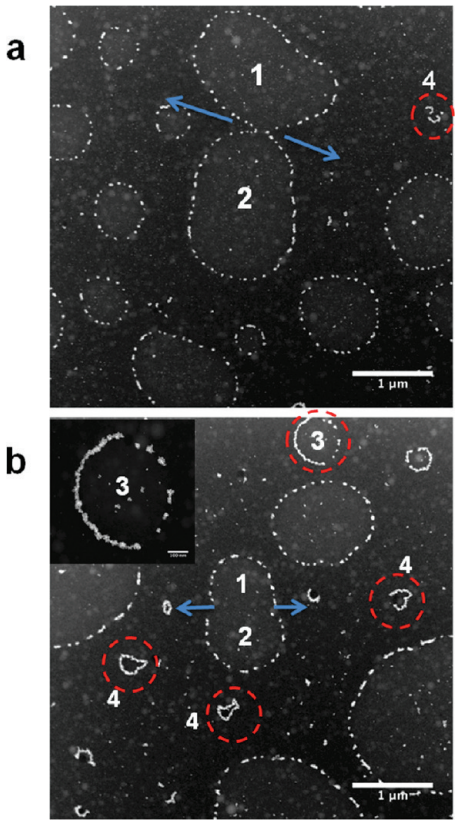


Figure 6. STEM images of PS-*b*-PnBMA with 3 wt % $AuPS_{10}$, annealed for times: t = 2340 min (part a) and 12 000 min (part b). The symbols 1 and 2 in the images denote two typical islands that have undergone coalescence; the process is more complete in part b. The island (encircled) labeled 3 has reduced in size considerably from a much larger size, due to OR (see inset and text). On the other hand, the groups of nanoparticles denoted by 4 are remnants of islands that shrunk and disappeared due to OR.

Finally, we comment on further details of the coarsening process. During coarsening the average distance between the nanoparticle clusters, along the perimeters of the islands, is not constant but fluctuates in separation distance due to local shape fluctuations of the boundaries of the islands. The fluctuations facilitate escape of the chains from the perimeter of the islands; the activation barrier for escape is lower in regions of low particle density. The boundary to the right of the island labeled 3 in Figure 6 shows evidence of a much lower number of particles per unit length, than to the left. The local shape fluctuations of the perimeter of an island enables the detachment of chains and facilitates the ripening process; this enables reshaping of the islands and therefore coalescence.[34,36]

In summary, we examined the dynamics of structural evolution of the surface topography, islands, in a thin film block copolymer/metallic nanoparticle hybrid system. The islands, ubiquitous in BCP thin films, are accommodated by line defects (edge dislocations) that constitute the boundaries of the islands in films of thickness $h < 2L$. The nanoparticles preferentially reside within the defects, along the boundaries of the islands. The topography of the pure BCP film coarsens via two mechanisms. During the initial stages coarsening occurs primarily by coalescence, whereas for longer times when the average separation distance between the islands increase, the Ostwald ripening (where the large islands grow at the expense of the smaller islands, driven by difference in the local chemical potential) becomes increasingly important. In the hybrid system, the rate of coarsening decreases appreciably and occurs primarily via coalescence. Ostwald ripening also occurs in the BCP/NP system, as shown by the images in Figures 2 and 6, but it makes only a small contribution to the structural evolution, compared to the pure BCP system. We anticipate that Ostwald ripening will have an increasingly important contribution to the structural evolution of the BCP/NP system at much longer times, when the separation distance between island increases. Finally, we note that our data are well described by distribution functions predicted by the classical theories. These theories assume that the structure may be characterized by a single length-scale, an average domain radius $\langle R \rangle$, and that the dynamics are self-similar. In this regard the coarsening dynamics in the system is akin to the behavior of a large class of systems, from alloys to magnetic systems that undergo coarsening.

AUTHOR INFORMATION

Notes

The authors declare no competing financial interest.

ACKNOWLEDGMENTS

This research was supported by the DOE office of Science, Basic Energy Sciences (BES), Synthesis and Processing Program, DOE no. DE-FG02-07ER46412.

REFERENCES

(1) Atwater, H. A.; Polman, A. *Nat. Mater.* **2010**, *9* (3), 205−213.
(2) Bockstaller, M.; Kolb, R.; Thomas, E. L. *Adv. Mater.* **2001**, *13* (23), 1783−1786.
(3) Coakley, K. M.; McGehee, M. D. *Chem. Mater.* **2004**, *16* (23), 4533−4542.
(4) Croce, F.; Appetecchi, G. B.; Persi, L.; Scrosati, B. *Nature* **1998**, *394* (6692), 456−458.
(5) Green, P. F. *Soft Matter* **2011**, *7* (18), 7914−7926.
(6) Haryono, A.; Binder, W. H. *Small* **2006**, *2* (5), 600−611.
(7) Nath, N.; Chilkoti, A. *Anal. Chem.* **2001**, *74* (3), 504−509.
(8) Shipway, A. N.; Katz, E.; Willner, I. *ChemPhysChem* **2000**, *1* (1), 18−52.
(9) Stoykovich, M.; Edwards, E.; Solak, H.; Nealey, P. *Phys. Rev. Lett.* **2006**, *97* (14), 147802.
(10) Stoykovich, M.; Muller, M.; Kim, S.; Solak, H.; Edwards, E.; De Pablo, J.; Nealey, P. *Science* **2005**, *308* (5727), 1442.
(11) Bockstaller, M. R.; Mickiewicz, R. A.; Thomas, E. L. *Adv. Mater.* **2005**, *17* (11), 1331−1349.
(12) Alivisatos, A. P.; Johnsson, K. P.; Peng, X.; Wilson, T. E.; Loweth, C. J.; Bruchez, M. P.; Schultz, P. G. *Nature* **1996**, *382* (6592), 609−611.
(13) Lin, Y.; Boker, A.; He, J.; Sill, K.; Xiang, H.; Abetz, C.; Li, X.; Wang, J.; Emrick, T.; Long, S.; Wang, Q.; Balazs, A.; Russell, T. P. *Nature* **2005**, *434* (7029), 55−59.
(14) Spatz, J. P.; Mössmer, S.; Hartmann, C.; Möller, M.; Herzog, T.; Krieger, M.; Boyen, H.-G.; Ziemann, P.; Kabius, B. *Langmuir* **1999**, *16* (2), 407−415.
(15) Sundrani, D.; Darling, S. B.; Sibener, S. J. *Nano Lett.* **2003**, *4* (2), 273−276.
(16) Kim, B. J.; Bang, J.; Hawker, C. J.; Kramer, E. J. *Macromolecules* **2006**, *39* (12), 4108−4114.
(17) Kim, B. J.; Chiu, J. J.; Yi, G.-R.; Pine, D. J.; Kramer, E. J. *Adv. Mater.* **2005**, *17* (21), 2618−2622.
(18) Kim, B. J.; Fredrickson, G. H.; Hawker, C. J.; Kramer, E. J. *Langmuir* **2007**, *23* (14), 7804−7809.
(19) Cheng, J. Y.; Ross, C. A.; Smith, H. I.; Thomas, E. L. *Adv. Mater.* **2006**, *18* (19), 2505−2521.

(20) Guo, Q.; Teng, X.; Rahman, S.; Yang, H. *J. Am. Chem. Soc.* **2002**, *125* (3), 630−631.
(21) Jo, A.; Joo, W.; Jin, W.-H.; Nam, H.; Kim, J. K. *Nat. Nanotechnol.* **2009**, *4* (11), 727−731.
(22) Bita, I.; Yang, J. K. W.; Jung, Y. S.; Ross, C. A.; Thomas, E. L.; Berggren, K. K. *Science* **2008**, *321* (5891), 939−943.
(23) Cheng, J.; Ross, C.; Thomas, E.; Smith, H.; Vancso, G. *Adv. Mater.* **2003**, *15* (19), 1599−1602.
(24) Gido, S.; Gunther, J.; Thomas, E.; Hoffman, D. *Macromolecules* **1993**, *26* (17), 4506−4520.
(25) Gido, S.; Thomas, E. *Macromolecules* **1994**, *27* (21), 6137−6144.
(26) Listak, J.; Bockstaller, M. *Macromolecules* **2006**, *39* (17), 5820−5825.
(27) Kim, J.; Green, P. F. *Macromolecules* **2010**, *43* (24), 10452−10456.
(28) Hamdoun, B.; Ausserré, D.; Joly, S.; Gallot, Y.; Cabuil, V.; Clinard, C. *J. Phys. II* **1996**, *6* (4), 493−501.
(29) Hamdoun, B.; Charara, J.; Zaiour, A. *J. Phys. IV* **2005**, *124*, 91−98.
(30) Orso, K. A.; Green, P. F. *Macromolecules* **1999**, *32* (4), 1087−1092.
(31) Turner, M. S.; Maaloum, M.; AusserrÃ©, D.; Joanny, J. F.; Kunz, M. *J. Phys. II* **1994**, *4* (4), 689−702.
(32) Bassereau, P.; Brodbreck, D.; Russell, T. P.; Brown, H. R.; Shull, K. R. *Phys. Rev. Lett.* **1993**, *71* (11), 1716−1719.
(33) Bray, A. J. *Condens. Matter* **1994**, *43*, 357.
(34) Lo, A.; Skodje, R. T. *J. Chem. Phys.* **2000**, *112* (4), 1966−1974.
(35) Brust, M.; Walker, M.; Bethell, D.; Schiffrin, D. J.; Whyman, R. *J. Chem. Soc., Chem. Commun.* **1994**, *7*, 801−802.
(36) Conti, M.; Meerson, B.; Peleg, A.; Sasorov, P. V. *Phys. Rev. E* **2002**, *65* (4), 046117.
(37) Green, P. F. *J. Polym. Sci., Part B: Polym. Phys.* **2003**, *41* (19), 2219−2235.
(38) Lifshitz, I. M.; Slyozov, V. V. *J. Phys. Chem. Solids* **1961**, *19*, 35−50.
(39) Limary, R.; Green, P. F. *Phys. Rev. E* **2002**, *66* (2), 021601.
(40) Limary, R.; Green, P. F. *Langmuir* **2003**, *19* (6), 2419−2424.
(41) Smoluchowski, M. v. *Phys. Z.* **1916**, 17.
(42) Wagner, C. *Z. Elektrochem. Angew. Phys. Chem.* **1961**, *65*, 581.
(43) Meli, L.; Green, P. F. *ACS Nano* **2008**, *2* (6), 1305−1312.

Macromolecules

Article

pubs.acs.org/Macromolecules

Double Gyroid Network Morphology in Supramolecular Diblock Copolymer Complexes

Ivana Vukovic,[†] Thomas P. Voortman,[†] Daniel Hermida Merino,[‡] Giuseppe Portale,[‡] Panu Hiekkataipale,[§] Janne Ruokolainen,[§] Gerrit ten Brinke,*[,†] and Katja Loos*[,†]

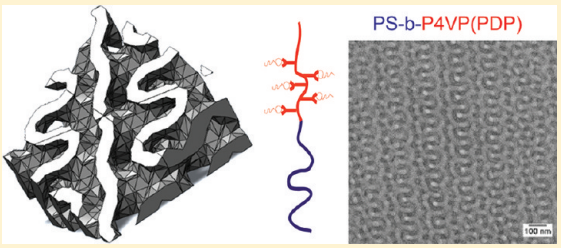
[†]Department of Polymer Chemistry, Zernike Institute for Advanced Materials, University of Groningen, Nijenborgh 4, 9747 AG Groningen, The Netherlands

[‡]Netherlands Organization for Scientific Research, DUBBLE beamline at the ESRF, 6 rue Jules Horowitz, BP 220, 38043, CEDEX 9, Grenoble, France, and Dutch Polymer Institute

[§]Molecular Materials, Department of Applied Physics, Aalto University (formerly Helsinki University of Technology), Puumiehenkuja 2, 02015 Espoo, Finland

Supporting Information

ABSTRACT: The double gyroid network morphology has been the focus of extensive research efforts as one of the most appealing block copolymer structures for practical applications. We performed an extensive study of the phase behavior of the supramolecular complex PS-*b*-P4VP(PDP)$_x$ to develop a systematic route to its double gyroid morphology. The morphological characterization of complexes was accomplished by transmission electron microscopy (TEM) and small-angle X-ray scattering (SAXS). Several compositions with the cubic $Ia\bar{3}d$ symmetry were found in a narrow region between the lamellar and the cylindrical phase. Experimental TEM images were compared to computer simulations of projections through multiple gyroid planes. Typical gyroid patterns—"double wave" and "wagon wheel"—were regularly found. The size of the gyroid unit cell was calculated from the SAXS data. The lattice parameter could be varied (from ca. 70 to 125 nm) by altering the molar mass of the block copolymer precursors. A number of complexes were found to exhibit characteristic biphasic morphologies—coexisting lamellar and gyroid phase or gyroid and cylindrical phase. Finally, gyroid complexes with different relative PDP ratios were obtained which provides the opportunity to generate nanoporous structures with tunable porosities by dissolving the amphiphiles.



INTRODUCTION

Self-assembly in block copolymers has attracted a lot of attention since the development of living anionic polymerization[1] and the subsequent experimental discovery of ordered mesostructures in the simplest linear AB diblock copolymers.[2−6] More complex systems such as triblock and multiblock copolymers, star-type and graft-type copolymers, blends of block copolymers with homopolymers, etc., are found to exhibit a broad variety of novel morphologies.[7−13]

The bicontinuous gyroid morphology has captivated researchers due to a wide range of possible technological applications, such as hybrid solar cells,[14] antireflection structures,[15] photonic crystals,[16] optical metamaterials,[17] etc. In comparison to classical phases (body-centered cubic spheres (BCC), hexagonally ordered cylinders (CYL), and lamellae (LAM)), a bicontinuous gyroid morphology appears over a narrow range of the copolymer composition f in the diblock copolymer phase diagram. It is mostly found in the weak-to-intermediate segregation regime ($10 < \chi N < 40$), and its region in the phase diagram gradually contracts as χN increases, possibly due to the packing frustration induced by narrowing interfaces in the strong segregation regime.[18] Therefore, careful selection of the block copolymer system parameters is required to target the gyroid region of the phase diagram. Another challenge that is of crucial importance for certain applications is the ability to control the domain size in the gyroid unit cell. For instance, interdomain spacing of several hundreds of nanometers is required for a visible-light photonic crystal[16] while it should be comparable to the exciton diffusion length (∼10 nm) for a hybrid solar cell application.[14]

Addition of another component to a block copolymer alters its phase behavior and can affect the appearance of new equilibrium morphologies, particularly between LAM and CYL phases.[19−21] Studies of the phase behavior of diblock copolymer/homopolymer blends have shown that bicontinuous phases can be stabilized by the presence of the homopolymer.[22,23] Another example is the appearance of the core−shell double gyroid morphology when the amphiphilic molecule PDP (pentadecylphenol) is added to the triblock copolymer P*t*BOS-*b*-PS-*b*-P4VP (poly(*tert*-butoxystyrene)-*b*-polystyrene-*b*-poly(4-vinylpyridine)).[24] Moreover, it is possible to tailor the morphology of the system in a simple fashion by varying the relative fraction of the additional component and thus saving the effort of

Received: February 9, 2012
Revised: March 28, 2012
Published: April 6, 2012

 © 2012 American Chemical Society dx.doi.org/10.1021/ma300273f | *Macromolecules* 2012, 45, 3503−3512

synthesizing a block copolymer to achieve the desired morphology.[25]

The focus of this study is the formation of the double gyroid network morphology in supramolecular complexes of amphiphilic PDP and PS-*b*-P4VP (polystyrene-*b*-poly(4-vinylpyridine)) diblock copolymers. PDP molecules interact via hydrogen bonds with pyridine rings to form PS-*b*-P4VP(PDP)$_x$ complexes (x denotes the ratio between PDP molecules and P4VP repeat units). The amphiphiles can be removed in a selective solvent to generate nanoporous structures.[26,27] If the nanoporous material has a continuous morphology, the critical alignment issue is overcome which provides the opportunity for several applications, such as membranes,[28] templates for inorganic materials, etc.[14,15,17,29,30] In our previous work we showed that gyroid PS-*b*-P4VP(PDP)$_x$ complexes can be exploited as precursors for well-ordered metal nanofoams.[31]

In the study of the phase diagram of the PS-*b*-P4VP(PDP)$_{1.0}$ complex, Valkama et al. have reported the formation of the double gyroid morphology in a sample with the weight fraction of PS (f_{PS}) 0.38 and the total molar mass (including PDP) 83 300 g mol^{-1}. When the total molar mass was increased to 129 000 g mol^{-1}, while f_{PS} was maintained constant, the complex adopted a lamellar morphology. The same behavior was noticed with the further increase of the total molar mass of the complex.[32] For the present study we prepared a large number of different PS-*b*-P4VP(PDP)$_x$ samples to systematically study the phase behavior of the supramolecular system in the region of the phase diagram in which the double gyroid morphology was expected. The systems investigated were divided into three groups according to the ratio between the molar mass of the PS block and the P4VP block in the starting block copolymer (this ratio is designated as r). Figure 1 schematically presents the

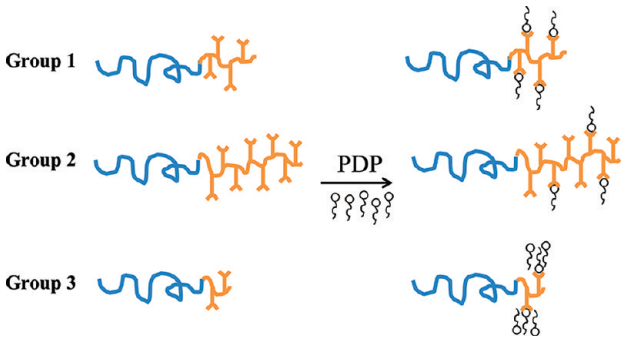


Figure 1. Schematic representation of the block copolymer precursors and the corresponding supramolecular complexes from groups 1, 2, and 3. Ratios r ($r = M_n(PS)/M_n(P4VP)$) for groups 1, 2, and 3 are $r \cong 2.45$, $r < 2.45$, and $r > 2.45$, respectively. The double gyroid morphology of the final supramolecular complex is expected for a comb block weight fraction f(P4VP(PDP)$_x$) of ca. 0.62.[32] To achieve this, different relative amounts x of PDP have to be added to the block copolymer precursors from groups 1, 2, and 3: $x \cong 1.0$, $x < 1.0$, and $x > 1.0$, respectively.

block copolymer precursors and the corresponding supramolecular complexes from groups 1, 2, and 3. Ratios r for groups 1, 2, and 3 were chosen such that double gyroid morphologies in supramolecular complexes, formed upon the addition of PDP, were expected for $x = 1.0$, $x < 1.0$, and $x > 1.0$, respectively. In each group, r was maintained relatively constant while the molar masses of the PS-*b*-P4VP block copolymers were altered which allowed us to move vertically in the phase diagram. Additionally, by adjusting the amount of PDP, the weight fractions of the blocks in the supramolecular complexes were changed and we could move along the x-axis in the phase diagram. Our aim was to understand which parameter values of the system give rise to the gyroid morphology, how we can tune the size of the gyroid unit cell as well as the porosity of the nanoporous gyroid templates, and what the possible limitations are in terms of the molar masses of the starting block copolymers and the size of the structures obtained.

EXPERIMENTAL SECTION

Materials. Diblock copolymers of polystyrene and poly(4-vinylpyridine) were obtained from Polymer Source Inc. The properties of the diblock copolymers studied are listed in Table 1. The polymers were used as received. 3-Pentadecylphenol (PDP) was acquired from Sigma-Aldrich (98 wt % purity) and was recrystallized twice from petroleum ether. Chloroform (p.a., LAB-SCAN) was used as received.

Table 1. Properties of the Diblock Copolymers PS-*b*-P4VP Used in This Study[a]

sample code	M_n(PS), g mol^{-1}	M_n(P4VP), g mol^{-1}	r	PDI
		Group 1		
S4VP-33.5k-1	24 000	9 500	2.53	1.10
S4VP-45.1k-1	31 900	13 200	2.42	1.08
S4VP-53.5k-1	37 500	16 000	2.34	1.30
S4VP-68.3k-1	48 000	20 300	2.36	1.13
		Group 2		
S4VP-21.5k-2	12 000	9 500	1.26	1.09
S4VP-43.5k-2	27 000	16 500	1.64	1.15
S4VP-56.0k-2	35 000	21 000	1.67	1.09
S4VP-65.0k-2	41 000	24 000	1.71	1.09
		Group 3		
S4VP-15.0k-3	11 000	4 000	2.75	1.09
S4VP-32.0k-3	25 000	7 000	3.57	1.10
S4VP-67.0k-3	50 000	17 000	2.94	1.15

[a]The division into three groups is made according to the ratio r between the molar masses of the PS and the P4VP block. The first number in the sample code denotes the total molar mass of the PS-*b*-P4VP block copolymer, and the second number denotes the group to which it belongs.

Preparation of the Polymer Films. Films of the supramolecular complexes were cast by dissolving the PS-*b*-P4VP diblock copolymer and PDP in chloroform. The concentration of polymer was maintained below 2 wt % to ensure homogeneous complex formation, and the solution was stirred for a couple of hours at room temperature. Afterward, the solution was poured into a glass Petri dish, which was subsequently placed into a saturated chloroform atmosphere. Chloroform was allowed to evaporate slowly during several days at room temperature. Subsequently, the samples were dried in vacuum at 30 °C overnight and annealed several days at 120 °C under N_2 atmosphere with 1 bar overpressure to make sure that the morphology represents the equilibrium structure of the melt state of the PS-*b*-P4VP(PDP) complex. Finally, samples were slowly cooled down to room temperature.

Characterization. Transmission electron microscopy was performed on a Philips CM12 transmission electron microscope operating at an accelerating voltage of 120 kV. Images were recorded on a Gatan slow-scan CCD camera. A piece of the film was embedded in an epoxy resin (Epofix, Electron Microscopy Sciences) and cured overnight at 40 °C. The sample was subsequently microtomed to a thickness of about 80 nm using a Leica Ultracut UCT-ultramicrotome and a Diatome diamond knife at room temperature. The microtomed sections were floated on water and subsequently placed on copper grids. To obtain contrast for TEM, the samples were stained with iodine (45 min).

dx.doi.org/10.1021/ma300273f | Macromolecules 2012, 45, 3503−3512

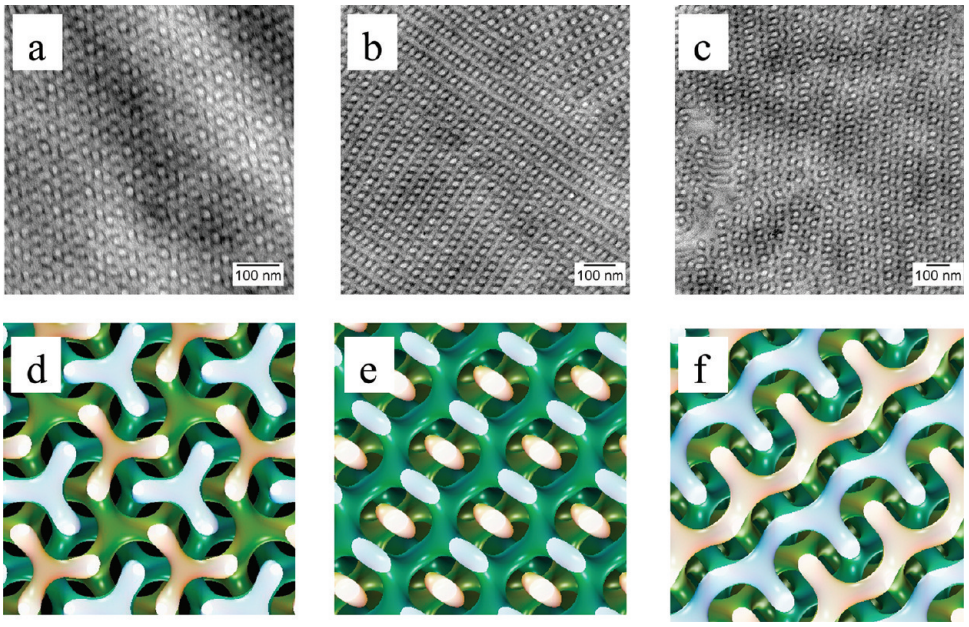


Figure 2. Bright-field TEM images of PS-*b*-P4VP(PDP)$_{1.0}$, f_{PS} = 0.38, M_{total} = 83 300 g mol^{-1} based on S4VP-45.1k-1; panels a, b, and c represent projections through the (111), (110), and (211) gyroid planes, respectively. TEM simulations of the (111), (110), and (211) planes are given in panels d, e, and f, respectively, as a comparison to experimental data.[35]

Small-angle X-ray scattering (SAXS) was performed on two different setups. The first one was at the Dutch-Belgian Beamline (DUBBLE) station BM26B of the European Synchrotron Radiation Facility (ESRF) in Grenoble (France). The sample-to-detector distance was ca. 5 m with a wavelength of 1.033 Å. A Dectris-Pilatus 1M detector with a resolution of 981 × 1043 pixels and a pixel size of 172 × 172 μm has been employed to record the 2D-SAXS scattering patterns. Standard corrections for sample absorption and background subtraction have been performed. The data were normalized with respect to the incident beam intensity in order to correct for primary beam intensity fluctuations. The scattering patterns from rat tail were used for the calibration of the wave vector scale of the scattering curve. The SAXS patterns were acquired at room temperature. The scattering vector q is defined as $q = 4\pi/\lambda \sin\theta$ with 2θ being the scattering angle.[33,34]

The second setup was on the SAXS device in the Nanomicroscopy Center at the Aalto University that consists of a Bruker MICROSTAR microfocus rotating anode X-ray source with Montel Optics (parallel beam, Cu Kα radiation λ = 1.54 Å), where the beam was further collimated using three sets of JJ X-ray 4-blade slits. A sample-to-detector distance of 4.64 m was used. The scattering intensities were measured using a 2D area detector (Bruker HiStar). The samples were measured at room temperature in vacuum.

RESULTS AND DISCUSSION

The weight fraction f of the comb block P4VP(PDP)$_x$ in the supramolecular PS-*b*-P4VP(PDP)$_x$ complex is related to the mass m of the different constituents by

$$f(\mathrm{P4VP(PDP)}) = \frac{m(\mathrm{PDP}) + m(\mathrm{P4VP})}{m(\mathrm{PDP}) + m(\mathrm{P4VP}) + m(\mathrm{PS})} \quad (1a)$$

The mass of PDP can be expressed as

$$m(\mathrm{PDP}) = \frac{m(\mathrm{P4VP})}{105\ \frac{\mathrm{g}}{\mathrm{mol}}} \times x \times 304\ \frac{\mathrm{g}}{\mathrm{mol}} \cong 3x \times m(\mathrm{P4VP}) \quad (1b)$$

Hence

$$f(\mathrm{P4VP(PDP)}) \cong \frac{3x + 1}{3x + 1 + r} \quad (1c)$$

Taking previous experimental results into account,[32] the double gyroid morphology is expected in complexes with a weight fraction of the comblike P4VP(PDP)$_x$ block of ca. 0.62.

Morphological Characterization of the PS-*b*-P4VP(PDP)$_x$ Samples from Group 1. When a stoichiometric ratio between PDP molecules and P4VP monomer units (x = 1.0) is aimed for, block copolymers with a ratio r between molar masses of PS and P4VP block of ca. 2.45 should be used as a precursors for the preparation of supramolecular complexes with potentially double gyroid morphology. The polymers of group 1 (Table 1) have been selected accordingly.

As reported before, our SAXS and TEM investigations confirm that the supramolecular complex PS-*b*-P4VP(PDP)$_{1.0}$ (f_{PS} = 0.38, M_{total} = 83 300 g mol^{-1})[32] prepared from S4VP-45.1k-1 (M_n(PS) = 31 900 g mol^{-1}, M_n(P4VP) = 13 200 g mol^{-1}) forms a double gyroid morphology. Bright-field TEM images representing projections through the (111), (110), and (211) planes of the gyroid unit cell are presented in Figures 2a, 2b, and 2c, respectively. The PS domains appear bright while the P4VP(PDP)$_{1.0}$ domains appear dark due to the iodine staining. Computer-simulated projections (Figures 2d, 2e, and 2f) of cross sections, cut parallel to (111), (110), and (211) gyroid planes, respectively, are obtained by TEMsim[35] and show a good agreement with the experimental data. The typical gyroid patterns, the "wagon wheel" (Figures 2a and 2d) and the "double wave" pattern (Figures 2c and 2f), confirm the morphological assignment. SAXS analysis (Figure 3) of the sample supports the TEM data. The first two reflections are positioned in the q ratio $\sqrt{6}:\sqrt{8}$, and they are attributed to the (211) and (220) spacings of the double gyroid morphology. The intensity ratio 10:1 between the first two peaks is a good indication of the bicontinuous $Ia\bar{3}d$ morphology (as discussed in the literature).[3] The first intensity maximum is centered at

dx.doi.org/10.1021/ma300273f | Macromolecules 2012, 45, 3503−3512

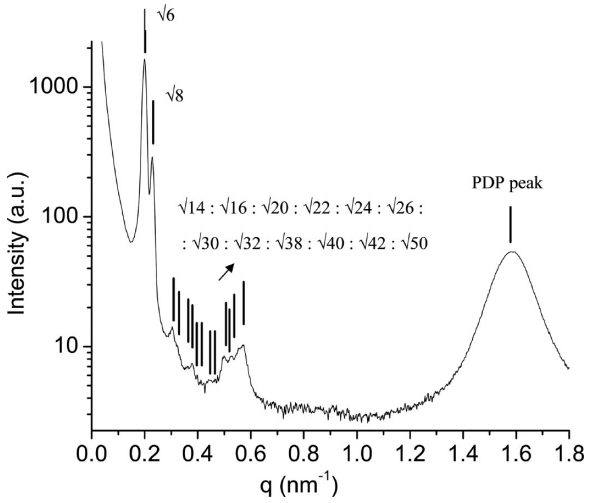


Figure 3. SAXS pattern of PS-*b*-P4VP(PDP)$_{1.0}$, f_{PS} = 0.38, M_{total} = 83 300 g mol^{-1} based on S4VP-45.1k-1. Lines indicate the expected reflections for the gyroid phase (cubic $Ia\bar{3}d$ symmetry), and they are positioned in the ratio $\sqrt{6}:\sqrt{8}:\sqrt{14}:\sqrt{16}:\sqrt{20}:\sqrt{22}:\sqrt{24}:\sqrt{26}:\sqrt{30}:\sqrt{32}:\sqrt{38}:\sqrt{40}:\sqrt{42}:\sqrt{50}$. The reflection at q = 1.58 nm^{-1} corresponds to the lamellar self-assembly within the P4VP(PDP)$_{1.0}$ domains.

q = 0.199 nm^{-1} corresponding to the d_{211} spacing equal to 31.6 nm and the lattice parameter a of 77.3 nm ($a = \sqrt{6}d_{211}$). Higher order gyroid peaks, although with relatively low intensity, are readily visible in the SAXS pattern (Figure 3). A peak centered at q = 1.58 nm^{-1} corresponds to lamellar structures with the lamellar period of 4 nm, formed in the comblike P4VP(PDP)$_{1.0}$ complex due to the microphase separation between the nonpolar PDP alkyl tails and the polar backbone.[36]

The block copolymer S4VP-33.5k-1 (M_n(PS) = 24 000 g mol^{-1}, M_n(P4VP) = 9500 g mol^{-1}) with shorter blocks but similar ratio between the molar masses of the PS and P4VP blocks is used to prepare a set of supramolecular samples by systematically changing the amount of PDP from 0.5 to 1.7, thus reducing f_{PS} from 0.51 to 0.30. As a function of x, the morphology of the complex changes along the pathway LAM ($0.5 \le x \le 0.8$) → GYR ($0.9 \le x \le 1.0$) → CYL ($1.1 \le x \le 1.7$). Figure 4 shows representative TEM images. Well-aligned lamellae of the sample with x = 0.7 are shown in Figure 4a. Figure 4b presents the projection through the (110) plane of the gyroid sample (x = 1.0), and hexagonally ordered cylinders of the sample with x = 1.3 are depicted in Figure 4c. The bicontinuous $Ia\bar{3}d$ morphology is found in the composition range $\Delta f_{PS} \ge 0.02$ (f_{PS} = 0.41 for x = 0.9 and f_{PS} = 0.39 for x = 1.0). SAXS patterns of two gyroid samples from this range are shown in Figure 5. The q ratios of $\sqrt{6}:\sqrt{8}$ and intensity ratios of nearly 10:1 between the first two reflections represent an unambiguous signature of the double gyroid morphology. The first-order reflections are equally positioned for both samples at q = 0.216 nm^{-1}, indicating the size of the unit cells to be 71.2 nm. This implies that the small variation of the PDP amount does not affect the size of the unit cell which can be exploited for the preparation of porous templates with the same interdomain spacing but somewhat different porosity. As calculated, the porosity of the templates prepared from these particular complexes can be varied from 42.5% to 45.1%. However, the size of the gyroid unit cell is influenced by the total molar mass of the starting copolymer, which allows us to

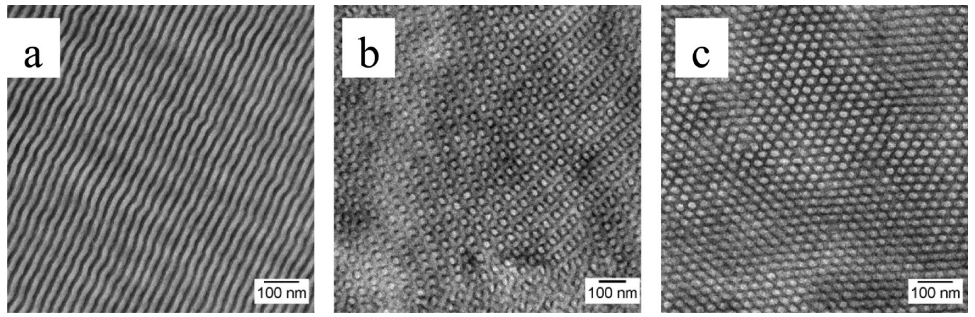


Figure 4. Bright-field TEM images of PS-*b*-P4VP(PDP)$_x$ complexes prepared from the diblock copolymer S4VP-33.5k-1 with x values of (a) 0.7, (b) 1.0, and (c) 1.3.

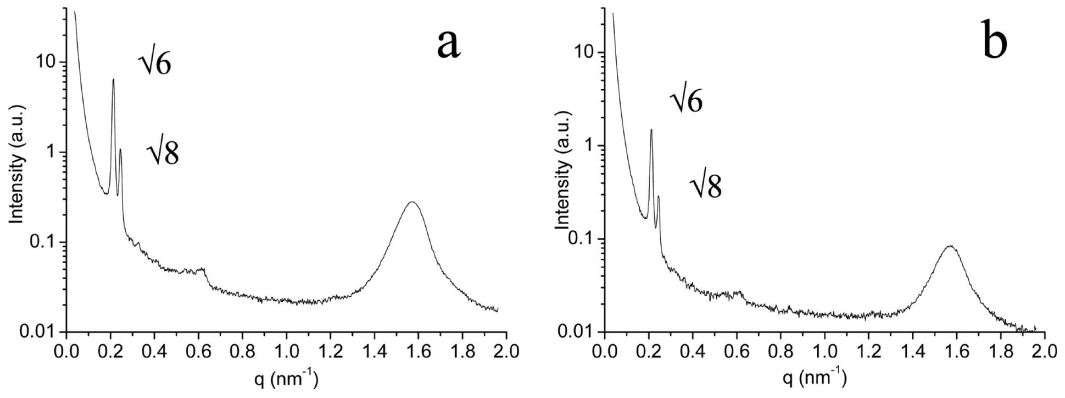


Figure 5. SAXS patterns of PS-*b*-P4VP(PDP)$_x$ complexes with adouble gyroid morphology. The samples are prepared from the diblock copolymer S4VP-33.5k-1 and have x = (a) 0.9 and (b) 1.0.

dx.doi.org/10.1021/ma300273f | *Macromolecules* 2012, 45, 3503−3512

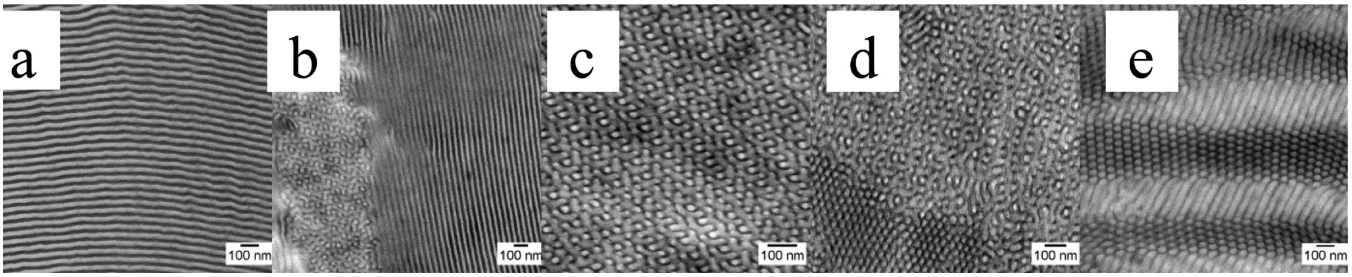


Figure 6. Bright-field TEM images of PS-*b*-P4VP(PDP)$_x$ complexes prepared from the diblock copolymer S4VP-53.5k-1 with x values of (a) 0.6, (b) 0.7, (c) 0.8, (d) 0.9, and (e) 1.0.

adjust the lattice parameter by varying the molar mass of the block copolymer precursor.

To further investigate the phase behavior of the supramolecular complex PS-*b*-P4VP(PDP)$_x$, another set of samples is prepared starting from the diblock copolymer with longer blocks S4VP-53.5k-1 (M_n(PS) = 37 500 g mol^{-1}, M_n(P4VP) = 16 000 g mol^{-1}). The PDP content is varied from x = 0.5 to x = 1.5, which implies a change in the weight fraction of the PS block from 0.49 to 0.30. The morphology of the complexes changes as follows: LAM ($0.5 \leq x \leq 0.6$) → LAM + GYR (x = 0.7) → GYR (x = 0.8) → GYR + CYL (x = 0.9) → CYL ($1.0 \leq x \leq 1.5$). Bright-field TEM images of several representative samples are given in Figure 6. Equally thick alternating PS and P4VP(PDP) lamellae of the sample with x = 0.6 are shown in Figure 6a, the gyroid "double wave" pattern of the sample with x = 0.8 is depicted in Figure 6c, and hexagonally packed cylinders of the sample with x = 1.0 are represented in Figure 6e. Additionally, biphasic morphologies appear as transitional phases between the lamellar and the gyroid phase (Figure 6b, sample with x = 0.7) as well as betweeen the gyroid and the cylindrical phase (Figure 6d, sample with x = 0.9). Biphasic morphologies do not really come as a surprise since theoretical studies on related supramolecular diblock copolymers show their presence in the phase diagram due to the supramolecular nature of the system.[37,38] Grain boundaries between the two coexisting phases can be easily observed in the TEM images. The double gyroid morphology is confirmed in one sample (x = 0.8), and if a slight horizontal move to any side in the phase diagram is made (to x = 0.7 or x = 0.9), the complexes enter the biphasic region. If this is compared with the previously discussed results (Figures 4 and 5), we notice a contraction of the gyroid region with an increase of the molar mass of the block copolymer precursor, as in the case of simple diblock copolymers.[18] The phase behavior of the complexes is further examined by SAXS. The first-order reflection of the lamellar sample (Figure 7) appears at q^* = 0.148 nm^{-1} (hence, lamellar period is 42.4 nm), and another reflection is found at the position $3q^*$. Even-order reflections ($2q^*$, $4q^*$, $6q^*$, etc.) are absent due to the symmetry of the alternating lamellae having equal thickness.[39] In the SAXS pattern of the gyroid sample, the peaks are found at the following positions: $\sqrt{6}q^*$, $\sqrt{8}q^*$, $\sqrt{14}q^*$, $\sqrt{22}q^*$, and $\sqrt{50}q^*$ as indicated with arrows. The first reflection of the gyroid sample coincides with the first reflection of the lamellar sample, implying the size of the gyroid unit cell to be 104 nm. The SAXS pattern of the sample with a coexisting lamellar and gyroid phase is also shown in Figure 7, and it is expected to represent a superposition of the former two patterns. The $\sqrt{6}$:$\sqrt{8}$ q ratio between the first two reflections and higher order peaks indicated with arrows confirm the

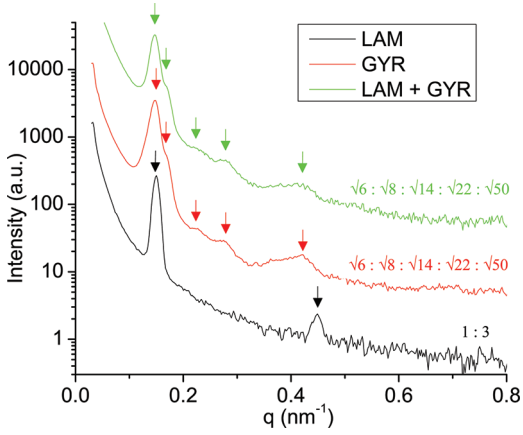


Figure 7. SAXS patterns of PS-*b*-P4VP(PDP)$_x$ complexes prepared from the diblock copolymer S4VP-53.5k-1 with x = 0.6 (black line), x = 0.7 (green line), and x = 0.8 (red line).

existence of the double gyroid regions in the sample. It is rather difficult to confirm the presence of the lamellar phase from SAXS results, since the $3q^*$ lamellar peak would be the only signal to contribute to the SAXS pattern, and it is positioned closely to the gyroid $\sqrt{50}q^*$ peak. The first peak in the SAXS pattern of the cylindrical sample (Figure 8) is centered at

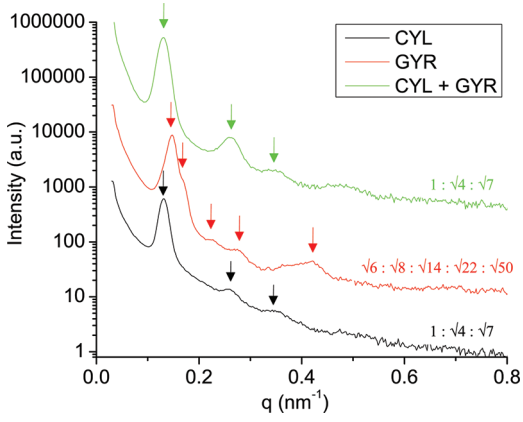


Figure 8. SAXS patterns of PS-*b*-P4VP(PDP)$_x$ complexes prepared from the diblock copolymer S4VP-53.5k-1 with x = 0.8 (red line), x = 0.9 (green line), and x = 1.0 (black line).

q^* = 0.131 nm^{-1} (hence, the calculated distance between the cylinders is 55.4 nm), and higher order peaks positioned at $\sqrt{4}q^*$ and $\sqrt{7}q^*$ confirm the morphological assignment. An identical SAXS pattern with well-defined higher order cylindrical peaks is found in the sample with a coexisting

dx.doi.org/10.1021/ma300273f | *Macromolecules* 2012, 45, 3503−3512

cylindrical and gyroid phase. The absence of gyroid peaks in the biphasic sample could imply that the cylinders represent the majority phase or that the gyroid phase has a low degree of ordering. To better resolve the first two reflections, the gyroid sample was measured for longer time (90 h), and the result is provided in the Supporting Information (Figure 1). Two signals positioned in the q ratio $\sqrt{6}:\sqrt{8}$ (q_1 = 0.148 nm^{-1} and q_2 = 0.171 nm^{-1}) can be clearly observed.

To examine the phase behavior of complexes with even higher molar mass and thus stronger segregation, a series of samples with x ranging from 1.0 to 1.7 is prepared from the block copolymer precursor S4VP-68.3k-1 (M_n(PS) = 48 000 g mol^{-1}, M_n(P4VP) = 20 300 g mol^{-1}). Here a direct transition from the lamellar to the cylindrical phase is found: LAM ($1.0 \leq x \leq 1.1$) → CYL ($1.2 \leq x \leq 1.7$), and the double gyroid morphology is not observed anymore. Representative TEM images are given in Figure 9. This suggests that the double

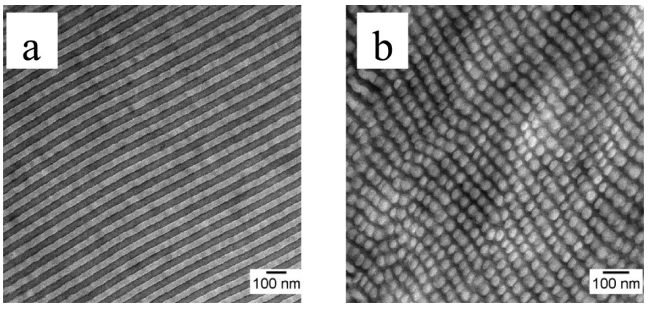


Figure 9. Bright-field TEM images of PS-*b*-P4VP(PDP)$_x$ complexes prepared from the diblock copolymer S4VP-53.5k-1 with values of x = (a) 1.0 and (b) 1.5.

gyroid phase does not exists in supramolecular complexes PS-*b*-P4VP(PDP)$_x$ based on block copolymer precursors of group 1 if the molar mass of the starting block copolymer exceeds a critical value.

The morphological characterization of PS-*b*-P4VP(PDP)$_x$ complexes from group 1 is summarized in Figure 10 and Table 2.

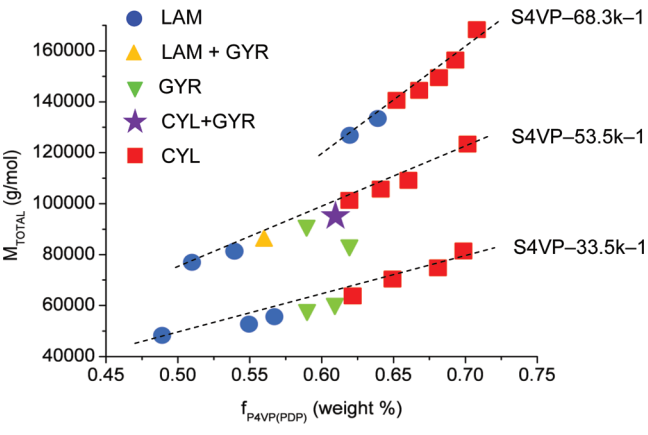


Figure 10. Phase diagram of supramolecular complexes PS-*b*-P4VP(PDP)$_x$ from group 1. The total molar mass of the complex is given on the y-axis while the weight fraction of the comb block is given on the x-axis. Samples connected with dashed lines are prepared from the same block copolymer precursor with code as given.

Morphological Characterization of the PS-*b*-P4VP-(PDP)$_x$ Samples from Group 2. This group of systems is of special interest since now the gyroid morphology is expected for $x < 1$. As has been demonstrated before, PDP molecules can be easily removed from the gyroid supramolecular complex PS-*b*-P4VP(PDP)$_x$ by selective dissolution. We are interested in applications where the porous nanotemplate is backfilled with metal, and subsequently, the polymer support is removed via pyrolysis to create well-ordered metal nanofoams with the inverse gyroid morphology. Since the porosity is inversely proportional to the amount of PDP in the starting supramolecular complex, values of x smaller than 1 are of specific interest.[31] A higher surface area, thus higher porosity of the metallic foam, is desirable for many applications, such as catalysts or actuators. As a guideline for the appearance of the gyroid phase we again prepare samples around $f_{P4VP(PDP)_x} \cong 0.62$.

Table 2. Morphological Characterization of Supramolecular Complexes PS-*b*-P4VP(PDP)$_x$ from Group 1

block copolymer code	x	f_{PS}	morphology
S4VP-45.1k-1	1.0	0.38	GYR
S4VP-33.5k-1	0.5	0.51	LAM
S4VP-33.5k-1	0.7	0.45	LAM
S4VP-33.5k-1	0.8	0.43	LAM
S4VP-33.5k-1	0.9	0.41	GYR
S4VP-33.5k-1	1.0	0.39	GYR
S4VP-33.5k-1	1.1	0.38	CYL
S4VP-33.5k-1	1.3	0.35	CYL
S4VP-33.5k-1	1.5	0.32	CYL
S4VP-33.5k-1	1.7	0.30	CYL
S4VP-53.5k-1	0.5	0.49	LAM
S4VP-53.5k-1	0.6	0.46	LAM
S4VP-53.5k-1	0.7	0.44	LAM + GYR
S4VP-53.5k-1	0.8	0.41	GYR
S4VP-53.5k-1	0.9	0.39	GYR + CYL
S4VP-53.5k-1	1.0	0.38	CYL
S4VP-53.5k-1	1.1	0.36	CYL
S4VP-53.5k-1	1.2	0.34	CYL
S4VP-53.5k-1	1.5	0.30	CYL
S4VP-68.3k-1	1.0	0.38	LAM
S4VP-68.3k-1	1.1	0.36	LAM
S4VP-68.3k-1	1.2	0.35	CYL
S4VP-68.3k-1	1.3	0.33	CYL
S4VP-68.3k-1	1.4	0.32	CYL
S4VP-68.3k-1	1.5	0.31	CYL
S4VP-68.3k-1	1.7	0.29	CYL

The total number of monomer units in the block copolymer precursors of group 2 varies from ca. 215 to 650, and as will be shown, the double gyroid morphology is indeed found in several samples. The TEM image and the SAXS pattern of a representative sample PS-*b*-P4VP(PDP)$_{0.75}$ prepared from the diblock copolymer S4VP-65.0k-2 are given in Figure 11. The gyroid reflections $\sqrt{6}q^*$, $\sqrt{8}q^*$, $\sqrt{30}q^*$, $\sqrt{38}q^*$, and $\sqrt{50}q^*$ are resolved in the SAXS pattern (Figure 9b). The lattice parameter a = 124 nm, as calculated from the position of the first-order reflection at q = 0.124 nm^{-1}. The TEM image (Figure 11a) represents the typical "wagon wheel" gyroid pattern.

In supramolecular complexes prepared from the diblock copolymer with the shortest blocks S4VP-21.5k-2 (M_n(PS) = 12 000 g mol^{-1}, M_n(P4VP) = 9500 g mol^{-1}), the double gyroid phase is found for x = 0.40, and when x is changed by ±0.05, the complex adopts a lamellar and cylindrical morphology.

For the PS-*b*-P4VP precursors with higher molar mass biphasic morphologies are mostly found. TEM images of samples

dx.doi.org/10.1021/ma300273f | Macromolecules 2012, 45, 3503−3512

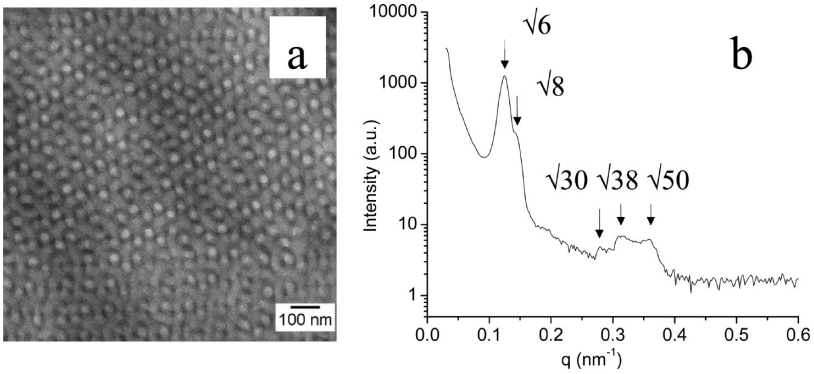


Figure 11. PS-*b*-P4VP(PDP)$_{0.75}$ complex prepared from the diblock copolymer S4VP-65.0k-2: (a) bright-field TEM image representing the projection through the gyroid (111) plane; (b) SAXS pattern of the gyroid sample.

with two coexisting phases are shown in Figure 12. Figure 12a shows a combination of lamellae and gyroids for a sample based on the S4VP-56.0k-2 precursor, whereas well-ordered grains of the gyroid and the cylindrical phase, separated by a transitional phase of poorly ordered cylinders, is depicted in Figure 12b for a sample based on the S4VP-65.0k-2 precursor. Much to our surprise, we observed the sequence GYR + CYL → GYR → CYL rather than the anticipated GYR → GYR + CYL → CYL sequence for the samples prepared from the highest molar mass S4VP-65.0k-2. As an additional surprise, the GYR + CYL region becomes broader with an increase of the molar mass of the block copolymer precursor. This demonstrates the complex nature of the system as compared to simple diblock copolymers. Not only do we have a comblike molecular architecture of the supramolecular block, but in addition the effective interaction between PS and P4VP(PDP)$_x$, and therefore the degree of segregation, depends on the relative amount of PDP, i.e. x.

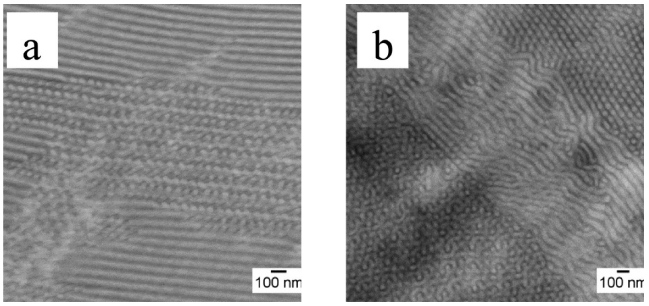


Figure 12. Bright-field TEM images of PS-*b*-P4VP(PDP)$_x$ complexes: (a) S4VP-56.0k-2 precursor, x = 0.53; (b) S4VP-65.0k-2 precursor, x = 0.7.

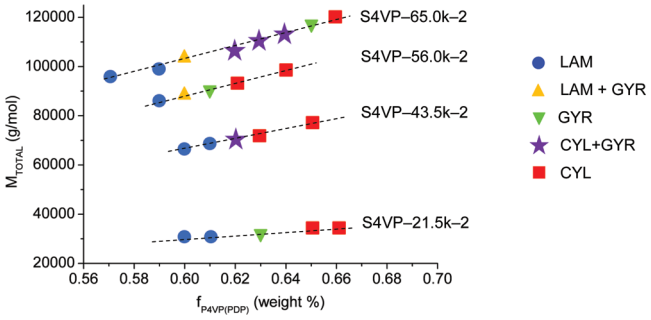


Figure 13. Phase diagram of supramolecular complexes PS-*b*-P4VP(PDP)$_x$ from group 2. The total molar mass of the complex is given at the y-axis while the weight fraction of a comb block is given at the x-axis. Samples connected with a dashed line are prepared from the same block copolymer precursor with the code as given.

The morphological characterization of PS-*b*-P4VP(PDP)$_x$ complexes from group 2 is summarized in Figure 13 and Table 3.

Table 3. Morphological Characterization of Supramolecular Complexes PS-*b*-P4VP(PDP)$_x$ from Group 2

block copolymer code	x	f_{PS}	morphology
S4VP-21.5k-2	0.3	0.40	LAM
S4VP-21.5k-2	0.35	0.39	LAM
S4VP-21.5k-2	0.4	0.37	GYR
S4VP-21.5k-2	0.45	0.35	CYL
S4VP-21.5k-2	0.5	0.34	CYL
S4VP-21.5k-2	1.0	0.24	CYL
S4VP-43.5k-2	0.5	0.40	LAM
S4VP-43.5k-2	0.53	0.39	LAM
S4VP-43.5k-2	0.57	0.38	GYR + CYL
S4VP-43.5k-2	0.6	0.37	CYL
S4VP-43.5k-2	0.7	0.35	CYL
S4VP-56.0k-2	0.5	0.41	LAM
S4VP-56.0k-2	0.53	0.40	LAM + GYR
S4VP-56.0k-2	0.57	0.39	GYR
S4VP-56.0k-2	0.6	0.38	CYL
S4VP-56.0k-2	0.7	0.36	CYL
S4VP-65.0k-2	0.45	0.43	LAM
S4VP-65.0k-2	0.5	0.41	LAM
S4VP-65.0k-2	0.55	0.40	LAM + GYR
S4VP-65.0k-2	0.6	0.38	GYR + CYL
S4VP-65.0k-2	0.65	0.37	GYR + CYL
S4VP-65.0k-2	0.7	0.36	GYR + CYL
S4VP-65.0k-2	0.75	0.35	GYR
S4VP-65.0k-2	0.8	0.34	CYL

Morphological Characterization of the PS-*b*-P4VP(PDP)$_x$ Samples from Group 3. Finally, we discuss the morphology of PS-*b*-P4VP(PDP)$_x$ complexes where a gyroid morphology is anticipated to occur for an excess of PDP molecules with respect to the number of pyridine groups. PS-*b*-P4VP polymers with ca. 150, 320, and 670 monomer units in total and r > 2.45 (Table 1, group 3) are used for this purpose.

Complexes produced from the polymer precursor S4VP-15.0k-3 (M_n(PS) = 11 000 g mol^{-1}, M_n(P4VP) = 4000 g mol^{-1}) with N = 150 and 1.1 ≤ x ≤ 1.5 (0.40 ≥ f_{PS} ≥ 0.34) have a disordered microphase separated morphology as shown by

dx.doi.org/10.1021/ma300273f | *Macromolecules* 2012, 45, 3503−3512

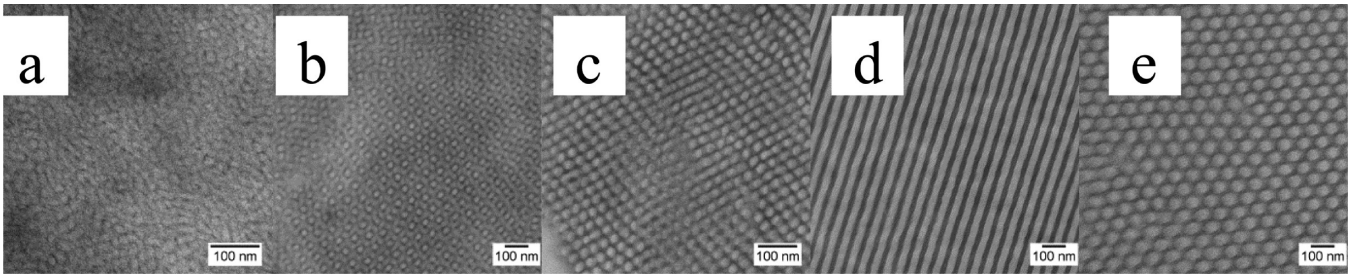


Figure 14. Bright-field TEM images of PS-*b*-P4VP(PDP)$_x$ complexes: (a) S4VP-15.0k-3 precursor, x = 1.1; (b, c) S4VP-32.0k-3 precursor, x = 1.6; (d) S4VP-67.0k-3 precursor, x = 1.1; (e) S4VP-67.0k-3 precursor, x = 1.5.

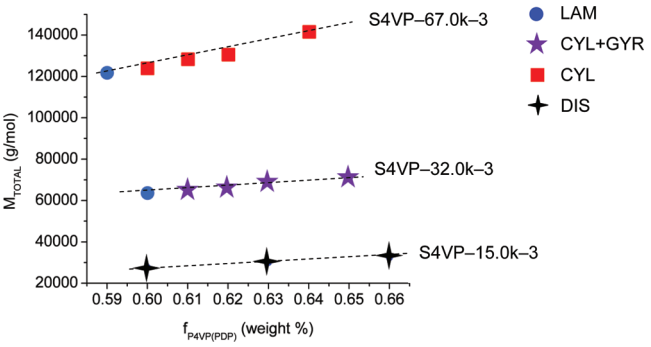


Figure 15. Phase diagram of supramolecular complexes PS-*b*-P4VP(PDP)$_x$ from group 3. The total molar mass of the complex is given at the *y*-axis while the weight fraction of a comb block is given at the *x*-axis. Samples connected with a dashed line are prepared from the same block copolymer precursor with code as given.

Table 4. Morphological Characterization of Supramolecular Complexes PS-*b*-P4VP(PDP)$_x$ from Group 3

block copolymer code	x	f_{PS}	morphology
S4VP-15.0k-3	1.1	0.40	DIS
S4VP-15.0k-3	1.3	0.37	DIS
S4VP-15.0k-3	1.5	0.34	DIS
S4VP-32.0k-3	1.5	0.40	LAM
S4VP-32.0k-3	1.6	0.39	GYR + CYL
S4VP-32.0k-3	1.7	0.38	GYR + CYL
S4VP-32.0k-3	1.8	0.37	GYR + CYL
S4VP-32.0k-3	1.9	0.35	GYR + CYL
S4VP-67.0k-3	1.1	0.41	LAM
S4VP-67.0k-3	1.17	0.40	CYL
S4VP-67.0k-3	1.24	0.39	CYL
S4VP-67.0k-3	1.3	0.38	CYL
S4VP-67.0k-3	1.5	0.36	CYL

TEM (Figure 14a). The value of the interaction parameter between PS and P4VP is on the order of $\chi_{S,4VP} \cong 0.35$.[40,41] Therefore, for the polymer precursor $\chi N \cong 50$, well within the ordered range. The disordered microphase-separated structures of the complexes confirm once again that the addition of PDP to PS-*b*-P4VP reduces the effective interaction parameter between the two phases, PS and P4VP(PDP), respectively.[31]

Samples obtained from the precursor S4VP-32.0k-3 (M_n(PS) = 25 000 g mol^{-1}, M_n(P4VP) = 7000 g mol^{-1}) with x ranging from 1.5 to 1.9 (f_{PS} varies from 0.40 to 0.35) exhibit a lamellar morphology LAM for x = 1.5 and a rather broad biphasic GYR + CYL region for $1.6 \leq x \leq 1.9$. Figures 14b and 14c present a gyroid grain (projection through the (110) plane) and a cylindrical grain as found in a representative biphasic sample (x = 1.6).

If the starting block copolymer has a sufficiently high molar mass (S4VP-67.0k-3, M_n(PS) = 50 000 g mol^{-1}, M_n(P4VP) = 17 000 g mol^{-1}) a direct transition from the lamellar to the cylindrical phase is found: LAM (x = 1.1) → CYL ($1.17 \leq x \leq 1.5$). Representative TEM images are provided in Figures 14d and 14e.

The morphological characterization of PS-*b*-P4VP(PDP)$_x$ complexes from group 3 is summarized in Figure 15 and Table 4.

CONCLUSION

A comprehensive study of the phase behavior of supramolecular complexes PS-*b*-P4VP(PDP)$_x$ from three different groups where the double gyroid morpholohy is anticipated to occur at $x < 1.0$, $x = 1.0$ and $x > 1.0$, respectively, has been conducted. A number of samples exhibiting the double gyroid network morphology were found. The morphological characterization of the complexes from group 1 (gyroid morphology expected for $x \cong 1.0$) indicated a contraction of the width of the gyroid region with an increase in molar mass of the polymer precursor PS-*b*-P4VP, followed by the absence of the cubic $Ia\bar{3}d$ symmetry above a critical value. This was also found for the samples from group 3 ($x > 1.0$). Samples from group 2 behaved differently, in the sense that for the highest molar mass employed a large biphasic window was found with one of the phases being the gyroid phase. Of course, it cannot be excluded that also for this group the gyroid morphology will cease to exist for even higher molar masses.

The size of the gyroid unit cell was tuned by varying the molar mass of the starting block copolymer from a = 71.2 nm to a = 124 nm. The porosities of the nanoporous templates obtained from gyroid supramolecular complexes PS-*b*-P4VP-(PDP)$_x$ by dissolving PDP can be tuned as well since the cubic $Ia\bar{3}d$ symmetry appeared in samples from all three groups, i.e., $x < 1.0$, $x = 1.0$, and $x > 1.0$. The results of this study show how to prepare double gyroid templates with tailored feature sizes and porosities.

ASSOCIATED CONTENT

Supporting Information

Figure 1. This material is available free of charge via the Internet at http://pubs.acs.org.

AUTHOR INFORMATION

Corresponding Author

*E-mail: k.u.loos@rug.nl (K.L.); g.ten.brinke@rug.nl (G.t.B.).

Notes

The authors declare no competing financial interest.

■ ACKNOWLEDGMENTS

We acknowledge Marc Stuart for his help with TEM.

■ REFERENCES

(1) Szwarc, M. 'Living' Polymers. *Nature* **1956**, *178*, 1168−1169.
(2) Bates, F. S.; Fredrickson, G. H. Block Copolymer Thermodynamics: Theory and Experiment. *Annu. Rev. Phys. Chem.* **1990**, *41*, 525−527.
(3) Hajduk, D. A.; Harper, P. E.; Gruner, S. M.; Honeker, C. C.; Kim, G.; Thomas, E. L.; Fetters, L. J. The Gyroid: A New Equilibrium Morphology in Weakly Segregated Diblock Copolymers. *Macromolecules* **1994**, *27*, 4063−4075.
(4) Schulz, M. F.; Bates, F. S.; Almdal, K.; Mortensen, K. Epitaxial Relationship for Hexagonal-to-Cubic Phase Transition in a Block Copolymer Mixture. *Phys. Rev. Lett.* **1994**, *73*, 86−89.
(5) Hamley, I. W. *The Physics of Block Copolymers*; Oxford University Press: Oxford, 1998.
(6) Meuler, A. J.; Hillmyer, M. A.; Bates, F. S. Ordered Network Mesostructures in Block Polymer Materials. *Macromolecules* **2009**, *42*, 7221−7250.
(7) Bates, F. S.; Fredrickson, G. H. Block Copolymers−Designer Soft Materials. *Phys. Today* **1999**, *52*, 32−38.
(8) Epps, T. H. III; Cochran, E. W.; Bailey, T. S.; Waletzko, R. S.; Hardy, C. M.; Bates, F. S. Ordered Network Phases in Linear Poly(isoprene-b-styrene-b-ethylene oxide) Triblock Copolymers. *Macromolecules* **2004**, *37*, 8325−8341.
(9) Abetz, V.; Simon, P. F. W. Phase Behavior and Morphologies of Block Copolymers. *Adv. Polym. Sci.* **2005**, *189*, 125−212.
(10) Tyler, C. A.; Qin, J.; Bates, F. S.; Morse, D. C. SCFT Study of Nonfrustrated ABC Triblock Copolymer Melts. *Macromolecules* **2007**, *40*, 4654−4668.
(11) Matsushita, Y. Creation of Hierarchically Ordered Nanophase Structures in Block Polymers Having Various Competing Interactions. *Macromolecules* **2007**, *40*, 771−776.
(12) Gobius du Sart, G.; Vukovic, I.; Alberda van Ekenstein, G. O. R.; Polushkin, E.; Loos, K.; ten Brinke, G. Self-Assembly of Supramolecular Triblock Copolymer Complexes. *Macromolecules* **2010**, *43* (6), 2970−2980.
(13) Faber, M.; Voet, V. S. D.; ten Brinke, G.; Loos, K. Preparation and Self-Assembly of Two-Length-Scale A-b-(B-b-A)$_n$-b-B Multiblock Copolymers. *Soft Matter* **2012**, *8*, 4479.
(14) Crossland, E. J. W.; Kamperman, M.; Nedelcu, M.; Ducati, C.; Wiesner, U.; Smilgies, D. M.; Toombes, G. E. S.; Hillmyer, M. A.; Ludwigs, S.; Steiner, U.; Snaith, H. J. A Bicontinuous Double Gyroid Hybrid Solar Cell. *Nano Lett.* **2009**, *9*, 2807−2812.
(15) Hsueh, H. Y.; Chen, H. Y.; She, M. S.; Chen, C. K.; Ho, R. M.; Gwo, S.; Hasegawa, H.; Thomas, E. L. Inorganic Gyroid with Exceptionally Low Refractive Index from Block Copolymer Templating. *Nano Lett.* **2010**, *10*, 4994−5000.
(16) Urbas, A. M.; Maldovan, M.; DeRege, P.; Thomas, E. L. Bicontinuous Cubic Block Copolymer Photonic Crystals. *Adv. Mater.* **2002**, *14*, 1850−1853.
(17) Vignolini, S.; Yufa, N. A.; Cunha, P. S.; Guldin, S.; Rushkin, I.; Stefik, M.; Hur, K.; Wiesner, U.; Baumberg, J. J.; Steiner, U. A 3D Optical Metamaterial Made by Self-Assembly. *Adv. Mater.* **2011**, DOI: 10.1002/adma.201103610.
(18) Cochran, E. W.; Garcia-Cervera, C. J.; Fredrickson, G. H. Stability of the Gyroid Phase in Diblock Copolymers at Strong Segregation. *Macromolecules* **2006**, *39*, 2449−2451.
(19) Matsen, M. W. Phase behavior of block copolymer/homopolymer blends. *Macromolecules* **1995**, *28* (17), 5765−5773.
(20) Hayashida, K.; Takano, A.; Arai, S.; Shinohara, Y.; Amemiya, Y.; Matsushita, Y. Systematic Transitions of Tiling Patterns Formed by ABC Star-Shaped Terpolymers. *Macromolecules* **2006**, *39* (26), 9402−9408.
(21) Lo, C. T.; Lee, B.; Pol, V. G.; Dietz Rago, N. L.; Seifert, S.; Winans, R. E.; Thiyagarajan, P. Effect of Molecular Properties of Block Copolymers and Nanoparticles on the Morphology of Self-Assembled Bulk Nanocomposites. *Macromolecules* **2007**, *40* (23), 8302−8310.
(22) Ajdari, A.; Leibler, L. Bending moduli and stability of copolymer bilayers. *Macromolecules* **1991**, *24*, 6803−6805.
(23) Xi, H.; Milner, S. T. Bicontinuous Phase in Diblock Copolymer Melts with Added Homopolymer. *Macromolecules* **1996**, *29* (7), 2404−2411.
(24) Gobius du Sart, G.; Vukovic, I.; Vukovic, Z.; Polushkin, E.; Hiekkataipale, P.; Ruokolainen, J.; Loos, K.; ten Brinke, G. Nanoporous Network Channels from Self-Assembled Triblock Copolymer Supramolecules. *Macromol. Rapid Commun.* **2011**, *32*, 366−370.
(25) Nandan, B.; Vyas, M. K.; Böhme, M.; Stamm, M. Composition-Dependent Morphological Transitions and Pathways in Switching of Fine Structure in Thin Films of Block Copolymer Supramolecular Assemblies. *Macromolecules* **2010**, *43*, 2463−2473.
(26) Ikkala, O.; ten Brinke, G. Functional Materials Based on Self-Assembly of Polymeric Supramolecules. *Science* **2002**, *295*, 2407−2409.
(27) Mäki-Ontto, R.; de Moel, K.; de Odorico, W.; Ruokolainen, J.; Stamm, M.; ten Brinke, G.; Ikkala, O. "Hair Tubes": Mesoporous Materials Containing Hollow Self-Organized Cylinders with Polymer Brushes at the Walls. *Adv. Mater.* **2001**, *13*, 117−121.
(28) Hillmyer, M. A. Nanoporous Materials from Block Copolymer Precursors. *Adv. Polym. Sci.* **2005**, *190*, 137−181.
(29) Crossland, E. J. W.; Ludwigs, S.; Hillmyer, M. A.; Steiner, U. Control of Gyroid Forming Block Copolymer Templates: Effects of an Electric Field and Surface Topography. *Soft Matter* **2010**, *6*, 670−676.
(30) Urade, V. N.; Wei, T. C.; Tate, M. P.; Kowalski, J. D.; Hillhouse, H. W. Nanofabrication of Double-Gyroid Thin Films. *Chem. Mater.* **2007**, *19*, 768−777.
(31) Vukovic, I.; Punzhin, S.; Vukovic, Z.; Onck, P.; De Hosson, J.; Th., M.; ten Brinke, G.; Loos, K. Supramolecular Route to Well-Ordered Metal Nanofoams. *ACS Nano* **2011**, *5* (8), 6339−6348.
(32) Valkama, S.; Ruotsalainen, T.; Nyka1nen, A.; Laiho, A.; Kosonen, H.; ten Brinke, G.; Ikkala, O.; Ruokolainen, J. Self-Assembled Structures in Diblock Copolymers with Hydrogen-Bonded Amphiphilic Plasticizing Compounds. *Macromolecules* **2006**, *39*, 9327−9336.
(33) Borsboom, M.; Bras, W.; Cerjak, I.; Detolleneare, D.; Glastra van Loon, D.; Goedtkindt, P.; Konijnenburg, M.; Lassing, P.; Kevine, Y. K.; Munneke, B.; Oversluizen, M.; van Tol, R.; Vlieg, E. The Dutch−Belgian Beamline at the ESRF. *J. Synchrotron Radiat.* **1998**, *5*, 518−520.
(34) Bras, W.; Dolbnya, I. P.; Detollenaere, D.; van Tol, R.; Malfois, M.; Greaves, G. N.; Ryan, A. J.; Heeley, E. Recent Experiments on a Combined Small-Angle/Wide-Angle X-ray Scattering Beam Line at the ESRF. *J. Appl. Crystallogr.* **2003**, *36*, 791−794.
(35) Available at https://secure.msri.org/about/sgp/jim/software/temsim/index.html.
(36) Ruokolainen, J.; Torkkeli, M.; Serimaa, R.; Komanschek, B. E.; Ikkala, O.; ten Brinke, G. Order−Disorder Transitions in Polymer−Surfactant Systems. *Phys. Rev. E* **1996**, *54*, 6646−6649.
(37) Angerman, H. J.; ten Brinke, G. Weak Segregation Theory of Microphase Separation in Associating Binary Homopolymer Blends. *Macromolecules* **1999**, *32*, 6813−6820.
(38) Feng, E. H.; Lee, W. B.; Fredrickson, G. H. Supramolecular Diblock Copolymers: A Field−Theoretic Model and Mean−Field Solution. *Macromolecules* **2007**, *40*, 693−702.
(39) Hamley, I. W.; Castelleto, V. Small-Angle Scattering of Block Copolymers in the Melt, Solution and Crystal States. *Prog. Polym. Sci.* **2004**, *29*, 909−948.
(40) Alberda van Ekenstein, G. O. R.; Meyboom, R.; ten Brinke, G.; Ikkala, O. Determination of the Flory−Huggins Interaction Parameter

of Styrene and 4-Vinylpyridine Using Copolymer Blends of Poly-(styrene-co-4-vinylpyridine) and Polystyrene. *Macromolecules* **2000**, *33*, 3752−3756.

(41) Zha, W.; Han, C. D.; Lee, D. H.; Han, S. H.; Kim, J. K.; Kang, J. H.; Park, C. Origin of the Difference in Order-Disorder Transition Temperature between Polystyrene-block-poly(2-vinylpyridine) and Polystyrene-block-poly(4-vinylpyridine) Copolymers. *Macromolecules* **2007**, *40*, 2109−2119.

Macromolecules

Article

pubs.acs.org/Macromolecules

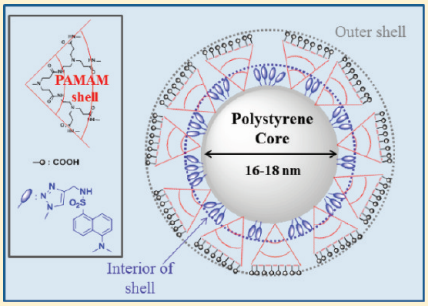
Azido-Coated Nanoparticles: A Versatile Clickable Platform for the Preparation of Fluorescent Polystyrene Core–PAMAM Shell Nanoparticles

Guillaume Rousseau, Hélène Fensterbank, Krystyna Baczko, Manuel Cano, Emmanuel Allard,* and Chantal Larpent

Institut Lavoisier de Versailles UMR-CNRS 8180, Université de Versailles-Saint-Quentin-en-Yvelines, 45 avenue des Etats-Unis, 78035 Versailles cedex, France

Supporting Information

ABSTRACT: The convergent synthesis of fluorescent polystyrene core–PAMAM shell nanoparticles in the 15–20 nm diameter range is presented using azido-coated nanoparticles (NP_{N3}) as a clickable platform. The coupling of the different partners occurs exclusively on the surface of the cross-linked polystyrene matrix owing to its nonswelling properties in water. PAMAM dendrons having an alkyne moiety at their focal point and peripheral carboxylic acid groups were covalently attached to the surface of azido-coated nanoparticles via a CuAAC reaction. Given the high density of azide anchoring groups on the NP surface (about 560 N_3 per NP) and the size of the PAMAM derivative, the grafting of dendrons was not complete, leaving azide units available for further functionalization with an alkyne dansyl derivative. These new dendron-coated nanoparticles, which possess a number of terminal functional groups comparable to the high eighth generation of PAMAM dendrimers, are obtained in a few steps without tedious chromatographic purification. Dendritic shell saturation levels of 70–85% were reached for these dendron-coated nanoparticles. The colloidal stability of the resulting scaffold was governed by the dendritic shell. Particularly, a pH-dependent electrostatic self-assembly process between the ammonium moieties of the cationic surfactant and carboxylate groups of PAMAM can be switched. This straightforward strategy gives access to dendron-coated nanoparticles as valuable building blocks for the construction of functional nanomaterials.



INTRODUCTION

Nanoparticles have attracted considerable interest over the past decade due to their unique physical and chemical properties that can be exploited in a wide range of applications such as in materials science[1] and biology.[2] Most of these applications require careful design of the nanoparticles and reliable strategies for constructing functional nanomaterials. Indeed, the properties of NPs are not only governed by their composition but are also influenced by their surface constitution. For example, many practical applications of inorganic nanoparticles require covering their surface with ligands to prevent NP aggregation, ensuring that their properties do not change, as well as to provide handles for convenient peripheral functionalization. The surface functionalization can be achieved through the use of polymers,[3] surfactants,[3,4] dendrimers, and other dendritic structures.[5]

Dendrimers and dendrons are the most intensely investigated subset of dendritic polymers.[6,7] Dendrimers are well-defined, monodispersed, three-dimensional macromolecules with a definite molecular weight. They contain three basic architectural components: a core, an interior of shells (generations) consisting of repeating branch-cell units, and terminal functional groups (the outer shell or periphery). The properties of dendrimers are dominated by the very high density of peripheral functional groups, although the internal cavities are also of a great significance due to their ability to encapsulate molecules or ions. Dendrons are associated with dendrimers since they represent a structural component of the parent dendrimer. Dendrons differ from dendrimers in their structure by their bifunctional nature. They possess a focal point that is functionalized differently than the periphery. This focal point allows dendrons to be grafted onto other molecules or solid supports.

Dendrimers are used as nanoreactors for templating metal nanoparticles leading to so-called dendrimer-encapsulated nanoparticles[8] (DENs) as well as surfactants adsorbing on the growing inorganic NPs affording dendrimer-stabilized nanoparticles (DSNs).[5] As far as dendrons are concerned, they can be associated with NPs through (i) direct ligand exchange processes,[9] (ii) direct-capping syntheses,[10] or (iii) covalent linkage.[11]

In parallel to the development of inorganic NPs, polymer nanoparticles have received considerable interest because well-documented polymerization techniques in microheterogeneous

Received: January 17, 2012
Revised: March 9, 2012
Published: April 6, 2012

ACS Publications © 2012 American Chemical Society

media can provide control over the size, charge, functionality, and colloidal stability.[12] Numerous particles incorporating functionalities on the surface and/or within the polymer core have been produced for a variety of applications.[13,14] In particular, the polymerization of hydrophobic monomers in an oil-in-water microemulsion was found to give access to stable aqueous suspension of well-defined ultrafine particles, so-called nanolatexes, in the nanosized diameter range (15−30 nm).[15] We have recently reported two strategies to prepare aqueous suspension of azido-functionalized polystyrene nanoparticles using this technique.[16] The two synthetic routes developed in this work led to structurally different nanoparticles in the 15−20 nm diameter range with azide groups located only on the surface (postfunctionalization route) or distributed in the core and on the surface (copolymerization route). The high surface-to-volume ratio of these nanometer-sized particles provides remarkable accessibility of the functional groups, ensuring multiple anchoring sites on the NPs surface. The grafting of hydrophobic and hydrophilic alkynes derivatives was particularly efficient using CuAAC reaction. Moreover, compared to previously clickable polymeric nanomaterials reported in the literature,[17] cross-linked polystyrene-based NPs are not swollen in water. Thus, the coupling of alkynes through CuAAC reaction can be performed only on the NPs surface, leaving the particle core available for further functional arrangements. We believe that these structurally programmed azide-functionalized NPs are promising clickable platforms for the synthesis of functional nano-objects, especially for the design of new dendronized polystyrene nanoparticles.

Chemical modification of polymer nanoparticles with dendrimers or dendrons has been scarcely studied. Hawker and Wooley reported a series of researches on the preparations of shell or core cross-linked nanoparticles from amphiphilic polymers assembled into micelles.[18] They used multifunctional dendritic cross-linkers that give rise to the simultaneous stabilization of supramolecular assemblies and the introduction of reactive groups within the shell or core domain. Gillies and co-workers have recently described a new approach for the surface functionalization of vesicles assembled from polymers with dendrons having alkyne moieties at their focal point via a Cu(I)-catalyzed azide and alkyne cycloaddition reaction.[19] This study reveals that the use of dendritic scaffolds to display peripheral biological ligands on the polymer surfaces leads to an enhanced binding affinity of these ligands. As the micrometer-scale sizes of these vesicles were unsuitable for in-vivo circulation, Gillies et al. further explored the development of micelles and vesicles conjugated to dendrons functionalized with peripheral amines, guanidines, or hydroxyl groups in the nanoscale range.[20] Larpent and co-workers have previously reported the postfunctionalization of already formed NPs with a phosphorus containing dendron to give dendronized NPs[21] as well as with polypropylenimine (PPI) dendrimer to afford polyaminodendrimer-coated NPs.[22] These studies have shown that the properties and reactivity in solution of the resulting NPs were governed by the dendritic shell. The polyaminodendrimer-coated NPs were also functionalized with various dyes and led to colored nanolatexes.[22]

Owing to the efficiency of the click CuAAC reaction on the azide NPs,[16] we decided to assess the grafting of dendrons onto the surface of azide-functionalized nanoparticles obtained from the postfunctionalization route. We can expect that given the high density of azide units on the surface of NP and the large size of dendrons, the grafting should not be complete. This should afford giant dendrimer-like particles[21] in which surface modification through peripheral moieties of the dendrons could be envisioned via self-assembling processes or covalent linkages. Unlike the polyaminodendrimer-coated NPs in which the surface functionalization is limited at this point to the PPI surface dendrimer,[22] modification of our nano-objects should not be limited to the dendron surfaces but could be extended at will to the surface of the polystyrene core via the residuals azide units.

Herein, we describe the preparation of core−shell functional nanostructures in the 15−20 nm diameter range by covalent attachment of a PAMAM dendron having an alkyne moiety at its focal point and peripheral carboxylic acids to azide coated polystyrene-based NP surfaces using CuAAC reaction.[23,24] The azido-coated nanoparticles were prepared using the post-functionalization route. Cross-linked polystyrene nanoparticles are not swollen in water. Therefore, the functionalization within the nanoparticles cannot occur. Dendrons have been preferred to dendrimers because their structure possesses a focal point that is functionalized differently than the peripheral moieties. Their focal point allows dendrons to be grafted onto the nanoparticles surface and stand the carboxylic acid units free for further surface functionalization. The use of dendrons also prevents the interparticle linkages which can be observed with dendrimers coated nanoparticles. Given the high density of azide anchoring groups on the NP surface as well as the size of PAMAM dendrons, the grafting of the dendron is not complete, leaving azide units located around the core. The nano-objects thereby obtained possess three basic architectural components: a polystyrene core bearing azide units on its surface, a PAMAM shell, and peripheral functional groups (the outer shell). This efficient strategy allows the synthesis of giant dendrimer-like particles from nanolatexes using earlier generations of PAMAM dendrons. Dendron-coated nanoparticles are obtained in a few steps without tedious chromatographic purification. Dendritic shell saturation levels of 70−85% were reached in these nano-objects in which the availability and reactivity of the remaining azides has been demonstrated by grafting a dansyl derivative.

EXPERIMENTAL SECTION

Materials. Dodecyltrimethylammonium bromide (DTAB, Fluka, 98%), sodium azide (Acros, 99%), copper(II) sulfate anhydrous (Fischer, 98%), sodium ascorbate (Acros, 99%), propargylamine hydrochloride (Sigma-Aldrich, 95%), dansyl chloride (Alfa-Aesar, 99%), methyl acrylate (Acros, 99%), and ethylenediamine (Fluka, 100%) were used as received. Triethylamine (Acros, 99%) was distilled under nitrogen before use. Dichloromethane was dried and distilled under CaH_2 prior to use. All other solvents were used as received. MilliRo Water and Milli-Q water were used for microemulsion polymerization and sample dilution, respectively.

PAMAM derivatives **1**-($G_{0.5}$) and **3**-($G_{1.5}$)[25] and dansyl derivative **5**[16] were prepared according to the previously published procedures.

Measurements. ^{1}H NMR and ^{13}C NMR spectra were recorded using a Bruker AM300 spectrometer at 300 MHz (^{1}H) and at 75 MHz (^{13}C) in DMSO-d_6 or $CDCl_3$. Chemical shifts δ were referenced to internal solvent $CDCl_3$ (7.27 and 77.00 ppm) or DMSO-d_6 (2.50 and 39.50 ppm).[26]

ESI-MS mass spectra were obtained with a Waters Xevo Qtof. The infrared spectra were recorded using a FTIR apparatus (Nicolet 550). Elemental analyses have been obtained from the Service Central d'Analyze (CNRS, Vernaison, France) and the Service de Microanalyse (ICSN, Gif-sur-Yvette, France). UV/vis analyses were performed on a Perkin-Elmer spectrophotometer UV/vis/NIR Lambda 19. Steady-state fluorescence measurements were recorded

on a spectrofluorimeter FluoroMax-3 equipped with a 150 W xenon lamp and a slit width of 5 nm. For all measurements the samples were diluted so that the maximum of absorbance is less than 0.1 to avoid reabsorption artifact. The mean hydrodynamic diameter and the polydispersity index (PDI) of the nanoparticles were measured by quasi-elastic light scattering (QELS) with a Brookhaven 90Plus. PDI ≤ 0.100 corresponds to reasonably narrow monomodal distribution latexes. The samples were diluted 100 times in MilliRo water and then filtered through a 0.22 μm membrane to remove dust. For each sample, the measurement was performed three times at a temperature of 25 °C with a detection angle of 90°. AFM measurements were made using tapping mode operation with a Digital Instrument 3100 and a Nanoscope IIIa controller. Tapping mode etched silicon probes from Veeco (TESP-SS, spring constant k_0: 20−80 N m^{-1} and constant force f_0: 300−371 kHz) with a 3.5−4.5 nm radius of curvature were used. Mica substrates were prepared by cleaving to produce a smooth surface prior to sample deposition. The nanolatexes were diluted 4 × 10^4 times in water (so that the final concentrations of nanoparticles and surfactant were respectively 2.25 × 10^{-4} and 2.5 × 10^{-4} g L^{-1}). 10 μL of the dilute solutions was deposited on 9 mm mica disks and allowed to dry at room temperature for 12 h. AFM images were analyzed using WSxM software 5.0 Develop 4.2.[27]

Dialyses were performed using either Spectra/Por regenerated cellulose membranes with 12 000−14 000 g mol^{-1} molecular weight cutoff (MWCO) or an ultrafiltration device (Vivascience, Vivaspin concentrator 20, PES) with a 50 000 g mol^{-1} MWCO.

Separation of the Resulting Polymers for IR and Elemental Analyses. The polymers were isolated and purified using the following procedure: the polymer was flocculated by adding 20 mL of methanol to 2 g of suspension and separated by centrifugation (8000 rpm, 15 min). The resulting white precipitate was extensively washed with demineralized water (stirring for 1 h followed by centrifugation) and finally dried at 50 °C (method A). When the polymer was not flocculated by adding methanol, the polymer was isolated by extensive dialysis of the suspension against water (at least 10 times), then by washing the polymer with hot water (200 mL), and finally drying at 50 °C (method B).

General Procedure for the Preparation PAMAM[CO_2H]$_n$. A solution of PAMAM[CO_2CH_3]$_n$ (**1**-($G_{0.5}$) or **3**-($G_{1.5}$)) in HCl (1 M) was stirred 3 days at RT and 3 days at 50 °C until completion of the reaction as monitored by ^{1}H NMR. The solvent was evaporated and the residue formed was dried in vacuum during 24 h.

Synthesis of Acid 2-($G_{0.5}$) PAMAM[CO_2H]$_4$. Starting from PAMAM[CO_2CH_3]$_4$ **1**-($G_{0.5}$) (6 g, 96 mmol) in HCl 1 M (500 mL) the target acid **2**-($G_{0.5}$) was obtained as a yellowish solid (5.4 g, 99%). ^{1}H NMR (300 MHz, DMSO-d_6) was performed at 323 K to improve the resolution, δ (ppm): 2.72−2.88 (m, 12H, H_4 and H_9), 3.18 (m, 4H, H_7), 3.34 (m, 12H, H_3 and H_8), 3.48 (m, 4H, H_6), 3.84 (m, 1H, H_1), 4.08 (dd, 2H, J = 1.6 Hz, J = 7.2 Hz, H_2), 8.51 (t, 2H, J = 3.8 Hz, H_5). ^{13}C NMR (75.5 MHz, DMSO-d_6) δ (ppm): 28.1, 28.4, 29.5, 33.6, 47.9, 48.0, 51.2, 72.8, 81.6, 169.4, 171.3, 171.5. IR (KBr) ν (cm^{-1}): 3237 (NH), 1712 (COOH), 1646, 1558 (CONH). HRMS ESI calcd for $C_{25}H_{42}N_5O_{10}$ [(M + H$^+$)]: 572.2932; found: 572.2930.

Synthesis of Acid 4-($G_{1.5}$) PAMAM[CO_2H]$_8$. Starting from PAMAM[CO_2CH_3]$_8$ **3**-($G_{1.5}$) (2 g, 14 mmol) in HCl 1 M (250 mL) the target acid **4**-($G_{1.5}$) was obtained as a yellowish solid (2.1 g, 100%). ^{1}H NMR (300 MHz, DMSO-d_6) was performed at 323 K to improve the resolution, δ (ppm): 2.75−2.88 (m, 28H, H_4, H_9 and H_{14}), 3.23−3.51 (m, 52H, H_3, H_{6-8} and H_{11-13}), 3.70 (m, 1H, H_1), 4.09 (m, 2H, H_2), 8.49 (m, 6H, H_5 and H_{10}). ^{13}C NMR (75.5 MHz, DMSO-d_6) δ (ppm): 28.2, 28.4, 29.2, 29.5, 33.4, 33.7, 48.0, 48.6, 49.0, 49.2, 51.3, 72.8, 81.7, 169.6, 169.7, 171.4, 171.6. IR (KBr) ν (cm^{-1}): 3223 (NH), 1717 (COOH), 1646, 1556 (CONH). HRMS ESI calcd for $C_{57}H_{98}N_{13}O_{22}$ [(M + H$^+$)]: 1316.6949; found: 1316.6960.

Synthesis of Azide-Functionalized Nanoparticles NP_{N3}. The synthesis of primary reactive chlorobenzyl-functionalized nanoparticles NP_{Cl} was obtained following the previously described procedures.[16] Details of the experimental procedures are provided in the Supporting Information. Azide-coated nanoparticles NP_{N3} were prepared by adding an aqueous solution of sodium azide (2.79 g in 10 mL of water) to 80 g of the freshly prepared crude suspension of NP_{Cl} the pH of which was previously adjusted to 7.5. The resulting suspension was stirred at room temperature for 1 week. The excess of sodium azide was then removed by dialysis through a porous cellulose membrane (MWCO 12000−14000D) toward an aqueous solution of DTAB (15 wt %) leading to a stable translucent aqueous suspension of azide-functionalized nanoparticles (NP_{N3}). Polymer particle content in suspension is 4.46 wt %. The polymer was isolated using method A. Chemical composition: C, 81.95; H, 7.08; N, 1.22% corresponding to an azide content of 0.29 mmol/g of polymer. Mean diameter (QELS): 18 nm (PDI: 0.08). IR (KBr) ν (cm^{-1}): 3084, 3060, 3022, 2922, 2849, 2094, 1602, 1508, 1495, 1450, 1232, 1153, 1065, 1030, 903, 834, 796, 762, 703, 539.

Synthesis of Acid-Terminated PAMAM-Functionalized Nanoparticles NP_PAMAM[CO_2H]$_4$. PAMAM derivative **2**-($G_{0.5}$) (80 mg, 0.140 mmol) was dissolved in 2 mL of water. The solution was added to 10 g of the aqueous suspension of azide-functionalized nanoparticles NP_{N3}. The pH was adjusted to 5.7 by adding NaOH (1M). Then, 2 mL of a freshly prepared aqueous solution of $CuSO_4$ (50 mg, 0.313 mmol) and sodium ascorbate (115 mg, 0.580 mmol) was added; the pH was again adjusted to 5.7. The resulting suspension was stirred at room temperature for 5 days. 76 mg of cyclam was added, and then the suspension was dialyzed against aqueous solution of DTAB (15 to 1.5 wt %). Polymer particle content in suspension is 1.8 wt %. The polymer was isolated using method B. Chemical composition: C, 82.91; H, 7.54; N, 2.72%. Mean diameter (QELS): 20 nm (PDI: 0.005). IR (KBr) ν (cm^{-1}): 3395, 3080, 3056, 3028, 2921, 2852, 2096, 1659, 1598, 1487, 1450, 1369, 1258, 1070, 1025, 899, 829, 797, 756, 698, 535.

Synthesis of PAMAM-Functionalized Nanoparticles NP_PAMAM[CO_2H]$_8$. Prepared using the same procedure as above starting from PAMAM derivative **4**-($G_{1.5}$) (187 mg, 0.142 mmol), 10 g of the aqueous suspension of NP_{N3} and 2 mL of aqueous solution of $CuSO_4$ (50 mg, 0.313 mmol) and sodium ascorbate (115 mg, 0.580 mmol). Polymer particle content in suspension is 1.5 wt %. Chemical composition: C, 81.93; H, 7.67; N, 2.78%. Mean diameter (QELS): 18 nm (PDI: 0.053). IR (KBr) ν (cm^{-1}): 3400, 3082, 3058, 3025, 2922, 2851, 2096, 1653, 1601, 1510, 1493, 1452, 1375, 1266, 1182, 1028, 905, 833, 796, 760, 699, 540.

Synthesis of Dansyl_PAMAM-Functionalized Nanoparticles NP_Dns_PAMAM[CO_2H]$_4$. Dansyl derivative **5** (10 mg, 0.035 mmol) was added to 6 g of the aqueous suspension of acid-terminated PAMAM-functionalized nanoparticles (polymer particle content in suspension is 1.8 wt %). The mixture was stirred at room temperature until complete solubilization of **5** (30 min). Then, 1 mL of a freshly prepared aqueous solution of $CuSO_4$ (19 mg, 0.119 mmol) and sodium ascorbate (44 mg, 0.222 mmol) were added. The resulting suspension was stirred at room temperature for 5 days. 29 mg of cyclam (0.145 mmol) was added, and then the suspension was dialyzed against aqueous solution of DTAB (5 wt %) using an ultrafiltration device (Vivascience, Vivaspin concentrator 20, 50 000 MWCO PES). The process was repeated until no dansyl derivative was detected in the filtrate. The polymer was isolated using method B. Chemical composition: C, 81.03; H, 7.24; N, 2.64; S, 0.63% corresponding to a dansyl and a dendrimer content of 0.20 and 0.11 mmol/g of polymer, respectively. Mean diameter (QELS): 18 nm (PDI: 0.088). IR (KBr) ν (cm^{-1}): 3379, 3082, 3058, 3025, 2922, 2850, 2096, 1668, 1601, 1493, 1452, 1329, 1266, 1145, 1071, 1029, 905, 831, 794, 760, 699, 623, 541.

Synthesis of Dansyl_PAMAM-Functionalized Nanoparticles NP_Dns_PAMAM[CO_2H]$_8$. Prepared using the same procedure as above starting from dansyl derivative **5** (30 mg, 0.104 mmol), 8 g of the aqueous suspension of NP_PAMAM[CO_2H]$_8$, and 1 mL of aqueous solution of $CuSO_4$ (21 mg, 0.132 mmol) and sodium ascorbate (49 mg, 0.247 mmol). 32 mg of cyclam (0.160 mmol) was used at the end of the reaction to sequester the copper. Chemical composition: C, 81.11; H, 7.19; N, 2.87; S, 0.75% corresponding to a dansyl and a dendrimer content of 0.23 and 0.06 mmol/g of polymer, respectively. Mean diameter (QELS): 21 nm (PDI: 0.113). IR (KBr) ν (cm^{-1}): 3392, 3082, 3058, 3025, 2922, 2850, 2096, 1653, 1601, 1510,

1493, 1452, 1329, 1266, 1145, 1071, 1029, 905, 838, 794, 760, 700, 623, 573, 541.

RESULTS AND DISCUSSION

The propargyl-functionalized PAMAM dendrons **1**-($G_{0.5}$) and **3**-($G_{1.5}$) were prepared by a divergent synthesis through a repetitive sequence involving a Michael addition using methyl acrylate and an amidation with ethylenediamine starting from propargylamine according to the previously described method.[25] We then investigated the hydrolysis of the methyl ester terminal groups under the conditions reported in the literature.[28] The reaction was performed with formic acid, and the conversion was monitored by ^{1}H NMR spectroscopy. Regardless of the conditions used (reaction run at room temperature or at 50 °C), the singlet methoxy proton chemical shift is still present in the ^{1}H NMR spectrum, indicating that the reaction is not complete even after a prolonged reaction time. In this regard, we tested the ester hydrolysis using HCl (1 M). The reaction mixture was stirred for 3 days at room temperature and then for three days at 50 °C and was followed by ^{1}H NMR. Under these optimized conditions, acid-terminated dendrons **2**-($G_{0.5}$) and **4**-($G_{1.5}$) were isolated in quantitative yields, and their structures were confirmed by ^{1}H and ^{13}C NMR spectroscopy as well as by IR spectroscopy and HRMS. The hydrolysis of the ester groups of **1**-($G_{0.5}$) and **3**-($G_{1.5}$) is evidenced by the absence of ^{1}H and ^{13}C NMR signals for the methoxy groups (δ_H 3.7 ppm and δ_C 51.0 ppm) along with the downfield shifts of all but the amide protons (Figure 1). Protonation of the tertiary amines of **2**-($G_{0.5}$) and **4**-($G_{1.5}$) probably accounts for the observed deshielding of the methylene and alkyne protons.

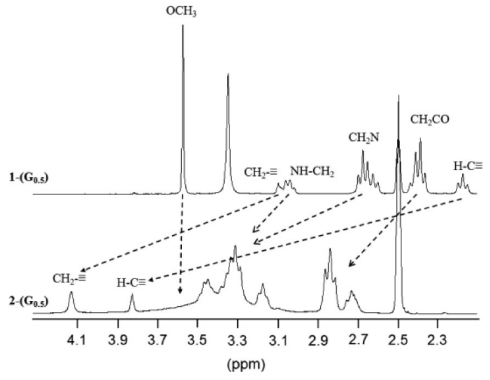
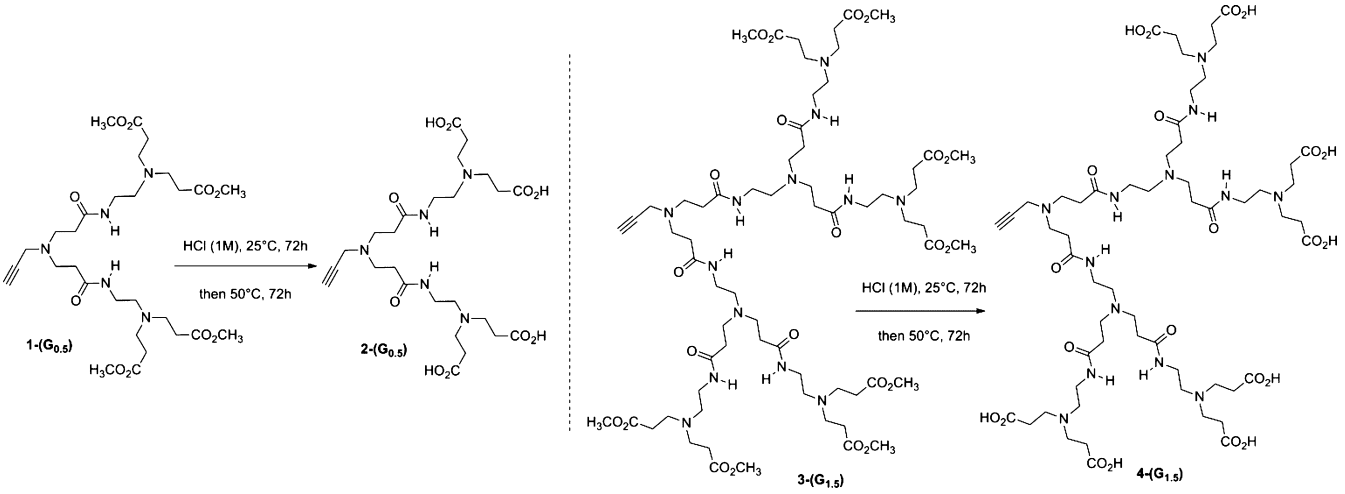


Figure 1. Comparison of ^{1}H NMR spectra of first-generation dendrons **1**-($G_{0.5}$) and **2**-($G_{0.5}$) (in their protonated forms) in DMSO-d_6 at 298 K.

In addition, the IR spectrum of **2**-($G_{0.5}$) shows the expected change in the absorption of the C═O stretching mode from ca. 1729 cm^{-1} for the esters groups to ca. 1712 cm^{-1} for the carboxylic acid moieties. Amide II band, due to NH bending vibrations, also shifts from 1532 cm^{-1} to ca. 1558 cm^{-1} after hydrolysis. Similar results were obtained in the case of second-generation dendron **4**-($G_{1.5}$).

Azido-coated nanoparticles (NP_{N3}) were prepared according to a previously described procedure.[16] In short, reactive benzyl chloride-functionalized nanoparticles (NP_{Cl}) were prepared by copolymerization of styrene, chloromethylstyrene, and divinylbenzene as a cross-linking agent in an oil-in-water microemulsion stabilized with a cationic surfactant (dodecyltrimethylammonium bromide, DTAB). The postfunctionalization reaction was carried out under mild conditions at room temperature by adding an excess of sodium azide (10 equiv per chlorine in the polymer) directly to the nonpurified and freshly prepared aqueous suspension of NP_{Cl}. In aqueous medium, the cross-linked polystyrene-based NPs were not swollen so that the grafting of azide units occurs exclusively on the surface. Unreacted sodium azide was easily removed from the suspension by dialysis at the end of reaction. The presence of azide groups is evidenced by the appearance of the characteristic N_3 stretching band at 2100 cm^{-1} in the IR spectrum (Figure 2a). Elemental analyses confirm this result with an azide load estimated to 0.29 mmol/g of polymer, which corresponds to about 560 N_3 per NP assuming a size of 18 nm for NP_{N3} and a polymer density of 1.05 (Table S1). This simple procedure affords a straightforward access to stable translucent aqueous suspension of azido-coated nanoparticles in the 16−18 nm diameter range. The suspension remained stable when the surfactant concentration was reduced down to 0.15 wt % by dialysis. Unlike the chlorobenzyl-functionalized nanoparticles in which the chlorobenzyl groups are hydrolyzed easily, the azide groups of NP_{N3} are remarkably stable, and the suspension can be stored for more than one year before use. The grafting of the PAMAM dendron was readily performed at room temperature

Scheme 1. Synthesis of Propargyl-Functionalized Acid-Terminated PAMAM Dendrons 2-($G_{0.5}$) and 4-($G_{1.5}$)



dx.doi.org/10.1021/ma300126h | Macromolecules 2012, 45, 3513−3522

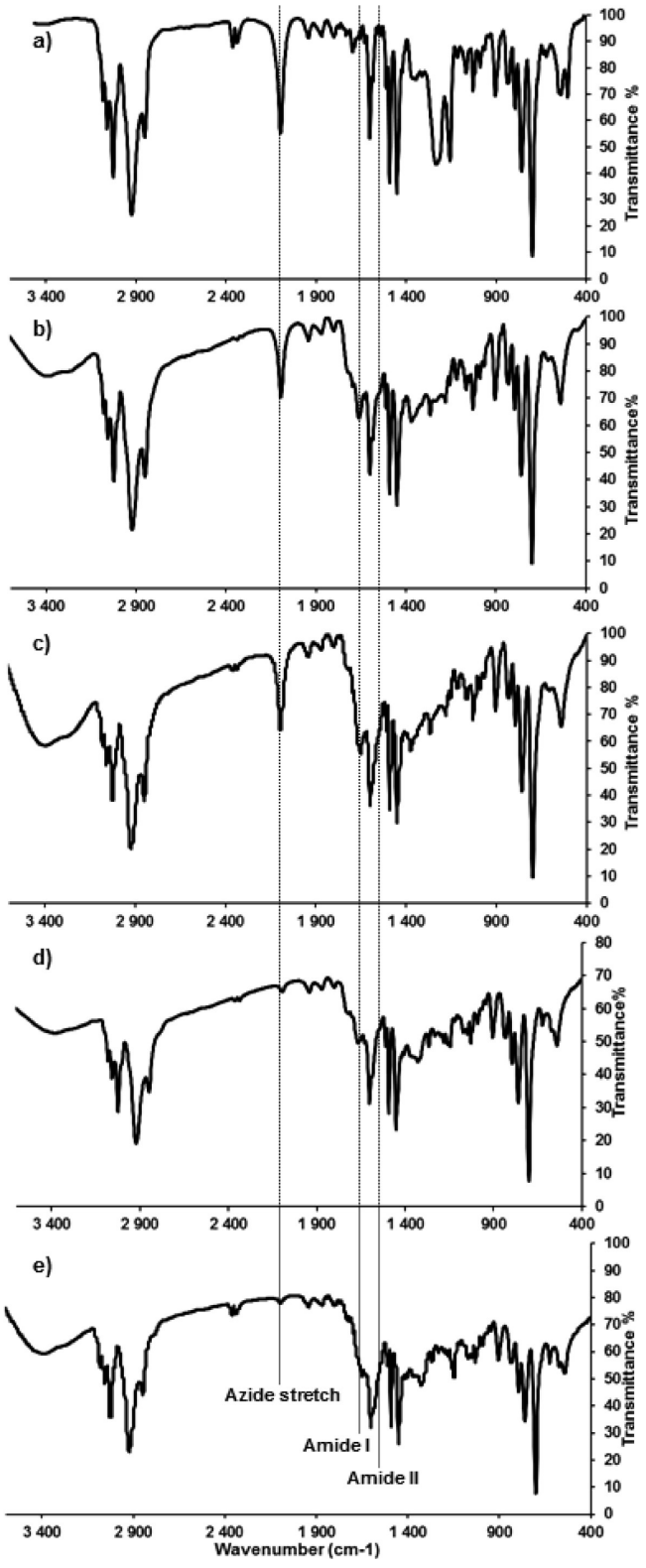


Figure 2. Infrared spectra (a) NP_{N3}, (b) NP_PAMAM$[CO_2H]_4$, (c) NP_PAMAM$[CO_2H]_8$, (d) NP_Dns_PAMAM$[CO_2H]_4$, and (e) NP_Dns_PAMAM$[CO_2H]_8$.

by adding a slight excess of **2**-($\mathbf{G}_{0.5}$) or **4**-($\mathbf{G}_{1.5}$) to the aqueous suspension of azido-coated nanoparticles NP_{N3} using click cycloaddition conditions to provide PAMAM-coated NPs. Owing to the likely affinity of cupric ions for acid-terminated PAMAM dendrons, we used copper sulfate and sodium ascorbate in excess (2.4 and 4.5 equiv, respectively, in relation to the azide content in the polymer) to obtain sufficient content of free copper for the click reaction. At the end of the reaction, cyclam, which has high affinity for cupric ions,[29] was added to easily sequester the excess of copper. The reaction was then purified by exhaustive dialysis against aqueous solutions of DTAB to ensure removal of the cyclam−copper complex, sodium ascorbate, and any unreacted dendrimers. The grafting of PAMAM dendrons on the surface of the nanoparticles can be proved by FT-IR measurement on the isolated and purified polymer (Figure 2b,c). The characteristic absorptions of amide bonds appear at 1660 and 1540 cm^{-1} for amide I and II modes, respectively, although the latter band is superimposed on an aromatic carbon−carbon vibration band. IR spectra also show a decrease of the intensity of the N_3 vibration band at 2100 cm^{-1}, which is more pronounced with **2**-($\mathbf{G}_{0.5}$) than with **4**-($\mathbf{G}_{1.5}$). Elemental analysis is in agreement with these results since nitrogen contents are similar regardless of the generation used (about 1.95 mmol of nitrogen/g of polymer). These facts indicate that the average number of the larger dendron grafted to the NP is lower than that of the smaller dendron. One can assume that the steric hindrance and electrostatic repulsion of the larger dendron ($\mathbf{G}_{1.5}$) are responsible for the lower surface reaction yield for this generation. The availability of unreacted azide groups on the surface of NPs was used as a handle for the attachment of an alkynyl-functionalized dansyl derivative. We have previously reported that the grafting of dansyl on azide-functionalized nanoparticles was almost quantitative using an excess of alkyne dansyl derivative **5** under click conditions.[16] In this work, the reaction was performed in the presence of $CuSO_4$ and sodium ascorbate between 4 equiv of **5** and the remaining azide moieties of the PAMAM-functionalized nanoparticles stabilized with an aqueous solution of 1.5 wt % DTAB, which also ensures the micellar solubilization of the hydrophobic dansyl derivative. After the reaction, exhaustive dialyses were performed to remove the copper catalyst and the unreacted dansyl **5**, until the absence of dye in the filtrate.

The coupling of dansyl was clearly evidenced for both PAMAM dendron-coated NPs by the almost complete disappearance of the azide vibration band in IR spectra of the isolated polymers, indicating a close to quantitative functionalization (Figure 2d,e).

This fact was confirmed by elemental analyses. The amounts of PAMAM and dansyl grafted on the NPs surface, deduced from the nitrogen and sulfur contents of the isolated polymers, were close to the azide content of the starting azide-functionalized nanoparticles (Table 1). One could estimate that the ratio of PAMAM to dansyl moieties grafted on the NPs was around 210/350 and 110/450 for the first and second generation, respectively. These dendron-coated nanoparticles are comparable to high generation PAMAM dendrimers in their functionality with about 840 and 880 peripheral carboxylic acid groups for the first and second generation, respectively.

Using the Mansfield−Tomalia−Rakesh[30] equation (1) for parking spheres on a sphere, the maximum number of dendrons that could be arranged around each nanoparticle was determined to be about 245 and 160 for the first and second generation, respectively.[31]

$$N_{max} = \frac{2\pi}{\sqrt{3}}\left(\frac{r_1}{r_2} + 1\right)^2 \quad (1)$$

dx.doi.org/10.1021/ma300126h | *Macromolecules* 2012, 45, 3513−3522

Scheme 2. Synthesis of Acid-Terminated PAMAM-Functionalized NP_PAMAM$[CO_2H]_n$ and Dansyl-Functionalized NP_Dns_PAMAM$[CO_2H]_n$ Nanoparticles

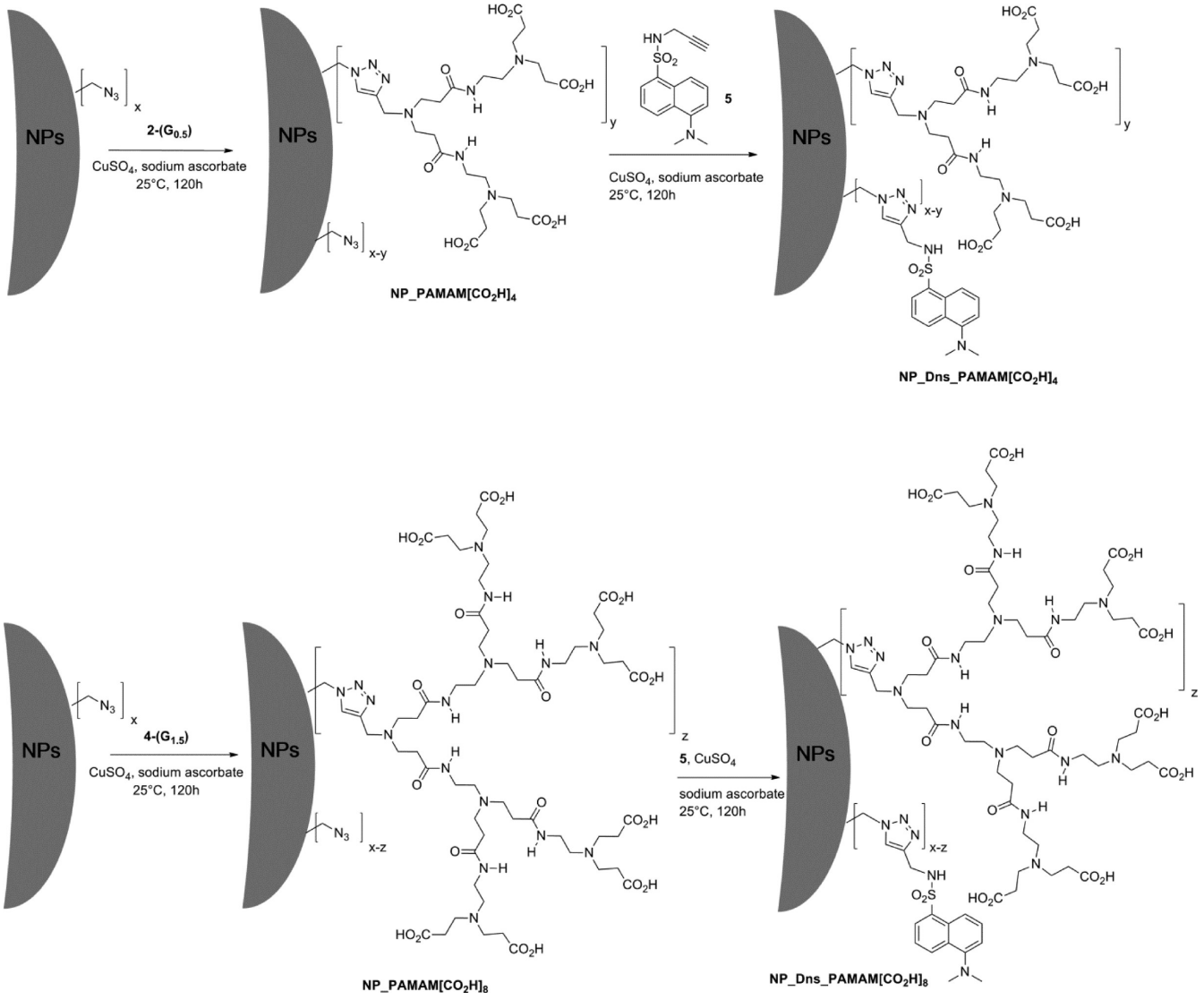


Table 1. Successive Surface Reactions on Azido-Coated Nanoparticles via CuAAC

		NP_PAMAM$[CO_2H]_n$			NP_Dns_PAMAM$[CO_2H]_n$			
list	starting suspension	reactant [x equiv]	D (nm) [PDI][b]	starting suspension	reactant [x equiv]	D (nm) [PDI][b]	PAMAM content[c]	dansyl content[d]
n = 4	NP_{N3}[a]	**2**-($G_{0.5}$) [1.1]	20 [0.005]	NP_PAMAM$[CO_2H]_n$	**5** [4]	18 [0.088]	0.11 (210)	0.20 (350)
n = 8	NP_{N3}[a]	**4**-($G_{1.5}$) [1.1]	18 [0.053]	NP_PAMAM$[CO_2H]_n$	**5** [4]	21 [0.113]	0.06 (110)	0.23 (450)

[a]Azide content in the polymer: 0.29 mmol/g polymer ; D = 18 nm (PDI = 0.08). [b]Particle diameter (D) and its polydispersity index (PDI) determined from QELS. [c]mmol/g of polymer deduced from elemental analysis (nitrogen and sulfur contents). In parentheses: number of PAMAM per NP deduced from the ratio PAMAM/dansyl grafted on the NPs and the content of azide per NP in the starting NP_{N3}. [d]mmol/g of polymer deduced from elemental analysis (nitrogen and sulfur contents). In parentheses: number of dansyl per NP deduced from the ratio PAMAM/dansyl grafted on the NPs and the content of azide per NP in the starting NP_{N3}.

These values, which corroborate fairly well with the experimental results, are indicative of a relatively dense dendritic shell. One can consider that about 85% and 70% of the dendritic shell saturation levels were reached for the first and second generation, respectively. These values are in the same order of magnitude than those obtained by Tomalia et al. in the case of core−shell tecto-dendrimers.[30d] The size and shape of the dendron-grafted NPs were measured in solution using QELS and in the dry state (deposited on a mica substrate) by atomic force microscopy (AFM). The dendron-functionalized NPs have narrow size distributions with mean hydrodynamic diameters of 18−21 nm, as determined by QELS. The dendron-coated NPs exhibit no significant change in diameter and polydispersity relative to the initial NPs (NP_{N3}), thus indicating that the particle size distribution is not modified by the grafting, regardless of the generation of the dendron. Figure 3 shows representative example of AFM image of dendron-functionalized NPs using the tapping mode, which

dx.doi.org/10.1021/ma300126h | Macromolecules 2012, 45, 3513−3522

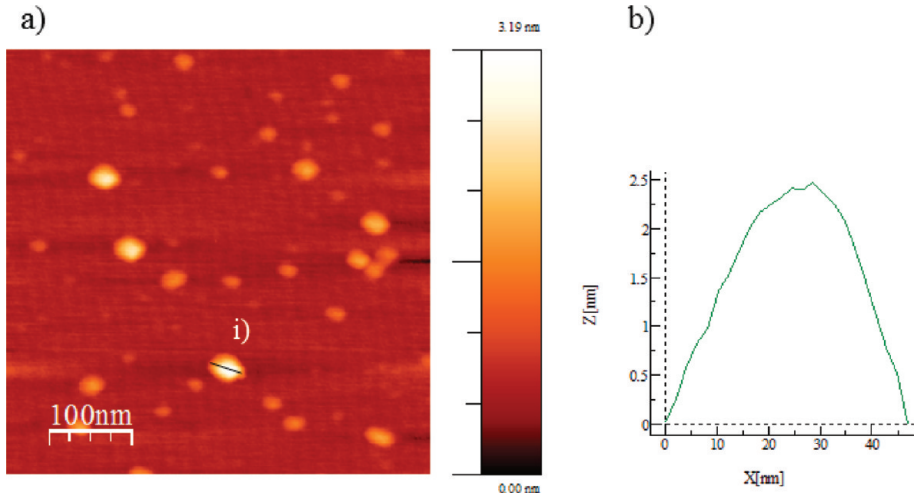


Figure 3. (a) Tapping mode AFM height image of a set of NP_Dns_PAMAM$[CO_2H]_4$ after deposition on a mica substrate. (b) Cross-sectional height profiles corresponding to (i) marked in panel a.

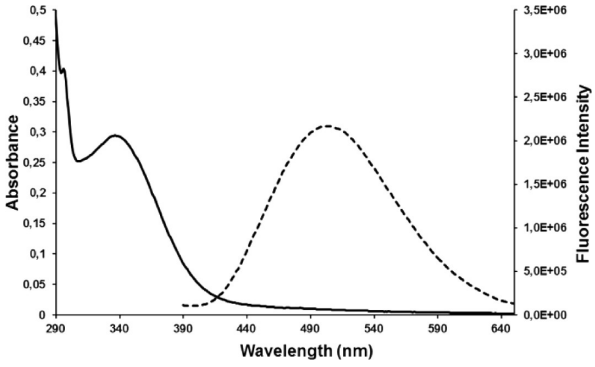


Figure 4. Absorption spectrum (full, 1 wt % DTAB content) and fluorescence emission spectrum (long-dash, λ_{exc} = 336 nm, 0.06 wt % DTAB content) of an aqueous suspension of NP_Dns_PAMAM-$[CO_2H]_4$.

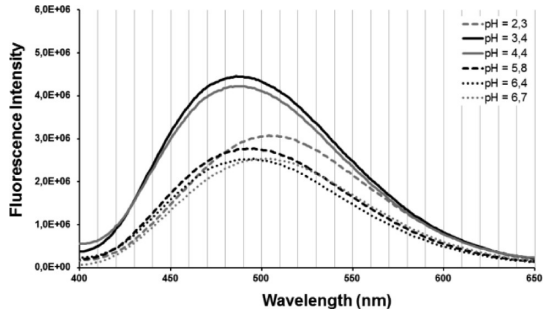


Figure 5. Fluorescence emission spectra of aqueous suspension of NP_dansyl_PAMAM$[CO_2H]_8$ (0.07 wt % DTAB content) for pH values ranging from 2.3 to 6.7. Dansyl was excited at 335 nm.

confirms their spherical morphology. The observation of separate, individual NPs of similar size randomly deposited on the mica surface is indicative of the absence of aggregation. The small height values of the NPs indicate that significant deformation occurs upon adsorption onto the mica AFM surface.[32] Although complicated by the finite size of the AFM tip, the larger lateral sizes of the particles obtained by AFM also supported deformation of the NPs on mica.

The absorption and fluorescence emission spectra of NP_Dns_PAMAM$[CO_2H]_4$ and NP_Dns_PAMAM$[CO_2H]_8$ at neutral pH displayed the characteristic features of dansyl units with a maximum absorption wavelength around 335−340 nm and a broad emission centered around 500 nm (Figure 4 and Figure S3). The blue-shifted emission observed for the dansyl units grafted on the NPs surface relative to the emission bands of dansyl derivatives in water (530−580 nm) indicates that the microenvironment of the dansyl moieties linked to the NP surface is less polar than a surrounding aqueous phase.[33,34] Furthermore, the position of the fluorescence emission band as well as the intensity varied significantly from 485 to 510 nm with changes of pH in the range of 2−7 (Figure 5 and Figures S6 and S7) while the absorption band did not varied. It is well-known that the fluorescence emission position and intensity of dansyl are strongly dependent on the polarity of the medium.[33,35] One may consider that the protonation of PAMAM dendrons induces a change in the local polarity close to the dansyl units to explain this result.

The colloidal stability of acid-terminated dendron-functionalized nanoparticles NP_PAMAM$[CO_2H]_n$ was first studied by decreasing the content of surfactant in the suspension in order to assess if the dendron shell could act as a protective layer and permit the stabilization of nanoparticles in surfactant free suspensions as already observed in dendritic-coated polymeric nanoparticles.[21,22] Experimental details of nanoparticles NP_PAMAM$[CO_2H]_n$-bis used for this study are provided in the Supporting Information. When the surfactant concentration was close to 0.3 wt % and the pH to 7, the aggregation of nanoparticles took place regardless of the grafted dendron while the initial nanolatexes (NP_{N3}) remained stable at this concentration (vide supra). This result suggests that the formation of ion pairs between ammonium moieties of DTAB and carboxylate groups of PAMAM dendrons occurs. This type of interaction has already been reported by Tomalia between PAMAM dendrimers and dodecylammonium bromide leading to generation-dependent surfactant aggregates.[36] The surfactant molecules self-assemble at the nanoparticle surface orienting their hydrophobic chains toward the aqueous solution, which leads to a colloidal destabilization of the suspension. Then, the colloidal stability of PAMAM dendron-coated NPs was assessed both in acidic and basic media (Figure 6). The experiment were performed in the presence of DTAB since the dialysis of dendron-coated nanoparticles against acidic

dx.doi.org/10.1021/ma300126h | Macromolecules 2012, 45, 3513−3522

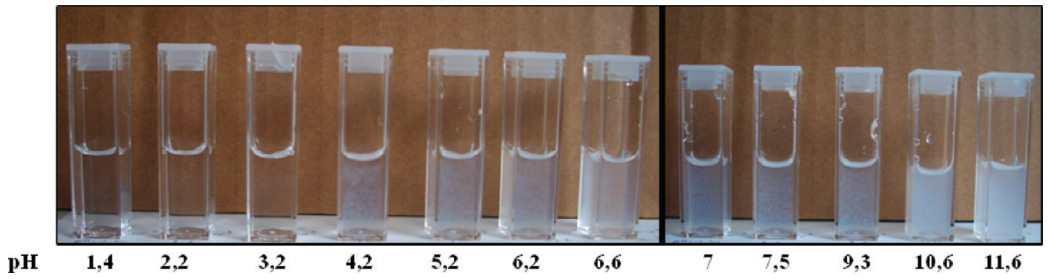


Figure 6. Pictures depicting the colloidal stability of NP_PAMAM$[CO_2H]_8$-bis versus pH.

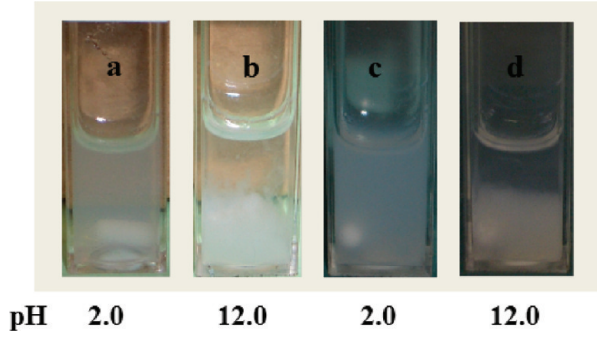


Figure 7. Photographs of NP_PAMAM$[CO_2H]_4$-bis (0.02 wt % DATB content) after standing 24 h: from the starting suspension (initial pH 2.0) after the first sequence final pH 2.0 (a), solution from (a) after basification pH 12.0 (b), from the starting suspension after three sequences final pH 2.0 (c), solution from (c) after basification pH 12.0 (d).

solution (pH = 2) led to the formation of hydrogel. The suspensions stabilized with 1.0 wt % of DTAB were diluted 50 times in HCl (concentrations range from 6×10^{-2} to 6×10^{-7} M) or in NaOH (concentrations range from 6×10^{-2} to 6×10^{-7} M). The suspensions of dendron-grafted NPs are stable at pH $\leq$ 3.2 regardless of the dendron generation. The pK_a values of internal tertiary amines moieties for PAMAM dendrimer are between 6.0 and 7.3.[37] At pH = 3, all the tertiary amines and carboxylic groups are protonated. The PAMAM dendron grafted to the surface of NPs could be assumed to be mainly in the protonated form at this pH, thus ensuring along with the remaining DTAB an electrostatic stabilization of the colloidal suspensions. So one could assume that, at acidic pHs ($\leq$3.2), the stabilization of the suspensions by electrostatic repulsions was kept and led to translucent suspension. Moreover, the size of the nanoparticles in acidic medium was not modified and was found to be in the 15−20 nm diameter range.

When the pH increased from 4 to 12, the suspensions turned cloudy and the polymer precipitated. Considering a pK_a value close to 4 for carboxylic acid groups,[38] the formation of ion pairs between ammonium units and carboxylate groups can be envisioned which leads to the immediate aggregation and precipitation of the nanoparticles. The reversibility of the electrostatic self-assembly process was then studied (Figure 7). The experiment was run on the previous diluted suspension using hydrochloric acid or sodium hydroxide to adjust the pH. The starting suspension (pH = 2) was basified then acidified (first sequence) and led to a cloudy aqueous suspension (as shown in Figure 7a) without precipitation of the polymer even after standing for 2 weeks (see Figure S10). This result indicates that some nanoparticles aggregate but that the overall charge on the resulting particles is large enough to prevent precipitation. This base−acid sequence process has been repeated three times and led to the same observation: polymer particles precipitated in basic medium after standing for 24 h and could be redispersed in acidic medium regardless of the generation. The sizes of the particles were determined at pH = 2 by QELS at the end of the three sequences. The resulting suspension of particle were polydisperse; the size of particles were found to be about 170 and 760 nm for NP_PAMAM-$[CO_2H]_4$-bis and 360 and 960 nm for NP_PAMAM$[CO_2H]_8$-bis. The precipitation of the polymer in basic medium does not allow the measurement of the hydrodynamic diameter by DLS analysis.

Although the initial size of the nanoparticles was altered, this reversible switchability would confer striking benefits, implying for instance the possible separation and redispersion of the polymeric particles. Furthermore, in agreement with a steric stabilization from the dendritic shell, aqueous suspensions of dendron-coated nanoparticles tolerated the addition of ethanol and remained stable up to 9:1 ethanol/water volumes regardless of the generation, while the initial nanolatex (NP_{N3}) suspension precipitated upon addition of ethanol.

CONCLUSION

This study demonstrates that azido-coated polymer nanoparticles (NP_{N3}) obtained by the postfunctionalization procedure can be used as a clickable platform for the convergent synthesis of fluorescent polystyrene core−PAMAM shell nanoparticles in the 15−20 nm diameter range. Owing to the nonswelling properties of cross-linked polystyrene matrix in water and to the fact that azide units are located only the surface, the grafting of PAMAM dendron and dansyl derivative occurs exclusively on the NP_{N3} surface. The reaction was particularly efficient with almost quantitative overall yield. The reaction proceeded under very mild conditions using $CuSO_4$ and sodium ascorbate as a catalytic system. The whole process was achieved in water without any added cosolvent in the presence of the surfactant which allowed the micellar solubilization of hydrophobic dansyl derivative. Remarkably, the use of earlier generation of PAMAM dendron ($\mathbf{G_{0.5}}$ and $\mathbf{G_{1.5}}$) allows the preparation in a few steps of dendron-coated nanoparticles which possess properties comparable to high eighth generation of PAMAM dendrimers in their functionality[39] and to core−shell tecto-dendrimer in their size.[40] Dendritic shell saturations levels of 85% and 70% were reached for the first and second generation, respectively. Dendron-coated nanoparticles can be considered as multifunctional systems composed of (i) an interior of shell with azide groups remaining after the grafting of PAMAM dendrons and located onto the NPs surface and (ii) an outer shell with peripheral carboxylic acid moieties. This approach allows the control of both the location and the distribution of a given

dx.doi.org/10.1021/ma300126h | Macromolecules 2012, 45, 3513−3522

chemical group in each part of the shell which carries out its designed task. This has been demonstrated by grafting of fluorescent dansyl derivative in the interior of shell. As far as peripheral carboxylic acid moieties are concerned, surface functionalization with various molecules (biomolecules or fluorescent dyes) can be envisioned via ion pair association or covalent linkages and are currently under investigation in our laboratory. Finally, the strategy presented here is quite general and should give a straightforward access to a variety of dendron-coated nanoparticles, thereby opening new perspectives in the field of materials science and biotechnology.

■ ASSOCIATED CONTENT

Supporting Information

Additional structures of **2-G**$(_{0.5})$ and **4-**$(\mathbf{G}_{1.5})$, experimental procedures, spectral characterization data, figures, and tables. This material is available free of charge via the Internet at http://pubs.acs.org.

■ AUTHOR INFORMATION

Corresponding Author

*E-mail: Emmanuel.Allard@chimie.uvsq.fr.

Notes

The authors declare no competing financial interest.

■ ACKNOWLEDGMENTS

M.C. thanks Fundacion Progreso y Salud (Ministry of Health from Junta de Andalucía) for the financial support through a Postdoctoral fellowship in Nanomedicine 2010−2012 (ref 0399). M.C. and E.A. thank B. Berrini for helpful assistance with the AFM measurements.

■ REFERENCES

(1) (a) Goesmann, H.; Feldmann, C. *Angew. Chem., Int. Ed.* **2010**, *49*, 1362−1395. (b) Shipway, A. N.; Katz, E.; Willner, I. *ChemPhysChem* **2000**, *1*, 18−52.

(2) De, M.; Ghosh, P. S.; Rotello, V. M. *Adv. Mater.* **2008**, *20*, 4225−4241.

(3) Astruc, D.; Lu, F.; Aranzaes, J. R. *Angew. Chem., Int. Ed.* **2005**, *44*, 7852−7872.

(4) Aiken, J. D.; Finke, R. G. *J. Mol. Catal. A: Chem.* **1999**, *145*, 1−44.

(5) Bronstein, L. M.; Shifrina, Z. B. *Chem. Rev.* **2011**, *111*, 5301−5344.

(6) *Dendrimers and Dendrons: Concepts, Syntheses, Applications*; Newkome, G. R., Moorefield, C. N., Voegtle, F., Eds.; Wiley-VCH: Weinheim, 2001.

(7) *Dendrimers and Other Dendritic Polymers*; Fréchet, J., Tomalia, D., Eds.; Wiley: Chichester, UK, 2001.

(8) (a) Crooks, R. M.; Zhao, M.; Sun, L.; Chechik, V.; Yeung, L. K. *Acc. Chem. Res.* **2001**, *34*, 181−190. (b) Astruc, D.; Boisselier, E.; Ornelas, C. *Chem. Rev.* **2010**, *110*, 1857−1959. (c) Vohs, J. K.; Fahlman, B. D. *New J. Chem.* **2007**, *31*, 1041−1051.

(9) (a) Guo, W.; Li, J. J.; Wang, A.; Peng, X. *Chem. Mater.* **2003**, *15*, 3125−3133. (b) Guo, W.; Li, J. J.; Wang, A.; Peng, X. *J. Am. Chem. Soc.* **2003**, *125*, 3901−3909. (c) Advincula, R. C. *Dalton Trans.* **2006**, 2778−2784. (d) Cutler, E. C.; Lundin, E.; Garabato, B. D.; Choi, D.; Shon, Y.-S. *Mater. Res. Bull.* **2007**, *42*, 1178−1185. (e) Danda, C.; Ponnapati, R.; Dutta, P.; Taranekar, P.; Patterson, G.; Advincula, R. C. *Macromol. Chem. Phys.* **2011**, *212*, 1600−1615. (f) Zhou, D.; Li, Y.; Hall, E. A. H.; Abell, C.; Klenerman, D. *Nanoscale* **2011**, *3*, 201−211. (g) Daniel, M.-C.; Grow, M. E.; Pan, H.; Bednarek, M.; Ghann, W. E.; Zabetakis, K.; Cornish, J. *New J. Chem.* **2011**, *35*, 2366−2374.

(10) (a) Mizugaki, T.; Murata, M.; Fukubayashi, S.; Mistudome, T.; Jitsukawa, K.; Kaneda, K. *Chem. Commun.* **2008**, 241−243. (b) Love, C. S.; Chechik, V.; Smith, D. K.; Brennan, C. *J. Mater. Chem.* **2004**, *14*, 919−923. (c) Gopidas, K. R.; Whitesell, J. K.; Fox, M. A. *J. Am. Chem. Soc.* **2003**, *125*, 6491−6502. (d) Jiang, G.; Wang, L.; Chen, T.; Yu, H.; Wang, J. *Nanotechnology* **2004**, *15*, 1716−1719. (e) Wang, R.; Yang, J.; Zheng, Z.; Carducci, M. D.; Jiao, J.; Seraphin, S. *Angew. Chem., Int. Ed.* **2001**, *40*, 549−552.

(11) (a) Heuzé, K.; Rosario-Amorin, D.; Nlate, S.; Gaboyard, M.; Bouter, A.; Clérac, R. *New J. Chem.* **2008**, *32*, 383−387. (b) Rosario-Amorin, D.; Wang, X.; Gaboyard, M.; Clérac, R.; Nlate, S.; Heuzé, K. *Chem.—Eur. J.* **2009**, *15*, 12636−12643. (c) Moussodia, R.-O.; Balan, L.; Merlin, C.; Mustin, C.; Schneider, R. *J. Mater. Chem.* **2010**, *20*, 1147−1155. (d) Kainz, Q. M.; Schätz, A.; Zöpfl, A.; Stark, W. J.; Reiser, O. *Chem. Mater.* **2011**, *23*, 3606−3613.

(12) (a) Pichot, C. *Curr. Opin. Colloid Interface Sci.* **2004**, *9*, 213−221. (b) Antonietti, M.; Tauer, K. *Macromol. Chem. Phys.* **2003**, *204*, 207−219.

(13) (a) Kunna, K.; Müller, C.; Loos, J.; Vogt, D. *Angew. Chem., Int. Ed.* **2006**, *45*, 7289−7292. (b) Mohammed, H. S.; Shipp, D. A. *Macromol. Rapid Commun.* **2006**, *27*, 1774−1778. (c) Voorn, D.-J.; Ming, W.; Herk, A. M. V. *Macromolecules* **2005**, *38*, 3653−3662. (d) Castelvetro, V.; Vita, C. D. *Adv. Colloid Interface Sci.* **2004**, *108−109*, 167−185. (e) Ford, W. T. *React. Funct. Polym.* **1997**, *33*, 147−158.

(14) (a) Amigoni-Gerbier, S.; Larpent, C. *Macromolecules* **1999**, *32*, 9071−9073. (b) Amigoni-Gerbier, S.; Désert, S.; Gulik, T.; Larpent, C. *Macromolecules* **2002**, *35*, 1644−1650. (c) Méallet-Renault, R.; Pansu, R.; Amigoni-Gerbier, S.; Larpent, C. *Chem. Commun.* **2004**, 2344−2345. (d) Cannizzo, C.; Amigoni-Gerbier, S.; Larpent, C. *Polymer* **2005**, *46*, 1269−1276. (e) Gouanvé, F.; Schuster, T.; Allard, E.; Méallet-Renault, R.; Larpent, C. *Adv. Funct. Mater.* **2007**, *17*, 2746−2756. (f) Allard, E.; Larpent, C. *J. Polym. Sci., Part A: Polym. Chem.* **2008**, *46*, 6206−6213. (g) Abid, J.-P.; Frigoli, M.; Pansu, R.; Szeftel, J.; Zyss, J.; Larpent, C.; Brasselet, S. *Langmuir* **2011**, *27*, 7967−7971. (h) Zhu, L.; Wu, W.; Zhu, M.-Q.; Han, J. J.; Hurst, J. K.; Li, A. D. Q. *J. Am. Chem. Soc.* **2007**, *129*, 3524−3526. (i) Tian, Z.; Shaller, A. D.; Li, A. D. Q. *Chem. Commun.* **2009**, 180−182. (j) Sun, H.; Almdal, K.; Andrese, T. L. *Chem. Commun.* **2011**, *47*, 5268−5270.

(15) (a) Larpent, C.; Tadros, C. F. *Colloid Polym. Sci.* **1991**, *269*, 1171−1183. (b) Antonietti, M.; Basten, R.; Lohmann, S. *Macromol. Chem. Phys.* **1995**, *196*, 441−466. (c) Hentze, H. P.; Kaler, E. W. *Curr. Opin. Colloid Interface Sci.* **2003**, *8*, 164−178. (d) Larpent, C. In *Surfactant Science Series, Colloid Polymers: Preparation and Biomedical Applications*; Elaissari, A., Ed.; Marcel Dekker: New York, 2003; Vol. *115*, Chapter 7, pp 145−187. (e) Yan, F.; Texter, J. *Soft Matter* **2006**, *2*, 109−118.

(16) Ouadahi, K.; Allard, E.; Oberleitner, B.; Larpent, C. *J. Polym. Sci., Part A: Polym. Chem.* **2012**, *50*, 314−328.

(17) Wesler, K.; Perera, M. D. A.; Aylott, J. W.; Chan, W. C. *Chem. Commun.* **2009**, 6601−6603.

(18) (a) Joralemon, M. J.; O'Reilly, R. K.; Hawker, C. J.; Wooley, K. L. *J. Am. Chem. Soc.* **2005**, *127*, 16892−16899. (b) O'Reilly, R. K.; Joralemon, M. J.; Hawker, G. J.; Wooley, K. L. *New J. Chem.* **2007**, *31*, 718−724.

(19) (a) Li, B.; Martin, A. L.; Gillies, E. R. *Chem. Commun.* **2007**, 5217−5219. (b) Martin, A. L.; Li, B.; Gillies, E. R. *J. Am. Chem. Soc.* **2009**, *131*, 734−741.

(20) Nazemi, A.; Amos, R. C.; Bonduelle, C. V.; Gillies, E. R. *J. Polym. Sci., Part A: Polym. Chem.* **2011**, *49*, 2546−2559.

(21) Larpent, C.; Geniès, C.; De Souza Delgado, A. P.; Caminade, A.-M.; Majoral, J.-P.; Sassi, J.-F.; Leising, F. *Chem. Commun.* **2004**, 1816−1817.

(22) (a) Larpent, C.; Cannizzo, C.; Delgado, A.; Gouanvé, F.; Sanghvi, P.; Gaillard, C.; Bacquet, G. *Small* **2008**, *4*, 833−840. (b) Cannizzo, C.; Amigoni-Gerbier, S.; Frigoli, M.; Larpent, C. *J. Polym. Sci., Part A: Polym. Chem.* **2008**, *46*, 3375−3386.

(23) Tornøe, C. W.; Christensen, C.; Meldal, M. *J. Org. Chem.* **2002**, *67*, 3057−3064.

(24) Rostovtsev, V. V.; Green, L. G.; Fokin, V. V.; Sharpless, K. B. *Angew. Chem., Int. Ed.* **2002**, *41*, 2596−2599.

(25) (a) Lee, J. W.; Kim, B.-K.; Kim, J. H.; Shin, W. S.; Jin, S.-H. *J. Org. Chem.* **2006**, *71*, 4988−4991. (b) Lee, J. W.; Kim, B.-K.; Kim, H. J.; Han, S. C.; Shin, W. S.; Jin, S.-H. *Macromolecules* **2006**, *39*, 2418−2422. (c) Lee, J. W.; Kim, H. J.; Han, S. C.; Kim, J. H.; Jin, S.-H. *J. Polym. Sci., Part A: Polym. Chem.* **2008**, *46*, 1083−1097.
(26) Gottlieb, H. E.; Kotlyar, V.; Nudelman, A. *J. Org. Chem.* **1997**, *62*, 7512−7515.
(27) Horcas, I.; Fernández, R.; Gómez-Rodriguez, J. M.; Colchero, J.; Gómez-Herrero, J.; Baro, A. M. *Rev. Sci. Instrum.* **2007**, *78*, 013705−1-013705−6.
(28) Tulu, M.; Aghatabay, N. M.; Senel, M.; Dizman, C.; Parali, T.; Dulger, B. *Eur. J. Med. Chem.* **2009**, *44*, 1093−1099.
(29) Thöm, V. J.; Hosken, G. D.; Hancock, R. D. *Inorg. Chem.* **1985**, *24*, 3378−3381.
(30) (a) Mansfield, M. L.; Rakesh, L.; Tomalia, D. A. *J. Chem. Phys.* **1996**, *105*, 3245−3249. (b) Tomalia, D. A. *Prog. Polym. Sci.* **2005**, *30*, 294−324. (c) Jensen, A. W.; Maru, B. S.; Zhang, X.; Mohanty, D. K.; Fahlman, B. D.; Swanson, D. R.; Tomalia, D. A. *Nano Lett.* **2005**, *5*, 1171−1173. (d) Uppuluri, S.; Swanson, D. R.; Piehler, L. T.; Li, J.; Hagnauer, G. L.; Tomalia, D. A. *Adv. Mater.* **2000**, *12*, 796−800.
(31) Equation 1; $r_1/r_2 > 1.20$, r_1 is the nanoparticle radius of starting azide-functionalized nanoparticles (determined from QELS). Even if the dendrons does not adopt a spherical geometry, one can estimate the radii of **2**-($\mathbf{G}_{0.5}$) (r_2 = 1.25 nm) and **4**-($\mathbf{G}_{1.5}$) (r_2 = 1.6 nm) considering that the dendrons have an extended conformation without correction for charge, solvation, etc., using Chem Bio3D Ultra 11.0 (MM2 calculation) software (Supporting Information, Figure S11).
(32) (a) Betley, T. A.; Hessler, J. A.; Mecke, A.; Banaszak Holl, M. M.; Orr, B. G.; Uppuluri, S.; Tomalia, D. A.; Baker, J. R., Jr. *Langmuir* **2002**, *18*, 3127−3133. (b) Dukette, T. F.; Mackay, M. E.; Van Horn, B.; Wooley, K. L.; Drockenmuller, E.; Malkoch, M.; Hawker, C. J. *Nano Lett.* **2005**, *5*, 1704−1709.
(33) (a) Nelissen, H. F. M.; Venema, F.; Uittenbogaard, R. M.; Feiters, M. C.; Nolte, R. J. M. *J. Chem. Soc., Perkin Trans. 2* **1997**, 2045−2053. (b) Montalti, M.; Prodi, L.; Zaccheroni, N.; Battistini, G.; Marcuz, S.; Mancin, F.; Rampazzo, E.; Tonellato, U. *Langmuir* **2006**, *22*, 5877−5881.
(34) Ouadahi, K.; Sbargoud, K.; Allard, E.; Larpent, C. *Nanoscale* **2012**, DOI: 10.1039/C2NR11413E.
(35) Wang, B.-B.; Zhang, X.; Jia, X.-R.; Li, Z.-C.; Ji, Y.; Yang, L.; Wei, Y. *J. Am. Chem. Soc.* **2004**, *126*, 15180−15194.
(36) Caminati, G.; Turro, N. J.; Tomalia, D. A. *J. Am. Chem. Soc.* **1990**, *112*, 8515−8522.
(37) (a) Cakara, D.; Kleimann, J.; Borkovec, M. *Macromolecules* **2003**, *36*, 4201−4207. (b) Diallo, M. S.; Christie, S.; Swaminathan, P.; Balogh, L.; Shi, X.; Um, W.; Papelis, C.; Goddard, W. A., III; Johnson, J. H., Jr. *Langmuir* **2004**, *20*, 2640−2651. (c) Kannaiyan, D.; Imae, T. *Langmuir* **2009**, *25*, 5282−5285.
(38) Van Duijvenbode, R. C.; Rajanayagam, A.; Koper, G. J. M.; Baars, M. W. P. L.; De Waal, B. F. M.; Meijer, E. W.; Borkovec, M. *Macromolecules* **2000**, *33*, 46−52.
(39) Sharma, A.; Desai, A.; Ali, R.; Tomalia, D. A. *J. Chromatogr., A* **2005**, *1081*, 238−244.
(40) Li, J.; Swanson, D. R.; Qin, D.; Brothers, H. M.; Piehler, L. T.; Tomalia, D. A.; Meier, D. J. *Langmuir* **1999**, *15*, 7347−7350.

Macromolecules

Article

pubs.acs.org/Macromolecules

Stimuli-Responsive Amphiphilic Polyelectrolyte Heptablock Copolymer Physical Hydrogels: An Unusual pH-Response

Maria-Teodora Popescu,[†,‡] Constantinos Tsitsilianis,[†,‡,*] Christine M. Papadakis,[§] Joseph Adelsberger,[§] Sandor Balog,[⊥] Peter Busch,[∥] Natalie A. Hadjiantoniou,[○] and Costas S. Patrickios[○]

[†]Department of Chemical Engineering, University of Patras, 26504, Patras, Greece

[‡]Institute of Chemical Engineering and High Temperature Chemical Processes, ICE/HT-FORTH, P.O. Box 1414, 26504 Patras, Greece

[§]Fachgebiet Physik weicher Materie, Physikdepartment, Technische Universität München, James-Franck-Strasse 1, 85747 Garching, Germany

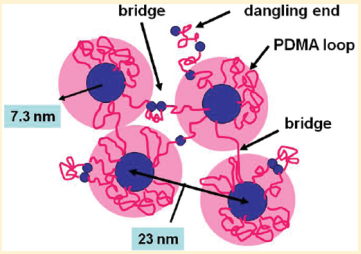
[⊥]Paul Scherrer Institut, 5232 Villigen PSI, Switzerland

[∥]Jülich Centre for Neutron Science at FRM II, Forschungszentrum Jülich GmbH, Lichtenbergstrasse 1, 85747 Garching, Germany

[○]Department of Chemistry, University of Cyprus, P.O. Box 20537, 1678 Nicosia, Cyprus

Supporting Information

ABSTRACT: An amphiphilic cationic polyelectrolyte based on poly[2-(dimethylamino)-ethyl methacrylate] (polyDMA) and poly(*n*-butyl methacrylate) (polyBuMA) with a BuMA−DMA−BuMA−DMA−BuMA−DMA−BuMA heptablock copolymer architecture was studied in aqueous media. This copolymer was found to form a physical hydrogel via the intermolecular hydrophobic association (physical cross-linking) of the BuMA blocks. The rheological properties of the heptablock hydrogels were investigated as a function of copolymer concentration, and pH. The results showed a peculiar pH-dependence of the rheological properties, remarkably different from those observed with associative telechelic polyelectrolytes. Aqueous solutions of this copolymer were free-flowing sols at low pH (below 2) and high pH (above 8), whereas they turned into gels at intermediate pH values. The rheological properties studied as a function of pH showed two additional stiff−soft−stiff gel transitions at pH 4.5 and 6.5. Small-angle neutron scattering revealed the formation of a 3D transient network of bridged flower-like micelles whose structural characteristics, i.e., micellar radius, hard-sphere radius and hard-sphere volume fraction, were smoothly evolving with the pD.



INTRODUCTION

Water-soluble associative polymers (AP) forming reversible hydrogels represent a very important class of polymeric materials with fascinating properties, which have attracted considerable attention in recent years. Amphiphilic block copolymers are the main polymeric materials in studies of reversible hydrogels, since they combine hydrophobic and hydrophilic segments and have the ability to spontaneously self-assemble in aqueous media. In dilute solutions, the hierarchical self-organization of molecular building blocks proceeds through various intra and/or intermolecular interactions. At higher concentration, a three-dimensional transient network is formed, composed of hydrophobic nanodomains (physical cross-links) interconnected by hydrophilic chains (elastic chains) imposing dramatic effects on the rheological properties of the solution. The considerable interest in these materials derives from their various applications as rheology modifiers in cosmetics and coatings, as well as injectable hydrogels and drug carriers in pharmaceutical formulations.[1−6]

Significant progress has been made in recent years on reversible hydrogels that can respond to an external stimulus like temperature, pH, light, and chemical triggers.[7−9] Because of our ability to build macromolecules with tunable macromolecular architectural characteristics (i.e., chain length of low polydispersity, block topology, hydrophobic/hydrophilic balance, and specific functionality) leading to self-assembly in specific environments, hydrogels with tunable properties, such as injectability and responsiveness (i.e., precise sol-to-gel transitions triggered by one or more stimuli), mesh size, and mechanical strength, can be designed.[10]

A remarkable number of studies have been devoted to triblock copolymers, composed of charged long chains end-capped by similar or different hydrophobic short blocks (stickers) also named telechelic or heterotelechelic polyelectrolytes.[11−27] In addition to this type of block copolymers, another class of associative gelators is that of hydrophobically modified polyelectrolytes bearing a number of hydrophobic blocks randomly distributed along the hydrophilic chain.[28−44]

Very recently, the gelation properties of a number of well-defined (i.e., comprising blocks with tunable degree of polymerization) amphiphilic polyelectrolyte multiblock copolymers based on hydrophobic (A) blocks of poly(*n*-butyl

Received: January 31, 2012
Revised: March 27, 2012
Published: April 3, 2012

 © 2012 American Chemical Society dx.doi.org/10.1021/ma300222d | *Macromolecules* 2012, 45, 3523−3530

methacrylate) (polyBuMA) and hydrophilic ionizable (B) blocks of poly[2-(dimethylamino)ethyl methacrylate] (polyDMA) with various topologies have been evaluated. In particular, two series of ABA triblock, BABAB pentablock, ABABABA heptablock, and BABABABAB nonablock copolymers with variable macromolecular structural parameters were studied. The first series comprised copolymers with constant length of the building blocks and varying overall molecular weight and composition, whereas the second series was composed of copolymers with constant overall molecular weight and hydrophobic content but variable size of the building blocks. It was found that the macromolecular characteristics such as the lengths of the hydrophilic and the hydrophobic segments (stickers) and, more importantly, the topology of the stickers along the chain had a profound influence on their gelation capability.

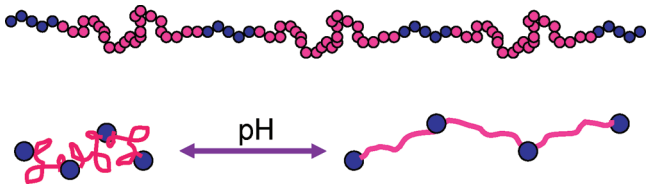
Rheological results showed that only the triblock ($BuMA_6$-*b*-DMA_{60}-*b*-$BuMA_6$) and the heptablock copolymers ($BuMA_5$-*b*-DMA_{25}-*b*-$BuMA_5$-*b*-DMA_{25}-*b*-$BuMA_5$-DMA_{25}-*b*-$BuMA_5$ and $BuMA_3$-*b*-DMA_{20}-*b*-$BuMA_3$-*b*-DMA_{20}-*b*-$BuMA_3$-*b*-DMA_{20}-*b*-$BuMA_3$) which bore hydrophobic blocks at both ends formed hydrogels at relatively low copolymer concentrations. Comparing the triblock and the heptablock copolymers having the same overall degree of polymerization, considerable different rheological properties were observed due to the different macromolecular topology. Preliminary data concerning the $BuMA_7$-*b*-DMA_{38}-*b*-$BuMA_7$-*b*-DMA_{38}-*b*-$BuMA_7$-*b*-DMA_{38}-*b*-$BuMA_7$ heptablock copolymer showed that this multiblock copolymer formed a free-standing hydrogel at concentrations above 3 wt %.[45]

In the present paper, we report a detailed study of the rheological properties of this heptablock amphiphilic polyelectrolyte in aqueous media. Its stimuli-responsive character, arising from the weak polyelectrolyte nature of its hydrophilic segments, leading to pH and ionic strength sensitivity, renders this particular system a highly interesting subject for fundamental investigation and also a promising matrix for drug delivery. Thus, the dependence of the rheological properties of its aqueous solutions on polymer concentration and pH was explored. The results showed a peculiar pH-dependence of the rheological properties, not observed in associative telechelic polyelectrolytes of the same nature.[15] Aqueous solutions of this polymer were free-flowing sols at low pH (below 2) and high pH (above 8), whereas they turned into gels at intermediate pH values. Both linear and nonlinear rheological properties studied as a function of pH showed two additional stiff-soft-stiff gel transitions around pH 4.5 and 6.5. The remarkable rheological properties of the heptablock physical gels were discussed in terms of their microstructure and were compared with other associative polyelectrolytes. Small-angle neutron scattering (SANS) was employed to determine the microstructure of the sol and the gels at different pH values.

EXPERIMENTAL SECTION

Polymer Synthesis. The copolymer under investigation was synthesized by group transfer polymerization (GTP)[46] and sequential monomer addition. Details of the synthesis are reported elsewhere.[47,48] The associating copolymer bears seven blocks, three of which are composed of the hydrophilic DMA (with N_{DMA} = 38 repeating units) and the other four comprise the hydrophobic BuMA (with N_{BuMA} = 7 repeating units).[49] The molecular weight and composition characteristics of the heptablock copolymer are: M_n = 21 500 g mol^{-1} and M_w/M_n =1.32 both determined using gel permeation chromatography (GPC), and BuMA content of 18.6 mol % calculated using ^{1}H NMR spectroscopy. The structure of the heptablock copolymer is illustrated in Scheme 1.

Scheme 1. Schematic Representation of the $BuMA_7$-*b*-DMA_{38}-*b*-$BuMA_7$-*b*-DMA_{38}-*b*-$BuMA_7$-*b*-DMA_{38}-*b*-$BuMA_7$ Heptablock Copolymer and Its Conformations in Water at High pH (Left, Uncharged) and Low pH (Right, Fully Charged)



Rheological Measurements. The rheological measurements were carried out using a stress controlled Rheometrics Scientific SR 200 rheometer, equipped with a cone and plate geometry (diameter =20 mm, cone angle =4°, truncation =11 μm). After each sample loading, a delay of 5 min was applied prior to any measurement, in order to erase any shear history. The temperature, fixed at 25 ± 0.1 °C, was controlled by a water bath circulator. Additional viscosimetric measurements were performed with a stress controlled rheometer (AR-2000ex, TA Instruments) in a cone−plate geometry with a steel cone of radius R = 3.0 cm and angle 2°. Samples were loaded such that the normal stress never exceeded 0.1 N. The linear viscoelastic regime was established by oscillatory strain sweeps using a frequency of 1 Hz. Dynamic oscillatory sweeps (in the linear regime at 25 °C) were performed for samples viscous enough to provide meaningful results. Steady shear measurements were similarly made at 25 °C, by increasing stepwise the shear stress and allowing for equilibration at each step for 120 s. The rheometer was equipped with a Peltier control system that allows accurate control of temperature (25 °C). A solvent trap was used to minimize changes in concentrations due to water evaporation.

For the rheological experiments, the copolymer solutions were directly prepared to the final desired concentration. The proper amount of polymer was weighed in a screw-capped vial. First, an equivalent amount of HCl (1 N) was added to ionize the tertiary amine groups of the polyDMA block, and then triply distilled water was added to the final volume. Vigorous stirring and multiple centrifugations were used for homogenization. The rheological measurements were conducted 24 h after homogenization.

Small-Angle Neutron Scattering (SANS). Copolymer solutions for small-angle neutron scattering (SANS) experiments were prepared in deuterated water and the pH (pD) was adjusted by adding deuterium chloride. The experiments were carried out using the SANS-II instrument[50] at the Swiss spallation neutron source, SINQ at Paul Scherrer Institut (PSI), Switzerland, and the SANS instrument KWS 2 of the Jülich Centre for Neutron Science (JCNS) outstation at the Forschungs-Neutronenquelle Heinz Maier-Leibnitz (FRM II) in Garching, Germany.

At PSI, the following wavelengths λ and sample-to-detector distances (SDD) were chosen: λ = 0.45 nm ($\Delta\lambda/\lambda$ = 10%) and SDD = 1.2 m; λ = 0.45 nm and SDD = 4.0 m; and λ = 1.05 nm and SDD = 6.0 m. This resulted in an overall q-range from 0.052 to 3.00 nm^{-1}. The collimation length was equal to the SDD in all cases, and the entrance and sample pinholes were 24 and 7.2 mm, respectively. Here, 2 wt % solutions in D_2O at pD 5.5 and 6.5 were diluted using D_2O prior to the measurements, so the resulting concentration was 1 wt %. Standard Hellma quartz cuvettes (light path of 1 mm) were used. The measurements were performed at room temperature for 30 min at SDD = 6 m, 20 min at SDD = 4 and 15 min at SDD = 1 m. Raw data were processed according to standard procedures and were calibrated for detector nonlinearity using the incoherent scattering from H_2O.

At FRM II, a wavelength λ = 0.7 nm ($\Delta\lambda/\lambda$ = 20%) and SDD of 1.53 and 7.53 m were chosen in order to cover the q-range from 0.044 to 2.1 nm^{-1}. The samples were contained between two Heraeus quartz glasses with a diameter of 2 cm and a thickness of 2 mm each. An O-ring separated the glasses from each other, resulting in a sample thickness of 1.5 mm. This sandwich was mounted in an oven consisting of an inner part which was heated electrically and an outer part which was cooled by temperature-controlled water. Measurements were carried out at 25 °C. The 4 wt % copolymer solutions in D_2O at pD values of 5.5 and 6.5 were measured. The accumulation time was 5 min for each SDD. To determine the detector sensitivity, poly(methyl methacrylate) was used. The intensities were corrected for dark current and background with boron carbide. The scattering of D_2O and the empty cell were subtracted from the sample scattering, taking the transmissions into account. The resulting intensities were azimuthally averaged. All data reductions were performed with the software QtiKWS provided by JCNS.

We present the azimuthally averaged scattering spectra as a function of the scattering vector, $q = (4\pi/\lambda) \times \sin(\theta/2)$ where θ is the scattering angle and λ is the wavelength. The azimuthally averaged scattering curves were analyzed using the NIST software in the IgorPro environment.[51] The following model was used to fit the intensity curves

$$I(q) = I_0[P_{sphere}(q)S_{PY}(q) + P_{forward}(q)] + \text{bkg} \quad (1)$$

where I_0 is a scaling factor including the geometrical factors of the experiment, the incoming neutron flux, the number of spheres, their volume and the neutron scattering length density contrast between BMA and D_2O. $P_{sphere}(q)$ denotes the form factor of core−shell spherical particles with a polydispersity of the core size, which models the polyBuMA core and the polyDMA shells of the micelles. The correlation between micelles was described by $S_{PY}(q)$, the Percus−Yevick structure factor for hard spheres (e.g., ref 52), which includes the hard-sphere radius, R_{HS}, corresponding to half the distance between the cores, and the hard-sphere volume fraction, ϕ. The forward scattering was modeled by the Porod term

$$P_{forward}(q) = \frac{K}{q^4} \quad (2)$$

where K is the Porod constant. bkg denotes the background left as a free fitting parameter.

RESULTS AND DISCUSSION

1. Effect of the Copolymer Concentration on the Rheological and the Structural Properties. Figure 1 shows characteristic flow curves obtained by steady-state shear viscosity measurements of the heptablock copolymer aqueous solutions at pH 6 (degree of ionization of polyDMA about α = 0.88) and at different copolymer concentrations. The solutions of 0.1 and 0.25 wt % polymer exhibited nearly Newtonian behavior (curves not shown). At concentrations higher than 1 wt % and up to 3 wt %, the viscosity profiles were characterized by a low-shear Newtonian plateau followed by shear thinning effects at higher shear stresses. As the copolymer concentration was increased above 3 wt %, significant changes in the flow behavior were observed. The zero-shear viscosity could not be determined by steady-state experiments since free-standing gels were formed as revealed also by the tube inversion test (inset of Figure 2). The solutions exhibited yield stress of the order of 30−60 Pa and what we see in Figure 1, for the high concentrations (c > 3 wt %), is a complex shear thinning regime (nonlinear behavior).

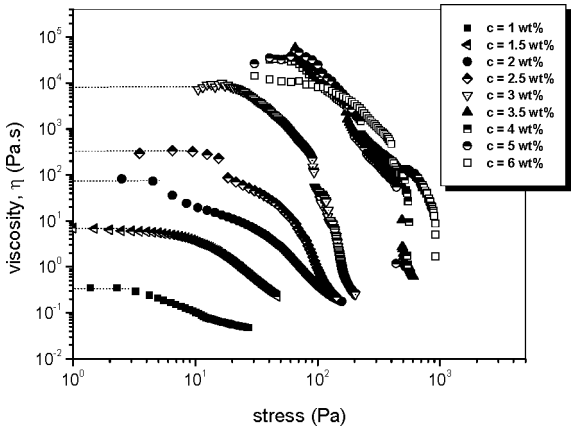


Figure 1. Steady shear viscosity profile for different concentrations of the heptablock copolymer in aqueous solution of pH 6 at 25 °C.

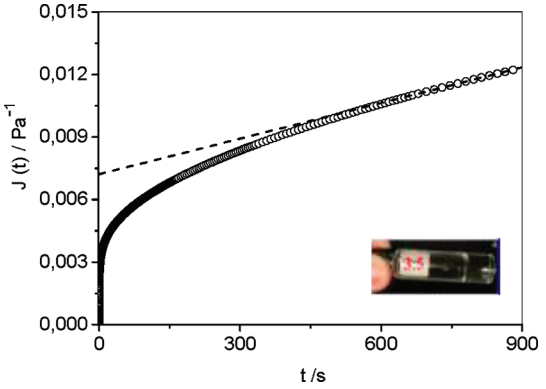


Figure 2. Compliance $J(t)$ versus time for a 3.5 wt % heptablock copolymer aqueous solution at pH 6. The dashed line represents the linear fit at the linear part of the curve. The inset shows that this solution forms a free-standing gel.

In order to characterize the free-standing gel at a 3.5 wt % polymer concentration, a creep experiment was conducted in the linear viscoelastic regime. In Figure 2, the compliance, $J(t)$, is plotted as a function of time after applying a stress adequately smaller than the yield stress (linear response). The figure shows a rapid increase in the compliance which became smoother and eventually linear at longer times. From the slope of the linear part of the curve, the zero-shear viscosity was determined to be $\eta_0 = 1.7 \times 10^5$ Pa·s which was about five times higher than the viscosity obtained at the lowest shear rate in the flow experiments. More importantly, the terminal relaxation time τ was calculated to be 1232 s through the equation $\tau = G_0/\eta_0$, where G_0 = 138 Pa was obtained from the intercept $[1/J_0(t)]$. This long relaxation time should be related to the long lifetime of the hydrophobic physical cross-links formed by the association of the $PBuMA_7$ blocks. The same order of magnitude in the characteristic times were reported for multiblock hydrophobic polyelectrolytes with the same degree of polymerization of the hydrophobic sequences (seven *N,N*-dihexylacrylamide).[42,43]

Figure 3 demonstrates the zero-shear viscosity as a function of concentration. At low concentrations and in the dilute regime, the solutions exhibited Newtonian response and the viscosity values were comparable to that of the medium. Above a critical concentration termed C_{gel}, the viscosity increased dramatically, indicating the onset of a 3D network formation. C_{gel} was determined at about 0.6 wt %, which was remarkably low for the polymer under investigation with such a low

dx.doi.org/10.1021/ma300222d | Macromolecules 2012, 45, 3523−3530

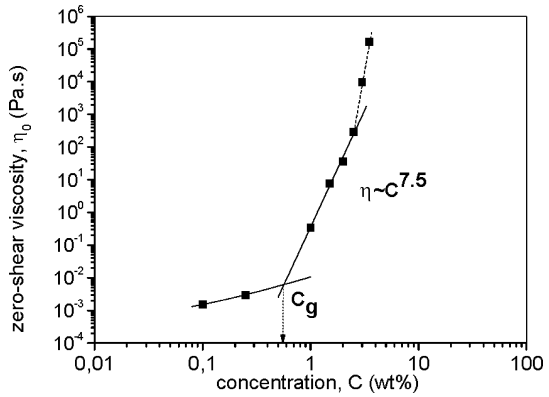


Figure 3. Double−logarithmic plot of the zero-shear viscosity, η_0, as a function of the concentration of the heptablock copolymer in aqueous solution at pH 6 and 25 °C.

molecular weight if compared to other multiblock copolymer APs of very high molecular weights of the order of millions.

Just above C_{gel}, the viscosity rose abruptly with a power-law exponent of 7.5. Because of the low degree of polymerization of the macromolecular chains, we are still in the semidilute unentangled regime in which intermolecular associations govern the viscoelastic behavior. Thus, the viscosity rose through intra to inter association (loop-to-bridge) transitions. Such high power-law exponents have been observed also for other AP systems like for instance in the polyMMA−polyDMA−polyMMA triblock copolymer[15] and the hydrophobically modified poly(dimethyl acrylamide).[39] However, considerable different concentration dependence of the viscosity was observed for high molecular weight multiblock associative polyelectrolytes. Just above the gelation threshold, the viscosity jumped about 3 orders of magnitude followed by a smooth rise with a power-law exponent of 2.[43]

Above C = 2.5 wt %, the viscosity rose even more steeply which could be attributed to the very high relaxation times. Such behavior has been reported for self-assembled triblock copolymers with pH-tunable exchange dynamics of the end-block stickers. At low pH, the relaxation times observed were very long (comparable to our system), implying that the system becomes kinetically frozen, behaving as an elastic soft solid.[25,26]

Although zero-viscosities could not be determined by the flow data at C > 3.5 wt %, the low-shear viscosities seem to be stabilized at this concentration regime (Figure 1). The same effect can also be seen in the concentration dependence of the dynamic viscosity at low frequencies (Figure S2, Supporting Information). Analogous tendency has been reported for multiblock associative polyelectrolytes.[43] This behavior may account for the fact that most of the likely bridges of the network have been formed.

SANS experiments were employed to explore the morphology of the network structure, which is responsible for the gelation phenomena observed upon increasing copolymer concentration. The SANS curve of the (liquid-like) 1 wt % solution at pD 6.5 is given in Figure 4. It shows a weak peak at 0.18 nm^{-1}, a shoulder at 0.4−0.5 nm^{-1}, a broad decay at 0.5−3 nm^{-1} and slightly increased forward scattering below 0.09 nm^{-1}. We attribute the peak at 0.18 nm^{-1} to the correlation between the polyBuMA cores, the shoulder to the form factor of the micelles presumably having a core−shell structure with polyBuMA cores and polyDMA shells, and the forward scattering to the presence of large aggregates of micelles. The

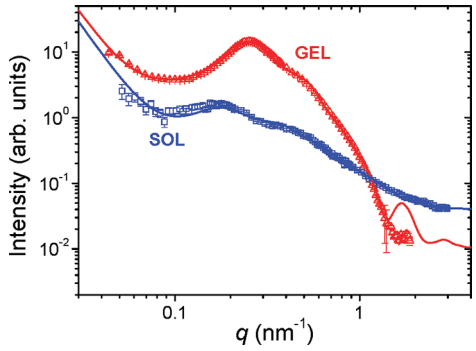


Figure 4. SANS curves from 1 wt % solution (□) and a 4 wt % gel (Δ), both at pD = 6.5. The lines are fits, see text.

fit of eq 1 matches well the curve. We find a core radius of R_{core} = 1.04 ± 0.07 nm, a micellar radius of R_{mic} = 5.62 ± 0.10 nm, a hard-sphere radius of R_{HS} = 16.3 ± 0.2 nm and a hard-sphere volume fraction of 0.15 ± 0.01. Thus, the 1 wt % sample consists of flower-like nearly unimolecular micelles (it can be calculated that 22 BuMA units can fit in a sphere with a radius equal to R_{core}, whereas a heptablock copolymer chain carries about 28 BuMA units) having small polyBuMA cores which are weakly correlated and are surrounded by the DMA_{38} blocks, some of which bridge different micelles. On large length-scales, the sample is slightly inhomogeneous, presumably due to the formation of large clusters of interconnected micelles as also have been observed by light scattering.[45]

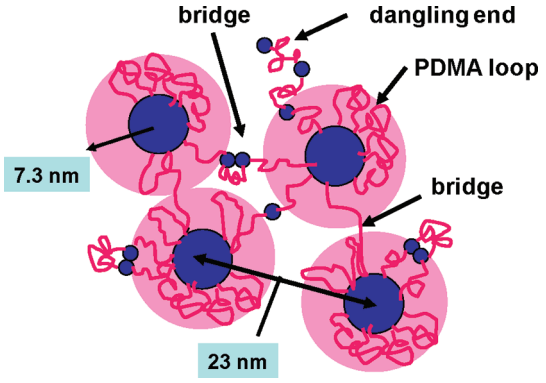
At higher concentration (4 wt %), the samples are gel-like. The peak of the structure factor is more pronounced than at 1 wt % and is shifted to higher q-values (0.25 nm^{-1}) than at 1 wt %, i.e. the hard-sphere radius is smaller than at 1 wt %, as expected. Equation 1 could again describe the SANS curve well. Good agreement was obtained, except above q = 1.4 nm^{-1} where the model overestimates the scattering. However it is important that this q-range corresponds to the vicinity of the edge of the neutron area detector, where the background subtraction can be critical, and therefore, deviations may occur.

The resulting radii of the core and the entire micelle are now R_{core} = 3.234 ± 0.003 nm and R_{mic} = 7.276 ± 0.007 nm, both values are thus higher than at 1 wt %. The higher the polymer concentration, the more $BuMA_7$ blocks are present in each core. The hard-sphere radius, R_{HS}, is 11.515 ± 0.005 nm, smaller than that at 1 wt %, as the cores are now much closer to each other than at 1 wt %. The hard-sphere volume fraction is 0.2416 ± 0.0003, higher than the one at 1 wt %. We conclude that, at 4 wt %, the micellar network is more densely packed than at 1 wt % and that the micelles display larger polyBuMA cores, i.e., higher aggregation numbers.

The physical picture of the hydrogel (4 wt %) which emerged from the SANS measurements is illustrated in Scheme 2. The heptablock topology of the amphiphilic copolymer dictates the formation of flower-like micelles with a mean core radius of 3.2 nm (implying a N_{agg} of about 24), a micellar radius of 7.3 nm and a corona thickness of 4.1 nm. Since the contour length of the hydrophilic polyelectrolyte segments is 9.6 nm (=38 × 0.254 nm,[47] corresponding to a stretched loop size of 4.8 nm), it seems that the corona chains (corona thickness calculated above = 4.1 nm) comprise rather stretched loops of polyDMA blocks (Scheme 2). Twice the average hard sphere radius, i.e., the mean distance between the centers of adjacent micelles, is about 23.0 nm which exceeds the contour length of

dx.doi.org/10.1021/ma300222d | Macromolecules 2012, 45, 3523−3530

Scheme 2. Schematic Representation of the Structure of the Micellar Transient Network at pD 6.5 and 4 wt % Heptablock Copolymer Concentration As Deduced from the Analysis of the SANS Data



one polyDMA segment. Thus, it may be that some of the bridging chains comprise two polyDMA segments, i.e., the two end-stickers to be located in different micellar cores and the two internal stickers forming pairwise associating groups (Scheme 2).

2. Effect of pH on the Rheological Properties. In the following, the influence of the pH on the rheological properties of the hydrogel formed at 4 wt % copolymer aqueous solutions was investigated by steady-state shear and dynamic oscillatory measurements.

Figure 5 displays characteristic flow curves, corresponding to pH 4.5, 5.5, and 6.5. From a first glance, it is obvious that the

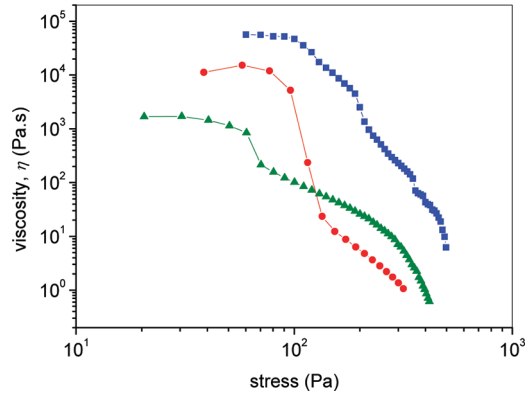


Figure 5. Viscosity profile at pH 4.5 (●), 5.5 (▲) and 6.5 (■) of 4 wt %. heptablock copolymer solutions at 25 °C.

rheological properties strongly depend on pH as expected from the weak polyelectrolyte nature of the hydrophilic segments (polyDMA) of which the degree of ionization (α) decreases monotonously upon increasing pH. However, the response of the copolymer to pH variations was more complex and unexpected. As can be seen in Figure 5, the viscosity dropped about 1 order of magnitude as the pH was increased from pH 4.5 (α = 0.96) to pH 5.5 (α = 0.92), while it rose again remarkably at pH 6.5 (α = 0.77) acquiring values even higher than those at pH 4.5. This effect was accompanied by a parallel decrease/increase of the corresponding yield stress (i.e., the stress above which shear-thinning was observed).

A more systematic study of the pH-dependence of the viscosity of 4 wt % heptablock copolymer aqueous solutions is depicted in Figure 6 where the low-shear viscosity (at $\gamma = 2 \times 10^{-3}$ s^{-1}) is plotted as a function of pH. Two sharp transitions

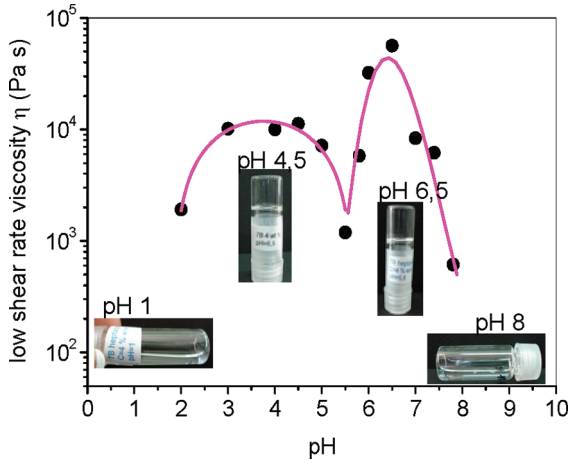


Figure 6. Variation of the low-shear viscosity, η (together with photographs of the samples), as a function of pH of a 4 wt % heptablock copolymer aqueous solution at 25 °C.

were observed at low and high pH; a sol−gel transition around pH 1.5 and a gel−sol transition close to pH 8 ($\alpha \sim 0.1$). In the gel phase region, the viscosity passed though two maxima, at pH 4.5 and 6.5, revealing a stiff gel-soft gel-stiff gel transition. The highest viscosity was observed at pH 6.5 above which the viscosity dramatically dropped several orders of magnitude down to pH 8.

The above-described peculiar complex pH-dependence of viscosity differs remarkably from that reported for the polyMMA−polyDMA−polyMMA triblock copolymer telechelic polyelectrolytes, comprising structurally similar hydrophobic/hydrophilic blocks but lacking internal stickers. In the latter case, the viscosity passed through a maximum at around pH 4.[15] This suggests that the additional internal stickers of the heptablock copolymer in the present study might be the reason for the observed complex behavior.

Oscillatory shear experiments were also performed at different pH values at constant copolymer concentration of 4 wt %. Figure 7 displays characteristic strain and frequency sweeps within the linear viscoelastic regime of the hydrogel. The hydrogel moduli exhibit significant pH-dependence, which is in good agreement with the steady-state results.

Moreover strain hardening effects can be seen in Figure 7a at pH 2, 4, 4.5, 5.5, and 7.4. As can be seen, the storage modulus increases above a certain strain prior to a sharp drop at higher strain values. This effect was not observed at pH 6.5 where the viscosity maximum appeared in Figure 6.

Figure 7b depicts the storage and the loss moduli as a function of frequency for several pH values. At pH 6.5, it appears that the hydrogel behaves as an elastic soft solid since G' and G'' are independent of frequency in the entire frequency range investigated. This behavior was also observed at pH 4.5 and 7.4 but with significantly lower G' and G'' magnitudes. Thus, the hydrogels exhibited superior viscosity and moduli values at pH 6.5 which corresponds to a degree of ionization of the polyDMA segments of 0.77. Furthermore, the pH dependence of the elastic modulus, G' and the dynamic complex viscosity, η^*, (at low frequency) exhibit again two maxima at pH 4.5 and 6.5 (see Figures S4 and S5, Supporting Information), which are consistent with the viscosity results.

dx.doi.org/10.1021/ma300222d | Macromolecules 2012, 45, 3523−3530

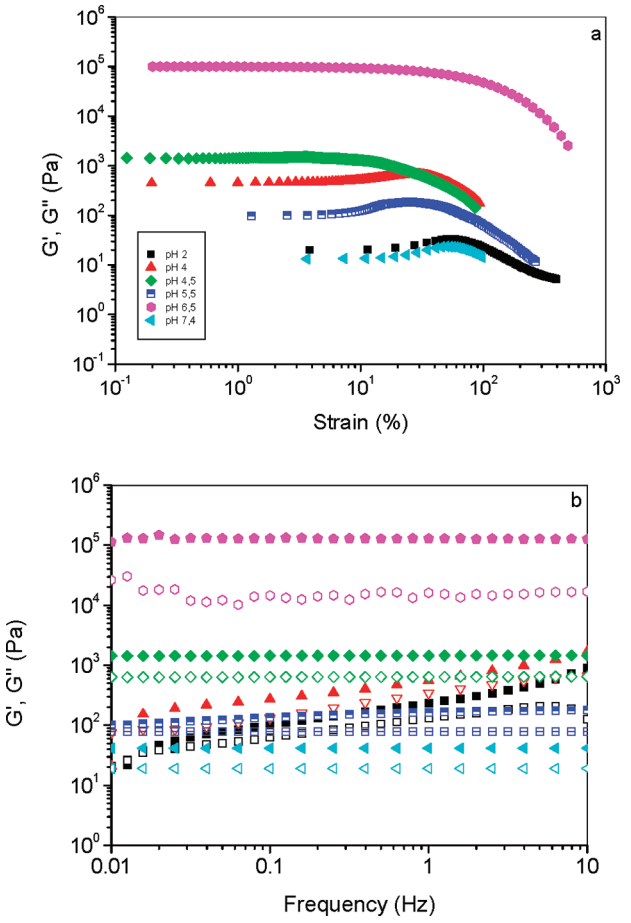


Figure 7. Strain-dependence of G' (a) and frequency dependence of G' and G'' (b) of 4 wt % heptablock copolymer solutions at 25 °C.

In order to understand better the influence of the pH on the viscoelastic properties of the hydrogels, SANS measurements were carried out at pD 4.0, 5.5, 6.5, and 7.5 and the results are shown in Figure 8. Again, good fits of eq 1 over most of the q-range (up to q = 1.4 nm^{-1}) were obtained. The resulting fitting parameters are compiled in Figure 9. All radii display a minimum at pD 5.5 (Figure 9a), implying that the aggregation number and the distance between the micelles also exhibit a minimum. The volume fraction of the correlated micelles is

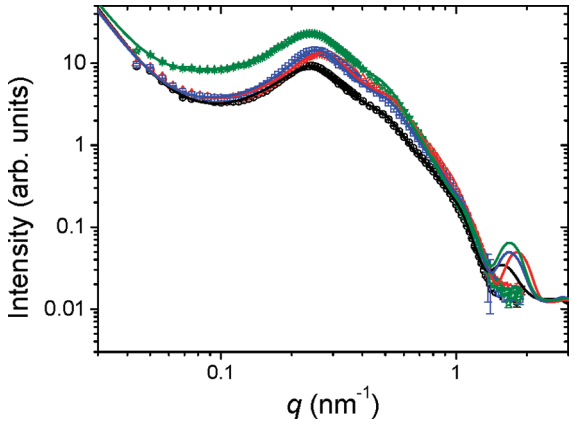


Figure 8. SANS curves from 4 wt % solutions at pD = 4.0 (black open circles), 5.5 (red open triangles up), 6.5 (blue open squares), and 7.5 (green open stars). The solid lines are fits; see text.

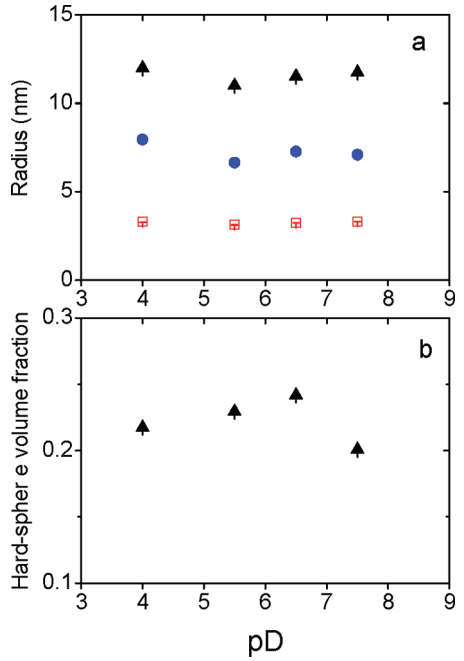


Figure 9. pD-dependence of 4 wt % solutions: (a) Core radius (open squares), micellar radius R_{mic} (closed circles) and hard-sphere radius R_{HS} (closed triangles up) and (b) hard-sphere volume fraction ϕ.

maximum at pD 6.5, thus the highest fraction of micelles is connected in clusters at this pD, which should result in a relatively stronger network. This could justify the maximum viscosity and modulus observed at pD 6.5. However, the influence of pD on the structural characteristics of the network as revealed from the SANS experiments cannot be directly correlated with the abrupt and complex variation of the rheological properties (e.g., minimum at pH 5.5 and sharp maximum at pH 6.5). It seems that rearrangements of the number of elastically effective chains (bridges) of the network and changes in the degree of their stretching should be the main reason for the viscosity behavior upon varying pH. These rearrangements may not be reflected necessarily in the variation of the aggregation number for instance.

As we have discussed previously,[45] the internal stickers along the chain were assumed to have different association potential from the end-stickers because the former bear at both ends charged (nonsticking) blocks which establish repulsions which may oppose association. This fact may account for the observed phenomena in the heptablock topology which were not observed in the triblock counterpart bearing only end-stickers. The SANS results showed that the bridging chains exceed the contour length of the DMA_{38} hydrophilic segment, indicating that several internal stickers could form pairwise associates. Further association of these stickers together with dangling ends ("open" end-sticker) seems to become attainable either by increasing copolymer concentration, or by varying the pH of the medium.

The strain-hardening effects also observed in Figure 6 (strain-dependence of G') in several pH conditions could also be attributed to the same effect that leads to an increase of the number density of the elastically active chains. Note that this effect has not been observed in the triblock counterpart.[15] The fact that the strain-hardening effect did not occur at pH 6.5, where the maximum elastic modulus was attained, may imply that the probable association of the stickers have been

dx.doi.org/10.1021/ma300222d | Macromolecules 2012, 45, 3523−3530

completed at will by simple pH adjustment and strain does not impose any further increase in the number of the elastic chains. This seems to be corroborated by the lower degree of ionization of the hydrophilic polyelectrolyte segments that become more flexible, favoring association of the hydrophobic blocks. Further increase of the pH up to 8 leads to complete deionization of the hydrophilic chains, resulting in the disruption of the network. A similar network disruption occurs at very low pH, and can be ascribed to electrostatic screening due to elevated ionic strength.

CONCLUSIONS

The unique rheological properties of aqueous solutions of an associative amphiphilic multiblock copolymer with chemical structure $BuMA_7$-*b*-DMA_{38}-*b*-$BuMA_7$-*b*-DMA_{38}-*b*-$BuMA_7$-*b*-DMA_{38}-*b*-$BuMA_7$ were explored. The behavior of the system and especially its ability to self-organize in a three-dimensional network (physical hydrogel) was governed by the interplay of the hydrophobic attractive interactions of the polyBuMA blocks, leading to formation of flower-like micelles, and the electrostatic repulsive interactions of the polyelectrolyte polyDMA blocks, which favored bridging of the micelles. The physical picture of the network structure, elucidated with the aid of the SANS measurements, consists of a three-dimensional network of bridged flower-like micelles.

The heptablock copolymer exhibited high gelation efficiency, resulting in the formation of a free-standing hydrogel at a copolymer concentration just above 3.5 wt %, characterized by viscosities more than 8 orders of magnitude higher than that of the aqueous medium. The critical gel concentration was determined at about 0.6 wt % (onset of network formation), which was remarkably low, rendering this multiblock amphiphilic polyelectrolyte to be a good candidate as rheology modifier. More importantly, the present system exhibited a different behavior as a function of copolymer concentration compared to the ABA type telechelic polyelectrolytes studied previously, which was ascribed to the additional internal hydrophobic stickers.

Since the hydrophilic segments of the copolymer exhibited weak polyelectrolyte features, this system displayed a rich behavior regarding its rheological properties in aqueous solutions as a function of pH. The rheological properties revealed a peculiar pH-dependence which has not been observed in telechelic polyelectrolytes of the ABA type composed of similar in nature blocks. In the sol−gel−sol transition, the viscosity passed through two maxima prior to a sharp decrease at high values of pH. The second viscosity maximum at pH 6.5 was attributed to a further contribution from the additional hydrophobic interactions of the internal stickers upon further decrease of the charge density of the polyDMA polyelectrolyte segments, resulting in the strengthening of the 3D network and in turn in the increase of the viscosity of the system.

This kind of polymeric materials may find application as thickeners in cosmetics, coatings, and other water-born formulations, and as injectable hydrogels[53] in pharmaceutical applications since they exhibit a sol state at pH 8 and a gel state at physiological pH.

ASSOCIATED CONTENT

Supporting Information

More rheological data concerning concentration and pH dependence of dynamic viscosities. This material is available free of charge via the Internet at http://pubs.acs.org/.

AUTHOR INFORMATION

Notes

The authors declare no competing financial interest.

ACKNOWLEDGMENTS

M.-T.P. and C.T. acknowledge support by University of Patras via the K. Karatheodory Program under contract number C897. CMP gratefully acknowledges support by the DFG priority program SPP1259 “Intelligente Hydrogele” (Pa771/4). N.A.H. and C.S.P. thank the Cyprus Research Promotion Foundation for a Doctoral Research Grant (Project ENISX/PENEK/0505/19) and the A. G. Leventis Foundation for financial support in establishing the NMR spectroscopy facilities at the University of Cyprus.

REFERENCES

(1) Rubinstein, M.; Dobrynin, A. V. *Curr. Opin. Colloid Interface Sci.* **1999**, *4*, 83.
(2) Berret, J.-F.; Calvet, D.; Collet, A.; Viguier, M. *Curr. Opin. Colloid Interface Sci.* **2003**, *8*, 296.
(3) Winnik, M. A.; Yekta, A. *Curr. Opin. Colloid Interface Sci.* **1997**, *2*, 424.
(4) Kimerling, S.; Rochefort, W. E.; Bhatia, S. R. *Ind. Eng. Chem. Res.* **2006**, *45*, 6885.
(5) Lee, K. Y.; Mooney, D. J. *Chem. Rev.* **2001**, *101*, 1869.
(6) Yu, L.; Ding, J. *Chem. Soc. Rev.* **2008**, *37*, 1473.
(7) Jeong, B.; Kim, S. W.; Bae, Y. H. *Adv. Drug Delivery Rev.* **2002**, *54*, 37.
(8) Pouliquen, G.; Tribet, C. *Macromolecules* **2006**, *39*, 373.
(9) Dayananda, K.; He, C.; Lee, D. S. *Polymer* **2008**, *49*, 4620.
(10) Tsitsilianis, C. *Soft Matter* **2010**, *6*, 2372.
(11) Tsitsilianis, C.; Iliopoulos, I.; Ducouret, G. *Macromolecules* **2000**, *33*, 2936.
(12) Tsitsilianis, C.; Iliopoulos, I. *Macromolecules* **2002**, *35*, 3662.
(13) Zaroslov, Y. D.; Fytas, G.; Pitsikalis, M.; Hadjichristidis, N.; Philippova, O. E.; Khokhlov, A. R. *Macromol. Chem. Phys.* **2005**, *206*, 173.
(14) Hietala, S.; Strandman, S.; Järvi, P.; Torkkeli, M.; Jankova, K.; Hvilsted, S.; Tenhu, H. *Macromolecules* **2009**, *42*, 1726.
(15) Bossard, F.; Aubry, T.; Gotzamanis, G.; Tsitsilianis, C. *Soft Matter* **2006**, *2*, 510.
(16) Katsampas, I.; Tsitsilianis, C. *Macromolecules* **2005**, *38*, 1307.
(17) Katsampas, I.; Roiter, Y.; Minko, S.; Tsitsilianis, C. *Macromol. Rapid Commun.* **2005**, *26*, 1371.
(18) Tsitsilianis, C.; Roiter, Y.; Katsampas, I.; Minko, S. *Macromolecules* **2008**, *41*, 925.
(19) Gotzamanis, G. T.; Tsitsilianis, C.; Hadjiyannakou, S. C.; Patrickios, C. S.; Lupitskyy, R.; Minko, S. *Macromolecules* **2006**, *39*, 678.
(20) Zhang, R.; Shi, T. F.; An, L. J. *J. Phys. Chem.* **2010**, *114*, 3449.
(21) Zhang, R.; Shi, T. F.; Li, H.; An, L. J. *J. Chem. Phys.* **2011**, *134*, 034903.
(22) Tsitsilianis, C.; Aubry, T.; Iliopoulos, I.; Norvez, S. *Macromolecules* **2010**, *43*, 7779.
(23) Borisova, O.; Billon, L.; Zaremski, M.; Grassl, B.; Bakaeva, Z.; Lapp, A.; Stepanek, P.; Borisov, O. *Soft Matter* **2011**, *7*, 10824.
(24) Bromberg, L. *Macromolecules* **1998**, *31*, 6148.
(25) Charbonneau, C.; Chassenieux, C.; Colombani, O.; Nicolai, T. *Macromolecules* **2011**, *44*, 4487.

(26) Charbonneau, C.; Chassenieux, C.; Colombani, O.; Nicolai, T. *Macromolecules* **2012**, *45*, 1025.
(27) Henderson, K. J.; Shull, K. R. *Macromolecules* **2012**, *45*, 1631.
(28) Hu, J.; Ge, Z.; Zhou, Y.; Zhang, Y.; Liu, S. *Macromolecules* **2010**, *43*, 5184.
(29) Ge, Z.; Zhou, Y.; Tong, Z.; Liu, S. *Langmuir* **2011**, *27*, 1143.
(30) Zhou, Y.; Jiang, K.; Song, Q.; Liu, S. *Langmuir* **2007**, *23*, 13076.
(31) Matsumiya, Y.; Matsumoto, M.; Watanabe, H.; Kanaya, T.; Takahashi, Y. *Macromolecules* **2007**, *40*, 3724.
(32) Selb, J.; Volpert, E.; Candau, F. *Polymer* **1998**, *39*, 1025.
(33) Jiang, J.; Malal, R.; Li, M. Y.; Colby, R. H.; Gersappe, D.; Rafailovich, M. H.; Sokolov, J.; Cohn, D. *Macromolecules* **2008**, *41*, 3646.
(34) Regalado, E. J.; Selb, J.; Candau, F. *Macromolecules* **1999**, *32*, 8580.
(35) Candau, F.; Regalado, E. J.; Selb, J. *Macromolecules* **1998**, *31*, 5550.
(36) Caputo, M.-R.; Selb, J.; Candau, F. *Polymer* **2004**, *45*, 231.
(37) Regalado, E. J.; Selb, J.; Candau, F. *Macromolecules* **2000**, *33*, 8720.
(38) Oh, H. J.; Joo, M. K.; Sohn, Y. S.; Jeong, B. *Macromolecules* **2008**, *41*, 8204.
(39) Cram, S. L.; Brown, H. R.; Spinks, G. M.; Hourdet, D.; Creton, C. *Macromolecules* **2005**, *38*, 2981.
(40) Branham, K. D.; Snowden, H. S.; McCormick, C. L. *Macromolecules* **1996**, *29*, 254.
(41) Braun, O.; Selb, J.; Candau, F. *Polymer* **2001**, *42*, 8499.
(42) Kujawa, P.; Audibert-Hayet, A.; Selb, J.; Candau, F. *Macromolecules* **2006**, *39*, 384.
(43) Kujawa, P.; Audibert-Hayet, A.; Selb, J.; Candau, F. *J. Polym. Sci., Part B: Polym. Phys.* **2004**, *42*, 1640.
(44) Candau, F.; Selb, J. *Adv. Colloid Interface Sci.* **1999**, *79*, 149.
(45) Popescu, M.-T.; Athanasoulias, I.; Tsitsilianis, C.; Hadjiantoniou, N. A.; Patrickios, C. S. *Soft Matter* **2010**, *6*, 5417.
(46) Webster, O. W.; Hertler, W. R.; Sogah, D. Y.; Farnham, W. B.; RajanBabu, T. V. *J. Am. Chem. Soc.* **1983**, *105*, 5706.
(47) Hadjiantoniou, N. A.; Patrickios, C. S. *Polymer* **2007**, *48*, 7041.
(48) Hadjiantoniou, N. A.; Triftaridou, A. I.; Kafouris, D.; Gradzielski, M.; Patrickios, C. S. *Macromolecules* **2009**, *42*, 5492.
(49) The copolymer under investigation has the same molecular characteristics as the heptablock copolymer reported in ref 45. In that reference, however, the chemical structure based on the nominal (theoretical) degrees of polymerization for each block was given as $BuMA_5$-*b*-DMA_{25}-*b*-$BuMA_5$-*b*-DMA_{25}-*b*-$BuMA_5$-*b*-DMA_{25}-*b*-$BuMA_5$.
(50) Strunz, P.; Mortensen, K.; Janssen, S. *Phys. B: Condens. Matter, Suppl. 1* **2004**, *350* (1−3), E783−E786.
(51) Kline, S. *J. Appl. Crystallogr.* **2006**, *39*, 895.
(52) Hiemenz, P. C. *Polymer Chemistry: The Basic Concepts*; New York: Marcel Dekker; 1984; p 6.
(53) Popescou, M.-T.; Mourtas, S.; Pampalakis, G.; Antimisiaris, S. G.; Tsitsilianis, C. *Biomacromolecules* **2011**, *12*, 3023.

Macromolecules

Article

pubs.acs.org/Macromolecules

Dissecting the Mechanism of the Heat-Induced Phase Separation and Crystallization of Poly(2-isopropyl-2-oxazoline) in Water through Vibrational Spectroscopy and Molecular Orbital Calculations

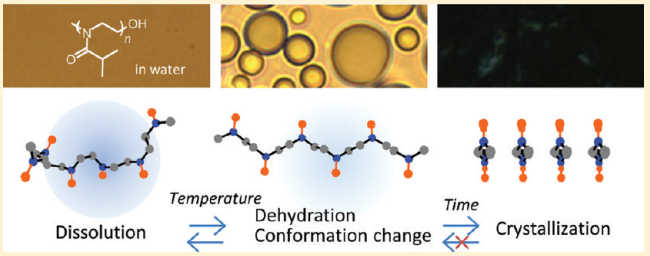
Yukiteru Katsumoto,*[,†] Aki Tsuchiizu,[†] XingPing Qiu,[‡] and Françoise M. Winnik*[,‡]

[†]Graduate School of Science, Hiroshima University, Kagamiyama 1-3-1, Higashi-Hiroshima 739-8526, Japan

[‡]Department of Chemistry and Faculty of Pharmacy, University of Montreal, CP 6128 Succursale Centre Ville, Montreal, QC H3C 3J7, Canada

Supporting Information

ABSTRACT: Aqueous solutions of amphiphilic polymers often undergo a heat-induced phase separation, which is known as the lower critical solution temperature (LCST) phase transition. In the case of aqueous poly(2-isopropyl-2-oxazoline) (PIPOZ) solutions, the phase separation is followed, upon prolonged heat treatment, by an irreversible crystallization of the polymer. Optical microscopy observation of a PIPOZ solution (60 g L^{-1}) in water revealed that liquid–liquid phase separation of the aqueous PIPOZ solution occurs at the cloud point (T_c) and that PIPOZ crystallizes in the polymer-rich liquid phase upon prolonged heating of the mixture at a temperature $T > T_c$. Vibrational spectroscopy combined with molecular orbital (MO) calculations and spectral measurements with model compounds were employed to monitor water/polymer interactions and changes in polymer conformation during the LCST-type phase separation. The thermally induced spectral variations suggest that the dehydration of the PIPOZ amide functions occurs gradually as the temperature is raised from 20 °C up to T_c. Upon prolonged heating of the phase-separated mixture at constant temperature (T_c + ~2 °C), the infrared spectrum of the polymer undergoes further changes ascribed to conformational transitions of the polymer backbone. These changes, which are irreversible upon cooling the solution below T_c, lead to the conformation taken by the polymer in the crystalline phase. This situation facilitates crystallization of the polymer by a nucleation/growth mechanism in the polymer-rich phase, a process akin to the crystallization of proteins from solution.



INTRODUCTION

Crystallization from solutions is a ubiquitous phenomenon that drives a variety of industrial manufacturing processes, geological events, laboratory manipulations, physiological pathways, and pathological situations. Under specified conditions, the process generates reproducibly particles with desired size, shape, crystal form, and purity. Yet, controlling the crystallization of molecular and nanoscale systems remains a challenge in physics, chemistry, and biology. For instance, although crystallization is central to protein characterization, there is still no set of rules for the rational *in vitro* production of protein crystals.[1] The phase behavior and association dynamics of protein solutions, however, are reasonably well understood.[2] It is generally assumed that protein crystallization proceeds via a two-step process involving, first, the formation of liquid droplets of high protein concentration and, second, the creation of ordered protein clusters within the dense liquid intermediate immediately prior to nucleation leading to protein crystals.[3] The development of ordered clusters is the rate-limiting step in this two-step nucleation model.[4] The classical nucleation model, which involves only one step, namely the generation of ordered crystalline nuclei from dense molecular clusters,[5] does not apply to the case of proteins in solutions due to the short range of their attractive interactions. Experimental evidence of liquid/liquid phase separation was reported in the case of lysozyme crystallization[6] as well as in solutions of normal and sickle cell hemoglobin.[7]

The phase behavior of synthetic polymer/solvent mixtures, in which both crystallization and liquid/liquid phase separation may occur, has been a topic of heated discussions since the early 1940s when Richards envisaged this situation for the first time.[8] Soon after, it was demonstrated experimentally with several polymer/solvent pairs for which the upper critical solution temperature (UCST) was located above the melting temperature.[9] In these systems, the liquid/liquid phase can be identified by the apparition of turbidity upon cooling the solution below a given temperature, the cloud point (T_c). Crystallization occurs by nucleation and growth within the polymer-rich liquid phase and can be detected by light scattering between crossed polars.[10] The phase diagram of a

Received: February 5, 2012
Revised: March 25, 2012
Published: April 4, 2012

ACS Publications © 2012 American Chemical Society

polymer/solvent system changes depending on the molecular weight of the polymer. A decrease in molecular weight lowers the UCST line but hardly affects the melting line. Hence, situations arise where the UCST lies below the melting temperature. Under equilibrium conditions, such a UCST line has no significance. However, under nonequilibrium conditions liquid/liquid separation may still take place if the energy barrier of crystallization is sufficiently high.[11] This phase separation process underlies an important processing technique in material sciences, known as thermally induced phase separation (TIPS), a process using nonequilibrium thermal quenching to create intricate liquid/liquid morphologies that are "frozen" upon crystallization of the polymer-rich liquid phase.[12] It is used in the fabrication of microcellular foams, microporous membranes,[13] and, more recently, scaffold materials in tissue engineering.[14] Poly(2-nonyl-2-oxazoline) and poly(2-isobutyl-2-oxazoline) in mixed ethanol/water solutions also undergo crystallization upon annealing below their UCST, by a process involving intermediate liquid/liquid separation.[15]

Liquid/liquid phase separation can also occur upon heating a polymer solution that undergoes a lower critical solution temperature (LCST)-type phase transition. The phenomenon has been observed in aqueous solutions of amorphous polymers. For example, in the course of a study of the heat-induced phase separation of aqueous poly(vinyl methyl ether), Tanaka observed that a temperature jump above the LCST line triggers the formation of a polymer-rich phase dispersed in the lean phase in the form of micrometer-sized droplets that remain stable up to 2 days with no sign of coalescence although they undergo fast Brownian motion.[16] Tanaka attributed this remarkable stability to a viscoelastic effect[17] that prevents polymer chains from interdiffusing upon collision of two moving droplets. The same effect has also been put forward to account for the formation of stable mesoglobules upon heat-induced phase separation of aqueous poly(*N*-isopropylacrylamide) (PNIPAM) solutions,[18] although in these solutions liquid/liquid phase separation, *per se*, has never been reported.

In the case of the solutions of semicrystalline polymers that undergo a LCST-type phase behavior, liquid/liquid phase separation may be accompanied by simultaneous or subsequent polymer crystallization. This phenomenon is well-known in the case of blends of amorphous and crystalline polymers.[19] As far as we are aware, there are few, if any, examples of polymer solutions where LCST-type liquid/liquid phase separation and crystallization compete or coexist. Aqueous solutions of poly(2-isopropyl-2-oxazoline) (PIPOZ, Figure 1), a crystalline polymer

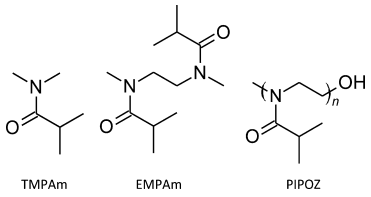


Figure 1. Chemical structures of TMPAm, EDMPAm, and PIPOZ.

with a melting temperature of ~200 °C,[20] present the necessary features, since they undergo an LCST-type phase separation around 40 °C,[21] and PIPOZ crystallizes from the solutions when they are heated to temperatures in the vicinity of 65 °C.[22,23] The possibility of a liquid/liquid phase separation prior to crystallization was invoked. However, direct evidence of the phenomenon was not provided.

Given the nontoxicity of polyoxazolines,[24] further studies of the temperature responsiveness of its aqueous solutions are easily justified, as they may lead the way to new biomedical applications of PIPOZ and its copolymers.[25] Driven by these opportunities, we set about to gain a detailed insight into the overall phenomenon by gathering local nanoscopic information, in addition to the thermodynamic data and mesoscopic structural observations currently available. Various spectroscopic tools can be used to gain local information about polymer conformation, association, and dynamics in solution, including magnetic resonance spectroscopy,[26] fluorescence spectroscopy,[27] electron paramagnetic spectroscopy,[28,18d] and infrared spectroscopy (IR).[29] The latter is particularly powerful to monitor local conformation changes of the polymer chain as well as changes in polymer/water interactions believed to play an important role in the LCST-type phase separation of aqueous polymer solutions. For instance, studies of the phase behavior of PNIPAM in water by IR spectroscopy gave direct evidence that heating the system brings about the dehydration of the polymer side chains,[30] in agreement with the theoretical treatment of the PNIPAM phase separation in water introduced by Okada and Tanaka.[31] In a previous report, we pointed out that conformational changes of the polymer also occur during the phase separation.[32] Moreover, a detailed analysis of the IR spectra with the aid of molecular orbital (MO) calculations led to the conclusion that intramolecular interactions among the side chains of PNIPAM compete with the hydration/dehydration process.[33]

In the first part of this article, we describe results of studies by optical microscopy, which allowed us to observe a liquid/liquid phase separation in aqueous PIPOZ solutions heated through their T_c. Polymer-rich micrometer-sized droplets formed above T_c. The droplets grew in size with increasing temperature. At sufficiently high temperature, PIPOZ crystallization took place within the droplets. Next, we examine by vibrational spectroscopy the heat-induced liquid−liquid phase separation of aqueous PIPOZ solutions and compare them to the vibrational spectra of new model compounds analogous to the dimer of the PIPOZ repeat unit. Analysis of the spectra of the model compounds combined with molecular orbital (MO) calculations yields a precise molecular picture of the temperature-induced changes in polymer conformation and hydration throughout the liquid/liquid phase separation. Our study provides important mechanistic insights onto the evolution of the liquid/liquid phase separation that leads the way to polymer crystallization. Overall, the phenomena observed bear remarkable similarities to the two-step nucleation of protein crystals from aqueous solutions.

EXPERIMENTAL SECTION

Materials. *N*,*N*,2-Trimethylpropionamide (TMPAm) was purchased from Wako Pure Chemical Ltd. PIPOZ was prepared as described previously.[34] The number-average molecular weight M_n, the polydispersity M_w/M_n, and the cloud point T_c of the samples are listed in Table 1. The cloud point of this sample was measured by turbidimetry. The dimer model compound, *N*,*N*′-1,2-ethanediylbis(*N*,2-dimethylpropanamide) (EDMPAm), was prepared by reaction of isobutyryl chloride with *N*,*N*′-dimethylethylenediamine in dry dichloromethane at 0 °C in the presence of triethylamine.[35] The crude amide was purified by fractional distillation at reduced pressure (bp 190−194 °C, 15 mmHg). The ^{1}H NMR spectrum of EDMPAm was obtained using a JEOL JNM-LAMBDA spectrometer (500 MHz, Natural Science Center for Basic Research and Development (N-BARD), Hiroshima University). ^{1}H NMR (500 MHz, DMSO-d_6 at

dx.doi.org/10.1021/ma300252e | *Macromolecules* 2012, 45, 3531−3541

Table 1. Characterization of PIPOZ Samples

sample	M_n/g mol^{-1}	M_w/M_n	T_c/°C	concn/wt %	solvent
PIPOZ-10K	10 400	1.06	44.0[a]	0.1	H_2O
			38.3	2.0	D_2O
PIPOZ-6K	5800	1.20	41.4	2.0	H_2O
			40.4	2.0	D_2O
			38.6	6.0	D_2O

[a]Reference 34.

120 °C): δ 1.09 (d, 12H, $-CH(CH_3)_2$), 2.76 (m, 2H, $-CH(CH_3)_2$), 3.07 (m, 6H, $-NCH_3$), 3.54 (s, 4H, $-N(CH_2)_2N-$). The chemical structures of PIPOZ, EDMPAm, and TMPAm are shown in Figure 1.

Procedures for Direct Monitoring of the Liquid–Liquid Phase Separation and Crystallization of PIPOZ. Samples of a PIPOZ solution (6 wt %) in water were held between two microscope slides as follows: The solution (10 μL) to be monitored was placed on a glass slide; a smaller glass coverslip was placed on top of the drop. The edge of the coverslip was sealed with an epoxy glue. The liquid spread over a circular area ~10 mm in diameter. The solution thickness, estimated from the solution volume and the area of the spread solution, was ~100 μm. The slides were mounted on the temperature control stage (THMS 600 with TMS94, Linkam) of a microscope (Axioskop 2, Carl Zeiss). The heating rate was 10 °C min^{-1}, unless otherwise specified.

Turbidimetry. The temperature dependence of transmittance of 650 nm light was monitored using a homemade apparatus equipped with a Si photodiode detector (S2386-18K, Hamamatsu Photonics). The temperature was controlled by a homemade thermostat with an accuracy of 0.1 °C. Heating rate was less than 0.2 °C min^{-1}. T_c was taken as the inflection point of the transmittance curves.

IR Spectroscopy. IR spectra were measured at a resolution of 2 cm^{-1} with coaddition of 512 scans using a Nicolet 6700 Fourier-transform IR spectrometer equipped with a liquid-nitrogen-cooled MCT detector. The attenuated total reflection (ATR) technique was employed to obtain IR spectra of polymer solutions (2 wt %). An ATR cell made of a horizontal ZnSe crystal (RI = 2.403) with an incident angle of 45° was filled with a polymer solution. The temperature of the ATR cell was controlled by a homemade thermoelectric device with an accuracy of ±0.1 °C. The cell was sealed by a toggle-clamp type cover to prevent solvent evaporation. Data processing, such as the background solvent spectrum subtraction, derivative calculation, and the nonlinear least-squares method, was performed by a software composed by one of the authors (Y.K.).[36] The pretreatment procedure for ATR/IR spectra of polymers in solutions, including the subtraction of the solvent spectrum from a sample spectrum, was described previously.[32]

Raman Spectroscopy. Raman spectra were recorded on a JASCO NRS-2100 Raman spectrometer equipped with a CCD detector (Princeton Instrument LN/CCD-1100 PBUVAR). The excitation wavelength of Raman scattering was 514.5 nm from an Ar ion laser (Spectra-Physics 2016). The spectral resolution and laser power at the sample position were 4 cm^{-1} and 200 mW, respectively. Raman spectra were acquired for a 10 wt % solution of EDMPAm in D_2O.

MO Calculations. All MO calculations were performed using the B3LYP functional with a 6-31+G(d) basis set.[37] For the calculation of solvent effects, the polarizable continuum model using the integral equation formalism variant (IEFPCM) was used. The computations were carried out on the GAUSSIAN 03 program.[38] Optimized geometries and vibrational frequencies of the model compounds were calculated. The zero-point energy correction was carried out. The harmonic wavenumbers ν_{harm} obtained were scaled by the wavenumber linear scaling (WLS) method: $\nu_{scale} = \nu_{harm} \times (1.003 - 0.000021 \times \nu_{harm})$.[39] WLS parameters were chosen so as to reproduce the experimental IR spectra in the fingerprint region. IR and Raman spectra were simulated by assuming a Lorentzian band shape with a bandwidth of 7 cm^{-1}.

RESULTS AND DISCUSSION

Direct Observation of the Temperature-Induced Phase Transitions of an Aqueous PIPOZ Solution. The temperature of an aqueous solution of PIPOZ-6K (6 wt %) placed between two sealed microscope slides was raised from 20 to 70 °C while recording the changes in appearance of a specific area of the specimen, as displayed in Figure 2a. Within a few seconds of reaching 48 °C, droplets of 1–2 μm in size

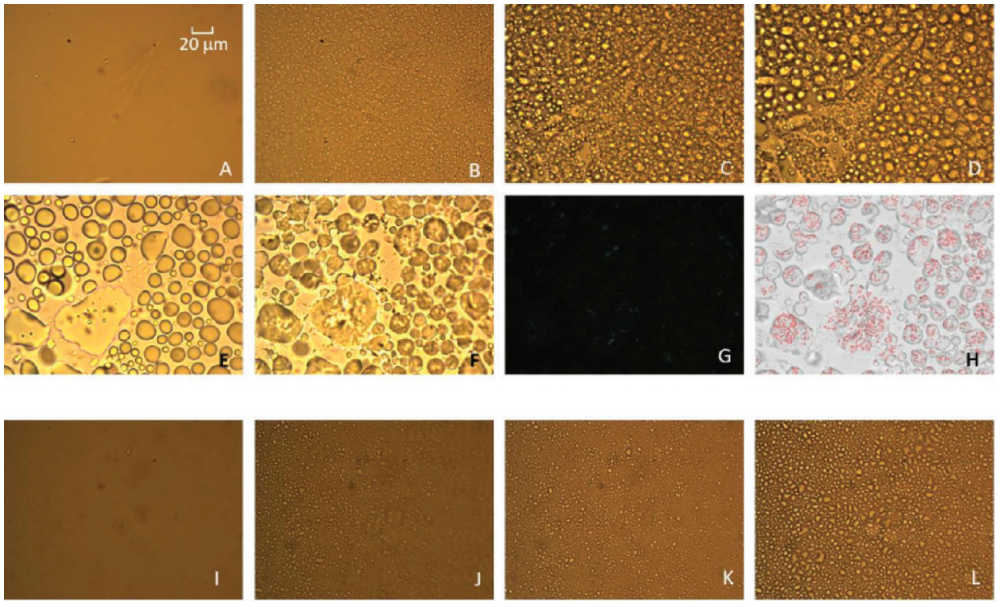


Figure 2. Optical micrographs of a solution of PIPOZ-6K in water (6 wt %) undergoing liquid/liquid phase separation and crystallization (heating rate = 10 °C min^{-1}): (A) 20 °C, (B) 48 °C, (C) 50 °C, (D) incubated for 2 h at 50 °C, (E) incubated for 2 h at 70 °C, (F) incubated for 30 h at 70 °C, (G) the transmittance image through crossed Nichols polarizers for (F). The image (H) is a composite of the gray-scaled (F) with the image (G) after applying the edge detection. The micrographs from (I) to (L) show the growth of droplets by heating at a rate of 0.3 °C min^{-1}: (I) 39.8, (J) 40.1, (K) 40.9, and (L) 41.2 °C.

dx.doi.org/10.1021/ma300252e | Macromolecules 2012, 45, 3531–3541

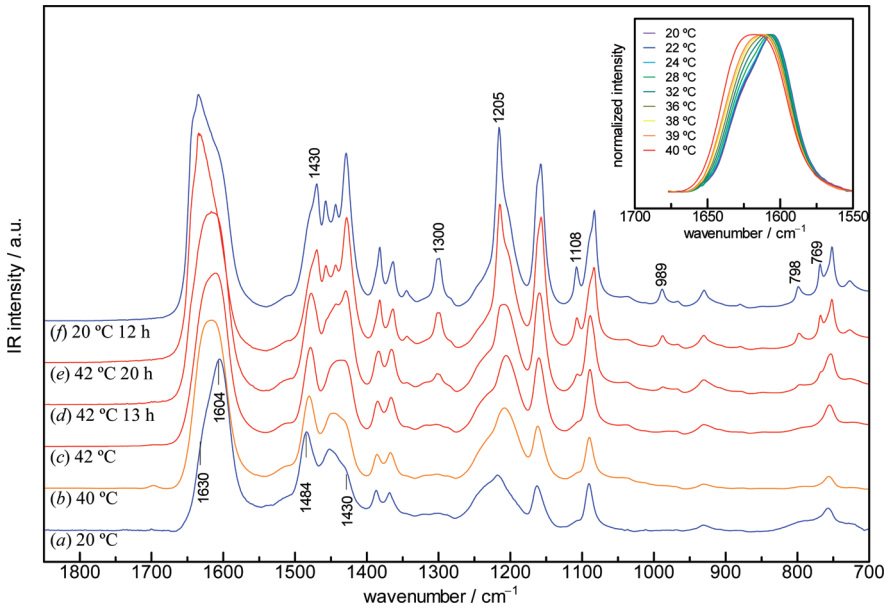


Figure 3. Temperature and time dependence of IR spectra of a solution of PIPOZ-10K in D_2O (2 wt %). The spectra shown were obtained after subtraction of the IR spectrum of D_2O from spectra measured under the following conditions. (a) 20 °C, (b) 40 °C, (c) 42 °C, (d) after incubation for 13 h at 42 °C, (e) after incubation for 20 h at 42 °C, (f) solution (e) cooled to 20 °C and kept at 20 °C for 12 h. The inset represents the temperature dependence of the $\nu_{C=O}$ band in water after baseline correction.

became visible, and in a matter of seconds they grew to sizes of 10−20 μm (Figure 2B). The droplets partook in Brownian motion, and their size grew by coalescence. We were concerned by the fact that the temperature of appearance of the droplets turned out to be significantly higher than the cloud point (38.6 °C) determined by turbidimetry for a 6 wt % aqueous solution of PIPOZ-6K (see Table 1). Such a difference may be due to the rather fast heating rate (10 °C min^{-1}) selected. We performed a control experiment, in which the stage was heated from 30 to 45 °C at a rate of 0.3 °C min^{-1} (Figures 2I−L). Under these conditions, droplet formation occurred between 38.5 and 40.0 °C, a temperature range that corresponds well to T_c of this solution, confirming that the heating rate affects the temperature of the liquid/liquid phase separation. However, the heating rate has no significant impact on the size of the droplets formed at a given temperature above T_c (see Figure 2L).

Several experimental protocols were carried out to convince us that (i) droplets are indeed formed and (ii) this is a true reversible liquid/liquid phase separation. A sample heated at a rate of 10 °C min^{-1} was kept at 50 °C for 2 h. The number of smaller droplets (2−5 μm) gradually decreased. After 2 h at 50 °C, most of the droplets had a diameter of 20−50 μm, with only a few larger drops (Figure 2D). There was no further coarsening at all, although the droplet density was high enough to cause frequent collisions. To test the reproducibility of the observations and the reversibility of the liquid/liquid phase separation, we heated several samples from 20 to 50 °C and always observed droplet formation. After being kept for a few minutes at 50 °C, each sample was cooled to 20 °C. A one-phase solution was recovered; no feature whatsoever could be seen by optical microscopy. The appearance of each sample was identical to the original state (Figure 2A). With several samples, we increased and decreased the sample temperature from 20 to 50 °C and back, several times, without any apparent changes in the kinetics of droplet appearance/disappearance that would indicate permanent alterations of the solution composition or microstructure. We attempted to determine the PIPOZ concentration of the polymer-rich phase using various *in situ* methods, including FTIR and Raman imaging, but failed to obtain reliable data. Then, we sought means to trigger the macroscopic liquid/liquid phase transition in a vial and to separate the dense layer. Analysis of this layer by refractometry or densitometry would lead to its polymer concentration. We placed a 1 mL aliquot of the PIPOZ solution in a conical vial and heated it to 50 °C. The solution became turbid as the temperature reached 40 °C. The turbidity persisted upon prolonged incubation at 50 °C, yet the suspension showed no tendency at all to separate into two liquid layers, confirming the stability against coalescence of the polymer-rich liquid droplets. This point will be addressed in detail in a forthcoming publication.[40]

Next, we used optical microscopy to visualize the crystallization of PIPOZ from hot water. A fresh sample was incubated at 50 °C for 2 h and rapidly heated to 70 °C. At this temperature, the droplets grew via coalescence, such that after a 2 h incubation their average diameter was on the order of 20−100 μm (Figure 2E). Examination of the sample through crossed Nichols polarizers failed to reveal any crystallization. Upon prolonged heating at 70 °C the droplets stopped growing. Their appearance changed, as seen in Figure 2F, which presents a micrograph of the same sample after a 30 h incubation at 70 °C. Droplets are no longer smooth. Their periphery appears rugged. Observation under polarized light revealed the blue hue of transmitted light characteristic of the presence of crystals (Figure 2G). Figure 2H, which is a composite of Figures 2G and 2F, presents evidence that crystallization occurred within the dense droplets and not in the continuous polymer-lean phase.

Temperature-Induced Conformational Changes of PIPOZ Chains in Water. *IR Spectra of Aqueous PIPOZ Solutions (20 °C < T < 42 °C).* All measurements were performed with a 2% PIPOZ-10K solution in deuterated water (T_c = 38.3 °C, see Table 1). We confirmed independently that PIPOZ in D_2O solution undergoes the liquid−liquid phase

dx.doi.org/10.1021/ma300252e | *Macromolecules* 2012, 45, 3531−3541

separation and following crystallization in the same manner as in H_2O, even though T_c of the D_2O solution is slightly lower than the T_c of the H_2O solution, as shown in Table 1 and discussed previously.[34] Control experiments confirmed that PIPOZ crystallizes from the solution in D_2O tested by IR spectroscopy heated to 70 °C, but not upon prolonged heating at 42 °C. Instrumental limitations prevented us from heating samples to 70 °C in the IR spectrometer sample compartment; hence, it was not possible to monitor PIPOZ crystallization by IR spectroscopy.

The IR spectrum of aqueous PIPOZ within this temperature range presents several bands in the 1550−700 cm^{-1} region, arising from the vibration modes of the polymer main chain and the isopropyl side groups. It also has a strong band around 1600 cm^{-1}, attributed to the C═O stretching ($\nu_{C=O}$) mode. In the spectrum recorded at 20 °C (trace a in Figure 3), this band consists of at least two overlapping bands centered at ca. 1630 and 1605 cm^{-1}. On the basis of previous studies,[41] we assigned the former band to the vibration of C═O groups with two hydrogen-bonded water molecules and the latter one to fully hydrated C═O groups. Tertiary amides in water, in general, have a unimodal $\nu_{C=O}$ band observed at ca. 1600 cm^{-1}.[41,42] The band at 1630 cm^{-1} is often present in the spectrum of hydrophilic polymers bearing tertiary amide substituents. It has been taken as an indication that the hydration of the amide C═O groups is somehow inhibited, possibly due to the steric hindrance imposed by neighboring monomeric units or due to interchain association.

The PIPOZ solution was heated to 40 °C, and its IR spectrum was recorded again. There were minor changes in the relative intensity of the bands at 1630 and 1605 cm^{-1}: the intensity of the band at 1630 cm^{-1} increased with increasing temperature (see inset Figure 3). The IR bands in the 1500−1400 cm^{-1} region also underwent slight changes. The solution temperature was raised to 42 °C, which is above T_c. There was no immediate change in the spectrum (see traces b and c in Figure 3). After a few minutes, this solution was cooled back to 20 °C. Its spectrum was identical to the initial spectrum (spectrum a in Figure 3). Subsequently, a fresh sample was heated to 42 °C and kept at this temperature for 20 h. IR spectra were recorded from time to time during incubation. As time progressed, the IR spectra underwent significant changes, as seen in Figure 3, where traces d and e are IR spectra of the PIPOZ solution incubated at 42 °C for 13 and 20 h, respectively. Qualitatively, one notices that after a 20 h incubation at 42 °C several IR bands become sharper and new bands appear at 1300, 1108, 989, 798, and 769 cm^{-1}. The relative intensities of bands around 1430 and 1205 cm^{-1} also vary remarkably.

At the end of the incubation, the sample was brought back to 20 °C, kept at this temperature for 12 h, and re-examined by IR spectroscopy. The spectrum recorded (trace f) was quite different from that of the original solution (spectrum a in Figure 3). It was remarkably similar to the spectrum recorded at 42 °C (spectrum e in Figure 3). Hence, the heat-induced spectral changes are irreversible, at least within the time frame probed here. The recovered solution was clear to the eye at room temperature, without visible sign of crystallization. Therefore, the spectral changes cannot be ascribed to PIPOZ crystallization. We set about to elucidate the mechanisms responsible for the remarkable changes in the IR spectrum of aqueous PIPOZ at 42 °C, with the help of MO calculations and spectral studies of a low molecular weight model compound, as described in the following sections.

Preferred Conformations of the Model Compound EDMPAm Based on MO Calculations, Spectral Simulations, and Experimental Results. The first step in this study was to select a suitable model compound as well as an adequate MO calculation method. We considered two model compounds: TMPAm and EDMPAm (Figure 1). They correspond to the monomer and dimer units of PIPOZ, respectively. The IR spectra of the two compounds in tetrachloromethane are presented in Figure 4A, together with the spectrum of PIPOZ

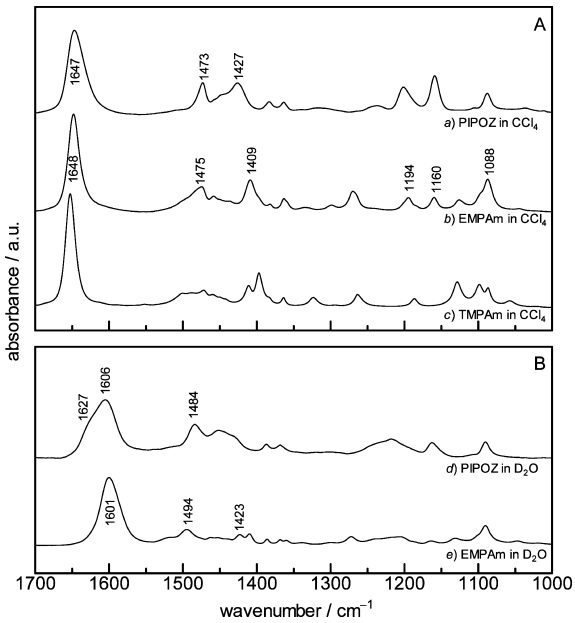


Figure 4. (A) IR spectra of PIPOZ, EDMPAm, and TMPAm in CCl_4. (B) IR spectra of PIPOZ and EDMPAm in D_2O.

in the same solvent. The IR spectrum of TMPAm is obviously different from that of the polymer. Hence, TMPAm was not considered further. The spectrum of EDMPAm reproduces reasonably well the spectrum of PIPOZ, in particular the bands near 1475, 1409, 1194, 1160, and 1088 cm^{-1} attributed to the skeletal vibrations of the polymer main chain ($-NCH_2CH_2N-$). To ascertain that EDMPAm is indeed a good model, we compared the spectra of EDMPAm and PIPOZ in aqueous solutions (Figure 4B). As in the case of the polymer, the $\nu_{C=O}$ band of EDMPAm undergoes a shift to shorter wavenumbers, from 1648 (CCl_4) to 1601 cm^{-1} (D_2O). The band remains unimodal, in contrast to the case of PIPOZ in water, for which the $\nu_{C=O}$ band has two contributions (see above). This was anticipated, given that the band at 1630 cm^{-1} in the spectrum of PIPOZ was attributed to polymer-specific steric hindrance caused by neighboring units as discussed above. The band near 1480 cm^{-1} in the spectrum of EMDPAm in CCl_4 shifts to a higher wavenumber in the spectrum in D_2O, a trend exhibited by PIPOZ as well.

The B3LYP/6-31+G(d) method was selected to carry out MO calculation-based spectral simulations. A test run using TMPAm convinced us that the method is suitable (see simulated and experimental spectra shown in Figure S1 in Supporting Information). To examine the conformation effects on the stability of EDMPAm, we developed a Ramachandran-type potential energy (PE) diagram for the dihedral angles of

dx.doi.org/10.1021/ma300252e | Macromolecules 2012, 45, 3531−3541

N−C−C−N (ϕ) and O=C−N−C(−C) (ψ). The angle ϕ defines the rotational conformers of the EDMPAm backbone, while ψ reflects those of the conformers of the isobutyryl side chain. Geometry optimization in redundant internal coordinates was performed for ϕ and ψ.[43] Since the effects of the relative orientation of the isopropyl group on the stability are minor, compared with those of ϕ and ψ, the rotation of isopropyl groups was not constrained in the geometrical optimization in redundant internal coordinate. The contour map of the PE diagram (Figure 5) reveals the existence of six

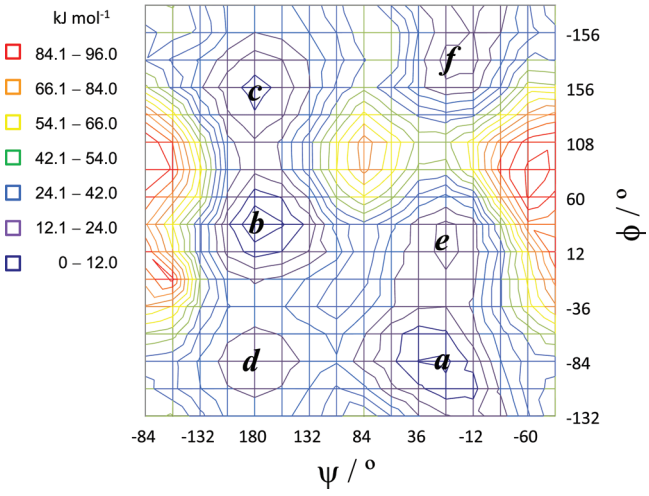


Figure 5. Ramachandran-type potential energy diagram for ϕ and ψ of EDMPAm obtained from the MO calculations at the B3LYP/6-31+G(d) level. The zero point energy is not corrected. See Supporting Information for the information on scan and constraint.

minima, corresponding to the EDMPAm conformers with (ϕ, ψ) ~ (180°, 0°) (a), (60°, 180°) (b), (−60°, 180°) (c), (180°, 180°) (d), (60°, 0°) (e), and (−60°, 0°) (f).

In the vicinity of each local minimum, there are several rotational conformers depending on the relative orientation of isopropyl groups, which gives rise to a secondary effect on the stability of the conformers. Thus, we carried out the geometrical optimization without any constraint for the conformers that are assumed to be found near the six local minima of the PE diagram. The calculation results for the representative conformers are summarized in Table 2 and Figure 6.[44] In the conformer designations, the letters (*a*, *b*, ...) correspond to the six minima in the PE diagram and the numbers (1, 2, ...) correspond to specific orientations of the isopropyl group. Judging from the relative energy ΔE shown in

Table 2. Relative Energy ΔE (kJ mol^{-1}) from the Energy of the Most Stable Conformer (*a*1), ϕ, and ψ for EDMPAm Conformers Optimized in Vacuum

ID	ΔE^a/kJ mol^{-1}	ϕ/deg	ψ/deg
*a*1	0.00	180.0	11.30
*a*2	0.446	177.9	14.12
*b*1	0.0867	62.60	182.7
*c*1	7.10	53.69	158.6
*d*3	16.2	170.0	175.6
*e*3	11.7	78.10	16.88
*f*4	11.7	−78.09	−2.87

[a]Zero point energy was corrected.

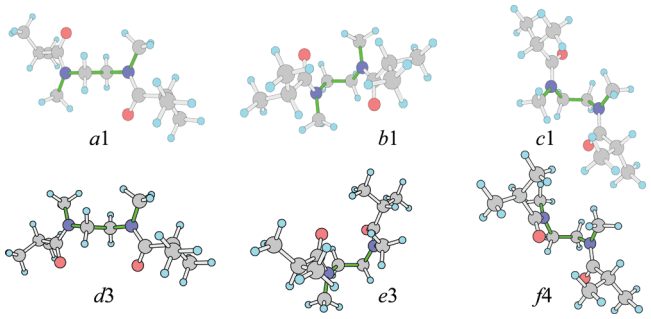


Figure 6. Optimized geometries of the representative conformers of EDMPAm in vacuum.

Table 2 (see Table S1 also), the conformers *a*1, *a*2, and *b*1 are observable in a nonpolar environment, such as in the gas phase and in nonpolar solvents, while in these conditions the population of the other conformers should be low.

In Figure 7, the simulated spectra of the three most stable conformers of EDMPAm—*a*1, *a*2, and *b*1—are confronted to

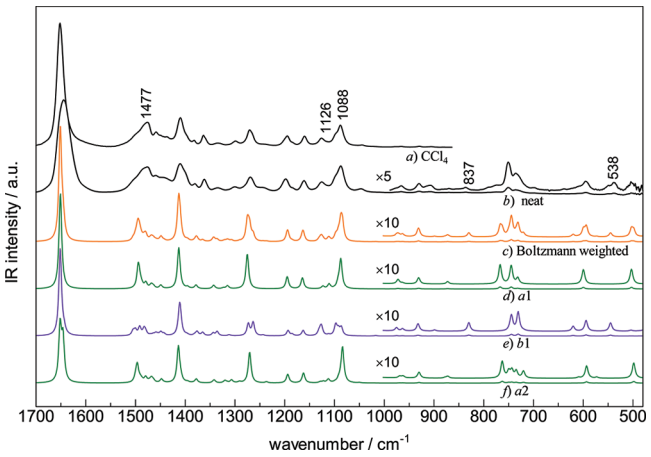


Figure 7. Experimental IR spectra of EDMPAm (a) in CCl_4 and (b) neat liquid and simulated IR spectra at the B3LYP/6-31+G(d) level for (d) *a*1, (e) *b*1, and (f) *a*2. Trace c is the Boltzmann-averaged spectrum of *a*1, *b*1, and *a*2.

the actual IR spectra of EDMPAm, neat and in CCl_4. The simulated spectra of the conformers *a*1 and *a*2 correspond reasonably well to the experimental spectra.[45] There are differences, however. Specifically, the bands at 1126, 837, and 538 cm^{-1} in the experimental spectra are conspicuously absent in the simulated spectrum. Also, the shape of the envelope near 750 cm^{-1} in the simulated IR spectrum of *a*1 or *a*2 is different from that in the experimental spectra. Bands at the wavenumbers mentioned above, or in close proximity to them, are present in the simulated spectrum of the conformer *b*1. Hence, the three conformers must coexist in EDMPAm in nonpolar solvents or neat. This conclusion is confirmed by the excellent agreement between the Boltzmann-weighted average of the simulated spectra of *a*1, *a*2, and *b*1 (Figure 7, trace c) and the experimental IR spectra of EDMPAm. It is generally acknowledged that Raman spectroscopy is more sensitive to skeletal conformational changes than IR spectroscopy. Therefore, as ancillary support to conclusions drawn from IR spectroscopy, we measured Raman spectra of EDMPAm neat and in CCl_4 (Figure S3). We also generated simulated Raman spectra of the conformers, which are presented in Figures S3 and S4, together

dx.doi.org/10.1021/ma300252e | *Macromolecules* 2012, 45, 3531−3541

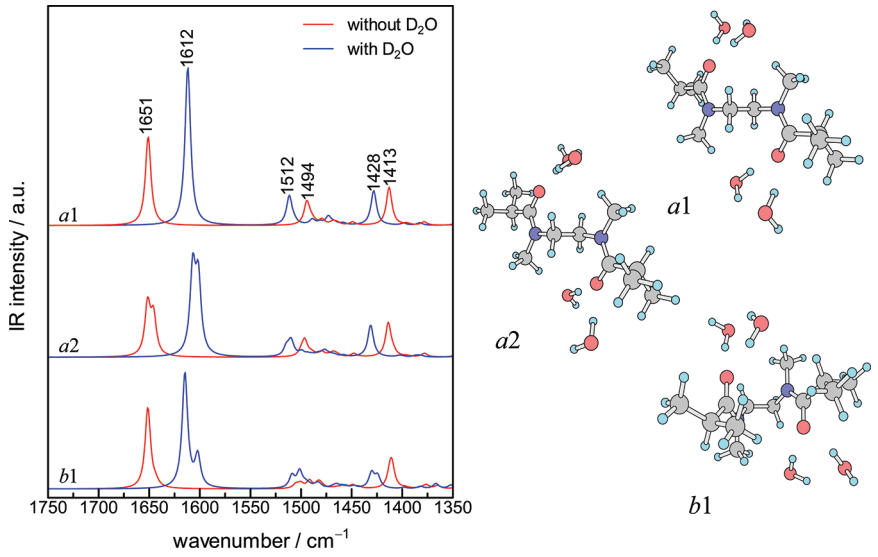


Figure 8. (right) Optimized conformations of the complex of EDMPAm and four D_2O molecules. (left) Simulated IR spectra of the various conformers of the complexes calculated by the B3LYP/6-31+G(d) method.

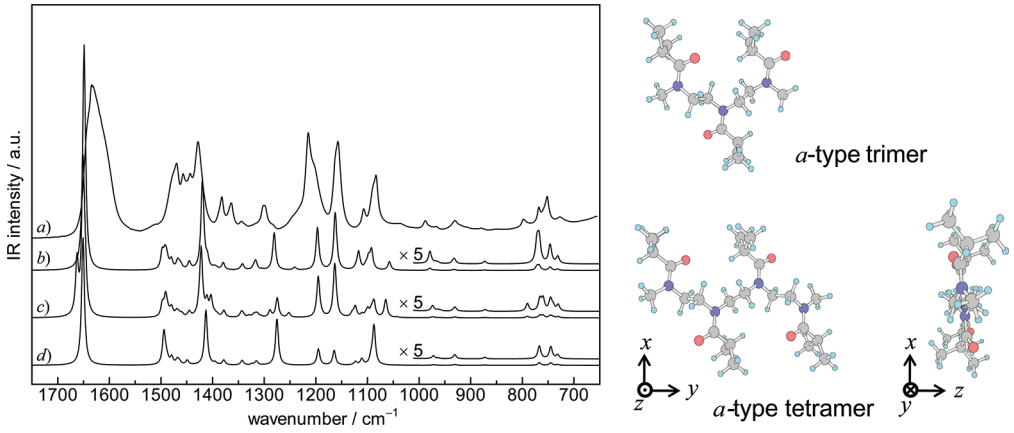


Figure 9. (left) (a) Experimental IR spectrum of a solution of PIPOZ in D_2O incubated for 20 h at 42 °C and the simulated IR spectra of (b) *a*-type tetramer, (c) *a*-type trimer, and (d) *a*-type dimer obtained by the B3LYP/6-31+G(d) method. (right) Optimized conformers of the multimers models.

with the Boltzmann-weighted simulated Raman spectrum for *a*1, *a*2, and *b*1. There is an excellent agreement between experimental and simulated Raman spectra.

Effects of Hydration on the Vibrational Spectra of EDMPAm and PIPOZ. The IR spectrum of EDMPAm in D_2O differs significantly from that in CCl_4 (Figure 4B). The largest changes are observed for the $\nu_{C=O}$ band, which for in the aqueous solution shifts to shorter wavenumbers by ca. 40 cm^{-1} and for the bands at 1475 and 1409 cm^{-1} (CCl_4), which shift by 15−18 cm^{-1} in the opposite direction in the spectrum of the D_2O solution. The Raman spectrum of EDMPAm in water (Figure S3) hardly differs from that of EDMPAm neat or in CCl_4 in the 1550−800 cm^{-1} spectral range, which indicates that there are no major differences in the conformer population in water compared to nonpolar solvents. The spectral region corresponding to $\nu_{C=O}$ vibrations frequency, in contrast, is affected by the change in solvent.

To facilitate the interpretation of the IR spectral changes observed, we carried out MO calculations for the hydrogen-bonded complexes between EDMPAm and water. The input geometries were those of the conformers *a*1, *a*2, and *b*1 to each of which were added four water molecules placed around the C═O group with a C═O···H−O hydrogen bond for each water molecule. In the optimized structures recovered from the calculations (Figure 8), the carbonyl group is linked to only two molecules of water, but the geometry of the conformers is not modified significantly, compared to the original *a*1, *a*2, and *b*1 conformers. The changes in the simulated spectra, shown in Figure 8, reflect accurately the spectral differences observed experimentally (Figure 4B), a key finding which warrants the validity of the methodology. The MO calculations and spectral simulations confirm that the spectral shifts observed reflect the hydration of the amide group of EDMPAm, rather than a change in the populations of its conformers, as strongly suggested also by the Raman spectra of EDMPAm solutions in CCl_4 and D_2O (Figure S3).

Conformation and Hydration Changes of PIPOZ in Water Concomitant with the Heat-Induced Phase Separation. As seen in Figure 3, a gradual increase in the temperature of a PIPOZ solution in water from 20 to 40 °C (below the macroscopic phase separation) is accompanied by a gradual change of the vibrational bands in the 1650−1430 cm^{-1} spectral window. Particularly significant is the gradual enhancement, as the temperature increases, of the intensity of the band

dx.doi.org/10.1021/ma300252e | *Macromolecules* 2012, 45, 3531−3541

near 1630 cm^{-1} associated with $\nu_{C=O}$ (inset, Figure 3). This indicates that the dehydration of the amide groups starts when the temperature is well below the temperature of macroscopic phase separation. As the solution temperature was brought to a temperature slightly above T_c, the overall sharpness of the spectrum increased gradually over time, and new bands appeared at 1430, 1330, 1205, 1108, 989, 798, and 769 cm^{-1} (see Figure 3). These bands are mainly associated with vibrations of the polymer main chain; their presence may indicate a significant change of the conformation of the polymer main chain, at least on the length scale probed by IR spectroscopy. To test this hypothesis, we carried out simulations of the IR spectra of the type-*a* conformers ($\phi \sim 180°$) of the trimer and tetramer analogues of the PIPOZ monomer units (Figure 9). Their simulated IR spectra correspond much more closely to the spectrum of PIPOZ in water after prolonged incubation at 42 °C, compared to those of the dimer model. For instance, in the multimer spectra the bands at 1197 and 1163 cm^{-1} are prominent, compared to the band at 1281 cm^{-1}, a key feature of the experimental PIPOZ spectrum as well. We determined that in their optimized form both multimers adopt an all-trans backbone conformation. Hence, the excellent match between the simulated trimer and tetramer IR spectra and the IR spectrum of PIPOZ solutions at 42 °C suggests that upon prolonged incubation at 42 °C the polymer main chain adopts a conformation in which the all-trans conformers (type *a*) become prevalent. As seen convincingly in Figure 5, for the conformational change from the *b*-type to the *a*-type to occur, it is necessary to pass though an intermediate conformer, such as the *e*-type or the *d*-type. In a nonpolar environment, these conformers seem hardly to exist under normal conditions because their relative energies are too high (Table 2). We carried out a geometrical optimization of representative conformers with the IEFPCM model using the solvent parameters for water. The results are compiled in Table 3. The most stable conformer is *a*1, and ΔE indicates that the

Table 3. Relative Energy ΔE (kJ mol^{-1}) from the Energy of the Most Stable Conformer (*a*1), ϕ, and ψ for EDMPAm Conformers Optimized in Aqueous Media

ID	ΔE^a/kJ mol^{-1}	ϕ/deg	ψ/deg
*a*1w	0.000	179.94	4.890
*b*1w	4.67	62.02	172.8
*c*1w	3.90	−62.33	−166.3
*d*3w	2.90	172.2	−1.38
*e*3w	8.23	70.05	11.65
*f*4w	8.44	−70.37	−12.42

[a]Zero point energy was corrected.

population of *a*1 is prominent in aqueous media. Interestingly, ΔE between *a*1 and *d*3, which is one of the candidate intermediates, is much smaller in aqueous media than that in vacuum, presumably because the dipole interaction between the side chains is shielded by solvent molecules. It should be emphasized that ΔE of *d*3 is smaller than that of *b*1 in aqueous media, indicating that the conformational change from *b*- to *d*-type occurs spontaneously.

One question still remains to be answered: why does the conformational change not occur in cold water? One reason could be that the energy barrier between the *b*- and *d*-type conformers is too high to be overcome at room temperature. To test this hypothesis, we calculated the angular dependence of ΔE for EDMPAm as a function of ψ and ϕ and plotted the results in Figures 10A and 10B, respectively. The energy

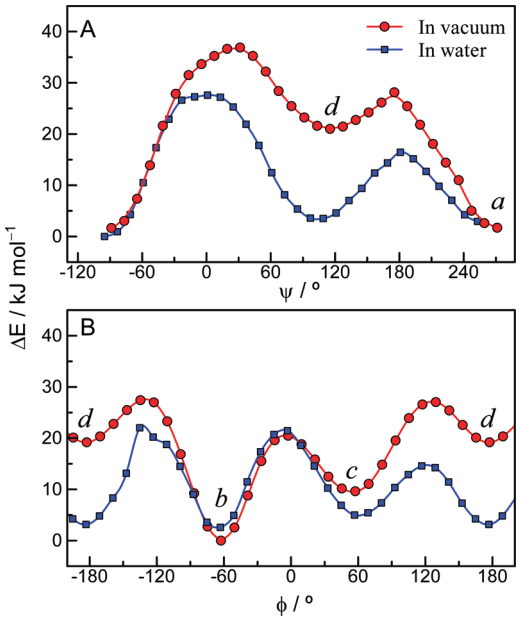


Figure 10. Plots of the changes of ΔE as a function of ϕ (B) and ψ(A) for EDMPAm in vacuum (circle) and in water (rectangle) calculated at the B3LYP/6-31+G(d) level.

barriers for the conformational change from *b* to *d* and from *d* to *a* are high, although the ΔE value of the *d*-conformer becomes very low in aqueous media. Thus, it is inferred that a thermal energy is required to induce the conformational change in the main chains of PIPOZ from *b*- to *a*-type. This may be the reason why the conformational change of PIPOZ occurs in hot water.

CONCLUSION

The direct visual observation of thin layers of PIPOZ solutions confined between sealed glass slides, reported in the first part of this article, revealed the following features of the heat-driven phase separation of PIPOZ aqueous solutions and eventual crystallization of PIPOZ from water: (i) the clouding of PIPOZ solutions noted by turbidimetry corresponds to the formation of two coexisting liquid phases; (ii) the dense (polymer-rich) liquid phase is metastable with respect to the dilute solution, i.e., a barrier for its decay exists, and it is not a simple density fluctuation; and (iii) the crystallization of PIPOZ takes place by nucleation in the dense liquid phase upon input of energy in the form of heat. The second section of the article focused on the changes in PIPOZ conformation and hydration, as seen by vibrational spectroscopy and MO calculations, during the liquid/liquid phase separation and upon prolonged heating at a temperature sufficiently low to preclude irreversible polymer crystallization. This part of the work revealed that (i) the polymer chains gradually dehydrate as the solution temperature nears macroscopic phase separation and (ii) in their dehydrated form the polymer chains undergo a conformational change and adopt a mostly all-trans conformation. A pictorial representation of phenomena unveiled in the study is given in Figure 11, where we draw connections between the two aspects of the work. In cold water ($T < T_c$) the polymer adopts a conformation in which the trans and gauche conformers

dx.doi.org/10.1021/ma300252e | Macromolecules 2012, 45, 3531−3541

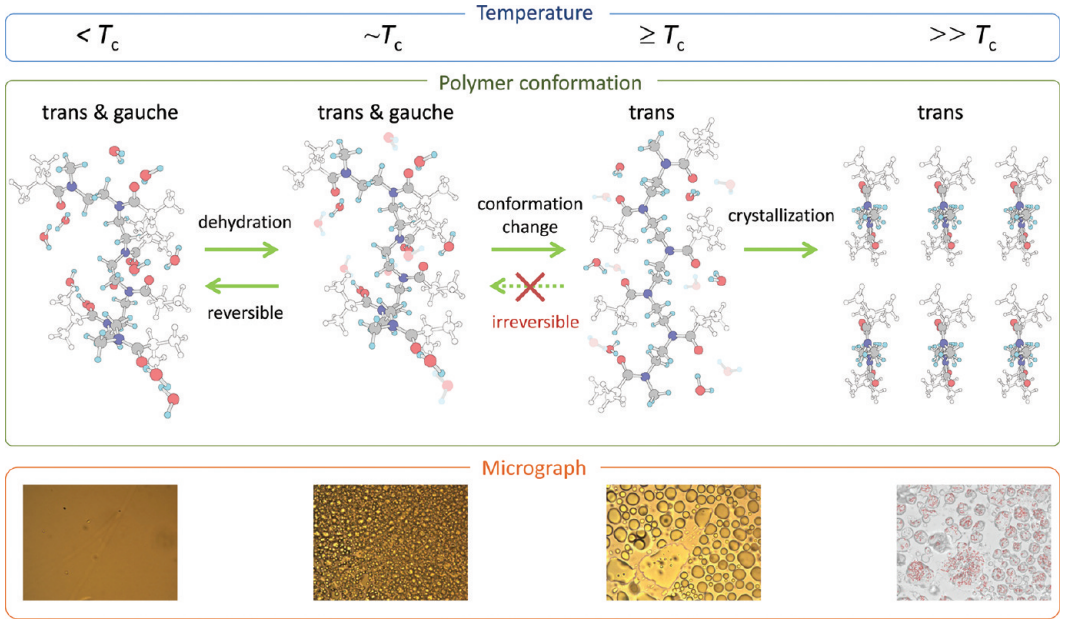


Figure 11. Schematic representation of the changes in the conformation of PIPOZ in water as a function of temperature and their correlation with the macroscopic phenomena observed by optical microscopy.

coexist. The chain is decorated with a hydrogen-bonded network of water molecules forming a hydration layer. Two or more water molecules of this layer form hydrogen bonds with the amide carbonyl group of each monomer unit (gauche or trans conformers). As the solution temperature increases, the hydration layer surrounding the polymer breaks gradually via cleavage of carbonyl/water hydrogen bonds, as revealed by shifts of the carbonyl bands in the IR spectrum and detected also by microcalorimetry.[21b] At a specific temperature, the solution undergoes liquid/liquid phase separation, and within the polymer-rich phase, the polymer chain adopts a mostly trans conformation. This conformation is stabilized over all others and remains the predominant one upon cooling of the sample below T_c. This conformation facilitates interchain dipolar interactions between amide fragments, which may promote partial organization of the chains in the dense liquid phase and facilitate nucleation and crystallization of PIPOZ. It is worth recalling here that in the crystalline phase PIPOX has an all-trans conformation as seen in Figure 11, which was confirmed by X-ray diffraction of PIPOZ precipitated from hot water.[46] In the first part of the study we observed that heating beyond 50 °C is required to induce crystallization, yet spectral data indicate that the conformational transition leading to the all-trans conformation occurs at a lower temperature. For crystallization to occur nucleation needs to take place. Our observations may indicate that nucleation requires further thermal energy and/or that it is the rate-determining step. In this context, the FT-IR measurement of the system up to 70 °C would be very interesting for understanding the nucleation process at the molecular level, if the process is indeed detectable spectroscopically.

PIPOZ is often compared to its structural isomer, poly(*N*-isopropylacrylamide) (PNIPAM) which has a −[CH_2−CH-(CONH−iPr)]− repeat unit. The two polymers share many similarities from the macroscopic viewpoint. They are soluble in polar organic solvents and in cold water. Their aqueous solutions undergo a phase separation upon heating beyond a temperature in the 30−40 °C range (T_c of PNIPAM: 32 °C).[47] But similarities vanish beyond such phenomenological observations. For instance, many reports on the phase separation of aqueous PNIPAM indicate that, above T_c, the polymer forms single chain globules that associate to large aggregates or mesoglobules.[18] There is no evidence that a liquid/liquid phase separation occurs concomitant with the LCST-type phase separation of aqueous PNIPAM solutions. While a "coil-to-globule" collapse is often invoked in descriptions of the phase separation of aqueous PIPOZ solutions, there is no direct evidence that such a chain contraction takes place. Our results advocate that the chains adopt a more extended conformation above T_c, compared to their conformation in cold water. The dehydration mechanism also differs for the two polymers, as demonstrated for instance by analysis of vibrational spectra. As shown in this study, spectral changes in the 1650−1430 cm^{-1} spectral region, which is sensitive to the hydration state of the amide carbonyl, occur over a wide temperature range in PIPOZ solutions, beginning at temperatures well below T_c. In contrast, the amide I band of PNIPAM in water does not change at all upon heating until T_c is reached, at which point a band appears at a wavenumber of ~1650 cm^{-1}, suggesting that the molecular environment around the PNIPAM chain undergoes a discontinuous change in the vicinity of T_c. The existence of C═O···H−N intrachain hydrogen bonds is believed to play an important part in the thermosensitivity of aqueous PNIPAM solutions.[32] In this context, it is interesting to recall that the temperature at which the network of water of hydration surrounding peptides starts to unravel upon heating is quite constant (~31 °C) independently of the peptide structure. A recent study suggests that this temperature is determined to a large extent by the cooperative hydration of the peptide backbone and by the H-bonds between water and the −HN−C═O structural motifs.[48] This unit is present in the structure of PNIPAM, which also undergoes cooperative hydration/dehydration[31] around 31 °C, but in the structure of PIPOZ this unit is replaced by the >N−C═O motif. Our study demonstrates that this structural difference has profound implications on the properties of the

dx.doi.org/10.1021/ma300252e | *Macromolecules* 2012, 45, 3531−3541

polymer in water and brings further evidence in support of the suggestion that networks of H-bonded water carry important information and may play some role in nonequilibrium biological processes.[48]

■ ASSOCIATED CONTENT

Supporting Information

Calculated and observed IR spectra of TMPAm, an example for the definition of redundant internal coordinates with scan and constraint information, the simulated IR and Raman spectra for the representative nine conformers of EDMPAm, the Raman spectra of EDMPAm; sum of the electronic and zero-point energy *E* (hartrees) and optimized geometries of EMPAm. This material is available free of charge via the Internet at http://pubs.acs.org.

■ AUTHOR INFORMATION

Corresponding Author

*Fax +81-82-424-7408, e-mail katsumot@hiroshima-u.ac.jp.

Notes

The authors declare no competing financial interest.

■ ACKNOWLEDGMENTS

This work was supported by the Grant-in-Aid for Scientific Research (No. 21750126) to Y.K. and by a grant of the Natural Science and Engineering Research Council of Canada to F.M.W. The authors thank Prof. T. Sato (University of Osaka, Japan) for stimulating discussions and useful suggestions. Dr. R. Obeid is thanked for supplying one of the PIPOZ samples.

■ REFERENCES

(1) Slabinski, L.; Jaroszewski, L.; Rodrigues, A. P. C; Rychlewski, L.; Wilson, I. A.; Lesley, S. A.; Godzik, A. *Protein Sci.* **2007**, *16*, 2472.
(2) Wolde, P. R. T.; Frenkel, D. *Science* **1997**, *277*, 1975.
(3) Pan, W.; Kolomeisky, A. B.; Vekilov, P. G. *J. Chem. Phys.* **2005**, *122*, 174905.
(4) (a) Erdemir, D.; Lee, A. Y.; Myerson, A. S. *Acc. Chem. Res.* **2009**, *42*, 621. (b) Filobelo, L. F.; Galkin, O.; Vekilov, P. G. *J. Chem. Phys.* **2005**, *123*, 014904.
(5) Kashchiev, D. *Nucleation: Basic Theory with Applications*; Butterworth-Heinemann: Oxford, 2000.
(6) (a) Galkin, O.; Vekilov, P. G. *Proc. Natl. Acad. Sci. U. S. A.* **2000**, *97*, 6277. (b) Galkin, O.; Vekilov, P. G. *J. Am. Chem. Soc.* **2000**, *122*, 156.
(7) Galkin, O.; Chen, K.; Nagel, R. L.; Hirsch, R. E.; Vekilov, P. G. *Proc. Natl. Acad. Sci. U. S. A.* **2002**, *99*, 8479.
(8) Richards, R. B. *Trans. Faraday Soc.* **1946**, *42*, 10.
(9) (a) Nakajima, A.; Fujiwara, H.; Hamada, F. *J. Polym. Sci., Part A-2: Polym. Phys.* **1966**, *4*, 507. (b) Nakajima, A.; Fujiwara, H. *J. Polym. Sci., Part A-2: Polym. Phys.* **1968**, *6*, 723. (c) Flory, P. J.; Mandelkern, L.; Hall, H. K. *J. Am. Chem. Soc.* **1951**, *73*, 2532. (d) Bueche, A. M. *J. Am. Chem. Soc.* **1952**, *74*, 65. (e) Quinn, F. A., Jr.; Mandelkern, L. *J. Am. Chem. Soc.* **1958**, *80*, 3178.
(10) Lee, H. K.; Myerson, A. S.; Levon, K. *Macromolecules* **1992**, *25*, 4002.
(11) (a) Chiu, G.; Mandelkern, L. *Macromolecules* **1990**, *23*, 5356. (b) Burghardt, W. R. *Macromolecules* **1989**, *22*, 2482.
(12) Graham, P. D.; McHugh, A. J. *Macromolecules* **1998**, *31*, 2565.
(13) (a) Matsuyama, H.; Iwatani, T.; Kitamura, Y.; Teramoto, M.; Sugoh, N. *J. Appl. Polym. Sci.* **2001**, *79*, 2449. (b) Tsai, F.-J.; Torkelson, J. M. *Macromolecules* **1990**, *23*, 775.
(14) Smith, I. O.; Liu, X. H.; Smith, L. A.; Ma, P. X. *Nanomed. Nanobiotechnol.* **2009**, *1*, 226.
(15) Diehl, C.; Dambowsky, I.; Hoogenboom, R.; Schlaad, H. *Macromol. Rapid Commun.* **2011**, *32*, 1753.
(16) Tanaka, H. *Macromolecules* **1992**, *25*, 6377.
(17) Tanaka, H. *J. Phys.: Condens. Matter* **2000**, *12*, R207.
(18) (a) Wu, C.; Li, W.; Zhu, X. X. *Macromolecules* **2004**, *37*, 4989. (b) Aseyev, V.; Tenhu, H.; Winnik, F. M. *Adv. Polym. Sci.* **2006**, *196*, 1. (c) Kujawa, P.; Aseyev, V.; Tenhu, H.; Winnik, F. M. *Macromolecules* **2006**, *39*, 7686. (d) Junk, M. J. N.; Li, W.; Schlüter, A. D.; Wegner, G.; Spiess, H. W.; Zhang, A.; Hinderberger, D. *J. Am. Chem. Soc.* **2011**, *133*, 10832.
(19) (a) Inaba, N.; Sato, K.; Suzuki, S.; Hashimoto, T. *Macromolecules* **1986**, *19*, 1690. (b) Tanaka, H. *Phys. Rev. Lett.* **1996**, *76*, 787. (c) Hu, H.; Shangguan, Y.; Zuo, M.; Zheng, Q. *J. Polym. Sci., Part B: Polym. Phys.* **2008**, *46*, 1923.
(20) (a) Bassiri, A.; Levy, A. *J. Polym. Sci., Part B* **1967**, *5*, 871. (b) Litt, M.; Rahl, F.; Roldan, L. G. *J. Polym. Sci., Part A-2: Polym. Phys.* **1969**, *7*, 463. (c) Obeid, R.; Tanaka, F.; Winnik, F. M. *Macromolecules* **2009**, *42*, 5818.
(21) (a) Uyama, H.; Kobayashi, S. *Chem. Lett.* **1992**, 1643. (b) Diab, C.; Akiyama, Y.; Kataoka, K.; Winnik, F. M. *Macromolecules* **2004**, *37*, 2556. (c) Park, J.-S.; Akiyama, Y.; Winnik, F. M.; Kataoka, K. *Macromolecules* **2004**, *37*, 6786. (d) Park, J.-S.; Kataoka, K. *Macromolecules* **2007**, *40*, 3599. (e) Zhao, J.; Hoogenboom, R.; Assche, G. V.; Mele, B. V. *Macromolecules* **2010**, *43*, 6853.
(22) Hoogenboom, R.; Thijs, H. M. L.; Jochems, M. J. H. C.; van Lankvelt, B. M.; Fijten, M. W. M.; Schubert, U. S. *Chem. Commun.* **2008**, *44*, 5758.
(23) Diehl, C.; Černoch, P.; Zenke, I.; Runge, H.; Pitschke, R.; Hartmann, J.; Tiersch, B.; Schlaad, H. *Soft Matter* **2010**, *6*, 3784.
(24) U.S. Food and Drug Administration (21 CFR 175.105) (note that the FDA approval is only valid for use as indirect food additives).
(25) (a) Schlaad, H.; Diehl, C.; Gress, A.; Matthias, M.; Demirel, A. L.; Nur, Y.; Bertin, A. *Macromol. Rapid Commun.* **2010**, *31*, 511. (b) Hoogenboom, R. *Angew. Chem., Int. Ed.* **2009**, *48*, 7978. (c) Viegas, T. X.; Bentley, M. D.; Harris, J. M.; Fang, Z.; Yoon, K.; Dizman, B.; Weimer, R.; Mero, A.; Pasut, G.; Francesco, M. V. *Bioconjugate Chem.* **2011**, *22*, 976.
(26) Spiess, H. W. *Macromolecules* **2010**, *43*, 5479.
(27) Kujawa, P.; Aseyev, V.; Tenhu, H.; Winnik, F. M. *Macromolecules* **2006**, *39*, 7686.
(28) (a) Winnik, F. M.; Ottaviani, M. F.; Bossman, S. H.; Pan, W.; Garcia-Garibay, M.; Turro, N. J. *J. Phys. Chem.* **1993**, *97*, 12998. (b) Junk, M. J. N.; Li, W.; Schluter, A. D.; Wegner, G.; Spiess, H. W.; Zhang, A.; Hinderberger, D. *Angew. Chem., Int. Ed.* **2010**, *49*, 5683.
(29) Everall, N.; Griffiths, P.; Chalmers, J. M. *Vibrational Spectroscopy of Polymers: Principles and Practice*; Wiley: New York, 2007.
(30) (a) Platé, N. A.; Levedeva, T. L.; Valuev, L. I. *Polym. J.* **1999**, *31*, 21. (b) Maeda, Y.; Higuchi, T.; Ikeda, I. *Langmuir* **2000**, *16*, 7503. (c) Maeda, Y.; Nakamura, T.; Ikeda, I. *Macromolecules* **2001**, *34*, 1391. (d) Percot, A.; Zhu, X. X.; Lafleur, M. *J. Polym. Sci., Polym. Phys. Ed.* **2000**, *38*, 907.
(31) Okada, Y.; Tanaka, F. *Macromolecules* **2005**, *38*, 4465.
(32) Katsumoto, Y.; Tanaka, T.; Sato, H.; Ozaki, Y. *J. Phys. Chem. A* **2002**, *106*, 3429.
(33) (a) Katsumoto, Y.; Tanaka, T.; Ihara, K.; Koyama, M.; Ozaki, Y. *J. Phys. Chem. B* **2007**, *111*, 12730. (b) Katsumoto, Y.; Kubosaki, N.; Miyata, T. *J. Phys. Chem. B* **2010**, *114*, 13312.
(34) Obeid, R.; Maltseva, E.; Thunemann, A. F.; Tanaka, F.; Winnik, F. M. *Macromolecules* **2009**, *42*, 2204.
(35) Buswell, M.; Fleming, I.; Chosh, U.; Mack, S.; Russel, M.; Clark, B. P. *Org. Biomol. Chem.* **2004**, *2*, 3006.
(36) The software, named SPINA, can be download from the following Web site: http://home.hiroshima-u.ac.jp/katsumot/spina.html.
(37) (a) Becke, A. D. *J. Chem. Phys.* **1993**, *98*, 5648. (b) Lee, C.; Yang, W.; Parr, G. R. *Phys. Rev. B* **1988**, *37*, 785.
(38) Frisch, M. J.; Trucks, G. W.; Schlegel, H. B.; Scuseria, G. E.; Robb, M. A.; Cheeseman, J. R.; Montgomery, Jr., J. A.; Vreven, T.; Kudin, K. N.; Burant, J. C.; Millam, J. M.; Iyengar, S. S.; Tomasi, J.; Barone, V.; Mennucci, B.; Cossi, M.; Scalmani, G.; Rega, N.; Petersson, G. A.; Nakatsuji, H.; Hada, M.; Ehara, M.; Toyota, K.;

Fukuda, R.; Hasegawa, J.; Ishida, M.; Nakajima, T.; Honda, Y.; Kitao, O.; Nakai, H.; Klene, M.; Li, X.; Knox, J. E.; Hratchian, H. P.; Cross, J. B.; Bakken, V.; Adamo, C.; Jaramillo, J.; Gomperts, R.; Stratmann, R. E.; Yazyev, O.; Austin, A. J.; Cammi, R.; Pomelli, C.; Ochterski, J. W.; Ayala, P. Y.; Morokuma, K.; Voth, G. A.; Salvador, P.; Dannenberg, J. J.; Zakrzewski, V. G.; Dapprich, S.; Daniels, A. D.; Strain, M. C.; Farkas, O.; Malick, D. K.; Rabuck, A. D.; Raghavachari, K.; Foresman, J. B.; Ortiz, J. V.; Cui, Q.; Baboul, A. G.; Clifford, S.; Cioslowski, J.; Stefanov, B. B.; Liu, G.; Liashenko, A.; Piskorz, P.; Komaromi, I.; Martin, R. L.; Fox, D. J.; Keith, T.; Al-Laham, M. A.; Peng, C. Y.; Nanayakkara, A.; Challacombe, M.; Gill, P. M. W.; Johnson, B.; Chen, W.; Wong, M. W.; Gonzalez, C.; Pople, J. A. Gaussian, Inc., Wallingford, CT, 2004.

(39) (a) Yoshida, H.; Ehara, A.; Matsuura, H. *Chem. Phys. Lett.* **2000**, *325*, 477. (b) Matsuura, H.; Yoshida, H. *Handbook of Vibrational Spectroscopy*; Chalmers, J. M., Griffiths, P. R., Eds.; John Wiley & Sons Inc.: New York, 2001; Vol. 3, p S4203. (c) Yoshida, H.; Takeda, K.; Okamura, J.; Ehara, A.; Matsuura, H. *J. Phys. Chem. A* **2002**, *106*, 3580.

(40) Takahashi, R.; Sato, T.; Terap, K.; Qiu, X.-P.; Winnik, F. M. *Macromolecules*, to be submitted.

(41) Katsumoto, Y.; Tanaka, T.; Ozaki, Y. *J. Phys. Chem. B* **2005**, *109*, 20690.

(42) For EMPAm in water, the unimodal $\nu_{C=O}$ band is also observed as seen in Figure 4.

(43) The definition of redundant internal coordinates with scan and constraint information can be found in the Supporting Information.

(44) The calculation results for all of possible confomers are listed in Table S1 of the Supporting Information.

(45) The simulated IR spectra for all conformers concerned with *a*, *b*, and *c* are represented in Figure S2. As seen in this figure, the relative orientation of the isopropyl groups plays a minor role in the IR spectrum of EDMPAm.

(46) Demirel, A. L.; Meyer, M.; Schlaad, H. *Angew. Chem., Int. Ed.* **2007**, *46*, 8622.

(47) Heskins, M.; Guillet, J. E. *J. Macromol. Sci., Chem.* **1968**, *A2*, 1441.

(48) Oleinikova, A.; Brovchenko, I. *J. Phys. Chem. Lett.* **2011**, *2*, 765.

Macromolecules

Article

pubs.acs.org/Macromolecules

Controlled Release from Model Blend Multilayer Films Containing Mixtures of Strong and Weak Polyelectrolytes

Yeongseon Jang,[†] Bulent Akgun,[‡,§] Hosub Kim,[†] Sushil Satija,[‡] and Kookheon Char*[,†]

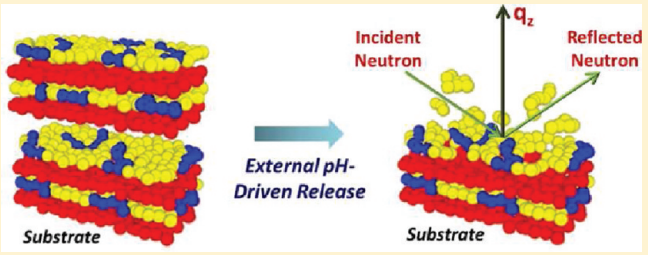
[†]The National Creative Research Initiative Center for Intelligent Hybrids, The WCU Program of Chemical Convergence for Energy & Environment, School of Chemical & Biological Engineering, Seoul National University, Seoul 151-744, Korea

[‡]NIST Center for Neutron Research, NIST, Gaithersburg, Maryland 20899-6102, United States

[§]Department of Materials Science and Engineering, University of Maryland, College Park, Maryland 20742, United States

Supporting Information

ABSTRACT: We have designed the controlled release platforms based on polyelectrolyte (PE) blend multilayer films to investigate the release mode and kinetics at the nanoscale level. The model blend multilayer films are composed of positively charged layers with weak polyelectrolytes (PEs) (linear poly(ethylenimine), LPEI) and negatively charged blend layers with mixtures of strong (poly(sodium 4-styrenesulfonic acid), PSS) and weak (poly(methacrylic acid), PMAA) PEs. The blend multilayer films ($[LPEI/PSS:PMAA]_n$) with well-defined internal structure were prepared by the spin-assisted layer-by-layer (LbL) deposition method. Release properties of the multilayer films were systematically studied as a function of blend ratio by neutron reflectivity (NR), ellipsometer, AFM, FT-IR spectroscopy, and quartz crystal microbalance with dissipation (QCM-D). Since PSS strong PEs serve as robust skeletons within the multilayer films independent of external pH variation, the burst disruption of pure weak PE multilayer films was dramatically suppressed, and the release kinetics could be accurately controlled by simply changing the PSS content within the blend films. These release properties of blend multilayer films form the basis for designing the controlled release of target active materials from surfaces.



INTRODUCTION

Great efforts have been devoted to develop thin film platforms for diverse biomedical applications. In particular, thin films which provide the controlled release of active biomolecules from the surfaces have the potentials to be used as bioactive coatings on implants. Among various techniques to prepare well-designed thin films, the layer-by-layer (LbL) deposition method has received great attention due to its versatility, biocompatible processing in aqueous environment, and the ability to insert therapeutic biomolecules at a desired position within the multilayer thin film. Moreover, the LbL deposition technique facilitates the programming of the release sequence of active materials by adjusting the molecular interactions between layers.[1−7]

Various types of multilayer thin films have been investigated for the controlled release by tuning diverse parameters including intrinsically degradable properties of polymers employed as well as external stimuli such as ionic strength, temperature, light, enzyme, electrical signal, and pH.[8−17] Particularly for pH-responsive release systems, multilayer films containing weak polyelectrolyte (PE) pairs have been exploited because the swelling and decomposition of multilayer films can easily be controlled by changing the solution pH. Most research on the weak PE multilayer films for biological applications has been focused on the structural change of the films at specific pH 7.4, the physiological condition in blood.[8,9] However, multilayer films solely composed of weak PEs show rapid morphological change within 20 min and subsequent disassembly when they are exposed to low pH solution ($1 \leq pH \leq 3$).[18,19] This rapid transition in the stability of weak PE multilayer films under acidic condition still remains as a critical obstacle for biomedical applications because pH in human body widely varies from 1.0 to 8.5.[20] Since most of drugs are rapidly degraded at pH 2, many material scientists and pharmacologists have focused on the design of controlled release systems to provide adequate release in gastric environment ($pH \leq 2$).[21−23]

To overcome the film instability of weak PE multilayers in extreme pH conditions, blended solutions consisting of both weak and strong PEs can be used by taking advantage of pH-independent characteristic of strong PEs.[24] The PE blend multilayer films generally offer versatility to control physical and biochemical properties such as film thickness, morphology, composition, and film stability for diverse potential applications.[25,26] In addition, the LbL deposition with blend solutions enables to insert expensive bioactive molecules effectively at a desired position and to release them in a controlled manner.[9]

However, the fundamental investigation on the internal rearrangement or the release of target molecules incorporated

Received: February 7, 2012
Revised: March 27, 2012
Published: April 3, 2012

 © 2012 American Chemical Society

within blend multilayer films has so far not been well understood because of the difficulty in detecting the change in internal film structure at the nanometer scale. One of useful tools for evaluating the structure of layers within a multilayer thin film is X-ray reflectivity (XRR) or neutron reflectivity (NR). Since the XRR is sensitive to electron density difference while NR is sensitive to the difference in coherent scattering length density (SLD), NR is more advantageous for the investigation of buried structure and interfacial roughness in polymer multilayer films which has a weak electron density contrast between layers. The strong neutron scattering contrast between different isotopes of hydrogen and deuterium is exploited to inscribe layering features of interest within a PE multilayer film.[27,28]

Herein, we report the release behavior of PE chains from model blend multilayer films containing mixtures of strong and weak anionic PEs (i.e., poly(sodium 4-styrenesulfonate) (PSS) and poly(methacrylic acid) (PMAA)). PSS is a strong anionic PE, which is always fully charged independent of pH of the solutions, whereas PMAA is a weak anionic PE and its charge density varies by the solution pH. Linear poly(ethylenimine) (LPEI) is used for weak cationic PE layers. The blend multilayer films ($[LPEI/PSS:PMAA]_n$) with well-defined internal structure are prepared by the spin-assisted layer-by-layer (LbL) deposition method,[29,30] and the release behavior of weak deuterated PMAA (*d*-PMAA) is systematically characterized by NR. Regularly spaced *d*-PMAA layers result in equally spaced peaks in SLD profiles, and the changes in peak shape and position after post-treatment give the ability to monitor internal rearrangement of model blend film using NR. In addition to NR measurements, changes in thickness, surface morphology, and film composition were thoroughly investigated as a function of blend ratio when the blend films were post-treated at pH 2 using ellipsometry, atomic force microscopy (AFM), and FT-IR. The *in situ* release kinetics of the model blend films were analyzed by quartz crystal microbalance with dissipation (QCM-D) measurements, providing insightful information relevant to the changes in film mass with nanogram unit.[31] The approaches taken in the present study represent the controlled release platforms based on blend multilayer films to overcome the weakness of pH-sensitive weak PE films in acidic environment. Furthermore, the results shown here would give some insights into the improved release property of target active macromolecules from blend multilayer thin films, offering versatile, adjustable stimuli-responsive polymeric release platforms.

EXPERIMENTAL SECTION

Materials. Linear poly(ethylenimine) (LPEI, M_w = 25 000 g/mol) and poly(methacrylic acid) (PMAA, M_w = 15 000 g/mol) were purchased from Polysciences.[32] Poly(sodium 4-styrenesulfonate) (PSS, M_w = 70 000 g/mol) and deuterated poly(methacrylic acid) (*d*-PMAA, M_w = 43 000 g/mol) were obtained from Aldrich[32] and Polymer Source,[32] respectively. All polymers were used as received. Silicon wafers, CaF_2 round crystal windows (Sigma-Aldrich[32]), and Au sensor crystals (QSX 301, Q-Sense[32]) were used as substrates to build blend multilayer films for further characterization.

Fabrication of Blend Multilayer Films. A LPEI solution and mixed solutions of PSS and PMAA were chosen for cationic and anionic polyelectrolyte solutions to prepare blend multilayer films. All the polymer solutions were prepared by dissolving polymers in 18 MΩ Milli-Q water with concentrations of 0.01 M (based on repeat units), and solution pH was adjusted to pH 5.0 by adding diluted HCl or NaOH solution. The blend ratio of the polyanion mixtures was varied based on the molarity of each polymer (i.e., PSS (M):PMAA (M) = 0:100, 10:90, 30:70, 100:0). Prior to multilayer deposition, all the substrates were cleaned with piranha solution (mixtures of 70 vol % H_2SO_4 and 30 vol % H_2O_2) for 20 min at room temperature and washed thoroughly with DI water, followed by drying under nitrogen stream. The blend multilayer films, $[LPEI/PSS_x:PMAA_{100-x}]_n$ (x: mole % of PSS in an anionic PE solution, n: number of bilayers), were prepared by the spin-assisted layer-by-layer (LbL) deposition method with a spin rate of 4000 rpm for 40 s for each deposition, followed by three consecutive washing steps for each polymer deposition with pH 5.0 DI water.

Post-Treatment of Blend Multilayer Films. The post-treatment for releasing multilayer films was performed by immersing the prepared multilayer films in pH 2.0 DI water for 10 min, which was proven to provide the sufficient disruption of multilayer films solely prepared with weak polyelectrolytes $(LPEI/PMAA)_{16}$. The post-treated blend multilayer films were washed thoroughly with pH 2.0 water, followed by the relevant drying process under N_2 stream.

Neutron Reflectivity (NR) Measurements. The internal structures of the blend multilayer films (in-plane averaged coherent SLD profile, surface and interface roughnesses, and total film and interlayer thicknesses) were characterized by NR measurements. The NR measurements were conducted at the NG7 horizontal reflectometer at National Institute of Standards and Technology (NIST) Center for Neutron Research (NCNR) using wavelength (λ) of 0.475 nm. Angular divergence of the beam was varied through the reflectivity measurement to get a constant footprint and a relative q_z resolution ($\Delta q_z/q_z$) ≈ 0.04 where $q_z = 4\pi \sin\theta/\lambda$ and θ is the incident and exit angle of the beam with respect to plane of the sample. For all the samples NR data were collected up to $q_{z,max}$ of 0.15 $Å^{-1}$. The NR experiments were performed in a closed chamber with $CaSO_4$ platelets to keep relative humidity close to zero. Samples are equilibrated in the closed chamber at least for 1 h, and then the measurements started. Previous experience with identical bilayers films showed that the 1 h is enough to reach equilibrium. Background subtraction and main beam normalization were made using the REFLPAK[33] software package provided by NIST. The structure of thin films in general cannot be determined by direct inversion of NR data to SLD profile due to the loss of phase information during the measurement. To obtain a real space depth profile first, a candidate model was chosen and the parameters (thickness, roughness, and SLD) of the model were varied using nonlinear regression until a simulated reflectivity curve calculated from the model structure using Parratt[34] formalism agrees sufficiently well with the experimental data. All the data were fitted using Parratt 32 and Motofit reflectivity analysis packages. Even though this is an indirect analysis method if preliminary information is obtained by other characterization techniques (e.g., AFM, XRR, and ellipsometer), thickness, roughness, and SLD of the layers in the film can be obtained with great precision.

Characterization of Blend Multilayer Films. The total film thicknesses were measured by a variable-angle multiwavelength ellipsometer (Gaertner L2W15S830, Gaertner Scientific Corp.[32]), and the surface morphologies of films were obtained with atomic force microscope (AFM) (Nanoscope IIIa, Digital Instrument[32]). Experimental results were reported by averaging the values of three independent measurements for film thickness and surface roughness. The changes in frequency (Δf_n) and dissipation (ΔD_n) of an Au sensor crystal (QSX301) coated with a blend multilayer film during the post-treatment were monitored by quartz crystal microbalance equipped with dissipation (QCM-D) (Q-Sense D300, Q-Sense[32]). The composition of blend multilayer films was characterized with FT-IR (FT-IR-200 spectrometer, JASCO Corp.[32]). The multilayer film for FT-IR measurement was prepared on a CaF_2 crystal, which is transparent to IR light.

RESULTS AND DISCUSSION

The controlled release platforms based on blend multilayer films, $[LPEI/PSS_x:PMAA_{100-x}]_n$ (x = 0, 10, 30, 100) were prepared by the spin-assisted LbL deposition employing

electrostatic interactions. To explore the pH-induced controlled release behavior of model blend multilayer films as a function of the blend ratio of weak (PMAA) and strong (PSS) PEs, film characteristics including thickness, internal structure, surface morphology, film mass, and film compositions before and after the post-treatment at pH 2.0 were investigated and discussed in detail in the following.

Growth Behavior of Blend Multilayer Films. Several studies using dip coating have reported that LbL films containing LPEI, in particular, exhibited the exponential growth behavior with the increase in bilayer number. Exponential growth phenomenon is based on the reversible internal rearrangement of mobile polymer chains such as LPEI.[35,36] Excess LPEI chains exhibit diffusion into the interior of a multilayer film as well as possessing chain mobility out to the film surface in each dipping process. Therefore, the dip-assisted LbL film containing LPEI shows the exponential growth behavior. However, in the case of the spin-assisted LbL deposition method, such interdiffusion behavior of LPEI chains is significantly suppressed, and the resulting films demonstrated linear growth behavior (Figure 1). The discrepancy between

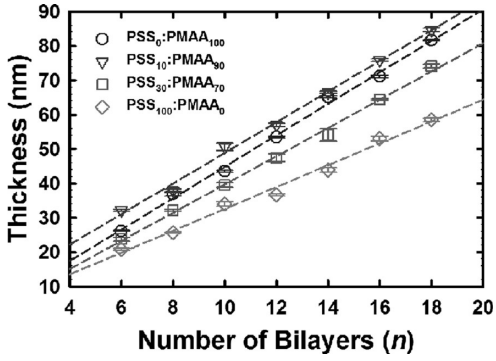


Figure 1. Thickness growth curves of blend multilayer films, $[\text{LPEI}/\text{PSS}_x\text{:PMAA}_{100-x}]_n$, as a function of number of bilayers. The films were assembled in pH 5.0 solutions, and thickness measurements were taken in ambient air.

conventional dip-assisted and spin-assisted LbL deposition is the different adsorption mechanisms (i.e., self-diffusion vs forced-diffusion process). The spin-assisted LbL deposition incorporates strong centrifugal force, viscous force, and air shear force along with intermolecular forces among adsorbing PE pairs.[29] In particular, the viscous force caused by fast solvent evaporation dramatically decreases the mobility and interdiffusion of LPEI chains within a multilayer film. Therefore, the spin-assisted LbL deposition allows us to construct a well-defined internal structure across the film thickness compared with the intermixed phase often seen in the dip-assisted LbL deposition.[37]

The multilayers were assembled with LPEI and PSS:PMAA blend solutions at pH 5.0, which is close to pK_a values of both weak PEs. The pK_a values of LPEI and PMAA weak PEs are around 4.8−5.0 and 5.5, respectively.[35,37] The electrostatic interactions between partially positive charges on LPEI chains and partially negative charges on PMAA chains form thick LbL-assembled multilayer films at pH 5.0 due to their coiled conformation. As has been well documented in the literature, the LbL film thickness can be controlled by simply changing the blend ratio of two anionic PEs in the adsorption solutions.[24−26,39,40] A representative example of PE blend multilayer films is the LbL deposition of cationic poly(allylamine hydrochloride) (PAH) solution and blended anionic solution with poly(acrylic acid) (PAA) and PSS. The relatively large thickness observed with PAH/PAA weak multilayer films is attributed to partially charged nature of PAA under the deposition conditions of pH 3.5, where PAA adsorbs in a highly coiled conformation. In contrast, a permanently negative charged PSS adopts a more stretched conformation due to higher charge per molecule and intramolecular electrostatic repulsions.[26] Similar to these $[\text{PAH}/\text{PSS:PAA}]_n$ blend multilayers, the decrease in the thickness growth rate of $[\text{LPEI}/\text{PSS}_x\text{:PAA}_{100-x}]_n$ films used in the present study was observed with increasing PSS fraction in the blend solutions. Notwithstanding, the linear growth of film thickness, regardless of the blend ratio between PSS and PMAA, is highly desirable for LbL systems in many occasions, and the spin-assisted LbL deposition to grow multilayered films circumvents problems typically associated with the dip-assisted LbL deposition: the spin-assisted LbL deposition yielding well-organized internal film structure considerably facilitates the monitoring of the changes in model deuterated PE layers inserted at desired position within multilayer films using NR.

Changes in the Internal Film Structure Monitored by NR. NR experiments have been performed on model blend multilayer films to monitor the changes in internal structure before and after post-treatment. As schematically represented in Figure 2, blend multilayer films for NR study were constructed

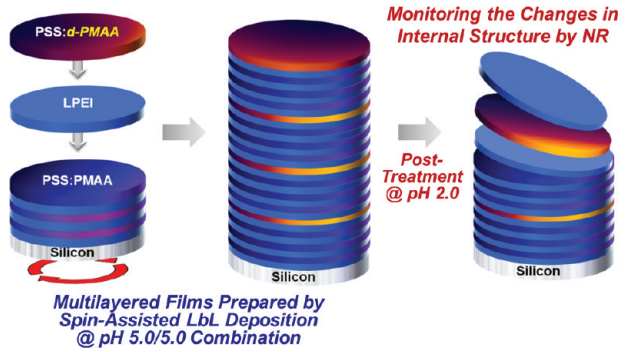


Figure 2. Schematic on the LbL deposition and post-treatment process of model blend multilayer films, $[(\text{LPEI}/\text{PSS}_x\text{:PMAA}_{100-x})_3(\text{LPEI}/\text{PSS}_x\text{:}d\text{-PMAA}_{100-x})_1]_4$, and their changes in internal structure for NR study.

by replacing PMAA with *d*-PMAA chains in the mixed polyanion solutions of PSS and PMAA in every fourth bilayer deposition to create neutron contrast. This configuration yields four spikes in the neutron SLD profile, and the changes in the height and the position of these spikes in the direction normal to the surface yield information on the diffusion and release of *d*-PMAA chains.

In order to investigate the effect of the strong PE PSS on the release behavior of weak PE *d*-PMAA chains from the multilayer films, model $[(\text{LPEI}/\text{PSS}_x\text{:PMAA}_{100-x})_3(\text{LPEI}/\text{PSS}_x\text{:}d\text{-PMAA}_{100-x})_1]_4$ multilayer films were constructed with different ratios of PSS and PMAA (i.e., PSS (M):*h*- or *d*-PMAA (M) = 0:100, 10:90, and 30:70) in blend polyanion solutions. Prior to NR measurements, the incorporated amount of PMAA within the blend multilayer films was calculated using quartz crystal microbalance (QCM) and the FT-IR measurements.[24] When the fraction of PSS in the blend polyanion solution is varied from 0 to 30 mol %, PSS and PMAA are incorporated

dx.doi.org/10.1021/ma3002615 | Macromolecules 2012, 45, 3542−3549

into the blend films with ratios similar to the feed ratios (Table S1 in Supporting Information). Therefore, herein, the blend ratios of PSS and PMAA in polyanion solutions can be considered as the ratios incorporated within the blended multilayer films.

Figure 3 illustrates the dramatic changes in the internal structure of multilayer films before and after the post-treatment at pH 2.0 depending on the blend ratio. The NR data were fitted with a classic box model for polyelectrolyte multilayer films, as previously described in prior works.[30,41−43] Each slab (protonated or deuterated layer) is characterized by SLD, thickness, and roughness in the fitting model. To fit the data, the model was constructed for an idealized LbL structure featuring sharp interfaces between adjacent layers. Initial individual layer thicknesses in the fitting model were taken from ellipsometry measurements and then adjusted to capture the Bragg peaks in the NR data. This LbL model was then modified iteratively until the reflectivity curve was best fitted to minimize χ^2.

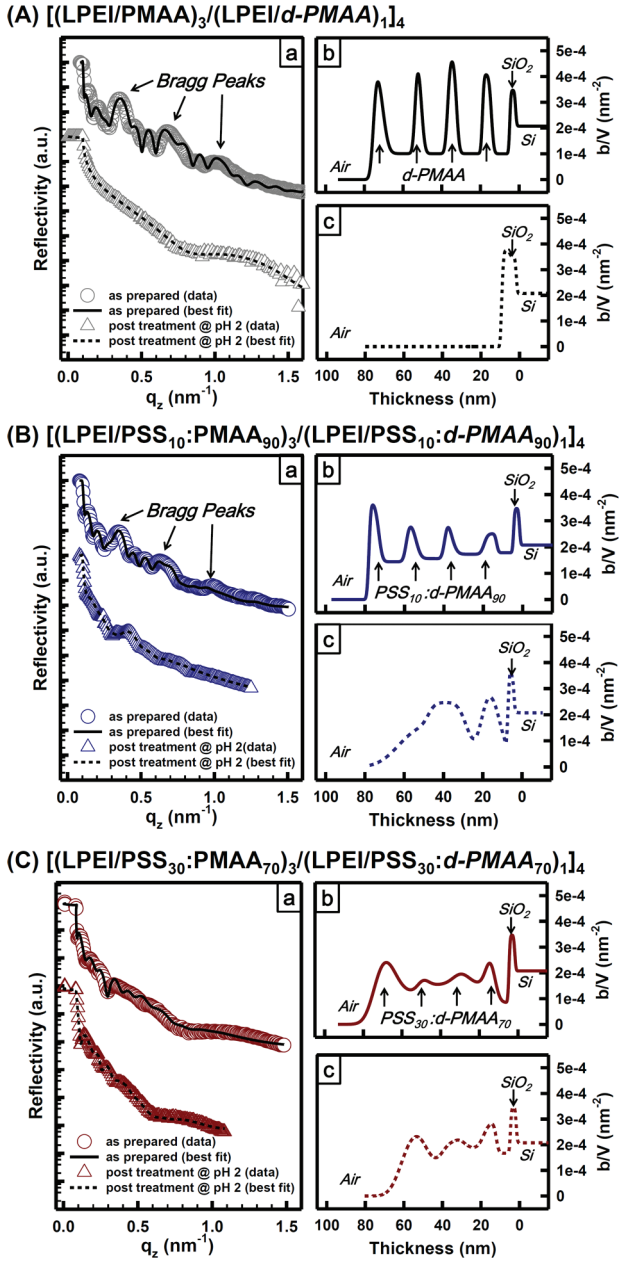


Figure 3. Neutron reflectivity (NR) curves with best fits and SLD profiles of blend multilayer films, $[(\text{LPEI/PSS:PMAA})_3(\text{LPEI/PSS:}d\text{-PMAA})_1]_4$. The changes in the internal structure of model multilayer films with different blend ratios of PSS:PMAA ((A) 0:100, (B) 10:90, and (C) 30:70) were monitored by NR. Films initially deposited at pH 5 are represented by circle symbols in (a) the reflectivity panels and solid lines in (b) the SLD panels while the films post-treated at pH 2 for 10 min are represented by triangle symbols in (a) the reflectivity panels and dashed lines in (c) the SLD panels.

The entire multilayer film prepared only with weak PEs (i.e., $[(\text{LPEI/PMAA})_3(\text{LPEI/}d\text{-PMAA})_1]_4$) was immediately disrupted upon the acidic post-treatment at pH 2.0 (Figure 3A) due to the complete loss of electrostatic interactions between the carboxylic groups of PMAA and the secondary amine groups of LPEI. Only 4.5 nm thick layers remained on the substrate after post-treatment due to strong physical interaction of the polymer chains in the first few bilayers with the underlying substrate. Since the pK_a value of PMAA PE is around 5.5,[38] ionized carboxylate groups (COO^-) in PMAA chains are protonated to their corresponding carboxylic acids (COOH) at pH 2.0, losing their negative charges that enable the association with LPEI. Subsequently, the positive charges in LPEI chains increases and the degree of ionization approaches 100% at pH 2.0 condition because the pK_a value of LPEI is approximately 4.8−5.0.[35] Therefore, the electrostatic interactions between negative charges on PMAA chains and positive charges on LPEI chains, which form well-ordered LbL-assembled multilayer films at pH 5.0, were significantly diminished during the post-treatment process, resulting in the precipitous disruption of the LbL film. Moreover, the disruption of the multilayer film is believed to be facilitated due to the long-ranged (inter- and intramolecular) electrostatic repulsive forces among increased positive charges of LPEI chains within the film.

However, rapid disruption of the entire multilayer film was prevented by incorporating 10% of strong PE PSS into the polyanion mixtures as well documented in Figure 3B. The multilayer film composed of $[(\text{LPEI/PSS}_{10}\text{:PMAA}_{90})_3(\text{LPEI/PSS}_{10}\text{:}d\text{-PMAA}_{90})_1]_4$ contains smeared Bragg peaks in the NR profile, implying that regularly spaced deuterated layers lose their neutron contrast to some extent within the film due to the mixing with protonated PE chains between the layers. The SLD profile for the blend multilayer film containing 10% PSS in Figure 3B shows that the protonated layers are more mixed with the *d*-PMAA:PSS layers in the blend film when compared with nonblend films. As a consequence of the high degree of intermixing at the substrate side of blend films, the blend multilayer film containing 10% PSS releases the weak PE *d*-PMAA from the surface, without showing the burst dissociation from the film. Since PSS chains are fully charged in aqueous solution in the pH range employed, permanent negative charges from the PSS chains are available to provide robust skeletons in blend multilayer films retaining the long-ranged electrostatic cross-linking with the positive charges of LPEI. Therefore, weak PE chains on the surface side move faster than those buried in the multilayer skeleton which is ionically cross-linked by PSS. This is consistent with the fact that the PE chains at the surface of the film has a larger diffusion coefficient than those within the film.[10]

Consequently, the release of weak PE PMAA from the blend multilayer films slowly transforms from the initial burst disruption to the surface attrition by increasing the amount of strong PE PSS in the mixtures of polyanions. As shown in

dx.doi.org/10.1021/ma3002615 | Macromolecules 2012, 45, 3542−3549

Table 1. Film Parameters Determined from NR Measurements for Model Blend Multilayer Films with Different Blend Ratios of PSS:PMAA ((A) 0:100, (B) 10:90, and (C) 30:70) before and after Treatment at pH 2

	as-prepared films			films post-treated at pH 2		
model blend multilayer films	total film thickness (nm)	external roughness (nm)	internal roughness (nm)	total film thickness (nm)	external roughness (nm)	internal roughness (nm)
A	70.5	1.4	1.3 ± 0.5	4.5	0.6	
B	73.4	0.8	1.5 ± 0.5	40.5	8.4	4.4 ± 2.3
C	69.5	4.2	3.5 ± 0.9	56.6	4.8	2.8 ± 1.1

Figure 3C, only weak PEs residing at the top layer of the blend film are released while *d*-PMAA chains buried deep inside the blend multilayer film are virtually intact or immobile most likely due to the ionic cross-linking effect of PSS within the film even after the post-treatment, as shown in the SLD profile (NR data and the fitted SLD profile for the blend multilayer with 20% PSS show the release behavior similar to the blend multilayer containing 30% PSS (see Figure S1 in Supporting Information)).

The degree of intermixing between individual deposition layers increases with the increase of the fraction of PSS in the mixtures of polyanions. The evidence for this observation originates from the peak broadening of *d*-PMAA layers in the blend films as well as the increased SLD values of protonated LPEI layers. Another clue for the intimate intermixing mediated by PSS is found from the sharpest and highest peak of *d*-PMAA at the surface (i.e., in contact with air side), elucidating that there is no virtual interpenetration at the surface. The PSS chains embedded within the multilayer film easily capture *d*-PMAA molecules residing upper or adjacent to LPEI layers. Thus, the release of *d*-PMAA is controlled by the content of PSS in the blend multilayer film, allowing the transition from a burst disruption to the surface erosion. The controlled release behavior of blend multilayer films was also confirmed by complementary experiments with ellipsometer, AFM, QCM, and FT-IR.

Changes in Film Thickness and Surface Morphology. The reduction in film thickness after the post-treatment was calculated as a function of the blend ratio of PSS and PMAA, based on the equation:

$$\text{thickness reduction (\%)} = \frac{t_i - t_f}{t_i} \times 100$$

where t_i and t_f are the initial as-prepared and final post-treated film thicknesses, respectively.

As shown in Figure 4, the $(\text{LPEI/PMAA})_{16}$ multilayer film containing weak PMAA polyanions only is almost disassembled after the post-treatment at pH 2.0. However, the thickness reduction remarkably decreases as the PSS content is increased within the multilayer film. The reduction in film thickness estimated from the ellipsometric data coincides with the thickness measurements obtained from the fitting of NR data. Fitting of NR data yields information on film parameters including total film/interlayer thickness as well as internal/external roughness of blend multilayer films before and after post-treatment, as summarized in Table 1. (All the error bars in this paper represents $\pm 1\sigma$.)

Changes in surface roughness before and after the post-treatment were obtained by AFM (Figure 5A) and could also be compared with the film parameters obtained from the NR data. The surface roughness is also very important for the critical transition of surface release properties which could, in turn, be related to pore size and molecular diffusion.[44,45] We

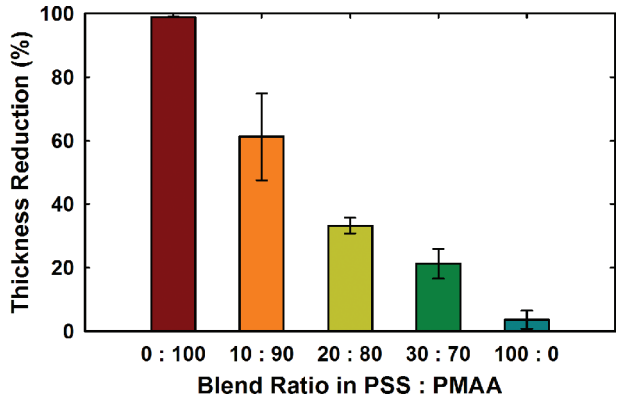


Figure 4. Thickness reduction (%) of blend multilayer films as a function of the blend ratio of PSS:PMAA polyanion mixtures, as measured by an ellipsometer.

thus quantitatively analyzed the root-mean-square (rms) surface roughness before and after the post-treatment as a function of the blend ratio (Table 1 and Figure 5B).

When a multilayer film is constructed with a pair of LPEI and PMAA, the roughness of the remaining very thin film is close to that of the Si substrate after the post-treatment because most likely the first few bilayers are conformal with the substrate. However, in the case of the blend multilayer film containing 10% PSS, some residual PEs remain with a roughened surface after the post-treatment, implying the appreciable release of polyelectrolyte chains (i.e., burst-out from the substrate but not entirely disrupted) with a small amount of PSS incorporated into the multilayer film. Consistent with the roughness values obtained by NR as well as the thickness reduction obtained from ellipsometer, the extent of surface morphological change during the pH treatment decreases as the content of PSS within the blend film is increased. We find that film stability against external pH has some correlations with the reduced change in film roughness (Figure 5B).

Release Kinetics. Release kinetics as a function of blend ratio of polyanions was monitored with *in situ* quartz crystal microbalance with dissipation (QCM-D) measurements. The relationship between frequency shift (Δf) and added or released mass per unit area (Δm) is linear, according to the Sauerbrey equation:[46]

$$\Delta m = -C\frac{\Delta f_n}{n}$$

where C is the proportionality constant related to intrinsic properties of quartz (C = 17.7 ng cm^{-2} Hz^{-1} for a 5 MHz quartz crystal) and n represents the overtone number (n = 1, 3, 5, 7). In addition, the dissipation change (ΔD_n), the loss of energy stored in a vibration cycle, indicates the physical characteristics of deposited layer such as viscosity, elasticity, and so forth. If ΔD_n is less than 2.0×10^{-6} and the plots of $\Delta f_n/n$

dx.doi.org/10.1021/ma3002615 | Macromolecules 2012, 45, 3542−3549

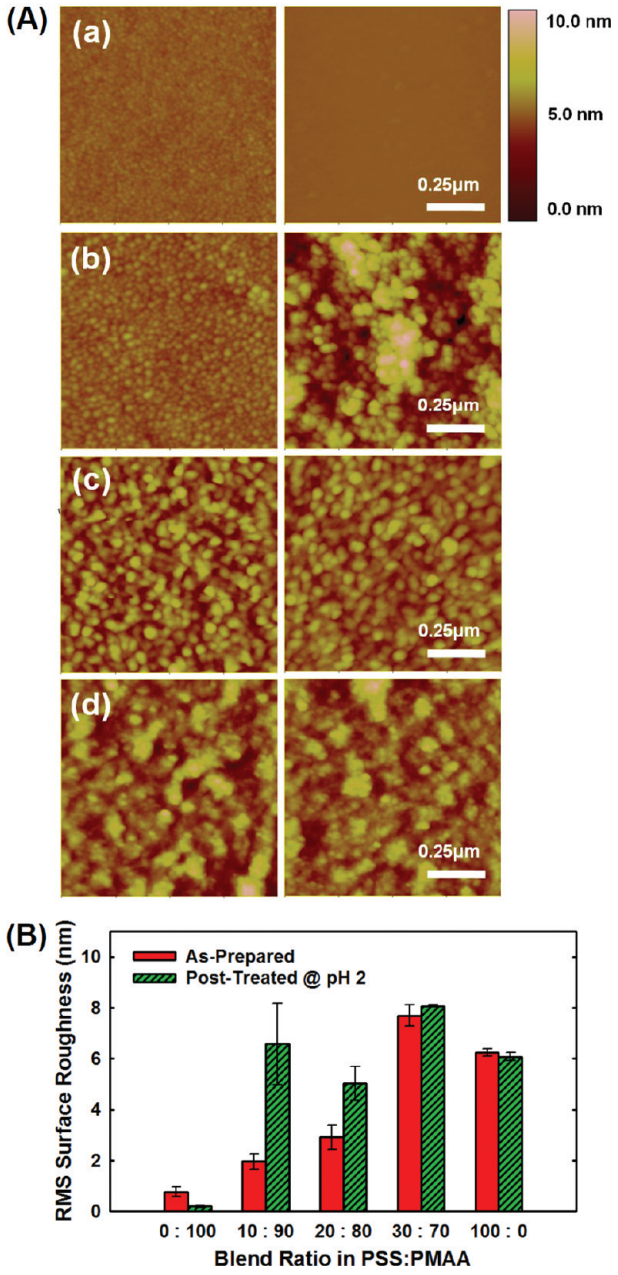


Figure 5. Changes in (A) surface morphology of as-deposited (left column) and post-treated (right column) blend multilayer films with different blend ratios of PSS:PMAA polyanions ((a) 0:100, (b) 10:90, (c) 30:70, (d) 0:100). (B) Changes in rms surface roughness as a function of blend ratio.

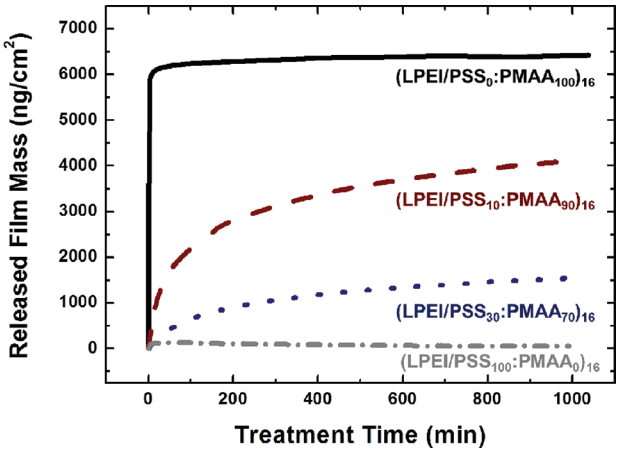


Figure 6. Release kinetics (released mass (ng/cm^2) plotted against time (min)) for blend multilayer films with different blend ratios of PSS and PMAA polyanions, monitored by QCM-D.

are superimposed with different overtones, the deposited layer has an elastic characteristic, and the physical properties such as mass and thickness of the elastic film can be estimated from the Sauerbrey equation.[47,48] In the present study, the released film masses (ng cm^{-2}) as a function of post-treatment time at pH 2.0 were calculated based on the Sauerbrey equation because the frequency changes ($\Delta f_n/n$) were superimposed with different overtone numbers (n = 3, 5, 7) as well as the dissipation energy of each multilayer was less than 2.0×10^{-6}, regardless of the blend ratio (Figure S2 in Supporting Information). The released film mass curves of blend multilayer films, shown in Figure 6, were calculated from the normalized frequency changes in third overtone ($\Delta f_3/3$). Detailed explanations of QCM experiments and data reduction are given in Supporting Information. As shown in Figure 6, an initial burst in the release profile of nonblended multilayer film containing LPEI and PMAA only was observed when the film is subject to post-treatment at pH 2.0, implying that the release behavior is induced directly from the substrate due to the absence of PSS. On the other hand, blended multilayer films containing 10% and 30% PSS show more retarded release rates when compared with the nonblend weak PE film. In the case of $(LPEI/PSS)_{16}$ multilayer film, it is clearly demonstrated that there is no change in the film mass even after the post-treatment at pH 2.0 for more than 1000 min.

The percentage of released film mass relative to the initial deposited mass was obtained from QCM measurements at different PSS blend ratios. The initial film masses were calculated using the Sauerbrey equation, based on the difference in absolute frequency (f_3) between a bare Au electrode and the electrodes coated with multilayer films. Compared with each initially deposited film mass, 81% of the original film mass is released from the multilayer film consisting of weak PEs only while 37% and 11% of masses of blended multilayer films containing 10% and 30% of PSS are lost from the film surface during the post-treatment at pH 2.0 for 1000 min. The differences in the released film masses with different strong PE contents demonstrate that the blend multilayer systems have great potential to control the amount of materials delivered as well as the rate of attrition.

Spectroscopic Changes in Film Composition. The reason why the blended films containing PSS PEs show the controlled release behavior is that the strong PSS PEs provide permanent negative charge density to associate with positive LPEI layer, and it could serve as robust skeletons of the films against external pH change. In order to verify the skeleton effect of PSS PEs within the multilayer films, independent of external pH, the composition of blend multilayer films has been analyzed with FT-IR.

Figure 7 shows the IR spectra of PSS in the blend multilayer films with different blend ratios of PSS and PMAA before (open symbols) and after (closed symbols) the post-treatment at pH 2.0 for 10 min. The FT-IR spectra of PSS shows the characteristic peak at 1035 cm^{-1} for the stretching vibration of SO_3^- groups.[48] The amount of PSS retained within the

dx.doi.org/10.1021/ma3002615 | Macromolecules 2012, 45, 3542−3549

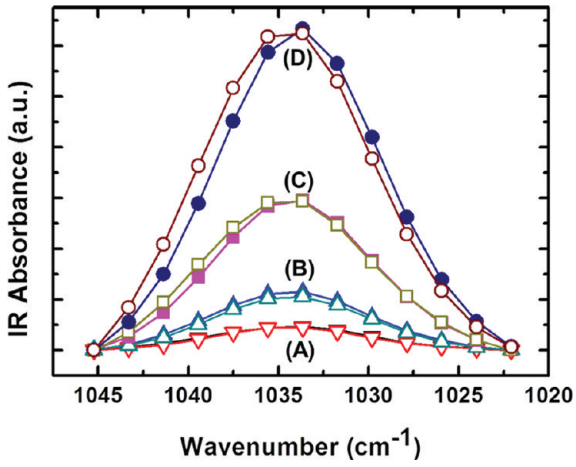


Figure 7. FT-IR spectra of PSS on the region of S═O stretching vibration of SO_3^- for as-prepared films (open symbols) and the films post-treated at pH 2 (closed symbols) with different blend ratios in PSS:PMAA polyanion mixtures ((A)▼, 10:90; (B) ▲, 20:80; (C) ■, 30:70; and (D) ●, 100:0).

multilayer films is almost constant even after the post-treatment, regardless of the blend ratios of PSS and PMAA.

On the other hand, weak PEs shows significant differences in IR absorbance when as-prepared films were subject to the post-treatment. Figure 8 shows that as the content of PSS is increased, the degree of decrease in the IR absorbance of PMAA is reduced and also more protonated PMAA chains confirmed by a peak at 1701 cm^{-1} remain within the blend film even after treatment. These results imply that every carboxylic group in PMAA chains is protonated at pH 2.0, but the protonated PMAA chains cannot easily escape from the blend multilayer films due to strong ionic cross-linking effect of PSS PEs. The remaining amount of LPEI also increases within the films as the PSS content within the multilayer film is increased (see Figure S3 in Supporting Information). These FT-IR analyses further support that pH-independent PSS chains serve as robust skeletons to resist the total disruption of $(LPEI/PMAA)_n$ weak PE multilayer films when the multilayer film is subject to treatment in acidic media. As a result, the burst disruption of multilayer films is dramatically suppressed, and the release kinetics could be finely tuned simply by varying the PSS content within the multilayer films.

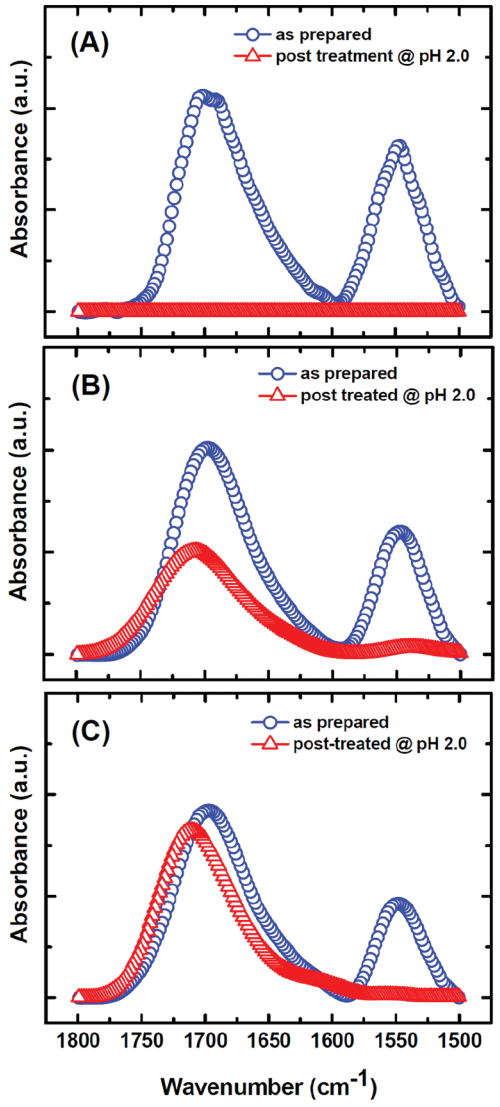


Figure 8. FT-IR absorption spectra of PMAA chains, in the regions at 1701 and 1540 cm^{-1} associated with COOH and COO^- groups for as-prepared films (circle symbols) and the films post-treated at pH 2.0 (triangle symbols) at different blend ratios in PSS:PMAA polyanion mixtures ((A) 0:100, (B) 10:90, (C) 30:70).

■ CONCLUSION

A model controlled release platform triggered in acidic conditions (i.e., pH 2.0) has been developed based on blend multilayer films incorporating the mixtures of strong and weak PEs. LbL systems containing $[LPEI/PSS_x:PMAA_{100-x}]_{16}$ have been prepared by the spin-assisted deposition method, which offers well-defined internal structure with linear growth behavior. The controlled release behavior as a function of blend ratio of PSS and PMAA has been investigated in terms of the changes in internal structure as well as the release kinetics at the nanoscale level. As the incorporation ratio of PSS is increased within the blend multilayer film, the precipitous disruption of a film solely composed of weak PEs is dramatically suppressed and switches to surface erosion. The released mass and kinetics of the film could be finely tuned as a function of the blend ratio. In addition, we have elucidated that PSS PEs provide the robust skeletons within the blend multilayer films, independent of pH variation, as shown by the comparison of the analysis of SLD profiles as well as FT-IR absorbance of model films before and after treatment. The approaches taken in the present study for the controlled release represent the improved release property of multilayer thin films. Therefore, the controlled release behavior of model blend multilayer systems triggered at low pH offers the opportunity to design versatile polymeric delivery platforms responding to external stimuli for various biomedical applications.

■ ASSOCIATED CONTENT

Ⓢ Supporting Information

Incorporation ratio of PMAA within the multilayer films (Table S1); NR curves with best fits and the SLD profiles of $[(LPEI/PSS_{20}:PMAA_{80})_3(LPEI/PSS_{20}:d\text{-}PMAA_{80})_1]_4$ (Figure S1); QCM raw data of model multilayer films (Figure S2); FT-IR spectra of LPEI (Figure S3) for as-prepared and post-treated samples. This material is available free of charge via the Internet at http://pubs.acs.org.

dx.doi.org/10.1021/ma3002615 | *Macromolecules* 2012, 45, 3542−3549

AUTHOR INFORMATION

Corresponding Author

*Tel +82-2-880-7431, fax +82-2-873-1548, e-mail khchar@plaza.snu.ac.kr.

Notes

The authors declare no competing financial interest.

ACKNOWLEDGMENTS

This work was financially supported by the National Research Foundation of Korea (NRF) funded by the Korea Ministry of Education, Science, and Technology (MEST) (The National Creative Research Initiative Program for "Intelligent Hybrids Research Center" (No. 2010-0018290), the Brain Korea 21 Program in SNU Chemical Engineering, and the WCU Program of Chemical Convergence for Energy and Environment (R31-10013)). Y. Jang is also grateful for the financial support from the Seoul Science Fellowship. We thank NIST Center for Neutron Research (NCNR) for assigning enough beamtime to conduct NR experiments at NG7 beamline. In addition, we appreciate Dr. Ki-Yeon Kim and Dr. Jung-Soo Lee for allowing us to use the REF-V beamline at the HANARO Center of Korea Atomic Energy Research Institute (KAERI).

REFERENCES

(1) Tang, Z. Y.; Wang, Y.; Podsiadlo, P.; Kotov, N. A. *Adv. Mater.* **2006**, *18* (24), 3203−3224.

(2) Boudou, T.; Crouzier, T.; Ren, K. F.; Blin, G.; Picart, C. *Adv. Mater.* **2010**, *22* (4), 441−467.

(3) Jang, Y.; Park, S.; Char, K. *Korean J. Chem. Eng.* **2011**, *28* (5), 1149−1160.

(4) Swiston, A. J.; Cheng, C.; Um, S. H.; Irvine, D. J.; Cohen, R. E.; Rubner, M. F. *Nano Lett.* **2008**, *8* (12), 4446−4453.

(5) Wood, K. C.; Boedicker, J. Q.; Lynn, D. M.; Hammond, P. T. *Langmuir* **2005**, *21* (4), 1603−1609.

(6) Ono, S. S.; Decher, G. *Nano Lett.* **2006**, *6* (4), 592−598.

(7) De Geest, B. G.; Sanders, N. N.; Sukhorukov, G. B.; Demeester, J.; De Smedt, S. C. *Chem. Soc. Rev.* **2007**, *36* (4), 636−649.

(8) Kim, B. S.; Smith, R. C.; Poon, Z.; Hammond, P. T. *Langmuir* **2009**, *25* (24), 14086−14092.

(9) Hong, J.; Kim, B. S.; Char, K.; Hammond, P. T. *Biomacromolecules* **2011**, *12* (8), 2975−2981.

(10) Jomaa, H. W.; Schlenoff, J. B. *Macromolecules* **2005**, *38* (20), 8473−8480.

(11) Wong, J. E.; Gaharwar, A. K.; Muller-Schulte, D.; Bahadur, D.; Richtering, W. *J. Colloid Interface Sci.* **2008**, *324* (1−2), 47−54.

(12) Volodkin, D. V.; Madaboosi, N.; Blacklock, J.; Skirtach, A. G.; Mohwald, H. *Langmuir* **2009**, *25* (24), 14037−14043.

(13) Wood, K. C.; Zacharia, N. S.; Schmidt, D. J.; Wrightman, S. N.; Andaya, B. J.; Hammond, P. T. *Proc. Natl. Acad. Sci. U. S. A.* **2008**, *105* (7), 2280−2285.

(14) Etienne, O.; Schneider, A.; Taddei, C.; Richert, L.; Schaaf, P.; Voegel, J. C.; Egles, C.; Picart, C. *Biomacromolecules* **2005**, *6* (2), 726−733.

(15) Kharlampieva, E.; Ankner, J. F.; Rubinstein, M.; Sukhishvili, S. A. *Phys. Rev. Lett.* **2008**, *100* (12), 128303.

(16) Jia, Y.; Fei, J.; Cui, Y.; Yang, Y.; Gao, L.; Li, J. *Chem. Commun.* **2011**, *47*, 1175−1177.

(17) Song, W.; He, Q.; Mohwald, H.; Yang, Y.; Li, J. *J. Controlled Release* **2009**, *139*, 160−166.

(18) Mendelsohn, J. D.; Barrett, C. J.; Chan, V. V.; Pal, A. J.; Mayes, A. M.; Rubner, M. F. *Langmuir* **2000**, *16* (11), 5017−5023.

(19) Lutkenhaus, J. L.; McEnnis, K.; Hammond, P. T. *Macromolecules* **2008**, *41* (16), 6047−6054.

(20) Vander, A. J.; Sherman, J. H.; Luciano, D. S. *Human Physiology: the Mechanisms of Body Function*; McGraw-Hill: New York, 1994.

(21) Estey, T.; Kang, J.; Schwendeman, S. P.; Carpenter, J. F. *J. Pharm. Sci.* **2006**, *95* (7), 1626−1639.

(22) Risbud, M. V.; Hardikar, A. A.; Bhat, S. V.; Bhonde, R. R. *J. Controlled Release* **2000**, *68*, 23−30.

(23) Rao, V. M.; Engh, K.; Qiu, Y. *Int. J. Pharm.* **2003**, *252*, 81−86.

(24) Cho, J. H.; Quinn, J. F.; Caruso, F. *J. Am. Chem. Soc.* **2004**, *126* (8), 2270−2271.

(25) Quinn, A.; Such, G. K.; Quinn, J. F.; Caruso, F. *Adv. Funct. Mater.* **2008**, *18* (1), 17−26.

(26) Quinn, A.; Tjipto, E.; Yu, A. M.; Gengenbach, T. R.; Caruso, F. *Langmuir* **2007**, *23* (9), 4944−4949.

(27) Decher, G. *Science* **1997**, *277* (5330), 1232−1237.

(28) Losche, M.; Schmitt, J.; Decher, G.; Bouwman, W. G.; Kjaer, K. *Macromolecules* **1998**, *31* (25), 8893−8906.

(29) Cho, J.; Char, K.; Hong, J. D.; Lee, K. B. *Adv. Mater.* **2001**, *13* (14), 1076−1078.

(30) Kharlampieva, E.; Kozlovskaya, V.; Chan, J.; Ankner, J. F.; Tsukruk, V. V. *Langmuir* **2009**, *25* (24), 14017−14024.

(31) Turon, X.; Rojas, O. J.; Deinhammer, R. S. *Langmuir* **2008**, *24* (8), 3880−3887.

(32) Commercial materials, instruments and equipment are identified in this paper in order to specify the experimental procedure as completely as possible. In no case does such identification imply a recommendation or endorsement by the National Institute of Standards and Technology nor does it imply that the materials, instruments, or equipment identified are necessarily best available for the purpose.

(33) Kienzle, P. A.; O'Donovan, K. V.; Ankner, J. F.; Berk, N. F.; Majkrzak, C. F. http://www.ncnr.nist.gov/reflpak, 2000−2006.

(34) Parratt, L. G. *Phys. Rev.* **1954**, *95* (2), 359−369.

(35) Yoo, P. J.; Zacharia, N. S.; Doh, J.; Nam, K. T.; Belcher, A. M.; Hammond, P. T. *ACS Nano* **2008**, *2* (3), 561−571.

(36) Yoo, P. J.; Nam, K. T.; Qi, J. F.; Lee, S. K.; Park, J.; Belcher, A. M.; Hammond, P. T. *Nat. Mater.* **2006**, *5* (3), 234−240.

(37) Lee, Y. M.; Park, D. K.; Choe, W. S.; Cho, S. M.; Han, G. Y.; Park, J.; Yoo, P. J. *J. Nanosci. Nanotechnol.* **2009**, *9* (12), 7467−7472.

(38) Chao, G. T.; Deng, H. X.; Huang, Q.; Jia, W. J.; Huang, W. X.; Gu, Y. C.; Tan, H. P.; Fan, L. Y.; Liu, C. B.; Huang, A. L.; Lei, K.; Gong, C. Y.; Tu, M. J.; Qian, Z. Y. *J. Polym. Res.* **2006**, *13* (5), 349−355.

(39) Hubsch, E.; Ball, V.; Senger, B.; Decher, G.; Voegel, J. C.; Schaaf, P. *Langmuir* **2004**, *20* (5), 1980−1985.

(40) Sui, Z. J.; Schlenoff, J. B. *Langmuir* **2004**, *20* (14), 6026−6031.

(41) Hiller, J.; Rubner, M. F. *Macromolecules* **2003**, *36* (11), 4078−4083.

(42) Kharlampieva, E.; Kozlovskaya, V.; Ankner, J. F.; Sukhishvili, S. A. *Langmuir* **2008**, *24* (20), 11346−11349.

(43) Fredin, N. J.; Zhang, J.; Lynn, D. *Langmuir* **2005**, *21*, 5801−5811.

(44) Quinn, J.; Caruso, F. *Langmuir* **2004**, *20*, 20−22.

(45) Felix, O.; Zheng, Z. Q.; Cousin, F.; Decher, G. *C. R. Chim.* **2009**, *12* (1−2), 225−234.

(46) Sauerbrey, G. *Z. Phys.* **1959**, *155* (2), 206−222.

(47) Vogt, B. D.; Lin, E. K.; Wu, W. L.; White, C. C. *J. Phys. Chem. B* **2004**, *108* (34), 12685−12690.

(48) Lee, H.-S.; Eckmann, D. M.; Lee, D.; Hickok, N. J.; Composto, R. J. *Langmuir* **2011**, *27* (20), 12458−12465.

(49) Kuo, C.-W.; Wen, T.-C. *Eur. Polym. J.* **2008**, *44* (11), 3393−3401.

Macromolecules

Article

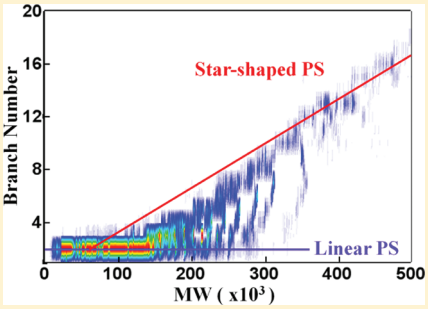
pubs.acs.org/Macromolecules

Characterization of Branched Polymers by Comprehensive Two-Dimensional Liquid Chromatography with Triple Detection

Seonyoung Ahn,† Hyojoon Lee,† Sekyung Lee, and Taihyun Chang*

Department of Chemistry and Division of Advanced Materials Science, Pohang University of Science and Technology (POSTECH), Pohang 790-784, Korea

ABSTRACT: In the branching analysis by size exclusion chromatography (SEC)/triple detection (concentration, light scattering, and viscosity detectors) method, the branch number is calculated from the extent of chain size contraction due to chain branching relative to the linear polymer of the same molecular weight (MW). A problem can arise from the fact that polymer chain size depends on both MW and chain branching. Since SEC separates polymers according to the chain size, an SEC fraction of randomly branched polymers may contain polymer species heterogeneous in both MW and chain architecture in general. As a solution of the problem, we propose a separation of polymers by interaction chromatography according to MW first and then measure the chain size distribution of polymers in the homogeneous MW fraction by SEC/triple detection. The analysis scheme is successfully established by online two-dimensional liquid chromatography combining temperature gradient interaction chromatography and SEC/triple detection.



INTRODUCTION

Long chain branching (LCB) is one of the important molecular characteristics which influences processability and performance of polymeric materials significantly.[1,2] Therefore, precise characterization of chain branching is a requisite step to understand the relationship between the molecular characteristic and the rheological and mechanical properties of the polymeric materials.[3,4] It is nontrivial to characterize LCB precisely. The most widely employed method to characterize the branch distribution is size exclusion chromatography separation coupled with triple (concentration, light scattering, and viscosity) detection (SEC/TD).[5−7] The method is based on the theoretical study by Zimm and Stockmayer in 1949, in which they worked out how the chain size (mean-square radius of gyration, R_g^2) is affected by chain branching.[8] Chain branching reduces R_g^2 relative to the linear chain of the same molecular weight (MW) and the ratio of R_g^2 values is defined as the chain contraction factor, g

$$g \equiv \frac{(R_g^2)_B}{(R_g^2)_L} \tag{1}$$

where the subscripts B and L denote branched and linear polymers, respectively. Later, Zimm and Kilb reported that the ratio of intrinsic viscosity, $[\eta]$, would give equivalent information on the chain size contraction upon branching.[9]

$$g' \equiv \frac{[\eta]_B}{[\eta]_L} \tag{2}$$

Since $[\eta]$ can be measured with a higher precision than R_g^2, particularly for low-MW polymers, g' is more frequently measured experimentally. However, an appropriate relationship between g and g' needs to be established to calculate branch numbers since the theoretical chain contraction factor is derived for R_g^2, not $[\eta]$.

The g factor has been derived for a few model branched chain architectures such as regular stars (having uniform MW arms)[8] and regular combs (having uniform MW branches).[10] Also, a number of experimental works have been carried out to verify the theoretical prediction and to establish a reliable experimental methodology for branching analysis of polymers.[7,11−14] Combining SEC separation and multiple detection, it is possible to separate polydisperse polymers into narrow (in elution volume) fractions and to measure MW, R_g^2, and $[\eta]$ for each eluting fraction online. If we assume that each fraction of SEC effluent contains polymers homogeneous in both MW and chain architecture, and if we have an appropriate g' function for the polymer system, one can map the bivariate distribution in MW and branch number of a branched polymer by SEC/TD method. The results in the literature cannot be said to be very successful and the deviations have been attributed to the following reasons.

(1) All theories dealing with g factor were developed for random-walk chain (Gaussian distribution of the chain segments) model while most of the experimental works carried out in good solvent condition including all the SEC/TD experiments.

(2) Because of the difficulty to measure R_g^2 precisely, in particular for the polymers with small R_g^2, the intrinsic viscosity was more frequently measured. But the relationship between g and g' is not well-established.

Received: September 30, 2011
Revised: March 20, 2012
Published: April 10, 2012

 © 2012 American Chemical Society dx.doi.org/10.1021/ma2021985 | *Macromolecules* 2012, 45, 3550−3556

In this paper, we would like to focus on another problem in the SEC/TD branching analysis. Although it is not frequently addressed in branching analyses by the SEC/TD method, an SEC fraction would not contain homogeneous polymer species.[15−17] Let alone the serious band broadening in SEC, SEC does not separate polymers according to MW but chain size. Polymers with different MW and different chain architecture can have the same chain size. If an SEC fraction does not contain polymers of homogeneous MW (local polydispersity), the basic assumption in the SEC/TD branching analysis based on the chain contraction factor of Zimm and Stockmayer is no longer valid. This problem may not be serious when the chain size has a monotonous dependence on MW such as regular star-shaped polymers, but it can be a source of error for branched polymers in general.

As a solution of the problem described above, we propose two-dimensional liquid chromatography (2D-LC) analysis. 2D-LC is a powerful tool for the analysis of complex polymers which have distributions in more than one molecular characteristic.[18−23] In most 2D-LC separations of synthetic polymers carried out so far, interaction chromatography (IC) has been used for the first-D LC separating the polymers by chemical heterogeneity while the second-D separation has been done by SEC separating the polymer chains with respect to the molecular size.[20,24−27] But IC can separate polymers according to MW as well with much higher resolution than SEC.[28,29] In particular, temperature gradient interaction chromatography (TGIC) has become a well-established technique to separate branched polymers according to MW nearly independent of long chain branching.[30−36]

Taking advantage of the sensitivity on MW of IC separation, a branched polymer system can be separated according to MW first and then SEC/TD analysis can be applied to the homogeneous MW fractions, which conforms to the analysis scheme based on chain contraction concept. In this study, we report online TGIC × SEC mode 2D-LC characterization of branched polymers by fractionating the samples into homogeneous MW fractions before the SEC/TD analysis. To demonstrate the problem in conventional SEC/TD analysis of branched polymer systems, we employed a model system: an artificial mixture of linear and star-shaped PS. The star-shaped PS was prepared by linking polystyryl anions with divinylbenzene to yield a series of star-shaped PS with different number of branches of equal length. Therefore, the mixture of star-shaped PS and linear PS has a bivariate distribution in both MW and branch number. Such an IC × SEC mode 2D-LC separation of branched polymers has been done earlier by Gerber et al. They demonstrated a mixture of star-shaped and linear polymers by off-line[32] as well as online[37] by IC x SEC mode 2D-LC. Gorbunov et al. reported a simulation result on the 2D-LC separation for the same mixture system.[38] However, they only demonstrated the separation itself, not on the branching analysis by multiple detection method. In this study, we successfully demonstrated that such a 2D-LC separation can be combined with triple detection to correctly characterize the complex branched polymer.

EXPERIMENTAL SECTION

Materials. The star-shaped polystyrene (PS) sample was synthesized by linking anionic-polymerized polystyryl anions with divinylbenzene (DVB). The polymerization of styrene was carried out in cyclohexane using *sec*-butyl Li as an initiator. Details of the synthetic procedure were reported previously.[39] Because of the synthetic mechanism, the PS sample contains regular star-shaped polymers of varying number of branches while each branch has a very narrow MW distribution. The linear PS was synthesized by anionic polymerization using *n*-butyl Li as an initiator, which is known to yield a broader MW distribution due to a relatively slow initiation rate of *n*-butyl Li.[33] To prepare a linear PS sample whose SEC elution volume fully overlaps with the star-shaped PS, three different MW linear PS were prepared and then mixed to obtain such a MW distribution. The characterization data of the polymer samples are given in Table 1.

Table 1. Molecular Weight Characteristics of Linear PS, Star-Shaped PS, and PS Mixture[a]

linear PS		star-shaped PS			PS mixture	
M_w	M_w/M_n	$M_{w,arm}$	M_w	M_w/M_n	M_w	M_w/M_n
127 000	1.46	30 000	152 000	2.01	144 000	1.89

[a]Determined by SEC/light scattering detection.

SEC Analysis. Two mixed bed columns (Polymer Lab. Mixed C, 300 × 7.8 mm i.d.) were used at a column temperature of 40 °C. Eluent was THF (Samchun, HPLC grade) at a flow rate of 0.8 mL/min. SEC chromatograms were recorded with a light scattering (LS)/refractive index (RI)/viscometer (DP) (Viscotek TDA 302) and a UV absorption detector (TSP, UV100 at 260 nm wavelength). The d*n*/d*c* value for PS in THF is 0.185 mL/g. Polymer samples were dissolved in THF at a concentration of ca. 1 mg/mL, and the injection volume was 100 μL.

RP-TGIC Analysis. For the reversed phase (RP)-TGIC analysis, a C18 bonded silica column (Nueleosil C18, 5 μm, 300 Å pore, 150 × 4.6 mm i.d.) was used. Mobile phase was a CH_2Cl_2/CH_3CN mixture (57/43, v/v, Samchun, HPLC grade) at a flow rate of 0.5 mL/min. Temperature of the column was controlled by circulating fluid from a programmable bath/circulator (ThermoHaake, C25P) through a homemade column jacket. The chromatograms were recorded with an LS (Wyatt, MiniDawn), RI (Shodex, RI-101), and a UV absorption (TSP, UV 2000 at 260 nm wavelength) detectors for online determination of absolute MW of polymers.

RP-TGIC × SEC 2D-LC Analysis. For the first-D RP-TGIC separation, the same experimental conditions as in the one-dimensional RP-TGIC analysis were used except for the flow rate. The flow rate of the first-D RP-TGIC was set low at 0.01 mL/min to synchronize with the second-D SEC separation. For the second-D SEC separation, one mixed bed column (Polymer Lab. Mixed C, 300 × 7.8 mm i.d.) was employed. Temperature of the SEC column was controlled at 60 °C by a column oven (Futecs, AT-4000). Eluent was THF (Samchun, HPLC grade) at a flow rate of 1.2 mL/min. The chromatograms were recorded with a triple detector (Viscotek TDA 302) for online determination of the absolute MW and intrinsic viscosity of polymers.

RESULTS AND DISCUSSION

To demonstrate the problem associated with "local polydispersity" in the conventional SEC/TD branching analysis, we selected a PS mixture as a model system consisting of equal amount of the linear PS and the star-shaped PS. Figure 1a displays SEC chromatograms of the three samples; the linear, the star-shaped, and the 1:1 mixture of the two. In the SEC chromatogram of the star-shaped PS, which has a distribution in branch number, is partially resolved as separate peaks. The lowest MW peak is the single arm and the two arm star (a linear PS with MW = 2 × MW_{arm}) appears as a shoulder of the main peak containing more highly branched species which are not resolved. It is a natural result of size-based SEC separation since the chain size of regular star-shaped polymers does not change much as the number of arm increases, and SEC resolution is not high due to the band broadening. The linear PS is a mixture of three PS samples prepared by anionic

dx.doi.org/10.1021/ma2021985 | Macromolecules 2012, 45, 3550−3556

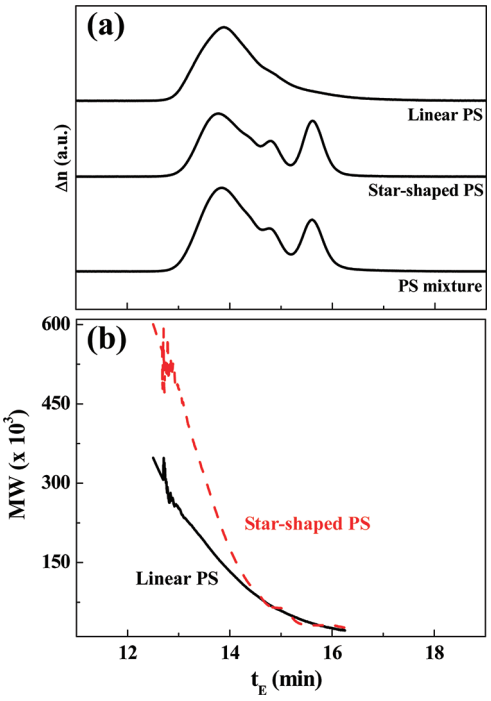


Figure 1. (a) SEC chromatograms of the linear PS, star-shaped PS, and PS mixture. (b) Molecular weight vs elution time plots of linear PS (solid line) and star-shaped PS (dashed line). Separation condition: two mixed bed columns (Polymer Laboratories, PL mixed C), THF eluent at the column temperature of 40 °C. Flow rate was 0.8 mL/min.

polymerization with *n*-butyl Li initiation. The three PS samples were mixed to give the overall peak shape similar to that of the star-shaped PS and at the same time to cover the entire elution volume range of the star-shaped PS. Therefore, the 1:1 mixture of the linear and star-shaped PS yields an SEC chromatogram showing the same general feature of the star-shaped polymer. Since the SEC separation is based on hydrodynamic volume, polymers with different MW can coelute due to the differences in their chain architectures.

Figure 1b displays the plots of MW vs SEC elution time for the star-shaped PS (dashed red line) and the linear PS (solid black line) determined by light scattering detection. Star-shaped PS elutes later than linear PS of the same MW. In other words, a star-shaped PS coelutes with a lower MW linear PS since a star-shaped polymer has a chain size smaller than the linear polymer of the same MW. Therefore, an SEC fraction of the PS mixture contains coeluting two different MW species: a linear PS of lower MW and a star PS of higher MW. Such local polydispersity may lead to an erroneous result in SEC/TD branching analysis.[15−17,40]

As the branch number of regular star-shaped polymers increases, the contraction factor decreases from 1. For regular star-shaped polymers, the following equation was derived to relate the branch number, f, to the chain contraction factor, g.[8]

$$g = \frac{3f - 2}{f^2} \tag{3}$$

The relationship between g and g' is often given by

$$g' \cong g^{\varepsilon} \tag{4}$$

The exponent ε depends on a number of factors including solvent, temperature, and chain architecture. The ε value has been reported to fall in a range of 0.5−1.5. For regular star-shaped polymers, it was found experimentally as 0.7−0.8 in good solvent conditions.[11]

Intrinsic viscosity vs MW plots of the three polymer samples are shown in Figure 2. Linear PS exhibits a linear dependence

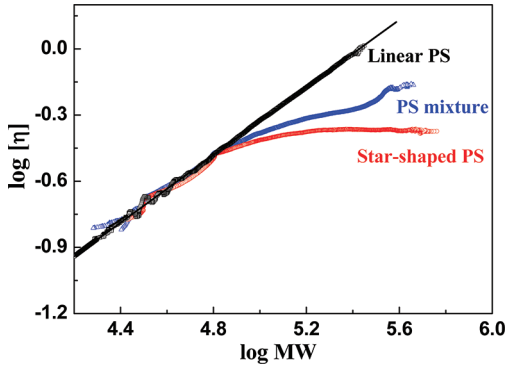


Figure 2. Intrinsic viscosity vs MW plots of linear PS (black square), star-shaped PS (red circle), and PS mixture (blue triangle).

of log [η] on log MW conforming to the Mark−Houwink relationship with a slope of 0.72, which is consistent with the literature values for linear random coils in the range of 0.7−0.74.[41] The intrinsic viscosity of star-shaped PS (red circle) is lower than linear PS (black square), indicating that chain branching leads to contraction of the chain size relative to the linear polymers at the same MW. The deviation increases as MW (thus branch number) increases. Since linear and star-shaped PS having the same hydrodynamic volume coelute in the SEC separation, the intrinsic viscosity of the PS mixture (blue triangle) falls in between the linear and star-shaped PS.

The g' values calculated from the intrinsic viscosities of the three samples are plotted as a function of MW in Figure 3a.

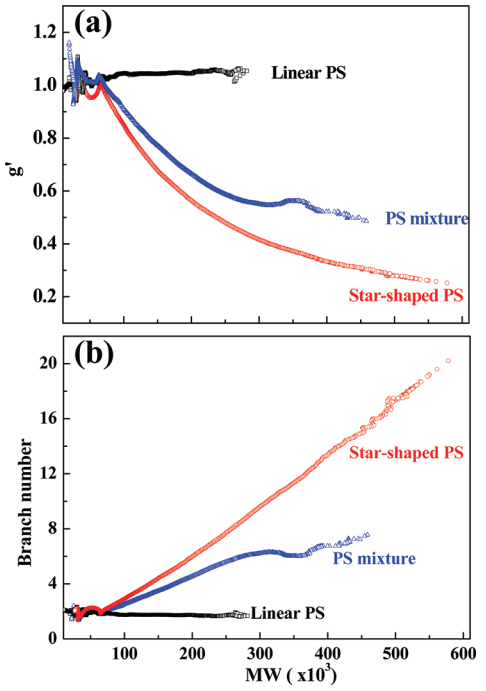


Figure 3. Plots of g' (a) and branching number f (b) vs molecular weight for linear PS (black square), star-shaped PS (red circle), and PS mixture (blue triangle).

dx.doi.org/10.1021/ma2021985 | *Macromolecules* 2012, 45, 3550−3556

The g' value of star-shaped PS decreases rapidly upon increase of MW. The g' values for the mixture fall in between the linear and star-shaped PS. In Figure 3b, the branch number, f, calculated according to eqs 3 and 4 is plotted against MW. The value of ε in eq 4 was determined with a priori information that $MW_{star} = f \times MW_{arm}$ for the regular star-shaped PS. The best fit of branch number vs MW_{star} was obtained when $\varepsilon = 0.7$ was used. The direct comparison of g and g' was not attempted, but this should be a good enough confirmation of the ε value for this study. Even though the resolution of SEC for the star-shaped PS is not so good and an SEC fraction contains a mixture of differently branched species to some extent, the elution sequence was maintained well and the analysis based on the chain contraction concept seems to work reasonably well. For the linear PS, the g' value (in Figure 3a) and the branch number (in Figure 3b) of linear PS were calculated relative to the best-fit Mark–Houwink equation displayed in Figure 2 (solid line), and it follows $f = 2$ closely over the entire MW range as expected. The PS mixture shows an intermediate branch number between the star-shaped PS and the linear PS. It is an expected result considering the coelution of linear and star-shaped PS. This result does not reflect the correct picture of the polymer system. The correct picture should be two separate lines of star-shaped PS and linear PS, indicating that the sample is a mixture of the two polymer species. Furthermore, the MW axis does not represent homogeneous polymer species but a weight-average MW of linear and star-shaped PS having the same chain size.

The problem displayed in Figure 3 arises from the fact that a SEC fraction contains polymer species polydisperse in both MW and chain architecture. To carry out the branching analysis based on the chain contraction concept, it is necessary to separate polymers according to MW first. IC is an adequate technique for the purpose.[42,43] TGIC is known to separate branched polymers according to MW nearly independent of chain architecture.[3,4,30−36] Figure 4 displays RP-TGIC chromatograms of the three polymer samples. A sharp peak appearing at $t_E \approx 5$ min in all three chromatograms is the injection solvent peak. In the star-shaped PS chromatogram, a series of the peaks corresponds to star-shaped PS with increasing branch number since MW_{star} is "quantized" by MW_{arm} with a narrow MW distribution. These peaks were not well resolved in the SEC separation (Figure 1a) due to its size-sensitive separation as well as band broadening. By virtue of its high resolution and sensitivity to MW, IC can resolve the branched polymer far better than SEC according to the branch number. Nonetheless, as the number of arms increases, the elution peaks start to overlap. This is mainly due to the overlap of the finite MW distribution of the branched species even though each star-shaped PS species has a very narrow MW distribution close to the Poisson distribution.[44]

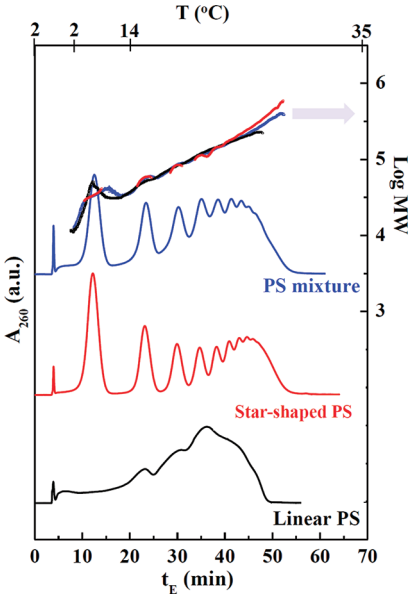


Figure 4. RP-TGIC chromatogram of three samples recorded by a UV detector. The molecular weights obtained by light scattering detection are also shown in the plot. The temperature program is shown in the top abscissa. Separation condition: Nucleosil C18, 500 Å pore, 7 μm particle, 150 × 4.6 mm i.d. Eluent: CH_2Cl_2/CH_3CN (57/43, v/v) at a flow rate of 0.5 mL/min.

The elution peak of linear PS is multimodal in contrast to the unimodal shape in SEC. The linear PS sample is a mixture of three different linear PS samples prepared by anionic polymerization using *n*-butyl Li initiator to cover the elution volume range of the star-shaped PS in SEC. The three linear PS components are partially resolved in the TGIC separation by virtue of the low band broadening in TGIC while they are hardly discernible in the SEC separation (Figure 1a). Plots of MW vs TGIC elution time of the three samples are also shown in Figure 4. The three PS samples show identical MW vs elution time plots, indicating the sensitivity of TGIC retention on MW not on chain architecture in contrast to SEC (Figure 1b).

If RP-TGIC/TD analysis is carried out based on the chain contraction factor concept, the problem of inhomogeneous MW fraction in SEC/TD analysis can be resolved. Nonetheless, it is not avoidable that an RP-TGIC fraction of the PS mixture is still a mixture of linear and star-shaped PS at the same MW. Therefore, it will provide a correct average branch number as a function of MW, but a full mapping of the branched structure of the polymer system is still not possible. If the linear and branched species in a homogeneous MW fraction obtained from RP-TGIC separation can be further separated according to the chain size, a full mapping of the branched structure could be achieved.

To pursue the idea, a 2D-LC separation was carried out by combining RP-TGIC and SEC as the first-D and the second-D LC separation, respectively. For the fast repetition of the second-D SEC separation, one GPC column and a fast flow rate had to be used at the cost of resolution to some extent. A triple detection system (light scattering, differential refractive index, viscosity detectors) was employed as the second-D LC detectors. The results of the online 2D-LC separation for the PS mixture are displayed in Figure 5 in which three 2D-LC chromatograms obtained by LS, RI, and viscosity detectors are shown in the form of contour map. They have similar shapes but with distinct intensity distribution. The characteristic intensity profile represent the different response of the three detectors: RI detector shows the concentration distribution while the LS detector signal is approximately proportional to MW × concentration, and the viscosity detector (differential pressure, DP) signal is approximately proportional to MW^{α} × concentration where α is the Mark–Houwink exponent.

In the 2D-LC chromatograms, unreacted arms and stars with a small number of arms show up as resolved peaks at RP-TGIC $t_E \approx 350$–450 min. Projections of a 2D-LC chromatogram to each axis corresponds to the 1D-LC chromatogram of the corresponding axis, and the general features of SEC and RP-TGIC chromatograms shown in Figures 1a and 4 can be observed.

dx.doi.org/10.1021/ma2021985 | *Macromolecules* 2012, 45, 3550−3556

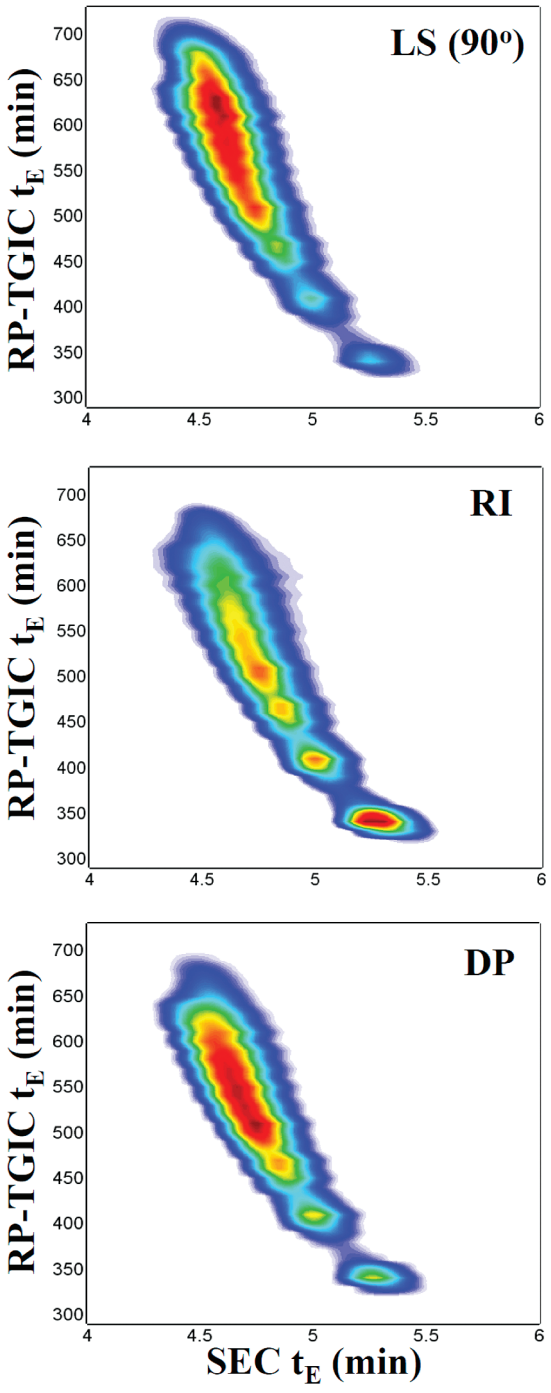


Figure 5. Contour plots of RP-TGIC × SEC 2D-LC chromatograms of the mixture of star-shaped PS and linear PS: first-D RP-TGIC: column (Nucleosil C18, 500 Å, 7 μm particle, 150 × 4.6 mm), eluent: CH_2Cl_2/CH_3CN (57/43, v/v) at a flow rate of 0.01 mL/min second-D SEC: PL mixed-C (Polymer Lab, 300 × 8 mm i.d.), THF eluent at a flow rate of 1.2 mL/min; column temperature: 60 °C.

But the 2D-LC chromatogram contains more information than two 1D-LC chromatograms. One feature we can see easily before the detailed analysis is the splitting of the chromatogram toward high-MW marked with arrows. If the resolution of the SEC separation is good, peak splitting between the linear PS and star-shaped PS would be like Figure 1b since RP-TGIC separates polymer according to MW. Because of the relatively poor resolution of SEC (to make the situation worse, only one SEC column was used to speed up the analysis), only a trace of peak splitting at the completion of the linear PS elution is observed.

We further examined the 2D-LC chromatogram as to whether the first-D TGIC separation indeed yielded the fractions with homogeneous MW. The three second-D SEC chromatograms of the TGIC fractions at t_E = 500, 550, and 600 min are displayed in Figure 6. In addition to the chromatograms (LS, RI, and DP

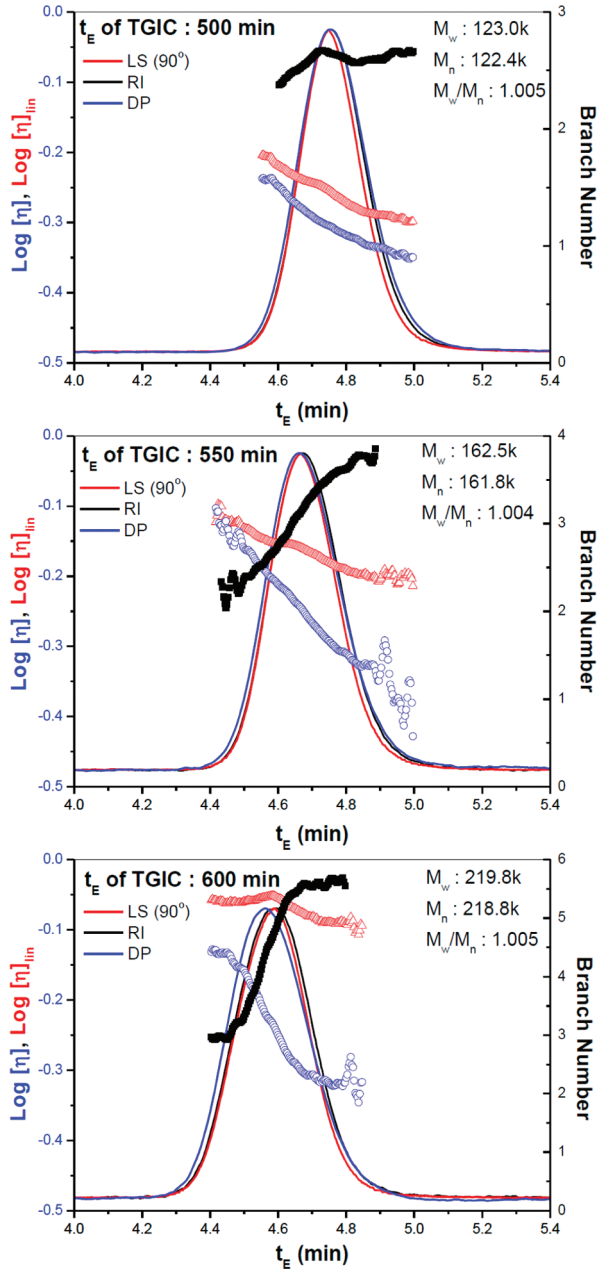


Figure 6. Second-D SEC chromatograms of the first-D TGIC fractions eluting at t_E = 500, 550, and 600 min. Normalized signal intensity from light scattering (red), refractive index (black), and viscosity (blue) detectors are plotted together. Log intrinsic viscosity of the sample (blue circle), log intrinsic viscosity of linear polymer of the same molecular weight as the sample (red triangle), and calculated branch number (black square) are also shown. M_w, M_n, and M_w/M_n are obtained by light scattering detection.

detection), intrinsic viscosity of the sample ($[\eta]$), MW (plotted as the equivalent intrinsic viscosity of linear PS of the same MW, $[\eta]_{lin}$, to compare with $[\eta]$ in the same scale), and branch

dx.doi.org/10.1021/ma2021985 | *Macromolecules* 2012, 45, 3550–3556

number calculated by eq 3 are also plotted. The deviation of $[\eta]$ from $[\eta]_{lin}$ reflects the extent of branching of the eluting polymer species. First of all, the M_w/M_n values measured by LS detection are very close to 1 (1.004 or 1.005) for all cases, indicating that the first-D TGIC separation successfully separated the mixture sample according to MW as expected.

At t_E = 500 min, polymer species of MW ~ 120 000 is eluted which contains 4-arm star-shaped PS. But they were not well separated from the linear PS because of the low resolution of SEC. As a result, the branch number of the whole polymer was obtained as ~2.5. As the number of branches increases, the SEC separation of the star-shaped PS from the linear PS of the same MW is getting better since the size difference increases as the number of branches increases. At t_E = 550 (MW ~ 160 000) and 600 min (MW ~ 220 000), the SEC chromatograms showed a clear drop of $[\eta]$ as the elution time increases, indicating that the branched polymers (~5-arm and ~7-arm star-shaped polymers, respectively) elutes at the late part of the peak while linear polymers of the same MW elutes at the early part. Nonetheless, the calculated branch number is still lower than the true value.

The same type of SEC/TD analysis based on chain contraction factor can be done for every set of the second-D SEC/TD chromatograms, and the result is displayed in Figure 7.

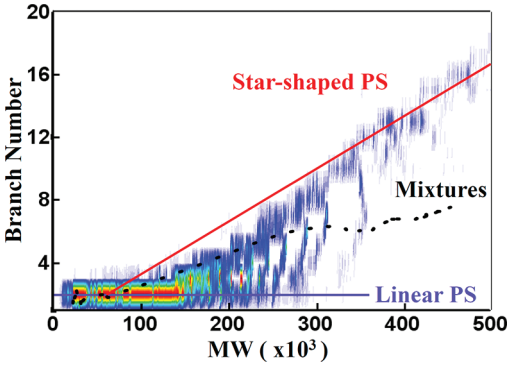


Figure 7. Plot of branch number vs MW for PS mixture. Solid lines are for star-shaped PS (red line) and linear PS (blue line). Black dotted line is the 1D-SEC analysis result (Figure 3b).

If everything was done perfectly, only two lines corresponding to linear and star-shaped polymers should be seen. However, the limited resolution in the fast second-D SEC separation leaves artifacts between the two lines. In addition, branch numbers of star-shaped PS were somewhat underestimated at low branch number region where SEC cannot resolve the star-shaped PS from the linear PS with the same MW very well. Nonetheless, by virtue of the first-D TGIC separation according to MW and the subsequent SEC/TD measurements, the distributions of both linear and star-shaped PS are clearly visible. As the number of branches increases, the branch analysis becomes more precise in contrast to the 1D-SEC/TD analysis shown in Figure 3b.

In summary, we investigated a problem in branching analysis by the SEC/TD method associated with "local polydispersity", coelution of polymer species of the same size but polydisperse in both chain architecture and MW. We demonstrated the problem by using a model system: a mixture of linear and star-shaped PS. To apply the chain contraction factor concept for the branching analysis, it is necessary to compare the chain size of polymers at the same MW. Therefore, the simple-minded SEC/TD analysis assuming homogeneous SEC fraction yields an incorrect picture in both MW and branch number. To improve the accuracy in the SEC/TD branching analysis, we propose 2D-LC, RP-TGIC × SEC separation as a potential solution in which branched polymers are first separated into homogeneous MW fractions by RP-TGIC and then the homogeneous MW fractions are subjected to SEC/TD analysis. We demonstrated that such a 2D-LC/TD method combined with Zimm–Stockmayer contraction factor concept could yield a far more accurate picture of the chain branching in complex polymer systems.

AUTHOR INFORMATION

Corresponding Author

*Tel: +82-54-279-2109; Fax: +82-54-279-3399; e-mail tc@postech.ac.kr.

Author Contributions

†Equal contributions.

Notes

The authors declare no competing financial interest.

ACKNOWLEDGMENTS

We acknowledge the support from NRF via NRL (R0A-2007-000-20125-0), SRC (R11-2008-052-03002), and WCU (R31-2008-000-10059-0) programs and from LGchem.

REFERENCES

(1) McLeish, T. C. B. *Adv. Phys.* **2002**, *51*, 1379–1527.
(2) Graessley, W. W. *Polymeric Liquids and Networks: Dynamics and Rheology*; Taylor & Francis Group: New York, 2008; p 550.
(3) Snijkers, F.; van Ruymbeke, E.; Kim, P.; Lee, H.; Nikopoulou, A.; Chang, T.; Hadjichristidis, N.; Pathak, J.; Vlassopoulos, D. *Macromolecules* **2011**, *44*, 8631–8643.
(4) Chen, X.; Rahman, M. S.; Lee, H.; Mays, J.; Chang, T.; Larson, R. *Macromolecules* **2011**, *44*, 7799–7809.
(5) Mori, S.; Barth, H. G. *Size Exclusion Chromatography*; Springer-Verlag: New York, 1999; p 208.
(6) Striegel, A. M. *Anal. Chem.* **2005**, *77*, 104A–113A.
(7) Striegel, A. M. *Encycl. Chromatogr., 3rd ed.* **2010**, *2*, 1417–1420.
(8) Zimm, B. H.; Stockmayer, W. H. *J. Chem. Phys.* **1949**, *17*, 1301–1314.
(9) Zimm, B. H.; Kilb, R. W. *J. Polym. Sci.* **1959**, *37*, 19–42.
(10) Casassa, E. F.; Berry, G. C. *J. Polym. Sci., Polym. Phys. Ed.* **1966**, *4*, 881–897.
(11) Burchard, W. *Adv. Polym. Sci.* **1999**, *143*, 113–194.
(12) Farmer, B. S.; Terao, K.; Mays, J. W. *Int. J. Polym. Anal. Charact.* **2006**, *11*, 3–19.
(13) Radke, W.; Müller, A. H. E. *Macromolecules* **2005**, *38*, 3949–3960.
(14) Roovers, J. *Polymer* **1979**, *20*, 843–849.
(15) Gaborieau, M.; Gilbert, R. G.; Gray-Weale, A.; Hernandez, J. M.; Castignolles, P. *Macromol. Theory Simul.* **2007**, *16*, 13–28.
(16) Castignolles, P.; Graf, R.; Parkinson, M.; Wilhelm, M.; Gaborieau, M. *Polymer* **2009**, *50*, 2373–2383.
(17) Gaborieau, M.; Castignolles, P. *Anal. Bioanal. Chem.* **2011**, *399*, 1413–1423.
(18) Berek, D. *Anal. Bioanal. Chem.* **2010**, *396*, 421–441.
(19) Im, K.; Park, H.-W.; Kim, Y.; Chung, B.; Ree, M.; Chang, T. *Anal. Chem.* **2007**, *79*, 1067–1072.
(20) Im, K.; Park, H.-W.; Lee, S.; Chang, T. *J. Chromatogr., A* **2009**, *1216*, 4606–4610.
(21) Pasch, H.; Adler, M.; Rittig, F.; Becker, S. *Macromol. Rapid Commun.* **2005**, *26*, 438–444.
(22) van der Horst, A.; Schoenmakers, P. J. *J. Chromatogr., A* **2003**, *1000*, 693–709.

(23) Edam, R.; Meunier, D. M.; Mes, E. P. C; Van Damme, F. A.; Schoenmakers, P. J. *J. Chromatogr., A* **2008**, *1201*, 208−214.
(24) Jiang, X.; Van der Horst, A.; Lima, V.; Schoenmakers, P. J. *J. Chromatogr., A* **2005**, *1076*, 51−61.
(25) Raust, J. A.; Brull, A.; Moire, C.; Farcet, C.; Pasch, H. *J. Chromatogr., A* **2008**, *1203*, 207−216.
(26) Ginzburg, A.; Macko, T.; Dolle, V.; Bruell, R. *J. Chromatogr., A* **2010**, *1217*, 6867−6874.
(27) Roy, A.; Miller, M. D.; Meunier, D. M.; de Groot, A. W.; Winniford, W. L.; Van Damme, F. A.; Pell, R. J.; Lyons, J. W. *Macromolecules* **2010**, *43*, 3710−3720.
(28) Lee, W.; Lee, H.; Cha, J.; Chang, T.; Hanley, K. J.; Lodge, T. P. *Macromolecules* **2000**, *33*, 5111−5115.
(29) Al Samman, M.; Radke, W.; Khalyavina, A.; Lederer, A. *Macromolecules* **2010**, *43*, 3215−3220.
(30) Lee, H.; Chang, T.; Harville, S.; Mays, J. W. *Macromolecules* **1998**, *31*, 690−694.
(31) Perny, S.; Allgaier, J.; Cho, D.; Lee, W.; Chang, T. *Macromolecules* **2001**, *34*, 5408−5415.
(32) Gerber, J.; Radke, W. *Polymer* **2005**, *46*, 9224−9229.
(33) Im, K.; Kim, Y.; Chang, T.; Lee, K.; Choi, N. *J. Chromatogr., A* **2006**, *1103*, 235−242.
(34) Ahn, S.; Im, K.; Chang, T.; Chambon, P.; Fernyhough, C. M. *Anal. Chem.* **2011**, *83*, 4237−4242.
(35) Chambon, P.; Fernyhough, C. M.; Im, K.; Chang, T.; Das, C.; Embery, J.; McLeish, T. C. B.; Read, D. J. *Macromolecules* **2008**, *41*, 5869−5875.
(36) Li, S. W.; Park, H. E.; Dealy, J. M.; Maric, M.; Lee, H.; Im, K.; Choi, H.; Chang, T.; Rahman, M. S.; Mays, J. *Macromolecules* **2011**, *44*, 208−214.
(37) Gerber, J.; Radke, W. *e-Polym.* **2005**, 45.
(38) Gorbunov, A. A.; Vakhrushev, A. V. *Polymer* **2009**, *50*, 2727−2735.
(39) Lee, H.-J.; Lee, K.; Choi, N. *J. Polym. Sci., Part A: Polym. Chem.* **2005**, *43*, 870−878.
(40) Tobita, H.; Saito, S. *Macromol. Theory Simul.* **1999**, *8*, 513−519.
(41) Brandrup, J., Immergut, E. H., Eds.; *Polymer Handbook*, 4th ed.; Wiley-Interscience: New York, 1998; p 1920.
(42) Chang, T. *Adv. Polym. Sci.* **2003**, *163*, 1−60.
(43) Chang, T. *J. Polym. Sci., Polym. Phys.* **2005**, *43*, 1591−1607.
(44) Ryu, J.; Im, K.; Yu, W.; Park, J.; Chang, T.; Lee, K.; Choi, N. *Macromolecules* **2004**, *37*, 8805−8807.

Macromolecules

Article

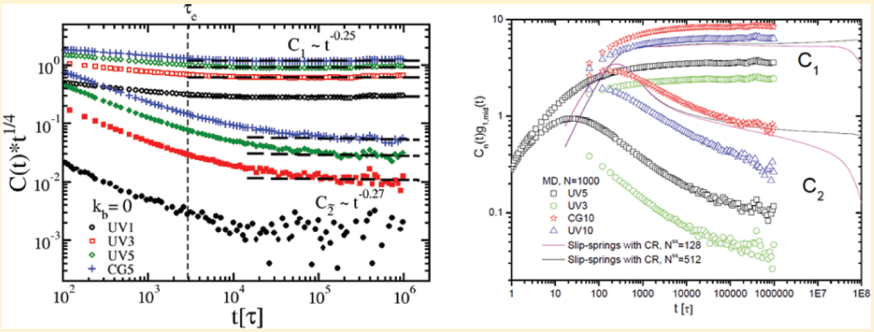
pubs.acs.org/Macromolecules

Segmental Dynamics in Entangled Linear Polymer Melts

Zuowei Wang,*[,†] Alexei E. Likhtman,[†] and Ronald G. Larson[‡]

[†]School of Mathematical and Physical Sciences, University of Reading, Whiteknights, Reading RG6 6AX, United Kingdom

[‡]Department of Chemical Engineering, University of Michigan, Ann Arbor, Michigan 48109-2136, United States



ABSTRACT: We present molecular dynamics (MD) and slip-springs model simulations of the chain segmental dynamics in entangled linear polymer melts. The time-dependent behavior of the segmental orientation autocorrelation functions and mean-square segmental displacements are analyzed for both flexible and semiflexible chains, with particular attention paid to the scaling relations among these dynamic quantities. Effective combination of the two simulation methods at different coarse-graining levels allows us to explore the chain dynamics for chain lengths ranging from $Z \approx 2$ to 90 entanglements. For a given chain length of $Z \approx 15$, the time scales accessed span for more than 10 decades, covering all of the interesting relaxation regimes. The obtained time dependence of the monomer mean square displacements, $g_1(t)$, is in good agreement with the tube theory predictions. Results on the first- and second-order segmental orientation autocorrelation functions, $C_1(t)$ and $C_2(t)$, demonstrate a clear power law relationship of $C_2(t) \sim C_1(t)^m$ with m = 3, 2, and 1 in the initial, free Rouse, and entangled (constrained Rouse) regimes, respectively. The return-to-origin hypothesis, which leads to inverse proportionality between the segmental orientation autocorrelation functions and $g_1(t)$ in the entangled regime, is convincingly verified by the simulation result of $C_1(t) \propto g_1(t)^{-1} \propto t^{-1/4}$ in the constrained Rouse regime, where for well-entangled chains both $C_1(t)$ and $g_1(t)$ are rather insensitive to the constraint release effects. However, the second-order correlation function, $C_2(t)$, shows much stronger sensitivity to the constraint release effects and experiences a protracted crossover from the free Rouse to entangled regime. This crossover region extends for at least one decade in time longer than that of $C_1(t)$. The predicted time scaling behavior of $C_2(t) \propto t^{-1/4}$ is observed in slip-springs simulations only at chain length of 90 entanglements, whereas shorter chains show higher scaling exponents. The reported simulation work can be applied to understand the observations of the NMR experiments.

1. INTRODUCTION

Dynamics in entangled polymer melts and concentrated solutions is prominently described by the tube theories.[1−5] The original tube theory predicts a number of scaling power laws for the time and molecular weight dependence of the rheological and dynamic behavior that are subject to continuous investigations.[1,2] Among them are the famous molecular weight dependence of the zero-shear viscosity, $\eta_0 \sim M^3$, and the chain self-diffusion coefficient, $D_{self} \sim M^{-2}$, predicted by the pure reptation model. Deviations from these integer powers, as observed in experiments with polymers of finite lengths, are attributed to additional relaxation mechanisms, such as the contour length fluctuations (CLFs) and constraint release (CR).[2,5−7] Development of quantitative theories for entangled polymers demands a clear understanding of these relaxation mechanisms, which can only be achieved from experiments[4,5,8−10] and computer simulations[11−15] on the microscopic scale. In such microscopic works the most widely studied observables are probably the segmental mean square displacement (MSD), $g_1(t)$, and the segmental orientation correlation functions, $C_n(t)$, because for them the tube model predictions are readily available to compare with.

The mean square segment displacement is experimentally accessible via neutron spin echo (NSE) spectroscopy[9,16] and NMR diffusometer.[17,18] For a highly entangled polymer chain, this quantity is predicted to undergo a series of time-dependent power law changes from $g_1(t) \sim t^{1/2}$ in the free Rouse regime, to $\sim t^{1/4}$ in the constrained Rouse regime, $\sim t^{1/2}$ in the reptation regime, and finally $\sim t^1$ in terminal diffusion regime.[2] The transition from the $t^{1/2}$ to $t^{1/4}$ power, marking the entry to the well-entangled regime, was evidenced by NSE experiments[9] and

Received: December 21, 2011
Revised: March 14, 2012
Published: April 9, 2012

 © 2012 American Chemical Society

molecular dynamics (MD) simulations of monodisperse linear polymer melts.[11,19]

Many NMR experiments measure the polymer segmental dynamics in terms of an orientation autocorrelation function of the second Legendre polynomial

$$C_{\tilde{2}}(t) \propto \langle P_2(\cos\tilde{\theta}(t))P_2(\cos\tilde{\theta}(0))\rangle \quad (1)$$

where $\tilde{\theta}(t)$ is the angle between the segmental orientation vector and a reference direction typically of the external magnetic field.[10,20−22] Using the return-to-origin (RTO) argument, Ball et al. proposed an inverse proportionality between this correlation function and the mean square segment displacement, $C_{\tilde{2}}(t) \propto g_1(t)^{-1}$ for time scales larger than the entanglement time τ_e, with an additional exponential correction close and beyond the Rouse time τ_R.[20] It follows that a power law decay of $C_{\tilde{2}}(t) \sim t^{-\alpha}$ with $\alpha = 1/4$ would be expected in the constrained Rouse regime ($\tau_e < t < \tau_R$), where $g_1(t) \sim t^{1/4}$. This $\sim t^{-1/4}$ scaling, however, has not been convincingly observed in NMR experiments. Measurements of Herrmann et al. on linear polybutadiene (PB) melts with chain length up to $Z \approx 9$ entanglements only rendered $\alpha \approx 0.5$ in this regime.[23] Graf et al. presented a $t^{-1/4}$ power law fitting to the data points obtained from PB melts with much longer chains ($Z \approx 76$),[21] but the applied NMR method itself may be subject to systematic errors.[10] The most recent NMR measurements on $C_{\tilde{2}}(t)$ were reported by Chávez and Saalwächter using linear PB melts with chain length ranging in $12 \leq Z \leq 1100$.[10,22] Interestingly, their results demonstrated a strong molecular weight dependence of α in the constrained Rouse regime. Even for the longest chain with $Z > 1000$, the asymptotic value of $\alpha \approx 0.29$ is still larger than the expected 1/4 power. The reason was considered to lie in the CR effects, which cause local chain motions less restricted than that predicted by the tube model.[10,22] This observation seems to be inconsistent with the chain diffusion coefficient data, where the CR effects were shown to diminish as Z increases beyond ~20[6,7] and also the NSE result of $g_1(t) \sim t^{1/4}$ for linear polyethylenes of molecular weight around 100 entanglements.[9] (Note, however, that the error bars in ref 9 are quite large compared with the NMR experiments.) One of the motivations for the current work is to address the time scaling behavior of $C_{\tilde{2}}(t)$ as well as its dependence on the CR effects and its correlation with other dynamical observables.

In computer simulations, the chain segmental orientation autocorrelation functions are generally calculated as

$$C_n(t) = \langle P_n(\mathbf{u}(t)\cdot\mathbf{u}(0))\rangle \quad (2)$$

where $P_n(x)$ is the Legendre polynomial of order n and $\boldsymbol{u}(t) = \boldsymbol{l}(t)/|\boldsymbol{l}(t)|$ is the unit segmental vector with $|\boldsymbol{l}(t)|$ being the segment length at time t. The triangular brackets here mean time and ensemble average and can also include averaging over different chain segments. For unentangled polymer chains, the Rouse model predicted a power law of $C_1(t) \sim t^{-1/2}$ and a scaling relation of $C_2(t) \propto C_1(t)^2$.[2,24] The applicability of the Rouse model has been discussed over a wide range of monomer concentration, temperature, and excluded volume interactions.[25−28] Simulation studies of $C_n(t)$ in the entanglement regime are much less frequent and are mostly on mildly entangled polymer melts.[12,13,29] Kreer et al. reported Monte Carlo simulation results on $C_1(t)$ and $g_1(t)$ for monodisperse linear polymer melts with various chain lengths.[12] The 1/4 power law expected in the constrained Rouse regime was not reached in both quantities for the longest chain of ~14 entanglements. The situation is similar in MD simulations using more realistic polymer chain models.[13,29] Accordingly, there is also a lack of numerical examination of the scaling relationship between the segmental orientation correlation functions of different orders, namely $C_2(t) \sim C_1(t)^m$ with m a certain constant, of well-entangled polymer systems. The $C_{\tilde{2}}(t) \propto C_1(t)^2$ relation, which only holds for the free Rouse regime, has been in some cases improperly applied to correlate experimental and simulation data in the entanglement regime.[23]

In the current work, we present the fine-grained MD[11] and coarse-grained slip-springs (SS)[30] simulations of the segmental dynamics of monodisperse entangled linear polymer melts. Particular attention is paid to the time scaling behavior of the segmental diffusion and orientation autocorrelation functions as well as the scaling relationship between them. Both flexible and semiflexible chains are studied in our MD simulations, with the longest chain length in each case above 15 entanglements.[15,19] The slip-springs model allows us to simulate melt systems with much longer chains up to time scales that are inaccessible to MD simulations.[30] The SS data presented here are for chain length up to $Z \approx 90$ and time scale reaching the terminal relaxation regime. By effectively mapping the slip-springs simulation results to the MD data, we are able to explore the dynamics of polymer chains with ~15 entanglements for a total timespan over 10 decades. More importantly, the slip-springs model has the unique advantage of being able to separate out the CR effects by switching such relaxations on and off in simulations,[31] which is essential for understanding the experimental observations.

This Article is organized as follows: Section 2 gives a brief overview of the theoretical descriptions of the segmental dynamics in entangled polymer melts. We describe the details of the MD and slip-springs simulation methods and the related system parameters in Section 3. The simulation results are presented and discussed in Section 4, and conclusions are summarized in Section 5.

2. THEORETICAL BACKGROUND

2.1. Segment Mean Square Displacement. The translational dynamics of a polymer segment is measured by its mean square displacement, $g_1(t) = \langle(\boldsymbol{r}(t) - \boldsymbol{r}(0))^2\rangle$, where $\boldsymbol{r}(t)$ is the coordinate of the segmental center of mass. On very short time scales, the segment motion is ballistic

$$g_1(t) = 3k_BTt^2/(N_sm),\ t \ll \tau_0 \quad (3)$$

where N_s is the number of monomers in the segment, k_B is the Boltzmann constant, T is the absolute temperature, and m is the mass of a monomer, respectively.

On larger time scales, the chain connectivity and uncrossability dominate the segmental diffusion behavior of entangled polymers. When neglecting the CR effects, the tube model predicts the following time scaling behavior of the mean

dx.doi.org/10.1021/ma202759v | Macromolecules 2012, 45, 3557−3570

square displacement of the central monomers of a well-entangled polymer chain[2,19,32]

$$g_1(t) \approx \begin{cases} b^2(t/\tau_0)^{1/2}, & \tau_0 < t < \tau_e \\ ab(t/\tau_0)^{1/4}, & \tau_e < t < \tau_R \\ \frac{ab}{N^{1/2}}(t/\tau_0)^{1/2}, & \tau_R < t < \tau_d \\ \frac{a^2}{N^2}(t/\tau_0), & \tau_d < t \end{cases} \quad (4)$$

where a is the tube Kuhn step defined from the tube length L via $La = Nb^2$, b is the statistical segment length, and we omit all numerical coefficients. The characteristic time scales are defined by $\tau_0 = \zeta b^2/(3\pi^2 k_B T)$, where ζ is the monomeric frictional coefficient, the entanglement time $\tau_e = N_e^2\tau_0$, Rouse time $\tau_R = Z^2\tau_e$ and terminal (disengagement) time $\tau_d = 3Z\tau_R$, respectively. $Z = N/N_e$ is the number of entanglements per chain and $N_e = a^2/b^2$ is the number of monomers in each entanglement strand.

2.2. Segmental Orientation Autocorrelation Functions. Following eq 2, the segmental orientation autocorrelation functions of orders 1 and 2 can be written explicitly as

$$C_1(t) = \langle \boldsymbol{u}(t)\cdot\boldsymbol{u}(0)\rangle \quad (5)$$

$$C_2(t) = \frac{1}{2}\langle 3[\mathbf{u}(t)\cdot\mathbf{u}(0)]^2 - 1\rangle \quad (6)$$

$C_1(t)$ is an analogue of chain end-to-end relaxation measured by dielectric spectroscopy,[4] and $C_2(t)$ is related to the orientation tensor (measured by optical methods) and to the stress modulus via the stress-optical law.[2,33] The second-order orientation correlation function is directly accessible by NMR experiments, as mentioned in the Introduction. Here we rewrite eq 1 as

$$C_{\tilde{2}}(t) = 5\langle P_2(\cos\tilde{\theta}(t))P_2(\cos\tilde{\theta}(0))\rangle \quad (7)$$

where $\tilde{\theta}$ is the angle between the unit segmental vector $\boldsymbol{u}$ and one of the Cartesian axes, giving $\cos\tilde{\theta}(t) = u_\alpha(t)$ with $\alpha = x$, y, or z. The normalization factor 5 in eq 7 results from $<\cos^4\tilde{\theta}(0)> = 1/5$. In practice, the statistics of the $C_{\tilde{2}}(t)$ results can be improved by averaging over all three Cartesian components u_α owing to the isotropic character of the melt system. In Appendix I, we demonstrate that when defined using the unit segmental orientation vector, the two second-order segmental orientation autocorrelation functions, $C_2(t)$ and $C_{\tilde{2}}(t)$, are equivalent to each other in equilibrium isotropic systems. Therefore, our following discussions on the second-order orientation correlation functions apply equally to both functions.

Initial Stage. On very short time scales, there is a universal relationship between $C_1(t)$ and $C_2(t)$. To illustrate this, we note that the angle $\theta(t)$ spanned by a rotating bond vector, defined by $\cos\theta(t) = \boldsymbol{u}(t)\cdot\boldsymbol{u}(0)$, is small over a small time interval t; therefore, we can use Taylor expansion

$$C_1(t) = \langle\cos\theta(t)\rangle \approx 1 - \langle\theta(t)^2\rangle/2 \quad (8)$$

$$C_2(t) = \frac{1}{2}\langle 3\cos^2\theta(t) - 1\rangle \approx 1 - 3\langle\theta(t)^2\rangle/2 \quad (9)$$

which can be more generally written as

$$C_n(t) \approx \exp\left(-\frac{n(n+1)}{4}\langle\theta(t)^2\rangle\right), \theta \ll 1 \quad (10)$$

This means that for small times these correlation functions must be related by a simple formula

$$C_{2(\tilde{2})}(t) \approx C_1(t)^3 \quad (11)$$

independent of the dynamics details. For example, it does not matter whether the rotational dynamics is ballistic or diffusive. This argument is more general than the one provided in ref 25.

Rouse Regime. On time scales $\tau_0 < t < \tau_e$, the chain connectivity dominates the rotational dynamics of the segments. The Rouse model predicts (see details in Appendix II)

$$C_1(t) \approx \frac{\sqrt{\pi}}{2}(t/\tau_0)^{-1/2}, \tau_0 < t < \tau_e \quad (12)$$

$$C_{2(\tilde{2})}(t) \approx C_1(t)^2 \approx \frac{\pi}{4}(t/\tau_0)^{-1} \quad (13)$$

In Appendix II, it should be noted that the normalization factor in $C_2(t)$, as defined in eq 6 for unit segmental orientation vectors, differs from that of the Rouse segment orientation vectors, $C_2^R(t)$ (eq A2-2), by a factor of 2 owing to the Gaussian-type fluctuations of the Rouse segment length.

Entangled Regime. When $t > \tau_e$, the topological constraints restrict the motion of the polymer chain to a tube-like region. The segmental displacement along the primitive path of the tube follows the subdiffusive motion of the Rouse model. Because the primitive path itself is a 3D random walk with a Kuhn step size a, the 3D MSD of the chain segment is related to its mean square curvilinear displacement along the tube, $\langle\Delta s(t)^2\rangle$, by $g_1(t) \approx a\langle\Delta s(t)^2\rangle^{1/2}$.[2,34]

Doi and Edwards indicated that the time correlation function of the segmental orientation vector, essentially defined as $C_1(t)$ in their book, represents the probability that at time t the chain segment remains in the original tube segment it occupied at time zero.[2] The same idea was later applied by Ball, Callaghan, and Samulski to describe the correlation function $C_{\tilde{2}}(t)$ measured in NMR experiments, where $C_{\tilde{2}}(t)$ is proposed to be the probability that $\langle\Delta s(t)^2\rangle \le a^2$.[20] It thus follows that all first- and second-order segmental orientation autocorrelation functions are proportional to the coarse-grained RTO probability[20]

$$P_{RTO}(t) \sim \frac{1}{\sqrt{2\pi\langle\Delta s(t)^2\rangle}}\exp(0) \sim g_1(t)^{-1} \quad (14)$$

and subsequently

$$C_1(t) \sim C_{\tilde{2}(2)}(t) \sim g_1(t)^{-1}, \tau_e < t \quad (15)$$

which is qualitatively different from eq 13. The time scaling behavior of these correlation functions in the entangled regime can then be conveniently estimated using the tube model predictions on $g_1(t)$, as given in eq 4. It is of particular interest in recent NMR experiments and computer simulations to examine the power law scaling in the constrained Rouse regime[10,12,22,23]

$$C_{1,\tilde{2}(2)}(t) \sim (t/\tau_e)^{-1/4}, \tau_e < t < \tau_R \quad (16)$$

dx.doi.org/10.1021/ma202759v | Macromolecules 2012, 45, 3557−3570

3. SIMULATION DETAILS

3.1. Molecular Dynamics. The linear polymers are represented by the standard Kremer−Grest bead−spring model.[11,35,36] All monomers interact via the purely repulsive Lennard-Jones (LJ) potential with the LJ parameter $\epsilon = 1.0k_BT$ and a cutoff radius of $r_c = 2^{1/6}\sigma$, where σ is the bead diameter. The monomers of the same chain are connected to their sequential neighbors by the finite extensible nonlinear elastic (FENE) potential with the spring constant $k = 30\epsilon/\sigma^2$ and the maximum bond length $R_0 = 1.5\sigma$. The combination of the LJ and FENE potentials leads to an average bond length $<l^2>^{1/2} = 0.97\sigma$. In addition, the chain stiffness is introduced by using a three-bead bending potential

$$U_{\text{bend}}(\vartheta) = k_b(1 - \cos\vartheta) \tag{17}$$

where ϑ is the angle in between two adjacent unit bond vectors. The strength of the bending potential is chosen to be $k_b = 0$ and 2ϵ for representing the flexible and semiflexible chains, respectively. The corresponding characteristic ratio and statistical segment length are $C_\infty = 1.82$ and $b = 1.31\sigma$ for the flexible chains, and $C_\infty = 3.40$ and $b = 1.79\sigma$ for the semiflexible ones, respectively. The primitive path analysis of Everaers et al. yielded the number of monomers per entanglement strand as $N_e^p = 65$ and 23 for these two types of chains.[37] When discussing the ratio between the mean square displacements of the end and middle monomers in Section 4.1.1, some extra data points, taken from our previous MD simulations using chain stiffness $k_b = 3\epsilon$, are also included.[30,33]

Trajectories of the monomers are obtained by integrating the following equation of motion using the velocity Verlet algorithm

$$m\ddot{\mathbf{r}}_i = -\nabla U(\mathbf{r}_i) - \Gamma\dot{\mathbf{r}}_i + \mathbf{W}_i(t) \tag{18}$$

where $\mathbf{r}_i$ is the coordinate of the ith monomer, m is the monomer mass, and Γ is the friction coefficient set to be $\Gamma = 0.5(mk_BT)^{1/2}/\sigma$. The system is coupled to a Langevin heat bath, and the stochastic force $\mathbf{W}_i$ is a Gaussian white noise related to the friction coefficient Γ by $<\mathbf{W}_i(t)\cdot\mathbf{W}_j(t')> = \delta_{ij}\delta(t-t')6k_BT\Gamma$. The simulations are performed in the NVT ensemble with periodic boundary conditions applied in all three dimensions of the cubic simulation box. The time step $\Delta t = 0.012\tau$ is used in all simulation runs, where $\tau = (m\sigma^2/k_BT)^{1/2}$ is the LJ time unit. The length and time scales in the systems are set by σ and τ, respectively. The global number density of the bonds is set to a fixed value of $\rho = 0.85\sigma^{-3}$ for all simulated systems.[35,36] The initial configurations of the monodisperse polymer melts are prepared using the equilibration method developed by Auhl et al. so as to start the simulations in close proximity to the equilibrium states.[36,38] Unless specified, simulation results will be presented in the reduced units of $m = \sigma = \epsilon = 1$.

3.2. Slip-Springs Model. The slip-springs model is a recently developed single-chain model for describing the dynamics of entangled polymers.[14] The basic building block of this model is a Rouse chain of N^{ss} beads. The confinement due to entanglements is introduced in a discrete manner using a set of virtual springs of N_s^{ss} monomers each. One end of each of these springs is fixed in space, and the other end is connected to the Rouse chain by a slip-link. On average, there is a slip-link every N_e^{ss} monomers. The chain can only slide through these slip-links, and this ensures that the long time dynamics is dominated by reptation. This model contains all mechanisms included in the tube model. Apart from the usual parameters of the Rouse model, there are three adjustable parameters related to entanglements: N_e^{ss}, N_s^{ss}, and ξ_s^{ss}, which is the friction of the slip-links when sliding along the chain contour. The values of N_s^{ss} and N_e^{ss} can be adjusted to fit the slip-springs model to MD data.[14,31] For reasons mentioned in ref 14, the ξ_s^{ss} value is fixed at $0.1\xi_0$, where ξ_0 is the bead friction of the Rouse chain.

The stochastic equations of motion for both the beads and the slip-links can be derived from the Hamiltonian of the system. Disentanglement of the chain from a slip-link and re-entanglement with a slip-link are accomplished by the destruction and the creation of slip-links at the chain ends. Constraint release is included by approximating the entanglements as binary events. The total number of entanglements is held constant during the simulations. This is reasonable for a large number of chains at equilibrium; in practice, the large number translates to running the simulations with at least 10 chains that affect each other's dynamics only through CR. Some of the mechanisms, like reptation, CR, and the sliding movement of the slip-links, can be individually deactivated to isolate their contribution to the relaxation of the chains. This is essential in the current work for separating out the CR effects on the segmental dynamics. The slip-springs equations of motion are solved numerically to the desired accuracy and with no uncontrolled approximations by means of Brownian dynamics simulations. Further details of the model can be found in previous publications.[14,39]

By construction, the polymer chain in the slip-springs model is Gaussian on all length scales. This avoids the problem of incorrect chain statistics around the scale of the tube step length in the tube model. The polymer chains in the MD simulations are not Gaussian on short length scales. Therefore, to map the slip-springs results onto MD data over all length scales will require the inclusion of repulsive potential between the monomers in the chain.[31] Because we are mainly interested in the slip-springs data on the time and length scales in the entanglement regime, the standard version of this model without repulsive potentials is used in the current work.[14] The system parameters are set to be $N_e^{ss} = 4$ and $N_s^{ss} = 0.5$, respectively. It has been shown that to map the slip-springs simulation data obtained with these standard parameters to the tube model requires the usage of $N_e \approx 5.7$ beads per entanglement length.[40] This means that our longest chains with $N^{ss} = 512$ have ~90 entanglements.

4. RESULTS AND DISCUSSION

4.1. Molecular Dynamics. The monodisperse linear polymer melts studied in our MD simulations are listed in Table 1. In each case, the side length of the cubic simulation box is significantly larger than the end-to-end distance of the polymer chains, so there is no self-entanglement involved. According to the N_e^p values estimated by primitive path analysis,[37] the chain lengths we simulated correspond to a range of the number of entanglements per chain $Z \approx 2-15$. It is noted that different analysis methods can lead to different estimations of the N_e and consequently Z values.[15,19,37,41] In the current work, these quantities are provided simply to give a guidance of the level of entanglements of the simulated chains. The uncertainties in their values have no qualitative effect on our discussions and conclusions. The MD simulation data are presented for a timespan of about eight decades, starting from one MD time step size $t = 0.012\tau$ to around $10^6\tau$ that is close to the Rouse time of the longest chains. Because the two second-order segmental orientation autocorrelation functions, $C_2(t)$

dx.doi.org/10.1021/ma202759v | Macromolecules 2012, 45, 3557−3570

Table 1. Systems Studied in Molecular Dynamics Simulations: Strength of Bending Potential k_b, Number of Monomers Per Chain N, Number of Chains Per Simulation Box M, and Total MD Simulation Time t_{tot}

$k_b(\epsilon)$	N	M	t_{tot} $(10^6\tau)$
0	100	500	1.0
	200	250	1.0
	350	200	2.3
	500	200	1.6
	1000	100	1.5
2	50	200	0.5
	80	400	1.0
	350	200	1.0

and $C_2(t)$, are equivalent, as demonstrated in Appendix II and verified in our MD simulations, we will only present the simulation results on $C_2(t)$.

4.1.1. Monomer Mean Square Displacement. The monomer MSD has been popularly measured in experiments and computer simulations of entangled polymers.[11,12,15,19,30,38] Analysis of this quantity was generally done by fitting the $g_1(t)$ curves to different power laws along the time axis and then comparing them with the Doi−Edwards predictions listed in eq 4. For melt systems composed of sufficiently long chains, one would expect that the $g_1(t > \tau_0)$ curves will display four distinctive relaxation regimes, each described by a well-defined scaling power. The characteristic times, that is, τ_e, τ_R, and τ_d, can then be determined from the intersections between the power law fittings of different regimes. However, the limited chain length and time scale accessible to current molecular simulations using atomistic or fine-grained chain models still make it formidable to achieve such a clear monomer MSD curve containing all four well-defined regimes, especially for the reptation regime of $\tau_R < t < \tau_d$.[30,42] In this work, we will extend our previous calculations of $g_1(t)$ to larger chain lengths in the flexible case and also to broader time spanning for all melt samples.[15,30] Within the time window we simulated, the simulation data show good agreement with the theoretical predictions discussed in Section 2.1, especially for the melts of largest chain lengths, which consequently allows us to estimate the entanglement time τ_e of the polymers with different stiffness. The obtained $g_1(t)$ results also serve as benchmarks for mapping the slip-springs simulation data to that of MD.

Figure 1 presents our MD data on $g_1(t)$ for the melt systems with various chain lengths and stiffness, which were obtained by taking an average of the g_1 curves of the middle 10 monomers of each chain. In addition, we have divided these data by $t^{1/4}$ to facilitate the comparison with the tube model prediction for the constrained Rouse regime $(\tau_e < t < \tau_R)$.[2] Figure 1 shows that in the unentangled regime the monomer MSDs of the chains with various lengths but same stiffness all follow a universal behavior. At very short time $t < 0.1\tau$, the monomer displacement is clearly ballistic, following the scaling of $g_1(t) = 3t^2$ in the dimensionless units of $k_BT = 1$ and $m = 1$. The MSD of the center of mass of the chain, $g_3(t) = \langle(r_{CM}(t) - r_{CM}(0))^2\rangle$, also obeys the power law of $g_3(t) = 3t^2/N$ (not shown). The chain connectivity takes effect on larger time scales, and the monomer displacement demonstrates a smooth crossover from ballistic motion to free Rouse diffusion behavior. No plateau-like feature is observed in this crossover region, indicating that there is no evident caging effect at the temperature and monomer volume fraction we studied.[28]

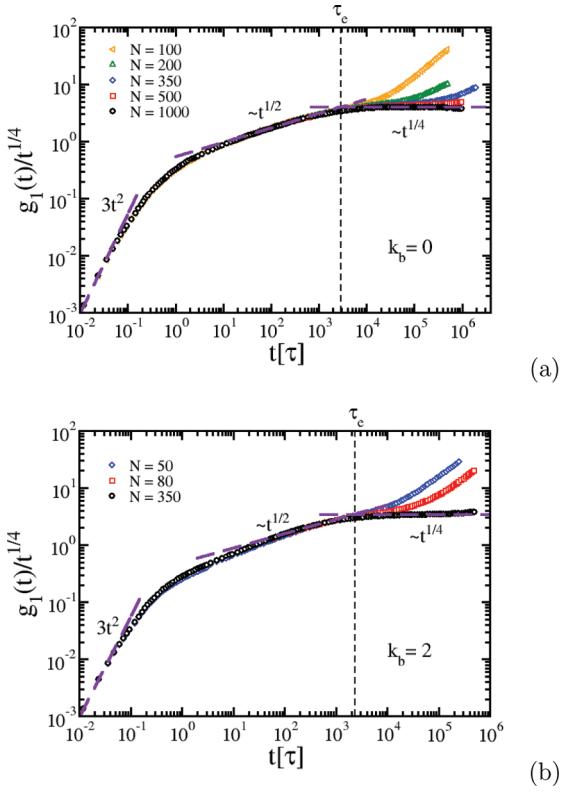


Figure 1. MD results of the mean square displacements of middle monomers of the flexible (a) and semiflexible (b) chains, normalized by the $t^{1/4}$ power law. The dashed lines show the power law fittings of $g_1(t)$ to the ballistic (t^2), free Rouse motion ($t^{1/2}$), and constrained Rouse ($t^{1/4}$) regimes.

The $g_1(t)$ curve of the longest chains in each case demonstrates a clear transition from the free Rouse to entanglement regime. The expected plateau-like region in $g_1(t)/t^{1/4}$ is approached at both chain stiffness. Power law fitting of $g_1(t) \propto t^{\alpha}$ to this entangled regime renders $\alpha = 0.25 \pm 0.02$ for the flexible chains and $\alpha = 0.28 \pm 0.02$ for the semiflexible ones. We can also fit these $g_1(t)$ data in different regimes directly to the scaling laws given in eq 4 and get rough estimates of the tube model parameters. As demonstrated in Figure 1, this gives $\tau_e \approx 2950$ and correspondingly $N_e \approx 50$ for the flexible chains, whereas $\tau_e \approx 2300$ with $N_e \approx 22$ for the semiflexible ones. We note, however, that these estimates are bound to be very approximate due to numerous assumptions of the tube model, and we list them just as a guidance and will not rely on them in the further discussion.

Another interesting, but less investigated, quantity for identifying entanglement effects is the ratio of the mean square displacements of the end and middle monomers of a chain, $g_{1,end}/g_{1,mid}$.[12,42] For a long ideal Rouse chain, this ratio is 2 on intermediate time scales $\tau_0 < t < \tau_R$ because the effective time-dependent friction on the middle monomer is twice that of the end one. In other words, this is because the chain end has to drag one piece of chain with it, whereas the chain middle has to drag two attached chains. For entangled polymers, the motion of the central chain segment is strongly confined by topological constraints, while the chain ends can still move freely to explore new tube segments. The end monomer diffusion is restricted only by the fact that they are attached to the inner segments, which are still entangled. As a result, the ratio between the MSDs of the two types of monomers increases with enhanced

dx.doi.org/10.1021/ma202759v | Macromolecules 2012, 45, 3557−3570

entanglement effects at intermediate times. The $g_{1,end}(t)/g_{1,mid}(t)$ curve is expected to reach a maximum around the Rouse time τ_R. After that, all monomers start to move coherently, and this ratio starts to decay back to 1. The asymptotic height of the maximum is theoretically predicted to be $4\sqrt{2}$ for the Evans–Edwards model, where a polymer chain diffuses through a lattice of impenetrable obstacles.[42,43] Our MD simulation data on $g_{1,end}(t)/g_{1,mid}(t)$ are presented in Figure 2. There the MSD data of the middle monomers,

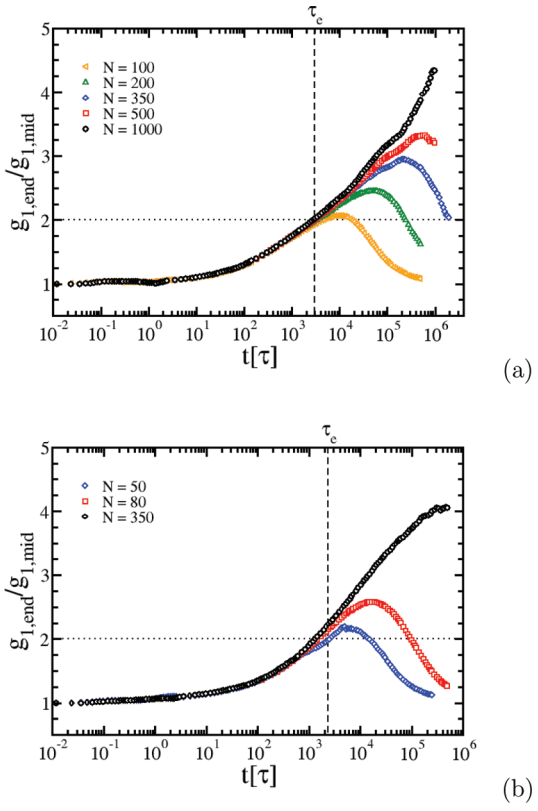


Figure 2. MD results on the ratio of the mean square displacements of the end and middle monomers, $g_{1,end}(t)/g_{1,mid}(t)$, of the flexible (a) and semiflexible (b) chains. The monomer MSD data in Figure 1 are used as $g_{1,mid}(t)$ of the middle monomers. The dotted horizontal line refers to the Rouse model prediction of $g_{1,end}/g_{1,mid}$ = 2 in the intermediate time regime.

$g_{1,mid}(t)$, are taken directly from Figure 1, whereas the $g_{1,end}(t)$ results are calculated by averaging over the 10 outermost monomers of each chain, that is, five end monomers on each side of the chain. Different from Monte Carlo simulations using lattice models where the initial value of $g_{1,end}/g_{1,mid}$ relies on the model details,[12,42] our MD result starts exactly from $g_{1,end}/g_{1,mid}$ = 1 in the ballistic regime. It then gradually increases to a maximum and starts to decay afterward. As expected, the height of the maximum is larger than two for all of the chain lengths we studied and increases with the chain length. This height value goes beyond four for the melts with the largest chain lengths. On very long time scales, typically several multiples of the terminal time of the entangled chains, the $g_{1,end}(t)/g_{1,mid}(t)$ ratio reduces to 1, as can be seen in Figure 2 from the results of the chains with few entanglements. The above observations are qualitatively consistent with the theoretical and related Monte Carlo simulation results obtained using the Evan–Edwards model.[42] The large difference between the diffusion mobilities of the end and middle monomers also elucidates the necessity of excluding the contributions from the fast moving chain ends for the sake of comparing the monomer MSD data with the tube model predictions.

In Figures 3 and 4, we analyze the maximum value of the ratio $g_{1,end}/g_{1,mid}$ and the time t_{max} at which it occurs. To

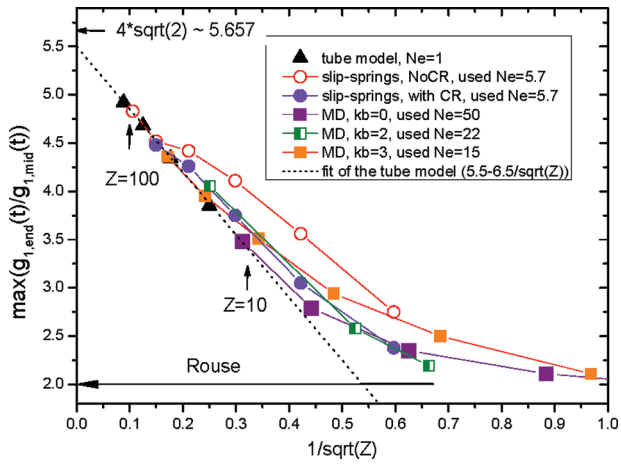


Figure 3. Maximum of the ratio $g_{1,end}/g_{1,mid}$ as a function of $Z^{-1/2}$ where Z is the approximate number of entanglements for the MD, slip-springs, and tube simulation models.

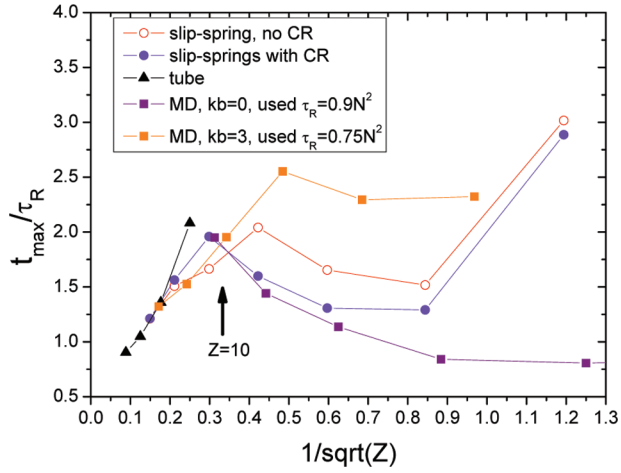


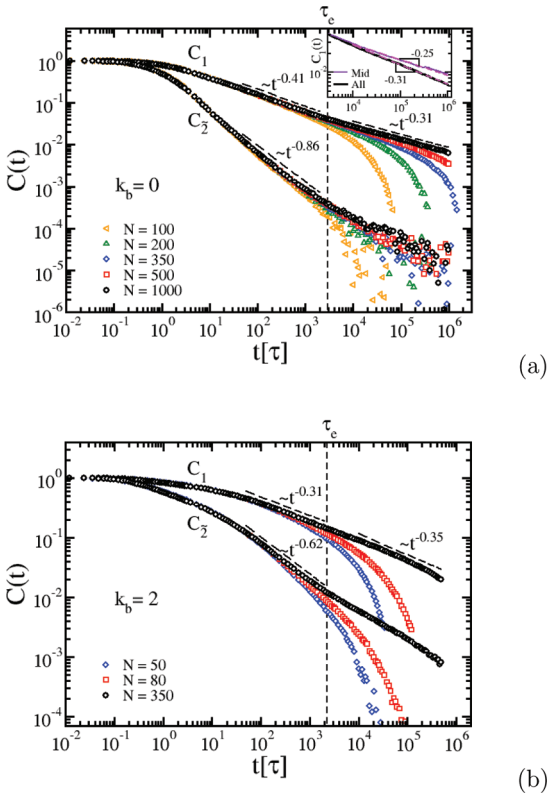
Figure 4. Time at the maximum of the ratio $g_{1,end}/g_{1,mid}$, normalized by the approximate Rouse time τ_R, as a function of $Z^{-1/2}$ for the MD, slip-springs and tube simulation models.

improve understanding, we also include results on the same quantities obtained from slip-springs simulations with and without CR, tube model simulations without CR, and one extra set of MD simulations with the bending potential strength k_b = 3ϵ. The tube model simulations are described in our previous publications,[15,44] in which the curvilinear motion of an entangled linear polymer is represented by the diffusion of a 1-D Rouse chain along a 3D random walk with the step size equal to that of the tube Kuhn step a. To put all of the models on the same graph, we plot them as a function of $Z^{-1/2}$, where $Z = N/N_e$ is approximate number of entanglements, as defined by the tube theory for each model. The values of N_e used for each model are listed in the legend. We see that (apart from the slip-springs without CR) all models fall onto a master curve, which starts from Rouse model prediction of 2 for small Z, and

dx.doi.org/10.1021/ma202759v | Macromolecules 2012, 45, 3557–3570

then asymptotically approaches theoretical prediction $4\sqrt{2}$. This graph illustrates that the convergence is very slow; that is, first-order corrections for finite Z are proportional to $Z^{-1/2}$, typical for the tube model.[32] Figure 4 shows that the maximum of $g_{1,end}/g_{1,mid}$ is achieved around Rouse time τ_R, and the results of tube model simulations, slip-springs with CR and MD of flexible chains, show the similar Z dependence, that is, increasing with Z at small number of entanglements but decreasing at $Z > 10$. We note, however, that MD results for the semiflexible chains with $k_b = 3$ show different Z dependence at small Z, which is probably related to the deviations from the random walk statistics on the length scale of entanglement.

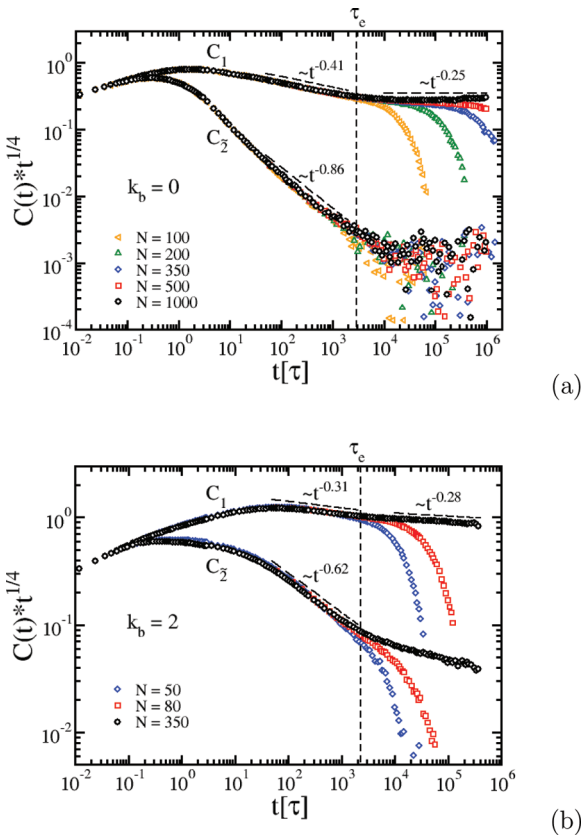
4.1.2. Segmental Orientation Autocorrelation Functions. Figures 5 and 6 present the MD simulation results on the orientation autocorrelation functions, $C_1(t)$ and $C_{\vec{2}}(t)$, of the unit bond vectors, $\boldsymbol{u}_i = (\boldsymbol{r}_{i+1} - \boldsymbol{r}_i)/|\boldsymbol{r}_{i+1} - \boldsymbol{r}_i|$, of different melt systems. The results are obtained by averaging over either the whole chain (Figure 5) or only the central part of the chain (Figure 6). The two $C_1(t)$ (or two $C_{\vec{2}}(t)$) curves of each system, calculated using these two different averaging methods, start by sitting on top of each other at early times but separate later by showing different decay rates. At a given time t, the discrepancy between the two sets of data decreases with the increase in the chain length. As the number of entanglements per chain reaches $Z \approx 15$, this difference becomes negligible below τ_e (not shown). Therefore, the asymptotic or envelope curves of $C_n(t < \tau_e)$ are well-defined by that of the longest chains at each chain stiffness, independent of the averaging scheme.



(a)

(b)

Figure 5. First- and second-order autocorrelation functions of the unit bond vectors, $C_1(t)$ and $C_{\vec{2}}(t)$, obtained from melts of flexible (a) and semiflexible (b) polymer chains. The results are averaged over all bonds along the chain. The τ_e values (vertical dashed lines) are taken from the $g_1(t)$ data fitting shown in Figure 1. In the inset of panel a, the $C_1(t)$ data calculated both over the whole chain (lower curve) and only over the central part of the chain (upper curve) are presented for the flexible chain melt with $N = 1000$.



(a)

(b)

Figure 6. Same types of autocorrelation functions as shown in Figure 5 but the results are obtained by averaging over bonds in the central parts of the chains. The data points are presented by multiplying the $t^{1/4}$ power, whereas the fitting powers given in the plots are those of the $C_n(t)$ functions themselves in different regimes.

The situation is very different on time scales $t > \tau_e$. We can first look at the $C_1(t)$ data of the chains with the highest length in each case. The power law exponent α, given by the $C_1(t) \propto t^{-\alpha}$ fitting in the entanglement regime, is found to be significantly larger in Figure 5 than that of the same melt system in Figure 6. This is further demonstrated in the inset of Figure 5a for the flexible chains with $N = 1000$. The $\alpha \approx 0.31$ value of these chains obtained by averaging over all bonds is rather close to those reported by NMR measurements[10,23] and Monte Carlo simulations[12] using linear polymers of similar number of entanglements per chain. There the whole chain averaging scheme was applied. The expected $\alpha = 1/4$ value was approached in Figure 6 by only considering the central chain segments, consistent with the $g_1(t)$ results in Figure 1. This again reflects the importance of ruling out the chain end contributions when comparing results obtained from limited chain lengths with the tube theory predictions made in the long chain limit. Therefore, all data analyses in the rest of this Article will be focused on the central parts of the linear chains.

Because the MD simulation data obtained from the melt systems with the highest chain lengths construct the envelope curves for all of the dynamic quantities we measured in this work, our following discussions on the segmental relaxation dynamics will be primarily based on these two representative samples. In the flexible chain case with $N = 1000$, the $C_n(t)$ results are averaged over the central 100 bonds, whereas in the

dx.doi.org/10.1021/ma202759v | Macromolecules 2012, 45, 3557−3570

semiflexible case with $N = 350$ the averages are taken over the central 50 bonds. In the time window covered by our MD runs, these correlation functions follow exactly the same time-dependent behavior as those obtained by averaging over the central 10 bonds but show smaller statistical errors.

Unentangled Regimes. The very short time scales correspond to the ballistic and monomer diffusion regimes. Figure 7 shows that the third power relation of $C_{\vec{2}}(t) = C_1(t)^3$

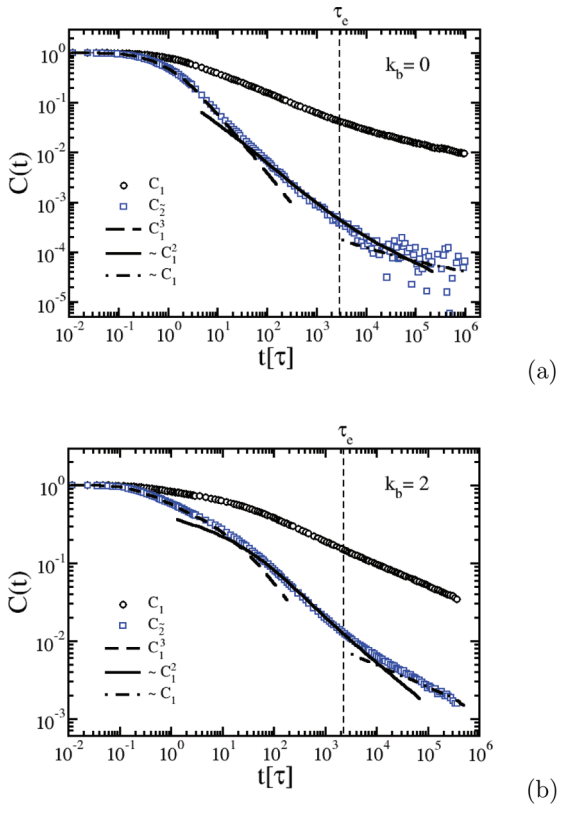


Figure 7. Scaling relationship between the first- and second-order orientation autocorrelation functions of the unit bond vectors for the polymer melts of (a) flexible chains of length $N = 1000$ and (b) semiflexible chains of length $N = 350$.

(eq 11) holds up to the time scale of $t \approx 10\tau$, about two decades in time beyond the ballistic region. After that, the rotation angle $\theta(t)$ becomes significant. Recent MD simulations of unentangled polymer melts showed qualitatively similar results, although using a different chain model.[25]

The segmental reorientation dynamics transfers to the Rouse diffusion behavior on larger time scales. The Rouse model predicts a scaling relation of $C_{\vec{2}}(t) \approx C_1(t)^2$ (eq 13), which is verified numerically in Figure 7. There the $C_1(t)^2$ data have been multiplied by a numerical coefficient b_1 for quantitatively matching the $C_{\vec{2}}(t)$ results. The b_1 values used in Figure 7 are 0.25 for the flexible chains and 0.56 for the semiflexible chains, respectively, both smaller than the 0.85 value predicted for ideal Rouse chains in Appendix II. This is understandable from the fact that at earlier times the second-order orientation correlation function of the segmental vector with unit length, $C_{\vec{2}}(t)$, decays in a third power of the first-order orientation correlation function, $C_1(t)^3$, rather than in a second power of $C_1(t)^2$. As a result, the value of $C_{\vec{2}}(t)$ is always smaller than $C_1(t)^2$ at any given time $t > 0$.

Figure 7 also illustrates that the Rouse regime in the segmental reorientation dynamics can be conveniently and reliably determined as the time region where $C_{\vec{2}}(t) \approx C_1(t)^2$. This regime is otherwise hard to define using the power law scaling because the ideal Rouse power laws of $C_1(t) \sim t^{-1/2}$ and $C_{\vec{2}}(t) \sim t^{-1}$ have not been observed in melts of real polymers, mostly attributed to the reduced number of Rouse modes caused by chain local stiffness. Such a deviation from the Rouse predictions is demonstrated in Figures 5 and 6, where we plot the power law fittings of $C_n(t) \sim t^{-\alpha}$ to the Rouse regime defined using the $C_{\vec{2}}(t) \propto C_1(t)^2$ relation. The obtained α values are all smaller than the corresponding Rouse values. The enhanced chain stiffness effect is clearly reflected in the smaller exponent values ($\alpha \approx 0.31$ and 0.62, respectively) obtained from the semiflexible chains than those ($\alpha \approx 0.41$ and 0.86) from the flexible chains. In the later case, the $C_{\vec{2}} \sim t^{-0.86}$ power is very close to the NMR result of $C_{\vec{2}} \sim t^{-0.85}$ found for linear PB melts, implying that the flexible bead−spring chain model can be used to mimic qualitatively the real polymers typically measured in recent NMR experiments.[22,23]

Entangled Regime. In Figure 6, the first-order orientation autocorrelation function of the unit bond vectors, $C_1(t)$, shows a clear crossover from the free Rouse to the entanglement regime and subsequently reaches a plateau-like region in the $C_1(t)t^{1/4}$ plot. At each chain stiffness, the onset of the plateau region occurs on roughly the same time scale as that of the corresponding $g_1(t)/t^{1/4}$ curve in Figure 1. Direct power law fitting of $C_1(t) \sim t^{-\alpha}$ for $t > 10^4\tau$ yields the exponents of $\alpha = 0.25 \pm 0.02$ for the flexible chains and $\alpha = 0.28 \pm 0.02$ for the semiflexible ones, both in good agreement with the power laws of $g_1(t)$ in the same regime.

As discussed above, the second-order orientation autocorrelation function, $C_{\vec{2}}(t)$, decays much faster than its first-order counterpart in the unentangled regime. Consequently, this function possesses much smaller values in the entanglement regime than that of $C_1(t)$. At the entanglement time τ_e estimated from the $g_1(t)$ data, its value is found to be $C_{\vec{2}}(\tau_e) \approx 4.1 \times 10^{-4}$ for the flexible chains, which is not far from the NMR data measured in various polymer species,[22] and 1.26×10^{-2} for the semiflexible chains, respectively. On time scales $t > \tau_e$, $C_{\vec{2}}$ of the semiflexible chains varies with time rather smoothly due to the relatively strong signals, whereas the data points of the flexible chains become very scattered and can hardly be used for any scaling analysis. Using the former case as an example, Figure 6b shows that the decaying rate of the $C_{\vec{2}}(t)$ function slows down after τ_e, but the plateau-like region in $C_{\vec{2}}(t)t^{1/4}$, as predicted by the RTO argument (eq 16), is not evidently reached even one decade after the onset time of the plateau in $C_1(t)t^{1/4}$. The prolonged crossover of the second-order orientation correlation function from the free Rouse to well-entangled behavior can also be seen in Figure 7b where the $C_{\vec{2}}(t)$ and rescaled $C_1(t)$ curves begin to match each other on the time scale $t \sim 10^5\tau \gg \tau_e$. This phenomenon will be addressed in more detail in the following subsections.

The $C_n(t)$ results presented in Figures 5 and 6 are calculated using the configuration frames recorded at a fixed time interval of 60τ or every 5000 MD time steps. The poor statistics in the $C_{\vec{2}}(t)$ data of the flexible chains imply that much denser sampling is still needed to get accurate results of these second-order bond vector correlation functions. This situation is similar to measuring the stress relaxation modulus in computer simulations where the stress has to be calculated at every time step to obtain a high signal-to-noise ratio.[30] One effective

dx.doi.org/10.1021/ma202759v | Macromolecules 2012, 45, 3557−3570

way of doing so is to apply the recently developed multiple-tau correlator algorithm to calculate the time correlation functions on the fly.[30,45,46] We notice that in the entanglement regime the polymer dynamics is dominated by topological constraints, which confine the chain diffusion to a tube-like region with the characteristic tube diameter a ($\propto N_e^{1/2}b$). As a consequence, the decay of the orientation autocorrelation functions of all chain segments, whose lengths are much smaller than the entanglement length N_e, should follow the same time-dependent behavior at $t > \tau_e$. It thus means that we can manage to improve the statistics of the $C_n(t)$ results by using coarse-grained chain segments to average out the fast fluctuations effectively on small length scales without losing any qualitative conclusions at larger length and time scales. This way we can also make full usage of the recorded trajectories that were generated over a substantial number of computer hours.

Coarse-Graining. We apply two different coarse-graining schemes to calculate the segmental orientation autocorrelation functions. In the first scheme, notated as *UVm*, we calculate $C_n(t)$ of the vectors linking monomers m bonds apart, that is, $\boldsymbol{u}_i^{UVm} = (\boldsymbol{r}_{i+m} - \boldsymbol{r}_i)/|\boldsymbol{r}_{i+m} - \boldsymbol{r}_i|$. Obviously, $m = 1$ corresponds to the unit bond vectors considered in Figure 6. The second scheme is termed as *CGm*, in which we subdivide the linear chain into N/m segments or blobs, each containing m monomers. The center of mass of the ith blob has the coordinate of

$$\mathbf{r}_i^{CG} = \frac{1}{m}\sum_{j=m(i-1)+1}^{mi}\mathbf{r}_j \tag{19}$$

The orientation correlation functions are then calculated for the vectors linking the centers of two adjacent blobs, $\boldsymbol{u}_i^{CG} = (\boldsymbol{r}_{i+1}^{CG} - \boldsymbol{r}_i^{CG})/|\boldsymbol{r}_{i+1}^{CG} - \boldsymbol{r}_i^{CG}|$. In both coarse-graining methods, the lengths of the segmental orientation vectors are normalized to unity. Therefore, the geometric argument on the equivalence of the two second-order orientation autocorrelation functions, $C_2(t) = C_{\vec{2}}(t)$, as proven in Appendix I, will still apply.

Figure 8 presents the $C_n(t)$ results calculated at different levels of coarse-graining for the two representative melt systems. For each system, the individual calculations are performed using the same central sections of the chains, namely, the middle 100 chemical bonds of the flexible chains of length $N = 1000$ and the middle 50 bonds of the semiflexible ones with $N = 350$, same as done in Figure 6. The results are only shown for the free Rouse and entanglement regimes for clarity. Because the coarse-graining process effectively smears out the contributions from the fast bond fluctuations on short time scales, all $C_n(t)$ data obtained at the coarse-graining level $m > 1$ demonstrate slower decaying rates in the Rouse regime than those of the unit bond vectors (Figure 6). Taking the melt of flexible chains as an example, when fitting the *UVm* data presented in Figure 8a to the power law of $C_1(t) \sim t^{-\alpha}$ in the Rouse regime (fitting not shown), the exponent is found to decrease continuously from $\alpha \approx 0.41$ at $m = 1$ to around 0.39 at $m = 3$ and 0.38 at $m = 5$. Correspondingly, the exponent of $C_{\vec{2}}(t)$ in the same regime drops from $\alpha \approx 0.86$ at $m = 1$ to around 0.82 at $m = 3$ and 0.80 at $m = 5$. The similar trend has been observed in the *CGm* results as well as in the melt of semiflexible chains. For the *CGm* calculations, we present only the *CG5* data in Figure 8 for clarity. Because the *CG5* scheme has a relatively higher level of coarse-graining than the *UV5*

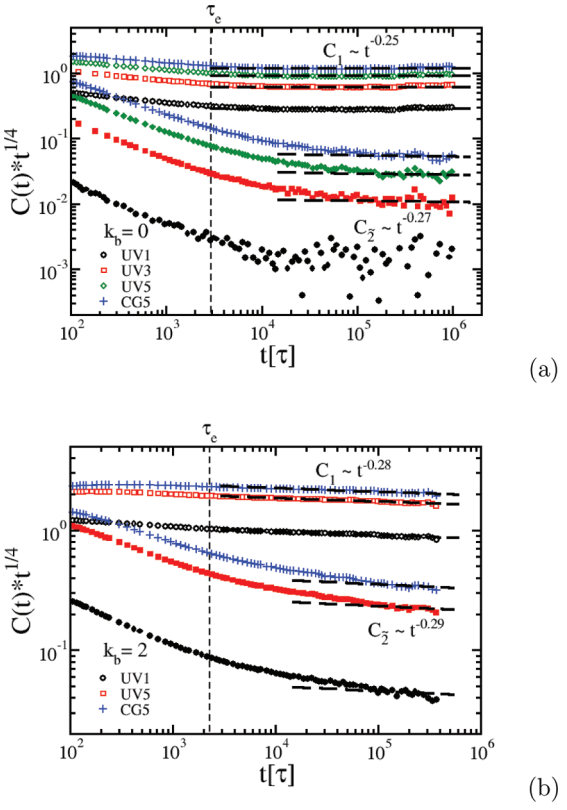


Figure 8. Segmental orientation autocorrelation functions calculated using various coarse-graining methods for the polymer melts of (a) flexible chains of length $N = 1000$ and (b) semiflexible chains of length $N = 350$. The *UV1* data sets are the same as those presented in Figure 6 for the same melt systems.

method, the resulted $C_n(t)$ curves also show somewhat lower scaling powers in the Rouse regime, that is, $\alpha \approx 0.36$ for $C_1(t)$ and 0.76 for $C_{\vec{2}}(t)$, than those given above for *UV5*.

Comparison of the power laws of the $C_n(t)$ functions in the Rouse regime also reveals that the Rouse-like scaling relation of $C_{\vec{2}}(t) \approx b_1 C_1(t)^2$ is well-preserved in the coarse-graining process. The value of b_1 is, however, brought closer to the ideal Rouse chain value. This can be attributed to the averaging out of the early time fast bond fluctuations. Therefore, before entering the Rouse regime, the numerical difference between $C_1(t)$ and $C_{\vec{2}}(t)$ of the coarse-grained segmental vectors is much smaller than that of the unit bond vectors. Depending on the levels of coarse-graining, the b_1 value obtained from the melt of flexible chains is found to increase from 0.25 for the unit bond vectors (Figure 7a) to 0.57 for *UV5*, 0.64 for *CG5*, and 0.75 for *CG10*, respectively. Similarly, this value changes from 0.56 for *UV1* (Figure 7b) to 0.77 for *UV5*, 0.81 for *CG5*, and about 0.85 for *CG10* in the melt of semiflexible chains. This is in perfect agreement with the Rouse model prediction of $b_1 \approx 0.85$, as shown in Appendix II.

On time scales $t > \tau_e$, all of the $C_1(t)$ curves obtained using different coarse-graining methods become parallel to each other and follow the same power law as that of the unit bond vectors. This is expected for the segmental relaxation dynamics in the entangled regime, as the segmental lengths used in the calculations are considerably smaller than N_e. As shown in Figure 8, the height of the plateau-like region in the $C_1(t)t^{1/4}$ curve relies on the decaying history of $C_1(t)$ on previous time scales and thus increases with increasing level of coarse-graining.

dx.doi.org/10.1021/ma202759v | *Macromolecules* 2012, 45, 3557–3570

The $C_{\vec{2}}(t)$ data behave similarly to their first-order counterparts. The stronger signals resulted from coarse-graining make it easier to visualize the significantly extended crossover region in $C_{\vec{2}}(t)$ from the free Rouse to well-entangled regimes, especially for the melts of flexible chains. At both chain stiffness values, the level-off of the $C_{\vec{2}}(t)t^{1/4}$ curves is found to become evident at $t \sim 10^5\ \tau$. Power fitting of $C_{\vec{2}}(t) \sim t^{-\alpha}$ to data points beyond this time yields the exponent $\alpha = 0.27 \pm 0.03$ for the flexible chains and $\alpha = 0.29 \pm 0.03$ for the semiflexible chains, both approaching the predicted 1/4 power law.[20] These results also support the relationship of $C_{\vec{2}}(t) \sim C_1(t)$ in the entanglement regime, as predicted in eq 16, but on time scales much larger than the entanglement time τ_e determined from $g_1(t)$ and $C_1(t)$.

In principle, one can also quantify the crossover behavior of the $C_n(t)$ functions by finding the intersections of their power law fittings in the free Rouse and entanglement regimes, as has been done in Figure 1 for determining the entanglement time τ_e. The intersection point corresponding to the $C_{\vec{2}}(t)$ function will apparently shift to larger time scale in comparison with that of $C_1(t)$. However, because the power laws fitted for these segmental orientation correlation functions do not exactly follow the theoretical predictions in both relaxation regimes (especially in the Rouse regime), the physical interpretation of their intersection points is not straightforward. The problem is further complicated by the change of the power laws in the Rouse regime when using different levels of coarse-graining. We thus leave this quantity for later study.

It is noted that our MD results on the power law exponents ($\alpha = 0.27 \pm 0.03$ for $k_b = 0$ and 0.29 ± 0.03 for $k_b = 2$, respectively) of $C_{\vec{2}}(t)$ in the entanglement regime are very close to the experimental value of $\alpha \approx 0.29$ obtained in NMR measurements of linear polymer melts with chain length up to 1100 entanglements, although the chain lengths studied in our simulations are only ~15 entanglements long.[10,22] However, as discussed above, our calculations of the segmental dynamic quantities have been focused on the central sections of the polymer chains, which effectively excludes the contributions from the fast moving chain ends. Therefore, our simulation results should yield power laws much closer to those obtained experimentally for very long chains. Moreover, it is also important to identify the right time scale at which the dynamic observable of interest approaches its asymptotic behavior. For $C_{\vec{2}}(t)$, this time scale is more than one decade later than that of other observables such as $C_1(t)$ and $g_1(t)$. If the power law fitting of $C_{\vec{2}}(t) \sim t^{-\alpha}$ is applied to the same time window (slightly after τ_e) as that used for fitting the $C_1(t)$ and $g_1(t)$ functions, a much higher α value will be wrongly obtained.

Return to Origin. The most straightforward way of examining the RTO argument is to plot the product of the segmental orientation autocorrelation functions, $C_n(t)$, and the mean square segmental displacement, $g_1(t)$. The tube theory predicts that this quantity should be constant in both entangled regimes, that is, for all times between entanglement time and reptation time

$$C_n(t)g_1(t) = const, \quad \tau_e < t < \tau_d \tag{20}$$

In other words, although $g_1(t)$ changes slope at the Rouse time τ_R, the product of $C_n(t)g_1(t)$ should not change. In addition, when referring to the Rouse model predictions of $g_1(t) \sim t^{1/2}$ (eq 4) and $C_1(t) \sim t^{-1/2}$ (eq 12), it also follows that $C_1(t)g_1(t) = const$ in the free Rouse regime ($\tau_0 < t < \tau_e$), supposing that the linear polymers behave as ideal Rouse chains. The constant can, however, be different from the constant in entangled regime.

The MD results on $C_n(t)g_1(t)$ are presented in Figure 9. In the Rouse regime, the time scaling of $C_1(t)$ deviates from the

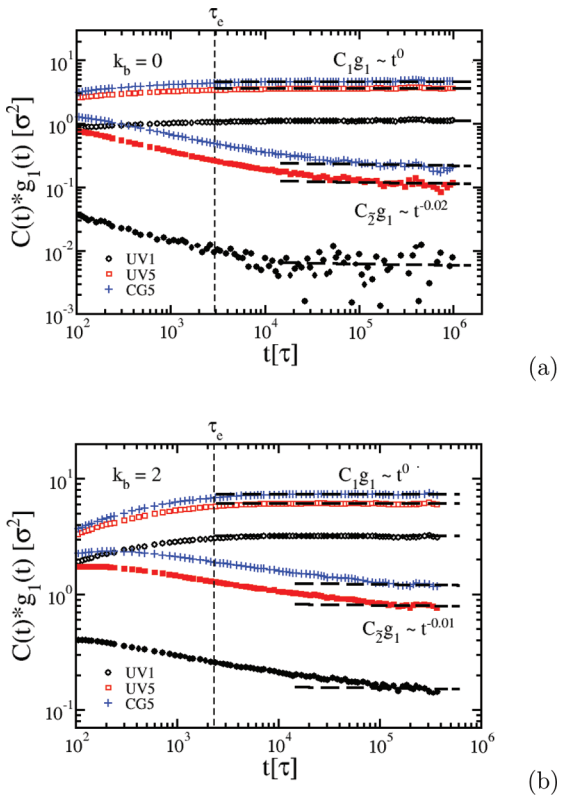


Figure 9. Products of the segmental orientation autocorrelation functions, $C_n(t)$, and the monomer mean square displacements, $g_1(t)$.

ideal Rouse chain behavior, and thus $C_1(t)g_1(t)$ grows with time, rather than being a constant. After the entanglement time τ_e, all of the $C_1(t)g_1(t)$ curves, regardless of the chain stiffness, become completely flat, which is in strong support of the RTO concept in eq 20. The significance of this result also lies in the fact that even though the power laws of both $g_1(t)$ and $C_1(t)$ of the semiflexible chains somewhat deviate from the ideal 1/4 value, their product remains constant. The prediction of eq 20 is also supported by the $C_{\vec{2}}(t)g_1(t)$ data, where a plateau-like region is also approached, although on much larger time scales. Note that the power law fittings to these plateau regions, as depicted in Figure 9, have relatively large error bars (±0.03) due to the limited time window accessed in MD simulations. Extension of the simulation runs to larger time scales is realized in our following slip-springs model simulations.

4.2. Slip-Springs Model. We start by mapping our MD simulations onto the slip-springs model using two adjustable parameters: N_0 is the number of MD monomers corresponding to one bead in slip-springs model and τ_{ss}^{MD}, which is the ratio of time units in both simulations (i.e., slip-springs time will be multiplied by τ_{ss}^{MD} to get the MD time). We obtain these two parameters from fitting the MD data on the MSDs of the middle monomers of the flexible chains ($k_b = 0$) with the slip-springs model. To this end, we performed a series of 20 slip-springs simulations with N^{ss} ranging from 10 to 256 and use *RepTate* software to interpolate between them. The results depend of course on the parameters of the slip-springs model.

dx.doi.org/10.1021/ma202759v | *Macromolecules* 2012, 45, 3557−3570

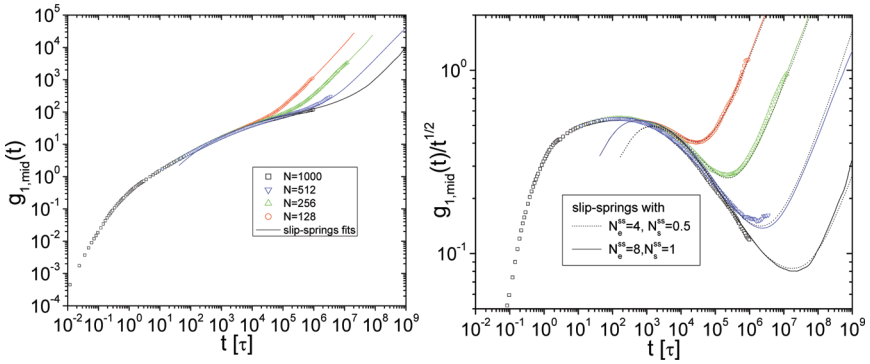


Figure 10. Mapping of the mean-square monomer displacements $g_1(t)$ between the slip-springs (lines) and MD simulations (symbols). The dotted and solid lines correspond to the slip-springs fits with different levels of coarse-graining. The time and length scale factors are discussed in the main text.

Figure 10 shows the resulting fits in two representations. The left panel shows normal representation with nine orders of magnitude along the vertical axis, which makes it very difficult to see any features. The right panel shows the same data divided by $\sqrt{t^{1/2}}$. This simple transformation reduces the vertical axis scale to 1.5 decades and makes comparison more effective and easy. It is this right panel representation, which we use for fitting.

The right panel in Figure 10 shows slip-springs fits with two levels of coarse graining: $N_e^{ss} = 4$, $N_s^{ss} = 0.5$, which are the standard settings, and two times less coarse-grained parameters with $N_e^{ss} = 8$, $N_s^{ss} = 1$. The fitting parameters are $\tau_{ss}^{MD} = 3370$, $N_0 = 9.74$ for the standard settings and $\tau_{ss}^{MD} = 840$, $N_0 = 4.87$ for the more fine-grained ones. Notice that the fitting parameters scale perfectly with the level of coarse graining, that is, two times more coarse simulations have four times longer elementary time and two times more MD monomers per one slip-springs bead. (See refs 14 and 31 for detailed discussion.) It is apparent that the more finegrained settings fit MD data better at early times, whereas the coarser simulations agree with them perfectly at later times but are exactly eight times cheaper. Therefore, we used finegrained simulations to get the accurate parameters and the coarser simulations for further discussion. We also notice that for standard settings $\tau_{ss}^{MD} = 3700$, $N_0 = 10$ give almost indistinguishable results.

We now simulate much longer chains with slip-springs model (corresponding to up to 5000 MD monomers) to understand different regimes and the role of constraint release on the segmental relaxation. Figure 11 shows slip-springs results

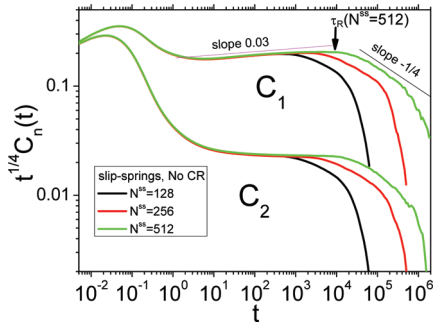


Figure 11. Slip-springs simulation results without constraint release for segmental relaxation functions $C_1(t)$ and $C_2(t)$ for different chain lengths.

without CR for different chain lengths, corresponding roughly to 22, 45, and 90 entanglements according to the tube theory mapping of slip-springs model ($N_e = 5.7$ for standard slip-springs setting[39]). All correlation functions are calculated by averaging over the central bonds of the chain. We see that both $C_1(t)t^{1/4}$ and $C_2(t)t^{1/4}$ show an extended plateau. In fact, $C_1t^{1/4}$ even shows a slightly positive slope of 0.03, corresponding to $C_1 \sim t^{-0.22}$. This is surprising feature of the slip-springs model, which probably means that the Rouse model for 1-D motion inside the tube is not completely adequate in this case. The effect is, however, very small. It is also apparent that after the Rouse time the slope of both functions changes to $C_n \sim t^{-0.5}$ in agreement with the tube theory expectations. However, one needs very long chains to see this second regime clearly (even without CR). The important thing to notice is that $C_2(t)$ attains a plateau later than $C_1(t)$, similarly to MD observations.

To elucidate the role of constraint release, we compare simulations with and without CR in Figure 12. The results are

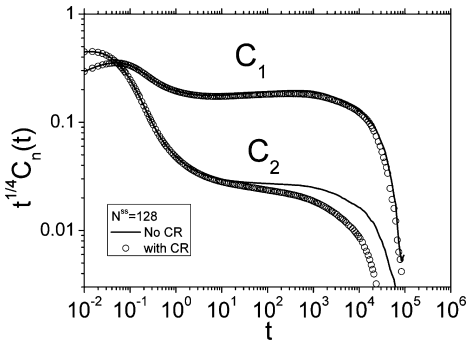


Figure 12. Slip-springs simulation results on $C_n(t)$ for $N^{ss} = 128$ with and without constraint release.

very interesting: the first-order segmental orientation correlation function C_1 is almost unaffected by CR, whereas the second-order correlation C_2 is affected significantly and shows about two times faster relaxation at the terminal time with CR. The situation is similar to contrasting the end-to-end vector relaxation with the stress (or orientation tensor) relaxations.[44] Therefore, CR makes it more difficult to observe a plateau in the $C_2(t)$ correlation function, which explains NMR findings of refs 10 and 22.

The clearest picture illuminating the role of CR is obtained from the return to origin plot Figure 13. We see that the product of the monomer mean square displacement $g_1(t)$ and $C_1(t)$ shows a perfect plateau in all regimes until the terminal time, and it is not affected by CR. In contrast, the same product with $C_2(t)$ attains a plateau only at late times and only without CR. The constraint release leads to a slope of $C_2(t)g_1(t)$, which persists until the terminal time. This slope seems to approach 0 asymptotically with increasing number of monomers N^{ss} but does

dx.doi.org/10.1021/ma202759v | Macromolecules 2012, 45, 3557–3570

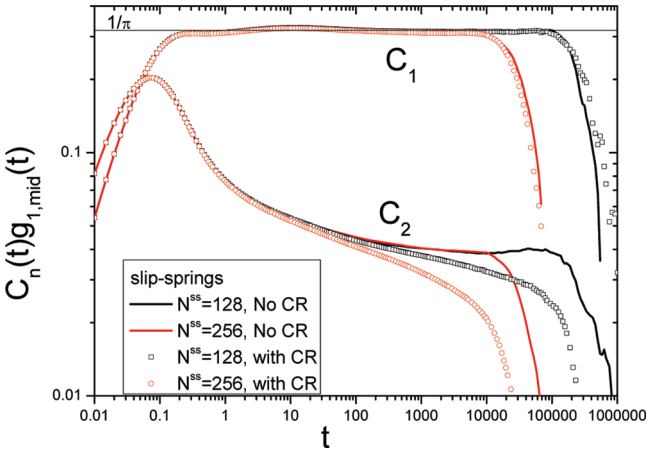


Figure 13. Return to origin plot for slip-springs simulations with and without constraint release.

so very slowly. We note that here we only analyze the middle monomer behavior. If all monomers are averaged over, then the results will be less clear, and we expect a significantly higher slope.

Finally, we attempt a direct comparison between slip-springs and MD simulations for the product of $C_n(t)g_1(t)$. To do that we multiply the slip-springs time scale by $\tau_{SS}^{MD} = 3370$ and the vertical scale by N_0b^2, where $N_0 = 9.74$ is the number of MD monomers in one slip-springs bead and $b^2 = R_e^2/N = 1.75$ is the statistical segment in MD simulations of flexible chains. As shown in Figure 14, the

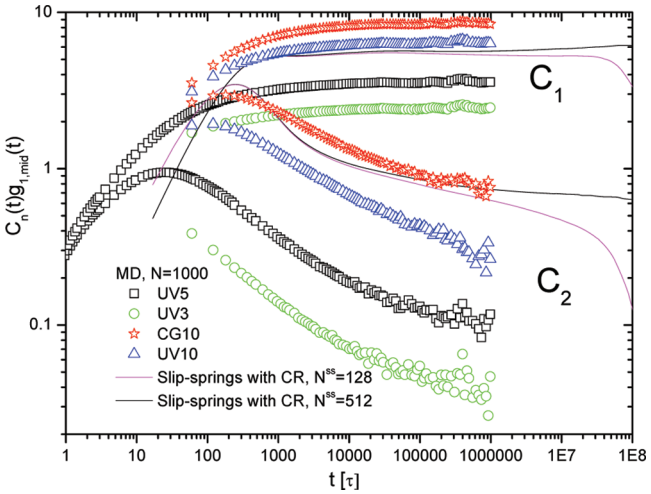


Figure 14. Comparison between MD and slip-springs simulations for the return to origin plot.

amplitude of the results strongly depends on the level of coarse graining. Moreover, the dependence on the level of coarse graining is not universal because the chains on small length scales do not obey perfect random walk statistics. Therefore, our results agree well, but only within a model-dependent vertical shift. Nevertheless, the results for $C_2(t)$ agree quite well with coarse-graining 10 (*CG10*, stars), which is close to our level of coarse-graining $N_0 = 9.74$, and results for $C_1(t)$ are close to *UV10* (triangles) method of coarse graining, which might be more suitable for $C_1(t)$ correlation function. We note that all coarse-graining results are exactly proportional to each other, and up to a vertical shift our slip-springs data for $N^{ss} = 128$ are in a very good agreement with the MD results for times larger than 1000τ, which is the same time when the mean squared displacement starts to agree (Figure 10).

5. CONCLUSIONS

The combination of MD and slip-springs simulations allows the complete range of polymer dynamics, from ballistic monomer motions all the way to complete relaxation by reptation to be accessed for polymers with up to 90 entanglements. Moreover, by averaging segmental dynamics over only the central part of the chain, scaling laws characteristic of much longer chains (up to around 1000 entanglements) can be effectively accessed. These simulations provide a rather comprehensive picture of relaxation dynamics, including Rouse-like, and reptation regimes, and allow the role of constraint release to be assessed. The simulation results are in agreement with available experimental data and provide a more complete picture than is possible from the experimental data alone.

This work was initiated, in part, because of new NMR experiments,[10,22] which reported that the segmental orientation correlation function $C_{\vec{2}}(t)$ does not show the tube-model predicted scaling of $t^{-0.25}$ in the constrained Rouse regime even for the polymers chain length $Z > 1000$ entanglements but instead decreases with slightly faster rate $t^{-0.29}$. In the present Article, we employed MD and slip-springs simulations to effectively separate contributions from different relaxation mechanisms and so revealed that there are three principal reasons for such delayed transition to asymptotic behavior predicted by the tube theory:

- The tube theory scaling predictions focus on the middle monomers, whereas experiments are naturally averaged over all monomers. As illustrated in Figures 5 and 6, this makes a large difference because the end monomers relax faster than the middle ones.
- The second-order segmental orientation correlation function $C_{2(\vec{2})}(t)$ shows an extended transition regime that goes well beyond the entanglement time τ_e; therefore, the expected slope $-1/4$ starts much (by more than one decade) later than that observed in the first-order correlation function $C_1(t)$.
- Constraint release further decreases the scaling exponent at later times, making it closer to experimentally observed exponent -0.29.

These findings suggest that the asymptotic behavior of $C_{\vec{2}}(t)$ can be expected in experimental measurements using long polymer chains with tailored architectures, where signals can be collected solely from central sections. To provide quantitative descriptions of the segmental relaxation curves obtained in NMR experiments and computer simulations from polymers of finite lengths, tube theories still need to be refined by taking a thorough consideration of the CR and CLF effects.

We have also demonstrated that the return to origin argument is valid for both the first- and second-order segmental orientation correlation functions. However, it holds much better for $C_1(t)$ than for $C_2(t)$, which is affected by CR and extended transition zone around τ_e.

APPENDIX I: EQUIVALENCE OF THE SECOND-ORDER ORIENTATION AUTOCORRELATION FUNCTIONS OF UNIT SEGMENTAL VECTORS

The two second-order segmental orientation correlation functions, $C_2(t)$ and $C_{\vec{2}}(t)$, as defined in eqs 6 and 7 using the unit segmental orientation vector, can be shown to be equivalent in equilibrium systems due to the spatial symmetry.

For a unit segmental vector, $\boldsymbol{u}$, the cosine of its orientation angle relative to one of the Cartesian coordinates α (x, y, or z)

dx.doi.org/10.1021/ma202759v | *Macromolecules* 2012, 45, 3557−3570

is simply $\cos\tilde{\theta} = u_\alpha$. Equation 7 can then be rewritten as

$$C_{\tilde{2}}(t) = 5\langle P_2(u_\alpha(t))P_2(u_\alpha(0))\rangle = \frac{45}{4}\langle u_\alpha^2(t)u_\alpha^2(0)\rangle - \frac{5}{4} \quad \text{(A1-1)}$$

where $\langle u_\alpha^2(0)\rangle = 1/3$ has been applied based on the equivalence of the three Cartesian axes. Similarly, eq 6 can be expanded as

$$C_2(t) = \frac{3}{2}\langle[\mathbf{u}(t)\cdot\mathbf{u}(0)]^2\rangle - \frac{1}{2} = \frac{9}{2}(\langle u_\alpha^2(t)u_\alpha^2(0)\rangle + 2\langle u_\alpha(t)u_\alpha(0)u_\beta(t)u_\beta(0)\rangle|_{\alpha\neq\beta}) - \frac{1}{2} \quad \text{(A1-2)}$$

The ensemble averages in eq A1-2 are invariant under the rotation of the reference coordinate frame. Rotating the Cartesian system (α, β, γ) around the γ axis clockwise by 45° to $(\alpha', \beta', \gamma)$, the components of the unit vector $\boldsymbol{u}$ in the new frame are given as $u_{\alpha'} = (u_\alpha + u_\beta)/\sqrt{2}$ and $u_{\beta'} = (-u_\alpha + u_\beta)/\sqrt{2}$. Using the rotational invariance, the cross term in the second step of eq A1-2 is given by

$$\langle u_\alpha(t)u_\alpha(0)u_\beta(t)u_\beta(0)\rangle = \langle u_{\alpha'}(t)u_{\alpha'}(0)u_{\beta'}(t)u_{\beta'}(0)\rangle = \frac{1}{2}(\langle u_\alpha^2(t)u_\alpha^2(0)\rangle - \langle u_\alpha^2(t)u_\beta^2(0)\rangle) \quad \text{(A1-3)}$$

Substituting this expression into eq A1-2 and then applying the relations of $\langle u_\alpha^2(t)u_\beta^2(0)\rangle = \langle u_\alpha^2(t)u_\gamma^2(0)\rangle$ and $u_\alpha^2(0) + u_\beta^2(0) + u_\gamma^2(0) = 1$, one directly gets

$$C_2(t) = \frac{45}{4}\langle u_\alpha^2(t)u_\alpha^2(0)\rangle - \frac{5}{4} = C_{\tilde{2}}(t) \quad \text{(A1-4)}$$

APPENDIX II: SEGMENTAL ORIENTATION AUTOCORRELATION FUNCTIONS OF A ROUSE CHAIN

We consider a Rouse chain with $N + 1$ beads located at positions $\{\boldsymbol{R}_i\}, i = 0,1,...,N$; the vector along its ith bond is given by $\mathbf{b}_i^R = (\boldsymbol{R}_{i+1} - \boldsymbol{R}_i)$. There are two ways of defining segment orientation functions $C_n(t)$. The definition used in the main text leads to the nonlinear averages and therefore is difficult to calculate analytically. If one normalizes the bond vector by the statistical segment $b = \langle(\boldsymbol{R}_{i+1} - \boldsymbol{R}_i)^2\rangle^{1/2}$ instead of the instantaneous bond lengths, it becomes straightforward to calculate $C_n(t)$ exactly using the Rouse modes. We shall distinguish correlation functions defined this way by the superscript "R". Below we perform short simulation of the Rouse chains and show that $C_n^R(t)$ normalized by the statistical segment follows exact analytical results, whereas the correlation functions $C_n(t)$ defined in the main text are exactly proportional to the $C_n^R(t)$ after the bond relaxation time.

The first- and second-order correlation functions of the Rouse bond vectors are defined by, respectively

$$C_1^R(t) = \frac{1}{b^2}\langle\mathbf{b}^R(t)\cdot\mathbf{b}^R(0)\rangle \quad \text{(A2-1)}$$

$$C_2^R(t) = \frac{1}{4}\left\langle\frac{3}{b^4}[\mathbf{b}^R(t)\cdot\mathbf{b}^R(0)]^2 - 1\right\rangle = 9\langle b_x^R(t)b_y^R(t)b_x^R(0)b_y^R(0)\rangle \quad \text{(A2-2)}$$

The normalization factor 1/4 in eq A2-2 originates from the fact that the fourth moment of the Rouse bond length is $\langle(b^R)^4\rangle = 5b^4/3$ owing to the Gaussian distribution of b^R.[25]

The first-order bond vector autocorrelation function of the Rouse chain can be found in the Doi and Edwards book[2,12]

$$C_1^R(t) = \frac{1}{N}\sum_{p=1}^{N}\exp\left(-\frac{p^2 t}{\tau_R}\right) \quad \text{(A2-3)}$$

with the Rouse time $\tau_R = N^2\tau_0$, the monomeric diffusion time $\tau_0 = \zeta b^2/3\pi^2 k_B T$, and the friction coefficient of the Rouse bead ζ.

On time scales $t \ll \tau_R$, large p terms in the summation dominate, which allows one to replace the summation by the integral over p. Thus, eq A2-3 predicts a power law time dependence

$$C_1^R(t) \approx \frac{\sqrt{\pi}}{2}(t/\tau_0)^{-1/2},\ \tau_0 \ll t \ll \tau_R \quad \text{(A2-4)}$$

which is proportional to the inverse of the mean-square displacement of the Rouse beads $\langle\Delta\mathbf{R}^2(t)\rangle$ on short time scales

$$C_1^R(t) \sim b^2/\langle\Delta\mathbf{R}^2(t)\rangle \sim (t/\tau_0)^{-1/2},\ t < \tau_R \quad \text{(A2-5)}$$

Figure 15 shows that simulation results for $C_1^R(t)$ (triangles) agree with eq A2-3 apart from the short times, where discreteness of the chain must be taken into account.

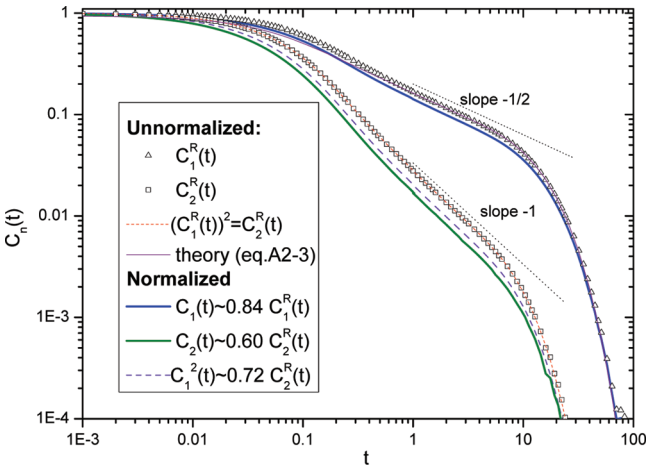


Figure 15. Rouse model simulations for $C_n(t)$ and $C_n^R(t)$ compared between themselves and with the theory. We have used Rouse chain of 17 beads with statistical segment $b^2 = 1$, bead friction $\zeta = 1$, and temperature $k_B T = 1$.

The second order correlation function $C_2^R(t)$ can be rewritten as

$$C_2^R(t) = \frac{1}{4}\left(\frac{3}{b^4}\sum_{\alpha,\beta=1}^{3}\langle b_\alpha^R(t)b_\alpha^R(0)b_\beta^R(t)b_\beta^R(0)\rangle - 1\right) = \frac{1}{4}\left(\frac{9}{b^4}(4\langle b_\alpha^R(t)b_\alpha^R(0)\rangle^2 + \langle b_\alpha^R(0)b_\alpha^R(0)\rangle^2) - 1\right) = \left(\frac{3}{b^2}\right)^2\langle b_\alpha^R(t)b_\alpha^R(0)\rangle^2 = C_1^R(t)^2 \quad \text{(A2-6)}$$

dx.doi.org/10.1021/ma202759v | Macromolecules 2012, 45, 3557−3570

where the indexes α,β = 1,2,3 correspond to the three Cartesian coordinates x,y,z. The second step in eq A2-6 was obtained by applying the formula

$$\langle abcd\rangle = \langle ab\rangle\langle cd\rangle+\langle ac\rangle\langle bd\rangle+\langle ad\rangle\langle bc\rangle \quad \text{(A2-7)}$$

for the Gaussian process with zero mean as well as the statistical independence of the different components of the bond vector $<b_\alpha^R(t_1)b_\beta^R(t_2)>|_{\alpha\neq\beta} = 0$ and the space isotropy $<b_\alpha^R(t_1)b_\alpha^R(t_2)> = <b_\beta^R(t_1)b_\beta^R(t_2)>$ for arbitrary times t_1 and t_2.[25] Finally, the ensemble average value of $<b_\alpha^R(t)b_\alpha^R(t)> = <b_\alpha^R(0)b_\alpha^R(0)> = b^2/3$ is applied in the third step. Figure 15 shows that indeed $C_2^R = (C_1^R)^2$ (squares and red dashed line).

We find from simulations that the functions $C_n(t)$ calculated by normalizing bond vectors by their instantaneous values become exactly proportional to the corresponding $C_n^R(t)$ functions, as illustrated in Figure 15 with the prefactors given in the legend. In particular, it follows that Rouse model predicts that $C_2(t) \approx 0.85C_1^2(t)$. Derivation of these prefactors is left as a challenge to an interested reader.

AUTHOR INFORMATION

Corresponding Author

*E-mail: zuowei.wang@reading.ac.uk.

Notes

The authors declare no competing financial interest.

ACKNOWLEDGMENTS

Z.W.W. acknowledges the support from the Foundation of Open Projects of Beijing National Laboratory for Molecular Sciences. A.E.L. acknowledges the support from EPSRC grant EP/H016686/1. R.G.L. acknowledges support from NSF under grant DMR 0906587. Any opinions, findings, and conclusions or recommendations expressed in this material are those of the authors and do not necessarily reflect the views of the National Science Foundation (NSF).

REFERENCES

(1) de Gennes, P. G. *J. Chem. Phys.* **1971**, *55*, 572−579.
(2) Doi, M.; Edwards, S. F. *The Theory of Polymer Dynamics*, 1st ed.; Clarendon Press: Oxford, U.K., 1988.
(3) Graessley, W. W. *Adv. Polym. Sci.* **1982**, *47*, 67−117.
(4) Watanabe, H. *Prog. Polym. Sci.* **1999**, *24*, 1253−1403.
(5) McLeish, T. C. B. *Adv. Phys.* **2002**, *51*, 1379−1527.
(6) Wang, S. *J. Polym. Sci., Part B: Polym. Phys.* **2003**, *41*, 1589−1604.
(7) Liu, C. Y.; Keunings, R.; C, C. B. *Phys. Rev. Lett.* **2006**, *97*, 246001.
(8) Kimmich, R.; Fatkullin, N. *Adv. Polym. Sci.* **2004**, *170*, 1−113.
(9) Wischnewski, A.; Monkenbusch, M.; Willner, L.; Richter, D.; Kali, G. *Phys. Rev. Lett.* **2003**, *90*, 058302.
(10) Chávez, F. V.; Saalwächter, K. *Phys. Rev. Lett.* **2010**, *104*, 198305.
(11) Kremer, K.; Grest, G. S. *J. Chem. Phys.* **1990**, *92*, 5057−5086.
(12) Kreer, T.; Baschnagel, J.; Muller, M.; Binder, K. *Macromolecules* **2001**, *34*, 1105−1117.
(13) Stephanou, P. S.; Baig, C.; Tsolou, G.; Mavrantzas, V. G.; Kroger, M. *J. Chem. Phys.* **2010**, *132*, 124904.
(14) Likhtman, A. E. *Macromolecules* **2005**, *38*, 6128−6139.
(15) Wang, Z. W.; Larson, R. G. *Macromolecules* **2008**, *41*, 4945−4960.
(16) Zamponi, M.; Wischnewski, A.; Monkenbusch, M.; Willner, L.; Richter, D.; Likhtman, A. E.; Kali, G.; Farago, B. *Phys. Rev. Lett.* **2006**, *96*, 238302.
(17) Pearson, D. S.; Fetters, L. J.; Graessley, W. W.; Strate, G. V.; von Meerwall, E. *Macromolecules* **1994**, *27*, 711−719.
(18) Fischer, E.; Kimmich, R.; Fatkullin, N.; Yatsenko, G. *Phys. Rev. E* **2000**, *62*, 775−782.
(19) Pütz, M.; Kremer, K.; Grest, G. S. *Europhys. Lett.* **2000**, *49*, 735−741.
(20) Ball, R. C.; Callaghan, P. T.; Samulski, E. T. *J. Chem. Phys.* **1997**, *106*, 7352−7361.
(21) Graf, R.; Heuer, A.; Spiess, H. W. *Phys. Rev. Lett.* **1998**, *80*, 5738−5741.
(22) Chávez, F. V.; Saalwächter, K. *Macromolecules* **2011**, *44*, 1549−1559.
(23) Herrmann, A.; Novikov, V. N.; Rossler, E. A. *Macromolecules* **2009**, *42*, 2063−2068.
(24) Rouse, P. E. *J. Chem. Phys.* **1953**, *21*, 1272−1280.
(25) Ottochian, A.; Molin, D.; Barbieri, A.; Leporini, D. *J. Chem. Phys.* **2009**, *131*, 174902.
(26) Barbieri, A.; Campani, E.; Capaccioli, S.; Leporini, D. *J. Chem. Phys.* **2004**, *120*, 437−453.
(27) Baschnagel, J.; Varnik, F. *J. Phys.: Condens. Matter* **2005**, *17*, R851−R953.
(28) Bennemann, C.; Baschnagel, J.; Paul, W.; Binder, K. *Comput. Theor. Polym. Sci.* **1999**, *9*, 217−226.
(29) Sun, Q.; Faller, R. *Macromolecules* **2006**, *39*, 812−820.
(30) Likhtman, A. E.; Sukumaran, S. K.; Ramirez, J. *Macromolecules* **2007**, *40*, 6748−6757.
(31) Sukumaran, S. K.; Likhtman, A. E. *Macromolecules* **2009**, *42*, 4300−4309.
(32) Likhtman, A. E.; McLeish, T. C. B. *Macromolecules* **2002**, *35*, 6332−6343.
(33) Cao, J.; Likhtman, A. E. *Phys. Rev. Lett.* **2010**, *104*, 207801.
(34) Rubinstein, M.; Colby, R. H. *Polymer Physics*, 1st ed.; Oxford University Press: New York, 2003.
(35) Kremer, K.; Grest, G. S.; Carmesin, I. *Phys. Rev. Lett.* **1988**, *61*, 566−569.
(36) Auhl, R.; Everaers, R.; Grest, G. S.; Kremer, K.; Plimpton, S. J. *J. Chem. Phys.* **2003**, *119*, 12718−12728.
(37) Everaers, R.; Sukumaran, S. K.; Grest, G. S.; Svaneborg, C.; Kremer, A. S. A. *Science* **2004**, *303*, 823−826.
(38) Zhou, Q.; Larson, R. G. *Macromolecules* **2007**, *40*, 3443−3449.
(39) Ramirez, J.; Sukumaran, S. K.; Likhtman, A. E. *J. Chem. Phys.* **2007**, *126*, 244904.
(40) Ramirez, J.; Sukumaran, S. K.; Likhtman, A. E. *Macromol. Symp.* **2007**, *252*, 119−129.
(41) Hoy, R. S.; Foteinopoulou, K.; Kröger, M. *Phys. Rev. E* **2009**, *80*, 031803.
(42) Schafer, L.; Baumgartner, A.; Ebert, U. *Eur. Phys. J. B* **1999**, *10*, 105−117.
(43) Ebert, U.; Schafer, L.; Baumgartner, A. *J. Stat. Phys.* **1998**, *90*, 1325−1373.
(44) Likhtman, A. E. Viscoelasticity and Molecular Rheology. In *Comprehensive Polymer Science*, 2nd ed.; Elsevier: Amsterdam, 2011.
(45) Ramirez, J.; Sukumaran, S. K.; Vorselaars, B.; Likhtman, A. E. *J. Chem. Phys.* **2010**, *133*, 154103.
(46) Magatti, D.; Ferri, F. *Appl. Opt.* **2001**, *40*, 4011−4021.

Macromolecules

Article

pubs.acs.org/Macromolecules

Effect of Cross-Linking on the Molecular Motions and Nanodomains Segregation in Polymethacrylates Containing Aliphatic Alcohol Ether Residues

M. Carsi,* M. J. Sanchis, and R. Diaz-Calleja

Instituto Tecnológico de la Energía (ITE), Universitat Politècnica de València, Valencia, Spain

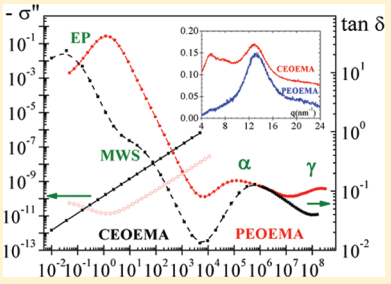
E. Riande*

Instituto de Ciencia y Tecnología de Polímeros (CSIC), Juan de la Cierva 3, 28008 Madrid, Spain

M. J. D. Nugent

Athlone Institute of Technology, Dublin Road, Athlone, County Westmeath, Ireland

ABSTRACT: The dielectric relaxation spectra of poly(2-ethoxyethyl methacrylate) in the frequency domain exhibits above T_g and at high frequencies a well-developed secondary γ relaxation. This process is followed in decreasing order of frequency for a relatively weak β relaxation and an ostensible glass−rubber relaxation which at high temperatures and low frequencies is dominated by electrode−polymer interfacial processes. By slightly cross-linking the polymer using 2.5% (mol) of 2-ethoxyethyldimethacrylate as cross-linking agent, the β relaxation disappears, the γ relaxation remaining. The activation energy of the γ relaxation for the cross-linked and un-cross-linked polymers is ca. 30 kJ·mol^{-1}, about 10 kJ·mol^{-1} below that of the β relaxation. Cross-linking shifts the location of the glass−rubber relaxation nearly 10 °C to higher temperatures, without widening the distribution of relaxation times. The X-rays pattern of the cross-linked polymer presents two peaks at q = 5.6 nm^{-1} and 12.76 nm^{-1}, resembling the X-ray patterns of poly(n-alkyl methacrylate)s. The peaks in poly(n-alkyl methacrylate)s were attributed to the formation of nanodomains integrated by side chains flanked by the backbone. However, whereas this heterogeneity produces an α_{PE} peak in poly(n-alkyl methacrylate)s with $n \geq 2$, this microheterogeneity gives rise to a Maxwell−Wagner−Sillars (MWS) relaxation in the cross-linked polymer located at lower frequencies than the glass rubber relaxation. Finally the interfacial-electrode conductive processes of the cross-linked and un-cross-linked polymeric systems are studied in the light of current theories.



1. INTRODUCTION

The time domain response of linear polymer chains without flexible side groups to a mechanic perturbation field Γ is given by $\Gamma(t) = \Gamma_0\,\Delta(t)$, where $\Delta(t)$ is the Heaviside step function. This involves at very short times, the local motions of the skeletal bonds. Over time, an increasing amount of the skeletal bonds intervene in the response until the whole chains move and flow takes place. In the frequency domain, the chain motions appear as relaxations in the mechanical loss spectra. At very low frequencies, the normal mode, which reflects the disentanglement of the chains, appears. The normal mode is followed at higher frequencies by the glass−rubber or α relaxation produced by segmental motions of the chains. At even higher frequencies, the so-called secondary relaxations are detected in the spectra. In order of increasing frequency, the secondary relaxations are named β, γ, δ, etc. The secondary relaxations are present in the liquid and glassy states while the glass−rubber and normal mode relaxations freeze at T_g.

Unfortunately, the response of polymers to perturbation fields can only be obtained in a few decades of time/frequency in the case of mechanical force fields so that obtaining information over a long frequency/time range requires the application of the temperature-frequency/time superposition principle which only holds for thermorheological simple systems. This disadvantage can be overcome using broadband dielectric spectroscopy (BDS), a technique which enables analysis of the chains response over more than 10 decades in the frequency domain. However, a disadvantage of the BDS technique is that the total dipole moments associated with most polymer chains do not scale with chains length, and therefore, the BDS technique is insensitive to chains disentanglement reflected in the normal mode process. Only the normal mode

Received: December 29, 2011
Revised: March 6, 2012
Published: April 6, 2012

ACS Publications © 2012 American Chemical Society

of chains with dipole moments parallel to the chain contour can be studied with the BDS technique.

The term methacrylates cover a wide variety of polymers differing in the nature of the alcohol residue. The first member of the series, poly(methyl methacrylate), is the most commonly used of the methacrylate family, mostly in automotive/home applications.[1] The polymer exhibits an ostensible β relaxation arising from rotation of the $C(CH_3)-C(O)OCH_3$ side group, located in the vicinity of the α relaxation. The position and relative intensity of the α/β relaxations depends on the nature, i.e., size and polarity, of the ester residue. If the residue results from *n*-alkyl alcohols (i.e., ethyl, propyl, butyl, etc.), it can be stated that longer alkyl groups will have a greater impact on the mechanical and dielectric properties of the polymers.[2−16] A great deal of work has been reported related with the influence of the size of the alkyl groups on the relaxations of these polymers.[17−27] Nanophase segregation of non polar alkyl side groups from the polar $-COO^-$ groups rigidly attached to the skeletal bonds of the chains, has been reported for these material types. The carboxyl groups presumably are concentrated at the surface of alkyl nanodomains formed by side groups of different structural units and different chains. Small domain sizes of the order of one nanometer have been detected by X-rays diffractograms of poly(alkyl acrylate)s (PnAAs) and poly(alkyl methacrylate)s (PnAMAs).[22,25,26]

The presence of nanophase separation has been confirmed by the study of the dynamics of amorphous side-chain polymers. Dielectric studies carried out for higher PnAMAs with the number of carbon atoms in the alkyl residue lying in the range $4 \leq C \leq 12$ have shown the existence of two coexisting relaxation processes with typical features of glass transitions: one detected at low temperatures associated with cooperative motions of the alkyl groups in the nanodomains and therefore it is a polyethylene (PE) like glass transition (α_{PE}). Another glass transition is detected at higher temperature resulting from cooperative motions of the skeletal bonds.[22,25] The spectra of poly(2,3-dimethoxybenzyl methacrylate) shows the glass−rubber relaxation followed at lower frequencies by another well developed relaxation attributed to a MWS process arising from the transport of electric charges in segregated nanodomains formed by the side chains surrounded by the skeletal bonds.[28]

In view of these antecedents, one of the aims of this work was to investigate whether the replacement of a methyl group for an ether group in poly(*n*-pentyl methacrylate) affects the segregation of hydrophilic and hydrophobic domains observed in poly(*n*-alkyl methacrylate)s. For that purpose the response of poly(2-ethoxyethyl methacrylate) (PEOEMA) to electric perturbation fields was studied at several temperatures over the wide frequency window $10^{-2}-10^{9}$ Hz. This polymer has been used as drug-eluting extent coating for percutaneous coronary interventions, providing durable, robust coatings with precise control over rapamycin elution rates.[29] The chemical structure of the repeating unit of PEOEMA is shown in Figure 1.

The effect of decreasing the mobility of the chains in the dielectric response to perturbation fields was studied in poly(2-ethoxy methacrylate-*co*-ethyldimethacrylate) containing 2.5% (mol) of the cross-linking agent, ethyldimethacrylate. The acronym of the cross-linked film will be CEOEMA. The parameters that define the relaxations of PEOEMA, i.e., dielectric strength, shape factors, and temperature dependence of the relaxations, were studied and compared with those of CEOEMA. Information on the possible formation of segregation domains was investigated by using X-rays techniques. MWS relaxations, and polymer−electrode interface conducting processes are also discussed.

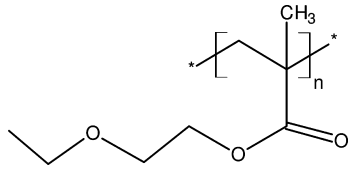


Figure 1. Structure of poly(2-ethoxyethyl methacrylate).

2. EXPERIMENTAL PART

Synthesis and Characterization of the Polymers. 2-Ethoxyethyl methacrylate was obtained by adding dropwise methachloroyl chloride to stirred 2-ethoxybutanol. The reaction was carried out at 0 °C for 6 h and the methacryloyl was separated from the reaction medium by distillation in vacuum. Ethylene dimethacrylate was obtained by reaction of ethylene glycol with methachloroyl chloride.

2-Ethoxyethyl methacrylate was polymerized in toluene solution and nitrogen atmosphere, at 50 °C, using α,α'-isobutyronitrile (AIBN) as initiator. The polymer, poly(2-ethoxyethyl methacrylate) (PEOEMA), was precipitated with methanol, dissolved in benzene and precipitated in methanol again and finally dried in vacuum at 60 °C. The number- and weight-average molecular weights of the sample, measured by GPC in chloroform solvent, were 82649 and 250774 g/mol, respectively.

A mixture of 2-ethoxy ethyl methacrylate and ethyldimethacrylate, containing 2.5% mol of the latter cross-linking agent, was copolymerized in bulk in a circular TEFLON mold. The copolymerization reaction was carried out at 50 °C using AIBN as initiator. The cross-linked film (CEOEMA) was maintained in hot toluene overnight to extract very small amounts of un-cross-linked polymer, washed several times with methanol and dried in vacuum at 60 °C.

Differential Scanning Calorimetry (DSC) Measurements. The glass transition temperatures of the PEOEMA and CEOEMA were determined with a DSC-7 Perkin-Elmer calorimeter, at a heating rate of 10 °C·min^{-1}. Taking as T_g the temperature at the middle point of the glass transition endotherm, the values of this quantity for PEOEMA and CEOEMA were −5 and +5 °C, respectively.

X-rays Characterization. Wide-angle X-ray diffraction (WAXS) patterns were recorded at room temperature using a Bruker D8 Advance diffractometer with Cu Kα radiation (λ = 0.1542 nm) operated at 40 kV and 4 mA. The diffraction scans were collected within the range of 2θ = 5−60° with a 2θ step of 0.024° and 0.5 s per step.

Dielectric Measurements. The experimental dielectric behavior of PEOEMA and CEOEMA was studied with a Novocontrol broadband dielectric spectrometer (Hundsagen, Germany) consisting of an Alpha analyzer to carry out measurements from 5×10^{-2} to 3×10^{6} Hz and an Agilent 4991A RF analyzer for measurements lying in the range $10^{6}-10^{9}$ Hz. Both devices were coupled to a Quattro temperature controller. Molded disk shaped samples of about 0.1 mm thickness and 20 mm and 10 mm diameter were used, respectively, for the low and high frequency analyzers. In order to keep the distance constant between the electrodes in the PEOEMA samples, especially at high temperatures, a silica spacer was utilized. The measurements were carried out in inert N_2 atmosphere from −150 to +150 °C for CEOEMA and from −150 to +70 °C for PEOEMA in 5 °C intervals. The experimental uncertainty was better than 5% in all cases.

3. RESULTS AND DISCUSSION

The isochrones corresponding to the real component of the complex dielectric permittivity of PEOEMA exhibit a plateau associated with the glass−rubber or α relaxation followed at higher temperature for a steep increase of this parameter in the

former polymer as temperature goes up. However, the isochrones for the real permittivity of CEOEMA present in addition to the plateau corresponding to the α relaxation another plateau at higher temperature associated with a relaxation, named α', the nature of which will be discussed latter. In increasing order of temperature the loss isochrones corresponding to PEOEMA present two absorptions named γ and β followed by the well developed α relaxation. As usual, at high temperatures and low frequencies the α relaxation is obscured by conductive contributions arising from interfacial electrode–polymer (EP) processes. The loss isochrones corresponding to CEOEMA only present the γ relaxation followed by the α and α' relaxations, the latter process strongly overlapping with the EP process. These features are reflected in the real and loss components of the complex dielectric permittivity represented in Figure 2.

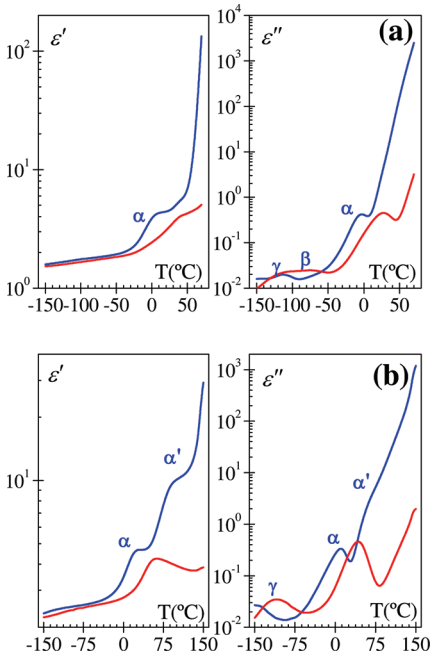


Figure 2. Temperature dependence of permittivity and loss permittivity at 10^0 (blue curve) and 10^3 (red curve) Hz for (a) PEOEMA and (b) CEOEMA.

A more complete description of the relaxation behavior of the polymers is shown in Figure 3 where the components of the complex dielectric permittivity in the frequency domain are presented at several temperatures for PEOEMA and CEOEMA, respectively.

The dielectric loss isotherms corresponding to the un-cross-linked polymer present at high frequencies a γ process followed in decreasing order of frequency by a weak β absorption and an ostensible glass–rubber relaxation dominated at low frequencies by strong interfacial electrode-polymer polarization (EP) processes. However, the dielectric loss isotherms for CEOEMA only exhibits at high frequencies a secondary single relaxation, named γ absorption, followed in decreasing order of frequency by the α relaxation which in the low frequency side overlaps with an apparently ostensible relaxation, named α' process. This latter absorption appears as a shoulder of the EP process. It is worth noting that the α'

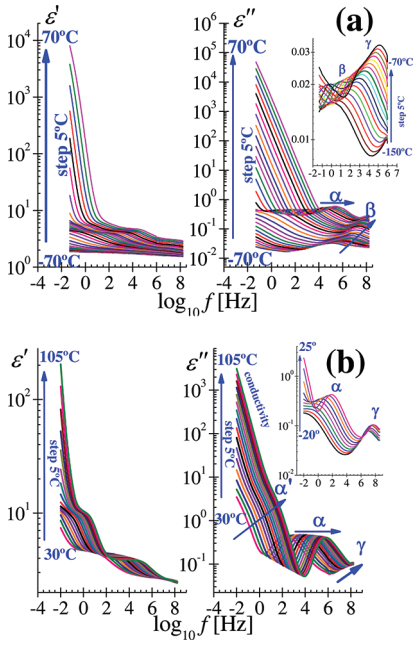


Figure 3. Dielectric permittivity and loss as a function of the frequency for PEOEMA (a) at temperatures between −70 and +70 °C, in 5 °C steps (inset between −150 and −70 °C, step of 5 °C) and for CEOEMA (b) between 30 and 105 °C, in 5 °C steps (inset between −20 and +25 °C, step of 5 °C).

relaxation is well-separated from the α and conductive processes in the isotherms corresponding to the real dielectric permittivity.

The β, α, and conductive processes are well-defined in the dielectric loss modulus of PEOEMA in the frequency domain, shown in Figure 4a. The rather narrow conductive peak of

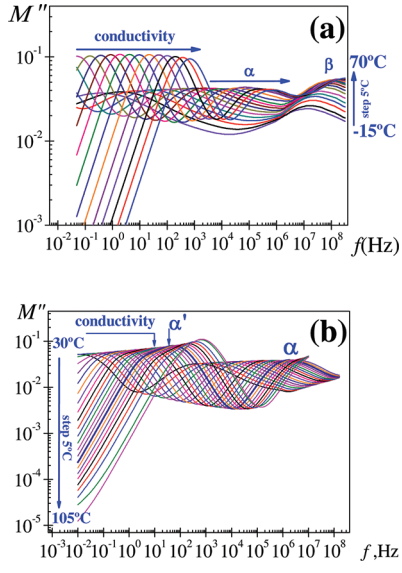


Figure 4. Dielectric loss modulus in the frequency domain, at several temperatures, for (a) PEOEMA and (b) CEOEMA.

PEOEMA widens in the case of CEOEMA as a result of the overlapping of the α' relaxation with the EP process (see Figure 4b).

dx.doi.org/10.1021/ma202811p | Macromolecules 2012, 45, 3571–3580

Splitting of the overlapping relaxations in the isotherms were carried out by means of Cole−Cole and Havriliak−Negami type equations[30]

$$\varepsilon^*(\omega) = \varepsilon_\infty + \sum_i \frac{\varepsilon_{0i} - \varepsilon_{\infty i}}{[1 + (j\omega\tau_i)^{a_i}]^{b_i}} - j\left(\frac{\sigma}{e_0\omega}\right)^s \quad (1)$$

where e_0 (=8.854 pF/m) is the free space dielectric permittivity, σ is the ionic conductivity arising from interfacial polymer-electrode phenomena, τ denotes a specific relaxation time associated with the process and s is a parameter very close to the unit. The subscript i in eq 1 refers to the absorptions γ, β, α and α' while the subscripts 0 and ∞ mean, respectively, relaxed and unrelaxed dielectric permittivity. The shape parameters a and b are related, respectively, to the departure of the complex ε'' vs ε' plot from a semicircumference, at low frequencies, and to the skewness of the plot along a straight line, at high frequencies. Owing to the symmetry of the secondary absorptions, the complex plots are arcs so that the shape parameter b is the unit. For a Debye type relaxation $a = b = 1$. For $T < T_g$, the contributions to $\varepsilon^*(\omega)$ of the α and α' relaxations as well as the ionic conductivity are nil. As usual, the HN and conductive parameters associated with each dipolar relaxation in eq 1 can be obtained by writing the real and loss component of the complex permittivity in the following way.

$$\varepsilon'(\omega) = \varepsilon_\infty + r^{-b/2}(\varepsilon_0 - \varepsilon_\infty)\cos b\theta \quad (2a)$$

$$\varepsilon''(\omega) = r^{-b/2}(\varepsilon_0 - \varepsilon_\infty)\sin b\theta + \left(\frac{\sigma}{e_0\omega}\right)^s \quad (2b)$$

where

$$r = [1 + (\omega\cdot\tau_0)^a \cos(a\pi/2)]^2 + [(\omega\tau_0)^a \sin(a\pi/2)]^2$$

$$\theta = \arctan\left[\frac{(\omega\cdot\tau_0)^a \sin(a\pi/2)}{1 + (\omega\tau_0)^a \cos(a\pi/2)}\right] \quad (3)$$

The HN and conductive fitting parameters were determined at several temperatures from a multiple nonlinear regression analysis of the experimental data. Examples of the deconvolutions of the loss dielectric curves for PEOEMA and CEOEMA at $T > T_g$ are shown in Figure 5.

In the inset of the figure the relative error associated with the values of the dielectric loss recalculated from the strengths and shape factors associated with the split relaxations are also shown. It can be seen that in most cases the relative error is about 7% or lower. In the most unfavorable cases (extreme frequencies), the error comes close to 10%.

The shape parameters associated with the relaxation processes of the samples are shown in Figure 6.

An inspection of the parameters corresponding to the α' process of CEOEMA indicates that the values of a slightly increase with increase temperature lying in the range 0.8−0.9 in the temperature interval 30°-105 °C. The closeness of the a parameter to the unit suggests that the α' relaxation exhibits a rather narrow distribution of relaxation times. As shown in Figure 6, the values of a for the α relaxation of CEOEMA are higher than those for the α' process at temperatures above 60 °C, smaller at temperatures below 60 °C, and in both cases they moderately increase with increasing temperature, though the increase is somewhat higher for the un-cross-linked

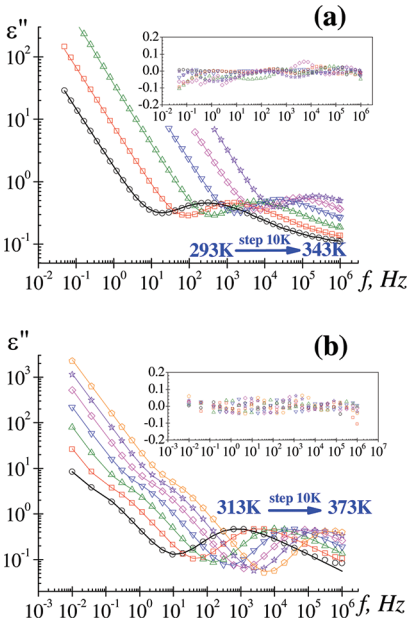


Figure 5. Reconstruction of the dielectric loss from the distribution of retardation times for PEOEMA (a) and CEOEMA (b) at several temperatures. Open circles represent the experimental data, and the continuous line represents the dielectric loss calculated as the sum of the individual processes. Inset: relative error calculated as $(\varepsilon_{CALC} - \varepsilon_{EXP})/\varepsilon_{EXP}$.

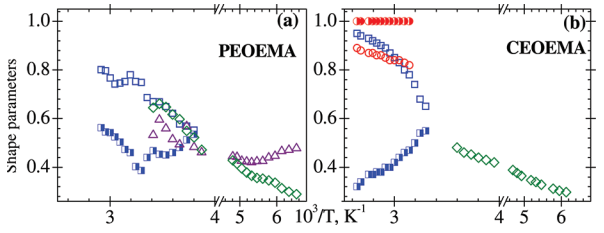


Figure 6. Temperature dependence of the shape parameter for (a) PEOEMA and (b) CEOEMA. α' process: a parameter (open circle) and b parameter (half right circle), α process: a parameter (open square) and b parameter (half right square), β process: a parameter (up triangle) and γ process: a parameter (diamond).

polymer. The b parameter corresponding to the α' relaxation is very close to the unit and independent of temperature. This fact indicates the absence of skewness in the high frequency side of the ε'' vs ε' plot, i.e. the α' relaxation is a symmetric process. However, the parameter b for the α relaxation decreases with increasing temperature, i.e., the skewness of the ε'' vs ε' plot increases with temperature. In both cases, the Cole−Cole plots at high temperature come close to a semicircle in the low frequency region. The values of the parameter a corresponding to the γ relaxations of PEOEMA and CEOEMA are rather close and in both cases they increase with increasing temperature. However, the temperature dependence of this parameter for the β relaxation of PEOEMA does not follow a definite trend.

The dielectric strength of the α' relaxation corresponding to CEOEMA, presented in Figure 7, increases with temperature. This behavior differs from that displayed by the α relaxation of CEOEMA and PEOEMA whose strength, as usual, decreases with increasing temperature. The dielectric strengths of the secondary relaxations, also shown in Figure 7, increase with increasing temperature. Moreover the strength of the

dx.doi.org/10.1021/ma202811p | Macromolecules 2012, 45, 3571−3580

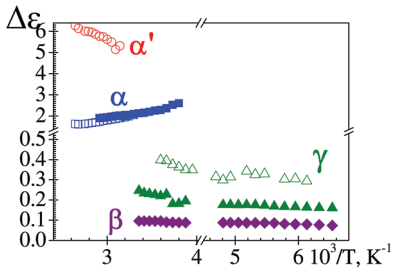


Figure 7. Temperature dependence of the strengths for the α (square), α' (circle), β (diamond), and γ (triangle) relaxations for PEOEMA (full symbols) and CEOEMA (open symbols).

γ relaxation of CEOEMA is nearly the sum of the γ and β dielectric strengths of PEOEMA.

Temperature Dependences of the Deconvoluted Relaxations. Arrhenius plots of the relaxation times associated with the different absorptions presented in the spectra of PEOEMA and CEOEMA are shown in Figure 8.

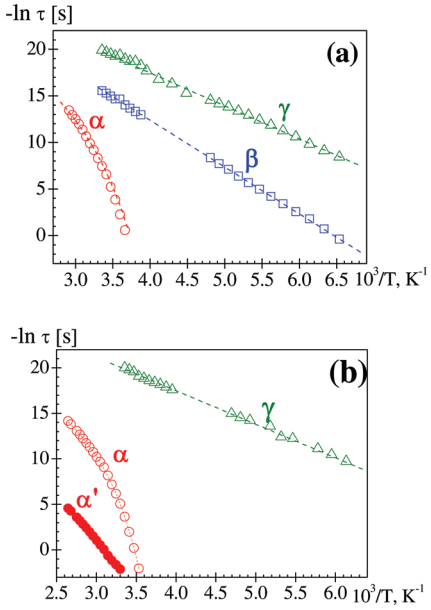


Figure 8. Arrhenius plots for the α' (full circles), α (open circles), β (square), and γ (triangles) relaxations for (a) PEOEMA and (b) CEOEMA.

The secondary relaxations are thermally activated processes and they obey Arrhenius behavior. The activation energies of the relaxations obtained from the slopes of Arrhenius plots are 41.6 ± 0.3 and 29.9 ± 0.4 kJ·mol^{-1} for the β and γ relaxations of PEOEMA. The activation energy of the unique secondary relaxation of CEOEMA is 30.1 ± 0.4 kJ·mol^{-1}. The fact that the activation energy of this relaxation is similar to that of the γ relaxation of PEOEMA suggests that the relaxation is also a γ process and so was labeled from the beginning.

The glass−rubber relaxation arises from segmental motions involving thermally activated conformational transitions depending on barrier potentials. As the system comes close to T_g, the free volume available to accommodate the conformations resulting from segmental motions is severely reduced in such a way that the time to complete relaxation undergoes a considerable increase, the α relaxation freezing at T_g. The temperature dependence of the relaxation times associated with the glass−rubber relaxation, presented in Figure 8 for PEOEMA and CEOEMA, is governed by the VFTH equation[31−33] which expressed in terms of the dimensionless fragility factor D_0[34−36] can be written as

$$\tau = \tau_0 \exp[D_0 T_V/(T - T_V)] \quad (4)$$

where the prefactor τ_0 is of the order of picoseconds, T_V is the Vogel temperature, i.e., the temperature at which hypothetically the excess entropy of the glassy system is nil and D_0 is respectively below and above 10 for fragile a strong glass forming liquids.

Comparison of eq 4. with the Doolittle equation, $\tau = \tau_0 \exp(\Phi/B)$, where Φ is the relative free volume and B is a parameter close to the unit, the ratio Φ/B at T_g[37,38] can be written as

$$\Phi_g/B = (T_g - T_V)/D_0 T_V \quad (5)$$

Moreover, the expansion coefficient at T_g is given by[39]

$$\alpha_f/B = (1/V)(\partial V/\partial T)_p/B = 1/D_0 T_V \quad (6)$$

The Vogel temperature, and the values at T_g of the fragility factor, relative free volume and the expansion coefficients for PEOEMA and CEOEMA are shown in Table 1. It can be seen

Table 1. Activation Energies and Prefactors of the Secondary Relaxation and Parameters of Vogel−Fulcher−Tammann−Hesse Equation $[\tau = \tau_0 \exp[D_0/(T/T_V) - 1]]$ for PEOEMA and CEOEMA

	sample	PEOEMA	CEOEMA
	$E_{\alpha\gamma}$ (kJ·mol^{-1})	29.9 ± 0.4	30.1 ± 0.4
	$-\ln \tau_{0,\gamma}$	32.0 ± 0.3	32.0 ± 0.2
	$E_{\alpha,\beta}$ (kJ·mol^{-1})	41.6 ± 0.3	—
	$-\ln \tau_{0,\beta}$	32.3 ± 0.2	—
α	$-\ln \tau_0$	25.3 ± 1.3	22.4 ± 0.2
	D_0	5.5 ± 0.4	5.2 ± 0.1
	T_v (K)	220.1 ± 3.4	233.6 ± 1.0
	ϕ_g/B (%)	4.0 ± 0.3	3.7 ± 0.1
	$\alpha_f \times 10^4$ (K^{-1})	8.3 ± 0.8	8.3 ± 0.2

that decreasing of the mobility of the chains by cross-linking hardly affects the values of these parameters.

The temperature dependence of the relaxation time associated with the α' process of CEOEMA is shown in Figure 8. Notice that the values of τ extend only over nearly half of the decades covered by the α relaxation. The relaxation times corresponding to the α' relaxation are larger than those associated with the α, though the divergence between them decreases as temperature increases. In spite of the fact that the data available for the relaxation times of the α' relaxation only cover a narrow span of temperature, an attempt at inspection of their temperature dependence suggests that both temperature and volume may intervenes in the development of the α' process.

The conductive contribution to the dielectric loss in eq 1 follows Arrhenius behavior as the plots of Figure 9 extending in the range of temperatures 0−105 °C, show. In general, the conductivity of CEOEMA is nearly three decades lower than that of PEOEMA, and the activation energies are 93.9 ± 1.2 and 122.9 ± 0.8 kJ·mol^{-1} for the former and latter systems, respectively.

dx.doi.org/10.1021/ma202811p | Macromolecules 2012, 45, 3571−3580

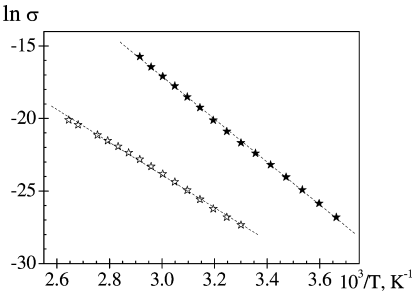


Figure 9. Arrhenius plot for the ionic conductivity, in S/m of PEOEMA (full star) and CEOEMA (open star).

4. DISCUSSION

A. Dipolar Relaxation Processes. Poly(*n*-alkyl methacrylates) with $n \geq 2$ are characterized for forming self-assembled alkyl domains, whose sizes depends on the side chains lengths, arising from aggregations of the side groups of different monomeric units. Heat capacity measurements carried out in these polymers present a two glass transition temperatures associated respectively with freezing of motions in within the alkyl domains (α_{PE}) and main chain dynamics.[20,40,41] The diffractogram patterns of WAXS and neutron-scattering spectra show two peaks respectively centered at $q \approx 5$ nm^{-1} (peak I) and 13.1 nm^{-1} (peak II). The value of q for peak I depends on the length of the *n*-alkyl group being 6, 5, and 4 nm^{-1} for poly(ethyl methacrylate), poly(buthyl methacrylate) and poly(hexyl methacrylate), respectively. The shifting of the peak to lower values of q with increasing alkyl length reflects main-chain correlations and therefore it is associated with average distance between the backbones. The value of q for peak II poly(*n*-alkyl methacrylate)s lies in the vicinity of 12−13 nm^{-1} and therefore the peak is thought to be correlated with average distances between side groups. With the aim to investigate whether main-chain and side-chain correlations still persist when a methyl group of the *n*-alkyl side chains are replaced by a methyl group, the WAXS diagrams of PEOEMA and CEOEMA were obtained. The diffractogram pattern of PEOEMA, presented in Figure 10, does not exhibit peak I, suggesting

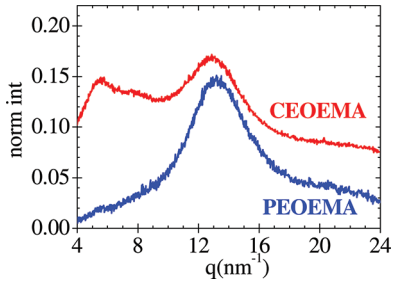


Figure 10. X-ray diffraction pattern for PEOEMA (blue) and CEOEMA (red).

that main-chain correlations are not important enough to be detectable. Only peak II, centered at $q \cong 12.8$ nm^{-1} remains, what means that segregation of side groups domains occurring in poly(*n*-butyl methacrylate) is absent in PEOEMA. However, the diffractogram of CEOEMA presents, in addition to the peak II that appears in PEOEMA ($q \cong 12.8$ nm^{-1}), a well-developed peak I centered at $q \cong 5.6$ nm^{-1}.

The similarity of the difractograms of CEOEMA and poly(*n*-alkyl methacrylates) suggests the existence of side-chains nanodomains in the cross-linked polymer flanked by the backbone, the average distance between the backbone being about 1.13 nm. It seems that cross-linking stabilizes the formation of the nanodomains. To explain this behavior it is necessary to remember that PEOEMA exhibits a great conformational versatility. The restriction that the formation of nanodoamins impose to the polymer segments to visit the whole conformational space, to which otherwise they would have access, involves a decrease of entropy ($\Delta S < 0$), which must be compensated by intermolecular interactions. Then the absence of nanodomains in PEOEMA is the result of the fact that $|\Delta H| < T|\Delta S|$, where ΔH is the change in enthalpy. Notice that ΔH is assumed to be negative. Owing to the fact that cross-linking decreases the conformational versatility of the chains, $T|\Delta S|$ for CEOEMA is smaller than in the case of PEOEMA in such a way that $|\Delta H_{\text{cross-linked}}| > T|\Delta S_{\text{cross-linked}}|$ and as a result the nanodomains in CEOEMA are stable. Finally, it should be pointed out that both the presence of a single endotherm in the DSC thermogram of CEOEMA and the symmetric nature of the α' relaxation rules out the possibility that the α' process is a glass−rubber relaxation.

Owing to the similarities of the reactivities of 2-ethoxyethyl methacrylate and ethyl dimethacrylate, CEOEMA can schematically be viewed as a network with statistically distributed molecules of cross-linking agent. Some portions of the chains may be flanked by cross-link points whereas others may appear as dangling chains. The fact that a single α relaxation appears suggests a rather effective cross-linking reaction. Cross-linking reduces the mobility of the chains and as a result the glass transition temperature of CEOEMA is nearly 10 °C above that of PEOEMA. The normalized α relaxation in the time domain for PEOEMA and CEOEMA was calculated from the retardation loss spectra[42,43] evaluated from the HN fit parameters by means of the following expression

$$\phi(t) = \frac{\int_{-\infty}^{\infty} L_{\alpha}(\ln \tau) e^{-t/\tau} \, d(\ln \tau)}{\int_{-\infty}^{\infty} L_{\alpha}(\ln \tau) \, d(\ln \tau)} \tag{7}$$

As usual, the function $\phi(t)$ is described by the KWW equation[44]

$$\phi(t) = \exp[-(t/\tau^*)^{\beta_{KWW}}] \tag{8}$$

where τ^* is a characteristic relaxation time and the stretch exponent (β_{KWW}) lies in the range 0−1. The KWW decay functions at different temperatures as well as the parameters that describe the functions are shown in Figure 11.

An inspection of the decay curves shows that contrary to what one would expect, the heterogeneity imposed in the system by cross-linking does not widen the distribution of relaxation times of the glass−rubber relaxation. In this regard, notice that at high temperature the values of β_{KWW} for CEOEMA are slightly larger than for PEOEMA.

The dynamic fragility factor describes the increase of the relaxation times as temperature comes closer to T_g. It is defined as[45,46]

$$m = \lim_{t \to \infty} \left(\frac{d(\log \tau)}{d(T_g/T)} \right) \tag{9}$$

A large dynamic parameter means that the temperature dependence of the glass−rubber relaxation comes closer to

dx.doi.org/10.1021/ma202811p | Macromolecules 2012, 45, 3571−3580

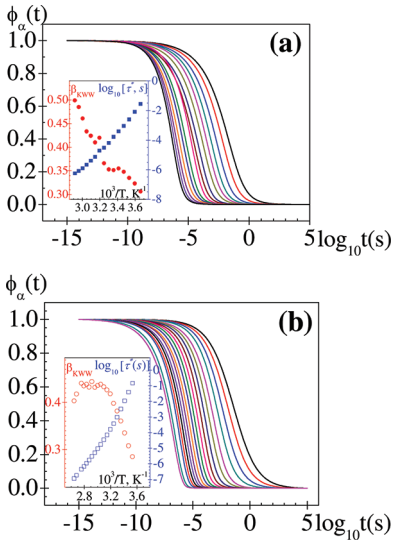


Figure 11. Normalized relaxation curves in the time domain for the α relaxation of (a) PEOEMA (273−343 K) and (b) CEOEMA (283−378 K). The decay curves are fitted by the KWW equation using the stretch exponents β_{KWW} and the characteristic relaxation times τ^* shown in the inset of the figure.

Arrhenius behavior. Taking T_g as reference and taking into account the VFTH equation

$$m = \frac{D_0 T_V}{2.303 T_g (1 - T_V/T_g)^2} \tag{10}$$

The values of m obtained for PEOEMA and CEOEMA are 61 and 74, respectively, indicating that a slight decrease in the chains mobility by effect of cross-linking produces a moderate increase in the dynamic fragility factor.

Local motions are reflected in the secondary relaxations. PEOEMA presents at high frequencies a γ relaxation presumably arising from motions of the side chains that change the orientation of the ether dipoles thus producing dielectric activity. At lower frequencies, a β relaxation appears that can be caused by combined motions of the ether and ester dipoles. It is worth noting that CEOEMA only exhibits the secondary γ relaxation. This fact suggests that the reduction in mobility caused by a slight cross-linking totally suppresses the β relaxation. This means that the β relaxation in PEOEMA may be produced by local motions of the backbone combined with motions of the side groups.

B). Interfacial and Electrode Polarization Processes. Interfacial polarization arising from the buildup of charges at the nanodomains interfaces may be responsible for the α' relaxation. Actually, transport of charges in the bulk over a considerable distance with respect to the atomic or segments produces the so-called Maxwell−Wagner−Sillars (MWS) relaxation.[47−49] This process has been reported for heterogeneous systems, i.e., silicone−polyester resins,[50] nylon/clay nanocomposites,[51−53] PZT fibers/epoxy resins,[54] polycarbonate/styrene−acrylonitrile multilayer composite,[55] amorphous−crystal interface in Nylon-1010,[56] etc. MWS relaxations were also reported for poly(dimethoxy benzyl methacrylate)s as a result of the heterogeneities produced in the melts by side chains segregations.[28] Although the symmetry of the α' relaxation, reflected in the fact that $b = 1$ in the Cole−Cole plot, fulfills one of the requirements of a MWS relaxation, the process is not described by a single relaxation time because a is close, but not equal, to 1. This suggests that the α' process is a distributed MWS relaxation produced by a variety of environments. The real component of the complex dielectric permittivity associated with the α' relaxation is well separated from both the dipolar relaxation in the high frequency region and EP processes at low frequencies. The separation is not so clear in the case of the dielectric loss. The relaxation can be interpreted by the Dyre model which assumes that charge transport in the bulk occurs by hopping of charge carriers in spatially varying random energy landscape.[57,58] According to the model

$$\varepsilon^*(\omega) = \varepsilon_0 + \frac{\sigma_0 \tau_e}{e_0 \ln(1 + \omega\tau_e)} \tag{11}$$

where ε_0 is the relaxed dielectric permittivity corresponding to the α relaxation, σ_0 the dc conductivity, e_0 the free space permittivity and τ_e. the time involved in overcoming the jump barrier in charge transport. Taking into account that $(1 + j\omega\tau_e) = (1 + \omega^2\tau_e^2)^{1/2} e^{j\tan^{-1}(\omega\tau_e)}$, the components of ε^* are given by

$$\varepsilon'(\omega) = \varepsilon_0 + \frac{1}{2}\frac{(\sigma_0/\varepsilon_0)\omega\tau_e \ln(1 + \omega^2\tau_e^2)}{(1/4)[\ln(1 + \omega^2\tau_e^2)]^2 + [\tan^{-1}(\omega\tau_e)]^2}$$

$$\varepsilon''(\omega) = \frac{1}{2}\frac{(\sigma_0/\varepsilon_0)\omega\tau_e \tan^{-1}(\omega\tau_e)}{(1/4)[\ln(1 + \omega^2\tau_e^2)]^2 + [\tan^{-1}(\omega\tau_e)]^2} \tag{12}$$

The parameters of the Dyre model were obtained at different temperatures by multiple nonlinear regression analysis of the values of ε' associated with the MWS relaxation. Figure 12 shows the Arrhenius plot for the values of $\omega_e = 1/\tau_e$ as well as

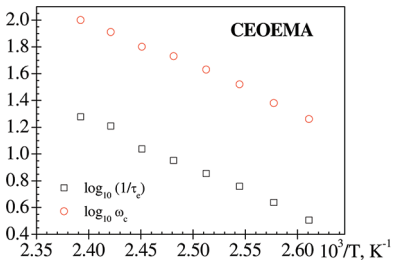


Figure 12. Arrhenius plots for the ω_c and $1/\tau_e$ parameters for CEOEMA.

the same plot for the critical frequency, ω_c, that describes the onset of the dispersion of the real component of the complex conductivity.

The values of ω_e and ω_c are rather close suggesting that they describe an identical underlying process, i.e. an electrical relaxation. However, owing to the rather narrow span of temperature covered by the experiments where ω_c and ω_e can be obtained, no definite conclusion can be reached regarding to whether these parameters are only thermally activated processes or whether they also depend on the volume. It should be noted that the temperature dependence of these parameters for ionic liquids over a wide span of temperature also depends on the volume.

dx.doi.org/10.1021/ma202811p | Macromolecules 2012, 45, 3571−3580

The increase observed in ε' at frequencies below those of the second plateau is caused by interfacial electrode-polymer polarization (EP) processes. These processes can be viewed as the result of relaxations of macrodipoles produced by charges located in the interface polymer−electrodes.[59] The charges proceed from impurities contained in solvents and chemical compounds used in the synthesis of the probes. The orientation of the macrodipole goes from the positive to the negative electrode. As shown in Figure 13, the EP process manifests

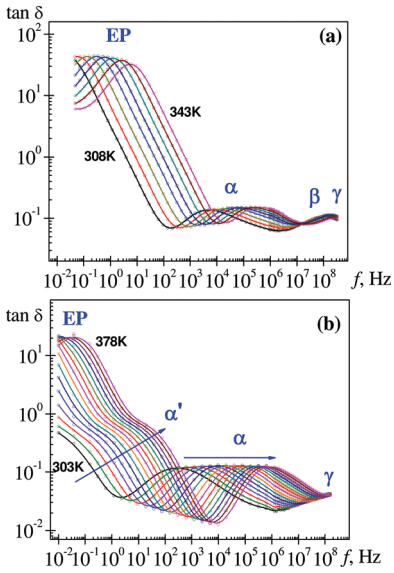


Figure 13. Loss tan δ in the frequency domain for (a) PEOEMA at 313−343 K and (b) CEOEMA at 303−373 K (at 5 K steps).

itself as a peak in tan δ isotherms in the frequency domain at very low frequencies. The peak is the result of the relaxation produced by the macrodipole following the electric field at very low frequencies.[60,61]

The macrodipole follows the electric field at low frequencies giving rise to a polarization process that can be represented by a Debye relaxation[62,63]

$$\varepsilon^*_{EP} = \varepsilon_r + \frac{\Delta\varepsilon_P}{1 + j\omega\tau_{EP}} \tag{13}$$

where ε_r is the value of ε' at the plateau of PEOEMA and the second plateau of CEOEMA, $\Delta\varepsilon_P = \varepsilon_{rEP} - \varepsilon_r$ where ε_{rEP} is the relaxed dielectric permittivity of the Debye process which according to the theory is related to the Debye length L_D by

$$\varepsilon_{rEP} = \varepsilon_r L/2L_D \tag{14}$$

where L is the thickness of the material sandwiched between the electrodes. By simplification of the expression obtained for tan δ_{EP} from eqs 13 and 14 (for details see the Supporting Information of ref 64), tan δ_{EP} can be written as

$$\tan\delta_{EP} = \frac{\omega\tau_{EP}}{1 + \omega^2{\tau_{EP}}^2(2L_D/L)} \tag{15}$$

where

$$\tau_{EP} = \frac{LF}{2\sigma}\left(\frac{e_0\varepsilon_r\sum_i z_i^2 c_i}{k_B T}\right)^{1/2} \tag{16}$$

In this expression F is the Faraday's constant, and z_i and c_i are respectively the valence and concentration of the ionic species i. The frequency at the peak maximum of tan δ_{EP} is given by

$$\omega_{max} = \frac{(L/2L_D)^{1/2}}{\tau_{EP}} \tag{17}$$

Then the value of tan δ_{EP} at the peak maximum is given by

$$\tan\delta_{EP} = \frac{1}{2}\left(\frac{L}{2D}\right)^{1/2} \tag{18}$$

Equations 16 and 17 in conjunction with the results for tan δ_{EP} in Figure 13 allow the estimation of the characteristic relaxation time τ_{EP} and Debye's length.

The variation of τ_{EP} with temperature for CEOEMA and PEOEMA are shown in Figure 14. It can be seen that the

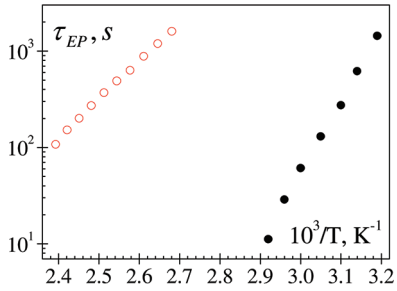


Figure 14. Temperature dependence of τ_{EP}(s) for PEOEMA (full symbols) and CEOEMA (open symbols).

characteristic time follows Arrhenius behavior with activation energy of 77.03 and 144.95 kJ·mol^{-1} for CEOEMA and PEOEMA. The results suggest that restrictions in chains mobility produced by cross-linking hinder the mechanism of charges transport in the polymer-electrodes interfaces.

The temperature dependence of Debye length, plotted in Figure 15, shows that L_D decreases as temperature increases for

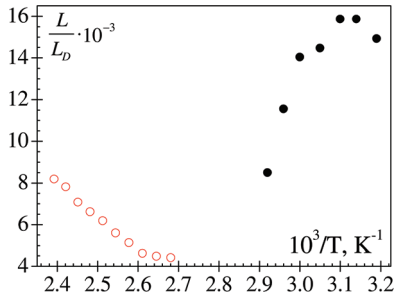


Figure 15. Temperature dependence of Debye length, $10^{-3}L/L_D$ for PEOEMA (full symbols) and CEOEMA (open symbols).

PEOEMA, while increases with temperature for CEOEMA. For example, L_D decreases from 600 to300 Å for PEOEMA when the temperature increases from 312 to 342 K. The value of L_D is higher for CEOEMA, but in this case this quantity decreases as temperature goes down, the change being from 2500 to 1250 Å when the temperature passes from 420 to 370 K. It is worth noting that temperature disrupts the electronic clouds surrounding ions and as a result L_D increases as temperature increases in very dilute electrolyte solutions. However, a decrease of the Debye's length with increasing temperature has been reported for some polymers.[65,66]

dx.doi.org/10.1021/ma202811p | Macromolecules 2012, 45, 3571−3580

The diffusion of ionic species in CEOEMA and PEOEMA can be roughly estimated by assuming that the diffusive species are monovalent. By taking into account that the concentrations of anions and cations are the same in this case, and expressing the conductivity in terms of the ionic mobility, μ_i, i.e., $\sigma = F\sum_i c_i\mu_i$, $i = +, -$, the geometric average of the diffusion coefficients of the ionic species can be written as

$$D_{\pm} = \frac{RT\sigma}{FC} \tag{19}$$

Notice that in the development of eq 19, use of the expression $\mu_i = FD_i/RT$ was made.

Arrhenius plots for $D_{\pm}$ of CEOEMA and PEOEMA, presented in Figure 16, show that the values of the ionic

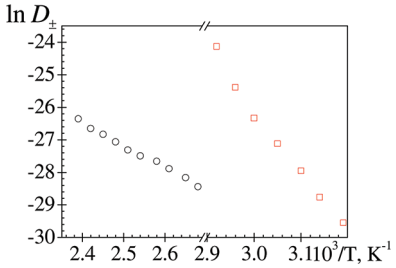


Figure 16. Temperature dependence of the geometric average diffusion coefficient of ionic species for PEOEMA (squares) and CEOEMA (circles).

diffusive coefficients corresponding to the latter polymer are higher than those corresponding to the cross-linked one. This means that reduction of the chains mobility by effect of cross-linking reduces ionic transport.

5. CONCLUSIONS

PEOEMA chains exhibit a well-developed γ absorption followed at lower frequencies by a weaker secondary β absorption. The fact that chains cross-linking eliminates the β relaxation suggests that whereas the γ absorption is associated with motions of the alcohol residue, the β relaxation presumably entails local motions of the backbone. In this context the β relaxation would be a Johari–Goldstein relaxation.[67,68]

Although cross-linking decreases the mobility of the chains, thus increasing the glass transition temperature, the temperature dependence of the stretching exponent of the glass–rubber relaxation suggests that cross-linking of the poly(2-ethoxy methacrylate) chains does not widen the distribution of relaxation times associated with this process.

Results have been reported in the literature showing the formation of side-chain nanodomains flanked by the backbone in poly(*n*-alkyl methacrylate)s. Cooperative motions in the nanodomains are reflected in an α_{PE} peak, in addition to the glass–rubber relaxation arising from cooperative motions of the backbone. The schematic replacement of one of the methylene groups of the side group of the repeat unit of poly(*n*-pentyl methacryate) for an ether group to yield poly(2-ethoxy methacrylate) chains eliminates the α_{PE} peak in this polymer. However, the fact that the X-rays pattern of slightly cross-linked poly(2-ethoxy methacrylate) is similar to that of poly(*n*-pentyl methacrylate), suggests the formation of nanodomains in these systems which give rise to a symmetric relaxation. We attribute this peak not to a cooperative process, but to a MWS relaxation arising from a long distance charge transport taking place in the bulk in heterogeneous systems.

Cross-linking seems to slowdown interfacial electrode–polymer processes.

AUTHOR INFORMATION

Notes

The authors declare no competing financial interest.

ACKNOWLEDGMENTS

We thank Dr. J. Guzman for providing us the CEOEMA sample. This work was financially supported by the DGCYT and CAM through the Grant MAT2008-06725-C03.

REFERENCES

(1) Mark, J. E., *Polymer Data Handbook*: Oxford University Press, Inc. 1999.
(2) Ishida, Y.; Yamafuji, K. *Kolloid Z.* **1961**, *177*, 97.
(3) Heijboer, J. In *Physics of Non-Crystalline Solids*; Prins, J. A., Ed.; North-Holland: Amsterdam, 1965;p 231.
(4) Sasabe, H.; Saito, S. *J. Polym. Sci.* **1968**, *A2–6*, 1401.
(5) Williams, G.; Watts, D. C. *Trans. Faraday Soc.* **1971**, *67*, 2793.
(6) Cowie, J. M. G. *J. Macromol. Sci., Part B* **1980**, *18* (4), 569–623.
(7) Gómez Ribelles, J. L.; Diaz-Calleja, R. *J. Polym. Sci.* **1985**, *23*, 1297.
(8) Diaz-Calleja, R.; Ribes Greus, A.; Gómez Ribelles, J. L. *Polymer* **1989**, *30*, 1433.
(9) Diaz-Calleja, R.; Ribes Greus, A.; Gómez Ribelles, J. L. *Polym. Commun.* **1989**, *30*, 270.
(10) Gómez Ribelles, J. L.; Ribes Greus, A.; Diaz-Calleja, R. *Polymer* **1990**, *31*, 223.
(11) McCrum, N. G.; Read, B. E.; Williams, G. In *Anelastic and Dielectric Effects in Polymeric Solids*; Dover: New York, 1991.
(12) Floudas, G.; Placke, P.; Stepanek, P.; Brown, W.; Fytas, G.; Ngai, K. L. *Macromolecules* **1995**, *28*, 6799.
(13) Meier, G.; Kremer, F.; Fytas, G.; Rizos, A. *J. Polym. Sci., Polym. Phys.* **1996**, *34*, 1391.
(14) Floudas, G.; Stepánek, P. *Macromolecules* **1998**, *31*, 6951–6957.
(15) Dudognon, E.; Bernès, A.; Lacabanne, C. *Macromolecules* **2001**, *34*, 3988–3992.
(16) Dudognon, E.; Bernès, A.; Lacabanne, C. *Macromolecules* **2002**, *35*, 5927–5931.
(17) Garwe, F.; Schönhals, A.; Beiner, M.; Schröter, K.; Donth, E. *J. Phys.: Condens. Matter* **1994**, *6*, 6941.
(18) Garwe, F.; Schönhals, A.; Lockwenz, H.; Beiner, M.; Schröter, K.; Donth, E. *Macromolecules* **1996**, *29*, 247–253.
(19) Schröter, K.; Unger, R.; Reissig, S.; Garwe, F.; Kahle, S.; Beiner, M.; Donth, E. *Macromolecules* **1998**, *31*, 8966.
(20) Arbe, A.; Genix, A.-C.; Arrese-Igor, S.; Colmenero, J.; Richter, D. *Macromolecules* **2010**, *43*, 3107–3119.
(21) Beiner, M.; Schröter, K.; Hempel, E.; Reissig, S.; Donth, E. *Macromolecules* **1999**, *32*, 6278.
(22) Beiner, M. *Macromol. Rapid Commun.* **2001**, *22*, 869.
(23) Beiner, M.; Kabisch, O.; Reichl, S.; Huth, H. *J. Non- Crystalline Solids* **2002**, *307*, 658.
(24) Hempel, E.; Beiner, M.; Huth, H.; Donth, E. *Thermochim. Acta* **2002**, *391*, 219.
(25) Beiner, M.; Huth, H. *Nat. Mater.* **2003**, *2*, 595.
(26) Hiller, S.; Pascui, O.; Kabisch, O.; Reichert, D.; Beiner, M. *New J. Phys.* **2004**, *6*, 10.
(27) Wind, M.; Graf, R.; Renker, S.; Spiess, H. W. *Macromol. Chem. Phys.* **2005**, *206*, 142–156.
(28) Sanchis, M. J.; Carsí, M.; Ortiz-Serna, P.; Domínguez-Espinosa, G.; Díaz-Calleja, R.; Riande, E.; Alegría, L.; Gargallo, L.; Radic, D. *Macromolecules* **2010**, *43*, 5723–5733.
(29) Cheng, P.; Driessen, A.; Tijsma, E.; Udipi, K. *J. Controlled Release* **2006**, *116* (2), e92–e94.

(30) Havriliak, S.; Havriliak, S. J., *Dielectric and Mechanical Relaxation in Materials*; Hanser: Munich, Germany, 1997; p 57.
(31) Vogel, H. *Z. Phys.* **1921**, *22*, 645.
(32) Fulcher, G. S. *J. Am. Ceram. Soc.* **1925**, *8*, 339.
(33) Tammann, G.; Hesse, W. *Z. Anorg. Allg. Chem.* **1926**, *156*, 245.
(34) Angell, C., A. In Complex Behavior of Glassy Systems; *Proceedings of the XIV Sitges Conference*; Sitges: Barcelona, Spain, 10−14 June 1996.
(35) Angell, C. A. in *Complex Behaviour of Glassy Systems*; Rubi, M.; Pérez-Vicente, C. Eds.; Springer: Berlin, 1997.
(36) Angell, C. A. *Science* **1995**, *262*, 1924.
(37) Doolittle, A. K. *J. Appl. Phys.* **1951**, *22*, 1471.
(38) Doolittle, A. K. *J. Appl. Phys.* **1952**, *23*, 236.
(39) Ferry, J. D. *Viscoelastic Properties of Polymers*, 2nd ed.; JohnWiley & Sons: New York, 1961.
(40) Hempel, E.; Beiner, M.; Huth, H.; Donth, E. *Thermochim. Acta* **2002**, *391*, 219−225.
(41) Hempel, E.; Huth, H.; Beiner, M. *Thermochim. Acta* **2003**, *403*, 105−114.
(42) Riande, E.; Díaz-Calleja, R., *Electrical Properties of Polymers*; Dekker: New York, 2004; Chapter 8.
(43) Kremer, F.; Schönhals, A. *In Broadband Dielectric Spectroscopy*; Springer: Berlin, 2003.
(44) Williams, G. *Adv. Polym. Sci.* **1979**, *33*, 60.
(45) Plazek, D. J.; Ngai, K. L. *Macromolecules* **1991**, *24*, 1222.
(46) Qin, Q.; McKenna, G. *J. Non-Cryst. Solids* **2006**, *352*, 2977.
(47) Maxwell, J. C., *Electricity and Magnetism*; Clarendon: Oxford, U.K., 1893.
(48) Wagner, K. W. *Arch. Elektrotech. (Berlin)* **1914**, *2*, 371.
(49) Sillars, R. W. *J. Inst. Electr. Eng. [1889−1940]* **1937**, *80*, 378.
(50) Arbe, A.; Genix, A.-C.; Colmenero, J.; Richter, D.; Fouquet, P. *Soft Matt.* **2008**, *4*, 1792.
(51) Perrier, G.; Bergeret, A. *J. Polym Sci: Part B: Polym Phys.* **1997**, *35*, 1349.
(52) Lee, Y-H.; Bur, A. J.; Roth, S. C.; Start, P. R. *Macromolecules* **2005**, *38*, 3828.
(53) Ortiz-Serna, P.; Díaz-Calleja, R.; Sanchis, M. J.; Riande, E.; Nunes, R.; Martins, A.; Visconte, L. *J. Non-Cryst. Solids* **2011**, *357*, 598−604.
(54) Hammami, H.; Arous, M.; Lagache, M.; Kallel, A. J. *All. Comp.* **2007**, *430*, 1.
(55) Daly, J. H.; Guest, M. J.; Hayward, D.; Pethrick, R. A. *J. Mater. Sci. Lett.* **1992**, *11*, 1271.
(56) Lu, H.; Zhang, X. J. *Macromol. Sci. Phys.* **2006**, *45*, 933.
(57) Dyre, J. C. *J. Phys. C: Solid State Phys.* **1986**, *19*, 5655.
(58) Dyre, J. C. *J. Appl. Phys.* **1988**, *64*, 5.
(59) Satti, G.; McLachlan, D. S. *J. Mater. Sci.* **2007**, *42*, 6477.
(60) Macdonald, J. R. *Phys. Rev.* **1953**, *92*, 4.
(61) Coelho, R. *J. Non-Cryst. Solids* **1991**, *131−133*, 1136.
(62) Coelho, R. *J. Non-Cryst. Solids* **1991**, *131−133*, 1136.
(63) Klein, R. J.; Zhang, S. H.; Dou, S.; Jones, B. H.; Colby, R. H.; Runt, J. *J. Chem. Phys.* **2006**, *124*, 144903.
(64) Sanchis, M. J.; Ortiz-Serna, P.; Carsí, M.; Díaz-Calleja, R.; Riande, E.; Gargallo, L.; Radić, D. *J. Phys. Chem. B* **2011**, *115*, 5730−5740.
(65) Compañ, V.; Sorensen, T. S.; Díaz-Calleja, R.; Riande, E. *J. Appl. Phys.* **1996**, *79*, 403.
(66) Compañ, V.; Guzmán, J.; Díaz-Calleja, R.; Riande, E. *J. Polym. Sci., Part B: Polym. Phys.* **1999**, *37*, 3027.
(67) Johari, G. P.; Goldstein, M. *J. Chem. Phys.* **1970**, *53*, 2372.
(68) Johari, G. P. *N. Y. Acad. Sci.* **1976**, *279*, 117.

Macromolecules

Article

pubs.acs.org/Macromolecules

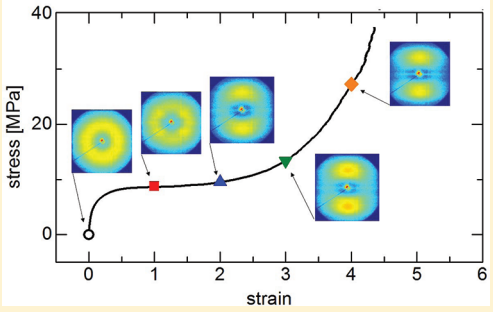
Microstructure and Segmental Dynamics of Polyurea under Uniaxial Deformation

Taeyi Choi,[†] Daniel Fragiadakis,[‡] C. Michael Roland,*[,‡] and James Runt*[,†]

[†]Department of Materials Science and Engineering, The Pennsylvania State University, University Park, Pennsylvania 16802, United States

[‡]Chemistry Division, Naval Research Laboratory, Code 6120, Washington, D.C. 20375, United States

ABSTRACT: Polyureas, formed by the rapid reaction between isocyanates and diamines, are attractive for various applications due to their outstanding mechanical properties, which can be tuned by varying component chemistry, molecular weight, and stoichiometry. Polyureas synthesized from a modified methylene diphenyl diisocyanate (Isonate 143 L) and polytetramethylene oxide-di-*p*-aminobenzoate (Versalink P1000) are widely utilized and investigated for energy absorbing applications such as impact mitigation and ballistic protection. In order to develop a more complete understanding of their mechanical response, we explore the effect of uniaxial strain on the phase separated microstructure and molecular dynamics. We utilize wide- and small-angle X-ray scattering to investigate amorphous segment and hard domain orientation, and broadband dielectric spectroscopy for interrogation of the dynamics. Uniaxial deformation was found to significantly perturb the phase-separated microstructure and chain orientation and result in a considerable slowing down and broadening of the polyurea soft phase segmental relaxation.



INTRODUCTION

Polyureas (PU) are formed from the reaction of isocyanates, usually based on diphenylmethane diisocyanate (MDI), with polyetheramines. The reaction is rapid with gel times measured in minutes, which means the reaction proceeds largely independently of ambient temperature and humidity, facilitating application of PU under diverse conditions. Polyureas have been used commercially since the early 1990s, with their processing and properties leading to widespread applications. In particular, the extensive hydrogen-bonding of PU leads to exceptional mechanical "toughness". Applications for PU include concrete coatings, repair of roofs and parking decks, and linears for storage tanks, freight ships, and truck beds. Prominent examples include the Boston tunnel project, the Incheon, Korea, airport, and the San Mateo, CA, bridge. PU coatings have also been found to mitigate the effects of bomb blasts on buildings by suppressing fragmentation, and thus have been applied to the Pentagon and various American embassies. A related application is the use of PU coatings as a means to up-armor military vehicles, such as the Humvee.

Reflecting the performance advantages of the material and the desire to further its application, there has been a large amount of experimental research lately aimed at better understanding the structure,[1] molecular dynamics,[2,3] mechanical properties[4−8] (especially at high strain rates), and performance as a coating for improving blast and impact resistance,[9−14] as well as efforts to create constitutive models[15,16] and sophisticated multiscale models[17] that predict the observed behaviors. The phase-separated microstructure of polyurea is crucial in determining molecular dynamics and mechanical properties, and its evolution during mechanical loading and unloading was recently studied by Rinaldi et al.[18] up to moderate strain.

The purpose of the present work was to determine how the structure of PU, its orientation, and the interaction of the phase domains, are affected by mechanical deformation. We employ X-ray scattering and dielectric relaxation spectroscopy to probe the changes in morphology and segmental dynamics brought about by extensional straining through the yield point up to failure. The polyurea selected for the study is used as an acoustic material on submarines, and is being explored as a protective barrier against impact and ballistic assault. We quantify the changes in structure and dynamics transpiring during deformation and their relationship to the strain history.

EXPERIMENTAL SECTION

The polyurea was formed by reaction of poly(tetramethylene oxide-di-*p*-aminobenzoate) (Versalink P1000, Air Products) and a polycarbodiimidemodified diphenylmethane diisocyanate (Isonate 143 L, Dow Chemical) at a 4:1 weight ratio. The molecular weight given by the manufacturer for the PTMO-amine component is M = 1238 ± 72 g/mol. The components were degassed under vacuum, mixed at 40 °C, and poured into a Teflon mold. Reaction was carried out at room temperature for 8 h, followed by an additional 12 h at 353 K.

Stress−strain measurements were carried out on an Instron 5500R with video extensometer; the nominal strain rate was 0.2 s^{-1}. Separate samples were held at 100%, 200%, 300%, and 400% strain until the

Received: January 18, 2012
Revised: March 26, 2012
Published: April 6, 2012

 © 2012 American Chemical Society

stress became constant, then clamped into aluminum frames and used for the X-ray scattering and dielectric spectroscopy experiments.

To investigate segment and hard domain orientations during uniaxial deformation, X-ray scattering experiments were conducted at two different length scales. To follow overall segment orientation, wide-angle X-ray diffraction (WAXD) patterns were measured on a Rigaku DMAX/rapid microdiffractometer in transmission mode, using a copper point-focused source (λ = 0.154 nm) at 50 kV and 40 mA. Small-angle X-ray scattering (SAXS) experiments were used to explore hard domain orientation and any changes in unlike segment mixing. The SAXS data were collected using a Molecular Metrology instrument with a Cu Kα radiation source (λ = 0.154 nm) at 45 kV and 66 mA, using a two-dimensional multiwire detector with a sample-to-detector distance of 1.5 m. Absolute scattered intensities were determined by comparing the spectra of the samples to that of a precalibrated, cross-linked polyethylene (S-2907) secondary standard.[19] SAXS and WAXD measurements were also conducted after specimens were relaxed for 24 h at ambient conditions in order to evaluate the extent of recovery after particular tensile strains.

Dielectric spectroscopy measurements were carried out using a parallel plate geometry with the sample in the form of a disk (15−20 mm diameter, 0.2−0.3 mm thick). Spectra were obtained as a function of temperature using a Novocontrol Alpha analyzer (10^{-2}−10^{6} Hz). The temperature was controlled using a Delta Design model 9023 oven. Both dry and hydrated samples were measured. For the former, samples were placed in a vacuum oven at 40 °C for several days, then quickly transferred to the test chamber and measured under dry nitrogen. "Hydrated" samples were exposed to saturated water vapor for several days prior to measurement. The final water content was 2.4, 2.6, 2.7, 2.9, and 3.2% for samples having respective strains of 0, 100, 200, 300, and 400% strain. In order to maintain constant water content, the hydrated samples were submerged in a fluorinated silicone oil during the dielectric measurements. It was verified that the presence of the oil did not significantly affect the measured spectra.

RESULTS AND DISCUSSION

Stress−Strain Behavior. Figure 1 shows a representative engineering stress−strain curve for the polyurea under investigation. Beyond an initial linear region, the material yields, with a long plateau of nearly constant stress, followed by a large upturn in stress prior to failure. The inset shows the permanent set (unrecovered strain) as a function of applied strain. This set is about 10% of the strain, becoming significant at applied strains exceeding 400%. The five points denoted in Figure 1 indicate the strains at which the structure and dynamics measurements were carried out; these correspond to the undeformed material, at the beginning and midpoint of the plateau, and at the initial and middle parts of the steep rise prior to failure, respectively.

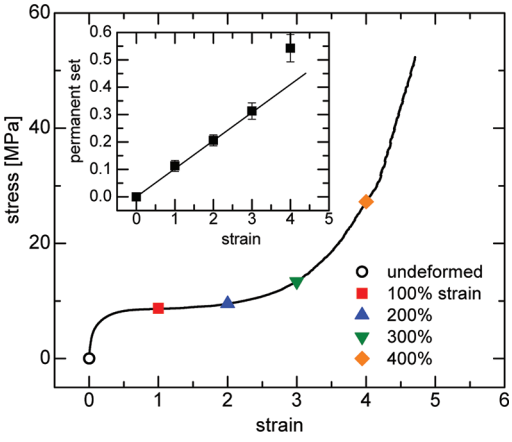


Figure 1. Representative stress−strain curve of polyurea under investigation. The points indicate the strains at which dielectric measurements were performed. Inset: permanent set (after relaxing to equilibrium) as a function of strain.

Chain Orientation: Wide-Angle X-ray Diffraction. The undeformed polyurea (Figure 2) exhibits predominately isotropic scattering, with slightly stronger scattered intensity on the equator, giving rise to a broad amorphous halo in the azimuthally averaged one-dimensional WAXD profiles shown in Figure 3. As the extension ratio increases, the scattered intensity becomes concentrated on the equator, indicating that the (amorphous) segments are increasingly oriented along the deformation direction.

2D X-ray diffraction patterns after relaxation from various strains are displayed in Figure 2. (The background color and contrast of the top and bottom row of Figure 2 are different, so only differences between the equators and meridians should be compared.) After relaxation, diffraction patterns have less equatorial intensity, indicating recovery of the aligned segments, although samples exposed to high strains (≥300%) exhibit some residual alignment and permanent deformation, consistent with the larger permanent set observed in Figure 1.

The corresponding azimuthally averaged scattered intensity profiles are displayed in Figure 3. Regardless of the extent of deformation, we only observe an amorphous halo at 2θ = 20° (4.4 Å), arising from the mean spacing between species, demonstrating that hard segments do not organize into a 3D crystalline structure under the deformation conditions employed herein.

To quantitatively evaluate the degree of segment orientation, the Hermans' orientation function (f_x) was calculated from the WAXD at angles between 2θ = 18−22° using[20,21]

$$f_x = \frac{3\langle \cos^2 \Phi \rangle - 1}{2} \tag{1}$$

$$\langle \cos^2 \Phi \rangle = \frac{\int_0^{90^\circ} I(\Phi) \sin \Phi \cos^2 \Phi \, d\Phi}{\int_0^{90^\circ} I(\Phi) \sin \Phi \, d\Phi} \tag{2}$$

where Φ is the azimuthal angle (equal to zero at the meridian and 90° at the equator). The function f_x varies from zero to unity for isotropic and perfect segment orientation, respectively. Orientation functions were also calculated in the same fashion from SAXS data. Figure 4 displays f_x vs uniaxial strain. With increasing strain (filled data points), f_x values increase from zero to 0.25 at 400% strain. After relaxation (open data points), f_x decreases significantly, for example, from 0.25 to 0.05 at 400% strain, demonstrating that most of the segment-level alignment is recovered after relaxation and that this phenomenon is dominated by soft segment relaxation.

Domain Orientation: Small-Angle X-ray Scattering. Two-dimensional SAXS patterns of deformed and relaxed samples (identical to those used in the WAXD experiments) at the various tensile strains are displayed in Figure 5. As expected, the undeformed material exhibits an isotropic scattering pattern. At 100% strain, a four-point intensity pattern along with two weaker reflections are observed, the scattering behavior arising due to shearing at the microdomain level, induced by the local torque exerted by the strained soft segments.[21−25] A similar four-point pattern was observed in deformed polyurea by

dx.doi.org/10.1021/ma300128d | Macromolecules 2012, 45, 3581−3589

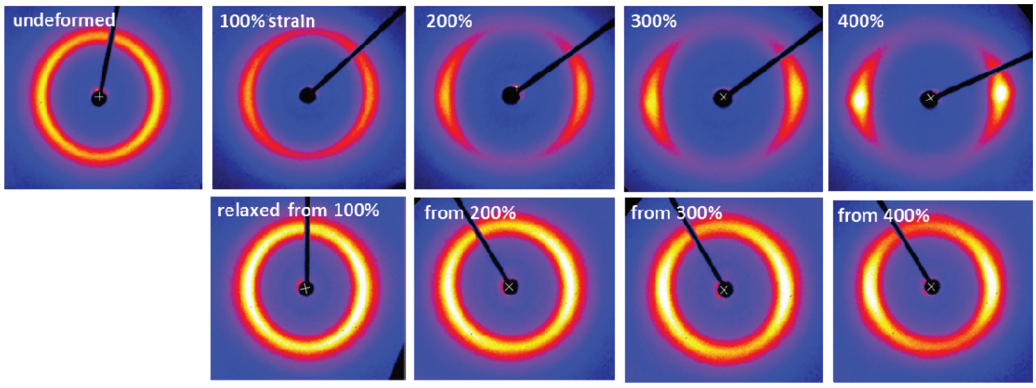


Figure 2. 2D WAXD patterns: (top row) undeformed polyurea and polyurea at 100%, 200%, 300% and 400% strain; (bottom row) polyureas after relaxation. The deformation direction is vertical.

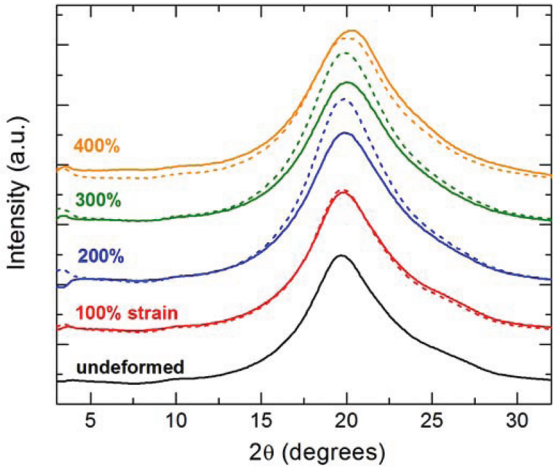


Figure 3. WAXD scattered intensity profiles as a function of 2θ (bottom to top): undeformed, 100%, 200%, 300%, and 400% strain. Key: solid lines, deformed samples; dashed lines, samples after relaxation.

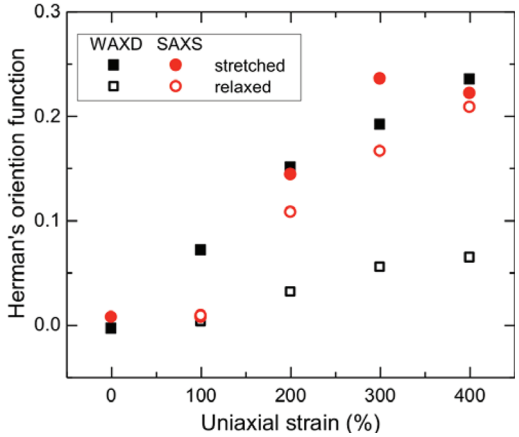


Figure 4. Hermans' orientation function for uniaxially deformed and relaxed polyureas: from WAXD measurements (squares) and from SAXS (circles).

Rinaldi et al.[18] The four and two-point patterns are seen clearly in Figure 6, which displays the angular intensity dependence vs azimuthal angle. At 100% strain, we observe a four point pattern with maxima at 55°, 125°, 235°, and 305°, and less intense reflections at 90° and 180°. At higher strains (≥200%), a meridional two-point scattering pattern emerges, arising from hard domain reorganization and orientation due to stress transferred from oriented soft segments.[21,25]

In addition to the strong scattered intensity on the meridian, streaks appear perpendicular to the stretching direction at 400% strain. Such behavior has been observed previously and ascribed to formation of nanofibrils on deformation.[21,24−26]

SAXS measurements were conducted on the identical samples after removing the tensile strain to characterize hard domain rearrangement. As displayed in Figure 5, for strains ≥200% significant scattering remains concentrated on the meridians after relaxation. The equatorial streaking for the 400% strained sample disappears after relaxation, illustrating that the nanofibrillar texture is not preserved on strain removal.

To quantify hard domain orientation, the Hermans' orientation factor from the SAXS data is plotted vs uniaxial strain in Figure 4. At strains ≥200%, f_x increases up to ∼0.2 and remains essentially constant after relaxation, indicating that hard domains are oriented (plastically deformed) at high strains, with negligible relaxation after removal of the strain. This is distinct from the substantial recovery at larger scale of oriented segments, as reflected in the WAXD analysis; clearly the latter is dominated by soft segments. Finally, the calculated orientation factor for the 100% strained sample is complicated by the hard domain reorganization at 100% strain, as seen in Figures 5 and 6, which is retained after relaxation.

Plots of azimuthally averaged absolute scattering intensities vs q before and after deformation are displayed in Figure 7. The mean interdomain spacing $(d = 2\pi/q_{max})$ and experimental electron density variances $(\overline{\Delta\eta^{2\prime}})$, which include the effects of intermixed segments and diffuse phase boundaries, are listed in Table 1. The variance is determined from the background corrected data[27] using

$$\overline{\Delta\eta^{2\prime}} = cQ = c\int \{I(q) - I_b(q)\}q^2\,dq \tag{3}$$

where Q is the invariant and the constant c is

$$c = \frac{1}{2\pi^2 i_e N_{av}{}^2} = 1.76 \times 10^{-24}\ \text{mol}^2/\text{cm}^2$$

The symbol i_e represents the Thompson's constant for the scattering from one electron (7.94×10^{-26} cm^2) and N_{av} is Avogadro's number.

In two-phase polyureas, the ratio of $\overline{\Delta\eta^{2\prime}}$ to the theoretical electron density variance for the case of complete unlike segment demixing $(\overline{\Delta\eta^{2\prime}}/\overline{\Delta\eta_c^{2}})$ provides a measure of the

dx.doi.org/10.1021/ma300128d | Macromolecules 2012, 45, 3581−3589

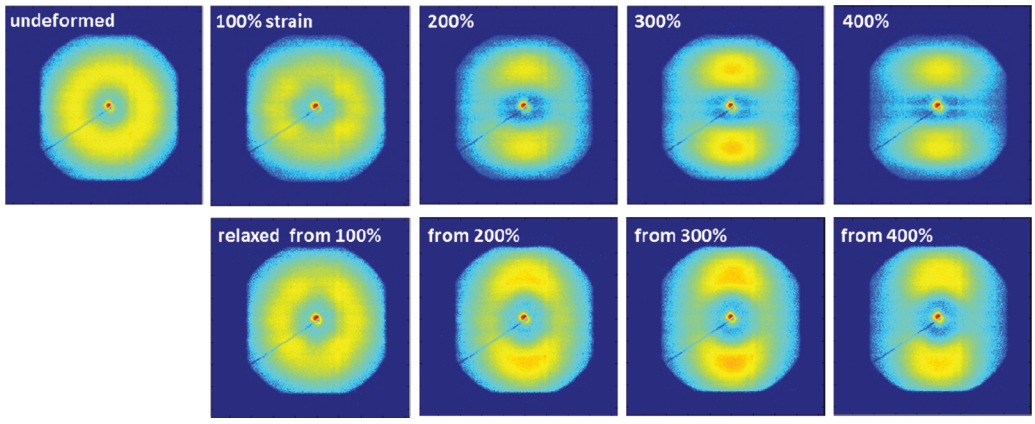


Figure 5. 2D SAXS patterns of polyurea: (top row) undeformed and deformed to various tensile strains; (bottom row) relaxed after deformation. Vertical deformation direction.

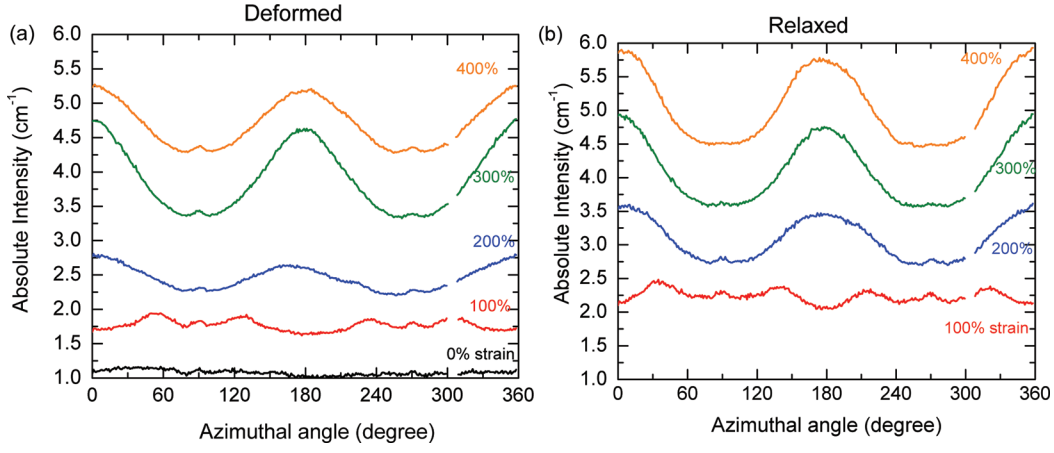


Figure 6. Background corrected absolute intensity plots vs azimuthal angle (a) under uniaxial deformation and (b) after relaxation. Curves have been shifted vertically for clarity by 1, 2, 3, and 4 cm^{-1} for 100%, 200%, 300%, and 400% strain, respectively.

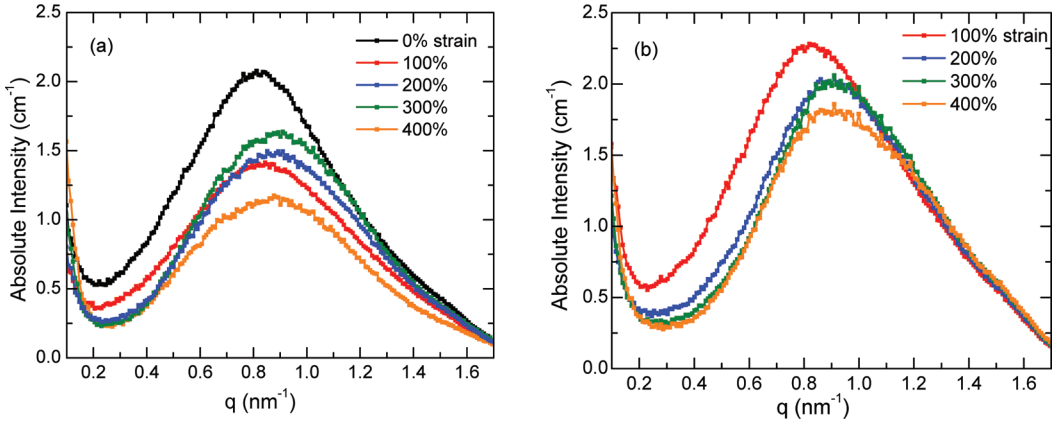


Figure 7. Background corrected absolute scattering intensity (azimuthally averaged) vs q (a) under uniaxial extension and (b) relaxed after deformation.

degree of microphase separation (equal to zero for complete mixing and unity for phase-separation without intermixing). The *hypothetical* electron density variance for a two-phase system ($\overline{\Delta\eta_c^2}$), assuming complete phase separation between hard and soft segments with sharp phase boundaries is given by[28]

$$\overline{\Delta\eta_c^2} = \phi_{hs}\phi_{ss}(\eta_{hs} - \eta_{ss})^2 = \phi_{hs}(1 - \phi_{hs})(\eta_{hs} - \eta_{ss})^2 \quad (4)$$

where ϕ_{hs} and ϕ_{ss} are the respective volume fractions of hard and soft segments in (hypothetical) completely phase-separated copolymers, and η_{hs} and η_{ss} are the corresponding electron densities. In our calculations of the completely demixed case, we assume that Isonate 143 L, polyurea linkages, and phenyl rings from the soft segment end groups comprise the hard phase, and the PTMO and two carbonate groups of the soft segments are in the soft phase. $\overline{\Delta\eta_c^2}$ is calculated based on

dx.doi.org/10.1021/ma300128d | *Macromolecules* 2012, 45, 3581−3589

Table 1. Mean Interdomain Spacing, Experimental Electron Density Variances, Boundary Size, and Variance Ratios for Microphase Separation, Boundary, and Intermixing Contributions to the Scattering from Deformed and Relaxed Polyureas

	$d = 2\pi/q_{max}$(nm)	$\overline{\Delta\eta^{2\prime}} \times 1000$ (mol e$^-$/cm^3)^2	degree of microphase separation $\overline{\Delta\eta^{2\prime}}/\overline{\Delta\eta_c^2}$	boundary size (σ, nm)	boundary diffuseness $\overline{\Delta\eta^{2\prime\prime}}/\overline{\Delta\eta^{2\prime}}-1$	intermixing within microphases $\overline{\Delta\eta_c^2}/\overline{\Delta\eta^{2\prime\prime}}-1$	phase separation (%)	boundary (%)	intermixing (%)
undeformed polyurea	7.4	2.11	0.38	0.54	0.74	0.52	38	36	26
				Deformed					
100% strain	7.4	1.44	0.26	0.54	0.94	1.00	26	36	38
200% strain	7.0	1.55	0.28	0.54	0.95	0.85	28	38	34
300% strain	7.0	1.63	0.29	0.53	0.96	0.74	29	40	31
400% strain	7.2	1.14	0.20	0.52	0.96	1.50	20	31	49
				Relaxed					
100% strain	7.7	2.30	0.41	0.55	0.94	0.25	41	46	12
200% strain	6.9	2.15	0.39	0.55	1.01	0.29	39	48	14
300% strain	6.9	2.16	0.39	0.55	1.06	0.25	39	50	12
400% strain	6.9	2.04	0.37	0.55	1.09	0.30	37	50	14

100% stoichoimetry of amine and isocyanate (4:1 weight ratio) using 144.5 g equiv weight for the isocyante and a functionality of Isonate 143 $L = 2.1$, as reported by the manufacturer.[29] Since $\overline{\Delta\eta_c^2}$ is calculated using the chemical composition of the polyurea, the theoretical value is the same for all samples in this study; $\overline{\Delta\eta_c^2} \times 1000 = 5.57$ (mol e$^-$/cm^3)^2.

Interface boundary diffuseness and segment intermixing can also be determined from the SAXS data as follows. With the assumption of a sigmoidal-gradient for the interface, the background corrected scattering intensity (in absolute units) is given by[20,30]

$$\begin{aligned} I_{obs}(q) &= I(q) - I_b(q) \\ &= I_{id}(q)H^2(q) \\ &= I_{id}(q)\exp(-\sigma^2q^2) \\ &= I_{id}(q)(1 - \sigma^2q^2) \end{aligned} \tag{5}$$

at large q, where $I_{id}(q)$ is the ideal scattering intensity, $H(q)$ is the Fourier transform of a smoothing function characterizing the shape and size of the diffuse boundaries, and σ is the diffuse boundary layer length. Because the ideal scattering intensity obeys Porod law's,[30] eq 5 can be written as:

$$I_{obs}(q) = \frac{K}{q^4}(1 - \sigma^2q^2) \tag{6}$$

Therefore, for data in the form of $q^4I(q)$ vs q^2, σ is obtained from the slope ($K\sigma^2$) and y-intercept (K) at larger q (see Table 1).

A second electron density variance ($\overline{\Delta\eta^{2\prime\prime}}$) can be calculated that removes the contribution to the scattering from diffuse boundaries.[28] $\overline{\Delta\eta^{2\prime\prime}}$ is defined as[27]

$$\overline{\Delta\eta^{2\prime\prime}} = c\int_0^\infty \frac{[(I(q) - I_b(q)]q^2}{H^2(q)}\,dq \tag{7}$$

where $H(q) = \exp((-(\sigma^2q^2)/2))$. The quantity $[\overline{\Delta\eta^{2\prime\prime}}/\overline{\Delta\eta^{2\prime}} - 1]$ is a measure of the boundary diffuseness, and similarly $[\overline{\Delta\eta_c^2}/\overline{\Delta\eta^{2\prime\prime}} - 1]$ provides a measure of the influence of intermixed segments on overall phase separation.

Values of these three ratios are displayed in Table 1. The final three columns in the table describe the findings in a somewhat different fashion. For the undeformed polyurea, $\overline{\Delta\eta^{2\prime}}/\overline{\Delta\eta_c^2} = 0.38$ (i.e., 38% phase separation). The relative contribution of the diffuse interface to the scattered intensity is 36%. The remainder of the deviation from $\overline{\Delta\eta_c^2}$, 26%, we attribute to unlike segment mixing within the microphases.

As seen in Table 1, the mean spacing between hard domains is 7 nm for all samples, regardless of deformation or relaxation. The value of σ (~0.55 nm) is also the same for all conditions; this quantity represents the standard deviation of the Gaussian function used in the sigmoidal-gradient model. This corresponds to 1.9 nm for the boundary layer thickness ($(12)^{1/2}\sigma$) in the easier to visualize but less physically realistic linear-gradient model.[30]

With increasing strain, intersegment microphase separation is significantly reduced, so that the intermixing contribution to the scattering increases. The boundary contribution is the same within experimental uncertainty for the undeformed and strained materials, except for the case of 400% strain where the boundary contribution decreases somewhat.[31] It is rather likely that hard domains consist of hard segments with little or no soft segments due to the strong interurea bidentate hydrogen bonding formed upon hard segment segregation. Therefore, the physical picture that emerges is hard domain orientation and disruption on straining polyurea to substantial levels, causing hard segments to become increasingly associated with the soft phase.

After relaxation for 24 h, all previously strained samples exhibit a similar level of microphase separation as the undeformed sample, indicating that hard segments rearrange significantly during relaxation. In addition, relaxation leads to an increase in the diffuse boundary contribution to the scattering, and a corresponding lower degree of unlike segment mixing. However, as demonstrated by the 2D SAXS results, the hard domains after relaxation retain substantial orientation after their deformation by the applied strain.

Segmental Dynamics. There have been several investigations of the effect of mechanical strain on the segmental dynamics of polymers, using dynamic mechanical[32−34] and broadband dielectric spectroscopies.[35−39] In single phase elastomers, strain has been observed to have no effect,[34,37] to speed up,[32] or to slow down[35,36] segmental relaxation, with even a nonmonotonic response to strain reported.[33] These effects have been rationalized in terms of two competing effects: the decrease of configurational entropy due to chain orientation leading to longer relaxation times, and a small decrease of density (due to

dx.doi.org/10.1021/ma300128d | Macromolecules 2012, 45, 3581−3589

the small, but finite compressibility) tending to speed up the dynamics. However, these effects are generally small, if observed at all, corresponding to changes of the glass transition temperature of a few degrees or less. Thermoplastic elastomers, on the other hand, can show very large effects of strain on their dynamics. We recently studied the effects of strain on the dynamics of a polyurethane based on poly(tetramethylene oxide) soft segments and MDI/1,4-butanediol hard segments, which has similarities to the present polyurea material. The polyurethane self-assembles into a morphology consisting of quasi-spherical hard domains embedded in a soft matrix,[40] compared to the highly elongated hard domains of the polyurea studied herein[41] and some other polyureas.[42] With increasing strain, the soft segment α-relaxation of the polyurethane becomes significantly slower and weaker, with a broader distribution of relaxation times.[43]

In Figure 8 are shown dielectric spectra of dry and hydrated polyurea, both unstretched and at the maximum studied strain (400%) at a representative temperature (298 K). In the temperature range studied, the chain segments in the hard domains are immobile, so that the loss peaks are due to the segmental dynamics of the soft phase. The apparent increase in the loss at low frequencies is due to a combination of dc conductivity, interfacial polarization (i.e., mobile ions trapped at the interfaces between hard and soft domains), and possibly other relaxation modes such as local motion of the hard segments.[44]

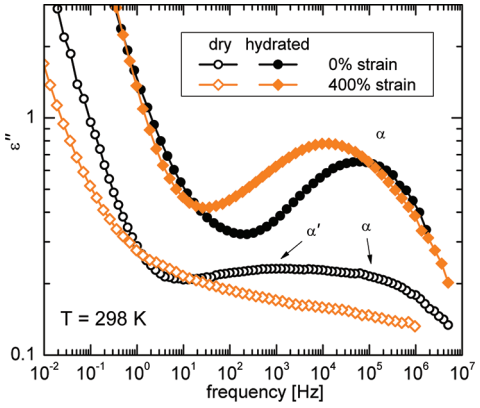


Figure 8. Dielectric loss spectra of dry (open symbols) and hydrated (filled symbols) polyurea at 298 K, undeformed and at 400% strain.

In the unstretched, dry polyurea, a very broad double peak is observed. On the basis of the behavior when changing stoichiometry, temperature, or pressure, we previously attributed the lower-frequency component (α' process) to segmental relaxation of the soft phase in the interfacial regions between the soft and hard domains, while the primary, higher-frequency component was ascribed to segmental relaxation in the soft phase distant from interfaces.[3] With increasing water content the two components combine into a single α-peak. This process reflects the overall segmental dynamics of the soft phase (slightly plasticized compared to the dry polyurea) and the temperature for which τ_α = 100 s roughly corresponds to the calorimetric glass transition temperature.[3]

At high strains, the segmental relaxation of the dry polyurea moves to lower frequency, broadens, and exhibits much weaker intensity; the peak becomes obscured by the background loss and cannot be further analyzed. In the hydrated sample, the segmental relaxation moves to lower frequencies but remains prominent even at high strains. Therefore, in the following, we show dielectric data only for hydrated samples under strain.

Figure 9 shows dielectric loss spectra of hydrated polyurea at 273 K at different static strains. With increasing extension, the peak moves systematically toward lower frequencies, and becomes more intense and broader. The increased amplitude of the peak in the hydrated sample is opposite to the behavior observed in the dry samples. However, it should not be attributed to increased mobility, but rather to the increase in equilibrium water content with increased strain (from 2.4% in the undeformed sample to 3.2% at 400% strain), since the intensity of the soft segment α-relaxation increases very strongly with increasing water content.[3] This increased hydration presumably arises due to the breakup of hard segments, effected by H-bond breakage between the urea segments, thus exposing additional, highly polar, hydration sites.

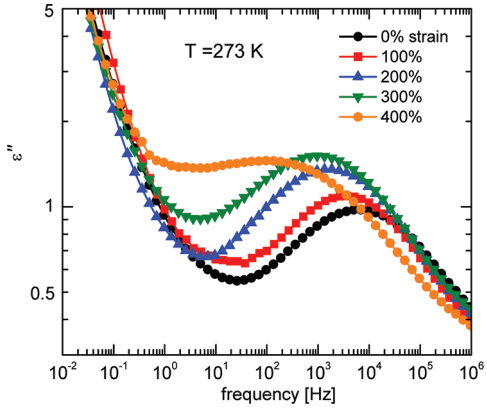


Figure 9. Dielectric spectra of hydrated polyurea at 273 K under uniaxial deformation. With increasing strain, the segmental relaxation peak moves to lower frequencies and broadens.

We fit the dielectric spectra to a sum of a Havriliak–Negami function[45] for the segmental process and a power law for the low-frequency loss:

$$\varepsilon^*(f) = \varepsilon_\infty + \frac{\Delta\varepsilon}{[1 + (if/f_{HN})^a]^b} + \frac{\sigma}{if^n}$$

where ε_∞ is the infinite frequency dielectric constant, $\Delta\varepsilon$ the intensity of the relaxation (contribution to the static dielectric constant), a and b are shape parameters, with $a, b > 0$ and $a < 1$, $ab \leq 1$, σ and n are temperature-dependent constants, and f_{HN} is related to the frequency of maximum loss $f_{max} = 1/(2\pi\tau_a)$ by

$$f_{max} = f_{HN}\left(\frac{\sin(\pi a/(2 + 2b))}{\sin(\pi ab/(2 + 2b))}\right)^{1/a}$$

Segmental relaxation frequencies are plotted against temperature in Figure 10. The α relaxation becomes slower with increasing strain over the entire frequency range; however, the effect is stronger close to T_g, as the curves converge at high temperatures. The relaxation times are well described over the measured range by the Vogel–Fulcher function.[46−48]

$$f_{max} = f_0 \exp\left(-\frac{B}{T - T_0}\right) \quad (8)$$

where T_0 (Vogel temperature), f_0, and B are constants. The parameters of eq 8 are listed in Table 2, along with the dynamic

dx.doi.org/10.1021/ma300128d | Macromolecules 2012, 45, 3581−3589

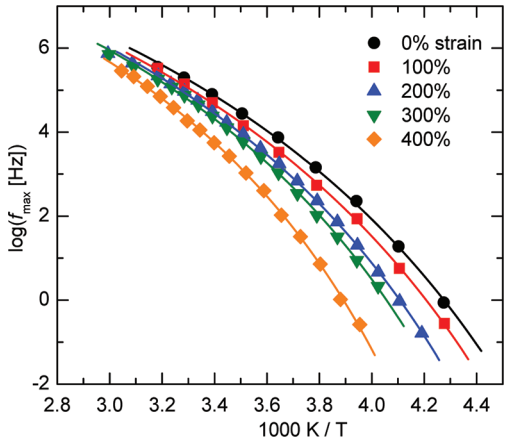


Figure 10. Segmental relaxation times of polyurea under uniaxial deformation. Lines are fits to the Vogel–Fulcher equation.

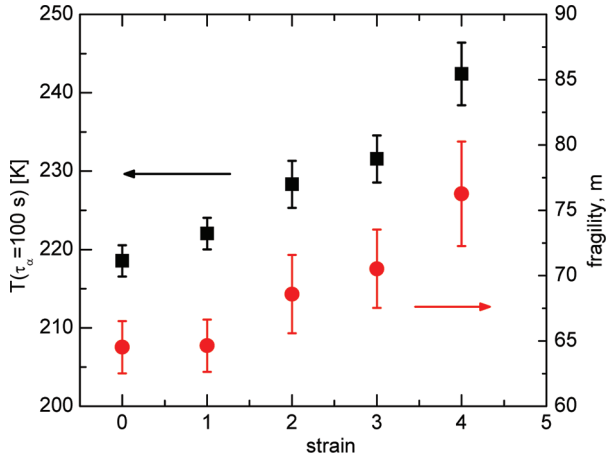


Figure 11. Glass transition temperature and fragility of uniaxially deformed polyurea (defined as the temperature where the segmental relaxation time is 100 s) as a function of applied strain.

glass transition temperature (defined as the temperature at which τ_a = 100 s). Strain has no effect on f_0, but significantly with decreasing temperature, as is usual for glass-forming systems. At constant temperature, the peak broadens with increasing strain. However, plotting the peak width against τ_α collapses the curves except for the highest (400%) strain. Therefore, the broadening at constant temperature at strains up to 300% is due only to the strain-induced shift toward lower frequencies, whereas at 400% strain the distribution of relaxation times actually broadens significantly. The breadth of the distribution of relaxation times reflects heterogeneity; both the dynamic heterogeneity inherent to the supercooled dynamics of liquids and polymers, and an additional contribution from the structural heterogeneity of the local chain environments; i.e., regions with different composition have different restrictions imposed on their motions by neighboring hard domains. With increasing strain, despite mixing of hard segments into the soft phase, this structural heterogeneity does not appear to change substantially below 400% strain.

Table 2. Parameters of Equation 8, Glass Transition Temperatures (Defined as the Temperature Where τ = 100 s) and Fragilities for Hydrated Deformed Polyurea

strain	log(f_0 / Hz)	B [K]	T_0 [K]	T_g [K]	m
undeformed polyurea	10.1	1506	71.2	218.6	64
100% strain	10.2	1603	169.4	222.0	65
200% strain	10.4	1638	175.5	228.3	69
300% strain	10.7	1754	175.9	231.5	71
400% strain	11.1	1894	183.2	242.4	76

increases T_g. Given the increased water content at higher strain, we might expect the material to be more plasticized at larger strains (although the effect would be minor); therefore, if compared at equivalent water content, the increase in T_g with strain may in fact be even larger. At 400% T_g is more than 20 K higher than for the undeformed sample. Also listed in Table 2 and plotted in Figure 11 is the fragility, defined as[49]

$$m = \left.\frac{\mathrm{d}(\log \tau)}{\mathrm{d}(T_0/T)}\right|_{T=T_g}$$

The fragility quantifies the non-Arrhenius character of the temperature dependence of τ_α; a stronger deviation from Arrhenius behavior corresponds to a more fragile system. With increasing strain, relaxation times become more sensitive to temperature, and the fragility increases. A similar strain dependence of T_g and m was observed for uniaxially oriented polyurethane.[43] The increased fragility with strain fits the general, albeit weak, correlation of fragility with T_g.[50] Fragility has been demonstrated to increase with increasing chemical cross-linking,[51,52] as well as intermolecular hydrogen bonding,[53] so the increase observed herein is consistent with greater constraints imposed on the soft segment motion due to more intimate association with hard segments. The latter contains some trifunctional units (chemical cross-links), as well as urea groups capable of forming hydrogen bonds with the ether oxygen atoms on the soft segments.

Figure 12 shows the full width at half-maximum of the segmental relaxation, quantifying the breadth of the distribution of relaxation times. The segmental process becomes broader

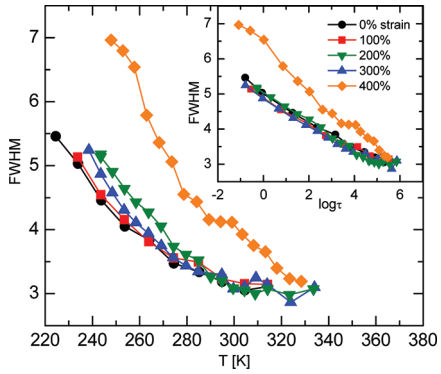


Figure 12. Full width at half-maximum of the segmental relaxation of uniaxially deformed polyurea as a function of temperature (also plotted as a function of segmental relaxation time in the inset).

SUMMARY

Previously it was shown that while high strain rates induce primarily an elastic response, with only modest permanent changes in morphology and sample dimensions, the situation is quite different for slow extension of elastomeric polyurea.[1] In this work, we examined the detailed dependence of the latter on the magnitude of the deformation. In the neo-Hookean

dx.doi.org/10.1021/ma300128d | Macromolecules 2012, 45, 3581–3589

region there is no permanent effect of strain, whereas deformations beyond the yield stress gives rise to unrecovered strain and orientation of the domains, along with disruption of the hard domains with consequent reduction in the degree of phase segregation. These morphological changes, in turn, cause significant slowing down of the segmental dynamics and broadening of its distribution of relaxation times and a large increase of apparent activation energy (fragility). The extent of these changes in the material varies continuously over the course of the deformation.

Polyurea is unrivaled in terms of the complexity of its mechanical behavior; nevertheless, extensive efforts have been made to model polyureas, particularly for impact applications.[15−18] As is generally the case for elastomers, the modeling efforts usually rely on assumptions of separability between strain and strain rate effects. Certainly this assumption breaks down at strain rates sufficient for the rubber to undergo a viscoelastic transition to the glassy state.[7] However, the present results demonstrate that even at very slow rates, the material *per se* and thus its mechanical response vary continuously over the course of deformation. Thus, realistic modeling of polyurea requires consideration of the instantaneous state of the morphology, which is convoluted with other factors such as strain nonlinearity, viscoelasticity, as well as other factors such as the effect of hydrostatic pressure and absorbed moisture.[2,3]

AUTHOR INFORMATION

Corresponding Author

*E-mail: (J.R.) runt@matse.psu.edu; (C.M.R.) mike.roland@nrl.navy.mil.

Notes

The authors declare no competing financial interest.

ACKNOWLEDGMENTS

T.C. and J.R. gratefully acknowledge the National Science Foundation, Polymers Program, under Grant DMR-0907139 and the Office of Naval Research Contract Number 4036-CU-ONR-1125 for their support of this research. D.F. acknowledges a postdoctoral fellowship from the National Research Council. The work at NRL was supported by the Office of Naval Research, Code 331.

REFERENCES

(1) Pathak, J. A.; Twigg, J. N.; Nugent, K. E.; Ho, D. L.; Lin, E. K.; Mott, P. H.; Robertson, C. G.; Vukmir, M. K.; Epps, T. H. III; Roland, C. M. *Macromolecules* **2008**, *41*, 7543−7548.

(2) Roland, C. M.; Casalini, R. *Polymer* **2007**, *48*, 5747−5752.

(3) Fragiadakis, D.; Gamache, R.; Bogoslovov, R. B.; Roland, C. M. *Polymer* **2010**, *51*, 178−184.

(4) Roland, C. M.; Casalini, R. *Polymer* **2007**, *48*, 5747−5752.

(5) Shim, J.; Mohr, D. *Int. J. Impact Eng.* **2009**, *36*, 1116−1127.

(6) Yi, J.; Boyce, M. C.; Lee, G. F.; Balizer, E. *Polymer* **2006**, *47*, 319−329.

(7) Bogoslovov, R. B.; Roland, M. *J. Appl. Phys.* **2007**, *102*, 063531.

(8) Sarva, S. S.; Deschanel, S.; Boyce, M. C.; Chen, W. *Polymer* **2007**, *48*, 2208−2213.

(9) Xue, L.; Mock, W. Jr.; Belytschko, T. *Mech. Mater.* **2010**, *42*, 981−1003.

(10) Bogoslovov, R. B.; Roland, C. M.; Gamache, R. M. *Appl. Phys. Lett.* **2007**, *90*, No. in press.

(11) Tekalur, S. A.; Shukla, A.; Shivakumar, K. *Compos. Struct.* **2008**, *84*, 271−281.

(12) Davidson, J. S.; Fisher, J. W.; Hammons, M. I.; Porter, J. R.; Dinan, R. J. *J. Struct. Eng.—ASCE* **2005**, *131*, 1194−1205.

(13) Jiao, T.; Clifton, R. J.; Grunschel, S. E. High strain rate response of an elastomer. In *Shock Compression of Condensed Matter—2005, Parts 1 and 2*; 2006; Vol. *845*, pp 809−812.

(14) Roland, C. M.; Fragiadakis, D.; Gamache, R. M. *Compos. Struct.* **2010**, *92*, 1059−1064.

(15) Shim, J.; Mohr, D. *Int. J. Plast.* **2011**, *27*, 868−886.

(16) Amirkhizi, A. V.; Isaacs, J.; McGee, J.; Nemat-Nasser, S. *Philos. Mag.* **2006**, *86*, 5847−5866.

(17) Grujicic, M.; Pandurangan, B.; King, A. E.; Runt, J.; Tarter, J.; Dillon, G. *J. Mater. Sci.* **2011**, *46*, 1767−1779.

(18) Rinaldi, R. G.; Boyce, M. C.; Weigand, S. J.; Londono, D. J.; Guise, M. W. *J. Polym. Sci., Part B: Polym. Phys.* **2011**, *49*, 1660−1671.

(19) Russell, T. P.; Lin, J. S.; Spooner, S.; Wignall, G. D. *J. Appl. Crystallogr.* **1988**, *21*, 629−638.

(20) Roe, R. J. *Methods of X-ray and Neutron Scattering in Polymer Science*; Oxford University Press: New York, 2000.

(21) Yeh, F.; Hsiao, B. S.; Sauer, B. B.; Michel, S.; Siesler, H. W. *Macromolecules* **2003**, *36*, 1940−1954.

(22) Bonart, R.; Morbitze., L.; Hentze, G. *J. Macromol. Sci.—Phys.* **1969**, *B3*, 337.

(23) Bonart, R. *J. Macromol. Sci., Part B* **1968**, *2*, 115−38.

(24) Desper, C. R.; Schneider, N. S.; Jasinski, J. P.; Lin, J. S. *Macromolecules* **1985**, *18*, 2755−2761.

(25) Waletzko, R. S.; Korley, L. T. J.; Pate, B. D.; Thomas, E. L.; Hammond, P. T. *Macromolecules* **2009**, *42*, 2041−2053.

(26) Ran, S. F.; Fang, D. F.; Sics, I.; Toki, S.; Hsiao, B. S.; Chu, B. *Rev. Sci. Instrum.* **2003**, *74*, 3087−3092.

(27) Garrett, J. T.; Runt, J.; Lin, J. S. *Macromolecules* **2000**, *33*, 6353−6359.

(28) Bonart, R.; Muller, E. H. *J. Macromol. Sci.—Phys.* **1974**, *B10*, 177−189.

(29) Polyols & Isocyanates for Coating, Adhesive, Sealant and Elastomer Applications in North America, Dow Chemical, 2009, http://www.dow.com/polyurethane/na/pdfs/109-01823.pdf

(30) Koberstein, J. T.; Morra, B.; Stein, R. S. *J. Appl. Crystallogr.* **1980**, *13*, 34−45.

(31) Sonnenschein, M. F.; Prange, R.; Schrock, A. K. *Polymer* **2007**, *48*, 616−623.

(32) Diaz-Calleja, R.; Riande, E.; Guzman, J. *Polymer* **1987**, *28*, 2190−2194.

(33) Riande, E.; Guzman, J.; Llorente, M. A. *J. Polym. Sci., Part B: Polym. Phys.* **1983**, *21*, 2473−2482.

(34) Munch, E.; Pelletier, J. M.; Sixou, B.; Vigier, G. *Polymer* **2006**, *47*, 3477−3485.

(35) Naoki, M.; Nakajima, K.; Nose, T.; Hata, T. *Polym. J.* **1974**, *6*, 283−294.

(36) Nakajima, K.; Naoki, M.; Nose, T. *Polym. J.* **1978**, *10*, 307−314.

(37) Adachi, H.; Adachi, K.; Kotaka, T. *Polym. J.* **1980**, *12*, 329−334.

(38) Diaz-Calleja, R.; Riande, E.; Guzman, J. *J. Polym. Sci., Part B: Polym. Phys.* **1990**, *28*, 1551−1563.

(39) Hernandez, M.; Lopez-Manchado, M. A.; Sanz, A.; Nogales, A.; Ezquerra, T. A. *Macromolecules* **2011**, *44*, 6574−6580.

(40) Hernandez, R.; Weksler, J.; Padsalgikar, A.; Choi, T.; Angelo, E.; Lin, J. S.; Xu, L.-C.; Siedlecki, C. A.; Runt, J. *Macromolecules* **2008**, *41*, 9767−9776.

(41) Castagna, A.; Dillon, G.; Runt, J. Manuscript in preparation.

(42) Das, S.; Yilgor, I.; Yilgor, E.; Wilkes, G. L. *Polymer* **2008**, *49*, 174−179.

(43) Lee, H.; Fragiadakis, D.; Martin, D.; Milne, A.; Milne, J.; Runt, J. *Macromolecules* **2010**, *43*, 3125−3127.

(44) Castagna, A.; Fragiadakis, D.; Lee, H.-K.; Choi, T.; Runt, J. *Macromolecules* **2011**, *44*, 7831−7836.

(45) Havriliak., S.; Negami, S. *J. Polym. Sci., Part C: Polym. Symp.* **1966**, 99.

(46) Fulcher, G. S. *J. Am. Ceram. Soc.* **1925**, *8*, 339−355.

(47) Tammann, G.; Hesse, W. *Z. Anorg. Allgem. Chem.* **1926**, 156.

(48) Vogel, H. *Phys. Z.* **1921**, *22*, 645−646.

(49) Bohmer, R.; Angell, C. A. *Phys. Rev. B* **1992**, *45*, 10091−10094.

(50) Qin, Q.; McKenna, G. B. *J. Non-Cryst. Solids* **2006**, *352*, 2977−2985.
(51) Kramarenko, V. Y.; Ezquerra, T. A.; Sics, I.; Balta-Calleja, F. J.; Privalko, V. P. *J. Chem. Phys.* **2000**, *113*, 447−452.
(52) Roland, C. M. *Macromolecules* **1994**, *27*, 4242−4247.
(53) Zhang, S. H.; Painter, P. C.; Runt, J. *Macromolecules* **2002**, *35*, 9403−9413.

Macromolecules

Article

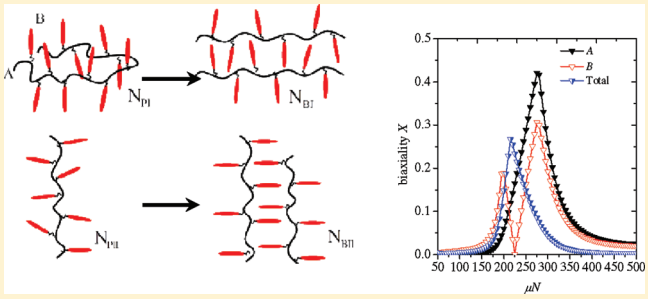
pubs.acs.org/Macromolecules

Uniaxial−Biaxial Nematic Phase Transition in Combined Main-Chain/Side-Chain Liquid Crystal Polymers Using Self-Consistent Field Theory

Guang Yang, Ping Tang,* and Yuliang Yang

State Key Laboratory of Molecular Engineering of Polymers and Department of Macromolecular Science, Fudan University, Shanghai 200433, China

ABSTRACT: We investigate the isotropic−anisotropic phase transitions and the conformation of combined main-chain/side-chain liquid crystal polymers (MCSCLCPs) by numerically solving semiflexible chain self-consistent field theory (SCFT) equations with the pseudospectral method. Two kinds of interactions are involved: the global coupling between backbone segments, between the backbone and side groups, and between the side mesogens and the local coupling between the polymer backbone and its attached side groups. When the hinges are flexible, both global and local effects prefer parallel alignments of backbone and side groups, forming only prolate uniaxial nematic phase N_{PIII}. When the hinges are relatively stiff, the competition between the global interaction preferring parallel orientations of the system and the perpendicular tendency of the two components due to the comb architecture results in rich phases with various orientation modes, including uniaxial prolate phases N_{PI}, N_{PII}, and oblate phase N_O and biaxial phases N_{BI}, N_{BII}, and N_{BIII}. The new phases N_O and N_{BIII} have not yet been reported by the previous theoretical results. We conclude that the occurrence of the biaxial phases results from not only the perpendicular toplogical structures between the oriented main chain and side groups but also the bending feature of the wormlike chain backbone, another necessary condition for N_{BI} and N_{BII}.



INTRODUCTION

Liquid crystal polymers (LCPs), which combine the liquid-crystalline behavior and polymeric properties, have desirable application prospects, such as optical switching and image storage, pressure and temperature sensors, shape-memory materials, protein structure studies, and so on.[1−4] LCPs have been divided into three main classes: main-chain LCPs composing of LC moiety (also called "mesogenic group") directly incorporated into backbone chain of a polymer, side-chain liquid crystal polymers (SCLCPs) in which pendant groups also playing roles as LC moiety connected to the backbone via flexible spacers,[5,6] and combined main-chain/side-chain liquid crystal polymers (MCSCLCPs), which consists of a main-chain LC backbone and side-chain LC groups.[7] In the SCLCPs, LC side groups can be linked to the backbone through either "terminal" (end-on SCLCPs) or "lateral" (side-on SCLCPs) attachment.[8] In addition, mesogen-jacked liquid crystal polymers (MJLCPs) exhibit special liquid crystal property of MCLCPs as a result of jacketing effect generated by the central rigid portion of the LC side groups laterally attached to the backbone chain without or with only quite short flexible spacers.[9] Such MJLCPs can also play the role as the semiflexible backbone in the synthesis of MCSCLCPs.[10]

During the past few decades, the complicated SCLCPs and MCSCLCPs have attracted intensive researches for academic interests on the study of the interplay of polymer chains and liquid crystal properties. Lots of experiments have devoted to investigate the influencing factors and their mutual effects on the nematic phase transitions, including the attachment (end-on or side-on SCLCPs),[11,12] the flexibility of backbone,[13,14] the length of the spacer,[15,16] molecular weight,[17,18] and mesogen graft density.[19,20] Moreover, the competition between the orientational ordering resulting from the main-chain or side-chain LC moieties and the drive to maximal entropy of the system leads to various phase structures. In order to accommodate the orientation of the LC moiety, the backbone chain coupled with the nematic ordering exhibits different conformations, including oblate ellipsoids,[11,20] prolate ellipsoids,[12,21] and biaxial phases.[10,22] Meanwhile, the orientational ordering of the LC side groups is also affected by the conformation of the backbone chain.[23] Therefore, theoretical calculation and computer simulation can help us understand the complicated phenomena of SCLCPs and MCSCLCPs.

How to describe the chain model of the system and the coupling effect on phase behavior between the main chain and side groups is the key issue in the theoretical researches on SCLCP and MCSCLCPs systems. At the earliest, Vasilenko and colleagues[24,25] developed a model by including the effect of excluded volume based on Flory type lattice theory to investigate the rodlike sections of SCLCPs. The Maier−Saupe mean-field theory which has been successfully used to understand the phase behavior of thermotropic liquid crystals was included in the SCLCPs by Brochard and co-workers[26] for

Received: December 24, 2011
Revised: March 16, 2012
Published: April 2, 2012

 © 2012 American Chemical Society dx.doi.org/10.1021/ma2027879 | *Macromolecules* 2012, 45, 3590−3603

describing the nematic interactions between liquid crystal units. They displayed the phase diagrams of the system based on Flory−Huggins theory of mixtures, whereas the backbone chain was assumed to be decoupled from the side groups. By considering the Maier−Saupe nematic interactions and the effect of chemical attachment between the backbone chain segments and the side groups, the so-called WWR model for nematic comblike polymers was proposed by Warner and co-workers.[27,28] In their work, the backbone was treated as a wormlike chain model and the rigid side groups hinged to it, as the teeth of the comb with their own mesogenic tendency. The competition between the polymers' conformational entropy and rod ordering effect resulted in three types of nematic phases depending on the volume fraction, temperature, nematic coupling, and stiffness. However, this theory treats the local stereochemical constraints on the relative orientation of backbone and its attached LC groups as a global (mean-field) interaction and gives no explanation about the influence of the spacer length on the orientational properties of the MCSCLCPs. For distinguishing these two different sources of interactions between backbone and side groups, Wessels and Mulder[6] included intrachain interactions (single-polymer effects) by hard-body repulsion between the connecting segments to mimics the stereochemical attachment. In that model, the excluded volume between the molecules had an identical formal structure for slender rods, which in some sense is unsuited to the stubby LC side groups. Recently, Wang and Wang[29] developed a freely jointed chain model by considering both the global Maier−Saupe interaction between the polymer main chain and the nematic field and the local coupling effect between the polymer backbone and its attached LC groups for investigating the thermodynamics and chain conformation of SCLCP systems. In this new model, the different behavior of side-on and end-on SCLCPs can be distinguished according to the local coupling effect supposed from experimental results, which realistically depend on the topological geometry that the point of the junction is located at the middle or at the end of the lateral group. Because correlations of global and local coupling effects on the side-on and end-on SCLCPs are different, the chain conformation of the side-on SCLCPs is always prolate and the end-on can be either oblate or prolate depending on the competitive effect of the two couplings. In general, most of the theoretical studies focused on the uniaxial nematic phases with either oblate or prolate backbone conformations,[6,29,30] while the biaxial nematic phases[10,31] and complex assembled phases in the MCSCLCPs[32] are quite limited to be theoretically studied. Considering the main-chain stiffness enhanced by the side rods and the biaxial nematic phases, the wormlike chain model[33] is suitable for describing the main chain's rigidity and the anisotropic liquid crystalline behavior of MCSCLCPs.

The self-consistent field theory (SCFT) has proved to be one of the most successful theoretical methods for investigating equilibrium phases of block copolymers[34] including comblike architectural polymers.[35] For the continuous wormlike chain model, however, solving the diffusion equation of the chain propagator $q(\mathbf{r},\mathbf{u},s)$ for describing the chain segment distribution becomes difficult due to the introduction of the extra parameter, namely a unit vector defined on a spherical surface $\mathbf{u}$ for describing the orientation of semiflexible segments. For the case of $\mathbf{r}$-independent nematic phase, the Legendre-expansion approach for solving $q(\mathbf{u},s)$, in the form of long-chain statistics, was initiated by Vroege and Odijk.[36] In the following, a spherical-harmonics expansion method coupled with real-space discretization was introduced by Cui et al.[37] to study the isotropic−nematic interface of the semiflexible polymers. Duchs and Sullivan[38] adopted the hybrid approach in ref 37 to solve the diffusion equation and study the phase behaviors of semiflexible diblock copolymers, consisting of a rigid and a flexible block. Recently, we developed a real-space method, which discretizes the orientation defined on a unit sphere with an icosahedron triangular mesh, and studied the self-assembly of semiflexible diblock copolymers both in 1D and 2D positional space implementation of SCFT.[39−41] Fredrickson[42] supposed that the pseudospectral (PS) algorithm with second-order accuracy seems be the best strategy for generating high-resolution solutions of the wormlike chain diffusion equation (Fokker−Planck equation). On the basis of the PS algorithm, Fredrickson and co-workers[43] studied the microstructures of flexible block copolymers assembled on a sphere, similar to the situation of the orientation $\mathbf{u}$ of the semiflexible segments on a unit sphere surface. In their work, a software package, SPHEREPACK 3.1,[44] was adopted for performing fast efficient transformations between the values of a 2D function $f(\mathbf{u})$ sampled on a grid on the unit sphere and its spherical harmonic coefficients. Furthermore, a SCFT model for rod−coil diblock copolymers consisting of continuous rigid rod with Maier−Saupe interaction can capture the experimental results in both bulk[45] and films[46] and is also suitable for side-chain LC block polymers.[47] Recently, a SCFT model implemented by the PS numerical approach was used to study the disorder−order transition of wormlike diblock copolymers.[48]

We develop a universal SCFT model to deal with MCSCLCPs with considering their comblike architecture and the exact connecting points of lateral groups. The MCSCLC molecules are treated as a wormlike backbone chain with its own intrinsic rigidity and nematic behavior from attached rigid rod side chains of some length to the backbone with varying flexibility hinges. The global nematic interactions favoring parallel alignment between backbone segments, between the backbone and side groups, and between the side mesogens are all described by Maier−Saupe orientational interactions. According to the experiments, if the side groups are attached to the main chain by flexible spacers (but not too long to decouple the interactions between side group and main chain), the backbone tends to parallel side groups for both end-on and side-on SCLCPs.[23,49,50] If the hinge is stiff, induced by a stiff main chain or the directly linked LC side chain, the perpendicular alignment between side groups and main chain is favorable to preserve the maximum conformational entropy.[18,20] Furthermore, the differences between side-on and end-on effects on the backbone conformation are unconspicuous once the side groups with high side-chain density dominate the phase structures, whereas the spacer length (the degree of rigidity of spacer) play important roles in the phase behaviors of SCLCPs.[15] Therefore, we use a coupling parameter μ_f proposed in ref 29 to describe the stiff extent of the attached spacer of MCSCLCPs in the form of a short-range or local interaction. $\mu_f N < 0$ prefers parallel alignments between the backbone segment and its own side group them whereas $\mu_f > 0$ represents the perpendicular attachment of the pendant. $\mu_f \leq 0$ and small values of positive μ_f indicate flexible spacers. Large value of positive μ_f indicates stiff spacers. This local coupling effect explicitly participates in the diffusion equation of the chain propagators, thus influencing the liquid crystal behavior of main and side chains. In this work, we try out the second-order pseudospectral SCFT approach with high numerical stability to

dx.doi.org/10.1021/ma2027879 | Macromolecules 2012, 45, 3590−3603

study the relatively simple nematic phase of MCSCLCPs. Not only uniaxial phases but also biaxial phases are obtained, and the effects of the stiffness of the main chain, nematic interaction, flexibility of spacer, and the component fraction on the liquid crystal behavior are investigated.

THEORETICAL FORMALISM

In this section, we briefly describe the SCFT theoretical framework for predicting the phase behavior of the MCSCLCPs. We consider incompressible side-chain polymer melts consisting of n identical polymer chains $A_{m+1}B_m$ in a volume V at the temperature T (hereafter we set $k_BT = 1$ with k_B being the Boltzmann constant). Each polymer consists of a semiflexible backbone chain denoted by A and m numbers of side rigid rods denoted by B, namely m branching points. The monomer units of semiflexible chain A and rigid rod of side chain B are characterized by statistical length a. We assume that chains A and B have the same bulk number density of the segment $\rho_0 = nN/V$, such that $ad^2 = \rho_0^{-1}$ (d is the diameter of the rod). The side chains divide the backbone chain as $m + 1$ equal parts (we called it "divided sections") with N_A segments of statistical length and each side chain B has N_B number of rod segments. N denotes the overall number of units of the side chain polymer and $N = (m + 1)N_A + mN_B$. Therefore, the volume fractions of the backbone chain A and the side groups B are given: $f_A = (m + 1)N_A/N$ and $f_B = mN_B/N$. Because the structure parameter m affects the phase diagram of the comb copolymer,[35] we fix $m = 10$ in this paper to focus on the influencing factors including the stiff extent of the main chain on the liquid crystal behaviors of MCSCLCPs. The composition of the species can be varied by changing the grafting density (the number of side chains per unit length of the backbone chain). In the results that we present, f_B is varied at the fixed N_B ($N_B = 20$), i.e., at fixed side-chain length by changing N_A. In fact, when m is fixed, the phase behavior of MCSCLCPs only depends on the radio of N_A/N_B, i.e., the volume fraction of the component f_B.

The semiflexible backbone chain A is parametrized with a continuous variable s which monotonically increases along the length of the polymer. $s = 0$ is at the beginning of backbone chain, and $s = (m + 1)N_A$ is at the other end of it. Using this parametrization, the space curves $\mathbf{r}_k(s)$ (where $k = 1, 2, ..., n$ indexes different polymers) are used to describe the different conformations of the polymer. The unit vector $\mathbf{u}_k(s)$ denotes the orientation of the kth polymer at the contour position s. Similarly, another vector $\mathbf{v}_{k,t}(s')$ ($t = 1, 2, ..., m$) denotes the orientation of the LC side group attached to the tth branching points. The nondimensional microscopic densities for the backbone chain $\hat{\phi}_A(\mathbf{r})$ and side groups $\hat{\phi}_B(\mathbf{r})$ are defined as

$$\hat{\phi}_A(\mathbf{r}) \equiv \frac{1}{\rho_0}\sum_{k=1}^{n}\int_0^{(m+1)N_A} ds\ \delta(\mathbf{r} - \mathbf{R}_k(s)) \tag{1}$$

$$\hat{\phi}_B(\mathbf{r}) \equiv \frac{1}{\rho_0}\sum_{k=1}^{n}\sum_{t=1}^{m}\int_0^{N_B} ds\ \delta(\mathbf{r} - [\mathbf{R}_k(N_At) + as\mathbf{v}_{k,t}(s)]) \tag{2}$$

Equation 2 is expressed in the form of end-on attached side groups, which can be expressed for side-on MCSCLCPs by changing the connecting points of the side groups.

In addition, the microscopic orientational order parameter for the backbone segments and side groups are defined as

$$\hat{\mathbf{S}}_A(\mathbf{r}) \equiv \frac{1}{\rho_0}\sum_{k=1}^{n}\int_0^{(m+1)N_A} ds\ \delta(\mathbf{r} - \mathbf{R}_k(s))\left(\frac{3}{2}\mathbf{u}_k\mathbf{u}_k - \frac{\mathbf{I}}{2}\right) \tag{3}$$

$$\hat{\mathbf{S}}_B(\mathbf{r}) \equiv \frac{1}{\rho_0}\sum_{k=1}^{n}\sum_{t=1}^{m}\int_0^{N_B} ds\ \delta(\mathbf{r} - [\mathbf{R}_k(N_At) + as\mathbf{v}_{k,t}(s)]) \times \left(\frac{3}{2}\mathbf{v}_{k,t}(s)\mathbf{v}_{k,t}(s) - \frac{\mathbf{I}}{2}\right) \tag{4}$$

where $\mathbf{I}$ is a 3×3 unit matrix. The incompressibility constraint is provided by enforcing that

$$\hat{\phi}_A(\mathbf{r}) + \hat{\phi}_B(\mathbf{r}) = 1 \tag{5}$$

Energetic interactions in the above model consist of the following four components:

$$H_1 = \frac{\xi}{2}\sum_{k=1}^{n}\int_0^{(m+1)N_A} ds\left|\frac{d\mathbf{u}_k(s)}{ds}\right|^2 \tag{6}$$

describing the total bending energy for the semiflexible components of the backbone chain with side rods attached, where ξ is the persistent length

$$H_2 = -\frac{\chi}{4}\int d\mathbf{r}\,(\hat{\phi}_A(\mathbf{r}) - \hat{\phi}_B(\mathbf{r}))^2 \tag{7}$$

describing the isotropic repulsion between unlike segments A and B, where χ is the Flory–Huggins interaction parameter between these segments which favors their phase separation

$$H_3 = -\frac{\mu_{AA}}{2}\int d\mathbf{r}\,\hat{\mathbf{S}}_A(\mathbf{r}):\hat{\mathbf{S}}_A(\mathbf{r}) - \frac{\mu_{BB}}{2}\int d\mathbf{r}\,\hat{\mathbf{S}}_B(\mathbf{r}):\hat{\mathbf{S}}_B(\mathbf{r}) - \mu_{AB}\int d\mathbf{r}\,\hat{\mathbf{S}}_A(\mathbf{r}):\hat{\mathbf{S}}_B(\mathbf{r}) \tag{8}$$

describing the Maier–Saupe interaction energy, where $\mu_{\kappa,\kappa'}$ ($\kappa, \kappa' = A, B$) represents the strength of anisotropically orientational interaction favoring the parallel alignment of orientational units, and

$$H_4 = \mu_f\sum_{k=1}^{n}\sum_{t=1}^{m}(\mathbf{u}_k(N_At)\cdot\mathbf{v}_{k,t}(0))^2 \tag{9}$$

indicating the local effect of flexibility of the spacer on the orientational alignment between the main chain and the side segments. Equation 9 representing the local coupling effect, was originally proposed in ref 29 where $\mu_f < 0$ represents side-on and $\mu_f > 0$ represents end-on SCLCPs, which are assumed to be determined by some experimental results. In our work, $\mu_f \leq 0$, indicating flexible spacers between the backbone segment and its own side group, and $\mu_f > 0$, preferring perpendicular attachment due to a stiff hinge.

Therefore, the partition function of the system is

$$Z \propto \int D\mathbf{R}_k(s)d\mathbf{u}_k(s)\delta\left[\mathbf{u}_k(s) - \frac{d}{ds}\mathbf{R}_k(s)\right]\delta[|\mathbf{u}_k(s)| - 1] \times \sum_{t=1}^{m}d\mathbf{v}_{k,t}(s')\exp[-\rho_0(H_1 + H_2 + H_3 + H_4)] \times \delta(\hat{\phi}_A(\mathbf{r}) + \hat{\phi}_B(\mathbf{r}) - 1) \tag{10}$$

dx.doi.org/10.1021/ma2027879 | Macromolecules 2012, 45, 3590–3603

By employing standard field-theoretical techniques, the quadratic interactions in the Hamiltonian can be decoupled by introducing fluctuating chemical potential fields with respect to the density and orientational order parameters.[51] In a nondimensional representation, all length scales of the system are denoted by the contour length $L \equiv aN$, and the continuous variable s and persistent length ξ are normalized by the overall molecular weight N. The partition function can be rewritten as a functional integral

$$Z \propto \prod_{P=A,B} \int D\phi_P D\omega_P \int D\eta D\mathbf{S}_P D\mathbf{M}_P \exp(-\rho_0 F) \tag{11}$$

The free energy per polymer chain is

$$\begin{aligned}\frac{\rho_0 F}{n} = \frac{1}{V}\int d\mathbf{r}\,[\chi N\phi_A(\mathbf{r})\phi_B(\mathbf{r}) - \sum_{P=A,B}\omega_P(\mathbf{r})\phi_P(\mathbf{r}) \\ + \eta(\mathbf{r})\Big(\sum_{P=A,B}\phi_P(\mathbf{r}) - 1\Big) - \frac{\mu_{AA}N}{2}\mathbf{S}_A(\mathbf{r}) \\ : \mathbf{S}_A(\mathbf{r}) - \frac{\mu_{BB}N}{2}\mathbf{S}_B(\mathbf{r}) : \mathbf{S}_B(\mathbf{r}) - \mu_{AB}N\mathbf{S}_A(\mathbf{r}) \\ : \mathbf{S}_B(\mathbf{r}) + \mathbf{M}_A(\mathbf{r}) : \mathbf{S}_A(\mathbf{r}) + \mathbf{M}_B(\mathbf{r}) : \mathbf{S}_B(\mathbf{r})] - \ln Q\end{aligned} \tag{12}$$

In the above equations, $\omega_P(\mathbf{r})$ is a purely imaginary conjugate field to the densities with species $P = (A,B)$, and $\eta(\mathbf{r})$ ensures the incompressibility of the system. $\mathbf{M}_P(\mathbf{r})$ is purely imaginary conjugate tensorial orientation field to the orientational parameter $\hat{\mathbf{S}}_P$. Q represents the single chain partition function of a MCSCLC polymer under the external fields $\omega_P(\mathbf{r})$, $\eta(\mathbf{r})$, and $\mathbf{M}_p(\mathbf{r})$, which is given by

$$\begin{aligned}Q \equiv \int D\mathbf{R}\,d\mathbf{u}\,d\mathbf{v}\,\delta\Big[\mathbf{u}(s) - \frac{d}{L\,ds}\mathbf{R}(s)\Big]\delta[|\mathbf{u}(s)| - 1] \\ \times \exp\Big\{-\frac{\xi}{2}\int_0^{f_A} ds\,\Big|\frac{d\mathbf{u}(s)}{ds}\Big|^2\Big\} \\ \times \exp\Big\{-\int_0^{f_A} ds\Big[\omega_A(\mathbf{R}(s)) - \mathbf{M}_A(\mathbf{R}(s)) : \Big(\frac{3}{2}\mathbf{uu} - \frac{\mathbf{I}}{2}\Big)\Big]\Big\} \\ \times \exp\{-\sum_{t=1}^{m}\int_0^{f_B/m} ds'[\omega_B(\mathbf{R}(tN_A/N) + Ls'\mathbf{v}_t(s')) \\ - \mathbf{M}_B(\mathbf{R}(tN_A/N) + Ls'\mathbf{v}_t(s')) : \Big(\frac{3}{2}\mathbf{v}_t\mathbf{v}_t - \frac{\mathbf{I}}{2}\Big)]\} \\ \times \exp[-\mu_f N\sum_{t=1}^{m}(\mathbf{u}(tN_A/N)\cdot\mathbf{v}_t(0))^2]\end{aligned} \tag{13}$$

According to the mean-field approximation, the complete SCFT equations for SCLCPs are obtained by minimizing the free energy functional eq 12 with respect to $\phi_P(\mathbf{r})$, $\omega_P(\mathbf{r})$, $\eta(\mathbf{r})$, $S_P(\mathbf{r})$, and $M_P(\mathbf{r})$. To reduce computational loads, we restrict the present study to only consider the nematic phases of the MCSCLCPs; thus, the density fields and orientation fields are homogeneous in the positional space; i.e., $\phi_A(\mathbf{r})$, $\phi_B(\mathbf{r})$, $\mathbf{S}_A(\mathbf{r})$, and $\mathbf{S}_B(\mathbf{r})$ reduce to f_A, f_B, $\mathbf{S}_A$, and $\mathbf{S}_B$, respectively. We should note that the side-on and end-on MCSCLCPs determined by the positional related fields in eq 13 could not be distinguished due to ignorance of heterogeneous phase in positional space. We further assume that each of the graft side groups are in the same conditions of the orientational fields, thus replacing $\mathbf{v}_t$ with $\mathbf{v}$. According to the above treatments, the free energy reduces as follows:

$$\begin{aligned}F = -\frac{\mu_{AA}N}{2}\mathbf{S}_A : \mathbf{S}_A - \frac{\mu_{BB}N}{2}\mathbf{S}_B : \mathbf{S}_B - \mu_{AB}N\mathbf{S}_A \\ : \mathbf{S}_B + \mathbf{M}_A : \mathbf{S}_A + \mathbf{M}_B : \mathbf{S}_B - \ln Q\end{aligned} \tag{14}$$

Minimizing the functional F, the SCFT equations are expressed as follows:

$$\mathbf{M}_A = \mu_{AA}N\mathbf{S}_A + \mu_{AB}N\mathbf{S}_B \tag{15}$$

$$\mathbf{M}_B = \mu_{BB}N\mathbf{S}_B + \mu_{AB}N\mathbf{S}_A \tag{16}$$

$$\begin{aligned}\mathbf{S}_A = \frac{1}{Q\int d\mathbf{u}}\sum_{t=1}^{m+1}\int_0^{N_A/N} ds\int d\mathbf{u}\,q(\mathbf{u}, s, t) \\ \times q(\mathbf{u}, N_A/N - s, m + 1 - t)\Big(\frac{3}{2}\mathbf{uu} - \frac{\mathbf{I}}{2}\Big)\end{aligned} \tag{17}$$

$$\begin{aligned}S_B = \frac{N_B}{NQ\int d\mathbf{u}\int d\mathbf{v}}\sum_{t=1}^{m}\int d\mathbf{u}\,d\mathbf{v}\,q(\mathbf{u}, N_A, t) \\ \times q(\mathbf{u}, N_A, m - t)\exp[-\mu_f N(\mathbf{u}\cdot\mathbf{v})^2] \\ \times \exp\Big[-\frac{N_B}{N}\Gamma_B(\mathbf{v})\Big]\Big(\frac{3}{2}\mathbf{vv} - \frac{\mathbf{I}}{2}\Big)\end{aligned} \tag{18}$$

where

$$Q = \frac{1}{\int d\mathbf{u}}\int d\mathbf{u}\,q(\mathbf{u}, N_A/N, m + 1) \tag{19}$$

The chain propagator of $m + 1$ sections of main chain $q(\mathbf{u},s,t)$ corresponds to the probability of finding a partial backbone chain of length $s \in [0, N_A/N]$ that starts from the end of each divided sections of A ($s = 0$) with the orientation $\mathbf{u}$, which satisfies the modified diffusion equation:

$$\begin{aligned}\frac{\partial q(\mathbf{u}, s, t)}{\partial s} = -\Gamma_A(\mathbf{u})q(\mathbf{u}, s, t) + \frac{1}{2\xi}\nabla_u^2 q(\mathbf{u}, s, t) \\ t = 1, 2, ..., m + 1\end{aligned} \tag{20}$$

The $\mathbf{r}$-independent diffusion equation in the external field is similar to that used by Chen[52] for studying the nematic ordering of semiflexible polymers. The initial conditions for the diffusion equation are

$$\begin{aligned}q(\mathbf{u}, 0, 1) = 1 \\ q(\mathbf{u}, 0, t + 1) = \Big\{q(\mathbf{u}, N_A/N, t)\int d\mathbf{v}\exp\Big[-\frac{N_B}{N}\Gamma_B(\mathbf{v})\Big] \\ \times \exp[-\mu_f N(\mathbf{u}\cdot\mathbf{v})^2]\Big\}/\int d\mathbf{v}\end{aligned} \tag{21}$$

where

$$\Gamma_A(\mathbf{u}) = -\mathbf{M}_A : \Big(\frac{3}{2}\mathbf{uu} - \frac{\mathbf{I}}{2}\Big) \tag{22}$$

$$\Gamma_B(\mathbf{v}) = -\mathbf{M}_B : \Big(\frac{3}{2}\mathbf{vv} - \frac{\mathbf{I}}{2}\Big) \tag{23}$$

dx.doi.org/10.1021/ma2027879 | Macromolecules 2012, 45, 3590−3603

Equations 15−18 form a closed set of self-consistent equations, which can be numerically implemented by combinatorial screening algorithm for Gaussian chain SCFT equations proposed by Drolet and Fredrickson.[34] In our work, the diffusion equation (20) is solved to obtain $q(\mathbf{u},s,t)$ with the pseudospectral (PS) operator splitting algorithm:[42,43]

$$q(\mathbf{u}, s + \Delta s, t) = \exp(-\Gamma(\mathbf{u})\Delta s/2) \exp\left(\frac{\Delta s}{2\xi}\nabla_{\mathbf{u}}^2\right) \times \exp(-\Gamma(\mathbf{u})\Delta s/2) q(\mathbf{u}, s, t) \quad (24)$$

The unit vector $\mathbf{u}$ is oriented in the three-dimensional plane, i.e., $\mathbf{u} = \mathbf{e}_x \sin\theta\cos\varphi + \mathbf{e}_y \sin\theta\sin\varphi + \mathbf{e}_z \cos\theta$. The software package "Spherepack 3.2"[44] enables us to evaluate the Laplacian of a function $f(\mathbf{u})$, i.e., $f(\theta,\phi)$, by implementing an efficient transforming between gird points on the sphere and its spherical harmonic coefficients. In this work, we perform the angular discretization through a 17-point evenly distributed points for θ and a 32-point evenly distributed points for ϕ. The discretization of contour variable s is chosen to be Δs = 0.002. In order to obtain relatively stable phases, we start the calculation referring to the Drolet Fredrickson combinatorial search[34] with both random initial orientation fields and completely aligned states including uniaxial and biaxial initial fields by ranging θ and ϕ from 0 to $\pi/2$, respectively. The final stable phase structure is thus determined as the one having the lowest free energy. Furthermore, the pseudodynamical evolutions are carried out to a convergence of 10^{-7} in free energy and a convergence of 10^{-4} in fields values. By contrast, we also perform the real-space solution of the diffusion equation (20) as developed in our previous work,[39] in which $\mathbf{u}$ on the spherical surface is discretized into icosahedron triangular mesh with M number of vertexes. Our tests show that the discrete points of s are at least twice of those in the above-mentioned PS method to ensure the numerical stability with the convergence of 10^{-5} in the free energy. Moreover, the PS method has faster convergences of the free energy and fields than the real-space method.

RESULTS AND DISCUSSION

According to our model, there are six factors influencing the nematic phase behaviors of MCSCLCPs including the main chain stiffness ξ, the orientational interactions between main chains $\mu_{AA}N$ and the side chain groups $\mu_{BB}N$, the volume fraction f_B, the global coupling effect $\mu_{AB}N$ preferring the anisotropic interactions between components A and B, and the local coupling effect μ_fN representing the spacers' flexibility. In the simulations of our explored parameter space, we obtain not only the uniaxial nematic phase but also complex biaxial nematic phase by varying the hinges flexibility μ_fN. It is common to construct MCSCLCPs with different hinge flexibility by altering the chemical composition of a spacer unit. When $\mu_fN \le 0$, MCSCLCPs have flexible spacers and favor parallel ordering between main chain and side groups. In this case, both the global interactions and local coupling play synergistic roles in the orientation of the system, favoring prolate conformation, as discussed in ref 29. Thus, we first focus on the influence of global interactions $\mu_{AB}N$ at different values of ξ and f_B in the absence of μ_fN, i.e., $\mu_fN = 0$. In fact, $\mu_fN = 0$ means that the side groups are decoupled from the backbone due to a very long or flexible spacer. We also consider the system conformation with different degree of main chain's rigidity including relatively flexible case ($\xi \le 0.1$) for comparison with the results reported in ref 29. When the side groups perpendicular attached to main-chain segment, i.e., $\mu_fN > 0$, more complex uniaxial and biaxial phase transitions occur. With the increase of the hinges stiffness, the phase behaviors become more complicated. In the case of the semiflexible main chain ($\xi = 1$), we investigate the phase transitions depending on the relationships between μ_fN, $\mu_{AA}N$, $\mu_{BB}N$, and $\mu_{AB}N$. Furthermore, the phase diagram in the μN−f_B plane in the case of $\mu_fN = 0.5\ \mu N$ is shown for $\xi = 1$. In our simulations, if all the global interactions $\mu_{AA}N$, $\mu_{BB}N$, and $\mu_{AB}N$ are considered to exist in the system, we assume $\mu_{AA} = \mu_{BB} = \mu_{AB} = \mu$ to simplify the influences of the chemical structure difference between A and A, B and B, and A and B.

A. Defining Various Nematic Phases. Molecular uniaxiality and biaxiality are two main characteristics for the ordering of nematic phase.[5] The uniaxial phase has the main directions of the molecules, which tend to be symmetrically parallel to the same common axis, while the biaxial phase can be expected with building blocks shaped in the form of long rectangles. For MCSCLCPs, however, even with main and side chains being geometrically uniaxial, biaxial phases may emerge because of the branch geometry,[16,22,31] quite different from the biaxial phase observed experimentally[53,54] in low molecular weight liquid crystals. In the self-consistent field theory of MCSCLCP system, the nematic phase is characterized by the Maier−Saupe orientational order parameter of the constituent species $\mathbf{S}_P$ (P = A, B), which is a traceless symmetric second-rank tensor. We normalize the orientational order parameter by volume fraction of A and B, respectively, i.e., $\mathbf{T}_P = \mathbf{S}_P/f_P$. After diagonalization of this orientational tensor, it becomes $\mathbf{T}_P = [\lambda_{x,P}\ \lambda_{y,P}\ \lambda_{z,P}]^{\mathrm{T}}\ \mathbf{I}$ with $\lambda_{x,P} + \lambda_{y,P} + \lambda_{z,P} = 0$. The average order parameters, i.e., eigenvalues elements $\lambda_{x,P}$, $\lambda_{y,P}$, and $\lambda_{z,P}$, determine the degree of orientations of main chain and side groups in x-, y-, and z-directions. We assume that $|\lambda_z|$ is always larger than $|\lambda_x|$, and $|\lambda_y|$; i.e., the principal axis is chosen as the z-directional orientation.

The normal convention of the uniaxial nematic phase ordered in the z-direction (main director) is that $\lambda_x = \lambda_y = -0.5\lambda_z$, and only one scalar order parameter λ_z is needed. $\lambda_z \in (0,1]$ represents prolate (rodlike) conformation while $\lambda_z \in [-0.5,0)$ represents oblate (disklike) conformation. Biaxial nematic phases exhibit additional orientational order of the system along a second macroscopic direction, the "short" axis, perpendicular to the primary nematic director. Therefore, after extracting the largest element $|\lambda_z|$ of the order parameter matrix, the biaxiality parameter is determined by the difference between the other two elements $X = |\lambda_x - \lambda_y|$. Therefore, $X = 0$ for uniaxial nematic phase while $\lambda_x \ne \lambda_y$ for biaxial nematic phase, in which two independent order parameters, λ_z and X, are required[31]

$$\lambda_x = -\frac{1}{2}\lambda_z + \frac{1}{2}X,\ \lambda_y = -\frac{1}{2}\lambda_z - \frac{1}{2}X \quad (0 \le X \le 0.5) \quad (25)$$

Because of the individual orientations of components A and B, they can create synergies for the entire system orientation and also can cancel out the effect of each other. With the assumed condition $\mu_{AA} = \mu_{BB} = \mu_{AB} = \mu$, there are only one united tensorial orientation field influencing the order parameters of the system, i.e., $\mathbf{M}_A = \mathbf{M}_B$. Therefore, the chain conformation of the overall system, λ_T, can be evolved from the order parameter of overall system, $\mathbf{T}_T = (\mathbf{S}_A + \mathbf{S}_B)/(f_A + f_B)$. The biaxiality of

dx.doi.org/10.1021/ma2027879 | Macromolecules 2012, 45, 3590−3603

the overall system is represents as X_T. For clarity, we use the symbols P_A, O_A, and B_A to note prolate, oblate, and biaxial phases of the main chain and P_B, O_B, and B_B for side groups, respectively. Previous theoretical work reported $N_{PI}(O_AP_B)$, $N_{PII}(P_AO_B)$, $N_{PIII}(P_AP_B)$[27,29] and biaxial phase $N_{BI}(B_AP_B)$ and $N_{BII}(P_AB_B)$,[31] with the schematics shown in Figure 1. Bladon et al.[31]

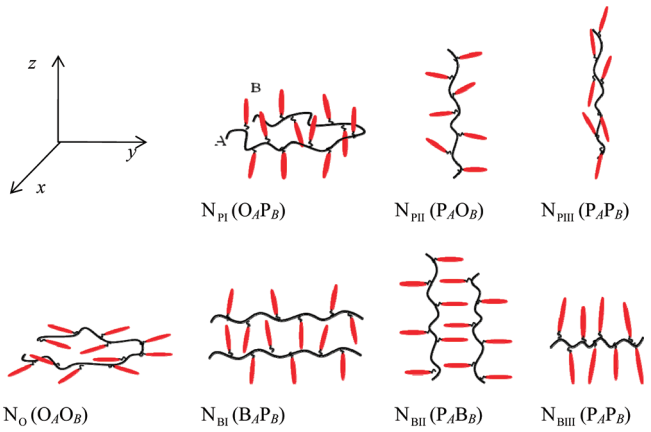


Figure 1. Schematic illustration of the nematic phase for end-on MCSCLCPs. P_A, O_A, and B_A indicate the prolate ellipsoidal order, oblate ellipsoidal order, and biaxial flat plane of the main chain A and P_B, O_B, and B_B for side groups B, respectively. $N_{PI}(O_AP_B)$, $N_{PII}(P_AO_B)$, and $N_{PIII}(P_AP_B)$ are uniaxial phases with prolate ellipsoid shapes; $N_O(O_AO_B)$ is uniaxial phase with oblate ellipsoid shape; $N_{BI}(B_AP_B)$, $N_{BII}(P_AB_B)$, and $N_{BIII}(P_AP_B)$ are biaxial phases. $N_{BI}(B_AP_B)$ and $N_{BII}(P_AB_B)$ signify that biaxialities are mainly contributed from A and B, respectively. The new phases N_O and N_{BIII} have not yet been reported in previous theoretical work.

suggested that N_{BI} and N_{BII} are evolved from N_{PI} and N_{PII}, respectively. The biaxial phase actually adopts a flattened prolate ellipsoidal shape with one of the components parallel to the z-direction and another ordered almost uniaxially along the x- or y-direction. If the largest value of uniaxial order parameter is given by the side-chain (main-chain) component, the phase is called N_{BI} (N_{BII}). We should note that the two phases are physically identical and simply related by a spatial rotation because the system is a flattened prolate ellipsoidal shape in the coordinate system.[31] In fact, for the biaxial phases N_{BI} and N_{BII} in our study, A and B each almost has a separate major axis of symmetry. In order to simplify the phase diagram, we will no longer distinguish them from N_{BI} or N_{BII}. In particular, we find two new phases shown in Figure 1. One is $N_O(O_AO_B)$ phase with both of the components displaying oblate shapes and orienting parallelly between each other, which is typically found when the orientations of A and B are comparable. Another new phase is a biaxial phase denoted as $N_{BIII}(P_AP_B)$ where both A and B present prolate shapes and perpendicularly orient along their individual primary directions. This phase occurs at quite large volume fractions of B and perpendicular oriented hinge units between the relativley stiff backbone and side groups.

B. Prolate Uniaxial Nematic Phase in the Case of $\mu_f N = 0$. For $\mu_f N = 0$, the tendency of mutual orthogonal orientation between main chain and side groups disappears, corresponding to the case of quite flexible hinges. The N_{PIII} phase, prolate ellipsoidal shape formed both by main chain A and side groups B, is obtained, because all the individual orientation interactions $\mu_{AA}N$ and $\mu_{BB}N$ and the global coupling $\mu_{AB}N$ all favor parallel orientations of LC side group and main chain segment. It was confirmed by the experiments that the natural tendency of the backbone chain was to adopt a prolate shape in the nematic phase when the hinges were flexible; i.e., the spacers connecting backbone and side groups were long enough.[49,55] We take the parameters of $\mu_f N = 0$, $\xi = 1$, $\mu_{AA} = \mu_{BB} = \mu_{AB} = \mu$ and $f_B = 0.476$ ($N_A/N_B = 1$) as an example to describe the I–N_{PIII} phase transition, as shown in Figure 2. The average order parameters

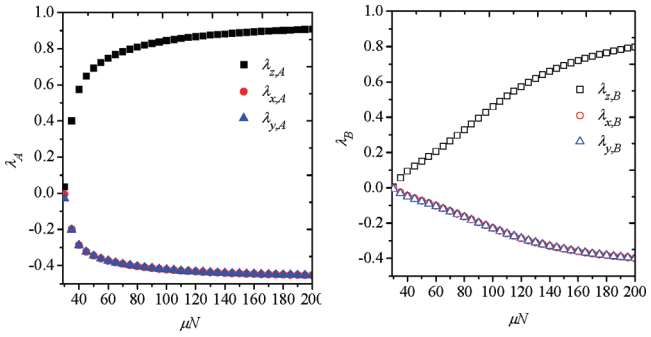


Figure 2. Orientational order parameters λ for MCSCLCPs with $f_B = 0.476$ ($N_A/N_B = 1$) and $\xi = 1$ as a function of orientational interaction μN in the case of $\mu_f N = 0$ and $\mu_{AA}N = \mu_{BB}N = \mu_{AB}N = \mu N$.

λ_A of the main chain increase rapidly with the μN increasing to 35, with $\lambda_{z,A} > 0$ and $\lambda_{x,A} = \lambda_{y,A}$ representing a uniaxial prolate spheroid of main chain A. At the same time, the side chains B begin to order in parallel with A, presenting prolate shape as well as A forming the N_{PIII} phase. Furthermore, $\lambda_{z,B}$ increases linearly when μN is increased from 35 to 130, whereas $\lambda_{z,A}$ increases rapidly to a high value ($\lambda_{z,A} = 0.8$) at $\mu N = 85$ and the value of $\lambda_{z,B}$ is always less than that of A at the same μN. This phenomenon indicates that the main chain A with some stiffness in this case dominates the ordering of nematic phases of MCSCLCPs.

I–N_{PIII} Phase Transition without Global Coupling ($\mu_{AB}N = 0$). In order to explore the interaction effects between main chain A and side groups B, we separate them by ignoring both global and local coupling effects between them, i.e., $\mu_{AB}N = 0$ and $\mu_f N = 0$. In the work of ref 29, the LC behavior of flexible backbone chains is induced by the orientation of rigid side groups; thus, the backbone chain remains isotropic when neglecting both global and local coupling effects. However, in our model, the main chain can also have LC behavior because of its instinct rigidity even without the global and local coupling effects. The transitions between isotropic phase and prolate nematic phase with different backbone's rigidities ξ are shown in Figure 3. In this case, the orientations of A and B have no relationship between each other. The ordering of A depends only on ξ, whereas that of B depends only on the structure parameter m. As long as ξ and m are fixed, the degrees of the ordering of main chain and side groups are relative to their individual self-orientation interactions, $\mu_{AA}N$ and $\mu_{BB}N$. The behavior of side groups B dominates in the right of the phase diagram because the strength of side-chain interaction governed by their volume fraction f_B is over the main chain. However, for the main chain, the effect of orientation not only depends on its volume fraction but also has relationship with ξ, thus displaying higher I–N_{PIII} for the case of low rigidity ($\xi = 0.1$) than that of $\xi = 1$. It should be noticed that the two components A and B still tend to be parallel to each other. According to mean-field Maier–Saupe orientational interactions adopted in our model, the parallel alignment of the orientation between backbone and

dx.doi.org/10.1021/ma2027879 | Macromolecules 2012, 45, 3590–3603

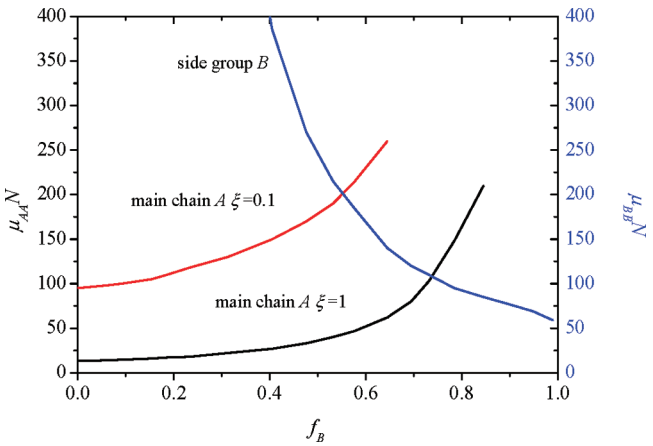


Figure 3. Phase transition lines from isotropic to prolate-shaped anisotropic phase for main chain *A* and side groups *B* plotted in the $\mu_{AA}N$–f_B and $\mu_{BB}N$–f_B planes without the global ($\mu_{AB}N = 0$) and local ($\mu_f N = 0$) coupling effects. The transition lines for *A* only depend on the stiffness ξ, and thus $\xi = 1$ and $\xi = 0.1$ are considered for comparison.

side groups remains to exist even in the case of $\mu_f N = 0$ and $\mu_{AB}N = 0$.

I–N_{PIII} Phase Transition in the Presence of Global Coupling ($\mu_{AB}N \neq 0$). The global coupling effect $\mu_{AB}N$ strengthens the parallel alignments of main chain *A* and side groups *B*. In this work, we combine them by using a uniform parameter μN ($\mu_{AB}N = \mu_{AA}N = \mu_{AB}N = \mu N$), and the I–$N_{PIII}$ phase transition is obtained when $\mu_f N = 0$. Figures 4a and 4b indicate the phase diagram plotted in the μN–f_B plane with relatively stiff main chain *A* ($\xi = 1$) and relatively flexible *A* ($\xi = 0.1$). The solid lines separate the uniaxial nematic phase N_{PIII} from isotropic phase I, and the dashed curves are chosen at an arbitrary value of $\lambda_{z,P} = 0.2$ for *A* and *B*, respectively. In Figure 4a, the main chain *A* with $f_B = 0$ begins to order at $\mu N = 13$ for $\xi = 1$. With the increase of f_B, the critical values of μN at the phase transition, noted as $(\mu N)_C$, enlarge with positive deviation from linear increase relationship. In the region of $0.5 < f_B < 0.89$, the change trend of $(\mu N)_C$ is negative deviation from linear increase. The value of $(\mu N)_C$ decreases when $f_B > 0.89$ and approaches $(\mu N)_C = 70$ with f_B being close to 1. One of the dashed curves representing *A* nearly coincides with the phase transiton line, but the other dashed curve representing *B* has relatively large disparity at small f_B. In contrast to the stiff main chain, the phase transition of relatively flexible main chain ($\xi = 0.1$) is shown in Figure 4b, which needs larger values of μN (lower temperature) compared with the case of $\xi = 1$. It is consistent with the experimental result of MCSCLCPs that enhancing the stiffness of the backbone gives rise to the nematic order of the system.[14] Moreover, the value of $(\mu N)_C$ increases initially before reaching the largest value at $f_B = 0.35$ when f_B is increased from 0.05 to 0.95. The highly ordered *A* and *B* (separated by dashed lines) appears simultaneously after $f_B = 0.35$.

The global interaction $\mu_{AB}N$ as well as different stiffness ξ of the main chain has significant effects on the I–N_{PIII} phase transition. The competition between the tendency to maximize the conformation entropy of main chain with different stiffness and the orientational order induced by the LC character of the system leads to the phase performances of MCSCLCPs. Thus, in Figure 4a, the LC behavior of the main chain *A* plays a great role for relative stiff backbone ($\xi = 1$) and the dashed line ($\lambda_{z,A} = 0.2$) presenting *A* nearly coincides with phase transition line. The addition of small volume fraction of *B* ($f_B < 0.5$) requires lower temperature to be ordered, thus leading to slightly higher of the transition line of the system than that of *A* in Figure 3. However, for relatively flexible backbone ($\xi = 0.1$), the phase transition occurs at large values of μN because the maximal conformation entropy of flexible chain controls over the ordering interactions of main-chain segments. This phenomenon is in agreement with the experimental result that increasing backbone's flexibility appeared to decrease the clearing temperature (larger μN was required to produce liquid crystal behavior) for the MCSCLCPs.[13] In this case, the side groups dominate the orientation of the system and the main chain and the overall system both display stronger orientations as the volume fraction of the side groups f_B is largely increased. The apparent persistence length seems to be increased due to the global interactions of the systems rather than the instinct property of MCSCLCPs, which is coincident with the experiment result.[18,19]

It is noted that our model also works for investigating the conformation of SCLCPs with quite flexible main chain.

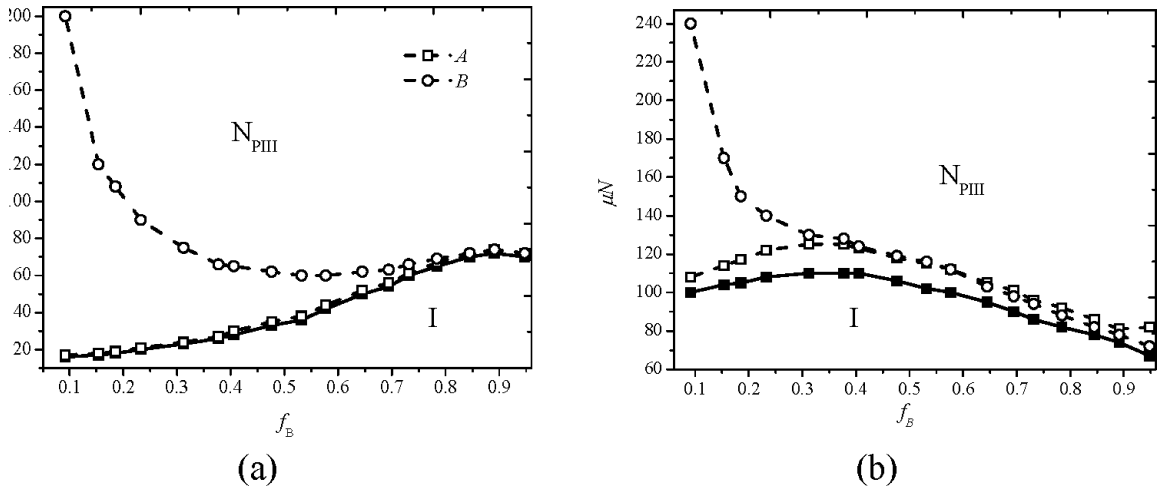


Figure 4. Phase diagram plotted in the μN–f_B plane for the MCSCLCPs with varying main-chain stiffness when $\mu_f N = 0$. (a) $\xi = 1.0$; (b) $\xi = 0.1$.

dx.doi.org/10.1021/ma2027879 | *Macromolecules* 2012, 45, 3590–3603

The mean-squared end-to-end distance vector for the wormlike chain satisfies the Kratky−Porod expression:[33]

$$\langle R^2\rangle = 2\xi L\left\{1 - \frac{\xi}{L}[1 - \exp(-L/\xi)]\right\} \quad (26)$$

In the flexible limit, $L/\xi \gg 1$, we obtain $R \approx (2\xi L)^{1/2}$, which is consistent with the ideal Gaussian chain scaling formula $R = bN^{1/2}$ if we define the contour length $L = Nb$ and $b = 2\xi$. In the rigid rod limit, i.e., $L/\xi \ll 1$, $R = L$. Therefore, the wormlike chain model allows perfect crossover from flexible chain to rigid rod chains. In our work, we set $\xi \leq 0.1$ for the relatively flexible polymer backbone, and in this case, the statistical behavior of the wormlike chain approaches that of the freely jointed chains. Therefore, conformation anisotropic radios $R_{\|}/R_{\perp}$ can be approximately calculated based on freely jointed chain model. We compare the conformation anisotropic radios $R_{\|}/R_{\perp}$ of the relatively flexible polymer backbone in uniaxial phases N_{PIII} with the results reported in ref 29. $\langle R_{\|}^2\rangle$ is the mean-square end-to-end distance vector in the direction parallel to the nematic axis (denoted along the z-direction), which is given by

$$\langle R_{\|}^2\rangle = \langle R_g^2\rangle\left(\frac{1}{3} + \frac{2}{3}\lambda_z\right) \quad (27)$$

where $\langle R_g^2\rangle$ is the mean-square radius of gyration for the wormlike chain with some given ξ values in the isotropic phase. $\langle R_{\perp}^2\rangle$ is the mean-square end-to-end distance vector in the perpendicular direction, which is given by

$$\langle R_{\perp}^2\rangle = \langle R_g^2\rangle\left(\frac{1}{3} - \frac{1}{3}\lambda_z\right) \quad (28)$$

Figure 5 shows the changes of the ratio $R_{\|}/R_{\perp}$ with respect to $\mu N - \mu N^*$ at different values of ξ. μN^* is the corresponding critical value of the orientational interaction at the phase transition. Similar to the analysis mentioned above, μN^* increases when the main chain becomes more flexible from $\xi = 0.1$ to $\xi = 0.05$ to $\xi = 0.01$, and the values of μN^* are 115, 165, and 260, respectively. For the most flexible main chain ($\xi = 0.01$), the degree of anisotropy, i.e., the ratio $R_{\|}/R_{\perp}$, increases slowly with increasing μN or decreasing the temperature. The coupling effect favoring parallel ordering between main chain and side groups is in agreement with that reported in ref 29.

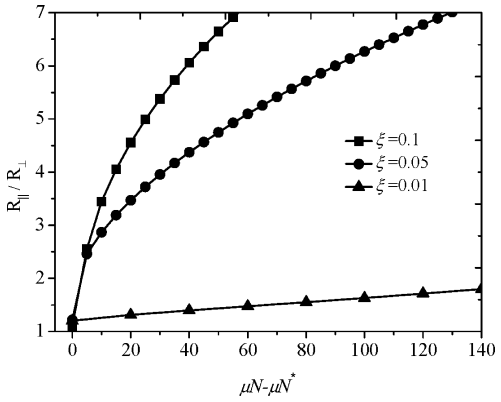


Figure 5. Main-chain conformation anisotropic ratio $R_{\|}/R_{\perp}$ for relatively flexible main chain ($\xi = 0.1$, $\xi = 0.05$, and $\xi = 0.01$) with $f_B = 0.476(N_A/N_B = 1)$ as a function of Maier−Saupe interaction $\mu N - \mu N^*$ under $\mu_f N = 0$. μN^* is the corresponding critical value at the phase transition.

However, compared to their results, the anisotropy radio of such a flexible main chain is smaller even with a large value of μN in our work. This is reasonable because the maximal conformation entropy of flexible chain dominates over the ordering between the main chain and side groups of the SCLCPs' phase behavior. Furthermore, we notice that the main chain's flexibility has strong influence on the conformation of the backbone. The relatively stiff main chains with larger value of ξ likely emerge anisotropic performances and can order strongly with large value of the anisotropy radio. The more stiffness the main chain possesses, the stronger tendency of the parallel alignment of the main chain segments.

C. Uniaxial to Biaxial Phase Transition in the Case of $\mu_f N > 0$. When the side groups are connected to the main chain via a short spacer or only a single covalent bond, we regard the hinges as being stiff. In this case, a perpendicular ordering alignment structure between backbone chain and side groups tends to form, denoted as $\mu_f N > 0$. There are two kinds of competitions in the MCSCLCPs. On one hand, the stretching energy of main chain with some bending modulus ξ must balance its conformation entropies, and the conformation will disturb the parallel alignment of side groups in some extent. On the other hand, the competitions between the global Maier−Saupe interaction preferring parallel ordering of main chain and side groups and the perpendicular tendency of the two components enhance the complexity of the MCSCLCPs phase behavior. Therefore, some complex phases are found, including uniaxial nematic phase N_{PI}, N_{PII}, and N_O and biaxial phase N_{BI}, N_{BII}, and N_{BIII}, which have been briefly introduced in section A. In this section, we first fix the volume fraction $f_B = 0.476(N_A/N_B = 1)$ and main chain's rigidity $\xi = 1$. We focus on the effects of local coupling $\mu_f N$ (stiff hinges with large positive value of $\mu_f N$), the competitions between $\mu_f N$ and LC orientational parameters $\mu_{AA}N$ and $\mu_{BB}N$ and the competition between $\mu_f N$ and the global coupling $\mu_{AB}N$ on the phase behaviors of MCSCLCPs. Furthermore, the phase diagram in μN−f_B plane for $\xi = 1$ is also shown in this work.

Phase Behavior Neglecting Global Coupling ($\mu_{AB}N = 0$). We first investigate the influence of local coupling $\mu_f N > 0$ on the phase behaviors of MCSCLCPs under $\mu_{AB}N = 0$ and $\mu_{AA}N = 0$. Figure 6 shows the order parameters as a function of $\mu_{BB}N$ with $\mu_f N = 0.05$ μN and $f_B = 0.476$. From Figure 6, the side groups B are weakly ordered in the z-direction ($|\lambda_{z,B}| \leq 0.2$) in the region $150 < \mu_{BB}N \leq 170$, forcing the backbone chain A into the xy plane with $\lambda_{z,A} < 0$. When $\mu_{BB}N$ is further increased, the ordering degree of B greatly increases, and A presents oblate shape with the same primary axis as well as B, forming the

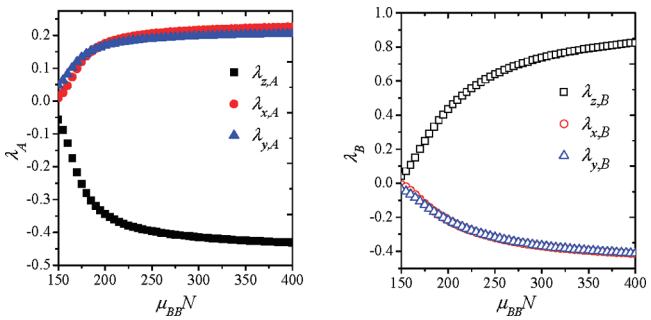


Figure 6. Orientational order parameters λ for MCSCLCPs with $f_B = 0.476$ $(N_A/N_B = 1)$ and $\xi = 1$ as a function of orientational interaction $\mu_{BB}N = \mu N$ in the case of $\mu_f N = 0.05\mu N$, $\mu_{AB}N = 0$, and $\mu_{AA}N = 0$.

dx.doi.org/10.1021/ma2027879 | Macromolecules 2012, 45, 3590−3603

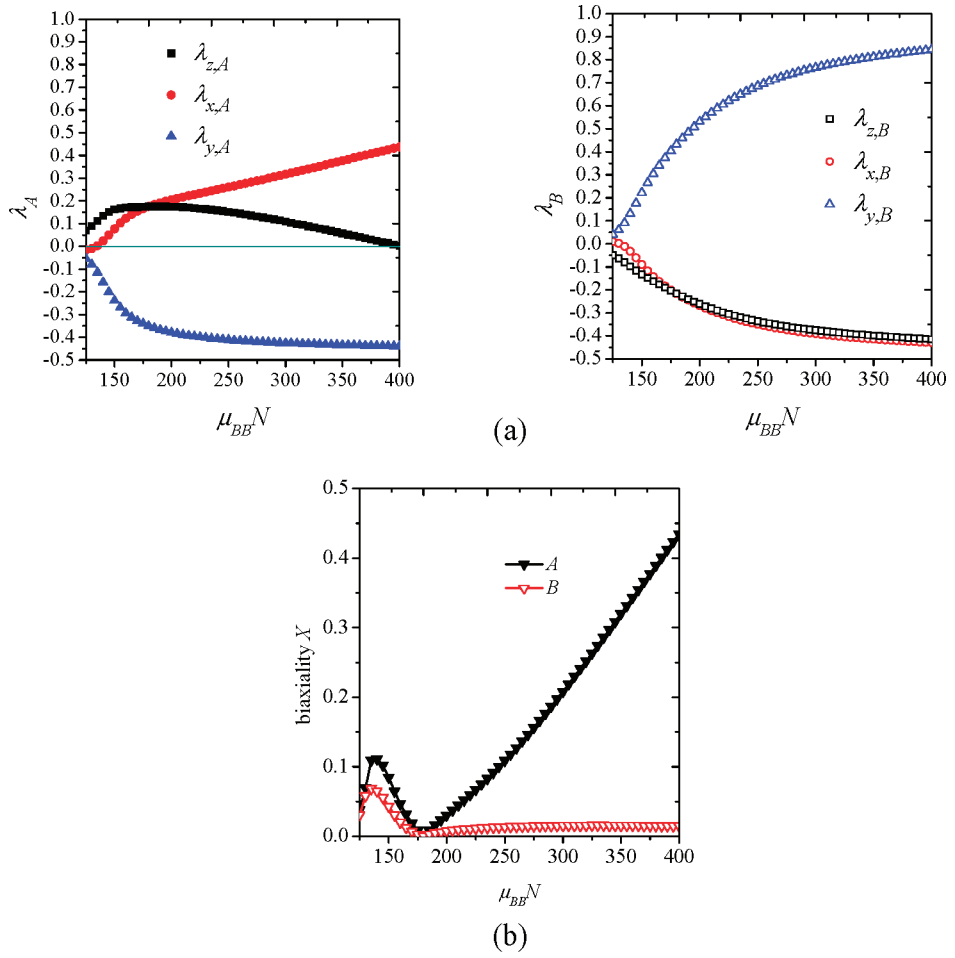


Figure 7. (a) Orientational order parameters λ and (b) the biaxiality parameter X for MCSCLCPs with $f_B = 0.476$ ($N_A/N_B = 1$) and $\xi = 1$ as a function of orientational interaction $\mu_{BB}N = \mu N$ in the case of $\mu_f N = 0.5\mu N$, $\mu_{AB}N = 0$, and $\mu_{AA}N = 0$.

uniaxial phase $N_{PI}(O_AP_B)$. Ignoring all of the global effect on A implies that the backbone is relatively flexible. The local rigidity arising from the linked segments forces the oblate comformation of A, which is similar to the freely joined chain model adopted in ref 29.

However, when $\mu_f N$ is further increased, the backbone with intrinsic bending energy induces different phase behaviors from the completely flexible backbone. Figure 7 shows the stronger local coupling effect with $\mu_f N = 0.5\mu N$, in contrast to Figure 6. Although side groups B order first when the anisotropic phase occurs with increasing their orientational parameter $\mu_{BB}N$, the main chain with some stiffeness ($\xi = 1$) orients along the z-direction induced by the rigid hinge effects. Thus, a weakly ordered uniaxial nematic phase $N_{PII}(P_AO_B)$ is formed at $\mu_{BB}N = 125$. With the further increase of $\mu_{BB}N$, the side groups with high ordering degree display prolate shape with the primary axis along the y-direction. The perpendicular alignment effect of the linkage is also increased by the higher ordered side groups and forces the backbone parallel into the xz plane at $\mu_{BB}N = 180$, forming the $N_{PI}(O_AP_B)$ phase. In the transition region ($130 < \mu_{BB}N < 165$), biaxial phases with small values of biaxiality parameter X occur, shown in Figure 7b. For the first-order unaixial−biaxial phase transitons, we can easily recognize the biaxial phases as long as the biaxiality parameter does not vanish. However, for the second-order phase transitons in this work, the appearance of biaxiality is continuous with the increase of $\mu_{BB}N$. Therefore, for the second-order unaixial−biaxial phase transitons, we define the transition points from uniaxial to biaxial phases as long as one of the biaxiality parameters of the two components is larger than an arbitrary relatively small value, such as 0.05. When $\mu_{BB}N > 210$, the side groups always orient along the y-direction whereas the backbone begins to stretch along the x-axis from the oblate shape in xz plane. Because of the order changes of A, the biaxial phase of the system occurs, forming the $N_{BI}(B_AP_B)$ phase. The biaxial phases are induced by the perpendicular toplogical structures between the main chain and side groups ($\mu_f N$) and main-chain bending feature ξ. It should be noticed that the bending energy ξ incorporated in the wormlike chain model is an essential parameter to form some special biaxial phases. When $\mu_f N$ is strong enough, the local coupling $\exp[-\mu_f N(\mathbf{u}\cdot\mathbf{v})^2]$ first effects on the propagator $q(\mathbf{u},s)$ in eq 21 of the connecting segement, inducing the perpendicular alignment between the side group and its own backbone segment. Then the operater $\nabla_{\mathbf{u}}^2/\xi$ with large value of ξ acting on the $q(\mathbf{u},s)$ in eq 20 drives the adjacent backbone segments to adopt wormlike chain conformation. Therefore, when the values of $\mu_f N$ and ξ are large enough, the biaxial behavior of the backbone N_{BI} can also be obtained even in the absence of the nematic interaction between the main-chain segments, such as $\mu_{AA} = 0$. It is also confirmed in experiments that the flexible backbone also appears as the wormlike chain conformation when the rods are stiffly linked to it.[18] In contrast, if the nematic interaction μ_{AA} is included in the freely jointed chain model without bending energy, we can

dx.doi.org/10.1021/ma2027879 | Macromolecules 2012, 45, 3590−3603

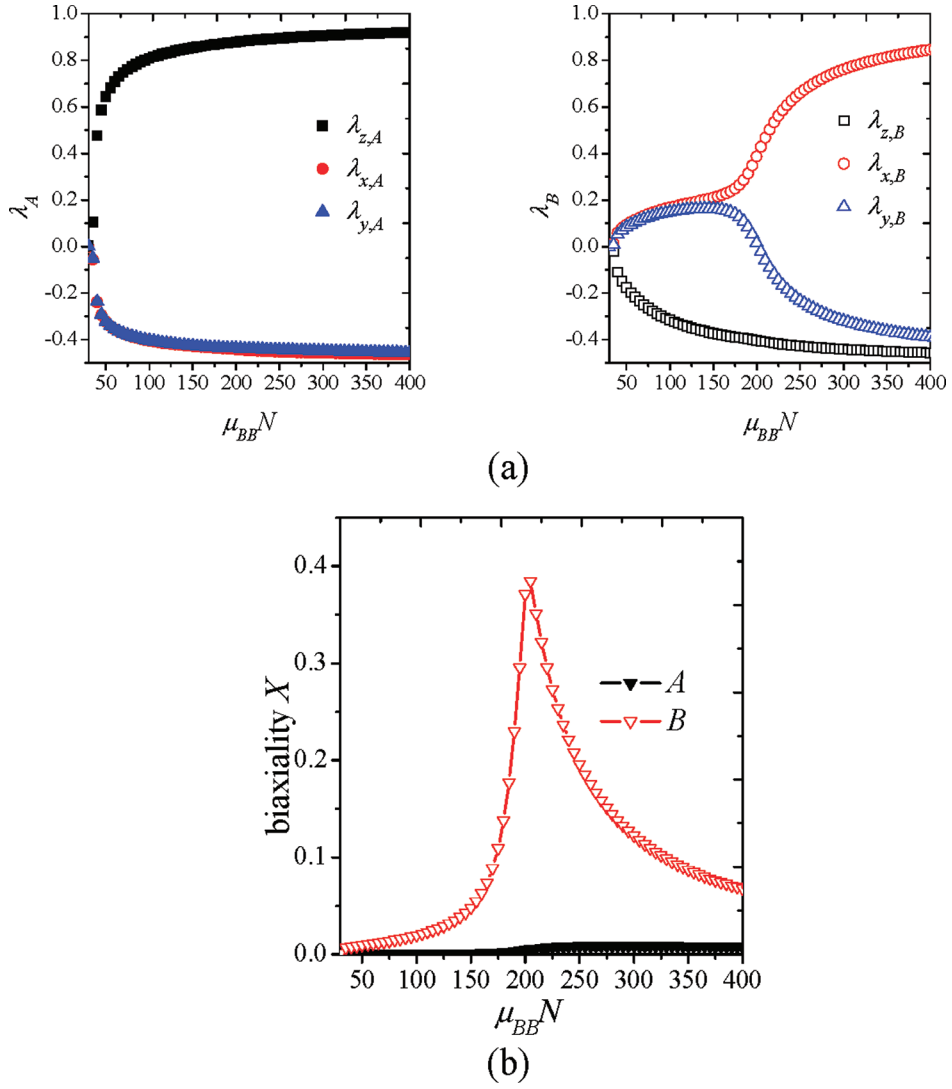


Figure 8. (a) Orientational order parameters λ and (b) the biaxiality parameter X for MCSCLCPs with $f_B = 0.476$ ($N_A/N_B = 1$) and $\xi = 1.0$ as a function of orientational interaction $\mu_{BB}N$ in the case of $\mu_fN = 0.05\mu N$, $\mu_{AA}N = \mu_{BB}N = \mu N$, and $\mu_{AB}N = 0$.

obtain the uniaxial nematic conformation of the main chain just like rod molecules and also the biaxial phase N_{BIII} with the backbone and side groups orientating along their individuals but with orthogonal primary directions. However, the freely jointed chain model cannot describe the biaxial behavior of the backbone such as N_{BI} and side groups such as N_{BII} phases in the following discussion.

The main chain A is treated as a wormlike chain in our model; thus, the orientational interaction of A, $\mu_{AA}N$, should be considered. In contrast to the results of Figure 6, the situations with $\mu_{AA}N = \mu_{BB}N = \mu N$ are shown in Figure 8. With the relatively stiff property ($\xi = 1$), the main-chain ordering influence is quite strong; thus, A orders first at $\mu N = 40$ to form a prolate shape with the primary axis orientated along the z-direction and forces the side groups B into the xy plane, forming the $N_{PII}(P_AO_B)$ phase. Even when $\mu_{BB}N$ is increased from 40 to 400, the A component always orients along the z-direction. Whereas, the components B undergo the transition from the oblate shape oriented in the xy plane to the biaxial nematic structure ordered in the x-direction at $\mu_{BB}N > 150$, forming the biaxial phase of the system $N_{BII}(P_AB_B)$. The order parameters of A are always larger than those of B; thus, the primary order of the system is consistent with the primary order of A, which is coincident with the theoretical results.[31] Moreover, we confirm that the biaxial nematic phase favors more conformation entropy of the system than the parallel orientations of them. The phase transition form N_{PII} to N_{BII} is induced by the competition between the orientational behaviors of LC moiety favoring parallel alignment of two components and the stiff hinge favoring orthogonal alignment.

Phase Behaviors in the Presence of Global Coupling ($\mu_{AB}N \neq 0$). In Figure 9, we focus on the effect of global coupling $\mu_{AB}N$ on the phase behaviors of MCSCLCPs while ignoring the interactions of A segments ($\mu_{AA}N = 0$). In this case, the two effects of $\mu_{AB}N$ favoring parallel alignment of A and B and the perpendicular hinge μ_fN counterbalance each other; thus, the anisotropic phase occurs until $\mu_{AB}N$ controls over μ_fN at large value of $\mu_{BB}N$ ($\mu_{BB}N = 200$). The backbone chain tends to be oblate to gain more chain conformation in the case of $\mu_{AA}N = 0$, and $\mu_{AB}N$ prefers parallel orientations between A and B. Thus, a new uniaxial phase N_O occurs in which both A and B display oblate shapes and the averaged orientational parameters are parallel to each other. The oblate spheroids determined by SANS were also mentioned in experiments.[11]

dx.doi.org/10.1021/ma2027879 | *Macromolecules* 2012, 45, 3590−3603

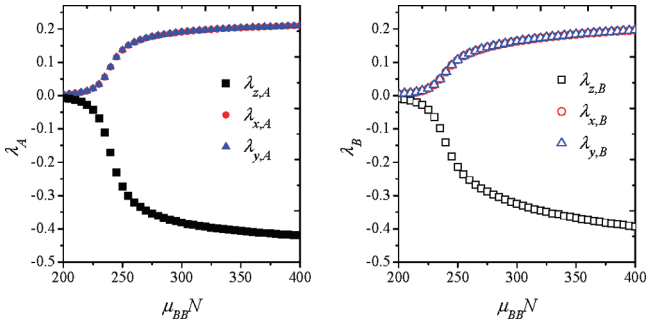


Figure 9. Orientational order parameters λ for MCSCLCPs with f_B = 0.476 (N_A/N_B = 1) and ξ = 1 as a function of orientational interaction $\mu_{BB}N$ in the case of $\mu_fN = 0.05\mu N$, $\mu_{AB}N = \mu_{BB}N = \mu N$, and $\mu_{AA}N = 0$.

If all the orientational parameters are taken into account, i.e., $\mu_{AA}N = \mu_{BB}N = \mu_{AB}N = \mu N$, the phase transitions are more complex. Figure 10 shows the order parameters and biaxiality parameter as a function of μN with local coupling $\mu_fN = 0.05\mu N$. Similar to the phenomenon in Figure 8, the N_{PII} phase occurs at μN = 50 because the main chain *A* orders first along the *z*-direction to form a prolate shape forcing the side groups *B* into the *xy* plane. When μN is further increased, *B* components with comparable volume fraction take the opportunity to order in the *xy* plane and orient along the *x*-direction to gain the beneficial orientational energy at $\mu N \approx 225$, forming the prolate shape of themselves. In the transition region of 175 < μN < 225, the side groups are oriented differently in 3D space, appearing biaxial orientations of *B*. The evolution of the side groups' orientations have an important effect on the main chain *A*, inducing the order parameters of *A* have deviations away from the *z*-axis. From Figure 10b, we see that the maximum value of the biaxiality *X* of *B* occurs at μN = 195, and that of the overall system subsequently occurs at μN = 210. Therefore, the biaxial phase of the system results from the transition from oblate shape to biaxial structure of *B* and the primary order of *A*, resulting in the phase of $N_{BII}(P_AB_B)$. When μN is further increased, the cost of the stretching energy of *A* will be intense due to the ordering of *B*, therefore forming biaxial shapes for both *A* and *B* at $\mu N \approx 275$. However, the separated orientations of *A* along the *z*- and *x*- directions while those of *B* are complementary, reducing the biaxiality of the overall system. We include this phase into N_{BII} phase. After that, the global interactions preferring parallel orientations of the two components compete the perpendicular effect of local coupling, and the conformation entropy of *A* dominates the phase behavoir. In this case, the uniaxial nematic phase N_O is found, similar to Figure 9.

Phase Diagram in μN–f_B Plane for ξ = 1. We present the phase diagram in the μN–f_B plane ($\mu_{AA}N = \mu_{BB}N = \mu_{AB}N = \mu N$) while fixing ξ = 1 and $\mu_fN = 0.5\ \mu N$ in Figure 11. It displays the principal ordered phases N_{PI}, N_{PII}, N_O, N_{BI}, N_{BII}, and N_{BIII} as well as the isotropic phase **I**. In order to compare the relative stability of the phases between isotropic and nematic phase, we started the free enery calculation with both random initial conditions and the given aligned states including uniaxial and biaxial initial fields. For each certain fixed composition, the phase boundary is constructed by comparing the free

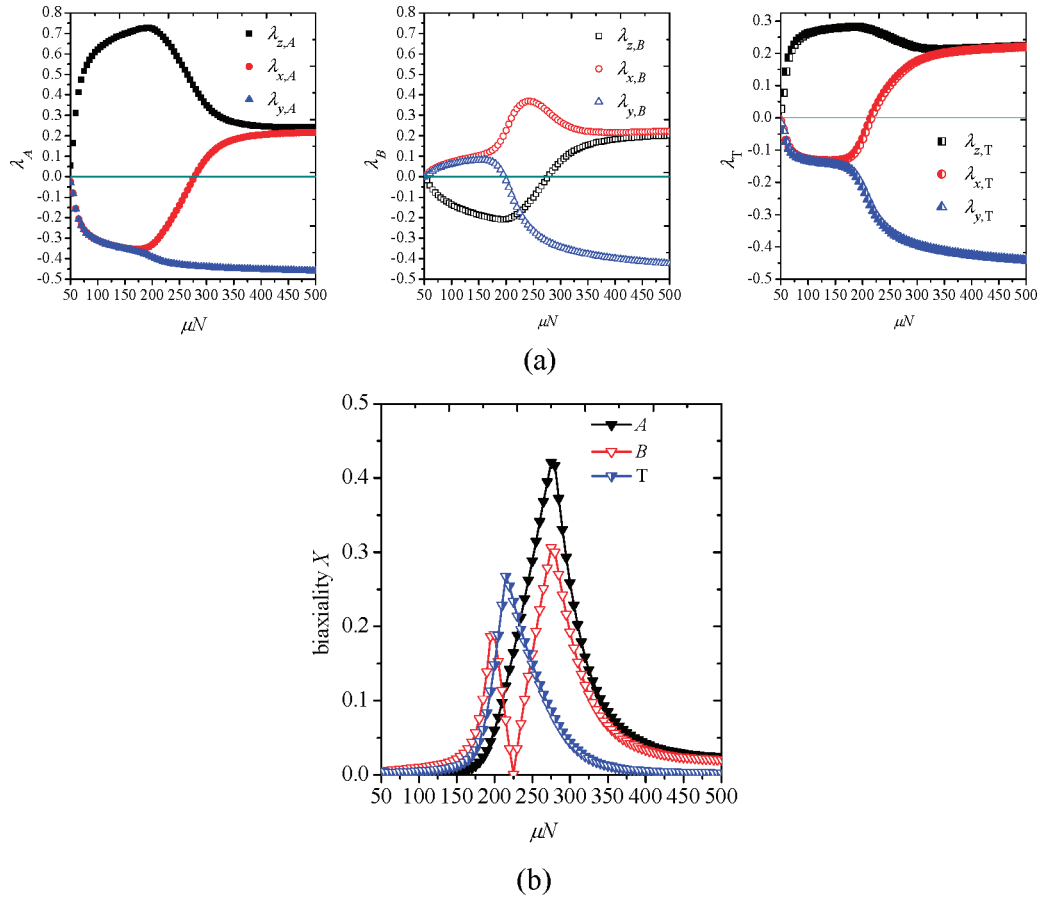


Figure 10. (a) Orientational order parameters λ and (b) the biaxiality parameter *X* for MCSCLCPs with f_B = 0.476 (N_A/N_B = 1) and ξ = 1 as a function of orientational interaction μN in the case of $\mu_fN = 0.05\mu N$ and $\mu_{AA}N = \mu_{BB}N = \mu_{AB}N = \mu N$.

dx.doi.org/10.1021/ma2027879 | *Macromolecules* 2012, 45, 3590–3603

energy of various phases including isotropic phase with the increase of μN by a step of $\Delta\mu N = 5$. The intersection point of these curves of the free energy is decided as the phase boundary point. The symbols in Figure 11 represent the calculated transition points, and the transition lines separating two different phases are simply a guide for the eyes. For each f_B, the discontinuities of the first-order partial derivative of the free energy determine the first-order phase transitions as a function of μN, denoted by the solid lines, otherwise defined as the second-order phase transitions, indicated by the dashed lines. The N'_{BII} (N'_{BI}) phase is biaxial phase where the side groups B (main chain A) display obvious biaxiality, i.e., $X_B \geq 0.05$ ($X_A \geq 0.05$), whereas the overall system displays prolate ellipsoid shape ($X_T < 0.05$) with such a small value volume fraction of the biaxial component. We distinguish them from N_{BII} and N_{BI} phases by dotted curves, respectively. In this phase diagram, the N_{PIII} phase in Figure 1 is not found, which is different from some theoretical reports about SCLCPs and MCSCLCPs.[27,31] It is reasonable that the effect of each side group and its local coupling have entered in the modified diffusion equation of the backbone and can accurately describe the topological structures of MCSCLCPs. Therefore, the backbone and the side groups prefer to be perpendicular between each other as long as one of the component dominates the order of system as increasing of μN.

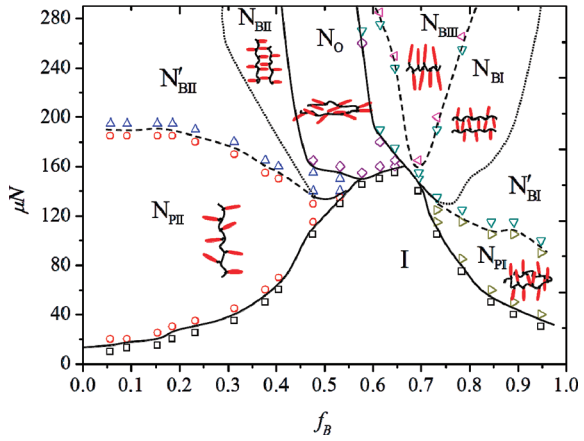


Figure 11. Phase diagram plotted in the μN–f_B plane for MCSCLCPs with the stiff hinge ($\mu_f N = 0.5\mu N$) in the case of the main-chain flexibility $\xi = 1.0$ and $\mu_{AA}N = \mu_{BB}N = \mu_{AB}N = \mu N$. The symbols represent the calculated transition points, and the transition lines are simply a guide for the eyes between the two side phases. The solid lines denote the first-order phase transitions, and the dashed lines denote second-order phase transitions. The $N'_{BII}(N'_{BI})$ phase separated from $N_{BII}(N_{BI})$ phase by dotted curves are biaxial phases where the side groups B (main chain A) display obvious biaxiality, i.e., $X_B \geq 0.05$ ($X_A \geq 0.05$), whereas the overall system displays prolate ellipsoid shape ($X_T < 0.05$).

To the left of the phase diagram, similar to the above analysis, the effect of the backbone with large volume fraction is dominant, and the side groups are forced into the xy plane, forming N_{PII} phase. With increasing of μN, the N'_{BII} phase is separated from N_{PII} phase, which is actually an prolate ellipsoid of the system, whereas the side groups B with small volume fraction display obvious biaxiality ($X_B \geq 0.05$). When μN is further increasd, the biaxial phase N_{BII} occurs because of the ordering of B. Moving toward to the middle of the phase diagram, the interaction effects of the A and B are comparable,

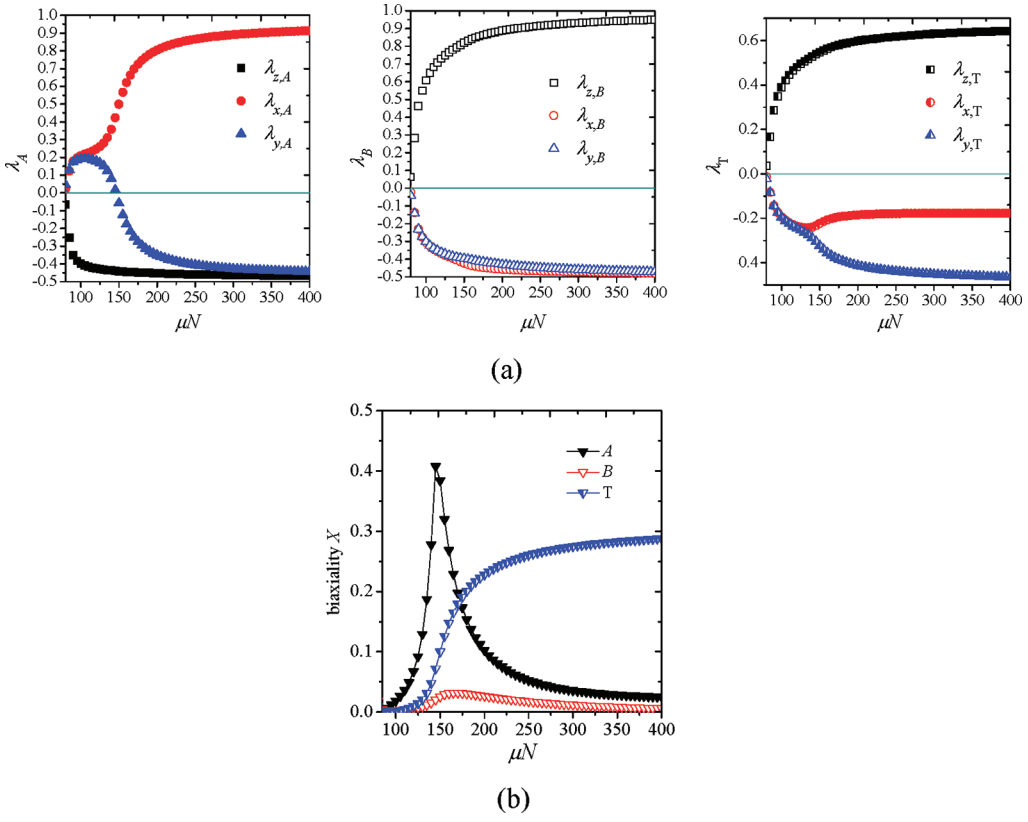


Figure 12. (a) Orientational order parameters λ and (b) biaxiality parameter X for MCSCLCPs with $f_B = 0.784$ ($N_A/N_B = 1/4$) and $\xi = 1$ as a function of orientational interaction μN in the case of $\mu_f N = 0.5\mu N$ and $\mu_{AA}N = \mu_{BB}N = \mu_{AB}N = \mu N$.

dx.doi.org/10.1021/ma2027879 | Macromolecules 2012, 45, 3590–3603

increasing the complexity of the phase transition. The uniaxial nematic phase N_O is formed when the global interactions dominate over the local coupling with large value of μN. Furthermore, due to the competitions between the parallel nematic interactions and the perpendicular local hinge effect, larger value of μN (lower temperature) are required to produce the phase transition from isotropic to anisotropic phase than the situation without local coupling effect ($\mu_f N = 0$) in Figure 4a, especially for almost equal volume fraction of the two components. It is also reported in the experiment that the introduction of stiff phenylsulfonyl side groups decreased the clearing temperature of the pure semiflexible polymers.[56]

To the right of the phase diagram, the orientational effect of the side groups become stronger. Increasing μN from the isotropic phase results in N_{PI}, N_{BI}, and N_{BIII} in turn. For instance, we analyze that phase transitions with $f_B = 0.784$ in detail, shown in Figure 12. The side groups begin to order at $\mu N = 80$ and force the backbone into the xy plane, forming the N_{PI} phase. The prolate shapes of B are always stable during the simulation region of μN. However, with the increase of μN, the backbone orders in the x-direction and displays biaxiality at $\mu N = 115$ with $X_A > 0.05$, as shown in Figure 12b. The biaxiality of the overall system occurs at $\mu N = 145$ with $X_T > 0.05$ following the biaxiality of A. When μN is further increased, the backbone stretches with strong ordering degree in the x-direction, and the biaxiality disappears at $\mu N > 270$ with $X_A < 0.05$. In this case, A and B present prolate shape of themselves, whereas the primary axises of A and B are perpendicular to each other, inducing the biaxial phase of the overall system with the order parameters parallel to xz plane, i.e., $N_{BIII}(P_AP_B)$. The biaxial phase N_{BIII} has never been reported before. In our study, the N_{BIII} phase is typically found at $0.65 < f_B < 0.7$, where the biaxiality of the overall system X_T is rapidly increased to 0.3 with $X_A < 0.05$ and $X_B < 0.02$ upon the appearance of the anisotropic phase. The biaxial phase N_{BIII} is obtained in the case of high backbone stiffness, comparable μ_{AA} and μ_{BB}, and stiff hinges, consistent with the biaxial molecular orientation in the experiments about the combined main-chain and side groups LC polymers.[10,16] Furthermore, the biaxial nematic phases are fond of side-on SCLCPs in experiments.[22,57] This is our bold guess, and a further study with both order parameters and microscopic densities distribution is expected to clarify the rich phase behaviors of side-on SCLCPs.

CONCLUSIONS

We use the SCFT method to investigate the isotropic−anisotropic phase transitions of the MCSCLCPs and the conformation of the system. A universal model is developed by treating the backbone as a wormlike chain with varying rigidity degree and attached with the rigid side groups hinged to it. The global nematic coupling and the local hinge effects are adopted to describe the interactions between the backbone and the side groups. The global nematic interactions favoring the parallel alignment between backbone segments, between the backbone side groups, and between the side mesogens are all described by Maier−Saupe orientational interactions. Whereas the local coupling effect involves the instantaneous values depending on the orientation vectors of the backbone segment and its own LC side groups, which was first proposed by Wang and Wang[29] for investigating the chain conformation of SCLCPs. Furthermore, the local coupling effect and the probability of each side group all act on the modified diffusion equation of the wormlike main chain, which is implemented by the pseudospectral operator splitting algorithm to obtain the chain propagator $q(\mathbf{u},s)$. The orientation degrees of the backbone chain and the side groups are all described by the corresponding unit vectors $\mathbf{u}\{\theta,\varphi\}$. By numerically solving the SCFT equations, we investigate the effects of rigidity of the main chain ξ, the self-nematic interactions $\mu_{AA}N$ and $\mu_{BB}N$, the global coupling $\mu_{AB}N$, the strength of local hinge $\mu_f N$, and the volume fraction f_B on the liquid crystal behaviors of MCSCLCPs. Rich ordered phases including uniaxial phases N_{PI}, N_{PII}, N_{PIII}, and N_O and biaxial phases N_{BI}, N_{BII}, and N_{BIII} are obtained in this work.

When the hinge is flexible, i.e., $\mu_f N = 0$, only prolate uniaxial nematic phase N_{PIII} are obtained where both of the main chain and side groups are parallelly ordered between each other. In this case, the relativley stiff main chain with intrinsic bending modulus dominates the phase transition from isotropic phase to nematic phases. Whereas for the relatively flexible backbone, the effects of side groups play more important role in the right of the phase diagram because the strength of side-chain interaction is governed by their volume fraction.

When the hinges are stiff with a large positive value of $\mu_f N$, the side groups prefer to be linked perpendicularly to the backbone and the comb geometrical structure of MCSCLCPs dominates the phase behaviors. The competitions between the global Maier−Saupe interaction preferring parallel orientations of the system, the perpendicular tendency of the two components, and the stretching energy of main chain with some bending modulus ξ but having to satisfy the conformation of maximum entropies result in complex transitions between uniaxial phases and biaxial phases. The uniaxial phases N_{PI} and N_{PII} are dominated by the order of the side groups and the main chain, respectively. The backbone of N_{PI} and side groups of N_{PII} forms oblate shapes. With the increase of μN, the biaxial phases N_{BI} and N_{BII} occur because the backbone chain and the side groups tend to order along their primary axis, respectively. The biaxial orderings of the backbone in N_{BI} and side groups in N_{BII} phases result from the accurate numerical calculation of the wormlike chain model with bending energy ξ. The new uniaxial phase N_O occurs when the global coupling effects with comparable volume fractions of backbone and side groups defeat the local coupling effects as well as the maximal entropy of the main chain. When the backbone has high chain stiffness and μ_{AA} is comparable to μ_{BB}, another new phase N_{BIII} is found as a biaxial phase, whereas the backbone and side groups are orientated along their individuals but with orthogonal primary directions. Furthermore, in contrast to the situation without local coupling effect, the phase transition from isotropic to anisotropic phase requires larger value of μN (lower temperature).

AUTHOR INFORMATION

Corresponding Author

*E-mail: pingtang@fudan.edu.cn.

Notes

The authors declare no competing financial interest.

ACKNOWLEDGMENTS

We thank financial support from the National Basic Research Program of China (Grant 2011CB605700). Funds from the NSF of China (Grants 20990231 and 91127033) are also acknowledged.

REFERENCES

(1) Ikeda, T.; Tsutsumi, O. *Science* **1995**, *268*, 1873.
(2) Blackwood, K. M. *Science* **1996**, *273*, 909.
(3) Ahn, S. K.; Deshmukh, P.; Gopinadhan, M.; Osuji, C. O.; Kasi, R. M. *ACS Nano* **2011**, *5*, 3085.
(4) Chakrabarti, P.; Pal, D. *Prog. Biophys. Mol. Biol.* **2001**, *76*, 1.
(5) de Gennes, P. G.; Prost, J. *The Physics of Liquid Crystals*, 2nd ed.; Clarendon Press: Oxford, UK, 1993.
(6) Wessels, P. P. F.; Mulder, B. M. *J. Phys.: Condens. Matter* **2006**, *18*, 9359.
(7) Reck, B.; Ringsdorf, H. *Makromol. Chem., Rapid Commun.* **1985**, *6*, 291.
(8) McArdle, C. B. *Side Chain Liquid Crystal Polymers*; Blackie: Glasgow, 1989.
(9) Zhou, Q. F.; Zhu, X. L.; Wen, Z. Q. *Macromolecules* **1989**, *22*, 491.
(10) Xie, H. L.; Jie, C. K.; Yu, Z. Q.; Liu, X. B.; Zhang, H. L.; Shen, Z. H.; Chen, E. Q.; Zhou, Q. F. *J. Am. Chem. Soc.* **2010**, *132*, 8071.
(11) Kempe, M. D.; Kornfield, J. A.; Lal, J. *Macromolecules* **2004**, *37*, 8730.
(12) Lecommandoux, S.; Noirez, L.; Achard, M. F.; Hardouin, F. *J. Phys. II* **1996**, *6*, 1231.
(13) Craig, A. A.; Imrie, C. T. *Macromolecules* **1999**, *32*, 6215.
(14) Riala, P.; Andreopoulou, A.; Kallitsis, J.; Gitsas, A.; Floudas, G. *Polymer* **2006**, *47*, 7241.
(15) Craig, A. A.; Imrie, C. T. *Macromolecules* **1995**, *28*, 3617.
(16) Piao, X. L.; Kim, J. S.; Yun, Y. K.; Jin, J. I.; Hong, S. K. *Macromolecules* **1997**, *30*, 2294.
(17) Percec, V.; Keller, A. *Macromolecules* **1990**, *23*, 4347.
(18) Kikuchi, M.; Lien, L. T. N.; Narumi, A.; Jinbo, Y.; Izumi, Y.; Nagai, K.; Kawaguchi, S. *Macromolecules* **2008**, *41*, 6564.
(19) Rousseau, D.; Marty, J. D.; Mauzac, M.; Martinoty, P.; Brandt, A.; Guenet, J. M. *Polymer* **2003**, *44*, 2049.
(20) Cotton, J. P.; Hardouin, F. *Prog. Polym. Sci.* **1997**, *22*, 795.
(21) Lecommandoux, S.; Achard, M. F.; Hardouin, F.; Brulet, A.; Cotton, J. P. *Liq. Cryst.* **1997**, *22*, 549.
(22) Severing, K.; Saalwachter, K. *Phys. Rev. Lett.* **2004**, *92*, 125501.
(23) Finkelmann, H.; Rehage, G. *Adv. Polym. Sci.* **1984**, *60−1*, 97.
(24) Vasilenko, S. V.; Shibaev, V. P.; Khokhlov, A. R. *Macromol. Chem. Phys.* **1985**, *186*, 1951.
(25) Auriemma, F.; Corradini, P.; Vacatello, M. *J. Chem. Phys.* **1990**, *93*, 8314.
(26) Brochard, F.; Jouffroy, J.; Levinson, P. *J. Phys. (Paris)* **1984**, *45*, 1125.
(27) Wang, X. J.; Warner, M. *J. Phys. A: Math. Gen.* **1987**, *20*, 713.
(28) Renz, W.; Warner, M. *Proc. R. Soc. London, Ser. A* **1988**, *417*, 213.
(29) Wang, R.; Wang, Z. G. *Macromolecules* **2010**, *43*, 10096.
(30) Carri, G. A.; Muthukumar, M. *J. Chem. Phys.* **1998**, *109*, 11117.
(31) Bladon, P.; Warner, M.; Liu, H. *Macromolecules* **1992**, *25*, 4329.
(32) Renz, W. *Mol. Cryst. Liq. Cryst.* **1988**, *155*, 549.
(33) Kratky, O.; Porod, G. *Recl. Trav. Chim* **1949**, *68*, 1106.
(34) Drolet, F.; Fredrickson, G. H. *Phys. Rev. Lett.* **1999**, *83*, 4317.
(35) Wang, R.; Jiang, Z. B.; Hu, J. L. *Polymer* **2005**, *46*, 6201.
(36) Vroege, G. J.; Odijk, T. *Macromolecules* **1988**, *21*, 2848.
(37) Cui, S. M.; Akcakir, O.; Chen, Z. Y. *Phys. Rev. E* **1995**, *51*, 4548.
(38) Duchs, D.; Sullivan, D. E. *J. Phys.: Condens. Matter* **2002**, *14*, 12189.
(39) Song, W. D.; Tang, P.; Zhang, H. D.; Yang, Y. L.; Shi, A. C. *Macromolecules* **2009**, *42*, 6300.
(40) Gao, J.; Tang, P.; Song, W. D.; Yang, Y. L. *Soft Matter* **2011**, *7*, 5208.
(41) Song, W. D.; Tang, P.; Qiu, F.; Yang, Y. L.; Shi, A. C. *Soft Matter* **2011**, *7*, 929.
(42) Fredrickson, G. H. *The Equilibrium Theory of Inhomogenous Polymers*; Clarendon Press: Oxford, 2005.
(43) Chantawansri, T. L.; Bosse, A. W.; Hexemer, A.; Ceniceros, H. D.; Garcia-Cervera, C. J.; Kramer, E. J.; Fredrickson, G. H. *Phys. Rev. E* **2007**, *75*, 031802.
(44) Adams, J. C.; Swarztrauber, P. N. SPHEREPACK 3.1: A Model Development Facility, 2003.
(45) Pryamitsyn, V.; Ganesan, V. *J. Chem. Phys.* **2004**, *120*, 5824.
(46) Yang, G. A.; Tang, P.; Yang, Y. L.; Wang, Q. A. *J. Phys. Chem. B* **2010**, *114*, 14897.
(47) Shah, M.; Pryarnitsyn, V.; Ganesan, V. *Macromolecules* **2008**, *41*, 218.
(48) Jiang, Y.; Zhang, W. Y.; Chen, J. Z. Y. *Phys. Rev. E* **2011**, *84*, 041803.
(49) Davidson, P.; Noirez, L.; Cotton, J. P.; Keller, P. *Liq. Cryst.* **1991**, *10*, 111.
(50) Hessel, F.; Finkelmann, H. *Polym. Bull.* **1985**, *14*, 375.
(51) Fredrickson, G. H.; Ganesan, V.; Drolet, F. *Macromolecules* **2002**, *35*, 16.
(52) Chen, Z. Y. *Macromolecules* **1993**, *26*, 3419.
(53) Chandrasekhar, S.; Sadashiva, B. K.; Ratna, B. R.; Raja, V. N. *Pramana* **1988**, *30*, L491.
(54) Matsuyama, A. *Mol. Cryst. Liq. Cryst.* **2011**, *540*, 42.
(55) Chen, X. F.; Shen, Z. H.; Wan, X. H.; Fan, X. H.; Chen, E. Q.; Ma, Y. G.; Zhou, Q. F. *Chem. Soc. Rev.* **2010**, *39*, 3072.
(56) Chang, S.; Han, C. D. *Macromolecules* **1996**, *29*, 2103.
(57) Hessel, F.; Herr, R. P.; Finkelmann, H. *Macromol. Chem. Phys.* **1987**, *188*, 1597.

Macromolecules

Article

pubs.acs.org/Macromolecules

Gas Sorption and Diffusion in Amorphous and Semicrystalline Nanoporous Poly(2,6-dimethyl-1,4-phenylene)oxide

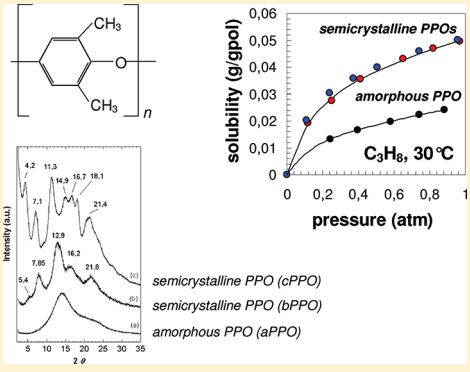
Michele Galizia,[†,*] Christophe Daniel,[‡] Gianluca Fasano,[‡] Gaetano Guerra,[‡] and Giuseppe Mensitieri[§]

[†]Department of Materials and Production Engineering, University of Naples Federico II, p.le Tecchio 80, 80125 Naples, Italy

[‡]Department of Chemistry, NANOMATES and INSTM Research Unit, University of Salerno, via Ponte Don Melillo, 84084 Fisciano (SA), Italy

[§]Department of Materials and Production Engineering and INSTM Research Unit, University of Naples Federico II, p.le Tecchio 80, 80125 Naples, Italy

ABSTRACT: In this contribution is presented an analysis of mass transport properties of low molecular weight compounds in amorphous PPO and in two semicrystalline PPOs obtained by treating with benzene and carbon tetrachloride the amorphous sample. It is found that semicrystalline samples are endowed with larger gas sorption capacity and diffusivity as compared to the amorphous ones: this behavior has been attributed prevalently to the nanoporous nature of the crystalline phases induced by treatment with solvents. In particular, sorption experiments, carried out at 30 °C with methane, carbon dioxide, propane and propylene, have shown that both semicrystalline PPOs display rather interesting features which make them suitable for use as membrane materials in gas separation processes, in view of the relatively high values of solubility and diffusivity. Moreover, these peculiar sorption and mass transport properties have been found to be virtually unaffected by thermal aging: in fact, sorption experiments conducted on amorphous and semicrystalline PPO after treatment at 65 °C for three months showed that sorption and transport properties of aged samples are the same as for the untreated ones. This is an important feature to ensure the stability of performances in membrane applications.



1. INTRODUCTION

Poly(2,6-dimethyl-1,4-phenylene)oxide (PPO) is an aromatic amorphous polymer (see Figure 1 for the repeating unit)

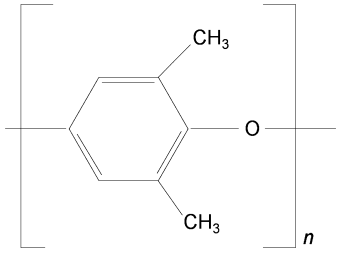


Figure 1. Repeating unit of PPO.

showing very high values of glass transition temperature and gas permeability. Previous works[1,2] report, for amorphous PPO, high levels of gas solubility, diffusivity and permeability, showing its suitability for use as a membrane for gas separations. Ideal separation factors were estimated for different penetrant couples of practical concern, such as methane/carbon dioxide and propane/propylene.[1,2] As pointed out by Toi et al.,[3] the permeation rate of PPO results several times larger than that of many other common glassy and even rubbery polymers. This finding, rather unusual in view of the very high glass transition temperature of PPO and considering the high rigidity of its molecular backbone, has been attributed to the relatively high fractional free volume, f, which was estimated to be about 18%.[4] It is recalled that f is defined as $(\hat{V}_{sp} - \hat{V}_0)/\hat{V}_{sp}$, where $\hat{V}_{sp}$ is the specific volume and $\hat{V}_0$ the occupied volume, as calculated through the Bondi's rule.

These features make PPO attractive for its exploitation as membrane material for gas separation, also in view of the fact that PPO is a commercial polymer with a cost which is well below that of common techno-polymers.

Quite interestingly, it has been found that semicrystalline PPO displaying nanoporous crystalline phases can be obtained by treatment with specific solvents.[5,6] As recently demonstrated by Guerra and co-workers,[7−14] semicrystalline PPO is characterized by peculiar and unexpected properties which resemble those of semicrystalline syndiotactic polystyrene (sPS) with nanoporous crystalline domains. In particular, it has been observed[7−15] that, in spite of the presence of a crystalline phase, the solubility of several low molecular weight compounds is significantly higher in semicrystalline PPO than in the totally amorphous PPO. In fact, this behavior has been attributed to sorption within the nanoporous crystalline phase.

Received: January 9, 2012
Revised: March 28, 2012
Published: April 13, 2012

 © 2012 American Chemical Society dx.doi.org/10.1021/ma3000626 | *Macromolecules* 2012, 45, 3604−3615

Usually, the description of gas solubility isotherms in semicrystalline polymers is based on the simple assumption that the penetrant molecules are accommodated only in the amorphous phase and that the crystalline domains do not contribute to the sorption process, because of its inaccessible and closely packed structure. Such an assumption has been widely confirmed by experimental evidence. As a consequence, the total gas solubility coefficient in the whole semicrystalline sample, S, can be generally scaled to that of the sole amorphous phase, S_a, according to the simple expression

$$S = \chi S_a \tag{1}$$

where χ is the volume fraction of amorphous phase.[16−18] The solubility coefficient is defined as the ratio between the equilibrium penetrant concentration inside the polymer (expressed as (cm^3 (STP)) /(cm^3 of polymer)) and the value of the external partial pressure of penetrant in contact with polymer. Nevertheless, in some cases this physical picture appears oversimplified, as for semicrystalline polymers displaying the mentioned nanoporous crystalline phases that contribute to sorption of low molecular weight compounds in a nonnegligible amount. One of the first reported cases is that of poly(4-methyl-1-pentene) (PMP).[19,20] Later, several authors demonstrated that, in some cases, the crystalline phase gives a contribution to the total solubility that even largely exceeds that of the amorphous phase: such a behavior was observed, for instance, in semicrystalline syndiotactic poly styrene (sPS).[8−14] In fact, in the case of carbon dioxide sorption capacity of the crystalline phase of sPS has been estimated to be about 20 times larger than that of the amorphous phase.[13]

As anticipated above, also the sorption capacity of semicrystalline nanoporous PPO has been reported to be significantly larger than that of totally amorphous PPO:[7] by taking advantage of such feature and by considering the relatively high diffusion coefficients measured, semicrystalline forms of PPO could be considered as suitable for use in membrane-based gas separation processes, where polymers that exhibit large values of permeability are required to guarantee high permeate fluxes. In general, any modification aimed at enhancing gas permeability is accompanied, both in neat polymers and in glassy polymers loaded with inorganic fillers,[21] by a decrease of selectivity. There is, then, a trade off between permeability and selectivity, as indicated by the Robeson upper bound in the selectivity vs permeability plot.[22,23] This issue is specifically addressed in this contribution with reference to the investigated semicrystalline PPOs. In view of its structural peculiarity related to the nanoporous structure of its crystalline domains, semicrystalline nanoporous PPO could be thought of as a special kind of *mixed matrix membrane* (MMM),[24−28] because the presence of crystalline domains acts by improving the gas transport properties, just as in the case of MMMs which are instead obtained by adding inorganic nanoparticles to polymer matrices. This aspect is of practical concern, since adding inorganic particles to polymers to improve the overall transport rate often causes a series of problems, among which the poor adhesion between polymer and filler is of particular relevance, since it leads to the formation of defective interphases. Moreover, in the case of porous fillers, like zeolites, the polymer chains can determine the blockage of pores and channels, reducing the benefits given by the inorganic phase. Conversely, the use of nanoporous semicrystalline polymers could avoid such problems since it would not require to couple the polymer matrix to an inorganic species: simply, by proper choosing the guest solvent and the process conditions for the treatment of amorphous PPO, it would be possible to tailor the fine structure of the nanoporous crystalline domains, limiting at the same time the formation of structural defects.

In the present contribution attention is focused on semicrystalline PPO, which is characterized by even larger gas permeability levels as compared to semicrystalline sPS, supplying a detailed analysis of mass transport properties in amorphous and semicrystalline samples and by highlighting the role played by the solvent used for the crystallization treatment and, in turn, by the associated nanoporous structure of crystalline phase in semicrystalline PPO.

2. THEORETICAL BACKGROUND

2.1. Permeability and Selectivity. The permeability of a polymer film to a gas or vapor penetrant is defined as the ratio between the penetrant flux, J, and the trans-membrane pressure gradient, according to the relationship[29]

$$P = \frac{J}{\Delta p/l} \tag{2}$$

where l is the membrane thickness. Permeability is commonly expressed in Barrers, where 1 barrer $=10^{-10}$ (cm^3(STP)·cm)/(cm^2·cmHg·s). When the solution-diffusion model holds and the sorption kinetics follow the Fick's law, the permeability can be estimated from sorption tests using the following expression:

$$P = S \times \bar{D} \tag{3}$$

Here S is the solubility coefficient and $\bar{D}$ the concentration-averaged penetrant diffusivity.

Besides permeability, another key parameter in membrane separation processes is the ideal selectivity, α_{ij}, defined, when the downstream pressure is much lower than that of the feed, as the ratio between the permeability of pure components i and j, i.e., P_i and P_j:

$$\alpha_{ij} = \frac{P_i}{P_j} = \left(\frac{S_i}{S_j}\right) \times \left(\frac{\bar{D}_i}{\bar{D}_j}\right) \tag{4}$$

It is noticed here that, as reported by several authors, the values of ideal selectivity obtained from pure vapor sorption or permeation data could be different from the real selectivity for gas or vapors mixtures, in the cases in which interactions take place among the penetrants and between the penetrants and the membrane material, and when the transport process is accompanied by significant matrix swelling.[30,31]

On the basis of solution-diffusion model, the ideal selectivity can be factored into two different contributions, namely solubility-selectivity (i.e., S_i/S_j) and diffusivity-selectivity (i.e., $\bar{D}_i/\bar{D}_j$). Usually, the diffusivity selectivity is the dominating term in glassy polymers that exhibit medium-low free volume fractions, while in high free volume glassy polymers the opposite behavior is observed, the overall selectivity being controlled by the solubility contribution. In the first case, one has the well-known size-sieving effect, in view of the fact that the selectivity is favorable to the lower molecular size components, while in the latter case the larger vapors, that are more soluble and condensable, result to be also more permeable.[30−32] In view of the fact that the solubility coefficient increases with the penetrant critical temperature, the solubility selectivity strongly depends on the difference of condensability between the penetrants considered.[33] On the other hand, the

dx.doi.org/10.1021/ma3000626 | Macromolecules 2012, 45, 3604−3615

diffusivity of lighter and less condensable gases is systematically higher than the one of larger size vapors. Then, a trade off exists between solubility selectivity and diffusivity selectivity: it is clear that the knowledge of both such parameters is of crucial importance in designing high performance membrane modules.[34]

2.2. Sorption Thermodynamics. Different models have been proposed to describe the sorption isotherms in amorphous glassy polymers: the dual mode sorption model[35] is certainly one of most widely known and used approaches to correlate both pure and mixed gas solubility in a wide series of glassy matrices.[36,37] Drawbacks of this simple model are, however, that it is not amenable to a predictive use and that the set of parameters determined from sorption data are often unable to describe the corresponding desorption isotherms.[37]

In the last two decades, more advanced models appeared in literature. Among them we consider in detail here the *nonequilibrium lattice fluid* (NELF) model, proposed by Doghieri and Sarti,[38] that, on the roots of rational thermodynamics, extended the Sanchez–Lacombe theory,[39,40] developed for equilibrium rubbery polymers, to the nonequilibrium case of glassy polymers, by choosing a proper order parameter to account for the departure of glassy state from the equilibrium conditions.[38,41,42] In particular, the polymer density, ρ_2, is used as an order parameter, in view of the fact that it gives a direct measurement of the degree of nonequilibrium of the glassy system. Differently from the case of equilibrium rubbery polymers, density of the polymer in the glassy-polymer/low molecular weight penetrant mixture cannot be retrieved from calculations based on equations of state. In fact ρ_2 plays the role of an internal state variable, which evolves at a rate that is dependent on the nonequilibrium values of state variables of the system. To simplify the matter, avoiding involvement of kinetics issues, in the application of NELF theory it is generally assumed that polymer density is frozen-in at the starting value of the unpenetrated glassy polymer, i.e., that its evolution kinetics is much slower than that characteristic of the gas sorption process.

On the basis of this approach, Doghieri and Sarti,[38,41,42] proposed the following expression for the chemical potential of a low molecular weight penetrant absorbed within a glassy polymer:

$$\mu_1^S(T, p, \omega_1, \rho_2) = \left(\frac{\partial G}{\partial n_1}\right)_{T,p,\rho_2,n_2} = RT\ln(\tilde{\rho}\phi_1) - RT\left[r_1^0 + \frac{r_1 - r_1^0}{\tilde{\rho}}\right]\ln(1-\tilde{\rho}) - r_1 + \tilde{\rho}[r_1^0 v^*_1(p^*_1 - p^* - \phi_2^2\Delta p^*)] \quad (5)$$

On this basis, the *pseudo phase equilibrium* between a pure gas penetrant phase and the penetrant absorbed in the glassy polymer phase can be hence obtained by equating the chemical potential of the penetrant in the external gaseous phase to that given by eq 5. The term *pseudoequilibrium* is used here in view of the fact that the phase equilibrium is attained for an apparently constant value of polymer density that is, actually, a nonequilibrium property.

In eq 5, the subscripts 1 and 2 stand for gas and polymer respectively, ω_i and ϕ_1 represent the mass and the volume fraction respectively of the component ith in mixture, r_1^0 and r_1 are the number of lattice sites occupied by a gas molecule in the pure state and in the glassy mixture, and $\tilde{\rho}$ is the mixture reduced density, defined as the ratio

$$\tilde{\rho} = \frac{\rho}{\rho^*} \quad (6)$$

where ρ is the density of polymer phase mixture and ρ^* a characteristic mixture parameter. The value of ρ can be calculated from the value of polymer density, ρ_2, by the following expression:

$$\rho = \frac{\rho_2}{\omega_2} \quad (7)$$

Finally, p^*_i and v^*_i are equation of state parameters for the pure species. The characteristic pressure, p^*, of the glassy polymer mixture can be calculated from the corresponding values for pure components, p^*_1 and p^*_2, through the following mixing rule:

$$p^* = \phi_1 p^*_1 + \phi_2 p^*_2 - \phi_1\phi_2(1 - k_{ij})(\sqrt{p^*_1} - \sqrt{p^*_2})^2 \quad (8)$$

The parameters p^*_1, p^*_2, and p^* are related to the cohesive energy density of species 1 and 2 and of the mixture, respectively; hence, they give an estimate of the extent of self- and mutual mean field interactions. In eq 8, k_{ij} represents an adjustable parameter that can be optimized on the basis of experimental solubility data, when available. Alternatively, it can be, in a first approximation, fixed to be equal to zero.[43] From a physical point of view, k_{ij} measures the deviation from the empirical geometric mean combination rule for p^*. Finally, v^*_i is related to a characteristic temperature of the substance through the relationship:

$$v^*_i = \frac{RT^*_i}{p^*_i} \quad (9)$$

Obviously, use of the NELF model requires the *a priori* knowledge of the characteristic parameters p^*_i, T^*_i, and ρ^*_i for both the penetrant and the polymer species: for the penetrant, they can be obtained by fitting experimental equilibrium liquid–vapor data with the Sanchez–Lacombe equation of state,[39] while for the polymer they can be determined by fitting, to the same equation of state, the experimental *PVT* data in the rubbery region, where equilibrium conditions hold (more on this later).

It is important to note that, in presence of swelling penetrants, one needs also to account for possible 'instantaneous' changes of the nonequilibrium frozen-in polymer density. In fact, in such cases the polymer density experiences a nonnegligible change, as long as the sorption proceeds, to accommodate penetrant molecules: experimental data collected on different systems suggest that the starting value of ρ_2 decreases linearly with the penetrant partial pressure,[44] according to the relationship

$$\rho_2 = \rho_2^0(1 - k_{sw}p) \quad (10)$$

where ρ_2^0 is the density of the pure unpenetrated polymer phase and k_{sw} is a swelling coefficient, that can be obtained directly from dilation experiments[45] or, indirectly, from the analysis of experimental solubility isotherms at relatively high pressures, where the swelling extent is larger, according to the procedure reported by Giacinti et al.[46] Here ρ_2 still represents a kinetically

dx.doi.org/10.1021/ma3000626 | Macromolecules 2012, 45, 3604–3615

frozen value of polymer density, which is different from the starting frozen-in density of pure glassy polymer since room is necessary to accommodate penetrant molecules. Conversely, sorption of nonswelling penetrants does not induce any appreciable variation of the matrix density and the entire sorption isotherm can be correctly predicted by imposing the swelling coefficient equal to zero and using k_{ij} as the only fitting parameter.

3. EXPERIMENTAL SECTION

3.1. Materials. The PPO used in this study was purchased by Sigma-Aldrich and presents weight-averaged and number-averaged molecular masses M_w= 59000 and M_n= 17000, respectively. Solvents used to prepare the semicrystalline samples (i.e., benzene and carbon tetrachloride) were purchased from Aldrich and used without further purification. For gas sorption measurements, high purity gases (>99.6%) supplied by Rivoira (Chivasso, Italy) were used as received.

PPO amorphous (in the following aPPO) films were obtained by compression molding after melting at 290 °C. The crystallization of these amorphous films has been induced by contacting them with vapors of different solvents at room temperature. The solvent was then removed from the crystallized films by treatment with a SFX 200 supercritical carbon dioxide extractor (ISCO Inc.), at 40 °C and 250 bar, with an extraction time of 300 min. Two different types of semicrystalline PPO samples were obtained by using two different solvents: bPPO, obtained by treatment with benzene and cPPO obtained by treatment with carbon tetrachloride.

3.2. X-ray, FTIR, and DSC Characterization. X-ray diffraction patterns were obtained on a Bruker D8 Advance automatic diffractometer operating with a nickel-filtered Cu Kα radiation. The degree of crystallinity of nanoporosous films was obtained from the X-ray diffraction data, by applying the standard procedure of resolving the diffraction pattern into two areas corresponding to the contributions of the crystalline and amorphous fractions.

Fourier transform infrared (FTIR) spectra were obtained at a resolution of 2.0 cm^{-1} with a Tensor 27 Bruker spectrometer equipped with deuterated triglycine sulfate (DTGS) detector and a Ge/KBr beam splitter. The frequency scale was internally calibrated to 0.01 cm^{-1} using a He−Ne laser. A total of 32 scans were signal averaged to reduce the noise.

The infrared based degree of crystallinity, X_C, can be evaluated according to the following relationship:[47,48]

$$K = \frac{l}{l'(1 - X_C)} \tag{11}$$

Here K is the subtraction coefficient used to reduce to baseline the contribution of the amorphous phase, l and l' are the thickness of the sample and of an amorphous PPO reference film. The ratio l/l' was estimated from the absorbance ratio of a conformationally insensitive peak, i.e., at 960 cm^{-1}.

Differential scanning calorimetry (DSC) analysis has been performed on amorphous and semicrystalline samples of PPO to gather information on glass transition and melting temperatures as well as, only for the semicrystalline samples, on enthalpy of melting. Test were performed on samples of around 10 mg sealed in a nonhermetic aluminum pan and under nitrogen atmosphere by using a Q1000 DSC apparatus (by TA Instruments, New Castle, DE) at a temperature scanning rate of 5 °C/min in the temperature range from 25 to 400 °C.

3.3. Sorption Measurements. Subatmospheric sorption experiments were carried out using a CAHN D200 electronic microbalance (CAHN Instruments, Madison, WI), with a sensitivity of 0.1 μg. The weighing unit element is put at the top of a close water-jacketed glass chamber containing the polymer sample hanged at the left arm of the balance, while an inert tare is suspended on the opposite arm, enclosed in a stainless steel case. All the system is vacuum tight, connected with service lines to the gas feeding system, to the vacuum pump and to the exhaust. The sampling chamber is thermostated with a water jacket equipped with a recirculation pump, to keep the temperature constant to within ±0.1 °C, while the pressure is monitored by a Baratron 121A (MKS Instruments, Andover, MA) manometer with a full scale of 1000 Torr, a resolution of 0.01% of the full scale range and an accuracy of 0.5% of the reading.

The experiments were performed by step increasing the penetrant partial pressure, after equilibrium conditions was reached at the previous sorption step: by following this procedure, the solubility and diffusivity values were determined in a stepwise manner, as a function of penetrant partial pressure. In particular, the gas solubility, expressed as grams of sorbed gas per gram of polymer, was estimated from the analysis of equilibrium sorption stage, while the diffusivity was retrieved from the analysis of the transient sorption stage, by assuming a Fickian behavior: this hypothesis was verified by fitting the experimental transient sorption data with the rigorous solution of the penetrant mass balance equation, for one-dimensional geometry. The evaluation of diffusion coefficients has been performed on the basis of the simplified linear correlation holding, for systems following Fick's law, between the mass absorbed and the square root of time, which is quite accurate up to sorption times for which the mass absorbed does not exceed the 60% of the total value[49] (i.e., $M_t/M_\infty < 0.6$), i.e.:

$$\frac{d(M_t/M_\infty)}{dt^{1/2}} = \left(\frac{16D}{l^2\pi}\right)^{1/2} \tag{12}$$

where D is the gas-polymer mutual diffusivity, M_t and M_∞ are the mass of penetrant absorbed at the time t and at equilibrium conditions, respectively, and l is the film thickness, that was estimated with a digital micrometer with an accuracy of ±1 μm. In applying eq 12 it has been assumed that diffusivity, during each sorption step, is rather constant in view of the limited associated step increase in pressure and, in turn, of the limited penetrant concentration change within the polymer.

It has to be noted here that, in view of the heterogeneous nature of the semicrystalline PPOs, the values of diffusivity determined for these samples are to be considered as spatial averages over the volume of the sample which reflects both the mass transport properties of the amorphous and of the crystalline domains, in a fashion which depends on the detailed morphological structure of the polymer. As a consequence, the reported values have to be considered only for qualitative comparison between amorphous and semicrystalline PPOs. Scaling of these values to PPO samples characterized by a different level of crystallinity and different orientation of crystals could be performed only once detailed information on the crystalline structure will be available.

3.4. PVT Experiments and Density Measurements. The pressure−volume−temperature properties for amorphous PPO were measured using a high pressure dilatometer provided by Gnomix (Boulder, CO).[30] In this apparatus, the polymer sample is kept under hydrostatic pressure using mercury as confining fluid: subsequent compression runs were performed at constant temperature by increasing the pressure in a stepwise manner and recording the corresponding change of polymer volume. When an isothermal compression was completed, the system temperature was increased and a new isothermal run was repeated. In the case at hand, the experiments were performed from 25 °C up to 320 °C, in a pressure range spanning from 0.1 to 100 MPa.

The volumetric data collected for amorphous PPO are reported in Figure 2a, in both rubbery and glassy states. The lattice fluid characteristic parameters were then estimated by fitting the experimental *PVT* data above the glass transition temperature with Sanchez−Lacombe equation of state[39] for pure fluids, i.e.

$$\tilde{\rho} = 1 - \exp\left[-\frac{\tilde{\rho}^2}{\tilde{T}} - \frac{\tilde{p}}{\tilde{T}} - \left(1 - \frac{1}{r}\right)\tilde{\rho}\right] \tag{13}$$

where $\tilde{\rho} = \rho/\rho^*$, $\tilde{T} = T/T^*$, and $\tilde{p} = p/p^*$. The values determined by a best fitting procedure for p^*, T^*, and ρ^* for amorphous PPO are reported in Table 1.

dx.doi.org/10.1021/ma3000626 | Macromolecules 2012, 45, 3604−3615

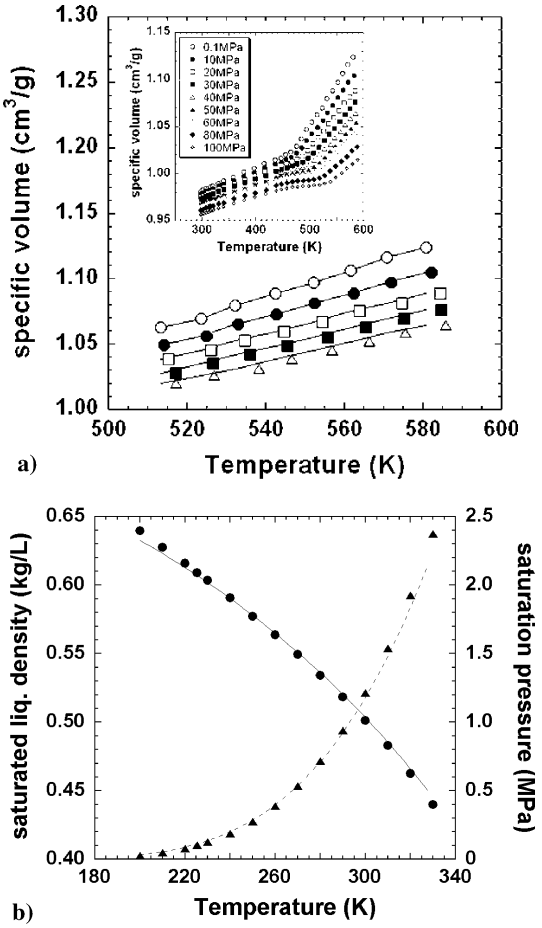


Figure 2. (a) Fitting of experimental PVT data to Sanchez–Lacombe equation of state for aPPO; (b) fitting of equilibrium data for propylene (●, saturated liquid density; ▲, vapor pressure) to Sanchez–Lacombe equation of state.

As observed by several authors,[51,52] the Sanchez–Lacombe equation of state is often unable to describe using a single set of parameters the volumetric properties of polymers with adequate reliability over very wide ranges of temperature and pressure. Hence, to improve the accuracy of the model in representing volumetric properties, data fitting with the Sanchez–Lacombe equation of state was performed in a range of experimental data close to the temperatures and pressures of interest: in fact, in this investigation, just the *PVT* data ranging from 0.1 to 40 MPa were used to retrieve the Sanchez–Lacombe parameters of amorphous PPO.

The lattice-fluid parameters of methane, carbon dioxide, and propane were taken from literature sources,[38,41−43] while, in the case of propylene, they were estimated by fitting simultaneously the vapor pressure and the saturated liquid density as a function of temperature to the Sanchez–Lacombe equation of state; to this aim, the experimental data for propylene were taken from technical literature.[53] The results of fitting for propylene are reported in Figure 2b, while in Table 1 are reported the calculated values for lattice-fluid parameters. As expected, the lattice-fluid scaling parameters for propylene do not depart very much from those of propane.

The density of amorphous and semicrystalline PPO was accurately measured by flotation at environment temperature and pressure. These values have been used: (a) to obtain absolute values of polymer density needed to compute the absolute PVT behavior of PPO, in view of the fact that Gnomix apparatus only supplies volume changes; (b) as the value of ρ_2 to be used in applying NELF model to aPPO; and (c) to convert the mass fraction of gas in volume fractions.

Parallel flotation experiments have showed that the density of totally amorphous PPO (1.016 ± 0.004 g/cm^3) is slightly higher than the one of the semicrystalline sample obtained after treatment with benzene (1.009 ± 0.002 g/cm^3): such result appears rather unusual and, as we will see later, it is consistent with the results of sorption experiments. A similar behavior has been previously observed in the case of semicrystalline syndiotactic polystyrene.[13] Unfortunately, it was not possible to estimate the density of cPPO due to the morphology of samples, which did not allow a reliable use of the flotation procedure. In fact, the samples crystallized with CCl_4 displayed a quite irregular shape which determined trapping of bubbles in the suspending solution around the sample. Since the value of density is needed to calculate *S* (appearing in eq 3) starting from the experimental values of solubility as a function of pressure, no estimate of permeability from eq 3 has been possible for cPPO. For this reason, in the following, the comparison of cPPO with bPPO will only be performed with reference to sorption behavior.

4. RESULTS AND DISCUSSION

4.1. X-ray, IR, and DSC Characterization. The X-ray diffraction patterns of aPPO, bPPO and cPPO film samples are shown in Figure 3. As already reported in a previous work,[7] the

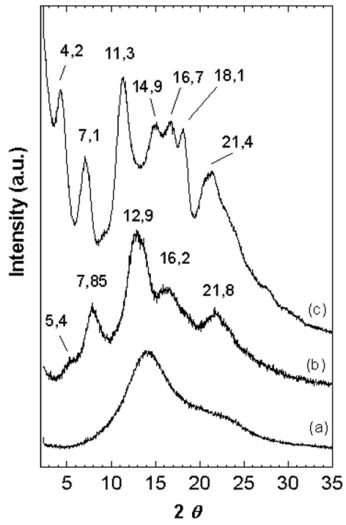


Figure 3. X-ray diffraction patterns of aPPO (curve a) and semicrystalline bPPO (curve b) and cPPO (curve c) film samples.

X-ray diffraction patterns of bPPO and cPPO films present peaks being located at definitely different diffraction angles

Table 1. NELF Model Parameters for aPPO, Penetrants, and Their Mixtures

	T^* (K)	p^* (MPa)	ρ^* (kg/L)	source	T_C (K)	V_C (cm^3/mol)	k_{sw} (MPa^{-1})	k_{ij}
aPPO	703	510	1.135	this work	–	–	–	–
C_3H_8	375	320	0.690	ref 43	369.8	203	0.044	0.035
C_3H_6	392	300	0.700	this work	364.9	181	0.042	0.007
CH_4	215	250	0.500	ref 41	190.4	99.2	≈0	−0.018
CO_2	300	630	1.515	ref 38	304.1	94	0.015	0.030

dx.doi.org/10.1021/ma3000626 | *Macromolecules* 2012, 45, 3604−3615

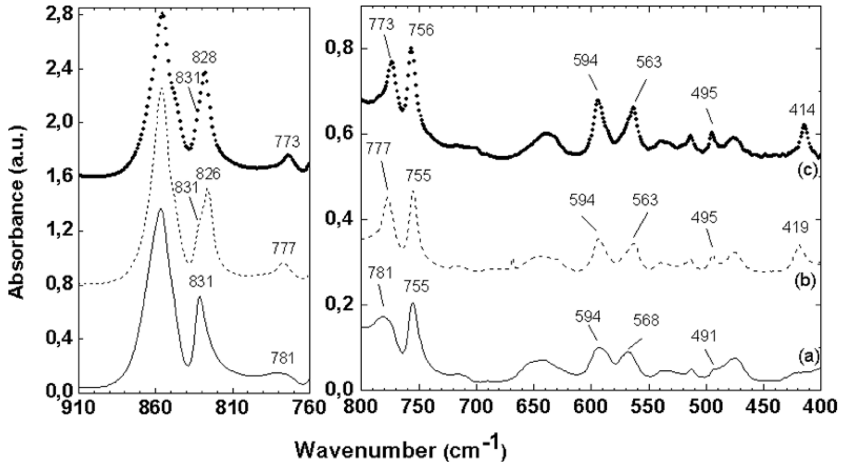


Figure 4. IR spectra of a aPPO film sample (curve a) and bPPO (curve b) and cPPO (curve c) film samples. The 910−400 cm^{-1} wavenumber region has been split in two graphs for the sake of clarity.

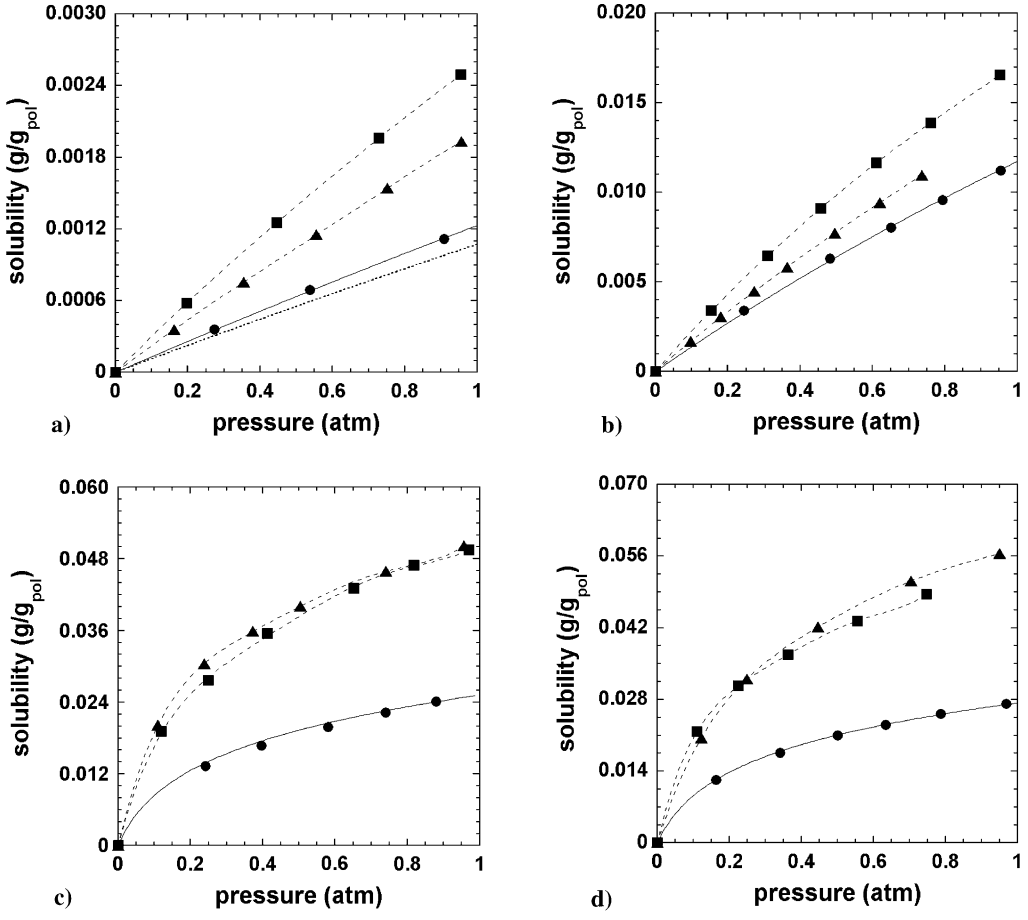


Figure 5. Sorption isotherms at 30 °C for (a) CH_4, (b) CO_2, (c) C_3H_8, and (d) C_3H_6 in aPPO (●), bPPO (■), and cPPO (▲). Continuous lines (−) represent two-parameters NELF model fitting. Dotted line (···), only in the case of methane, represents NELF model prediction with no fitting parameters. Dashed lines (---) are only guides for the eye.

which indicate the formation of different crystalline modifications. Both modifications, according to molecular sorption and surface area measurements, are nanoporous.

In Figure 4 are reported the IR spectra in the 910−400 cm^{-1} wavenumber range of amorphous and semicrystalline PPO films, whose X-ray diffraction patterns have been reported in Figure 3. As can be observed, the IR spectrum of fully amorphous PPO sample (curve a) in the 910−400 cm^{-1} region is markedly different from those of both semicrystalline PPO samples. In particular: (i) the broad bands of aPPO located at 781, 594, 563, and 491 cm^{-1} become sharper in semicrystalline samples; (ii) in the 410−420 cm^{-1} region, the semicrystalline samples display a sharp IR band which is negligible in the aPPO; (iii) the IR spectrum of aPPO presents a sharp band at 831 cm^{-1} which becomes, in semicrystalline PPO samples, the shoulder of a new band located at a lower wavenumber.

dx.doi.org/10.1021/ma3000626 | *Macromolecules* 2012, 45, 3604−3615

Following an approach developed for syndiotactic polystyrene, the degree of crystallinity of semicrystalline PPO samples has been determined by subtracting the contribution of the amorphous phase. The spectral subtraction was accomplished by choosing the K parameter (see Experimental Section) so as to reduce the typical aPPO band at 831 cm^{-1} to the baseline. The degree of crystallinity, was found to be 32% for both the samples crystallized with benzene and carbon tetrachloride. This indicates that the amount of polymer chains in ordered conformation is similar for the two nanoporous-crystalline samples.

It is worth adding that for the crystalline sample obtained by treating aPPO with benzene the degree of crystallinity determined from the X-ray diffraction pattern (curve b of Figure 3) by applying the standard procedure of resolving the diffraction pattern into two areas corresponding to the contribution of the crystalline and amorphous fractions was found to be 32% which is similar to the value obtained from the IR spectrum.

Finally, we note that the IR spectra of the two semicrystalline PPO films, although very similar, exhibit significant variations, due to different chain conformation or packing in the nanoporous crystalline phase. In particular, bPPO (curve b) presents peaks located at 826, 777, and 419 cm^{-1} while cPPO (curve c) presents peaks located at 828, 773, and 414 cm^{-1}.

Differential scanning calorimetry has been performed on aPPO, bPPO, and cPPO determining glass transition temperature, T_g, and, for semicrystalline samples, melting temperature, T_m, and melting enthalpy of the crystalline phase, ΔH_m. Values of T_g resulted, for all the samples, around 211 °C, thus suggesting that the presence of crystals does not alter significantly the mobility of the amorphous phase. Melting temperatures were also very close for the two semicrystalline samples. In particular, for the case of bPPO it was determined T_m = 239.6 °C and a melting enthalpy equal to 12.8 J/g, that corresponds to a ΔH_m for the crystal equal to 1.16 kcal/mol. On the basis of this information, the entropy of melting of the crystal, ΔS_m, was estimated to be 2.27 cal/(mol K), from the relationship $\Delta S_m = \Delta H_m/T_m$. Both the value of ΔH_m and of ΔS_m are lower than those generally found in semicrystalline polymers.[15] This result points to weak interchain interactions, consistently with the hypothesis of a nanoporous crystalline phase, aspect that has already been evidenced by Alentiev et al.[15] in their investigation on semicrystalline PPO.

4.2. Solubility. Sorption experiments of methane, carbon dioxide, propane, and propylene were performed at 30 °C on both aPPO and semicrystalline bPPO and cPPO samples. For all the penetrants investigated, the solubility was determined to be lower for aPPO as compared with semicrystalline PPOs, indicating that the sorption capacity of the whole sample increases after crystallization with solvents: such a behavior is consistent with the lower density showed by the semicrystalline bPPO with respect to the amorphous sample, which points, in turn, to a lower density and higher associated sorption capacity of the crystalline phase. This trend is clearly opposite to the one commonly observed in semicrystalline polymers, where the gas solubility results to be proportional to the volume fraction of the amorphous phase, according to the linear model proposed by Michaels et al.[16−18] In parts a−d of Figures 5 are reported the sorption isotherms for all the penetrants tested in amorphous and semicrystalline PPOs as a function of the penetrant partial pressure: they are concave to the pressure axis for carbon dioxide, propane and propylene, as expected on the basis of the typical behavior of glassy amorphous polymers and of the Langmuir-type adsorption in well-defined nanocavities of crystalline nanoporous structures, while a quite linear trend is observed in the case of methane, likely due to the fact that in this case the absorbed amount at equilibrium is far enough from saturation value. Moreover, the solubility increases systematically with the penetrant critical temperature, following the order $CH_4 < CO_2 < C_3H_6 \approx C_3H_8$.

In particular, by reporting for each penetrant the logarithm of experimental solubility coefficient at infinite dilution in amorphous PPO as a function of the penetrant critical temperature, a good linear trend is observed, that can be rigorously justified from the theoretical point of view on the basis the NELF model.[33] In Figure 6 is reported a comparison

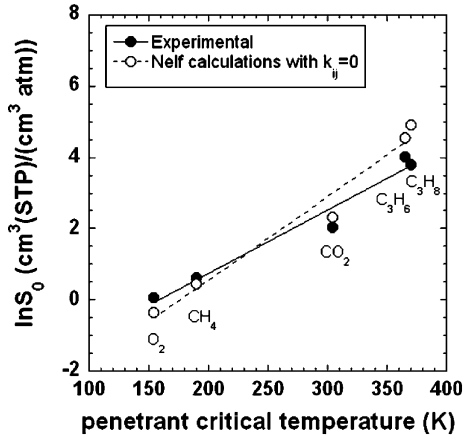


Figure 6. Experimental and calculated solubility coefficients at infinite dilution in aPPO as a function of penetrant critical temperature.

between experimental and theoretical solubility coefficients at infinite dilution (as predicted by using NELF model with k_{ij} = 0) as a function of the penetrant critical temperature which shows that the NELF model is able to give a reasonable representation of the linear trend displayed by experimental data: the greater departure showed by the theoretical values with respect to the experimental data in the case of larger hydrocarbons can be justified by considering that, to use NELF model in a predictive fashion, the binary interaction parameter has been set equal to zero. The experimental infinite dilution solubility S_0 was calculated for each penetrant by extrapolating at vanishing pressure the experimental solubility coefficient, i.e.

$$S_0 = \lim_{p \to 0}\left(\frac{C}{p}\right) \tag{14}$$

where C is the gas concentration expressed in $cm^3(STP)/cm^3$ and p the respective equilibrium pressure. In Figure 6 the value of S_0 at 30 °C for oxygen (T_C =154.6 K), taken from literature sources,[33] was also represented for comparison purposes.

The entire experimental sorption isotherms in aPPO were also compared with the theoretical predictions of NELF model, whose scaling parameters for the polymer species were estimated by fitting the experimental PVT data to the Sanchez−Lacombe equation of state, according to the procedure described above. As is shown in Figures 5a-d, the model provides a very good fitting of experimental data in the whole pressure range inspected and for all the penetrants. For nonswelling penetrants, methane in our case, only k_{ij} was used as fitting parameter, assuming k_{sw} = 0.

dx.doi.org/10.1021/ma3000626 | Macromolecules 2012, 45, 3604−3615

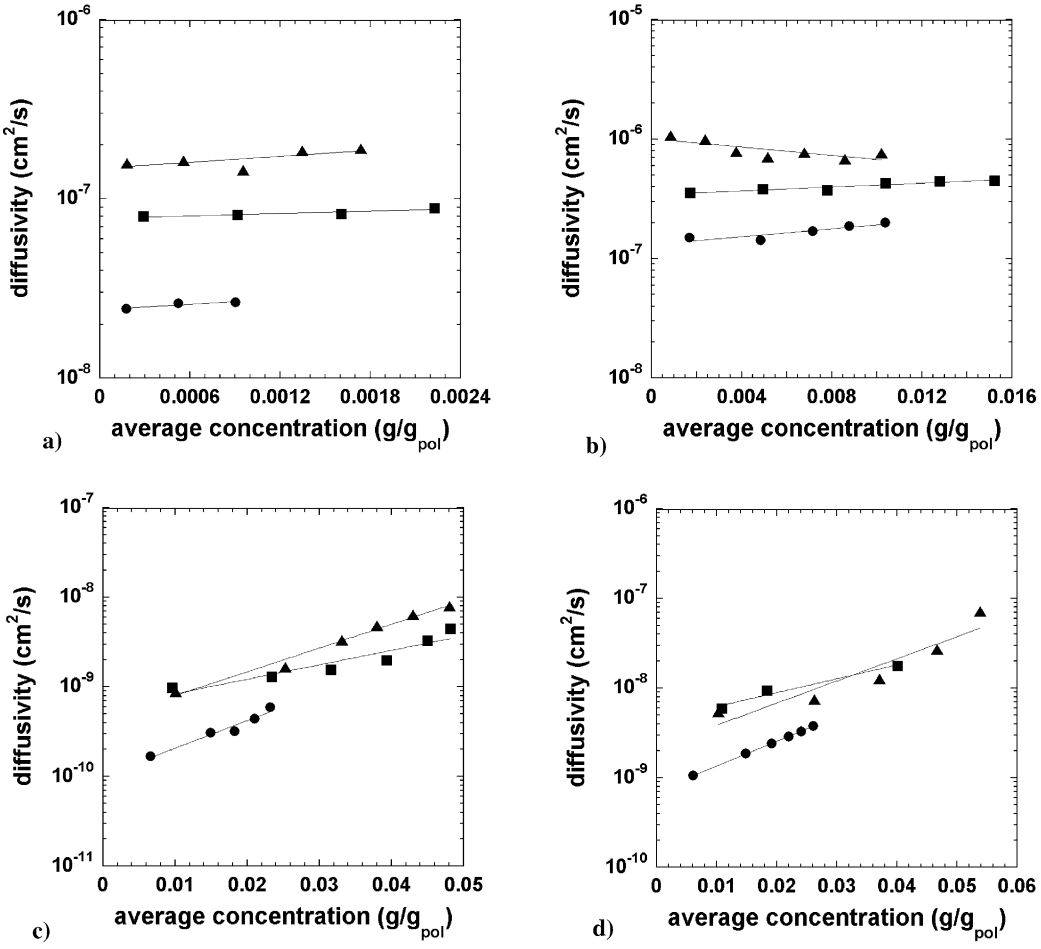


Figure 7. Diffusivity isotherms at 30 °C for (a) CH_4, (b) CO_2, (c) C_3H_8, and (d) C_3H_6 in aPPO (●), bPPO (■), and cPPO (▲). Continuous lines represent an exponential interpolation.

Conversely, for swelling penetrants, i.e. carbon dioxide, propane and propylene, both k_{ij} and k_{sw} were used as fitting parameters: in particular, the latter was determined following the procedure proposed by Giacinti et al.[45] In other words, by taking advantage of the linear relationship holding for the polymer density as a function of the penetrant partial pressure, the swelling coefficient can be retrieved by applying eq 10, i.e.:

$$k_{sw} = \left[\frac{\rho_2^0 - \rho_2(p)}{\rho_2^0}\right]\frac{1}{p} \tag{15}$$

where ρ_2^0 is the pure polymer density before sorption experiments, that is known from density measurements, and ρ_2 the density at pressure p, as retrieved by fitting the corresponding solubility datum with the NELF model. For all the swelling penetrants tested, the corresponding value of k_{sw} was optimized using the solubility datum available at the highest pressure. The binary interaction parameter as well the swelling coefficient determined by the fitting procedure for each polymer/penetrant couple are reported in Table 1. As a matter of fact, the values of k_{ij} do not depart very much from zero for all the polymer/penetrant pairs. Moreover, the experimental solubility data for methane are reasonably represented by the NELF model also when it is used in a completely predictive way, i.e., by setting the binary parameter identically equal to zero: a comparison between the two different modeling approaches ($k_{ij} = 0$ and $k_{ij} \neq 0$) for nonswelling penetrant (CH_4) is reported in Figure 5a.

The extent of swelling, as calculated through the NELF model, follows the order $CO_2 < C_3H_6 \approx C_3H_8$, consistently with the lower molecular size of carbon dioxide with respect to the hydrocarbon vapors. In all the cases, however, the amorphous sample shows a very good dimensional stability, in view of the fact that the percentage volume dilation induced by sorption of propane does not exceed the 0.45% at atmospheric pressure, as it is possible to estimate from the respective values of k_{sw}: such aspect is of crucial importance in separation processes, where materials endowed with adequate dimensional stability are required.

As anticipated above, semicrystalline PPOs display a higher sorption capacity than aPPO, due to their ability to host gas molecules in their crystalline nanocavities, according to a Langmuir-type adsorption mechanism. We did not attempt to retrieve quantitative information on gas solubility in the pure crystalline phase from sorption isotherms for semicrystalline PPOs and aPPO. In fact, for the amorphous phase of semicrystalline PPOs, the assumption of the same solubility of aPPO, which is needed to perform this calculation, is not necessarily fair.

It is noticed that, by comparing the mass transport properties of bPPO and cPPO, no appreciable differences were found in the case of propane and propylene: in these cases, the same solubility was measured in the two semicrystalline matrices,

dx.doi.org/10.1021/ma3000626 | Macromolecules 2012, 45, 3604−3615

that, in turn, results roughly doubled with respect to the one measured in the aPPO. Conversely, by considering carbon dioxide and methane, nonnegligible differences emerged between the solubilities in bPPO and cPPO: for instance, in the case of methane the solubility in bPPO results about double than in aPPO, while the solubility in cPPO is roughly 1.5 times larger than the one measured in the amorphous sample. Analogously, in the case of carbon dioxide the sorption capacity of bPPO is about 1.5 times larger than that of aPPO, while for cPPO this ratio reduces to 1.2. In summary, for the more condensable hydrocarbons both the semicrystalline matrices show the same sorption capacity, while for the less condensable gases a rather different solubility was measured in bPPO and cPPO.

4.3. Diffusivity. For all the penetrants tested, a Fickian behavior was observed during the transient sorption stage and, on the basis of eq 12, the average diffusivity was estimated as a function of penetrant average concentration: the results are reported in Figure 7a–d for amorphous and semicrystalline PPOs. We remark here that, as already pointed out in the Experimental Section, the calculated values of diffusivity for semicrystalline PPOs have to be considered as a spatially averaged property, in view of the heterogeneous nature of the sample. No attempt was made to calculate values of diffusivity for the pure crystalline phase since details on the structure and orientation of the crystalline domains have not been yet fully clarified.

Very interestingly, a significant increase of the diffusivity was observed for all penetrants by moving from amorphous to semicrystalline PPO: this behavior is consistent with the experimental density data of polymer samples and can be attributed to the nanoporous nature of crystalline domains. The values of diffusivities suggest that, in mass transport processes, the semicrystalline phases of PPO keep the size sieving effect proper of amorphous PPO, by promoting a more rapid diffusion for lighter gases. The relevant result of larger diffusivities for semicrystalline PPOs as compared to aPPO appears quite unexpected in view of the fact that usually the presence of semicrystalline regions act by increasing the tortuosity of the penetrant molecular path thus reducing the diffusivity. In fact, generally, crystallites do not contribute to the sorption and diffusion processes, acting like a constraint for the amorphous phase and as a geometrical obstacle to diffusion. In the present case the picture is rather different, because the crystalline phase evidently takes part to the sorption and transport processes, as a consequence of its nanoporous structure, with mass transport rates even higher than those proper of the amorphous domains.

It is explicitly noticed here that, although also for semicrystalline sPS with nanoporous crystalline phases the solubility of low molecular weight compounds has been reported to be significantly higher than in the amorphous sPS,[8,11−14] the distinguishable feature of a higher diffusivity for low molecular weight compounds in the semicrystalline samples is present only in the case of PPO.

As expected, in both amorphous and semicrystalline PPO the diffusion coefficient results to be strongly dependent on the penetrant size: the lowest values for diffusivity were measured in the case of propane, that is the larger sized penetrant inspected, while the highest diffusivities were obtained in the case of carbon dioxide. As it is well-known, the penetrant critical volume is a good scaling parameter to compare the diffusivities of different gases in polymer matrices: indeed by reporting the infinite dilution diffusivity at 30 °C in aPPO, extrapolated from the experimental diffusivity isotherms, as a function of critical volume for all the gas and vapors tested, a monotonous decreasing trend was found, as shown in Figure 8.

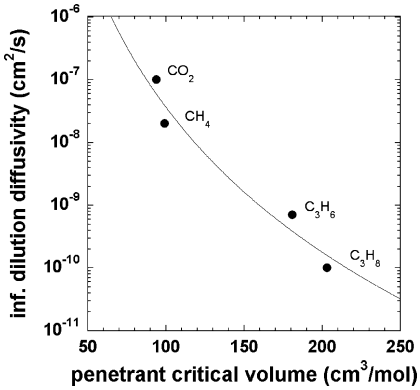


Figure 8. Infinite dilution diffusivity in aPPO as a function of penetrant critical volume.

Finally, it is observed that the diffusivity in all samples increases exponentially with the concentration, specially for propane and propylene. This effect is likely related to the behavior of amorphous domains as a consequence of the matrix dilation: such behavior is consistent with the NELF calculations, which indicates that hydrocarbon vapors induce the higher matrix swelling. A completely different behavior is showed by methane, due to its poor ability to swell the polymer matrix: in this case the diffusivity does not change very much with the penetrant concentration.

4.4. Permeability and Ideal Selectivity. The gas permeabilities of aPPO and bPPO were estimated as the product $\bar{D} \times S$, according to eq 3: as expected on the basis of sorption data discussed above, for each penetrant the permeability increases moving from amorphous to semicrystalline sample. A comparison among the different penetrants tested shows that the permeability is a decreasing function of the penetrant critical volume, just like the diffusivity, and indeed it follows the order $C_3H_8 < C_3H_6 < CH_4 < CO_2$.

Moreover, the analysis of ideal selectivities clearly reveals for aPPO and bPPO a diffusivity-controlled permeability: for example, at 0.24 atm the ideal selectivity CO_2/C_3H_8 is 225, corresponding to a diffusivity selectivity of 970 and a solubility-selectivity of 0.23. This result clearly indicates that, though the solubility selectivity is favorable to the more condensable penetrant, i.e., C_3H_8, the selectivity is globally favorable to CO_2, as a consequence of the diffusivity contribution.

Also for the couple CO_2/CH_4 a size sieving effect was observed: in particular, the total ideal selectivity for carbon dioxide was calculated to be about 20 in aPPO, in good agreement with previous results reported in literature.[1] In Figure 9 the ideal selectivity CO_2/CH_4 calculated for both aPPO and bPPO is represented as a function of CO_2 permeability and compared with the values reported in literature for PTMSP,[54] 6FDA-based polyimides[55] and TR (thermally rearranged) polymers:[56] the latter matrices, containing benzoxazole-phenylene or benzothiazole-phenylene structures, exhibit an exceptionally high separation ability for the pair CO_2/CH_4 in view of the fact that their performances can reach and overcome the upper bound calculated by Robeson[28] in 2008. Such comparative analysis suggests that the

dx.doi.org/10.1021/ma3000626 | Macromolecules 2012, 45, 3604−3615

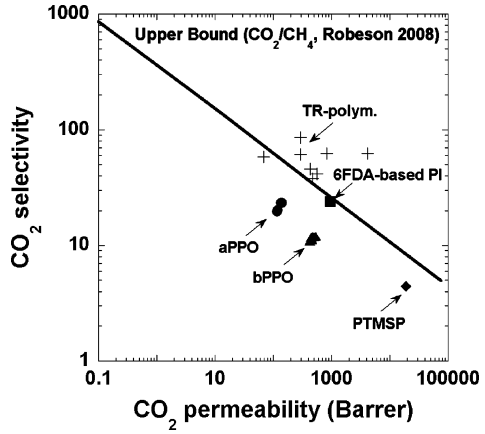


Figure 9. Selectivity–permeability diagram for the mixture carbon dioxide-methane in aPPO, bPPO, and other polymers.

separation capability of both aPPO and bPPO, although lower than those offered by TR polymers or 6FDA-based polyimides, are still better than those showed by PTMSP in term of selectivity. Moreover, because of the low pressure reached in the sorption experiments (<1 atm), it is reasonable to assume that the ideal selectivities estimated from pure gas sorption data do not differ very much from the actual values in mixed gas conditions, as also suggested by Robeson.[28]

A comparison among the permeation properties of aPPO and bPPO for the CO_2/CH_4 mixture reveals that the ideal selectivity decreases moving from amorphous to semicrystalline sample, as shown in the same Figure 9: such loss of selectivity is reasonably related to the porosity shown by the crystalline phases of PPO.

An estimation of ideal selectivity was made also for the couple propane–propylene, that is of relevant concern in petrochemical industry: in agreement with previous results reported in literature,[57,58] an ideal selectivity of about 10 for propylene was found for both aPPO and bPPO. Also in this case the selectivity is globally controlled by the diffusivity, which is largely favorable for propylene, in view of the fact that the two vapors show practically the same solubility.

5. EFFECTS OF THERMAL ANNEALING ON GAS TRANSPORT PARAMETERS

Many studies are reported in the literature showing that the mass transport properties of glassy polymers are strongly dependent on their thermal and mechanical history, as well on the film production procedure. For instance, a thermal treatment generally promote the densification of polymer matrix, with a consequent reduction of its sorption capacity and gas permeation rate: this behavior can be attributed to the nonequilibrium state that a polymer experiences below its glass transition temperature.

In this work, samples of aPPO and bPPO were annealed at 65 °C under vacuum for 3 months: after treatment, a sorption run of carbon dioxide and methane was performed on both the samples and the results were compared with those of untreated aPPO and bPPO. Very interestingly, as shown in parts a and b of Figure 10, both solubility and diffusivity resulted unaffected by thermal annealing, indicating a good thermal stability of both amorphous and semicrystalline matrices. Such aspect is of crucial importance, in view of the fact that often a long exposure to medium-high temperatures determines a sensitive

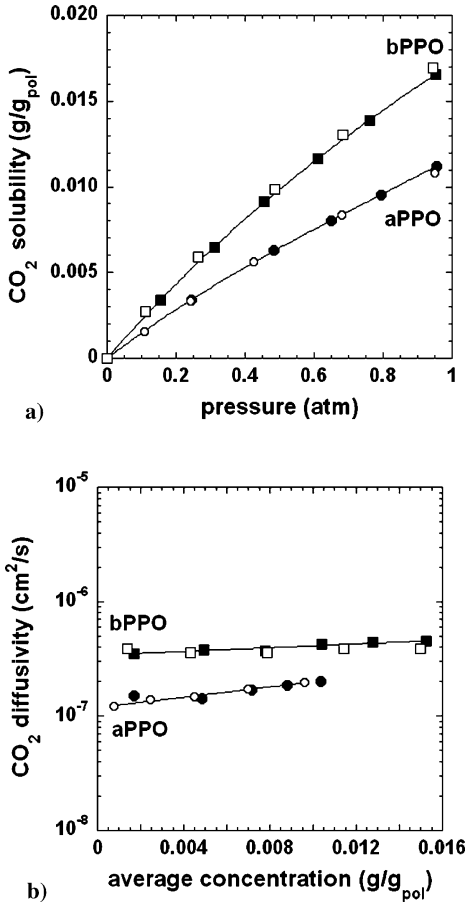


Figure 10. Carbon dioxide solubility (a) and diffusivity (b) isotherms at 30 °C in fresh (filled symbols) and annealed (open symbols) aPPO and bPPO.

reduction of gas transport parameters, like in the case of glassy PTMSP, the most permeable polymer known so far: as observed by Giacinti et al.,[59] indeed, a treatment at 45 °C for 6 month suppresses the solubility of *n*-pentane in PTMSP of about 25%, while a less marked decrease of diffusivity was observed. It is worth noticing that, though both PPO and PTMSP are characterized by high values of the glass transition temperature, the strong instability showed by the latter can be ascribed to its higher degree of free volume, which ranges from 28 to 30%. In parts a and b of Figure 10, the carbon dioxide sorption and diffusion isotherms in fresh and annealed aPPO and bPPO are reported as a function of penetrant partial pressure and penetrant average concentration, respectively: similar results, not reported here for the sake of brevity, were obtained from methane sorption experiments. This behavior is consistent with that reported in literature by Daniel et al.,[7] which observed, at least in the case of large size solvents (C_6H_6, CCl_4), an essentially unaltered uptake after several hours of thermal treatment in air, up to 100 °C.

The good stability showed by PPO can be explained in view of the rigidity of its backbone, related to the presence of the aromatic rings, as well as of its high glass transition temperature, that exceeds that of most of the other glassy polymers, like polystyrene, polycarbonate or polysulphone, coupled with a lower free volume.

dx.doi.org/10.1021/ma3000626 | Macromolecules 2012, 45, 3604–3615

6. DISCUSSION

The unusual behavior of semicrystalline PPO, which displays gas solubility and diffusivity significantly higher than its totally amorphous counterpart, has been rationalized by invoking an involvement of the nanoporous crystalline phase in mass transport. As a matter of fact, there is the possibility that such a behavior could be also ascribed, at least in part, to the existence of a third, amorphous, phase in the semicrystalline samples, beside the bulk amorphous phase and the crystalline phase. This peculiar amorphous domain, originated by the constraint imposed by the crystals on some amorphous regions, has been reported as the "rigid amorphous phase",[60,61] constituted by amorphous backbones with a mobility hindered by the presence of the crystalline phase. An example is the case of the O_2/PET[61] system, for which results of permeation measurements have been rationalized by arguing that the rigid amorphous phase develops an extra excess-hole free volume upon cooling thus promoting a larger oxygen solubility of this amorphous fraction.

In principle, the presence of a rigid amorphous phase could also contribute to the behavior observed for semicrystalline PPO. However, it is to be noted that, at best of our knowledge, there is no case in which a semicrystalline polymer displays higher solubility and diffusivity of low molecular weight compounds as compared to its totally amorphous counterparts. The only relevant exception is the case of semicrystalline sPS samples, exhibiting, in fact, the nanoporous-crystalline δ and ε phases, which present a solubility of suitable guest molecules higher than that of amorphous PS samples, although diffusivities are still lower. In the case of sPS, it has been undoubtedly demonstrated that solubility occurs within the crystalline domains. The presently reported data for PPO actually represent the first case in which both solubility and diffusivity for semicrystalline samples are higher than for the corresponding fully amorphous samples and this finding does speak in favor of a determinant role played by the crystalline regions. Since the structure of the material is, at this stage, not yet resolved, any quantitative prediction of mass transport properties of semicrystalline PPO is not yet possible. Information on the properties of the phases involved as well as on the arrangements of these phases within the sample is needed to obtain macroscopic transport properties by volume averaging. Moreover, preliminary results indicate a large increase of sorption capacity of guest molecules in semicrystalline PPO as a function of grade of crystallinity: this finding, taken together with the results of a detailed structural characterization reported by Daniel et al.[7] in a previous work and of DSC analysis, further supports the fact that the unusual behavior showed by semicrystalline PPO can be mostly attributed to the nanoporous nature of its crystalline phase.

7. CONCLUSIONS

The mass transport properties of amorphous PPO and of semicrystalline nanoporous PPO obtained after treatment with benzene and carbon tetrachloride of aPPO were determined and analyzed for gases and hydrocarbon vapors: the investigated semicrystalline samples are characterized by a gas solubility and diffusivity which are much larger than in the case of totally amorphous PPO. This unexpected behavior can be justified by considering the nonnegligible sorption capacity of the crystalline domains, against what is commonly observed in semicrystalline polymers: such results are further supported by the fact that the density of amorphous PPO is slightly higher than that of semicrystalline samples.

Because of its peculiar mass transport properties, semicrystalline PPO could be a potential candidate for membrane-based gas separation processes: in this respect, interesting values of ideal selectivity were obtained for the pairs CO_2/CH_4 and propylene/propane, which are of strong practical concern in petrochemical industry.

In the case of amorphous PPO, the experimental solubility isotherms compared well with the NELF model calculations, after determination of polymer characteristic parameters: interestingly, the swelling coefficient estimated at atmospheric pressure for more bulky penetrants, namely carbon dioxide, propane, and propylene appear relatively low, indicating a reduced tendency of aPPO to swell in presence of high soluble vapors.

Finally, the mass transport parameters of both amorphous and semicrystalline samples resulted rather insensitive to thermal aging. In fact, a thermal treatment of three months at 65 °C, did not induce any significant change in solubility and diffusivity of carbon dioxide and methane, against what it is commonly observed in other glassy matrices.

AUTHOR INFORMATION

Corresponding Author

*E-mail: michele.galizia@unina.it. Telephone: (+39)-081-7682512. Fax: (+39)-081-7682404.

Notes

The authors declare no competing financial interest.

REFERENCES

(1) Story, B. J.; Koros, W. J. *J. Membr. Sci.* **1992**, *67*, 191.
(2) Ilinitch, O. M.; Semin, G. L.; Chertova, M. V.; Zamaraev, K. I. *J. Membr. Sci.* **1992**, *66*, 1.
(3) Toi, K.; Morel, G.; Paul, D. R. *J. Appl. Polym. Sci.* **1982**, *27*, 2997.
(4) Huang, Y.; Paul, D. R. *J. Polym. Sci. B: Polym. Phys.* **2007**, *45*, 1390.
(5) Wenig, W.; Hammel, R.; MacKnight, W. J.; Karasz, F. E. *Macromolecules* **1976**, *9*, 253.
(6) Barrales-Rienda, J. M.; Fatou, J. M. G. *Kolloid-Z. Z. Polym.* **1971**, *244*, 317.
(7) Daniel, C.; Longo, S.; Fasano, G.; Vitillo, J.; Guerra, G. *Chem. Mater.* **2011**, *23*, 3195.
(8) Manfredi, C.; Del Nobile, M. A.; Mensitieri, G.; Guerra, G.; Rapacciuolo, M. *J. Polym. Sci. B: Polym. Phys.* **1997**, *35*, 133.
(9) De Rosa, C.; Guerra, G.; Petraccone, V.; Pirozzi, B. *Macromolecules* **1997**, *30*, 4147.
(10) Petraccone, V.; Ruiz de Ballesteros, O.; Tarallo, O.; Rizzo, P.; Guerra, G. *Chem. Mater.* **2008**, *20*, 3663.
(11) Rapacciuolo, M.; De Rosa, C.; Guerra, G.; Mensitieri, G.; Apicella, A.; Del Nobile, M. A. *J. Mater. Sci. Lett.* **1991**, *10*, 1084.
(12) Cotugno, S.; Guerra, G.; Mensitieri, G.; Musto, P.; Venditto, V. *Macromolecules* **2002**, *35*, 2296.
(13) Larobina, D.; Sanguigno, L.; Venditto, V.; Guerra, G.; Mensitieri, G. *Polymer* **2004**, *45*, 429.
(14) Mensitieri, G.; Larobina, D.; Guerra, G.; Venditto, V.; Fermeglia, M.; Pricl, S. *J. Polym. Sci. B: Polym. Phys.* **2008**, *46*, 8.
(15) Alentiev, A.; Drioli, E.; Gokzhaev, M.; Golemme, G.; Ilinich, O.; Lapin, A.; Volkov, V.; Yampolskii, Yu. *J. Membr. Sci.* **1998**, *138*, 99.
(16) Michaels, A. S.; Bixler, H. J.; Fein, H. L. *J. Appl. Phys.* **1964**, *35*, 3165.
(17) Michaels, A. S.; Bixler, H. J. *J. Polym. Sci.* **1961**, *50*, 393.
(18) Michaels, A. S.; Bixler, H. J. *J. Polym. Sci.* **1961**, *50*, 413.
(19) Puleo, A. C.; Paul, D. R.; Wong, P. K. *Polymer* **1989**, *30*, 1357.

(20) Pope, D. S.; Koros, W. J. *J. Polym. Sci. B: Polym. Phys.* **1996**, *34*, 1861.
(21) Ferrari, M. C.; Galizia, M.; De Angelis, M. G.; Sarti, G. C. *Ind. Eng. Chem. Res.* **2010**, *49*, 11920.
(22) Robeson, L. M. *J. Membr. Sci.* **1991**, *62*, 165.
(23) Robeson, L. M. *J. Membr. Sci.* **2008**, *320*, 390.
(24) Diaz, K.; Lopez-Gonzalez, M.; del Castillo, L. F.; Riande, E. *J. Membr. Sci.* **2011**, *383*, 206.
(25) Goh, P. S.; Ismail, A. F.; Sanip, S. M.; Ng, B. C.; Aziz, M. *Sep. Purif. Technol.* **2011**, *81*, 243.
(26) Noble, R. D. *J. Membr. Sci.* **2011**, *378*, 393.
(27) Aroon, M. A.; Ismail, A. F.; Matsuura, T.; Montazer-Rahmati, M. M. *Sep. Purif. Techol.* **2010**, *75*, 229.
(28) Adams, R.; Carson, C.; Ward, J.; Tannenbaum, R.; Koros, W. J. *Microporous Mesoporous Mater.* **2010**, *131*, 13.
(29) Ghosal, K.; Freeman, B. D. *Polym. Adv. Tech.* **1994**, *5*, 673.
(30) Raharjo, R. D.; Freeman, B. D.; Paul, D. R.; Sarti, G. C.; Sanders, E. S. *J. Membr. Sci.* **2007**, *306*, 75.
(31) Das, M.; Koros, W. J. *J. Membr. Sci.* **2010**, *365*, 399.
(32) Galizia, M. *Mass transport in polymeric and nanocomposite membranes for gas separation*, Ph.D. Thesis, University of Bologna, 2010 (in Italian).
(33) De Angelis, M. G.; Sarti, G. C.; Doghieri, F. *J. Membr. Sci.* **2007**, *289*, 106.
(34) Singh, A.; Freeman, B. D.; Pinnau, I. *J. Polym. Sci., B: Polym. Phys.* **1998**, *36*, 289.
(35) Barrer, R. M.; Barrie, J. A.; Slater, J. *J. Polym. Sci.* **1958**, *27*, 177.
(36) Sanders, E. S.; Koros, W. J.; Hopfenberg, H. B.; Stannett, V. *J. Membr. Sci.* **1984**, *18*, 59.
(37) Bondar, V. I.; Kamiya, Y.; Yampolskii, Y. *J. Polym. Sci., B: Polym. Phys.* **1996**, *34*, 369.
(38) Doghieri, F.; Sarti, G. C. *Macromolecules* **1996**, *29*, 7885.
(39) Sanchez, I. C.; Lacombe, R. H. *J. Phys. Chem.* **1976**, *80*, 2352.
(40) Sanchez, I. C.; Lacombe, R. H. *Macromolecules* **1978**, *11*, 1145.
(41) Sarti, G. C.; Doghieri, F. *Chem. Eng. Sci.* **1998**, *19*, 3435.
(42) Doghieri, F.; Sarti, G. C. *J. Membr. Sci.* **1998**, *147*, 73.
(43) De Angelis, M. G.; Merkel, T. C.; Bondar, V. I.; Freeman, B. D.; Doghieri, F.; Sarti, G. C. *J. Polym. Sci., B: Polym. Phys.* **1999**, *37*, 3011.
(44) Fleming, G. K.; Koros, W. J. *Macromolecules* **1990**, *23*, 1353.
(45) De Angelis, M. G.; Merkel, T. C.; Bondar, V. I.; Freeman, B. D.; Doghieri, F.; Sarti, G. C. *Macromolecules* **2002**, *35*, 1276.
(46) Giacinti Baschetti, M.; Doghieri, F.; Sarti, G. C. *Ind. Eng. Chem. Res.* **2001**, *40*, 3027.
(47) Guerra, G.; Manfredi, C.; Musto, P.; Tavone, S. *Macromolecules* **1998**, *31*, 1329.
(48) Albunia, A. R.; Musto, P.; Guerra, G. *Polymer* **2006**, *47*, 234.
(49) Crank, J. *The Mathematics of Diffusion*; Academic Press: New York, 1968.
(50) Zoller, P.; Fakhreddine, Y. A. *Thermochem. Acta* **1994**, *238*, 397.
(51) Pottinger, M. T.; Laurence, R. L. *J. Polym. Sci., Polym. Phys. Ed.* **1984**, *22*, 903.
(52) Hariharan, R.; Freeman, B. D.; Carbonell, R. G.; Sarti, G. C. *J. Appl. Polym. Sci.* **1993**, *50*, 1781.
(53) Perry, R. H.; Green, D. W. *Chemical Engineers' Handbook*, 7th ed.; McGraw-Hill: New York, 1999 (section 2).
(54) Mizumoto, T.; Masuda, T.; Higashimura, T. *J. Polym. Sci. A: Polym. Chem.* **1993**, *31*, 2555.
(55) Nagel, C.; Gunther-Schade, K.; Fritsch, D.; Strunskus, T.; Faupel, F. *Macromolecules* **2002**, *35*, 2071.
(56) Park, H. B.; Jung, C. H.; Lee, Y. M.; Hill, A. J.; Pas, S. J.; Mudie, S. T.; Van Wagner, E.; Freeman, B. D.; Cookson, D. J. *Science* **2007**, *318*, 254.
(57) Staudt-Bickel, C.; Koros, W. J. *J. Membr. Sci.* **2000**, *170*, 205.
(58) Tanaka, K.; Taguchi, A.; Hao, J.; Kita, H.; Okamoto, K. *J. Membr. Sci.* **1996**, *121*, 197.
(59) Giacinti Baschetti, M.; Ghisellini, M.; Quinzi, M.; Doghieri, F.; Stagnaro, P.; Costa, G.; Sarti, G. C. *J. Mol. Struct.* **2005**, *739*, 76.
(60) Okazaki, I.; Wunderlich, B. *J. Polym. Sci., Part B: Polym. Phys.* **1996**, *34*, 2941.
(61) Lin, J.; Shenogin, S.; Nazarenko, S. *Polymer* **2002**, *43*, 4733.

Macromolecules

Article

pubs.acs.org/Macromolecules

Fast X-ray Phase-Contrast Imaging of Electrospinning Polymer Jets: Measurements of Radius, Velocity, and Concentration

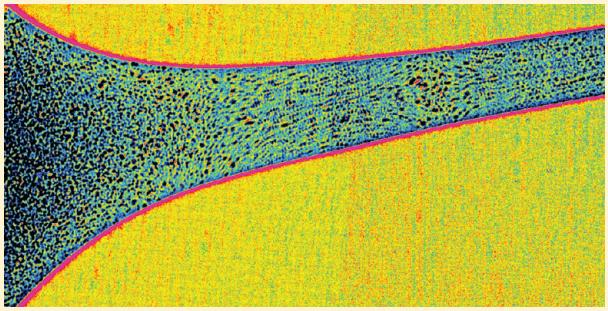
Israel Greenfeld,*[,†] Kamel Fezzaa,[‡] Miriam H. Rafailovich,[§] and Eyal Zussman[†]

[†]Department of Mechanical Engineering, Technion - Israel Institute of Technology, Haifa 32000, Israel

[‡]Advanced Photon Source, Argonne National Laboratory, Argonne, Illinois 60439, United States

[§]Department of Materials Science and Engineering, State University of New York, Stony Brook, New York 11794-2275, United States

ABSTRACT: The study of electrospinning polymer solution jets, and the evolution of the polymer entangled network during electrospinning, is of interest for understanding of the microstructure of the resulting nanofibers. Fast X-ray phase-contrast imaging was applied to investigate the flow of the first 10 mm of a straight jet of electrospinning PEO and PMMA semidilute solutions. The jet radius, velocity, and absorbance were measured at high resolution (0.67 μm/pixel) and at extremely short exposure time (<0.5 μs), under a wide range of electrospinning conditions and solution concentrations. The flow field, measured by tracing silica microbeads, revealed laminar flow with axial velocities that implied significant mass loss due to evaporation. X-ray absorption measurements provided evidence for substantial polymer concentration rise along the jet, particularly at the jet boundaries, evidence of rapid evaporation. Furthermore, at high strain rates, the polymer concentration rose at the jet center as the velocity increased along the jet, implying polymer network lateral contraction due to axial stretching. Our findings confirm the theoretically predicted counteracting effects of evaporation and stretching on the polymer matrix within the jet.



1. INTRODUCTION

Electrospinning is characterized by high strain rates of the order 10^3 s^{-1}.[1−7] Such stretching can potentially improve the structural order within as-spun nanofibers and enhance their mechanical properties.[8−12] At the same time, rapid solvent evaporation during electrospinning can lead to increased polymer concentrations at the jet boundary,[13−16] sometimes forming a solid skin and a heterogeneous and porous structure.[11,15,17] Hence, study of electrospinning polymer solution jets, and specifically of the evolution of the polymer entangled network during electrospinning,[11] is of interest in clarifying the microstructure of as-spun nanofibers. Experimental data on the jet dynamics during the initial stage of electrospinning, and particularly on the flow regime within the jet, are needed in order to characterize the hydrodynamic environment to which the polymer network is subjected. Furthermore, data on the distribution of the polymer within the jet can shed light on the conflicting processes of stretching and evaporation for different material properties and electrospinning conditions.

The geometry and velocity of electrospinning jets were studied by optical microscopy[1,5] and by tracing large particles (50−70 μm) using high-speed visible light imaging.[18] Stretching and orientation of polymer chains have been observed in electrospinning jets using birefringence,[19] Raman,[20] and X-ray diffraction[21] techniques. Imaging of electrospinning jets using in-line fast X-ray phase-contrast imparts several advantages. The method has been used to study flow dynamics, particularly fuel jets and sprays,[22−24] and offers an extremely short exposure time (<0.5 μs), essential for capturing the inherently unstable electrospinning jet, and, at the same time, provides high spatial resolution (0.67 μm/pixel). Owing to the weak interaction of X-ray with matter, it has high penetrability, and its essentially monochromatic beam enables measurement of transmission absorption and analysis of the polymer concentration within the jet. The method also provides enhanced phase boundary contrast, enabling accurate measurement of small objects, as well as accurate velocimetry using particles as small as 1 μm.[24] At the same time, the scattering of X-rays penetrating a small object is significant[25] and requires correction of absorption measurements.

In this work, we apply fast X-ray phase-contrast imaging toward analysis of up to 10 mm of the initial portion of electrospinning jets (the straight and stable section) to extrapolate high-resolution (0.67 μm/pixel) measurements of the jet radius, velocity, and absorbance. Semidilute solutions of PEO (poly(ethylene oxide)) and PMMA (poly(methyl methacrylate)) were measured under a wide range of electrospinning conditions (electric field and flow rate) and solution concentrations. The jet flow field, measured by tracing silica microbeads mixed in the polymer solutions, showed laminar flow with axial velocities that implied significant mass

Received: February 1, 2012
Revised: March 29, 2012
Published: April 10, 2012

ACS Publications © 2012 American Chemical Society

loss due to evaporation. Absorption along and across the jet was calculated from beam transmission measurements, after correcting for the scattering effect. Substantial polymer concentration increase was observed along the jet, as early as 2−3 mm from the jet start, evidence of rapid evaporation. This concentration rise occurred particularly along the jet's boundaries. At the same time, high strain rates (e.g., due to high electric field), sufficiently distant from the orifice, led to a rise in polymer concentration at the jet center as well. This latter phenomenon is testimonial of the lateral inward contraction of the polymer network due to the axial stretching.

2. EXPERIMENTAL SECTION

2.1. Equipment Setup and Operation. The experiment was conducted at 32-ID Beamline, Advanced Photon Source (APS), Argonne National Lab, using a partially coherent undulator X-ray white beam. The experimental setup of the X-ray imaging system and the electrospinning chamber are presented in Figures 1a and 2a,b.

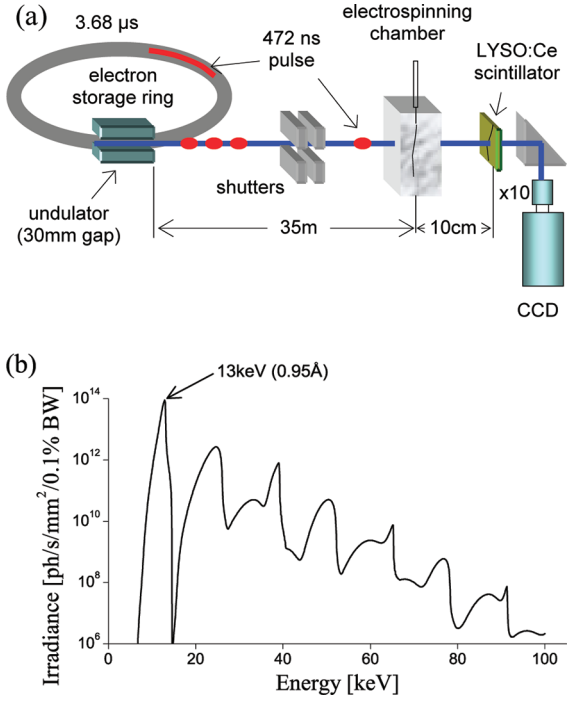


Figure 1. Experimental setup. (a) X-ray beam path: a millisecond shutter was set up in series with a very fast galvano-based shutter that opened the path for less than 100 μs each second. The beam penetrated the jet and was converted to a digital image via a scintillator. The CCD camera was timed to capture the first pulse after the very fast shutter opened. (b) X-ray beam flux: the dominant harmonic is indicated.

The X-ray beam was generated from the synchrotron's electron storage ring with a dominant harmonic at a beam energy of 13 keV, corresponding to a wavelength of 0.95 Å (Figure 1b). The dominant peak was ∼100 times more intense than the harmonics, rendering the beam practically monochromatic, an essential feature in view of the strong dependence of material X-ray mass absorption coefficients on beam energy. The X-ray beam was emitted as short pulses, each 472 ns long, issued at intervals of 3.68 μs. A millisecond mechanical shutter opened the beam path at 1 Hz in order to protect the imaging system from overheating, and was followed by a very fast galvano-based shutter that opened the beam path for less than 100 μs each second.

The X-ray pulses penetrated the electrospinning jet, and their transmission was converted to visible light by a fast scintillator crystal (LYSO:Ce, 40 ns decay time), positioned at a distance of 10 cm from the spinning jet. A camera, timed to capture the first pulse passing through the very fast shutter, captured the image via a folding mirror and a ×10 objective optics, using a 1280H × 1024 V CCD detector with a pixel size of 6.7 × 6.7 μm^2. The beam size of 1 × 1 mm^2 was slightly larger than the camera's effective field-of-view. A typical X-ray image of the jet is shown in Figure 2c. Note the white corona at the jet boundaries due to edge diffraction. During particle tracing experiments, two-pulsed images were captured for each frame, separated by a time interval of 3.68 μs multiples, up to a maximum of 147.2 μs.

The electrospinning chamber (Figure 2a,b) consisted of a PMMA-based enclosure with Kapton-film windows. The chamber was mounted on a remotely controlled motorized stage, which allowed for control of *x*,*y*,*z* positioning of the electrospinning chamber, and for sequential capturing of images at 0.5 mm steps along the jet during a single session (see image example in Figure 2d). Because of the unstable nature of electrospinning jets and the small field-of-view of the camera, images could only be captured at distances of up to 10 mm from the jet start. The image frame was recorded 20 times at 1 s intervals for each stage position, with a gray scale depth of 16 bits. Dark images (no X-ray) and background images (no jet) were also collected to allow for image correction.

In order to avoid prolonged exposure of the jet to X-ray radiation that might degrade the polymer or affect the solvent, the following measures were taken. After allowing sufficient time for the jet flow to become steady, the camera was triggered to capture the first pulse released by the very fast shutter. In the absorption measurement experiments, only a single pulse was captured, and the jet was consequently exposed to the beam for 0.47 μs. In the particle tracing experiments, the beam path was left open until the second image was captured, and therefore the jet was exposed to 3−41 pulses, depending on the selected time interval, and consequently the cumulative exposure time varied between 1.4 and 19.4 μs. The corresponding fluence (time-integrated flux) of the beam spectrum shown in Figure 1b was several orders of magnitude below typical X-ray damaging fluences.[26] Also, owing to the beam small size, irradiation was restricted to the jet section that was currently imaged, about 1 mm long, while the rest of the jet was not exposed to the beam. Finally, the experimental evidence from the particle tracing experiments using different exposure times has shown that the measured jet radius and particles velocity were not sensitive to exposure time, implying that the beam did not influence the jet dynamics or evaporation.

2.2. Materials and Test Cases. PEO (M_w 600 kDa) and PMMA (M_w 70 kDa) were purchased from Sigma-Aldrich. PEO was dissolved in water at concentrations of 3 and 5 wt %; PMMA was dissolved in $CHCl_3$ (chloroform) at concentration of 15 wt %. Glycerol was purchased from Sigma-Aldrich. During velocimetry tests, the PEO solutions were mixed with silica (SiO_2) microbeads, purchased from Polysciences Europe GmbH, at volume fraction of 0.9 vol %. The microbeads size ranged from 1 to 10 μm (98% of microbeads), with a mean size of 1.94 ± 0.76 μm (STD), measured using ImageJ. The relevant properties of the materials and solutions used in the experiment are listed in Table 1.

The polymer solutions were injected using a standard syringe pump, into a 25 gauge capillary needle (internal diameter 0.26 mm) installed on top of the electrospinning chamber, at flow rates *Q* ranging from 1 to 8 mL/h. A 20 gauge needle (internal diameter 0.6 mm) was used for the PEO 5% particle tracing experiments. The polymer solution was drawn from the capillary needle by an electric field, created by a standard high-voltage power supply, with electric potential ranging from 4 to 14 kV. The gap between the needle and the collector tip was adjusted to fall within a range of 2.5−6.5 cm (Figure 2a), resulting in a nominal electric field *E* of 0.6−4 kV/cm. The experiments were conducted at room temperature, at a relative humidity of 40%. Tests 1−17 and their conditions are presented in Figure 3.

2.3. Particle Tracing. Velocity measurements and characterization of the flow regime inside the electrospinning jet were achieved by X-ray particle tracing. The measurements were carried out on PEO 3% and 5% solutions, mixed with silica microbeads (tests 14−18). The microbeads provided good X-ray image contrast, with an absorption coefficient ∼10 times higher than that of the PEO solutions (refer to

dx.doi.org/10.1021/ma300237j | Macromolecules 2012, 45, 3616−3626

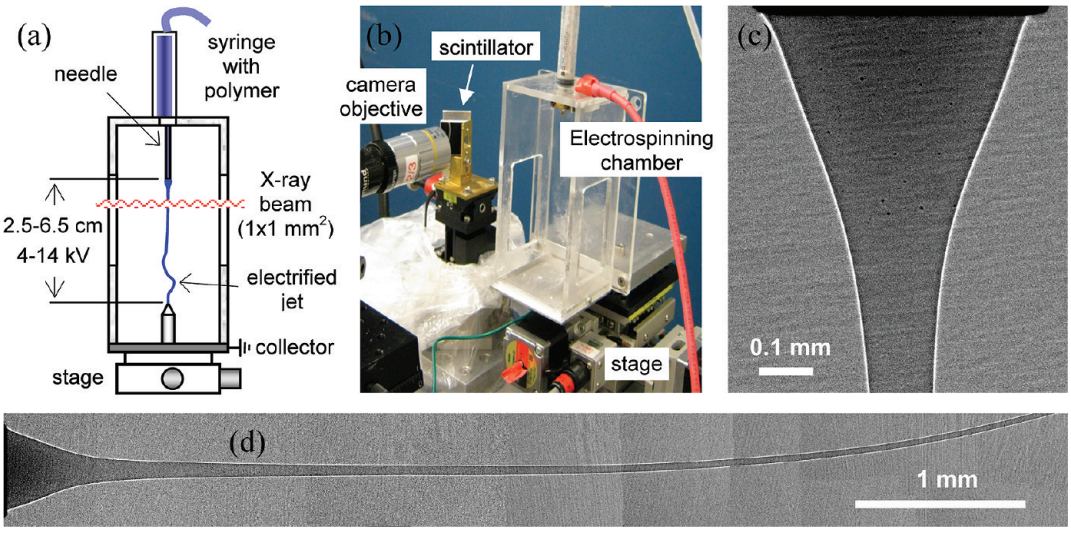


Figure 2. Electrospinning setup. (a) Electrospinning chamber: the polymer solution is pumped into the syringe and drawn by the electric field toward the collector. The initial rectilinear portion of the jet is imaged by sequentially moving the motorized stage upward at 0.5 mm steps. (b) Electrospinning chamber and imaging target (scintillator). (c) Representative X-ray image: electrospinning solution of 5 wt % PEO (M_w = 600 kDa) in water; electric field 1.6 kV/cm, flow rate 3.2 mL/h. (d) Same test case, presenting a jet section 6 mm long, reconstructed from 12 sequential images.

Table 1. Characteristic Properties of Tested Materials and Solutions[a]

material/polymer	M_w [Da]	solvent	c [%]	μ [Pa s]	γ [mN/m]	σ [mS/m]	ρ_p (ρ_s) [g/cm^3]	ε_p (ε_s)[b] [cm^2/g]	α_0 [1/cm]
glycerol	92		100	0.9	64[c]	0.006[d]	1.26	1.75	2.21
PMMA	70K	chloroform	15	~0.1	28[c]		1.2 (1.5)	1.45 (23.3)	28.9
PEO	600K	water	3	1.2[e]	72[e]	1.4[e]	1.12 (1)	1.51 (2.29)	2.28
PEO	600K	water	5	12[e]	75[e]	1.6[e]	1.12 (1)	1.51 (2.29)	2.26
silica (microbeads)							2.65	8.27	21.9

[a]Molecular weight M_w, concentration c, zero-shear viscosity μ, surface tension γ, conductivity σ, mass absorption coefficient of polymer (solvent) ε_p (ε_s), density of polymer (solvent) ρ_p (ρ_s), and absorption coefficient α_0. [b]Reference 27. [c]Reference 28. [d]SmartMeasurement.[29] [e]Estimate based on Theron et al.[30]

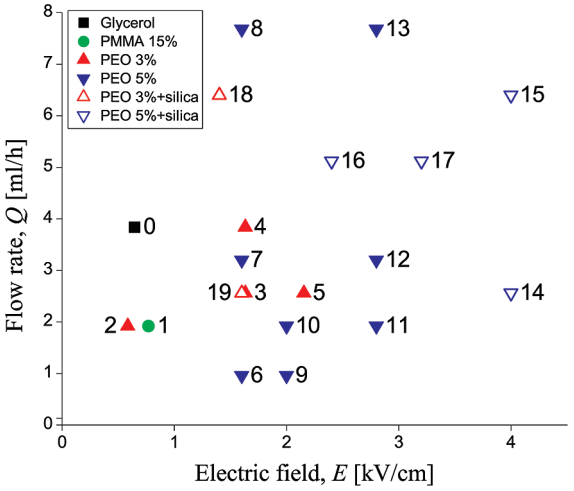


Figure 3. Map of X-ray tests and their respective solutions, flow rates Q, and applied electric fields E. Refer to Table 1 for corresponding material properties.

Table 1). Each jet section was exposed twice to X-ray radiation, within a short time interval, and both exposures were recorded on a single image. The time intervals used were 7.4, 18.4, 36.8, 73.6, and 147.2 μs. Velocity vectors were calculated by tracing particles, as shown in Figure 4, and adjusting for the lateral displacement of the jet during the time interval between exposures. Typically, shorter intervals were applied in regions of high velocity, whereas longer intervals were needed for regions of low velocity. The resulting velocity vectors were two-dimensional projections of a three-dimensional flow, but since the vertical velocity component was dominant this inaccuracy is negligible.

The small size of the particles (mean size ~2 μm) and their low volume fraction in the solution (0.9 vol %), as well as their homogeneous dispersion within the fluid (Figure 4), ensured minimal influence of the particles on the jet flow properties and accurate velocity measurement. Suspensions with particles volume fraction up to 1 vol % may be considered as dilute,[31] and therefore the effect of the particles on viscosity was negligible. Theoretical and experimental studies of the flow of particle-laden fluids in confined spaces[24,32] have shown that for small particles ($d/H \leq 0.2$, where d is the particle size and H the small dimension of the flow) and low Reynolds numbers ($Re = \rho v D_H/\mu < O(1)$, where ρ is the fluid density, v is the fluid velocity, and D_H is the hydraulic diameter), the particles will not cross streamlines while moving along the flow, and their velocity will be within less than 2% from the undisturbed fluid velocity. These conditions apply to the present tracing tests, where $d < 10$ μm, $H \cong D_H < 1$ mm, $\rho \cong 1$ g/cm^3, $v < 1$ m/s, and $\mu \leq 12$ Pa s, and therefore $d/H < 0.01$ and $Re < 0.1$.

The effects of particle gravity and buoyancy are negligible, in view of the high hydrodynamic forces in the electrospinning jet. The inertial force can be neglected as well (the ratio between the inertial force, $(\pi/6)\rho_p d^3 \dot{v}$, and the hydrodynamic force, $3\pi\mu d v$, acting on a particle assuming a spherical shape, is $\rho_p d^2 s/(18\mu) \cong 10^{-6} \ll 1$, where ρ_p = 2.65 g/cm^3 is the particle density and $s = \dot{v}/v < 10^3$ 1/s is the flow strain rate).

2.4. Radiation Transmission and Absorption. Characterization of the polymer concentration distribution within the jet was achieved by measuring the X-ray transmission through the jet and calculating

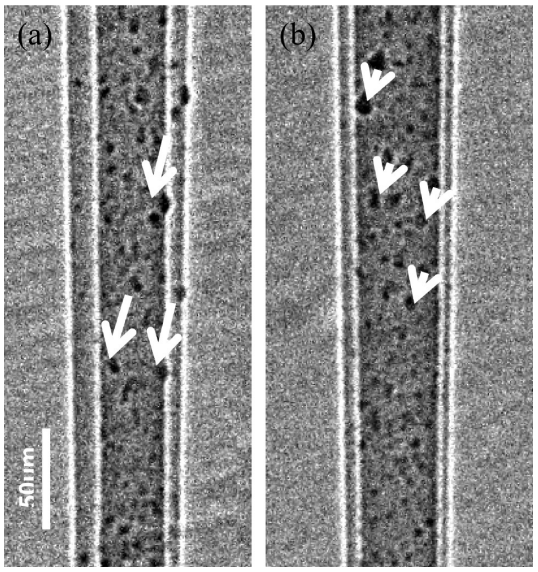


Figure 4. Particle tracing technique using two-pulsed X-ray images. The horizontal offset is due to the jet lateral displacement during the time interval between exposures. Representative velocity vectors (prior to correction of the lateral displacement) are indicated by arrows, correlating particles in the first image to the same particles in the second image. The solution was PEO 5% mixed with 0.9 vol % silica microbeads, electrospun under an electric field of 4 kV/cm and with a flow rate of 2.6 mL/h (test 14). The measurement was taken at distance z = 1.6 mm from the jet start, with a time interval between exposures of (a) Δt = 147.2 μs and (b) Δt = 73.6 μs.

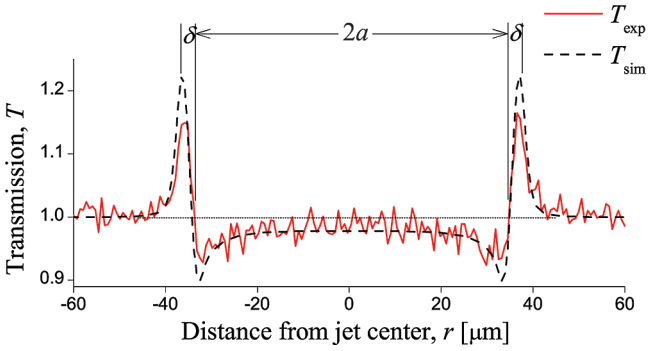


Figure 5. Example of the measured X-ray transmission T_{exp} at a cross section of the jet, based on test 3 (PEO 3%, 1.6 kV/cm, 2.6 mL/h) experimental data, overlaid on the simulated transmission T_{sim}. The estimated measurement error is 1.5%. The jet radius was measured at 1 pixel resolution (0.67 μm) both axially and radially. The radius a was obtained by measuring the distance between the two diffraction peaks, and subtracting δ = 1.5 μm, corresponding to the beam wavelength.

the corresponding absorption coefficient at each point. Using polymer−solvent pairs that have disparate mass absorption coefficients (refer to Table 1), the measured variations in the local absorption coefficient could be converted to polymer concentration variations.

Each raw image (see example in Figure 6a) was processed, using the recorded dark and background images, for the purpose of removing the background spatial nonuniformity and normalizing the background intensity to 1. The resulting transmission of each pixel, $T_{exp}(r,z)$, where r and z respectively denote the radial and axial positions of the pixel in the jet, was obtained by further adjustment for the residual local background offset. The measured transmission T_{exp} (Figure 6b) was normalized by a simulated transmission, $T_{sim}(r,z)$ (Figure 6c), that assumed a homogeneous jet without concentration variations. Normalization provided correction for scattering effects such as dispersion and edge diffraction. Polymer macromolecular orientation as a result of stretching had a negligible effect, since X-ray is absorbed by the atoms along the beam path regardless of their bonding state.[27,33]

The transmission T_{sim} was calculated by a wave propagation simulation designed to account for the overall optical effects of the partially coherent beam and the test setup, by combining absorption and scattering effects. The simulation was based on the Fresnel equation, which, in the paraxial approximation,[34] takes the form of a convolution of the object (projected sample) and a term called propagator. The code used FFTs to calculate the convolution in reciprocal space and then inverse FFTs to retrieve the intensity in real space at the detector location. The code included the most relevant experimental parameters, such as jet geometry and energy-dependent absorption coefficients and refraction indices, as well as source size, energy spectrum, and detector point spread function.

Figure 5 depicts T_{exp} and T_{sim} at a typical cross section of the jet. Note the slight increase in the measured transmission at the jet center, with respect to the simulated transmission. Since the polymer mass absorption coefficient is lower than that of the solvent (see Table 1), absorption decreases and polymer concentration increases. Note also the increase in the measured transmission close to the jet boundary ($r = \pm a$), reflecting a concentration increase near the edge as well.

Using the Beer−Lambert absorption law, and normalizing T_{exp} by T_{sim}, the average change in the apparent absorption coefficient, $\Delta\alpha_{app}(r,z)$, can be expressed by

$$\Delta\alpha_{app}(r, z) = -\frac{1}{d(r, z)} \ln \frac{T_{exp}(r, z)}{T_{sim}(r, z)} \quad (1)$$

where $d(r,z) = 2a(z)(1 - [r/a(z)]^2)^{1/2}$ is the beam penetration distance at a radial position r and $a(z)$ is the jet radius at an axial position z.[11] The measurement of the jet radius a was performed by detecting the edge diffraction white peaks and adjusting for a diffraction width of δ = 1.5 μm corresponding to the beam wavelength (refer to Figure 5).

The measured transmission of the X-ray beam, T_{exp}, is the result of incident beam attenuation consequential of both absorption and scattering of the materials within the jet. Scattering effects of the collimated beam become significant with nonzero distances between the jet and the imaging target (the scintillator) and are relatively larger at smaller jet diameters and at regions closer to the jet boundary. Thus, the apparent absorption coefficient α_{app}, obtained from pixel intensity measurements by eq 1, consists of an absorption term α_{abs} and a scattering term α_{scat}, such that $\alpha_{app} = \alpha_{abs} + \alpha_{scat}$.[33]

In the case of a homogeneous fluid without concentration variations, the scattering contribution can be assessed by comparing the solution absorption coefficient α_0 to the simulated apparent absorption coefficient extrapolated from jet geometry, $\alpha_{sim}(r,z) = -\ln T_{sim}(r,z)/d(r,z)$. While α_0 accounts for absorption only, $\alpha_{sim}(r,z)$ factors in both absorption and scattering. Assuming, as a first-order approximation, that the ratio between these two parameters is retained when concentration variations are present within the fluid, we can introduce a correction factor, $\alpha_0/\alpha_{sim}(r,z)$, to eq 1:

$$\Delta\alpha(r, z) \cong \frac{\alpha_0}{\alpha_{sim}(r, z)} \Delta\alpha_{app}(r, z) = \alpha_0 \left[\frac{\ln T_{exp}(r, z)}{\ln T_{sim}(r, z)} - 1 \right] \quad (2)$$

where $\Delta\alpha(r,z) = \alpha(r,z) - \alpha_0$ is the change in the local absorption coefficient with respect to the solution's initial absorption coefficient.

The absorption coefficient of polymer solutions is given by $\alpha(r,z) = \varepsilon_p c_p(r,z) + \varepsilon_s c_s(r,z)$,[33] where ε_p and ε_s denote the X-ray mass absorption coefficients of the polymer and solvent and c_p and c_s denote the mass concentrations. Using the relationship $c_s/\rho_s = 1 - c_p/\rho_p$, the change in the local polymer concentration, $\Delta c_p(r,z)$, is linearly dependent on $\Delta\alpha(r,z)$:[11]

dx.doi.org/10.1021/ma300237j | Macromolecules 2012, 45, 3616−3626

$$\Delta c_p(r, z) = c_p(r, z) - c = \frac{\Delta\alpha(r, z)\rho_p}{\varepsilon_p\rho_p - \varepsilon_s\rho_s} \quad (3)$$

where c is the solution's initial concentration and ρ_p and ρ_s are the densities of the polymer and solvent, respectively. Using c as the concentration scale, the relative concentration change may be expressed by $\Delta c_p/c$ and the relative concentration by $c_p/c = 1 + \Delta c_p/c$.

The values of the parameters ρ_p, ρ_s, c, ε_p, ε_s, and α_0, used in the analysis of the experimental data, are provided in Table 1. An example of the two-dimensional distribution of $\Delta\alpha$ and Δc_p within the jet is shown in Figure 6d. Note that due to the pixel noise remaining after background removal, further data smoothing was required.

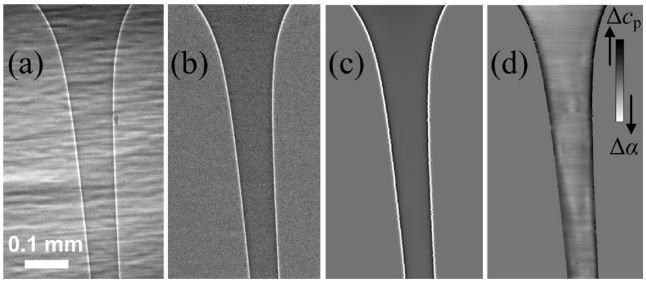
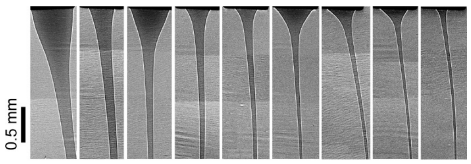


Figure 6. Radiation transmission and absorption processing steps. Example based on test 11 (PEO 5%, 2.8 kV/cm, 1.9 mL/h) data. (a) Raw image. (b) Image after background removal and normalization, T_{exp}. (c) Wave propagation simulation, T_{sim}, assuming a homogeneous jet. (d) Distribution of the absorption coefficient $\Delta\alpha$ (eq 2) and polymer concentration Δc_p (eq 3) (smoothed). Dark regions denote low absorption and high concentration, while bright regions denote high absorption and low concentration.

3. RESULTS AND DISCUSSION

3.1. Jet Radius. Jet radius measurements were carried out on electrospinning PEO 3% solutions (tests 2–5), PEO 5% solutions (tests 6–13), a PMMA 15% solution (test 1), and glycerol (test 0). Image examples shown in Figure 7



Test #	8	13	7	12	11	6	4	3	5
c %	5	5	5	5	5	5	3	3	3
E kV/cm	1.6	2.8	1.6	2.8	2.8	1.6	1.6	1.6	2.2
Q mL/h	7.7	7.7	3.2	3.2	1.9	1	3.8	2.6	2.6

Figure 7. Representative test cases of 3% and 5% PEO. The flow in each image was steady state, at test conditions provided in the table. The jet diameter narrows (from left to right) when the electric field is higher and the flow rate and solution concentration are lower.

demonstrate that the jet diameter narrows earlier along the jet when under higher electric fields and lower flow rates and polymer concentrations. Additionally, these process variables influence the opening angle and height of the Taylor cone at the beginning of the jet, as also shown by Reznik et al.[35] and Feng,[36] as well as the degree of wetting of the lower face of the stainless steel needle. The jet radius reduction ratios within up to 8 mm from the jet start ranged between 5 and 24 for the PEO tests, 10 for the PMMA test, and 31 for the glycerol test. The radius profiles versus the position along the jet are depicted in Figure 8.

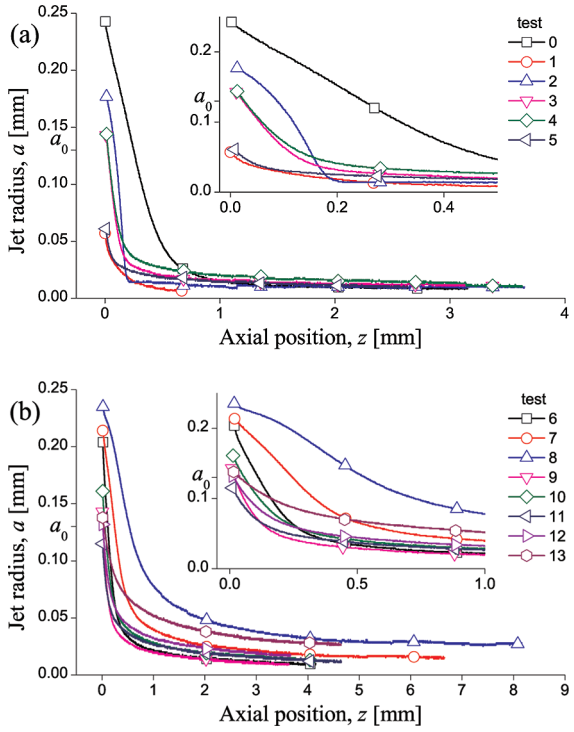


Figure 8. Measured jet radius a at position z along the jet. The jet profile is measured at 1 pixel resolution (0.67 μm), both axially and radially. The insets magnify the early portion of the jet. a_0 = 0.13 mm designates the capillary inner radius. (a) Glycerol (test 0), PMMA 15% (test 1), and PEO 3% (tests 2–5). (b) PEO 5% (tests 6–13).

Analysis of electrically driven fluid jets has shown that the jet reaches an asymptotic regime sufficiently far from the needle orifice. The dimensionless jet radius $\hat{a}$ can be expressed by a power law of the form $\hat{a} \sim \hat{z}^{-\beta}$, where $\hat{z}$ is the dimensionless distance from the orifice and β is a positive exponent.[37−41] The values of β vary, depending on the fluid type and analysis method. For Newtonian fluids, assuming a negligible viscosity effect, the exponent was estimated as $\beta = 1/4$.[37] Using a power-law rheologic constitutive equation, this estimate was generalized to non-Newtonian jets having a flow index >2, to $\beta \geq 1/2$,[38] which converged to $\beta = 1/2$ for jets with a high flow index. Other estimates for Newtonian fluids were $\beta = 1$ (hyperbolic shape), for both viscosity-dominated[40] and capillary-dominated[41] flows. The jet viscoelastic rheology was modeled by Reneker et al. using Maxwell damper-spring elements, providing a complete description of the jet dynamics throughout both the straight and bending-instability regions.[4] Running this model for the jet straight region, we observed a good asymptotic fit to a power law, with $\beta \cong 1/4$ over a wide range of the dimensionless parameters (voltage, elastic modulus, and electric charge). Solvent evaporation, added to the model by Yarin et al., was shown to have a major effect on the jet radius at the bending-instability region, while only a minor effect at the straight region.[42]

Using the orifice internal radius a_0 as the length scale, the power law takes the form

dx.doi.org/10.1021/ma300237j | Macromolecules 2012, 45, 3616−3626

$$\frac{a}{a_0} = \frac{1}{k}\left(\frac{z}{a_0}\right)^{-\beta} \quad (4)$$

where the dimensionless parameter k determines the jet radius reduction rate. The radius measurements of all tests can be collapsed onto a common asymptotic curve (k = 1), by multiplying each profile displayed in Figure 8, by a suitable value of k. The results are depicted in Figure 9a and apply when

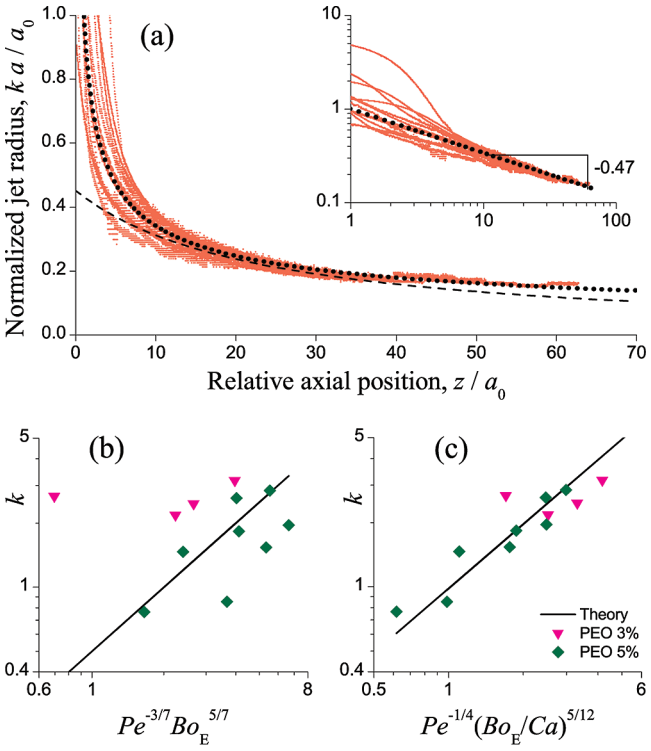


Figure 9. Comparison of measured jet radius to theory at distances of $z/a_0 > 10$ from the orifice. (a) Normalized jet radius ka/a_0 at position z/a_0 along the jet, for the combined data of tests 0–13, where each test set is multiplied by the constant k pertaining to that test. The power fit (dotted line) corresponds to $a/a_0 = (z/a_0)^{-0.47}$, where the exponent is measured in the inset graph. The hyperbolic fit (dashed line) corresponds to $a/a_0 = (z/a_0 + p)^{-1}$, where p = 23.1. (b) Measured coefficient k for tests 2–13 (PEO), compared to the theoretical dimensionless prediction (solid line) for capillary-dominated flow. The predicted value is adjusted by a constant of order 1. (c) As in (b), but for viscosity-dominated flow.

the distance from the orifice, z, is larger than ~10 times the orifice's internal radius, a_0. The slope of the asymptote was measured as $\beta = 0.47 \cong 1/2$ (inset in Figure 9a) and compared with a hyperbolic fit.

The parameter k depends on the flow type. The flow is considered viscosity-dominated when the viscosity, flow rate, and electric field are high, yielding smaller surface tension stresses than viscous and electric stresses. Conversely, the flow is considered capillary-dominated when the surface tension stresses are comparably higher than the viscous and electric stresses. Using dimensionless numbers, theoretical expressions for k are given by $k_{vis} \sim \varepsilon_m^{1/6} Pe^{-1/4} (Bo_E/Ca)^{5/12}$ for viscosity-dominated flow,[40] and $k_{cap} \sim \varepsilon_m^{2/7} Pe^{-3/7} Bo_E^{5/7}$ for capillary-dominated flow,[41] where $\varepsilon_m \cong 1$ is the permeability of the medium (air), $Pe = 2v_0/(\sigma a_0)$ is the Péclet number, $Bo_E = a_0E^2/\gamma$ is the electric Bond number, and $Ca = \mu v_0/\gamma$ is the capillary number. $v_0 = Q/(\pi a_0^2)$ is the jet initial velocity. The dimensional counterparts are the following: $k_{vis}^d \sim \varepsilon_m^{1/6} a_0^{2/3} v_0^{-2/3} \sigma^{1/4} \mu^{-5/12} E^{5/6}$ and $k_{cap}^d \sim \varepsilon_m^{2/7} a_0^{2/7} v_0^{-3/7} \sigma^{3/7} \gamma^{-5/7} E^{10/7}$. Note that k_{vis} is independent of the surface tension γ, while k_{cap} is independent of the viscosity μ. The measured values of k were compared with these theoretical predictions, assuming both capillary-dominated (Figure 9b) and viscosity-dominated (Figure 9c) flows. A good fit to the theoretical model was achieved when assuming viscosity-dominated flow.

Reznik et al.[41] provide an additional criterion for determining the flow type, using the dimensionless number $B = Bo_E CaI/Pe$, where I is the overall electric current led by the jet. When $B \leq 0.01$, the flow is dominated by capillarity, and when $B \geq 1$, the flow is dominated by viscosity. However, when $0.01 < B < 1$, both surface tension and viscous stresses influence the jet shape. Based on the data provided in Table 1, $0.1 < B < 0.9$ for the PEO 3% tests, which is within the interim regime, while $3 < B < 40$ for the PEO 5% tests, which falls within the viscosity-dominated regime. Thus, we can conclude that the experimental results for the PEO tests are in good agreement with the theoretical models. It should be clarified that this analysis applies to the straight section of the jet, before the onset of bending instability, which introduces a dramatic decrease in jet radius and an increase in jet surface area, causing rapid evaporation.[4,6,7,42−44]

At regions closer to the orifice, namely within the Taylor cone (Figure 10a), viscous stresses are lower and the effect of surface tension becomes more significant, while the effects of flow rate and electric field remain similar to those at the asymptotic region of the jet. We use the dimensionless number $Bo_E/Pe = (1/2)a_0^2 v_0^{-1} \sigma\gamma^{-1} E^2$ to express these effects for the

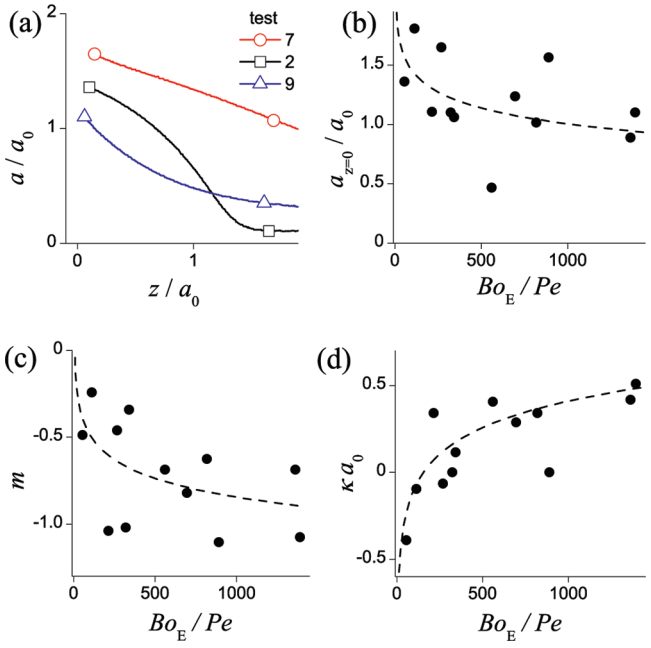


Figure 10. Jet radius profile near the orifice and its dependence on the dimensionless number Bo_E/Pe for tests 2–13 (PEO). (a) Typical cases of the jet radius a/a_0 at position z/a_0 along the jet: straight (test 7: PEO 5%, 1.6 kV/cm, 3.2 mL/h, Bo_E/Pe = 267), convex (test 2: PEO 3%, 0.6 kV/cm, 1.9 mL/h, Bo_E/Pe = 55), and concave (test 9: PEO 5%, 2 kV/cm, 1 mL/h, Bo_E/Pe = 1390). (b) Initial jet radius $a_{z=0}/a_0$. (c) Initial jet slope m. (d) Initial jet curvature κa_0.

dx.doi.org/10.1021/ma300237j | Macromolecules 2012, 45, 3616−3626

PEO tests (Figure 10). When the electric field was lower and the flow rate and surface tension were higher (smaller Bo_E/Pe), the wetting of the needle was larger (Figure 10b), the initial slope of the profile was smaller (Figure 10c), and the curvature of the profile became negative (Figure 10d). In other words, the Taylor cone became larger and convex. On the other hand, when $Bo_E/Pe > 1000$, the Taylor cone features tended to converge to the following conditions: no wetting $a_{z=0} \cong a_0$, slope $m = da/dz \cong -1$, and curvature $\kappa \cong 1/(2a_0)$.

The initial semivertical angle of the Taylor cone in these PEO tests varied between 13° and 48°. By comparison, Reznik et al.[35] have experimentally and theoretically shown that at an electric field with Bo_E above a critical value, jetting sets in, and the jet acquires an almost conical shape with a semivertical angle of 30°, significantly smaller than the 49.3° angle of the Taylor cone.

3.2. Jet Velocity. An upper-bound estimate for jet velocity v (Figure 11a,b) and strain rate s (velocity gradient) (Figure 11c)

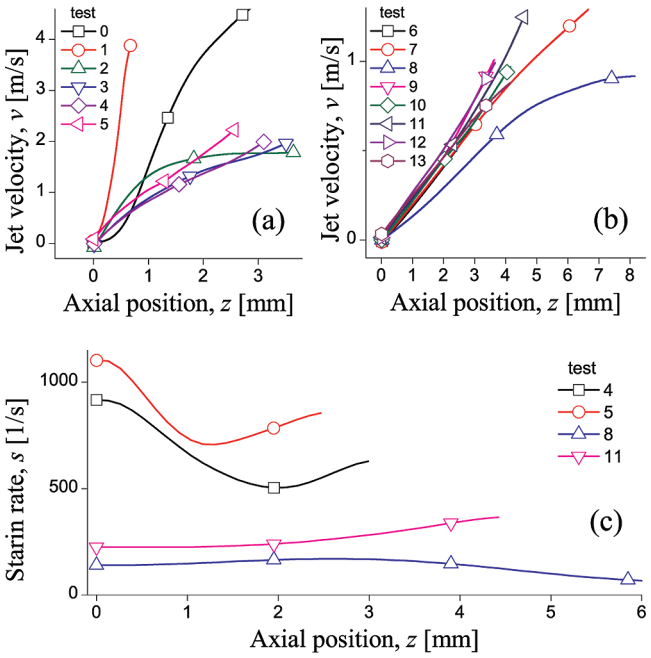


Figure 11. Estimated jet velocity $v = Q/(\pi a^2)$ at position z along the jet, assuming mass conservation. (a) Glycerol (test 0), PMMA 15% (test 1), and PEO 3% (tests 2–5). (b) PEO 5% (tests 6–13). (c) Examples of strain rate s.

can be obtained from the radius measurements by assuming mass conservation (i.e., no evaporation), that is, $v = Q/(\pi a^2)$, where Q is the volumetric flow rate. Typical estimated maximal values were $v \sim 2$ m/s and $s \sim 1000$ 1/s for the PEO 3% tests, $v \sim 1$ m/s and $s \sim 200$ 1/s for the PEO 5% tests, $v \sim 4$ m/s and $s \sim 7000$ 1/s for the PMMA 15% test, and $v \sim 5$ m/s and $s \sim 2000$ 1/s for the glycerol test. Note the nonmonotonic evolution of the strain rate in Figure 11c, which indicates the transition from the capillary-dominated region (Taylor cone) to the viscosity-dominated region.

Using the power law of eq 4, the asymptotic velocity sufficiently far from the orifice can be written as

$$\frac{v}{v_0} = k^2\left(\frac{z}{a_0}\right)^{2\beta} \cong \frac{k^2 z}{a_0} \qquad (5)$$

where, as before, $\beta = 0.47 \cong 1/2$. The corresponding dimensionless strain rate $\hat{s}$ saturates to approximately $\hat{s} = sa_0/v_0 \cong k^2$. Thus, for the studied viscosity-dominated test conditions, the jet strain rate, expressed by k_{vis}^2, increases with the electric field E and conductivity σ and decreases with the velocity v_0 (or flow rate Q) and viscosity μ (or solution concentration c). Note that the "grouping" of the graphs in Figure 11 is due to the sensitivity of k_{vis}^2 to the widely disparate viscosity values between the groups (see Table 1).

Measurements of the jet vertical velocity using particle tracing, v_p, are presented for PEO 5% tests 14 (4 kV/cm, 2.6 mL/h) and 15 (4 kV/cm, 6.4 mL/h) and are compared to velocity estimation based on the mass conservation assumption, v_c (Figure 12). The comparison revealed a large deviation

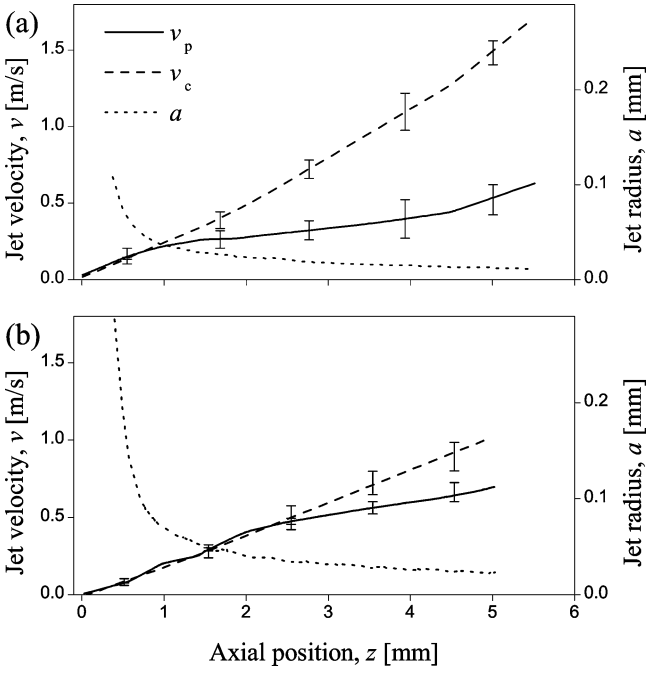


Figure 12. Examples of vertical velocity measurements using silica microbeads, v_p, compared to velocity estimation from the measured radius a assuming mass conservation, v_c. Electrospinning of PEO 5%, under an electric field of 4 kV/cm. (a) Test 14: flow rate of 2.6 mL/h, 589 data points. (b) Test 15: flow rate of 6.4 mL/h, 696 data points.

between the two measurement methods, which intensified with the distance from the orifice and was more pronounced at the lower flow rate (Figure 12a). The difference in strain rate is by a factor of ~2. v_p and v_c coincide close to the orifice, but they begin to separate at a jet diameter of $2a \cong 50$ μm, significantly larger than the particle mean size (~2 μm), thereby ruling out any possibility of adverse effects of the particles on flow. The possible impact of the X-ray beam, especially due to ionization of the air surrounding the jet, can also be ruled out in view of the good correlation between the methods at the beginning of the jet. It also seems unlikely that the dynamic evolution of the polymer network could affect the particles velocity to the extent observed.

Thus, this measurement and comparison suggest a very rapid evaporation, at a distance of only a few millimeters from the jet start. Note that the asymptotic ratio of jet surface area to volume, inversely proportional to the jet radius, is about twice as large in the 2.6 mL/h case compared to the 6.4 mL/h case, accounting for the higher evaporation rate in lower flow rate.

dx.doi.org/10.1021/ma300237j | Macromolecules 2012, 45, 3616–3626

The solvent used in these tests was water, a nonvolatile solvent; however, the relative humidity was fairly low (40%).

The use of particles provides a high-resolution internal view of the flow field within the jet. The image in Figure 13a displays

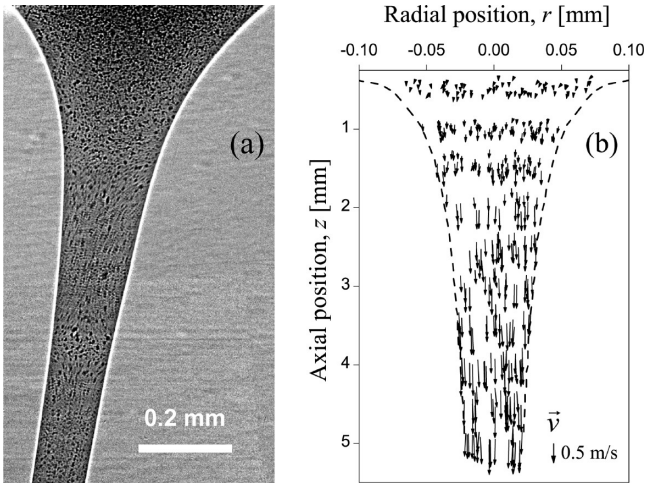


Figure 13. Typical flow field during electrospinning of PEO 5% solution in water, mixed with 0.9 vol % silica microbeads, under an electric field of 4 kV/cm and flow rate of 6.4 mL/h (test 15). (a) Two-pulsed X-ray image of a 1 mm long jet section, captured with a 73.6 μs time interval between exposures. (b) Velocity vector field, $\vec{v}$, generated by particle tracing in a 5 mm long jet section (note the uneven axis scales).

an example of the flow regime during the initial formation of the jet. As seen, flow lines emerge when the velocity is fast enough, and the flow appears to be laminar, as expected from the low Reynolds number. The flow field velocity measurements (Figure 13b) showed a predominantly vertical velocity that seemed to be uniformly distributed across the jet.

However, fitting the data of test 15 (PEO 5%, 4 kV/cm, 6.4 mL/h) to a parabolic shape, as suggested by Reznik et al.,[41] revealed a Poiseuille distribution of the vertical velocity across the jet (Figure 14a), with lower velocity at the jet center when compared to the jet boundary. By contrast, vertical velocity distribution was close to uniform in the lower flow rate case (test 14: PEO 5%, 4 kV/cm, 2.6 mL/h, Figure 14b), possibly

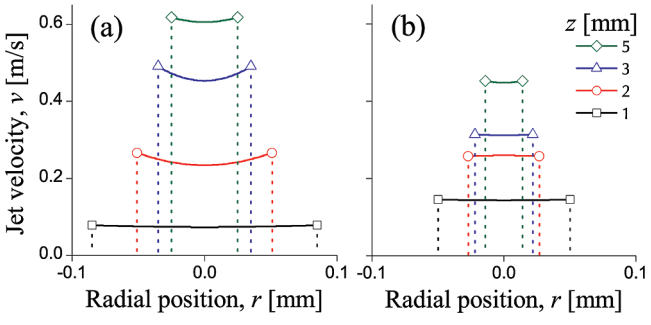


Figure 14. Examples of vertical velocity distribution across the jet, at given locations z along the jet, as a function of the radial distance r from the jet center. The values were averaged along the X-ray beam path and were obtained by parabolic fitting of the test data. Electrospinning was done for PEO 5% solution in water, mixed with 0.9 vol % silica microbeads, under an electric field of 4 kV/cm. (a) Test 15: flow rate of 6.4 mL/h ($\bar{R}^2 > 0.95$). (b) Test 14: flow rate of 2.6 mL/h ($\bar{R}^2 > 0.75$).

due to the smaller jet radius. The sign of the velocity profile curvature in test 15 was opposite to that predicted by Reznik et al. for a viscosity-dominated flow. This phenomena could be influenced by the nonuniform distribution of the polymer (section 3.3) .

3.3. Polymer Concentration Distribution. Measurements of X-ray absorption variations within the jet were carried out on PEO 3% solutions (tests 2–5), PEO 5% solutions (tests 6–13), and a PMMA 15% solution (test 1). The resulting concentration variations are attributed to the effects of evaporation and polymer network stretching. In view of the partial correction for scattering effects (eq 2), these results should be regarded as indicating trends.

As concentration variations are expected to assume circular symmetry at a jet cross section, measurement of radiation transmission through the center of a jet should yield the average absorption change of the jet at a given axial position z. The resulting evolution of the average absorption coefficient, $\Delta\alpha$, along the centerline of the jet of several test cases, is shown in Figure 15a. As seen, the absorption coefficient tends to

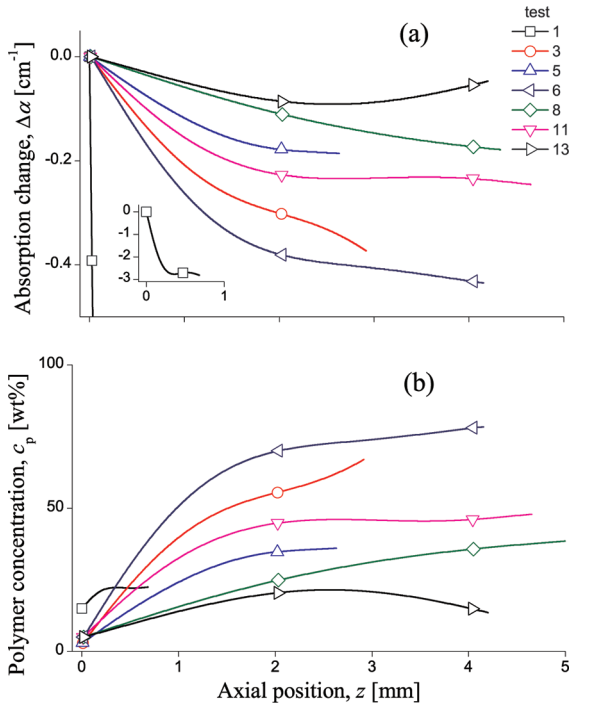


Figure 15. Measured average change in X-ray absorption and polymer concentration, in relation to the distance z from the orifice, based on radiation transmission measurements along the jet centerline. Test 1 is PMMA 15% (inset), tests 3 and 5 are PEO 3%, and tests 6–13 are PEO 5%. (a) Absorption coefficient change, $\Delta\alpha$. (b) Polymer concentration, c_p [wt %].

decrease with the distance from the orifice. At the jet beginning, the rate of decrease is high but slows at increasing distances and sometimes even reverses (e.g., test 13: PEO 5%, 2.8 kV/cm, 7.7 mL/h). Note the high absorption change in test 1 (PMMA 15%, 0.8 kV/cm, 1.9 mL/h, see inset in Figure 15a) due to the high disparity in mass absorption coefficients between PMMA and chloroform.

The polymers in these tests have lower X-ray mass absorption coefficients than their respective solvents (refer to Table 1), and therefore the decrease in the absorption coefficient reflects an increase in polymer concentration (Figure

dx.doi.org/10.1021/ma300237j | Macromolecules 2012, 45, 3616–3626

15b). The results show a significant rise in concentration within the first few millimeters from the jet start, indicating substantial mass loss due to evaporation. This observation supports the similar finding obtained from the velocity measurements in section 3.2. The slowing down, and even reversal, of the concentration change rate along the jet may imply an onset of additional mechanisms, such as polymer chains disentanglement or skin solidification, which retards evaporation rates. Further evaporation may leave voids in the jet core and allow partial relaxation of the polymer matrix.[11]

A common behavior emerges when examining the polymer relative concentration change, $\Delta c_p/c$, recorded in tests 3−12 (PEO in water), as a function of the relative jet radius, a/a_0 (Figure 16). A steep rise in polymer concentration was

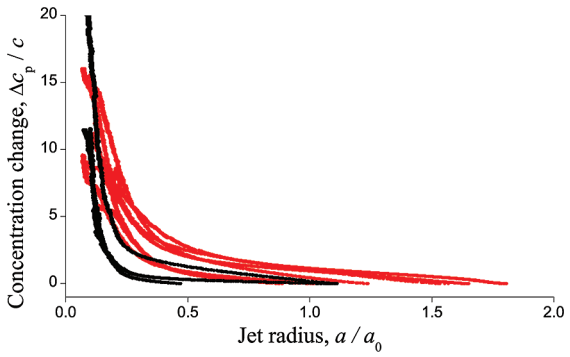


Figure 16. Relative concentration change $\Delta c_p/c$ vs relative jet radius a/a_0, derived from the X-ray absorption measurements at jet center of tests 3−5 (PEO 3%, black lines) and tests 6−12 (PEO 5%, red lines).

observed at $a/a_0 \cong 0.2$, marking a critical radius of ∼25 μm, below which rapid evaporation is initiated. Interestingly, velocity measurements demonstrated a similar value, marking the radius at which rapid evaporation began (Figure 12). As noted by Yarin et al.,[42] rapid evaporation starts upon rapid increase in the ratio of the jet surface area to volume, which is inversely proportional to the jet radius.

The concentration change rate can be estimated from the slope of the plot in Figure 16 in the asymptotic region, using the power dependence

$$\frac{\Delta c_p}{c} \sim \left(\frac{a}{a_0}\right)^{-\phi} \tag{6}$$

where the measured exponent is $\varphi \cong 2 \pm 0.5$ for PEO tests 3−12. Since this concentration change is due to evaporation, the corresponding local mass loss rate is then $\sim c(a/a_0)^{-2}$ in the measured region or, in other words, inversely proportional to the jet cross-sectional area.

Absorption measurements across the jet at different axial positions (Figure 17) revealed nonuniform distribution of the polymer, with high concentration boundary layer formed as a result of evaporation. In addition, a peak emerged at the jet center, starting at cross sections $z \geq 1$ mm from the orifice. Our previous theoretical and experimental study[11] attributed this rise to polymer network stretching during electrospinning, which causes lateral contraction of the network, thereby increasing polymer concentration at the center. Polymer chains entangled in a network were shown to approach full extension when the jet vertical velocity was approximately $v/v_0 \cong N_s^{1-\nu}$, where N_s is the number of monomers in a subchain (a section

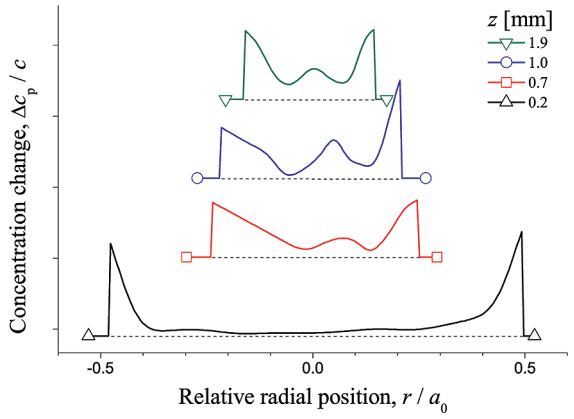


Figure 17. Typical polymer relative concentration change across the jet, $\Delta c_p/c$, vs the relative radial distance from the jet center, r/a_0, for several axial positions z along the jet. The data are derived from the X-ray absorption measurements of PEO 5%, under an electric field of 2.8 kV/cm and flow rate of 1.9 mL/h (test 11). The dashed horizontal lines represent zero concentration change, $\Delta c_p/c = 0$, corresponding to a homogeneous jet with uniform concentration $c_p = c$.

of a polymer chain between two adjacent entanglement nodes) and ν is Flory's exponent. Considering a PEO 5% solution, this criterion predicts significant stretching at a relative radius of $a/a_0 \cong 0.4$, which occurs close to the jet start, in good agreement with the result observed in Figure 17.

Evaporation and stretching impart contradicting effects on the polymer concentration distribution. Evaporation tends to increase concentration at the jet boundary, while stretching leads to its increase at the jet center. Fast stretching of the solution jet counteracts polymer network relaxation due to evaporation and skin formation and causes lateral inward contraction of the network. Material properties and electrospinning conditions influence the relative impact of stretching and evaporation on the polymer matrix and eventually determine the resulting macrostructure of nanofibers (see examples of homogeneous and porous structures in Greenfeld et al.[11]).

The balance between these two processes is demonstrated in Figure 18, which compares the concentration along the jet centerline to that along an offset of half-radius ($a/2$) from the centerline. The comparison is done within the same solution (PEO 5% in water) to avoid concentration effects on evaporation. Under an electric field of 2.8 kV/cm and flow rate of 1.9 mL/h (test 11, Figure 18a), the concentration at the center was higher than at the offset, for sufficiently small jet relative radius a/a_0, indicating noticeable stretching. When reducing the electric field to 2 kV/cm and leaving the flow rate unchanged (test 10, Figure 18b), the concentrations at the center and at the offset remained similar, evidence for balanced effects of evaporation and stretching on polymer distribution at the jet core. Finally, when leaving the electric field unchanged (as in test 11) and increasing the flow rate to 7.9 mL/h (test 13, Figure 18c), a higher concentration was observed at the offset than at the center, evidence for dominant evaporation.

Similar behavior was observed when testing PEO 3%. For example, test 5 (2.2 kV/cm, 2.6 mL/h) involved higher electric field and lower flow rate than test 4 (1.6 kV/cm, 3.8 mL/h) and yielded higher concentrations at the center when compared to the offset. These trends are in agreement with the theoretical prediction,[11] which has shown that the local axial stretching of polymer chains, and consequently their lateral contraction, are

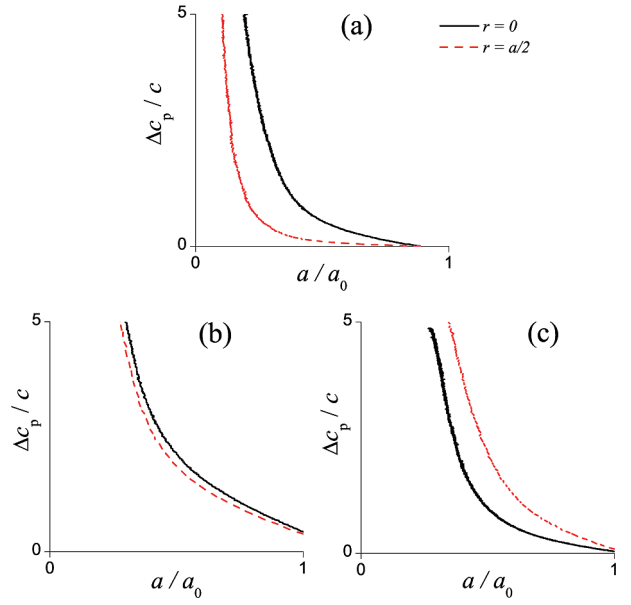


Figure 18. Comparison of the relative concentration change $\Delta c_p/c$ at the jet center ($r = 0$) to that measured at a radial offset from the center ($r = a/2$, averaged over the range $0.4a$ to $0.6a$), presented vs the relative jet radius a/a_0. The data were derived from the X-ray absorption measurements of PEO 5% in (a) test 11 (2.8 kV/cm, 1.9 mL/h), (b) test 10 (2 kV/cm, 1.9 mL/h), and (c) test 13 (2.8 kV/cm, 7.9 mL/h).

proportional to the jet relative local velocity v/v_0, and hence, in view of eq 5), are proportional to k_{vis}^2. Regardless of these findings, it should be noted that high concentration at the jet boundary was observed in all tests.

4. CONCLUSIONS

Fast X-ray phase-contrast imaging was applied for high-resolution investigation of the initial straight section of electrospinning polymer jets, extending up to 10 mm from the orifice. The experiment aimed at providing data on the flow field and polymer concentration distribution within the jet, which can help describe the state of the polymer network during electrospinning.

Details relating to jet radius, velocity, and strain rate were measured for a range of electrospinning conditions and polymer solutions. Particle tracing velocimetry allowed for flow regime viewing inside the jet, characterized by laminar flow and dominant vertical velocity. The velocity was found to be slower than an estimation based on mass conservation assumption, indicating a substantial mass loss due to evaporation at a very early stage of the process.

Measurement of pixel intensities were converted to X-ray radiation absorption coefficients that allowed for estimation of the polymer distribution within the jet. Concentrations were found to rapidly increase below a critical radius, evidence of rapid evaporation. The rate of mass loss due to evaporation seemed to be much higher than theoretical predictions.[42] In addition, the concentration variation across the jet revealed high concentrations at the jet boundary due to evaporation as well as a concentration rise at the jet center. The latter phenomenon is attributed to polymer stretching that causes lateral contraction of the polymer network toward the jet center and is in good agreement with theoretical models.[11] Moreover, it was shown that evaporation is dominant when stretching is weaker (e.g., at lower electric field and/or higher flow rate), canceling the concentration peaks measured at the jet center.

The balance between the effects of evaporation and stretching determines the polymer network nonequilibrium conformation during electrospinning and can help clarify the reasons for the diverse macrostructures and properties found in solid nanofibers. In particular, the size-dependent mechanical, thermomechanical, and thermodynamic properties of as-spun nanofibers,[8,9,12,45] such as the rise of the elastic modulus at small diameters, are attributed to the internal molecular and supermolecular structure of the polymer matrix in nanofibers.[11]

X-ray imaging during electrospinning can provide internal flow and concentration data, unattainable by other in-situ measurement methods. The current implementation of the method is, however, limited to the initial section of the jet that is sufficiently stable to be captured within the small field of view of the imaging system. Nevertheless, further investigation downstream, at narrower jet diameters on the order of micrometers, can provide evidence for polymer chains disentanglement and reveal nonuniform flow regime due to rapid evaporation, possibly with streamlines toward the jet boundary. Such observations may be important for electrospinning applications such as drug delivery and coatings.

AUTHOR INFORMATION

Corresponding Author

*Tel 972 4 957 1287; fax 972 4 957 1291; e-mail green_is@netvision.net.il.

Notes

The authors declare no competing financial interest.

ACKNOWLEDGMENTS

We gratefully acknowledge the financial support of the United States−Israel Binational Science Foundation (BSF Grant 2006061), the RBNI−Russell Berrie Nanotechnology Institute, and the Israel Science Foundation (ISF Grant 770/11). Use of the Advanced Photon Source, an Office of Science User Facility operated for the U.S. Department of Energy (DOE) Office of Science by Argonne National Laboratory, was supported by the U.S. DOE under Contract DE-AC02-06CH11357. We acknowledge Dr. Arkadii Arinstein for insightful discussions on polymer dynamics. We thank Dr. Rene Van-Hout for valuable advice on X-ray image processing.

REFERENCES

(1) Han, T.; Yarin, A. L.; Reneker, D. H. *Polymer* **2008**, *49* (6), 1651−1658.
(2) Gupta, P.; Elkins, C.; Long, T. E.; Wilkes, G. L. *Polymer* **2005**, *46* (13), 4799−4810.
(3) Reneker, D. H.; Yarin, A. L.; Zussman, E.; Xu, H. *Adv. Appl. Mech.* **2007**, *41*, 43−195.
(4) Reneker, D. H.; Yarin, A. L.; Fong, H.; Koombhongse, S. *J. Appl. Phys.* **2000**, *87* (9), 4531−4547.
(5) Bellan, L. M.; Craighead, H. G.; Hinestroza, J. P. *J. Appl. Phys.* **2007**, *102* (9), 094308.
(6) Hohman, M. M.; Shin, M.; Rutledge, G.; Brenner, M. P. *Phys. Fluids* **2001**, *13* (8), 2201−2220.
(7) Shin, Y. M.; Hohman, M. M.; Brenner, M. P.; Rutledge, G. C. *Polymer* **2001**, *42* (25), 9955−9967.
(8) Burman, M.; Arinstein, A.; Zussman, E. *Appl. Phys. Lett.* **2008**, *93* (19), 193118.
(9) Arinstein, A.; Burman, M.; Gendelman, O.; Zussman, E. *Nat. Nanotechnol.* **2007**, *2* (1), 59−62.

(10) Burman, M.; Arinstein, A.; Zussman, E. *Europhys. Lett.* **2011**, *96*, 16006.
(11) Greenfeld, I.; Arinstein, A.; Fezzaa, K.; Rafailovich, M. H.; Zussman, E. *Phys. Rev. E* **2011**, *84* (4), 041806.
(12) Zussman, E.; Arinstein, A. *J. Polym. Sci., Part B: Polym. Phys.* **2011**, *49* (10), 691−707.
(13) Guenthner, A. J.; Khombhongse, S.; Liu, W. X.; Dayal, P.; Reneker, D. H.; Kyu, T. *Macromol. Theory Simul.* **2006**, *15* (1), 87−93.
(14) Dayal, P.; Kyu, T. *Phys. Fluids* **2007**, *19* (10), 107106.
(15) Dayal, P.; Liu, J.; Kumar, S.; Kyu, T. *Macromolecules* **2007**, *40* (21), 7689−7694.
(16) Koombhongse, S.; Liu, W. X.; Reneker, D. H. *J. Polym. Sci., Part B: Polym. Phys.* **2001**, *39* (21), 2598−2606.
(17) Casper, C. L.; Stephens, J. S.; Tassi, N. G.; Chase, D. B.; Rabolt, J. F. *Macromolecules* **2004**, *37* (2), 573−578.
(18) Deitzel, J. M.; Krauthauser, C.; Harris, D.; Pergantis, C.; Kleinmeyer, J. *Polym. Nanofibers* **2006**, *918*, 56−73.
(19) Larrondo, L.; Manley, R. S. J. *J. Polym. Sci., Part B: Polym. Phys.* **1981**, *19* (6), 921−932.
(20) Stephens, J. S.; Frisk, S.; Megelski, S.; Rabolt, J. F.; Chase, D. B. *Appl. Spectrosc.* **2001**, *55* (10), 1287−1290.
(21) Priebe, M.; Kalbfleisch, S.; Tolkiehn, M.; Koster, S.; Abel, B.; Davies, R. J.; Salditt, T. *New J. Phys.* **2010**, *12*, 1−12.
(22) MacPhee, A. G.; Tate, M. W.; Powell, C. F.; Yue, Y.; Renzi, M. J.; Ercan, A.; Narayanan, S.; Fontes, E.; Walther, J.; Schaller, J.; Gruner, S. M.; Wang, J. *Science* **2002**, *295* (5558), 1261−1263.
(23) Wang, Y. J.; Liu, X.; Im, K. S.; Lee, W. K.; Wang, J.; Fezzaa, K.; Hung, D. L. S.; Winkelman, J. R. *Nat. Phys.* **2008**, *4* (4), 305−309.
(24) Im, K. S.; Fezzaa, K.; Wang, Y. J.; Liu, X.; Wang, J.; Lai, M. C. *Appl. Phys. Lett.* **2007**, *90* (9), 091919.
(25) Sasov, A. *European Conference for Non-Destructive Testing (ECNDT)* **2006**, *We.1.5.4*, 1−6.
(26) Richter, A. G.; Guico, R.; Shull, K.; Wang, J. *Macromolecules* **2006**, *39* (4), 1545−1553.
(27) Gullikson, E. X-Ray Interactions with Matter. http://henke.lbl.gov/optical_constants/.
(28) www.surface-tension.de. Surface tension values of some common test liquids.
(29) http://www.smartmeasurement.com. Conductivity of common fluids.
(30) Theron, S. A.; Zussman, E.; Yarin, A. L. *Polymer* **2004**, *45* (6), 2017−2030.
(31) Thomas, D. G. *J. Colloid Sci.* **1965**, *20* (3), 267−277.
(32) Staben, M. E.; Davis, R. H. *Int. J. Multiphase Flow* **2005**, *31* (5), 529−547.
(33) Roe, R. J., *Methods of X-ray and Neutron Scattering in Polymer Science*; Oxford University Press: New York, 2000; p xiv, 331 p.
(34) Reeves, R. V.; White, J. D. E.; Dufresne, E. M.; Fezzaa, K.; Son, S. F.; Varma, A.; Mukasyan, A. S. *Phys. Rev. B* **2009**, *80* (22), 224103.
(35) Reznik, S. N.; Yarin, A. L.; Theron, A.; Zussman, E. *J. Fluid Mech.* **2004**, *516*, 349−377.
(36) Feng, J. J. *Phys. Fluids* **2002**, *14* (11), 3912−3926.
(37) Kirichenko, V. N.; Petrianovsokolov, I. V.; Suprun, N. N.; Shutov, A. A. *Dokl. Akad. Nauk SSSR* **1986**, *289* (4), 817−820.
(38) Spivak, A. F.; Dzenis, Y. A. *Appl. Phys. Lett.* **1998**, *73* (21), 3067−3069.
(39) Hohman, M. M.; Shin, M.; Rutledge, G.; Brenner, M. P. *Phys. Fluids* **2001**, *13* (8), 2221−2236.
(40) Higuera, F. J. *J. Fluid Mech.* **2006**, *558*, 143−152.
(41) Reznik, S. N.; Zussman, E. *Phys. Rev. E* **2010**, *81* (2), 026313.
(42) Yarin, A. L.; Koombhongse, S.; Reneker, D. H. *J. Appl. Phys.* **2001**, *89* (5), 3018−3026.
(43) Thompson, C. J.; Chase, G. G.; Yarin, A. L.; Reneker, D. H. *Polymer* **2007**, *48* (23), 6913−6922.
(44) Fridrikh, S. V.; Yu, J. H.; Brenner, M. P.; Rutledge, G. C. *Phys. Rev. Lett.* **2003**, *90* (14), 144502.
(45) Ji, Y.; Li, C.; Wang, G.; Koo, J.; Ge, S.; Li, B.; Jiang, J.; Herzberg, B.; Klein, T.; Chen, S.; Sokolov, J. C.; Rafailovich, M. H. *EPL* **2008**, *84* (5), 56002.

Macromolecules

Article

pubs.acs.org/Macromolecules

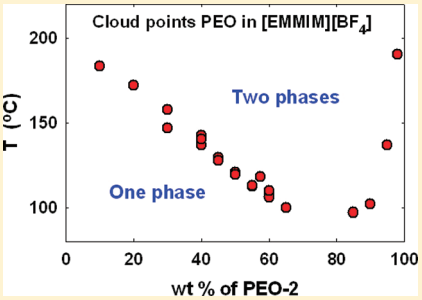
Unusual Lower Critical Solution Temperature Phase Behavior of Poly(ethylene oxide) in Ionic Liquids

Hau-Nan Lee,[†] Nakisha Newell,[†] Zhifeng Bai,[†] and Timothy P. Lodge*[,†,‡]

[†]Department of Chemistry and [‡]Department of Chemical Engineering and Materials Science, University of Minnesota, Minneapolis, Minnesota 55455, United States

Supporting Information

ABSTRACT: We describe the LCST-type phase behavior of poly(ethylene oxide) (PEO) dissolved in imidazolium-based tetrafluoroborate ionic liquids (ILs). Phase diagrams were determined by a combination of small-angle neutron scattering (SANS) and cloud point (CP) measurements. Unlike typical LCST phase diagrams of polymer solutions, the PEO/IL phase diagram is either roughly symmetric with a critical composition near 50% polymer or asymmetric with a critical composition shifted to an even higher concentration of PEO. As the molecular weight decreases from 20 500 to 4200 g/mol, the critical temperature (T_c) increases slightly (~10 °C). However, a larger increase in T_c (27 °C) was observed as the molecular weight decreases from 4200 to 2100 g/mol, likely due to the increasing importance of hydrogen bonds between the −OH end groups of PEO and the fluorine atoms of the anions. This inference is supported by the strong dependence of the phase diagram on the identity of the PEO end groups (hydroxy vs methoxy). Furthermore, replacing the most acidic proton of the imidazolium ring (in the C_2 position) with a methyl group lowers the T_c and changes the shape of the phase diagram significantly, suggesting that the hydrogen bonds between the H atoms on the C_2 position of the imidazolium ring and the O atoms of PEO play an important role in determining the LCST phase behavior of this system.



INTRODUCTION

Ionic liquids (ILs) are a class of solvents with appealing physical properties such as negligible vapor pressure, good chemical and thermal stability, and wide liquid temperature ranges. They have been called "designer solvents" due to the readily tunable solvation properties accessible by varying the chemical structure of the cation or anion.[1] Combinations of ILs with polymers have been proposed for many applications such as polymer electrolytes[2] in lithium batteries.[3] Self-assembled systems such as ion gels,[4] micelles,[5,6] and vesicles[7] can also be obtained by incorporating block copolymers into ILs. Possible applications include membranes for gas separations,[8,9] gels for thin-film transistors,[10−13] and micelles/vesicles for molecular storage and transport systems.[14,15] In order to optimize materials for these applications, knowledge of the phase behavior of polymers in ILs over a wide range of temperature is essential.[16,17]

A full understanding of polymer solution phase behavior has proven to be challenging. The narrow liquid range and high vapor pressure of water or organic solvents limit the experimental temperature range. In contrast to water or organic solvents, the nonvolatility and good thermostability of ILs provide a great opportunity to investigate the phase behavior over a much wide range of temperature. Furthermore, in polymer/IL systems, both LCST and UCST phase behavior have been reported. For example, Ueki and Watanabe demonstrated the UCST phase behavior of poly(*N*-isopropylacrylamide) in 1-ethyl-3-methylimidazolium bis{(trifluoromethyl)sulfonyl}amide ([EMIM][TFSA]).[18] Later, Watanabe and co-workers showed that poly(benzyl methacrylate) and its derivatives[19−25] exhibit LCST phase behavior in 1-alkyl-3-methylimidazolium bis{(trifluoromethyl)sulfonyl}amide [C_nMIM][TFSA]. They hypothesized that the formation of ordered structures via the cation−π interactions[26] between the IL cations and the aromatic groups in the polymers leads to the LCST phase behavior. Watanabe and co-workers also discovered that poly(ethyl glycidyl ether) (PEGE) showed LCST phase behavior in [EMIM][TFSA].[27] In this case they proposed that the hydrogen bonds between PEGE and [EMIM][TFSA] are the primary driving force of the LCST phase behavior. More recently, we reported the LCST-type phase behavior of poly(*n*-butyl methacrylate) (PnBMA) dissolved in [C_nMIM][TFSA], and the LCST of PnBMA can be tuned over a wide range (>230 °C) by mixing two different alkylmethylimidazolium ILs, without modifying the chemical structure of the polymers.[28] One common feature of these UCST or LCST polymer/IL systems is that they all exhibit asymmetric temperature−composition phase diagrams, with the critical composition shifted to low concentrations of polymer, qualitatively consistent with the predictions of Flory−Huggins theory.

In a previous study using optical transmittance, we reported that PEO exhibits unusual temperature−composition phase

Received: February 18, 2012
Revised: March 30, 2012
Published: April 10, 2012

 © 2012 American Chemical Society dx.doi.org/10.1021/ma300335p | *Macromolecules* 2012, 45, 3627−3633

diagrams in 1-ethyl-3-methylimidazolium tetrafluoroborate ([EMIM][BF_4]), in which the critical composition inferred from cloud points (CP) shifts to high concentrations of PEO.[29] The LCST of this system can be tuned by varying molecular weight of PEO or by modifying the chemical structures of the IL. The present work extends the previous study by experimentally examining the influence of hydrogen bonding between the components on the LCST phase behavior and by utilizing small-angle neutron scattering (SANS) to access the spinodal curves, thereby reinforcing the location of the critical point. Phase diagrams determined by both SANS and CP measurements are presented.

EXPERIMENTAL SECTION

Materials. 1-Ethyl-3-methylimidazolium tetrafluoroborate ([EMIM][BF_4]), 1-ethyl-2,3-dimethylimidazolium tetrafluoroborate ([EMMIM][BF_4]), and deuterated 1-ethyl-3-methylimidazolium tetrafluoroborate ([EMIM-D_5][BF_4]) were synthesized in house; the details of synthetic procedures can be found in the Supporting Information. The PEO homopolymers used in this study were purchased from Aldrich. The M_n and M_w/M_n of these PEOs were determined by size exclusion chromatography (SEC) and matrix-assisted laser desorption/ionization time-of-flight (MALDI-TOF) measurements and are summarized in Table 1. The details of polymer characterization are described in the Supporting Information.

Table 1. Sample Characteristics

samples	M_n (kg/mol)	M_w/M_n
PEO-20(−OH)[a]	20.5	1.03
PEO-11(−OH)[a]	10.7	1.07
PEO-4(−OH)[a]	4.2	1.26
PEO-2(−OH)[b]	2.1	1.01
PEO-2($-OCH_3$)[b]	1.7	1.08
PEO-2(−OH, $-OCH_3$)[b]	1.9	1.02

[a] M_n and M_w/M_n of PEO-20(−OH), PEO-11(−OH), and PEO-4(−OH) were determined by size exclusion chromatography (SEC) with THF containing 1 vol % of tetramethylethylenediamine (TMEDA) as the eluent. [b] M_n and M_w/M_n of PEO-2(−OH), PEO-2($-CH_3$) and PEO-2(−OH, $-OCH_3$) were determined by MALDI-TOF mass spectrometry. The numbers indicate the molecular weight in kg/mol. The −OH or $-OCH_3$ functional groups in parentheses indicate the types of PEO end groups.

Preparation of PEO/IL Solutions. A procedure was utilized to prepare PEO/IL solutions for CP and SANS measurements to minimize water content. For CP measurements, PEO and IL were combined in ampules and heated to ~80 °C, with stirring, to melt the PEO and make homogeneous PEO/IL solutions. The solutions were then dried under vacuum (<50 mTorr) for at least 48 h to remove moisture. Finally, the ampules were flame-sealed in an argon atmosphere to prevent moisture, contamination, and degradation of components at high temperatures. A similar method was applied to prepare solutions of PEO in deuterated IL for the SANS measurements. After drying in a vacuum oven, the solutions were transferred into quartz banjo cells or between two quartz disks with a path length of ~1.0−1.4 mm.

Cloud Point Measurements. The CPs of PEO/IL were determined by optical transmittance measurements at 632.8 nm at a heating rate of roughly 1 °C/min. The temperature dependence of transmittance was monitored using a laser power detector while the solution was stirred in a temperature-controlled oil bath. The CP is taken as the temperature at which the transmittance drops to 80%.

Small-Angle Neutron Scattering. SANS experiments were performed on the NG-7 30 m instrument at the National Institute of Standards and Technology. The sample temperature was controlled to within 0.5 °C by placing the cells in a heating block and monitored with a thermocouple in contact with the heating block. A sample-to-detector distance of 3 m, a monochromated neutron wavelength λ = 7 Å, and a wavelength spread of $\Delta\lambda/\lambda$ = 0.115 were used to cover a scattering wave vector range q = 0.01−0.13 $Å^{-1}$. The scattering vector is defined as $q = (4\pi/\lambda)\sin(\theta/2)$, where λ and θ are the neutron wavelength and scattering angle, respectively. Using established procedures,[30] the two-dimensional scattering spectra were reduced by azimuthal integration to yield the one-dimensional form of intensity $I(q)$ vs q, corrected for background detector efficiency, empty cell scattering, and sample transmission and then converted to absolute intensity with direct beam flux measurements. Finally, incoherent scattering from the sample was subtracted.

RESULTS AND DISCUSSION

Could Point Measurements of PEO in ILs. LCST phase behavior of PEOs in [EMIM][BF_4] or [EMMIM][BF_4] was investigated using CP measurements. Figure 1 shows the temperature dependence of the transmittance at 632.8 nm for PEO-20(−OH) in [EMIM][BF_4] with different concentrations. Transmittance of 100% indicates a single-phase solution, and a decrease in transmittance indicates that the solution undergoes liquid−liquid phase separation. As shown in Figure 1, at low temperatures, PEO-20(−OH) in [EMIM][BF_4] systems are completely miscible. However, as the temperature increases above the LCST, the solution becomes cloudy and the transmittance rapidly decreases. The CPs of 1, 5, 10, 20, and 30 wt % of PEO-20(−OH) in [EMIM][BF_4] are determined to be 129.9, 125.4, 123.8, 121.8, and 119.5 °C, respectively. The change in solubility with temperature is completely reversible; upon cooling, the solution becomes clear again.

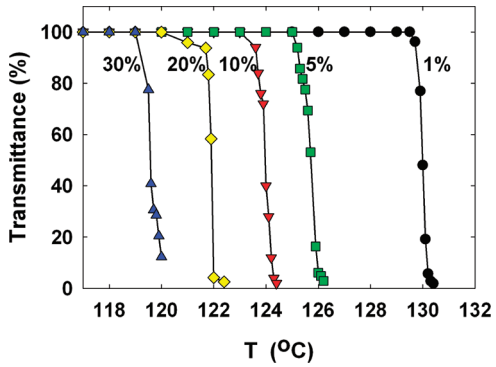


Figure 1. Temperature dependence of transmittance at 632.8 nm for PEO-20(−OH) in [EMIM][BF_4] measured at a heating rate of ~1 °C/min. Weight fractions of PEO-20(−OH) in solutions are indicated.

Figure 2 shows the temperature−composition phase diagrams for different molecular weight PEOs in [EMIM][BF_4]. The phase diagrams were constructed by plotting the CPs determined by the transmittance measurements illustrated in Figure 1. All curves are convex downward, and the critical temperatures (T_c) are estimated to be 119, 121, 130, and 157 °C for PEO-20(−OH), PEO-11(−OH), PEO-4(−OH), and PEO-2(−OH), respectively. T_c slowly increases as the molecular weight decreases from 20 500 to 4200 g/mol; the molecular weight dependence of T_c in this molecular weight range is relatively weak. However, a more substantial increase in T_c (27 °C) was observed as the molecular weight decreases from 4200 to 2100 g/mol. In addition, unlike the typical LCST phase diagram of polymer solutions and blends,[27,31] the PEO/

dx.doi.org/10.1021/ma300335p | Macromolecules 2012, 45, 3627−3633

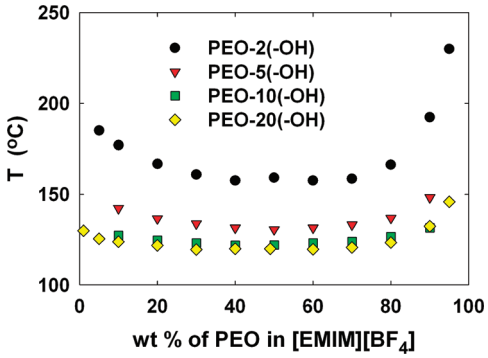


Figure 2. CP curves for PEOs in [EMIM][BF_4]. The values of CP were determined from transmittance measurements such as shown in Figure 1.

[EMIM][BF_4] phase diagrams are roughly symmetric with a critical composition of ~50 wt %.

In an LCST-type phase separation in a polymer solution, it is often the case that there is a large negative contribution to excess entropy of mixing.[32] In aqueous polymer solutions, the formation of hydrogen bonds between polymer chains and water molecules lowers the enthalpy and enhances the mixing; however, the specific molecular orientations required by these bonds result in negative ΔS_{mix}. As the temperature increases above the LCST, the growing entropic contribution to the free energy is dominant and results in phase separation. A typical example is PEO in aqueous solution.[33−36] In the PEO/[EMIM][BF_4] system, the LCST phase transition is likely caused by the competition between formation of polymer−cation and cation−anion hydrogen bonds. On the basis of the results of several experimental,[37,38] theoretical,[38] and computational[39] works, it is reasonable to infer that there are hydrogen bonds between the O atoms of PEO and the H atoms of the imidazolium cations, between the H atoms of PEO end groups and F atoms, and between F atoms and the H atoms of the imidazolium rings, as illustrated schematically in Figure 3. Consequently, similar to aqueous PEO solutions,[33−36] it is possible that the directional interactions between components result in well-oriented solvation around the PEO, providing the negative contribution to ΔS_{mix} that is typical of LCST phase behavior.

It is likely that the hydrogen bonds between the H atoms on the C_2 position of the imidazolium rings and the O atoms of PEO play an important role in determining the LCST phase behavior of the PEO/IL system, as suggested by Watanabe and co-workers.[27] To test this hypothesis, we performed CP measurements on PEO-2(−OH) in [EMIM][BF_4] and [EMMIM][BF_4]. [EMMIM][BF_4] is structurally similar to [EMIM][BF_4], except that a methyl group replaces the H atom in the C_2 position of the ring. As shown in Figure 4b, this small change in IL structure has a significant influence on the phase behavior. No change in phase behavior was observed when PEO concentrations are low; however, as the PEO concentration increased above 30 wt %, there is a pronounced reduction in the CP value. Replacing the most acidic proton of

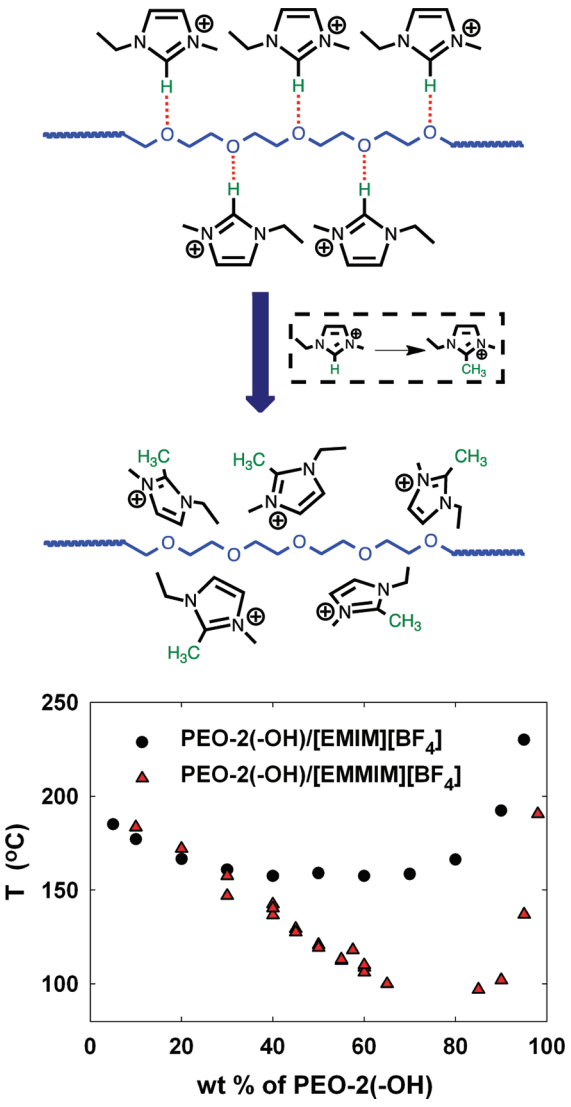


Figure 4. Effect of hydrogen bonding between the protons of the [EMIM] ring and the oxygens of the PEO main chain. (a) Schematic illustration of the hydrogen bonding between the [EMIM] ring and PEO. (b) Cloud point curves for PEO-2(−OH) in [EMIM][BF_4] and [EMMIM][BF_4].

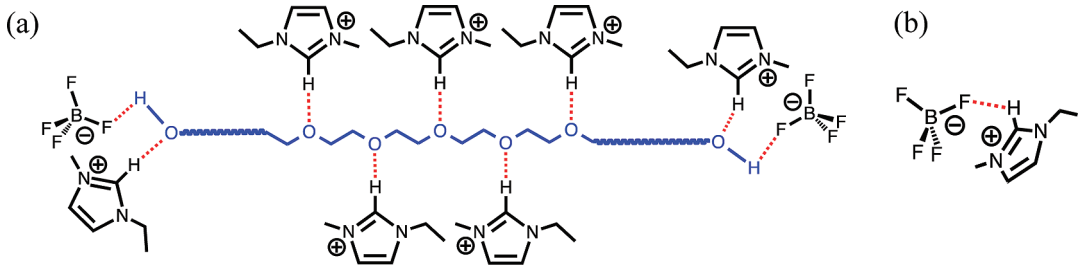


Figure 3. Schematic illustration of hydrogen bonding between (a) [EMIM][BF_4] and PEO and (b) [EMIM] and [BF_4].

dx.doi.org/10.1021/ma300335p | Macromolecules 2012, 45, 3627−3633

the imidazolium ring with a methyl group lowers its hydrogen bond forming capability with the PEO chain, as illustrated in Figure 4a. As a result, without this strong interaction, the miscibility between IL and PEO decreases, and the CP curve shifts down. Interestingly, the PEO/[EMMIM][BF_4] phase diagram is strongly asymmetric with the critical composition (~80 wt %) shifted to an even higher PEO concentration.

Another observation in Figure 2 is that the molecular weight dependence of T_c is relatively weak in the high molecular weight regime; however, a large increase in T_c was observed as the molecular weight drops below 4200 g/mol. Based on the Flory–Huggins theory, the critical T_c can be obtained, assuming that the interaction parameter (χ) at T_c follows the functional form

$$\chi_c = \frac{\alpha}{T_c} + \beta = \frac{1}{2}\left(\frac{1}{N} + \frac{2}{\sqrt{N}} + 1\right) \quad (1)$$

where N is proportional to the degree of polymerization, α/T_c is the enthalpic part of χ_c, and β is the entropic part of χ_c. Rearranging eq 1

$$T_c = \frac{\alpha}{\frac{1}{2}\left(\frac{1}{N} + \frac{2}{\sqrt{N}} + 1\right) - \beta} \quad (2)$$

In an LCST system, α is negative, implying a net attractive interaction between the components, such as hydrogen bonding, whereas β is positive and is associated with the detailed intermolecular packing. In the high molecular weight regime, the observation of a weak molecular weight dependence of T_c confirms that β (i.e., the entropic term) provides the dominant contribution to determine the phase behavior.

As the molecular weight decreases, the fraction of the −OH end groups of PEO increases. The increasing number of hydrogen bonds between the −OH end groups and the F atoms of IL likely increases the enthalpic contribution and enhances the overall solvation of PEO. To test this hypothesis, we performed CP measurements on low molecular weight PEOs (M_w ~ 2000 g/mol) with different end groups in [EMIM][BF_4] (Figure 5a). As shown in Figure 5b, we have considered three types of PEO termination: both hydroxyl end groups, PEO-2(−OH), one methyl end group and one hydroxyl end group, PEO-2(−OH, $-OCH_3$), and both methyl end groups, PEO-2($-OCH_3$). Not much change in CP was observed in the low polymer concentration regime (<10 wt %); however, beyond 10 wt %, the CP curve clearly shifts down as the number of $-OCH_3$ end group increases. In addition, the change in CP value continually increases as the polymer concentration increases. For example, at 90 wt %, the CP of PEO-2($-OCH_3$) is 65 °C lower than that of PEO-2(−OH), but only ~10 °C decrease in CP was observed at 10 wt %. Similar to the LCST phase behavior of PEO/water solution,[36] the contribution of the end group to the solvation becomes especially important at high polymer concentration (low IL content). As a result, the phase diagram becomes more asymmetric and the critical composition is shifted to a higher concentration of PEO.

SANS Determination of the Spinodal Curve. Often, a CP curve lies between the coexistence curve (binodal) and stability limit (spinodal). For polymer solutions, a CP obtained with slow temperature variation is usually closer to the coexistence curve. To complete the phase diagram, the spinodal curve is also needed. SANS measurements were performed to determine the spinodal temperatures for PEO-20(−OH), PEO-2(−OH, $-OCH_3$), and PEO-2($-OCH_3$) in [EMIM-D_5][BF_4]. The SANS technique is a good monitor of phase separation because it is sensitive to composition fluctuations that are enhanced close to the phase boundary. A partially deuterated IL (Figure 6d) was used to enhance scattering contrast. We deuterated the ethyl side group of the imidazolium to avoid perturbing the interactions between PEO and IL, since, as compared to the H atoms on the ethyl side chain, the H atom on the C_2 position of the imidazolium likely forms a stronger hydrogen bond with PEO.[27] In Figure 6a–c, we show the influence of deuteration on the phase behavior. For all three PEOs, the measured CP drops by a few degrees, indicating that the deuteration of IL only slightly lowers the miscibility of PEO and IL. More importantly, the shape of the CP curves is not changed, suggesting that the interactions between PEO and IL are not altered. The slight decrease in miscibility after deuteration of the solvent is generally observed in many polymer solutions; for example, the UCST of polystyrene in deuterated cyclohexane is about 4 °C higher than that in hydrogenated cyclohexane.[40]

Figure 7a shows the SANS results from 50 wt % of PEO-2(−OH) in [EMIM-D_5][BF_4]. The scattering intensity increases with increasing temperature due to increased composition fluctuations when approaching the phase boundary. Figure 7b shows the Ornstein–Zernike plots ($1/I(q)$ vs q^2) for the same data shown in panel a. A linear fit yields $1/I(0)$ as intercept. As the spinodal temperature T_s is approached, $I(0)$

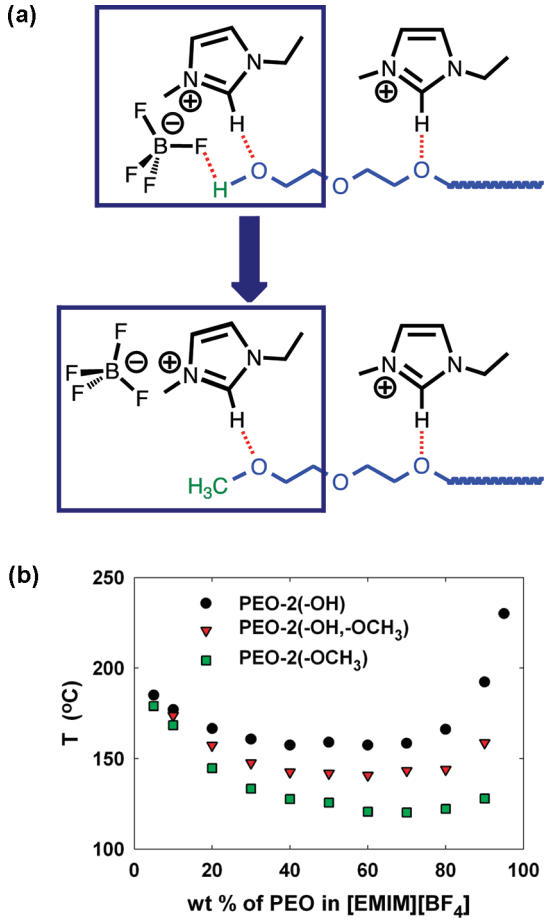


Figure 5. (a) Schematic illustration of the influence of the −OH and $-OCH_3$ end groups. (b) CP curves for PEO-2 with three different end group combinations in [EMIM][BF_4].

dx.doi.org/10.1021/ma300335p | Macromolecules 2012, 45, 3627–3633

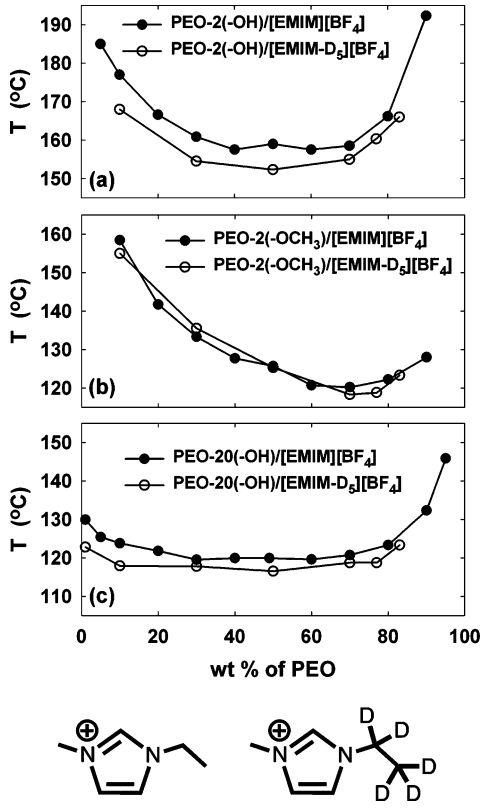


Figure 6. Comparison of the CPs for: (a) PEO-2(−OH), (b) PEO-2(−OCH_3), and (c) PEO-20(−OH) in protonated ([EMIM][BF_4]) and deuterated ([EMIM-D_5][BF_4]) ionic liquids. (d) Chemical structures of protonated and deuterated [EMIM] cations.

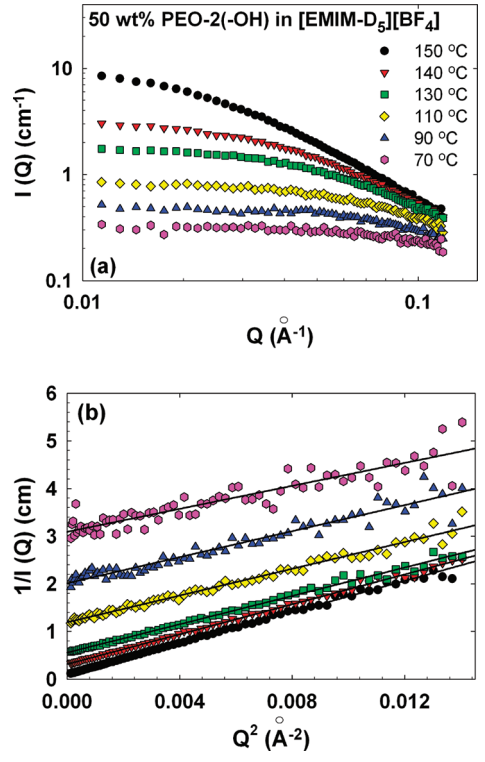


Figure 7. Selected SANS data. (a) Scattered intensity for 50 wt % of PEO-2(−OH) in [EMIM-D_5][BF_4] at different temperatures. (b) Ornstein−Zernike plots for the SANS data shown in (a).

diverges. Therefore, T_s can be estimated from the intercept of a $1/I(0)$ vs $1/T$ plot of data taken at various temperatures. In the case of 50 wt % PEO-2(−OH) in [EMIM-D_5][BF_4] shown in Figure 8, the values of $1/I(0)$ obtained from linear fits to the

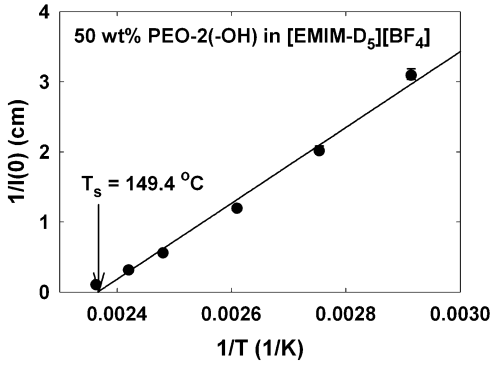


Figure 8. $1/I(0)$ vs $1/T$ plot for 50 wt % of PEO-2(−OH) in [EMIM-D_5][BF_4]. The intercept of the $1/I(0)$ vs $1/T$ plot represents the spinodal temperature (T_s).

Ornstein−Zernike plots (Figure 7b) are plotted as a function of $1/T$. The behavior is linear, and the intercept obtained for $1/I(0) = 0$ represents a spinodal temperature (T_s = 149.4 °C).

Figures 9, 10, and 11 show the spinodal temperatures determined from SANS measurements for PEO-2(−OH),

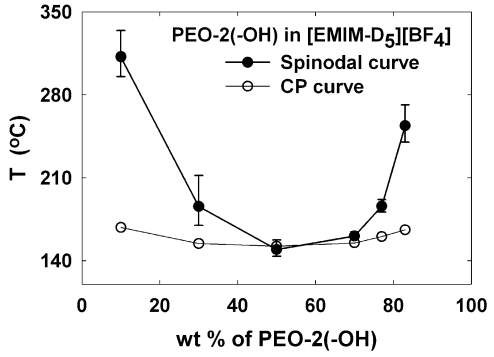


Figure 9. Temperature−composition phase diagram for PEO-2(−OH) in [EMIM-D_5][BF_4]. The spinodal temperatures were determined from the SANS measurements as illustrated in Figures 7 and 8. The CPs were determined from the transmittance measurements.

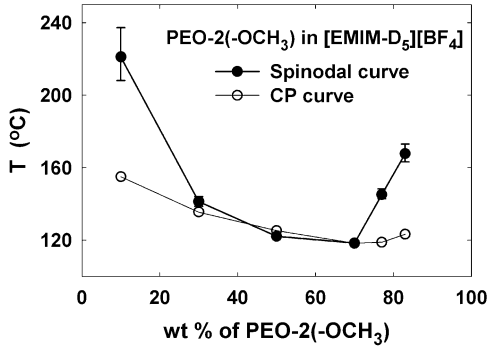


Figure 10. Temperature−composition phase diagram for PEO-2(−OCH_3) in [EMIM-D_5][BF_4]. The spinodal temperatures and CPs were determined from the SANS and transmittance measurements, respectively.

dx.doi.org/10.1021/ma300335p | *Macromolecules* 2012, 45, 3627−3633

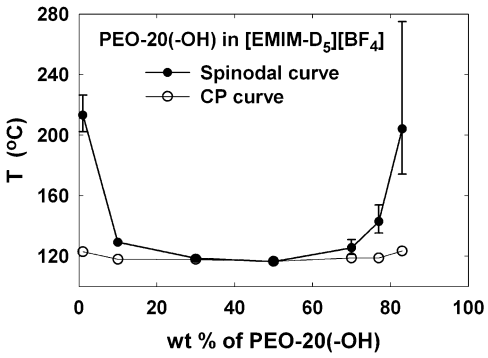


Figure 11. Temperature−composition phase diagram for PEO-20(−OH) in [EMIM-D_5][BF_4]. The spinodal temperatures and CPs were determined from the SANS and transmittance measurements, respectively.

PEO-2(−OCH_3), and PEO-20(−OH) in [EMIM-D_5][BF_4]. Although the error bars due to the uncertainty of extrapolation are significant, it is clear that PEO/[EMIM-D_5][BF_4] has an LCST-type phase behavior. CP curves are also plotted in the same figures. The binodal curve separates the one-phase region at low temperature from the two-phase region at low temperature. The spinodal line separates the unstable and metastable regions within the two-phase region. As expected, the binodal and spinodal curves meet at a critical point.

Unlike the typical LCST phase diagram of polymer solutions, the PEO/IL phase diagram is either roughly symmetric with a critical composition of ∼50 wt % (Figures 2, 9, and 11) or strongly asymmetric with a critical composition shifted to a high concentration of PEO (Figures 4, 5, and 10). The origin of this unusual phase diagram could be related to a strong dependence of the interaction parameter on concentration, as proposed by Schafer-Soenen et al.[41] Another argument provided by de Gennes suggests that the formation of a dense polymer phase may lead to an unusual phase diagram.[42] Away from the standard θ point, he predicted that in certain polymer systems with strong interactions between the components such as PEO/water there may be a tendency for separation into a dense polymer phase and a phase with very dilute swollen polymer chains.[42] In any event, it is clear that this combined data set provides an excellent opportunity to test more sophisticated predictive theories of polymer phase behavior.

CONCLUSION

In this paper, we report an LCST-type liquid−liquid phase behavior of PEO in imidazolium-based tetrafluoroborate ILs. The nonvolatility and good thermostability of ILs and PEOs allow investigation of the phase behavior over a wide range of temperature and composition. Phase diagrams determined by SANS and CP measurements exhibit unusual behavior; they are either symmetric with a critical composition of ∼50 wt % or strongly asymmetric with a critical composition shifted to a high concentration of PEO. The experimental data support the hypothesis that hydrogen bonds between components provide the driving force for the LCST phase behavior.

ASSOCIATED CONTENT

Supporting Information

SEC and MALDI experimental procedures and synthesis procedures of ionic liquids. This material is available free of charge via the Internet at http://pubs.acs.org.

AUTHOR INFORMATION

Corresponding Author

*E-mail: lodge@umn.edu.

Notes

The authors declare no competing financial interest.

ACKNOWLEDGMENTS

This work was supported by the National Science Foundation through Award DMR-0804197. Helpful discussions with Prof. J. Lipson, Dr. Takeshi Ueki and Prof. M. Watanabe are appreciated.

REFERENCES

(1) Hough, W. L.; Smiglak, M.; Rodriguez, H.; Swatloski, R. P.; Spear, S. K.; Daly, D. T.; Pernak, J.; Grisel, J. E.; Carliss, R. D.; Soutullo, M. D.; Davis, J. H.; Rogers, R. D. *New J. Chem.* **2007**, *31*, 1429−1436.
(2) Susan, M. A.; Kaneko, T.; Noda, A.; Watanabe, M. *J. Am. Chem. Soc.* **2005**, *127*, 4976−4983.
(3) Shin, J. H.; Henderson, W. A.; Passerini, S. *J. Electrochem. Soc.* **2005**, *152*, A978−A983.
(4) He, Y. Y.; Boswell, P. G.; Buhlmann, P.; Lodge, T. P. *J. Phys. Chem. B* **2007**, *111*, 4645−4652.
(5) He, Y. Y.; Li, Z. B.; Simone, P.; Lodge, T. P. *J. Am. Chem. Soc.* **2006**, *128*, 2745−2750.
(6) Lee, H. N.; Bai, Z.; Newell, N.; Lodge, T. P. *Macromolecules* **2010**, *43*, 9522−9528.
(7) Bai, Z.; Lodge, T. P. *J. Am. Chem. Soc.* **2010**, *132*, 16265−16270.
(8) Bara, J. E.; Lessmann, S.; Gabriel, C. J.; Hatakeyama, E. S.; Noble, R. D.; Gin, D. L. *Ind. Eng. Chem. Res.* **2007**, *46*, 5397−5404.
(9) Gu, Y.; Lodge, T. P. *Macromolecules* **2011**, *44*, 1732−1736.
(10) Cho, J. H.; Lee, J.; He, Y.; Kim, B.; Lodge, T. P.; Frisbie, C. D. *Adv. Mater.* **2008**, *20*, 686.
(11) Cho, J. H.; Lee, J.; Xia, Y.; Kim, B.; He, Y. Y.; Renn, M. J.; Lodge, T. P.; Frisbie, C. D. *Nat. Mater.* **2008**, *7*, 900−906.
(12) Lee, K. H.; Zhang, S.; Lodge, T. P.; Frisbie, C. D. *J. Phys. Chem. B* **2011**, *115*, 3315−3321.
(13) Zhang, S.; Lee, K. H.; Frisbie, C. D.; Lodge, T. P. *Macromolecules* **2011**, *44*, 940−949.
(14) He, Y. Y.; Lodge, T. P. *J. Am. Chem. Soc.* **2006**, *128*, 12666−12667.
(15) Bai, Z. F.; He, Y. Y.; Young, N. P.; Lodge, T. P. *Macromolecules* **2008**, *41*, 6615−6617.
(16) Rodriguez, H.; Rogers, R. D. *Fluid Phase Equilib.* **2010**, *294*, 7−14.
(17) Winterton, N. *J. Mater. Chem.* **2006**, *16*, 4281−4293.
(18) Ueki, T.; Watanabe, M. *Chem. Lett.* **2006**, *35*, 964−965.
(19) Kodama, K.; Nanashima, H.; Ueki, T.; Kokubo, H.; Watanabe, M. *Langmuir* **2009**, *25*, 3820−3824.
(20) Ueki, T.; Arai, A. A.; Kodama, K.; Kaino, S.; Takada, N.; Morita, T.; Nishikawa, K.; Watanabe, M. *Pure Appl. Chem.* **2009**, *81*, 1829−1841.
(21) Ueki, T.; Karino, T.; Kobayashi, Y.; Shibayama, M.; Watanabe, M. *J. Phys. Chem. B* **2007**, *111*, 4750−4754.
(22) Ueki, T.; Watanabe, M. *Langmuir* **2007**, *23*, 988−990.
(23) Ueki, T.; Watanabe, M. *Macromolecules* **2008**, *41*, 3739−3749.
(24) Ueki, T.; Yamaguchi, A.; Ito, N.; Kodama, K.; Sakamoto, J.; Ueno, K.; Kokubo, H.; Watanabe, M. *Langmuir* **2009**, *25*, 8845−8848.
(25) Fujii, K.; Ueki, T.; Niitsuma, K.; Matsunaga, T.; Watanabe, M.; Shibayama, M. *Polymer* **2011**, *52*, 1589−1595.

(26) Ma, J. C.; Dougherty, D. A. *Chem. Rev.* **1997**, *97*, 1303−1324.
(27) Tsuda, R.; Kodama, K.; Ueki, T.; Kokubo, H.; Imabayashi, S.; Watanabe, M. *Chem. Commun.* **2008**, 4939−4941.
(28) Lee, H. N.; Lodge, T. P. *J. Phys. Chem. B* **2011**, *115*, 1971−1977.
(29) Lee, H. N.; Lodge, T. P. *J. Phys. Chem. Lett.* **2010**, *1*, 1962−1966.
(30) Kline, S. R. *J. Appl. Crystallogr.* **2006**, *39*, 895−900.
(31) Jung, J. G.; Bae, Y. C. *J. Polym. Sci., Part B: Polym. Phys.* **2010**, *48*, 162−167.
(32) Rowlinson, J. S.; Swinton, F. L. *Liquids and Liquid Mixtures*, 3rd ed.; Butterworth: London, 1982.
(33) Dormidontova, E. E. *Macromolecules* **2002**, *35*, 987−1001.
(34) Kjellander, R.; Florin, E. *J. Chem. Soc., Faraday Trans. 1* **1981**, *77*, 2053.
(35) Hammouda, B.; Ho, D.; Kline, S. *Macromolecules* **2002**, *35*, 8578−8585.
(36) Dormidontova, E. E. *Macromolecules* **2004**, *37*, 7747−7761.
(37) Suarez, P. A. Z.; Einloft, S.; Dullius, J. E. L.; de Souza, R. F.; Dupont, J. *J. Chim. Phys.-Chim. Biol.* **1998**, *95*, 1626−1639.
(38) Katsyuba, S. A.; Dyson, P. J.; Vandyukova, E. E.; Chernova, A. V.; Vidis, A. *Helv. Chim. Acta* **2004**, *87*, 2556−2565.
(39) Costa, L. T.; Ribeiro, M. C. C. *J. Chem. Phys.* **2006**, *124*, 8.
(40) Strazielle, C.; Benoit, H. *Macromolecules* **1975**, *8*, 203−205.
(41) Schafer-Soenen, H.; Moerkerke, R.; Berghmans, H.; Koningsveld, R.; Dusek, K.; solc, K. *Macromolecules* **1997**, *30*, 410−416.
(42) de Gennes, P. G. *Pure Appl. Chem.* **1992**, *64*, 1585−1588.

Macromolecules

Note

pubs.acs.org/Macromolecules

Polystyrene-*block*-poly(ethylene oxide) Reverse Micelles and Their Temperature-Driven Morphological Transitions in Organic Solvents

Lian Wang,[†,‡] Xinfei Yu,[†,*] Shuguang Yang,[†] Joseph X. Zheng,[†] Ryan M. Van Horn,[†] Wen-Bin Zhang,[†] Junting Xu,[‡,*] and Stephen Z. D. Cheng[†,*]

[†]Department of Polymer Science, College of Polymer Science and Polymer Engineering, The University of Akron, Akron, Ohio 44325-3909, United States

[‡]MOE Key Laboratory of Macromolecular Synthesis and Functionalization, Department of Polymer Science and Engineering, Zhejiang University, Hangzhou 310027, China

Supporting Information

INTRODUCTION

It has been widely reported that amphiphilic diblock copolymers can self-assemble into micelles when selective solvent is added into copolymer solution with its common solvent above the critical micelle concentration (CMC) of the copolymer.[1−12] For amphiphilic diblock copolymers containing water-soluble blocks, various nanoscale morphologies in aqueous solution such as sphere, cylinder, and vesicle and their transformations have been extensively investigated due to their potential biomedical applications.[13−15] Generally speaking, formation of micelles of block copolymers in solution could be controlled by the molecular architecture, the size of each block, polymer concentration, etc.[16,17] Micellar morphologies of block copolymers could be affected by the solvent quality, the solvent/nonsolvent ratio, the polymer concentration, the pH value, additives such as salts, ions, and homopolymer, and/or the temperature.[18−22] Theoretical calculations of micelle free energies were conducted to predict and explain those morphological formations based on mean-field theory in thermodynamic equilibrium. A micelle's free energy is commonly attributed to the free energy of the core, F_{core}, the free energy of the interface, $F_{interface}$, and the free energy of the corona, F_{corona}. Micelle morphology with a lower overall free energy would be more stable under one set of specific experimental conditions.[23,24] On the other hand, the formation of diblock copolymer micelles containing water-soluble blocks in organic solvent (reverse micelles) has also received a variety of attention due to their applications in encapsulation and as nanoreactors.[25−27] The transformation of reverse micelles so far, however, has been rare due to the difficulties of tuning the solvent properties.

Micellization of polystyrene-*block*-poly(ethylene oxide) (PS-*b*-PEO) in a selective solvent was first observed several decades ago.[3] Recently, micellization and morphological transitions of an asymmetric PS-*b*-PEO block copolymer in *N*,*N*-dimethylformamide (DMF)/water and DMF/acetonitrile was systematically studied in our previous work.[21,28,29] Micellar morphologies were found to be dependent on the water content and polymer concentrations. Furthermore, temperature was found to drive the micellar morphologies in DMF/water mixtures. With an increase in temperature, morphological changes were observed from vesicles to worm-like cylinders and then to spheres. In this letter, reverse micelles of PS-*b*-PEO were investigated in mixed organic solvents, in which 1,4-dioxane was utilized as the common solvent and cyclohexane was the selective solvent. The reverse micelles contain PEO blocks as the micellar core and PS blocks as the corona. The effect of temperature on the micellar morphological changes was further investigated. Transmission electron microscopy (TEM) and light scattering (LS) experiments were conducted to study the micellar morphologies and their transformation process. Finally, the origin of morphological changes with temperature was illustrated by the free energy calculation of micelles as a first approximation.

EXPERIMENTAL SECTION

Materials and Preparation of Micelle Solutions. A diblock copolymer PS_{164}-*b*-PEO_{827} was purchased from Polymer Source Inc. The degrees of polymerization for the PS and PEO blocks are 164 and 827, respectively. The M_n, M_w, and polydispersity of this diblock copolymer, characterized by size exclusion chromatography, were 52.8 kg/mol, 56.0 kg/mol, and 1.06, respectively. The M_ns of the PS and PEO blocks were calculated utilizing nuclear magnetic resonance experiments to be 16.4 kg/mol and 36.4 kg/mol, respectively. The volume fraction of the PEO blocks was 0.76.

This PS_{164}-*b*-PEO_{827} was first dissolved in 1,4-dioxane with stirring at room temperature for one day and filtered through a 0.2 μm filter before using. Cyclohexane was filtered through a 0.2 μm filter and then slowly added into the polymer solution (with a rate of 0.01 mL/min) with vigorous stirring. After reaching the preset 1,4-dioxane/cyclohexane ratio, solutions were held with mild stirring at room temperature for 3 days until equilibrium was reached. Equilibrated micellar solutions were kept standing without stirring for 1 day before morphological observations by TEM. For studying the temperature effect on the morphological transitions, the micellar solutions in vials were kept at the desired temperature in a temperature-controlled oil bath equipped with a digital temperature controller having an accuracy of ±0.1 °C. During cooling, the micellar solutions were equilibrated at the preset temperature for at least 12 h before morphological observations.

Instruments and Characterizations. Observations of micelle morphology were conducted on a Philips TECNAI TEM with an accelerating voltage of 120 kV. The micelle solution was quenched into excess cyclohexane to fix the micellar morphologies. A drop of quenched micellar solution was placed on the carbon-coated grid.

Received: February 10, 2012
Revised: April 1, 2012
Published: April 9, 2012

ACS Publications © 2012 American Chemical Society

dx.doi.org/10.1021/ma3002752 | *Macromolecules* 2012, 45, 3634−3638

Excess solution was removed with filter paper after a few minutes. The grids were then dried at room temperature and atmospheric pressure for at least one day before TEM observation. Owing to the high glass transition temperature of the PS blocks after the solvent drying and severe restriction of PEO block mobility in selective solvent, the micellar morphology could be fixed on the grids during solvent evaporation.

Dynamic and static light scattering (DLS and SLS) experiments were carried on a Brookhaven Instrument coupled with a BI-200SM goniometer and BI-9000AT correlator. An EMI-9863 photo multiplier tube is used for photon counting. A Meller Griot 35 mW He−Ne laser was utilized as the light source with wavelength 632.8 nm. A cylindrical glass scattering cell (with a diameter of 12 mm) was positioned at the center of a thermostated bath (with an accuracy of the temperature control at ±0.01 °C) using decahydronaphthalene for refractive index matching. The measurements were carried out at a 90° scattering angle. The glass scattering cells were thoroughly cleaned by ultrasonication in THF and acetone to eliminate any dust and impurity.

RESULTS AND DISCUSSION

Reverse Micelles of PS_{164}-*b*-PEO_{827} Block Copolymers. In this study, 1,4-dioxane was chosen as the common solvent, and cyclohexane was selected as the selective solvent. PS_{164}-*b*-PEO_{827} was first dissolved in 1,4-dioxane with an initial polymer concentration of 0.5 (wt) %. Cyclohexane was added very slowly until the final cyclohexane concentration reached 80 (wt) %, and the final concentration of PS_{164}-*b*-PEO_{827} was 0.1 (wt) %. Figure 1a shows a TEM bright field (BF) image of spherical micelles of PS_{164}-*b*-PEO_{827}. Figure 1b shows dynamic light scattering results of the spherical micelles. The DLS results indicate that the apparent hydrodynamic diameter of the spherical micelles ($D_{h,app}$) is centered at 49 nm, which is larger than the size observed by TEM (28.4 nm, Figure 1a). This is probably due to the collapse of the micelles (especially the coronas) caused by solvent evaporation during TEM sample preparation. By combining DLS and TEM results, the spherical morphology were confirmed to be the authentic aggregation form in the micelle solution.

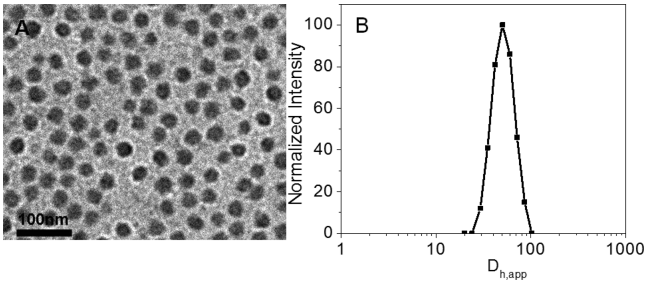


Figure 1. (a) TEM BF image of spherical micelles of PS_{164}-*b*-PEO_{827}. (b) Size distribution of spherical micelles after CONTIN analysis of the DLS results.

Temperature-Induced Morphological Transition of Micelles. Temperature dependent experiments were conducted in a thermal bath with a precision of ±0.1 °C. The micelle solutions were kept at the preset temperatures for more than 3 h and monitored by DLS experiments. When the light scattering intensities reached a constant, the micelle solutions were then used for TEM sample preparation (assuming that the morphological change is completed and that the solution is now under thermodynamic equilibrium). Figure 2 illustrates the dependence of light scattering intensity with temperature during cooling for the micelle solution with 80 (wt) % cyclohexane at 0.1 (wt) % PS_{164}-*b*-PEO_{827}. A sharp change in the scattering intensity has been observed within a temperature range of 0 °C < T < 10 °C. This sharp increase in scattering intensity reflects the existence of a micellar morphological transformation. The variation of apparent hydrodynamic diameter ($D_{h,app}$) has also been included in Figure 2. The value of $D_{h,app}$ increases from 50 to 168 nm when the temperature decreases from +25 to −10 °C, which corresponds to the scattering intensity change. Below −10 °C, the intensity does not substantially change until the lowest temperature available for experiments, −25 °C, is reached. At such a low temperature, it is expected that the diblock copolymer may possess little mobility. The larger value of $D_{h,app}$ suggests that a new association with a larger size may be constructed when decreasing the temperature.

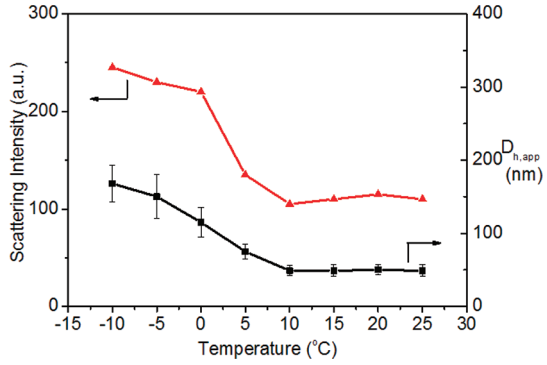


Figure 2. Light scattering intensity (red) and apparent hydrodynamic diameter (black) of PS_{164}-*b*-PEO_{827} as a function of temperature.

Figure 3 shows a set of TEM BF images of the micellar morphologies during the cooling process. At room temperature (25 °C), spherical micelles are formed as shown in Figure 1a. A mixture of spherical micelles and cylindrical micelles are observed in Figure 3a when the temperature decreased to 5 °C; however, spherical micelles remain the majority. Further decreasing the temperature to 0 °C, the micellar morphology changed into pure cylinders (Figure 3b). The micelle morphology further evolved into a mixture of vesicles and cylinders at −5 °C (Figure 3c).

Micelle Free Energy Calculations. The driving force for micelle formation and morphological transformations is the tendency to minimize the overall micelle free energy under a specific set of experimental conditions. The overall micelle free energy can be expressed as[23]

$$F = F_{core} + F_{interface} + F_{corona} \quad (1)$$

where the term F_{core} is the free energy of the core that involves deformation of the core block conformations such as stretching or compressing, leading to deviation from its random coil conformation. In this case, this corresponds to the PEO block. The term $F_{interface}$ is determined by the surface tension between the core and solvent at the interface. The term F_{corona} relates to the steric and electrostatic (if ionic block exists, however that is not the case here) interactions between corona blocks and solvent. Here, it is the PS block.

F_{core} can be correlated to the degree of stretching or compression (S_c) of the PS blocks in the core and calculated as[18]

$$S_c = R_{core}/R_0 \quad (2)$$

dx.doi.org/10.1021/ma3002752 | Macromolecules 2012, 45, 3634−3638

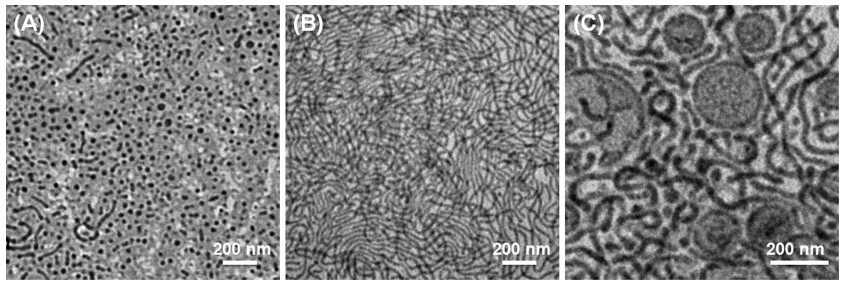


Figure 3. Morphology transition of PS_{164}-*b*-PEO_{827} on cooling for a micelle solution with 0.1 (wt) % polymer concentration at 80 (wt) % cyclohexane content in dioxane/cyclohexane system: (a) mixture of spheres and cylinders at 5 °C; (b) pure cylinders at 0 °C; (c) mixture of vesicles and cylinders at −5 °C.

Table 1. Physical Parameters and Free Energy Calculations of Reverse Micelles at Three Different Temperatures

temp (°C)	morph.	$R_{core}(nm)^a$	$S_c{}^b$	$s(nm^2)^c$	F_{core}/kT	$F_{interface}/kT$	F_{corona}/kT	$F_{overall}/kT$
25	sphere	14.2 ± 1.0	0.79 ± 0.06	12.0 ± 0.8	0.6 ± 0.1	30.3 ± 2.0	2.2 ± 0.1	33.1 ± 2.2
0	cylinder	12.0 ± 0.6	0.67 ± 0.03	9.5 ± 0.5	1.4 ± 0.1	25.6 ± 1.3	2.8 ± 0.3	29.8 ± 1.7
−5	vesicle	8.4 ± 0.4	0.47 ± 0.02	6.8 ± 0.4	5.6 ± 0.5	18.6 ± 1.1	4.0 ± 0.5	28.2 ± 2.1

[a] R_{core} is the diameter of spherical and cylindrical micelles and half of wall thickness for vesicles. [b] S_c is the degree of stretching of PEO blocks in the micellar core. [c] *s* is the interfacial area per chain.

where R_{core} is the radius of the PEO core in the spherical and cylindrical micelles. In the case of vesicles, half of the wall thickness was utilized as R_{core}. The quantity R_0 is the unperturbed end-to-end distance of the PEO chain which can be calculated from the equation[30]

$$R_0 = 0.094(M)^{0.5} \tag{3}$$

where M is the number-average molecular weight of the PEO blocks. The value of R_0 is calculated to be 17.9 nm when the PEO block's molecular weight is 36.4 kg/mol.

As a result, the PEO blocks are slightly compressed in the core of the spherical micelle with an average R_{core} of 14.2 nm. The average R_{core} of the cylindrical micelles is found to be 12.0 nm, reflecting a higher degree of compression of the PEO blocks. The PEO block has the highest degree of compression in the vesicles with an average R_{core} of 8.4 nm. The calculated values of S_cs are listed in Table 1, which decreases from 0.79 for spheres to 0.47 for vesicles. Therefore, the free energy of compressed PEO blocks in the micellar core can be calculated based on the following equation:[28]

$$F_{core}/(kT) = k_j(1/S_c)^2 \quad (S_c < 1) \tag{4}$$

Here, k_j is the numerical coefficients of a dense PEO core: $j = 1$ for lamella, $k_1 = \pi^2/8$; $j = 2$ for cylinder, $k_2 = \pi^2/16$; and $j = 3$ for sphere, $k_3 = 3\pi^2/80$. The calculated free energy of the micellar core increases from 0.6 kT for spheres to 5.6kT for the vesicles with highest compressibility.

The second term, $F_{interface}$, relates to the interfacial free energy between the core (PEO) blocks at the interface and the solvents. Therefore

$$F_{interface} = \gamma s \tag{5}$$

where s is the interfacial area per chain, and γ is surface tension, which is related to $\chi_{PEO-solvent}$ described by the following equation:

$$\gamma = (kT/a_{PEO}{}^2)(\chi_{PEO-solvent}/6)^{0.5} \tag{6}$$

where a_{PEO} is the length of a PEO monomer. The term $\chi_{PEO-solvent}$ is dependent on temperature as follows:[31]

$$\chi_{PEO-solvent} = \alpha + \frac{\beta}{T} \tag{7}$$

where α and β are constants depending on the solvent properties. It was deduced from experimental data that $\alpha = -0.84$ and $\beta = 565$ (see Supporting Information).[32,33] The value of $\chi_{PEO-solvent}$ is thus highly temperature dependent, and it changes from 1.06 at 25 °C to 1.27 at −5 °C.

The interfacial area per chain (s_j) can be calculated based on the following equation:

$$s_j = jV_{PEO}N_{PEO}/(fR_{core}) \tag{8}$$

where $j = 1$ for lamella, $j = 2$ for cylinder, and $j = 3$ for sphere; V_{PEO} is the volume of the PEO monomer, N_{PEO} is the degree of polymerization of the PEO blocks, and f is the volume fraction of the PEO blocks in the core which may be treated as unity due to the high content of selective solvent, driving the PEO chains to pack densely to avoid interaction with selective solvent. The calculated values of $F_{interface}$ are listed in Table 1 and decrease from 30.3 kT for spheres to 18.6 kT for vesicles.

The third term, F_{corona}, is based on the expression proposed by Zhulina et al. in their theory of diblock copolymer micelles.[24] The corona could be treated as chains tethered on a planar substrate when the corona is much shorter than the core block. This free energy is expressed by:

$$F_{corona}/(kT) = \hat{C}_H\hat{C}_F N_{PS}(sa_{PS}{}^{-2})^{-1/2\nu} \tag{9a}$$

where N_{PS} is the degree of polymerization of PS block and a_{PS} is the PS monomer length. Cyclohexane is a θ-solvent for the PS blocks at a critical temperature of 34.5 °C. The mixed solvent may be recognized as an approximate θ-solvent when the content of cyclohexane reaches 80%. Therefore, ν, the scaling exponent, is equal to 0.5. The $\hat{C}_H$ and $\hat{C}_F$ values are numerical prefactors, and in the case of Θ-solvent, they are

$$\hat{C}_H = 0.68(l/a_{PS})^{1/4} \tag{9b}$$

$$\hat{C}_F = 1.38(l/a_{PS})^{-3/4} \tag{9c}$$

dx.doi.org/10.1021/ma3002752 | *Macromolecules* 2012, 45, 3634−3638

where l is the Kuhn length of PS. The calculated values of F_{corona} increases from 2.2 kT for spheres to 4.0 kT for vesicles as shown in Table 1.

The change of free energy for different micellar morphologies can be estimated based on calculations above. During the cooling process, $\chi_{PEO-solvent}$ increases up to 20% and leads to an increase of the surface tension between the PEO core bock and solvents. Spherical morphologies with the highest surface area become unfavorable and transfer to cylinders and finally to vesicles. F_{core}/kT and F_{corona}/kT increase due to the increased compressibility and crowding for the micellar PEO core blocks and PS corona blocks, respectively. These two free energy terms, however, are balanced by the reduction of $F_{interface}/kT$, which is dominant. Therefore, the overall free energy of the micelles decreases from spheres to cylinders and to vesicles with a reduction in temperature as shown in Table 1.

Although the interfacial free energy is demonstrated to be the main driving force for the morphology transitions induced by decreasing temperature in this system, it is surprising that the reversible transformations when increasing to room temperature is not able to be observed in our experimental time range (24 h). This may be due to the transition kinetics possessing a large hysteresis. It is thus speculated that both blocks are so restricted under these solvent and temperature conditions that the morphological transformations may take a much longer time to occur during heating to room temperature. As such, the recovery of those micellar morphologies after the transformations require a substantially longer period of time compared with our current experimental conditions. This surprising observation and a three-dimensional morphological phase diagram combining the polymer concentration, solvent composition and temperature are still under investigations to understand the morphological transformation mechanism for these reverse micelles.

CONCLUSION

In summary, reverse micelles with PEO blocks as the micelle cores and PS blocks as the micelle corona have been obtained by dissolving PS_{164}-b-PEO_{827} in 1,4-dioxane and slowly adding selective solvent (cyclohexane). Reverse spherical micelles formed at a cyclohexane content of 80 (wt) % at room temperature. The effects of temperature on the micellar morphologies have been investigated. TEM and DLS experimental observations have shown that pure spherical micelles transformed into a mixture of spheres and cylinders at 5 °C. Uniform cylindrical micelles formed at 0 °C. A mixture of cylinders and vesicles appeared as temperature decreased to −5 °C. As a first approximation, the free energies of micelles with various morphologies were calculated to understand the thermodynamic reasons for the morphological transformations. The results revealed that the $F_{interface}$ term dominates the morphology transformations due to the specific fact that $\chi_{PEO-solvent}$ is highly temperature dependent.

ASSOCIATED CONTENT

Supporting Information

Calculations of $\chi_{PEO-solvent}$, a table of solubility parameters and calculated $\chi_{PEO-solvent}$, and a figure showing the dependence of $\chi_{PEO-solvent}$ on temperature. This material is available free of charge via the Internet at http://pubs.acs.org.

AUTHOR INFORMATION

Corresponding Author

*E-mail: (S.Z.D.C.) scheng@uakron.edu. Telephone: +1-330-972-6931. (X.Y.) E-mail: xy5@uakron.edu. Telephone: +1-330-972-8281. (J.X.) E-mail: xujt@zju.edu.cn. Telephone: +86-571-87953164.

Notes

The authors declare no competing financial interest.

ACKNOWLEDGMENTS

This work was supported by the Division of Materials Research at the National Science Foundation (DMR-0906898). Dr. Xu would like to thank the financial support from the National Foundation of China (20974099) and State Key Laboratory of Chemical Engineering. Lian Wang acknowledges her support from the Chinese Scholarship Council.

REFERENCES

(1) Evans, F.; Wennerstrom, H. *The colloidal domain: where physics, chemistry, biology, and technology meet*, 2nd ed.; Wiley-VCH: New York, 1999.
(2) de Gennes, P. G. *Macromolecules* **1980**, *13*, 1069−1075.
(3) Wilhelm, M.; Zhao, C. L.; Wang, Y.; Xu, R.; Winnik, M. A.; Mura, J. L.; Riess, G.; Croucher, M. D. *Macromolecules* **1991**, *24*, 1033−1040.
(4) Prochazka, K.; Kiserow, D.; Ramireddy, C.; Tuzar, Z.; Munk, P.; Webber, S. E. *Macromolecules* **1992**, *25*, 454−460.
(5) Wu, G.; Chu, B. *Macromolecules* **1994**, *27*, 1766−1773.
(6) Zhang, L.; Eisenberg, A. *Science* **1995**, *268*, 1728−1731.
(7) Chen, E.-Q.; Xia, Y.; Graham, M. J.; Foster, M. D.; Mi, Y.; Wu, W.-L.; Cheng, S. Z. D. *Chem. Mater.* **2003**, *15*, 2129−2135.
(8) Liu, X.; Kim, J.-S.; Wu, J.; Eisenberg, A. *Macromolecules* **2005**, *38*, 6749−6751.
(9) Duxin, N.; Liu, F.; Vali, H.; Eisenberg, A. *J. Am. Chem. Soc.* **2005**, *127*, 10063−10069.
(10) Bang, J.; Jain, S.; Li, Z.; Lodge, T. P.; Pedersen, J. S.; Kesselman, E.; Talmon, Y. *Macromolecules* **2006**, *39*, 1199−1208.
(11) Du, B.; Mei, A.; Yin, K.; Zhang, Q.; Xu, J.; Fan, Z. *Macromolecules* **2009**, *42*, 8477−8484.
(12) Jain, S.; Bates, F. S. *Science* **2003**, *300*, 460−464.
(13) Rösler, A.; Vandermeulen, G. W. M.; Klok, H.-A. *Adv. Drug. Deliver, Rev.* **2001**, *53*, 95−108.
(14) Kataoka, K.; Harada, A.; Nagasaki, Y. *Adv. Drug. Deliver, Rev.* **2001**, *47*, 113−131.
(15) Fuks, G.; Mayap Talom, R.; Gauffre, F. *Chem. Soc. Rev.* **2011**, *40*, 2475−2493.
(16) Zhou, Z.; Li, Z.; Ren, Y.; Hillmyer, M. A.; Lodge, T. P. *J. Am. Chem. Soc.* **2003**, *125*, 10182−10183.
(17) Förster, S.; Antonietti, M. *Adv. Mater.* **1998**, *10*, 195−217.
(18) Zhang, L.; Eisenberg, A. *J. Am. Chem. Soc.* **1996**, *118*, 3168−3181.
(19) Shen, H.; Eisenberg, A. *J. Phys. Chem. B* **1999**, *103*, 9473−9487.
(20) Liu, F.; Eisenberg, A. *J. Am. Chem. Soc.* **2003**, *125*, 15059−15064.
(21) Yang, S.; Yu, X.; Wang, L.; Tu, Y.; Zheng, J. X.; Xu, J.; Van Horn, R. M.; Cheng, S. Z. D. *Macromolecules* **2010**, *43*, 3018−3026.
(22) Yu, X.; Zhong, S.; Li, X.; Tu, Y.; Yang, S.; Van Horn, R. M.; Ni, C.; Pochan, D. J.; Quirk, R. P.; Wesdemiotis, C.; Zhang, W.-B.; Cheng, S. Z. D. *J. Am. Chem. Soc.* **2010**, *132*, 16741−16744.
(23) Zhang, L.; Eisenberg, A. *Polym. Adv. Technol.* **1998**, *9*, 677−699.
(24) Zhulina, E. B.; Adam, M.; LaRue, I.; Sheiko, S. S.; Rubinstein, M. *Macromolecules* **2005**, *38*, 5330−5351.
(25) Alexandridis, P.; Andersson, K. *J. Phys. Chem. B* **1997**, *101*, 8103−8111.
(26) Eastoe, J.; Hollamby, M. J.; Hudson, L. *Adv. Colloid Interface Sci.* **2006**, *128−130*, 5−15.

(27) Van Horn, W. D.; Ogilvie, M. E.; Flynn, P. F. *J. Am. Chem. Soc.* **2009**, *131*, 8030−8039.
(28) Bhargava, P.; Zheng, J. X.; Li, P.; Quirk, R. P.; Harris, F. W.; Cheng, S. Z. D. *Macromolecules* **2006**, *39*, 4880−4888.
(29) Bhargava, P.; Tu, Y.; Zheng, J. X.; Xiong, H.; Quirk, R. P.; Cheng, S. Z. D. *J. Am. Chem. Soc.* **2007**, *129*, 1113−1121.
(30) Rubinstein, M.; Colby, R. H. *Polymer Physics*, 1st ed.; Oxford University Press: London, 2003.
(31) Barton, A. F. M., *Handbook of Polymer-Liquid Interaction Parameters and Solubility Parameters*. CRC Press: Boston, MA, 1990.
(32) Monique, G. *Polymer* **1983**, *24*, 865−870.
(33) Fernández-Berridi, M. J.; Martin; Guzmán, G.; Iruin, J. J.; Elorza, J. M. *Polymer* **1983**, *24*, 417−422.

Macromolecules

Note

pubs.acs.org/Macromolecules

Isomeric Effects on the Phase Behavior of Polystyrene-*block*-poly(pentyl methacrylate) Copolymers

Hong Chul Moon, Jong Gyun Kim, and Jin Kon Kim*

National Creative Research Initiative Center for Block Copolymer Self-Assembly, Department of Chemical Engineering, Pohang University of Science and Technology, Pohang, Kyungbuk 790-784, Republic of Korea

Supporting Information

1. INTRODUCTION

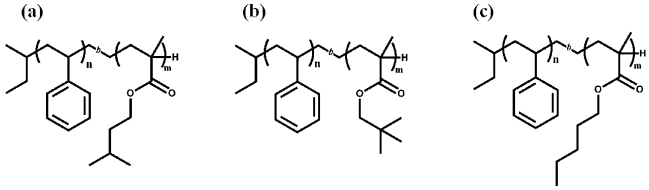
Self-assembly and phase behavior of block copolymers have been studied extensively due to the various periodic nanostructures such as lamellae, cylinders, gyroids, and spheres.[1−4] The key parameters affecting the phase behavior of block copolymers are the volume fraction (f) of one of block, the degree of polymerization (N), and the Flory−Huggins segmental interaction parameter (χ).[1]

Among many block copolymers, weakly interacting polystyrene-*block*-poly(n-alkyl methacrylate) copolymers (PS-*b*-PnAMA) have received strong attention because of different phase behaviors depending on the number of carbons (n) in the alkyl chain of PnAMA block.[5−17] For example, only the order-to-disorder transition (ODT) was observed for n = 1 and $n \geq 6$,[5−7] while the lower disorder-to-order transition (LDOT) was found for n = 2, 3, and 4.[5,6,8−11] Interestingly, PS-*block*-poly(n-pentyl methacrylate) copolymer (PS-*b*-PnPMA), which corresponds to n = 5, showed a closed-loop phase behavior having both LDOT and upper order-to-disorder transition (UODT).[12−15] Since the block copolymers with the closed-loop phase behavior had very high pressure coefficient of the transition temperature,[15] we have tried to find other block copolymers having the closed-loop phase behavior. One example is that when the PnPMA block is replaced by the random copolymer of n = 4 and n = 6 (i.e., poly(n-butyl-*ran*-n-hexyl) methacrylate: Pn(B-*r*-H)MA) or n = 1 and n = 8 (i.e., poly(n-octyl-*ran*-methyl) methacrylate: Pn(O-*r*-M)MA), both PS-*b*-Pn(B-*r*-H)MA and PS-*b*-Pn(O-*r*-M)MA showed the closed-loop type phase behavior.[16,17] This is because the average interaction force between PS and Pn(B-*r*-H)MA (or Pn(O-*r*-M)MA) is similar to that between PS and PnPMA.

We note that the isomers of one of the blocks in the block copolymers dramatically changes phase behavior.[18−20] For instance, Han and co-workers[18] synthesized polystyrene-*block*-polybutadiene (PS-*b*-PB) copolymers with two different PBs prepared by 1,2-addition or 1,4-addition, while the total molecular weights and the weight fractions of PS block are very similar. They found that the ODT temperature (T_{ODT}) of PS-*b*-PB(1,2) is higher than that of PS-*b*-PB(1,4). The difference in the T_{ODT} arises from a higher segmental interaction parameter (χ) between PS and PB(1,2) than that between PS and PB(1,4). A similar χ difference was also observed between PS and PI.[19] Zha et al.[20] showed that the T_{ODT} of polystyrene-*block*-poly(4-vinylpyridine) copolymer (PS-*b*-P4VP) is much higher than that of polystyrene-*block*-poly(2-vinylpyridine) copolymer (PS-*b*-P2VP) at similar molecular weight and weight fraction of PS block, although the only difference between P2VP and P4VP is the location of nitrogen in the pyridine moiety. This is attributed to $\chi_{PS-P4VP}$ having greater than $\chi_{PS-P2VP}$ arising from the larger dipole polarization of P4VP than P2VP.

Thus, when the isomers of poly(pentyl methacrylate) (PPMA) are used instead of PnPMA, it would be possible for one to have the closed-loop phase behavior in PS-*b*-PPMA. Among eight possible isomers in poly(pentyl methacrylate) block, we chose two isomers of PPMA in this study: poly(isopentyl methacrylate) (PisoPMA) and poly(neopentyl methacrylate) (PneoPMA) whose chemical structures are shown in Scheme 1. We found that when the molecular weight was judiciously controlled, PS-*b*-PneoPMA showed the closed-loop type phase behavior similar to PS-*b*-PnPMA whose chemical structure is given in Scheme 1c. On the other hand, PS-*b*-PisoPMA exhibited only ODT. The result shows that the isomeric effect indeed dramatically changes the phase behavior of weakly interacting block copolymers.

Scheme 1. Chemical Structures for (a) PS-*b*-PisoPMA, (b) PS-*b*-PneoPMA, and (c) PS-*b*-PnPMA



2. EXPERIMENTAL SECTION

Materials. Symmetric PS-*b*-PisoPMA and PS-*b*-PneoPMA with various molecular weights were synthesized by sequential anionic polymerization. All chemicals were purchased from Sigma-Aldrich except neopentyl methacrylate (neo-PMA) and isopentyl methacrylate (iso-PMA) monomers which were purchased from Monomer-Polymer and Dajac Laboratories. Tetrahydrofuran (THF) was stirred with CaH_2 for 24 h followed by vacuum-distillation into sodium/benzophenone mixture and stirred until the solution became deep violet color, indicating oxygen and moisture-free state. Styrene, neo-PMA, and iso-PMA were allowed to stir with CaH_2 for 24 h. Then, styrene was vacuum-distilled and vigorously stirred with dibutylmagnesium for 4 h, while neo-PMA and iso-PMA were vacuum-distilled with trioctylaluminum and stirred for 10 min. All of the monomers and

Received: February 20, 2012
Revised: March 28, 2012
Published: April 6, 2012

ACS Publications © 2012 American Chemical Society

THF were finally distilled once again before use. *sec*-BuLi was used as an initiator in the presence of LiCl. The purified styrene was polymerized for 1 h, and then either iso-PMA or neo-PMA was injected dropwise and allowed to react for 5 h at THF of −78 °C under extremely pure argon gas. Finally, the reaction was terminated by adding anhydrous 2-propanol. Because a small difference in total molecular weight can greatly affect phase transitions, we blended higher and lower molecular weight of neat block copolymers to control the total molecular weight. All the blends were prepared using benzene solution. After they were mixed completely, solvent was removed by freeze-drying at room temperature followed by thermal annealing at 150 °C for 24 h in a vacuum oven.

Molecular Characterization. The number-average molecular weight (M_n) and polydispersity index (PDI) of all the block copolymers were measured by size exclusion chromatography (SEC: Waters 2414 refractive index detector) based on PS standards. Two 300 mm (length) × 7.5 mm (inner diameter) columns including particle size of 5 μm (PLgel 5 μm MIXED-C: Polymer Laboratories) was used with THF as an eluent and a flow rate of 1 mL/min at 30 °C. The weight fraction of each block was determined by ^{1}H nuclear magnetic resonance spectra (^{1}H NMR: Bruker Avance III 400) with a solvent of chloroform-*d* ($CDCl_3$). The molecular characteristics for the samples are summarized in Table 1.

Table 1. Molecular Characteristics of Polymers Employed in This Study

sample code	M_n[a]	PDI[b]	w_{PS}[c]	L/H (w/w) blend ratio	transition type
PS-*b*-PisoPMA-L	24 400	1.11	0.53	1.00/0.00	fully disordered
PS-*b*-PisoPMA-B1	29 700			0.50/0.50	fully disordered
PS-*b*-PisoPMA-B2	31 800			0.35/0.65	ODT
PS-*b*-PisoPMA-B3	34 100			0.20/0.80	ODT
PS-*b*-PisoPMA-H	37 900	1.05	0.51	0.00/1.00	ODT
PS-*b*-PneoPMA-L	28 600	1.06	0.52	1.00/0.00	fully disordered
PS-*b*-PneoPMA-B1	30 800			0.44/0.56	closed-loop
PS-*b*-PneoPMA-B2	30 980			0.40/0.60	closed-loop
PS-*b*-PneoPMA-B3	31 110			0.37/0.63	closed-loop
PS-*b*-PneoPMA-B4	31 400			0.30/0.70	UODT
PS-*b*-PneoPMA-B5	31 900			0.20/0.80	UODT
PS-*b*-PneoPMA-H	32 800	1.07	0.52	0.00/1.00	UODT

[a]Calculated by $(M_n)_{blend} = [\ (w_1/M_{n,1}) + (w_2/M_{n,2})\ ]^{-1}$, where w_i and $M_{n,i}$ are weight fraction and the number-average molecular weight of block polymer *i*, respectively, in the blend. [b]Polydispersity index. [c]Weight fraction of PS in block copolymer determined by ^{1}H NMR spectra.

Depolarized Transmitted Light Scattering. Vertically polarized light from a HeNe laser having wavelength of 632.8 nm passed through the sample and a horizontal analyzing polarizer onto a photodetector. All the samples were molded with a thickness and a diameter of 1 mm and 5 mm, respectively, between two glass disks, and then the depolarized light intensity was recorded as a function of temperature at a heating rate of 0.5 °C/min.

Rheological Properties. Dynamic temperature sweep of storage (G') and loss moduli (G'') under isochronal condition upon heating at a rate of 0.5 °C/min were measured with Advanced Rheometric Expansion System (TI Instrument) with parallel plates of 25 mm diameter. The angular frequency (ω) and the strain amplitude were 0.1 rad/s and 0.05, respectively, which lie in the linear viscoelasticity range. Isothermal frequency sweeps (ω = 0.02−100 rad/s) of G' and G'' at a strain amplitude of 0.05 were conducted at three temperatures of 150, 200, and 230 °C.

Small-Angle X-ray Scattering (SAXS). SAXS profiles ($I(q)$ vs q ($= (4\pi/\lambda) \sin\theta$; here q and 2θ are the scattering vector and scattering angle, respectively) were obtained on beamline BL10C at the Photon Factory (Japan), where X-ray wavelength was 0.1488 nm. The scattered X-rays were collected by position sensitive proportional counters (PSPC) detector with detection length of 20 mm. The sample-to-detector distance was 2 m. The sample thickness and the exposure time were 1.0 mm and 300 s, respectively.

Transmission Electron Microscopy (TEM). The PS-*b*-PneoPMA-B3 was annealed at three different temperatures, 150, 200, and 230 °C, for 24 h followed by rapid quenching with liquid nitrogen. Ultrathin sections were prepared using a Leica Ultracut Microtome (EM UC6 Leica Ltd.) at room temperature with thickness of ∼40 nm. The specimens were exposed to RuO_4 vapor for 5 min at room temperature to stain PS microdomains selectively. Finally, the TEM images were obtained with a bright-field TEM (S-7600 Hitachi Ltd.) operating at 80 kV.

3. RESULTS AND DISCUSSION

Figure 1a shows temperature sweep of storage modulus (G') for neat PS-*b*-PisoPMA-H and PS-*b*-PisoPMA-L. G' of PS-*b*-PisoPMA-H dropped abruptly near at 260 °C, which is defined

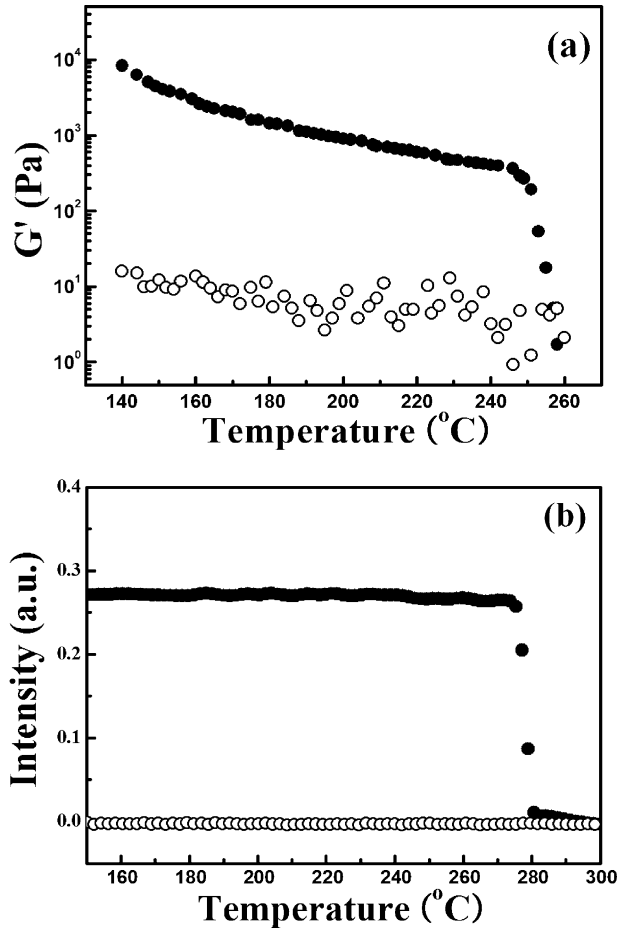


Figure 1. (a) Variations of dynamic storage modulus G' at ω = 0.1 rad/s during heating at a rate of 0.5 °C/min for neat PS-*b*-PisoPMA-H (●) and PS-*b*-PisoPMA-L (○). (b) Temperature dependence of optical birefringence intensity for neat PS-*b*-PneoPMA-H (●) and PS-*b*-PneoPMA-L (○).

dx.doi.org/10.1021/ma3003449 | *Macromolecules* 2012, 45, 3639−3643

as the T_{ODT}. On the other hand, G' of PS-*b*-PisoPMA-L having relatively low molecular weight was very low, suggesting that it has fully disordered state over the entire experimental temperatures. Figure 1b gives temperature dependence of optical birefringence intensity for neat PS-*b*-PneoPMA-H and PS-*b*-PneoPMA-L. PS-*b*-PneoPMA-H showed a precipitous drop in the birefringence signal at ~278 °C, corresponding to the T_{UODT}. But, PS-*b*-PneoPMA-L had fully disordered state over the entire experimental temperature because of no birefringence.

Since the phase behavior of PS-*b*-PnPMA was dramatically changed by a small difference (even less than 10%) in total molecular weight,[12−14] we carefully controlled the total molecular weight of PS-*b*-PisoPMA and PS-*b*-PneoPMA by mixing higher and lower molecular weights of their block copolymers, as shown in Table 1. Figure 2 gives the temperature dependence of depolarized transmitted light scattering for all the samples. For the PS-*b*-PisoPMA system, only T_{ODT} was observed at experimentally accessible temperature ranges ($T_g < T < T_d$, in which T_g and T_d are the glass transition temperatures of the microphase-separated PS (102 °C) and PisoPMA (67 °C), and T_d is the degradation temperature (>300 °C)[21] of the block copolymer (see Figure S1 in the Supporting Information). The T_{ODT} decreased gradually with increasing the amount of PS-*b*-PisoPMA-L. Once the amount of PS-*b*-PisoPMA-L in the blend was larger than 50 wt %, the blend became fully disordered state (Figure 2a).

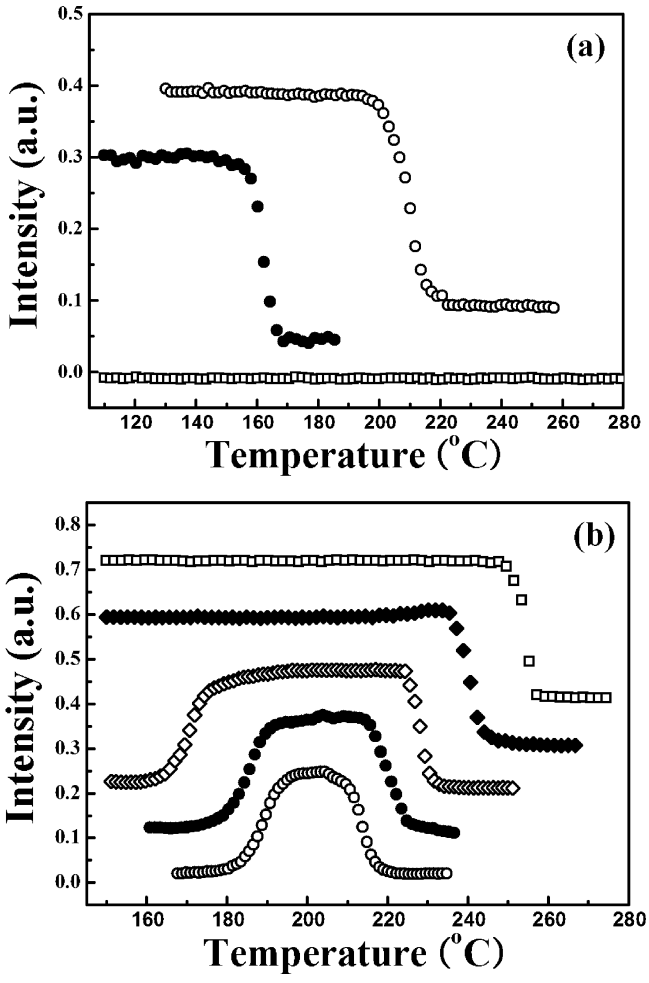


Figure 2. Temperature dependence of optical birefringence intensity during heating at a rate of 0.5 °C/min for (a) PS-*b*-PisoPMA-B1 (□), PS-*b*-PisoPMA-B2 (●), and PS-*b*-PisoPMA-B3 (○) and (b) PS-*b*-PneoPMA-B1 (○), PS-*b*-PneoPMA-B2 (●), PS-*b*-PneoPMA-B3 (◇), PS-*b*-PneoPMA-B4 (◆), and PS-*b*-PneoPMA-B5 (□). To avoid the overlap in (a) and (b), the intensities were shifted vertically by a factor of 0.05 and 0.1, respectively.

Interestingly, the PS-*b*-PneoPMA system showed quite different phase behavior from PS-*b*-PisoPMA system, as shown in Figure 2b. At small amounts of PS-*b*-PneoPMA-L in the blend, only UODT was observed. However, 37/63 (w/w) PS-*b*-PneoPMA-L/PS-*b*-PneoPMA-H blend began to show both T_{LDOT} and T_{UODT} above $T_{g,PS}$ (103 °C) and $T_{g,PneoPMA}$ (118 °C), which is characteristic of the closed-loop phase behavior. The size of the closed-loop decreased with increasing the amount of PS-*b*-PneoPMA-L in the blend.

The closed-loop phase behavior of PS-*b*-PneoPMA was also confirmed by SAXS, rheometry, and TEM. Figure 3a shows SAXS profiles at various temperatures for PS-*b*-PneoPMA-B3 (37/63 w/w PS-*b*-PneoPMA-L/PS-*b*-PneoPMA-H blend). At low temperatures (less than 160 °C), a small and broad peak originating from the correlation hole was found, indicating that it was in the disordered state. At 162.5 °C, the peak became sharp and narrow, which corresponds to T_{LDOT}. With further increase in temperature, SAXS intensity decreased again at 217.5 °C, which is the T_{UODT}. The symmetric PS-*b*-PneoPMA-B3 should show lamellar microstructure at temperatures between T_{LDOT} and T_{UODT}, but only a first-order peak was observed without showing higher order peaks. This is because of small scattering length density difference (0.25%) between styrene and neo-PMA. The detailed calculation of the scattering length density of styrene and neo-PMA is given in section 1 of the Supporting Information. A plot of inverse maximum intensity ($1/I_{max}$) of SAXS profiles in Figure 3a versus inverse temperature ($1/T$) is given in Figure 3b, from which T_{LDOT} and T_{UODT} are determined to be 162.5 and 217.5 °C, respectively. Figure 3c indicates temporal changes of storage modulus G' of PS-*b*-PneoPMA-B3. With increasing temperature, G' was decreased, and then it started to increase at T_{LDOT}. Finally, G' dropped precipitously again at T_{UODT}. The transition temperatures, T_{LDOT} and T_{UODT}, measured by rheological method were in good agreement with the values determined by SAXS. To elucidate three distinct states, we also conducted isothermal frequency sweeps for PS-*b*-PneoPMA-B3 at three representative temperatures: 150 °C (<T_{LDOT}), 200 °C, and 230 °C (>T_{UODT}). The plot of log G' vs log G'' is given in Figure 3d. The slope of this plot at both 150 and 230 °C is close to 2, while the slope at 200 °C is less than 2. Since a block copolymer with the disordered state shows the slope of 2,[14,22] we conclude that PS-*b*-PneoPMA-B3 has the disordered state at 150 and 230 °C, while it has an ordered state at 200 °C. The same conclusion is also obtained from the plots of log G' vs log ω as well as log G'' vs log ω for PS-*b*-PneoPMA-B3 (see Figure S2 in the Supporting Information). TEM images obtained at three representative temperatures also support the closed-loop phase behavior. Since PS block was selectively stained by RuO_4, it looked dark. TEM images at a temperature lower than T_{LDOT} (Figure 3e) and another temperature higher than T_{UODT} (Figure 3g) represent the concentration fluctuation of the disordered state. On the other hand, lamellar microdomains were clearly observed at 200 °C (Figure 3f). The formation of the lamellar microdomains is quite expected because of the

dx.doi.org/10.1021/ma3003449 | *Macromolecules* 2012, 45, 3639−3643

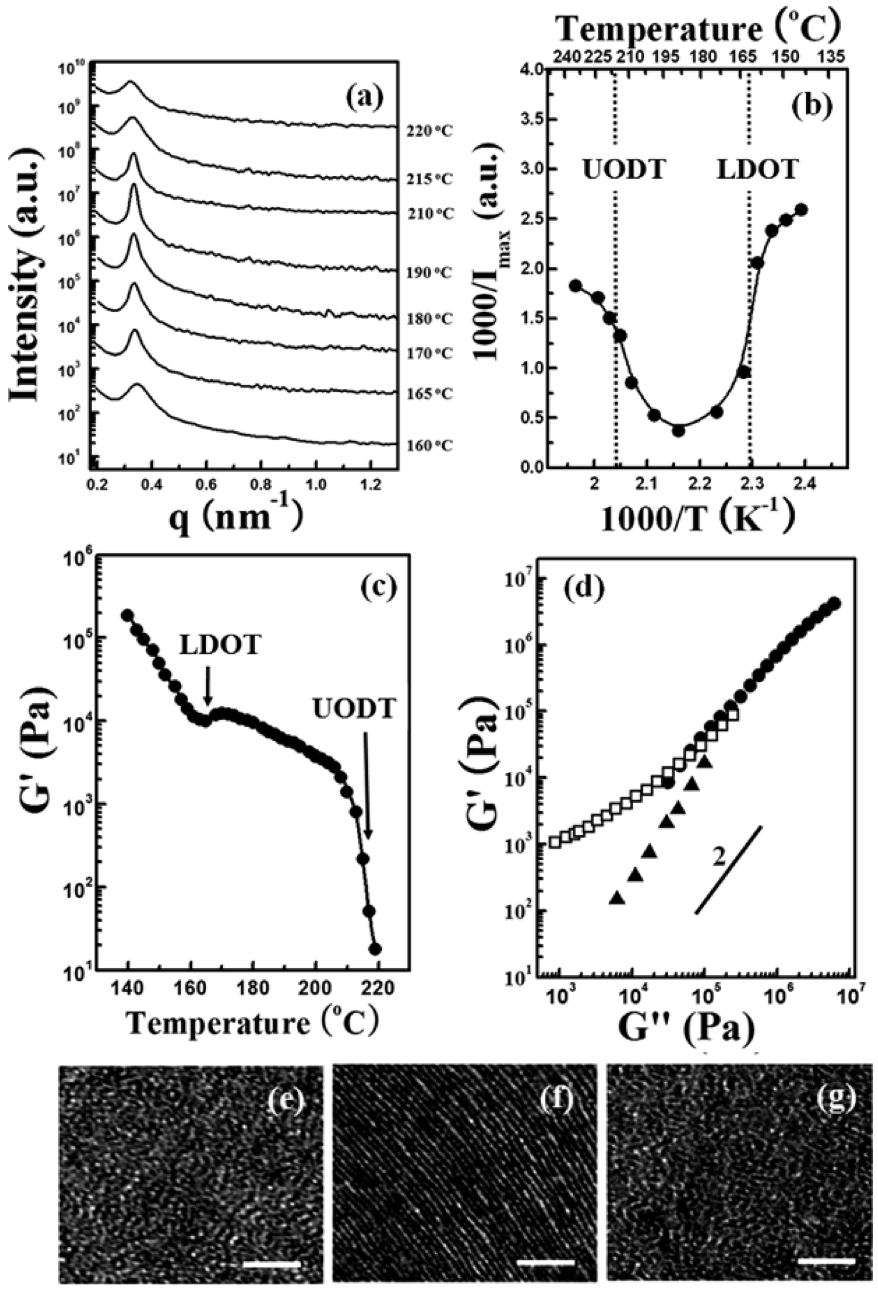


Figure 3. (a) SAXS profiles at various temperatures where the SAXS profiles were vertically shifted to avoid the overlap each other by a factor of 10. (b) Plot of $1/I_{max}$ versus $1/T$. (c) Variation of G' at ω = 0.1 rad/s during heating at a rate of 0.5 °C/min. (d) G' vs G'' plots at three representative temperatures: 150 (●), 200 (□) and 230 °C (▲). Corresponding TEM images (scale bar is 100 nm) at (e) 150, (f) 200, and (g) 230 °C for PS-*b*-PneoPMA-B3.

symmetric composition (the weight fraction of PS block of 0.52).

The molecular weight dependence of transition temperatures for PS-*b*-PisoPMA and PS-*b*-PneoPMA is plotted in Figure 4. While the T_{ODT} for PS-*b*-PisoPMA was simply decreased as total molecular weight decreased (Figure 4a), the closed-loop size having both of T_{LDOT} and T_{UODT} was shrunk dramatically, even at very small total molecular weight difference (~1000) for PS-*b*-PneoPMA. Interestingly, the total molecular weight for PS-*b*-PneoPMA to show the close-loop phase behavior was ~30 000, which is quite smaller than that (~50 000) for PS-*b*-PnPMA,[12] PS-*b*-Pn(B-*r*-H)MA,[16] and PS-*b*-Pn(O-*r*-M)MA.[17] Although the exact reason is not clear, it might be attributed to the different molecular geometries of pentyl methacrylate block: a spherical shape of neopentyl chains versus a linear shape of *n*-pentyl chains. The effective χ between PS and PnPMA is given by two terms: (1) free volume effect which reduces the miscibility and (2) the directional interaction which enhances the miscibility.[16,17] The free volume for PneoPMA is larger than that for PnPMA because of the bulkier neopentyl chains compared with linear shape of *n*-pentyl chains. Thus, the difference of the free volume between PS and PneoPMA is larger than that between PS and PnPMA. Also, the directional interaction of PS and PneoPMA is smaller than that of PS and PnPMA. This is because the bulkier group is not effective to give the directional interaction. Combining these two effects, we conclude that χ between PS and PneoPMA is larger than that between PS and PnPMA. This speculation is consistent

dx.doi.org/10.1021/ma3003449 | *Macromolecules* 2012, 45, 3639−3643

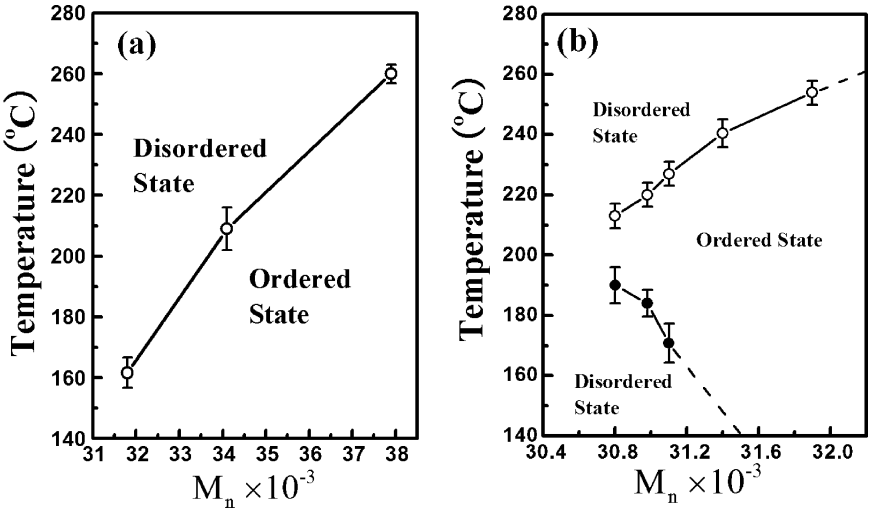


Figure 4. Dependence of the transition temperatures on the total molecular weight for (a) PS-*b*-PisoPMA and (b) PS-*b*-PneoPMA.

with the result given in Figure 4b. Namely, since the phase behavior is determined by χN (here, N is the total number of the segments, which is proportional to the total molecular weight), the molecular weight of PS-PneoMA exhibiting the disordered state was smaller than that of PS-*b*-PnPMA.

In summary, we synthesized PS-*b*-PisoPMA and PS-*b*-PneoPMA copolymers via sequential anionic polymerization to investigate the isomeric effect on the phase behavior of PS-*b*-PPMA. After careful adjustment of total molecular weight, PS-*b*-PneoPMA showed the closed-loop type phase transition having both of LDOT and UODT, but the molecular weight range for the existence of the closed-loop was lower than PS-*b*-PnPMA. On the other hand, PS-*b*-PisoPMA exhibited only ODT.

■ ASSOCIATED CONTENT

Ⓢ Supporting Information

Calculation for the scattering length density of styrene and neopentyl methacrylate, DSC thermograms for PS-*b*-PisoPMA-H and PS-*b*-PneoPMA-H, and frequency sweep of G' and G'' for PS-*b*-PneoPMA-B3 at three representative temperatures. This material is available free of charge via the Internet at http://pubs.acs.org.

■ AUTHOR INFORMATION

Corresponding Author

*E-mail: jkkim@postech.ac.kr.

Notes

The authors declare no competing financial interest.

■ ACKNOWLEDGMENTS

This work was supported by the National Creative Research Initiative Program supported by the National Research Foundation of Korea (NRF). SAXS experiment was supported by PAL through the abroad beamtime program of Synchrotron Radiation Facility Project under MEST and has been performed under the approval of the Photon Factory Program Advisory Committee (Proposal No. 2011G257).

■ REFERENCES

(1) Leibler, L. *Macromolecules* **1980**, *13*, 1602−1617.
(2) Bates, F. S.; Fredrickson, G. H. *Annu. Rev. Phys. Chem.* **1990**, *41*, 525−557.
(3) Kim, J. K.; Lee, J. I.; Lee, D. H. *Macromol. Res.* **2008**, *16*, 267−292.
(4) Kim, J. K.; Yang, S. Y.; Lee, Y.; Kim, Y. *Prog. Polym. Sci.* **2010**, *35*, 1325−1349.
(5) Ryu, D. Y.; Shin, C.; Cho, J.; Lee, D. H.; Kim, J. K.; Lavery, K. A.; Russell, T. P. *Macromolecules* **2007**, *40*, 7644−7655.
(6) Ruzette, A.-V. G.; Banerjee, P.; Mayes, A. M.; Pollard, M.; Russell, T. P.; Jerome, R.; Slawecki, T.; Hjelm, R.; Thiyagarajan, P. *Macromolecules* **1998**, *31*, 8509−8516.
(7) Zhao, Y.; Sivaniah, E.; Hashimoto, T. *Macromolecules* **2008**, *41*, 9948−9951.
(8) Russell, T. P.; Karis, T. E.; Gallot, Y.; Mayes, A. M. *Nature* **1994**, *368*, 729−731.
(9) Karis, T. E.; Russell, T. P.; Gallot, Y.; Mayes, A. M. *Macromolecules* **1995**, *28*, 1129−1134.
(10) Chen, W.; Wei, X.; Balaz, A. C.; Matyjaszewski, K.; Russell, T. P. *Macromolecules* **2011**, *44*, 1125−1131.
(11) Weidisch, R.; Stamm, M.; Schubert, D. W.; Arnold, M.; Budde, H.; Höring, S. *Macromolecules* **1999**, *32*, 3405−3411.
(12) Ryu, D. Y.; Jeong, U.; Kim, J. K.; Russell, T. P. *Nat. Mater.* **2002**, *1*, 114−117.
(13) Ryu, D. Y.; Jeong, U.; Lee, D. H.; Kim, J.; Youn, H. S.; Kim, J. K. *Macromolecules* **2003**, *36*, 2894−2902.
(14) Ryu, D. Y.; Lee, D. H.; Jeong, U.; Yun, S. H.; Park, S.; Kwon, K.; Sohn, B. H.; Chang, T.; Kim, J. K.; Russell, T. P. *Macromolecules* **2004**, *37*, 3717−3724.
(15) (a) Ryu, D. Y.; Lee, D. J.; Kim, J. K.; Lavery, K. A.; Russell, T. P.; Han, Y. S.; Seong, B. S.; Lee, C. H.; Thiyagarajan, P. *Phys. Rev. Lett.* **2003**, *90*, 235501−1−4. (b) Jo, A.; Joo, W.; Jin, W.-H.; Nam, H.; Kim, J. K. *Nat. Nanotechnol.* **2009**, *4*, 727−731.
(16) Moon, H. C.; Han, S. H.; Kim, J. K.; Li, G. H.; Cho., J. *Macromolecules* **2008**, *41*, 6793−6799.
(17) Moon, H. C.; Han, S. H.; Kim, J. K.; Cho., J. *Macromolecules* **2009**, *42*, 5406−5410.
(18) Han, C. D.; Choi, S.; Lee, K. M.; Hahn, S. F. *Macromolecules* **2004**, *37*, 7290−7300.
(19) Han, C. D.; Lee, K. M.; Choi, S.; Hahn, S. F. *Macromolecules* **2002**, *35*, 8045−8055.
(20) Zha, W.; Han, C. D.; Lee, D. H.; Han, S. H.; Kim, J. K.; Kang, J. H.; Park, C. *Macromolecules* **2007**, *40*, 2109−2119.
(21) Chuai, C.; Almdal, K.; Lyngaae-Jørgensen, J. *J. Appl. Polym. Sci.* **2004**, *91*, 609−620.
(22) Han, C. D.; Baek, D. M.; Kim, J. K. *Macromolecules* **1990**, *23*, 561−570.

Macromolecules

Note

pubs.acs.org/Macromolecules

Removal of Solubilizing Side Chains at Low Temperature: A New Route to Native Poly(thiophene)

Eva Bundgaard,*[,†] Ole Hagemann,[†] Morten Bjerring,[‡] Niels Chr. Nielsen,[‡] Jens W. Andreasen,[†] Birgitta Andreasen,[†] and Frederik C. Krebs[†]

[†]Department of Energy Conversion and Storage, Technical University of Denmark, Frederiksborgvej 399, DK-4000 Roskilde, Denmark

[‡]Centre for Insoluble Protein Structures (inSPIN), Interdisciplinary Nanoscience Centre (iNANO) and Department of Chemistry, Langelandsgade 140, Aarhus University, DK-8000 Aarhus C, Denmark

Supporting Information

The possibility for solution processing of conjugated polymers is undoubtedly the major reason for their tremendous success within many areas of application. Conjugated polymers are actively being employed within all areas of organic electronics and are almost exclusively applied as thin films through deposition from a dilute solution followed by drying. The most popular technique has until now been spincoating, which as a batch process enables the simple and fast formation of even films over many square centimeters.[1] Alternative film-forming techniques are gradually entering the scene, enabling even larger areas to be formed, also using continuous roll-to-roll processes.[1] The conjugated polymers have a rigid backbone that does not automatically grant solubility in a solvent; therefore, the successful approach has so far been to employ solubilizing side chains attached to the rigid conjugated polymer backbone. Aliphatic or ether side chains have been in almost exclusive use, whereas there are a number of reports where ionic or polar side chains have been employed. The choice of side chain has been ruled by the desired solvent for film forming. In historic terms, the early conjugated polymers were intractable materials arrived at through electrochemical or chemical polymerization of unsubstituted monomers. Those materials were difficult to process when polymerized, and the most successful approach at the time was electropolymerization and subsequent study of the material on the electrodes.[2] A breakthrough was the precursor routes to conjugated polymers such as poly(acetylene) through the Durham route[3] and poly(phenylenevinylene) through the Gilsch[4] or the sulphinyl route.[5] Later, the dithiocarbamate route followed.[6] The precursor route allows for solution processing the materials where the final conjugated polymer is achieved post-processing. Both soluble and insoluble polymer materials can be processed through a precursor route, and in the mid-1990s synthetic routes to conjugated polymers with good solubility through side chains attached to the backbone were reported, and for the past two decades these have dominated the field.[7] Once the film is formed, however, there is often little need for the side chains that in most instances behave passively with respect to film function (e.g., visible absorption, carrier transport), and they may even adversely affect the properties of the film by incurring poor morphological stability,[8] poor photochemical stability, and so on.[9] From this point of view, there has recently been a drive to develop solution proccessable routes to conjugated polymer films that are then made insoluble post-formation vis-à-vis the original precursor routes, except that the conjugated backbone is in place already during solution processing of the film. There have been two overall approaches to this, the first one being the use of functionalized side chains allowing for cross-linking post-film formation. Side chains carrying a bromine atom, a vinyl group, an azide group, or an oxetane group can be cross-linked in the solid state through irradiation with light or through the use of a catalyst for ring-opening polymerization.[10] The second approach is perhaps the most difficult but also the most elegant from a fundamental point of view and presents a method whereby the side chains are there during film formation and then subsequently removed post-film formation, yielding a conjugated polymer film without side chains, which presents the largest optical density achievable for a given thickness. There have, however, been few routes to this, and they all require a very high temperature heating step. An example is the tertiary esters[11] that required ∼300 °C. This is too high for use beyond the laboratory setting and brings with it problems of thermally induced defects and undesirable side reactions. Studies aimed at lowering the temperature for side-chain removal have achieved a lowering to around 150−200 °C through systematic studies of side-chain chemistry and use of acid catalysis.[12]

The ultimate aim is a room-temperature process where the side-chain removal is achieved by chemical means and not through a high-temperature step. The control of a chemical reaction using temperature implies that the reaction is spontaneous at some temperature, and to ensure stability of the material in its processable form, the treatment temperature must be significantly elevated with respect to the storage temperature (ambient temperature). This led us to explore new means, and we prepared silane-substituted poly(thiophene), as shown in Scheme 1.

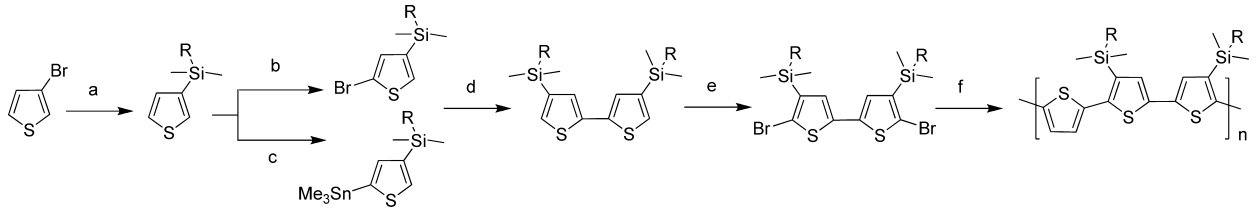
The polydimethyloctylsilylterthiophene (PDMOST) was found to solution process very well and was also found to enable the removal through treatment with acids. We employed many agents for the removal of the silane including trifluoromethanesulfonic acid (TfOH), tetrabutylammonium-

Received: January 11, 2012
Revised: March 16, 2012
Published: April 2, 2012

ACS Publications © 2012 American Chemical Society

dx.doi.org/10.1021/ma300075x | Macromolecules 2012, 45, 3644−3646

Scheme 1. Synthesis of PDMOST[a]



[a]R = octyl. (a) (1) *n*BuLi, Et_2O, −78 °C, (2) Cl-$SiMe_2$Oc. (b) (1) *n*BuLi, THF, −78 °C, (2) CBr_4. (c) (1) *n*BuLi, THF, −78 °C, (2) Me_3SnCl. (d) (1) Pd_2dba_3, tri-*o*-tolylphosphine, toluene, 110 °C. (e) (1) NBS, K_2CO_3, THF. (f) (1) 2,5-di-(trimethyltin)-thiophene, Pd_2dba_3, tri-*o*-tolylphosphine, toluene, 110 °C.

fluoride (TBAF), and the acids: HBr, HCl, trichloroacitic acid (TCA), and dichloroacitic acid (DCA). TfOH, which was used in a similar procedure,[12c] did not show the successful control, and the cleaved polymer started to precipitate before all side chains had been cleaved, and the result was a film that was not smooth (see Supporting Information.) However, TCA was found to be most efficient in organic solvents and could be mixed into the coating solution or applied post-film formation. Subsequent drying of the film led to a pure insoluble poly(thiophene), PT film. In previous studies, it was demonstrated how P3MHOCT could be converted into PT at 300 °C.[11]

Solid-state NMR spectroscopy here proved to be extremely useful, and the choice of PT was particularly instructive because the soluble polymer is random in nature and the ^{13}C CP/MAS NMR spectrum presents a complex set of signals including both signals from aliphatic groups as well as the thiophene moieties. On the contrary, native PT only presents two distinct carbon atoms from the thiophene unit. Upon successful formation of native PT, the solid-state ^{13}C CP/MAS NMR spectrum thus becomes very simple and presents only two distinct peaks. In Figure 1, we demonstrate how native PT can be formed by solution processing PDMOST, followed by acid treatment at room temperature. Figure 1 also demonstrates the color and solubility difference between PDMOST before and after acid treatment, that is, a yellow film that is soluble in chloroform for the noncleaved polymer and a red insoluble film for the cleaved polymer. The solid-state ^{13}C CP/MAS NMR spectrum provides unequivocal proof of the efficiency of this low-temperature method. The ^{13}C CP/MAS NMR spectrum was found to match the material arrived at through the high-temperature route, as shown in Figure 1.

The treatment at room temperature may result in voids in the polymer film due to the removal of the side chains, which in the case of PDMOST accounts for 57% of the molecular weight and therefore a very significant part of the volume in the film. In the case of PT arrived at through the thermal route, very dense films are obtained and the question of whether a low-temperature method such as the one we present here would yield a dense or a porous film was thus investigated. Through the use of X-ray reflectivity that probes a very large area of the sample (square centimeteres), we found that the film collapses upon the removal of the side chains, thus yielding a compact PT film at room temperature identical to the PT film arrived at through the high-temperature method.

In Figure 2, X-ray reflectivity data as a function of scattering vector $Q_z = 4\pi \sin\theta/\lambda$ (θ is the scattering angle, λ is the X-ray wavelength), show the changes in film thickness and density when the polymer is cleaved and washed. The critical angle is directly related to the electron density and thus, knowing the

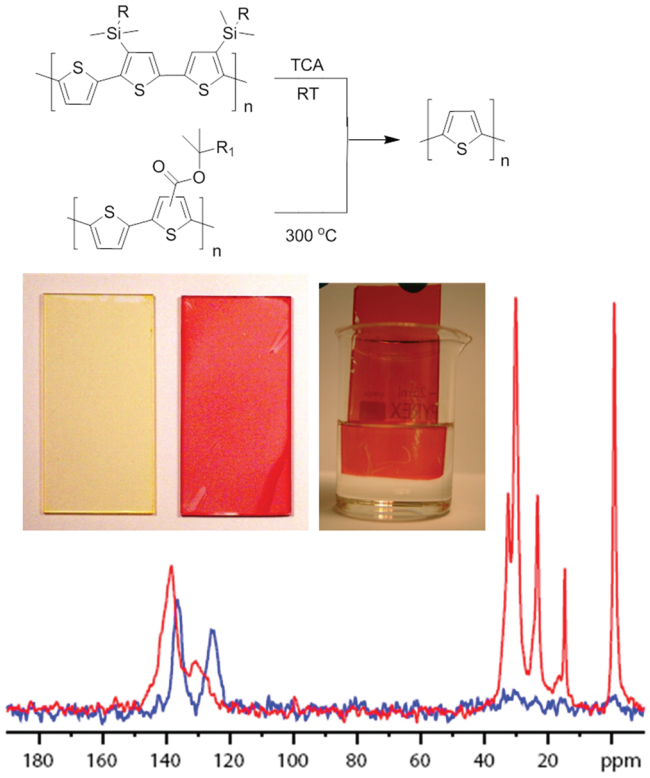


Figure 1. Removal of side chains. Top: two different routes to native polythiophene; the route reported here at room temperature and a previous reported route using high temperature.[11] Middle: Demonstration of color change upon the removal of the side chains (yellow to red) and the demonstration of insolubility of the cleaved polymer film when immersed in chloroform. Bottom: ^{13}C CP/MAS solid-state NMR spectra demonstrating the removal of the aliphatic side chains, that is, PDMOST before (red) and after (blue) acid treatment.

chemical composition, the mass density. The data show a clear increase in density of the film when washed, from 1.0 g/cm^3 for PDMOST to 1.2 g/cm^3 for the native PT film, and a reduction in film thickness from 127 to 49 nm. The removal of side chains corresponds to a mass loss of 57%, and with the concomitant reduction in thickness, this should result in a film density of 1.1 g/cm^3 for an initial density of 1.0 g/cm^3. The higher final density indicates a further densification by washing. In summary, we have demonstrated the facile removal of solubilizing side chains at room temperature using acid catalysis. This allows for traditional solution processing of the functional material into thin films, followed by insolubilization enabling subsequent solution processing. This is likely to have implications within the field of large area coating and printing of multilayer organic film on heat-sensitive substrates.

dx.doi.org/10.1021/ma300075x | *Macromolecules* 2012, 45, 3644−3646

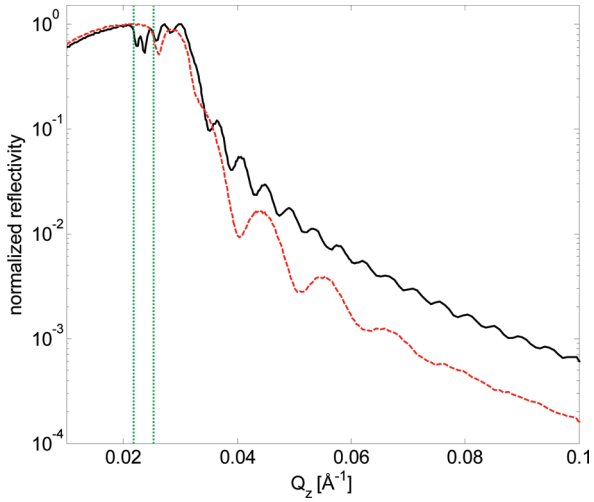


Figure 2. X-ray reflectivity of spin-coated film of acid-treated PDMOST. Black line: the reflectivity of a spin coated film of cleaved polymer; red dashed line: the reflectivity of the same film after washing with chloroform. Green dotted vertical lines: the position of the scattering vectors corresponding to the critical angle for total reflection for the film.

■ ASSOCIATED CONTENT

Supporting Information

Experimental synthetic details, UV−vis, TGA, DCS curves, and AFM images. This material is available free of charge via the Internet at http://pubs.acs.org.

■ AUTHOR INFORMATION

Corresponding Author

*E-mail: evbu@dtu.dk.

Notes

The authors declare no competing financial interest.

■ ACKNOWLEDGMENTS

This work was supported by the Danish National Research Foundation (*Danish-Chinese Centre for Organic-Based Photovoltaic Cells with Morphology Control*) and *Centre for Insoluble Protein Structures (inSPIN)*). We gratefully acknowledge Martin Meedom Nielsen who wrote the code for analyzing the X-ray reflectometry data.

■ REFERENCES

(1) (a) Gevorgyan, S. A.; Krebs, F. C. *Mol. Org. Electron. Devices* **2010**, 291−309. (b) Huebler, A. C.; Kempa, H. *Organic Photovoltaics: Materials, Device Physics and Manufacturing Technologies*; Brabec, C., Dyakonov, V., Scherf, U., Eds.; Wiley-VCH: Weinheim, Germany, 2008. (c) Krebs, F. C. *Sol. Energy Mater. Sol. Cells* **2009**, *93*, 394−412.

(2) (a) Yamamoto, T.; Kokubo, H. *Electrochim. Acta* **2005**, *50*, 1453−1460. (b) Li, Y. *Curr. Trends Polym. Sci.* **2002**, *7*, 101−111.

(3) (a) Feast, W. J.; Winter, J. N. *J. Chem. Soc., Chem. Commun.* **1985**, 202−203. (b) Bott, D. C.; Brown, C. S.; Chai, C. K.; Walker, N. S.; Feast, W. J.; Foot, P. J. S.; Calvert, P. D.; Billingham, N. C.; Friend, R. H. *Synth. Met.* **1986**, *14*, 245−269. (c) Furlani, A.; Napoletano, C.; Russo, M. V.; Feast, W. J. *Polym. Bull.* **1986**, 16.

(4) (a) Gilch, H. G.; Wheelwri, W. L. *J. Polym. Sci., Part A-1* **1966**, *4*, 1337−1347. (b) Spreitzer, H.; Becker, H.; Kluge, E.; Kreuder, W.; Schenk, H.; Demandt, R.; Schoo, H. *Adv. Mater.* **1998**, *10*, 1340−1343.

(5) (a) Louwet, F.; Vanderzande, D.; Gelan, J.; Mullens, J. *Macromolecules* **1995**, *28*, 1330−1331. (b) Louwet, F.; Vanderzande, D.; Gelan, J. *Synth. Met.* **1995**, *69*, 509−510. (c) Louwet, F.; Vanderzande, D.; Gelan, J. *Synth. Met.* **1992**, *52*, 125−130.

(6) Henckens, A.; Dyussens, I.; Lutsen, L.; Vanderzande, D.; Cleij, T. J. *Polymer* **2006**, *47*, 123−131.

(7) Garay, R. O.; Mayer, B.; Karaz, F. E.; Lenz, R. W. *J. Polym. Sci., Part A: Poly. Chem.* **1995**, *33*, 525−531.

(8) (a) Gadisa, A.; Oosterbaan, W. D.; Vandewal, K.; Bolsée, J.-C.; Bertho, S.; D'Haen, J.; Lutsen, L.; Vanderzande, D. J. M.; Manca, J. V. *Adv. Funct. Mater.* **2009**, *19*, 3300−3306. (b) Bertho, S.; Janssen, G.; Cleij, T. J.; Conings, B.; Moons, W.; Gadisa, A.; D'Haen, J.; Goovaerts, E.; Lutsen, L.; Manca, J.; Vanderzande, D. J. M. *Sol. Energy Mater. Sol. Cells* **2008**, *92*, 753−760.

(9) (a) Manceau, M.; Bundgaard, E.; Carlé, J. E.; Hagemann, O.; Helgesen, M.; Søndergaard, R.; Jørgensen, M.; Krebs, F. C. *J. Mater. Chem.* **2011**, *21*, 4132−4141. (b) Rivaton, A.; Chambon, S.; Manceau, M.; Gardette, J.-L.; Lemaître, N.; Guillerez, S. *Polym. Degrad. Stab.* **2010**, *95*, 278−284.

(10) (a) Kim, B. J.; Miyamoto, Y.; Ma, B.; Fréchet, J. M. J *Adv. Funct. Mater.* **2009**, *19*, 2273−2281. (b) Bang, J.; Bae, J.; Löwenheilm, P.; Spiessberger, C.; Given-Beck, S. A.; Russel, T. P.; Hawker, C. J. *Adv. Mater.* **2007**, *19*, 4552−4557. (c) Liu, Y.-L.; Hsiue, G.-H.; Chiu, Y.-S.; Jeng, R.-J. *J. Polym. Sci., Part A: Polym. Chem.* **1994**, *32*, 3201−3204. (d) Wei, X.; Li, L.; Kalish, J. P.; Chen, W.; Russel, T. P. *Macromolecules* **2011**, *44*, 4269−4275. (e) Kim, H. J.; Han, A.-R.; Cho, C.-H.; Kang, H.; Cho, H.-H.; Lee, M. Y.; Fréchet, J. M. J.; Oh, J. H.; Kim, B. J. *Chem. Mater.* **2012**, *24*, 215−221. (f) Kang, D. J.; Kwon, T.; Kim, M. P.; Cho, C.-H.; Jung, H.; Bang, J.; Kim, B. J. *ACS Nano* **2011**, *5*, 9017−9027.

(11) (a) Krebs, F. C.; Spanggaard, H. *Chem. Mater.* **2005**, *17*, 5235−5237. (b) Liu, J. S.; Kadnikova, E. N.; Liu, Y. X.; McGehee, M. D.; Fréchet, J. M. J. *J. Am. Chem. Soc.* **2004**, *126*, 9486−9487.

(12) (a) Diliën, H.; Vandenbergh, J.; Banishoeb, F.; Adriaensens, P.; Cleij, T. J.; Lutsen, L.; Vanderzande, D. J. M. *Macromolecules* **2011**, *44*, 711−718. (b) Søndergaard, R.; Norrman, K.; Krebs, F. C. *J. Polym. Sci., Part A: Polym. Chem.* **2011**, *50*, 1127−1132. (c) Jakob, S.; Moreno, A.; Zhang, X.; Bertschi, L.; Smith, P.; Schlüter, A. D.; Sakamoto, J. *Macromolecules* **2010**, *43*, 7916−7918.